

The BABAR Physics Book: Physics at an Asymmetric B Factory

This book presents the results of a year-long workshop devoted to a review of the physics opportunities of the BABAR experiment at the PEP-II *B* Factory, at the Stanford Linear Accelerator Center Laboratory.

* Work supported in part by US Department of Energy contract DE-AC02-76SF00515.

SLAC National Accelerator Laboratory, Menlo Park, CA 94025

This page was intentionally left blank.

The BABAR Collaboration

LAPP Annecy, Annecy-le-Vieux, France

D. Boutigny, I. De Bonis, Y. Karyotakis, R. Lafaye, V. Tisserand

INFN Sezione di Bari, Bari, Italy

C. Evangelista, A. Palano

Beijing Glass Research Institute, Beijing, China

G. Chen, S. Ren, O. Wen, H. Yu, F. Zhang, Y. Zheng

Institute of High Energy Physics, Beijing, China

G. Chen, Y. Guo, H. Lan, H. Mao, N. Qi, P. P. Xie, W. G. Yan, C. Zhang, W. Zhao, Y. Zhu

University of Bergen, Bergen, Norway

A. Borgland, G. Eigen, B. Stugu

Ruhr-Universität Bochum, Bochum, Germany

H. Koch, M. Kunze, B. Lewandowski, K. Peters, H. Schmücker, M. Steinke

University of Bristol, Bristol, UK

J. C. Andress, N. Dyce, B. Foster, A. Mass, J. McFall

University of British Columbia, Vancouver, British Columbia, Canada

C. Hearty, M. H. Kelsey, J. McKenna

Brunel University, London, UK

B. Camanzi, T. J. Champion, A. K. McKemey, J. Tinslay

Budker Institute of Nuclear Physics, Novosibirsk, Russia

V. E. Blinov, A. D. Bukin, A. R. Buzykaev, S. F. Ganzhur, V. N. Ivanchenko, A. A. Korol,
E. A. Kravchenko, A. P. Onuchin, S. I. Serednyakov, Yu. I. Skovpen, V. I. Telnov

California Institute of Technology, Pasadena, California, USA

E. Chen, G. P. Dubois-Felsmann, D. G. Hitlin, Y. G. Kolomensky, S. Metzler, B. B. Naranjo,
F. C. Porter, A. Ryd, A. Samuel, M. Weaver, S. Yang, R. Zhu

University of California, Irvine, Irvine, California, USA

A. Lankford, M. Mandelkern, D.P. Stoker, G. Zioulas

University of California, Los Angeles, Los Angeles, California, USA

C. Buchanan, S. Chun

University of California, San Diego, La Jolla, California, USA

J. G. Branson, R. Faccini, C. Hast, D. B. MacFarlane, E. Potter, S. Rahatlou, G. Raven,
V. Sharma, F. Wilson

University of California, Santa Barbara, Santa Barbara, California, USA

D.A. Bauer, C. Campagnari, A. Eppich, P. Hart, N. Kuznetsova, O. Long, A. Lu, J.D. Richman,
M. Witherell, S. Yellin

University of California, Santa Cruz, Santa Cruz, California, USA

J. Beringer, D. E. Dorfan, A. M. Eisner, A. Frey, A. A. Grillo, C. A. Heusch, R. P. Johnson,
W. S. Lockman, M. Munson, T. Pulliam, H. Sadrozinski, T. Schalk, B. A. Schumm, A. Seiden,
M. Turri

University of Cincinnati, Cincinnati, Ohio, USA

S. Devmal, T. Geld, B. T. Meadows, D. Renner, M. D. Sokoloff

Colorado State University, Fort Collins, Colorado, USA

J. L. Harton, R. Malchow, A. Soffer, W. H. Toki, R. J. Wilson, W. Yang

University of Colorado, Boulder, Colorado, USA

S. Fahey, W. T. Ford, F. Gaede, K. M. Hall, T. L. Hall, D. R. Johnson, H. Krieg, U. Nauenberg,
P. Rankin, J. Roy, S. Sen, J. G. Smith, D. L. Wagner, M. Zhao

Technische Universität Dresden, Dresden, Germany

T. Brandt, J. Brose, M. L. Kocian, R. Müller-Pfefferkorn, K. R. Schubert, R. Schwierz, B. Spaan,
R. Waldi

University of Edinburgh, Edinburgh, UK

R. Bernet, P. Clark, S. Gowdy, S. Playfer

INFN Sezione di Ferrara, Ferrara, Italy

S. Dittongo, M. Folegani, L. Piemontese

INFN Laboratori Nazionali di Frascati, Frascati, Italy

F. Anulli, A. Asmone, R. Baldini-Ferrolì, A. Calcaterra, D. Falciari, G. Finocchiaro, I. M. Peruzzi,
M. Piccolo, R. de Sangro, Z. Yu, A. Zallo

INFN Sezione di Genova, Genova, Italy

A. Buzzo, R. Contri, G. Crosetti, M. Lo Vetere, M. Macri, M. R. Monge, M. Pallavicini,
R. Parodi, C. Patrignani, M. G. Pia, E. Robutti, A. Santroni

Imperial College, London, UK

P. D. Dauncey, R. Martin, J.A. Nash, P. Sanders, D. Smith, P. Strother

Iowa State University, Ames, Iowa, USA

H. B. Crawley, A. Firestone, J. Lamsa, W. T. Meyer, E. I. Rosenberg

University of Iowa, Iowa City, Iowa, USA
R. Bartoldus, T. Dignan, R. Hamilton, U. Mallik

Lawrence Berkeley National Laboratory, Berkeley, California, USA
B. Abbott, G. S. Abrams, A. Breon, D. N. Brown, R. N. Cahn, A. R. Clark, C. T. Day, Q. Fan,
R. G. Jacobsen, R. W. Kadel, J. Kadyk, R. Kapur, A. Karcher, R. Kerth, S. Kluth, J. F. Kral,
C. LeClerc, M. Levi, D. Li, T. Liu, G. Lynch, M. Marino, A. Meyer, A. Mokhtarani, P. J. Oddone,
J. Ohnemus, S. J. Patton, M. Pripstein, D. R. Quarrie, N. A. Roe, A. Romosan, M. Ronan,
V. G. Shelkov, A. V. Telnov, W. A. Wenzel

Lawrence Livermore National Laboratory, Livermore, California, USA
P. D. Barnes, R. M. Bionta, D. Fujino, M. N. Kreisler, M. Mugge, X. Shi, K. A. Van Bibber,
D. Wright, C. R. Wuest

University of Liverpool, Liverpool, UK
M. Carroll, G. Dahlinger, J. R. Fry, E. Gabathuler, R. Gamet, M. George, S. McMahon,
C. Touramanis

University of Louisville, Louisville, Kentucky
D. Brown, C. Davis, J. Pavlovich, A. Trunov

University of Manchester, Manchester, UK
J. Allison, R. Barlow, A. Khan, G. Lafferty, A. McNab, N. Savvas, A. Walkden, J. Weatherall

University of Maryland, College Park, Maryland, USA
C. Dallapiccola, D. Fong, A. Jawahery, D. A. Roberts, A. Skuja

Massachusetts Institute of Technology, Cambridge, Massachusetts, USA
R. F. Cowan, R. K. Yamamoto

University of Massachusetts, Amherst, Amherst, Massachusetts, USA
K. Baird, G. Blaylock, J. Button-Shafer, K. Flood, S. S. Hertzbach, R. Kofler, C. S. Lin, J. Wittlin

McGill University, Montréal, Quebec, Canada
P. Bloom, M. Milek, P. M. Patel, J. Trischuk

INFN Sezione di Milano, Milano, Italy
A. Forti, F. Lanni, F. Palombo, V. Pozdnyakov

University of Mississippi, University, Mississippi, USA
J. M. Bauer, L. Cremaldi, V. Eschenburg, R. Kroeger, J. Reidy, D. Sanders, J. Secret,
D. Summers

Université of Montréal, Montréal, Quebec, Canada
A. Hasan, J. Martin, R. Seitz, P. Taras, A. Woch, V. Zacek

Mount Holyoke College, South Hadley, Massachusetts, USA

H. Nicholson, C. S. Sutton

INFN Sezione di Napoli, Napoli, ItalyG. P. Carlino, N. Cavallo, G. De Nardo, F. Fabozzi, C. Gatto, L. Lista, P. Paolucci, D. Piccolo,
C. Sciacca**Northern Kentucky University, Highland Heights, Kentucky, USA**

M. Falbo-Kenkel

University of Notre Dame, Notre Dame, Indiana

J. Bishop, N. M. Cason, A. Garcia, J. M. LoSecco, W. D. Shephard

Oak Ridge National Laboratory, Oak Ridge, Tennessee, USA

R. Alsmiller, T. A. Gabriel

LAL Orsay, Orsay, FranceM. Benkebil, G. Grosdidier, A. Hoecker, V. Lepeltier, A. Lutz, S. Plaszczynski, M.-H. Schune,
A. Valassi, G. Wormser, F. Zomer**INFN Sezione di Padova, Padova, Italy**

F. Dal Corso, F. Galeazzi, M. Morandin, M. Posocco, R. Stroili, C. Voci

Ecole Polytechnique Palaiseau, LPNHE, Palaiseau, France

L. Behr, G. R. Bonneaud, E. Roussot, C. Thiebaux, G. Vasileiadis, M. Verderi

LPNHE Université de Paris VI et VII, Paris, FranceM. Benayoun, H. Briand, J. Chauveau, P. David, C. de la Vaissière, L. Del Buono, O. Hamon,
F. Le Diberder, Ph. Leruste, J. Lory, L. Martin, J.-L. Narjoux, N. Regnault, L. Roos, S. Versillé**INFN Sezione di Pavia, Pavia, Italy**

A. Leona, A. Leona, E. Mandelli, P. F. Manfredi, A. Perazzo, L. Ratti, V. Re, V. Speciali

University of Pennsylvania, Philadelphia, Pennsylvania, USA

C. Cretsinger, E. Frank, L. Gladney, V. Suraiya

INFN Sezione di Pisa, Pisa, ItalyC. Angelini, G. Batignani, S. Bettarini, M. Bondioli, G. Calderini, M. Carpinelli, F. Costantini,
F. Dutra, F. Forti, M. A. Giorgi, A. Lusiani, S. Mettarini, M. Morganti, F. Morsani, M. Rama,
G. Rizzo, G. Simi, G. Triggiani, R. Vitale**Prairie View A& M University, Prairie View, Texas, USA**

M. Haire, D. Judd, K. Paick, D. Wagoner

Princeton University, Princeton, New Jersey, USAJ. Albert, C. Lu, K. T. McDonald, V. Miftakov, S. F. Schaffner, A. J. S. Smith, A. Tumanov,
E. W. Varnes

Queen Mary & Westfield College, London, UK

J. J. Back, P. F. Harrison, A. J. Martin

University di Roma ‘La Sapienza’ and INFN Sezione di Roma, Rome, Italy

G. Cavoto, F. Ferrarotto, F. Ferroni, E. Lamanna, S. Mazzoni, S. Morganti, G. Piredda, M. Rotondo

Royal Holloway & Bedford New College, London, UK

M. G. Green, I. Scott, E. Tetteh-Lartey

Rutgers University, Rutgers, New Jersey, USA

P. F. Jacques, M. S. Kalelkar, G. Mancinelli, R. J. Plano

Rutherford Appleton Laboratory, Chilton, Didcot, UK

T. Adye, U. Egede, B. Franek, N. I. Geddes, G. P. Gopal

CEA, DAPNIA, CE-Saclay, Gif-sur-Yvette, France

R. Aleksan, G. De Domenico, S. Emery, A. Gaidot, G. Hamel de Monchenault, A. de Lesquen, G.W. London, B. Mayer, A. Salnikov, G. H. Vasseur, C. Yeche, M. Zito

Shanghai Institute of Ceramics (SICCAS), Shanghai, China

D. Yan, Z. Yin

University of South Carolina, Columbia, South Carolina, USA

N. Coptly, M. Purohit

Stanford Linear Accelerator Center, Stanford, California, USA

I. Adam, P. L. Anthony, D. Aston, A. Bajic, E. Bloom, A. M. Boyarski, F. Bulos, J. Cohen-Tanugi, M. R. Convery, D. P. Coupal, D. H. Coward, N. De Groot, J. Dorfan, M. Doser, W. Dunwoodie, T. Glanzman, G. L. Godfrey, J. L. Hewett, T. Himel, W. R. Innes, C. P. Jessop, L. Keller, P. C. Kim, P. F. Kunz, W. G. J. Langeveld, D. W. G. S. Leith, K. Lingel, V. Luth, H. L. Lynch, G. Manzin, H. Marsiske, T.S. Mattison, R. Messner, K. Moffeit, M. Morii, R. Mount, D.R. Muller, C.P. O’Grady, T.J. Pavel, R. Pitthan, B. N. Ratcliff, L. S. Rochester, V. Savinov, R. H. Schindler, J. Schwiening, G. Sciolla, V. V. Serbo, A. Snyder, A. Stahl, D. Su, M. K. Sullivan, M. Talby, H. A. Tanaka, J. Va’vra, S. R. Wagner, A. Weinstein, W. J. Wisniewski, C. C. Young

Stanford University, Stanford, California, USA

P. Burchat, C. H. Cheng, D. Kirkby, T. I. Meyer, E. Nehrlich, C. Roat, R. Zaliznyak

University of Texas, Dallas, Dallas, Texas, USA

J. H. Cooke III, J. M. Izen, X. C. Lou, M. Turcotte

INFN Sezione di Torino, Torino, Italy

F. Bianchi, B. DiGirolamo, D. Gamba, P. Grosso, A. Romero, A. Smol, A. Vitelli, D. Zanin

INFN Sezione di Trieste, Trieste, Italy

L. Bosisio, G. Castelli, G. Della Ricca, L. Lanceri, G. Musolino, P. Poropat, M. Prest, E. Vallazza,
G. Vuagnin

TRIUMF, Vancouver, British Columbia, Canada

R. Henderson

Vanderbilt University, Nashville, Tennessee, USA

R. S. Panvini

University of Victoria, Victoria, British Columbia, Canada

A. DeSilva, R. V. Kowalewski, J. M. Roney

University of Wisconsin, Madison, Madison, Wisconsin, USA

H. Band, E. Charles, S. Dasu, P. Elmer, J. Johnson, J. Nielsen, W. Orejudos, Y. Pan, R. Prepost,
I. Scott, J. Walsh, S. L. Wu, H. Zobernig

Participating Theorists

D. Atwood, *Iowa State University*; P. Ball, *European Laboratory for Particle Physics, CERN*; I. Bigi, *University of Notre Dame*; F. M. Borzumati, *Universität Zürich*; C. G. Boyd, *Carnegie Mellon University*; G. C. Branco, *Instituto Superior Técnico, Lisbon*; V. M. Braun, *Nordisk Institut for Teoretisk Fysik, NORDITA*; F. Buccella, *INFN Sezione di Naples*; G. Buchalla, *European Laboratory for Particle Physics, CERN*; G. Burdman, *University of Wisconsin*; R. N. Cahn, *Lawrence Berkeley National Laboratory*; J. Charles, *Laboratoire de Physique Théorique et Hautes Energies, Orsay*; M. Ciuchini, *INFN Sezione di Rome*; F. E. Close, *Rutherford Appelton Laboratory*; P. Colangelo, *INFN Sezione di Bari*; F. De Fazio, *INFN Sezione di Bari*; A. S. Dighe, *International Centre for Theoretical Physics, Trieste*; I. Dunietz, *Fermi National Accelerator Laboratory*; A. F. Falk, *Johns Hopkins University*; R. Fleischer, *European Laboratory for Particle Physics, CERN*; J. M. Flynn, *University of Southampton*; M. C. Gonzalez-Garcia, *Universidad de València*; B. Grinstein, *University of California, San Diego*; Y. Grossman, *Stanford Linear Accelerator Center*; D. Guetta, *INFN Sezione di Bologna*; J. L. Hewett, *Stanford Linear Accelerator Center*; G. Isidori, *Laboratori Nazionali de Frascati*; A. L. Kagan, *University of Cincinnati*; Y. Y. Keum, *APCPT, Seoul National University*; A. Khodjamirian, *Universität Würzburg*; J. H. Kühn, *Universität Karlsruhe*; A. Le Yaouanc, *Laboratoire de Physique Théorique et Hautes Energies, Orsay*; L. Lellouch, *European Laboratory for Particle Physics, CERN*; Z. Ligeti, *University of California, San Diego*; D. London, *Université de Montréal*; M. Lusignoli, *INFN Sezione di Rome*; T. Mannel, *Universität Karlsruhe*; G. Martinelli, *INFN Sezione di Rome*; A. Masiero, *INFN Sezione di Padova*; B. Mayer, *Centre d'Etudes Nucléaires de Saclay*; G. Michelon, *International Centre for Theoretical Physics, Trieste*; E. Mirkes, *Universität Karlsruhe*; E. Nardi, *Antioquia University*; M. Neubert, *European Laboratory for Particle Physics, CERN*; U. Nierste, *DESY Deutsches Elektronen-Synchrotron*; Y. Nir, *The Weizmann Institute of Science*; L. Oliver, *Laboratoire de Physique Théorique et Hautes Energies, Orsay*; N. Paver, *INFN Sezione di Trieste*; R. D. Peccei, *University of California, Los Angeles*; O. Pene, *Laboratoire de Physique Théorique et Hautes Energies, Orsay*; A. A. Petrov, *Johns Hopkins University*; A. Pich, *Universidad de València*; A. Pugliese, *INFN Sezione di Rome*; H. R. Quinn, *Stanford Linear Accelerator Center*; L. Reina, *University of Wisconsin*; G. Ricciardi, *INFN Sezione di Naples*; T. G. Rizzo, *Stanford Linear Accelerator Center*; R. Rückl, *Universität Würzburg*; C. T. Sachrajda, *University of Southampton*; D. Silverman, *University of California, Irvine*; L. Silvestrini, *Università di Roma*; A. Soni, *Brookhaven National Laboratory*; B. F.L. Ward, *University of Tennessee*; J. D. Wells, *Stanford Linear Accelerator Center*; M. B. Wise, *California Institute of Technology*; M. P. Worah, *Stanford Linear Accelerator Center*; D. Wyler, *Universität Zürich*

Preface

This book presents the results of a year-long workshop devoted to a review of the physics opportunities of the BABAR experiment at the PEP-II *B* Factory, at the Stanford Linear Accelerator Center laboratory. The workshop meeting schedule was as follows:

University of Rome “La Sapienza”	11th–14th November 1996
Princeton University	17th–20th March 1997
LAL Orsay	16th–19th June 1997
California Institute of Technology	22nd–24th September 1997

The workshop brought together a number of theorists with experimentalists from the BABAR Collaboration. Each chapter represents the contribution of a working group and presents both a theoretical summary of the relevant topics and the results of related simulation studies. The working group convenors, listed below, were teams that included both theorists and experimentalists.

The book represents the status of work around the beginning of 1998. Both the state of the theory and of the experiment’s simulation and analysis tools continue to advance. The results presented here are thus not a final view of what the experiment can achieve, but represent an interim study. The studies are more detailed and comprehensive than those made at the time of the Technical Design Report, but still lack many features that will be needed for the real data analysis. The book is intended as a guide to the work that still needs to be done, and as a detailed introduction which will assist new members, joining the Collaboration, and, we hope, other researchers in the field.

Working Groups and Conveners

The BABAR workshops were divided into the following working groups with the conveners named. Chapters 5–12 and 14 of this book directly represent the work done in these groups.

Determinations of β

Y. Karyotakis, L. Oliver, J. Smith, W. Toki

Determinations of α and Direct CP Violation.

M. Giorgi, H. Jawahery, F. LeDiberder, D. London, A. Soni

Methods of Measuring γ

P. Dauncey, R. Fleischer, L. Lanceri

Semileptonic B Decays and the Extraction of V_{ub} , V_{cb} from B decays

T. Mannel, M. Neubert, K. Schubert, M. Witherell

Rare B Decays within the Standard Model

J. Hewett, A. Masiero, S. Playfer, S. Wagner

Hadronic B Meson Decays

I. Bigi, A. Petrov, P. Rankin, R. Waldi, D. Wyler

Non- CP B Physics

J. Chauveau, J. Izen, G. Martinelli, U. Nierste

Charm, τ , QCD and Two-photon Physics

P. Burchat, F. Gilman, R. Peccei, A. Pich, A. Seiden

Overall Determinations of the CKM Matrix

G. Eigen, B. Grinstein, Y. Nir, M. Schune

In addition, Chapter 1 was convened by H. Quinn and Y. Nir; Chapter 2 was convened by A. Falk, and Chapters 3 and 4 were convened by P. F. Harrison and M. Pia. Chapter 13 was convened by J. Hewett, A. Masiero, and Y. Nir.

Acknowledgments

Preliminary organisation of the BABAR workshops was managed by the International Organising Committee:

- Roy Aleksan
- Marcello Giorgi
- Paul Harrison (Program Coordinator)
- David Hitlin
- Helen Quinn (Theory Coordinator)
- Klaus Schubert
- Marie-Helene Schune
- Walter Toki
- Mike Witherell

The organisers gratefully acknowledge the financial support of:

- Accademia Nazionale dei Lincei
- California Institute of Technology
- DAPNIA-Saclay/CEA
- Dipartimento di Fisica dell'Università di Roma "La Sapienza"
- IN2P3/CNRS
- Istituto Nazionale di Fisica Nucleare
- National Science Foundation
- Princeton University Physics Department

- Particle Physics and Astronomy Research Council
- Université de Paris XI, Orsay
- US Department of Energy

and of the local workshops organisations:

- Dipartimento di Fisica dell'Università di Roma "La Sapienza": Gabriella Bucci and Marcella Mastrofini and staff
- Princeton University: Elaine Remillard and staff
- Laboratoire de l'Accélérateur Linéaire (LAL), Orsay: Marie-Helene Schune and her local organizing committee and Nicole Mathieu and her staff.
- California Institute of Technology: Betty Smith and staff

The editors would like to thank particularly Bob Cahn, Theresa Champion, Adam Falk, Klaus Schubert, and Jim Smith for their assistance during the editing of this Book. They would also like to thank Sharon Jensen of the SLAC Theory Group and the production staff of the SLAC Technical Publications Department for their invaluable and indefatigable work during the editing and production of the book.

Contents

1	A CP Violation Primer	1
1.1	CP Violation in Field Theories	2
1.1.1	Field Transformations	2
1.2	Neutral B Mesons	5
1.2.1	Mixing of Neutral B Mesons	5
1.2.2	Phase Conventions	7
1.2.3	Time Evolution of Neutral B_d Mesons	8
1.2.4	Two-Time Formalism for Coherent $B\bar{B}$ States	9
1.3	The Three Types of CP Violation in B Decays	12
1.3.1	CP Violation in Decay	12
1.3.2	CP Violation in Mixing	14
1.3.3	CP Violation in the Interference Between Decays With and Without Mixing	15
1.4	CP Violation in the Standard Model	17
1.4.1	The CKM Picture of CP Violation	17
1.4.2	Unitarity of the CKM Matrix	19
1.4.3	Measuring CKM Parameters with CP -Conserving Processes	23
1.5	Expected CP Asymmetries — Standard Model Predictions	24
1.5.1	CP Violation in Mixing	24
1.5.2	Decay-Amplitude Weak-Phase Structure	25
1.5.3	Low-Energy Effective Hamiltonians	28
1.5.4	Decay Asymmetry Predictions in the Standard Model — General Patterns	29

1.5.5	Decay Asymmetry Predictions in the Standard Model — Some Sample Modes	32
1.5.6	Effects of Physics Beyond the Standard Model	34
1.6	Some Comments about the K System	35
1.6.1	The Neutral K System	35
1.6.2	Measuring CP Violation in the K System	37
1.6.3	The ε_K and ε'_K Parameters	38
2	Introduction to Hadronic B Physics	43
2.1	The Operator Product Expansion	46
2.1.1	General Considerations	46
2.1.2	Example I: Weak b Decays	47
2.1.3	Radiative Corrections	49
2.1.4	Example II: Penguins and Box Diagrams	50
2.1.5	Summary	51
2.2	The Heavy-Quark Expansion	52
2.2.1	Separation of Scales	52
2.2.2	Heavy-Quark Symmetry	53
2.2.3	Heavy-Quark Effective Theory	54
2.2.4	Application of the HQE to B Decays	56
2.2.5	Limitations of the HQE	59
2.3	Light Flavor Symmetry	60
2.3.1	Chiral Lagrangians	60
2.3.2	Heavy-Hadron Chiral Perturbation Theory	61
2.3.3	Factorization, Color Flow, and Vacuum Saturation	62
2.4	Lattice Gauge Theory	64
2.5	QCD Sum Rules	66

2.6	Quark Models and Related Methods	68
2.7	Further Reading	70
3	An Introduction to the BABAR Experiment	73
3.1	e^+e^- B Factories and PEP-II	73
3.1.1	Cross-Sections at the $\Upsilon(4S)$	74
3.1.2	Data Taking in the Continuum	75
3.2	Overview of the BABAR Detector	78
3.3	The Silicon Vertex Tracker	81
3.3.1	Physics Requirements and Performance Goals	81
3.3.2	Silicon Vertex Tracker Layout	82
3.3.3	The Silicon Microstrip Detectors	84
3.3.4	Silicon Vertex Tracker Readout	85
3.3.5	Silicon Vertex Tracker Space Resolution	86
3.3.6	Calibration and Alignment	88
3.4	The Drift Chamber	88
3.4.1	Drift Chamber Design	89
3.4.2	Drift Chamber Electronics	92
3.4.3	Prototype Results	92
3.5	The DIRC	93
3.5.1	DIRC Concept and Hardware Overview	94
3.5.2	DIRC Acceptance	95
3.5.3	DIRC Performance	95
3.6	The Electromagnetic Calorimeter	96
3.6.1	Performance Goals and Layout	96
3.6.2	Crystal Subassemblies and Readout	99
3.6.3	Calibration	100

3.7	The Muon and Neutral Hadron Detector	102
3.7.1	The Detector Layout	102
3.7.2	The Active Detectors	104
3.7.3	The Readout System	104
3.8	The Trigger	105
4	Snapshot of BABAR Software and Analysis Tools	111
4.1	Simulation	111
4.1.1	Event Generators	112
4.1.2	Full Detector Simulation	113
4.1.3	Fast Detector Simulation: Aslund	115
4.2	Reconstruction	118
4.2.1	Tracking	119
4.2.2	Reconstruction in the Electromagnetic Calorimeter	121
4.3	Charged Particle Identification	125
4.3.1	Charged Hadron Identification	126
4.3.2	Electron Identification	129
4.3.3	Muon Identification	135
4.3.4	Identification of Particles with Neural Networks	138
4.4	Neutral Particle Identification	144
4.4.1	π^0 and Photon Identification	144
4.4.2	K_L^0 Identification	145
4.5	Vertexing and Kinematic Fitting	153
4.5.1	Vertex Reconstruction	153
4.5.2	Kinematical Fitting	155
4.6	Reconstruction of Particle Decays	159
4.6.1	K_S^0	159

4.6.2	<i>D</i> and <i>D</i> *	160
4.7	Multivariate Analysis Tools	165
4.7.1	Presentation of the Different Methods	165
4.7.2	Description of Cornelius	169
4.8	Tagging	171
4.8.1	Direct- and Reverse-Sign Classes	171
4.8.2	The Tagging Strategy	172
4.8.3	Definition of Discriminating Variables	173
4.8.4	Definition of Categories of Events Treated	175
4.8.5	Performances of the Tagging Methods	176
4.8.6	Measuring the Tagging Performance with Real Data	178
4.8.7	Future Prospects and Improvements	180
4.8.8	Conclusions	180
4.9	Tools for Continuum Identification	181
4.9.1	Criteria for Continuum Identification	181
4.9.2	A Common Procedure for Background Fighting	185
4.9.3	Performance	186
4.10	Extraction of <i>CP</i> Asymmetries	187
4.10.1	Fit Equations	187
4.10.2	Adding Flavor-Tagging Information	189
4.10.3	Likelihood Estimate of <i>A</i>	190
4.10.4	Error of the Likelihood Estimate	191
4.10.5	The Kin Variable	193
4.11	Data Production	194
5	Determination of β	199
5.1	Theoretical Review of $\sin 2\beta$ Measurements	199

5.1.1	Decays That Can Measure β	199
5.1.2	Uncertainties: Penguins and FSI phases	204
5.1.3	Angular Analyses to Extract CP Amplitudes	213
5.1.4	Isospin Analysis	221
5.1.5	Modeling the Uncertainty on β	222
5.1.6	Measurement of β in Inclusive Decays	229
5.1.7	Discrete Ambiguities	231
5.1.8	Summary of Data on Decays Measuring β	236
5.2	Experimental Considerations for $\sin 2\beta$ Analyses	241
5.3	Charmonium + Kaon modes	242
5.3.1	$B^0 \rightarrow J/\psi K_S^0$	243
5.3.2	$B^0 \rightarrow J/\psi K_L^0$	247
5.3.3	$B^0 \rightarrow \psi' K_L^0$	253
5.3.4	$B^0 \rightarrow \chi_{c1} K_L^0$	255
5.4	Charmonium + K^{*0} Modes	258
5.4.1	Event Selection	260
5.4.2	Measurement of $\sin 2\beta$ with the Decay $B^0 \rightarrow J/\psi K^{*0}$	264
5.5	$D^+ D^-$, $D^* D$, and $D^* D^*$ Final States	265
5.5.1	Study of $B^0 \rightarrow D^+ D^-$	265
5.5.2	Study of $B^0 \rightarrow D^{*+} D^{*-}$	275
5.5.3	Estimates for the $D^* D$ Mode	291
5.5.4	Measurement of CP Asymmetries and Extraction of β	292
5.6	Penguin Modes	301
5.6.1	$B^0 \rightarrow \eta' K_S^0$	302
5.6.2	Analysis of $B^0 \rightarrow \eta' K_L^0$	306
5.6.3	Analysis of ϕK^{*}	307

5.6.4	Estimates for $B \rightarrow \phi K_s^0$	315
5.6.5	Analysis of $B^0 \rightarrow \phi K_L^0$	315
5.7	Summary and Conclusions	318
5.7.1	Summary of Results	318
5.7.2	Systematic Errors	321
5.7.3	Conclusion	322
6	Determinations of α and Direct CP Violation	327
6.1	Theoretical Background: The Role of Penguins and α -Extraction	327
6.1.1	Extraction of α -Ignoring Penguins	328
6.1.2	Extraction of α in the Presence of Penguins	330
6.2	Penguins and Direct CP Violation	346
6.2.1	Varieties of Direct CP Violation	346
6.2.2	Illustrative Examples of Direct CP	348
6.3	Overview of the Experimental Studies	353
6.4	B -Decay Modes with Two Pions	353
6.4.1	The $\pi^+\pi^-$ Decay Mode	354
6.4.2	The $\pi^0\pi^0$ Decay Mode	359
6.4.3	The $\pi^+\pi^0$ Decay Mode	361
6.4.4	Extraction of CP Asymmetries from the $B^0 \rightarrow \pi^+\pi^-$ Decay Mode . . .	364
6.4.5	Isospin Analysis	368
6.4.6	α without $B^0 \rightarrow \pi^0\pi^0$?	370
6.4.7	Conclusions	376
6.5	B Decay Modes with Three Pions	376
6.5.1	Event Selection	378
6.5.2	Analysis	388
6.5.3	Conclusion	403

6.6	<i>B</i> -Decay Modes with Four Pions	404
6.6.1	Overview	404
6.6.2	The $a_1\pi$ Decay Modes	405
6.6.3	The $\rho\rho$ Decay Modes	429
6.6.4	Summary and Conclusion for Four-Pion Channels	437
6.7	Conclusions	438
6.8	Charged <i>B</i> Decays and Direct <i>CP</i> Violation	441
6.8.1	$B^- \rightarrow \eta h^-$	442
6.8.2	$B^- \rightarrow D^- D^0$	443
6.8.3	Outlook	444
7	Methods of Measuring γ	449
7.1	Introduction and Motivation for Measuring γ	449
7.2	An Overview of Methods for Extracting γ	449
7.3	Experimental Errors in Extracting γ from Triangles	453
7.4	Methods Using $B \rightarrow DK$ Decays	456
7.4.1	Theoretical Framework	456
7.4.2	Experimental Feasibility Studies	460
7.5	Methods Using Flavor Symmetries	466
7.5.1	Theoretical Framework	466
7.5.2	A Simple Strategy for Extracting γ	470
7.5.3	Constraints from Combined $B_{u,d} \rightarrow \pi K$ Branching Ratios	473
7.5.4	Experimental Feasibility Studies	478
7.6	Partial Reconstruction of $B_d \rightarrow D^{(*)\pm} \pi^\mp$	481
7.6.1	Theoretical Framework	483
7.6.2	The Experimental Approach	484
7.7	Strategies to Determine γ from B_s Decays	491

7.8	Summary of Results and Overall γ Reach	493
8	Semileptonic B Decays and the Extraction of V_{cb} and V_{ub}	499
8.1	Exclusive Semileptonic B Decays to Charmed Mesons	499
8.1.1	Heavy-Quark Symmetry	499
8.1.2	Determination of $ V_{cb} $	502
8.1.3	Dispersive Bounds and Unitarity Constraints on Form Factors	505
8.1.4	Tests of Heavy-Quark Symmetry	507
8.1.5	B Decays to p -Wave Charm Mesons	508
8.2	Exclusive Semileptonic B Decays to Light Mesons and Determination of $ V_{ub} $	512
8.2.1	Heavy-to-Light Form Factors from Lattice QCD	513
8.2.2	Dispersive Bounds on Heavy-to-Light Form Factors	515
8.2.3	Heavy-to-Light Form Factors from Light-Cone Sum Rules	517
8.2.4	Using Semileptonic D Decays and Dispersive Bounds to Extract $ V_{ub} $	520
8.3	Inclusive Semileptonic $b \rightarrow c$ Decays	521
8.3.1	Determination of $ V_{cb} $	526
8.3.2	Aspects of Inclusive B Decays	529
8.4	$ V_{ub} $ from Inclusive Semileptonic $b \rightarrow u$ Decays	530
8.5	Theory Summary	532
8.6	Studying Semileptonic Decays with the BABAR Detector	534
8.6.1	The Experimental Environment	534
8.6.2	Semileptonic Event Generators	534
8.6.3	Reconstruction of the Other B	535
8.7	Measuring $ V_{cb} $ Using HQET in Exclusive Decays	538
8.8	Measuring $ V_{ub} $ Using Exclusive Decays	539
8.9	Measuring $ V_{cb} $ with Inclusive Decays	540
8.10	Measuring $ V_{ub} $ with Inclusive Decays	544

8.11	Conclusions	547
9	Rare B Decays within the Standard Model	557
9.1	Leptonic Decays	557
9.1.1	$B \rightarrow \ell \nu_\ell$	559
9.1.2	$B^0 \rightarrow \ell^+ \ell^-$	564
9.1.3	$B \rightarrow \ell \nu \gamma, \ell^+ \ell^- \gamma$	566
9.2	$b \rightarrow s(d) + X$ Transitions	572
9.2.1	$B \rightarrow X_s \gamma, X_d \gamma$	577
9.2.2	$B \rightarrow X_s \gamma \gamma$	590
9.2.3	$B \rightarrow X_s \ell \ell, X_d \ell \ell$	592
9.2.4	$B \rightarrow X_s \nu \bar{\nu}$	608
9.2.5	$B \rightarrow X_s + \text{Gluon}$	613
9.3	Model-Independent Test of the Standard Model	625
9.4	Summary	627
10	Hadronic B Meson Decays	639
10.1	Exclusive Hadronic Decays: The Factorization Ansatz in Nonleptonic Decays of Heavy Mesons	640
10.1.1	The BSW Approach	647
10.1.2	Phenomenology of Nonfactorizable Contributions	653
10.1.3	Towards an Understanding of Factorization. Departures from Factorization	653
10.1.4	Tests of Factorization	659
10.1.5	Factorization in Multibody Decays	665
10.2	The Role of Final State Interactions in B Decays	667
10.3	Heavy-Quark Chiral Perturbation Theory	678
10.4	Inclusive Properties of B Meson Decays	681

10.4.1	Fully Integrated Rates	681
10.4.2	Semi-inclusive Transitions	685
10.4.3	Charm Production and Charm Counting	685
10.4.4	Production of Light Hadrons	690
10.5	<i>B</i> Meson Decays to Baryons	694
10.5.1	Exclusive Decays to Baryons	700
10.5.2	<i>CP</i> Violation in Baryonic Decays	702
11	Non-<i>CP</i> <i>b</i> Physics	709
11.1	Overview	709
11.2	The Determination of Δm_B	710
11.2.1	Theory of $B^0-\bar{B}^0$ Mixing	710
11.2.2	Measurement of Δm_B	717
11.3	Lifetimes	726
11.3.1	Lifetimes and Inclusive Semileptonic Decays	726
11.3.2	Lifetime Ratios	737
11.3.3	The Semileptonic Branching Fraction	741
11.3.4	<i>B</i> -Lifetime Ratio Measurement at BABAR	743
11.4	Bottomonium Physics	753
11.4.1	$\Upsilon(4S)$ Resonance Parameters	753
11.4.2	$\Upsilon(4S)$ Decays to <i>B</i> -Meson Pairs	757
11.4.3	Non $B\bar{B}$ Decays of the $\Upsilon(4S)$	761
11.5	The Case for $\Upsilon(5S)$ Running	766
11.5.1	CDF B_s Reach	767
11.5.2	Partial B_s Reconstruction	767
11.5.3	B_s -Meson Lifetime Differences	770
11.5.4	B_s Production Cross-Section	773

11.5.5	PEP-II Options for Running Above the $\Upsilon(4S)$	775
11.6	Summary and Conclusions	775
12	Charm, τ, QCD, and Two-Photon Physics	783
12.1	Charm Physics	784
12.1.1	Searches for New Physics	795
12.1.2	Purely Leptonic Decays of D and D_s	804
12.1.3	Semileptonic Decays	807
12.1.4	Hadronic Charm Decays	815
12.2	τ Physics	820
12.2.1	Present Status	820
12.2.2	Limits on the ν_τ Mass	826
12.2.3	Determination of the Strange-Quark Mass	827
12.2.4	CP Violation in Hadronic τ Decays	828
12.2.5	Lorentz Structure of τ Decays	829
12.2.6	Rare τ Decays	832
12.2.7	τ Electric Dipole Moment	835
12.3	Two-Photon Physics	837
12.3.1	Monte Carlo Simulations and BABAR Rate Estimates	838
12.3.2	Resonance Production	839
12.3.3	Exclusive Hadron Production and QCD	842
12.4	Light-Meson Spectroscopy in B , D_s , and D Decays	844
12.4.1	B decays	846
12.4.2	D and D_s Decays	848
12.5	Baryon Formation	853
12.6	General Conclusions on Non- B Physics	856

13	Physics Beyond the Standard Model	867
13.1	Baryogenesis	868
13.2	Model-Independent Analysis of Mixing	870
13.2.1	The Basic Assumptions and Results	870
13.2.2	Discrete Ambiguities	872
13.2.3	The (ρ, η) Plane	874
13.2.4	The $(\sin 2\alpha, \sin 2\beta)$ Plane	876
13.2.5	Final Comments	876
13.3	New Physics Effects in CP -Violating B Decays	878
13.3.1	Effects in Decays	878
13.3.2	Formalism	879
13.3.3	The Different Decay Channels	880
13.3.4	Standard Model Corrections	882
13.3.5	Overview of New Physics Possibilities	884
13.4	Supersymmetry	887
13.4.1	The Supersymmetric CP Problems	887
13.4.2	Classes of Supersymmetric Models	888
13.4.3	Supersymmetry without R -parity	891
13.4.4	Model-Independent Analysis	897
13.5	Models with Extra Scalars	903
13.5.1	The General MHDM	903
13.5.2	B Physics Implications	905
13.5.3	2HDM	906
13.6	Models with Additional Quarks	907
13.6.1	Isosinglet Quarks	907
13.6.2	Fourth Generation	909

13.7	Left-Right Symmetric Model	911
13.8	Models with Additional Strong Dynamics	916
13.8.1	FCNC Effects in Topcolor-Assisted Technicolor	917
13.8.2	Model-Independent Analysis	919
13.9	Summary	920
14	Overall Determinations of the CKM Matrix	933
14.1	The Problem of Theoretical Uncertainties	934
14.2	Individual Constraints on the Unitarity Triangle	934
14.2.1	The $ V_{ub}/V_{cb} $ Constraint	938
14.2.2	The Δm_{B_d} Constraint	939
14.2.3	The ϵ_K Constraint	942
14.2.4	The Status of ϵ'/ϵ	943
14.2.5	Impact of $K \rightarrow \pi \nu \bar{\nu}$ Decays	944
14.2.6	Determination of $\sin 2\beta$	945
14.2.7	Determination of $\sin 2\alpha$	946
14.3	The Determination of the CKM Parameters	948
14.3.1	Method for Extracting CKM Parameters	948
14.3.2	Present Constraints on the Unitarity Triangle	949
14.3.3	Including BaBar CP Asymmetry Measurements	958
14.3.4	Determination of $f_{B_d} \sqrt{B_{B_d}}$ and B_K using CP Asymmetries	964
14.3.5	In Case of Incompatibility	965
14.3.6	Other Possible Future Constraints	967
14.4	Conclusions	969
A	The Effective $\Delta B = 1$ Hamiltonian	973
B	Some Remarks on Form-Factor Models	981

B.1	Introduction	981
B.1.1	Why Use Quark Models?	981
B.1.2	General Features of Quark Models for Form Factors	982
B.2	Hybrid Models and Purely Phenomenological Models	986
B.2.1	Hybrid Models	986
B.2.2	Discussion of the Idea of Nearby-Pole Dominance	987
B.2.3	Purely Phenomenological Models	989
B.3	Full Quark Model Approaches	990
B.3.1	Bethe-Salpeter Approach	990
B.3.2	Three-Dimensional Approaches	991
B.3.3	Classification of Three-Dimensional Approaches	992
B.3.4	Connection between Bethe-Salpeter Formalism and Three-Dimensional Models	996
B.3.5	Quantitative Predictions of Three-Dimensional Models	997
B.4	Conclusions	998
C	Standard Model Parameters from Lattice QCD	1003
C.1	Evaluation of Physical Quantities in Lattice Simulations	1004
C.2	Main Sources of Uncertainty	1007
C.3	Quark Masses	1008
C.4	Leptonic Constants of Pseudoscalar Heavy Mesons	1010
C.5	B^0 - \bar{B}^0 and K^0 - \bar{K}^0 Mixing	1012
C.6	Semileptonic Decays of D and B Mesons	1014
C.6.1	Semileptonic D Decays	1015
C.6.2	Semileptonic $B \rightarrow D$ and $B \rightarrow D^*$ Decays	1016
C.6.3	Semileptonic $B \rightarrow \rho$ and $B \rightarrow \pi$ Decays and the Rare Decay $\bar{B} \rightarrow K^* \gamma$	1017
C.7	The Parameters of the HQET	1021

C.7.1	The Evaluation of the Mass of a Heavy Quark	1022
C.7.2	Kinetic Energy of a Heavy Quark	1023
C.7.3	The Matrix Element of the Chromomagnetic Operator	1025
C.8	Exclusive Nonleptonic Decays of Heavy Mesons	1025
D	Standard Model Parameters from QCD Sum Rules	1031
D.1	Quark Masses	1037
D.1.1	Non-Strange-Quark Masses: $m_u + m_d$	1038
D.1.2	Strange-Quark Mass: m_s	1039
D.1.3	Charm-Quark Mass: M_c	1040
D.1.4	Beauty-Quark Mass: M_b	1041
D.2	Leptonic Constants of Pseudoscalar Heavy Mesons	1042
D.3	B_{B_d} and B_K	1044
D.4	Heavy-to-Light Decay Form Factors from Light-Cone Sum Rules	1045
D.4.1	Semileptonic Decays	1045
D.4.2	Rare Decays	1049
D.4.3	Strong Coupling Constants	1049
D.4.4	The Heavy-Quark Limit	1050
D.4.5	Theoretical Accuracy and Possible Developments	1050

A CP Violation Primer

This chapter is a primer on the subject of CP violation. It is intended as an introductory background for physicists joining the BABAR experiment. Much of the emphasis is on the physics relevant to that experiment. However other related topics are briefly reviewed and summarized.

The subject of CP symmetry and its violation is often referred to as one of the least understood in particle physics. Perhaps a better statement would be to say that it is experimentally one of the least constrained. CP symmetry violation is an expected consequence of the Standard Model with three quark generations, but is one of the least well-tested parts of that model. The only part of CP violation that currently is considered puzzling by theorists is the lack of CP violation in strong interactions. That subject is outside the realm of this document and of BABAR experiments. The CP violation that shows up in a small fraction of weak decays is accommodated simply in the three-generation Standard Model Lagrangian. All it requires is that CP is not imposed as a symmetry.

However, while it is known that CP violation occurs, because it has been observed in K decays [1], it is not yet known whether the pattern of CP violation predicted by the minimal Standard Model is the one found in nature. The K -decay observations, together with other measurements, place constraints on the parameters of the Standard Model mixing matrix (the CKM matrix [2, 3]) but do not yet provide any test. A multitude of CP -violating effects are expected in B decays, some of which are very cleanly predicted by the Standard Model. If enough independent observations of CP violation in B decays can be made then it will be possible to test the Standard Model predictions for CP violation. Either the relationships between various measurements will be consistent with the Standard Model predictions and fully determine the CKM parameters or there will be no single choice of CKM parameters that is consistent with all measurements.

This latter case, of course, would be much more interesting. It would indicate that there is a contribution of physics beyond the Standard Model. There may be enough information in the pattern of the inconsistencies to learn something about the nature of the new physics contributions. Thus the aim of the game is to measure enough quantities to impose redundant constraints on Standard Model parameters, including particularly the convention-independent combinations of CP -violating phases of CKM matrix elements.

One may well ask, after the many successes of the Standard Model, why one would expect violations to show up in such a low-energy regime. The best answer is simply that it has not yet been tested. Theorists will give a variety of further reasons. Many extensions of the Standard

Model have additional sources of *CP*-violating effects, or effects which change the relationship of the measurable quantities to the *CP*-violating parameters of the Standard Model.

In addition there is one great puzzle in cosmology that relates to *CP* violation, and that is the disappearance of antimatter from the Universe [4]. In grand unified theories, or even in the Standard Model at sufficiently high temperatures, there are baryon number-violating processes. If such processes are active then thermal equilibrium produces equal populations of particles and antiparticles. Thus in modern theories of cosmology the net baryon number of the universe is zero in the early high-temperature epochs. Today it is clearly not zero, at least in our local region. A full discussion of the cosmological arguments is not possible here. It suffices to remark that there is large class of theories in which the baryon number asymmetry is generated at the weak-phase transition [5]. Such theories, however, must include *CP* violation from sources beyond the minimal Standard Model. Calculations made in that model show that it does not generate a large enough matter-antimatter imbalance to produce the baryon number to entropy ratio observed in the universe today. This is a hint that *CP* violation from beyond Standard Model sources is worth looking for. It is by no means a rigorous argument. There are theories in which baryon number is generated at a much higher temperature and then protected from thermalization to zero by $B \Leftrightarrow L$ (baryon number minus lepton number) symmetry. Such theories do not in general require any new low-energy *CP*-violation mechanism. Neither do they forbid it.

More generally, since there is *CP* violation in part of the theory, any extension of the Standard Model cannot be required to be *CP* symmetric. Any additional fields in the theory bring possible additional *CP*-violating couplings. Even assumptions such as soft or spontaneous *CP* symmetry breaking leave a wide range of possibilities. Further experimental constraints, from experiments such as the *B* factory, are needed.

Section 1.1 begins by discussing the way *CP* violation appears in a field theory Lagrangian [6]. Sections 1.2–1.6, follow the discussion in [7].¹ Section 1.2 turns to the quantum mechanics and time dependence of neutral meson systems, and Section 1.3 gives a model-independent treatment of the possible types of *CP* violation. Following that, Section 1.4 presents the Standard Model version of *CP* violation, and Section 1.5 gives the predictions and relationships for various decays that arise from that theory. Finally, in Section 1.6, the situation for *K*-decays is reviewed.

1.1 *CP* Violation in Field Theories

1.1.1 Field Transformations

This section provides a basic introduction to the field theory basis of *CP* symmetry breaking. The fundamental point is that *CP* symmetry is broken in any theory that has complex coupling

¹For a recent, excellent, and very detailed review see [8].

constants in the Lagrangian which cannot be removed by any choice of phase redefinition of the fields in the theory.

Three discrete operations are potential symmetries of a field theory Lagrangian [6]: Two of them, *parity* and *time reversal* are spacetime symmetries and constitute part of the Poincaré group. Parity, denoted by P , sends $(t, \mathbf{x}) \rightarrow (t, \Leftrightarrow\mathbf{x})$, reversing the handedness of space. Time reversal, denoted by T , sends $(t, \mathbf{x}) \rightarrow (\Leftrightarrow t, \mathbf{x})$, interchanging the forward and backward light-cones. A third (non-spacetime) discrete operation is *charge conjugation*, denoted by C . This operation interchanges particles and antiparticles. The combination CP replaces a particle by its antiparticle and reverses momentum and helicity. The combination CPT is an exact symmetry in any local Lagrangian field theory.

What is the status of these symmetry operations in the real world? From experiment, it is observed that electromagnetic and strong interactions are symmetric with respect to P , C and T . The weak interactions violate C and P separately, but preserve CP and T to a good approximation. Only certain rare processes, all involving neutral K mesons, have been observed to exhibit CP violation. All observations to date are consistent with exact CPT symmetry. (Gravitation couples to the energy-momentum tensor and is thus C , P , and T invariant. This is supported by the universality of the gravitational coupling for different types of matter, with different baryon number to mass ratios.)

To understand whether a given theory can accommodate CP violation, one needs to know the transformation properties of the fields under the various discrete symmetries. In particular for a Dirac spinor:

$$P\psi(t, \mathbf{x})P = \gamma^0\psi(t, \Leftrightarrow\mathbf{x}), \quad (1.1)$$

$$T\psi(t, \mathbf{x})T = \Leftrightarrow\gamma^1\gamma^3\psi(\Leftrightarrow t, \mathbf{x}), \quad (1.2)$$

$$C\psi(t, \mathbf{x})C = \Leftrightarrow i(\bar{\psi}(t, \mathbf{x})\gamma^0\gamma^2)^T. \quad (1.3)$$

The Lagrangian, being a Lorentz scalar, can only depend on terms bilinear in fermion fields (and not on single fermion fields). The transformation properties of various fermion bilinears under CP are summarized in the table below. Here the shorthand $(\Leftrightarrow 1)^\mu \equiv 1$ for $\mu = 0$ and $(\Leftrightarrow 1)^\mu \equiv \Leftrightarrow 1$ for $\mu = 1, 2, 3$ (namely, $(\Leftrightarrow 1)^\mu a^\mu = a_\mu$) is used.

term	$\bar{\psi}_i\psi_j$	$i\bar{\psi}_i\gamma^5\psi_j$	$\bar{\psi}_i\gamma^\mu\psi_j$	$\bar{\psi}_i\gamma^\mu\gamma^5\psi_j$	(1.4)
$CP\Leftrightarrow$ transformed term	$\bar{\psi}_j\psi_i$	$\Leftrightarrow i\bar{\psi}_j\gamma^5\psi_i$	$\Leftrightarrow(\Leftrightarrow 1)^\mu\bar{\psi}_j\gamma^\mu\psi_i$	$\Leftrightarrow(\Leftrightarrow 1)^\mu\bar{\psi}_j\gamma^\mu\gamma^5\psi_i$	

Similarly, the CP transformation properties of scalar (H), pseudoscalar (A) and vector boson (W) fields, and also of the derivative operator are given by

term	H	A	$W^{\pm\mu}$	∂_μ	(1.5)
$CP\Leftrightarrow$ transformed term	H	$\Leftrightarrow A$	$\Leftrightarrow(\Leftrightarrow 1)^\mu W^{\mp\mu}$	$(\Leftrightarrow 1)^\mu\partial_\mu$	

Taking into account the Lorentz invariance and hermiticity of the Lagrangian, the above *CP* transformation rules imply that each of the combinations of fields and derivatives that appear in the Lagrangian transforms under *CP* to its hermitian conjugate. However, there are coefficients in front of these expressions which represent either coupling constants or particle masses and which do not transform under *CP*. If any of these quantities are complex, then the coefficients in front of *CP*-related terms are complex conjugates of each other. In such a case, *CP* is not necessarily a good symmetry of the Lagrangian. When the rates of physical processes that depend on these Lagrangian parameters are calculated, there can be *CP*-violating effects, namely rate differences between pairs of *CP* conjugate processes. Examples are given below.

Note, however, that not all Lagrangian phases are physically meaningful quantities. Consider the Lagrangian that contains the most general set of complex coupling constants consistent with all other symmetries in the theory. That is to say *CP* symmetry is not imposed, and hence any coupling is allowed to be complex (unless the Hermitian structure of the Lagrangian automatically requires it to be real). Now any complex field in the Lagrangian can be redefined by an arbitrary phase rotation; such rotations will not change the physics, but will change the phases of some set of terms in the Lagrangian. Consider for example a typical Yukawa-type term,

$$y_{ij}H\bar{\psi}_i\psi_j + \text{hermitian conjugate.} \quad (1.6)$$

The phase of y_{ij} can be changed by redefining the phase of any one of the three fields H , ψ_i , ψ_j that enter this term. In general such redefinitions will also change the phase of any other terms in the Lagrangian that involve these same fields, unless the complex conjugate field appears with the same power in the same term. Some set of couplings can be made real by making such field redefinitions. However if any non-zero phases for couplings remain after all possible field redefinitions have been used to eliminate as many of them as possible, then there is *CP* violation. It is a matter of simple counting for any Lagrangian to see whether this occurs. If all phases can be removed in this way then that theory is automatically *CP*-conserving. In such a theory it is impossible to introduce any *CP* violations without adding fields or removing symmetries so that additional couplings appear. (This is the case for the Standard Model with only two generations and a single Higgs multiplet.)

If some phases survive the redefinitions, there is, in general, convention-dependence as to where the complex phases appear. One can choose to make certain terms real and leave others complex, but a different choice, related to the first by field redefinitions, has the same physical consequences. Only those differences between pairs of phases that are unchanged by such redefinitions are physically meaningful. How such phase differences manifest themselves as *CP*-violating effects will be shown below. First some conventions and notation for neutral B mesons need to be established.

1.2 Neutral B Mesons

1.2.1 Mixing of Neutral B Mesons

This section treats the quantum mechanics of the two state system of neutral B mesons. Unless otherwise specified, this discussion is completely model independent and does not depend on Standard Model specific results. It will however use features of the flavor and weak-interaction structure of the Standard Model, which will inevitably also be part of any extension of that theory.

The systems of interest are neutral self-conjugate pairs of mesons. There are two such systems involving b quarks: B_d mesons, made from one b -type quark or antiquark and one d type; and B_s mesons from one b and one s . Like the neutral K mesons, the neutral B mesons are complicated by the fact that different neutral states are relevant to the discussion of different physical processes: there are two flavor eigenstates, which have definite quark content and are most useful to understand particle production and particle decay processes; and there are eigenstates of the Hamiltonian, namely states of definite mass and lifetime, which propagate through space in a definite fashion. If CP were a good symmetry, the mass eigenstates would also be CP eigenstates, namely under a CP transformation they would transform into themselves with a definite eigenvalue ± 1 . But since CP is not a good symmetry, the mass eigenstates can be different from CP eigenstates (see further discussion below). In any case the mass eigenstates are not flavor eigenstates, and so the flavor eigenstates are mixed with one another as they propagate through space. The flavor eigenstates for B_d are $B^0 = \bar{b}d$ and $\bar{B}^0 = \bar{d}b$. (The convention is that B^0 is the isospin partner of B^+ ; therefore it contains the \bar{b} quark. This is similar to the K mesons, where K^0 , the isospin partner of K^+ , contains the \bar{s} quark.) The conventional definitions for the B_s system are $B_s = \bar{b}s$ and $\bar{B}_s = \bar{s}b$. Unless explicitly stated the following general discussion applies to both B systems, and a similar notation can be used also for K^0 or D^0 mesons. However, the two neutral K mesons have very different lifetimes (while their masses are almost identical), so that it is more convenient to define the states by the half-life, K_L and K_S for the long-lived and short-lived state, respectively. For the neutral D mesons, the mixing rate is much slower than the decay rate so that flavor eigenstates are the most convenient basis.

An arbitrary linear combination of the neutral B -meson flavor eigenstates,

$$a|B^0\rangle + b|\bar{B}^0\rangle, \quad (1.7)$$

is governed by a time-dependent Schrödinger equation

$$i\frac{d}{dt}\begin{pmatrix} a \\ b \end{pmatrix} = H\begin{pmatrix} a \\ b \end{pmatrix} \equiv (M \Leftrightarrow \frac{i}{2}\Gamma)\begin{pmatrix} a \\ b \end{pmatrix} \quad (1.8)$$

for which M and Γ are 2×2 Hermitian matrices. CPT invariance guarantees $H_{11} = H_{22}$.

The off-diagonal terms in these matrices, M_{12} and Γ_{12} , are particularly important in the discussion of *CP* violation. They are the dispersive and absorptive parts respectively of the transition amplitude from B^0 to \bar{B}^0 . (Note that both of these can be complex quantities because of complex coupling constants.) In the Standard model these contributions arise from the box diagrams with two W exchanges. The large mass of the B makes the QCD calculation of these quantities much more reliable than the corresponding calculation for K mixing. The dispersive part, M_{12} , is clearly short-distance dominated (*i.e.*, large-quark momenta in the box diagram) and long-distance effects are expected to be negligible. For the dispersive part, one calculates the cut of the quark box diagram and uses the argument of *quark-hadron duality* (see Chapter 2) to relate this quantity to the corresponding hadronic quantity. This is similar to the calculation of $R_{e^+e^-}$, the ratio of hadron to leptonic cross-sections for e^+e^- scattering. While there is no rigorous argument that quark-hadron duality holds at a single energy scale (known as local quark-hadron duality), it can be shown to be true when averaged over a sufficient range. However in a region where there are no thresholds the value of this cut does not vary rapidly with energy and hence one expects the quark calculation to be reliable. Combining heavy quark behavior with QCD calculation one obtains an estimate for Γ_{12} that is expected to be valid up to corrections of order $1/N_C$ and/or Λ/m_b where $N_C = 3$ is the number of colors and Λ is the scale that defines how the QCD coupling evolves with energy. New physics effects, that is physics from additional diagrams that arise in models beyond the Standard Model, are not expected to have significant effects on Γ_{12} because any additional particles in such theories are required to be massive and hence do not give new cut contributions at this scale, but such effects can significantly alter M_{12} , as is discussed in Chapter 13, Section 13.2.

The light B_L and heavy B_H mass eigenstates are given by

$$|B_L\rangle = p|B^0\rangle + q|\bar{B}^0\rangle, \quad (1.9)$$

$$|B_H\rangle = p|B^0\rangle \leftrightarrow q|\bar{B}^0\rangle. \quad (1.10)$$

The complex coefficients p and q obey the normalization condition

$$|q|^2 + |p|^2 = 1. \quad (1.11)$$

Note that $\arg(q/p^*)$ is just an overall common phase for $|B_L\rangle$ and $|B_H\rangle$ and has no physical significance.

The mass difference Δm_B and width difference $\Delta\Gamma_B$ between the neutral B mesons are defined as follows:

$$\Delta m_B \equiv M_H \leftrightarrow M_L, \quad \Delta\Gamma_B \equiv \Gamma_H \leftrightarrow \Gamma_L, \quad (1.12)$$

so that Δm_B is positive by definition. Finding the eigenvalues of (1.8), one gets

$$(\Delta m_B)^2 \leftrightarrow \frac{1}{4}(\Delta\Gamma_B)^2 = 4(|M_{12}|^2 \leftrightarrow \frac{1}{4}|\Gamma_{12}|^2), \quad (1.13)$$

$$\Delta m_B \Delta\Gamma_B = 4 \mathcal{R}e(M_{12}\Gamma_{12}^*). \quad (1.14)$$

The ratio q/p is given by

$$\frac{q}{p} = \frac{\Delta m_B \leftrightarrow \frac{i}{2} \Delta \Gamma_B}{2(M_{12} \leftrightarrow \frac{i}{2} \Gamma_{12})} = \frac{2(M_{12}^* \leftrightarrow \frac{i}{2} \Gamma_{12}^*)}{\Delta m_B \leftrightarrow \frac{i}{2} \Delta \Gamma_B}, \quad (1.15)$$

1.2.2 Phase Conventions

(This section follows the discussion in [9].) The states B^0 and \bar{B}^0 are related through CP transformation:

$$CP|B^0\rangle = e^{2i\xi_B}|\bar{B}^0\rangle, \quad CP|\bar{B}^0\rangle = e^{-2i\xi_B}|B^0\rangle. \quad (1.16)$$

The phase ξ_B is *arbitrary*. The freedom in defining it comes from the fact that flavor conservation (in particular b -flavor) is a symmetry of the strong interactions. A phase transformation,

$$|B_\zeta^0\rangle = e^{-i\zeta}|B^0\rangle, \quad |\bar{B}_\zeta^0\rangle = e^{+i\zeta}|\bar{B}^0\rangle, \quad (1.17)$$

has therefore no physical effects. In the new basis, CP transformations take the form

$$(CP)_\zeta|B_\zeta^0\rangle = e^{2i(\xi_B - \zeta)}|\bar{B}_\zeta^0\rangle, \quad (CP)_\zeta|\bar{B}_\zeta^0\rangle = e^{-2i(\xi_B - \zeta)}|B_\zeta^0\rangle. \quad (1.18)$$

The various quantities discussed in this chapter change with the phase transformation (1.17):

$$M_{12}^\zeta = e^{2i\zeta}M_{12}, \quad \Gamma_{12}^\zeta = e^{2i\zeta}\Gamma_{12}, \quad (q/p)_\zeta = e^{-2i\zeta}(q/p). \quad (1.19)$$

Decay amplitudes, defined by

$$A_f = \langle f|H|B^0\rangle, \quad (1.20)$$

$$\bar{A}_f = \langle f|H|\bar{B}^0\rangle, \quad (1.21)$$

are also affected by the phase transformation (1.17):

$$(A_f)_\zeta = e^{-i\zeta}A_f, \quad (\bar{A}_f)_\zeta = e^{+i\zeta}\bar{A}_f. \quad (1.22)$$

From the transformation of states (1.17), and the transformation of q/p in (1.19), one learns that

$$|B_{L\zeta}\rangle = e^{i\zeta'}|B_L\rangle, \quad |B_{H\zeta}\rangle = e^{i\zeta'}|B_H\rangle, \quad (1.23)$$

namely both mass eigenstates are rotated by a common phase factor, which has no physical significance.

Similar phase freedom exists in defining the CP transformation law for a possible final state f and its CP conjugate $e^{2i\xi_f}\bar{f}$. The quantity ξ_f depends on the flavor content of f and is related to the quark flavor symmetries (c , u , s , d) of the strong interactions.

However, the freedom in defining the phase of the flavor eigenstates (which are defined through strong interactions only) does not mean that the full Lagrangian, which involves also weak interactions, is invariant under such phase redefinitions. Indeed, the differences of flavor redefinition phases appear as changes in the phases of the quark mixing matrix elements and of the Yukawa couplings of quarks to Higgs fields (or any other Lagrangian terms that cause couplings between different flavor eigenstates in more general models). While both (q/p) and A_f acquire overall phase redefinitions when these phase rotations are made, the quantity

$$\lambda = \frac{q \bar{A}_f}{p A_f} \quad (1.24)$$

has a convention-independent phase that has physical significance, as will be seen when the possible types of *CP* violations are examined below.

Another subtle point that has to do with the arbitrariness of the phase ξ_B in the *CP* transformation law (1.16) is the following. If $|q/p| = 1$, it is always possible to choose a *CP* transformation (1.16) such that the mass eigenstates (1.9) and (1.10) are eigenstates of this transformation. Such a definition is, however, not meaningful, because there is no relationship between the so-called *CP* quantum numbers for state with different flavor content. For example, the state B_H can be chosen to be odd under such an appropriately defined transformation, but can decay into a final two-pion state (which is even under the conventionally defined *CP* transformation) even without *CP* violating phases in the decay amplitude.

1.2.3 Time Evolution of Neutral B_d Mesons

The two neutral B_d mesons are expected to have a negligible difference in lifetime,

$$\Delta\Gamma_{B_d}/\Gamma_{B_d} = \mathcal{O}(10^{-2}). \quad (1.25)$$

Note that $\Delta\Gamma_{B_d}$ has not been measured. The difference in width is produced by decay channels common to B^0 and \bar{B}^0 . The branching ratios for such channels are at or below the level of 10^{-3} . As various channels contribute with differing signs, one expects that their sum does not exceed the individual level, hence $\Delta\Gamma_{B_d} \ll \Gamma_{B_d}$ is a rather safe and model-independent assumption [10]. (For B_s^0 mesons the lifetime difference may be significant [11].)

On the other hand, Δm_{B_d} has been measured [12],

$$x_d \equiv \Delta m_{B_d}/\Gamma_{B_d} = 0.73 \pm 0.05. \quad (1.26)$$

From (1.25) and (1.26) one learns that, model-independently,

$$\Delta\Gamma_B \ll \Delta m_B. \quad (1.27)$$

Equations (1.25) and (1.27) imply that, to $\mathcal{O}(10^{-2})$ accuracy, Eqs. (1.13), (1.14) and (1.15) simplify into

$$\Delta m_B = 2|M_{12}|, \quad \Delta \Gamma_B = 2 \mathcal{R}e(M_{12}\Gamma_{12}^*)/|M_{12}|, \quad (1.28)$$

$$q/p = \Leftrightarrow |M_{12}|/M_{12}. \quad (1.29)$$

Any B state can then be written as an admixture of the states B_H and B_L , and the amplitudes of this admixture evolve in time

$$a_H(t) = a_H(0)e^{-iM_H t} e^{-\frac{1}{2}\Gamma_H t}, \quad a_L(t) = a_L(0)e^{-iM_L t} e^{-\frac{1}{2}\Gamma_L t}. \quad (1.30)$$

A state which is created at time $t = 0$ as initially pure B^0 , is denoted $|B_{\text{phys}}^0\rangle$, it has $a_L(0) = a_H(0) = 1/(2p)$. Similarly an initially pure \bar{B}^0 , $|\bar{B}_{\text{phys}}^0\rangle$, has $a_L(0) = \Leftrightarrow a_H(0) = 1/(2q)$. The time evolution of these states is thus given by

$$|B_{\text{phys}}^0(t)\rangle = g_+(t)|B^0\rangle + (q/p)g_-(t)|\bar{B}^0\rangle, \quad (1.31)$$

$$|\bar{B}_{\text{phys}}^0(t)\rangle = (p/q)g_-(t)|B^0\rangle + g_+(t)|\bar{B}^0\rangle, \quad (1.32)$$

where

$$g_+(t) = e^{-iMt} e^{-\Gamma t/2} \cos(\Delta m_B t/2), \quad (1.33)$$

$$g_-(t) = e^{-iMt} e^{-\Gamma t/2} i \sin(\Delta m_B t/2), \quad (1.34)$$

and $M = \frac{1}{2}(M_H + M_L)$.

For some purposes, it is useful to go beyond the leading approximation for $\frac{q}{p}$, the relevant expression is:

$$\frac{q}{p} = \Leftrightarrow \frac{M_{12}^*}{|M_{12}|} \left[1 \Leftrightarrow \frac{1}{2} \mathcal{I}m \left(\frac{\Gamma_{12}}{M_{12}} \right) \right]. \quad (1.35)$$

1.2.4 Two-Time Formalism for Coherent $B\bar{B}$ States

At a B factory, that is an e^+e^- collider operating at the $\Upsilon(4S)$ resonance, the B^0 and \bar{B}^0 mesons produced from the decay of the Υ are in a coherent $L = 1$ state. One way to view this state is that each of the two particles evolve in time as described above for a single B . However they evolve in phase, so that at any time, until one particle decays, there is always exactly one B^0 and one \bar{B}^0 present. (This is yet one more particle physics case of the classic Einstein-Podolsky-Rosen situation.) However once one of the particles decays the other continues to evolve, and thus there are possible events with two B or two \bar{B} decays, whose probability is governed by the time between the two decays.

The two particles from the Upsilon decay are identified by the angle θ that they make with the e^- beam direction in the Upsilon rest frame. Then the two- B state

$$\begin{aligned} S(t_f, t_b) &= \frac{1}{\sqrt{2}} \{ B_{\text{phys}}^0(t_f, \theta, \phi) \bar{B}_{\text{phys}}^0(t_b, \pi \leftrightarrow \theta, \phi + \pi) \\ &\quad \leftrightarrow \bar{B}_{\text{phys}}^0(t_f, \theta, \phi) B_{\text{phys}}^0(t_b, \pi \leftrightarrow \theta, \phi + \pi) \} \sin(\theta) \end{aligned} \quad (1.36)$$

can be written as

$$\begin{aligned} S(t_f, t_b) &= \frac{1}{\sqrt{2}} e^{-(\Gamma/2 + iM)(t_f + t_b)} \{ \cos[\Delta m_B(t_f \leftrightarrow t_b)/2] (B_f^0 \bar{B}_b^0 \leftrightarrow \bar{B}_f^0 B_b^0) \\ &\quad \leftrightarrow i \sin[\Delta m_B(t_f \leftrightarrow t_b)/2] (\frac{q}{p} B_f^0 B_b^0 \leftrightarrow \frac{q}{p} \bar{B}_f^0 \bar{B}_b^0) \} \sin(\theta_f), \end{aligned} \quad (1.37)$$

where t_f is the proper time of the B_f , the B particle in the forward half-space at angle ($\theta_f < \pi/2, \phi_f$) and t_b is the proper time for the backward-moving B_b , at ($\pi \leftrightarrow \theta_f, \phi_f + \pi$). Since the B 's have equal (though back-to-back) momenta in this frame, until such time as one or the other of these particles decays $t_f = t_b$ and Eq. (1.37) contains one B^0 and one \bar{B}^0 . However decay stops the clock for the decayed particle. Then the terms that depend on $\sin[\Delta m_B(t_f \leftrightarrow t_b)/2]$ begin to play a role.

From Eq. (1.37) one can derive the amplitude for decays where one of the two B 's decays to any state f_1 at time t_1 and the other decays to f_2 at time t_2 . One obtains

$$\begin{aligned} A(t_1, t_2) &= \frac{1}{\sqrt{2}} e^{-(\Gamma/2 + iM)(t_1 + t_2)} \zeta(t_1, t_2) \{ \cos[\Delta m_B(t_1 \leftrightarrow t_2)/2] (A_1 \bar{A}_2 \leftrightarrow \bar{A}_1 A_2) \\ &\quad \leftrightarrow i \sin[\Delta m_B(t_1 \leftrightarrow t_2)/2] (\frac{q}{p} A_1 A_2 \leftrightarrow \frac{q}{p} \bar{A}_1 \bar{A}_2) \} \sin(\theta_1), \end{aligned} \quad (1.38)$$

where A_i is the amplitude for a B^0 to decay to the state f_i , \bar{A}_i is the amplitude for a \bar{B}^0 to decay to the *same* state f_i (see Eqs. (1.20) and (1.21)). Any state that identifies the flavor of the parent B ('tagging decays') has either A_f or $\bar{A}_f = 0$. (The fact that $\sin(2\pi \leftrightarrow \theta) = -\sin(\theta)$ is used to write Eq. (1.38) with θ_1 running over angles $(0, \pi)$.) In Eq. (1.38) to keep signs consistent with Eq. (1.37) the shorthand

$$\zeta(t_1, t_2) = \begin{cases} +1 & t_1 = t_f, t_2 = t_b, \\ \leftrightarrow 1 & t_1 = t_b, t_2 = t_f \end{cases} \quad (1.39)$$

is introduced, but this overall sign factor will disappear in the rate.

It is now straightforward to calculate the time-dependent rate for producing the combined final states f_1, f_2 . One finds

$$\begin{aligned} R(t_1, t_2) &= C e^{-\Gamma(t_1 + t_2)} \{ (|A_1|^2 + |\bar{A}_1|^2)(|A_2|^2 + |\bar{A}_2|^2) \leftrightarrow 4 \operatorname{Re}(\frac{q}{p} A_1^* \bar{A}_1) \operatorname{Re}(\frac{q}{p} A_2^* \bar{A}_2) \\ &\quad \leftrightarrow \cos(\Delta m_B(t_1 \leftrightarrow t_2)) [(|A_1|^2 \leftrightarrow |\bar{A}_1|^2)(|A_2|^2 \leftrightarrow |\bar{A}_2|^2) + 4 \operatorname{Im}(\frac{q}{p} A_1^* \bar{A}_1) \operatorname{Im}(\frac{q}{p} A_2^* \bar{A}_2)] \\ &\quad + 2 \sin(\Delta m_B(t_1 \leftrightarrow t_2)) [\operatorname{Im}(\frac{q}{p} A_1^* \bar{A}_1)(|A_2|^2 \leftrightarrow |\bar{A}_2|^2) \leftrightarrow (|A_1|^2 \leftrightarrow |\bar{A}_1|^2) \operatorname{Im}(\frac{q}{p} A_2^* \bar{A}_2)] \}. \end{aligned} \quad (1.40)$$

Here an integral over all directions for either B has been performed, so the angular dependence has dropped out of the expressions, and an overall normalization factor C has appeared. The approximation $|q/p| = 1$ has also been used.

To measure CP asymmetries one looks for events where one B decays to a final CP eigenstate f_{CP} at time t_f , while the second decays to a tagging mode, that is a mode which identifies its b -flavor, at time t_{tag} . For example, take a tagging mode with $A_2 = 0$, $\bar{A}_2 = \bar{A}_{\text{tag}}$. This then identifies the *other* B -particle as a B^0 at time $t_2 = t_{\text{tag}}$ at which the tag decay occurs. Note that this is true even when the tag decay occurs after the CP eigenstate decay. In this case the state of the other B at any time $t_f < t_{\text{tag}}$ must be just that mixture that, if it had not decayed, would have evolved to become a B^0 at time $t_f = t_{\text{tag}}$. The double time expression reduces to the form

$$R(t_{\text{tag}}, t_{f_{CP}}) = C e^{-\Gamma(t_{\text{tag}} + t_{f_{CP}})} |\bar{A}_{\text{tag}}|^2 |A_{f_{CP}}|^2 \{1 + |\lambda_{f_{CP}}|^2 + \cos[\Delta m_B(t_{f_{CP}} \leftrightarrow t_{\text{tag}})](1 \leftrightarrow |\lambda_{f_{CP}}|^2) \leftrightarrow 2 \sin[\Delta m_B(t_{f_{CP}} \leftrightarrow t_{\text{tag}})] \mathcal{I}m(\lambda_{f_{CP}})\} \quad (1.41)$$

where

$$\lambda_{f_{CP}} \equiv \frac{q \bar{A}_{f_{CP}}}{p A_{f_{CP}}} = \eta_{f_{CP}} \frac{q \bar{A}_{\bar{f}_{CP}}}{p A_{f_{CP}}}. \quad (1.42)$$

The second form for $\lambda_{f_{CP}}$ here uses the property

$$\bar{A}_{f_{CP}} = \eta_{f_{CP}} \bar{A}_{\bar{f}_{CP}}, \quad (1.43)$$

where $\eta_{f_{CP}}$ is the CP eigenvalue of the state f_{CP} . The amplitudes $A_{f_{CP}}$ and $\bar{A}_{\bar{f}_{CP}}$ are related by CP and differ only in the signs of the weak phase for each term, while $\eta_{f_{CP}} = \pm 1$, so the second form is useful in calculating the expected asymmetries, and explains the extra minus sign that appears for a CP odd final state.

For the case where the tag final state has $\bar{A}_2 = 0$, $A_2 = A_{\text{tag}}$, which identifies the second particle as a \bar{B} at time t_{tag} , an expression similar to Eq. (1.41) applies, except that the signs of both the cosine and the sine terms are reversed. The fact that $|q/p| = 1$ means that the amplitudes for the two opposite tags are the same. Thus the difference of these rates divided by their sum, which measures the time-dependent CP asymmetry[13], is given by

$$a_{f_{CP}} = \frac{(1 \leftrightarrow |\lambda_{f_{CP}}|^2) \cos(\Delta m_B t) \leftrightarrow 2 \mathcal{I}m \lambda_{f_{CP}} \sin(\Delta m_B t)}{1 + |\lambda_{f_{CP}}|^2}, \quad (1.44)$$

where $t = t_{f_{CP}} \leftrightarrow t_{\text{tag}}$.

It is useful to note that the above expressions can be integrated over the variable $(t_1 + t_2)$, which for $t_1 \geq 0$ and $t_2 \geq 0$ can take values between $|t_1 \leftrightarrow t_2|$ and infinity. Thus one can fit the dependence on the variable $t_1 \leftrightarrow t_2$ without having to measure the Υ decay time. The fact that the variable $t_1 \leftrightarrow t_2$ can be related to the distance between the locations of the two decays is of course the prime reason for building an energy-asymmetric collider for the B factory. If one had to integrate over

this variable as well all information on the coefficient of $\sin(\Delta m_B(t_1 \leftrightarrow t_2))$ would be lost in the above expressions, and the experiment would be sensitive only to those *CP*-violating effects that give $|\lambda| \neq 1$. (Note that this is a consequence of the coherent production of the two B states, in a hadronic environment, where the B 's are produced incoherently, time-integrated rates are always integrals from $t = 0$ to infinity and hence retain information about the $\sin(\Delta m_B t)$ behavior.)

1.3 The Three Types of *CP* Violation in B Decays

The possible manifestations of *CP* violation can be classified in a model-independent way:

1. *CP* violation in decay, which occurs in both charged and neutral decays, when the amplitude for a decay and its *CP* conjugate process have different magnitudes;
2. *CP* violation in mixing, which occurs when the two neutral mass eigenstates cannot be chosen to be *CP* eigenstates;
3. *CP* violation in the interference between decays with and without mixing, which occurs in decays into final states that are common to B^0 and \bar{B}^0 . (It often occurs in combination with the other two types but, important for BABAR, there are cases when, to an excellent approximation, it is the only effect.)

In each case it is useful to identify a particular *CP*-violating quantity that is independent of phase conventions and discuss the types of processes that depend on this quantity.

1.3.1 *CP* Violation in Decay

For any final state f , the quantity $|\frac{\bar{A}_f}{A_f}|$ is independent of phase conventions and physically meaningful. There are two types of phases that may appear in A_f and \bar{A}_f .

Complex parameters in any Lagrangian term that contributes to the amplitude will appear in complex conjugate form in the *CP* conjugate amplitude. Thus their phases appear in A_f and \bar{A}_f with opposite signs. In the Standard Model these phases occur only in the CKM matrix which is part of the electroweak sector of the theory, hence these are often called “weak phases.” The weak phase of any single term is convention dependent. However the difference between the weak phases in two different terms in A_f is convention independent; the initial and final states are the same for every term and thus any phase rotation of the fields that appear in these states will affect all terms in the same way.

A second type of phase can appear in scattering or decay amplitudes even when the Lagrangian is real. Such phases do not violate CP , since they appear in A_f and $\bar{A}_{\bar{f}}$ with the same sign. Their origin is the possible contribution from intermediate on-shell states in the decay process, that is an absorptive part of an amplitude that has contributions from coupled channels. Usually the dominant rescattering is due to strong interactions, hence the designation “strong phases” for the phase shifts so induced. Again only the relative strong phases of different terms in a scattering amplitude have physical content, an overall phase rotation of the entire amplitude has no physical consequences.

Thus it is useful to write each contribution to A in three parts: its magnitude A_i , its weak-phase term $e^{i\phi_i}$, and its strong phase term $e^{i\delta_i}$. Then, if several amplitudes contribute to $B^0 \rightarrow f$, the amplitude A_f (see (1.20)) and the CP conjugate amplitude $\bar{A}_{\bar{f}}$ (see (1.21)) are given by:

$$A_f = \sum_i A_i e^{i(\delta_i + \phi_i)}, \quad \bar{A}_{\bar{f}} = e^{2i(\xi_f - \xi_B)} \sum_i A_i e^{i(\delta_i - \phi_i)}, \quad (1.45)$$

where ξ_f and ξ_B are defined in 1.2.2. (If f is a CP eigenstate then $e^{2i\xi_f} = \pm 1$ is its CP eigenvalue.) The convention-independent quantity is then

$$\left| \frac{\bar{A}_{\bar{f}}}{A_f} \right| = \left| \frac{\sum_i A_i e^{i(\delta_i - \phi_i)}}{\sum_i A_i e^{i(\delta_i + \phi_i)}} \right|. \quad (1.46)$$

When CP is conserved, the weak phases ϕ_i are all equal. Therefore, from Eq. (1.46) one sees that

$$|\bar{A}_{\bar{f}}/A_f| \neq 1 \implies CP \text{ violation}. \quad (1.47)$$

This type of CP violation is here called *CP violation in decay*. It is often also called *direct CP violation*. It results from the CP -violating interference among various terms in the decay amplitude. From Eq. (1.46) it can be seen that a CP violation of this type will not occur unless at least two terms that have different weak phases acquire different strong phases, since:

$$|A|^2 \Leftrightarrow |\bar{A}|^2 = \Leftrightarrow 2 \sum_{i,j} A_i A_j \sin(\phi_i \Leftrightarrow \phi_j) \sin(\delta_i \Leftrightarrow \delta_j). \quad (1.48)$$

Any CP asymmetries in charged B decays,

$$a_f = \frac{\Gamma(B^+ \rightarrow f) \Leftrightarrow \Gamma(B^- \rightarrow \bar{f})}{\Gamma(B^+ \rightarrow f) + \Gamma(B^- \rightarrow \bar{f})}, \quad (1.49)$$

are from CP violation in decay. In terms of the decay amplitudes

$$a_f = \frac{1 \Leftrightarrow |\bar{A}/A|^2}{1 + |\bar{A}/A|^2}. \quad (1.50)$$

CP violation in decays can also occur for neutral meson decays, where it competes with the other two types of CP violation effects described below. There is as yet no unambiguous experimental

evidence for *CP* violation in decays. (As explained in 1.6.3, a measurement of $\text{Re } \varepsilon'_K \neq 0$ would constitute such evidence.)

The magnitude and strong phase of any amplitude involve long distance strong interaction physics, and cannot be calculated from first principles. Thus quantities that depend only on the weak phases are much cleaner than those that require knowledge of the relative magnitudes or strong phases of various amplitude contributions. There is however a large literature and considerable theoretical effort that goes into the calculation of amplitudes and strong phases. In many cases one can only relate experiment to Standard Model parameters through such calculations. The techniques that are used are expected to be more accurate for *B* decays than for *K* decays because of the larger *B* mass, but theoretical uncertainty remains significant. The calculations generally contain two parts. First, the operator product expansion and QCD perturbation theory are used to write any underlying quark process as a sum of local quark operators with well-determined coefficients. Second, the matrix elements of the operators between the initial and final hadron states must be calculated. This is where the theory is weakest and the results most model dependent. Ideally lattice calculations should be able to provide accurate determinations for the matrix elements, and in certain cases this is already true, but much remains to be done. In the following chapter an overview of the principal methods used in such calculations is given. Further details on the status of various theoretical approaches are presented in relevant chapters and in the appendices.

1.3.2 *CP* Violation in Mixing

A second quantity that is independent of phase conventions and physically meaningful is

$$\left| \frac{q}{p} \right|^2 = \left| \frac{M_{12}^* \Leftrightarrow \frac{i}{2} \Gamma_{12}^*}{M_{12} \Leftrightarrow \frac{i}{2} \Gamma_{12}} \right|. \quad (1.51)$$

When *CP* is conserved, the mass eigenstates must be *CP* eigenstates. In that case the relative phase between M_{12} and Γ_{12} vanishes. Therefore, Eq. (1.51) implies

$$|q/p| \neq 1 \implies \text{CP violation.} \quad (1.52)$$

This type of *CP* violation is here called *CP violation in mixing*; it is often referred to as *indirect CP violation*. It results from the mass eigenstates being different from the *CP* eigenstates. *CP* violation in mixing has been observed unambiguously in the neutral kaon system.

For the neutral *B* system, this effect could be observed through the asymmetries in semileptonic decays:

$$a_{\text{sl}} = \frac{\Gamma(\overline{B}_{\text{phys}}^0(t) \rightarrow \ell^+ \nu X) \Leftrightarrow \Gamma(B_{\text{phys}}^0(t) \rightarrow \ell^- \nu X)}{\Gamma(\overline{B}_{\text{phys}}^0(t) \rightarrow \ell^+ \nu X) + \Gamma(B_{\text{phys}}^0(t) \rightarrow \ell^- \nu X)}. \quad (1.53)$$

In terms of $|q/p|$,

$$a_{\text{sl}} = \frac{1 \Leftrightarrow |q/p|^4}{1 + |q/p|^4}, \quad (1.54)$$

which follows from

$$\langle \ell^- \nu X | H | B_{\text{phys}}^0(t) \rangle = (q/p) g_-(t) A^*, \quad \langle \ell^+ \nu X | H | \overline{B}_{\text{phys}}^0(t) \rangle = (p/q) g_-(t) A. \quad (1.55)$$

As can be seen from the discussion in Section 1.2.3, effects of CP violation in mixing in neutral B_d decays, such as the asymmetries in semileptonic decays, are expected to be small, $\mathcal{O}(10^{-2})$. Moreover, to calculate the deviation of q/p from a pure phase, one needs to calculate Γ_{12} and M_{12} . This involves large hadronic uncertainties, in particular in the hadronization models for Γ_{12} . The overall uncertainty is easily a factor of 2–3 in $|q/p| \Leftrightarrow 1$ [10]. Thus even if such asymmetries are observed, it will be difficult to relate their rates to fundamental CKM parameters.

1.3.3 CP Violation in the Interference Between Decays With and Without Mixing

Finally, consider neutral B decays into final CP eigenstates, f_{CP} [14, 15, 16]. Such states are accessible in both B^0 and \overline{B}^0 decays. The quantity of interest here that is independent of phase conventions and physically meaningful is λ of Eq. (1.42), $\lambda = \eta_{f_{CP}} \frac{q}{p} \frac{\overline{A}_{f_{CP}}}{A_{f_{CP}}}$. When CP is conserved, $|q/p| = 1$, $|\overline{A}_{f_{CP}}/A_{f_{CP}}| = 1$, and furthermore, the relative phase between (q/p) and $(\overline{A}_{f_{CP}}/A_{f_{CP}})$ vanishes. Therefore, Eq. (1.42) implies

$$\lambda \neq \pm 1 \implies CP \text{ violation.} \quad (1.56)$$

Note that both CP violation in decay (1.47) and CP violation in mixing (1.52) lead to (1.56) through $|\lambda| \neq 1$. However, it is possible that, to a good approximation, $|q/p| = 1$ and $|\overline{A}/A| = 1$, yet there is CP violation:

$$|\lambda| = 1, \quad \text{Im } \lambda \neq 0. \quad (1.57)$$

This type of CP violation is called *CP violation in the interference between decays with and without mixing* here; sometimes this is abbreviated as “interference between mixing and decay.” As explained in Section 1.6, this type of CP violation has also been observed in the neutral kaon system.

For the neutral B system, CP violation in the interference between decays with and without mixing can be observed by comparing decays into final CP eigenstates of a time-evolving neutral B state that begins at time zero as B^0 to those of the state that begins as a \overline{B}^0 :

$$a_{f_{CP}} = \frac{\Gamma(B_{\text{phys}}^0(t) \rightarrow f_{CP}) \Leftrightarrow \Gamma(\overline{B}_{\text{phys}}^0(t) \rightarrow f_{CP})}{\Gamma(B_{\text{phys}}^0(t) \rightarrow f_{CP}) + \Gamma(\overline{B}_{\text{phys}}^0(t) \rightarrow f_{CP})}. \quad (1.58)$$

It was shown above (1.44) that this time-dependent asymmetry is given by:

$$a_{f_{CP}} = \frac{(1 \Leftrightarrow |\lambda_{f_{CP}}|^2) \cos(\Delta m_B t) \Leftrightarrow 2 \Im \lambda_{f_{CP}} \sin(\Delta m_B t)}{1 + |\lambda_{f_{CP}}|^2}. \quad (1.59)$$

This asymmetry will be non-vanishing if any of the three types of *CP* violation are present. However, for decays such that $|\lambda| = 1$ (the ‘clean’ modes — see below), (1.44) simplifies considerably:

$$a_{f_{CP}} = \Leftrightarrow \Im \lambda_{f_{CP}} \sin(\Delta m_B t). \quad (1.60)$$

One point concerning this type of asymmetries is worth clarifying. Consider the decay amplitudes of B^0 into two different final *CP* eigenstates, A_a and A_b . A non-vanishing difference between $\eta_a \lambda_a$ and $\eta_b \lambda_b$,

$$\eta_a \lambda_a \Leftrightarrow \eta_b \lambda_b = \frac{q}{p} \left(\frac{\bar{A}_a}{A_a} \Leftrightarrow \frac{\bar{A}_b}{A_b} \right) \neq 0, \quad (1.61)$$

would establish the existence of *CP* violation in $\Delta b = 1$ processes. For this reason, this type of *CP* violation is also called sometimes “direct *CP* violation.” Yet, unlike the case of *CP* violation in decay, no nontrivial strong phases are necessary. The richness of possible final *CP* eigenstates in B decays makes it very likely that various asymmetries will exhibit (1.61). (A measurement of $\mathcal{B}(K_L \rightarrow \pi \nu \bar{\nu}) \gtrsim 10^{-11}$ can establish the existence [17, 18, 19] of a similar effect, a $\Delta s = 1$ *CP* violation that does not depend on strong phase shifts.) Either this type of observation or the observation of *CP* violation in decay would rule out superweak models for *CP* violation.

CP violation in the interference between decays with and without mixing can be cleanly related to Lagrangian parameters when it occurs with no *CP* violation in decay. In particular, for B_d decays that are dominated by a single *CP*-violating phase, so that the effect of *CP* violation in decay is negligible, $a_{f_{CP}}$ is cleanly translated into a value for $\Im \lambda$ (see (1.60)) which, in turn, is cleanly interpreted in terms of purely electroweak Lagrangian parameters. (As discussed below, $\Im \varepsilon_K$ which describes *CP* violation in the interference between decays with and without mixing in the K system, is cleanly translated into a value of ϕ_{12} , the phase between $M_{12}(K)$ and $\Gamma_{12}(K)$. It is difficult, however, to interpret ϕ_{12} cleanly in terms of electroweak Lagrangian parameters.)

When there is *CP* violation in decay at the same time as in the interference between decays with and without mixing, the asymmetry (1.58) depends also on the ratio of the different amplitudes and their relative strong phases, and thus the prediction has hadronic uncertainties. In some cases, however, it is possible to remove any large hadronic uncertainties by measuring several isospin-related rates (see *e.g.*, [20, 21, 22]) and thereby extract a clean measurement of CKM phases. This is discussed in further detail in Chapters 5 and particularly 6.

There are also many final states for B decay that have *CP* self-conjugate particle content but are not *CP* eigenstates because they contain admixtures of different angular momenta and hence different parities. In certain cases angular analyses of the final state can be used to determine the amplitudes for each different *CP* contribution separately. Such final states can then also be used for clean comparison with theoretical models [23]. This is discussed in more detail in Chapter 5.

1.4 CP Violation in the Standard Model

1.4.1 The CKM Picture of CP Violation

In the Standard Model (SM) [24] of $SU(3)_C \times SU(2)_L \times U(1)_Y$ gauge symmetry with three fermion generations, CP violation arises from a single phase in the mixing matrix for quarks [3]. Each quark generation consists of three multiplets:

$$Q_L^I = \begin{pmatrix} U_L^I \\ D_L^I \end{pmatrix} = (3, 2)_{+1/6}, \quad u_R^I = (3, 1)_{+2/3}, \quad d_R^I = (3, 1)_{-1/3}, \quad (1.62)$$

where $(3, 2)_{+1/6}$ denotes a triplet of $SU(3)_C$, doublet of $SU(2)_L$ with hypercharge $Y = Q \Leftrightarrow T_3 = +1/6$, and similarly for the other representations. The interactions of quarks with the $SU(2)_L$ gauge bosons are given by

$$\mathcal{L}_W = \Leftrightarrow \frac{1}{2} g \overline{Q_{Li}^I} \gamma^\mu \tau^a \mathbf{1}_{ij} Q_{Lj}^I W_\mu^a, \quad (1.63)$$

where γ^μ operates in Lorentz space, τ^a operates in $SU(2)_L$ space and $\mathbf{1}$ is the unit matrix operating in generation (flavor) space. This unit matrix is written explicitly to make the transformation to mass eigenbasis clearer. The interactions of quarks with the single Higgs scalar doublet $\phi(1, 2)_{+1/2}$ of the Standard Model are given by

$$\mathcal{L}_Y = \Leftrightarrow G_{ij} \overline{Q_{Li}^I} \phi_{Rj}^I \Leftrightarrow F_{ij} \overline{Q_{Li}^I} \tilde{\phi} u_{Rj}^I + \text{Hermitian conjugate}, \quad (1.64)$$

where G and F are general *complex* 3×3 matrices. Their complex nature is the source of CP violation in the Standard Model. With the spontaneous symmetry breaking, $SU(2)_L \times U(1)_Y \rightarrow U(1)_{\text{EM}}$ due to $\langle \phi \rangle \neq 0$, the two components of the quark doublet become distinguishable, as are the three members of the W^μ triplet. The charged current interaction in (1.63) is given by

$$\mathcal{L}_W = \Leftrightarrow \sqrt{\frac{1}{2}} g u_{Li}^I \gamma^\mu \mathbf{1}_{ij} d_{Lj}^I W_\mu^+ + \text{h.c.} \quad (1.65)$$

The mass terms that arise from the replacement $\mathcal{R}e(\phi^0) \rightarrow \sqrt{\frac{1}{2}}(v + H^0)$ in (1.64) are given by

$$\mathcal{L}_M = \Leftrightarrow \sqrt{\frac{1}{2}} v G_{ij} \overline{d_{Li}^I} d_{Rj}^I \Leftrightarrow \sqrt{\frac{1}{2}} v F_{ij} \overline{u_{Li}^I} u_{Rj}^I + \text{Hermitian conjugate}, \quad (1.66)$$

namely

$$M_d = Gv/\sqrt{2}, \quad M_u = Fv/\sqrt{2}. \quad (1.67)$$

The phase information is now contained in these mass matrices. To transform to the mass eigenbasis, one defines four unitary matrices such that

$$V_{dL} M_d V_{dR}^\dagger = M_d^{\text{diag}}, \quad V_{uL} M_u V_{uR}^\dagger = M_u^{\text{diag}}, \quad (1.68)$$

where M_q^{diag} are diagonal and real, while V_{qL} and V_{qR} are complex. The charged current interactions (1.65) are given in the mass eigenbasis by

$$\mathcal{L}_W = \Leftrightarrow \sqrt{\frac{1}{2}} g \overline{u_{Li}} \gamma^\mu \overline{V}_{ij} d_{Lj} W_\mu^+ + \text{h.c.} \quad (1.69)$$

(Quark fields with no superscript denote mass eigenbasis.) The matrix $\overline{V} = V_{uL} V_{dL}^\dagger$ is the (unitary) mixing matrix for three quark generations. As such, it generally depends on nine parameters: three can be chosen as real angles (like the Cabibbo angle) and six are phases. However, one may reduce the number of phases in \overline{V} by a transformation

$$\overline{V} \implies V = P_u \overline{V} P_d^*, \quad (1.70)$$

where P_u and P_d are diagonal phase matrices. This is a legitimate transformation because it amounts to redefining the phases of the quark-mass-eigenstate fields, as was discussed earlier:

$$q_{Li} \rightarrow (P_q)_{ii} q_{Li}, \quad q_{Ri} \rightarrow (P_q)_{ii} q_{Ri}, \quad (1.71)$$

which does not change the real diagonal mass matrix M_q^{diag} . The five phase differences among the elements of P_u and P_d can be chosen so that the transformation (1.70) eliminates five of the six independent phases from \overline{V} ; thus V has one irremovable phase. This phase is called the Kobayashi-Maskawa phase [3], δ_{KM} , and the mixing matrix is called the Cabibbo-Kobayashi-Maskawa (CKM) matrix [2]. It is interesting to note that the same procedure applied to a two-generation Standard Model Lagrangian with a single Higgs field would remove all *CP*-violating phases — that theory could not accommodate *CP* violation without the addition of extra fields. It was this observation that led Kobayashi and Maskawa to suggest a third quark generation long before there was any experimental evidence for it.

The irremovable phase in the CKM matrix allows possible *CP* violation. To see this, recall the *CP* transformation laws (1.4) and (1.5),

$$\overline{\psi}_i \psi_j \rightarrow \overline{\psi}_j \psi_i, \quad \overline{\psi}_i \gamma^\mu W_\mu (1 \Leftrightarrow \gamma_5) \psi_j \rightarrow \overline{\psi}_j \gamma^\mu W_\mu (1 \Leftrightarrow \gamma_5) \psi_i. \quad (1.72)$$

Thus the mass terms and gauge interactions are obviously *CP*invariant if all the masses and couplings are all real. In particular, consider the coupling of W^\pm to quarks. It has the form

$$g V_{ij} \overline{u}_i \gamma_\mu W^{+\mu} (1 \Leftrightarrow \gamma_5) d_j + g V_{ij}^* \overline{d}_j \gamma_\mu W^{-\mu} (1 \Leftrightarrow \gamma_5) u_i. \quad (1.73)$$

The *CP* operation interchanges the two terms except that V_{ij} and V_{ij}^* are not interchanged. Thus, *CP* is a good symmetry only if there is a mass basis and choice of phase convention where all couplings and masses are real.

CP is not necessarily violated in the three generation Standard Model. If two quarks of the same charge had equal masses, one mixing angle and the phase could be removed from V . This can be written as a condition on quark mass differences: *CP* violation requires

$$(m_t^2 \Leftrightarrow m_c^2)(m_c^2 \Leftrightarrow m_u^2)(m_t^2 \Leftrightarrow m_u^2)(m_b^2 \Leftrightarrow m_s^2)(m_s^2 \Leftrightarrow m_d^2)(m_b^2 \Leftrightarrow m_d^2) \neq 0. \quad (1.74)$$

(The squared masses appear here because the sign of a fermion mass term is not physical.) Likewise, if the value of any of the three mixing angles were 0 or $\pi/2$, then the phase could be removed. Finally, *CP* would not be violated if the value of the single phase were 0 or π . These last eight conditions are elegantly incorporated into one, parameterization-independent, condition [25]. To find this condition, note that unitarity of the CKM matrix, $VV^\dagger = \mathbf{1}$, requires that for any choice of $i, j, k, l = 1, 2, 3$

$$\mathcal{I}m[V_{ij}V_{kl}V_{il}^*V_{kj}^*] = J \sum_{m,n=1}^3 \epsilon_{ikm}\epsilon_{jln}. \quad (1.75)$$

Then, the conditions on the mixing parameters are summarized by

$$J \neq 0. \quad (1.76)$$

The fourteen conditions incorporated in (1.74) and (1.76) can all be written as a single requirement of the mass matrices in the interaction basis [25]:

$$\mathcal{I}m\{\det[M_d M_d^\dagger, M_u M_u^\dagger]\} \neq 0 \Leftrightarrow \textit{CP} \text{ violation}. \quad (1.77)$$

This is a convention-independent condition. The quantity J is of much interest in the study of *CP* violation from the CKM matrix. The maximum value that J could in principle assume is $1/(6\sqrt{3}) \approx 0.1$, but it is found to be $\lesssim 4 \times 10^{-5}$, providing a concrete meaning to the notion that *CP* violation in the Standard Model is small.

The fact that the three generation Standard Model with a single Higgs multiplet contains only a single independent *CP*-violating phase makes the possible *CP*-violating effects in this theory all very closely related. It is this that makes the pattern of *CP* violations in *B* decays strongly constrained in this model. The goal of the *B* factory is to test whether this pattern occurs.

1.4.2 Unitarity of the CKM Matrix

The unitarity of the CKM matrix is manifest using an explicit parameterization. There are various useful ways to parameterize it, but the standard choice is the following [26]:

$$V = \begin{pmatrix} c_{12}c_{13} & s_{12}c_{13} & s_{13}e^{-i\delta} \\ \Leftrightarrow s_{12}c_{23} \Leftrightarrow c_{12}s_{23}s_{13}e^{i\delta} & c_{12}c_{23} \Leftrightarrow s_{12}s_{23}s_{13}e^{i\delta} & s_{23}c_{13} \\ s_{12}s_{23} \Leftrightarrow c_{12}c_{23}s_{13}e^{i\delta} & \Leftrightarrow c_{12}s_{23} \Leftrightarrow s_{12}c_{23}s_{13}e^{i\delta} & c_{23}c_{13} \end{pmatrix}, \quad (1.78)$$

where $c_{ij} \equiv \cos \theta_{ij}$ and $s_{ij} \equiv \sin \theta_{ij}$. In this parameterization

$$J = c_{12}c_{23}c_{13}^2 s_{12}s_{23}s_{13} \sin \delta. \quad (1.79)$$

This shows explicitly the requirement that all mixing angles are different from 0, $\pi/2$ and $\delta \neq 0, \pi$.

The unitarity of the CKM matrix implies various relations among its elements. A full list of these relations can be found in Ref. [8]. Three of them are very useful for understanding the Standard Model predictions for *CP* violation:

$$V_{ud}V_{us}^* + V_{cd}V_{cs}^* + V_{td}V_{ts}^* = 0, \quad (1.80)$$

$$V_{us}V_{ub}^* + V_{cs}V_{cb}^* + V_{ts}V_{tb}^* = 0, \quad (1.81)$$

$$V_{ud}V_{ub}^* + V_{cd}V_{cb}^* + V_{td}V_{tb}^* = 0. \quad (1.82)$$

Each of these three relations requires the sum of three complex quantities to vanish and so can be geometrically represented in the complex plane as a triangle. These are “the unitarity triangles.” Note that the term “Unitarity Triangle” is reserved for the relation (1.82) only (for reasons soon to be understood).

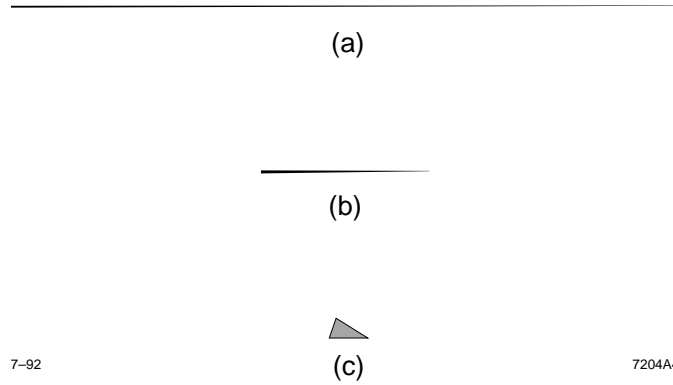


Figure 1-1. The three unitarity triangles a) $V_{ud}V_{us}^* = 0$, b) $V_{us}V_{ub}^* = 0$, and c) $V_{ud}V_{ub}^* = 0$, drawn to a common scale.

It is instructive to draw the three triangles, knowing the experimental values (within errors) for the various $|V_{ij}|$. This is done in Fig. 1-1. In the first two triangles, one side is much shorter than the other two, and so they almost collapse to a line. This would give an intuitive understanding of why *CP* violation is small in the leading *K* decays (the first triangle) and in the leading *B_s* decays (the second triangle). Decays related to the short sides of these triangles (for example, $K_L \rightarrow \pi\nu\bar{\nu}$) are rare but could exhibit significant *CP* violation. The most exciting physics of *CP* violation lies in the *B* system, related to the third triangle. The openness of this triangle predicts large *CP* asymmetries in *B* decays.

Equation (1.75) has striking implications for the unitarity triangles:

1. All unitarity triangles are equal in area.
2. The area of each unitarity triangle equals $|J|/2$.
3. The sign of *J* gives the direction of the complex vectors.

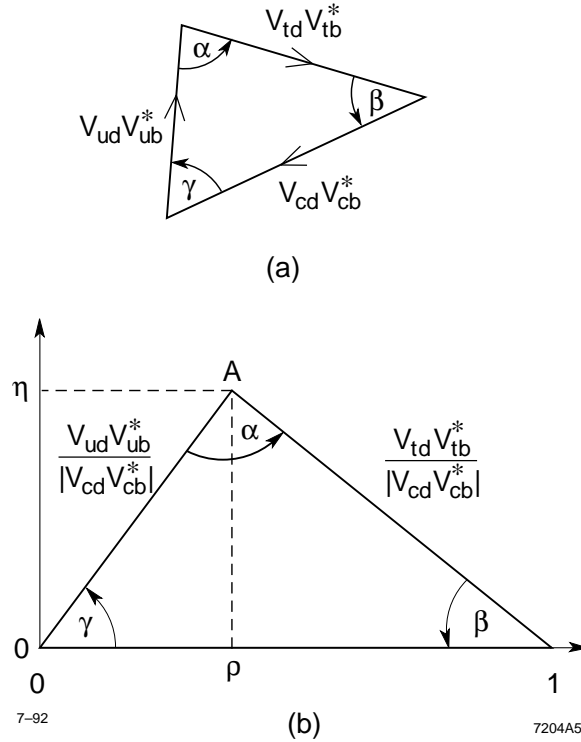


Figure 1-2. The rescaled Unitarity Triangle, all sides divided by $V_{cb}^*V_{cd}$.

The rescaled Unitarity Triangle (Fig. 1-2) is derived from (1.82) by (a) choosing a phase convention such that $(V_{cd}V_{cb}^*)$ is real, and (b) dividing the lengths of all sides by $|V_{cd}V_{cb}^*|$; (a) aligns one side of the triangle with the real axis, and (b) makes the length of this side 1. The form of the triangle is unchanged. Two vertices of the rescaled Unitarity Triangle are thus fixed at $(0,0)$ and $(1,0)$. The coordinates of the remaining vertex are denoted by (ρ, η) . It is customary these days to express the CKM-matrix in terms of four Wolfenstein parameters (λ, A, ρ, η) with $\lambda = |V_{us}| = 0.22$ playing the role of an expansion parameter and η representing the CP -violating phase [27]:

$$V = \begin{pmatrix} 1 \Leftrightarrow \frac{\lambda^2}{2} & \lambda & A\lambda^3(\rho \Leftrightarrow i\eta) \\ \Leftrightarrow \lambda & 1 \Leftrightarrow \frac{\lambda^2}{2} & A\lambda^2 \\ A\lambda^3(1 \Leftrightarrow \rho \Leftrightarrow i\eta) & \Leftrightarrow A\lambda^2 & 1 \end{pmatrix} + \mathcal{O}(\lambda^4). \quad (1.83)$$

λ is small, and for each element in V , the expansion parameter is actually λ^2 . Hence it is sufficient to keep only the first few terms in this expansion. The relation between the parameters of (1.78) and (1.83) is given by

$$s_{12} \equiv \lambda, \quad s_{23} \equiv A\lambda^2, \quad s_{13}e^{-i\delta} \equiv A\lambda^3(\rho \Leftrightarrow i\eta). \quad (1.84)$$

This specifies the higher order terms in (1.83).

The definition of (λ, A, ρ, η) given in (1.84) is useful because it allows an elegant improvement of the accuracy of the original Wolfenstein parameterization. In particular, up to $O(\lambda^6)$ corrections,

$$V_{us} = \lambda, \quad V_{cb} = A\lambda^2, \quad V_{ub} = A\lambda^3(\rho \Leftrightarrow i\eta), \quad (1.85)$$

$$V_{td} = A\lambda^3(1 \Leftrightarrow \bar{\rho} \Leftrightarrow i\bar{\eta}), \quad (1.86)$$

$$\mathcal{I}m V_{cd} = \Leftrightarrow A^2 \lambda^5 \eta, \quad \mathcal{I}m V_{ts} = \Leftrightarrow A\lambda^4 \eta, \quad (1.87)$$

where

$$\bar{\rho} = \rho(1 \Leftrightarrow \lambda^2/2), \quad \bar{\eta} = \eta(1 \Leftrightarrow \lambda^2/2). \quad (1.88)$$

These are excellent approximations to the exact expressions [28]. Depicting the rescaled Unitarity Triangle in the $(\bar{\rho}, \bar{\eta})$ plane, the lengths of the two complex sides are

$$R_b \equiv \sqrt{\bar{\rho}^2 + \bar{\eta}^2} = \frac{1 \Leftrightarrow \lambda^2/2}{\lambda} \left| \frac{V_{ub}}{V_{cb}} \right|, \quad R_t \equiv \sqrt{(1 \Leftrightarrow \bar{\rho})^2 + \bar{\eta}^2} = \frac{1}{\lambda} \left| \frac{V_{td}}{V_{cb}} \right|. \quad (1.89)$$

The three angles of the Unitarity Triangle are denoted by α, β and γ [29]:

$$\alpha \equiv \arg \left[\Leftrightarrow \frac{V_{td}V_{tb}^*}{V_{ud}V_{ub}^*} \right], \quad \beta \equiv \arg \left[\Leftrightarrow \frac{V_{cd}V_{cb}^*}{V_{td}V_{tb}^*} \right], \quad (1.90)$$

The third angle is then

$$\gamma \equiv \arg \left[\Leftrightarrow \frac{V_{ud}V_{ub}^*}{V_{cd}V_{cb}^*} \right] \equiv \pi \Leftrightarrow \alpha \Leftrightarrow \beta. \quad (1.91)$$

These are physical quantities and, as discussed below, can be measured by *CP* asymmetries in various *B* decays. The consistency of the various measurements provide tests of the Standard Model.

The angle β gives, to a good approximation, the Standard Model phase between the neutral *B* mixing amplitude and its leading decay amplitudes. It is interesting to define the analog phases for the *B_s* meson, β_s , and the *K* meson, β_K :

$$\beta_s \equiv \arg \left[\Leftrightarrow \frac{V_{ts}V_{tb}^*}{V_{cs}V_{cb}^*} \right], \quad \beta_K \equiv \arg \left[\Leftrightarrow \frac{V_{cs}V_{cd}^*}{V_{us}V_{ud}^*} \right]. \quad (1.92)$$

The angles β_s and β_K can be seen to be the small angles of the second and first unitarity triangles, (1.81) and (1.80), respectively.

It is straightforward to express the angles of the triangle in terms of $\bar{\rho}$ and $\bar{\eta}$. For example, the following two relations are useful:

$$\sin 2\alpha = \frac{2\bar{\eta}[\bar{\eta}^2 + \bar{\rho}(\bar{\rho} \Leftrightarrow 1)]}{[\bar{\eta}^2 + (1 \Leftrightarrow \bar{\rho})^2][\bar{\eta}^2 + \bar{\rho}^2]}, \quad \sin 2\beta = \frac{2\bar{\eta}(1 \Leftrightarrow \bar{\rho})}{\bar{\eta}^2 + (1 \Leftrightarrow \bar{\rho})^2}. \quad (1.93)$$

Note that unitarity is a fundamental property of any field theory. When one speaks of testing the unitarity of the CKM matrix one is not looking for violations of unitarity, but for violations of the consequences of unitarity in the three generation theory. Such violations would simply imply the presence of other channels, particles not included in the Standard Model theory, contributing in some way to the decays under study. To call these effects “unitarity violations” is perhaps misleading, but it is the common terminology of the field.

1.4.3 Measuring CKM Parameters with *CP*-Conserving Processes

Six of the nine absolute values of the CKM entries are measured directly, namely by tree-level processes. (All numbers below are taken from [12].) Nuclear beta decays give

$$|V_{ud}| = 0.9736 \pm 0.0010. \quad (1.94)$$

Semileptonic kaon and hyperon decays give

$$|V_{us}| = 0.2205 \pm 0.0018. \quad (1.95)$$

Neutrino and antineutrino production of charm off valence *d* quarks give

$$|V_{cd}| = 0.224 \pm 0.016. \quad (1.96)$$

Semileptonic *D* decays give

$$|V_{cs}| = 1.01 \pm 0.18 \quad (1.97)$$

Semileptonic exclusive and inclusive *B* decays give

$$|V_{cb}| = 0.041 \pm 0.003. \quad (1.98)$$

The endpoint spectrum in semileptonic *B* decays gives

$$|V_{ub}/V_{cb}| = 0.08 \pm 0.02. \quad (1.99)$$

Using unitarity constraints, one can narrow some of the above ranges (most noticeably, that of $|V_{cs}|$) and put constraints on the top mixings $|V_{ti}|$. The full information on the absolute values of the CKM elements (as given by [12]) from both direct measurements and three generation unitarity is summarized by

$$|V| = \begin{pmatrix} 0.9745 \Leftrightarrow 0.9757 & 0.219 \Leftrightarrow 0.224 & 0.002 \Leftrightarrow 0.005 \\ 0.218 \Leftrightarrow 0.224 & 0.9736 \Leftrightarrow 0.9750 & 0.036 \Leftrightarrow 0.046 \\ 0.004 \Leftrightarrow 0.014 & 0.034 \Leftrightarrow 0.046 & 0.9989 \Leftrightarrow 0.9993 \end{pmatrix}. \quad (1.100)$$

Note that the only large uncertainties are in $|V_{ub}|$ and $|V_{td}|$. However, the two are related through (1.82). Thus, the unitarity triangle is a very convenient tool for presenting constraints from indirect measurements on the most poorly determined parameters.

The most useful *CP* conserving indirect measurement, namely a Standard Model loop level process, is mixing in the $B^0 \leftrightarrow \bar{B}^0$ system. The experimental result is

$$x_d \equiv \frac{\Delta m_B}{\Gamma_{B^0}} = 0.73 \pm 0.05. \quad (1.101)$$

Note that this value averages over measurements at the $\Upsilon(4S)$ of

$$\chi_d \equiv \frac{\Gamma(B^0 \rightarrow \ell^- X)}{\Gamma(B^0 \rightarrow \ell^\pm X)} = \frac{x_d^2}{2(1 + x_d^2)}, \quad (1.102)$$

and measurements at the Z^0 of

$$\Delta m_B = x_d / \tau_{B^0}. \quad (1.103)$$

The Standard Model accounts for this quantity by the box diagrams with intermediate top quarks [30]:

$$M_{12} = \Leftrightarrow \frac{G_F^2}{12\pi^2} \eta m_B (B_B f_B^2) m_t^2 f_2(m_t^2/m_W^2) (V_{tb} V_{td}^*)^2 e^{-2i\xi_B}, \quad (1.104)$$

$$x_d = 2\tau_b |M_{12}|. \quad (1.105)$$

In Eq. (1.104) the quantity η is a QCD correction factor and $f_2(y)$ is a kinematic function calculated from the box diagrams. Both are positive quantities. Using [12] $B_B f_B^2 = (1.2 \pm 0.2)(173 \pm 40 \text{ MeV})^2$ and $m_t = 174 \pm 16 \text{ GeV}$ as input, (1.105) gives

$$|V_{tb}^* V_{td}| = 0.009 \pm 0.003, \quad (1.106)$$

which significantly improves over the unitarity constraint (1.100).

The above ranges for the V_{ij} 's give the following 90% CL range for the *CP*-violating measure $|J|$:

$$|J| = (3.0 \pm 1.3) \times 10^{-5} \sin \delta. \quad (1.107)$$

1.5 Expected *CP* Asymmetries — Standard Model Predictions

1.5.1 *CP* Violation in Mixing

As mentioned above, in the B_d system the result $\Gamma_{12} \ll M_{12}$ is model independent. Moreover, within the Standard Model and assuming that the box diagram (with a cut) is appropriate to estimate Γ_{12} , one can actually calculate the two quantities from the quark diagrams of Fig. 1-3. The calculation gives [10]

$$\frac{\Gamma_{12}}{M_{12}} = \Leftrightarrow \frac{3\pi}{2} \frac{1}{f_2(m_t^2/m_W^2)} \frac{m_b^2}{m_t^2} \left(1 + \frac{8}{3} \frac{m_c^2}{m_b^2} \frac{V_{cb} V_{cd}^*}{V_{tb} V_{td}^*} \right). \quad (1.108)$$

This confirms the order of magnitude estimate, $|\Gamma_{12}/M_{12}| \lesssim 10^{-2}$. The deviation of $|q/p|$ from unity is proportional to $\mathcal{I}m(\Gamma_{12}/M_{12})$ which is even further suppressed by another order of magnitude. Thus, to a very good approximation,

$$\frac{q}{p} = \frac{M_{12}^*}{|M_{12}|} = \frac{V_{tb}^* V_{td}}{V_{tb} V_{td}^*} e^{2i\xi_B}. \quad (1.109)$$

Note that (1.108) allows an estimate of CP violation in mixing, namely

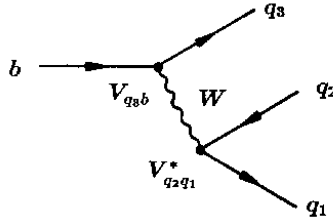
$$1 \Leftrightarrow \left| \frac{q}{p} \right| = \frac{1}{2} \mathcal{I}m \frac{\Gamma_{12}}{M_{12}} = \frac{4\pi}{f_2(m_t^2/m_W^2)} \frac{m_c^2}{m_t^2} \frac{J}{|V_{tb} V_{td}^*|^2} \sim 10^{-3}. \quad (1.110)$$

The last term is the ratio of the area of the Unitarity Triangle to the length of one of its sides squared, so it is $\mathcal{O}(1)$. The only suppression factor is then (m_c^2/m_t^2) . The uncertainty in the calculation comes from the use of a quark diagram to describe Γ_{12} and could easily be of order 30%, but not three orders of magnitude. (A similar expression to (1.109) holds for B_s , except that the last term is $J/|V_{tb} V_{ts}^*|^2 \sim 10^{-2}$, as can be seen from the relevant unitarity triangle in Fig. 1-1.)

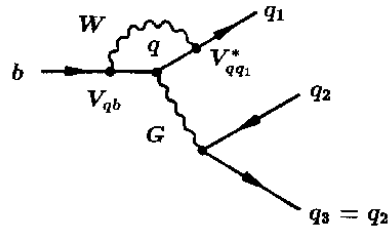
1.5.2 Decay-Amplitude Weak-Phase Structure

Most channels have contributions from both tree and three types of penguin diagrams [31]. The latter are classified according to the identity of the quark in the loop, as diagrams with different intermediate quarks may have both different strong phases and different weak phases. On the other hand, the subdivision of tree processes into spectator, exchange, and annihilation diagrams is unimportant in this respect since they all carry the same weak phase. In addition to gluonic penguins there are also electroweak penguin contributions, with a photon or Z boson. In certain cases the latter contribution can be significant because it is enhanced by a factor M_t^2/M_Z^2 which partially compensates the relative suppression of electroweak versus QCD couplings.

Tree Diagrams:



QCD Penguin Diagrams:



EW Penguin Diagrams:

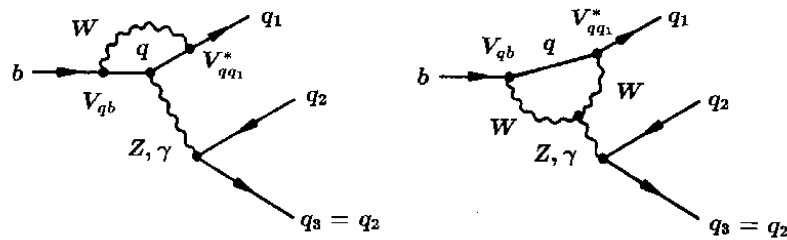


Figure 1-3. Quark diagrams contributing to b decays.

Figure 1-3 shows the quark diagrams for tree, penguin and electroweak penguin contributions. While quark diagrams can be easily classified in this way, the description of B decays is not so neatly divided into tree and penguin contributions once long distance physics effects are taken into account. Rescattering processes can change the quark content of the final state and confuse the identification of a contribution. There is no physical distinction between rescattered tree diagrams and long-distance contributions to the cuts of a penguin diagram. While these issues complicate estimates of various rates they can always be avoided in describing the weak-phase structure of B -decay amplitudes. The decay amplitudes for $b \rightarrow q\bar{q}q'$ can always be written as a sum of three terms with definite CKM coefficients:

$$A(q\bar{q}q') = V_{tb}V_{tq'}^*P_{q'}^t + V_{cb}V_{cq'}^*(T_{c\bar{c}q'}\delta_{qc} + P_{q'}^c) + V_{ub}V_{uq'}^*(T_{u\bar{u}q'}\delta_{qu} + P_{q'}^u). \quad (1.111)$$

Here P and T denote contributions from tree and penguin diagrams, excluding the CKM factors. As they stand, the P terms are not well defined because of the divergences of the penguin diagrams. Only differences of penguin diagrams are finite and well defined. (However, as will be seen,

introduction of a common high momentum cut off in the loop diagrams does not affect the final answer, since it depends only on differences of penguin amplitudes. This can be seen by using Eqs. (1.81) and (1.82) to eliminate one of the three terms, by writing its CKM coefficient as minus the sum of the other two.

In the case of $q\bar{q}s$ decays it is convenient to remove the $V_{tb}V_{ts}^*$ term. Then

$$\begin{aligned} A(c\bar{c}s) &= V_{cb}V_{cs}^*(T_{c\bar{c}s} + P_s^c \Leftrightarrow P_s^t) + V_{ub}V_{us}^*(P_s^u \Leftrightarrow P_s^t), \\ A(u\bar{u}s) &= V_{cb}V_{cs}^*(P_s^c \Leftrightarrow P_s^t) + V_{ub}V_{us}^*(T_{u\bar{u}s} + P_s^u \Leftrightarrow P_s^t), \\ A(s\bar{s}s) &= V_{cb}V_{cs}^*(P_s^c \Leftrightarrow P_s^t) + V_{ub}V_{us}^*(P_s^u \Leftrightarrow P_s^t). \end{aligned} \quad (1.112)$$

In these expressions only differences of penguin contributions occur, which makes the cancelation of the ultraviolet divergences of these diagrams explicit. Further, the second term has a CKM coefficient that is much smaller than the first. Hence this grouping is useful in classifying the expected direct CP violations. (Note that terms $b \rightarrow d\bar{d}s$, which have only penguin contributions, mix strongly with the $u\bar{u}s$ terms and hence cannot be separated from them. Thus P terms in $A(u\bar{u}s)$ include contributions from both $d\bar{d}s$ and $u\bar{u}s$ diagrams.)

In the case of $q\bar{q}d$ decays the three CKM coefficients are all of similar magnitude. The convention is then to retain the $V_{tb}V_{td}^*$ term because, in the Standard Model, the phase difference between this weak phase and half the mixing weak phase is zero. Thus only one unknown weak phase enters the calculation of the interference between decays with and without mixing. One can choose to eliminate whichever of the other terms does not have a tree contribution. In the cases $q = s$ or d , since neither has a tree contribution either term can be removed. Thus the amplitudes can be written

$$\begin{aligned} A(c\bar{c}d) &= V_{tb}V_{td}^*(P_d^t \Leftrightarrow P_d^u) + V_{cb}V_{cd}^*(T_{c\bar{c}d} + P_d^c \Leftrightarrow P_d^u), \\ A(u\bar{u}d) &= V_{tb}V_{td}^*(P_d^t \Leftrightarrow P_d^c) + V_{ub}V_{ud}^*(T_{u\bar{u}d} + P_d^u \Leftrightarrow P_d^c), \\ A(s\bar{s}d) &= V_{tb}V_{td}^*(P_d^t \Leftrightarrow P_d^u) + V_{cb}V_{cd}^*(P_d^c \Leftrightarrow P_d^u). \end{aligned} \quad (1.113)$$

Again only differences of penguin amplitudes occur. Furthermore the difference of penguin terms that occurs in the second term would vanish if the charm and up quark masses were equal, and thus is GIM (Glashow-Illiopoulos-Maiani) suppressed. However, particularly for in modes with no tree contribution, ($s\bar{s}d$), the interference of the two terms can still give significant direct CP violation, and thus complicate the simple predictions for the interference of decays with and without mixing [32] obtained by ignoring this term.

The penguin processes all involve the emission of a neutral boson, either a gluon (strong penguins) or a photon or Z boson (electroweak penguins). Excluding the CKM coefficients, the ratio of the contribution from the difference between a top and light quark strong penguin diagram to the

contribution from a tree diagram is of order

$$r_{PT} = \frac{P^t \Leftrightarrow P^{\text{light}}}{T_{q\bar{q}q'}} \approx \frac{\alpha_s}{12\pi} \ln \frac{m_t^2}{m_b^2}. \quad (1.114)$$

This is a factor of $\mathcal{O}(0.03)$. However this estimate does not include the effect of hadronic matrix elements, which are the probability factor to produce a particular final state particle content from a particular quark content. Since this probability differs for different kinematics, color flow, and spin structures, it can be different for tree and penguin contributions and may partially compensate the coupling constant suppression of the penguin term. Electroweak penguin difference terms are even more suppressed since they have an additional α_{em}/π or α_w/π compared to tree diagrams, but certain Z -contributions are enhanced by the large top quark mass and so can be non-negligible [33].

1.5.3 Low-Energy Effective Hamiltonians

The most efficient tool to analyze B decays is that of the low-energy effective Hamiltonian. The meaning and use of this tool is discussed further in the following chapter. Here the conventional notations used for the B decay Hamiltonian are simply noted. This section is based on Ref. [34], where a more detailed discussion can be found.

Low-energy effective Hamiltonians are constructed using the operator product expansion (OPE) which yields transition matrix elements of the structure

$$\langle f | \mathcal{H}_{\text{eff}} | i \rangle \propto \sum_k \langle f | Q_k(\mu) | i \rangle C_k(\mu), \quad (1.115)$$

where μ denotes an appropriate renormalization scale. The OPE allows one to separate the ‘‘long-distance’’ contributions to that decay amplitude from the ‘‘short-distance’’ parts. Whereas the former pieces are not calculable and are relegated to the nonperturbative hadronic matrix elements $\langle f | Q_k(\mu) | i \rangle$, the latter are described by perturbatively calculable Wilson coefficient functions $C_k(\mu)$.

In the case of $|\Delta B| = 1$, $\Delta C = \Delta U = 0$ transitions one finds

$$\mathcal{H}_{\text{eff}} = \mathcal{H}_{\text{eff}}(\Delta B = \Leftrightarrow 1) + \mathcal{H}_{\text{eff}}(\Delta B = \Leftrightarrow 1)^\dagger \quad (1.116)$$

with

$$\mathcal{H}_{\text{eff}}(\Delta B = \Leftrightarrow 1) = \frac{G_F}{\sqrt{2}} \left[\sum_{j=u,c} V_{jq}^* V_{jb} \left\{ \sum_{k=1}^2 Q_k^{jq} C_k(\mu) + \sum_{k=3}^{10} Q_k^q C_k(\mu) \right\} \right]. \quad (1.117)$$

Here G_F denotes the Fermi constant, the renormalization scale μ is of $\mathcal{O}(m_b)$, the flavor label q in $\{d, s\}$ corresponds to $b \rightarrow d$ and $b \rightarrow s$ transitions, respectively, and Q_k^{jq} are four-quark operators that can be divided into three categories:

(i) current-current operators:

$$\begin{aligned} Q_1^{jq} &= (\bar{q}_\alpha j_\beta)_{V-A} (\bar{j}_\beta b_\alpha)_{V-A} \\ Q_2^{jq} &= (\bar{q}_\alpha j_\alpha)_{V-A} (\bar{j}_\beta b_\beta)_{V-A}. \end{aligned} \quad (1.118)$$

(ii) QCD penguin operators:

$$\begin{aligned} Q_3^q &= (\bar{q}_\alpha b_\alpha)_{V-A} \sum_{q'} (\bar{q}'_\beta q'_\beta)_{V-A} \\ Q_4^q &= (\bar{q}_\alpha b_\beta)_{V-A} \sum_{q'} (\bar{q}'_\beta q'_\alpha)_{V-A} \\ Q_5^q &= (\bar{q}_\alpha b_\alpha)_{V-A} \sum_{q'} (\bar{q}'_\beta q'_\beta)_{V+A} \\ Q_6^q &= (\bar{q}_\alpha b_\beta)_{V-A} \sum_{q'} (\bar{q}'_\beta q'_\alpha)_{V+A}. \end{aligned} \quad (1.119)$$

(iii) EW penguin operators:

$$\begin{aligned} Q_7^q &= \frac{3}{2} (\bar{q}_\alpha b_\alpha)_{V-A} \sum_{q'} e_{q'} (\bar{q}'_\beta q'_\beta)_{V+A} \\ Q_8^q &= \frac{3}{2} (\bar{q}_\alpha b_\beta)_{V-A} \sum_{q'} e_{q'} (\bar{q}'_\beta q'_\alpha)_{V+A} \\ Q_9^q &= \frac{3}{2} (\bar{q}_\alpha b_\alpha)_{V-A} \sum_{q'} e_{q'} (\bar{q}'_\beta q'_\beta)_{V-A} \\ Q_{10}^q &= \frac{3}{2} (\bar{q}_\alpha b_\beta)_{V-A} \sum_{q'} e_{q'} (\bar{q}'_\beta q'_\alpha)_{V-A}. \end{aligned} \quad (1.120)$$

Here α and β denote $SU(3)_C$ color indices, $V\pm A$ refers to the Lorentz structures $\gamma_\mu(1 \pm \gamma_5)$, respectively, q' runs over the quark flavors active at the scale $\mu = \mathcal{O}(m_b)$, *i.e.*, $q' \in \{u, d, c, s, b\}$, and $e_{q'}$ are the corresponding electrical quark charges. The current-current, QCD, and EW penguin operators are related to the tree, QCD, and EW penguin processes, depicted in Fig. 1-3.

In the case of transitions of the type $b \rightarrow q\bar{u}c$ and $b \rightarrow q\bar{c}u$ with $q \in \{d, s\}$, only current-current operators contribute. The structure of the corresponding low-energy effective Hamiltonians is completely analogous to (1.117). To obtain it, one replaces both the CKM factors $V_{jq}^* V_{jb}$ and the flavor contents of the current-current operators (1.118) straightforwardly with the appropriate quark flavor structure, and omits the sum over penguin operators.

1.5.4 Decay Asymmetry Predictions in the Standard Model — General Patterns

As mentioned above, direct CP violations require two contributions to the decay process which differ in both their strong phases and their weak phases so that $|\bar{A}/A| \neq 1$. Purely leptonic and semileptonic decays are dominated by a single diagram and thus are unlikely to exhibit any measurable direct CP violation. Nonleptonic decays often have two terms that are comparable in

magnitude and hence could have significant direct *CP* violations. The theoretical calculation of *CP* asymmetries of the type (1.50) requires knowledge of strong phase shifts and of absolute values of various amplitudes, as can be seen from (1.46). The estimates therefore necessarily have hadronic uncertainties. In contrast, a clean relationship between measured asymmetries and CKM phases is obtained when studying *CP* violation in the interference between decays with and without mixing for *CP* eigenstate modes dominated by a single term in the decay amplitude.

B decays can thus be grouped into five classes. Classes 1 and 2 are expected to have relatively small direct *CP* violations and hence are particularly interesting for extracting CKM parameters from interference of decays with and without mixing. In the remaining three classes, direct *CP* violations could be significant and the neutral decay asymmetries cannot be cleanly interpreted in terms of CKM phases.

1. Decays dominated by a single term: $b \rightarrow c\bar{c}s$ and $b \rightarrow s\bar{s}s$. The Standard Model cleanly predicts zero (or very small) direct *CP* violations because the second term is Cabibbo suppressed. Any observation of large direct *CP*-violating effects in these cases would be a clue to beyond Standard Model physics. The modes $B^+ \rightarrow \psi K^+$ and $B^+ \rightarrow \phi K^+$ are examples of this class. The corresponding neutral modes have cleanly predicted relationships between CKM parameters and the measured asymmetry from interference between decays with and without mixing.
2. Decays with a small second term: $b \rightarrow c\bar{c}d$ and $b \rightarrow u\bar{u}d$. The expectation that penguin-only contributions are suppressed compared to tree contributions suggests that these modes will have small direct *CP* violation effects, and an approximate prediction for the relationship between measured asymmetries in neutral decays and CKM phases can be made.
3. Decays with a suppressed tree contribution: $b \rightarrow u\bar{u}s$. The tree amplitude is suppressed by small mixing angles, $V_{ub}V_{us}^*$. The no-tree term may be comparable or even dominate and give large interference effects. An example is $B \rightarrow \rho K$.
4. Decays with no tree contribution: $b \rightarrow s\bar{s}d$. Here the interference comes from penguin contributions with different charge 2/3 quarks in the loop. An example is $B \rightarrow KK$.
5. Radiative decays: $b \rightarrow s\gamma$. The mechanism here is the same as in case 4 except that the leading contributions come from electromagnetic penguins. An example is $B \rightarrow K^*\gamma$.

Recent CLEO results on $\mathcal{B}(B \rightarrow K\pi)$ and $\mathcal{B}(B \rightarrow \pi\pi)$ [35] suggest that the matrix element of penguin operators is enhanced compared to that of tree operators. If this enhancement is significant, then some of the decay modes listed in Class 2 might actually fit better to Class 3; that is it becomes more difficult to relate a measured asymmetry to a CKM phase. For example, it is possible that $b \rightarrow u\bar{u}d$ decays have comparable contributions from tree and penguin amplitudes. On the other hand, this would also mean that some modes listed in Class 3 could be dominated by a

single penguin term. For such cases an approximate relationship between measured asymmetries in neutral decays and CKM phases can be made. This is discussed in greater detail in Chapter 5.

It is useful to summarize all this discussion in two tables. The first table shows all cases for $b \rightarrow q\bar{q}'s$ while the second gives $b \rightarrow q\bar{q}'d$.

The last line in the first table of Table 1-1 are methods to measure the angle γ in $B_d \rightarrow DK$ decays. These modes have no penguin contributions, but can have direct CP violation due to interference of D^0 and \bar{D}^0 in decays to common final states. D decays to c -flavor-distinguishing states are then used to measure individual amplitude strengths. Thus the value of γ can be extracted, up to a fourfold ambiguity, via these modes if rates are high enough to make the relevant measurements accurately. These methods are discussed in more detail in Chapter 7. Again in the second table of Table 1-1 the final entry refers to direct CP violation studies in $B_d \rightarrow D\pi$ or $B_s \rightarrow DK$ decays through interference of common D^0 and \bar{D}^0 channels [36, 37]. Here one of the B -decay amplitudes is doubly Cabibbo suppressed, so the only hope for large interference effects is in a channel which is a doubly Cabibbo-suppressed decay of the other D state. Rates will be small, but the direct CP violation could be a large effect. Tagging via the second B is necessary to identify b -flavor. Charged $B \rightarrow D\pi$ can be similarly studied (with no tagging needed) [38].

1.5.5 Decay Asymmetry Predictions in the Standard Model — Some Sample Modes

The decay $B \rightarrow \psi K_S$ is an example of Class 1. A new ingredient in the analysis is the effect of $K \leftrightarrow \bar{K}$ mixing. For decays with a single K_S in the final state, $K \leftrightarrow \bar{K}$ mixing is essential because $B^0 \rightarrow K^0$ and $\bar{B}^0 \rightarrow \bar{K}^0$, and interference is possible only due to $K \leftrightarrow \bar{K}$ mixing. This adds a factor of

$$\left(\frac{p}{q}\right)_K = \frac{V_{cs}V_{cd}^*}{V_{cs}^*V_{cd}} e^{-2i\xi_K} \quad (1.121)$$

into (\bar{A}/A) . The quark subprocess in $\bar{B}^0 \rightarrow \psi\bar{K}^0$ is $b \rightarrow c\bar{c}s$ which is dominated by the W -mediated tree diagram:

$$\frac{\bar{A}_{\psi K_S}}{A_{\psi K_S}} = \eta_{\psi K_S} \left(\frac{V_{cb}V_{cs}^*}{V_{cb}^*V_{cs}}\right) \left(\frac{V_{cs}V_{cd}^*}{V_{cs}^*V_{cd}}\right) e^{-2i\xi_B}. \quad (1.122)$$

The CP eigenvalue of the state is $\eta_{\psi K_S} = \pm 1$. Combining (1.109) and (1.122), one finds

$$\lambda(B \rightarrow \psi K_S) = \pm \left(\frac{V_{tb}^*V_{td}}{V_{tb}V_{td}^*}\right) \left(\frac{V_{cb}V_{cs}^*}{V_{cb}^*V_{cs}}\right) \left(\frac{V_{cs}^*V_{cb}}{V_{cs}V_{cb}^*}\right) \implies \mathcal{I}m \lambda_{\psi K_S} = \sin(2\beta). \quad (1.123)$$

The second term in (1.112) is of order $r_T \sin^2 \theta_C$ for this decay and thus Eq. (1.123) is clean of hadronic uncertainties to $\mathcal{O}(10^{-3})$. This measurement will thus give the theoretically cleanest

$B \rightarrow q\bar{q}s$ Decay Modes

Quark Process	Leading Term	Secondary Term	Sample B_d Modes	B_d Angle	Sample B_s Modes	B_s Angle
$b \rightarrow c\bar{c}s$	$V_{cb}V_{cs}^* = A\lambda^2$ tree + penguin ($c-t$)	$V_{ub}V_{us}^* = A\lambda^4(\rho - i\eta)$ penguin only ($u-t$)	$J/\psi K_S$	β	ψK_S $D_s \bar{D}_s$	β_S
$b \rightarrow s\bar{s}s$	$V_{cb}V_{cs}^* = A\lambda^2$ penguin only ($c-t$)	$V_{ub}V_{us}^* = A\lambda^4(\rho - i\eta)$ penguin only ($u-t$)	ϕK_S	β	ϕK_S	0
$b \rightarrow u\bar{u}s$	$V_{cb}V_{cs}^* = A\lambda^2$ penguin only ($c-t$)	$V_{ub}V_{us}^* = A\lambda^4(\rho - i\eta)$ tree + penguin ($u-t$)	$\pi^0 K_S$ ρK_S	competing terms	$\phi\pi^0$ $K_S K_S$	competing terms
$b \rightarrow c\bar{u}s$	$V_{cb}V_{us}^* = A\lambda^3$	0	$D^0 K$ \searrow common $\bar{D}^0 K$ \nearrow modes	γ	$D^0 \phi$ \searrow common $\bar{D}^0 \phi$ \nearrow modes	γ
$b \rightarrow u\bar{c}s$	$V_{ub}V_{cs}^* = A\lambda^3(\rho - i\eta)$					

 $b \rightarrow q\bar{q}d$ Decay Modes

Quark Process	Leading Term	Secondary Term	Sample B_d Modes	B_d Angle * (leading terms only)	Sample B_s Modes	B_s Angle * (leading term)
$b \rightarrow c\bar{c}d$	$V_{cb}V_{cd}^* = -A\lambda^3$ tree + penguin ($c-u$)	$V_{tb}V_{td}^* = A\lambda^3(1 - \rho + i\eta)$ penguin only ($t-u$)	$D^+ D^-$	$*\beta$	ψK_S	β_S
$b \rightarrow s\bar{s}d$	$V_{tb}V_{td}^* = A\lambda^3(1 - \rho + i\eta)$ penguin only ($t-u$)	$V_{cb}V_{cd}^* = A\lambda^3$ penguin only ($c-u$)	$\phi\pi$ $K_S \bar{K}_S$	competing terms	ϕK_S	competing terms
$b \rightarrow u\bar{u}d$	$V_{ub}V_{ud}^* = A\lambda^3(\rho - i\eta)$ tree + penguin (uc)	$V_{tb}V_{td}^* = A\lambda^3(1 - \rho + i\eta)$ penguin only ($t-c$)	$\pi\pi; \pi\rho$ πa_1	$*\alpha$	$\pi^0 K_S$ $\rho^0 K_S$	competing terms
$b \rightarrow c\bar{u}d$	$V_{cb}V_{ud}^* = A\lambda^2$	0	$D^0 \pi^0$ \searrow common $\bar{D}^0 \pi^0$ \nearrow modes	γ	$D^0 K_S$ \searrow common $\bar{D}^0 K_S$ \nearrow modes	γ
$b \rightarrow u\bar{c}d$	$V_{ub}V_{cd}^* = -A\lambda^4(\rho - i\eta)$					

Table 1-1. Decay modes for $b \rightarrow q\bar{q}s$ and $b \rightarrow q\bar{q}d$

determination of a CKM parameter, even cleaner than the determination of $\sin \theta_C$ from $K \rightarrow \pi \ell \nu$. (If $\mathcal{B}(K_L \rightarrow \pi \nu \bar{\nu})$ were measured, it would give a comparably clean determination of $\sin \beta$ [39].)

The channel $B \rightarrow \psi K^*$ has a similar amplitude structure, but, since the two vector particles can have either even or odd relative angular momentum, the final state is not a pure CP eigenstate. The two different CP states can be separated by an analysis of the angular distribution of the decays [23]. This requires more data to get a comparable accuracy for $\sin 2\beta$, but on the other hand the branching ratio to this channel is somewhat higher and it appears to be dominated by a single CP eigenstate [40], so it may in fact give comparably accurate and equally clean results.

A second example of a theoretically clean mode in Class 1 is $B \rightarrow \phi K_S$. The quark subprocess involves flavor changing neutral current and cannot proceed via a tree-level Standard Model diagram. The leading contribution comes from penguin diagrams. The two terms in Eq. (1.112) are now both differences of penguins, but the second term is CKM suppressed and thus of order 0.02 compared to the first. Thus CP violation in the decay is at most a few percent and can be neglected in the analysis of asymmetries in this channel. The analysis is similar to the ψK_S case, and the asymmetry is proportional to $\sin(2\beta)$.

The same quark subprocesses give theoretically clean CP asymmetries also in B_s decays. The list of clean modes is given in Table 1-1.

The best known example of Class 2 is $B \rightarrow \pi\pi$. The quark subprocess is $b \rightarrow u\bar{d}$ which is dominated by the W -mediated tree diagram. Neglecting for the moment the second, pure penguin, term in Eq. (1.113) one finds

$$\frac{\bar{A}_{\pi\pi}}{A_{\pi\pi}} = \eta_{\pi\pi} \frac{V_{ub}V_{ud}^*}{V_{ub}^*V_{ud}} e^{-2i\xi_B}. \quad (1.124)$$

The CP eigenvalue for two pions is $+1$. Combining (1.109) and (1.124), gives

$$\lambda(B \rightarrow \pi^+\pi^-) = \left(\frac{V_{tb}^*V_{td}}{V_{tb}V_{td}^*} \right) \left(\frac{V_{ud}^*V_{ub}}{V_{ud}V_{ub}^*} \right) \implies \mathcal{I}m \lambda_{\pi\pi} = \sin(2\alpha). \quad (1.125)$$

The pure penguin term in Eq. (1.113) has a weak phase, $\arg(V_{td}^*V_{tb})$, different from the term with the tree contribution, so it modifies both $\mathcal{I}m \lambda$ and (if there are nontrivial strong phases) $|\lambda|$. Recent results from CLEO suggest that the $B \rightarrow K\pi$ rate is comparable to or larger than the $B \rightarrow \pi\pi$ rate. This in turn indicates that the penguin contribution to $B \rightarrow \pi\pi$ channel is significant, probably 10% or more. This then introduces CP violation in decay, unless the strong phases cancel (or are zero, as suggested by factorization arguments). The resulting hadronic uncertainty can be eliminated using isospin analysis [20]. This requires a measurement of the rates for the isospin-related channels $B^+ \rightarrow \pi^+\pi^0$ and $B^0 \rightarrow \pi^0\pi^0$ as well as the corresponding CP conjugate processes. The rate for $\pi^0\pi^0$ is expected to be small and the measurement is difficult, but even an upper bound on this rate can be used to limit the magnitude of hadronic uncertainties.

Related but slightly more complicated channels with the same underlying quark structure are $B \rightarrow \rho^0\pi^0$ and $B \rightarrow a_1^0\pi^0$. Again an analysis involving the isospin-related channels can be used to help

eliminate hadronic uncertainties from *CP* violations in the decays. Channels such as $\rho\rho$ and $a_1\rho$ could in principle also be studied, using angular analysis to determine the mixture of *CP*-even and *CP*-odd contributions.

The analysis of $B \rightarrow D^+D^-$ proceeds along very similar lines. The quark subprocess here is $b \rightarrow c\bar{c}d$, and so the tree contribution gives

$$\lambda(B \rightarrow D^+D^-) = \eta_{D^+D^-} \left(\frac{V_{tb}^* V_{td}}{V_{tb} V_{td}^*} \right) \left(\frac{V_{cd}^* V_{cb}}{V_{cd} V_{cb}^*} \right) \implies \mathcal{I}m \lambda_{DD} = \leftrightarrow \sin(2\beta) \quad (1.126)$$

since $\eta_{D^+D^-} = +1$. Again, there are hadronic uncertainties due to the pure penguin term in (1.113), but they are estimated to be small. (See, however, [41].)

Now consider Class 4 decays, for example the case $B \rightarrow \phi\pi^0$. Here both terms in (1.113) are significant, though the second is GIM suppressed; that is it would vanish if charm and up quark masses were equal. Neglecting this term early studies predict no *CP* asymmetry in this channel in the Standard Model. However it has been shown that the presence of the second term can introduce asymmetries that may be as large as 10% [32]. Hence this channel cannot readily be used to look for violations of Standard Model predictions, unless one can reliably bound the size of the penguin effects.

In all cases the above discussions have neglected the distinction between strong penguins and electroweak penguins. The CKM phase structure of both types of penguins is the same. The only place where this distinction becomes important is when an isospin argument is used to remove hadronic uncertainties due to penguin contributions. These arguments are based on the fact that gluons have isospin zero, and hence strong penguin processes have definite ΔI . Photons and *Z*-bosons on the other hand contribute to more than one ΔI transition and hence cannot be separated from tree terms by isospin analysis. In most cases electroweak penguins are small, typically no more than ten percent of the corresponding strong penguins and so their effects can safely be neglected. However in Cases 3 to 5, where tree contributions are small or absent, their effects may need to be considered. A full review of the role of electroweak penguins in *B* decays has been given by Fleischer [34].

1.5.6 Effects of Physics Beyond the Standard Model

A more detailed examination of the effects in a variety of theories beyond the Standard Model is given in Chapter 13 of this book and in various reviews [42]. Here only some very general observations are in order.

By now the Standard Model and its particle content are so well established that any future theory will certainly contain them. However extensions that go beyond the Standard Model inevitably introduce additional fields. Along with them there often come additional coupling constants and hence the possibility of additional *CP*-violating phases. Even if no new phases occur there can be changes in the relationship between various physical quantities and CKM matrix element

magnitudes and phases. Effects of physics beyond the Standard Model can manifest themselves in two ways, as additional contributions to the mixing of B^0 and \bar{B}^0 states, and/or as additional contributions to some set of decays.

An additional contribution to the mixing would have two effects: a change in the relationship between x_d and $|V_{td}V_{tb}|$ which led to Eq. (1.106) and a change in the relationship between the phase of q/p and the phase of $V_{tb}V_{td}^*$. However, since all λ_f have a common factor q/p , it would not change the relative phases between various λ_f .

Additional contributions to the decays can only be unambiguously and model-independently observed in cases where an amplitude is dominated by a single weak-phase term in the Standard Model. Then such terms destroy the relationship between the asymmetry and a CKM matrix phase and so lead to inconsistencies. For example, various modes that have the same Standard Model asymmetry may actually give different asymmetries [43]. In cases where two competing terms with different weak phases occur in the Standard Model expression, any additional term, whatever its phase, can always be absorbed into these two terms, appearing simply as changes in their magnitudes. Since these magnitudes cannot as yet be calculated in a model-independent and reliable fashion, this makes it quite difficult to identify changes from the Standard Model in these cases. However by a systematic study of expected patterns and improved theoretical calculations of matrix elements, one may be able to identify the impact of contributions beyond the Standard Model in these cases as well.

1.6 Some Comments about the K System

This section briefly reviews the K system in order to understand (a) the similarities and differences between neutral K and neutral B mesons and (b) the implications of CP violation as measured in K decays for future measurements of B decays.

1.6.1 The Neutral K System

In marked difference from the neutral B mesons, the neutral K meson states differ significantly in their lifetimes:

$$\tau_S = (0.8927 \pm 0.0009) \times 10^{-10} \text{ s}, \quad \tau_L = (5.17 \pm 0.04) \times 10^{-8} \text{ s}, \quad (1.127)$$

where the sub-indices S and L stand for the short-lived and long-lived mass eigenstates, respectively. Indeed, for the K system it is more useful to define the eigenstates by the lifetimes,

$$|K_S\rangle = p|K^0\rangle + q|\bar{K}^0\rangle, \quad (1.128)$$

$$|K_L\rangle = p|K^0\rangle \Leftrightarrow q|\bar{K}^0\rangle, \quad (1.129)$$

namely $\Delta\Gamma_K < 0$ by definition. (The p, q coefficients are of course different in the B and K systems. The notation $(q/p)_K$ for the ratio in the K system is used wherever the distinction is necessary.) The mass difference in the K system is measured to be

$$\Delta m_K \equiv M_L \Leftrightarrow M_S = (3.491 \pm 0.009) \times 10^{-15} \text{ GeV}. \quad (1.130)$$

Equations (1.127) and (1.130) provide a convenient empirical approximation:

$$\Delta\Gamma_K \approx \Leftrightarrow 2\Delta m_K, \quad (1.131)$$

which is quite different from the B_d system (1.27).

The calculation of $(q/p)_K$ according to (1.15) proceeds a little differently than for the B_d case. To understand the situation in the K system, it is useful to define a phase ϕ_{12} according to

$$\frac{M_{12}}{\Gamma_{12}} \equiv \Leftrightarrow \left| \frac{M_{12}}{\Gamma_{12}} \right| e^{i\phi_{12}}. \quad (1.132)$$

Since *CP*-violating effects in the K system are known to be small, $\phi_{12} \ll 1$, so that ϕ_{12} can be used as a small expansion parameter. To leading order in ϕ_{12} , Eqs. (1.13) and (1.14) give

$$\Delta m_K = 2|M_{12}|, \quad \Delta\Gamma_K = \Leftrightarrow 2|\Gamma_{12}|. \quad (1.133)$$

Consequently, Eq. (1.132) can be rewritten, to first order in ϕ_{12} , as

$$\frac{M_{12}}{\Gamma_{12}} = \frac{\Delta m_K}{\Delta\Gamma_K} (1 + i\phi_{12}). \quad (1.134)$$

In some arbitrary phase convention,

$$\Gamma_{12} = |\Gamma_{12}| e^{-2i\xi_K}. \quad (1.135)$$

Using (1.134) and (1.135), gives from (1.15):

$$\left(\frac{q}{p} \right)_K = e^{2i\xi_K} \left[1 \Leftrightarrow i\phi_{12} \frac{1 + i\frac{\Delta\Gamma_K}{2\Delta m_K}}{1 + \left(\frac{\Delta\Gamma_K}{2\Delta m_K} \right)^2} \right]. \quad (1.136)$$

Thus $(q/p)_K$ is, to a good approximation, a pure phase. Actually, (1.136) implies that in the *CP* limit ($\phi_{12} = 0$), the *CP* transformation law is $CP|K^0\rangle = e^{2i\xi_K}|\bar{K}^0\rangle$. The K_S and K_L states are *CP* eigenstates to $\mathcal{O}(\phi_{12}) \sim 10^{-3}$ approximation.

As a result of the large lifetime difference between the neutral kaons, kaon experiments can easily separate the mass eigenstates and investigate K_L and K_S decays independently. This is impossible in B experiments, so there one will follow the decays of $B_{\text{phys}}^0(t)$ and $\bar{B}_{\text{phys}}^0(t)$ instead.

To compare the effects of CP violation in mixing, note that Eqs. (1.133) and (1.28) imply that $|q/p|_K$ and $|q/p|_{B_d}$ are both very close to 1. CP violation in mixing is then small in both systems. However, while for the B_d system the reason for that is the small lifetime difference, in the K system the reason is the smallness of the relevant CP -violating phase.

Finally, consider CP violation in the interference of mixing and decay. This could give a theoretically clean observable, provided that the decay is dominated by a single weak phase or a single strong phase. It is not difficult to find K decays into final CP eigenstates where $|\bar{A}/A| = 1$ to a good approximation: for example, the $\Delta I = 1/2$ rule implies that $K \rightarrow \pi^0\pi^0$ and $K \rightarrow \pi^+\pi^-$ are both dominated by a single strong phase. The difference in width, Γ_{12} , is completely dominated by the two pion intermediate state and therefore

$$\arg(\Gamma_{12}) = \arg(A_{2\pi}^* \bar{A}_{2\pi}) = \arg(\bar{A}_{2\pi}/A_{2\pi}). \quad (1.137)$$

In the approximation that $(\bar{A}_{2\pi}/A_{2\pi})$ is a pure phase, thus

$$\frac{\bar{A}_{2\pi}}{A_{2\pi}} = \Leftrightarrow \frac{\Delta\Gamma_K}{2\Gamma_{12}^*} = e^{-2i\xi_K}. \quad (1.138)$$

(See (1.135) for the last equation.) However, Eq. (1.136) shows that in the approximation where q/p is a pure phase, it is given by $q/p = e^{2i\xi_K}$. Thus, the prediction for CP asymmetry in $K \rightarrow 2\pi$ which is clean of hadronic uncertainties is simply zero:

$$\lambda(K \rightarrow \pi\pi) = 1 \implies \mathcal{I}m \lambda_{\pi\pi} = 0. \quad (1.139)$$

It should hold (as it does!) to $\mathcal{O}(10^{-3})$. To learn something about CP violation it is necessary to go beyond this approximation and use

$$\frac{q}{p} \frac{\bar{A}_{\pi\pi}}{A_{\pi\pi}} = 1 \Leftrightarrow i\phi_{12} \frac{1 + i\frac{\Delta\Gamma_K}{2\Delta m_K}}{1 + \left(\frac{\Delta\Gamma_K}{2\Delta m_K}\right)^2}. \quad (1.140)$$

Thus a value of ϕ_{12} can be cleanly extracted from measurements of CP violation in $K \rightarrow \pi\pi$. However, the translation of ϕ_{12} into electroweak parameters requires the knowledge of either the long distance contribution to M_{12} or the matrix element of the relevant four quark operator between K^0 and \bar{K}^0 states. This introduces large hadronic uncertainties into the calculation.

1.6.2 Measuring CP Violation in the K System

CP violation was first (and so far only) measured in K decays [1]. A number of complementary measurements have been made. CP asymmetries in the semileptonic K decays,

$$\delta(\ell) = \frac{\Gamma(K_L \rightarrow \pi^- \ell^+ \nu_\ell) \Leftrightarrow \Gamma(K_L \rightarrow \pi^+ \ell^- \bar{\nu}_\ell)}{\Gamma(K_L \rightarrow \pi^- \ell^+ \nu_\ell) + \Gamma(K_L \rightarrow \pi^+ \ell^- \bar{\nu}_\ell)}, \quad (1.141)$$

have been measured, giving

$$\delta(\mu) = (3.04 \pm 0.25) \times 10^{-3}, \quad \delta(e) = (3.33 \pm 0.14) \times 10^{-3}. \quad (1.142)$$

These asymmetries are manifestations of *CP* violation in mixing:

$$\delta = \frac{1 \Leftrightarrow |q/p|_K^2}{1 + |q/p|_K^2}, \quad (1.143)$$

hence the statement above that $|q/p|_K$ is very close to unity.

The asymmetries in the two-pion channels,

$$\eta_{00} = \frac{A(K_L \rightarrow \pi^0 \pi^0)}{A(K_S \rightarrow \pi^0 \pi^0)}, \quad \eta_{+-} = \frac{A(K_L \rightarrow \pi^+ \pi^-)}{A(K_S \rightarrow \pi^+ \pi^-)}. \quad (1.144)$$

have been measured:

$$|\eta_{00}| = (2.275 \pm 0.019) \times 10^{-3}, \quad \phi_{00} = 43.5 \pm 1.0^\circ, \quad (1.145)$$

$$|\eta_{+-}| = (2.285 \pm 0.019) \times 10^{-3}, \quad \phi_{+-} = 43.7 \pm 0.6^\circ. \quad (1.146)$$

A straightforward evaluation gives

$$\eta_{00} = \frac{pA_{00} \Leftrightarrow q\bar{A}_{00}}{pA_{00} + q\bar{A}_{00}} = \frac{1 \Leftrightarrow \lambda_{00}}{1 + \lambda_{00}}, \quad \eta_{+-} = \frac{pA_{+-} \Leftrightarrow q\bar{A}_{+-}}{pA_{+-} + q\bar{A}_{+-}} = \frac{1 \Leftrightarrow \lambda_{+-}}{1 + \lambda_{+-}}. \quad (1.147)$$

As shown below, η_{00} and η_{+-} are affected by all three types of *CP* violation: $|q/p| \neq 1$ and $\text{Im } \lambda \neq 0$ give $\mathcal{O}(10^{-3})$ effects, while $|\bar{A}/A| \neq 1$ gives an $\mathcal{O}(10^{-6})$ effect.

1.6.3 The ε_K and ε'_K Parameters

There is a possible contribution to (1.147) from direct *CP* violation. This is due to the fact that there are two isospin channels, leading to final $(2\pi)_{I=0}$ and $(2\pi)_{I=2}$ states:

$$\langle \pi^0 \pi^0 | = \sqrt{\frac{1}{3}} \langle (\pi\pi)_{I=0} | \Leftrightarrow \sqrt{\frac{2}{3}} \langle (\pi\pi)_{I=2} |, \quad (1.148)$$

$$\langle \pi^+ \pi^- | = \sqrt{\frac{2}{3}} \langle (\pi\pi)_{I=0} | + \sqrt{\frac{1}{3}} \langle (\pi\pi)_{I=2} |. \quad (1.149)$$

However, the possible interference effects are small because (on top of the smallness of the relevant *CP*-violating phases) the final $I = 0$ state is dominant (this is the $\Delta I = 1/2$ rule). Isospin amplitudes can be defined by

$$A_I = \langle (\pi\pi)_I | H | K^0 \rangle, \quad \bar{A}_I = \langle (\pi\pi)_I | H | \bar{K}^0 \rangle. \quad (1.150)$$

Experimentally, $|A_2/A_0| \approx 1/20$. Instead of η_{00} and η_{+-} one defines two combinations, ε_K and ε'_K , in such a way that the possible direct CP -violating effects are isolated into ε'_K .

The definition of ε_K is

$$\varepsilon_K \equiv \frac{1}{3}(\eta_{00} + 2\eta_{+-}) = \frac{1 \Leftrightarrow \lambda_0}{1 + \lambda_0}, \quad (1.151)$$

where $\lambda_0 \equiv (q/p)_K(\bar{A}_0/A_0)$ and the equation holds to first order in A_2/A_0 (at zeroth order $\eta_{00} = \eta_{+-} = \varepsilon_K$). As, by definition, only one strong channel contributes to λ_0 , there is indeed no direct CP violation in (1.151).

Note that ε_K is a manifestation of CP violation in both mixing and the interference between decays with and without mixing (to see this explicitly, examine Eqs. (1.136) and (1.140)):

$$\left| \frac{q}{p} \right|_K \Leftrightarrow 1 = \phi_{12} \frac{\frac{\Delta\Gamma_K}{2\Delta m_K}}{1 + \left(\frac{\Delta\Gamma_K}{2\Delta m_K} \right)^2}, \quad (1.152)$$

$$2\varepsilon_K \approx 1 \Leftrightarrow \left(\frac{q}{p} \right)_K \frac{\bar{A}_0}{A_0} = \phi_{12} \frac{i \Leftrightarrow \frac{\Delta\Gamma_K}{2\Delta m_K}}{1 + \left(\frac{\Delta\Gamma_K}{2\Delta m_K} \right)^2}. \quad (1.153)$$

As $\Delta\Gamma_K \approx \Leftrightarrow 2\Delta m_K$, the deviation of $|q/p|_K$ from unity (CP violation in mixing) and the deviation of $\mathcal{I}m[(q/p)_K(\bar{A}_0/A_0)]$ from zero (CP violation in the interference between decays with and without mixing) are both $\mathcal{O}(\phi_{12})$ and thus contribute to ε_K at the same order. One can interpret Eqs. (1.152) and (1.153) to imply that $\mathcal{R}e(\varepsilon_K)$ is a manifestation of CP violation in mixing while $\mathcal{I}m(\varepsilon_K)$ is a manifestation of CP violation in the interference between decays with and without mixing. As (1.153) predicts $\arg(\varepsilon_K) \approx \pi/4$, the magnitudes of the two phenomena are similar.

One can define ε'_K by

$$\varepsilon'_K \equiv \frac{1}{3}(\eta_{+-} \Leftrightarrow \eta_{00}) = \frac{2(\lambda_{00} \Leftrightarrow \lambda_{+-})}{3(1 + \lambda_{00})(1 + \lambda_{+-})} \approx \frac{1}{6} \frac{q}{p} \left(\frac{\bar{A}_{00}}{A_{00}} \Leftrightarrow \frac{\bar{A}_{+-}}{A_{+-}} \right), \quad (1.154)$$

where the last equality used (1.145) which gives $\lambda_{00} \approx \lambda_{+-} \approx 1$. One can further evaluate (1.154) in terms of A_0 and A_2 with the help of the relationships given in Eqs. (1.148) and (1.149). The approximations $(q/p)(\bar{A}_0/A_0) \approx 1$ and $|A_2/A_0| \ll 1$ give

$$\varepsilon'_K = \frac{i}{\sqrt{2}} \left| \frac{A_2}{A_0} \right| e^{i(\delta_2 - \delta_0)} \sin(\phi_2 \Leftrightarrow \phi_0). \quad (1.155)$$

In the derivation of (1.155), since it is a good approximation to replace q/p with a pure phase, one sees that there is no CP violation in mixing in ε'_K . Equations (1.154) and (1.155) imply that $\mathcal{R}e(\varepsilon'_K)$ is a manifestation of CP violation in decay while $\mathcal{I}m(\varepsilon'_K)$ is a manifestation of CP violation in the interference between decays with and without mixing. For recent experimental results, see [44].

References

- [1] J. H. Christenson *et al.*, *Phys. Rev. Lett.* **13**, 138 (1964).
- [2] N. Cabibbo, *Phys. Rev. Lett.* **10**, 531 (1963).
- [3] M. Kobayashi and T. Maskawa, *Prog. Th. Phys.* **49**, 652 (1973).
- [4] A. D. Sakharov, *ZhETF Pis. Red.* **5**, 32 (1967); *JETP Lett.* **5**, 24 (1967).
- [5] A. G. Cohen, D. B. Kaplan and A. E. Nelson, *Ann. Rev. Nucl. Part. Sci.* **43**, 27 (1993).
- [6] M. E. Peskin and D.V. Schroeder, *An Introduction to Quantum Field Theory*, Addison-Wesley Publishing Company (1995).
- [7] Y. Nir, Lectures presented in the 20th SLAC Summer Institute, SLAC-PUB-5874 (1992); Y. Nir and H. R. Quinn, *Ann. Rev. Nucl. Part. Sci.* **42**, 211 (1992).
- [8] A. J. Buras and R. Fleischer, (1997) hep-ph/9704376, to appear in *Heavy Flavours II*, World Scientific, eds. A. J. Buras and M. Linder.
- [9] W. Grimus, *Fortschr. Phys.* **36**, 201 (1988).
- [10] I. I. Bigi *et al.*, in *CP Violation*, ed. C. Jarlskog, World Scientific, Singapore (1992).
- [11] I. Dunietz, *Phys. Rev. D* **52**, 3048 (1995);
M. Beneke, G. Buchalla, and I. Dunietz, *Phys. Rev. D* **54**, 4419 (1996);
A. S. Dighe *et al.*, *Phys. Lett. B* **369**, 144 (1996).
- [12] All experimental data are taken from: R. M. Barnett *et al.*, *Phys. Rev. D* **54**, 1 (1996).
- [13] Ya. I. Azimov, N. G. Uraltsev and V. A. Khoze *Sov. J. Nucl. Phys.* **45**, 878 (1987).
- [14] A. B. Carter and A. I. Sanda, *Phys. Rev. Lett.* **45**, 952 (1980); *Phys. Rev. D* **23**, 1567 (1981) .
- [15] I. I. Bigi and A. I. Sanda, *Nucl. Phys.* **B193**, 85 (1981); *Nucl. Phys.* **B281**, 41 (1987).
- [16] I. Dunietz and J. Rosner, *Phys. Rev. D* **34**, 1404 (1986).
- [17] L. S. Littenberg, *Phys. Rev. D* **39**, 3322 (1989).
- [18] G. Buchalla and A. J. Buras, *Nucl. Phys.* **B400**, 225 (1993);
A. J. Buras, *Phys. Lett. B* **333**, 476 (1994).
- [19] Y. Grossman and Y. Nir, *Phys. Lett. B* **398**, 163 (1997).

- [20] M. Gronau and D. London, *Phys. Rev. Lett.* **65**, 3381 (1990).
- [21] Y. Nir and H. R. Quinn, *Phys. Rev. Lett.* **67**, 541 (1991).
- [22] H. J. Lipkin *et al.*, *Phys. Rev. D* **44**, 1454 (1991).
- [23] I. Dunietz *et al.*, *Phys. Rev. D* **43**, 2193 (1991).
- [24] S.L. Glashow, *Nucl. Phys.* **22**, 579 (1961);
S. Weinberg, *Phys. Rev. Lett.* **19**, 1264 (1967);
A. Salam, in *Proceedings of the 8th Nobel Symposium*, ed. N. Swartholm, Almquist and Wiksells, Stockholm (1968).
- [25] C. Jarlskog, *Phys. Rev. Lett.* **55**, 1039 (1985);
- [26] L. L. Chau and W. Y. Keung, *Phys. Rev. Lett.* **53**, 1802 (1984).
- [27] L. Wolfenstein, *Phys. Rev. Lett.* **51**, 1945 (1983).
- [28] A. J. Buras, M. E. Lautenbacher and G. Ostermaier, *Phys. Rev. D* **50**, 3433 (1994).
- [29] C. O. Dib *et al.*, *Phys. Rev. D* **41**, 1522 (1990).
- [30] T. Inami and C. S. Lim, *Prog. Th. Phys.* **65**, 297 (1981); **65**, 772(E) (1982).
- [31] M. Bander, S. Silverman and A. Soni, *Phys. Rev. Lett.* **43**, 242 (1979).
- [32] R. Fleischer, *Phys. Lett. B* **341**, 205 (1995);
A. J. Buras and R. Fleischer, *Phys. Lett. B* **341**, 379 (1995).
- [33] R. Fleischer, *Z. Phys. C* **62**, 81 (1994);
N. G. Deshpande and X.-G. He, *Phys. Lett. B* **336**, 471 (1994).
- [34] R. Fleischer, *Int. J. Mod. Phys. A* **12**, 2459 (1997).
- [35] R. Godang *et al.*, (CLEO Collaboration), *Phys. Rev. Lett.* **80**, 3456 (1998).
- [36] M. Gronau and D. Wyler, *Phys. Lett. B* **265**, 172 (1991).
- [37] D. Atwood, I. Dunietz and A. Soni, *Phys. Rev. Lett.* **78**, 3257 (1997).
- [38] I. Dunietz, *Phys. Lett. B* **427**, 179 (1998).
- [39] G. Buchalla and A. J. Buras, *Phys. Rev. D* **54**, 6782 (1996).
- [40] M. S. Alam *et al.*, (CLEO Collaboration), *Phys. Rev. D* **50**, 43 (1994).
- [41] M. Ciuchini *et al.*, *Phys. Rev. Lett.* **79**, 978 (1997).

- [42] C. O. Dib, D. London and Y. Nir, *Int. J. Mod. Phys. A* **6**, 1253 (1991);
M. Gronau and D. London, *Phys. Rev. D* **55**, 2845 (1997);
Y. Grossman, Y. Nir and R. Rattazzi, (1997) hep-ph/9701231, to appear in *Heavy Flavours II*, eds. A. J. Buras and M. Lindner, Advanced Series on Direction in High Energy Physics, World Scientific Publishing, Singapore.
- [43] Y. Grossman and M. Worah, *Phys. Lett. B* **395**, 241 (1997).
- [44] G. D. Barr *et al.*, (NA31 Collaboration), *Phys. Lett. B* **317**, 233 (1993);
L. K. Gibbons *et al.*, (E731 Collaboration), *Phys. Rev. Lett.* **70**, 1203 (1993).

Introduction to Hadronic B Physics

The purpose of this chapter is to provide an overview of theoretical techniques essential to the study of B mesons and their decays. Of course, there is an enormous literature on this subject, and it is not our goal here to review it all. Rather, this chapter will provide a general context within which to place the theoretical treatments of specific processes found later in this book. The focus here will be on general issues of philosophy and approach. No attempt is made in this chapter to include references to the voluminous literature of individual contributions on each topic. Subsequent more detailed chapters will, it is hoped, remedy this situation.

A key factor in the experimental interest in b physics is the potential insight it affords into physics at very short distances. In particular, it is hoped that the high precision study of phenomena such as CP violation, rare decays, and flavor changing processes will provide precious insights into new interactions associated with the flavor sector of whatever theory lies beyond the Standard Model. However, in order for this information to become available, it is necessary to confront the fact that the b quarks, which are the ultimate objects of study, are bound by strong dynamics into color neutral hadrons. While understood in principle, the nonperturbative nature of these bound states makes problematic the extraction of precision information about physics at higher energies from even the most clever and precise experiments on B mesons. To explore new physics effects one faces a daunting theoretical challenge to untangle them from the effects of nonperturbative QCD.

This is not a problem which has been solved in its entirety, nor is it likely ever to be. Rather, what is available is a variety of theoretical approaches and techniques, appropriate to a variety of specific problems and with varying levels of reliability. There are a few situations in which one can do analyses which are rigorous and predictive, and many in which what can be said is more imprecise and model dependent. The result is an interesting interplay between theory and experiment, where one often cannot measure what one can compute reliably, nor compute reliably what one can measure. In the search for quantities which can be both predicted and measured, one must be creative and flexible in the choice of theoretical techniques. While approaches which are based directly on QCD, and which allow for quantitative error estimates, are clearly to be preferred, more model-dependent methods are often all that are available and thus have an important role to play as well.

The theoretical methods discussed in this chapter fall roughly into three categories. First, there are effective field theories such as the Heavy-Quark Expansion (HQE) and Chiral Perturbation Theory (ChPT). Effective field theories derive their predictive power by exploiting systematically a small

expansion parameter. For nonperturbative QCD, this parameter cannot be the strong coupling constant α_s ; instead, it is a ratio of mass scales obtained by considering a particular limit or special kinematics. Second, there are the approaches of lattice QCD and QCD sum rules, which are based on QCD but do not exploit a large separation of scales. While in principle these techniques are rigorous, they suffer in their current practical implementations from a degree of uncontrolled model dependence. In the case of the lattice, this problem will improve with the availability of ever more powerful computers. Third, there are quark models, which do not purport to be derived from QCD. Instead, in using models one introduces some new degrees of freedom and interactions which, it is hoped, capture or mimic some behavior of the true theory. The advantage of models is their flexibility, since a model may be tuned to particular processes or hadronic states. The disadvantage is that models are intrinsically *ad hoc*, and it is difficult to assess their reliability. For this reason, one should use them only when no better options are available.

Effective field theories are based on the idea that in a given process, only certain degrees of freedom may be important for understanding the physics. In particular, it is often the case that kinematical considerations that restrict the momenta of external particles effectively restrict the momenta of virtual particles as well. Thus it is sensible to remove from the theory intermediate states of high virtuality. Their absence may be compensated by introducing new “effective” interactions between the degrees of freedom which remain. Effective field theories are often constructed using the technique of the operator product expansion, which provides an elegant and general conceptual framework.

Both the HQE and ChPT are effective field theories which are derived from formal limits of QCD in which the theory exhibits new and useful symmetries. In the case of the HQE, the limit is $m_b, m_c \rightarrow \infty$, where a “spin-flavor” symmetry yields a variety of predictions for heavy-hadron spectroscopy and semileptonic decays. For ChPT, the limit is $m_u, m_d, m_s \rightarrow 0$, which leads to exact predictions for the emission and absorption of soft pions. In both cases, the quark masses are large or small compared to the scale of nonperturbative QCD, typically hundreds of MeV. What makes an effective field theory powerful is that the deviations from the limiting behavior may be organized in a systematic expansion in a small parameter. Hence one can both improve the accuracy of an analysis and derive quantitative error estimates. An effective field theory is predictive precisely because it is under perturbative control.

While the HQE and ChPT are powerful tools where they may be applied, their use is restricted to a small number of processes involving certain initial and final states. Unfortunately, the HQE and ChPT have nothing to say about the vast majority of processes and quantities available for experimental study at a B Factory. Similar considerations affect lattice QCD. Because of both computational and theoretical limitations, reliable lattice predictions are confined largely to spectroscopy and matrix elements with restricted kinematics. QCD sum rules, also for technical reasons, may only be used in limited circumstances.

Thus a serious problem remains, namely that many quantities of experimental and phenomenological importance cannot be analyzed by methods which are systematic and well understood. For

inclusive weak decays, some exclusive semileptonic decays, and some static properties, effective field theories or the lattice give controlled theoretical predictions. But for the description of exclusive hadronic weak decays, most exclusive semileptonic decays, strong decays, fragmentation, and many other interesting aspects of B physics, only a variety of model-dependent approaches are available. While no model is “correct,” some models are better than others. A successful model should be motivated by some physical picture, should reproduce much more data than there are input parameters, and should behave correctly in appropriate limits, such as obeying heavy-quark symmetry as $m_b \rightarrow \infty$. It will not be possible in this chapter to discuss or even enumerate all of the models which are used in B physics, but it is generally true that every model ought to be judged by criteria such as these.

Because there is no single theoretical framework which suffices for all of B physics, it is often necessary to utilize a variety of methods in one theoretical analysis. Usually, this is desirable, as a combination of complementary approaches can lead to conclusions which are much more robust. But at the same time, one must be careful to be consistent in the use and definition of theoretical concepts and quantities, and particularly in their translation from one context to another. Otherwise one is led easily to error and confusion.

An excellent illustration of how problems can arise is given by the definition of the heavy-quark mass. Clearly there is *something* which is meant by “the b mass” because to say that the b quark is heavy is to say that the parameter m_b is large compared to Λ_{QCD} . Whatever the b mass is, it is presumably somewhere close to 4 or 5 GeV. But the situation becomes more complicated when one tries to pin down m_b more precisely than that.

On the one hand, it is known that the b quark acquires its mass from its coupling, of strength λ_b , to the “Higgs vacuum expectation value” v , so $m_b = \lambda_b v$. The quark mass which is directly related to this coupling is known as the “current mass” or “short-distance mass.” Its value depends on the renormalization scheme, such as $\overline{\text{MS}}$, which is used to define the theory. In perturbation theory, there is also a pole in the b -quark propagator, the position of which corresponds to the rest energy of a freely propagating b quark. This “pole mass” is closer to an intuitive notion of an invariant, relativistic mass. Unfortunately, because of confinement, a freely propagating b quark cannot actually exist, and the pole mass is not defined nonperturbatively. In fact, even within perturbation theory the pole mass is ill behaved and can only be defined to a fixed finite order α_s^n . Hence there is really a family of pole masses, namely the “1-loop pole mass,” the “2-loop pole mass,” and so on, none more “accurate” or intuitively accessible than another. There are also “Wilsonian” running masses $m_b(\mu)$, which are defined with additional subtractions in the infrared.

An analogous variety of b -quark masses is defined in lattice calculations. While it is typically understood how these lattice b masses are related to each other, relating them to pole or current masses defined in continuum QCD can be problematic. For example, lattice field theory, both perturbative and nonperturbative, is regulated and subtracted differently from field theory in the continuum, and the relationship between the various schemes often is not straightforward. Similar ambiguities can affect the b -quark masses which appear in QCD sum rules. Finally, there are the

many quark masses introduced in models, which are free parameters with *no* rigorous relationship either to each other or to masses defined in QCD. A typical example is the “constituent-quark mass” of the nonrelativistic quark model. No matter how precisely one fits the constituent-quark mass to data, it can never be used as an input into a lattice or HQE calculation. The most that can be said is that all of these various masses probably are within several hundred MeV of each other.

It is important to understand that there is no more precise way to unify these many masses into a single universal quantity. The ambiguity in m_b is unimportant, so long as its definition is *consistent* within a given analysis, and ultimately one predicts measurable quantities in terms of other measurable quantities. This issue will be treated with care in the detailed discussions found in subsequent chapters. The problem is that it is difficult to make an m_b defined on the lattice consistent with one defined in the continuum, and impossible to make a model-dependent m_b consistent with either. Hence there can be limits *in principle* to the accuracy which one can obtain when a variety of methods are combined in a single analysis.

The rest of this chapter consists of elementary introductions to the most important theoretical techniques in B physics. After a general discussion of operator product expansions and effective field theories, Heavy-Quark Effective Theory and Chiral Perturbation Theory are introduced. The next two sections contain discussions of lattice QCD and QCD sum rules, and the chapter will close with a brief discussion of quark models. None of these ideas will be developed in much depth; rather, they will serve as a background to the variety of detailed theoretical analyses to be presented in subsequent chapters. More extended and technical discussions of some of these topics are given in Appendices A–D.

2.1 The Operator Product Expansion

2.1.1 General Considerations

A central observation which underlies much of the theoretical study of B mesons is that physics at a wide variety of distance (or momentum) scales is typically relevant in a given process. At the same time, the physics at different scales must often be analyzed with different theoretical approaches. Hence it is crucial to have a tool which enables one to identify the physics at a given scale and to separate it out explicitly. Such a tool is the operator product expansion, used in conjunction with the renormalization group. Here a general discussion of its application is given.

Consider the Feynman diagram shown in Fig. 2-1, in which a b -quark decays nonleptonically. The virtual quarks and gauge bosons have virtualities μ which vary widely, from Λ_{QCD} to M_W and higher. Roughly speaking, these virtualities can be classified into a variety of energy regimes: (i) $\mu \gg M_W$; (ii) $M_W \gg \mu \gg m_b$; (iii) $m_b \gg \mu \gg \Lambda_{\text{QCD}}$; (iv) $\mu \approx \Lambda_{\text{QCD}}$. Each of these momenta

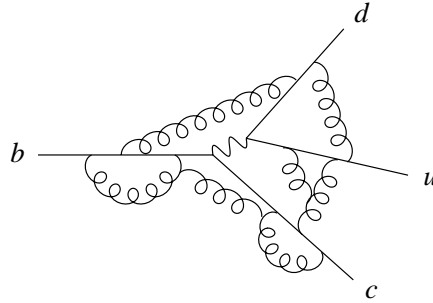


Figure 2-1. *The nonleptonic decay of a b quark.*

corresponds to a different distance scale; by the uncertainty principle, a particle of virtuality μ can propagate a distance $x \approx 1/\mu$ before being reabsorbed. At a given resolution Δx , only some of these virtual particles can be distinguished, namely those that propagate a distance $x > \Delta x$. For example, if $\Delta x > 1/M_W$, then the virtual W cannot be seen, and the process whereby it is exchanged would appear as a point interaction. By the same token, as Δx increases toward $1/\Lambda_{\text{QCD}}$, fewer and fewer of the virtual gluons can be seen explicitly. Finally, for $\mu \approx \Lambda_{\text{QCD}}$, it is probably not appropriate to speak of virtual gluons at all because at such low momentum scales QCD becomes strongly interacting and a perturbation series in terms of individual gluons is inadequate.

It is useful to organize the computation of a diagram such as is shown in Fig. 2-1 in terms of the virtuality of the exchanged particles. This is important both conceptually and practically. First, it is often the case that a distinct set of approximations and approaches is useful at each distance scale, and one would like to be able to apply specific theoretical techniques at the scale at which they are appropriate. Second, Feynman diagrams in which two distinct scales $\mu_1 \gg \mu_2$ appear together can lead to logarithmic corrections of the form $\alpha_s \ln(\mu_1/\mu_2)$, which for $\ln(\mu_1/\mu_2) \sim 1/\alpha_s$ can spoil the perturbative expansion. A proper separation of scales will include a resummation of such terms.

2.1.2 Example I: Weak b Decays

As an example, consider the weak decay of a b quark, $b \rightarrow c\bar{u}d$, which is mediated by the decay of a virtual W boson. Viewed with resolution $\Delta x < 1/M_W$, the decay amplitude involves an explicit W propagator and is proportional to

$$\bar{c}\gamma^\mu(1-\gamma^5)b\bar{d}\gamma_\mu(1-\gamma^5)u \times \frac{(ig_2)^2/4}{p^2 - M_W^2}, \quad (2.1)$$

where p^μ is the momentum of the virtual W . Since $m_b \ll M_W$, the kinematics constrains $p^2 \ll M_W^2$, so the virtuality of the W is of order M_W , and it travels a distance of order $1/M_W$ before

decaying. Viewed with a lower resolution, $\Delta x > 1/M_W$, the process $b \rightarrow c\bar{u}d$ appears to be a local interaction, with four fermions interacting via a potential which is a δ function where the four particles coincide. This can be seen by making a Taylor expansion of the amplitude in powers of p^2/M_W^2 ,

$$\bar{c}\gamma^\mu(1-\gamma^5)b\bar{d}\gamma_\mu(1-\gamma^5)u \times \frac{g_2^2}{8M_W^2} \left[1 + \frac{p^2}{M_W^2} + \frac{p^4}{M_W^4} + \dots \right]. \quad (2.2)$$

The coefficient of the first term is just the usual Fermi decay constant, $G_F/\sqrt{2}$. The higher order terms correspond to local operators of higher mass dimension. In the sense of a Taylor expansion, the momentum-dependent matrix element (2.1), which involves the propagation of a W boson between *two* spacetime points, is identical to the matrix element of the following infinite sum of local operators:

$$\frac{G_F}{\sqrt{2}} \bar{c}\gamma^\mu(1-\gamma^5)b \left[1 + \frac{(i\partial)^2}{M_W^2} + \frac{(i\partial)^4}{M_W^4} + \dots \right] \bar{d}\gamma_\mu(1-\gamma^5)u, \quad (2.3)$$

where the derivatives act on the entire current on the right. This expansion of the nonlocal product of currents in terms of local operators, sometimes known as an *operator product expansion*, is valid so long as $p^2 \ll M_W^2$. For B decays, the external kinematics requires $p^2 \leq m_b^2$, so this condition is well satisfied. In this regime, one may consider a nonrenormalizable *effective field theory*, with interactions of dimension six and above. The construction of such a low-energy effective theory is also known as *matching*. As it is nonrenormalizable, the effective theory is defined (by construction) only up to a cutoff, in this case M_W . The cutoff is explicitly the mass of a particle which has been removed from the theory, or *integrated out*. If one considers processes in which one is restricted kinematically to momenta well below the cutoff, the nonrenormalizability of the theory poses no technical problems. Although the coefficients of operators of dimension greater than six require counterterms in the effective theory (which may be unknown in strongly interacting theories), their matrix elements are suppressed by powers of p^2/M_W^2 . To a *given order* in p^2/M_W^2 , the theory is well defined and predictive.

From a modern point of view, in fact, such nonrenormalizable effective theories are actually preferable to renormalizable theories, because the nonrenormalizable terms contain information about the energy scale at which the theory ceases to apply. By contrast, renormalizable theories contain no such explicit clues about their region of validity.

In principle, it is possible to include effects beyond leading order in p^2/M_W^2 in the effective theory, but in practice, this is usually quite complicated and rarely worth the effort. Almost always, the operator product expansion is truncated at dimension six, leaving only the four-fermion contact term. Corrections to this approximation are of order $m_b^2/M_W^2 \sim 10^{-3}$.

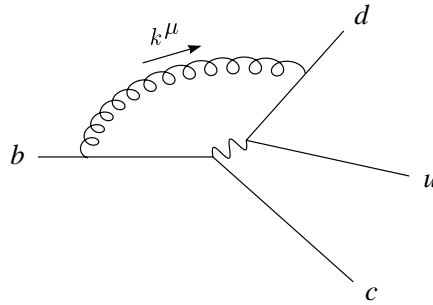


Figure 2-2. The nonleptonic decay of a b quark at one loop.

2.1.3 Radiative Corrections

At tree level, the effective theory is constructed simply by integrating out the W boson because this is the only particle in a tree-level diagram which is off-shell by order M_W^2 . When radiative corrections are included, gluons and light quarks can also be off-shell by this order. Consider the one-loop diagram shown in Fig. 2-2. The components of the loop momentum k^μ are allowed to take all values in the loop integral. However, the integrand is cut off both in the ultraviolet and in the infrared. For $k > M_W$, it scales as d^4k/k^6 , which is convergent as $k \rightarrow \infty$. For $k < m_b$, it scales as $d^4k/k^3 m_b M_W^2$, which is convergent as $k \rightarrow 0$. In between, all momenta in the range $m_b < k < M_W$ contribute to the integral with roughly equivalent weight.

As a consequence, there is potentially a radiative correction of order $\alpha_s \ln(M_W/m_b)$. Even if $\alpha_s(\mu)$ is evaluated at the high scale $\mu = M_W$, such a term is not small in the limit $M_W \rightarrow \infty$. At n loops, there is potentially a term of order $\alpha_s^n \ln^n(M_W/m_b)$. For $\alpha_s \ln(M_W/m_b) \sim 1$, these terms need to be resummed for the perturbation series to be predictive. The technique for performing such a resummation is the *renormalization group*.

The renormalization group exploits the fact that in the effective theory, operators such as

$$O_I = \bar{c}_i \gamma^\mu (1 - \gamma^5) b^i \bar{d}_j \gamma_\mu (1 - \gamma^5) u^j \quad (2.4)$$

receive radiative corrections and must be subtracted and renormalized. (Here the color indices i and j are explicit.) In dimensional regularization, this means that they acquire, in general, a dependence on the renormalization scale μ . Because physical predictions are of necessity independent of μ , in the renormalized effective theory it must be the case that the operators are multiplied by coefficients with a dependence on μ which compensates that of the operators. It is also possible for operators to mix under renormalization, so the set of operators induced at tree level may be enlarged once radiative corrections are included. In the present example, a second operator with different color structure,

$$O_{II} = \bar{c}_i \gamma^\mu (1 - \gamma^5) b^j \bar{d}_j \gamma_\mu (1 - \gamma^5) u^i, \quad (2.5)$$

is induced at one loop. The interaction Hamiltonian of the effective theory is then

$$\mathcal{H}_{\text{eff}} = C_I(\mu)O_I(\mu) + C_{II}(\mu)O_{II}(\mu), \quad (2.6)$$

and it satisfies the differential equation

$$\mu \frac{d}{d\mu} \mathcal{H}_{\text{eff}} = 0. \quad (2.7)$$

By computing the dependence on μ of the operators $O_i(\mu)$, one can deduce the μ -dependence of the *Wilson coefficients* $C_i(\mu)$. In this case, a simple calculation yields

$$C_{I,II}(\mu) = \frac{1}{2} \left[\left(\frac{\alpha_s(M_W)}{\alpha_s(\mu)} \right)^{6/23} \pm \left(\frac{\alpha_s(M_W)}{\alpha_s(\mu)} \right)^{-12/23} \right]. \quad (2.8)$$

For $\mu = m_b$, these expressions resum all large logarithms proportional to $\alpha_s^n \ln^n(M_W/m_b)$.

The decays which are observed involve physical hadrons, not asymptotic quark states. For example, this nonleptonic b decay can be realized in the channels $B \rightarrow D\pi$, $B \rightarrow D^*\pi\pi$, and so on. The computation of partial decay rates for such processes requires the analysis of hadronic matrix elements such as

$$\langle D\pi | \bar{c}\gamma^\mu(1 - \gamma^5)b \bar{u}\gamma_\mu(1 - \gamma^5)d | \bar{B} \rangle. \quad (2.9)$$

Such matrix elements involve nonperturbative QCD and are extremely difficult to compute from first principles. However, they have no intrinsic dependence on large mass scales such as M_W . Because of this, they should naturally be evaluated at a renormalization scale $\mu \ll M_W$, in which case large logarithms $\ln(M_W/m_b)$ will not arise in the matrix elements. By choosing such a low scale in the effective theory (2.6), all such terms are resummed into the coefficient functions $C_i(m_b)$. As promised, the physics at scales near M_W has been separated from the physics at scales near m_b , with the renormalization group used to resum the large logarithms which connect them. In fact, nonperturbative hadronic matrix elements are usually evaluated at an even lower scale $\mu \approx \Lambda_{\text{QCD}} \ll m_b$, explicitly resumming all perturbative QCD corrections.

2.1.4 Example II: Penguins and Box Diagrams

In the previous example of nonleptonic decays, the operator O_I appeared when the matching at tree level was performed. It is also possible to find new operators in the effective theory which appear only when the matching is performed at one loop. The most common such operators are those which arise from penguin and box diagrams, such as those shown in Fig. 2-3. These diagrams are important in b physics typically because they lead to flavor-changing interactions at low energies which are suppressed at tree level in the Standard Model. Hence the transitions mediated by these operators are potentially a sensitive probe of new physics.

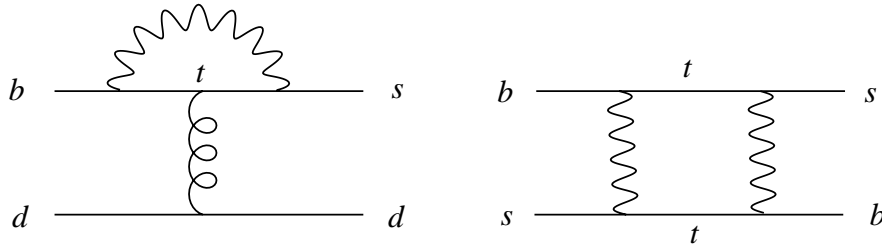


Figure 2-3. Penguin diagram (left) and box diagram (right).

Both penguins and box diagrams can lead, via the operator product expansion, to four-quark operators with new flavor or color structure, such as

$$\bar{s}\gamma^\mu T^a b \bar{d}\gamma_\mu T^a d, \quad (2.10)$$

which mediates nonleptonic B decay, or

$$\bar{b}\gamma^\mu\gamma^5 d \bar{b}\gamma_\mu\gamma^5 d, \quad (2.11)$$

which is responsible for $B^0-\bar{B}^0$ mixing. Penguins can also lead to new flavor-changing magnetic interactions, such as

$$\bar{s}\sigma^{\mu\nu} T^a b G_{\mu\nu}^a, \quad (2.12)$$

when the d -quark line in Fig. 2-3 is removed. The gluon could also be replaced by a photon or a Z boson. From the point of view of the low-energy effective theory, it is unimportant that these operators arise at one loop at high energy. They can mix with four-fermion operators induced at tree level, insofar as such mixing is allowed by the flavor and Lorentz symmetries of the effective theory. In fact, the renormalization of penguin-induced operators can be quite complicated, due to the nature of their flavor structure; two loop calculations may be required to resum the leading logarithms $\alpha_s^n \ln^n(M_W/m_b)$.

2.1.5 Summary

Low-energy effective theories are constructed using the operator product expansion and the renormalization group. This procedure implements an important separation of scales, isolating the physics which involves virtualities $\mu \gg m_b$ and accounting for it systematically in a double expansion in powers of α_s and m_b/M_W , where M_W is the matching scale at which heavy particles are integrated out of the theory. This procedure may be generalized to integrate out heavy particles of many different kinds. For reference, Appendix A includes the complete $\Delta B = 1$ effective Hamiltonian responsible for B decays.

This analysis explicitly does not address those parts of a process which are dominated by low momenta, which will typically be more difficult to deal with. By breaking the problem up according

to momentum scale, one may compute systematically in perturbation theory where it is possible to do so. However, the accuracy obtained in this part of the calculation is useful only if one can also account for physics at lower energy. The chief limitation on the accuracy of most theoretical calculations in b physics is, in fact, from these lower energy effects.

2.2 The Heavy-Quark Expansion

2.2.1 Separation of Scales

This section considers physics characterized by virtualities $\mu \approx m_b$ and below. The previous section discussed how physics at higher scales is accounted for in QCD perturbation theory because at high energies $\alpha_s(\mu)/\pi \ll 1$. Although $m_b \ll M_W$, at this “low” energy it is still the case that $\alpha_s(m_b)/\pi \approx 0.1 \ll 1$, and $\Lambda_{\text{QCD}}/m_b \sim 0.1 \ll 1$. Hence one seeks a technique analogous to the operator product expansion by which to exploit the presence of such small parameters.

The status of the b quark in a B meson is different from that of a virtual W in a weak decay because the b is real, not virtual, and the B carries nonzero b -number which persists in the asymptotic state. Hence it is not appropriate to integrate out the b in the same sense as the W was integrated out, removing it from the theory entirely. Rather, when bound into a hadron with light degrees of freedom of typical energies $E \sim \Lambda_{\text{QCD}}$, the b makes excursions from its mass shell by virtualities only of order Λ_{QCD} . What can be integrated out is not the b itself, but rather those parts of the b field which take it far off shell. The result will be an effective theory of a static b quark, in its rest frame.

Processes with hard virtual gluons, which drive the b far off shell, will lead to perturbative corrections in the effective theory of order $\alpha_s(m_b)$. They may be included as before. In addition, *power corrections* appear, analogous to the higher order operators appearing in Eq. (2.3). In this case, it will be necessary to include the leading higher-dimension operators to achieve results of the desired accuracy. These power corrections will lead to terms of order $(\Lambda_{\text{QCD}}/m_b)^n$. The appearance of the scale Λ_{QCD} serves as a reminder that these corrections involve nonperturbative physics and will typically not be calculable from first principles. Instead, the inclusion of power corrections will require the introduction of new phenomenological parameters, whose values are controlled by nonperturbative QCD. These parameters have precise field-theoretic definitions, and they will be introduced in a systematic manner. Their appearance will not spoil the inherent predictability of the theory, although in practice they will increase the number of quantities which must be determined from experiment before accurate predictions can be made.

Finally, for some applications (notably the analysis of exclusive semileptonic B decays), it will be useful to treat the c quark as heavy, that is, to perform an expansion also in powers of Λ_{QCD}/m_c .

In this case, clearly, the leading power corrections will be important and will have to be well understood for the theory to be predictive.

2.2.2 Heavy-Quark Symmetry

Let us, for generality, consider a hadron H_Q composed of a heavy quark Q and “light degrees of freedom” consisting of quarks, antiquarks, and gluons, in the limit $m_Q \rightarrow \infty$. The Compton wavelength of the heavy-quark scales as the inverse of the heavy-quark mass, $\lambda_Q \sim 1/m_Q$. The light degrees of freedom, by contrast, are characterized by momenta of order Λ_{QCD} , corresponding to wavelengths $\lambda_\ell \sim 1/\Lambda_{\text{QCD}}$. Since $\lambda_\ell \gg \lambda_Q$, the light degrees of freedom cannot resolve features of the heavy quark other than its conserved gauge quantum numbers. In particular, they cannot probe the actual *value* of λ_Q . Although the structure of the hadron H_Q is determined by nonperturbative strong interactions, the typical momenta exchanged by the light degrees of freedom with each other and with the heavy quark are of order $\Lambda_{\text{QCD}} \ll m_Q$, against which the heavy quark Q does not recoil. In this limit, Q acts as a static source of electric and chromoelectric field.

There is an immediate implication for the spectroscopy of heavy hadrons. Since the interaction of the light degrees of freedom with the heavy quark is independent of m_Q , then so is the spectrum of excitations. It is these excitations which determine the spectrum of heavy hadrons H_Q . Since the *splittings* $\Delta_i \sim \Lambda_{\text{QCD}}$ between the various hadrons H_Q^i are entirely due to the properties of the light degrees of freedom, they are independent of Q and, in the limit $m_Q \rightarrow \infty$, do not scale with m_Q . For example, if $m_b, m_c \gg \Lambda_{\text{QCD}}$, then the light degrees of freedom are in exactly the same state in the mesons B_i and D_i , for a given i . The offset $B_i - D_i = m_b - m_c$ is just the difference between the heavy-quark masses. By no means does the relationship between the spectra rely on an approximation $m_b \approx m_c$.

This picture is enriched by recalling that the heavy quarks and light degrees of freedom also carry angular momentum. The heavy quark has spin quantum number $S_Q = \frac{1}{2}$, which leads to a chromomagnetic moment $\mu_Q \propto g/2m_Q$. Note that $\mu_Q \rightarrow 0$ as $m_Q \rightarrow \infty$, and the interaction between the spin of the heavy quark and the light degrees of freedom is suppressed. Hence the light degrees of freedom are insensitive to S_Q ; their state is independent of whether $S_Q^z = \frac{1}{2}$ or $S_Q^z = -\frac{1}{2}$. Thus each of the energy levels B_i and D_i is actually doubled, one state for each value of S_Q^z . In summary, the light degrees of freedom in a heavy hadron are the same when combined with any of the four heavy-quark states:

$$b(\uparrow), \quad b(\downarrow); \quad c(\uparrow), \quad c(\downarrow). \quad (2.13)$$

The result is an $SU(4)$ symmetry which leads to nonperturbative relations between physical quantities.

Suppose the light degrees of freedom have total angular momentum J_ℓ , which is integral for baryons and half-integral for mesons. When combined with the heavy-quark spin $S_Q = \frac{1}{2}$, physical hadron states can be produced with total angular momentum

$$J = \left| J_\ell \pm \frac{1}{2} \right|. \quad (2.14)$$

If $J_\ell \neq 0$, then these are two degenerate states. For example, the lightest heavy mesons have $J_\ell = \frac{1}{2}$, leading to a doublet with $J = 0$ and $J = 1$. When effects of order $1/m_Q$ are included, the chromomagnetic interactions split the states of given J_ℓ but different J . This ‘‘hyperfine’’ splitting is not calculable perturbatively, but it is proportional to the heavy-quark magnetic moment μ_Q . Since $\mu_Q \propto 1/m_Q$, one can construct a relation which is a nonperturbative prediction of heavy-quark symmetry,

$$m_{B^*}^2 - m_B^2 = m_{D^*}^2 - m_D^2. \quad (2.15)$$

Experimentally, $m_{B^*}^2 - m_B^2 = 0.49 \text{ GeV}^2$ and $m_{D^*}^2 - m_D^2 = 0.55 \text{ GeV}^2$. The correction to this prediction is of order $\Lambda_{\text{QCD}}^3(1/m_c - 1/m_b) \sim 0.1 \text{ GeV}^2$, so it works about as well as one should expect. Note that the relation (2.15) involves not only the heavy-quark symmetry, but also the systematic inclusion of the leading-symmetry-violating effects.

So far, heavy-quark symmetry has been formulated for hadrons in their rest frame. One can easily boost to a frame in which the hadrons have arbitrary four-velocity $v^\mu = \gamma(1, \mathbf{v})$. The symmetry will then relate hadrons $H_b(v)$ and $H_c(v)$ with the same velocity but with different momenta. This distinguishes heavy-quark symmetry from ordinary symmetries of QCD, which relate states of the same momentum. It will often be convenient to label heavy hadrons explicitly by their velocity: $B(v)$, $B^*(v)$, and so on.

2.2.3 Heavy-Quark Effective Theory

It is quite useful to make heavy-quark symmetry manifest within QCD by taking the limit $m_b \rightarrow \infty$ of the QCD Lagrangian. This is done by making the dependence of all quantities on m_b explicit, and then developing the Lagrangian in a series in inverse powers of m_b . The idea is to write the Lagrangian in a form in which the action of the heavy-quark symmetries is well-defined at each order in the expansion, so the effect of symmetry breaking corrections can be studied in a systematic way. The resulting Lagrangian is known as the Heavy-Quark Effective Theory (HQET). The HQET is similar to an effective theory which results from an operator product expansion, in the sense that the only virtualities p which are allowed satisfy $p \ll m_b$, with effects of greater virtuality absorbed into the coefficients of higher dimension operators. The difference is that in this case, the heavy b quark is not explicitly removed from the effective theory.

In the heavy-quark limit, the velocity v^μ of the b quark is conserved. Thus one may write its four-momentum in the form $p_b^\mu = m_b v^\mu + k^\mu$, where $m_b v^\mu$ is the *on-shell* part and k^μ is the *residual momentum*. In this decomposition, $k^\mu \sim \Lambda_{\text{QCD}}$ represents the fluctuations in p_b^μ due to

the exchange of soft gluons with the rest of the B meson. Only the on-shell part of p_b^μ scales with m_b . Also, mixing between the “quark” and “anti-quark” components of the Dirac spinor is suppressed by powers of $2m_b$, the mass gap between the positive- and negative-energy parts of the wavefunction. Hence an effective heavy-quark field h_v can be defined,

$$h_v(x) = \frac{1 + \not{v}}{2} e^{im_b v \cdot x} b(x), \quad (2.16)$$

where the Dirac matrix $(1 + \not{v})/2$ projects out the “quark” part of the field. Furthermore, since $i\partial^\mu h_v(x) = (p_b^\mu - m_b v^\mu)h_v(x) = k^\mu h_v(x)$, derivatives acting on h_v scale as Λ_{QCD} , rather than as m_b .

The next step is to express the QCD Lagrangian, $\mathcal{L} = \bar{b}(i\not{D} - m_b)b$, in terms of the m_b -independent field h_v . At lowest order in $1/m_b$, the result is

$$\mathcal{L}_{\text{HQET}} = \bar{h}_v i v \cdot D h_v. \quad (2.17)$$

At leading order, $\mathcal{L}_{\text{HQET}}$ respects the heavy spin and flavor symmetries explicitly. Both bottom and charm quarks can be treated as heavy by introducing separate effective fields $h_v^{(b)}$ and $h_v^{(c)}$ and duplicating $\mathcal{L}_{\text{HQET}}$. The theory has a simple heavy-quark propagator and quark-gluon vertex which are manifestly independent of m_b and have no Dirac structure.

The effective theory is also expanded perturbatively in $\alpha_s(m_b)$. In particular, the quark mass m_b is shifted to m_b^{pole} , the *pole mass* at n loops. The pole mass is a quantity which makes sense only at finite order in perturbation theory. One must always be careful to be consistent in the convention by which one chooses to define it.

The mass of the B meson may be expanded in powers of m_b ,

$$m_B = m_b + \bar{\Lambda} + \mathcal{O}(1/m_b), \quad (2.18)$$

where $\bar{\Lambda} \sim \Lambda_{\text{QCD}}$ is the energy contributed by the light degrees of freedom. Its precise definition depends on the convention by which one chooses to define the heavy-quark pole mass. The parameter $\bar{\Lambda}$ depends on the flavor, excitation energy, and total angular momentum of the light degrees of freedom.

When one includes the leading $1/m_{b,c}$ corrections, the heavy spin and flavor symmetries are broken by the subleading terms. The leading Lagrangian (2.17) is modified by the addition of two terms,

$$\mathcal{L}^{(1)} = \frac{1}{2m_b} (O_1 + O_2) = \frac{1}{2m_b} \left(\bar{h}_v (iD)^2 h_v + \bar{h}_v \frac{1}{2} g G_{\mu\nu} \sigma^{\mu\nu} h_v \right), \quad (2.19)$$

neglecting terms which vanish by the classical equations of motion. Note that the “kinetic” operator O_1 violates the heavy-flavor symmetry, while the “chromomagnetic” operator O_2 violates both the spin and flavor symmetries. When radiative corrections are included, the operator O_2 is renormalized, and its coefficient develops a logarithmic dependence on m_b .

The subleading operators O_1 and O_2 contribute to the mass of the B meson through their expectation values,

$$\lambda_1 = \langle B | \bar{h}_v (iD)^2 h_v | B \rangle / 2m_B, \quad (2.20)$$

$$\lambda_2 = \langle B | \bar{h}_v \frac{1}{2} g G_{\mu\nu} \sigma^{\mu\nu} h_v | B \rangle / 6m_B. \quad (2.21)$$

The matrix elements λ_1 and λ_2 are often referred to by the alternate names $\mu_\pi^2 = -\lambda_1$ and $\mu_G^2 = 3\lambda_2$. The parameter μ_π^2 actually differs from λ_1 in that it is defined with an explicit infrared subtraction. Because they are defined in the effective theory, the parameters λ_1 and λ_2 do not depend on m_b . The expansion of m_B now takes the form

$$\begin{aligned} m_B &= m_b + A - \frac{\lambda_1 + 3\lambda_2}{2m_b} + \dots, \\ m_{B^*} &= m_b + \bar{A} - \frac{\lambda_1 - \lambda_2}{2m_b} + \dots. \end{aligned} \quad (2.22)$$

Because O_2 violates the heavy-spin symmetry, it is the leading contribution to the splitting between B and B^* . From the measured mass difference, $\lambda_2 \approx 0.12 \text{ GeV}^2$. On the other hand, the parameters \bar{A} and λ_1 must be measured indirectly. Estimates from models yield the ranges $200 \text{ MeV} < \bar{A} < 700 \text{ MeV}$ and $-0.5 \text{ GeV}^2 < \lambda_1 < 0$. Measurement of various features of inclusive semileptonic B decays will provide experimental information on \bar{A} and λ_1 in the future.

2.2.4 Application of the HQE to B Decays

A variety of applications of the HQE to B decays will be discussed in later chapters. Here a few general comments and two illustrative examples are given. In principle, the value of using an effective theory such as the HQE is that there is a framework within which one can estimate the error in a calculation, due to uncomputed terms of a definite size. Even when the accuracy is not so good, it is under control in the sense that one can understand the magnitude of the error to be expected. In any application of the HQE, then, two sorts of questions must be addressed in addition to the computation itself:

1. What are the sizes of the leading uncomputed corrections in the expansion in powers of α_s and $1/m_b$ (or $1/m_c$, as appropriate)? With what accuracy are the parameters known which appear in the expansion?
2. What *other* assumptions or approximations have been made, beyond those that go into the HQE itself?

2.2.4.1 Exclusive semileptonic B decays

The paradigmatic application of heavy-quark symmetry is to semileptonic B decay in the limit $m_b, m_c \rightarrow \infty$. This decay is mediated by the quark transition $b \rightarrow c \ell \bar{\nu}$. Suppose the weak decay occurs at time $t = 0$. What happens to the light degrees of freedom? Since the b quark does not recoil, for $t < 0$ they see simply the color field of a point source moving with velocity v . At $t = 0$, this point source changes (almost) instantaneously to a new velocity v' ; the color neutral leptons do not interact with the light hadronic degrees of freedom as they fly off. The light quarks and gluons then must reassemble themselves about the recoiling color source. There is some chance that this nonperturbative process will lead the light degrees of freedom to reassemble themselves back into a D meson. The amplitude for this to happen is a function $\xi(w)$ of the product $w = v \cdot v'$ of the initial and final velocities of the heavy color sources.

Clearly, the kinematic point $v = v'$, or $w = 1$, is a special one. In this corner of phase space, where the leptons are emitted back to back, there is no recoil of the source of color field at $t = 0$. As far as the light degrees of freedom are concerned, *nothing happens!* Hence the amplitude for them to remain in the ground state is exactly unity. This is reflected in a nonperturbative normalization of $\xi(w)$ at zero recoil,

$$\xi(1) = 1. \quad (2.23)$$

This normalization condition is of great phenomenological use. There are important corrections to this result for finite heavy-quark masses m_b and, especially, m_c .

The weak decay $b \rightarrow c$ is mediated by a left-handed current $\bar{c}\gamma^\mu(1-\gamma^5)b$, which can also change the orientation of the spin S_Q of the heavy quark during the decay. Since the only difference between a D and a D^* is the orientation of S_c , heavy-quark symmetry implies relations between the hadronic matrix elements which describe the semileptonic decays $B \rightarrow D\ell\bar{\nu}$ and $B \rightarrow D^*\ell\bar{\nu}$. These matrix elements are parameterized by six form factors, which are independent nonperturbative functions of w . In the heavy-quark limit, they are all proportional to $\xi(w)$, a powerful constraint on the structure of semileptonic decays.

Now consider more closely the structure of the theoretical expansion for the decay $B \rightarrow D^*\ell\bar{\nu}$, which may be used to measure the CKM matrix element $|V_{cb}|$. Near the zero-recoil point, the transition is dominated by a single form factor, $h_{A_1}(w)$, with the normalization condition $h_{A_1}(1) = 1$ in the heavy-quark limit. For general m_B and m_{D^*} , the differential decay rate may be written

$$\frac{d\Gamma}{dw} = G_F^2 |V_{cb}|^2 K(m_B, m_{D^*}, w) F^2(w), \quad (2.24)$$

where $K(m_B, m_{D^*}, w)$ is a known kinematic function and $F(w)$ has an expansion at $w = 1$ of the form

$$F(1) = \eta_A(\alpha_s) \left[1 + \frac{0}{m_c} + \frac{0}{m_b} + \mathcal{O}\left(\frac{1}{m_b^2}\right) \right]. \quad (2.25)$$

The perturbative function $\eta_A(\alpha_s)$ has been computed to two loops, with the result $\eta_A = 0.960$. The leading HQE corrections arise at order $1/m_{b,c}^2$ rather than at order $1/m_{b,c}$, and have been estimated

to be approximately 5%. A more detailed analysis of this decay will be given in a later chapter. For now, the point is to note how the double expansion in powers of α_s and $1/m_{b,c}$ appears in a physical quantity. This analysis is also typical because it applies only to a very particular case of enhanced symmetry, namely the decay rate as $w \rightarrow 1$. The extrapolation of the data to this limit requires both experimental ingenuity and more theoretical input beyond the HQE.

2.2.4.2 Duality and inclusive semileptonic decays

As a second example, consider the *inclusive* decay $B \rightarrow X_c$, where X_c is any final state containing a charm quark. The analysis of inclusive decays, although it relies on a similar expansion, is different from the treatment of exclusive decays. In this case, it is useful to observe that the energy released into the final state by the decay of the heavy b quark is large compared to the QCD scale. Hence the final hadronic state need not be dominated by a few sharp resonances. If resonances are indeed unimportant, then there is a factorization between the short-distance part of the decay (the disappearance of the b quark) and the long-distance part (the eventual hadronization of the decay products). This factorization implies that for sufficiently inclusive quantities it is enough to consider the short-distance part of the process, with the subsequent hadronization taking place with unit probability. Note that what is important here is that the b quark is heavy, with no restriction placed on the charm mass. In fact, a smaller charm-quark mass is better because it increases the average kinetic energy of the decay products.

This factorization, known as *local parton-hadron duality*, is an example of a crucial assumption which lies outside of the HQE itself. What is its status? Clearly, local duality must hold as $m_b \rightarrow \infty$ with all other masses held fixed. In this limit, wavelengths associated with the b -quark decay are arbitrarily short and cannot interfere coherently with the hadronization process. On the other hand, it is not known how to estimate the size of corrections to local duality for m_b large but finite. There is no analog of the heavy-quark expansion appropriate to this question, and no way to estimate systematically deviations from the limit $m_b \rightarrow \infty$. Although we will incorporate an expansion in powers $1/m_b$ in the calculation of inclusive quantities, the behavior of this expansion does not address directly the issue of violations of duality. The duality hypothesis, while entirely reasonable for inclusive B decays, is not independently verifiable except by the direct confrontation of theoretical calculations with the data.

For semileptonic B decays, $B \rightarrow X_c \ell \bar{\nu}$, the situation has additional interesting features. On the one hand, in the region of phase space where the leptons carry away most of the available energy, the final hadronic state is likely to be dominated by resonances and local duality is likely to fail. (In some B decays, local duality can be shown to hold even in the resonance region; however, this requires a more subtle and less intuitive argument than the one on which this discussion is based.) On the other hand, if one integrates over the lepton phase space to compute an inclusive quantity such as the total semileptonic width, then one needs not local duality but rather the weaker notion of *global parton-hadron duality*. (The use here and elsewhere in this book of this term, while it

reflects current practice, is ahistorical. This notion originally was known simply as *duality*, while *global duality* was first introduced to describe the technical assumption that one can neglect distant cuts in computing the semileptonic B decay rate, which is an important and distinct issue. Both terminologies remain in use in the literature.)

In essence, the argument is as follows. Let q be the momentum carried away by the leptons. The semileptonic width is an integral of a differential width, written schematically as $d\Gamma/dq$, which must be calculated under the hypothesis of local duality. For certain ranges of q (q^2 near its kinematic maximum), local duality clearly fails. However, $d\Gamma/dq$ has a known analytic structure as a function of q , with cuts and poles, corresponding to thresholds and resonances, which are confined to the real axis. If the integration contour in q is deformed away from the resonances, *into the complex plane*, then it may be possible to compute the integral without knowing the integrand everywhere along the original (real) contour of integration. From one point of view, complex q forces the final state away from the mass shell, where long-distance effects can become important. From another, the integral over q imposes an average over the invariant mass s_H of the hadrons in the final state, which smears out the effect of resonances when they do contribute. This property, that quantities averaged over s_H may be computable even when differential ones are not, is global duality. The most important feature is the *smearing* of the perturbative calculation over the resonance region. Note that global duality does not apply to purely hadronic B decays, for which $s_H = m_B^2$ is fixed.

Once the issue of duality has been addressed, the actual expansions obtained for inclusive decays are very similar to those for exclusive decays. For example, the total charmless semileptonic B decay width takes the form

$$\Gamma(B \rightarrow X_u \ell \bar{\nu}) = \frac{G_F^2 |V_{ub}|^2}{192\pi^3} m_b^5 \left[1 - 2.41 \frac{\alpha_s}{\pi} + \frac{\lambda_1 - 9\lambda_2}{2m_b^2} + \dots \right]. \quad (2.26)$$

The leading corrections to this expression are of order α_s^2 , α_s/m_b and $1/m_b^3$. Note that the $1/m_b^2$ corrections are far more tractable than in the exclusive decay: first, because $1/m_c^2$ does not appear, and second, because they may all be written in terms of the two parameters λ_1 and λ_2 , one of which is already known. Finally, note the strong dependence on the mass m_b , which is equivalent via the mass expansion (2.22) to a dependence on $\bar{\Lambda}$. This is a significant source of uncertainty in the expression for the rate. The extensive recent theoretical efforts to reduce this uncertainty will be discussed in detail in Chapter 8. Similarly, the technically-more-complicated case of $B \rightarrow X_c \ell \bar{\nu}$ is left until this later more-detailed discussion.

2.2.5 Limitations of the HQE

While the heavy-quark expansion and the HQET are powerful tools in the analysis of many aspects of B spectroscopy and decay, there are important issues into which they provide little direct insight.

What the HQE provides is a framework within which the dependence of quantities on the large mass m_b may be extracted systematically. However, once this has been accomplished, the task usually remains of analyzing those parts of the process which are characterized by long distances, small momenta, and nonperturbative dynamics. For a few quantities, such as the exclusive and inclusive decay rates discussed in this section, the calculation can be organized so that such effects appear only at subleading order, with the leading order terms controlled by heavy-quark symmetry. But this is not the typical situation in B phenomenology; one is usually required to analyze quantities and processes for which the nonperturbative nature of QCD is a dominant effect.

By necessity, such analyses involve a wide variety of methods, techniques, approximations and ansatzes. Some of the most important approaches are briefly discussed in the rest of this chapter. But even where the heavy-quark limit is not itself predictive, it still has an important role to play. Any model or effective theory which purports to describe B mesons must obey the heavy-quark limit. By the same token, it is often possible to enhance or extend a model by building heavy-quark symmetry in explicitly. The information provided by the heavy-quark limit will prove to be very useful in this broader context.

2.3 Light Flavor Symmetry

2.3.1 Chiral Lagrangians

Complementary to the heavy-quark limit, new symmetries of QCD also arise in the limit of vanishing light-quark masses. As $m_u, m_d, m_s \rightarrow 0$, the quarks of left and right helicity decouple from each other. In this limit, the invariance of the Lagrangian separately under rotations among (u_L, d_L, s_L) and (u_R, d_R, s_R) gives rise to an $SU(3)_L \times SU(3)_R$ chiral flavor symmetry. In the QCD vacuum, this symmetry is dynamically broken to the diagonal subgroup $SU(3)_V$ by the quark condensate $\langle \bar{q}_i q_j \rangle \neq 0$. As a consequence, there are eight Goldstone bosons in the light spectrum, which we identify with the physical π , K , and η . Since the actual u , d , and s -quark masses are small but nonzero, the π , K , and η are light but not exactly massless.

The spontaneous breaking of chiral symmetry is characterized by a scale $\Lambda_\chi \sim 1$ GeV, which is related to the value of the quark condensate. For light masses $m_\pi, m_K, m_\eta \ll \Lambda_\chi$ and small momenta $p \ll \Lambda_\chi$, QCD exhibits a separation of energy scales which can be used as the basis for an effective field theory. This *chiral Lagrangian* describes low-energy interactions in a systematic expansion in powers of p/Λ_χ and m_q/Λ_χ . Since the fundamental degrees of freedom, the eight “pions” π , K and η , are the Goldstone bosons associated with the spontaneous symmetry breaking $SU(3)_L \times SU(3)_R \rightarrow SU(3)_V$, they transform in a complicated nonlinear way under the full symmetry group. It is convenient to assemble them into a matrix Π_{ab} , which is in turn

exponentiated,

$$\Sigma_{ab} = [\exp(2i\Pi/f_\pi)]_{ab} , \quad (2.27)$$

where $f_\pi \approx 130$ MeV is the pion decay constant and a, b are flavor indices which take values u, d , or s . The unusual looking field Σ has the property that it transforms simply under $SU(3)_L \times SU(3)_R$.

The chiral Lagrangian is the most general function of Σ consistent with the symmetries, constructed order by order in powers of $1/\Lambda_\chi$. At lowest order, the Lagrangian is completely fixed,

$$\mathcal{L} = \frac{f_\pi^2}{4} \partial^\mu \Sigma_{ab}^\dagger \partial_\mu \Sigma_{ba} + \dots , \quad (2.28)$$

where the flavor indices are summed over and the ellipsis indicates operators suppressed by Λ_χ^n . The exponential form of the Σ field allows this simple Lagrangian to describe interactions between arbitrarily large numbers of pions. Indeed, one of the useful features of Chiral Perturbation Theory (ChPT) is its ability to relate scattering amplitudes involving different numbers of external particles.

All hadrons other than the pions, such as vector mesons or baryons, have masses of order Λ_χ . Hence for external momenta $p \ll \Lambda_\chi$ they can only appear as virtual states. Their effect on the effective theory is reproduced by higher dimension operators involving Σ , such as

$$\frac{f_\pi^2}{\Lambda_\chi^2} \text{Tr} \left[\partial^\mu \Sigma^\dagger \partial^\nu \Sigma^\dagger \partial_\mu \Sigma \partial_\nu \Sigma \right] , \quad (2.29)$$

where the trace is over flavor indices. Because one cannot solve QCD, the couplings of these operators are unknown constants which must be determined phenomenologically. In practice, the Lagrangian (2.28) has been generalized to include operators containing up to four derivatives or one power of the light-quark masses, as well as effects from electromagnetic and flavor changing currents. By now, most of the couplings have been extracted from experiment. Typical predictions, such as π - K radiative reactions or π - π scattering, are accurate at the 10–30% level, although in some cases, such as the extraction of $|V_{us}|$ from $K \rightarrow \pi \ell \bar{\nu}$, the uncertainties are much smaller. It is important to keep in mind that these predictions are valid only so long as external momenta are small compared to $\Lambda_\chi \sim 1$ GeV.

2.3.2 Heavy-Hadron Chiral Perturbation Theory

Although heavy hadrons have masses much larger than Λ_χ , it is still possible to incorporate them into ChPT. This is because it is only the light degrees of freedom in the hadron, whose mass does not scale with the heavy quark, which interact with external pions. This extension of the effective theory, known as Heavy-Hadron Chiral Perturbation Theory (HHChPT), incorporates the

heavy-quark spin-flavor symmetry in an expansion in derivatives, light-quark masses, and inverse heavy-quark masses. It describes soft pions interacting with a static heavy hadron.

A simple example of where such a formalism is useful is the semileptonic decay $B \rightarrow \pi \ell \bar{\nu}$. Over most of the Dalitz plot, the pion is much too energetic for chiral symmetry to apply. However, in the region where the pion is soft, the form factor $f_+(q^2)$ which determines the differential rate can be determined reliably. For a sufficiently soft pion, the dominant contribution to $B \rightarrow \pi \ell \bar{\nu}$ comes from the process where $B \rightarrow B^* \pi$, with the virtual B^* then decaying leptonically. The strength of the $B \rightarrow B^* \pi$ transition is proportional to a universal coupling constant g , which may be determined from the rate for the decay $D^* \rightarrow D \pi$. The amplitude for $B \rightarrow \pi \ell \bar{\nu}$ at lowest order in HHChPT is then

$$f_+(q^2) = \frac{g M_B^2 f_B / f_\pi}{M_{B^*}^2 - q^2}, \quad (2.30)$$

which is simply a statement of nearest pole dominance, which holds rigorously in the combined heavy-quark and chiral limit. Physically, pole dominance holds because in this limit the mass splitting between the B and B^* vanishes, whereas the energy gap to the nearest excited resonance remains finite. Thus, for arbitrarily soft pions, the B^* is the only resonance which can affect the form factor. Note that the heavy- and light-flavor symmetries relate B_s, D and D_s states to the B , so there are analogous form factors in $B_s \rightarrow K \ell \bar{\nu}$, $D_s \rightarrow K \ell \bar{\nu}$, and $D \rightarrow \pi \ell \bar{\nu}$.

As is typical in chiral calculations, the amplitude relations hold only where the pions are soft. There will be corrections to these relations at higher order, when loop graphs and explicit symmetry breaking terms are included. Most calculations within HHChPT are done at leading order, or include only some of the numerically important corrections. Since the number of unknown coefficients tends to proliferate at higher order, such results are usually presented as estimates of the size of symmetry breaking effects. Chiral Lagrangians are particularly useful for exploring the light-flavor dependence of quantities arising from pion loops and other infrared physics.

2.3.3 Factorization, Color Flow, and Vacuum Saturation

The problem with chiral calculations is that they only apply when the external pions are soft, and for most processes of phenomenological interest, nothing constrains this to be the case. For example, it is not very useful to apply such techniques to exclusive nonleptonic decays such as $B \rightarrow D \pi$, since the π has momentum $p = 2.3 \text{ GeV} > \Lambda_\chi$. If one attempts to use the chiral Lagrangian here, one finds that the effects of higher dimension operators, which scale as $(p/\Lambda_\chi)^2$, are unsuppressed, and the theory loses its predictive power. The hadrons in the final state continue to interact long after the weak decay, and there is no clean separation of scales. The situation is even more complicated for multiple pion production ($B \rightarrow D \pi \pi, \dots$), which is governed over most of the phase space not by low-energy theorems but by the nonperturbative dynamics of QCD fragmentation. In the absence of a solution to QCD, exclusive nonleptonic decays remain one of

the most intractable problems in B physics. All that one has is a variety of models, based on ideas such as light cone wavefunctions or fragmenting strings, which describe the data with varying degrees of success.

In the absence of any theory based on first principles, phenomenological approaches are often used instead. The most popular of these is the hypothesis of *factorization*, which applies to certain two body nonleptonic decays. A simple example is $B \rightarrow D\pi$, which is mediated by the quark transition $b \rightarrow c\bar{u}d$. Immediately after the weak decay, the quarks typically find themselves with a large momentum and in the middle of a medium of gluons and light quark-antiquark pairs, with which they subsequently interact strongly. However, if the $\bar{u}d$ pair has a small invariant mass, $m(\bar{u}d) \approx m_\pi$, then these two quarks will remain close together as they move through the colored medium. If, in addition, they are initially in a color singlet state, then they will interact with the medium not individually but as a single color dipole. Since the distance between the \bar{u} and the d grows slowly, it is possible that the pair will have left the colored environment completely before its dipole moment is large enough for its interactions to be significant. In this case, the pair will hadronize as a single π . Such a phenomenon is known as “color transparency.”

If, by contrast, the $\bar{u}d$ pair has a large invariant mass, then the quarks will interact strongly with the medium. In this case, their reassembly into a single π is extremely unlikely. As a result, it is reasonable to hypothesize that the decay $B \rightarrow D\pi$ is dominated by the former scenario, and that the matrix element actually factorizes,

$$\langle D\pi | \bar{c}\gamma^\mu(1 - \gamma^5)b \bar{d}\gamma_\mu(1 - \gamma^5)u | \bar{B} \rangle = \langle D | \bar{c}\gamma^\mu(1 - \gamma^5)b | \bar{B} \rangle \times \langle \pi | \bar{d}\gamma_\mu(1 - \gamma^5)u | 0 \rangle. \quad (2.31)$$

The result is something much simpler: $\langle \pi | \bar{d}\gamma_\mu(1 - \gamma^5)u | 0 \rangle$ is related to f_π , and $\langle D | \bar{c}\gamma^\mu(1 - \gamma^5)b | \bar{B} \rangle$ may be extracted from semileptonic B decays. With this ansatz, it is possible to obtain relations among various two body decays which can then be tested experimentally. A proper analysis is fairly complicated because it is necessary to take into account short-distance perturbative corrections and other formally subleading effects. In particular, when the leading QCD radiative corrections are included, the matrix element (2.31) develops a dependence on the renormalization scale μ which cannot be compensated within the factorization ansatz. Thus even the question of whether a matrix element factorizes has no scale invariant meaning. A complete discussion is reserved for later chapters.

There is a heuristic distinction which is often made in the discussion of nonleptonic B decays, between contributions to decays which are “color allowed” and those which are “color suppressed.” In the spirit of factorization, it is often convenient to use Fierz identities to rewrite the effective Hamiltonian as a sum of products of quark bilinears which could interpolate certain exclusive final states. For example, if one were interested in the semi-inclusive process $B \rightarrow X_s\psi$, it would be useful to re-express the combination

$$C_1 \bar{s}_i\gamma^\mu(1 - \gamma^5)c^j \bar{c}_j\gamma_\mu(1 - \gamma^5)b^i + C_2 \bar{s}_i\gamma^\mu(1 - \gamma^5)c^i \bar{c}_j\gamma_\mu(1 - \gamma^5)b^j, \quad (2.32)$$

where i and j are color indices, as

$$(C_1 + \frac{1}{3}C_2) \bar{c} \gamma^\mu (1 - \gamma^5) c \bar{s} \gamma_\mu (1 - \gamma^5) b + 2C_2 \bar{c} T^a \gamma^\mu (1 - \gamma^5) c \bar{s} T^a \gamma_\mu (1 - \gamma^5) b. \quad (2.33)$$

Then the first term can be factorized in the sense of Eq. (2.31), while the second cannot. If the coefficient $C_1 + \frac{1}{3}C_2$ of the factorizable term is large, that is, if $C_1 + \frac{1}{3}C_2 \gg 2C_2$, then the amplitude is said to be “color allowed”; if the reverse is true, then it is said to be “color suppressed.” It is often supposed that amplitudes which have the wrong color structure to factorize are intrinsically small. Of course, soft gluons can always be exchanged to rearrange the color structure, so this distinction does not survive radiative corrections. However, the neglect of nonfactorizable amplitudes is a common phenomenological starting point for analyses of nonleptonic B decays, where it is often useful to have some guess as to which four-quark operators are the most important for mediating a given transition.

Another common ansatz, which is similar in spirit to factorization, is *vacuum saturation*. The computation of $B^0 - \bar{B}^0$ mixing requires the hadronic matrix element $\langle \bar{B}^0 | \bar{b} \gamma^\mu \gamma^5 d \bar{b} \gamma_\mu \gamma^5 d | B^0 \rangle$, where the four-quark operator has been induced by an interaction (such as a box diagram) at very short distances. In vacuum saturation, one inserts a complete set of states between the two currents, and then assumes that the sum is dominated by the vacuum. This ansatz is neither stable under radiative corrections, nor really well defined, since $\bar{b} \gamma^\mu \gamma^5 d \bar{b} \gamma_\mu \gamma^5 d$ is an indivisible local operator. The result is of the form

$$\langle \bar{B}^0 | \bar{b} \gamma^\mu \gamma^5 d \bar{b} \gamma_\mu \gamma^5 d | B^0 \rangle = A f_B^2 m_B^2 B_B, \quad (2.34)$$

where A is a known constant and B_B absorbs the error induced by keeping only the vacuum intermediate state. Deviations of B_B from unity parameterize corrections to the ansatz. Vacuum saturation becomes exact in the formal limit $N_c \rightarrow \infty$, where N_c is the number of colors, since then the mesons are noninteracting. This limit is often cited as a justification of the ansatz. As it turns out, calculations in lattice QCD do seem to prefer a value for B_B which is close to unity. One may use HHChPT to estimate the uncertainty in the light-flavor dependence of the ratio B_{B_s}/B_{B_d} .

2.4 Lattice Gauge Theory

An important alternative to the analytic analyses presented so far is the attempt to solve QCD directly via a numerical simulation. As for any quantum field theory, QCD may be defined by a partition function,

$$Z = \int [dA_\mu][d\bar{\psi}_i][d\psi_i] e^{iS(A_\mu, \bar{\psi}_i, \psi_i)}, \quad (2.35)$$

where the *functional integral* is over all configurations with given gauge potential A_μ and quarks ψ_i . The action,

$$S(A_\mu, \bar{\psi}_i, \psi_i) = \int d^4x \left[-\frac{1}{4} G^{\mu\nu} G_{\mu\nu} + \bar{\psi}_i (i\not{D} - g\not{A} - m) \psi_i + \dots \right], \quad (2.36)$$

is supplemented by sources for the quarks and gluons, and by gauge fixing terms. The functional Z and its derivatives are enough to determine all of the correlation functions of the theory. The program of *lattice gauge theory* is to perform the integral in the action by discretizing space-time on a grid of spacing a , and then to compute Z by summing over a finite but representative set of configurations of A^μ and ψ_i . In principle, given enough configurations and a fine enough grid, such an analysis provides an arbitrarily accurate solution to QCD.

However, there are a number of important practical difficulties with this program, which effectively restrict its accuracy and rigor, and the uses to which it may be put. The first is that any realistic analysis requires an enormous amount of computer power. While such resources continue to improve at a remarkable pace, it will be long in the future before it will be possible to analyze processes in which a wide range of momentum scales is important. Effectively, this limits the use of the lattice for the study of exclusive nonleptonic B decays or π - π scattering. For the time being, it is the static, rather than the dynamical, properties of QCD which are most amenable to a lattice treatment.

Another practical limitation of lattice QCD is that it is extremely expensive to include quark loops in the computation. It is possible to save a huge factor in computing time by working in the *quenched* or *valence approximation*, in which quark loops are neglected entirely. Quenching is really more an ansatz than an approximation, in the sense that it is difficult to estimate reliably the error which it induces. It can be argued that in certain contexts, such as heavy quark-antiquark bound states, the primary effect of quenching is to renormalize the effective coupling of the gluons, which can be compensated by adjusting the coupling g at the lattice scale. But in most cases, quenching is just a necessary simplification of the calculation, with a largely unknown effect on the results. With the emergence of a new generation of computers capable of $\sim 10^{12}$ flops, some unquenched calculations will become feasible. Then it will begin to be possible to study the effects of quenching in more quantitative detail.

Other practical difficulties in lattice QCD are more tractable. Because of the nature of the propagator, massless quarks induce singularities in lattice calculations, so one must work with light quarks of mass $m \sim 100$ MeV or larger and then extrapolate to physical $m_u \sim 5$ MeV and $m_d \sim 10$ MeV. The nature of this extrapolation is strongly affected by quenching. It is also necessary to work at nonzero lattice spacing a , and finite overall lattice size L , extrapolating to $a \rightarrow 0$ and $L \rightarrow \infty$ at the end. These extrapolations are believed to be reasonably under control in most calculations. Finally, it turns out to be extremely difficult to incorporate chiral quarks in lattice computations, although this is not an important problem for a vector theory such as QCD.

Even given these limitations, the progress in lattice QCD in the past ten years has been phenomenal. This is due both to advances in computing technology, and perhaps more important, to the development of new theoretical methods particular to the lattice. New techniques which are relevant to the study of heavy quarks include the *static approximation*, *nonrelativistic QCD*, and *improved actions*. The first of these is the analogue of HQET for heavy quarks on the lattice, which actually predates (and inspired) the development of HQET in the continuum. Static techniques are

necessary because the Compton wavelength of the b -quark scales as $1/m_b$ and is much smaller than any lattice spacing a in use, so fully dynamical b quarks are extremely difficult to simulate. The static limit has proven very useful for the computation of heavy-hadron spectra and decay constants. Nonrelativistic QCD, a somewhat different expansion in powers of $1/m$, is relevant to the study of heavy quark-antiquark bound states. Such analyses have become so accurate that lattice determinations of quarkonium splittings, when compared with data, provide a measurement of α_s which may be competitive with precision measurements at the Z pole. Finally, it has been understood how to “improve” the action $S(A_\mu, \psi_i, \bar{\psi}_i)$ by including discretization effects order by order in a , thereby allowing the same accuracy to be obtained with larger lattice spacing. Since for a lattice of a given size in physical units, the number of points scales as $1/a^4$, the result can be a significant saving in computer resources.

In summary, the lattice will continue to be an important tool for B physics, but it is not a universal approach for the numerous important quantities which cannot as yet be treated analytically. Lattice QCD has been very successful for certain quantities, such as the bag constant B_B and the splittings in the Υ system. For others, such as bottom meson and baryon spectroscopy, decay constants, and semileptonic form factors, the situation continues to improve. A collection of lattice results relevant to B phenomenology is given in Appendix C, along with additional discussion of lattice methods. On the other hand, there are quantities, such as exclusive nonleptonic decays or fragmentation functions, where lattices of impractical size and granularity would be required to obtain useful predictions. For such processes, there is no rigorous theoretical calculation based on first principles.

2.5 QCD Sum Rules

Another theoretical approach which is based, in principle, on QCD is that of *QCD sum rules*. The idea is to exploit parton-hadron duality as fully as possible, by studying inclusive quantities with kinematic or other restrictions which require them to be dominated by a single exclusive intermediate state. In this way one can learn something about nonperturbative physics, which controls the detailed properties of bound states, within a calculation based on a perturbative expansion.

The construction of QCD sum rules has a number of technical subtleties. This section only outlines the ingredients and the general structure, leaving specific applications to later chapters. A discussion which contains considerably more detail, along with some results, is found in Appendix D. The method involves the study of correlation functions in QCD, as a function of external momenta. The correlation functions of a quantum field theory contain all the information about the theory, and hence in principle this method has access to every observable of QCD. In practice, it is only feasible to study two-point and some three-point functions, so QCD sum rules are useful primarily for computing spectra, decay constants and form factors.

The main features of the method will be illustrated here with a simple example from B physics. One attractive feature of sum rules is that they can be formulated within HQET, thereby incorpo-

rating heavy-quark symmetry automatically. In HQET, the current $\bar{h}_v \gamma^5 q$ can create a B meson, or other excited states B_n with the same quantum numbers. Since the b quark is static, the appropriate measure of the mass of a state is the excitation energy $\nu_n = (m_{B_n}^2 - m_b^2)/2m_b$, which is independent of m_b as $m_b \rightarrow \infty$. The object of study is the two point function

$$\Pi(\omega) = i \int d^4x e^{ik \cdot x} \langle 0 | T \{ \bar{q} \gamma^5 h_v(x), \bar{h}_v \gamma^5 q(0) \} | 0 \rangle, \quad (2.37)$$

where $\omega = v \cdot k$ is the energy injected into the correlator. For general ω , the correlator $\Pi(\omega)$ receives contributions from all intermediate states B_n . Hence $\Pi(\omega)$ may be written in the form

$$\Pi(\omega) = \sum_n \frac{F_n^2}{\nu_n - \omega - i\epsilon}, \quad (2.38)$$

where F_n is the coupling of the current to the excited state B_n . The correlator (2.37) and sum over states (2.38) are often referred to, respectively, as the ‘‘theoretical’’ and ‘‘phenomenological’’ sides of the sum rule.

The goal is now two-fold: first, to compute the correlator (2.37) in QCD, and second, to isolate the contribution of the ground state B to the sum (2.38), so that its properties can be extracted. These two goals conflict, as they require different limits of ω . A perturbative calculation of the correlator is appropriate for ω far from resonances, $\omega \gg \Lambda_{\text{QCD}}$, or even better, in the unphysical region $\omega \rightarrow -\infty$. On the other hand, the ground state will only dominate the sum for ω small and near the B resonance. The compromise is to work in a regime of intermediate ω , where it is hoped that, with some technical improvements, both the correlator and the sum over states can be treated accurately. These improvements are the source of most of the complications in the method.

The first step is to rewrite $\Pi(\omega)$ as a dispersion integral over its imaginary part, which receives contributions from real intermediate states,

$$\Pi(\omega) = \int_0^\infty d\nu \frac{\rho(\nu)}{\nu - \omega - i\epsilon}, \quad (2.39)$$

where $\rho(\nu) \propto \text{Im}\Pi(\nu)$. For simplicity, local subtractions, which may be required to make this expression well behaved, have been omitted here. Note the similarity between the theoretical expression (2.39) and the phenomenological sum over states (2.38). While it is certainly not true that $\rho(\nu_n) = F_n^2$ at each point, global duality allows the two expressions for $\Pi(\omega)$ to coincide once both sides have been integrated. For ω large enough, it suffices to compute the density $\rho(\nu)$ as a power series in α_s . But for intermediate ω , it is necessary also to include corrections to $\Pi(\omega)$ of order $1/\omega^n$. These corrections appear in the form of *condensates*, new nonperturbative quantities characteristic of QCD. It is usually enough to include the condensates of dimension ≤ 5 , whose values have been extracted at the $\sim 30\%$ level from other processes:

$$\begin{aligned} \langle \bar{q}q \rangle &\approx -(0.23 \text{ GeV})^3, \\ \langle \alpha_s G^{\mu\nu} G_{\mu\nu} \rangle &\approx (0.45 \text{ GeV})^4, \\ \langle g \bar{q} \sigma^{\mu\nu} q G_{\mu\nu} \rangle &\approx -(0.40 \text{ GeV})^5. \end{aligned} \quad (2.40)$$

The condensates are universal quantities which, it is hoped, capture the leading nonperturbative effects of the QCD vacuum and allow the correlator to be computed accurately even for ω not asymptotically large.

The next step is to focus on the ground state B . The excited states B_n are all quite broad and unlikely to induce rapid variations in $\Pi(\omega)$, and it is assumed that above some scale ω_0 , the integral over the excited states can accurately be described by parton-hadron duality. Actually, it is hoped that the scale ω_0 may be chosen as a *threshold*, in the sense that the entire contribution of the excited states (and none of the ground state) may be modeled by the perturbative dispersion integral for $\nu > \omega_0$. The contribution of the excited states is then subtracted from both expressions, leaving an upper cutoff ω_0 on the dispersion integral (2.39), and only the ground state $n = 0$ in the sum over intermediate states (2.38).

The object of the analysis is now to equate the theoretical and phenomenological sides of the sum rule and attempt to fit the coupling F and the energy ν of the ground state B . To do so, one must fix values for the threshold ω_0 and the energy ω , neither of which is given *a priori*. (In Borel sum rules, ω is exchanged for a “Borel parameter” T .) While there exists a prescription for choosing these parameters, it is not based directly on QCD, but rather derives from the requirement that the sum rule be self-consistent, that is, dominated neither by the condensates nor by the excited states. In fact, therein lies a fundamental source of uncertainty in the practical application of QCD sum rules. While it is certainly encouraging that ω_0 and ω usually may be chosen to make the sum rule consistent and well behaved, there is no way to test whether the *consistent* choice is, in fact, the *correct* one. It is not clear, from first principles, how the stability of a sum rule corresponds to its accuracy.

The absence of a reliable estimate of the error from choosing ω_0 and ω , as well as of the error from truncating the sum over intermediate states, leaves QCD sum rule analyses with systematic uncertainties which are difficult to quantify. In this respect, they are a lot like lattice gauge theory calculations in the quenched approximation. Both methods are based, in principle, on QCD, which is their most attractive feature. However, in their practical implementation it is unavoidable that uncontrolled model dependence emerges. The result in each case is a bit of a hybrid, a valuable theoretical tool which one must rely on only with considerable care.

2.6 Quark Models and Related Methods

This section discusses quark models and their relatives. While a QCD analysis is always preferable to a model, there are unfortunately many processes and quantities of interest for which models are the only recourse. The variety of models, even commonly used ones, is indeed enormous, and there is no hope to survey the field here. More information about specific models may be found in Appendix B. This brief section explains what is meant by a model, and why a model is distinct from

QCD. Many models are invented for a very limited purpose, to capture some particular feature of hadron phenomenology such as spectroscopy, fragmentation, or weak decay. Here the focus is on a popular model with more general ambitions, the *nonrelativistic quark model*. This is probably the most intuitively accessible model, and it serves as an excellent illustrative example. Appendix B contains some discussion of a number of models used to estimate hadron form factors relevant in semi-leptonic decays.

Consider a ρ^+ meson. In QCD, this state is a complicated collection of quarks, antiquarks, and gluons, carrying overall flavor quantum numbers. Note that although a ρ^+ has the flavor of a $u\bar{d}$ pair, there are in fact many u , \bar{u} , d , and \bar{d} quarks in a ρ^+ , and it is not correct to assign the flavor of the overall ρ^+ to any particular ones. In the nonrelativistic quark model, however, a meson is treated as a bound state of a single quark and antiquark. Entirely new degrees of freedom have been introduced, since these *constituent* u and d quarks are only indirectly related to the quarks of QCD. They have large masses of order 300 MeV (in contrast to the *QCD-current* quark masses of 5 – 10 MeV), they have small magnetic moments, they are nonrelativistic, they are not pair produced, and they interact with each other through an instantaneous potential. This is an ansatz, not an approximation to or a limit of QCD.

Given these new degrees of freedom, one can then guess a potential and solve the Schrödinger equation to find quark wavefunctions. Magnetic interactions and other effects are introduced as necessary, as perturbations to the nonrelativistic potential. The wavefunctions then may be used to fit or predict physical observables such as spectra, decay constants, or transition rates. Note that the very idea of a nonrelativistic wavefunction is foreign to QCD, so there is no meaningful sense in which the solutions which are obtained are “correct.” All that one can ask is that the model be “predictive,” in that it fit many independent pieces of data with few adjustable parameters.

In principle, models should be constrained to reproduce the known behavior of QCD in its various limits, but this is not always possible. The chiral limit is a particular problem: it is difficult to tune the nonrelativistic quark model to obtain a massless pion when the u and d current masses vanish. By contrast, heavy-quark symmetry provides useful constraints, and it can be used to tune aspects of the quark model when it is applied to bottom and charmed hadrons.

The central problem with models is that it is difficult to accompany their predictions with meaningful error estimates. Since they do not arise as an expansion of QCD, there is no small parameter and no systematic corrections to a controlled limit. It is very difficult to guess, when a model is extended to a new region, at what level to trust its predictions. For example, the nonrelativistic quark model typically works very well for hadron spectroscopy, but this fact gives little insight into its reliability in predicting form factors. It is common practice, unfortunately, to cite uncertainties due to “model dependence” which are obtained by surveying the predictions of a variety of models. This exercise certainly provides more insight into the tastes of model builders than into the accuracy of their predictions.

Of the wide variety of models currently in use, just a few of the most popular ones for B physics are listed here. The Isgur-Scora-Grinstein-Wise model is a version of the nonrelativistic quark model which is tuned to the study of semileptonic B decays. The Bauer-Stech-Wirbel model is a quark model on the light front, used for weak B and D decays and the exploration of the factorization hypothesis. String fragmentation and flux tube models are used to study heavy-quark fragmentation. The Skyrme model, derived from the chiral Lagrangian, is a model of light baryons which has been extended to describe heavy baryons as well. An alternative tool for studying baryons is the nonrelativistic diquark model. The ACCMM (Altarelli *et al.*) model is used to include initial bound state effects in inclusive B decays. What these models, and others like them, have in common is that they are tuned to specific particles or specific processes, for which they typically work reasonably well. By contrast, their predictivity in new contexts is hard to assess reliably. Since it is unavoidable that models will continue to be an indispensable tool in B phenomenology, it is important always to remain mindful of their limitations.

2.7 Further Reading

This chapter has given only the briefest discussion to a few topics in the theory of hadronic B physics. Many of the ideas introduced here will be developed in considerably more detail in subsequent chapters, when they are applied to specific processes and analyses. The purpose here has been to provide a background and some context for these later applications. Because of the very general level of the discussion in this chapter, references to the original literature have not been included. In subsequent chapters where these methods are applied the relevant references are given. The reader who wishes to explore any of these topics further at an introductory level is invited to consult the many textbooks and reviews which now exist.

A few examples are:

- Effective Hamiltonians and operator product expansions
 - *Dynamics of the Standard Model*, John Donoghue, Eugene Golowich and Barry R. Holstein, Cambridge University Press (1992)
 - G. Buchalla, A. J. Buras and M. E. Lautenbacher, *Rev. Mod. Phys.* **68**, 1125 (1996)
- The heavy-quark expansion
 - M. Neubert, *Phys. Rep.* 245, 259 (1994)
 - M. Shifman, in *QCD and Beyond*, Proceedings of TASI 95, ed. D. Soper, World Scientific (1996)
 - B. Grinstein, in *CP Violation and the Limits of the Standard Model*, Proceedings of TASI 94, ed. J. F. Donoghue, World Scientific (1995)

- Chiral perturbation theory
 - J. Gasser and H. Leutwyler, *Phys. Rep.***87**, 77 (1982)
- Lattice gauge theory
 - *Phenomenology and Lattice QCD*, Proceedings of the Uehling Summer School on Phenomenology and Lattice QCD, eds. G. Kilcup and S. Sharpe, World Scientific (1995)
 - S. Sharpe, in *CP Violation and the Limits of the Standard Model*, Proceedings of TASI 94, ed. J. F. Donoghue, World Scientific (1995)

and

- QCD sum rules
 - Stephan Narison, *QCD Spectral Sum Rules*, World Scientific (1989).

This page was intentionally left blank.

An Introduction to the BABAR Experiment

The primary goal of the BABAR experiment is the systematic study of CP asymmetries in the decays of neutral B mesons. In addition to this, a sensitive measurement of the CKM matrix element, V_{ub} can be made, and a number of rare B meson decays may be measured, together enabling good constraints to be put on fundamental parameters of the Standard Model. A range of other physics may also be studied at BABAR, including other B physics, the physics of charm and tau leptons, and two-photon physics. Many of the methods for doing this are described in later chapters of this book.

The particular channels in which it is hoped that BABAR will be able to measure CP asymmetries include the following:

- For $\sin 2\beta$: $B^0 \rightarrow J/\psi K_S^0$, $B^0 \rightarrow J/\psi K_L^0$, $B^0 \rightarrow J/\psi K^{*0}$, $B^0 \rightarrow D^+ D^-$, $B^0 \rightarrow D^{*+} D^{*-}$, *etc.*
- For $\sin 2\alpha$: $B^0 \rightarrow \pi^+ \pi^-$, $B^0 \rightarrow \pi^+ \pi^- \pi^0$, $B^0 \rightarrow a_1 \pi$

The CP asymmetries in question may be quite large, needing only a few hundred reconstructed events in the appropriate channel to observe. The branching ratios to reconstructible final states are very small, however, *e.g.*, $\sim 10^{-5}$ for $J/\psi K_S^0$ and for $\pi^+ \pi^-$, so that in excess of 10^7 $B^0 \bar{B}^0$ pairs need to be produced, in order to measure the asymmetries with errors at the 10% level or better.

In order to observe the asymmetries, three things need to be measured: the exclusive final state needs to be fully reconstructed; the flavor (beauty or anti-beauty) of the decaying particle needs to be tagged; the proper time of the B^0 decay with respect to its production needs to be measured, as (in most cases), the asymmetry cancels to zero in time-integrated measurements at $e^+ e^-$ machines.

The BABAR experiment was designed and optimized to achieve the goals specified above. The PEP-II B Factory was designed to deliver the B mesons to the experiment.

3.1 $e^+ e^- B$ Factories and PEP-II

In the late 1980s, studies [1] indicated that the best source of B mesons for such a physics program was an $e^+ e^-$ collider, operating at the $\Upsilon(4S)$ resonance, but in an *asymmetric* mode, *i.e.*, with

beams of unequal energy, resulting in B^0 mesons with significant momenta in the laboratory frame (the small Q -value of the $\Upsilon(4S) \rightarrow B\bar{B}$ decay results in B mesons almost at rest in the center of mass frame). This enables the B^0 mesons' decay times to be inferred from their now-measurable decay lengths. The machine must also have unprecedented luminosity; of the order of a few $\times 10^{33} \text{ cm}^{-2} \text{ s}^{-1}$, or more, in order to provide enough B mesons. The PEP-II B Factory was designed with just these characteristics.

There are several advantages of the e^+e^- environment over the hadronic environment, for doing such physics, namely:

- A high signal-to-background ratio, with $\sigma_{b\bar{b}}/\sigma_{TOT} \simeq 0.28$.
- Clean events, with a mean charged multiplicity of ~ 11 .
- Low interaction rates $\sim 10 \text{ Hz}$ (physics rate).
- The possibility to reconstruct final states containing π^0 s and photons, thereby allowing the possibility to make measurements in many more channels.
- Straightforward extrapolation from existing experiments.

There are two major advantages of the $\Upsilon(4S)$ resonance over the situation at LEP. The first is the absence of any fragmentation products, thereby reducing the possibility of combinatorial backgrounds. The second advantage is the existence of several kinematic constraints, namely knowledge of the exact 4-momentum of the two- B meson system and also knowledge of the momentum magnitudes of the two B mesons individually in the center-of-mass frame. These constraints help considerably in suppressing backgrounds.

PEP-II will have two rings, one of 9 GeV (for electrons) and one of 3.1 GeV (for positrons), housed in the former PEP tunnel. This results in a $\beta\gamma$ for the resulting B mesons of 0.56 in the laboratory frame. The machine will use the already-existing SLAC linac as an injector. The machine construction schedule allows for phased commissioning of the various components. The design luminosity goal is $3 \times 10^{33} \text{ cm}^{-2} \text{ s}^{-1}$.

3.1.1 Cross-Sections at the $\Upsilon(4S)$

The cross-sections for the production of fermion pairs at the $\Upsilon(4S)$ are shown in Table 3-1¹. They are discussed in more detail in Section 11.4.1.2. The $B\bar{B}$ cross-section can be calculated from

¹All quark-antiquark cross-sections except $b\bar{b}$ are calculated with the `Jetset 7.4` event generator for $\sqrt{s} = 10.58 \text{ GeV}$. Radiative corrections are included; hence the cross-sections include radiative events for which acceptance will be low.

Table 3-1. Production cross-sections at $\sqrt{s} = M(\Upsilon(4S))$. The e^+e^- cross-section is the effective cross-section, expected within the experimental acceptance.

$e^+e^- \rightarrow$	Cross-section (nb)
$b\bar{b}$	1.05
$c\bar{c}$	1.30
$s\bar{s}$	0.35
$u\bar{u}$	1.39
$d\bar{d}$	0.35
$\tau^+\tau^-$	0.94
$\mu^+\mu^-$	1.16
e^+e^-	~ 40

known $\Upsilon(4S)$ properties and the beam-energy spread of the machine. Since the BABAR beam spread is very close to being the same as it is for CLEO, we take the peak cross-section obtained in CLEO and adjust for the slightly larger beam spread expected in BABAR. This yields a peak cross-section of 1.05 nb with an uncertainty of less than 0.1 nb (the BABAR TDR [2] used 1.15 nb for most analyses).

While in principle the $q\bar{q}$ cross-section can be calculated if the value of $R \equiv \sigma_{q\bar{q}}/\sigma_{\mu^+\mu^-}$ is known, initial-state radiation assures that the value depends sensitively on the minimum value of center-of-mass energy that is required in an analysis. Events with very hard radiated photons look more like 2-photon processes than typical $q\bar{q}$ events. For most purposes in this book, it is only necessary to know how to normalize the Monte Carlo samples that have been generated. In this case we use the cross-section calculated from `Jetset 7.4` with the usual photon-energy cutoff of $0.99E_{\text{beam}}$, corresponding to a minimum center-of-mass energy of 1.06 GeV. This cross-section is found to be 3.39 nb.

3.1.2 Data Taking in the Continuum

It is intended to run PEP-II at the $\Upsilon(4S)$ resonance, for the majority of its running. However, off-resonance data are essential for all precision measurements of B meson decays since Monte Carlo simulations for B decay backgrounds from the continuum are less reliable than their direct determination from real data (the non- $B\bar{B}$ physics (charm, tau, ...) does not require any data taking off the $\Upsilon(4S)$ resonance since these data come simultaneously with $B\bar{B}$ events). For decays with very little background, like $B^0 \rightarrow J/\Psi K_S^0$ with background/signal ratios $B/S < \text{a few } \%$, a very high fraction of data taking on the $\Upsilon(4S)$ resonance gives the smallest error on the CP

asymmetry for these events. For decays with higher continuum background, like $B^0 \rightarrow \pi^+\pi^-$ with $B/S = \mathcal{O}(1)$, the smallest errors on $\mathcal{B}(B \rightarrow \pi^+\pi^-)$ and $A_{CP}(B \rightarrow \pi^+\pi^-)$ are obtained with a much larger fraction of continuum data taking. The same holds for all inclusive studies like $B \rightarrow \ell\nu X$. In this section, a recipe is derived for choosing the optimal fraction of continuum data taking.

In order to reach a minimal error on S , the cross-section \times branching ratio for a signal, in the presence of a continuum background with a magnitude B (for the analogous quantity), a given integrated luminosity, $\mathcal{L} = \int \dot{\mathcal{L}} dt$ should be shared between two fractions, $(1-c)\mathcal{L}$ on the $\Upsilon(4S)$, and $c\mathcal{L}$ in the continuum. Assuming that the error is predominantly statistical, the optimal value for c depends on $b = B/S$. This can be seen as follows. The numbers of events on the $\Upsilon(4S)$ and in the continuum are respectively

$$N(\Upsilon(4S)) = (1-c)\mathcal{L}(1+b)S, \quad N(\text{continuum}) = c\mathcal{L}bS, \quad (3.1)$$

so that S can be obtained from

$$S = \frac{N(\Upsilon(4S))}{(1-c)\mathcal{L}} - \frac{N(\text{continuum})}{c\mathcal{L}}. \quad (3.2)$$

Propagating the errors, and substituting for the N s gives

$$\sigma(S) = \left[\frac{(1-c)\mathcal{L}(1+b)S}{(1-c)^2\mathcal{L}^2} + \frac{cb\mathcal{L}S}{c^2\mathcal{L}^2} \right]^{1/2} = E \cdot \sqrt{S/\mathcal{L}} \quad (3.3)$$

where

$$E = E(c) = E(c|b) = \sqrt{\frac{c+b}{c(1-c)}}. \quad (3.4)$$

The function E describes the increase of the error on the signal cross-section with respect to the condition $b = c = 0$. Its dependence on c , for values of b between 0 and 1 is shown in Figure 3.1.2. In all cases, the minimum obtained is very shallow, and wide ranges of c give very similar statistical errors for the signal cross-section. Table 3-2 gives the optimal continuum fraction c_{\min} , $E(c_{\min})$, $E(0.15)/E(c_{\min})$, and $E(0.20)/E(c_{\min})$.

It may be concluded that small luminosity fractions in the continuum, around one sixth of the total integrated luminosity, cover the optimal conditions for background to signal ratios up to 0.50. The price for channels without background is very low; their errors increase only by 10 percent with respect to $c = 0$, *i.e.*, with no continuum running at all.

This conclusion leads to a recommendation for the initial running conditions of BABAR: choose $c = 0.174$. At this continuum fraction, the errors on channels with no background increase by exactly 10%, the errors are minimal for $b \approx 0.05$, and the errors increase by less than 10% for all b values up to 0.40. Figure 3.1.2 shows $E(0.174, b)$, $E(c_{\min}, b)$, and $E(0.174, b)/E(c_{\min}, b)$, *i.e.*, the error increase at $c = 0.174$ with respect to $b = c = 0$, the error increase at the optimal c , and the ratio of the two, as a function of b .

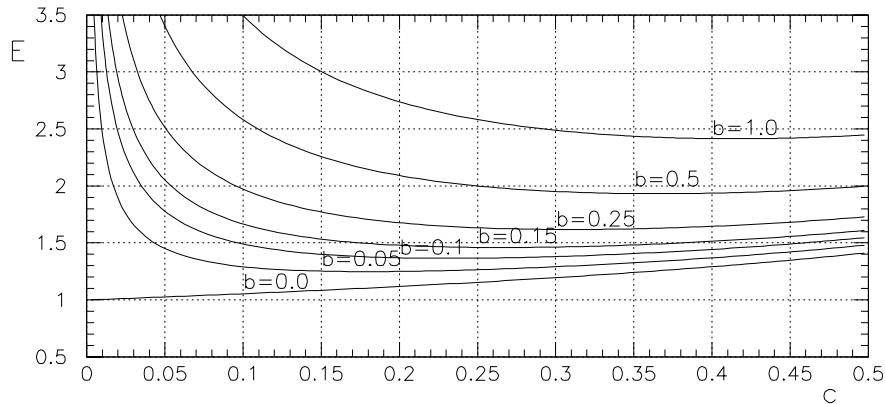


Figure 3-1. increase of the signal error with respect to $b = c = 0$ as a function of the continuum luminosity fraction c for various background to signal ratios b .

Table 3-2. The optimal fraction c_{\min} of continuum luminosity, the increase of signal errors with respect to $b = c = 0$, and the increase ratios at two c values, for seven background to signal ratios b .

b	c_{\min}	$E(c_{\min})$	$\frac{E(0.15)}{E(c_{\min})}$	$\frac{E(0.20)}{E(c_{\min})}$
0.00	0.00	1.00	1.08	1.12
0.05	0.18	1.25	1.00	1.00
0.10	0.23	1.37	1.02	1.00
0.15	0.27	1.46	1.05	1.01
0.25	0.31	1.62	1.09	1.04
0.50	0.37	1.93	1.17	1.08
1.00	0.41	2.41	1.24	1.14

Continuum running with the recommended fraction of around one sixth of the total integrated luminosity should be done at a center-of-mass energy around 60 MeV below the $\Upsilon(4S)$ mass. For the storage ring operation, the easiest option might be to keep the low-energy ring at 3.109 GeV and to decrease the high-energy ring from 9.000 to 8.900 GeV. This choice would change the boost from 0.5568 by a negligible amount to 0.5505.

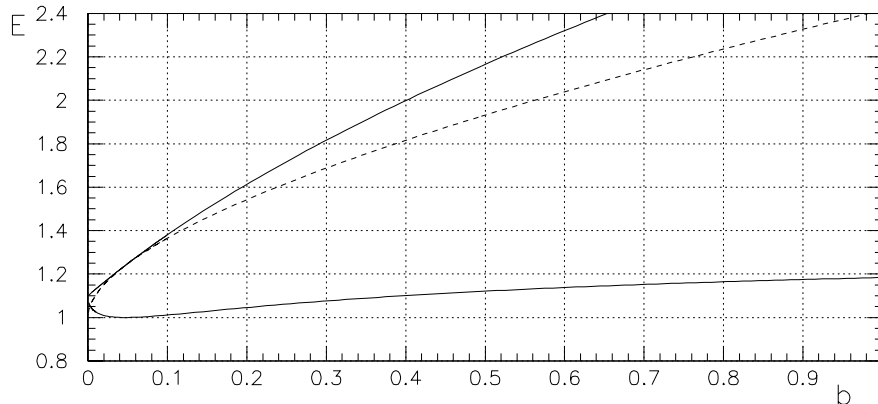


Figure 3-2. Increase of the signal error at a continuum luminosity fraction $c = 0.174$ (upper solid curve) with respect to $b = c = 0$, the same increase at the optimal luminosity fraction c_{\min} (dashed curve), and ratio of the two (lower solid curve) as function of the background to signal ratio $b = B/S$.

3.2 An Overview of the BABAR Detector

In order to achieve the physics goals stated in the introduction to this chapter, and to function optimally, the BABAR detector needs:

- The maximum possible acceptance in the center-of-mass system. The asymmetry of the beams in BABAR causes the decay products to be boosted forward in the laboratory frame. This puts the solid angle in the forward direction at a premium. Although the boost is rather a small one, optimizing the detector acceptance leads to an asymmetric detector.
- To accommodate machine components close to the interaction region. The high luminosities needed to achieve the physics goals at BABAR necessitate unusual beam optics with machine elements coming very close to the interaction region.
- Excellent vertex resolution. The B mesons travel almost parallel to the z -axis, so that their decay time difference is measured via a difference in the z -components of their decay positions. This stresses the z -component of vertex resolution. The experiment needs the best possible vertex resolution in order to help in the discrimination of beauty, charm, and light-quark vertices. Vertex resolution also stresses the importance of minimizing multiple scattering.
- To do tracking over the range $\sim 60 \text{ MeV} < p_t < \sim 4 \text{ GeV}$.
- Discrimination between e, μ, π, K and p over a wide kinematic range. Tagging of the flavor of B -meson decays is needed in many analyses, and this can be done with high efficiency

and purity only if electrons, muons and kaons can be well identified. In addition, π -K discrimination at high momenta (2–4 GeV) is essential in order to distinguish between the decay channels $B^0 \rightarrow \pi^+\pi^-$ and $B^0 \rightarrow K^\pm\pi^\mp$, $B^0 \rightarrow \rho^+\pi^-$ and $B^0 \rightarrow K\rho$ and $B^0 \rightarrow K^*\pi$.

- To detect photons and π^0 s over the wide energy range $\sim 20 \text{ MeV} < E < \sim 5 \text{ GeV}$.
- To have neutral hadron identification capability.

The BABAR detector was designed to provide all the above features. A schematic of the detector is shown in Fig. 3-3. Major subsystems of the detector include:

1. A Silicon Vertex Tracker (SVT). This provides precise position information on charged tracks, and also is the sole tracking device for very low-energy charged particles.
2. A Drift Chamber (DCH) filled with a helium-based gas, in order to try to minimize multiple scattering. This provides the main momentum measurement for charged particles and helps in particle identification through energy loss measurements.

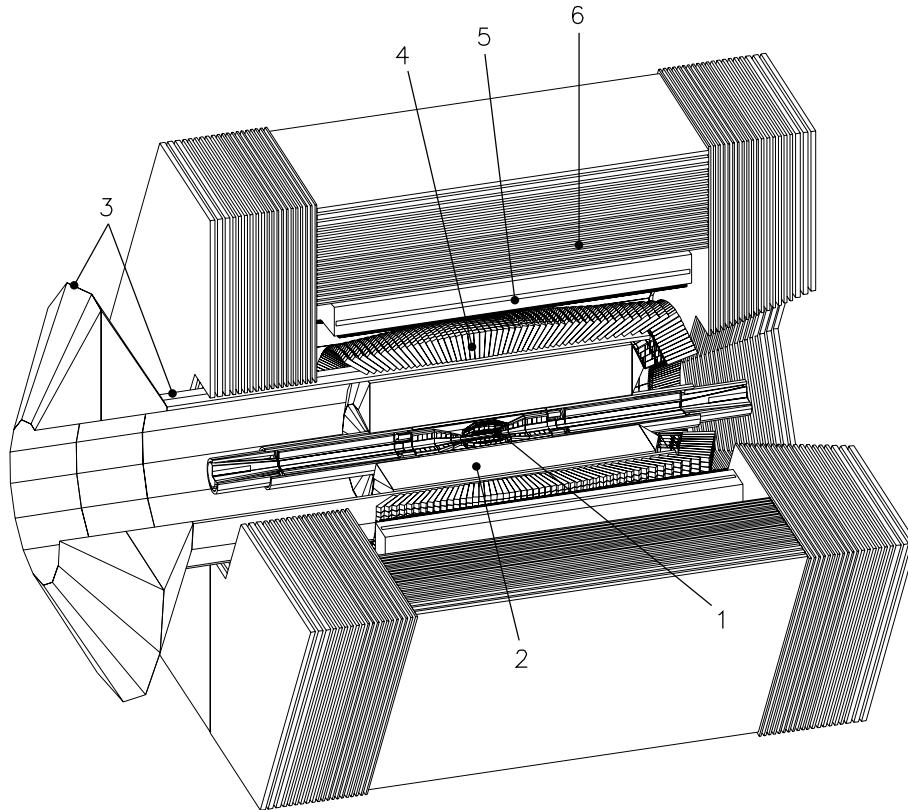


Figure 3-3. Layout of the BABAR detector. See text for key.

3. A Detector of Internally Reflected Cherenkov light (DIRC). This is designed and optimized for charged hadron particle identification.
4. A Caesium Iodide Electromagnetic Calorimeter (EMC). It has a forward endcap, but none in the backward direction, for reasons of economy, as it was found that the boost prevents more than a tiny fraction of neutrals from going in the extreme backward direction. In addition to neutral electromagnetic particles, the calorimeter provides good electron identification down to about 0.5 GeV, and information for neutral hadron identification.
5. A superconducting coil, which provides a 1.5 T solenoidal magnetic field.
6. An Instrumented Flux Return (IFR) for muon identification down to about 0.6 GeV and neutral hadron identification. The latter is of particular interest in the CP -violating time-dependent asymmetries in $B^0 \rightarrow J/\psi K_L^0$ as a cross-check to the result in the $B^0 \rightarrow J/\psi K_S^0$ channel.

As always, the detector is constrained by space, time, and financial considerations. In addition, however, it is more than usually constrained by the machine considerations already mentioned. A number of the design parameters of the BABAR detector are listed in Table 3-3.

Table 3-3. *Detector design performance parameters. Acceptance coverages are quoted for the Center of Mass system.*

Parameter	Value [2]
Tracking coverage ($/4\pi$)	0.92
σ_{p_t}/p_t (%) (1 GeV pions at 90°)	0.36
σ_{z_0} (μm) (1 GeV pions at 90°)	52
Calorimetry coverage ($/4\pi$)	0.90
X_0 in front of Calorimeter (at 90°)	0.25
σ_E/E (%) (1 GeV γ at all angles)	1.8
γ efficiency within acceptance (at 100 MeV)	0.92
Charged Hadron ID coverage ($/4\pi$)	0.84

The BABAR detector, was extensively described in the Technical Design Report (TDR) [2]. Since that time, a number of features of the design have changed. These changes include the following:

- A slight increase in the amount of material in the beam-pipe and beam support tube;
- The re-design of the drift chamber, including the forward end-plate;

- The removal from the design of the forward aerogel threshold counter;
- The removal of the inner ring of CsI crystals from the forward end-cap;
- Numerous small changes in the geometry of the Instrumented Flux Return, in order to accommodate other pieces of the detector, its supports and services.

In this Chapter, the main features of each of the detector systems are reviewed, paying particular attention to those features which have changed since the design quoted in the TDR. Individual expected performances of systems will be summarized here. The anticipated performances of the detector as a whole, as seen in the latest full simulations at the time of writing, will be summarised in Chapter 4, and subsequent chapters.

3.3 The Silicon Vertex Tracker

3.3.1 Physics Requirements and Performance Goals

The main task of the BABAR vertex detector is to reconstruct the decay vertices of the two primary B mesons in order to determine the time between the two decays. This determination will allow the measurement of time-dependent CP asymmetries in B^0 decays. For a given track, the best angular information is provided by the inner points, measured by the silicon vertex detector, because the precision on the outer points is limited by multiple scattering. In addition, charged particles with transverse momenta lower than $100 \text{ MeV}/c$ will not reach the drift chamber, so for these particles the silicon vertex tracker provides the complete tracking information. The drift chamber reaches full efficiency only for tracks with p_t larger than about $180 \text{ MeV}/c$. For these reasons this subdetector is called the Silicon “vertex tracker” rather than the “vertex detector,” henceforth referred to as the silicon vertex tracker.

The basic requirement from CP violation physics on the silicon vertex tracker is to measure the separation z between the two B vertices with a precision of better than one half the mean separation, that is $\sim 250 \mu\text{m}$ at PEP-II [3]. This corresponds to a single vertex precision of better than $80 \mu\text{m}$, which is readily achievable with silicon micro-strip detectors. However, obtaining a better precision will help with pattern recognition, vertex reconstruction and background rejection. The silicon vertex tracker was designed to reach the best practicable resolution. Multiple scattering sets the lower limit for the useful point resolution: resolutions of $10\text{--}15 \mu\text{m}$ for the inner layers, and $30\text{--}40 \mu\text{m}$ for the outer ones, will ensure that the impact parameter resolution will be dominated by the uncertainty given by multiple scattering [4].

It is a general requirement, for a collider detector, to cover as much solid angle as possible. As PEP-II is an asymmetric collider, particular care must be taken to cover the forward region.

The accelerator bending magnets limit the maximum acceptance to 17.2° , in both forward and backward directions. To allow the maximum forward coverage, machine components such as cooling systems *etc.*, are located in the backward region. Taking into account the unavoidable dead spaces due to mechanical supports, electronics and cabling, the active parts of the silicon vertex tracker will cover the polar angle between 20.1° and 150.2° .

A near-perfect overall track reconstruction efficiency is needed to handle the high background level foreseen at PEP-II. Moreover, low-momentum tracks, like slow pions in D^* decays, will be mostly contained in the silicon vertex tracker volume; in this case only the silicon vertex tracker information can be used for track reconstruction. In addition, the silicon vertex tracker must be efficient for particles like K_S^0 which decay within the active volume.

As the impact parameter resolution is dominated by the precision of the measurement closest to the interaction point; both high efficiency and good point resolution are needed for the inner layers, requiring redundancy for this measurement. Also an outer point redundant measurement is needed to allow a better alignment with the drift chamber measurements. The third detector, placed in the middle region, will help the track reconstruction in particular when the tracks' helices are completely contained in the silicon vertex tracker volume.

At PEP-II the radiation near the interaction region is nonuniform in azimuth, peaking in the bending plane of the machine, with a maximum of 240 krad/yr for the innermost layer detectors, and 110 krad/yr for the electronics in the same layer. The system is designed to withstand at least ten times the expected annual dose for the lifetime of the experiment, of about ten years.

Particular attention is being paid to the reliability of the detector, given the high statistics needed for CP violation studies. The detector will be mounted in a zone of the BABAR apparatus which is not easily accessible, so that a shutdown period would be required if intervention were necessary.

3.3.2 Silicon Vertex Tracker Layout

As can be seen in Fig. 3-4 and 3-5, the BABAR silicon vertex tracker consists of five concentric cylindrical layers of double-sided silicon detectors with 90° stereo. Each layer is divided in azimuth into modules. The inner three layers have six detector modules and are traditional barrel-style structures. The outer two consist respectively of 16 and 18 detector modules, and employ a new arch structure in which the detectors are electrically connected across an angle. The bend in the arch modules increases the solid angle coverage and avoids very large track incidence angles. The two outer layers are further divided into "a" and "b" modules, with "a"-type modules situated at slightly smaller radii than the corresponding "b"-type ones (see Fig. 3-5), to allow the detectors to overlap. For the inner "barrel"-like modules, overlap is guaranteed by a pin-wheel type arrangement.

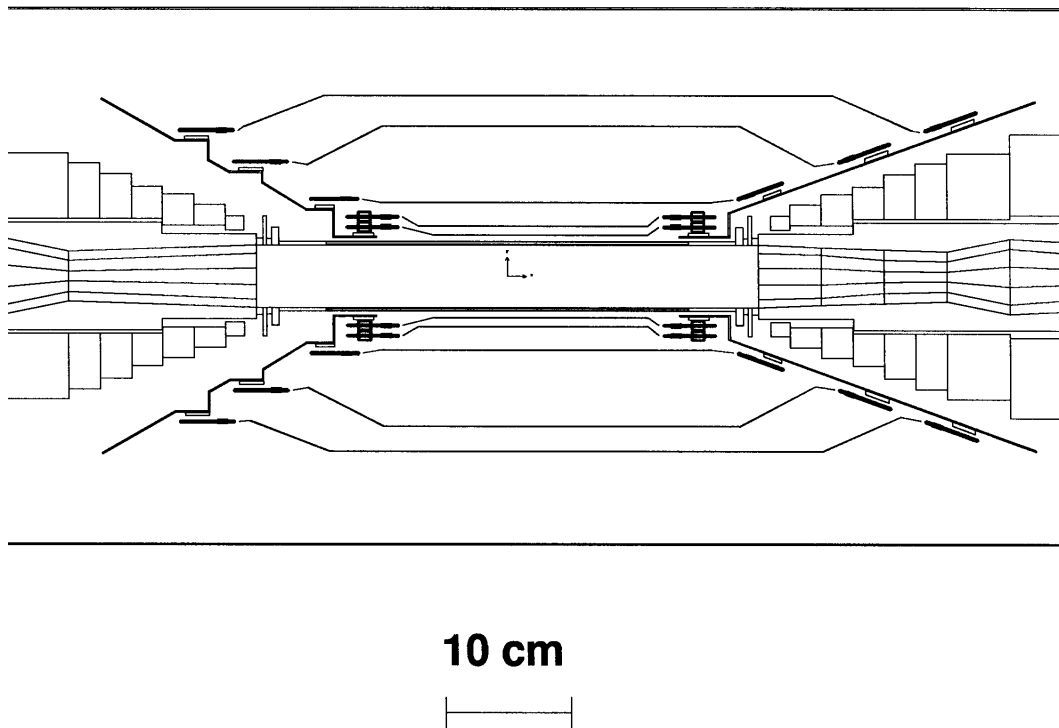


Figure 3-4. Detail of the inner part of the apparatus, showing the cross-sectional view of the silicon vertex tracker in a plane containing the beam axis.

Each module is divided into two electrically separated forward and backward half-modules, the shorter (if they are not exactly symmetrical) always being the forward one. In order to follow the designed structure of the fourteen half-modules, detectors with six different wafer geometries are needed.

The inner sides of the detectors have strips oriented perpendicular to the beam direction to measure the z coordinate (z -side), whereas the outer sides, with longitudinal strips, allow the ϕ coordinate measurement (ϕ -side). The read-out electronics will be placed outside the active area, the z -side strips will be connected to them with flexible Upilex fanout circuits glued to the inner faces of the half-modules. In the two outer modules, the number of z strips exceeds the number of readout channels, so some fraction of the strips is “ganged”, *i.e.*, two strips are connected to the same readout channel. The “ganging” is performed by the fanout circuits. The ϕ strips are daisy-chained between detectors, resulting in a total strip length of up to 26 cm and a maximum capacitance of 35 pF. Also, for the ϕ -side, a short fanout extension is needed to connect the ends of the strips to the readout electronics.

Half-modules contain from two to four detectors. The connections between two adjacent detectors on the ϕ -side, and with the fanout on both sides, are made with wire bonds. The bending of the

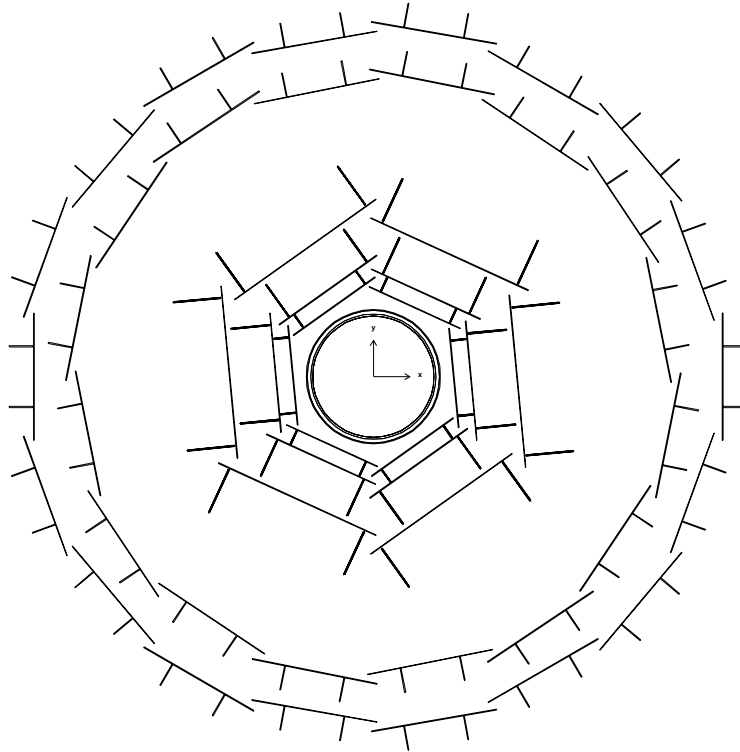


Figure 3-5. *Layout of the BABAR silicon vertex tracker. Cross-sectional view in the plane orthogonal to the beam axis.*

outer detector of external layers is done after the wire bonding. The modules are supported on Kevlar ribs mounted to the end cones located in the forward and backward directions. A carbon-fiber space frame supports the assembly, which is mounted on the bending magnets using kinematic mounts. The space frame is needed to allow some motion of the magnet during the assembly procedure.

The BABAR silicon vertex tracker will have 340 silicon detectors in total, covering an area of about 1 m^2 , with a total of $\sim 150,000$ readout channels. Details of the silicon vertex tracker parameters are shown in Table 3-4: here the intrinsic point resolution is calculated for tracks incident at 90° , assuming a signal-to-noise ratio, $S/N = 20 : 1$.

3.3.3 The Silicon Microstrip Detectors

Silicon vertex detectors use double-sided silicon strip detectors, AC coupled with polysilicon bias resistors [5]. They have p^+ strips on the p-side and n^+ strips on the opposite, n-side. The n^+ strips on the n-side must be interleaved by p^+ implants (p-stops). They are fabricated on $(300 \pm 30) \mu\text{m}$

Table 3-4. *Some parameters of the silicon vertex tracker layout.*

	Layer 1	Layer 2	Layer 3	Layer 4a	Layer 4b	Layer 5a	Layer 5b
Radius (mm)	32	40	54	124	127	140	144
Modules/Layer	6	6	6	8	8	9	9
Wafers/Module	4	4	6	7	7	8	8
Readout pitch (μm)							
ϕ	50	55	55	80–100		80–100	
z	100	100	100	210		210	
Floating Strips							
ϕ	—	—	—	1		1	
z	1	1	1	1		1	
Intrinsic Resol.(μm)							
ϕ	10	10	10	10–12		10–12	
z	12	12	12	25		25	

thick high-resistivity silicon with [111] orientation. Six types of detectors (I to VI) are needed, having different physical dimensions, number of strips and readout pitches. The readout pitch is sometimes larger than the strip pitch. This is due to the floating strips, which are biased but not connected to preamplifiers, capacitively dividing the charge between adjacent channels, which are connected to the readout system.

The wafers of the “barrel” detector (I to V) have orthogonal strips on the two sides. The strips which read the z coordinates are on the junction side for the model I, II and III detectors, and on the ohmic side for models IV and V. On the “wedge” detectors, due to their shape, the strips are not orthogonal on the two sides. Strips which read the z coordinates (ohmic side) have constant width and pitch, whereas the strips which read the ϕ coordinates (junction side) have different starting and ending pitches. Also, the strip width is scaled to maintain a constant width/pitch ratio over the whole detector.

3.3.4 Silicon Vertex Tracker Readout

The front-end signal processing will be performed by ICs mounted on hybrid circuits [6] which distribute power and signals, and thermally interface the ICs to the cooling system. The chips are fabricated in a radiation-hard CMOS technology.

Signals from strips are amplified, shaped, and compared with a threshold. The time interval during which they exceed the threshold is approximately logarithmically related to the charge induced on the strips. The length of this interval, called “time over threshold” (TOT), is digitally recorded and, in the case of level-1 trigger acknowledgment, is read by the data acquisition system.

The TOT method has several advantages with respect to the traditional linear analog readout: due to the logarithm relation the dynamic range is compressed, reducing the number of bits needed for the recording. In addition, since digitization is accomplished in the front-end chips, cost, power, and space requirements are reduced. In Fig. 3-6(b) different readout modes are compared for a $100\ \mu\text{m}$ readout pitch and one floating strip configuration, showing that the expected resolution for the ideal TOT readout scheme is comparable with that of an analog readout.

The readout chips amplify, shape, and digitize the input signals, in parallel for all channels [7, 8]. The signals are buffered for the duration of level-1 trigger latency. Buffered data are stored until a read command is received, in the case of trigger acknowledgment. Due to the large anticipated trigger rate, data acquisition, digitization, buffering and readout occur simultaneously during normal operations to allow a high acquisition rate.

The acquired data will be transmitted from the hybrid on flexible cables to passive impedance matching cards, situated at about 40 cm from the front-end electronics; from there, twisted pair cables will carry the signals to multiplexer modules, located on the detector platform. These modules will convert the signals, transmitting them to the remote readout electronics on optical fibers.

3.3.5 Silicon Vertex Tracker Space Resolution

A Monte Carlo simulation of the intrinsic resolution for $300\ \mu\text{m}$ thick silicon, as a function of track incidence angle for different strip and readout pitches, is shown in Fig. 3-6(a) and (b) [2]; a noise level of $1200\ e^-$ and a perfect analog readout are assumed. According to these simulations, a $100\ \mu\text{m}$ readout pitch with one intermediate floating strip gives better readout results, both at low and at high incidence angles, being equivalent to $50\ \mu\text{m}$ readout pitch at low angle (but $50\ \mu\text{m}$ readout pitch degrades significantly at high angle), and to $100\ \mu\text{m}$ readout with no floating strips at high angle (this configuration has worse resolution at low angle).

In 1995 prototypes of the detectors, reproducing all the relevant configurations of physical and readout strip pitch and ganging, were tested in an SPS beam at CERN [9], with a classical analog readout. For a geometry corresponding to the z side of the inner layers, the achieved resolution at 90° incidence angle was $13\ \mu\text{m}$. Figure 3-6 shows the measured resolution *vs.* track incidence angle for the z side of a detector with $25\ \mu\text{m}$ strip pitch and $100\ \mu\text{m}$ readout pitch; the result is in good agreement with the simulated one. Several other configurations were tested with different pitches and numbers of floating strips, giving full confidence in the design of the silicon vertex

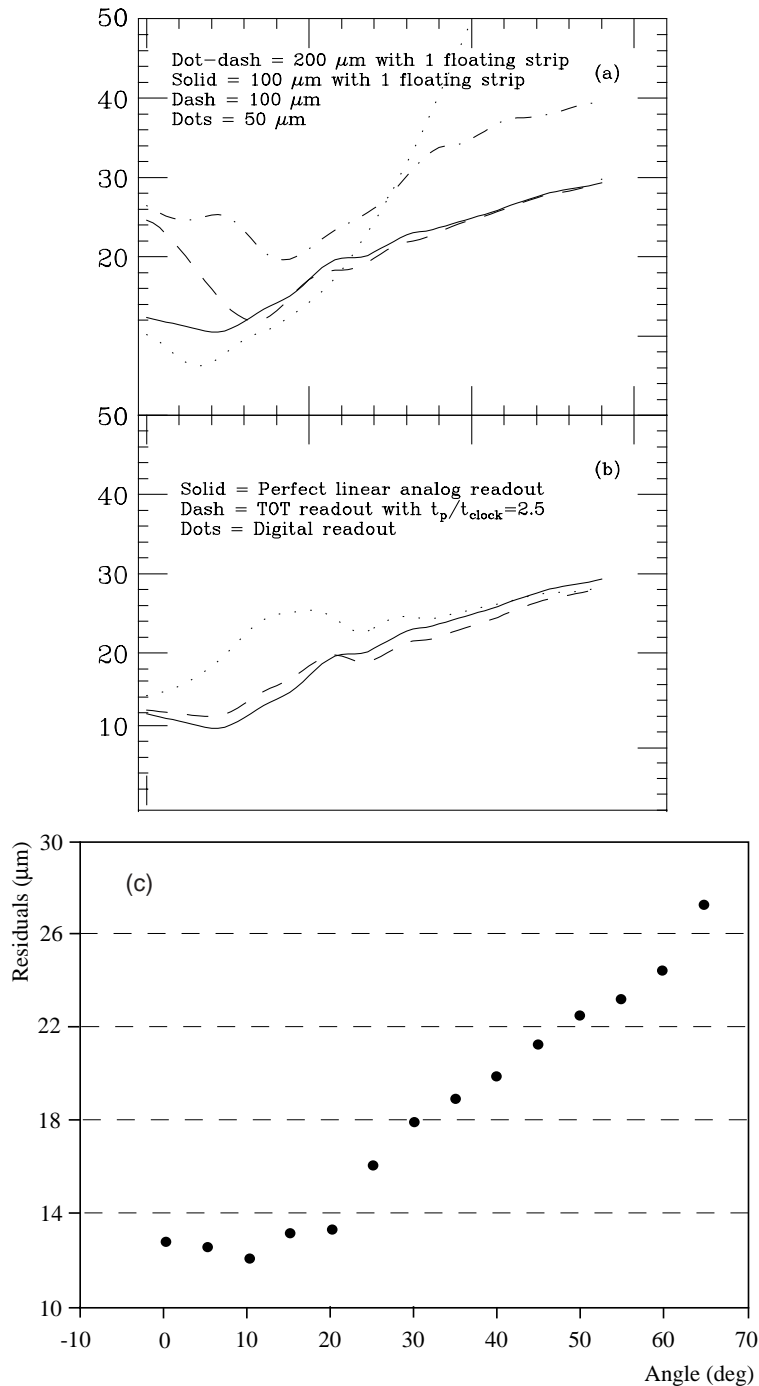


Figure 3-6. (a) Simulated intrinsic resolution vs. dip angle for various strip configurations assuming perfect analog readout. (b) same as (a), assuming 100 μm readout pitch and one floating strip, for various readout techniques [2]. (c) Measured resolution vs. track incidence angle for the z side of a detector with 25 μm strip pitch and 100 μm readout pitch. The result is from the July 1995 test-beam [9].

tracker and the Monte Carlo prediction of its performance. More recently, final detector modules of layers 2 and 5a were tested with prototype TOT readout chips, confirming the basic features of the system.

3.3.6 Calibration and Alignment

Procedures for calibration, reconstruction and alignment are currently under development.

The front-end electronics is calibrated by injecting known amounts of charge into the preamplifiers and varying the TOT thresholds. This method will also be used frequently during data taking to monitor the stability of the TOT response function for each channel.

Different point reconstruction algorithms are used, according to the number of strips collecting the released charge in a given wafer, as a function of the angle of incidence of the incoming particle. They are being optimized to take into account also the detailed knowledge of unavoidable detector defects collected during construction which will be stored in a database.

Global and local alignment algorithms using reconstructed particle tracks are under development. They will monitor the position of each wafer in the experiment at the required precision level.

3.4 The Drift Chamber

The drift chamber is the main tracking device of the BABAR detector. It provides up to 40 measurements of space coordinates per track, ensuring high reconstruction efficiency for tracks with transverse momentum greater than $100 \text{ MeV}/c$. Combined with the silicon vertex tracker, the BABAR tracking system provides excellent spatial and momentum resolution required for exclusive reconstruction of the CP decays of B mesons.

The performance goals of the drift chamber, motivated in detail in [2], are to provide spatial resolution better than $140 \mu\text{m}$, averaged over the cell in the R - ϕ plane, and to supply particle identification for low momentum tracks by dE/dx , with a resolution of 7% (for 40 measurements). For tracks with momentum above $1 \text{ GeV}/c$, a resolution of $\sigma_{p_t} \approx 0.3\% \times p_t$ is expected. The angular acceptance in the forward region must extend down to the beam-line components, *i.e.*, 300 mr. In addition, the drift chamber is designed to provide one of the principal triggers for the experiment.

For low momentum tracks, the momentum resolution is limited by the multiple scattering in the inner cylinder of the drift chamber as well as in the silicon vertex tracker. The material in the drift chamber also affects the performance of the DIRC and the electromagnetic calorimeter. The mechanical structure of the drift chamber is built using light materials and the gas mixture is

Helium-based. The read-out electronics are mounted on the rear endplate to minimize the material in the forward region.

The high luminosity of PEP-II imposes a stringent demand on the deadtime tolerated both for the chamber itself and for its readout electronics. Background from synchrotron radiation is expected to cause high signal occupancy, especially in the innermost sense wires. A small-cell cylindrical chamber design was chosen to minimize the drift time, and a fast and highly pipelined design was adopted for the front-end electronics, in order to eliminate the readout deadtime.

The detailed engineering design of the drift chamber was finalized after the time of the BABAR Technical Design Report [2]. An up-to-date description of the design can be found in [10]. In the following sections, the main features of the final design are summarized.

3.4.1 Drift Chamber Design

A schematic side view of the BABAR drift chamber is shown in Fig. 3-7. The BABAR drift chamber is a 280 cm-long cylinder, with an inner radius of 23.6 cm and an outer radius of 80.9 cm. The flat endplates are made of aluminum. Since the BABAR events will be boosted in the forward direction, the design of the detector is optimized to reduce the material in the forward end. The forward endplate is made thinner (12 mm) in the acceptance region of the detector compared to the rear endplate (24 mm), and all the electronics is mounted on the rear endplate. The inner cylinder is made of 1 mm beryllium, which corresponds to 0.28% radiation lengths (X_0). The outer cylinder consists of 2 layers of carbon fiber on a Nomex core, corresponding to 1.5% X_0 .

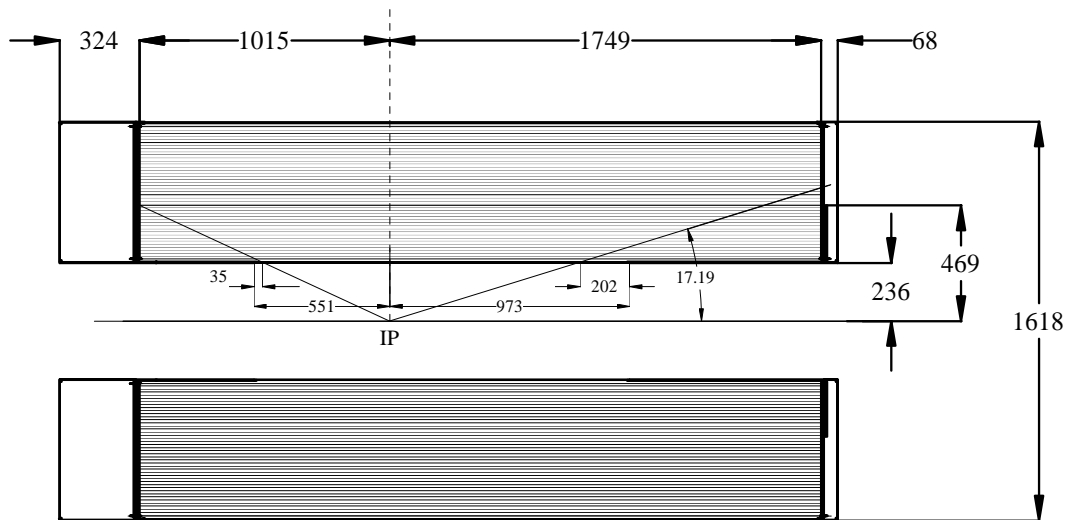


Figure 3-7. Side view of the BABAR drift chamber. The dimensions are in mm.

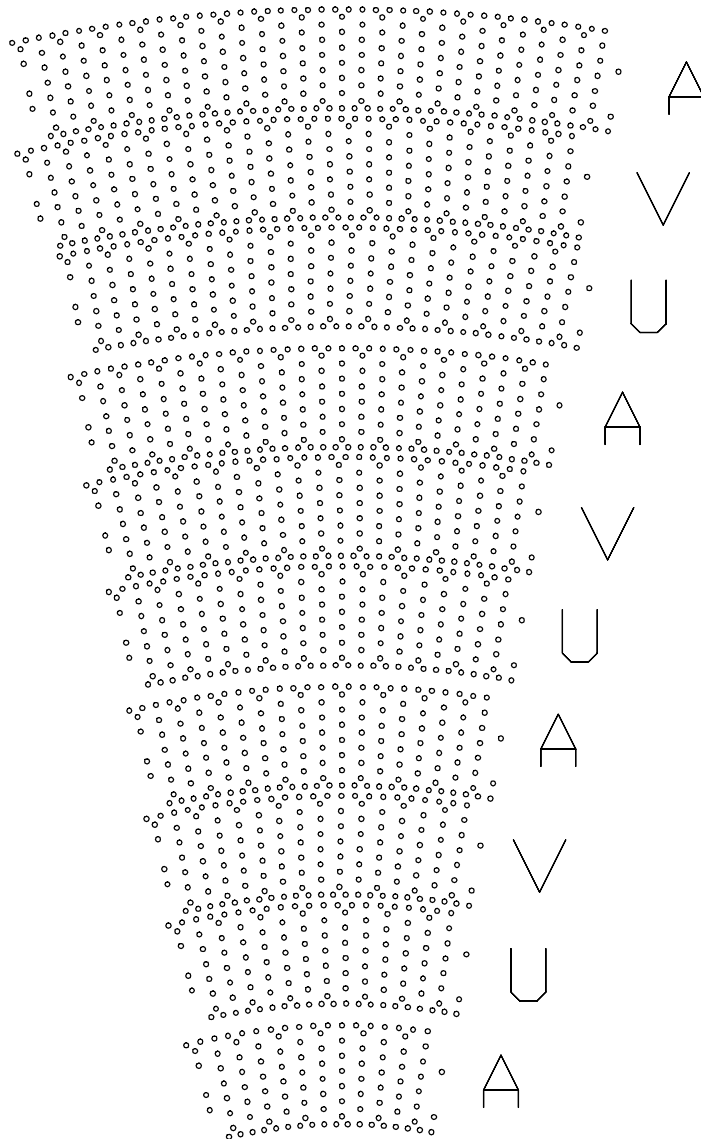


Figure 3-8. Cell layout in the BaBar drift chamber.

The drift cells are arranged in 10 superlayers of 4 layers each, for a total of 40 layers. Axial (A) and stereo (U, V) superlayers alternate, following the pattern AUVUVAUVA as shown in Fig. 3-8. The stereo angle varies from a minimum of 40 mrad in the innermost stereo superlayer, to a maximum of 70 mrad in the outermost stereo superlayer. The 7104 cells are hexagonal with typical dimension of $1.2 \times 1.8 \text{ cm}^2$. Figure 3-9 shows the 50 ns isochrones in a typical cell in a 1.5 T magnetic field.

The sense wires are $20 \mu\text{m}$ gold-plated tungsten-rhenium, the field wires are $120 \mu\text{m}$ and $80 \mu\text{m}$ gold-plated aluminum. The chosen gas mixture, Helium-isobutane (80%:20%), provides good spatial and dE/dx resolution and reasonably short drift time, while minimizing the material. The gas and the wires total $0.3\% X_0$ for tracks at 90° [11].

Nominal voltages of 1960 V for the sense wires and 340 V for the field-shaping wires at the boundaries of the superlayers are supplied by HV assemblies mounted on the feedthroughs of the rear endplate. Other field wires are connected to the ground through metal feedthroughs on the rear endplate. The forward endplate carries no components other than the feedthroughs.

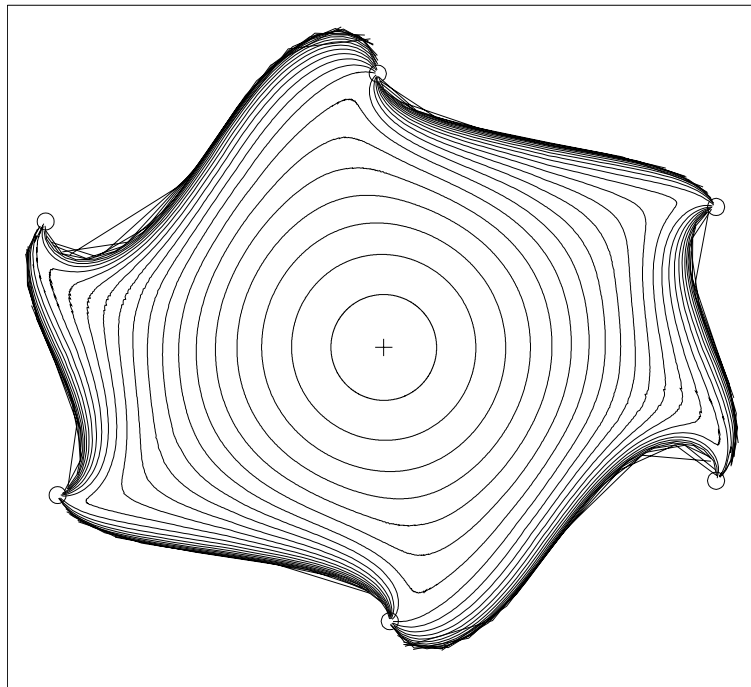


Figure 3-9. 50 ns isochrones in a typical BABAR drift chamber cell.

3.4.2 Drift Chamber Electronics

The BABAR drift chamber electronics is designed not to degrade the intrinsic performance of the chamber by more than 10%. For the drift-time measurement, the electronics detects the leading edge of the signal from the charge arriving at the sense wire and digitizes the time with 1 ns resolution. The dE/dx measurement requires summing the total charge in the pulse. The approach adopted is to apply a slow shaper, then digitize the pulse with a 6-bit 15 MHz FADC.

In order to achieve the required channel density, the electronics design uses a 4-channel amplifier-discriminator IC [12] and an 8-channel CMOS TDC/FADC IC [13]. The amplifier, digitizer, and the trigger interface electronics are mounted on the rear endplate, on top of the HV Assembly. They are contained in 48 wedge-shaped aluminum boxes called Front-End Assemblies (FEAs) that are water-cooled.

The data from the TDCs and FADCs are written through a 12 μ s trigger latency buffer into 4 levels of event buffers to minimize the dead time. The electronics provides prompt trigger signals by sending the hit information from all 7104 channels to the Level 1 Trigger system at a sampling frequency of 3.75 MHz. The system is designed to maintain good performance in severe background conditions. The expected single-cell efficiency for the trigger signal is greater than 95%.

3.4.3 Prototype Results

A full-length prototype of the BABAR drift chamber was built at SLAC in 1996. This test chamber consists of 214 drift cells (930 wires) and reproduces a portion of the first 4 superlayers of the final chamber. The main goals of this prototype are the validation of the design choices, test of the assembly procedures, and provision of a test bench for the electronics and for the development of the online and offline software.

The tracks used for the analysis are cosmic rays with a minimum momentum of 0.8 GeV/c. The typical data set was recorded using the nominal gas mixture (He:isobutane 80:20) and the nominal settings of the high voltages (1960 V for sense wires). The gas gain was $\approx 7 \times 10^4$ and the discriminator threshold was ≈ 2.5 electrons. The resolution for this configuration [14] was $\approx 100 \mu$ m in the central part of the cell and 131 μ m averaged over the cell (Fig. 3-10). The dE/dx resolution was studied by comparing the truncated mean of the signal charges measured in the inner and outer 8 layers of the 16-layer prototype chamber [15]. The result, extrapolated to 40 layers, corresponds to a predicted dE/dx resolution of 6.8% for the BABAR drift chamber. These results meet the goals for the BABAR drift chamber and confirm the validity of both the mechanical and the electronics design.

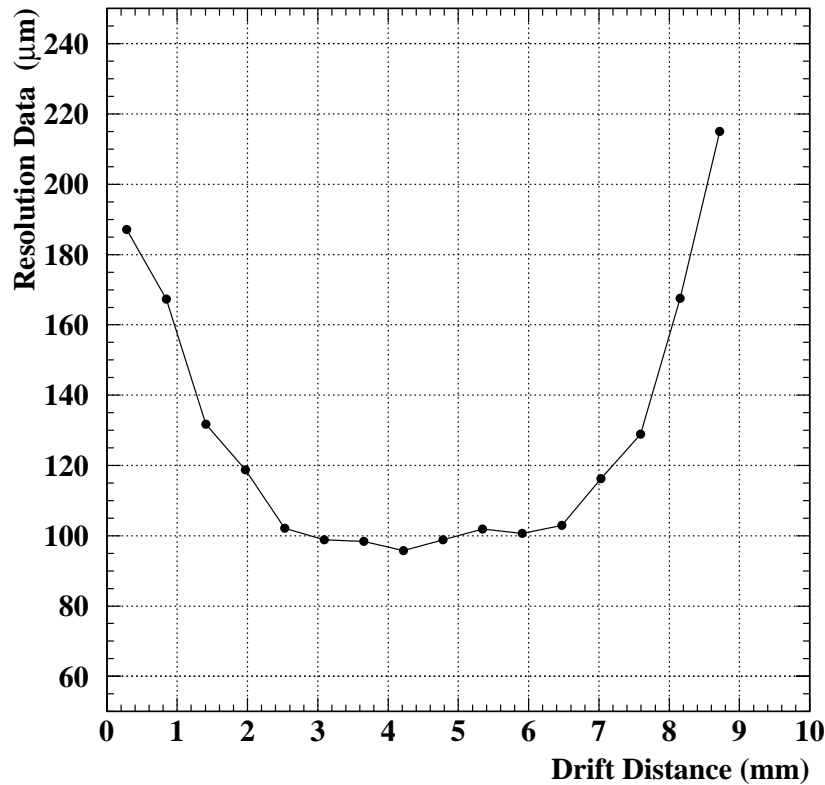


Figure 3-10. Spatial resolution obtained in the Prototype drift chamber with sense wire voltage at 1960 V.

3.5 The DIRC

The DIRC, an acronym for **D**etection of **I**nternally **R**elected Cherenkov (light), is a new type of Cherenkov-based detector devoted to particle identification (PID). In particular, the DIRC is designed to provide excellent kaon identification, not only for tagging purposes, where kaon momenta extend up to about 2.0 GeV/c, but also at higher momenta for *rare* B meson decay processes. In order to distinguish between the two-body decay modes $B^0 \rightarrow \pi^+\pi^-$ and $B^0 \rightarrow K^+\pi^-$, the DIRC must be able to separate pions from kaons up to about 4.0 GeV/c at large dip angles in the laboratory frame. The DIRC will also participate in muon identification in the momentum range where the IFR is still inefficient (typically below ~ 750 MeV/c).

3.5.1 DIRC Concept and Hardware Overview

The DIRC inverts the traditional concept of ring-imaging Cherenkov counters (RICH) in that it relies on the detection of Cherenkov photons trapped in the radiator due to total internal reflection [16].

The DIRC radiator consists of 144 long, straight bars of synthetic quartz with rectangular section, arranged in a 12-sided polygonal barrel. The bars have transverse dimensions of 1.7 cm thick by 3.5 cm wide, and are 4.9 m long. The DIRC radiator extends through the steel of the solenoid flux return in the backward direction, to bring the Cherenkov light, through successive total internal reflections, outside the tracking and magnetic volumes. Only this end of the bars is instrumented. A mirror placed at the other end on each bar reflects forward-going photons to the instrumented end. The Cherenkov angle at which a photon was produced is preserved in the propagation, modulo a certain number of discrete ambiguities, some of which can be resolved by the photon arrival-time measurement. Remaining ambiguities are dealt with by the pattern recognition during Cherenkov angle reconstruction.

At the instrumented end, the Cherenkov image is allowed to expand. The expansion medium is purified water, whose refractive index matches reasonably well that of the bars, thus minimizing the total internal reflection at the quartz-water interface. The region containing water is called the Standoff Box. Cherenkov photons are detected in the visible and near-UV range by a close-packed array of linear focused 2.82 cm diameter photomultiplier tubes (PMTs), lying on an approximately toroidal surface. A small piece of quartz with a trapezoidal profile glued at the back end of each bar allows for significant reduction in the area requiring instrumentation because it folds one half of the image onto the other half, while also reflecting photons with large angles in the radial direction back into the detection array. The dimensions of the Standoff Box are such that geometrical errors on angle measurements due to the finite size of bars and PMTs are of the order of the irreducible error due to quartz achromaticity. Six m³ of water are needed to fill the Standoff Box, and about 11,000 PMTs to cover the detection area. The PMTs are operated directly in water, and are equipped with light concentrators. The PMTs are about 1.2 m away from the end of the quartz bar. Magnetic shielding around the Standoff Box is further needed to maintain the magnetic fringe field at an acceptable level for PMT operation.

The DIRC technique was chosen for some of its many advantages. It presents an amount of material comparable to that of other techniques (14% of an X_0 for a particle at normal incidence). The DIRC occupies only 8 cm of radial space, which allows for a relatively large radius for the drift chamber while keeping the volume (and thus the cost) of the CsI Calorimeter reasonably low. Furthermore, its material is located close to the front faces of the crystals and has minimal impact on the Calorimeter performance for soft photon detection. Also, the DIRC performance tends to improve with the steepness of incidence of particles, as more light is generated and trapped at steeper angles, which matches well the needs of a detector at an asymmetric B Factory. Finally, the DIRC design is rather robust, involving conventional photodetectors and well-known materials.

The main uncertainty resides in the photoelectron yield, which depends on various parameters such as transparencies of quartz, water and glues, reflectivities of mirrors and light collectors, and on the quality of quartz polishing. However, extensive beam tests with a large prototype of the DIRC [17] give some confidence in the DIRC simulation model currently used in the `BBsim` full-simulation program.

3.5.2 DIRC Acceptance

In the nominal 1.5 T magnetic field, the DIRC radiator polygon, with an internal radius of 80 cm, can only be reached by particles produced (at the IP) with transverse momenta larger than ~ 250 MeV/c. The DIRC bars extend 178 cm forward from the IP (up to 60 deg in dip angle), covering 87% of the polar solid angle in the center-of-mass frame. The azimuthal coverage is 93%, since there are gaps between bars at the 12 sides of the radiator polygon.

3.5.3 DIRC Performance

The refractive index of quartz is close to 1.474. In a quartz radiator, the Cherenkov threshold for kaons (~ 460 MeV/c) is well below the value of momentum for which there is no possible confusion between a pion and a kaon through ionization loss measurement (dE/dx) in the drift chamber (~ 700 MeV/c): the two systems are remarkably complementary as far as π/K separation is concerned. The difference in Cherenkov angle between a pion and a kaon at 4.0 GeV/c is as small as 6.5 mr (the same difference occurs between a muon and a pion at 700 MeV/c). A good π/K separation therefore requires resolutions on the Cherenkov angle for a track of 2 mr or better. The single photoelectron resolution, intrinsically limited by geometry and quartz achromaticity, is of order 9 mr, largely independent of the track momentum and dip angle. Designed track resolutions are obtained by combining measurements from the large number of photoelectrons generally observed for each track. As an example, the expected number of photoelectrons for an ultrarelativistic particle at 60 deg of dip angle is larger than 50. This number drops to around 25 at some smaller dip angles, but momentum spectra are then much softer.

The DIRC performance depends also on the accuracy of extrapolated track parameters and their errors, as provided by the tracking software. The best accuracy is obtained with a Kalman filter fit, which takes into account correctly the effects of scattering and energy loss in the material along the trajectory, including the material between the last drift chamber hit and the quartz bar. At low momenta, the uncertainty on the track direction due to multiple scattering in the drift chamber outer wall, the DIRC supports and the bar itself, actually dominates the error on the Cherenkov angle measurement. Cherenkov resolutions are greatly improved at low momenta by a full constrained fit of the Cherenkov image. This is particularly relevant for μ/π separation below 750 MeV/c.

The DIRC reconstruction provides for each charged track, together with an estimation of the Cherenkov angle and its error, a confidence level for each of the five mass hypotheses (e , μ , π , K and p). The probability for a kaon in the DIRC acceptance to be given the largest confidence level for the kaon hypothesis is of order 95% or larger for all dip angles and all momenta above the kaon threshold, while the fraction of pions misidentified as kaons is lower than 3% up to momenta of ~ 3 GeV/ c . These results are fully satisfactory for tagging needs. Studies of the benchmark mode $B^0 \rightarrow K^+ \pi^-$ show excellent results as well, with efficiencies of order 97% and contaminations lower than 3 for both pions and kaons, except for kaons in the very upper tail of the momentum spectrum (above 4 GeV/ c), where the efficiency drops to 90%. A study of a sample of isotropically generated muons shows that the probability of correctly assigning muon as the best hypothesis to a muon in the DIRC acceptance, is larger than 80% below 750 MeV/ c and is 95% at 500 MeV/ c . The DIRC can also be used in veto-mode when there are not enough associated photons, or when a Cherenkov image cannot be reconstructed, for a track whose extrapolated trajectory crosses the radiator. However, efficiencies and purities in this mode are strongly dependent on the level and nature of machine induced backgrounds. Most protons at PEP-II have small velocity. Even above the proton Cherenkov threshold (~ 940 MeV/ c), the Cherenkov cone hardly opens. At small dip angles, the effective proton threshold, for which some fraction of the Cherenkov cone is trapped by total internal reflection, is as high as 2 GeV/ c . Protons are therefore identified most of the time in veto mode, above the kaon threshold. Below the kaon threshold, kaons and protons cannot be distinguished.

3.6 The Electromagnetic Calorimeter

3.6.1 Performance Goals and Layout

The physics requirements of BaBar led to a calorimeter design [2] based on quasi-projective CsI(Tl) crystals over a solid angle corresponding to $-0.775 \leq \cos \theta \leq 0.962$ in the laboratory frame, and $-0.916 \leq \cos \theta \leq 0.895$ in the center-of-mass frame. Useful physics coverage is slightly less since one has to stay away from the forward and backward edges to avoid excessive shower leakage. The properties of CsI(Tl) are summarized in Table 3-5. The crystal scintillation light is read-out by photodiodes because of the strong magnetic field in which the calorimeter lies.

The target energy resolution for photons at a polar angle of 90° is:

$$\frac{\sigma_E}{E} = \frac{1\%}{\sqrt[4]{E(\text{GeV})}} \oplus 1.2\%. \quad (3.5)$$

The constant term arises from front and rear leakage ($\leq 0.5\%$), inter-calibration errors (0.25%), and light collection non-uniformity ($\leq 0.5\%$). This expression includes neither electronic noise,

Table 3-5. *Properties of Thallium-doped CsI.*

Properties	CsI(Tl)
Radiation Length (cm)	1.85
Molière Radius (cm)	3.6
Absorption Length for 5 GeV pions (cm)	41.7
Density (g/cm ³)	4.53
$dE/dx _{mip}$ (MeV/cm)	5.6
Light Yield (Photons/MeV $\times 10^3$)	40–50
Light Yield Temperature Coef. (%/°C)	0.1
Peak Emission (nm)	565
Refractive Index at Emission Maximum	1.79
Decay Time (ns)	940
Hygroscopic	slight
Radiation Hardness (rad)	10^3 – 10^4

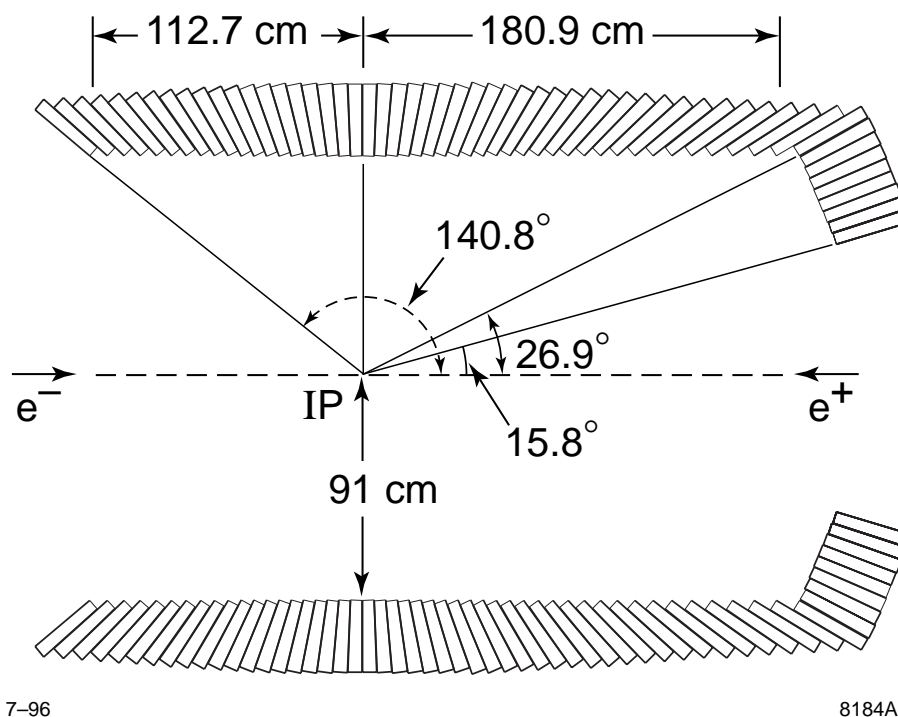
nor beam-background noise. The energy resolution degrades towards the ends of the barrel as a consequence of the staggered arrangement of crystals and the increasing amount of inactive material in front of the calorimeter.

The angular resolution is determined by the transverse crystal size and average distance to the interaction point. The target angular resolution for photons at a polar angle of 90° is:

$$\sigma_{\theta,\phi} = \frac{3 \text{ mr}}{\sqrt{E(\text{GeV})}} + 2 \text{ mr}. \quad (3.6)$$

As in CLEO-II, the minimum detectable energy for photons is about 10–20 MeV. It is expected to be largely determined by beam- and event-related backgrounds in the calorimeter even at energies as low as a few MeV, since the intrinsic CsI(Tl) efficiency should be close to 100%.

The calorimeter consists of a cylindrical barrel section and a forward conic endcap, as shown in Fig. 3-11. Radially, the barrel is located outside the particle ID system and within the magnet cryostat. It weighs 23.5 metric tonnes and is supported off each end of the coil cryostat. The barrel has an inner radius of 91 cm and an outer radius of 136 cm. It is located asymmetrically about the interaction point. The active crystal volume starts at a radius of 91.9 cm its inner radius extending 112.7 cm in the backward direction and 180.9 cm in the forward direction. The barrel crystals cover a solid angle corresponding to $\pi - 684 \text{ mr} \leq \theta \leq 470 \text{ mr}$ ($-0.775 \leq \cos \theta \leq 0.892$) in the laboratory frame, and $-0.916 \leq \cos \theta \leq 0.715$ in the center-of-mass frame.



7-96

8184A1

Figure 3-11. The EMC layout: Side view showing dimensions (in mm) of the calorimeter barrel and forward endcap.

The barrel consists of 5760 CsI(Tl) crystals, arranged in 48 polar-angle (θ) rows of distinct crystal sizes, each having 120 identical crystals in azimuthal angle (ϕ). The crystals are grouped in 280 modules, each spanning 7×3 crystals in θ and ϕ , respectively (except for the most-backward module, which has only 6 crystals in θ). The modules are made from $300 \mu\text{m}$ thick carbon fiber composite (CFC) material and held from the rear by an aluminum strongback. They are mounted in an aluminum support cylinder, which in turn is fixed to the coil cryostat.

By supporting the crystals from the rear, minimal material is placed in front of them. The EMC front material consists of two 1 mm-thick cylinders of aluminum, separated by foam, which provide a gas seal and rf shielding. Additional front material due to the liquid radioactive source calibration system consists of the equivalent of another 3 mm of aluminum. (All thicknesses are quoted at perpendicular incidence.) Cooling, cables, and services are located at the back of each module and thus do not add to the inactive-materials budget.

The total amount of external material in front of the calorimeter barrel (endcap) is about $0.25X_0$ ($0.20X_0$) at a polar angle of 90° (20°), the major contributors being the DIRC (drift chamber endplate) with about $0.14X_0$ in both cases. Areas of particular concern are the forward and backward end of the barrel, where the material grows to $0.5X_0$ and $0.39X_0$, respectively.

CFC and crystal wrapping material introduce gaps between the crystal active material of about 1.25 mm in each of the θ and ϕ directions. In order to minimize the loss of photons traversing these gaps, all θ gaps (except the one at 90°) are nonprojective by ± 15 mr for most of the barrel, increasing to $+45$ mr within the most-forward module. The gaps in ϕ are fully projective; this allows for identical crystals within a θ ring, at the cost of up to 2.5% of photons traversing inactive material between crystals.

The forward endcap is a conic section, with front and back surfaces tilted at 22.7° with respect to the vertical. The endcap weighs about 3.2 metric tonnes. It is supported off the barrel support cylinder to enable precision alignment relative to the barrel; this is to minimize the barrel/endcap gap, which is expected to be about 2 mm. At present, the endcap contains 820 CsI(Tl) crystals, arranged in 8 θ rings, starting at an inner radius of 55.3 cm from the beam line. It covers the solid angle range corresponding to $468 \text{ mr} \leq \theta \leq 275 \text{ mr}$ ($0.893 \leq \cos \theta \leq 0.962$) in the laboratory frame, and $0.718 \leq \cos \theta \leq 0.895$ in the center-of-mass frame. A 9th ring is currently filled with lead shielding blocks, but could be instrumented with CsI(Tl) crystals to provide coverage down to a polar angle of 250 mr. The ϕ segmentation of the endcap is not the same in all rings. In the outermost three rings, it is matched to that of the barrel with 120 crystals. In subsequent inner rings it decreases to 100 and 80 crystals. The crystal non-projectivity, 45 mr at the barrel/endcap gap, is 45 mr in the outer endcap ring and then reduced to the regular 15 mr over the next rings.

As in the barrel, the endcap crystals are grouped in modules: there are 20 modules around in azimuth, each with currently 41 crystals (potentially 45 crystals if the innermost ring is instrumented). The modules are of a CFC construction similar to the one in the barrel and are also held from behind by aluminum strongbacks, mounted to an aluminum backplate. Inactive EMC front material is very similar to that in the barrel; and again, all cooling, cables, and services are mounted behind the crystals or at polar angles below the acceptance.

3.6.2 Crystal Subassemblies and Readout

The crystals are of trapezoidal shape with typical transverse dimensions of $47 \times 47 \text{ mm}^2$ at the front face, flaring out towards the back to about $60 \times 60 \text{ mm}^2$ ($55 \times 55 \text{ mm}^2$) in the central (forward) part of the barrel. Crystal dimensions in the endcap match those of the barrel at the barrel/endcap interface, reducing to $46 \times 53 \text{ mm}^2$ for the innermost ring. Front face dimensions vary by no more than 2 mm across the barrel, and are square to within 2 mm; variations are somewhat larger in the endcap — up to 8 mm — due to the changing azimuthal segmentation.

In an effort to keep the CsI volume down, crystal lengths change with polar angle, taking into account the effect of the boost on the photon energy spectrum: all crystals in the backward half of the barrel have a length of $16.1X_0$ (29.76 cm); towards the forward end of the barrel, crystal lengths increase in steps of $0.5X_0$ every 7 crystals (*i.e.*, every module), up to a length of $17.6X_0$ (32.55 cm) in the most-forward barrel module; all endcap crystals are of $17.6X_0$ (32.55 cm) length,

except the two innermost rings which had to be shortened by $1X_0$ due to space limitations. Crystal dimensions have tolerances of about $250\ \mu\text{m}$ transversely, and about 1 mm longitudinally.

A crystal subassembly consists of a CsI(Tl) crystal covered with a white, diffuse reflector wrapped in thin aluminum foil, and a readout package located at the rear. The readout package consists of two silicon PIN diodes, closely coupled to the crystal and to two low-noise, charge-sensitive preamplifiers, all enclosed in a metallic housing (which is tightly connected to the aluminum foil) to shield against rf noise. All components are selected to have uniform and high light collection, together with minimal noise from the readout electronics, in order to achieve optimal energy resolution. Mostly for reliability reasons, but also to increase signal/noise, two independent readout and electronics chains are implemented, starting with the diodes.

The diffuse reflector consists of two $150\ \mu\text{m}$ layers of Tyvek 1056D, covering the front and all side faces. It is wrapped in one layer of $30\ \mu\text{m}$ aluminum foil. The area of the rear surface not viewed by the diodes is covered by a white plastic reflector plate (Trovidur, coated with NE561 paint). The two Hamamatsu S2744-08 diodes ($10 \times 20\ \text{mm}^2$ each) are glued with epoxy to a slightly oversized, 1 mm thick Polystyrene carrier plate, which in turn is glued with epoxy to the crystal. Each diode is connected via a 3 cm long flexible flat cable to its own preamplifier IC, which sits on a printed circuit board located in a metal box whose side walls rest on the rear plastic reflector plate.

This setup results in an average light yield per crystal of 7300 pe/MeV, varying between 5000 and 10000. Using a “long-shaping-time” digital filter, the incoherent electronic noise has been measured as about 900 e per crystal, resulting in an average equivalent noise energy of less than 150 keV per crystal. That renders incoherent electronic noise a negligible contribution to the calorimeter’s energy resolution for typical cluster sizes of 9 to 25 crystals, even at the lowest energies. The beam background noise, even at nominal levels, completely overwhelms electronic noise: it is estimated as about 350 keV (1000 keV) per crystal at $\times 1$ ($\times 10$) background.

Using a variety of techniques (*e.g.*, surface roughening), every crystal has been compensated, resulting in the light collection efficiency along the length of the crystal being uniform to within $\pm 2\%$ ($\pm 6\%$) for the front (back) half of the crystal. At that level, non-uniformity contributes less than 0.5% (absolute) to the constant term in the energy resolution. Concern remains, though, that radiation damage might increase this. There is also concern about how a change in the light collection profile can be monitored.

3.6.3 Calibration

In order to realize the intrinsic performance of which a CsI calorimeter is capable, it is crucial to provide for precise means of setting its energy scale and for monitoring short- and long-term variations of its response. The calibration and monitoring system [18] for the BABAR calorimeter consists of the following:

- A charge injection system to linearize the response of the FEE to better than 0.1% over all of the four ADC ranges;
- A liquid radioactive source system using 6.1 MeV photons from the ^{16}N β - γ cascade for setting the initial energy scale per crystal to better than 0.5%, and monitoring long term variations;
- A light pulser system for conveniently tracking short term changes to better than 0.5%; and
- A detailed program of using physics processes to determine the energy scale for individual crystals as well as clusters to better than 0.25% and 0.5%, respectively.

The main tasks of the radioactive source system are to determine single-crystal calibration constants and to provide an absolute monitor of changes in light collection due to crystal radiation damage or to degradation of optical couplings, surfaces, or wrappings. For both functions, the most crucial feature of the source is that it provides an absolutely known and stable photon-energy deposit in a single crystal. The source provides a readily-determined low-energy point on the photon response curve. It will be the primary means of calibration during initial running, when it will also help establish the Bhabha calibration procedure. Together with Bhabhas, it will provide continuing calibration of the energy dependence of single-crystal response, a necessity in the potentially hostile PEP-II environment. Reliance on the source is heavier still for those crystals which are not hit by coincident Bhabha events.

Calibration using colliding beam events entails measuring the response of the system to a particle of known type, known energy, and known position at the calorimeter. The events to be used are those providing constraints: two-body final states such as e^+e^- (Bhabhas), $\gamma\gamma$, and $\mu^+\mu^-$, as well as radiative Bhabha and $\gamma\gamma\gamma$ states, and a clean subset of $\pi^0 \rightarrow \gamma\gamma$ decays in more complex states. The nonradiative Bhabha events play a special role: because of their high yield, they are used both to track the crystal gains in time and — with small geometry-dependent corrections determined from simulation and from $\gamma\gamma$ events — to provide intercalibration of crystals. They also give the overall scale at the highest possible energies. At design luminosity, it takes less than 12 hours of data to achieve 0.25% accuracy per crystal.

Radiative Bhabha events are used to study the photon-energy response in the energy range from a few hundred MeV to a few GeV. Photons from radiative Bhabhas cover the whole kinematically allowed range of photon energy versus polar angle. They are used to derive an energy-dependent correction to the energy of *showers*, initially measured using a combination of the Bhabha and radioactive-source single-crystal constants. In order to achieve the best possible calibration from radiative Bhabha events, geometric effects such as variations in crystal length and stagger need to be taken into account. This requires energy-response curves in bins of polar angle, likely as small as individual crystal rings. At design luminosity, it takes less than two weeks to collect the data required to calibrate the energy response of a crystal ring to 0.25%.

Many of the photons produced in $B\bar{B}$ events have very low energy, and almost all of them originate from decays of neutral pions, $\pi^0 \rightarrow \gamma\gamma$. Exclusive B reconstruction efficiency is very sensitive to our ability to reconstruct π^0 s effectively and with the best possible mass resolution. Fortunately, that very population of π^0 s can be used to check the photon-energy response by employing the π^0 mass constraint on pairs of well-separated photon showers. Although this technique is complicated, it is expected to be used in the energy range from approximately 20 MeV up to near 1 GeV, where there is overlap with other calibration methods (*e.g.*, radiative Bhabhas). It remains to be seen how well the method works at the very lowest energies, as the background level there increases rapidly. (This is due to fake photons from within the event as well as from beam background.) The accuracy of such a calibration should approach 0.5%, depending on photon energy and the actual background conditions. This assumes that any variations in crystal response are monitored over the time it takes to collect the necessary statistics.

3.7 The Muon and Neutral Hadron Detector

3.7.1 The Detector Layout

The large iron structure needed as magnet yoke is segmented and instrumented with Resistive Plate Counters (RPCs), in order to provide muon identification and (in tandem with the calorimeter) neutral hadron detection. This system, called the Instrumented Flux Return (IFR), consists of a central part (Barrel), and two plugs (End Caps), which complete the solid angle coverage down to 300 mrad in the forward direction and 400 mrad in the backward direction.

A novel feature of the BABAR experiment is the graded segmentation of the iron, which varies from 2 to 10 cm, increasing with the radial distance from the interaction region. This segmentation is the result of detailed Monte Carlo studies which have shown that muon identification at low momentum and K_L^0 detection improve, for a given amount of absorber, as the thickness of the iron plates decreases. This effect, however, is most important in the first absorption length, so by grading the segmentation it is possible to improve the performance without increasing too much the number of layers.

The iron is segmented into 18 plates, giving a total thickness of 65 cm in the Barrel and 60 cm in the End Caps. The innermost nine plates are 2 cm thick, followed by four of 3 cm and three of 5 cm; the two outermost plates are 10 cm thick in the Barrel, with one 5 cm and one 10 cm in the End Caps. The gaps housing the RPCs are 3.2 cm wide, except the ones between the 2 cm Barrel plates where more room, 3.5 cm, is allowed for housing the RPCs.

In the Barrel region there are 21 active detector layers: a double layer cylindrical RPC surrounding the Electromagnetic Calorimeter, an inner layer of planar RPCs between the solenoidal coil and the iron, 17 layers in the gaps, and one last layer outside the iron structure. The total area covered

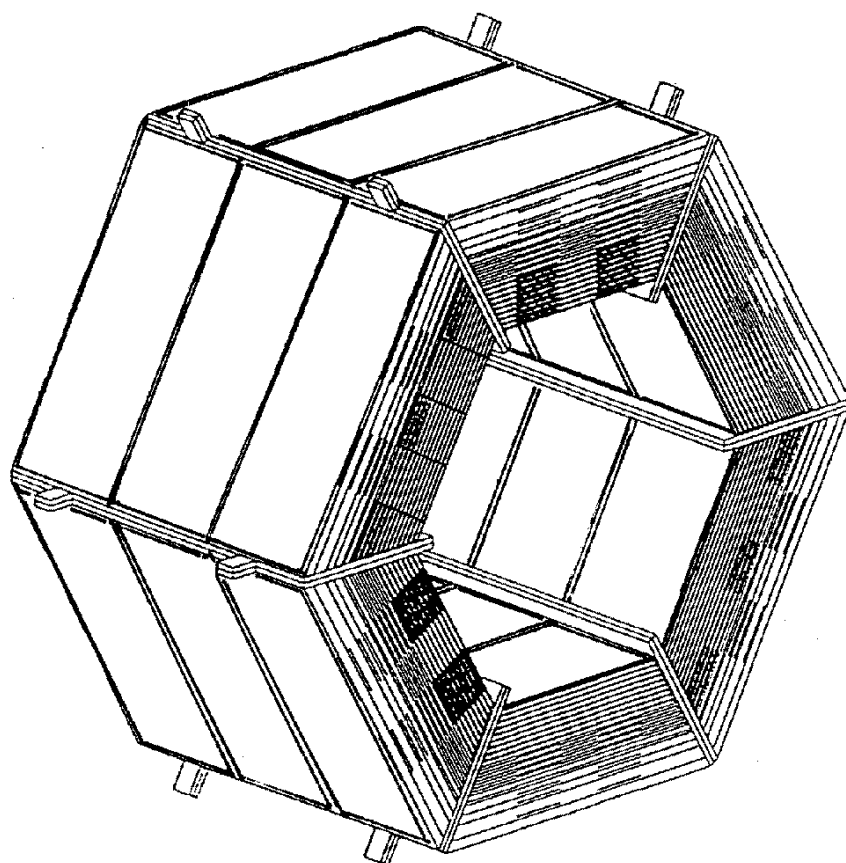


Figure 3-12. *The IFR Barrel: layout of the RPC Modules.*

by detector exceeds 1000 m^2 . The cylindrical RPC is another novel feature of the BABAR detector. It consists of 8 chambers, in two layers, for maximum efficiency. Each chamber covers one quarter of a cylinder, 147 cm in radius, and is made by joining 4 modules, for a total of 32 modules, each of approximate size $115 \text{ by } 190 \text{ cm}^2$.

Each planar Barrel chamber covers the whole gap and consists of three modules, joined along their long sides (in the direction perpendicular to the beam axis), as shown in Fig. 3-12; each RPC module is 125 cm wide and 181 cm to 320 cm long, depending on the radial distance from the interaction region. The Barrel yoke is divided into sextants, so there are 114 chambers and 342 independent modules.

Each End Cap door has a hexagonal shape and is divided vertically into two halves to allow access to the inner detectors; each half door is divided into three sections by horizontal spacers which are needed to withstand the magnetic forces; so there are 6 chambers in each layer of one door.

There are 18 detector layers, with the first starting behind the innermost iron plate, for a total of 216 modules, and $\approx 1000 \text{ m}^2$ detector surface.

3.7.2 The Active Detectors

The active volume is filled with a gas mixture based on comparable quantities of Argon and Freon 134A ($C_2H_2F_4$), and a small amount (a few %) of Isobutane. This choice was driven by the need to operate the RPCs with a nonflammable and environmentally safe gas mixture: the mixture traditionally used in RPCs [19] has a large fraction of isobutane, $\approx 40\%$, and does not satisfy the safety standards for BaBar. With the choice used here, the chambers can work in streamer mode, and it has been proved to yield good performance. Long-term effects of this new gas have been studied over a period of two years on the first-built chambers, which have been kept in continuous operation. Typical examples of efficiencies, single rates and currents as a function of the operating Voltage are shown in Fig. 3-13. The estimate of the absolute efficiency of the RPCs was computed on a sample of events in which full spatial reconstruction and tracking of the cosmic muons was performed.

The distribution of $\simeq 100$ RPCs shows an average value of 97.2% at 8 kV, [20] with losses due essentially to the dead areas corresponding to the spacers. All modules were tested with cosmic rays prior to assembly; finished chambers were also tested with cosmic rays before insertion into the iron.

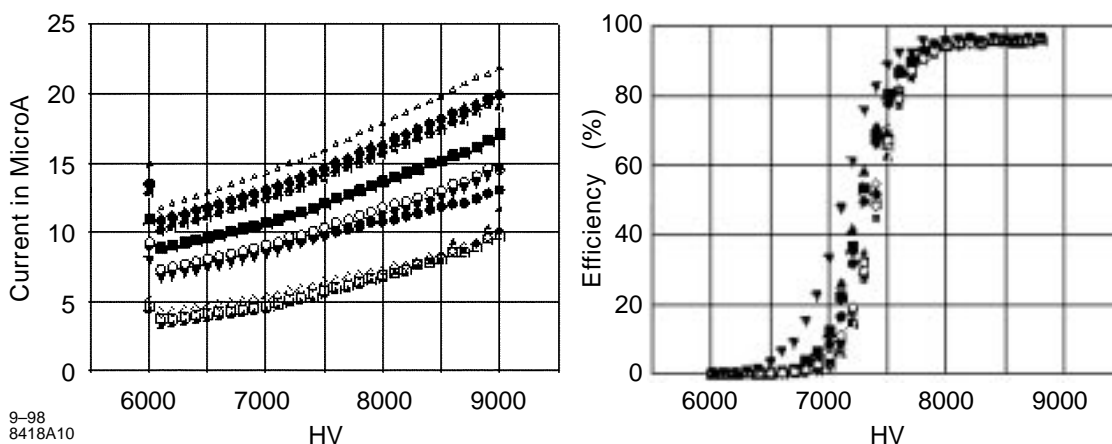


Figure 3-13. Typical results obtained with a set of 12 RPCs, as a function of HV: Left: Currents; Right: Plateau curves.

3.7.3 The Readout System

The external pick-up electrodes are made of aluminum strips glued on a plastic support and coupled, with a suitable 4 mm thick insulator, to the bakelite sheets. On the other side, a $40 \mu\text{m}$

aluminum plane is connected to ground and insulated from the iron by a laminated mylar sheet. Both sides of the RPC are read-out with such strip electrodes, which run along the chamber lengthwise and crosswise, respectively, to provide 3-dimensional information.

In the Barrel, the strips which run along each module measure the direction along the beamline, *i.e.*, the z coordinate; this strip plane faces the ground side of the RPCs. The strip-width is 36.5 mm, and the gap between strips is 2 mm, for a total pitch of 38.5 mm: there are 32 longitudinal strips on each module. The other plane of strips is glued across three modules on the HV electrode, and allows the measurement of the ϕ angle; the pitch is different in each layer, increasing with the radial coordinate from 19.7 to 33.5 mm, to give exactly 96 strips in each chamber.

In the End Cap chambers, the strips run horizontally and vertically, to measure the x and y coordinates, respectively. The horizontal strips are glued on the HV side of each module; their width is 26.4 mm, and the gap between strips is 2 mm, for a total pitch of 28.4 mm. The vertical strips are glued across two modules, on the Ground side, and have a 38 mm pitch. Strip pitch is the same throughout all End Cap chambers. Typically each one has 64 horizontal strips and 64 vertical; due to the conical shape of the central hole in the forward door and the presence of cutouts for services, the chambers come in many different sizes and the strip planes vary accordingly.

One end of each strip is connected to the ground plane with a $2\text{K}\Omega$ resistor, the other side is connected to the input of the Front End readout Cards (FEC), which have 16 channels each. In the Barrel, the readout cards for layers 1–16 are positioned directly on the chambers, six cards at one end are connected to the odd-numbered strips, the other six at the opposite end are connected to the even-numbered strips; adjacent strips are read by different cards so that in case of a card failure there are no dead areas. The FECs for the cylindrical RPC and for layers 17–19 are housed in external small custom-built crates (minicrates), located on the top of the Barrel.

In the End Cap, the chambers can be accessed only by one side, adjacent strips are, however, always connected to two different cards; for lack of space in the gaps, only the FECs for the horizontal strips are positioned on the chambers, the others are in external minicrates, on the back of the doors.

The FECs are interfaced to the readout module, which is a BABAR standard, by a set of custom built modules [21].

3.8 The Trigger

The BABAR trigger has two levels: Level 1 which executes in hardware and Level 3 which executes in software after the event assembly. The trigger system Requirements Document contains a detailed description [22].

The primary performance measure of a trigger system is its efficiency for benchmark physics processes. The Level 1 trigger system is designed to achieve very high efficiency and good understanding of the efficiency. The charged track trigger requires at least two tracks in the drift chamber: one long track with $p_t > 0.18$ GeV/c and one short track with $p_t > 0.12$ GeV/c. The energy trigger requires two clusters in the electromagnetic calorimeter, both with reconstructed energy deposits above a threshold that is efficient for muons. The orthogonality of the requirements allows good cross-calibration of trigger efficiency. Under nominal background conditions, this ‘open trigger’ is simulated to produce a rate of 1.5 KHz, while yielding 100% efficiency inside the fiducial region of the detector for B and τ physics and $> 99\%$ for $\gamma\gamma$ physics.

With no further restrictions, the total trigger rate for this open trigger is simulated to be about 16 KHz at 10 times nominal beam backgrounds, which is greater than the specification of 2 KHz. The rate can be reduced further rather simply, for example by using a correlated trigger which requires either one charged track and two energy clusters, or two back-to-back clusters with one of the cluster energies above 0.5 GeV. Most simulated backgrounds may alternatively be reduced by introducing a p_t cut on the track with the largest transverse momentum and an energy cut on the largest energy deposit.

While a detailed simulation of the trigger electronics is available, most properties of the trigger can be obtained from the acceptance curves for the individual trigger objects (tracks and clusters). There are three drift chamber trigger objects: long tracks (A), short tracks (B) and long tracks with a configurable cut on $p_t(A')$. The calorimeter trigger reports three main trigger objects, corresponding to three configurable energy thresholds for clusters. The energy lowest threshold object (M) defaults to > 0.12 GeV, low enough to be quite efficient for minimum ionizing muons. The solid angle acceptance for these can be seen in Fig. 3-14.

The global trigger selects events using any combination of these objects, using requirements on the number of objects, optionally subject to separation cuts in azimuth and to matching between tracks and clusters.

The efficiency for events such as $B^0 \rightarrow \pi^+\pi^-$, $\bar{B}^0 \rightarrow \mu X$ is simulated to be close to 100% for any reasonable variation of the proposed trigger. There are so many charged tracks and photons with high momentum in such events that the efficiency is very robust.

Tau events with 1 + 1 prongs and low-mass two-photon production are more demanding of the trigger, and therefore have been given attention in the trigger design. Even under worst-case scenarios of backgrounds and drift chamber cell inefficiencies, requirements are met for these challenging topologies. For example, efficiencies larger than about 95% inside the fiducial volume are expected for events with $\tau^+ \rightarrow e^+\nu\bar{\nu}$, $\tau^- \rightarrow \mu^-\bar{\nu}\nu$. The crucial performance parameter for such events is not the efficiency itself, but the systematic error in determining the efficiency. Since the efficiencies for τ events are dominated by the angular acceptance of the experiment, they should be measurable with great precision.

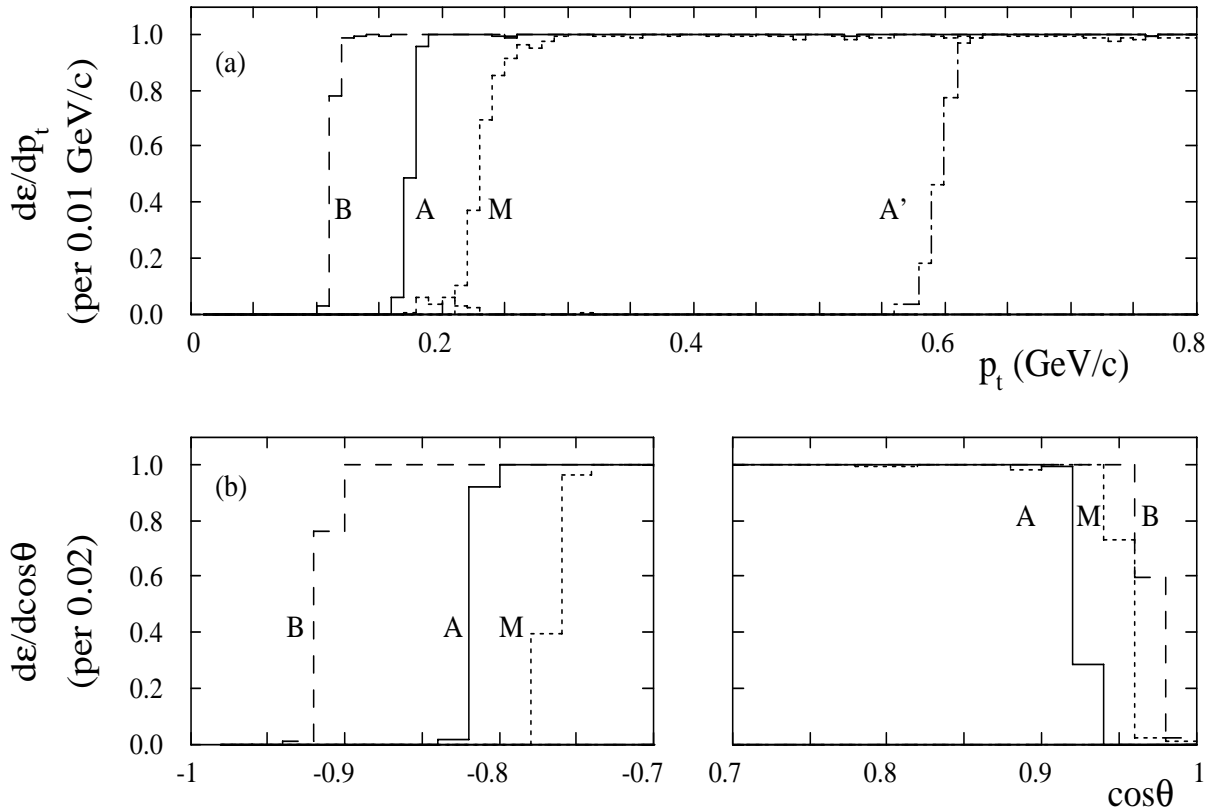


Figure 3-14. Differential efficiencies for single muons to be identified as trigger objects A, A', B or M, as a function of (a) p_t with $|\cos\theta| < 0.7$ and (b) $\cos\theta$ with $p_t > 0.4\text{GeV}/c$.

The Level 3 trigger contains a flexible combination of tools to reduce backgrounds while keeping the physics. Under nominal background conditions, it has been demonstrated that the output rate to mass storage can be kept to the specified value of 100 Hz. Preliminary studies indicate that simulated above-nominal conditions can also be handled, using information from the full event. For example, a hierarchy of increasingly complex algorithms obtain more and more accurate precision on track impact parameters from the Level 1 trigger track segments, the drift chamber hits and the silicon vertex tracker hits. The Level 3 trigger is not expected to reduce significantly the efficiencies delivered by Level 1. In Level 3, the only physics processes that need to be prescaled are two-photon processes used to match data from previous experiments and Bhabhas. The rates of all other physics processes amount to only 20 Hz of the 100 Hz budget at the design luminosity.

References

- [1] P. Oddone, in *Proceedings of the UCLA Workshop: Linear Collider $B\bar{B}$ Factory Conceptual Design*, edited by D. Stork, World Scientific (1987), p. 243.
- [2] “Technical Design Report,” (BaBar Collaboration), SLAC-REP-372 (1995).
- [3] A. Snyder, “The Effect of Vertex Cuts on CP Reach,” BaBar Note # 177 (1994).
- [4] F. Forti, “TRACKERR Studies for Optimization of Vertex Detector Resolution,” BaBar Note # 195 (1994).
- [5] D. Barbieri *et al.*, “Silicon Sensors for the BaBar Vertex Tracker,” submitted to *Nuovo Cimento*.
- [6] F. Lanni and F. Palombo, *Nucl. Instr. Methods* **A379**, 399 (1996).
- [7] R. Johnson *et al.*, “Silicon Vertex Detector Readout Chip, Requirement Specification,” BaBar Note # 213 (1995).
- [8] R. Johnson *et al.*, “Silicon Vertex Detector Readout Chip (Target Design Specifications),” BaBar Note # 214 (1995).
- [9] M. Bari *et al.*, “Results from the BaBar Silicon Vertex Tracker Test Beam,” BaBar Note # 278 (1996).
- [10] G. Sciolla, The BaBar Drift Chamber, in *Proceedings of the 8th Vienna Wire Chamber Conference*, SLAC-PUB-7779 (1998).
- [11] A. Boyarski, D. Briggs, P. Burchat, *Nucl. Instr. Methods* **A323**, 267 (1992).
- [12] D. Dorfan *et al.*, to be published.
- [13] A. Chau *et al.*, *IEEE Trans. Nucl. Sci.* **43**, 1720 (1996).
- [14] D. Coupal *et al.*, “Spatial Resolution Studies for the BaBar Drift Chamber based on the Prototype II Cosmic Data,” BaBar Drift Chamber Technical Note TNDC-98-83 (1998).
- [15] V. Blinov, “BaBar Drift Chamber dE/dx Resolution Study based on Proto-II Data,” BaBar Drift Chamber Technical Note TNDC-98-79 (1998).
- [16] B. N. Ratcliff, SLAC-PUB-5946 (1992); P. Coyle *et al.*, *Nucl. Instr. Methods* **A343**, 292 (1994).
- [17] R. Aleksan *et al.*, *Nucl. Instr. Methods* **A397**, 261 (1997).

-
- [18] R. Bernet *et al.*, “Calibration and Monitoring for the BABAR Calorimeter,” BABAR Note # 363, (1997).
- [19] R. Santonico and R. Cardarelli, *Nucl. Instr. Methods* **A187**, 377 (1981).
- [20] F. Anulli, in *Proceedings of La Biodola*.
- [21] N. Cavallo, in *Proceedings of La Biodola*.
- [22] The Trigger Group, N. Dyce *et al.*, “BABAR Trigger System Design Requirements,” Version 4.71, August 8, (1997).

This page was intentionally left blank.

A Snapshot of BABAR Software and Analysis Tools

This chapter presents an overview of the software tools used in the physics analyses reported in this book. It includes a review of the simulation and reconstruction tools, and of some physics analysis tools which were developed during the work.

The chapter reflects the status of the development of BABAR simulation, reconstruction and analysis tools at the time it was written. The results quoted do not represent the ultimate performance of the BABAR detector, or its software, but only those found in the simulation and used for the reported analyses.

Some features of the BABAR experimental environment, such as machine backgrounds, misalignment and calibration effects, were not included in the event simulation at this early stage of the experiment. Such effects will be taken into account in later studies. In some areas, such as the simulation of hadronic showers at low energies, Monte Carlo simulations are known to be imprecise and model-dependent, and this uncertainty should be borne in mind when considering the results of these studies. Strategies and procedures for extracting the relevant measurements for calibration and validation of the detector and its software using real BABAR data are under development.

4.1 Simulation

The physics studies described in this book are based on simulated data. The simulation process begins with event generation, for which BABAR uses a combination of a new generator, `EvtGen`, and the more familiar `Jetset 7.4`. Two different detector simulations were used to model the simulation of the BABAR detector response: a fast parametric Monte Carlo called `Aslund` and a detailed `Geant321`-based ([1]) simulation of the experiment, called `BBSim`. Both simulation packages were interfaced to the event generators via the `Beget` package.

4.1.1 Event Generators

Two different event generators were used to perform the studies in this book: `EvtGen` [2] and `Jetset 7.4` [3]. The former was used for B decays to exclusive final states and the latter for generic continuum and inclusive B decay simulation.

The interface to both event generators is called `Beget` [4]. This simulates the smearing of the beam energies and the position of the interaction point. The beam-energy smearing is modeled as a single Gaussian for each of the beams with widths of 5.5 MeV and 3.1 MeV for the high-energy and low-energy beams respectively. The smearing of the interaction region in the x and y coordinates is 160 μm and 6 μm , respectively, and is simulated by a single Gaussian in each case. The beam position in z is modeled as a flat distribution, 1 cm long. `Beget` also provides access to other generators, such as `KORALB` which can be used for the generation of $\tau^+\tau^-$ events, the event generator for Bhabhas; the two-photon generator; and many others.

The main generator for $B\bar{B}$ physics is called `EvtGen`. This implements a large number of physics processes in detail. This includes the generation of the asymmetries in CP -violating decays as well as many other decays, such as semileptonic decays. `EvtGen` provides a framework into which decay models may be added as modules. These modules can have a variety of different functionality. The most useful type calculates amplitudes for the decay. As an example consider the decay $D^* \rightarrow D\pi$. Here a vector ($J = 1$) particle, the D^* , decays to two scalar particles. This decay is described by 3 amplitudes, one for each possible state of the D^* . The state of the particle is related to the helicity.

The generator uses the amplitudes to simulate many decay distributions of the D^* , *e.g.*, it can be used to generate the correct angular distribution in $B \rightarrow D^*\ell\nu$, $D^* \rightarrow D\pi$ or in $B \rightarrow D^*D^*$, $D^* \rightarrow D\pi$, including all the correlations.

`EvtGen` introduces mixing by generating decays of the $\Upsilon(4S)$ to the proper mixture of $B^0\bar{B}^0$, $\bar{B}^0\bar{B}^0$, and B^0B^0 final states, with the correct distributions of Δt . CP asymmetries are generated in modules that modify the generated lifetime distributions of the two B s produced in the decay of the $\Upsilon(4S)$. Generic models are available for simulating two-body decays to a pair of scalar mesons, a scalar and a vector meson, a scalar and a tensor meson, or a pair of vector mesons. Besides these generic models there are special models for generating 3π and 4π final states. Currently, the generator assumes that the other B always provides a flavor tag.

The generator uses a main decay file (`DECAY.DEC`) which provides a fairly complete table for decays of particles below the $\Upsilon(4S)$. However, the generator handles only exclusive final states, *i.e.*, it does not perform any fragmentation. In order to provide a complete table of decays, it uses `Jetset 7.4` to produce the final states that are not enumerated as exclusive states. This is implemented in such a way that if `Jetset 7.4` produces a final state that is listed as an exclusive decay, it will be rejected and a new decay is generated by `Jetset 7.4`. This ensures that there is no double-counting. For the decays of B mesons, about 50% are accounted for by exclusive states,

while the other 50% are produced by `Jetset 7.4`. `Jetset 7.4` is also used to generate the $c\bar{c}$ states and weakly decaying baryons. The original `Jetset 7.4` decay table was modified in order to be in line with recent measurements.

4.1.2 Full Detector Simulation

The full detector simulation is structurally divided into two parts: event generation and particle tracking, followed by the detector response simulation. The full simulation is used for detailed detector performance, design optimization, and physics analysis studies. It complements the `Aslund` fast simulation described in the next section in that it provides much greater detail and realism in terms of detector geometry, particle interactions in the detector, decays, showers, magnetic field, detector response, *etc.*, at the expense of execution speed. The detailed simulation is described in greater detail below; the fast parametrized simulation is described in the following section. A simplified data flow model of the simulation is shown in Figure 4-1.

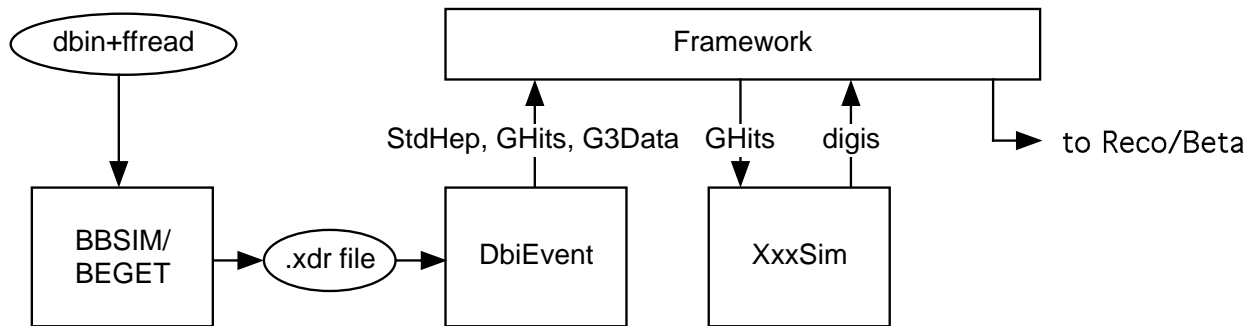


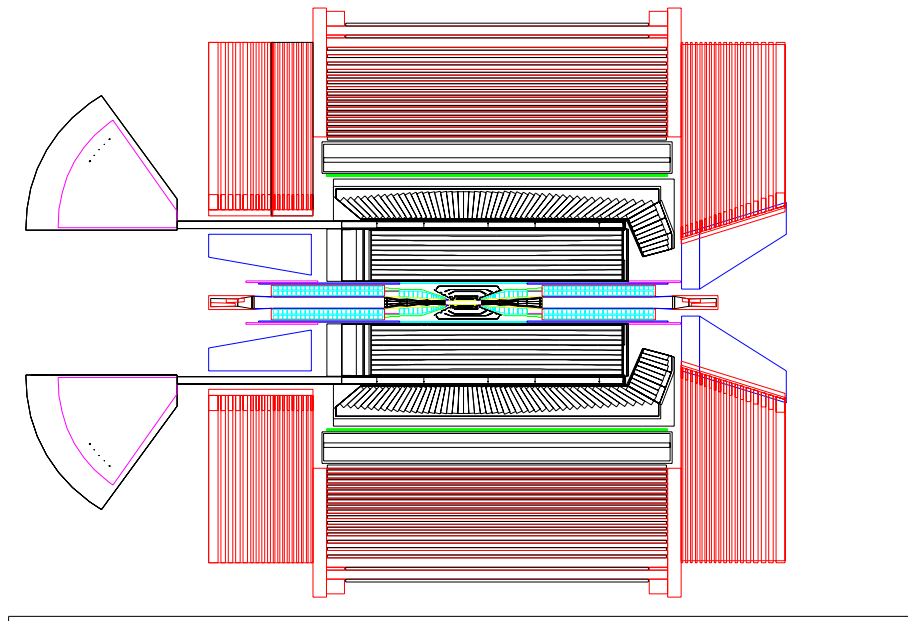
Figure 4-1. Simplified dataflow diagram for the full simulation.

`BBSim` is based on the CERN detector description and simulation tool, `Geant 321` [1]. `Geant 321` provides tools to construct the detector geometry; to step charged and neutral particles through the detector, simulating the full variety of interactions and decays that each particle species may undergo; to register Monte Carlo track hits (referred to as `GHits` in `BABAR` terminology); and to display the detector components, particle trajectories, and track hits.

`BBSim` is organized as a set of driver, framework, utility, and subsystem packages as shown in Table 4-1. Each subsystem-specific package consists of a standard set of routines which are called from the framework package at various stages of the simulation. In the initialization phase, the detailed subsystem geometries are built from parameters specified in an ASCII geometry database. The model includes the definition of materials, shapes, positions and orientations of the sensitive and insensitive subdetector components, and the tracking media quantities associated with the sensitive detectors. For the data simulations in this book, a constant magnetic field $B_z = +1.5\text{T}$ inside the coil was used. A cut-view of the assembled detector is shown in Figure 4-2.

Table 4-1. Packages in BBSim.

Subsystem	Package Name	Output
Driver package	gnbase	-
Infrastructure package	gnbbg	-
Utility package	gnutil	-
Beam Line, Beam Pipe, and Support Tube	gnbpip	-
Silicon Vertex Detector	gnssvd	SvtGHit
Drift Chamber	SvtSimGeom	DchGHit
DIRC	gndirc	DrcGTrkHits, DrcGHits
Electromagnetic Calorimeter	gnemca	EmcGHits
Coil and Instrumented Flux Return	gnmuon	IfrGHits

**Figure 4-2.** Side cut view of the BABAR detector as modeled in BBSim.

In the event loop phase, events are first generated by `Beget`, and the results stored. Long-lived particles (“primaries”) from the event generation step are stepped through the detector and allowed to interact or decay. In `BBsim`, hadronic interactions may be simulated using either `Gheisha` [5] (default), `Fluka` [6] or `GCalor` [7]. Secondaries resulting from interactions or decay are tracked as well. However, when recording the Geant3-level genealogy (`G3Data`), only the kinematics of primaries and secondaries resulting from decays are recorded. Particle `GHits` are scored in the active detector components. The `GHit` contains all the information needed to perform the subsequent detector response simulation. This usually includes a position, a direction, the time of flight from the production vertex, the energy lost, the Monte Carlo track number, and an identifier for the sensitive detector, together with other subsystem-specific quantities.

At the end of the event, all of the subsystem `GHits` are written along with the generator- and Geant321-level Monte Carlo truth to an output file. The output file is then read into the `BABAR` Offline Framework and the subsystem digitization is performed using the `GHit` information as input.

To validate the geometry of the parameterized `Aslund` simulation against that of `BBsim`, material scans of the `BBsim` detector are periodically performed. Figure 4-3 compares the amount of material traversed as a function of polar angle from the interaction point, averaged over azimuth, in the `BBsim` material simulation (solid lines) and in `Aslund` (open circles). As can be seen, the amount of material is the same in both cases.

4.1.3 Fast Detector Simulation: `Aslund`

`Aslund` is a fast, parameterized Monte Carlo simulation of the `BABAR` detector. It is interfaced to the two generator packages, `Jetset 7.4` [3] and `EvtGen`, described in Section 4.1.1, via the `Beget` interface. The parametrization includes the tracking system, particle identification with the dE/dx and the `DIRC`, neutral clusters (only) in the electromagnetic calorimeter, and the inner flux return. These will be reviewed in the next sections.

4.1.3.1 The tracking system

The simulation of the tracking is performed with a package called `TrackErr` [8]. The program enables the description of any cylindrically symmetric tracking system and computes the fully correlated error matrix and the smeared track quantities. In the calculation of the parameters, the program takes into account the geometrical description of the silicon vertex detector and the drift chamber. The magnetic field is assumed to be uniform and parallel to the detector’s axis of symmetry. The program first searches for all the layers in the Drift Chamber intersected by the helical trajectory but, without taking into account the energy loss and multiple scattering along the

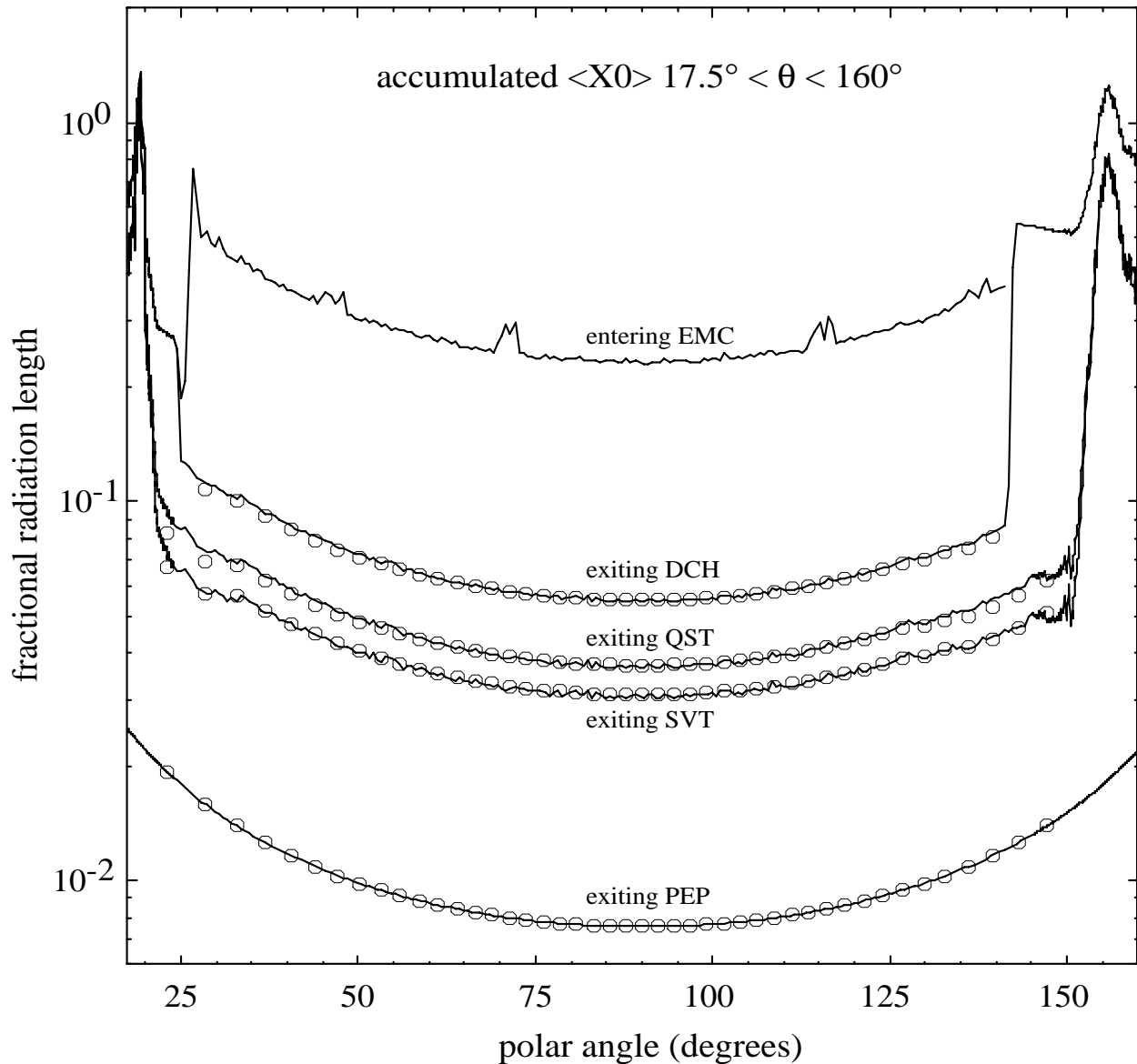


Figure 4-3. Material traversed in fractions of a radiation length as a function of angle with respect to the z-axis, averaged over azimuth, as estimated in `BBSim` (solid lines) and `Aslund` (open circles) after exiting: the beam pipe (PEP), the Silicon Vertex Tracker (SVT), the Quadrupole Support Tube (QST), the Drift chamber (DCH), and entering the Electromagnetic Calorimeter (EMC).

trajectory. This assumption is an important limitation of the program in the case of tracks with a significant amount of energy loss. Another limitation is the reconstruction efficiency, which is taken to be 100% when the track is in the fiducial volume of the tracking system (≥ 4 silicon vertex detector hits or drift chamber layers). The detection efficiency per layer is assumed to be 100%. Once all the hits have been found, the smeared track parameters, as well as the error matrix, are calculated at the origin. A comparison of the parametrization with the full simulation showed an agreement within 15% for the mass resolution in the decay $B^0 \rightarrow \pi^+ \pi^-$.

4.1.3.2 The DIRC parametrization

Once a track is calculated to hit a quartz bar, the DIRC simulation is activated. It needs as an input, the 4-vector of the track, the coordinate of the track impact in the quartz bar, and the error on the measurement of the azimuthal and dip angle of the track. Given these quantities, the simulation returns the number of Cherenkov photons detected by the photomultipliers and the error on this measurement. Also it computes the number of standard deviations for each of the five hypotheses (e^\pm , π^\pm , K^\pm , μ^\pm , p^\pm). The parametrization is still based on the TDR design, which is not up-to-date in some areas, (mirror replaced by the wedge). The wedge made of quartz should increase the number of photons, especially at small dip angles.

A comparison of the parametrization output with the full DIRC simulation, which takes into account all types of effects, has been made. The study showed that a polynomial correction was needed in the fast simulation. The first one provides a dip angle correction to the absorption. The second one is related to the number of Cherenkov photons as a function of the dip angle. Finally, the last one concerns the resolution as a function of the momentum. The performances of the fast simulation for the K - π separation with the DIRC TDR design has shown good agreement with the full simulation for tracks with momenta above 1 GeV/c. However, for tracks with momenta near the Cherenkov threshold, the results are less reliable.

4.1.3.3 The EMC parametrization

The EMC fast simulation is based on the results obtained from the full simulation of the detector `BBsim`. The momentum vector, the polar angle, and the azimuthal angle of the neutral particle interacting with the electromagnetic calorimeter are smeared according to the distributions [9] obtained from `BBsim`. These distributions are in eight bins in energy and $\cos \theta_{\text{lab}}$ which vary from 0.02 GeV to 5.12 GeV and -0.920 to 0.960 respectively. Therefore, the smearing is performed as a function of these two quantities. Also, a factor of efficiency detection is applied according to the corresponding bin in energy and $\cos \theta_{\text{lab}}$. As a result of this parametrization, the π^0 mass distribution shows a tail at low mass which reflects the amount of material in front of the EMC.

The simulation of this system also includes the photon background coming from PEP-II. The distribution of the number of background photons has a mean of 1.6 and a width of 3.1. The energy spectrum has an exponential shape and the θ distribution is peaked in the forward region of the detector.

The two main limitations of the EMC parametrization are that:

- It does not treat the showers caused by charged tracks. It cannot therefore be used to simulate electron identification or to simulate the difficulties of total energy reconstruction.
- It does not simulate overlapping showers, for example, those coming from high-energy π^0 s.

4.1.3.4 The IFR parametrization

ASLUND simulates both charged and neutral particles in the IFR. In the case of charged particles, it treats muons and pions. These are expected to be reconstructed by the detector within the fiducial acceptance $0.350 < \theta < 2.75$ and for energies above ~ 400 MeV. The muon reconstruction efficiency and the pion contamination is based on the algorithm described in Reference [10]. The dependence of the reconstruction efficiency on track energy and polar angle is not included.

For the neutral hadrons, namely the K_L^0 , n , and \bar{n} , the detection efficiency in the IFR fast simulation is a function of the momentum, the polar angle, and azimuthal angle. First, the simulation checks if the hadron interacts with the EMC and extracts the energy deposited. Then, the hadron's angles are smeared according to results obtained with BBsim.

4.2 Reconstruction

The BABAR reconstruction software [11] is organized as a set of *Modules*, which process sequentially the data in an *Event*. The order of execution of these is controlled by a *Framework*, which provides command line facilities for controlling execution and access to the Tcl/Tk scripting language. The reconstruction package used for most of the studies in this book contained approximately 65 such modules, arranged in *Sequences* to do subdetector-specific processing (hit finding, *etc.*), followed by pattern recognition, fitting, and subdetector-specific particle identification.

The results of these computations will eventually be saved in an event store currently being constructed. As this was not available at the time of the current studies, temporary support for BABAR Event Analysis Summary Tapes (Beast tapes) was developed. This allowed certain of the high-level reconstruction results to be stored after computation and read back into simple analysis software. Only limited information could be made available in this way at the time these analyses were performed, so that the results obtained cannot be considered optimised.

The output of reconstruction is accessed through an analysis toolkit called `Beta` [12]. `Beta` provides code enabling the analyst to treat charged tracks and clusters as four-vectors, bypassing many of the details of the reconstruction results. It also provides access to vertexing, particle identification, Monte-Carlo simulation truth information, and reconstruction of sequential decay chains. `Beta` can be used with either the output of the fast simulation, `Aslund`, the summary tapes (`Beast`), or the full reconstruction, so that the same analysis program can generally be used for each kind of input. `Beta` also serves as a “point of access” to the underlying reconstruction information, so that the analysis program can select events of interest using simple four-vector-based cuts before invoking more powerful, but slower, detailed reconstruction.

The complete code base for this system is available to the collaboration from a central CVS repository. This is used by a set of release tools (`SoftRelTools`) to create periodically “releases” of the software, which have been compiled, linked, and tested. These are then used to create the various analysis programs. During the period leading up to the completion of the analyses for this book, four major releases were created, each with an enhanced set of features.

4.2.1 Tracking

For the studies in this report which used full simulation, it was necessary to pass the output of the detector simulation through a preliminary version of the full `BABAR` reconstruction program. In these studies, all track-finding and fitting was done using only simulated data; *i.e.*, no Monte Carlo truth was employed in reconstructing tracks.

4.2.1.1 Pattern recognition

Tracks are found independently in the two tracking devices, the silicon vertex detector and the drift chamber; different algorithms are used in each. The silicon vertex detector algorithm first combines $r - \phi$ and z hits in the same silicon wafer to form space points, and then does an exhaustive search for good helical tracks, requiring hits in at least four out of the five layers of silicon.

Two drift chamber algorithms are run in sequence. The first drift chamber algorithm finds straight-line track segments in all ten superlayers. It then combines segments to form first a circular track (using axial segments only, and with a strong bias toward tracks coming from the interaction point), and then a helical track (by adding stereo segments to the axial track).

The second drift chamber track-finding algorithm uses circular superlayer segments in three adjacent superlayers (all eight possibilities are tried) to form a trial helix. If the helix is of sufficient quality, it is projected forward and backward, and other segments are added. This algorithm is designed to find tracks not coming from the primary vertex (such as K_s^0 and other decays), tracks

which only pass through a small number of superlayers (large dip angle tracks), and low p_T tracks (loopers).

Another piece of code merges the separately-found drift chamber and silicon vertex detector tracks; it projects each silicon vertex detector and drift chamber track to the support tube and looks for good matches. Those that match are combined into a single track, which is placed in the output list of good tracks; any silicon vertex detector or drift chamber tracks that fail to be merged are copied and placed in the output list as well.

4.2.1.2 Fitting

After pattern recognition, all tracks are initially fitted with a simple helix fitter, which ignores interactions with materials. After merging of drift chamber and silicon vertex detector tracks, the merged tracks are assigned track parameters based on a weighted average of the two input tracks. All tracks in the output list (merged or not) are then refitted with a Kalman filter fitter, using as a mass hypothesis the mass of the pion. (Access to multiple fits for different mass hypotheses was not available at the time of these studies, although support for this is under development.) The effects of multiple scattering and energy loss in the detector are included in the fit; the detector description used in the calculation of material effects includes a fairly detailed model of the vertex detector, including support structure, models of the beampipe and support tube, and a simple model of the drift chamber (treating the gas as a set of concentric cylinders). All physics analyses using full simulation, presented in this book, were done using the Kalman filter's best estimate of the track at the interaction point; this should give the best estimate of the particle momentum, except in the case of K_s^0 s decaying outside the beampipe. In the latter case, the K_s^0 finders used do correct for the curvature along a track from the interaction point to the decay vertex, as will be seen later.

4.2.1.3 Limitations

There are a number of pieces missing from the tracking code described here. Looping tracks and decays in flight are often found as two pieces, and no attempt has yet been made to join them. Drift chamber hits from tracks which do not have enough p_T to be found in the drift chamber are not associated with found silicon vertex detector tracks; no attempt is made yet at joint silicon vertex detector/drift chamber pattern recognition. These defects (all of which will be remedied before BABAR data become available) mean that current results are a pessimistic estimate of the quality of tracking in BABAR.

On the other hand, a number of effects that will degrade tracking performance have not yet been modeled. These include some detector inefficiencies and defects, misalignments, mixing of background and signal events, and electronic noise (drift chamber). Consequently, the track-

finding efficiencies found in the various analyses should be treated as rough estimates of the efficiencies that will be obtained with real data.

4.2.1.4 Performance

Figures 4-4 (a)–(d) illustrate the performance of the BABAR tracking measured using full simulation, in the same version of the code as used for the physics analyses in this book. Figure 4-4 (a) shows $\delta p/p$ as a function of p at $p = p_T = 90^\circ$ in the lab. frame, while Fig. 4-4 (b) shows $\delta p_T/p_T$ as a function of $\cos \theta$ in the lab. frame. Both these distributions compare very favorably with those in the TDR [13]. Figures 4-4 (c) and (d) show the resolution obtained on the r - ϕ and z_0 impact parameters respectively as a function of momentum.

4.2.2 Reconstruction in the Electromagnetic Calorimeter

The main task of the calorimeter is to measure the energies and positions of neutral and charged clusters (primarily photons and electrons, but also, *e.g.*, K_L^0 s) with the best possible resolution and efficiency over the full energy range and solid angle. In addition, the calorimeter contributes to particle identification which utilizes information on the cluster's total energy and its lateral distribution. The results are then used to

- Reconstruct single photons in, *e.g.*, radiative decays;
- Reconstruct π^0 s (even at high energy, when the photon showers overlap);
- Aid in electron, muon, and charged and neutral hadron identification (via cluster energy and transverse shower shape);
- Aid in K_L^0 reconstruction (position measurement); and
- Aid in neutrino reconstruction (via missing energy).

4.2.2.1 Clusters and bumps in the EMC

The reconstruction of clusters starts from a list of crystals with energy above some threshold, nominally 0.5 MeV. (This is the lowest threshold commensurate with the expected level of electronics noise; beam background may require this to be raised significantly.) The energy in a crystal is calculated by applying electronics and physics-process-derived calibration constants to pedestal-subtracted ADC counts.

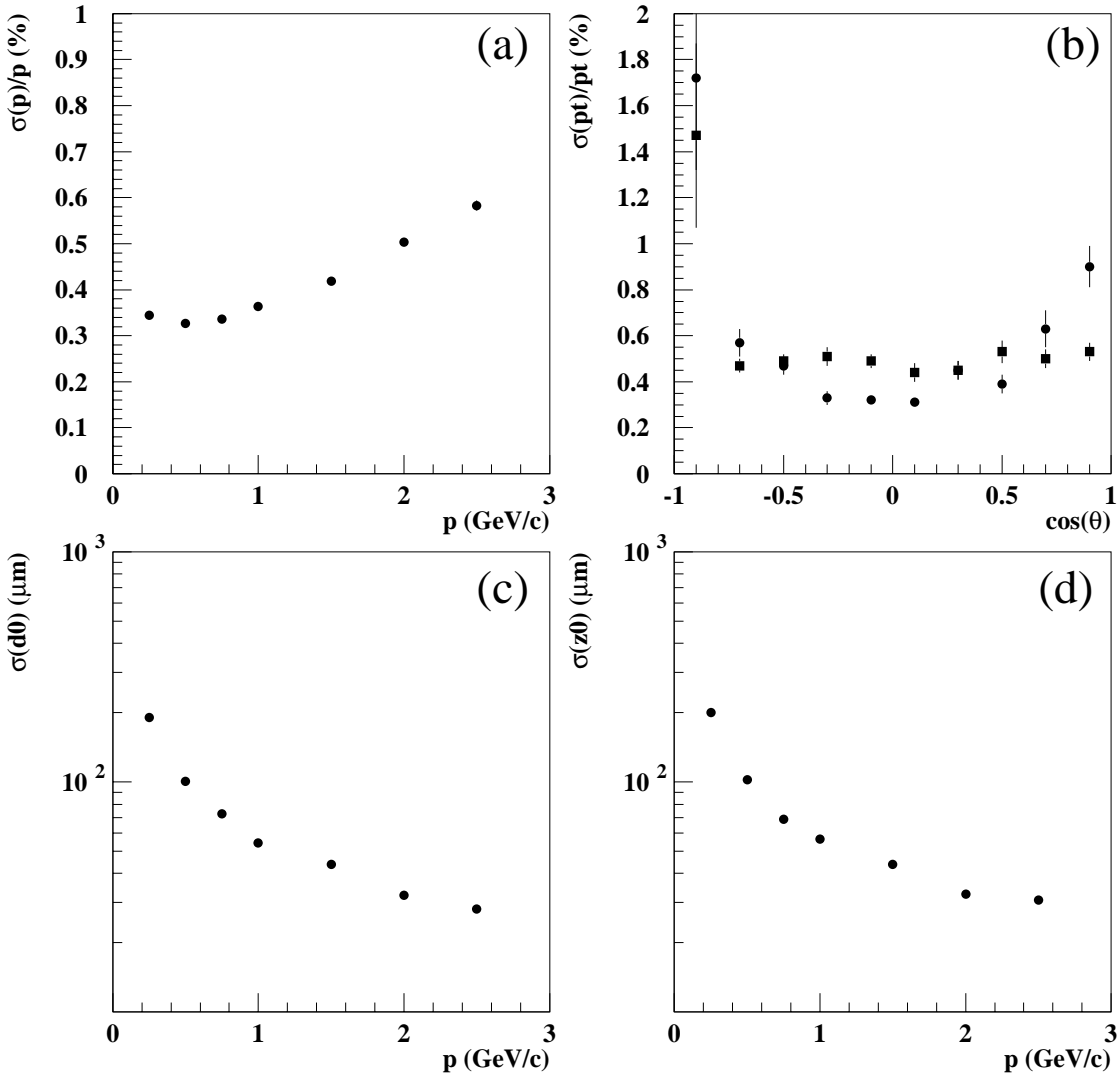


Figure 4-4. Performance of the BABAR tracking measured using full simulation: (a) $\delta p/p$ as a function of p for pion tracks at 90° in the lab. (b) $\delta p_T/p_T$ as a function of $\cos \theta$ in the lab. Circles are for $0.3 < p < 0.7$ GeV/c and Squares are for $1.8 < p < 2.2$ GeV/c. (c) Impact parameter in r - ϕ plane as a function of momentum. (d) Impact parameter in r - z projection as a function of momentum.

A cluster is a set of adjacent crystals, with the sum of their energies above some threshold, nominally 20 MeV. (This threshold is driven by event-related fake clusters, but, again, beam background may require it to be raised significantly.) “Adjacent” here means: neighboring crystals that touch on a side or a corner. A cluster is the energy deposit caused by one or more particles interacting in the calorimeter.

An attempt is made to split clusters into bumps. A bump is created from a local maximum within the cluster, such that it represents the fraction of the cluster energy deposit caused by a single-particle interaction. Thus, clusters and bumps are identical in the case that there is one and only one local maximum; otherwise, a cluster contains more than one bump. In identifying bumps, care has to be taken to discount so-called splitoffs — shower fluctuations that manifest themselves as additional local maxima in a cluster. This can only be done reliably for clusters caused by electromagnetic interactions: using the readily predictable shower shape, spurious local maxima can be eliminated.

Neutral, electromagnetic multi-bump clusters can be caused by random overlap of multiple photons or by the overlapping photon showers from the decay of a high-energy π^0 . (For example, a two-bump cluster with 500 MeV energy is most likely caused by random overlap, whereas one with 3 GeV is a merged- π^0 candidate.) For genuine multi-bump clusters, the bump parameters can be unfolded by assigning the proper fractions of energy in shared crystals, using the expected exponential lateral shower profile. It should be noted, though, that merged- π^0 s, once identified as such, are better reconstructed from the cluster parameters rather than from the bump parameters of the individual photons.

Charged clusters created by electrons can be treated reliably in much the same way as photon/ π^0 clusters. Care should, and can, be taken to deal with potentially overlapping showers from bremsstrahlung and to take into account the bending effect of the magnetic field. Clusters caused by ionizing-only particles, most notably muons, are straight-forward to handle: they are usually single-bump clusters made of a rather small number of crystals, depending on the particle’s path through the crystals — which can be reliably predicted by swimming tracks from the tracking detectors. As for clusters caused by particles interacting hadronically, charged or neutral, there is no reliable way to suppress spurious bumps, since hadronic showers are highly irregular and suffer from large fluctuations.

In the software, clusters and bumps are represented by classes known as `EmcCluster` and `EmcBump` (which “inherits” from `EmcCluster`). These classes provide a number of basic services, most notably: the energy function which reports the sum of the energies recorded in all crystals that are part of the cluster (bump), and functions which return the θ and ϕ coordinates of the cluster centroid. The cluster centroid is calculated from the energy-weighted front-center angles of all crystals participating in the cluster. Several other functions are provided, which include characterization of the transverse cluster shape for particle identification purposes.

All bumps and neutral clusters are then made into “candidates” (class name `EmcCand`) to be used for physics analysis. In the process, their energy and position get calibrated assuming a certain particle hypothesis. The default (and only) particle type considered at the moment is that of the photon. For the energy, calibration entails applying an energy- and polar-angle-dependent correction, which corrects for losses due to leakage and inactive material, and nonuniform light collection. Position calibration applies an S-shaped correction to the measured cluster centroid, in order to remove a bias inherent in the center-of-gravity method (due to the finite granularity of the calorimeter).

4.2.2.2 Matching tracks to calorimeter clusters

In order to identify charged and neutral particles, it is necessary to discriminate between calorimeter clusters deposited by each of these types of particle. This is done by attempting to “match” geometrically clusters to nearby reconstructed charged tracks found in the tracking detectors, as candidate charged-particle clusters.

The matching is done by finding track-cluster separations in the r - ϕ and z coordinates, near the point of entry of the tracks to the calorimeter. The calorimeter barrel is modeled as a cylinder, with its axis along the z axis, while the end-cap is represented as a truncated cone of the appropriate angle, coaxial with the z axis. The intersection of a track is found with the appropriate surface and the reconstructed centroid position of a cluster is projected onto the front face of the calorimeter by assuming that the cluster direction lies along the radial direction from the interaction point. The separations in r - ϕ and z between a track and cluster are then simply calculated as the difference of these two projected intersection points. The curvature of a charged track means that its entry-direction into the calorimeter is not in the radial direction and the corresponding cluster centroid is in general displaced accordingly in the ϕ projection. Hence, the mean separation in r - ϕ is non-zero and has a sign which depends on the particle’s charge. The mean “shift” increases with decreasing particle momentum as the curvature increases.

The shapes of the distributions of the track-cluster shifts in the two projections were calibrated using the `BBsim` Monte Carlo simulation of the BABAR detector. It is found that the distributions of the separations for a given momentum differ between electrons, muons, and pions, the pion distributions being the widest. Furthermore, pions are the most populous particles in BABAR. Therefore the separation distributions for pions are used as a measure of the goodness of geometrical matching between tracks and clusters, in order to determine whether a given track-cluster pair is consistent as being deposited by the same charged particle.

By considering single-pion Monte Carlo events, and using only the highest energy cluster if there is more than one, the matching method was found to be approximately 95% efficient for the barrel and 90% efficient for the end-cap, for track-cluster pairs with a matching confidence level greater than 0.1%. This inefficiency is due mainly to non-Gaussian fluctuations in the distribution of

the pion separations and is much smaller for electron tracks, which have smaller deviations than pions. Further work is underway to improve the matching efficiency. For production, a matching confidence level of 10^{-6} was used as the default, in order to keep the matching efficiency high.

4.3 Charged Particle Identification

The identification of charged particles — both hadrons and leptons — is relevant for the reconstruction of many beauty and charm decay channels and plays an essential role in the determination of the B flavor.

All BABAR detectors contribute in a complementary way to charged particle identification: the silicon vertex detector and the drift chamber provide dE/dx measurements; the DIRC is a Cherenkov ring-imaging device; the electromagnetic calorimeter discriminates electrons, muons, and hadrons according to their energy deposit and their shower shape; and the IFR characterizes muons and hadrons according to their different transverse and longitudinal interaction pattern in the segmented iron.

The software for particle identification is structured in two stages: first, the information from each detector is analyzed independently to provide a response — in terms of a likelihood and a confidence level — for each charged particle hypothesis (e, μ, π, K, p), without performing any selection; then algorithms combining the information from the various detectors are applied to perform particle selections.

Due to the wide momentum spectrum covered and the variety of requirements imposed by the different characteristics of many physics channels, flexible selection tools have been developed, allowing the optimization of the efficiency and purity of the selection according to the physical context of the application.

The cases of ambiguous identification of a particle in terms of more than one acceptable hypothesis are handled differently according to the context of the application: for instance, while only an unambiguous particle hypothesis is acceptable as an input to the tagging algorithm, many of the exclusive channel reconstruction algorithms accepted multiple identification hypotheses for the same reconstructed track, the identification of a particle among the various hypotheses being subject also to compatibility with the decay kinematics. Analyses are structured, however, in such a way that the same identified track cannot be used more than once in any given final state reconstructed.

The performances of the particle identification tools reported in the following sections were based on simulated events and are dependent on the model of hadronic simulation — the Geant 3.21 package Gheisha [5] — adopted in the event production for this book.

4.3.1 Charged Hadron Identification

There are two main purposes of the charged hadron identification in BABAR: the B -flavor tagging which relies on the correlation between the charge of a kaon and the flavor of the decaying B^0 from which it originated, and the identification of exclusive final states, such as $B^0 \rightarrow \pi^+\pi^-$. Since the relative abundances of pions, kaons, and protons in B decays are approximately 7:1:0.2, the B -flavor tagging requires good kaon identification with minimal pion contamination. The average π (K) momentum ranges between about 0.3 (0.45) GeV/ c in the backward direction to about 0.75 (1.1) GeV/ c in the forward direction. Therefore in the generic case, good K/π separation is especially important at low momentum.

The reconstruction of CP -violating modes, such as $B^0 \rightarrow \pi^+\pi^-$ and $B^0 \rightarrow \rho\pi$, and the measurement of V_{ub} in charmless decays require high pion identification efficiency with minimal kaon contamination, particularly in the high momentum region (3 – 4.5 GeV/ c). Hadron identification is also useful to reduce the continuum background, since the sample of background tracks hard enough to mimic a $\pi\pi$ event is enriched in kaons and protons.

High kaon efficiency (but not necessarily strong pion rejection) is needed for reconstruction of D and D^* decays. Efficient K/π separation is also required for τ physics, particularly in the study of $K\pi\pi$ and $KK\pi$ systems.

For all the above reasons, good K/π separation must be achieved over a broad momentum range (up to about 4.5 GeV/ c). Particularly difficult is the separation at high momenta where the difference in velocity at a given momentum (and hence Cherenkov angle and dE/dx) between pion and kaon becomes rather small.

Particle identification information for charged hadrons is available from three detectors: the DIRC, the silicon vertex detector, and the drift chamber. The latter two provide the measurement of the ionization dE/dx and are effective at the low momenta (below 700 MeV/ c for K/π discrimination) where the DIRC performance degrades. On the other hand, about half of the tagging kaons and most of the kaons from the exclusive B decays are hard and are identified exclusively by the DIRC. Thus, to achieve effective identification over the full momentum range, one needs to combine information from all available subsystems.

4.3.1.1 The DIRC

For each charged track which intersects it, the DIRC reconstruction provides an estimate of the corresponding Cherenkov angle and its error. In addition, the corresponding confidence level for each mass hypothesis (e , μ , π , K , and p) is calculated. A charged track is identified by the hypothesis with the highest confidence level. In the following, efficiency is defined as the fraction of particles identified correctly within the acceptance of a detector. For a generic $B\bar{B}$

event sample, the kaon efficiency for the DIRC is on the order of 85%, above the kaon threshold (93% for momenta greater than 700 MeV/c), while the fraction of pions misidentified as kaons is less than 2.5% up to about 3 GeV/c.

Below the Cherenkov threshold, the DIRC can also be used in the *veto* mode. In this region the kaon efficiency drops to about 50% with the fraction of pions misidentified as kaons being about 7%. Efficiency and purity in the veto mode strongly depend on the level and nature of the machine-induced backgrounds.

Most of the pions from $B^0 \rightarrow \pi^+\pi^-$ fall in the barrel region. For events where both pions are in the tracking acceptance, the fraction of pions which miss the DIRC is about 11%: 4% due to cracks between the quartz bars and about 7% in the forward region. Studies on the continuum events show excellent results, with kaon efficiencies of order 97% and contamination lower than 3%, except for kaons in the very upper tail of the momentum spectrum (above 4 GeV/c) where the efficiency drops to 90%.

4.3.1.2 dE/dx measurements

In the version of the simulation used at the time of writing, measurements of the ionization dE/dx are available from both the silicon vertex detector and the drift chamber. These provide information on the velocity of a charged particle, and therefore can be used for identification purposes at low momenta. For both detectors, a truncated average dE/dx is calculated for every track, and a likelihood and significance level for a given mass hypothesis are obtained.

In the case of the silicon vertex detector, the best K/π separation is achieved by selecting the mass hypothesis with the highest confidence level greater than a certain cut (typically, 0.05 for the silicon vertex detector). The average kaon efficiency in the silicon vertex detector is 85% below 700 MeV/c, and the fraction of pions misidentified as kaons is $\approx 1\%$. The analogous quantities for the drift chamber are 53% and 2% respectively. The optimal performance is presently achieved by using dE/dx information from the silicon vertex detector, and using the drift chamber identification only when the silicon vertex detector information is not available. The average kaon efficiency in this case is 82% below 700 MeV/c, and the fraction of misidentified pions is 1%.

It remains to be demonstrated in practice that the silicon vertex detector can really provide dE/dx measurements with the discrimination power indicated in the present version of the simulation.

4.3.1.3 Performance of charged hadron identification at low momenta

Figure 4-5 shows the momentum dependence of the kaon efficiency and pion misidentification probability for the DIRC and dE/dx measurements together at low momenta.

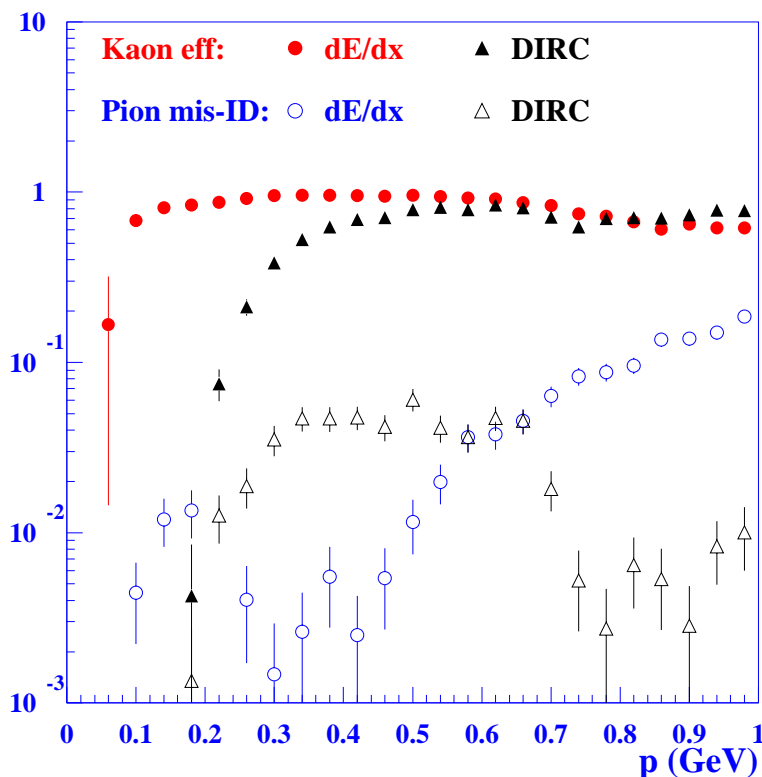


Figure 4-5. Kaon identification efficiency for the DIRC (solid triangles) and dE/dx in the silicon vertex detector and drift chamber (solid circles), and pion mis-identification probability for the DIRC (open triangles) and dE/dx (open circles).

4.3.1.4 Kaon identification

The signals provided by the different detectors are, to a good approximation, uncorrelated. This offers the prospect of relatively straightforward methods of combining the information from all sub-systems in a statistical fashion. The dE/dx information provides better K/π separation at low momenta, but this rejection power deteriorates quickly at high momenta. For this reason, kaons are identified using dE/dx below $p = 700$ MeV/c, and using the DIRC at higher momenta. The particle selectors offer two modes: loose and tight. Figure 4-6 shows the kaon efficiency and pion mis-identification probability in the *loose* mode, optimized to provide the best product of efficiency and dilution factor for kaons in generic B^0 decays. Averaged over the entire momentum range, the kaon efficiency is 78%, and the pion contamination is 4.5%.¹ A better pion rejection (at the expense of reduced kaon efficiency) can be achieved by applying simultaneous cuts on kaon significance level in all detectors (silicon vertex detector and drift chamber at low momenta, and in DIRC, silicon vertex detector, and drift chamber at high momenta). Kaon efficiency and pion

¹This number includes acceptance effects and kaon decays in flight.

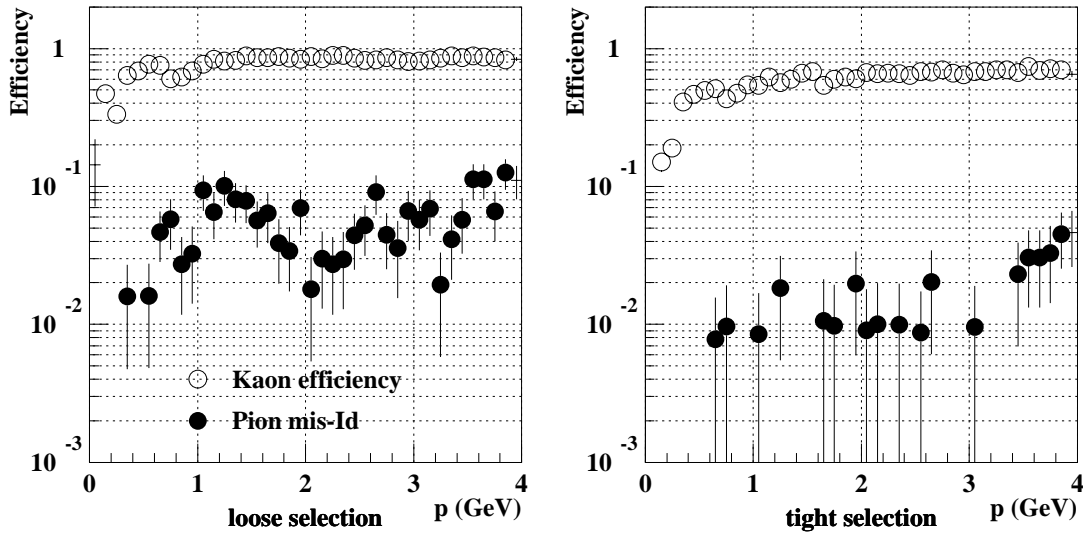


Figure 4-6. Kaon identification efficiency and pion mis-identification probability (per track) for the loose (left) and tight (right) modes. The data used were from a sample of generic B^0 decays.

rejection for this *tight* selection are shown in Fig. 4-6. An average kaon efficiency of 58% and an average pion contamination of 0.6% are achieved.

4.3.1.5 Proton identification

Most protons in the detector have small velocity, and even above the Cherenkov threshold, the cone opening angle is very small. At small dip angles, the effective threshold is increased because some fraction of the Cherenkov cone is trapped by total internal reflection and is as high as 2 GeV/c. In the DIRC, protons are therefore identified most of the time in the veto mode, above the kaon threshold, while below such threshold kaons and protons cannot be distinguished by the DIRC alone. On the other hand, dE/dx measurements provide good p/π separation up to 1.4 GeV/c, and p/K separation up to 1 GeV/c. The selection is similar to the kaon identification: dE/dx is used below 1.2 GeV/c, and the DIRC is used above 1.2 GeV/c. The proton efficiency and pion mis-identification probability for both *loose* and *tight* selections are shown in Fig. 4-7.

4.3.2 Electron Identification

The identification of leptons is of crucial importance for the tagging of B decays, as well as for the studies of semileptonic and leptonic charm and beauty decays; it also plays a role in the reconstruction of heavy quarkonia, such as in the process $B^0 \rightarrow J/\psi K_s^0$.

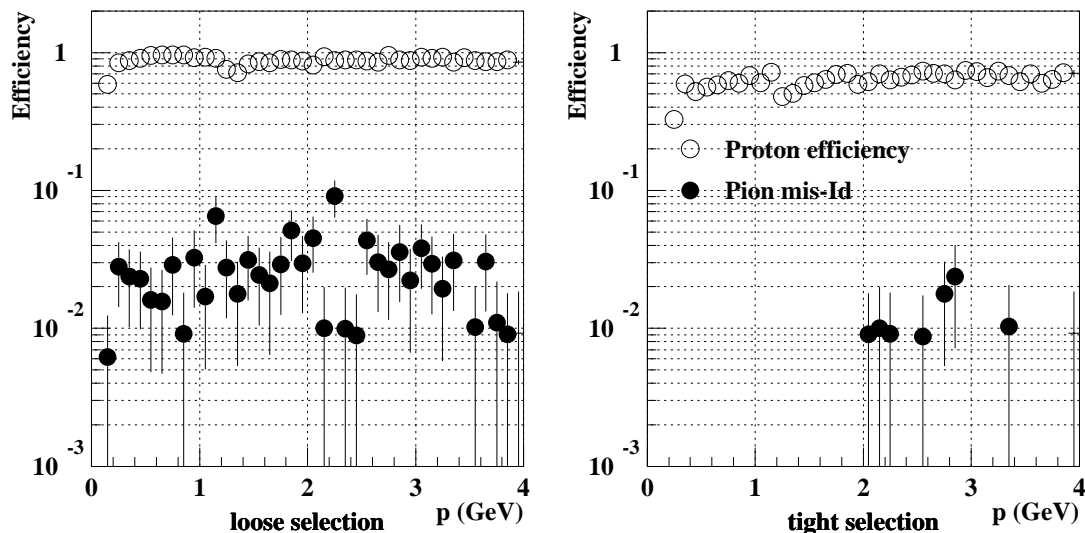


Figure 4-7. Proton identification efficiency and pion mis-identification probability (per track) for the loose (left) and tight (right) modes. The data used were from a sample of single particle events, generated isotropically, and flat in momentum.

Flexible tools for lepton identification are necessary to cope with the different physics requirements: leptons for flavor tagging represent a very challenging task, since both high purity and high efficiency are required over a wide momentum spectrum, while the identification of high-energy leptons from quarkonium decays is more straightforward.

The identification of electrons is done using information predominantly from the electromagnetic calorimeter, but also using information from the DIRC and dE/dx in the tracking devices at lower momenta. There are two main methods of discriminating between electrons and other particles in the calorimeter. The first uses the ratio E/p , the energy deposited by a particle in the calorimeter to its measured momentum in the tracking devices, which provides good discrimination above about 400 MeV/c. The second method uses the spatial distribution of energy deposited in the calorimeter, which is rather different between electrons, muons, and hadrons.

4.3.2.1 Electron identification using E/p

The ratio E/p , where E is the measured energy of a shower in the calorimeter and p is the measured momentum of the corresponding charged track, provides good discrimination between electrons and other charged particle species. When an electron enters the calorimeter, it produces an electromagnetic shower consisting of photons, electrons and positrons, which together deposit the energy of the original electron. In an ideal calorimeter therefore, electrons should have an E/p ratio close to unity. Muons on the other hand deposit energy only as a single ionizing particle. Charged hadrons sometimes pass through the calorimeter without interacting, appearing

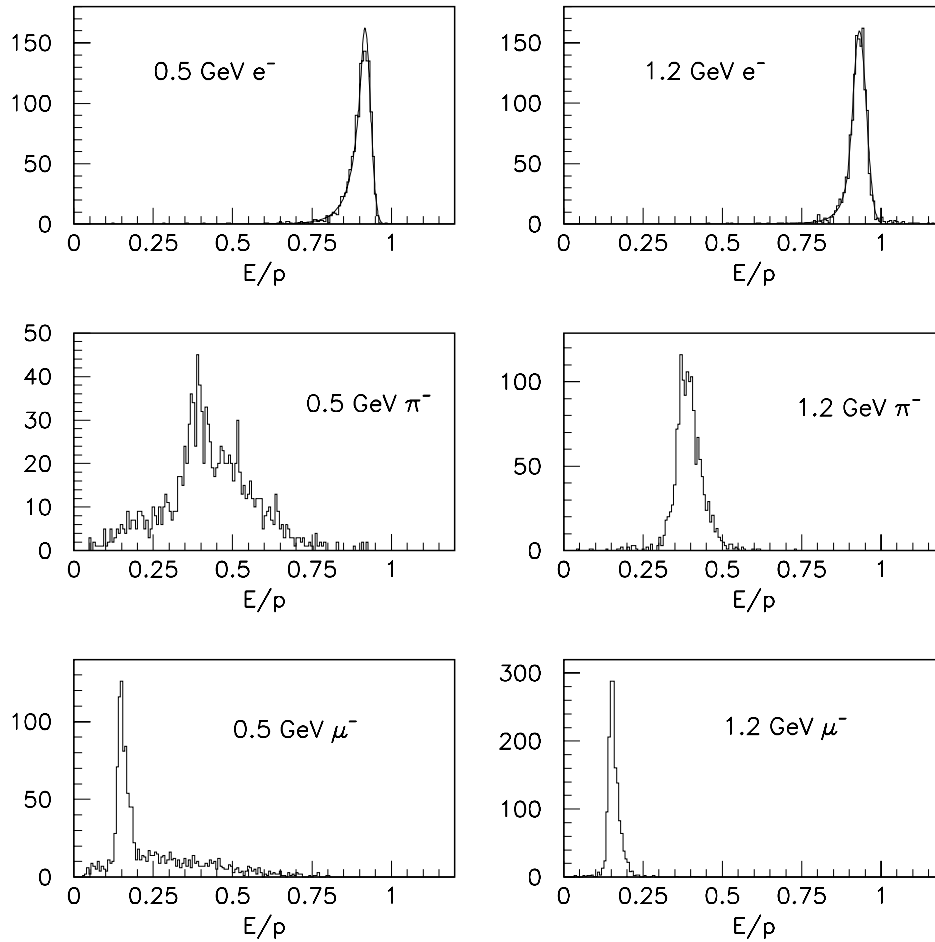


Figure 4-8. E/p ratios for electrons, pions, and muons with track-cluster matching significance levels $\geq 1\%$ for momenta 0.5 GeV/c and 1.2 GeV/c. The electron E/p distributions were fitted to a Gaussian with a power law tail on the low side.

like muons, and sometimes interact, leaving a larger fraction of their energy in the calorimeter, although rarely their full energy. Muons and charged hadrons therefore generally have values of E/p less than unity. E/p distributions for electrons, pions, and muons with track-cluster matching significance levels $\geq 1\%$ are shown in Figure 4-8. The electron distributions were fitted to a Gaussian with a power law tail on the low side.

In a real calorimeter, the value of E/p for electrons will be slightly different from unity, due to shower leakage and other resolution effects. For high-energy electrons, the E/p ratio can be greater than unity, owing to the effects of bremsstrahlung, in which the emitted photon(s) can be merged with the electron shower, whereas the measured momentum (after the bremsstrahlung) is reduced. These effects can be seen in the figures. Muons have only a single well-defined peak characteristic of the energy deposition of a single minimum-ionizing particle, while the pion distributions have

such peaks, supplemented by broad tails at higher E/p values, corresponding to those pions that have interactions and produce partially-contained showers. As can be seen, the separation in E/p between electrons and the other species of charged particle is not perfect, and there will be some contamination from pions and muons, especially for particles with momenta well below 1 GeV/c, in which there is significant overlap between the E/p distributions of the different species.

A candidate can be considered to be an electron if its E/p ratio is consistent with that expected for an electron. One way to check this is to calculate the significance level for the electron hypothesis, defined as the fraction of the area under the E/p curve (on a given side of the peak) with E/p values further from the peak than the measured value. Other methods might involve just cutting on the E/p value directly, or using the likelihood technique. The E/p distributions of electrons, pions, and muons were parameterized separately in bins of track momentum and direction, and this information was used to calculate the significance levels. By construction, significance level distributions should be flat, independent of track momentum and direction, as was found to be the case, except for track-cluster pairs with E/p values much larger than unity, owing to the effects of bremsstrahlung, as explained above. This leads to artificially low significance levels for tracks in this region.

A way to deal with the problem of low significance levels for high E/p values is to note that the backgrounds, pions and muons, have low E/p values, so that only those E/p values on the low side of the peak need to have a consistency check. Thus each significance level is supplemented by a flag, corresponding to whether it is on the low or high side of the E/p peak.

The electron identification efficiency for a given cut can be defined simply by the ratio $\eta = \frac{N_e}{N_0}$, where N_0 is the total number of matched track-cluster pairs, and N_e is the number of matched track-cluster pairs classified as electrons. This also gives the misidentification probabilities when applied to non-electron samples. Using samples of single-particle events, it was found that, for samples of track-cluster pairs matched at the 1% level, the electron identification efficiency was approximately 96% when cutting on an electron significance level value of 2% (only for E/p values on the low side of the E/p peak). This efficiency can be increased by reducing the E/p significance level cut value. However, this will also increase the pion and muon contamination. Figure 4-9 shows how the electron identification efficiency varies with pion misidentification probability. It was found that for a good electron identification efficiency ($\approx 96\%$) the pion/muon contamination is of the order of a few tenths of a percent ($\approx 0.2\%$).

4.3.2.2 Improving electron identification using lateral shower shape

As mentioned in the last section, hadrons sometimes interact with the calorimeter by ionization and excitation alone, and sometimes they interact hadronically, initiating a hadronic shower. In the latter case, they can deposit a large fraction of their energy in the calorimeter, which can make them difficult to distinguish from electrons when looking at E/p alone. The longitudinal and

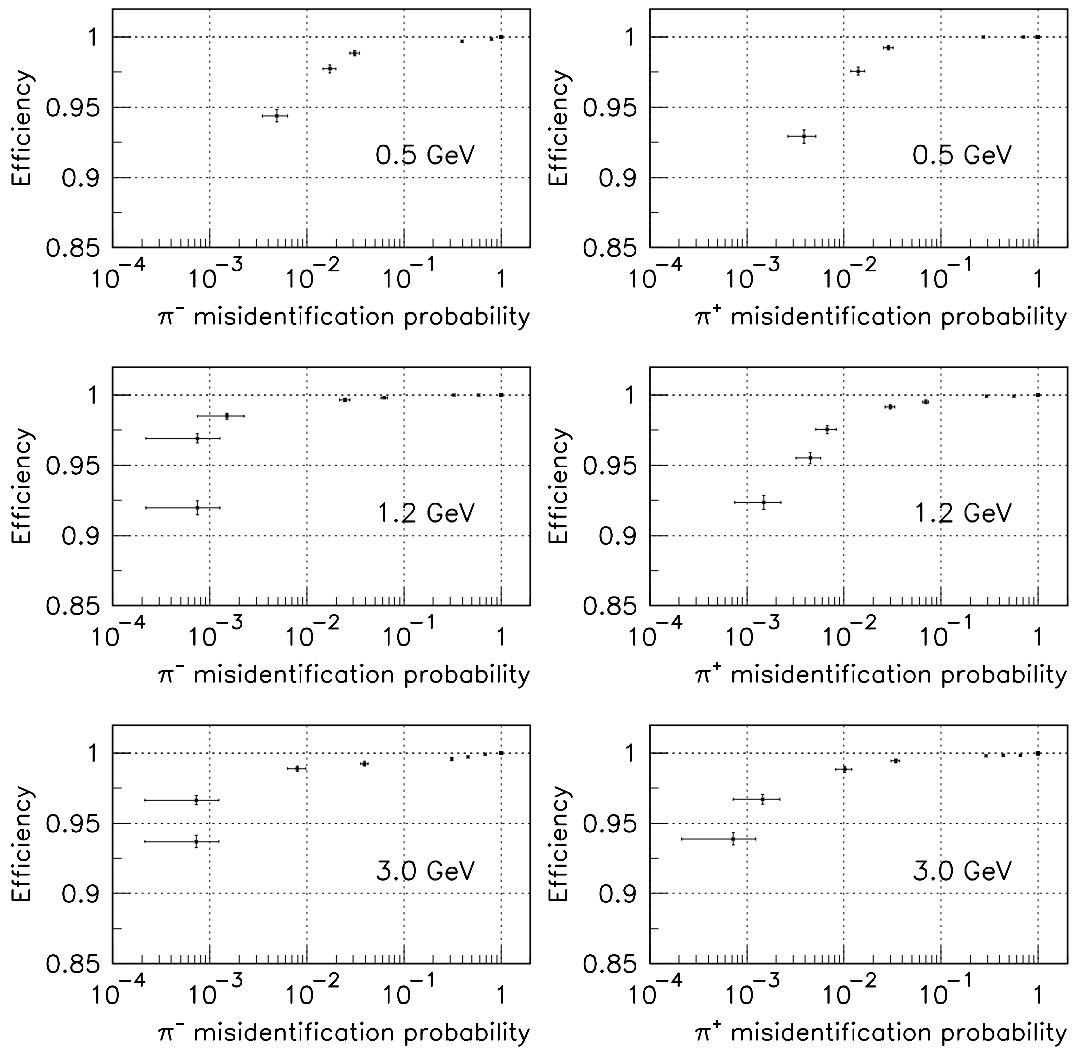


Figure 4-9. Electron (positron) identification efficiency vs pion mis-identification probability to be an electron (positron) for the momenta 0.5, 1.2, and 3.0 GeV/c.

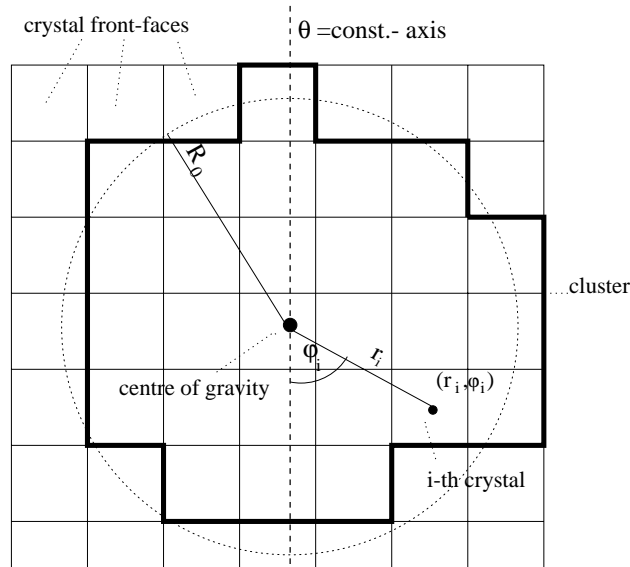


Figure 4-10. Definition of the variables r_i , φ_i and R_0 .

lateral energy distributions of hadronic showers differ significantly from those of electromagnetic showers, being characterized by the longer length scale of the nuclear interaction length, compared with the radiation length.

In order to describe the lateral energy distributions of showers, the following variables are defined: N , the number of crystals associated with the shower; E_i , the energy deposited in the i -th crystal, numbering them such that $E_1 > E_2 > \dots > E_N$; and r_i, φ_i , the polar coordinates in the plane perpendicular to the line pointing from the interaction point to the shower center (see Fig. 4-10). Using these variables, one can define [14] the variable

$$LAT = \frac{\sum_{i=3}^N E_i r_i^2}{\sum_{i=3}^N E_i r_i^2 + E_1 r_0^2 + E_2 r_0^2}, \quad (4.1)$$

where r_0 is the average distance between two crystals, which is approximately 5 cm for the BaBar calorimeter. This variable is constructed to discriminate between electromagnetic and hadronic showers based on their average properties. The summation in the numerator omits the two crystals containing the highest amounts of energy. Electrons deposit most of their energy in two or three crystals, so that the value of LAT is small for electromagnetic showers. Multiplying the energies by the squared distances enhances the effect for hadronic showers, compared with electronic.

Another approach [15] is to expand the lateral energy distribution into various moments which contain information about the azimuthal distribution (with respect to the particle's initial direction)

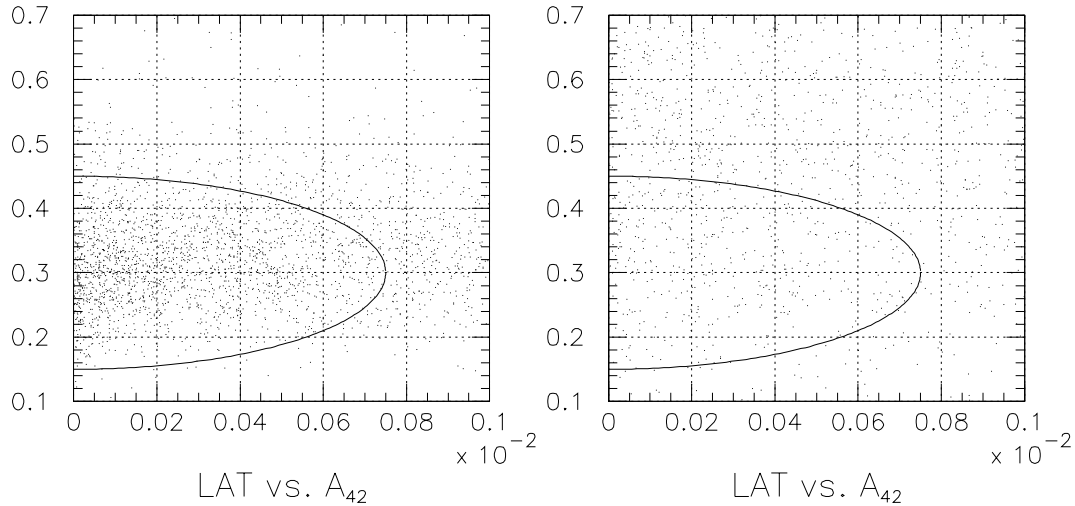


Figure 4-11. Distributions of LAT, and a φ -sensitive moment for electrons (left) and pions (right) at $p = 1 \text{ GeV}/c$ and $E > 0.4 \text{ MeV}$.

of the shower shape. For example, the value of the moment will be zero when the energy distribution is isotropic in φ and large if it is quite anisotropic. In general, since hadronic showers are far more irregular and less isotropic in φ than electromagnetic ones, the moment should be larger for pions than electrons.

In order to find an enhanced discriminating variable for the shower shape classification, a combination of variables is used, combining discrimination based on the way the energy is distributed with respect to the distance from the center, and on deviations from the rotationally invariant shape expected for an electromagnetic shower. Figure 4-11 illustrates this. LAT is small for electrons, and the distribution of the moment A_{42} is very narrow for electrons compared with pions, which occupy a larger volume in the LAT- A_{42} plane. By using a (preliminary) combination of these parameters and E/p , the pion-misidentification rate was found to be reduced in Monte Carlo events, as shown in Fig. 4-12.

In summary, this preliminary inclusion of shower shape information reduces the probability of misidentifying pions as electrons by factors of between 1.5 and 2 at momenta between 0.6 and 1 GeV/c. By using more sophisticated analysis methods like neural networks and including the track-cluster separations in r - ϕ , a further reduction of the pion contamination could be achieved.

4.3.3 Muon Identification

Muon identification and pion rejection are performed in the IFR with detailed information on the patterns of the interactions of muons and pions in the iron.

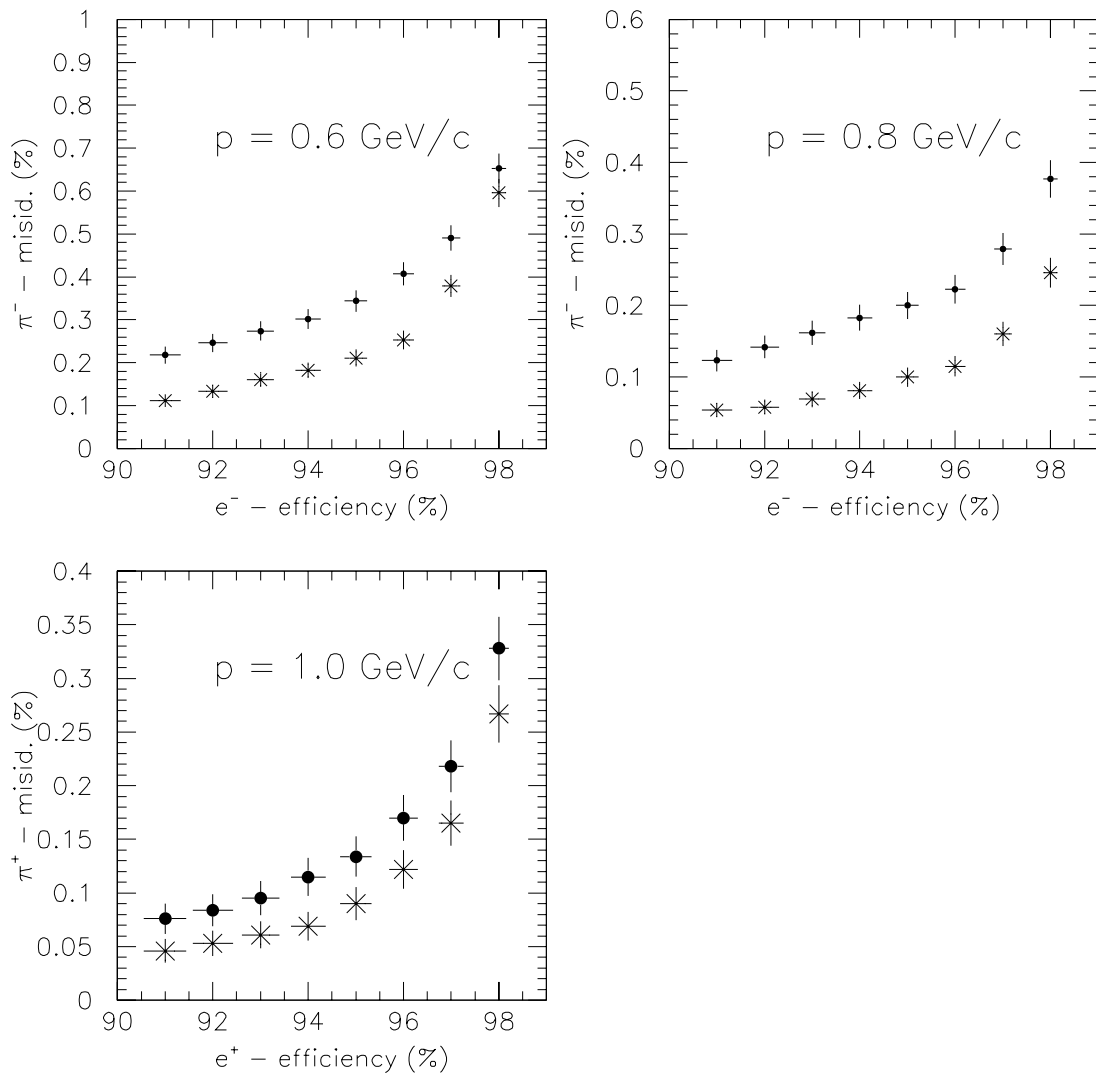


Figure 4-12. Efficiencies and misidentification probabilities using only E/p (\bullet) and additional shower shape information (\times).

4.3.3.1 Track finding in the IFR

The track finding in the IFR is not a critical aspect of muon identification since the average occupancy in this detector is rather low, and a tiny fraction of tracks overlap each other.

IFR tracks are first reconstructed in two-dimensional projections in each sector using a clustering algorithm based on a maximum hit-distance criterion. The two orthogonal views of each cluster are associated together checking for the compatibility of the 2D hit patterns. Finally, using the extrapolation into the IFR of the charged tracks measured by the tracking systems, clusters belonging to different sectors are merged into a composite cluster. Such clusters are considered as candidates for muons or charged hadrons and are subsequently processed by a discrimination algorithm.

4.3.3.2 μ/π discrimination in the IFR

The IFR muon identification works by discriminating between the two hypotheses that the detected track has been produced by a muon or a pion. Other hadron hypotheses (K^\pm , proton) have very similar patterns in the IFR to pions and are discriminated from the pion hypotheses by the other PID sub-systems in BABAR.

Several discriminating variables are considered in order to separate muons from pions. The quantities used in the current algorithm depend on the detailed pattern of the IFR clusters, namely, the penetration depth in the iron of the track, the transverse size of the cluster, which identifies the showering pions, and “missed” planes along the path, which may be caused by neutral particles coming from the pion hadronic shower. The inner (cylindrical) RPC layers are included in the algorithm.

Studies done outside the current reconstruction framework [10] show that variables based on the extrapolation of the drift chamber tracks to the IFR can give a significant improvement in muon identification. Such variables have not been considered yet in the current implementation.

In order to combine the rejection power of all the considered variables, a likelihood ratio criterion is applied. The probability distribution of each variable $x_i, i = 1, \dots, n$ is computed in 16 momentum bins from 0 to 4 GeV/ c and in different angular regions which correspond to the barrel, the forward and backward endcaps, and the overlapping regions in between.

Once an IFR cluster is defined, the likelihood ratio R is calculated as:

$$R = \log_{10}(P_\pi/P_\mu), \quad (4.2)$$

where the probabilities to be a muon or a pion P_μ and P_π respectively, are defined as:

$$P_{\mu/\pi} = \prod_{i=1}^n P_{\mu/\pi}(x_i). \quad (4.3)$$

The distribution of R is then normalized, in order to obtain a flat distribution for the right particle hypothesis. Such a normalized value defines the significance level for a given particle mass hypothesis. In order to identify muon candidates, a cut on the significance level for the pion hypothesis may be applied, *e.g.*,

$$C_{\pi} < 0.05. \quad (4.4)$$

The efficiencies obtained for muon identification as a function of momentum with this cut are shown in Fig. 4-13.

4.3.3.3 Combining the IFR with other detector information

The IFR muon identification capabilities decrease progressively at low momenta. Here, the information from other detectors can improve the muon/hadron discriminating power. In fact, at momenta smaller than ~ 400 MeV/ c , charged tracks do not even reach the IFR because of the effect of the magnetic field, and energy loss in the inner detector systems. The muon identification efficiency and corresponding pion mis-id probability for the IFR alone are shown in the top left plot of Fig. 4-14. An attempt has been made to improve muon identification capabilities below 400 MeV/ c in the form of a selection algorithm which makes use of detector systems other than the IFR at low momenta. For instance, the DIRC can be used to identify muons for charged tracks with $p > 250$ MeV/ c . The muon efficiency and pion mis-id probability for the DIRC are shown in the top right plot of Fig. 4-14.

The current muon selector can be set to one of three criteria depending on the desired efficiency and purity of the resulting sample. For instance, the “loose” criterion uses silicon vertex detector dE/dx for the momentum range 50 MeV/ $c < p < 130$ MeV/ c , the DIRC for 250 MeV/ $c < p < 850$ MeV/ c and the IFR for higher momenta. Often, information from two separate sub-detectors is combined such that a candidate particle must pass significance level cuts from two different measurements in order to be selected. Whether or not this is done is dependent on the momentum range in question and which criteria (and therefore algorithm) is being used. An example is the “tight” selection which uses the significance level from the energy deposited in the EMC in conjunction with the DIRC for the momentum range 350 MeV/ $c < p < 550$ MeV/ c and uses both the DIRC and the IFR to discriminate in the range 550 MeV/ $c < p < 850$ MeV/ c . The “verytight” selection algorithm uses the combinations described for the “tight” criterion, but uses both IFR and DIRC out to $p = 1.5$ GeV/ c to achieve a purer sample of muons. The outputs of the “loose” and “tight” selection algorithms are shown in the bottom two plots of Fig. 4-14.

4.3.4 Identification of Particles with Neural Networks

Traditional probability theory assumes an accuracy and precision of categorization of the world that may not be available in many important problems. Artificial neural networks estimate dis-

97/09/06 08.20

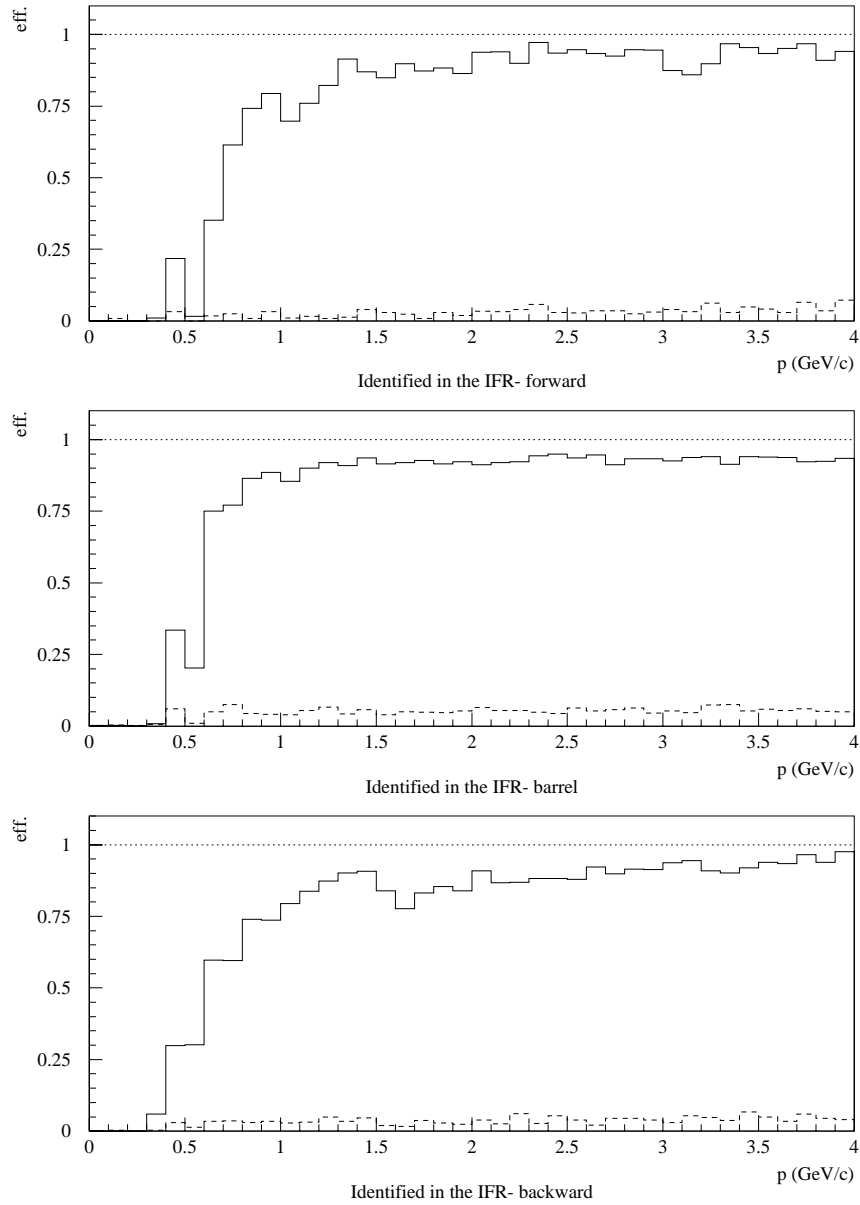


Figure 4-13. Muon efficiency for muons (solid line) and pions (dashed line) as a function of momentum for forward (top), barrel (middle), and backward (bottom). The sample used here has a flat distribution in θ and ϕ .

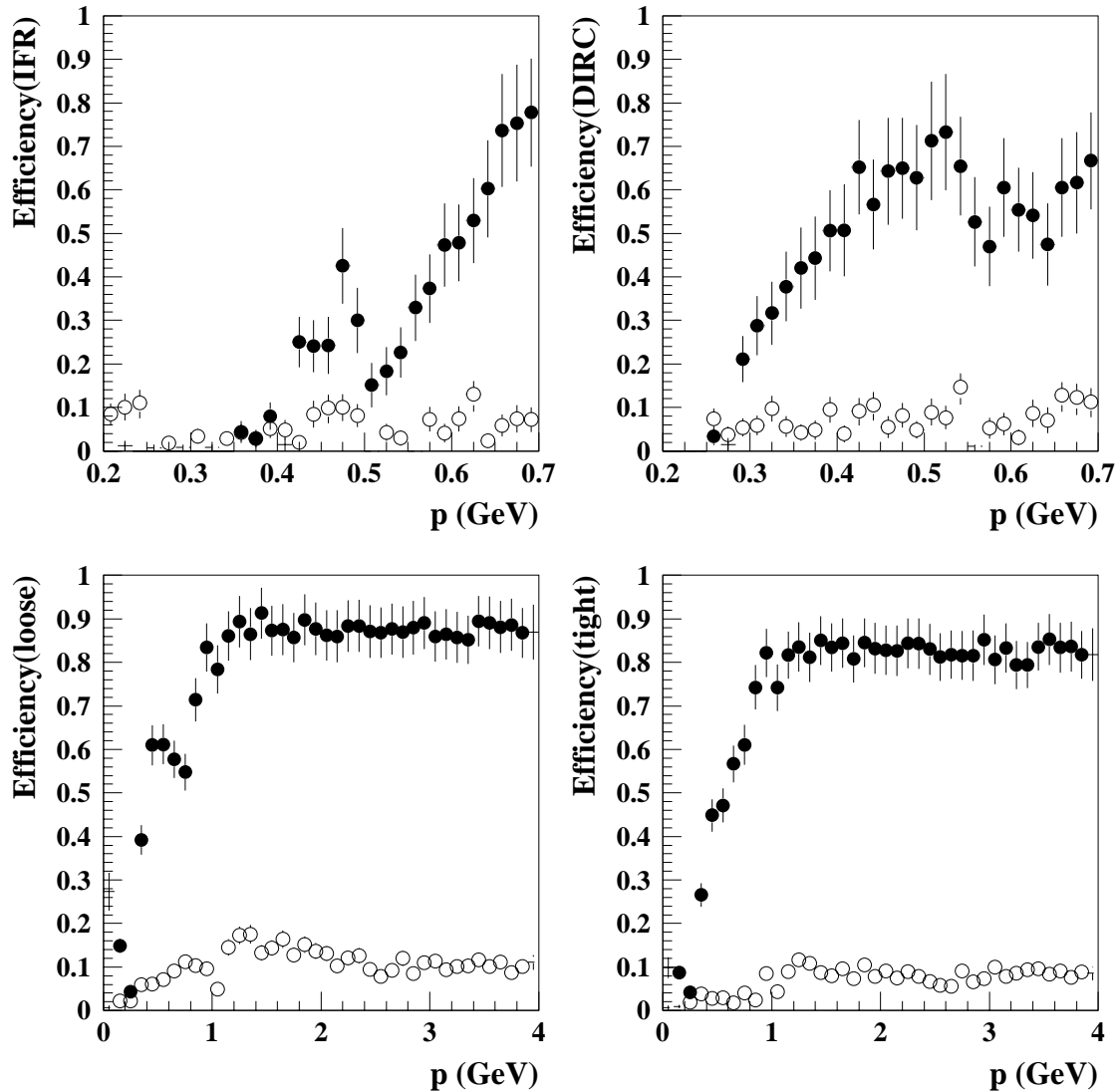


Figure 4-14. The top two plots show muon efficiency (filled circles) and pion mis-id probability (open circles) for the IFR (left) and the DIRC (right) in the momentum range $200 \text{ MeV}/c < p < 700 \text{ MeV}/c$. The lower two plots show the output of the muon selector in both “loose” (left) and “tight” (right) selection mode for $p < 4 \text{ GeV}/c$ (where the symbols have the same meaning as before).

crimination functions from sample data, as do conventional statistical methods. However, for each individual problem, statistical approaches require that it is known (or at least can be modeled) how outputs depend functionally on inputs. Neural networks on the other hand do not require such a model. Since neural networks do not implement a specific mathematical model, the same architecture and dynamics can be applied to a wide variety of problems.

Neural networks consist of many simple computing elements — generally simple nonlinear summing joints (called neurons) — linked together by connections of varying strength. This weight matrix stores pattern or function information with distributed encoding. There are many neural network architectures. The multilayer perceptron groups a fixed number of neurons in layers: input layer–hidden layers–output layer. The network has to be optimized in an iterative process fitting the problem at hand. A more elegant approach is the self-organizing growing network where each neuron has the same basic functionality, and network topology evolves during training in a dynamical growth process.

Neural networks ultimately learn to adapt to a priori unknown probability density functions, even in the presence of strong correlations in the data. Here, supervised learning uses class-membership information, known for instance exactly from Monte Carlo-generated training samples. Unsupervised learning on the other hand uses unlabeled samples, *i.e.*, experimental data. Neither supervised nor unsupervised learning systems assume knowledge or a specific behavior of the underlying probability density function.

In BaBar neural network tools are available in the field of particle identification (NNSelectors) and event tagging (Cornelius). Up to now multilayer perceptrons have been trained with Monte Carlo-generated event samples in supervised mode; in the future unsupervised training might play an important role and offer an elegant solution in domains where no reliable Monte Carlo simulation yet exists (*e.g.*, low-energy pions, K_L , beam backgrounds). All networks are implemented with the Neural Network Objects package (NNO) [16].

4.3.4.1 Methodology

Artificial neural networks are currently being investigated for identification of charged (e , μ , π , K , p) and neutral (γ , π^0 , K_L^0) particles [17]. The use of neural networks allows for a coherent treatment of all particles with the identical computer program. The knowledge about a specific system is not in the code, but is located in a separate network weight file. Thus modification of a particle selector's behavior requires a reload rather than a recode. Neural networks for particle identification offer the following benefits in comparison to a combination of conventional cuts:

- Single cut parameter to adjust purity/background ratio (variable criterion);
- Higher efficiency at the same background level with smoothly changing momentum dependence;

- Easy reprogramming by retraining to adapt to varying experimental conditions; it is possible to load a different weight file depending on conditions;
- Robustness with respect to varying or even missing inputs (graceful degradation);
- Neural networks are model-free estimators; there is no need to implement a specific mathematical model (likelihood, significance level);
- Neural networks inherently take into account any kind of correlation.

7-40-20-1 and 5-20-10-1 multilayer perceptrons have been trained with Monte Carlo-generated single particle samples in the whole momentum and angular range. The following data are used as the input vector, without cuts:

- Track momentum and θ ,
- Silicon vertex detector dE/dx
- DIRC Cherenkov angle,
- EMC energy,
- Number of DIRC photons, and
- Number of IFR hits.

The target vector holds a one in the presence of the particle under investigation or zero for any other particle.

4.3.4.2 Performance

The most important feature of neural network selectors (NNOSelectors) is that the purity/background ratio can be adjusted with a single cut on the network output node as if smoothly operating a slider. In the following, this cut was adjusted so that the resulting efficiency matched the efficiency of the conventional selectors. Table 4-2 indicates that at comparable efficiencies lower background levels are in principle achieved with neural network selectors.

Table 4-2. Inclusive single-track efficiency in percent for the NNSelectors at different cuts on the output node as compared to conventional selectors. Efficiency is defined as number of correctly assigned tracks divided by the total number of tracks.

Selector	e^{+-}	μ^{+-}	π^{+-}	K^{+-}	p^+	p^-
ElectronSelection (tight)	83	0	0	0	0	5
NNOElectronSelection (Cut=0.9)	83	0	0	0	0	0
MuonSelection (loose)	1	83	12	23	9	10
NNOMuonSelection (Cut=0.5)	5	85	11	13	2	2
PionSelection (loose)	92	87	79	12	3	15
NNOPionSelection (Cut=0.3)	8	14	78	27	18	22
PionSelection (tight)	26	42	58	16	13	26
NNOPionSelection (Cut=0.6)	2	3	59	7	3	9
KaonSelection (loose)	0	2	4	78	14	6
NNOKaonSelection (Cut=0.6)	1	2	6	73	9	9
KaonParamSelection (tight)	2	1	4	66	11	5
NNOKaonSelection (Cut=0.8)	0	1	3	65	1	3
ProtonSelection (loose)	1	0	6	3	89	82
NNOProtonSelection (Cut=0.3)	2	2	5	7	84	82

4.3.4.3 Future improvements

Further improvements and optimizations of the neural network selectors are currently under investigation:

- There is the possibility that different networks produce a similar response for the same track. According to the central limit theorem a better performance could be achieved by taking into account all individual outputs rather than just accepting the best value. This is technically realized by introduction of a top-level gating network which learns to weight and add together the outputs of the individual particle identification experts.
- Efficiency could be improved by consideration of additional detector information like specific energy loss in the drift chamber and timing information from the instrumented flux return.

- The transition from supervised, trained, multilayer perceptrons to unsupervised, self-organizing networks would allow independence from the Monte Carlo-generated samples: unsupervised training without labeled samples could boost the performance of pion or K_L^0 selectors once experimental data become available.

4.4 Neutral Particle Identification

4.4.1 π^0 and Photon Identification

The identification of π^0 s and photons in the EMC is performed by examining the transverse shower shape of reconstructed clusters.

An EMC cluster is defined as a contiguous array of crystals, all with energy above some threshold (nominally 0.5 MeV), whose total energy exceeds another threshold, nominally 20 MeV. A cluster is the energy disposition resulting from the interaction of one or more particles.

Two particles with small angular separation create energy deposits which overlap, resulting in a contiguous region which is reported as one cluster. In an attempt to resolve this situation, regions of local maxima are located and separated according to criteria based on an electromagnetic shower hypothesis. Such regions are referred to as bumps. A bump represents the energy deposit of a single particle and contains one and only one local maximum. (Thus, bumps may be thought of as clusters with one local maximum; a cluster always contains one or more bumps.)

The lateral distribution of energy within a cluster depends heavily on the nature of the incident particle. Electromagnetic particles deliver a rather regular and characteristically cylindrically symmetric shape in their lateral energy distribution, with the fall-off in energy from the center being exponential. In contrast, hadronic particles produce irregular and less predictable energy deposits, often resulting in more than one cluster per incident hadron. Those extra clusters, so-called (hadronic) splitoffs, are likely not identified as charged and may result in fake neutral showers.

Decays of π^0 s into two photons fall into two categories: for π^0 energies below about 1 GeV, the two photons are sufficiently far apart to produce two well-separated clusters (ideally with one bump each). In that case, the π^0 is reconstructed from the two photon 4-momenta. As the energy of the π^0 increases (beyond ~ 1.5 GeV), the photons have decreasing separation, to the extent that they are no longer distinguishable as separate clusters. Further, the division of the cluster into bumps becomes increasingly difficult, to the extent that at the very highest energies (for example, in the decay $B \rightarrow \pi^0\pi^0$) two photons may enter adjacent crystals or even the same crystal, making such a separation impossible.

Fortunately the distribution of energy within such clusters provides a mechanism by which such cases may be identified. The *second moment*, S , of a cluster is defined as:

$$S = \frac{\sum_{i=0}^{i=n} E_i (\Delta\theta_i)^2}{\sum_{i=0}^{i=n} E_i} \quad (4.5)$$

where $\Delta\theta_i$ is defined as

$$\Delta\theta_i = \begin{pmatrix} \theta_{clus} - \theta_i \\ \phi_{clus} - \phi_i \end{pmatrix} \quad (4.6)$$

and

$$\theta_{clus} = \frac{\sum_{i=0}^{i=n} E_i \theta_i}{\sum_{i=0}^{i=n} E_i}, \quad (4.7)$$

with a similar expression for ϕ . At medium to high energy, the resulting second moment distribution for π^0 s is reasonably well separated from that of photons (see Fig. 4-15). Moreover, the quantity $E^2 S$, after subtracting a constant offset due to the non-zero value of this quantity even for massless photons, is proportional to the mass of the incident particle, and can thus be used to identify such merged π^0 s. Their 4-momentum is measured from the cluster energy and center-of-gravity, after proper calibration.

This method works very well for distinguishing between medium- to high-energy photons and π^0 s, as can be seen in Figs. 4-16 and 4-17. It also provides a way of identifying photons in their own right (see Fig. 4-18), with two caveats though: for small energy deposits resulting in few crystals contributing to the sums in the above equations, S ceases to be well behaved due to the granularity of the calorimeter; moreover, the nature of the backgrounds to be discriminated against changes dramatically as a function of energy. As a result, other methods need to be developed to identify low-energy photons with high efficiency and low contamination.

4.4.2 K_L^0 Identification

A large fraction ($\approx 85\%$) of all K_L^0 s with momenta greater than 0.5 GeV/c produce at least one hit in the IFR chambers. Previous analyses [18], done outside the full reconstruction environment, indicated that it is possible to obtain a good detection efficiency for K_L^0 in the channel $B \rightarrow J/\psi K_L$ by requiring a minimum of four IFR layers hit. The IFR is not a calorimeter and is not used for energy measurements: it can measure only the flight-direction of the K_L^0 s. The detection efficiency and the angular resolution can be improved if the interaction starts in the EMC (which happens in $\approx 55\%$ of $B \rightarrow J/\psi K_L$ events) and information from the EMC is added (see Fig. 4-19). In about one third of cases, the interaction starts in the flux return iron, and the IFR is the only detector involved.

The K_L^0 reconstruction is now being implemented [19] in the standard BABAR reconstruction framework. Preliminary results using the full BBSim simulation are shown in Fig. 4-20.

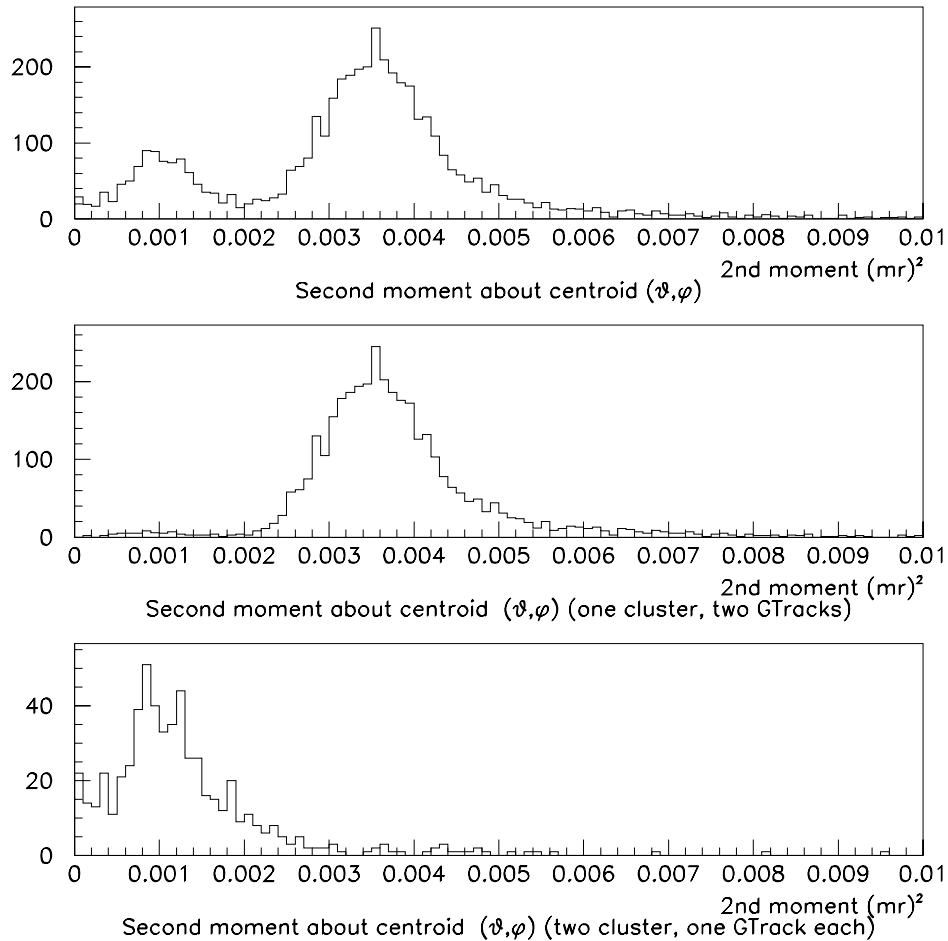


Figure 4-15. Distribution of the second moment of clusters in theta, phi space for 3GeV π^0 s. At this energy, some π^0 s form separated photon clusters, giving the left-hand peak, and some form one merged cluster, giving the right-hand peak. This may be seen by the separation of the two distributions using Monte Carlo truth.

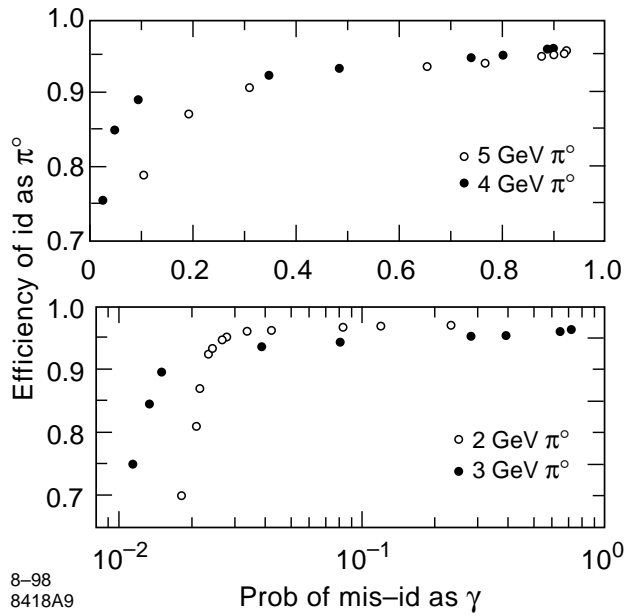


Figure 4-16. π^0 efficiency vs. photon misidentification probability for π^0 energies between 2 GeV and 5 GeV.

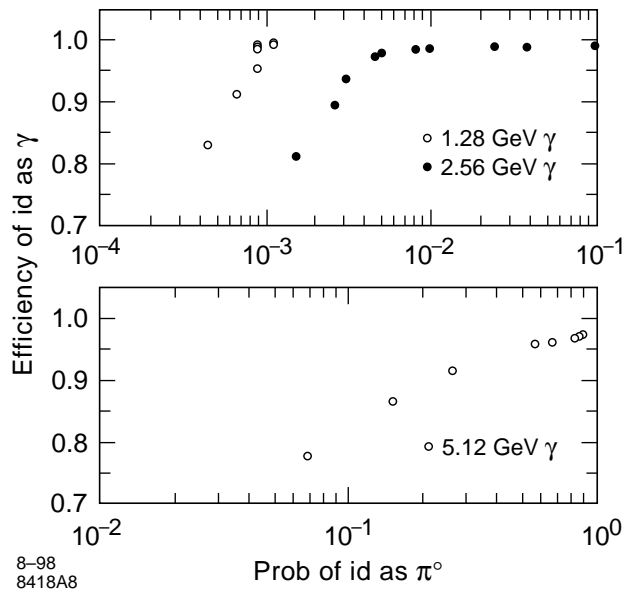


Figure 4-17. Photon efficiency vs. π^0 mis-identification probability for photon energies between 1.28 GeV and 5.12 GeV.

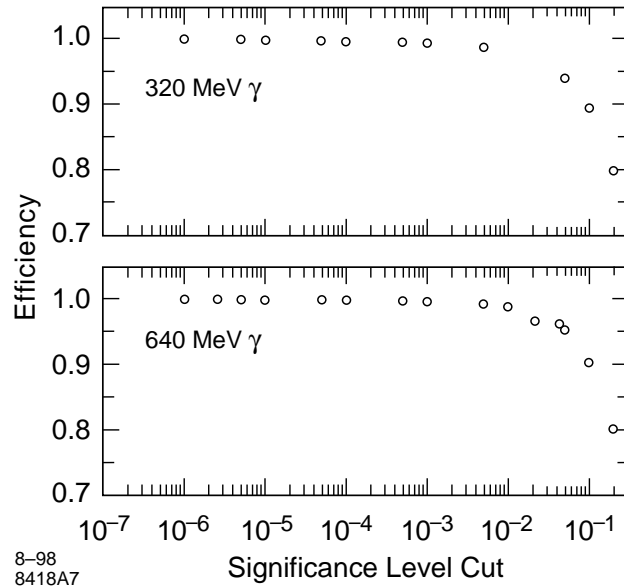


Figure 4-18. Photon efficiency vs. significance level cut for photon energies of 320 MeV and 640 MeV.

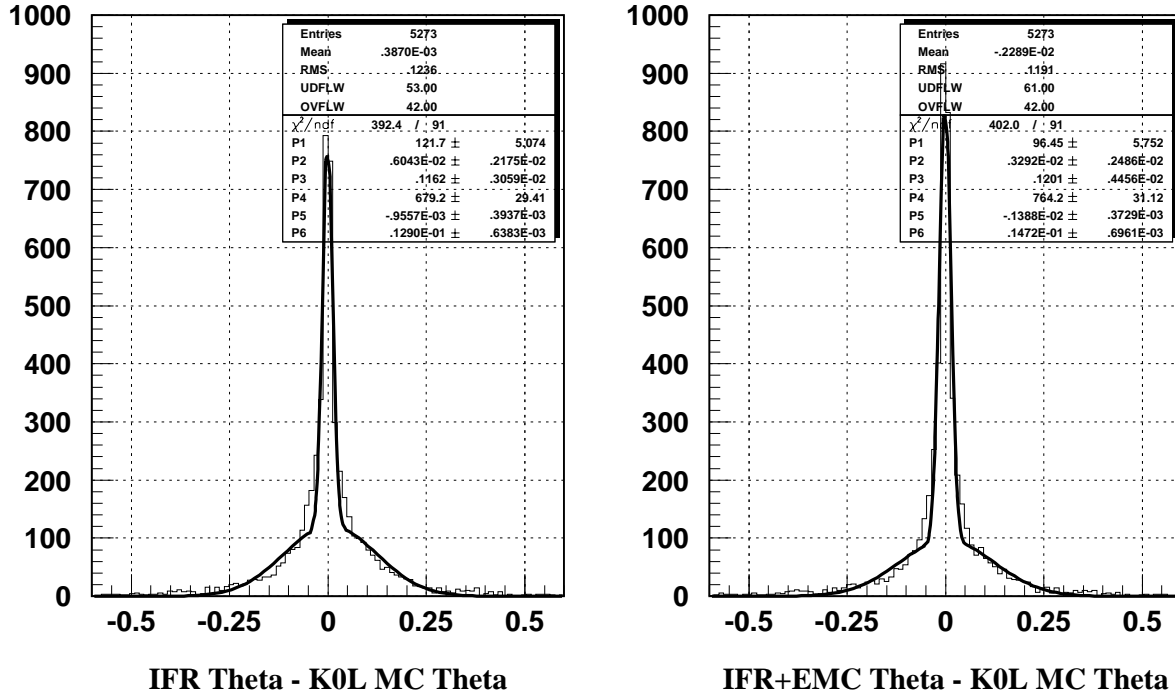


Figure 4-19. Comparison of angular resolution for K_L^0 in the IFR between cases with no interaction in the calorimeter (left) and those with an initial interaction in the calorimeter (right).

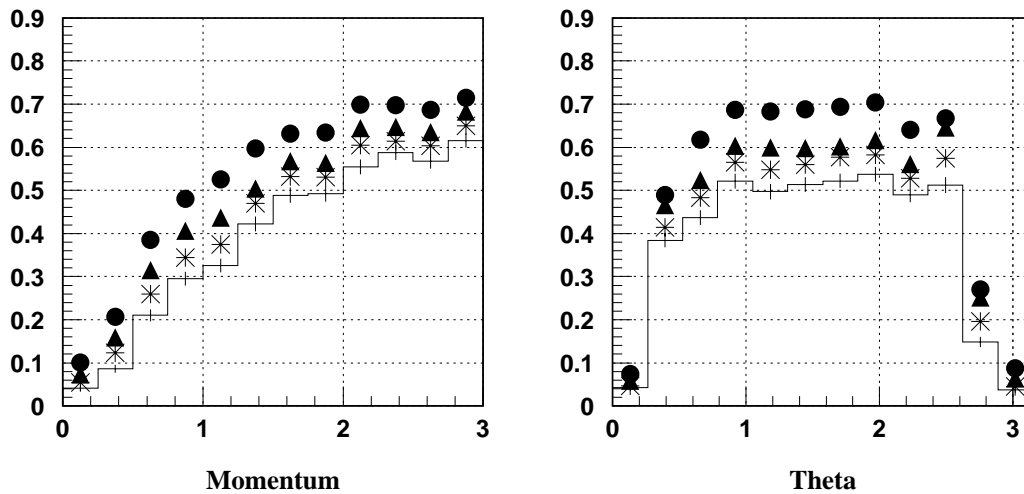


Figure 4-20. K_L^0 reconstruction efficiency as a function of momentum and theta.

As in the earlier studies, the results depend somewhat on the hadronic shower simulation used. Unfortunately, existing simulations do not all describe consistently the interactions of K_L^0 at low momenta. All the hadronic interaction models accessible through Geant 321 do, however, agree on the general characteristics of the response to penetrating hadrons, namely that:

- There is a high multiplicity of hadronic shower topologies, distributed over a wide part of the IFR detector;
- Shower longitudinal development depends on momentum and particle direction;
- Shower transversal development depends on the particular pattern of showering physics processes;
- There is a significant fraction of early hadronic showers in the inner calorimeter.

The design for the reconstruction of K_L^0 is based on the general detector response characteristics.

The K_L^0 reconstruction starts by selecting *neutral* clusters, from the available 3-dimensional IFR clusters in each event, by checking that no reconstructed track extrapolates (using a swimmer algorithm) to the IFR cluster position. An algorithm attempts to combine such neutral clusters, as being associated to the same hadronic shower on the basis of a vicinity criterion. The final object output by this process is a neutral cluster aggregate which combines both IFR and Inner RPC response to the particle. Such an object can have components found in different geometric sectors of the IFR and can provide a first estimate of the neutral hadron flight direction.

An association is formed between the above IFR aggregate and calorimeter clusters, assuming that the position of the EMC cluster provides the position of the first interaction, that the shower develops into a cone of tuned opening angle, and taking into account the covariance matrix of the IFR aggregate. Each created association has a significance level based on the χ^2 of the match, which can be used to select different match qualities. The IFR-EMC association is used to create an object representing the neutral hadron. This object provides the implementation of different algorithms for the computation of the flight direction and is available for the physics analysis.

A good resolution for the K_L^0 flight direction helps provide a clean reconstruction of the signal channel $B^0 \rightarrow J/\psi K_L^0$. Different direction-finding strategies have been studied and are useful for comparison and cross-check purposes:

- Position in the IFR only: this method is based on the response of the the IFR alone to the hadron.
- Position in the Inner RPC: this method exploits the response in the Inner RPC, if present in the neutral aggregate.
- First layer method: the average position of single hits in the first layer only is used as estimate of the flight direction.
- Optimal hit method: the 'optimal' hit is defined as the hit minimizing the distance from the position obtained by the full IFR response.
- Calorimeter cluster position: this method exploits the available information from the IFR-EMC association and applies in the cases of early hadronic showers.

4.4.2.1 K_L^0 calibration

The K_L^0 detection efficiency can be evaluated using the detailed Monte Carlo simulation; the lack of experimental data available now makes the hadron shower simulation not entirely reliable at low momenta, and the results depend somewhat on the hadronic shower generator used. Hence, it is important to find a calibration channel so that identification and detection efficiency can be tested directly with data.

The ideal calibration channel would have a branching ratio much larger than $\sim 5 \times 10^{-5}$, which is the combined branching ratio of the reference channel $B^0 \rightarrow J/\psi K_L^0$, ($J/\psi \rightarrow \ell^+ \ell^-$), and should be as pure as possible, to enable the identification of K_L^0 on an event-by-event basis. Unfortunately there is no single B -decay mode with a K_L^0 in the final state with a branching ratio much larger than the reference channel which can be kinematically selected. A copious source of K_L^0 however, is the decay $\phi \rightarrow K_s^0 K_L^0$, which is produced abundantly, both in the continuum and in $\Upsilon(4S)$ events. The inclusive ϕ production rate is very high, $\sim 8\%$ per event, and roughly the same for $\Upsilon(4S)$

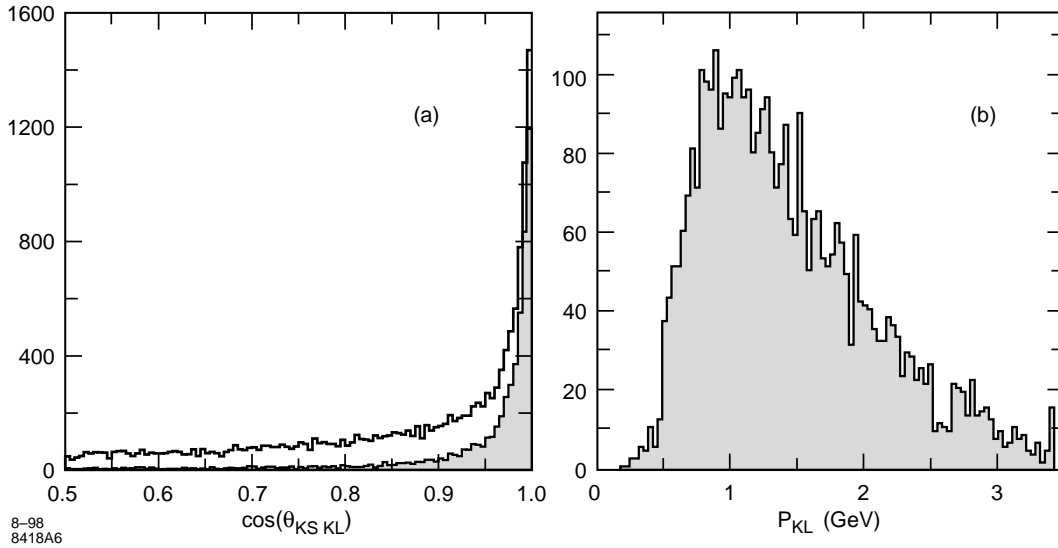


Figure 4-21. (a) Opening angle between K_S^0 and K_L^0 ; (b) Momentum spectrum of K_L^0 from ϕ decays.

events as for continuum events. The continuum cross-section is ~ 3.5 times the peak cross-section of $\Upsilon(4S) \rightarrow B^0 \bar{B}^0$, so that the number of K_L^0 from this calibration channel is ~ 3000 times more than the reference channel.

The expected distribution of the opening angle between the two kaons in the laboratory frame, has a peak at small angles, due to the average ϕ velocity and to the very small K_L^0 momentum in ϕ center of mass frame. The inclusive angular distribution between any K_S^0 and any K_L^0 from hadronic e^+e^- interactions (both $\Upsilon(4S)$ and continuum events) is shown in Fig. 4-21(a). In any such event where a K_S^0 is selected, there is a good probability to find a K_L^0 within a cone of $\sim 10^\circ$, enabling K_L^0 to be selected and their direction to be estimated using observed K_S^0 . The corresponding K_L^0 momentum spectrum is shown in Fig. 4-21(b). It can be seen that it covers most of the critical range where the detection efficiency needs to be tested. The K_L^0 from the reference B decay and from other interesting channels typically have momenta of 1–3 GeV/c. In the higher momentum range, the detection efficiency is expected to flatten out anyway.

Further selection criteria can be found to enhance the signal from ϕ decays with respect to the background. From the study of K_L^0 from ϕ decay, it is also possible to determine the K_L^0 momentum, P_L , with reasonable resolution, from the measurement of the momentum P_S of the K_S^0 and the opening angle α , with the relationship:

$$M_\phi^2 = 2m_K^2 + 2[E_L E_S - P_L P_S \cos \alpha]. \quad (4.8)$$

This equation has two solutions for P_L , and thus introduces a two-fold ambiguity. The ambiguous cases can be reduced strongly as follows. First of all, only those events are selected where the

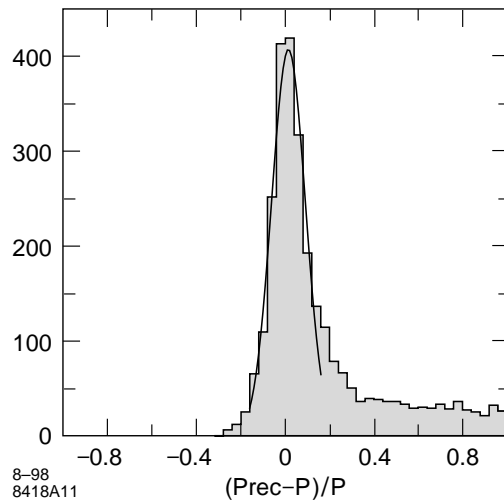


Figure 4-22. Fractional difference between true and reconstructed K_L^0 momenta.

solution corresponding to the lower momentum gives a value too small for detection, ($P_L \leq 500$ MeV). Furthermore the correct solution is fairly flat in the ϕ center-of-mass reference frame (the ϕ being mostly unpolarized and the detection efficiency affecting mostly very forward angles). On the contrary the wrong solution is strongly backward-peaked. In cases where only one of the two solutions is in the backward hemisphere, the solution in the forward hemisphere is likely to be correct. This criterion also drastically reduces the combinatorial background, since for these events, both solutions are likely to correspond to backward emission. An additional cut on P_S may halve this background without affecting very much the events from ϕ decay.

Applying these criteria after a K_S^0 has been selected, a K_L^0 from ϕ decay is expected in a 10° cone in $\sim 10\%$ of the cases with a few percent contamination from the combinatorial background. The efficiency is $\approx 50\%$. The sample is very large and further cuts can be envisaged if the need should arise to reduce the background further. In Fig. 4-22, the fractional difference between true and reconstructed momenta in such a sample is shown. The distribution shows a tail corresponding to $\sim 10\%$ of the events, where the wrong solution has been chosen and the momentum is overestimated. The K_L^0 momentum is measured with $\sim 8\%$ resolution, mainly due to the uncertainty on the K_L^0 direction.

The detection efficiency may be measured as a function of momentum from a sample of K_L^0 selected in this way. It can be normalized by using $\phi \rightarrow K^+ K^-$ events.

4.5 Vertexing and Kinematic Fitting

4.5.1 Vertex Reconstruction

This section is a brief introduction to the vertexing tools in use in BABAR. Vertexing is the process of finding the best estimate of the three-dimensional point of intersection of a number of tracks. Errors present in all measurements mean that there is no unique point through which all reconstructed tracks pass, so that the problem must be solved by some kind of optimization process.

In addition to finding the intersection of long-lived tracks, the vertexing tools should provide additional features. The quality of the fit should be reported, aiding the removal of incorrect fits, in which tracks that in reality do not meet have been vertexed.

4.5.1.1 Algorithms

Vertexing of charged tracks is complicated by the presence of the magnetic field and material in which particles can scatter. To the extent that the field is uniform and the material is thin, the trajectories of a charged particle can be approximated by a helix. The vertexing of neutral “tracks” is hindered by the fact they lack most spatial information and are reconstructed from energy deposits in the calorimeter. The precision of a neutral track can be improved if it can be identified with a decay vertex and perhaps kinematically fit.

Most vertex reconstruction algorithms work by minimizing the sum of the squares of the distance of closest approach of a set of tracks to a point. The curvature of tracks makes the problem nonlinear. The general procedure for solving nonlinear problems is to linearize them and look for a local solution. This procedure is iterated from the local solution until convergence is obtained. A drawback of such methods is that they require an initial guess of the location of the vertex. In general the primary interaction point is an unbiased choice for this first guess, but the convergence radius of such methods is only a few cm[20]. This is good enough for B and D decays, but can be a problem for long-lived particles such as K_S^0 , Λ , or other hyperons. To handle this case, a tool has been developed using a global method [21] that solves analytically the nonlinear equations to provide a first guess well within the convergence radius. The performance of this tool has been shown to be a significant improvement over traditional methods. Several examples of its application can be found in *e.g.*, Section 4.5 and Chapters 5 and 6.

4.5.1.2 Primary vertex reconstruction

The size of the interaction point (IP) at the PEP-II interaction region is about 150 μm in x , 6 μm in y , and 1 cm in z . For many physics analyses and reconstruction tasks, it is desirable to have a more accurate estimate of the primary interaction vertex. For instance, reconstruction of γ and

π^0 candidates will, in many cases, use the primary vertex as the point of origin in constructing momentum vectors.

The primary vertex is estimated on an event-by-event basis from a vertex fit which uses selected charged tracks in the event and knowledge of the average IP position. The selected tracks are those with an impact parameter less than 1 mm in the x - y plane, with respect to the nominal IP. This requirement removes most charged tracks associated with particles which decay a relatively long distance from the interaction point, such as K_s^0 mesons. Although the performance of this algorithm is dependent on the type of event, the efficiency for reconstructing a primary vertex is always above 99%.

For events where the e^+e^- collision produces light quarks, the reconstructed primary vertex is a good estimate of the true primary interaction point. In this case the resolution is about $63 \mu\text{m}$ in x , $7 \mu\text{m}$ in y , and $62 \mu\text{m}$ in z . For charm and $B\bar{B}$ events, the reconstructed primary vertex resolution is degraded due to the effects of the charm and B meson lifetimes. The resolution for charm events is about $87 \mu\text{m}$ in x , $9 \mu\text{m}$ in y and $99 \mu\text{m}$ in z . For $B\bar{B}$ events, both B mesons travel along the positive z direction in the lab frame, and so the reconstructed primary vertex will be shifted in the positive z direction from the e^+e^- interaction point. The vertex reconstructed by this algorithm therefore represents something like the average B decay position (the midway point between the two decays). In many applications this is, in fact, the quantity one is most interested in. The resolution, using the midway point between the two B decay vertices as a reference, is $101 \mu\text{m}$ in x , $10 \mu\text{m}$ in y , and $115 \mu\text{m}$ in z .

4.5.1.3 Reconstruction of the tagging- B vertex

Vertex reconstruction of the tag B is more complicated than that of the CP B . In the latter case one has all the final-state tracks of the B_{CP} decay chain, and one can choose those which should originate from the B decay vertex and use those for vertexing. B_{tag} vertex reconstruction on the other hand is done with all the remaining charged tracks in the event. This means that most of the time there is not a complete decay tree, and there are tracks which are daughters of long-lived intermediate particles and cannot be used to reconstruct the vertex.

In the B_{tag} finder tool three algorithms are used for inclusive vertex reconstruction.

1. Vertex Fit (VF): this method is used when at least two tracks are available.
2. Simple Impact Parameter (SIP): this is a one-track method. The point on the track nearest to the B_{CP} is selected and it is assumed as the B_{tag} vertex.
3. Lepton Impact Parameter (LIP): this is also a one-track method which is applied only to high-energy primary leptons from semileptonic decays: $B \rightarrow X\ell\nu$. In this case, the point on the track nearest to the nominal detector origin is used as the B_{tag} vertex.

All three methods are applied after a suitable track selection. The cuts applied for track selection depend on the algorithm used. As a first step, tracks from secondary vertices that are too far from the nominal interaction point to be vertexed, and tracks too near to the detector acceptance boundary that could be badly reconstructed are eliminated. This selection is based on the d_0 and z_0 impact parameters and on the polar angle θ . If more than one track remains, the vertex fit algorithm is used, and cuts on the vertex χ^2 probability and on the pseudo-track mass are made. The first cut is obviously to remove vertices with a bad fit and the second one to remove secondary vertices. If only one track remains, a cut on its momentum is made. The aim of this cut is to remove low momentum particles which are badly reconstructed due to multiple scattering effects. If the track passes this cut the simple impact parameter method is used.

The spatial information of leptons can be very useful in the B_{tag} vertex reconstruction. In order to maximize its benefit, it is necessary to distinguish between primary and secondary leptons. This can be achieved by making a cut on the momentum of the leptons. Primary leptons from semileptonic decays, especially from $B \rightarrow D\ell\nu$ decays, have a high momentum in the $\Upsilon(4S)$ rest frame. Among leptons in the charged track list the one with highest momentum is selected and a cut is made on its momentum. In this case the impact parameter method is used. The two “one-track” methods are used with different tracks (generic tracks and leptonic tracks) depending on how well the track (and consequently its z_0 impact parameter) is reconstructed. In the lepton case it is not necessary to search for another point on the lepton track because the z_0 choice is a good enough approximation.

All three methods are used in each event. The VF and SIP methods are exclusive. This means that in a given event, only one of these situations occurs. However they can each coexist with the LIP method. If this is the case, an arithmetic mean is made between the z coordinate (z_{tag}) calculated with one of the first two methods and the z coordinate (z_{lep}) calculated using the lepton. More details on the B_{tag} vertex reconstruction tool, including the results obtained in the $a_1\pi$ analysis, can be found in Ref. [22].

4.5.2 Kinematical Fitting

This section is a brief introduction to the kinematic fitting tools used in BABAR. Kinematic fitting is the process of using kinematic constraints, such as masses, and energy and momentum conservation, to improve our knowledge of an event. Kinematic fitting can provide improved parameters for charged and neutral tracks. It can assist in particle identification and in event classification. It can also be useful in resolving ambiguous vertices. An ambiguous vertex is one in which multiple tracks seem to come from a unique point in the detector, but the sum of energy and momenta for the tracks associated with the point do not correspond to the decay of a known particle.

4.5.2.1 Algorithms

The classic fitter, Squaw [23], is still in use and has been adapted for use in BABAR [24]. The adaptations include extending the underlying Fortran code to support up to 50 tracks and putting C++ wrappers around the code.

Squaw uses the method of χ^2 minimization of the measured track parameters, combined with Lagrangian multipliers to impose the constraints.

$$f(x, x^*) = 0 \quad (4.9)$$

$$M = 2f\alpha + (x - m)^T G(x - m) + (x^* - m^*)^T G^*(x^* - m^*) \quad (4.10)$$

Here x and x^* are the track parameters to be fitted and m and m^* are those that have been measured. G and G^* are the weight matrices, the inverse of the covariance matrices, for each of the tracks. The vector of constraints is represented in the form $f = 0$ and M is the function to be minimized. α is the vector of Lagrangian multipliers. The code distinguishes between well-measured variables, m , and badly measured ones, m^* . Minimization of M with respect to the set of x , x^* , and α leads to a set of coupled nonlinear equations. These are solved using traditional methods of linearization and iteration. Chapter VI of Ref. [23] provides more details of the fitting methods used.

Squaw is a *kinematic* fitter and does not use any spatial information in doing the minimization. Only the momenta and momenta errors are employed. Another kinematic fitter, BetaKfit [25], has also been developed for use in BABAR. The main difference from the Squaw fitter is that it employs both kinematic and spatial information in the fitting. The Least Squares method used in BetaKfit minimizes the sum:

$$S^2 = \sum_i (m_i - h_i(\bar{\xi}))^T W_i (m_i - h_i(\bar{\xi})) + A(\bar{\xi}), \quad (4.11)$$

taking into account kinematic and spatial constraints $\bar{f}(\bar{\xi}) = 0$, where m_i is a vector of the track's measured parameters and W_i is its weight matrix. The vector of fitted parameters, $\bar{\xi}$ includes the positions of the vertices and the momenta of registered tracks. The function $h_i(\bar{\xi})$ is a mapping from the fitted parameters to the track parameters. An additional term $A(\bar{\xi})$, which may appear in S^2 , accounts for the independent measurements of some function of the track parameters; this may be a beam energy, for example. In these fits, charged tracks are represented by five parameters and neutral tracks are represented by three parameters.

For now, there exist two implementations of the BetaKfit fitter — one is an interface to the FitVer package developed for the DELPHI experiment [26], and another is a native C++ implementation of the algorithm. Both, however, use the same interface. Constrained minimization in both these implementations uses the penalty function method, and minimization is performed with the Minuit package [27].

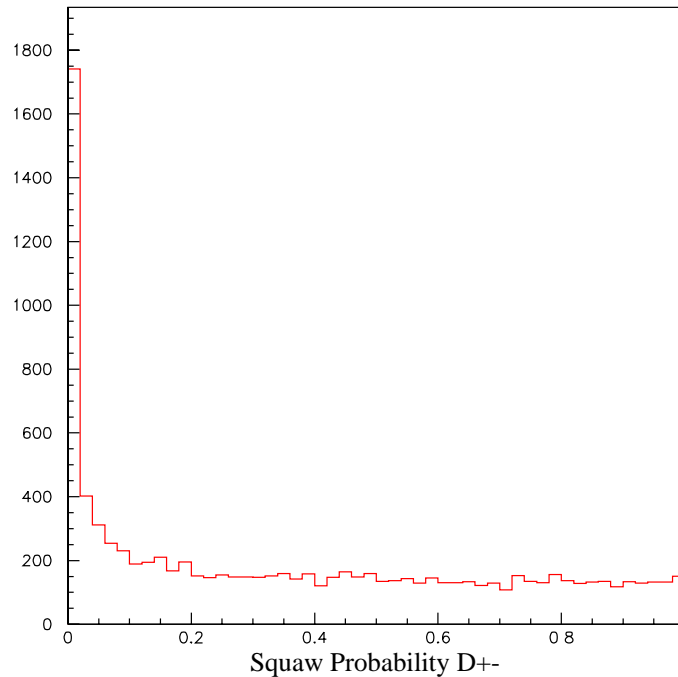


Figure 4-23. The confidence level distribution of a set of kinematic fits to the decay $D \rightarrow K\pi\pi$. The kinematic fit is done on events with 12 charged tracks with 100% $K-\pi$ ambiguity. The peak at low probability is mostly misfits. Even with the ambiguity of 90 combinations per event, less than 15% give poor fits with confidence levels significantly greater than zero.

4.5.2.2 Applications and performance

One application of kinematic fitting is in the reduction of vertexing ambiguities. When there are multiple charged tracks from the decay of different short-lived particles emerging from a very small region, it is quite possible that the association of tracks to vertices based purely on spatial coincidence can lead to multiple solutions, including many incorrect ones. Since all of the interesting vertices are associated with the decay of particles with known masses, this constraint can be used to select the correct association of daughter particles. The kinematic fit will also permit the association of calorimeter neutrals with a vertex, since this cannot be done with spatial information.

Figure 4-23 shows the confidence level distribution for kinematic fits to the $D^\pm \rightarrow K\pi\pi$ decay mode. The fitted events had 12 charged tracks each. No particle identification was used in the fits, so every track was tested against both the π and K hypothesis. Figure 4-24 shows the two-dimensional plot of the kinematic fit confidence level plotted against the spatial vertexing confidence level. Both the kinematic and spatial confidence level can be combined to get an overall probability for the decay hypothesis.

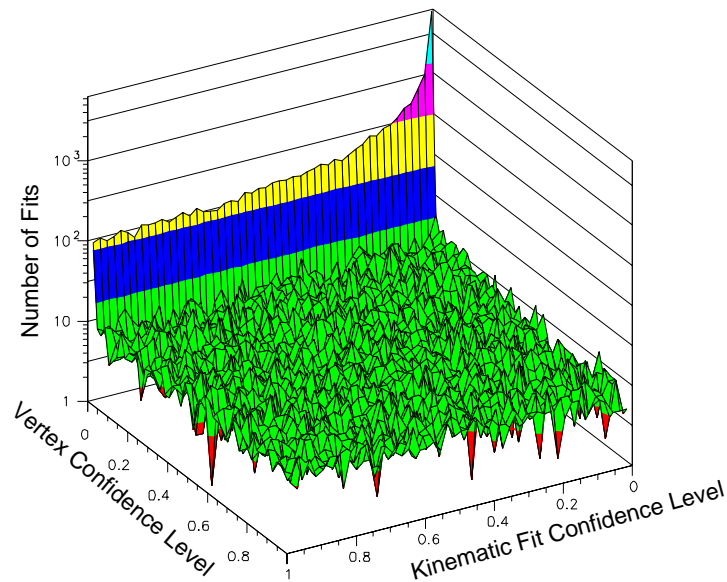


Figure 4-24. Two-dimensional confidence level distribution for a set of fits to the decay hypothesis $D \rightarrow K\pi\pi$. The kinematic fit confidence level is shown from right to left; the vertex fit confidence level is shown from rear to front.

Table 4-3. BetaKfit resolution parameters for Aslund-generated events. Decay modes - 1) $B^0 \rightarrow D^+D^-$ with both D s decaying to $K\pi\pi$; 2) $B^0 \rightarrow D^+D^-$ with both D s decaying to $K_S^0\pi \rightarrow \pi^+\pi^-\pi$; 3) $B^0 \rightarrow \rho\pi$ with $\rho \rightarrow \pi^0\pi$.

Decay mode	mass constraint	$\sigma_z(B^0)$, μm	$\sigma_M(B^0)$, MeV/c^2
1) D^+D^-	none	48	9.6
1) D^+D^-	D^+D^-	48	5.3
2) $D[K^0]$	none	53	10.8
3) $\rho\pi$	none	44	28

Table 4-3 summarizes performances achieved with the BetaKfit fitter. An example of clear improvement is the mass resolution of B^0 in the decay $B^0 \rightarrow D^+D^-$ when each D decays into $K\pi\pi$. The resolution improves dramatically from 9.6 MeV to 5.3 MeV when the masses of both D s are fixed.

4.6 Reconstruction of Particle Decays

4.6.1 K_s^0

Reconstruction of K_s^0 mesons in BABAR plays a crucial role both in the search for “golden channel” events, $B^0 \rightarrow J/\psi K_s^0$, and in the reconstruction of D mesons. The reconstruction procedure of the charged mode, $K_s^0 \rightarrow \pi^+ \pi^-$, is the same in both cases, but the selection of input tracks and output K_s^0 candidates could be very different. A general-purpose K_s^0 finder combines oppositely-charged input tracks and finds a common vertex. An invariant-mass cut can be applied, and other variables for possible cuts are provided to allow users to set the values of cuts according to their analyses. This tool uses the analytic method introduced previously in Section 4.5.1 [21].

In the following, K_s^0 s from B^0 decays in events such as $B^0 \rightarrow J/\psi K_s^0$ with $\bar{B}^0 \rightarrow X$, and K_s^0 s from D mesons in events such as $B^0 \rightarrow D^{*+} D^{*-}$ with $\bar{B}^0 \rightarrow X$ are considered. Figure 4-25 shows the signal mass resolution and combinatorial background contamination (in the same events) for K_s^0 s from B and D mesons. A signal mass resolution of about 3.5 MeV is obtained in both cases, but for K_s^0 s from D mesons there are longer tails. Table 4-4 shows the efficiencies obtained using an invariant-mass cut at three times the signal resolution from the nominal K_s^0 mass. In order to clean up the selection, a number of other cuts may be used. For example, the vertexing algorithm itself can be used as a background-suppression tool, cutting on the χ^2 probability of the found vertex, or a simple cut can be applied on the decay length of the K_s^0 .

K_s^0 s that are direct decay products of a B meson tend to have larger momenta (Fig. 4-26) than the combinatorial background, so that a momentum cut can be used to help suppress the background in such cases (although this would not be useful in a generic K_s^0 finder). The relatively long K_s^0 lifetime typically results in vertices detached from the primary event vertex and impact parameters larger than those of the primary tracks (Fig. 4-27). Effects of further cuts on the χ^2 probability, momentum, and impact parameters of daughters pions are shown in Table 4-5. In the table, the efficiency of combined cuts is equal to the product of efficiencies of single cuts, *i.e.*, the chosen cuts are independent of each other. The lower row in the table shows an overall efficiency, including the efficiency of cuts and the tracking efficiency (83%, including geometrical acceptance). These

Table 4-4. Effect of a 3σ invariant-mass cut ($487 \text{ MeV}/c^2 < m < 509 \text{ MeV}/c^2$).

Channel	Efficiency(%)
K_s^0 from B^0	79
K_s^0 from D	69

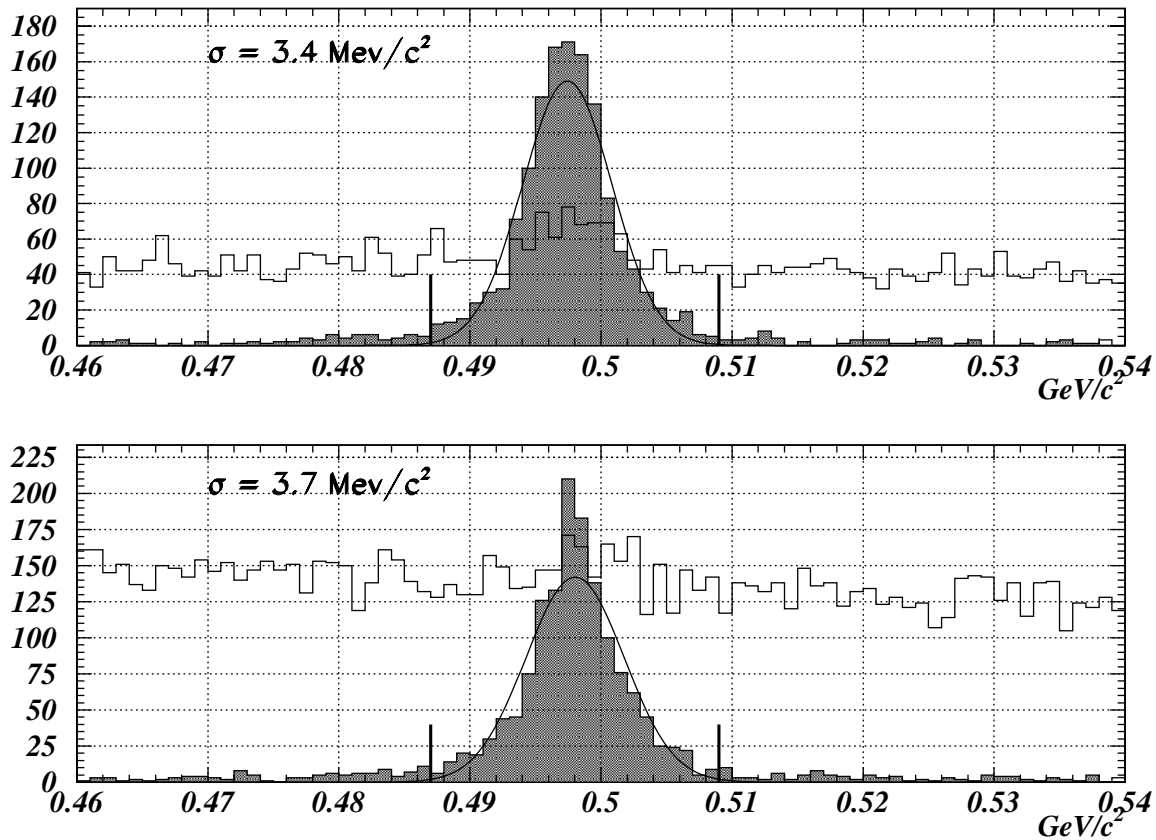


Figure 4-25. Invariant-mass plots for K_S^0 s from (top) B and (bottom) D mesons. The filled (unfilled) histogram is signal (combinatorial background within the event).

efficiencies are, of course, valid only for the particular cuts chosen, and with the reconstruction version available at the time of writing.

4.6.2 D and D^*

In this section the reconstruction of the charmed mesons, which will be used for the study of CP asymmetries, for charm physics and B physics and for understanding the detector will be discussed. Due to the mass threshold in the D^* decay, the D^0 resonance is the most interesting state and is the only one described in this part.

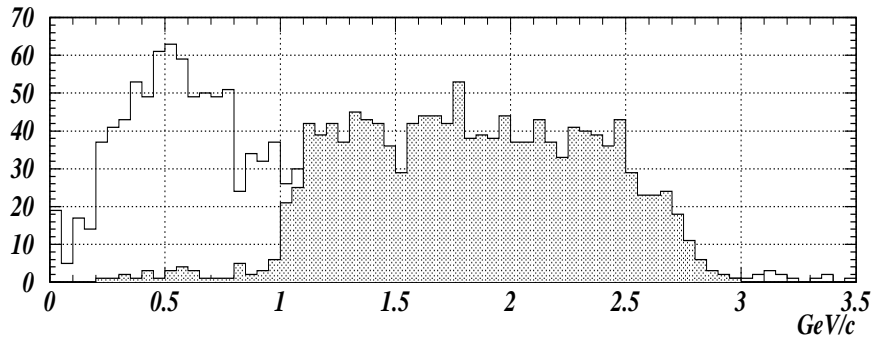


Figure 4-26. Momentum distribution of K_s^0 s from B^0 decays: the filled histogram is signal and the empty histogram is background.

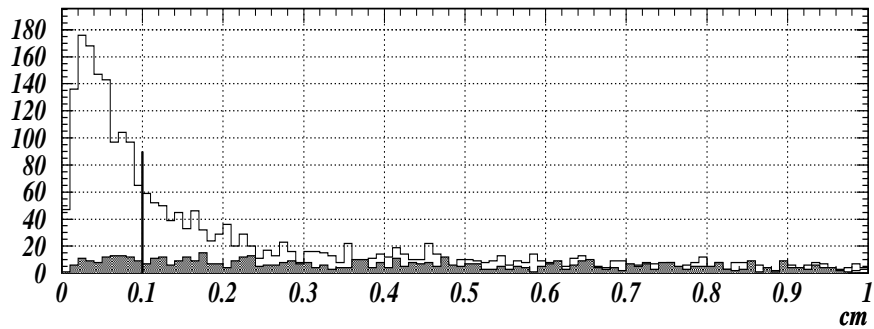


Figure 4-27. Distribution of $|d_0(\pi^+)| + |d_0(\pi^-)|$ in K_s^0 s from D mesons: the filled histogram is signal and the empty histogram is background. A possible cut is shown, whose effects are reported in Table 4-5.

Table 4-5. Efficiencies of cuts applied after a mass cut on K_s^0 s coming from B^0 and D decays.

	Efficiency(%) for K_s^0 from B^0	Efficiency(%) for K_s^0 from D
$p(\chi^2) > 0.01$	98	96
$1. < P_{K^0} < 3.$	98	N/A
$ d_0(\pi^+) + d_0(\pi^-) > 0.07(0.1)$	95	94
Combined cuts	91	89
Combined $\times \epsilon_{mass} \times \epsilon_{trk}$	60	51

4.6.2.1 D^0 reconstruction

The following decay channels have been considered with the daughter branching ratios in parentheses:

- $D^0 \rightarrow K^- \pi^+$ (3.8%)
- $D^0 \rightarrow K^- \pi^+ \pi^0$ (13.9%)
- $D^0 \rightarrow K^- \pi^+ \pi^+ \pi^-$ (7.5%)

The momentum range of the charged kaon (between 0.5 and 4 GeV/c) is well suited to the DIRC so that the standard BABAR particle ID described earlier can be used to identify it. A good vertex for the D^0 decay tracks is useful in decreasing the combinatoric background. In the $K\pi\pi\pi$ channel a further identification of the pions is required. In a sample of 10,000 $B^0\bar{B}^0 \rightarrow X$ events, a clean D^0 signal can be obtained only for the $K\pi$ mode (Fig. 4-28). In this channel, a resolution of $\sigma \simeq 6$ MeV is achieved. Nevertheless all the decay modes will be used for reconstructing the D^* .

4.6.2.2 $D^{*\pm}$ reconstruction

In this section, the decay $D^* \rightarrow D^0 \pi^+$ (68%) is considered. The D^0 is reconstructed and mass cuts of three standard deviations are applied on the candidates. The soft pion (below 400 MeV/c) is required to have charge opposite to that of the kaon. The usual $\Delta m = M(D\pi) - M(D)$ must exhibit a sharp peak around 145 MeV/c². The signals obtained in a sample of 10000 $B^0\bar{B}^0 \rightarrow X$ are displayed for the different D^0 channels in Fig. 4-29.

The combination of all three modes shows a good signal/background ratio and a Δm resolution of about 1 MeV/c². The reconstruction efficiencies were obtained using the full simulation and

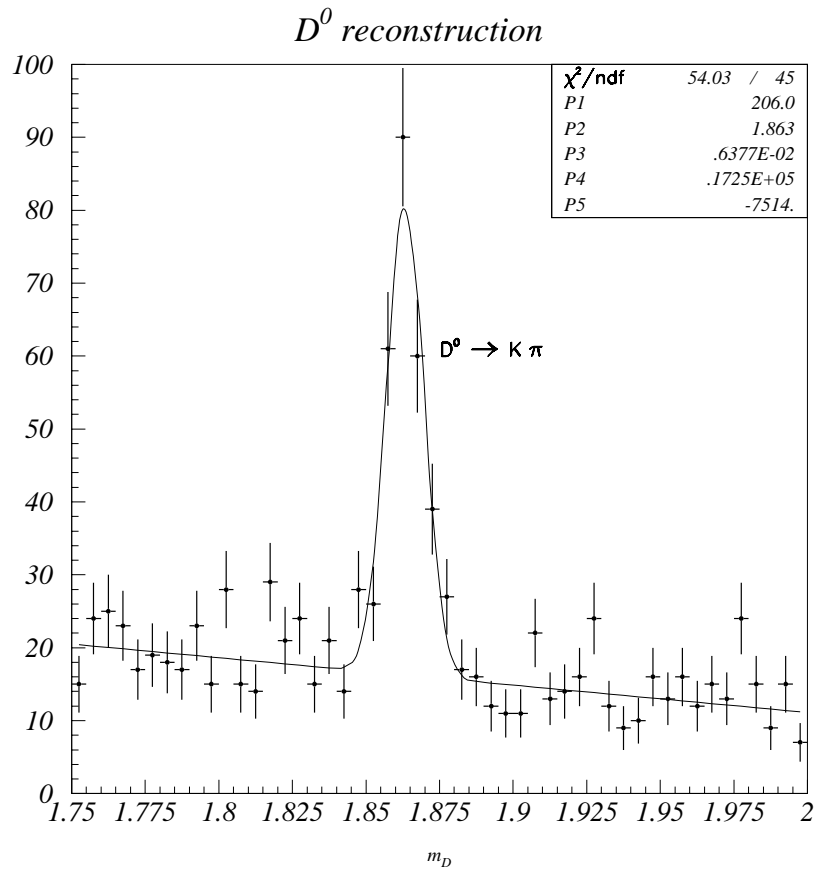


Figure 4-28. $K\pi$ invariant mass reconstructed from a sample of 10,000 $B^0\bar{B}^0$ decays.

Table 4-6. D^* reconstruction efficiencies measured using full simulation/reconstruction for the different D^0 decay modes.

ϵ_{rec}	$D^0 \rightarrow K\pi$	$D^0 \rightarrow K\pi\pi^0$	$D^0 \rightarrow K\pi\pi\pi$
Acceptance (D^0 tracks)	0.85	0.85	0.5
K identification	0.8	0.8	0.8
π identification	0.9	0.9	0.73
π^0 reconstruction	-	0.3	-
vertexing + mass cuts	0.97	0.97	0.95
Acceptance for soft π	0.7	0.7	0.7
Total	0.41	0.12	0.19

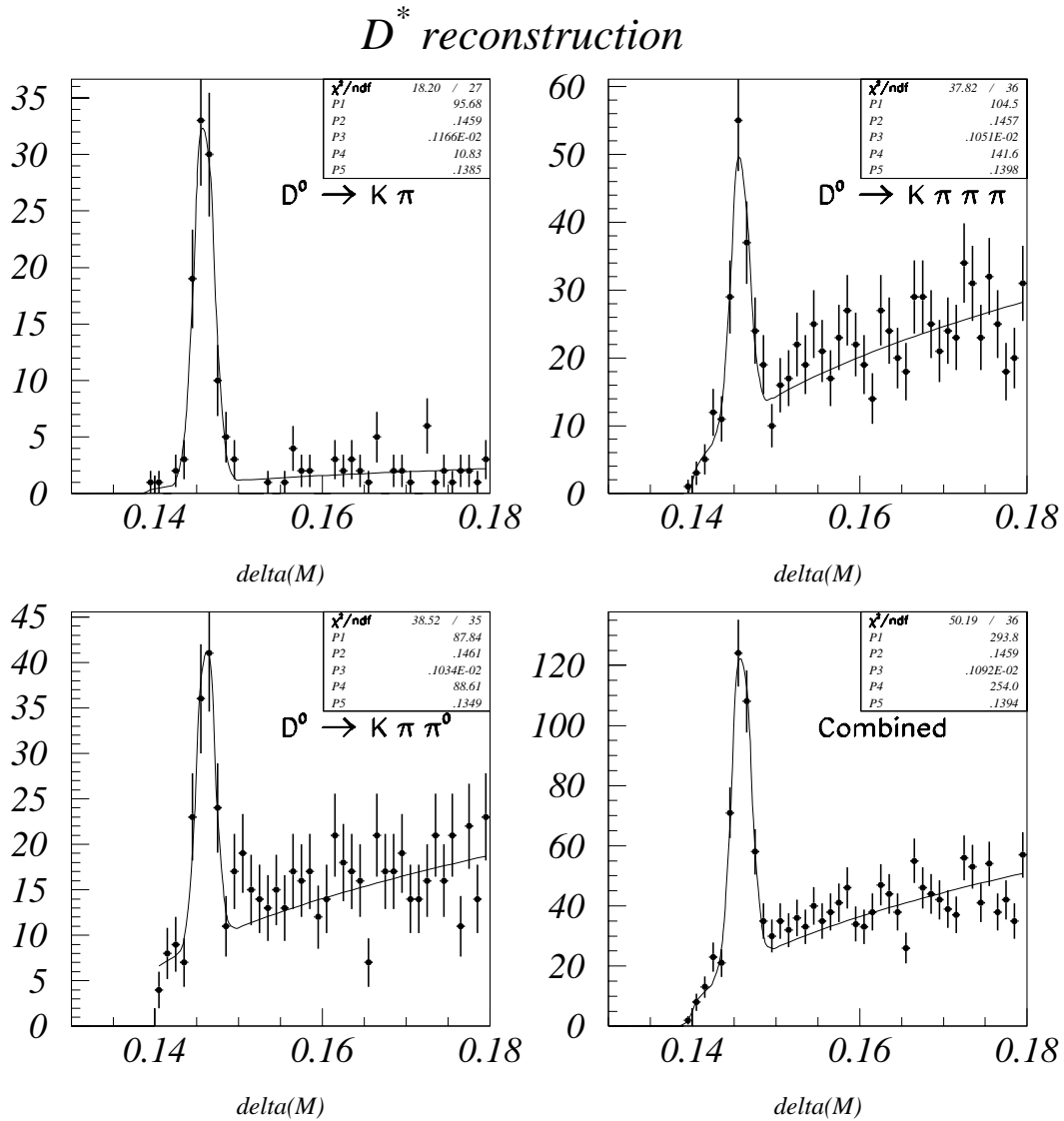


Figure 4-29. Δm distributions obtained in a sample of 10000 $B^0 \bar{B}^0$ events, for the different D^0 decay channels. Multiple entries, which occur frequently in the $K3\pi$ mode, have been removed by selecting the best D^0 candidate.

reconstruction chain and are given in Table 4-6. The π^0 reconstruction efficiency is presently low and this number should improve with time when better algorithms become available.

4.7 Multivariate Analysis Tools

In standard analyses one often has to characterize events for acceptance or rejection. This task is generally performed by applying cuts on various distributions which distinguish signal events from background. This approach is not always the optimal solution to the problem because all the information (the shapes of the variable distributions, the correlations between the variables) is not exploited, and this leads to a loss in signal efficiency. Statistical methods based on multivariate analysis have been developed over many years to tackle this kind of problem. For historical reasons these methods have been focused on linear problems which are easily tractable. In order to deal with nonlinearities, artificial neural networks have been shown to be a powerful tool in the discrimination task, and during the last decade they have been more and more extensively used in the particle physics community, either for searches for new particles (top, Higgs) or in B physics at LEP.

In the specific case of the BABAR experiment, in order to measure CP violation it will be necessary to suppress the huge $q\bar{q}$ background to a level of some 10^{-5} , or even less, and to tag with a reasonably high efficiency the CP -mode B candidate after reconstruction. In the first step of the background rejection, one deals with loose cuts, in which the signal sample is preserved with the maximum possible efficiency, but for the tagging and the remaining background suppression, the use of multivariate analysis provides a quantity which can be used as a weight for the event to originate from a b or \bar{b} quark or continuum background.

4.7.1 Presentation of the Different Methods

In this section, the different multivariate analysis methods used in the rest of this book are summarized. In order to separate a signal from its background, the simplest approach consists of applying cuts to the discriminating variables. First, a method (Genetic Algorithm) which allows the optimization of a set of cuts is presented. Then, a likelihood method (Parameterized Approach) which deals with the shape of the distributions of the discriminating variables is described. Finally, two methods are presented, (Fisher and Neural Network approaches) in which the correlations between the variables are taken into account respectively by a linear or nonlinear combination of the variables.

In the following discussion, the case where one has to discriminate between two classes of events is considered. One class is associated with the signal — the events to be characterized. The other

class is referred to as background. These methods are collected together in a single package called `Cornelius` which returns the probabilities for an event to belong to the two classes, according to any of the different methods.

4.7.1.1 Method to optimize cut approaches: genetic algorithms

Genetic Algorithms [28] are search algorithms based on the mechanics of Darwinian evolution: survival of the fittest. Each possible solution to a given problem (*e.g.*, a set of cuts on some discriminating variables) is considered an *individual*: each cut may be regarded as one *gene*, the set of cuts comprising the individual. The genetic algorithm is designed to find the best solution to the problem from a *population* of possible solutions. The algorithm calculates a *fitness* value for each individual (set of cuts). This is specified by the user with his/her problem in mind, and could be, for example, a measure of the signal to background ratio for each set of cuts (individual). Then the worst candidate solutions (the least fit) are removed from the population. The algorithm then acts on the surviving solutions using three fundamental (genetic) operators: *reproduction*, *crossover* and *mutation*: more individuals are “spawned” from combinations of the surviving ones in order to form a new (descendant) population, which retains the best characteristics of the previous one. The individuals comprising the population improve, on average, after each iteration, *i.e.*, they gain better and better *fitness* values.

In experimental particle physics it has been demonstrated [29] [30] that genetic algorithms can help in physics analysis when statistical significance optimization is needed. Applications of genetic algorithms [29] include distinguishing signal from background (in rare decays) and flavor tagging.

4.7.1.2 The parameterized approach

The Parameterized Approach (PA) [31] is based on the use of relative likelihood and is constructed from the distributions of the discriminating variables for the two classes of events (1 and 2) which should be distinguished. Ideally, for N discriminating variables, the likelihood for an event to belong to the class α ($\alpha = 1$ or 2) is given by the N -dimensional density distribution $g^\alpha(x_1, \dots, x_N)$. To characterize this event one can then construct the ratio of the likelihood for the two hypotheses:

$$X_{PA} = \frac{g^1(x_1, \dots, x_N)}{g^1(x_1, \dots, x_N) + g^2(x_1, \dots, x_N)}. \quad (4.12)$$

In practice, it is difficult to obtain N -dimensional distributions for $g^1(x_1, \dots, x_N)$ and $g^2(x_1, \dots, x_N)$. Hence in the PA, the approximation may be made that the discriminating variables are uncorrelated, *i.e.*, that:

$$g^\alpha(x_1, \dots, x_N) = \prod_{i=1}^N g_i^\alpha(x_i), \quad (4.13)$$

where $g_i^1(x_i)$ ($g_i^2(x_i)$) is the one-dimensional density distribution of the variable x_i for events of Class 1 (2). Several points should be emphasized:

- By construction, X_{PA} tends to 1 for Class 1 events and tends to 0 for Class 2 events.
- If a discriminating variable x_i is not useful, ($g_i^1(x_i) \simeq g_i^2(x_i)$ over all the range considered for x_i), it does not dilute the information from the other discriminating variables.
- If there is no correlation between the different discriminating variables the combined variable X_{PA} is optimal.
- In the case where there are correlations between the discriminating variables, some information is lost. Nevertheless the use of X_{PA} as a new discriminating variable (cf. Probability building below) insures that no bias is introduced into the analysis. However, care should be taken not to incorporate too many correlated variables, to avoid a dilution of the discriminating power of the PA.

Despite the above advantages, the PA may be improve for a given application by the use of two-dimensional distributions for the highly correlated pairs of variables.

4.7.1.3 Linear multidimensional methods (Fisher, Mahalanobis)

In Linear Discriminant Analysis (LDA) [32], also known as the Fisher method, the initially selected N variables which characterise the events are combined linearly to provide the best separation between the two classes of events. The discrimination task consists of determining an axis in the R^N space of the discriminating variables such that the two classes are maximally separated. In order to apply this method, one needs only the mean values of each variable over the full sample, $(\bar{\mathbf{x}})$, the means over each class, $(\bar{\mathbf{x}}_1, \bar{\mathbf{x}}_2)$, and the total variance-covariance matrix, $T_{\mu\nu}$. This matrix may be separated into two components: $T_{\mu\nu} = W_{\mu\nu} + B_{\mu\nu}$ where $W_{\mu\nu}$ and $B_{\mu\nu}$ are the Within- and Between-class matrices respectively. W reflects the dispersion of the events relative to the center of gravity of their own class, and B represents the distance of a class to the total center of gravity.

The distance between the projected points will naturally be maximum along the direction defined by the line between \mathbf{x}_1 and \mathbf{x}_2 . Then the segment $(\bar{\mathbf{x}}_1, \bar{\mathbf{x}}_2)$ is the projection axis. In his original work [32], Fisher proposed to normalize the projected distance by the quadratic sum of the projected dispersion of each class. Mathematically, discriminating an event means: compare the value of a discriminating function (the projection) for the event (\mathbf{x}), given by

$$X_{FI} = \frac{\sqrt{n_1 n_2}}{n} (\bar{\mathbf{x}}_1 - \bar{\mathbf{x}}_2)^T W^{-1} \mathbf{x} \quad (4.14)$$

with some threshold value. For the case of interest here, the threshold is

$$\theta_0 = \frac{\sqrt{n_1 n_2}}{n} (\bar{\mathbf{x}}_1 - \bar{\mathbf{x}}_2)^T W^{-1} (\bar{\mathbf{x}}_1 + \bar{\mathbf{x}}_2) / 2 \quad (4.15)$$

where n_1, n_2 are the number of events in each sample and n is the total number of events. More generally, as will be discussed below, one merely calculates the probability for X_{FI} to be in each class and uses these probabilities rather than making a cut. The Mahalanobis analysis uses the full covariance matrix instead of the W matrix. An event is classified in Class 1 if $X_{FI} > \theta_0$. Otherwise, it is classified in Class 2. It is often preferable to compare to 0, in which case the discriminating function is simply redefined by $X_{FI} - \theta_0$.

4.7.1.4 Nonlinear multidimensional methods (neural networks)

A natural extension of the previous linear approaches is to use a nonlinear one [33], *e.g.*, neural networks (see also Section 4.3.4). Here, the focus is on the multilayer perceptron architecture (MLP) using back-propagation of the error. The basic building block of the architecture of the NN is a processing element called a neuron. To this single neuron j is associated N input variables x_k and a response, the output z_j . The inputs are linearly combined according to some parameters called weights, ω_{jk} . A constant term (the threshold θ_j) can be added to the weighted sum of the inputs, giving the signal Z which will activate the neuron:

$$Z = \sum_{k=1}^N \omega_{jk} x_k + \theta_j \quad (4.16)$$

The activation of the neuron j is simulated by evaluation of a nonlinear function $a(x)$ at the point Z ,

$$z_j = a(Z) \quad (4.17)$$

where the activation function is generally given by the sigmoid function

$$a(x) = \frac{1}{2}(1 + \tanh x). \quad (4.18)$$

For the tagging, background fighting, and particle ID studies, two different packages were used: the feed-forward NN developed by the JETNET group [34], and the C++ package (NNO [16]). In the MLP architecture ($N : N_h : 1$), the neurons are put into layers. The data flow is directed from the first layer of N data inputs (discriminating variables) to the last layer, which gives the response of the NN, through N_h neurons placed in hidden layers in between. The weights ω_{1j} and ω_{jk} of the connection between the neurons, respectively (output layer–hidden layer) and (hidden layer–input layer), are determined by minimizing the error function:

$$E = \frac{1}{2n} \sum_{p=1}^n (X_{NN} - t_1^p)^2, \quad (4.19)$$

where X_{NN} is the output parameter defined as a function of the input parameters x_k by:

$$X_{NN} = a\left(\sum_{j=1}^{N_h} \omega_{1j} a\left(\sum_{k=1}^N \omega_{jk} x_k + \theta_j\right) + \theta_1\right), \quad (4.20)$$

where n is the number of patterns (number of events used for the training) and t_1^p is the desired value of the output parameter. This parameter, t_1^p , is fixed to 0 if the pattern p is a background event and t_1^p is fixed to 1 if the pattern p is a signal event.

4.7.2 Description of `Cornelius`

Considering the large choice of multivariate analysis methods and the need to compare their performances, it was considered desirable to provide common software for all of them. In order to achieve this goal, a general purpose package, named `Cornelius`,² was developed. This groups together the above described methods (except genetic algorithms). It handles the input/output requirements of each multivariate method, and translates the outputs into probabilities.

In general, the output of each method can be used in two ways: one can either apply a cut on the output value to associate an event to a given class, or one can derive from the distributions of the output a probability for an event to belong to a given class.³ In order to exploit the full information carried by these methods, one should use the probabilities (cf. [35]). If there are two classes of events, the relative probability for an event to originate from Class 1 is defined by:

$$p_1 = \frac{f_1 F_1(X)}{f_1 F_1(X) + f_2 F_2(X)} \quad (4.21)$$

where the f_i are the fractions of events coming from class i ($f_1 + f_2 = 1$) and F_i the density distribution of the output variable X (*i.e.*, $X = X_{NN}, X_{FI} \dots$), normalized to unity. An example is provided in Figure 4-30, where the F_i distributions are shown and the corresponding p_1 distribution.⁴

By default, `Cornelius` is set up to perform tagging (cf. Section 4.8), but it also provides the user with various tools and options. In particular, for a user wishing to use the package for another specific application, it handles the learning phase of the multivariate methods and proceeds to an evaluation of the best set of variables to be retained.

Among the features of the package is the possibility for the user to treat events differently depending on the reconstructed final state: one may introduce different categories of final states. An event may belong to several such categories and one must predefine a ranking between them. For example, when used for tagging, the package treats differently events with one lepton and events with one lepton and a Kaon, using different variables. In that case, the chosen hierarchy uses the second category because its discriminating power is better.

²Combined Optimal Reconstruction with NEural network and Likelihood for Identification USage.

³This does not apply to the genetic algorithms method, as there the output is a binary one.

⁴Some peaks may appear in the probability distribution. This is simply due to relation (4.21) when $F_1(X) \propto F_2(X)$ within a given range in X .

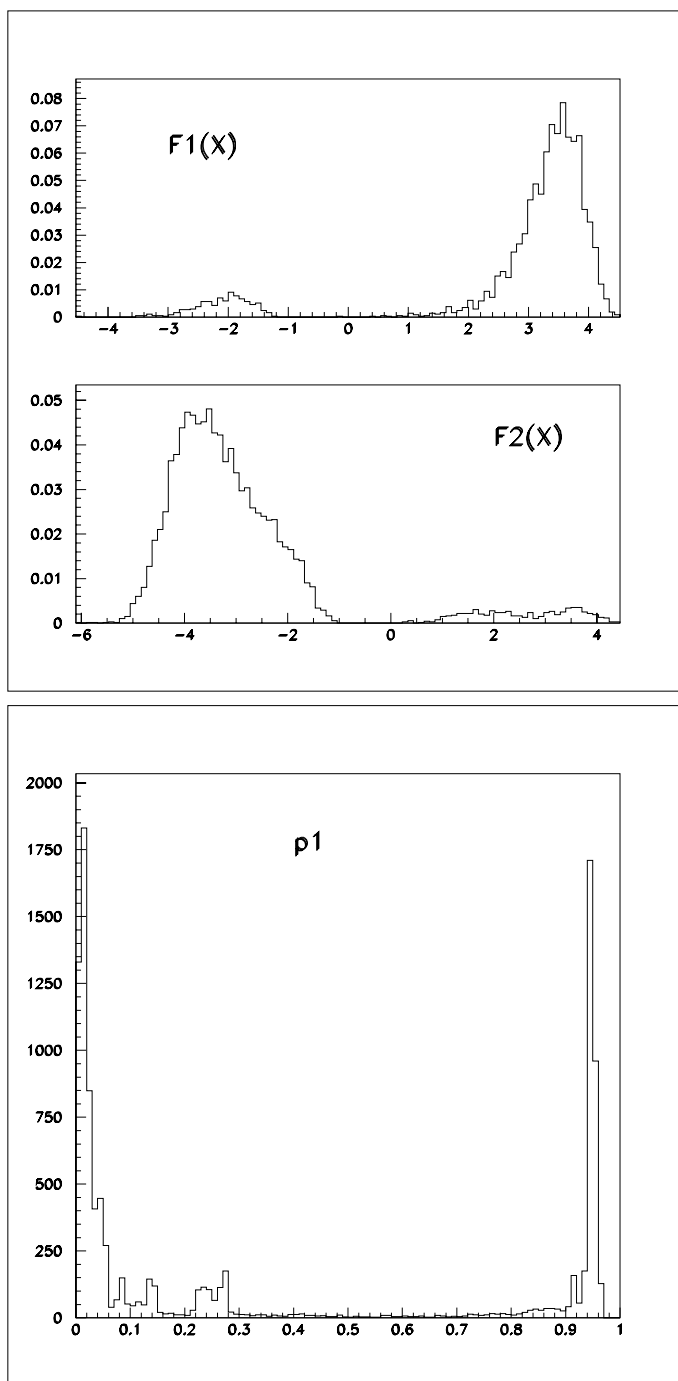


Figure 4-30. Example of the distribution of the output of the FI method (on the left) and the related probability (on the right). These distributions are obtained with the discriminating variables defined for the tagging category (lepton+kaon) (cf. Section 4.8.4).

4.8 Tagging

The physical asymmetries which need to be measured in order to establish CP violation depend on the time difference $t_{CP} - t_{tag}$ between the decay of the CP -mode B meson, B_{CP} , and the decay of the recoiling meson B_{tag} , and on the flavor of the b quark (b or \bar{b}) of this tagging- B . The purpose of the tagging is to identify this flavor.

4.8.1 Direct- and Reverse-Sign Classes

The b -quark flavor is derived from the correlation between the sign of the charge of the quark and signed characteristics of the decay products. The presence of a lepton in the final state provides the most simple example of such a correlation. If the lepton stems from a semi-leptonic decay of the B meson, as in Fig. 4-31(a), the sign of the charge of the lepton is identical to q_b , the sign of the b quark. However, the lepton may originate from a cascade, in which case the sign of its charge may be opposite to that of q_b , as in Fig. 4-31(b), or the same as q_b , as in Fig. 4-31(c). Whereas it is not possible to distinguish between the two types of cascade decays, leptons from the semi-leptonic decays ($b \rightarrow c$) may be distinguished from those coming from cascade decays by using the momentum of the lepton in the $\Upsilon(4S)$ rest frame, since the spectrum of those is known to be harder than the spectrum of the cascade decays.

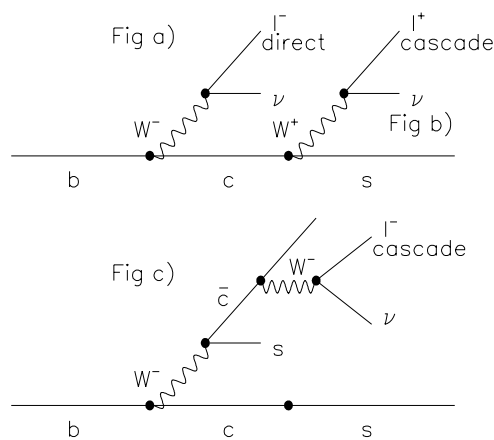


Figure 4-31. (a) Direct production of a lepton. (b) Cascade production of a lepton with reverse sign. (c) Cascade production of a lepton with direct sign.

More generally, events can be sorted into two classes: the direct-sign class, in which the sign attributed to the decay products is the same as the sign of the q_b , and the reverse-sign class, in which the sign attributed to the decay products is the opposite of the sign of q_b . It is the purpose of the tagging to perform the most efficient discrimination between these two classes, hence performing the best identification of the flavor of the tagging B .

4.8.2 The Tagging Strategy

The classification of events in the direct-sign class or in the reverse-sign class is based on a category (*e.g.*, a lepton is present in the final state (see below)) and on kinematical and/or topological quantities (*i.e.*, a set of discriminating variables) characterizing the tagging- B decay products. As discussed in Section 4.7.2, two approaches can be adopted to tag events on the basis of a set of discriminating variables. One can either use a fixed criterion to associate each event to a given class, or one can associate to each event, a probability to belong to each class. This latter approach is the method advocated here.

The measured CP asymmetries are quantities which are diluted by two effects:

- The tagging efficiency ϵ_{tag}^c , which is the fraction of events which can be associated to a tagging category. This parameter contains the branching ratio of the decay channel and the particle ID efficiency of the tagging particles.
- The tagging separation $\langle s^2 \rangle$, which is a measurement of the tagging purity. In the fixed criterion approach, the separation is a fixed number which can be written as

$$\langle s^2 \rangle = (1 - 2w)^2, \quad (4.22)$$

where w is the wrong tag probability, *i.e.*, the probability that the criterion associates an event to the wrong class. In the probability approach, the separation is given by

$$\langle s^2 \rangle = \left\langle \left(\frac{p_R - p_D}{p_R + p_D} \right)^2 \right\rangle = \langle (1 - 2p_D)^2 \rangle = \langle (1 - 2p_R)^2 \rangle, \quad (4.23)$$

where p_D (p_R) is the relative probability (cf. Section 4.7.2) for the tagging B of a given event to belong to the direct-sign (reverse-sign) class.

In both approaches, apart from other detector and background effects, the statistical uncertainty on the measured asymmetries for events tagged in a given category (c) is inversely proportional to the product of the tagging efficiency and the separation:

$$\sigma \propto \frac{1}{\sqrt{\epsilon_c^{\text{tag}} \langle s_c^2 \rangle}}. \quad (4.24)$$

Hence, as far as CP violation is concerned, the absolute separation, defined by the sum:

$$S^2 = \sum_{category} \epsilon_c^{tag} \langle s_c^2 \rangle , \quad (4.25)$$

plays the role of a selection efficiency common to all CP channels. It is therefore a crucial task to maximize this quantity, in order to maximize the sensitivity of the experiments to CP violation, without introducing large systematics effects.

4.8.3 Definition of Discriminating Variables

The tagging is performed using variables computed after the explicit removal from the event of the tracks belonging to the CP final state. Thus the correlation between the tagging performance and the CP final state under study are minimized. The discriminating variables computed are based on the information associated with the leptons (muons and electrons) and the charged kaons from the decay of the tagging B^0 .

In order to discriminate between direct-sign leptons, mostly produced by the $b \rightarrow c$ transitions, and reverse-sign leptons produced by the cascade decays of the c quarks, many topological and kinematical variables (see Fig. 4-32) have been studied. A systematic study of the performance of each variable has enabled the definition of the following set of discriminating variables:

1. P_l^* , the lepton momentum in the $\Upsilon(4S)$ center of mass (CM) system
2. M_{recoil} , the recoil mass of the lepton.
3. P_{miss} , the missing momentum of the event.
4. θ_{miss} in the B^0 CM, the angle between the lepton direction and the missing momentum of the tagging B .
5. θ_{min}^W in the B^0 CM, the angle between the the direction of the reconstructed virtual W and the particle closest to this direction. The direction of the virtual W is approximated by the sum of the lepton and missing momenta.
6. E_{90}^W , the energy in the B^0 CM in the 90 degree cone defined around of the direction of the reconstructed virtual W .
7. $Asym$, the asymmetry in the B^0 CM between the projection with respect to the lepton direction of the sum of all the particle momenta in the lepton hemisphere, and the projection of the sum of the other particles' momenta.
8. Q^2 , the invariant mass of the virtual W from the lepton momentum and the reconstructed neutrino momentum.

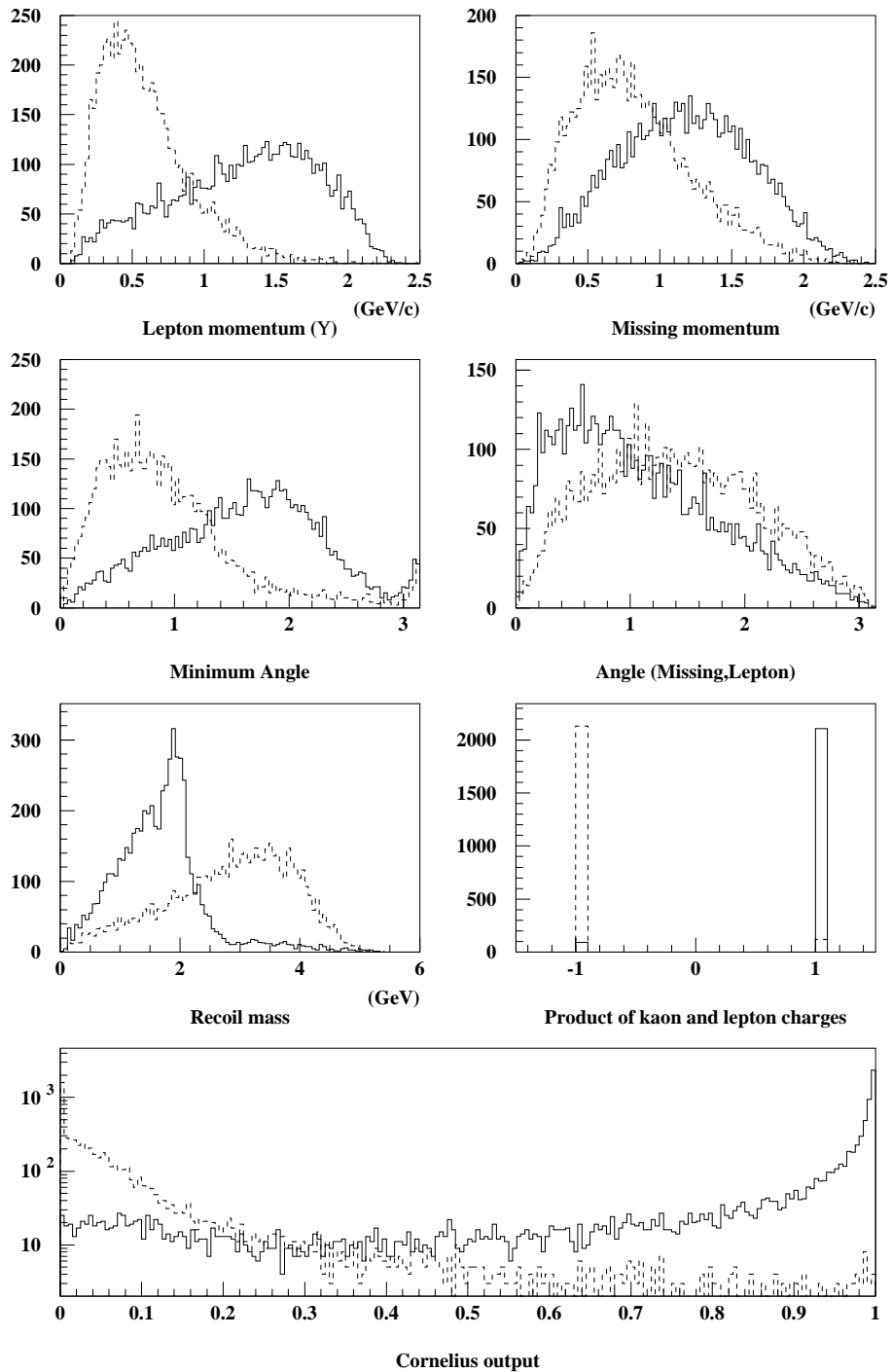


Figure 4-32. Distributions of the discriminating variables (P_l^* , M_{recoil} , P_{miss} , θ_{miss} , θ_{min}^W , $Q_l Q_K$) of the lepton and the Cornelius output for "direct-sign" (solid line) and "reverse-sign" (dotted line).

9. $Q_l Q_K$, the product of the charge of the lepton and that of the kaon.
10. $Q_{l1} Q_{l2}$, the product of the charges of the two leptons.

In the case of the tagging performed with the charged kaons, the sign of the kaon's charge is a very efficient discriminating variable. However, the discrimination between the direct-sign and reverse-sign kaons may be improved by introducing two variables:

1. N_{imp} , the number of tracks in the event with impact parameter ≥ 1 mm in the transverse plane.
2. M_{miss} , the missing mass of the tagging B^0 .

When two kaons (of any charge) are produced by the same B^0 , the kaon information is not useful for tagging. The purpose of these two discriminating variables is to identify the events with an associated neutral kaon. N_{imp} helps to discriminate events with decays of long-lived particles, such as K_S^0 , and M_{miss} allows the identification of Significant mass loss as K_L^0 .

4.8.4 Definition of Categories of Events Treated

In tagging studies, the events are separated into several different categories: events with at least one lepton, events with one lepton and one kaon, and events with a single kaon. This splitting into categories allows the treatment of about 60% of the events produced. In order to take into account the fact that the discriminating variables may have different shapes due to the different nature of the particle identification algorithms, a separate category is created for electrons and muons. Therefore, for the three methods (PA, LDA, and NN), there are five categories with a set of discriminating variables:

Lepton: P_l^* , M_{recoil} , P_{miss} , θ_{miss} , θ_{min}^W .

Lepton and kaon: $Q_l Q_K$.

Kaon: N_{imp} , M_{miss} .

In order to increase the performance of the NN method, a special category has been created. In this, the above five categories (lepton, lepton+kaon) are merged into a single category where all the variables are treated at the same time. Moreover, some variables linked to a second lepton are added. The set of 15 variables used for this category is as follows:

1st Lepton: P_l^* , M_{recoil} , P_{miss} , θ_{miss} , θ_{min}^W , E_{90}^W , $Asym$, Q^2 .

Kaon: $Q_l Q_K$, N_{imp} , M_{miss} .

2nd Lepton: P_l^* , M_{recoil} , E_{90}^W , $Q_{l1} Q_{l2}$.

4.8.5 Performances of the Tagging Methods

The performances obtained for the different methods implemented in `Cornelius` and for different categories of event (one or two categories for the leptons) are summarized in Table 4-7. These results were obtained using the full simulation and reconstruction chain of BABAR and were generated with the standard event generator, `EvtGen`. The identification of the reconstructed tracks was performed with a preliminary (and unoptimised) version of the particle identification tools, a later version of which was described in Section 4.3.

The three different methods are seen to each have approximately the same performance. However, a slight gain, essentially due to the increase in the number of discriminating variables (15 instead of 5), is observed when the lepton and lepton+kaon categories are merged into a single category.

In terms of separation, the total performance of around 23% reported in Table 4-7 may be considered a lower limit of the eventual tagging performance, in view of the fact that these results were obtained with unoptimised particle ID software. In order to obtain an upper limit on the performance, the same tagging method and the same set of discriminating variables was used with perfect particle ID (using Monte Carlo truth information). A total separation of 36% was achieved, as seen in Table 4-8.

It was found that the absolute performance of the tagging software is very sensitive to the assumed branching ratios in the event generator; for example, the recent measurement of the branching ratio, $\mathcal{B}(\bar{B} \rightarrow D\bar{D}X) = 7.9 \pm 2.2\%$ ⁵ by CLEO [36], leads to a loss of $\simeq 20\%$ of leptonic separation. This is because in this channel, secondary leptons are produced with the same sign as direct leptons in the decay of the \bar{D} (cf. Fig. 4-31-c).

With the tools used at the time of this tagging study, it is very difficult to give an accurate figure for the eventual tagging performance of BABAR, but the final number is likely to be between the two limits 23% and 36%. A value of 30% has been used for the estimates of eventual CP -reach in the rest of this book.

⁵These recent results are included in `EvtGen`.

Table 4-7. Comparison between the different discriminating methods (PA, LDA, and NN) obtained using fully reconstructed $B\bar{B}$ sim events with preliminary particle ID software.

Tagging Category	Methods	Separation $\langle s^2 \rangle$ (%)	Tagging Efficiency ϵ_{tag} (%)	Absolute Separation $\epsilon_{\text{tag}} \langle s^2 \rangle$ (%)
<i>Electron</i> (1)	PA	34.6	12.9	4.5
	LDA	34.2	12.9	4.4
	NN	36.0	12.9	4.6
<i>Electron</i> + <i>Kaon</i> (2)	PA	60.2	6.0	3.6
	LDA	62.6	6.0	3.8
	NN	60.6	6.0	3.6
<i>Muon</i> (3)	PA	31.5	7.9	2.5
	LDA	31.1	7.9	2.5
	NN	34.6	7.9	2.7
<i>Muon</i> + <i>Kaon</i> (4)	PA	51.8	4.6	2.4
	LDA	57.0	4.6	2.6
	NN	57.5	4.6	2.6
<i>Electron</i> (5)	NN	44.4	18.9	8.4
<i>Muon</i> (6)	NN	42.9	12.5	5.4
<i>Kaon</i> (7)	PA	39.3	24.2	9.5
	LDA	39.5	24.2	9.6
	NN	39.5	24.2	9.6
TOTAL (1)+(2) (3)+(4)+(7)	PA		55.6	22.5
	LDA		55.6	22.9
	NN		55.6	23.1
TOTAL (5)+(6)+(7)	NN		55.6	23.4

Table 4-8. Comparison between the different discriminating methods (PA, LDA, and NN) obtained with fully reconstructed `BBSim` events and using perfect (MC-truth) particle ID.

Tagging Category	Methods	Separation $\langle s^2 \rangle$ (%)	Tagging Efficiency ϵ_{tag} (%)	Absolute Separation $\epsilon_{\text{tag}} \langle s^2 \rangle$ (%)
<i>Lepton</i> (1)	PA	41.5	25.7	10.7
	LDA	42.0	25.7	10.8
	NN	43.1	25.7	11.1
<i>Lepton</i> + <i>Kaon</i> (2)	PA	77.6	13.8	10.7
	LDA	77.4	13.8	10.7
	NN	81.1	13.8	11.2
<i>Lepton</i> (3)	NN	58.0	39.5	22.9
<i>Kaon</i> (4)	PA	60.0	21.3	12.8
	LDA	59.9	21.3	12.8
	NN	60.8	21.3	13.0
TOTAL (1)+(2)+(4)	PA		60.8	34.2
	LDA		60.8	34.3
	NN		60.8	35.3
TOTAL (3)+(4)	NN		60.8	35.9

4.8.6 Measuring the Tagging Performance with Real Data

The uncertainty on the tagging purity has a direct impact on every CP violation measurement because $A_{\text{meas}} = (1 - 2w)A_{\text{phys}}$, where A_{meas} and A_{phys} are the measured and the true asymmetry. Moreover, the tagging algorithm depends crucially on a number of features of the distributions of the discriminating variables, including their correlations. Therefore, it is mandatory to be able to measure the performances of the tagging algorithms with a data sample, independent of the Monte Carlo simulation, and to extract the distributions of the discriminating variables used in the algorithm.

Although a number of checks can be done on a generic $B\bar{B}$ sample, studying the multiplicities of leptons and kaons, for example, and momentum spectra *etc.*, the most important studies are those on a sample that is independently tagged, where for example, one B^0 meson has been completely reconstructed in an exclusive state [37]. The tagging algorithm can then be applied to the recoil neutral B meson, in the same way as for a CP analysis. The measurement of the wrong tag probability, w , can then be done very easily. In fact,

$$w = \frac{f_{\text{mix}} - \chi}{1 - 2\chi} \quad (4.26)$$

where f_{mix} is the fraction of events that are classified as mixed according to the tagging and χ is the time-integrated mixing probability.⁶

A more sophisticated approach is to use the time information by fitting the time distributions of events that have been classified as mixed and unmixed with

$$M(t) = (1 - 2w)m(t) + wu(t) \quad \text{and} \quad U(t) = (1 - 2w)u(t) + wm(t). \quad (4.27)$$

Here, $m(t)$ and $u(t)$ are the time distributions of true mixed and unmixed events convoluted with the experimental resolution. Using this method, the experimental error on w is 50% lower than using the time-integrated method discussed above.

The efficiency ϵ_{rec} of the exclusive reconstruction of a B^0 can be estimated in two ways: using the `Aslund` efficiencies for the reconstruction of the modes $B^0 \rightarrow D^{(*)}h$ where $h = \pi, \rho, \pi\pi\pi$, a value $\epsilon_{\text{rec}} = 2 \times 10^{-3}$ is obtained. As a lower limit, it will be assumed that this efficiency will be at least as large as at CLEO, where it was 0.3×10^{-3} [38].⁷ Taking conservatively the latter figure, a sample of 10^4 tagged B^0 would be obtained for 30 fb^{-1} , leading to an error on $1 - 2w$ of 0.7%. The same method can be applied in the case of the probability approach by considering the value of $\langle s^2 \rangle$ on this tagged sample.

Using the same sample, it is possible to extract the distributions of the discriminating variables for direct and reverse signs. In this case, as previously discussed, both a time-integrated measurement and a time-dependent fit can be used. Both approaches have been implemented and tested on data generated with the fast simulation program `Aslund`. A method using the tagged sample to train a neural network has also been developed and tested on simulated data.

Thus, the performances of the tagging algorithms can be checked and measured using the data themselves, completely independent of the Monte Carlo simulation. The precision of this measurement, which is a source of systematic error for every CP violation analysis, will be below 1% for one year of nominal luminosity, much lower than the overall statistical error.

⁶The small contamination which will be present in the tagged sample has been neglected and it has been assumed that the flavor of the completely reconstructed B^0 meson is known without ambiguity. A realistic analysis can easily take these small effects into account.

⁷Though the BABAR acceptance is slightly smaller than that of CLEO, improvements in particle ID should make up for this loss.

4.8.7 Future Prospects and Improvements

Within the present version of the tagging package, several improvements have been considered. In addition, the intrinsic performance of the particle identification will improve. Various studies have been performed to improve the lepton categories, and discriminating variables such as those related to the information of the soft pion produced in the decay of a $D^{*\pm} \rightarrow D^0\pi^\pm$ have been reviewed [39].

For the Kaon-alone category, the discriminating variables applied improve the separation by a few percent. A more elaborate program has already been started to improve the tagging. It relies on the fact that b quarks decay almost exclusively to c quarks. As a consequence the exclusive reconstruction of charm mesons (and baryons) provides very good tagging information. D^0 , D^+ , and D_s^- mesons can be used as \bar{B}^0 tags. Compared to the more classical kaon-tag method, charm tagging offers three advantages:

- A higher tagging purity for charm tagged events already correctly tagged with kaons;
- When a D meson is reconstructed, a correct assignment of an opposite sign to the tagging kaon (the improvement occurs mainly when two kaons are produced but only one identified);
- Addition of new tags for previously untagged events.

Preliminary estimates show that D decay modes containing up to four charged tracks and two π^0 s could provide a relative enhancement of the overall tagging performance of the order of 20%. Work is in progress to determine to what extent large multiplicity D decays can really be used for this purpose. If proven, this new tagging method will be incorporated into *Cornelius*.

4.8.8 Conclusions

A general package, named *Cornelius*, has been set up for multivariate analyses. It offers several different methods (presently a Likelihood approach, a Fisher discriminant, and a Neural Network) to discriminate between hypotheses given a set of discriminating variables. Its main application is currently the $B^0 \bar{B}^0$ tagging for CP violation studies. It provides the *probability* that each event is a B^0 or a \bar{B}^0 . Rather than using a deterministic estimate of the type of event (with some fraction of wrong tags) this probability may be input to the final likelihood fit (for the extraction of the amount of CP violation) giving results which are much closer to optimal. The so-called *dilution* factor used in the deterministic approach $(1 - 2w)^2$ (with w being the fraction of wrong tags) is replaced by the *separation*, which is a measurement of the overlap of the output distributions for the two hypotheses tested.

The absolute separation (*i.e.*, accounting for the tagging efficiency) obtained for the tagging lies in the range 23–36%, depending on whether one uses the Monte Carlo truth information for identifying leptons and kaons (36%) or the preliminary version of the general particle identification tools (23%). It must be stressed that the particle identification is in a preliminary stage at the time of these studies and substantial improvements are expected before BABAR begins to take real data. For this reason, the average of 30% has been used for all the CP violation analyses presented in this book.

Finally, the tagging performance relies on some input distributions obtained from the Monte Carlo. They will eventually be extracted directly from the data, thereby minimizing systematics, once sufficient data become available.

4.9 Tools for Continuum Identification

The issue of continuum background suppression is an important one for BABAR, where typically the branching ratios for the channels of interest are very small. The challenge is to achieve background rejection factors in many analyses, of at least 10^5 , with as little loss of signal as possible. Many of the techniques and variables traditionally used for background suppression are well known and applicable to a range of analyses. A set of tools has therefore been developed for dealing with the general procedure of discriminating signal from continuum background.

4.9.1 Criteria for Continuum Identification

A powerful method for discriminating signal events from $q\bar{q}$ background events exploits the differences in their characteristic topologies. In a true signal event, the primary e^+e^- pair produces a $B\bar{B}$ pair via the $\Upsilon(4S)$ resonance. In the $\Upsilon(4S)$ rest frame, the B mesons have low momenta, so that the decay of each B meson is nearly isotropic. An additional feature of a signal event is that there is no correlation between the directions of the decay products coming from each of the two B mesons.

In a light-quark (u, d, s) continuum event, however, the event shape has a pronounced two-jet structure, so there is a strongly preferred direction characterizing the whole event. B candidates from such an event will therefore tend to have less isotropic decay shapes in the $\Upsilon(4S)$ rest frame, and there will also be correlations between the directions of the decay products of the two B meson candidates, since they will tend to lie within the two jets. In a $c\bar{c}$ event, the jet structure is still present, but is less pronounced, and so the methods described here using shape variables will provide less discriminating power for this type of background.

A set of discriminating variables used for continuum identification and suppression has been chosen. The list is by no means exhaustive, and other variables may be added subsequently. In addition to characteristic shape variables for the event, the list includes properties of the CP candidate, and kinematic variables.

The variables in use are described below. Some of them can be applied generally to any decay, while others require modification according to the number of bodies in the final state of the B candidate decay. For the two-body case, the characteristic direction is clearly defined by the B decay axis, while for the three-body case, a suitable characteristic direction is the normal to the B decay plane. The choice of reference frame is another issue which can affect the discriminating power of the variables used. For global event variables, it is appropriate to use the $\Upsilon(4S)$ rest frame, while for variables using properties of the B decay products, the B rest frame is used. In practice, this distinction does not make very much difference, as the two frames are very similar, owing to the small momentum of the B in the $\Upsilon(4S)$ rest frame.

Another consideration when using each of these variables is the choice of the subset of the event to which it should be applied. For some variables, only the charged tracks in the event are used, while others apply to all charged and neutral candidates. For discrimination purposes, a variable may be applied globally to the event, or just to the decay products of one (the CP B) or other (the tag- B) candidate in the event (the latter is hereafter referred to as the ‘rest of the event’).⁸ All of the event shape variables described here are calculated as standard for the entire event and for the tag- B candidate, when these tools are invoked.

- **B^0 mass:** In each analysis the CP B decay is reconstructed for each event producing a set of ‘candidate’ particles. The invariant mass of the decay products from a signal candidate should be equal to the B mass, up to resolution effects. There are no real B mesons produced in continuum background events, so that the distribution of invariant mass for reconstructed B^0 candidates in these events has a wide range. The distribution is slowly falling in the region of the B mass. These effects are illustrated in Fig. 4-33 (a).
- **The Momenta of the CP B^0 and its decay products:** In a signal event the momentum of each B in the $\Upsilon(4S)$ rest frame is kinematically constrained to be ~ 0.35 GeV/c, while the B candidates produced from continuum events exhibit a wide range of momenta, as shown in Fig. 4-33 (b).
- **Sum of the transverse momenta of the rest of the event with respect to the B direction:** For a $q\bar{q}$ event, the transverse components of momenta for the rest of the event are small with respect to the B candidate direction, due to the jet structure, whereas for a $B\bar{B}$ event there is no such correlation.

⁸Though it is convenient to speak in terms of the CP B decays, the discussion in this section is general and applies equally to charged- B decays.

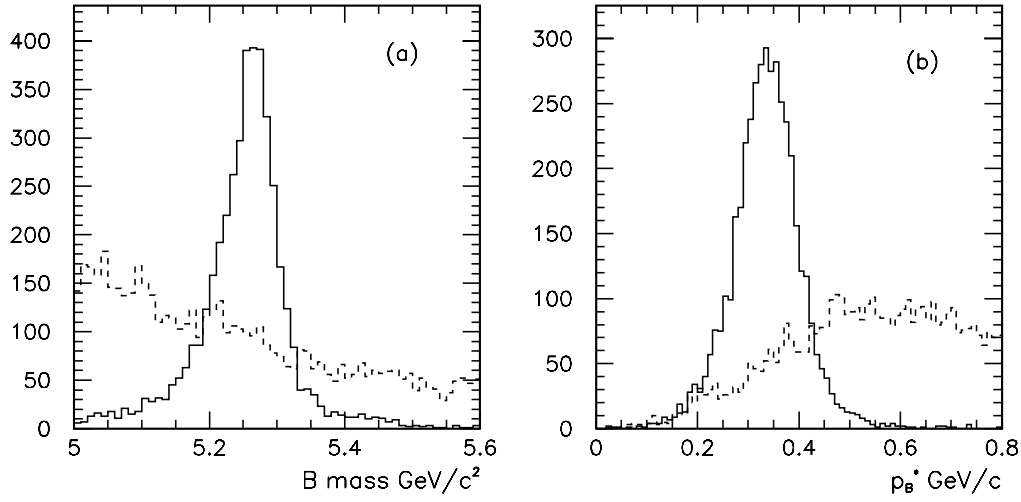


Figure 4-33. (a) B invariant mass, (b) momentum of the B in the $\Upsilon(4S)$ rest frame (signal: solid line, light-quark continuum: dotted line).

- **Thrust:** The thrust axis of an event, \hat{T} , is defined to be the direction which maximizes the sum of the longitudinal momenta of the particles. Thrust, T , is related to this direction [40] by

$$T = \frac{\sum_i |\hat{T} \cdot \mathbf{p}_i|}{\sum_i |\mathbf{p}_i|}. \quad (4.28)$$

The allowed range of T is (0.5, 1), where $T \sim 1$ corresponds to a highly directional event, and $T = 0.5$ corresponds to an isotropic event. Thrust distributions for a typical signal and continuum background are shown in Fig. 4-34 (a).

In a typical background event for a two-body decay, the decay products of the B^0 candidate each lie in one of the two jets and are therefore approximately back-to-back. Thus the decay axis of the B^0 candidate is roughly collinear with the thrust axis for the rest of the event. For a true signal event, the B^0 decay axis is uncorrelated with the thrust axis of the rest of the event, which in that case comes from the decay of the other B^0 meson.

For background discrimination, the cosine of the angle between the thrust axis of the rest of the event is taken with each of the following:

- The B direction,
 - Each B decay product direction,
 - The thrust axis of the CP B decay mode, and
 - The normal to the B decay plane, for a 3-body decay (see Fig. 4-35 (b)).
- **Sphericity:** As with thrust, sphericity provides good separation of $q\bar{q}$ continuum events and signal due to the jet structure of $q\bar{q}$ events. Sphericity is a measure of the sum of the

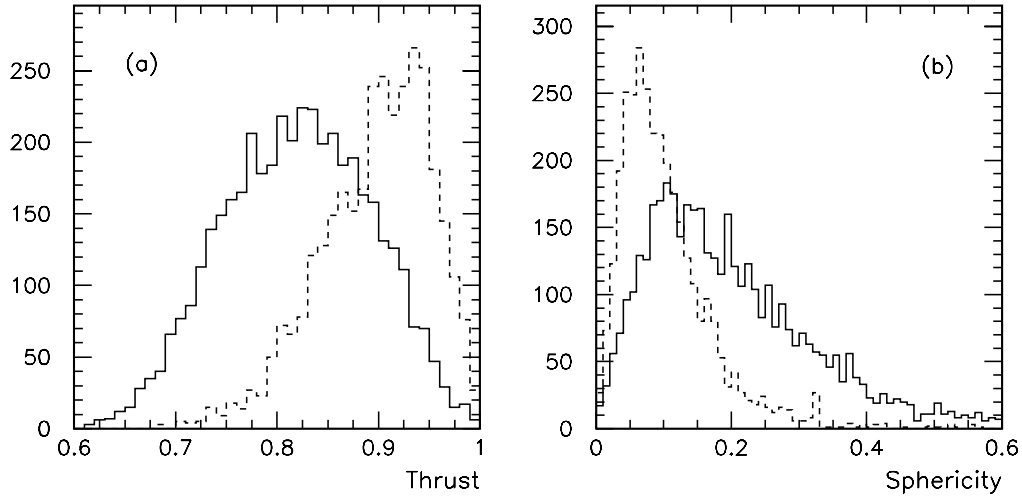


Figure 4-34. Examples of event-shape variables for the whole event: (a) thrust, (b) sphericity (signal: solid line, light-quark continuum: dotted line).

squares of transverse momenta for each track with respect to the event axis. Defined over the interval (0,1), with highly directional events having low sphericity, and isotropic events corresponding to sphericity = 1.

Sphericity is defined [41] as,

$$S = \frac{3}{2}(\lambda_2 + \lambda_3), \quad (4.29)$$

where λ_2 and λ_3 are the two larger eigenvalues of the diagonalized sphericity tensor

$$S^{\alpha\beta} = \frac{\sum_i p_i^\alpha p_i^\beta}{\sum_i p_i^2}, \quad (4.30)$$

where $\alpha, \beta = 1, 2, 3$ corresponds to the x, y, z components respectively. Sphericity distributions for a typical signal and continuum background are shown in Fig. 4-34 (b).

The Sphericity Axis of the system is determined by the direction of the eigenvector corresponding to the largest eigenvalue. The sphericity axis of the rest of the event is used in an analogous way to the thrust axis of the rest of the event (*e.g.*, see Fig. 4-35 (a)).

- **Aplanarity:** Aplanarity is a measure of the transverse component of momentum out of the event plane. It is related to the smallest eigenvalue of the sphericity tensor [41] by

$$A = \frac{3}{2}\lambda_3. \quad (4.31)$$

In the case of a totally planar event, $\lambda_3 = 0$, so the Aplanarity is zero. In an isotropic event the three eigenvalues are of equal magnitude ($\frac{1}{3}$), and the Aplanarity takes a maximum value of $\frac{1}{2}$.

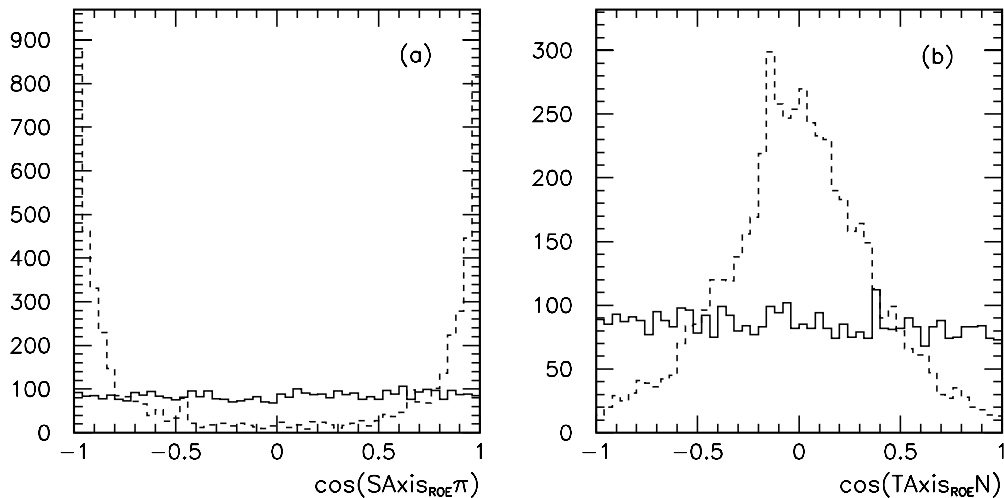


Figure 4-35. Examples of event shape variables (a) cosine of the angle between the sphericity axis of the rest of the event and the daughter pion (for the channel $B \rightarrow \rho\pi$), (b) cosine of the angle between the normal to the B decay plane and the thrust axis for the rest of the event (signal: solid line, light-quark continuum: dotted line).

- **Fox-Wolfram Moments:**

The Fox-Wolfram moments, H_l , are defined [42] as,

$$H_l = \sum_{i,j} \frac{|\mathbf{p}_i| \cdot |\mathbf{p}_j|}{E_{\text{vis}}^2} P_l(\cos\theta_{ij}) \quad (4.32)$$

where P_l are the Legendre polynomials, $\mathbf{p}_{i,j}$ are the particle momenta, θ_{ij} is the opening angle between particles i and j , and E_{vis} is the total visible energy of the event.

Neglecting particle masses, energy-momentum conservation requires that $H_0 = 1$. For 2-jet events, $H_1 = 0$ and $H_l \sim 1$ for l even, and $H_l \sim 0$ for l odd. For this application the ratio of Fox-Wolfram 2nd to 0th moments is used as the discriminating variable.

4.9.2 A Common Procedure for Background Fighting

A common procedure [43] has been developed to provide background suppression for any analysis. Many of the more general of the discriminating variables described above are automatically calculated, while the basic structure of these tools allows further variables to be calculated easily and added to the procedure. Each stage in the procedure is controlled by a module, as described below:

Filtering: Filtering is an optional step, allowing the application of a set of preliminary selections to every reconstructed event, in order to isolate a sample of events, each of which contains at least

one candidate B meson in the desired channel. The aim is to reduce the background sample by a significant fraction (typically one to two orders of magnitude), providing a condensed sample which contains the most dangerous $q\bar{q}$ background events for the signal channel considered, and of course, the signal. The cuts are loose enough to maintain signal efficiency as far as possible and are typically made on the masses and momenta of the CP -mode candidates.

User Analysis Module: This runs on the filtered or unfiltered events, and typically applies the same or a similar preselection as in filtering. Its output is a list of B candidates for each event. This list, together with details of the decay products for each reconstructed CP mode, are then passed to the background fighting module, BtaBgFighter.

Background Fighting: This tool has been set up to provide an interface between the various functions used to calculate a set of background discriminating variables, and the subsequent multivariate analysis tools (*e.g.*, `Cornelius`, see Section 4.7), which can be used to optimize background suppression. The aim is that it should supply a general list of variables which can apply to any channel, and that it should be straightforward to add further variables which are customized for particular channels. The output of the tool is an n-tuple containing the distributions for each variable.

Cornelius Training: This requires two n-tuples of the discriminating variables to be supplied, for signal and background events respectively. For the neural network approach at least 5000 entries are needed in each n-tuple to achieve good performance.

Cornelius Output: Having been trained on a $q\bar{q}$ sample, `Cornelius` can be implemented in the analysis in order to provide continuum suppression. A probability of being signal/background is attached to each event, and the user can then select events based on this criterion.

4.9.3 Performance

The effectiveness of the procedure described above is dependent on both the discriminating power of the individual variables, and on the correlations between them. Selecting the final set of discriminating variables to use for background suppression must also take into account the type of multivariate analysis method employed, as correlations between the variables are handled differently in the various methods (see Section 4.7).

An example of the output of training `Cornelius`, on fully reconstructed events, is shown in Fig. 4-36 for the $B \rightarrow \rho\pi$ channel. The final separation achieved, using the PA method and four discriminating variables, was 75%. The separation at each stage of the training process is shown in the figure on the right. The PA method is most effective when the variables are uncorrelated, and it can be seen in this example that adding a fourth variable provides no additional discriminating power. A neural network method, however, can handle correlations effectively, so in general it is possible to use more variables in the training process.

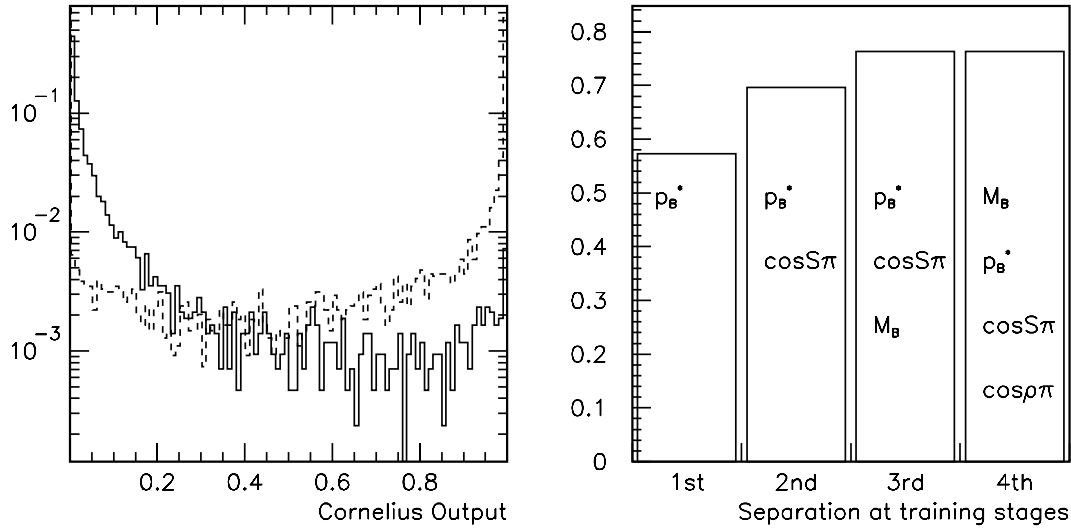


Figure 4-36. Results of Cornelius training with the PA method (Section 4.7) on four discriminating variables. Left: distribution of the final separation (see Sections 4.7 and 4.8) of signal and background; Right: the value of separation (on the vertical axis) achieved during the training process using different sets of the discriminating variables (signal: solid line, light-quark continuum: dotted line).

4.10 Extraction of CP Asymmetries

This section presents a discussion of methods [44] of extracting the CP asymmetry from B or \bar{B} decays to CP eigenstates in $\Upsilon(4S) \rightarrow B\bar{B}$ events produced in an asymmetric collider. It begins with a discussion of the equations that describe the Δz distributions of the data. That is followed by a discussion of the distribution, given perfect knowledge of the B flavor tag recoiling against the CP eigenstate, and then follows a discussion of a more realistic experimental situation with tagging that contains some misidentification or *mistagging*. Then a formula is presented for providing CP error estimates assuming Gaussian smearing of the vertex and including tagging efficiency and backgrounds. Finally, there is an introduction to alternative methods of fitting and displaying the CP results with the Kin variable.

4.10.1 Fit Equations

The time evolution of the process

$$\Upsilon(4S) \rightarrow R_+(\Delta z_+) \rightarrow f_{CP} B_{\text{tag}} \text{ or } f_{CP} \bar{B}_{\text{tag}} \quad (4.33)$$

is given by Eq. (1.41) as

$$R(t_{\text{tag}}, t_{CP}) \propto e^{-\Gamma t_{CP}} e^{-\Gamma t_{\text{tag}}} [1 + A \sin(\Delta m(t_{\text{tag}} - t_{CP})/\Gamma) + B \cos(\Delta m(t_{\text{tag}} - t_{CP})/\Gamma)] \quad (4.34)$$

where t_{CP} and t_{tag} , are the proper times of the decay to the CP eigenstate, f_{CP} , and the decay of the recoiling B or \bar{B} tag, and the coefficients, A and B are

$$A = -\frac{2Im\lambda_f}{1 + |\lambda_f|^2}, \quad B = \frac{1 - |\lambda_f|^2}{1 + |\lambda_f|^2}. \quad (4.35)$$

If the coefficient A is non-zero there will be CP violation. The coefficients A and B for a B tag will be equal in magnitude and opposite in sign to those for a \bar{B} tag. Integration of the above expression for $R(t_{\text{tag}}, t_{CP})$ over the time variable, $t_{\text{tag}} + t_{CP}$, yields the dependence in terms of the single variable, $t_{\text{tag}} - t_{CP}$, which is the time difference between the two decays:

$$R_{\pm}(t_{\text{tag}} - t_{CP}) \propto e^{-\Gamma|t_{\text{tag}} - t_{CP}|} [1 \pm A \sin(\Delta m(t_{\text{tag}} - t_{CP})/\Gamma) \pm B \cos(\Delta m(t_{\text{tag}} - t_{CP})/\Gamma)] \quad (4.36)$$

where the \pm sign depends on whether the recoiling tag is a B or a \bar{B} . Experimentally, the time difference is actually determined in the laboratory from the difference in the z positions of the decay to the CP eigenstate, f_{CP} , and of the recoiling B or \bar{B} tag. They are related by Lorentz transformation as follows:

$$\gamma\beta c(t_{CP} - t_{\text{tag}}) \cong z_{CP} - z_{\text{tag}} \equiv \Delta z, \quad (4.37)$$

where $z_{\text{tag}}(z_{CP})$ is the z position of the B_{tag} (B_{CP}) decay in the laboratory and $\gamma\beta \cong 0.56$ is the Lorentz transformation factor between the laboratory frame and the $\Upsilon(4S)$ rest frame. The measurement of Δz in the laboratory is exact for decays along the z -axis and has a small correction for decays that deviate from the z -axis. Usually this correction is ignored in the fit.

The observed measurements will be smeared by the finite resolution of the vertex measurements. If the errors are Gaussian, the observed distribution f_{\pm} , will be the convolution integral

$$f_{\pm}(\Delta z = \Delta t/(\gamma\beta c)) = \int_{-\infty}^{\infty} e^{-(t' - \Delta t)^2/2\sigma^2} e^{-\Gamma|t'|} \cdot [1 \pm A \sin(\Delta m t'/\Gamma) \pm B \cos(\Delta m t'/\Gamma)] dt' \quad (4.38)$$

The expected vertex separation will be approximately $\gamma\beta c\tau \cong 0.56 \times 468 \mu\text{m} = 260 \mu\text{m}$ and the experimental vertex resolution in the z direction is $\sim 130 \mu\text{m}$. Hence $\Gamma\sigma \cong 0.5$ and $\Delta m\sigma \cong 0.35$. Given these parameters, the $f_{\pm}(\Delta z')$ distribution for $-\infty < \Delta z' < \infty$ will be a slightly skewed, smeared exponential centered on zero. The CP asymmetry occurs in the odd functional part of $f(\Delta z')$. This asymmetry is more readily apparent by forming the forward-backward asymmetry of $f_{\pm}(\Delta z') - f_{\pm}(-\Delta z')$, which appears as a Lorentzian distribution for non-zero CP violation and flat for zero CP violation.

4.10.2 Adding Flavor-Tagging Information

Since there are not pure samples of B and \bar{B} tags, what is really measured is the probability that the recoil tag is a B or a \bar{B} . Denoting this probability b and \bar{b} respectively, then an observed CP event will have a probability

$$P = b e^{-\Gamma t} [1 + A \sin \Delta m t] + \bar{b} e^{-\Gamma t} [1 - A \sin \Delta m t] = e^{-\Gamma t} [(b + \bar{b}) + (b - \bar{b}) A \sin \Delta m t]. \quad (4.39)$$

If the probabilities, b and \bar{b} , of the events being a B or a \bar{B} are measured according to some variable x (e.g., from Cornelius), then the joint probability distribution of the decay is

$$e^{-\Gamma t} [(b(x) + \bar{b}(x)) + (b(x) - \bar{b}(x)) A \sin \Delta m t] dx dt, \quad (4.40)$$

where the number of B events in a differential dx is $b(x)dx$. To simplify the discussion, assume the variable x varies between -1 and 1, where the selection is optimized such that when x is near 1, the tag is a B , and when x is near -1, the tag is a \bar{B} . The above can be rewritten as

$$f(t, x, A) dx dt = e^{-\Gamma t} [1 + q(x) A \sin \Delta m t] n(x) dx dt, \quad (4.41)$$

where $q(x) = (b(x) - \bar{b}(x)) / (b(x) + \bar{b}(x))$ and $n(x) = b(x) + \bar{b}(x)$. Note the $b(x)$ and $\bar{b}(x)$ distributions must be known (either from measurement or accurate Monte Carlo simulation) and their relative normalizations must be determined.

When vertex resolution is included, the above becomes a convolution integral, with

$$f(t, x, A, \sigma_t) dx dt = \left[\int \frac{1}{\sqrt{2\pi}\sigma_t} e^{-\frac{1}{2}\left(\frac{t-t'}{\sigma_t}\right)^2} e^{-\Gamma|t'|} [1 + q(x) A \sin \Delta m t'] n(x) dt' \right] dx dt \quad (4.42)$$

This represents the probability distribution of the CP events as a function of the two measured observables, t and x and the fitting parameter A . The notation can be simplified by writing

$$f(t, x, A, \sigma) dx dt = [E(t) + Aq(x) S(t)] n(x) dx dt \quad (4.43)$$

with

$$E(t) = \int \frac{1}{\sqrt{2\pi}\sigma_t} e^{-\frac{1}{2}\left(\frac{t-t'}{\sigma_t}\right)^2} e^{-\Gamma|t'|} dt', \quad (4.44)$$

$$S(t) = \int \frac{1}{\sqrt{2\pi}\sigma_t} e^{-\frac{1}{2}\left(\frac{t-t'}{\sigma_t}\right)^2} e^{-\Gamma|t'|} \sin \Delta m t' dt'. \quad (4.45)$$

The functions $E(t)$ and $S(t)$ have simple analytic forms obtained from complex error function integrals. These error functions can be approximated by computer programs and used to fit the distributions.

4.10.3 Likelihood Estimate of A

In the maximum-likelihood approach, the value of A is chosen which maximizes the log likelihood,

$$\ln \mathcal{L} = \ln \prod_{i=1}^N f(t_i, x_i, A, \sigma_t) = \sum_{i=1}^N \ln f(t_i, x_i, A, \sigma_t) \quad (4.46)$$

$$\begin{aligned} \ln \prod_{i=1}^N f(t_i, x_i, A, \sigma_t) &= \sum_{i=1}^N \ln [(1 + Aq(x) S(t) / E(t)) E(t) n(x)] \\ &= \sum_{i=1}^N \ln (1 + Aq(x) S(t) / E(t)) + C . \end{aligned} \quad (4.47)$$

Since the maximum depends only on terms which include A , the other terms are absorbed into C with the result

$$\ln \mathcal{L}' = \sum_{i=1}^N \ln \left(1 + A \frac{qS}{E} \right) . \quad (4.48)$$

The value of A that maximizes $\ln \mathcal{L}'$ is the likelihood estimate of A , and the one standard deviation error on A occurs where the value of $\ln \mathcal{L}'$ decreases by 0.5. Usually the maximum and error are determined numerically maximizing $\ln \mathcal{L}'$ using a program such as `Minuit`.

If one prefers to estimate A without fitting, the log likelihood can be expanded:

$$\begin{aligned} \ln \mathcal{L}' &= \sum_{i=1}^N \ln \left(1 + A \frac{qS}{E} \right) = A \sum_{i=1}^N \left(\frac{qS}{E} \right) - \frac{1}{2} A^2 \sum_{i=1}^N \left(\frac{qS}{E} \right)^2 + \\ &\quad \frac{1}{3} A^3 \sum_{i=1}^N \left(\frac{qS}{E} \right)^3 - \frac{1}{4} A^4 \sum_{i=1}^N \left(\frac{qS}{E} \right)^4 + \dots \end{aligned} \quad (4.49)$$

The value of A that maximizes the log likelihood occurs when the derivative of the log likelihood is zero.

$$0 = \frac{\partial \ln \mathcal{L}}{\partial A} = \sum_{i=1}^N \frac{\frac{qS}{E}}{1 + A \frac{qS}{E}} \quad (4.50)$$

$$0 = \sum_{i=1}^N \left(\frac{qS}{E} \right) - A \sum_{i=1}^N \left(\frac{qS}{E} \right)^2 + A^2 \sum_{i=1}^N \left(\frac{qS}{E} \right)^3 - A^3 \sum_{i=1}^N \left(\frac{qS}{E} \right)^4 + \dots \quad (4.51)$$

In the limit that A is small, this equation can be solved for A :

$$0 = \sum_{i=1}^N \frac{q(x_i) S(t_i) / E(t_i)}{1 + A q(x_i) S(t_i) / E(t_i)} \simeq \sum_{i=1}^N q(x_i) S(t_i) / E(t_i) - A [q(x_i) S(t_i) / E(t_i)]^2 \quad (4.52)$$

$$A \simeq \frac{\sum_{i=1}^N q(x_i) S(t_i) / E(t_i)}{\sum_{i=1}^N [q(x_i) S(t_i) / E(t_i)]^2}, \quad (4.53)$$

The values of $q(x_i)$, $S(t_i)$ and $E(t_i)$ for each event are used to evaluate the sums. Note that the term $q(x_i) S(t_i) / E(t_i)$ is equivalent to the reduced Kin (see next section). This short cut is easy to calculate and allows a fairly precise estimate when A is less than 1, but it is slightly less precise than the likelihood estimate. It is easy to see from Eq. (4.51) that this is equivalent to a moment analysis, where moments of powers of $q(x_i) S(t_i) / E(t_i)$ are formed and the appropriate ratios yield Eq. (4.53).

4.10.4 Error of the Likelihood Estimate

The uncertainty in the likelihood estimate of A can be calculated from

$$\frac{1}{\sigma_A^2} = N \int \frac{1}{f} \left(\frac{\partial f}{\partial A} \right)^2 dx, \quad (4.54)$$

where N is the number of events and f is the probability distribution function. In the present case, there are two random variables leading to a double integral:

$$\frac{1}{\sigma_A^2} = N \int_{-1}^1 \int_{-\infty}^{\infty} \frac{1}{f} \left(\frac{\partial f}{\partial A} \right)^2 n(x) dt dx. \quad (4.55)$$

For the case where vertex resolution is ignored, this becomes

$$\frac{1}{\sigma_A^2} = N \int_{-1}^1 \int_{-\infty}^{\infty} \frac{e^{-\Gamma|t|} q^2 \sin^2 \Delta mt}{1 + q(x) A \sin \Delta mt} n(x) dt dx, \quad (4.56)$$

while the case with vertex resolution becomes

$$\frac{1}{\sigma_A^2} = N \int_{-1}^1 \int_{-\infty}^{\infty} \frac{q(x)^2 S^2(t)}{[E(t) + A q(x) S(t)]} n(x) dx dt = N \int_{-1}^1 \int_{-\infty}^{\infty} \frac{\left(\frac{q(x) S(t)}{E(t)} \right)^2}{\left[1 + A \frac{q(x) S(t)}{E(t)} \right]} E(t) n(x) dx dt, \quad (4.57)$$

where N is the number of CP events. The above formula is the exact likelihood error estimate for A .

If $q(x)$ is near 1, then this can be approximated as

$$\frac{1}{\sigma_A^2} \approx N \int_{-1}^1 \int_{-\infty}^{\infty} \frac{\left(\frac{q(x)S(t)}{E(t)}\right)^2}{\left[1 + A \frac{S(t)}{E(t)}\right]} E(t) n(x) dx dt \approx N \int_{-1}^1 q^2(x) n(x) dx \int_{-\infty}^{\infty} \frac{\left(\frac{S(t)}{E(t)}\right)^2}{\left[1 + A \frac{S(t)}{E(t)}\right]} E(t) dt . \quad (4.58)$$

Finally,

$$\sigma_A \approx \frac{\sigma_0}{\sqrt{N} \sqrt{\langle q^2 \rangle}} , \quad (4.59)$$

where

$$\langle q^2 \rangle \equiv \int_{-1}^1 q^2(x) n(x) dx \quad (4.60)$$

and

$$\sigma_0 \equiv \frac{1}{\sqrt{\int_{-\infty}^{\infty} \frac{\left(\frac{S(t)}{E(t)}\right)^2}{\left[1 + A \frac{S(t)}{E(t)}\right]} E(t) dt}} . \quad (4.61)$$

With this approximation for the CP error, the number of events, the tagging error and vertex error parts are separated in a simpler expression for σ_A .

The σ_0 term has been tabulated in Ref. [45] for different values of A , Δm , and measurement errors. The error increases for larger values of σ_t , but decreases for large A . Table 4-9 gives the error on A for the case of $A=0.7$ and $\Delta m/\Gamma=0.75$, for different values of measurement resolutions, σ_z , in units of $\gamma\beta c\tau$.

Table 4-9. Single event error on A as a function of the error on Δz

$\sigma_0(A, \Delta m/\Gamma, \sigma_z)$ for $A=0.7$ and $\Delta m/\Gamma=0.75$ for 1 event						
$\sigma_z/\gamma\beta c\tau$	0	.25	.50	.75	1.0	2.0
$\sigma_0(A, \Delta m/\Gamma, \sigma_z)$	1.36	1.42	1.59	1.85	2.17	3.66

The uncertainty in the flavor determination of the recoiling B tag is contained in the factor $\langle q^2 \rangle$. This factor can be rewritten as a product of the tagging efficiency ϵ and $(1 - 2w)^2$, where w is the B flavor misidentification probability. This results in

$$\sigma_A(A, \Delta m/\Gamma, \sigma_t, N, w) = \frac{\sigma_0(A, \Delta m/\Gamma, \sigma_t)}{\sqrt{N} \sqrt{\epsilon} (1 - 2w)} . \quad (4.62)$$

Often fitting nomenclature designates the *effective tagging efficiency* as the product of the efficiency to measure the tag and $(1 - 2w)^2$, and the inverse of $\sigma_0(A, \Delta m/\Gamma, \sigma_t)$ is sometimes called the *dilution factor*. If the measurement error is $\sigma_z/\gamma\beta c\tau=0.5$ and the effective tagging efficiency is 0.3, at least 135 reconstructed events would be needed to achieve a four standard deviation measurement for $A = 0.7$.

An error due to symmetric backgrounds can also be included, which scales as, $\sqrt{(N_S + N_B)}/N_S$, where N_S is the number of signal events and N_B is the number of background events. This can be obtained from the estimator equation by letting N represent the sum of background and signal, and letting $f(x)$ include both the normalized background and signal distribution. Thus the combined error on A , σ_A , including the value of A , the resolution σ_z , the mixing $\Delta m/\Gamma$, the number of signal events N_S , the number of background N_B , the tagging efficiency ϵ , and the tagging misidentification rate w is

$$\sigma_A(A, \Delta m/\Gamma, \sigma_z, N_S, \epsilon, w, N_B) = \frac{\sigma_0(A, \Delta m/\Gamma, \sigma_z)\sqrt{N_S + N_B}}{\sqrt{\epsilon}(1 - 2w)N_S}. \quad (4.63)$$

The above equation will be used in later sections to estimate the precision of measuring the CP asymmetry, with a correction applied when the backgrounds are not symmetric. Since the backgrounds should be peaked near zero and the CP events should be more displaced, providing more sensitivity to the parameter A , the above is an over-estimate of the effect of background on σ_A .

4.10.5 The Kin Variable

For any final state analysis, the likelihood can be rewritten as a sum of two terms:

$$\mathcal{L} = \sum_{i=1}^N \ln f_i = \mathcal{L}_0 + \mathcal{L}_{CP}, \quad (4.64)$$

with:

$$\mathcal{L}_0 = \sum_{i=1}^N \ln \left(\frac{1}{2}(f_i + \bar{f}_i) \right), \quad (4.65)$$

$$\mathcal{L}_{CP} = \sum_{i=1}^N \ln(1 + K_i), \quad (4.66)$$

where:

- f_i is the density distribution for event i , taking into account detector and background effects.
- \bar{f}_i is the density distribution for a virtual event, defined as the CP conjugate of event i .

- K_i is the Kin variable [46], defined by:

$$K_i = \frac{f_i - \bar{f}_i}{f_i + \bar{f}_i}. \quad (4.67)$$

The first component of the likelihood \mathcal{L}_0 is by construction CP invariant and therefore contains no information on the possible CP violation present in the data. In contrast, the second term \mathcal{L}_{CP} embeds all information about CP violation. The Kin variable depends on Δz , but also on the tagging and background information available for event i :

$$K = (F_+ - F_-) \frac{R_+ - R_-}{R_+ + R_-} \frac{1}{1 + R_{\text{tag}} B} \quad (4.68)$$

where F_{\pm} are the relative probabilities for the event to follow the R_{\pm} time and phase-space distribution, the latter including detector effects, B is the time and phase-space dependent background over signal ratio, and R_{tag} is a correction term accounting for the tagging response for background events [47]. The Kin variable bears interesting properties due to the fact that its distribution is of the form:

$$\Psi(K) = \Psi_0(K)(1 + K), \quad (4.69)$$

where $\Psi_0(K)$ is an even function. Its properties are best illustrated by considering the $B^0 \rightarrow J/\psi K_S^0$ channel where $R_+ - R_- \propto \sin 2\beta$ and where the Kin variable is thus linear in $\sin 2\beta$:

$$K_i = \sin 2\beta \mathcal{K}_i. \quad (4.70)$$

The reduced Kin variable \mathcal{K} allows the immediate determination of the CP -violating parameter through:

$$\sin 2\beta = \frac{\sum_{i=1}^N \mathcal{K}_i}{\sum_{i=1}^N \mathcal{K}_i^2} \pm \frac{1}{\sqrt{\sum_{i=1}^N \mathcal{K}_i^2}} \sqrt{1 - \sin^2 2\beta \frac{\sum_{i=1}^N \mathcal{K}_i^4}{\sum_{i=1}^N \mathcal{K}_i^2}}, \quad (4.71)$$

where the statistical uncertainty is only slightly larger than that achieved in a likelihood analysis. The occurrence of CP violation is displayed by the asymmetry in the \mathcal{K} distribution. The adequacy of the Monte Carlo simulation used to compute f_i , and hence to measure $\sin 2\beta$, can be checked by dividing the data distribution of \mathcal{K} by Ψ_0 : the result must be a straight line of slope $\sin 2\beta$. The \mathcal{K} distributions obtained from different final states where CP violation is due to $\sin 2\beta$, can be merged directly into a single histogram, thereby permitting simultaneous handling of a variety of channels.

4.11 Data Production

For the analyses in this book, approximately 10 million events were generated with full simulation. These were generated in numerous exclusive physics channels, as well as in various inclusive

Table 4-10. *The number of events produced for each of the general types of event.*

Type of Event	Number of Events (10^6)
Continuum (u, d, s)	3.6
Continuum (c)	2.4
Generic $B^0 \bar{B}^0$	1.3
Generic $B^+ B^-$	1.3
Exclusive Physics Channels	1.2

modes for use in background studies. The numbers of events generated in the various inclusive modes are summarized in Table 4-10). In addition, over 2 million events containing only a single particle per event were simulated and reconstructed. The single particle events (as well as the physics events) were used to aid the development of the sub-detector reconstruction algorithms (such as electromagnetic calorimeter cluster-finding, tracking, *etc.*) and were also used to develop particle identification algorithms. The results of these technical studies have been described in earlier sections of this book.

The events were generated using the BABAR event generation packages Beget (for control of the input parameters) and EvtGen (see Section 4.1.1) to handle the dynamics of the decays. The generated data were then passed through the full detector simulation package, BBSim, described in Section 4.1.2, and were written out to tape as raw hits. These simulated events were then passed through the full reconstruction software (see Section 4.2), the high-level results of which were written out to Beast tapes. This large-scale production was carried-out at six different sites around the world. It used more than 61000 CPU hours and required more than 1200 GB of storage space.

Eight million events from the inclusive background samples on Beast tape were passed through 10 different physics filter algorithms (see Section 4.9), each one corresponding to a different exclusive physics channel, and were written out to filter summary Beast tapes. These filtered event samples, and the exclusive physics samples, were used as input to many of the physics analyses which are described in the rest of this book.

References

- [1] “GEANT, Detector Description and Simulation Tool,” CERN Program Library Long Writup W5013, (1994).
- [2] A. Ryd *et al.*, EvtGen User Guide:
<http://www.slac.stanford.edu/BFROOT/doc/LIGHT/6.7.5/src/EvtGen/guide/>
- [3] T. Sjöstrand, “PYTHIA 5.7 and JETSET 7.4 Physics and Manual,” CERN-TH 7112/93 (1993).
- [4] D. Wright, “BEGET: The B -Factory Event Generator Version 21,” BaBar Note # 149, (1994).
- [5] H. C. Fesefeldt, Technical Report PITHA 85-02, III, Physikalisches Institut, RWTH Aachen Physikzentrum, 5100 Aachen, Germany, (1985).
- [6] P. A. Aarnio *et al.*, FLUKA86 User’s Guide, CERN Technical Report TIS-RP-168, (1986); Enhancements to the FLUKA86 Program (FLUKA87), CERN Technical Report TIS-RP-190, (1987).
- [7] C. Zeitnitz and T. A. Gabriel, “The Geant-Calor Interface User’s Guide”:
http://dipmza.physik.uni-mainz.de/~www_aleph/zeitnitz_c/gcalor_manual.ps, (1996).
- [8] W. Innes, “TRACKERR: A Program for Calculating Tracking Errors,” BaBar Note # 121, (1993).
- [9] P. F. Harrison, A. Hasan and L. Moneta, “Electromagnetic Calorimeter Resolutions: Parameterisation in Aslund,” BaBar Note # 249, (1995).
- [10] L. Lista *et al.*, “Muon Identification in the IFR,” BaBar Note # 413, (1998).
- [11] E. D. Frank *et al.*, “Architecture of the BaBar Reconstruction System,” to be published in *Computer Phys. Comm.*
- [12] B. Jacobsen, “Beta: A High-level Toolkit for BaBar Physics Analysis,” submitted to *Comp. Phys. Comm.*
- [13] *Technical Design Report*, (BaBar Collaboration), SLAC-Report-372 (1995).
- [14] A. Drescher *et al.*, *Nucl. Instr. Methods* **A237**, 464 (1985).
- [15] R. Sinkus and T. Voss, *Nucl. Instr. Methods* **A391**, 360 (1997).
- [16] M. Kunze and J. Steffens, *Nucl. Instr. Methods* **A389**, 12 (1997).

- [17] M. Kunze, <http://www.ep1.ruhr-uni-bochum.de/marcel/PidNNO/PidNNOResults.html>
- [18] R. Baldini-Ferroli *et al.*, “A Study of CP Violation in $B^0 \rightarrow J/\psi K_L^0$ using a Highly Segmented IFR,” *BaBar Note* # 198, (1995); “Further Study of $B^0 \rightarrow J/\psi K_L^0$,” *BaBar Note* # 223, (1995).
- [19] D. Falciari and R. de Sangro, “Neutral Hadrons Reconstruction in BaBar,” *BaBar Note* (in preparation).
- [20] P. Billoir and S. Qian, *Nucl. Instr. Methods* **A311**, 139 (1992).
- [21] E. Dedrick, J. M. LoSecco and W. D. Shephard, “Analytic Vertex Estimation,” *BaBar Note* # 378, (1997).
- [22] A. Forti, F. Lanni and F. Palombo, “Measurement of the CKM Alpha Angle in the Processes $B_d^0 \rightarrow a_1^{-+} \pi^{+-} \rightarrow \pi^+ \pi^- \pi^+ \pi^-$,” *BaBar Note* # 423, (1998).
- [23] O. I. Dahl *et al.*, “SQUAW Kinematic Fitting Program,” Group A Programming Note P-126, University of California, Lawrence Radiation Laboratory, Berkeley, California (1968).
- [24] J. M. LoSecco, “Kinematic Fitting for BaBar,” *BaBar Note* # 352, (1997).
- [25] Description pending, see README file in BetaKfit package in SRT.
- [26] A. Ouraou, <http://infodan.in2p3.fr/delphi/user/ouraou/fitver.html>
- [27] F. James, CERN program library long writeup D506 (1992).
- [28] D. E. Goldberg, “Genetic Algorithms in Search Optimization and Machine Learning” Addison Wesley (1989).
- [29] G. Organtini, *Int. Jour. Mod. Phys.* **C6**, 605 (1995).
- [30] G. Cavoto and F. Ferroni, “A Genetic Algorithm for Cut Optimization at BaBar,” *BaBar Note* # 377, (1997).
- [31] F. Le Diberder, *et al.*, “Treatment of Weighted Events in a Likelihood Analysis of B_s Oscillations or CP Violation,” *BaBar Note* # 132, (1994).
- [32] R. A. Fisher, *Annals of Eugenics* **7**, 179 (1936);
M. S. Srivastava and E. M. Carter, “An Introduction to Applied Multivariate Statistics,” North Holland, Amsterdam (1983).
- [33] C. M. Bishop, “Neural Networks for pattern recognition,” Oxford University Press (1995).
- [34] C. Peterson, T. Rönngvaldsson and L. Lönnblad, *Comput. Phys. Commun.* **81**, 185 (1994).

- [35] A. Gaidot *et al.*, BABAR Note # 461, in preparation.
- [36] T. E. Coan *et al.*, (CLEO Collaboration), *Phys. Rev. Lett.* **80**, 1150 (1998).
- [37] Tagging Group, BABAR Note # 427 in preparation.
- [38] M. Athanas *et al.*, (CLEO Collaboration), *Phys. Rev. Lett.* **73**, 3503 (1994).
- [39] R. Waldi, “Flavour Tagging Studies for the BABAR TDR,” BABAR Note # 204 (1995).
- [40] S. Brandt *et al.*, *Phys. Lett.* **12**, 57 (1964);
E. Fahri, *Phys. Rev. Lett.* **39**, 1587 (1977).
- [41] J. D. Bjorken and S. J. Brodsky, *Phys. Rev. D* **1**, 1416 (1970).
- [42] G. C. Fox and S. Wolfram, *Nucl. Phys.* **B149**, 413 (1979).
- [43] T.J. Champion, “Using BetaTools for Physics Analysis,” BABAR Note # 424, (1990).
- [44] W. Toki, “Parametrization of Decay Length Distributions with Errors,” BABAR Note # 35, (1990);
For alternate approaches see:
Reference [45];
A. Snyder, “CP Extraction Tool,” BABAR Note # 188, (1994);
For a simplification of the expressions see:
P. Marrocchesi, “An Unbinned Maximum Likelihood Analysis of CP Violation,”
BABAR Note # 257, (1995).
- [45] F. Le Diberder, “Precision on CP Violation Measurements and Requirement on the Vertex Resolution,” BABAR Note # 34, (1990).
- [46] S. Versillé and F. Le Diberder, “The KIN Variable,” BABAR Note # 406, (1998); “The KIN Variable and CP Thinking Revisited,” BABAR Note # 421, (1998).
- [47] S. Versillé, “Simultaneous Handling of Tagging and Background Fighting,”
BABAR Note # 408, (1998).

Determination of β

This chapter presents results on methods of extracting the angle β of the unitarity triangle. It starts with a theoretical introduction, which is followed by a general discussion of some experimental considerations. Then the results of Monte Carlo-based analyses are presented in successive sections on: modes with charmonium and a kaon, modes with charmonium and a K^{*0} , modes with two charmed mesons and modes which have dominant penguin contributions. The chapter concludes with a summary of the expected CP -reach for nominal BABAR luminosity.

5.1 Theoretical Review of $\sin 2\beta$ Measurements

The first subsection gives an overview of the three classes of decay for which the CP asymmetry can be related (at least naively), to $\sin 2\beta$. These are discussed in more detail in Section 5.1.2, which gives a detailed discussion of the calculation of CP asymmetries for each class, and the resultant theoretical uncertainties in the extraction of $\sin 2\beta$. Uncertainties due to hadronic effects are quite different in the three classes. In general the discussion is model-independent, although in some instances, for the purpose of illustration, it appeals to models. Following that, the ideas and methods of angular analysis are presented in Section 5.1.3. This can be used to separate CP -odd and CP -even contributions in certain vector-vector modes. The application of isospin analysis to modes of interest for the determination of $\sin 2\beta$ is discussed in Section 5.1.4. Section 5.1.6 discusses the measurement of β in inclusive decays and Section 5.1.7 addresses the question of discrete ambiguities. The theoretical introduction ends with a summary of existing data, since these determine input numbers for simulation analyses.

5.1.1 Decays That Can Measure β

The angle β of the unitarity triangle is defined by [1]:

$$\beta = \text{Arg} \left(-\frac{V_{cd}V_{cb}^*}{V_{td}V_{tb}^*} \right). \quad (5.1)$$

The time-dependent asymmetry for any CP eigenstate f is given by

$$a_f(t) = \frac{\Gamma(B^0(t) \rightarrow f) - \Gamma(\bar{B}^0(t) \rightarrow f)}{\Gamma(B^0(t) \rightarrow f) + \Gamma(\bar{B}^0(t) \rightarrow f)} = C_f \cos \Delta mt + S_f \sin \Delta mt \quad (5.2)$$

where

$$C_f = \frac{1 - |\lambda_f|^2}{1 + |\lambda_f|^2} \quad S_f = -\frac{2\text{Im}\lambda_f}{1 + |\lambda_f|^2}. \quad (5.3)$$

f is a CP eigenstate, $\lambda_f = \frac{q}{p} \frac{\bar{A}(f)}{A(f)}$, and $A(f)$, $\bar{A}(f)$ are the amplitudes of the decays $B_d^0 \rightarrow f$, $\bar{B}_d^0 \rightarrow f$. Present data constrain the CP phase, β , in the Standard Model to lie within the limits [2]:

$$10^\circ \leq \beta \leq 35^\circ \quad . \quad (5.4)$$

In the modes discussed in this chapter, a naive leading result is predicted, with corrections that differ according to the type of mode, of the form

$$\lambda_f \cong \eta_f e^{-2i\beta} \quad a_f(t) \cong \eta_f \sin 2\beta \sin \Delta mt \quad (5.5)$$

where $\eta_f = \pm 1$ for $CP(f) = \pm 1$.

The decay modes that can be helpful in the determination of β [3, 4, 5, 6, 7] can be classified into three main types, here called Types I, II, and III, according to the underlying quark processes.

5.1.1.1 Type I decays

Color-suppressed modes $b \rightarrow c\bar{c}s$: $B_d^0, \bar{B}_d^0 \rightarrow \text{Charmonium} + K_s^0(K_L^0)$ and the corresponding modes with K^* , where the K^* decays into a CP eigenstate $K^* \rightarrow K_s^0\pi^0(K_L^0\pi^0)$.

The diagram for the tree amplitude in these modes is shown in Fig. 5-1. For such modes, *e.g.*, $J/\psi K_s^0$ ($CP = -$),

$$\lambda(B_d \rightarrow J/\psi K_s^0) = - \left(\frac{V_{tb}^* V_{td}}{V_{tb} V_{td}^*} \right) \left(\frac{V_{cs}^* V_{cb}}{V_{cs} V_{cb}^*} \right) \left(\frac{V_{cd}^* V_{cs}}{V_{cd} V_{cs}^*} \right) \quad (5.6)$$

where the first term comes from B_d^0 - \bar{B}_d^0 mixing, the second from the ratio $\frac{\bar{A}(f)}{A(f)}$ and the third from K^0 - \bar{K}^0 mixing. Hence,

$$\text{Im} \lambda(B_d \rightarrow J/\psi K_s^0) = \sin 2\beta \quad . \quad (5.7)$$

For decays of Type I, the tree amplitudes are color-suppressed because of the topology of Fig. 5-1. However the dominant penguin contribution has the same weak phase as the tree, as will be shown below. The only term with a different weak phase is a penguin contribution that is Cabibbo suppressed by $\mathcal{O}(\lambda^2)$ where λ is the Wolfenstein parameter. Thus, to good accuracy, and independent

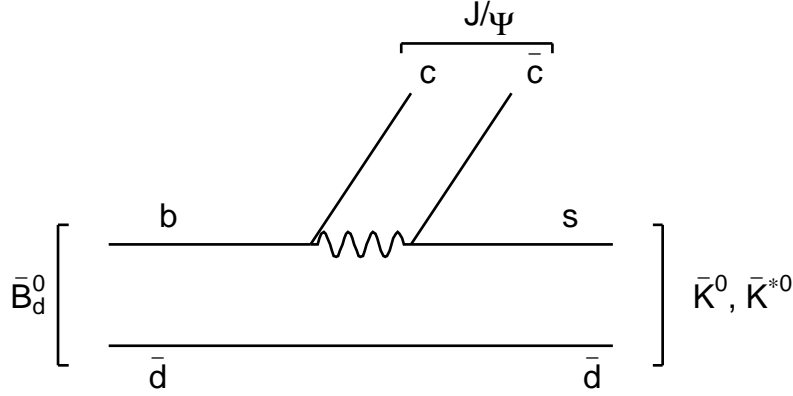


Figure 5-1. $\bar{B}_d^0 \rightarrow \text{charmonium} + \bar{K}^0 (\bar{K}^{*0})$ decays, color-suppressed (Type I).

of any assumptions about factorization, color suppression, or the role of final state interactions, $|\lambda_f| = 1$ for this mode, and the simple relationship between the CP asymmetry and $\sin 2\beta$ has negligible theoretical uncertainty.

The CP of a two-body state has a $(-1)^L$ dependence on the relative angular momentum of the two particles. When two non-zero spin particles are produced from a B decay, they can have either even or odd relative angular momentum, and thus final states (those which are otherwise CP self-conjugate) are a mixture of even and odd CP . In such cases, *e.g.*, Vector-Vector (VV), such as $J/\psi K^*$, an angular analysis is needed to separate the amplitudes of definite CP . This adds an experimental complication, but once this analysis is applied, these modes are as clean, theoretically, as the vector-pseudoscalar case.

5.1.1.2 Type II decays

Cabibbo-suppressed modes $b \rightarrow c\bar{c}d$: $B_d^0, \bar{B}_d^0 \rightarrow D\bar{D}, D\bar{D}^*, D^*\bar{D}, D^*\bar{D}^*$, *etc.*

The tree diagram for these modes is shown in Fig. 5-2. The dominant tree amplitude, *e.g.*, for D^+D^- , is:

$$\lambda(B_d \rightarrow D^+D^-) = \left(\frac{V_{tb}^*V_{td}}{V_{tb}V_{td}^*} \right) \left(\frac{V_{cd}^*V_{cb}}{V_{cd}V_{cb}^*} \right)$$

$$\text{Im}\lambda(B_d \rightarrow D^+D^-) = -\sin 2\beta \quad (5.8)$$

since $CP(D^+D^-) = +$. In these modes, the tree amplitude is CKM suppressed. Hence, the contribution of penguin graphs with a different weak phase is potentially significant. Such effects

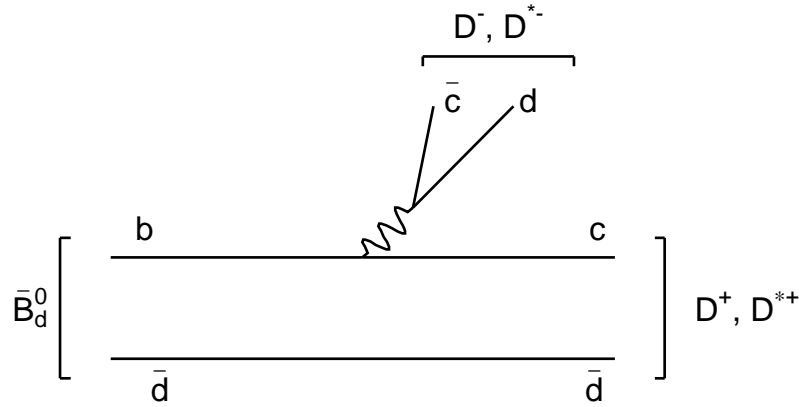


Figure 5-2. $\bar{B}_d^0 \rightarrow D^+ D^-$ decay, Cabibbo-suppressed and color-allowed (Type II).

are an example of direct CP violation, and result in $|\lambda_f| \neq 1$. This complicates the expression for the measured asymmetry to the form given in Eq. (5.3). Hence, as will be shown below, if this complication is ignored in the extraction of $\sin 2\beta$, the value obtained is shifted from the correct one by an amount which depends on the ratio of tree to penguin contributions and their relative weak phases. Calculations for these quantities depend on models and have large uncertainties, as is typical for such low-energy hadronic effects. This translates into significant theoretical uncertainties in the extracted value of $\sin 2\beta$. Eventual reduction of these uncertainties is possible as models, and final-state interaction effects are constrained by comparison with data in a variety of channels.

In addition, for the VV case, $D^* \bar{D}^*$, one again needs an angular analysis to separate the amplitudes of definite CP .

5.1.1.3 Type III decays

Penguin-only or penguin-dominated modes, $b \rightarrow s\bar{s}s$ or $d\bar{d}s$: $B_d^0, \bar{B}_d^0 \rightarrow \pi^0 K_S^0(K_L^0), \eta' K_S^0(K_L^0), \phi K_S^0(K_L^0)$ etc., and the corresponding modes with K^* : $B_d^0, \bar{B}_d^0 \rightarrow \pi^0, \eta'$ or ϕ , etc., and $K^*(K^* \rightarrow K_S \pi^0(K_L \pi^0))$ [8].

In some of these modes, tree contributions are completely absent (e.g., for $\phi K, \phi K^*$). In others a $u\bar{u}s$ tree contribution can enter for the same modes, but it is both color-suppressed and Cabibbo-suppressed, thus the penguin contributions are expected to dominate. As shown in Table 1-1, one can always use the unitarity relationship to group the three penguin terms as two terms with different weak phases, one with coefficient $V_{cs}^* V_{cb}$ (charm minus top) and a second with the

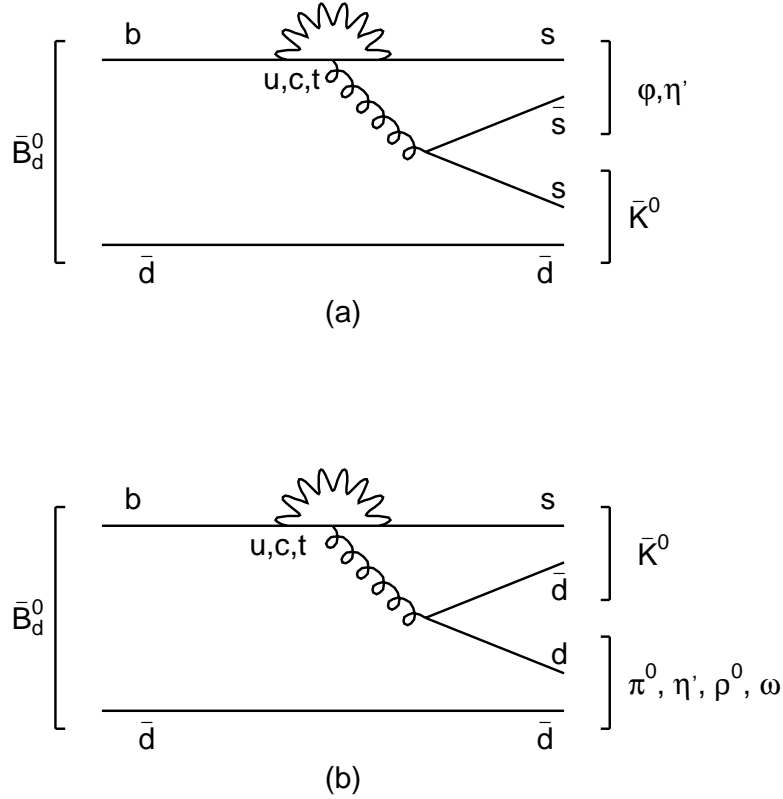


Figure 5-3. Penguin-dominated \bar{B}_d^0 decays (Type III).

Cabibbo-suppressed coefficient $V_{us}^* V_{ub}$ (up minus top). Examples of the diagrams for such modes are given in Fig. 5-3. Ignoring the Cabibbo-suppressed terms the asymmetry is given by

$$\lambda(B_d \rightarrow \phi K_S) \cong - \left(\frac{V_{tb}^* V_{td}}{V_{tb} V_{td}^*} \right) \left(\frac{V_{cs}^* V_{cb}}{V_{cs} V_{cb}^*} \right) \left(\frac{V_{cd}^* V_{cs}}{V_{cd} V_{cs}^*} \right)$$

$$\text{Im} \lambda(B_d \rightarrow \phi K_S) \cong \sin 2\beta. \quad (5.9)$$

Except for ϕK , ϕK^* , the theoretical status of Type III decays is less clear than for Types I and II, as will be discussed below. In the VV case like ϕK^* , one needs of course angular analysis.

Penguin-only modes (Type III modes) also include the radiative penguin transitions $B_d^0, \bar{B}_d^0 \rightarrow \gamma + K^*(K^* \rightarrow K_S \pi^0(K_L \pi^0))$, although in this case, the asymmetries are quite small in the Standard Model.

5.1.2 Uncertainties: Penguins and FSI phases

This section discusses in some detail the different contributions to the amplitudes for the decay modes that can be used to determine β . The focus is on contributions that modify the time-dependent asymmetries away from the clear-cut case $a_f(t) = \eta_f \sin 2\beta \sin \Delta mt$. This occurs when there are two contributions to the amplitude with different weak phases. Calculations of the relative size, or the relative strong phases, of the various contributions are model-dependent, and involve the typical uncertainties of low-energy hadronic calculations. Theoretical uncertainties are thereby introduced into the value of $\sin 2\beta$ determined from such modes. Throughout this section, factorization is assumed, whenever needed, to estimate the relative sizes of terms. More detailed model assumptions are discussed point by point as they arise.

Using the Operator Product Expansion (see Section 2.1), the amplitude of a decay $B \rightarrow f$, $A(f) = \langle f | H_{eff} | B \rangle$, can be written as sums of products of the form $C_i(\mu) \langle f | O_i(\mu) | B \rangle$. The amplitude contains CKM factors $V_{Uq}^* V_{Ub}$ ($U = u, c, t; q = d, s$), which are physical quantities independent of the renormalization scale, μ . Hence, the μ -dependence of the short-distance coefficients, $C_i(\mu)$, must cancel the μ -dependence of the matrix elements of local operators $\langle f | O_i(\mu) | B \rangle$. The matrix elements are complicated objects, containing the long-distance QCD effects, not included in the short-distance coefficients $C_i(\mu)$, namely soft gluons, rescattering, final-state interaction (FSI) phases, *etc.* The coefficients $C_i(\mu)$ are computed for $\mu \cong m_b$. For diagrams with penguin topology with c and u quarks in the loop the amplitudes also include long distance effects, where these quarks are on or close to mass-shell. Such effects are not reliably given by the short-distance calculation of the operator coefficient. Therefore, one needs to write a completely general expression of the amplitude $A(f)$ that includes in principle all such nonperturbative effects. This section considers only CP eigenstates and avoids spin complications. Our analysis generalizes easily to non- CP eigenstates such as *e.g.*, $D\bar{D}^* + \bar{D}D^*$. Angular analysis for VV modes will be discussed in more detail in Section 5.1.3.

While it is a general and model-independent result that the CP asymmetry for Type I decays gives $\sin 2\beta$ directly, it is useful for comparison purposes (and also for model testing) to cast this calculation in the same form as will be used subsequently for other modes. For this type of decay, from the general form of the CKM matrix and of the effective weak Hamiltonian ($\Delta B = 1$, $\Delta C = 0$, $\Delta U = 0$, $\Delta S = 1$) written in Appendix A, the $B_d^0, \bar{B}_d^0 \rightarrow f$ amplitudes can be written, in general:

$$\begin{aligned} A(f) &= A(B \rightarrow f) = V_{us} V_{ub}^* M^{(u)} + V_{cs} V_{cb}^* M^{(c)} + V_{ts} V_{tb}^* M^{(t)} \\ \bar{A}(f) &= A(\bar{B} \rightarrow f) = V_{us}^* V_{ub} M^{(u)} + V_{cs}^* V_{cb} M^{(c)} + V_{ts}^* V_{tb} M^{(t)}. \end{aligned} \quad (5.10)$$

The amplitudes $M^{(u)}$, $M^{(c)}$, and $M^{(t)}$ are completely general, defined by their CKM factors and the expression of H_{eff} in terms of local operators. (Note that technically, the separate penguin graphs are ill-defined because they are divergent. However, formally, they can be simply defined

by introducing a cutoff on the loop momenta in the penguin diagrams at some large value (well above m_{top}) since the unitarity relationship guarantees the cancellation of the high momentum (divergent) contributions between the three graphs. The eventual answers depend only on the differences between two penguin graphs with different quarks in the loop, and thus are independent of the cutoff prescription. All such divergences are correctly handled in the usual operator product treatment; large loop momenta are integrated out in defining the residual local operators and their coefficients.) The separate terms in Eq. (5.10) are:

1. The amplitude $V_{cs}V_{cb}^*M^{(c)} \cong A\lambda^2 M^{(c)}$ contains the dominant tree amplitude contributing to $J/\psi K(K^*)$ (Fig. 5-1). $M^{(c)}$ is the matrix element of the operator $C_1O_1^{(c)} + C_2O_2^{(c)}$. Assuming factorization, this is proportional to $a_2 = C_1 + \frac{C_2}{N_c} \cong 0.2$, where $C_1 = \mathcal{O}(\alpha_s)$, $C_2 = \mathcal{O}(1)$ and $N_c = 3$ is the number of colors. Thus $a_2 \rightarrow \mathcal{O}(\alpha_s)$ in the large N_c limit (Fig. 5-4a) (in fact, α_s and $1/N_c$ are of comparable magnitude). This term also contains the penguin contribution with the c quark in the loop [9]. This has a possible (small) long-distance part, represented by (Fig. 5-4b).
2. The u -penguin term $V_{us}V_{ub}^*M^{(u)} \cong A\lambda^4(\rho + i\eta)M^{(u)}$ has a different weak phase than the dominant term. However, it is suppressed by $\mathcal{O}(\lambda^2)$ as well as the factor α_s in the penguin coefficients. Any long distance part is also suppressed by the Zweig rule (creation of a color singlet $c\bar{c}$ pair by soft gluons in Fig. 5-4b). The amplitude $M^{(u)}$ is the matrix element of the combination of current-current operators $C_1O_1^u + C_2O_2^u$ [9] and corresponds to a long distance u -penguin (Fig. 5-4b with the u quark in the loop), describing rescattering of the type $\bar{B}_d^0 \rightarrow (s\bar{u})(u\bar{d}) \rightarrow (c\bar{c})(s\bar{d}) \rightarrow J/\psi \bar{K}(\bar{K}^*)$. This term is presumably very small.
3. The amplitude $V_{ts}V_{tb}^*M^{(t)} \cong -A\lambda^2 M^{(t)}$ corresponds to the usual short-distance penguin contribution (top quark in the loop). $M^{(t)}$ is the matrix element of the sum of local penguin operators $C_3O_3 + \dots + C_{10}O_{10}$ (Fig. 5-4 where the dot represents the penguin operators). Using the unitarity relation, one can write $V_{ts}V_{tb}^* = -V_{cs}V_{cb}^* - V_{us}V_{ub}^*$ and regroup this term into the other two terms.

With the notation $T = M^{(c)} - M^{(t)}$, $P = M^{(u)} - M^{(t)}$,

$$\begin{aligned} A(f) &= V_{cs}V_{cb}^*T + V_{us}V_{ub}^*P \\ \bar{A}(f) &= V_{cs}^*V_{cb}T + V_{us}^*V_{ub}P \end{aligned} \quad (5.11)$$

Since $\frac{V_{us}^*V_{ub}}{V_{cs}V_{cb}^*} \sim \mathcal{O}(\lambda^2)$, and P is suppressed relative to T by penguin short-distance coefficients or by the Zweig rule, there is a clear hierarchy between the two terms. Therefore, in this class of decays, λ_f defined above, is close to a pure phase $\lambda_f = \eta_f e^{-2i\beta}$. The time-dependent asymmetry has the simple form

$$a_f(t) = -\text{Im} \left(\frac{q}{p} \frac{\bar{A}(f)}{A(f)} \right) \sin \Delta mt = \eta_f \sin 2\beta \sin \Delta mt. \quad (5.12)$$

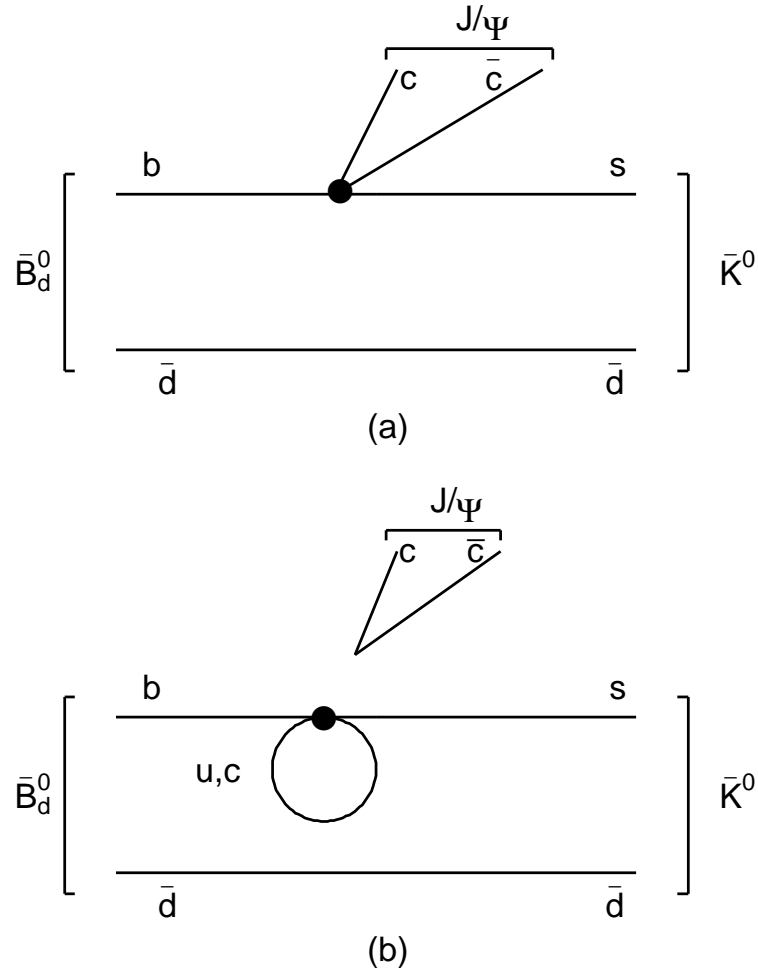


Figure 5-4. Contributions of local operators to Type I decays, $\bar{B}^0 \rightarrow \text{Charmonium} + \bar{K}^0 (\bar{K}^{*0})$. The dot represents the local operators (current-current or penguin). Figure 5-4b represents the long distance u and c -penguins, with the $c\bar{c}$ pair created by soft gluons.

The determination of β using modes of this type is thus safely free of hadronic uncertainties.

For Type II decays, the dominant contributions to the $B, \bar{B} \rightarrow f$ amplitudes (e.g., $f = D\bar{D}$) are Cabibbo suppressed (Fig. 5-2), of the order $A(f) \sim \lambda^3 a_1$, with $a_1 = \mathcal{O}(1)$ (for color-allowed modes). Assuming factorization, $a_1 = C_2 + \frac{C_1}{N_c}$, with $C_2 = \mathcal{O}(1)$. Then

$$\begin{aligned}
 A(f) &= V_{ud}V_{ub}^*M^{(u)} + V_{cd}V_{cb}^*M^{(c)} + V_{td}V_{tb}^*M^{(t)} \\
 \bar{A}(f) &= V_{ud}^*V_{ub}M^{(u)} + V_{cd}^*V_{cb}M^{(c)} + V_{td}^*V_{tb}M^{(t)}.
 \end{aligned}
 \tag{5.13}$$

The different terms are:

1. The amplitude $V_{cd}V_{cb}^*M^{(c)} \cong -A\lambda^3 M^{(c)}$ is Cabibbo suppressed relative to the decays of Type I. $M^{(c)}$ is the matrix element of the current-current operators $C_1O_1^{(c)} + C_2O_2^{(c)}$ (Fig. 5-5a). It contains the tree amplitude (Fig. 5-2) and also the contribution of Fig. 5-5c with the c quark in the loop. $M^{(c)}$ is color-allowed in decays like D^+D^- , and color suppressed in decays of the type $D^0\bar{D}^0$ (Fig. 5-5b). This dominant decay amplitude is the one related to β .
2. The amplitude $V_{td}V_{tb}^*M^{(t)} \cong A\lambda^3(1 - \rho - i\eta)M^{(t)}$ corresponds to the usual short-distance penguin contribution (Fig. 5-5 where the dot represents the local penguin operators). It is Cabibbo suppressed and also suppressed by the small penguin short-distance QCD coefficients, $a_P \sim \mathcal{O}(10^{-2})$. It has a different weak phase than the dominant term; in the Standard Model, this is the weak phase of the mixing amplitude.
3. The amplitude $V_{ud}V_{ub}^*M^{(u)} \cong A\lambda^3(\rho + i\eta)M^{(u)}$ is the u -penguin term [9], which includes also the long-distance contribution (Fig. 5-5c) with the u quark in the loop. This term also has a different weak phase than the dominant term. This term is not Zweig rule suppressed because it can describe rescattering processes of the type $\bar{B}_d^0 \rightarrow (u\bar{d})(d\bar{u}) \rightarrow (c\bar{d})(d\bar{c}) \rightarrow D^+D^-$.

Using the unitarity $V_{ud}^*V_{ub} + V_{cd}^*V_{cb} + V_{td}^*V_{tb} = 0$, and the notation $T \equiv M^{(c)} - M^{(u)}$, $P \equiv M^{(t)} - M^{(u)}$, the amplitudes may be written

$$\begin{aligned} A(f) &= V_{cd}V_{cb}^*T + V_{td}V_{tb}^*P \\ \bar{A}(f) &= V_{cd}^*V_{cb}T + V_{td}^*V_{tb}P . \end{aligned} \quad (5.14)$$

Again here T denotes the tree-dominated term while P is a penguin-only contribution. However the relative size of the two terms in Eq. (5.14) is quite different from Type I decays. The CKM coefficients are comparable in magnitude. Only the $\mathcal{O}(\alpha_s)$ OPE coefficient of penguin graphs suppresses P relative to T .

Hence the P terms cannot be neglected in this case. Using the fact that the weak phase of the mixing, $q \sim V_{td}V_{tb}^*$, cancels the weak phase of the coefficient of P , $V_{tb}V_{td}^*$, the ratio of amplitudes can be written

$$\lambda_f = \eta_f \frac{e^{-i\beta} - |R|e^{i\delta}}{e^{i\beta} - |R|e^{i\delta}} \quad (5.15)$$

using the definitions

$$R = z r \quad z = \frac{V_{td}^*V_{tb}}{V_{cd}^*V_{cb}} \quad r = \frac{P}{T} = |r|e^{i\delta} . \quad (5.16)$$

where, z is the ratio of CKM matrix elements, and r is the ratio of the penguin-only term P to the tree-dominated term T . $\eta_f = +1$ for D^+D^- is the CP eigenvalue of the state f , and δ is the relative strong phase between the amplitudes P and T . It is important to keep in mind that $|R|$

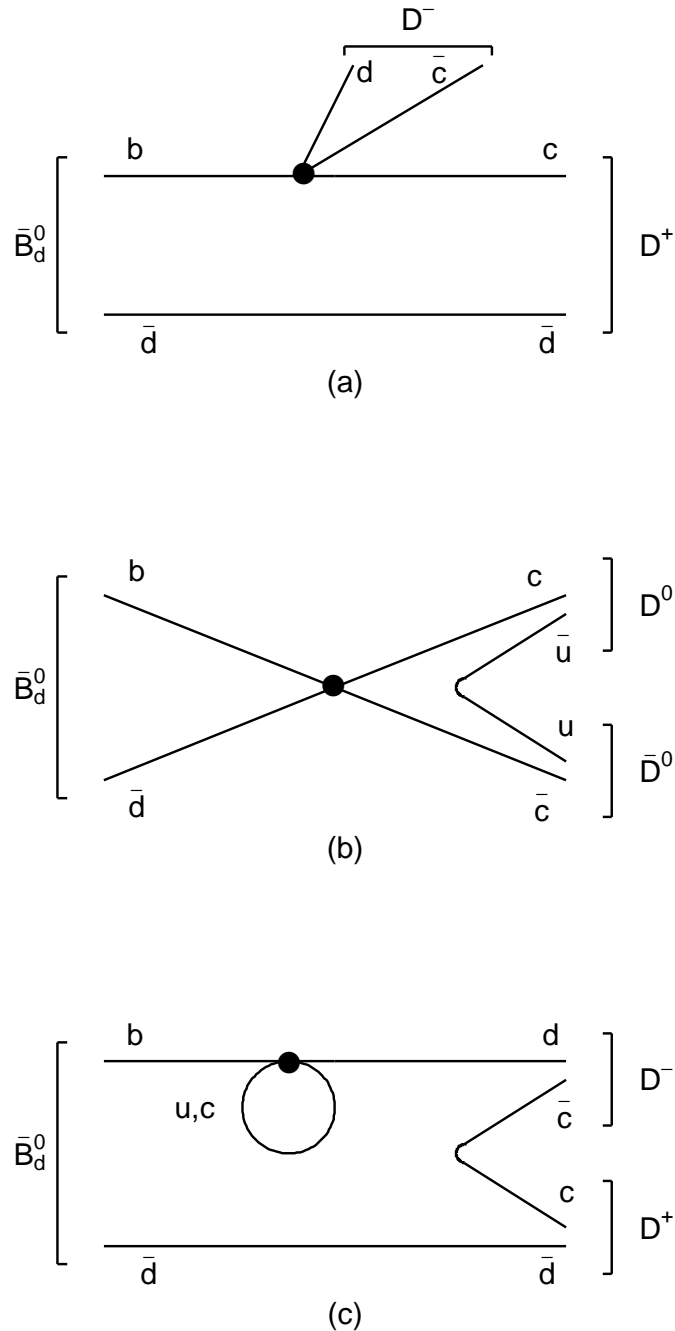


Figure 5-5. Contributions of local operators to Type II decays, $\bar{B}_d^0 \rightarrow D\bar{D}$. The dot represents the local operators (current-current or penguin). Figure 5-5c represents the long-distance u and c penguins induced by local operators.

depends on the CKM ratio z , and is therefore also a function of the weak angles α, β . The small $|R|$ limit is not *a priori* justified.

In Type II decays, the coefficients C_f and S_f in Eq. (5.3) are now

$$C_f = \frac{-2|R| \sin \beta \sin \delta}{1 + |R|^2 - 2|R| \cos \beta \cos \delta} \quad S_f = \eta_f \frac{\sin 2\beta - 2|R| \sin \beta \cos \delta}{1 + |R|^2 - 2|R| \cos \beta \cos \delta}. \quad (5.17)$$

For small $|R|$,

$$C_f \cong -2|R| \sin \beta \sin \delta \quad S_f \cong \eta_f (\sin 2\beta + 2|R| \sin \beta \cos 2\beta \cos \delta). \quad (5.18)$$

In Section 5.1.5, factorization and models are used to calculate R and estimate the theoretical uncertainty in the extraction of $\sin 2\beta$ for some Type II decays.

For Type III decays, the dominant amplitudes are of the penguin type, (Figs. 5-3a and 5-3b). The tree amplitude can pollute the determination of β in some channels like $\pi^0 K_S$, *etc.* From the general form of the CKM matrix, the $B, \bar{B} \rightarrow f$ amplitudes for this type of decay can be written, in general:

$$\begin{aligned} A(f) &= V_{us} V_{ub}^* M^{(u)} + V_{cs} V_{cb}^* M^{(c)} + V_{ts} V_{tb}^* M^{(t)} \\ \bar{A}(f) &= V_{us}^* V_{ub} M^{(u)} + V_{cs}^* V_{cb} M^{(c)} + V_{ts}^* V_{tb} M^{(t)} \end{aligned} \quad (5.19)$$

because in the modes under consideration, there is a single s quark from the $\bar{K}(\bar{K}^*)$ in the final state and the other mesons η', ϕ , *etc.*, do not have open flavor.

These modes will be useful to measure β , if the CKM term $V_{ts} V_{tb}^*$ (*i.e.*, the short-distance penguin operators) clearly dominate the other contributions. This is still a matter of discussion and depends on the particular decay mode considered.

The different terms are:

1. The amplitude $V_{ts} V_{tb}^* M^{(t)} \cong -A\lambda^2 M^{(t)} + \mathcal{O}(\lambda^4)$ is the dominant short-distance penguin term contributing to this class of modes (Figs. 5-3a, b and Fig. 5-6 with the dot representing the local penguin operators). This contribution is of the order $\lambda^2 a_P$ where a_P is a combination of the short-distance penguin coefficients $C_{3,\dots,6}$, and thus is suppressed by α_s . Therefore the rates are expected to be small, of $\mathcal{O}(10^{-5})$ for any of these modes.
2. The amplitude $V_{us} V_{ub}^* M^{(u)} \cong A\lambda^4(\rho + i\eta) M^{(u)}$ is CKM suppressed and has a different CKM phase than the top penguin term (Fig. 5-6a with $q = u$, and Fig. 5-6b with the u quark in the loop).
3. The amplitude $V_{cs} V_{cb}^* M^{(c)} \cong A\lambda^2 M^{(c)}$ is c -penguin term, which includes long-distance effects (Fig. 5-6b with the c quark in the loop).

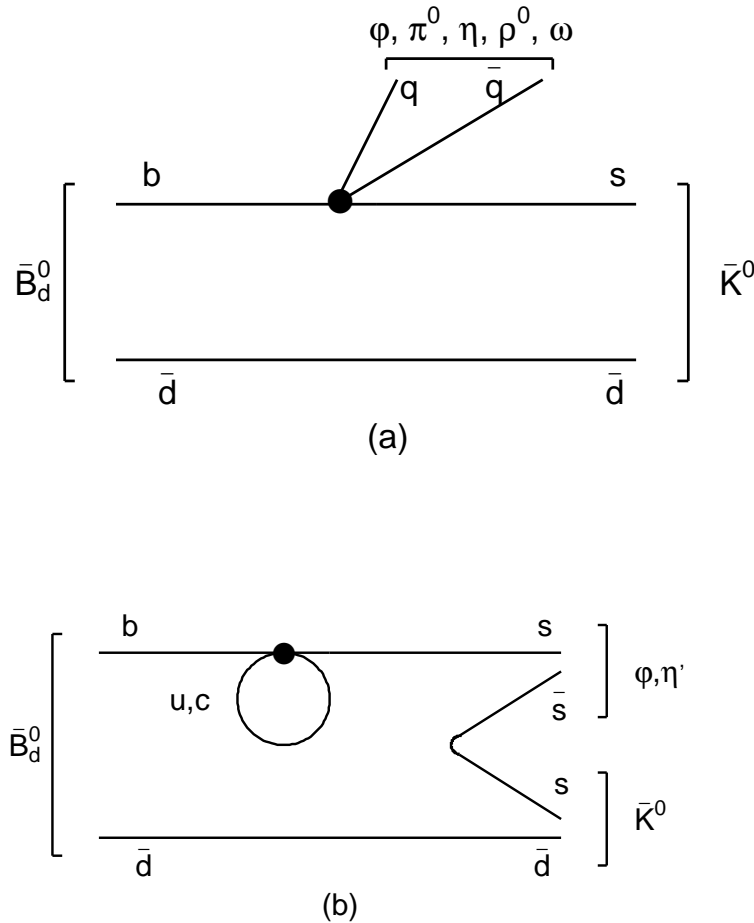


Figure 5-6. Contributions of local operators to penguin-dominated, Type III decays, $\bar{B}_d^0 \rightarrow \phi K_S, \eta' K_S, \text{ etc.}$ The dot represents the local operators. In Fig. 5-6a, for $q = u$ there are contributions from current-current and penguin local operators. For $q = d, s$, only penguin operators contribute. Figure 5-6b represents the long-distance u and c penguins induced by local operators.

Once again, unitarity can be used to group these terms into two, one with the CKM coefficient $V_{cs}V_{cb}^*$ and the other with the Cabibbo-suppressed CKM coefficient $V_{us}V_{ub}^*$. If the first of these terms dominated the decay then the asymmetry would be proportional to $\sin 2\beta$. Therefore, these modes will be useful to measure β if $|V_{us}V_{ub}^*(M^{(u)} - M^{(t)})| \ll |V_{cs}V_{cb}^*(M^{(c)} - M^{(t)})|$.

Note that the terms $M^{(u)}$ and $M^{(c)}$ differ only in their dependence on the mass of the quark in the penguin diagram loop, and hence their short-distance parts are comparable in size. The possible long-distance parts, plus any tree graph $b \rightarrow u\bar{u}s$ contribution to $M^{(u)}$ lead to large theoretical uncertainties in the relationship between the asymmetry and the value of β in some modes.

The relative sizes of these terms for different modes can be quite different:

1. In modes of the type $\phi K(K^*)$, $M^{(u)}$ contains a long-distance u penguin (Fig. 5-6b with the u quark in the loop), describing rescattering, *e.g.*, $\bar{B}_d^0 \rightarrow (s\bar{u})(u\bar{d}) \rightarrow (s\bar{s})(s\bar{d}) \rightarrow \phi\bar{K}^0$. There is a corresponding long-distance c contribution to $M^{(c)}$. The size of these two terms is expected to be comparable, so that the ratio $\frac{|V_{us}V_{ub}^*(M^{(u)}-M^{(t)})|}{|V_{cs}V_{cb}^*(M^{(c)}-M^{(t)})|}$ is expected to be of order $|\lambda^2|$. Hence the asymmetry in these modes gives a measurement of $\sin 2\beta$ which has quite small theoretical uncertainties, though not quite as small as for the Type I modes where the second term is suppressed by a further factor of α_s .
2. In modes of the type $\pi^0 K(K^*)$, $\eta' K(K^*)$, $\rho^0 K(K^*)$, $\omega K(K^*)$ $M^{(u)}$ has a (color-suppressed) tree amplitude contribution (Fig. 5-6a with the dot representing the current-current operators). Therefore one expects a magnitude $\frac{V_{us}V_{ub}^*(M^{(u)}-M^{(t)})}{V_{cs}V_{cb}^*(M^{(c)}-M^{(t)})}$ of order $\lambda^2 a_2/c_P \sim 0.4$ where $c_P \sim -0.02$ is typically a short-distance penguin coefficient, and $a_2 \sim 0.2$ is the color-suppression factor. Thus, in this latter case it seems that the term with a different weak phase must be included in relating the asymmetry measurement to β . Uncertainties in this quantity will lead to significant uncertainties in β as measured by these modes.

For these latter modes it is convenient to write

$$\begin{aligned} A(f) &= V_{us}V_{ub}^*T + V_{cs}V_{cb}^*P \\ \bar{A}(f) &= V_{us}^*V_{ub}T + V_{cs}^*V_{cb}P \end{aligned} \quad (5.20)$$

where $T = M^{(u)} - M^{(t)}$, $P = M^{(c)} - M^{(t)}$. The notation T is used because this term contains the tree contribution wherever there is such a contribution. Note, however, if applying this notation for ϕK_S , T represents a difference of two penguin terms.

Thus for the modes of Type III one gets

$$\lambda_f = \eta_f \left(\frac{V_{tb}^*V_{td}}{V_{tb}V_{td}^*} \right) \left(\frac{V_{us}^*V_{ub}T + V_{cs}^*V_{cb}P}{V_{us}V_{ub}^*T + V_{cs}V_{cb}^*P} \right) \left(\frac{V_{cd}^*V_{cs}}{V_{cd}V_{cs}^*} \right) \quad (5.21)$$

that gives

$$\lambda_f = \eta_f \frac{e^{-i\beta} - |R|e^{i\alpha} e^{i\delta}}{e^{i\beta} - |R|e^{-i\alpha} e^{i\delta}} \quad (5.22)$$

where now

$$R = z r \quad z = \frac{V_{ub}V_{us}^*}{V_{cb}V_{cs}^*} \quad r = \frac{T}{P} = |r|e^{i\delta} \quad (5.23)$$

$\eta_f = -1$ for ϕK_S , $\eta' K_S$, $\pi^0 K_S$, *etc.*, and δ is the relative strong phase between the amplitudes T and P . Again here, the quantity $|R|$ depends on the weak phases α and β through $|z|$. In Eq. (5.23) the small phase of V_{cd} , of $\mathcal{O}(\lambda^5)$, is neglected.

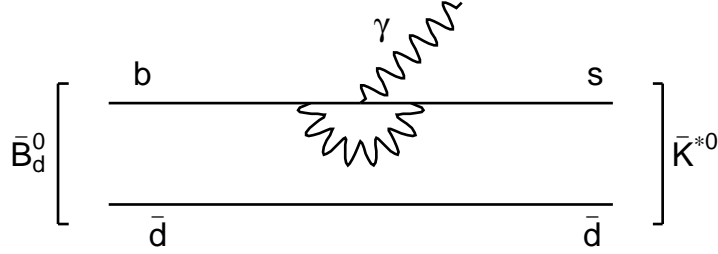


Figure 5-7. The decay $\bar{B}_d^0 \rightarrow \bar{K}^{*0} \gamma$.

The correction $|R|$ differs according to the decay mode. Naively, one expects

$$|R| \cong \lambda^2 \sqrt{\rho^2 + \eta^2} \quad \text{for } \phi K_S, \text{ etc.}$$

$$|R| \cong \lambda^2 \sqrt{\rho^2 + \eta^2} \left| \frac{a_2}{a_P} \right| \quad \text{for } \pi^0 K_S, \text{ etc.} \quad (5.24)$$

where $\left| \frac{a_2}{a_P} \right|$ is the ratio of the color suppression factor $a_2 \cong 0.2$ of the tree diagram, and $|a_P| \sim$ few %, of the order of the penguin short-distance coefficients. $|R|$ is small for ϕK_S while it could be not negligible for $\pi^0 K_S$, etc.

To summarize, the correction to $\lambda_f = \eta_f e^{-2i\beta}$ is expected to be small in modes of the type $\phi K(K^*)$, and presumably also for $\eta' K(K^*)$, but it could be quite sizeable for the modes of the type $\pi^0 K(K^*)$, $\rho^0 K(K^*)$, as will be shown in the calculations in Section 5.1.5 which are made within the factorization assumption. The preceding discussion of the uncertainty on β for given decay modes holds for both QCD and electroweak penguins, because the weak phase affecting both types of operators is the same (see Appendix A).

The radiative penguin transitions [10] that are related to β in the Standard Model are $B_d^0, \bar{B}_d^0 \rightarrow \gamma + K^*(K^* \rightarrow K_S \pi^0(K_L \pi^0))$ (Fig. 5-7). In the Standard Model, the photon in the transition $b \rightarrow s \gamma$ is dominantly left-handed and only a fraction $\frac{m_s}{m_b}$ of the amplitude corresponds to a right-handed photon, where the quark masses are current masses. Thus, the final-state $K^* \gamma$ (with e.g., $K^* \rightarrow K_S \pi^0$) is not a pure CP eigenstate, but consists to a good approximation (neglecting the ratio $\frac{m_s}{m_b}$) of equal admixtures of states with $CP = +$ and $CP = -$. The expected CP asymmetry is therefore quite small, suppressed by the factor $\frac{m_s}{m_b} \cong 0.03$:

$$A(t) \cong 2 \frac{m_s}{m_b} \sin 2\beta \sin \Delta m t. \quad (5.25)$$

Thus, this mode could be a good candidate to look for CP violation beyond the Standard Model [2, 10].

5.1.3 Angular Analyses to Extract CP Amplitudes

Decays to two particles with non-zero spin need an angular analysis to extract β from an asymmetry measurement. Examples are $J/\psi K^*$ ($J/\psi \rightarrow \ell^+ \ell^-$, $K^* \rightarrow K\pi$), $\psi' K^*$ ($\psi' \rightarrow J/\psi \pi\pi$), $D^* \bar{D}^*$ ($D^* \rightarrow D\pi$), ϕK^* ($\phi \rightarrow K\bar{K}$), *etc.*, and also the AV mode $\chi_{1c} K^*$ ($\chi_{1c} \rightarrow J/\psi \gamma$).

In all such channels, there are three partial waves $L = 0, 2$ (parity-violating decay of the B), $L = 1$ (parity conserving decay), L being the relative angular momentum between the two vector particles. The CP of the final state depends on the partial wave, since it contains a factor $(-1)^L$. Thus, even when the decays of the two particles lead to a set of CP -self-conjugate particles, one has a final state that is an admixture of CP -odd and CP -even eigenstates. Since the asymmetry has opposite sign for the two CP states they tend to cancel, or “dilute” the overall asymmetry.

If there is no separation of the CP components of *e.g.*, $J/\psi K^{*0}$ ($K^{*0} \rightarrow K_S \pi^0$), then the CP asymmetry has a dilution factor $D < 1$ coming from the cancellation of the two different CP components:

$$a(t) = D \sin 2\beta \sin \Delta mt \quad (5.26)$$

where D is given by

$$D = \frac{\Gamma_{CP=+} - \Gamma_{CP=-}}{\Gamma_{tot}} = \frac{\Gamma_0 + \Gamma_{\parallel} - \Gamma_{\perp}}{\Gamma_{tot}} = 1 - \frac{2\Gamma_{\perp}}{\Gamma_{tot}}. \quad (5.27)$$

Here, Γ_0 , Γ_{\parallel} and Γ_{\perp} are partial widths corresponding to an angular momentum decomposition based on the decay topology, which will be explained below. However, when angular analysis allows separation of the different CP components, one can obtain $\sin 2\beta$ without dilution.¹

Although the amplitudes are in general time-dependent, in an appropriate basis the angular dependence and the time dependence factorize; this greatly simplifies this treatment [11, 12]. The simplest cases are described here, those in which V decays into two spin $\frac{1}{2}$ or two 0^- particles, namely the main cases $J/\psi K^*$ ($J/\psi \rightarrow \ell^+ \ell^-$, $K^* \rightarrow K\pi$), $D^* \bar{D}^*$ ($D^* \rightarrow D\pi$) and ϕK^* ($\phi \rightarrow K\bar{K}$). The mode $\chi_{1c} K^*$ will be discussed in Section 5.3.

In these decays into two vector mesons, $B \rightarrow V_1 V_2$, there are three different angular momentum projections that can be used: the helicity basis, the transversity basis and the partial wave decomposition. They are completely equivalent, but quantities defined in these different basis states have different physical interpretations, and thus lead to slightly different physical insights

¹There are many different factors that tend to decrease the measured asymmetry that are all referred to as “dilution factors” in the literature. The cancellation between the asymmetry from two different CP components in an otherwise CP eigenstate is the most common dilution factor in theoretical papers. Other reductions coming from experimental effects, such as the presence of a CP conserving background contribution in the data sample and the reduction in magnitude of the measured asymmetry from the smearing of the $\sin \Delta mt$ term due to z -resolution are also sometimes called dilution effects. Since these effects all have different causes and thus different cures it is well to keep them separate.

about the underlying process. There are two general approaches that can be used in applying the angular analysis. The first approach, generally the way theorists think about the problem, is to isolate a particular CP contribution by projecting it out via some weighted integral over the data and then performing a fit for β by looking at the CP asymmetry in this projected quantity. The more experimentally-oriented approach is simply to perform a multivariate analysis where a maximum-likelihood procedure simultaneously fits for β and for the chosen basis amplitudes. Further restrictions on the non- CP -violating parameters can be obtained from time-integrated and/or untagged data samples, and possibly from isospin-related charged channels.

In the helicity basis, there are three amplitudes A_λ , ($\lambda = 0, \pm 1$) corresponding to the helicity of V_1 or V_2 in the decay $B \rightarrow V_1 V_2$. The transverse amplitudes are defined as spin projections for one vector particle parallel and perpendicular to the plane of the decay of the other. The amplitude A_0 remains unchanged, the other two transversity amplitudes are defined as the following linear combinations of the helicity amplitudes [13]:²

$$A_{\parallel} = \frac{1}{\sqrt{2}}(A_{+1} + A_{-1}) \quad A_{\perp} = \frac{1}{\sqrt{2}}(A_{+1} - A_{-1}). \quad (5.28)$$

The helicity formalism gives a straightforward determination of the longitudinal rate, while the transversity formalism is convenient for the determination of the CP -odd component of the decay rate, allowing a ready interpretation of the $\sin 2\beta$ measurement.

Finally there is the partial wave decomposition corresponding to the possible S , P and D orbital angular momenta (relative orbital angular momentum $L = 0, 1, 2$ between V_1 and V_2). In terms of the transversity amplitudes, the partial wave amplitudes read [14]

$$S = \frac{1}{\sqrt{3}}(\sqrt{2}A_{\parallel} - A_0), \quad P = A_{\perp}, \quad D = \frac{1}{\sqrt{3}}(A_{\parallel} + \sqrt{2}A_0). \quad (5.29)$$

Note that the $(-1)^L$ -odd P -wave term is also the transversity amplitude A_{\perp} , while the other two transversity amplitudes are combinations of the $(-1)^L$ -even S - and D -wave amplitudes. The preceding relations are valid for any time t . To make the time dependence explicit it is convenient to use the transversity basis, since those amplitudes each contribute to only one CP eigenstate. One finds

$$\begin{aligned} A_0(t) &= A_0(0)e^{-imt} e^{-\Gamma t/2} \left(\cos \frac{\Delta mt}{2} + i\eta\lambda_f \sin \frac{\Delta mt}{2} \right) \\ A_{\parallel}(t) &= A_{\parallel}(0)e^{-imt} e^{-\Gamma t/2} \left(\cos \frac{\Delta mt}{2} + i\eta\lambda_f \sin \frac{\Delta mt}{2} \right) \\ A_{\perp}(t) &= A_{\perp}(0)e^{-imt} e^{-\Gamma t/2} \left(\cos \frac{\Delta mt}{2} - i\eta\lambda_f \sin \frac{\Delta mt}{2} \right) \end{aligned} \quad (5.30)$$

²These two combinations correspond respectively to G_{1+} and G_{1-} in the notation of Dunietz *et al.*, [12].

where $\lambda_f = \frac{q}{p} \frac{\bar{A}(f)}{A(f)}$ and the CP of the final state is $\eta_f(-1)^L$, where η_f is the intrinsic CP (for example $\eta(J/\psi(K_S\pi^0)_{K^*}) = +1$) and L is the partial wave between V_1 and V_2 . The factor $(-1)^L$ is explicit in Eq. (5.30) and accounts for the negative sign in the expression for $A_\perp(t)$. From these expressions one can deduce the time dependence in the helicity basis or for S , P and D .

Note that these expressions are valid if a single CKM phase contributes, a safe assumption in the case of $J/\psi K^*$. However, for $D^*\bar{D}^*$, where penguin effects can be sizeable, in general λ_f is not the same for the different transversity amplitudes because the ratio of penguin to tree contributions will be different for the different amplitudes. In general one should assume different $\lambda_0, \lambda_\parallel, \lambda_\perp$.

The corresponding amplitudes for the decay of $\bar{B}_{phys}^0(t)$ into the CP eigenstate f

$$\begin{aligned}\bar{A}_0(t) &= \eta\bar{A}_0(0)e^{-imt} e^{-\Gamma t/2} \left(\cos \frac{\Delta mt}{2} + i\eta\lambda_f^{-1} \sin \frac{\Delta mt}{2} \right) \\ \bar{A}_\parallel(t) &= \eta\bar{A}_\parallel(0)e^{-imt} e^{-\Gamma t/2} \left(\cos \frac{\Delta mt}{2} + i\eta\lambda_f^{-1} \sin \frac{\Delta mt}{2} \right) \\ \bar{A}_\perp(t) &= -\eta\bar{A}_\perp(0)e^{-imt} e^{-\Gamma t/2} \left(\cos \frac{\Delta mt}{2} - i\eta\lambda_f^{-1} \sin \frac{\Delta mt}{2} \right).\end{aligned}\quad (5.31)$$

The algebra that gives predicted time-dependent angular distributions has been given in detail in [12]. To write the angular distribution, the following conventions (Fig. 5-8) are used: \mathbf{p}_1 denotes the three-momentum of the K_S in the K^{*0} rest frame; \mathbf{p}_2 the three-momentum of the l^+ in the J/ψ rest frame; \hat{v} is the unit vector along the direction of flight of the K^{*0} and $\hat{c}(\hat{d})$ is the unit vector along the projection of \mathbf{p}_1 (\mathbf{p}_2) orthogonal to \hat{v} ($-\hat{v}$). Three angles are now defined in the helicity frame by

$$\begin{aligned}\cos \theta_1 &= \hat{v} \cdot \mathbf{p}_1 / |\mathbf{p}_1| & \cos \theta_2 &= -\hat{v} \cdot \mathbf{p}_2 / |\mathbf{p}_2| \\ \cos \phi &= \hat{c} \cdot \hat{d} & \sin \phi &= (\hat{c} \times \hat{v}) \cdot \hat{d}\end{aligned}\quad (5.32)$$

In the helicity basis the three angles are then defined to be the polar angle of the l^+ in the J/ψ rest frame θ_2 ; the polar angle of the K in the K^* rest frame θ_1 ; and the angle between the K^* decay plane and the J/ψ decay plane ϕ , that can take values from 0 to 2π .

Then the full angular distribution of the B decay in the helicity basis:

$$\begin{aligned}\frac{1}{\Gamma} \frac{d^3\Gamma}{d \cos \theta_1 d \cos \theta_2 d\phi} &= \frac{9}{16\pi} \frac{1}{|A_0|^2 + |A_{+1}|^2 + |A_{-1}|^2} \\ &\left\{ \frac{1}{4} (1 + \cos^2 \theta_2) \sin^2 \theta_1 (|A_{+1}|^2 + |A_{-1}|^2) + \sin^2 \theta_2 \cos^2 \theta_1 |A_0|^2 \right. \\ &\quad \left. - \frac{1}{2} \sin^2 \theta_1 \sin^2 \theta_2 [\cos 2\phi \text{Re}(A_{+1}A_{-1}^*) - \sin 2\phi \text{Im}(A_{+1}A_{-1}^*)] \right. \\ &\quad \left. + \frac{1}{4} \sin 2\theta_1 \sin 2\theta_2 [\cos \phi \text{Re}(A_{+1}A_0^* + A_{-1}A_0^*) - \sin \phi \text{Im}(A_{+1}A_0^* - A_{-1}A_0^*)] \right\}.\end{aligned}\quad (5.33)$$

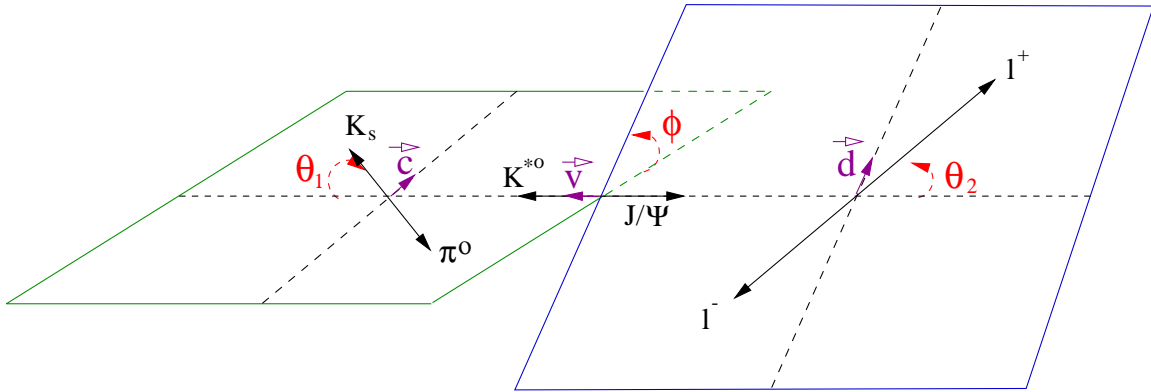


Figure 5-8. Helicity frame for $\bar{B}_d^0 \rightarrow J/\psi \bar{K}^{*0} \rightarrow \ell^+ \ell^- \bar{K} \pi$. The vectors \hat{c} , \hat{v} and \hat{d} are defined in the text.

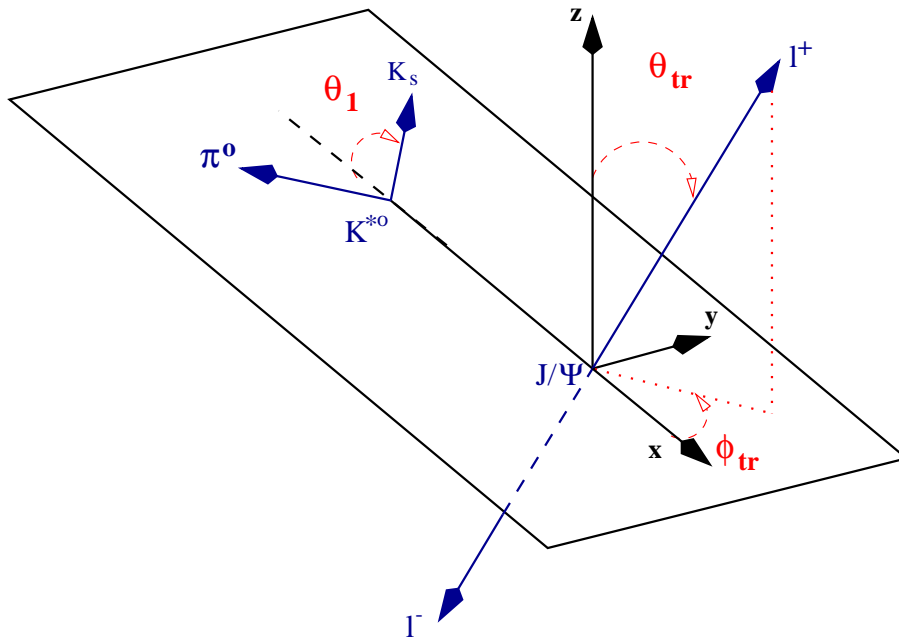


Figure 5-9. Transversity frame for $\bar{B}_d^0 \rightarrow J/\psi \bar{K}^{*0} \rightarrow \ell^+ \ell^- \bar{K} \pi$.

In Eq. (5.33) the amplitudes depend on time, and the angular distribution for the decay of $B_d^0(t)$ is normalized here at time t . It could be more convenient in practice to normalize to the total rate, tagged or untagged, integrated over time.

The longitudinal polarization ratio R_0 is defined by

$$R_0 = \frac{\Gamma_0}{\Gamma} = \frac{|A_0|^2}{|A_0|^2 + |A_{+1}|^2 + |A_{-1}|^2} \quad (5.34)$$

and the proportion of transverse polarization will then be $R_T = 1 - R_0$. Integrating over the angle ϕ gives

$$\frac{1}{\Gamma} \frac{d^2\Gamma}{d \cos \theta_1 d \cos \theta_2} = \frac{9}{32}(1 - R_0) \sin^2 \theta_1 (1 + \cos^2 \theta_2) + \frac{9}{8} R_0 \cos^2 \theta_1 \sin^2 \theta_2. \quad (5.35)$$

Then, a one-parameter fit in the $\cos \theta_1 - \cos \theta_2$ plane is sufficient to determine the longitudinal polarization R_0 . However, Γ_T has two pieces, corresponding to the parity conserving (P -wave) amplitude (VV part of the weak interaction) and to the parity-violating ($S + D$ waves) amplitude (AV part of the interaction).

In the transversity formalism the angles are defined as follows: In the J/ψ rest frame, the momentum \mathbf{p}_ψ defines the Ox axis; the plane $K\pi$ contains the Oy axis with $p_y(K) > 0$; Oz is the normal to $K\pi$ plane; θ_{tr} is the so-called transversity angle between ℓ^+ and Oz , and the projection of ℓ^+ on the $K\pi$ plane in the J/ψ rest frame and the Ox axis define the azimuthal angle ϕ_{tr} . The third angle θ_1 is defined like in the helicity basis (Fig. 5-9).

The K^* linear polarization lies in the $K\pi$ plane because the VPP coupling $K^*K\pi$ is of the form $\varepsilon_{K^*} \cdot (p_K - p_\pi)$, and one can consider the K^* linear polarization to be $\varepsilon_{K^*} = \hat{x}$ (longitudinal) or $\varepsilon_{K^*} = \hat{y}$ (transverse). The three transversity amplitudes are then defined by the direction of the polarization of J/ψ :

$$\begin{aligned} A_0 &: \quad \varepsilon_{K^*} = \hat{x} & \varepsilon_\psi = \hat{x} & \quad (CP = +) \\ A_{\parallel} &: \quad \varepsilon_{K^*} = \hat{y} & \varepsilon_\psi = \hat{y} & \quad (CP = +) \\ A_{\perp} &: \quad \varepsilon_{K^*} = \hat{y} & \varepsilon_\psi = \hat{z} & \quad (CP = -). \end{aligned}$$

Thus the notation becomes transparent: A_{\parallel} means transverse polarization parallel to the plane of the other decay, and A_{\perp} means transverse polarization perpendicular to that plane [14].

The relation between the angles in the helicity and the transversity basis is

$$\begin{aligned} \cos \theta_2 &= \sin \theta_{tr} \cos \phi_{tr} \\ \sin \theta_2 \sin \phi &= \cos \theta_{tr} \\ \sin \theta_2 \cos \phi &= \sin \theta_{tr} \sin \phi_{tr} \quad . \end{aligned} \quad (5.36)$$

Thus, the angular distribution writes for the transversity basis is:

$$\frac{1}{\Gamma} \frac{d^3\Gamma}{d \cos \theta_{\text{tr}} d \cos \theta_1 d \phi_{\text{tr}}} = \frac{9}{32\pi} \frac{1}{|A_0|^2 + |A_{\parallel}|^2 + |A_{\perp}|^2} \quad (5.37)$$

$$\left\{ 2 \cos^2 \theta_1 (1 - \sin^2 \theta_{\text{tr}} \cos^2 \phi_{\text{tr}}) |A_0|^2 + \sin^2 \theta_1 (1 - \sin^2 \theta_{\text{tr}} \sin^2 \phi_{\text{tr}}) |A_{\parallel}|^2 \right.$$

$$+ \sin^2 \theta_1 \sin^2 \theta_{\text{tr}} |A_{\perp}|^2 + \sin^2 \theta_1 \sin 2\theta_{\text{tr}} \sin \phi_{\text{tr}} \text{Im}(A_{\parallel}^* A_{\perp})$$

$$\left. + \frac{1}{\sqrt{2}} \sin 2\theta_1 \sin^2 \theta_{\text{tr}} \sin 2\phi_{\text{tr}} \text{Re}(A_0^* A_{\parallel}) - \frac{1}{\sqrt{2}} \sin 2\theta_1 \sin 2\theta_{\text{tr}} \cos \phi_{\text{tr}} \text{Im}(A_0^* A_{\perp}) \right\}.$$

The combination $|A_0|^2 + |A_{\parallel}|^2$ describes the parity-even ($S + D$ waves) while $|A_{\perp}|^2$ corresponds to the parity-odd (P -wave) components. Define the proportion of parity-odd component as

$$R_{\perp} = \frac{|A_{\perp}|^2}{|A_0|^2 + |A_{\parallel}|^2 + |A_{\perp}|^2} . \quad (5.38)$$

Integrating over ϕ_{tr} and θ_1 one obtains

$$\frac{1}{\Gamma} \frac{d\Gamma}{d \cos \theta_{\text{tr}}} = \frac{3}{8} (1 - R_{\perp}) (1 + \cos^2 \theta_{\text{tr}}) + \frac{3}{4} R_{\perp} \sin^2 \theta_{\text{tr}} \quad (5.39)$$

and the parity-odd component can be extracted by a one-parameter fit. This time-independent analysis applies to charged B decays as well as to neutral B decays without tagging. This analysis has been done by CLEO for $J/\psi K^*$, this measurement which provides a necessary input in the simulations for CP this mode.

The CLEO fit on these distributions gives [13]

$$R_0 = 0.52 \pm 0.07 \pm 0.04, \quad R_{\perp} = 0.16 \pm 0.08 \pm 0.04 \quad (5.40)$$

and the relative phases $\varphi(A)$ with the convention $\varphi(A_0) = 0$

$$\varphi(A_{\parallel}) + \pi = 3.00 \pm 0.37 \pm 0.04 \quad \varphi(A_{\perp}) = -0.11 \pm 0.46 \pm 0.03 \quad (5.41)$$

(the π comes from the CLEO choice of angle convention). These results are consistent with relative reality of the amplitudes A_{\parallel} , A_{\perp} , A_0 , as expected within the hypothesis of factorization [15, 16].

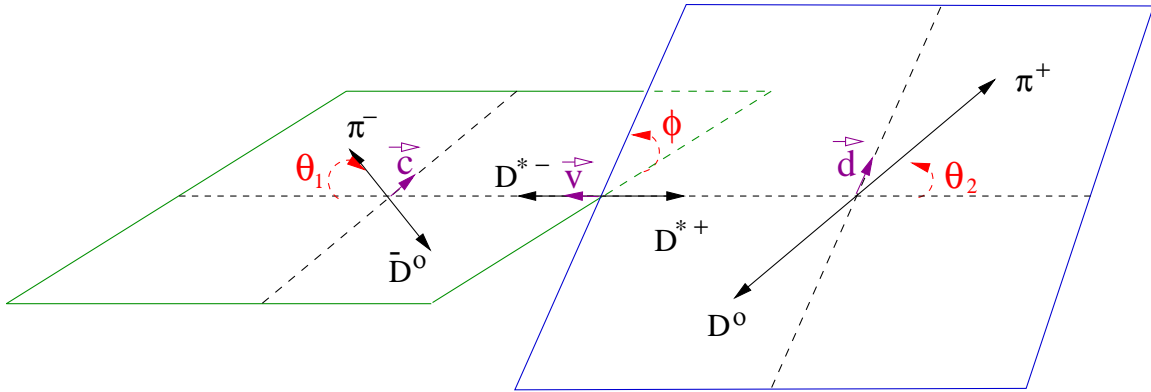


Figure 5-10. Helicity frame for $B \rightarrow D^{*+} D^{*-} \rightarrow D^0 \pi^+ \bar{D}^0 \pi^-$. The vectors \hat{c} , \hat{v} , and \hat{d} are used to define the angles like in the $J/\psi K^*$ case, described in the text.

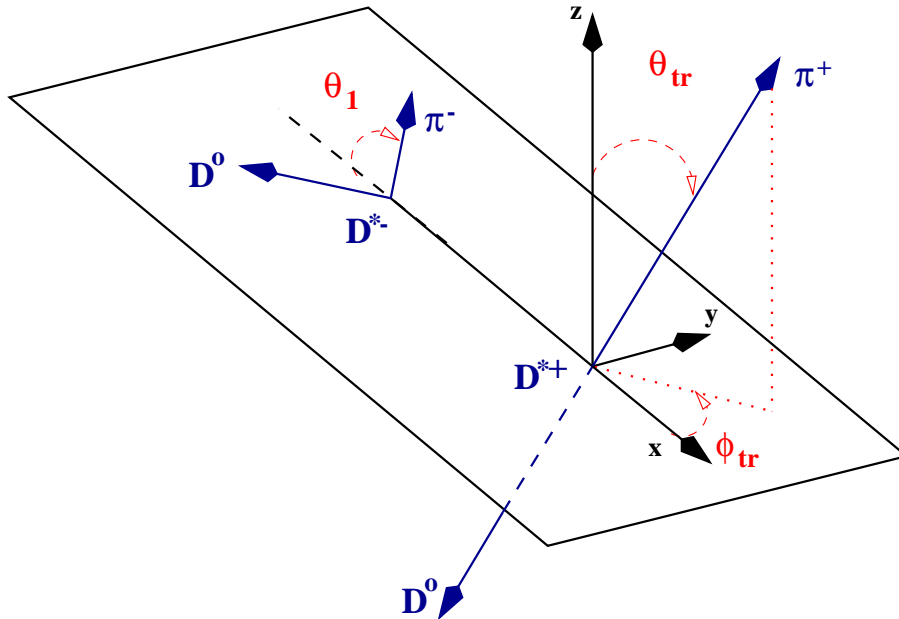


Figure 5-11. Transversity frame for $B \rightarrow D^{*+} D^{*-} \rightarrow D^0 \pi^+ \bar{D}^0 \pi^-$.

The angular distribution in the helicity and the transversity frames for the mode $B_d^0 \rightarrow D^{*+}D^{*-} \rightarrow D^0\pi^+\bar{D}^0\pi^-$ are given below [17]. In the helicity basis, the angles are defined as follows: θ_1 is the polar angle of π^- in the D^{*-} rest frame, θ_2 is the polar angle of π^+ in the D^{*+} rest frame, and ϕ is the azimuthal angle between the D^{*+} and D^{*-} decay planes (Fig. 5-10).

$$\begin{aligned} \frac{1}{\Gamma} \frac{d^3\Gamma}{d \cos \theta_1 d \cos \theta_2 d\phi} &= \frac{9}{16\pi} \frac{1}{|A_0|^2 + |A_{+1}|^2 + |A_{-1}|^2} \\ &\left\{ \frac{1}{2} \sin^2 \theta_1 \sin^2 \theta_2 (|A_{+1}|^2 + |A_{-1}|^2) + 2 \cos^2 \theta_1 \cos^2 \theta_2 |A_0|^2 \right. \\ &+ \sin^2 \theta_1 \sin^2 \theta_2 [\cos 2\phi \operatorname{Re}(A_{+1}A_{-1}^*) - \sin 2\phi \operatorname{Im}(A_{+1}A_{-1}^*)] \\ &\left. - \frac{1}{2} \sin 2\theta_1 \sin 2\theta_2 [\cos \phi \operatorname{Re}(A_{+1}A_0^* + A_{-1}A_0^*) - \sin \phi \operatorname{Im}(A_{+1}A_0^* - A_{-1}A_0^*)] \right\}. \end{aligned} \quad (5.42)$$

Integrating over the angle ϕ gives

$$\frac{1}{\Gamma} \frac{d^2\Gamma}{d \cos \theta_1 d \cos \theta_2} = \frac{9}{16} (1 - R_0) \sin^2 \theta_1 \sin^2 \theta_2 + \frac{9}{4} R_0 \cos^2 \theta_1 \cos^2 \theta_2. \quad (5.43)$$

Then, a one-parameter fit in the $\cos \theta_1 - \cos \theta_2$ plane is sufficient to determine the fraction of longitudinal polarization R_0 .

In the transversity basis, the angles are the polar angle θ_1 of the π^- in the D^{*-} rest frame (like in the helicity basis), the polar angle θ_{tr} between the normal to the D^{*-} decay plane and the π^+ line of flight and the relative azimuthal angle ϕ_{tr} (Fig. 5-11). The angular distribution writes then

$$\begin{aligned} \frac{1}{\Gamma} \frac{d^3\Gamma}{d \cos \theta_1 d \cos \theta_{\text{tr}} d\phi_{\text{tr}}} &= \frac{9}{16\pi} \frac{1}{|A_0|^2 + |A_{\parallel}|^2 + |A_{\perp}|^2} \\ &\left\{ 2 \cos^2 \theta_1 \sin^2 \theta_{\text{tr}} \cos^2 \phi_{\text{tr}} |A_0|^2 + \sin^2 \theta_1 \sin^2 \theta_{\text{tr}} \sin^2 \phi_{\text{tr}} |A_{\parallel}|^2 \right. \\ &+ \sin^2 \theta_1 \cos^2 \theta_{\text{tr}} |A_{\perp}|^2 - \sin^2 \theta_1 \sin 2\theta_{\text{tr}} \sin \phi_{\text{tr}} \operatorname{Im}(A_{\parallel}^* A_{\perp}) \\ &- \frac{1}{\sqrt{2}} \sin 2\theta_1 \sin^2 \theta_{\text{tr}} \sin 2\phi_{\text{tr}} \operatorname{Re}(A_0^* A_{\parallel}) \\ &\left. + \frac{1}{\sqrt{2}} \sin 2\theta_1 \sin 2\theta_{\text{tr}} \cos \phi_{\text{tr}} \operatorname{Im}(A_0^* A_{\perp}) \right\}. \end{aligned} \quad (5.44)$$

Integrating over ϕ and θ_1 one obtains

$$\frac{1}{\Gamma} \frac{d\Gamma}{d \cos \theta_{\text{tr}}} = \frac{3}{4} (1 - R_{\perp}) \sin^2 \theta_{\text{tr}} + \frac{3}{2} R_{\perp} \cos^2 \theta_{\text{tr}} \quad (5.45)$$

and the parity-odd component can be extracted by a one-parameter fit.

5.1.4 Isospin Analysis

The isospin structure of QCD penguin diagrams is, in general, more restricted than that of the tree contributions. Hence, isospin analysis can be a useful tool in some channels for separating the effects of these two types of contribution. This is discussed in greater detail in Chapter 6, since the method is most useful for channels that measure α , as it can achieve a clean separation of a tree-only contribution. For the β modes no such clean separation can be made, but it is possibly still useful to apply isospin analyses to these channels as it provides tests that help to gain an understanding of and further constraints on penguin contributions, and on the validity of the factorization approximation.

In Type I decays, charmonium $+K(K^*)$, the transition is pure $\Delta I = 0$, implying the equality of the amplitudes $A(\bar{B}_d^0 \rightarrow (c\bar{c})\bar{K}^0) = A(B_u^- \rightarrow (c\bar{c})K^-)$. This simple isospin relationship shows that measurements of the charged modes can be used to constrain the time-independent quantities that also enter into the neutral decay channels. While none of these quantities is needed to extract $\sin 2\beta$ such relationships between channels provide useful cross checks for the understanding of experimental data.

For Type II decays, as the $D\bar{D}$ modes, there are three possible charge states $\bar{B}_d^0 \rightarrow D^+D^-$, $D^0\bar{D}^0$, $B^- \rightarrow D^-D^0$. Since the interaction H_w is $\Delta I = \frac{1}{2}$, with final isospin then either 0 or 1 for *both* tree and penguin operators, these cannot be separated via isospin analysis.

In the isospin basis the final $D\bar{D}$ can be in a state $I = 0$ or $I = 1$. Isospin symmetry says that each isospin amplitude has a unique strong phase, although they are not necessarily the same for current-current (tree) and penguin operators. This last can be understood from the fact that the kinematics of the two diagrams are different and hence the mixing of the two-body state with higher multiplicity states of the same isospin is different for the two terms, this then results in different rescattering phases. One can write [18]

$$\begin{aligned} A(\bar{B}_d^0 \rightarrow D^+D^-) &= \frac{1}{2}\bar{A}_1 + \frac{1}{2}\bar{A}_0 \\ A(\bar{B}_d^0 \rightarrow D^0\bar{D}^0) &= \frac{1}{2}\bar{A}_1 - \frac{1}{2}\bar{A}_0 \\ A(B^- \rightarrow D^0D^-) &= \bar{A}_1. \end{aligned} \tag{5.46}$$

This implies the isospin triangular relation

$$A(\bar{B}_d^0 \rightarrow D^+D^-) + A(\bar{B}_d^0 \rightarrow D^0\bar{D}^0) = A(B^- \rightarrow D^0D^-) \tag{5.47}$$

and a similar one for the CP -conjugated processes. Relations of the same form hold separately for the modes $\bar{B} \rightarrow D\bar{D}^*$, $\bar{D}D^*$ and for the different spin amplitudes of $\bar{B} \rightarrow D^*\bar{D}^*$.

From these relationships it is clear that one can find the magnitudes and relative phases of the various isospin amplitudes from a measurement of the three rates. In principle this allows one to

define and measure an asymmetry for each isospin separately. These two quantities both would be proportional to $\sin 2\beta$ if penguin effects were negligible, but the non-negligible penguins introduce a shift to both.

However, from vector current conservation and the assumption of factorization, $A(\bar{B}_d^0 \rightarrow D^0 \bar{D}^0) = 0$, since the only possible diagram is of the exchange type (Fig. 5-5b). For the other modes, the amplitudes in the neutral mode, *e.g.*, $A(\bar{B}_d^0 \rightarrow D^{*0} \bar{D}^0)$, $A(\bar{B}_d^0 \rightarrow D^0 \bar{D}^{*0})$ or $A(\bar{B}_d^0 \rightarrow D^{*0} \bar{D}^{*0})$, current conservation is not applicable, but these are suppressed by a color factor a_2 and also by a form factor at large q^2 , $F^{cc}(m_B^2)$. Neglecting the exchange diagram, one predicts equality between the other two modes, as in $A(B^- \rightarrow D^0 D^-) = A(\bar{B}_d^0 \rightarrow D^+ D^-)$. Thus the factorization assumption predicts $A_{00} = 0$, which implies that $A_1 = A_0$, and in fact separately $T_1 = T_0$ and $P_1 = P_0$. Thus, up to terms due to rescattering, the two definite-isospin asymmetries, and hence the overall asymmetry, are the same. Clearly the size of A_{00} and its CP conjugate \bar{A}_{00} provide a test of factorization, but the isospin analysis gives little new information in these channels. Note that the preceding discussion is not changed by Electroweak penguin operators, since these are also $\Delta I = \frac{1}{2}$.

For the Type III modes, insofar as these are penguin-dominated, there is nothing to be gained by isospin analysis. For $d\bar{d}s$ modes there is a small tree-contribution. Here the possible application of isospin analysis would be to isolate a pure-penguin term, whereas in the α channels the aim is to isolate a pure-tree term. While the latter is possible, the former is not, because the tree terms contribute to every possible isospin state, while the penguins contribute only to a restricted class.

Thus the general conclusion is that isospin analysis is not particularly useful in the β channels.

5.1.5 Modeling the Uncertainty on β

Decays of Type II or III can help to measure $\sin 2\beta$, based on the naively expected order of magnitude of penguins and current-current operators respectively. As discussed above, corrections due to the suppressed terms may be significant. These corrections can be calculated using theoretical models, but this introduces a theoretical uncertainty in the extracted value of β , due to the uncertainty of the model-dependent calculation. As a first approximation for this uncertainty, one can take the size of the shift introduced in a simple model as the uncertainty in β . As understanding of the validity of these models is improved by confronting them with data, the actual shift may become better determined and the uncertainty in the shift reduced. In this section, the uncertainty on β for decays of Types II and III is estimated as the shift in β calculated using factorization [19] and neglecting the relatively small effect of electroweak penguins.

5.1.5.1 Type II modes

For Type II (Cabibbo-suppressed) modes, within the factorization assumption, there are no final-state interactions and hence FSI phases $\rightarrow 0$. From the general formalism of decays of B_d^0 , \bar{B}_d^0 to common modes that are CP conjugate pairs but not necessarily CP eigenstates [20], one can write the time-dependent rates for the different $D\bar{D}$, $D\bar{D}^* + D^*\bar{D}$, $D^*\bar{D}^*$ modes in the form

$$\begin{aligned} R(B_d^0(t) \rightarrow f) &\sim [1 + R \cos(\Delta mt) + \eta_f D \sin[2(\beta + \Delta\beta)] \sin(\Delta mt)] \\ R(\bar{B}_d^0(t) \rightarrow f) &\sim [1 - R \cos(\Delta mt) - \eta_f D \sin[2(\beta + \Delta\beta)] \sin(\Delta mt)] \end{aligned} \quad (5.48)$$

where $\eta_f = +$ for $D\bar{D}$ and for $(D^*\bar{D}^*)_{CP=+}$, and also for $D\bar{D}^* + \bar{D}D^*$ in some theoretical limit (see Section 5.1.6), and $\eta_f = -$ for $(D^*\bar{D}^*)_{CP=-}$ and

$$D = \frac{2|A| |\bar{A}|}{|A|^2 + |\bar{A}|^2} \quad R = \frac{|A|^2 - |\bar{A}|^2}{|A|^2 + |\bar{A}|^2} \quad (5.49)$$

since one has:

$$\frac{q}{p} \frac{\bar{A}(f)}{A(f)} = \eta_f \frac{|\bar{A}|}{|A|} e^{-2i(\beta + \Delta\beta)} \quad (5.50)$$

The effect of penguins is to shift the angle β by an amount $\Delta\beta$, and also to affect the dilution factor D . Since within factorization the FSI phase is neglected, for CP eigenstates $D = 1$. For non- CP eigenstates, since $D^2 + R^2 = 1$ and D can be measured from the $\cos \Delta mt$ dependence.

For the purpose of modeling the shift $\Delta\beta$, one can write the amplitudes for the different decays $D\bar{D}$, $D\bar{D}^*$, $D^*\bar{D}$, $D^*\bar{D}^*$ (up to irrelevant overall phases) [21]:

$$\begin{aligned} A(\bar{B}_d^0 \rightarrow D^+ D^-) &= \frac{G_F}{\sqrt{2}} f_D (m_B^2 - m_D^2) f_0^{cb}(m_D^2) \\ &\times \left[V_{cd}^* V_{cb} a_1 - V_{td}^* V_{tb} \left(a_4 + a_6 \frac{2M_D^2}{(m_b - m_c)(m_c + m_d)} \right) \right] \\ A(\bar{B}_d^0 \rightarrow D^+ D^{*-}) &= \frac{G_F}{\sqrt{2}} 2f_{D^*} m_B f_+^{cb}(m_{D^*}^2) p (V_{cd}^* V_{cb} a_1 - V_{td}^* V_{tb} a_4) \\ A(\bar{B}_d^0 \rightarrow D^{*+} D^-) &= -\frac{G_F}{\sqrt{2}} 2f_D m_B A_0^{cb}(m_D^2) p \\ &\times \left[V_{cd}^* V_{cb} a_1 - V_{td}^* V_{tb} \left(a_4 - a_6 \frac{2M_D^2}{(m_b + m_c)(m_c + m_d)} \right) \right] \end{aligned} \quad (5.51)$$

and the amplitudes $D^{*+} D^{*-}$ are:

$$\bar{A}_0 = A(\bar{B}_d^0 \rightarrow D^{*+}(\lambda=0) D^{*-}(\lambda=0)) = \frac{G_F}{\sqrt{2}} m_{D^*} f_{D^*}$$

$$\left[(m_B + m_{D^*}) \left(\frac{2p^2 + m_{D^*}^2}{m_{D^*}^2} \right) A_1^{cb}(m_{D^*}^2) - \frac{m_B^2}{m_B + m_{D^*}} \frac{2p^2}{m_{D^*}^2} A_2^{cb}(m_{D^*}^2) \right] \times (V_{cd}^* V_{cb} a_1 - V_{td}^* V_{tb} a_4) \quad (5.52)$$

$$\bar{A}_{\parallel} = G_F m_{D^*} f_{D^*} (m_B + m_{D^*}) A_1^{cb}(m_{D^*}^2) (V_{cd}^* V_{cb} a_1 - V_{td}^* V_{tb} a_4) \quad (CP = +)$$

$$\bar{A}_{\perp} = G_F m_{D^*} f_{D^*} \frac{2m_B}{m_B + m_{D^*}} V^{cb}(m_{D^*}^2) p (V_{cd}^* V_{cb} a_1 - V_{td}^* V_{tb} a_4) \quad (CP = -).$$

In the preceding equations, $a_1 = C_2 + \frac{C_1}{N_c}$, $a_4 = C_4 + \frac{C_3}{N_c}$, $a_6 = C_6 + \frac{C_5}{N_c}$, with the short-distance coefficients C_i given in Appendix A. Since in this approximation the various form factors in the DD and DD^* case appear only as overall quantities, multiplying both the leading and the naively suppressed term, their actual form does not affect the estimated value of the shift $\Delta\beta$. This is also true for the transverse amplitude A_{\perp} in the D^*D^* case. Thus the model gives

$$\begin{aligned} (\Delta\beta)_{DD} &= \text{Arg} \left[1 + (1 - \rho - i\eta) \frac{1}{a_1} \left(a_4 + a_6 \frac{2M_D^2}{(m_b - m_c)(m_c + m_d)} \right) \right] \\ (\Delta\beta)_{D^*D} &= \text{Arg} \left[1 + (1 - \rho - i\eta) \frac{1}{a_1} \frac{1}{2} \left(2a_4 - a_6 \frac{2M_D^2}{(m_b + m_c)(m_c + m_d)} \right) \right] \\ (\Delta\beta)_{D^*D^*} &= \text{Arg} \left[1 + (1 - \rho - i\eta) \frac{1}{a_1} a_4 \right]. \end{aligned} \quad (5.53)$$

The two penguin terms in $(\Delta\beta)_{DD}$ have the same sign, while the two terms in $(\Delta\beta)_{D^*D}$ have opposite signs: the penguin correction is smaller in DD^* than in DD . For the purpose of illustration, the uncertainties on masses and short-distance coefficients are neglected, and the correction $\Delta\beta$ is computed in terms of ρ and η . Using the numerical values $a_1 = 1.04$, $a_4 = -0.031$, $a_6 = -0.042$ and the current masses $m_b = 4.7 \text{ GeV}/c^2$, $m_c = 1.2 \text{ GeV}/c^2$, one finds

$$\begin{aligned} (\Delta\beta)_{DD} &\cong \text{Arg}[1 - 0.088(1 - \rho - i\eta)] \\ (\Delta\beta)_{D^*D} &\cong \text{Arg}[1 - 0.010(1 - \rho - i\eta)] \\ (\Delta\beta)_{D^*D^*} &\cong \text{Arg}[1 - 0.029(1 - \rho - i\eta)] \end{aligned} \quad (5.54)$$

Since both $\sin 2\beta$ and $\Delta\beta$ are functions of (ρ, η) , the allowed region in the $\rho - \eta$ plane due to the constraints coming from ε_K , $B_d^0 - \bar{B}_d^0$ mixing and $|V_{ub}|$ will result in an allowed domain in the plane $\Delta\beta - \sin 2\beta$. In Fig. 5-12 the allowed domains from Eq. (5.54) are plotted for each these modes.

5.1.5.2 Type III (Penguin-dominated) modes

In the same way one can estimate, using the factorization assumption, the correction $\Delta\beta$ due to the tree diagram in the penguin-dominated modes like $\pi^0 K_S$, $\rho^0 K_S$, $\pi^0 (\bar{K}^{*0})_{K_S \pi^0}$ or $\rho^0 (\bar{K}^{*0})_{K_S \pi^0}$.

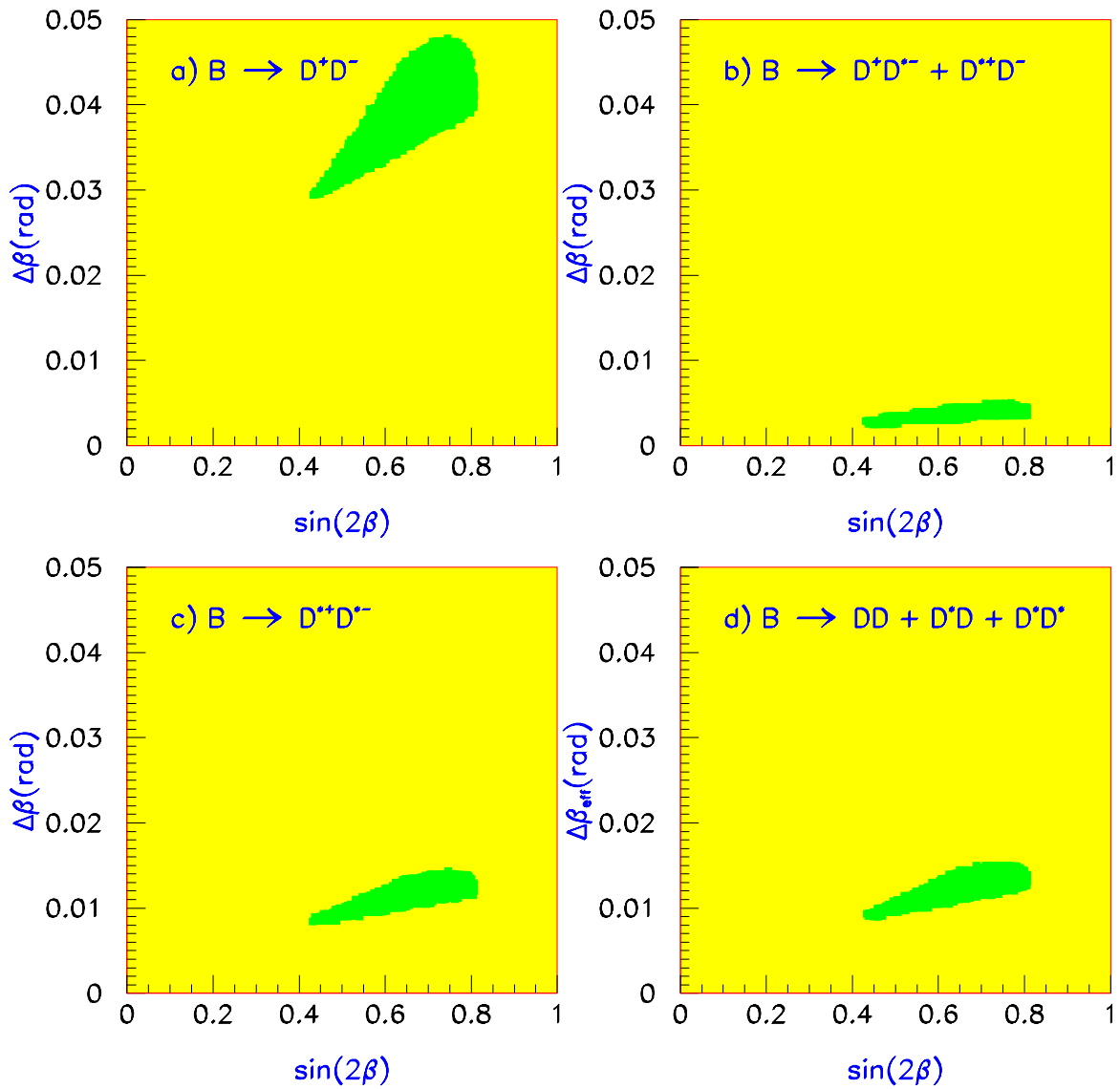


Figure 5-12. Uncertainty $\Delta\beta$ due to penguins in Cabibbo-suppressed (Type II) decays, assuming factorization.

Again one can use the model estimate of the shift as an estimate of the uncertainty in the shift. Note that the modes ϕK_S , $\phi \bar{K}^{*0}$ do not have any tree contribution, and the determination of β is free from ambiguities.

To illustrate the expected shift $\Delta\beta$ for the other modes, consider the amplitudes assuming factorization:

$$A(\bar{B}_d^0 \rightarrow \pi^0 \bar{K}^0) = \frac{G_F}{\sqrt{2}} f_P (m_B^2 - m_P^2) f_0^{ub}(m_P^2) \frac{1}{\sqrt{2}} \times [V_{us}^* V_{ub} a_2 + V_{ts}^* V_{tb} (a_4 + a_6 C_P)] \quad (5.55)$$

$$A(\bar{B}_d^0 \rightarrow \rho^0 \bar{K}^0) = \frac{G_F}{\sqrt{2}} 2 f_P m_B A_0^{qb}(m_P^2) p \frac{1}{\sqrt{2}} \times [V_{us}^* V_{ub} a_2 R_{VP} + V_{ts}^* V_{tb} (a_4 - a_6 C_P)]$$

$$A(\bar{B}_d^0 \rightarrow \pi^0 \bar{K}^{*0}) = \frac{G_F}{\sqrt{2}} 2 f_V m_B f_0^{qb}(m_V^2) p \frac{1}{\sqrt{2}} (V_{us}^* V_{ub} a_2 R_{PV} + V_{ts}^* V_{tb} a_4)$$

where $C_P \cong \frac{2m_K^2}{m_b m_s}$, $R_{PV} = R_{VP}^{-1}$ is the ratio $f_P A_0^{qb}(m_P^2)/f_V f_0^{qb}(m_V^2)$, and the amplitudes for $\rho^0 \bar{K}^{*0}$ are:

$$A_0 = \frac{G_F}{\sqrt{2}} \frac{1}{\sqrt{2}} (V_{us}^* V_{ub} a_2 + V_{ts}^* V_{tb} a_4) m_V f_V \quad (5.56)$$

$$\left[(m_B + m_V) \left(1 + \frac{2p^2}{m_V^2} \right) A_1^{qb}(m_V^2) - \frac{m_B^2}{m_B + m_V} \frac{2p^2}{m_V^2} A_2^{qb}(m_V^2) \right]$$

$$A_{\parallel} = G_F \frac{1}{\sqrt{2}} (V_{us}^* V_{ub} a_2 + V_{ts}^* V_{tb} a_4) m_V f_V (m_B + m_V) A_1^{qb}(m_V^2)$$

$$A_{\perp} = G_F \frac{1}{\sqrt{2}} (V_{us}^* V_{ub} a_2 + V_{ts}^* V_{tb} a_4) m_V f_V \frac{2m_B}{m_B + m_V} V^{qb}(m_V^2) p .$$

In all these formulae P and V stand for light pseudoscalar and vector mesons. $SU(3)$ symmetry has been used to reduce the number of independent form factors. This is essential to the estimate and introduces a further source of uncertainty into it. Moreover, for the sake of simplicity, $R_{PV} = R_{VP}^{-1} = 1$ is used, although this could be an overestimation in view of the actual ratio f_P/f_V .

Then the shift on β for the different modes are:

$$(\Delta\beta)_{\pi^0 K_S} = \text{Arg} \left[1 - (\rho - i\eta) \frac{\lambda^2 a_2}{a_4 + a_6 C_P} \right] \quad (5.57)$$

$$(\Delta\beta)_{\rho^0 K_S} = \text{Arg} \left[1 - (\rho - i\eta) \frac{\lambda^2 a_2}{a_4 - a_6 C_P} \right]$$

$$(\Delta\beta)_{\pi^0(\bar{K}^{*0})_{CP}} = \text{Arg} \left[1 - (\rho - i\eta) \frac{\lambda^2 a_2}{a_4} \right]$$

$$(\Delta\beta)_{\rho^0(\bar{K}^{*0})_{CP}} = \text{Arg} \left[1 - (\rho - i\eta) \frac{\lambda^2 a_2}{a_4} \right]$$

In this latter case \bar{K}^{*0} is assumed to decay in a CP eigenstate, and $\rho^0 \bar{K}^{*0}$ to be in a definite partial wave, and hence a definite CP .

Numerically, one finds (using $m_s \cong 150 \text{ MeV}/c^2$)

$$(\Delta\beta)_{\pi^0 K_S} = \text{Arg} [1 + 0.169(\rho - i\eta)] \quad (5.58)$$

$$(\Delta\beta)_{\rho^0 K_S} = \text{Arg} [1 + 3.49(\rho - i\eta)]$$

$$(\Delta\beta)_{\pi^0(\bar{K}^*)_{CP}} = \text{Arg} [1 + 0.322(\rho - i\eta)]$$

$$(\Delta\beta)_{\rho^0(\bar{K}^*)_{CP}} = \text{Arg} [1 + 0.322(\rho - i\eta)] \quad .$$

In the $\rho^0 K_S$ case, the model predicts that the tree is of the same order as the penguin due to the near cancellation between the a_4 and a_6 coefficients in the penguin term (the same cancellation that gives a small $\Delta\beta$ for the DD^* channel). It is clear that this mode cannot be used for the extraction of β . Further the branching ratio for this mode is predicted to be very small. This suppression of the $\rho^0 K_S$ amplitudes implies that electroweak penguins may be important in this mode; these were not included in the above estimates.

This calculation predicts the hierarchy $\mathcal{B}(\rho^0 \bar{K}^0) \ll \mathcal{B}(\pi^0 \bar{K}^{*0}) < \mathcal{B}(\pi^0 \bar{K}^0)$. The mode ωK_S is known from isospin arguments alone to be sizeable because $B^- \rightarrow \omega K^-$ has been observed with a branching ratio of $\mathcal{O}(10^{-5})$ (Table 5-5). This rate is not surprisingly high taking into account both QCD and electroweak penguin contributions, although a factorization calculation gives an unstable result owing to the uncertainties on the short-distance coefficients. Tests of these and other model predictions may serve to help reduce the uncertainty in the shift of β .

In the Fig. 5-13 the allowed domains in the plane $\Delta\beta - \sin 2\beta$ for these modes are plotted. This can be used to estimate the theoretical uncertainty on $\sin 2\beta$. The correction for $\pi^0 K^*$ and $\rho^0 K^*$ is substantial (for the former this is possibly an overestimation in view of the value adopted for R_{PV}); only the mode $\pi^0 K_S$ seems favorable in view of this naive calculation.

The channel $\eta' K_S$ is interesting. The modes $\bar{B}_d^0 \rightarrow \eta' \bar{K}^0$ and $B^- \rightarrow \eta' K^-$ have been observed with a large branching ratio of the order of 5×10^{-5} (Table 5-5). An estimation of the rate can be made using the same model assumptions as above, with H_{eff} of Appendix 1. The mode is found to be penguin-dominated. Taking into account the two possible topologies for $\eta' \bar{K}^0$ of Figs. 5-3 ($\eta' = \eta_1, \cos \theta + \eta_8 \sin \theta$), the model gives:

$$\begin{aligned} \mathcal{B}(\bar{B}_d^0 \rightarrow \eta' \bar{K}^0) &\cong 3 \times \mathcal{B}(B_d^0(\bar{B}_d^0) \rightarrow K^\mp \pi^\pm) = \\ &= 3 \times (1.50 \pm 0.51) \times 10^{-5} \end{aligned} \quad (5.59)$$

where the $SU(3)$ singlet f_1 and octet f_8 pseudoscalar decay constants are taken to be equal $f_1 = f_8 = f_K$. In this rough calculation, the finite chiral-limit quantity is estimated by $\sqrt{3}\langle 0|\bar{q}\gamma_5 q|\eta_1\rangle \cong$

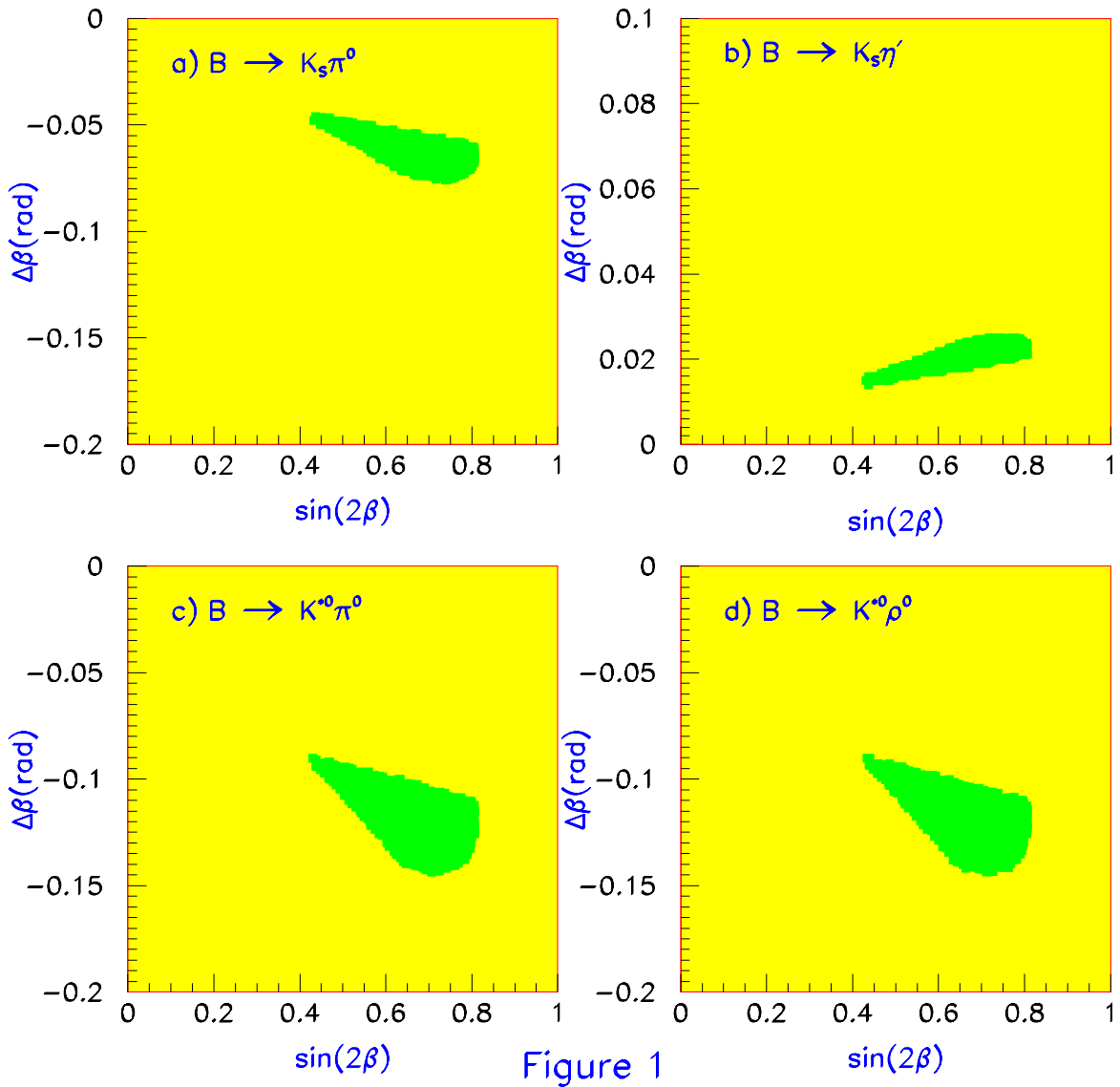


Figure 5-13. Uncertainty $\Delta\beta$ due to the tree diagram in penguin-dominated (Type III) decays, assuming factorization.

$\langle 0 | \bar{s} \gamma_5 q | K \rangle$ [22]. This naive estimate qualitatively reproduces the measured rate [23], and the shift in β is found to be small:

$$(\Delta\beta)_{\eta' K_S} \cong \text{Arg}[1 - 0.05(\rho - i\eta)] \quad . \quad (5.60)$$

This shift is plotted in Fig. 5-13.

The η' is coupled to two gluons through the chiral anomaly. Contributions of this type have the penguin topology. If they are large, the ratio of tree to penguin contributions, and hence the shift of β , for $\eta' K_S$ could be even smaller. A small $c\bar{c}$ component in the η' wave function has also been assumed [24] in some models to fit the large rate. Such contributions would not invalidate the measurement of $\sin 2\beta$ since the CKM phase of these terms is exactly that assumed for the dominant term.

5.1.6 Measurement of β in Inclusive Decays

This section examines CP asymmetries in inclusive decays $B_d^0, \bar{B}_d^0 \rightarrow D\bar{D} + X$ ($\Delta S = 0$). It has been suggested that such a measurement could be useful in the analysis of the earliest BaBar results. However, since both CP -odd and CP -even modes contribute such an asymmetry cannot be interpreted as a measurement of $\sin 2\beta$ unless the fraction of each sign CP state can be reliably calculated.

5.1.6.1 CP asymmetry in the sum of all DD type modes.

Heavy-quark symmetry and factorization be used to estimate the the CP properties of the sum of the ground state decay modes $B_d^0, \bar{B}_d^0 \rightarrow D\bar{D} + D\bar{D}^* + \bar{D}D^* + D^*\bar{D}^*$. The total branching ratio is predicted to be about 2×10^{-3} (Table 5-4).

The state $D\bar{D}$ is a $CP = +$ state. Now consider $D\bar{D}^* + \bar{D}D^*$. Note that in the heavy-quark limit D and D^* are degenerate partners of the same multiplet. Define two states of definite CP :

$$\frac{1}{\sqrt{2}}(|D^*(\lambda = 0, \mathbf{p})\bar{D}(-\mathbf{p}) \rangle \pm |D(\mathbf{p})\bar{D}^*(\lambda = 0, -\mathbf{p}) \rangle) \quad (CP = \mp) \quad . \quad (5.61)$$

In the limit of heavy-quark symmetry, the transformation of H_w under the operator $CP \times \exp\left(i\frac{\pi}{2}\sigma_z^{(c)}\right)$ implies that the spectator diagram (Fig. 5-5a) produces only the $CP = +$ combination, while the exchange diagram (Fig. 5-5b) gives only the $CP = -$ one [21]. The exchange diagram contribution is presumably small since: 1) it is suppressed by the short-distance factor $a_2 \cong 0.2$; and 2) there is a form factor suppression $A_0(q^2)$ because of the large $q^2 = m_B^2$ in the s -channel. Thus, $D\bar{D}^* + \bar{D}D^*$ is predicted to be in a $CP = +$ state to a good approximation [21].

$D^*\bar{D}^*$ could be in a $CP = +$ state ($S + D$ waves) or a $CP = -$ state (P wave). This contribution can be estimated in the heavy-quark limit. In this limit and within the factorization assumption the decays $D\bar{D}$, $D\bar{D}^*$, $\bar{D}D^*$, and $D^*\bar{D}^*$ are related to the decay constant $f_D = f_{D^*}$ and to the form factors $B \rightarrow D$ (D^*) that are given by the Isgur-Wise function $\xi(w)$. In the non-leptonic decays under consideration, the value of w is fixed: $w = \frac{m_B}{2m_D}$. One can write the CP asymmetry for the whole ground state sum as

$$a(t) = D_{g.s.} \sin 2\beta \sin \Delta mt \quad (5.62)$$

with the dilution factor given by the pure kinematic quantity

$$D_{g.s.} = 1 - \frac{2\Gamma_{\perp}}{\Gamma_{g.s.}} = 1 - \frac{4(w^2 - 1)}{4(w^2 - 1) + (2w - 1)^2(w + 1)^2} \quad w = \frac{m_b}{2m_c} \quad (5.63)$$

where $\Gamma_{g.s.} = \Gamma(D\bar{D} + \bar{D}D^* + D\bar{D}^* + D^*\bar{D}^*)$ is the total ground state width. With real masses, this gives $D_{g.s.} \cong 0.95$. Even though these modes are Cabibbo suppressed, the whole sum $D\bar{D} + D\bar{D}^* + \bar{D}D^* + D^*\bar{D}^*$ represents a statistical gain of a factor 6 relatively to the golden mode $J/\psi K_S^0$. However, the poorer detection efficiency in the former case puts $D\bar{D} + D\bar{D}^* + \bar{D}D^* + D^*\bar{D}^*$ and $J/\psi K_S^0$ on roughly equal footing. Further, as discussed above there is a theoretical uncertainty in the extraction of β from these modes due to the terms from penguin diagrams that contribute with a different weak phase.

As a check on the validity and the heavy-quark-limit estimate, the CP properties of $D\bar{D}^* + \bar{D}D^*$ system can in principle be measured by looking for example at the three-body angular-distribution

$$D^+D^{*-} + D^-D^{*+} \rightarrow D^+D^-\pi^0 \quad .$$

In the center of mass of the D^+D^- , the relative partial wave of the π^0 will give the CP of the system ($L = \text{even}$, $CP = -$; $L = \text{odd}$, $CP = +$), and the two components $CP = +$, $CP = -$ could be hopefully separated. This will not be easy, however, because the π is very soft.

5.1.6.2 CP asymmetry in total $b \rightarrow c\bar{c}d$

It has been pointed out recently [25] that inclusive B decays can be useful in the measure of the CP angles. In the case of β , the method would need to isolate $\Delta C = 0$ $\Delta S = 0$, but with charmed particles in the final states, *i.e.*, decays of the form $b(\bar{b}) \rightarrow c\bar{c}d(\bar{d})$. The estimated total branching ratio to such states is about 1%. The time-dependent asymmetry can be written in the form of Eqs. (5.2) and (5.3),

$$\lambda_f = -\frac{M_{12}^*}{|M_{12}|} \frac{\Gamma_{f,12}}{\Gamma_{f,11}} \quad , \quad \Gamma_{f,ij} = \sum_k \langle i|f_k\rangle \langle f_k|j\rangle \quad (5.64)$$

In these formulas, i, j indicate B_d^0 or \bar{B}_d^0 and f the type of final states, *i.e.*, $\Delta C = 0$, $\Delta S = 0$ with charm. The calculation of [25] estimates the ratio of CP -odd to CP -even final states. It is found

that the relative size of penguin-only compared to tree-dominated contributions to the total rate is small. One obtains a predicted dilution factor

$$\text{Im } \lambda_f \cong -0.41 \sin 2\beta. \quad (5.65)$$

However this calculation requires strong assumptions and thus has a significant theoretical uncertainty. The feasibility of such a measurement is worth studying. However care must be taken in comparing any measurement to this predicted asymmetry because cuts made to reduce background could possibly affect the CP -odd and CP -even states differently, so the expected dilution factor may need to be re-estimated for the actual experimental situation. Further theoretical work is also needed to estimate the uncertainties in the dilution factor.

5.1.7 Discrete Ambiguities

The measurement of $\sin 2\beta$ can only determine β up to a four-fold ambiguity [26]: $\{\beta, \frac{\pi}{2} - \beta, \pi + \beta, \frac{3\pi}{2} - \beta\}$, with β defined by convention to lie between 0 and 2π . In addition to the values of $\sin 2\beta$, one needs to determine the signs of $\cos 2\beta$ and $\sin \beta$, and also those of $\cos 2\alpha$ and $\sin \alpha$. These four signs resolve the ambiguities completely. As far as β is concerned,

- $\text{sign}(\cos 2\beta)$ would resolve the $\beta \rightarrow \frac{\pi}{2} - \beta$ ambiguity.
- $\text{sign}(\sin \beta)$ would resolve the $\beta \rightarrow \pi + \beta$ ambiguity.

Within the Standard Model, the present data on the CKM matrix elements reduces the allowed range, implying that 2β is in the first quadrant $0 < \beta < \frac{\pi}{4}$ and that $0 < \alpha < \pi$, and that there is a correlation between the values of α and β . The ambiguities in β and α could hide a beyond-Standard-Model result that has a different sign pattern, because the related ambiguous solution is consistent with the Standard Model. Thus it is interesting to attempt to resolve these ambiguities.

5.1.7.1 Determination of $\text{sign}(\cos 2\beta)$

1) Interference between opposite CP amplitudes in $J/\psi K^*$.

The first question here is whether it is possible to lift the ambiguity $\beta \rightarrow \frac{\pi}{2} - \beta$ by examining the interference terms between opposite CP terms in $J/\psi \bar{K}^*$ or $D^* \bar{D}^*$. These terms are interference terms between CP -even and CP -odd amplitudes, of the form

$$\text{Im } A_{\perp}(t)A_{\parallel}^*(t) \quad \text{Im } A_{\perp}(t)A_0^*(t)$$

Table 5-1. Observables in transversity frame for $J/\psi(K^{*0})_{CP}$

Time-dependent observable	Time dependence	Time-independent observable
$ A_{\parallel} ^2$ ($CP=+$) $ A_{\perp} ^2$ ($CP=-$) $ A_0 ^2$ ($CP=+$)	$\sin \Delta mt$	$\sin 2\beta$
$\text{Re } A_{\parallel} A_0^*$	constant $\sin \Delta mt$	$\cos[\varphi(A_{\parallel}) - \varphi(A_0)]$ $\cos[\varphi(A_{\parallel}) - \varphi(A_0)] \sin 2\beta$
$\text{Im } A_{\perp} A_{\parallel}^*$	$\sin \Delta mt$ $\cos \Delta mt$	$\cos[\varphi(A_{\perp}) - \varphi(A_{\parallel})] \cos 2\beta$ $\sin[\varphi(A_{\perp}) - \varphi(A_{\parallel})]$
$\text{Im } A_{\perp} A_0^*$	$\sin \Delta mt$ $\cos \Delta mt$	$\cos[\varphi(A_{\perp}) - \varphi(A_0)] \cos 2\beta$ $\sin[\varphi(A_{\perp}) - \varphi(A_0)]$

that can be obtained from the transversity analysis [12, 13, 14], as was shown above. For example

$$\text{Im } A_{\perp}(t)A_{\parallel}^*(t) \sim \text{Im } A_{\perp}(0)A_{\parallel}^*(0) \cos \Delta mt - \text{Re } A_{\perp}(0)A_{\parallel}^*(0) \eta \cos 2\beta \sin \Delta mt \quad (5.66)$$

contains a term in $\cos 2\beta$. To lift the ambiguity one needs the sign of $\cos 2\beta$, but there is the unknown sign of the coefficient $\text{Re } A_{\perp}(0)A_{\parallel}^*(0)$, due to the strong interactions.

The relative phase between $A_{\parallel}(0)$ and $A_{\perp}(t)$ and between $A_{\parallel}(0)$ and A_0 have been measured by CLEO. CLEO reports the phases (5.41), consistent with the relative reality of the amplitudes $A_0, A_{\parallel}, A_{\perp}$ as given by the factorization assumption. However there is a discrete ambiguity that leads to a difficulty. As pointed out above, looking at the time-dependent formulae in Appendix B of Dunietz *et al.*, [12] one sees that one can measure by angular analysis the time-dependent observables $|A_{\parallel}|^2, |A_{\perp}|^2, |A_0|^2, \text{Re } A_{\parallel}A_0^*, \text{Im } A_{\perp}A_0^*, \text{Im } A_{\perp}A_{\parallel}^*$ and, separating the constant, $\sin \Delta mt$ and $\cos \Delta mt$ terms, one can measure the time-independent observables quoted in the Table 5-1.

The terms containing $\cos 2\beta$ are of the form $\cos \delta_{FSI} \cos 2\beta \sin \Delta mt$, where δ_{FSI} is some strong phase. CLEO results concern the time-independent angular distribution (the non-vanishing terms at $t = 0$ in the Table 5-1, the constant and $\cos \Delta mt$ terms):

$$\cos \varphi(A_{\parallel}), \quad \sin [\varphi(A_{\perp}) - \varphi(A_{\parallel})], \quad \sin \varphi(A_{\perp})$$

(in the convention $\varphi(A_0) = 0$). These quantities remain invariant under

$$\varphi(A_{\parallel}) \rightarrow -\varphi(A_{\parallel}) \quad \varphi(A_{\perp}) \rightarrow \pi - \varphi(A_{\perp}) \quad (5.67)$$

while the terms proportional to $\cos 2\beta$ change sign

$$\begin{aligned}\cos [\varphi(A_{\perp}) - \varphi(A_{\parallel})] \cos 2\beta &\rightarrow -\cos [\varphi(A_{\perp}) - \varphi(A_{\parallel})] \cos 2\beta \\ \cos \varphi(A_{\perp}) \cos 2\beta &\rightarrow -\cos \varphi(A_{\perp}) \cos 2\beta \quad .\end{aligned}\quad (5.68)$$

Thus there is a sign ambiguity on $\cos[\varphi(A_{\perp}) - \varphi(A_{\parallel})]$ and on $\cos \varphi(A_{\perp})$ and therefore a sign ambiguity on $\cos 2\beta$ remains. One of the solutions for $\text{sign}(\cos[\varphi(A_{\perp}) - \varphi(A_{\parallel})])$ and $\text{sign}(\cos \varphi(A_{\perp}))$ will correspond to the relative sign between CP -even and CP -odd amplitudes as given by factorization. The other solution will correspond to the situation in which the relative sign has been exactly reversed by a very large FSI. Thus the measurement of the relative phases plus the hypothesis of factorization can give a model-dependent result on the $\beta \rightarrow \frac{\pi}{2} - \beta$ ambiguity. Clearly, however, if this leads to a value for β inconsistent with that extracted from other measurements using the Standard Model, the factorization hypothesis will need to be examined more closely.

2) Dalitz plot analyses through D^{**} .

To lift the ambiguity $\beta \rightarrow \frac{\pi}{2} - \beta$ one can try, in analogy with Dalitz-plot analysis for α in B_d^0 , $\bar{B}_d^0 \rightarrow \pi^+ \rho^-$, $\rho^+ \pi^- \rightarrow \pi^+ \pi^- \pi^0$ [27], for example the Dalitz-plot interference $D^+ D^- \pi^0$ through $D^*(\mathcal{B}(D^{*+} \rightarrow D^+ \pi^0) = 30 \%)$:

$$B_d^0, \bar{B}_d^0 \rightarrow D^+ D^{*-}, D^{*+} D^- \rightarrow D^+ D^- \pi^0$$

This decay mode and other interesting channels are studied in detail in [28]. The time-dependent rates are

$$\begin{aligned}|A_t(\bar{B}_d^0 \rightarrow D^+ D^- \pi^0)|^2 &= e^{-\Gamma t} \frac{1}{2} [|\bar{A}_1|^2 + |\bar{A}_2|^2] \\ &\left\{ (|f^+|^2 + |f^-|^2) + D \, 2\text{Re}[f^+(f^-)^*] \right. \\ &- \cos \Delta mt [R (|f^+|^2 - |f^-|^2) - D \sin \delta \, 2\text{Im}[f^+(f^-)^*]] \\ &- \sin \Delta mt [D(\sin(2\beta - \delta)|f^+|^2 + \sin(2\beta + \delta)|f^-|^2) + \sin 2\beta \, 2\text{Re}[f^+(f^-)^*] \\ &\left. + R \cos 2\beta \, 2\text{Im}[f^+(f^-)^*] \right\}\end{aligned}\quad (5.69)$$

and $|A_t(B_d^0 \rightarrow D^+ D^- \pi^0)|^2$ is obtained by changing the sign of the coefficients of the $\cos \Delta mt$ and $\sin \Delta mt$ terms. $f^+(f^-)$ are the Breit-Wigner of the decays $D^{*+} \rightarrow D^+ \pi^0 (D^{*-} \rightarrow D^- \pi^0)$, and

$$D = \frac{2|\bar{A}_1| |\bar{A}_2|}{|\bar{A}_1|^2 + |\bar{A}_2|^2} \quad R = \frac{|\bar{A}_1|^2 - |\bar{A}_2|^2}{|\bar{A}_1|^2 + |\bar{A}_2|^2} \quad \delta = \arg(\bar{A}_1 \bar{A}_2^*) \quad (5.70)$$

where $\bar{A}_1 = A(\bar{B} \rightarrow D\bar{D}^*)$ is the amplitude of emission of \bar{D}^* , and $\bar{A}_2 = A(\bar{B} \rightarrow \bar{D}D^*)$ is the amplitude of emission of \bar{D} . The sign of $\cos 2\beta$ can in principle be measured, and lift the

ambiguity. However, the interference effect is expected to be very small, essentially because the D^* is so narrow ($\Gamma(D^*) < 0.1$ MeV), and the effect is unobservable.

But one could try D^{**} in the different decay modes $D\pi$ and $D^*\pi$ and look at the various Dalitz plots $D\bar{D}\pi, D\bar{D}^*\pi, \bar{D}D^*\pi, D^*\bar{D}^*\pi$, *e.g.*, [28]

$$\begin{aligned} B_d^0, \bar{B}_d^0 &\rightarrow D^+ D^{*-} + D^- D^{*+} \rightarrow D^+ D^- \pi^0 \\ B_d^0, \bar{B}_d^0 &\rightarrow D^{*+} D^{*-} + D^{*-} D^{*+} \rightarrow D^{*+} D^{*-} \pi^0 \\ B_d^0, \bar{B}_d^0 &\rightarrow D^+ D^{*-} + D^{*-} D^{*+} \rightarrow D^+ D^{*-} \pi^0 . \end{aligned}$$

The first excited level $\ell = 1$ has the following states: $D_{1/2}^{**}(0^+)$, $D_{1/2}^{**}(1^+)$, $D_{3/2}^{**}(1^+)$ and $D_{3/2}^{**}(2^+)$, where $j = \frac{1}{2}, \frac{3}{2}$ is the total angular momentum of the light quark relative to the heavy quark. $D_{3/2}^{**}(1^+)$ and $D_{3/2}^{**}(2^+)$ have been seen clearly in semileptonic b decay: $D_1^{**}(2420)$ decays only in $D^*\pi$, while $D_2^{**}(2460)$ decays in $D\pi, D^*\pi$ (in a proportion 1.8, taking into account phase space). Below a quantitative model of the $D\bar{D}\pi$ Dalitz plot through the distribution Eq. (5.69) is made to study measurement of $\cos 2\beta$. One should however emphasize that, unlike the 3π case, this analysis does not allow the penguin contribution to be separated, and hence a theoretical uncertainty in the value of $\sin 2\beta$ remains. Another Dalitz-plot analysis that could measure $\text{sign}(\cos 2\beta)$ is $D^+ D^- K_S$ via D_s^{**} [28] (provided rates are favorable in the interesting regions). This mode is in principle quite interesting because it is CKM allowed and free of penguins.

3) Cascade decay $B_d \rightarrow J/\psi K^0 \rightarrow J/\psi (\pi^- \ell^+ \nu_\ell)$.

A nice remark has been made recently [29] that can also help to measure $\cos 2\beta$. While the time-dependent rate (t_B is the time at which the B meson decays)

$$\Gamma [B_d^0(\bar{B}_d^0) \rightarrow J/\psi K_S^0] \sim e^{-\Gamma_B t_B} [1 \mp \sin 2\beta \sin \Delta m_B t_B] \quad (5.71)$$

only allows the measurement of $\sin 2\beta$, the cascade decay rate

$$\Gamma [B_d^0(\bar{B}_d^0) \rightarrow J/\psi K \rightarrow J/\psi \pi^\mp \ell^\pm \nu] \quad (5.72)$$

can give information also on $\cos 2\beta$ due to the interference with K^0 - \bar{K}^0 mixing. The form rates, dependent on t_B and t_K , can be written as (the times of decay of B and K respectively):

$$\begin{aligned} &e^{-\Gamma_B t_B} \left\{ e^{-\gamma_S t_K} [1 \mp \sin 2\beta \sin(\Delta m_B t_B)] + \right. \\ &e^{-\gamma_L t_K} [1 \pm \sin 2\beta \sin(\Delta m_B t_B)] \left. \begin{array}{l} \pm \\ \mp \end{array} 2e^{-\frac{1}{2}(\gamma_S + \gamma_L)t_K} \right. \\ &\left. \cdot [\cos(\Delta m_B t_B) \cos(\Delta m_K t_K) + \cos 2\beta \sin(\Delta m_B t_B) \sin(\Delta m_K t_K)] \right\}. \quad (5.73) \end{aligned}$$

One observes that a term in $\cos 2\beta$ appears due to the interference between B_d^0 - \bar{B}_d^0 mixing and K^0 - \bar{K}^0 mixing. The angle β here is not polluted by penguins.

5.1.7.2 Determination of $\text{sign}(\sin \beta)$

The determination of $\text{sign}(\sin \beta)$ [26] would lift the ambiguity $\beta \rightarrow \pi + \beta$. However, this needs some model-dependent input. It can be done by comparing Type I and Type II decays, for example $J/\psi K_S^0$ versus $D^+ D^-$. The comparison of the coefficients of $\sin \Delta mt$ in both classes (see Eqs. (5.12) and (5.17)):

$$\begin{aligned} S_{J/\psi K_S^0} &= -\sin 2\beta \\ S_{D^+ D^-} &= \frac{\sin 2\beta - 2|R_{DD}| \sin \beta \cos \delta_{DD}}{1 + |R_{DD}|^2 - 2|R_{DD}| \cos \beta \cos \delta_{DD}} \end{aligned} \quad (5.74)$$

can give the $\text{sign}(\sin \beta)$ if $\text{sign}(\cos 2\beta)$ and $\text{sign}(\cos \delta_{DD})$ are known. The $\text{sign}(\cos 2\beta)$ could be determined by the method described above. The determination of $\text{sign}(\cos \delta_{DD})$ needs model-dependent input. Without loss of generality one can keep the leading order in $|R_{DD}|$, that gives:

$$S_{J/\psi K_S^0} + S_{D^+ D^-} = 2|R_{DD}| \cos \delta_{DD} \cos 2\beta \sin \beta. \quad (5.75)$$

Within factorization, $\text{sign}(\cos \delta_{DD}) = +$ (see Eqs. (5.14) and (5.52) and the fact that $a_4, a_6 < 0$)

$$\text{sign}(S_{J/\psi K_S^0} + S_{D^+ D^-}) = \text{sign}(\cos 2\beta \sin \beta). \quad (5.76)$$

Note that the present Standard-Model range gives $\text{sign}(\cos 2\beta \sin \beta) > 0$, and the asymmetry in $D^+ D^-$ is larger in magnitude than in $J/\psi K_S^0$, and opposite in sign.

5.1.7.3 Modeling the extraction of $\cos 2\beta$ from Dalitz plot analyses

The Dalitz plot analysis of *e.g.*, $B_d^0, \bar{B}_d^0 \rightarrow D^+ D^- \pi^0$ through D^* , can be modeled in the factorization approximation. This analysis seems hopeless because the D^* is very narrow, and, in addition, a further problem is that the interference term in $\cos 2\beta$ that lifts the ambiguity is too small, since its coefficient R vanishes in the heavy-quark limit assuming factorization, $A \cong \bar{A} \sim f_D \xi \left(\frac{m_B}{2m_D} \right)$.

For the D^{**} channels proposed above [28] an estimate of the magnitude of the coefficient of the $\cos 2\beta$ term can be made by assuming factorization. To study the different Dalitz plots one needs to estimate the current matrix elements $B \rightarrow D, D^*$ and $B \rightarrow D_{1/2}^{**}(0^+, 1^+), D_{3/2}^{**}(1^+, 2^+)$ and the decay constants $f_D = f_{D^*}$, and the different $f_{D^{**}}$.

The current matrix elements for $B \rightarrow D(D^*)$ in the heavy-quark limit are given in terms of the Isgur-Wise function $\xi(w)$ and the transition $B \rightarrow D_{1/2}^{**}(0^+, 1^+), D_{3/2}^{**}(1^+, 2^+)$ are given in terms of the IW functions $\tau_{1/2}(w), \tau_{3/2}(w)$ [30]. On the other hand, in the heavy-quark limit $D_{1/2}^{**}(0^+, 1^+)$ have equal decay constants $f_D^{(1/2)}$ while $f_D^{(3/2)} = 0$.

Thus factorization plus heavy-quark symmetry predicts

$$A(\bar{B} \rightarrow D\bar{D}_{3/2}^{**}(1^+)) = A(\bar{B} \rightarrow D\bar{D}_{3/2}^{**}(2^+)) = 0 \quad \rightarrow \quad R = 1. \quad (5.77)$$

Table 5-2. Theoretical and experimental branching ratios (\mathcal{B}) for semi-leptonic $B \rightarrow D, D^*, D^{**}$ decays.

	Theoretical \mathcal{B} (Orsay Quark Model [31])	Experimental Branching Ratio	
		PDG 1997 [32]	New Measurements
$\bar{B}^0 \rightarrow D^+ \ell^- \bar{\nu}$	2.35%	$(1.9 \pm 0.5)\%$	$(1.87 \pm 0.15 \pm 0.32)\%$ [33]
$B^- \rightarrow D^0 \ell^- \bar{\nu}$	2.35%	$(1.6 \pm 0.7)\%$	$(1.94 \pm 0.15 \pm 0.34)\%$ [33]
$\bar{B}^0 \rightarrow D^{*+} \ell^- \bar{\nu}$	6.86%	$(4.68 \pm 0.25)\%$	
$B^- \rightarrow D^{*0} \ell^- \bar{\nu}$	6.86%	$(5.3 \pm 0.8)\%$	
$B \rightarrow D_{3/2}^{**}(2^+) \ell \nu$	0.70%		
$B \rightarrow D_{3/2}^{**}(1^+) \ell \nu$	0.45%		
$B \rightarrow D_{1/2}^{**}(1^+) \ell \nu$	0.07%		
$B \rightarrow D_{1/2}^{**}(0^+) \ell \nu$	0.06%		

On the other hand, since numerically one has $\tau_{1/2}(w) \ll \xi(w)$, and moreover $f_D^{(1/2)}$ is predicted to be of the same order of magnitude as f_D [31] there is an expected hierarchy

$$\begin{aligned}
 |A(\bar{B} \rightarrow D \bar{D}_{1/2}^{**}(0^+))| &\gg |A(\bar{B} \rightarrow D_{1/2}^{**}(0^+) \bar{D})| \\
 |A(\bar{B} \rightarrow D \bar{D}_{1/2}^{**}(1^+))| &\gg |A(\bar{B} \rightarrow D_{1/2}^{**}(1^+) \bar{D})|.
 \end{aligned} \tag{5.78}$$

This also implies $|R| \cong 1$.

From these selections rules and the fact that $\tau_{1/2}(w) \ll \xi(w)$ one sees that indeed the coefficient of the $\cos 2\beta$ term will be maximal for the $D^+ D^- \pi^0$ Dalitz plot.

In the Table 5-2 are given the semileptonic branching ratios in the Bakamjian-Thomas scheme (Orsay Quark Model [31]). This model predicts covariant form factors with Isgur-Wise scaling (see also Appendix B). For the decay constants the heavy-quark-model values for the same model are used; namely $f_D^{(1/2)} \sim f_D$, taking $f_D \cong 210$ MeV from lattice calculations.

In the Figs. 5-14a and 5-14b show the Dalitz plot $B_d \rightarrow D^+ D^- \pi^0$ via $D_{1/2}^{**}(0^+)$ and $D_{3/2}^{**}(2^+)$ at $t = 0$. One can clearly see the D -wave decay of the 2^+ state. As an illustration, Figs. 5-14c and 5-14d also show the $\sin 2\beta$ and $\cos 2\beta$ terms for $\Delta mt = \frac{\pi}{2}$ and $\beta = \frac{\pi}{6}$ [28].

5.1.8 Summary of Data on Decays Measuring β

This section summarizes the existing data on the decay modes discussed in this chapter. Table 5-3 gives the measured or expected branching ratios of the Type I decays $\bar{B} \rightarrow$ charmonium $\bar{K}(\bar{K}^*)$

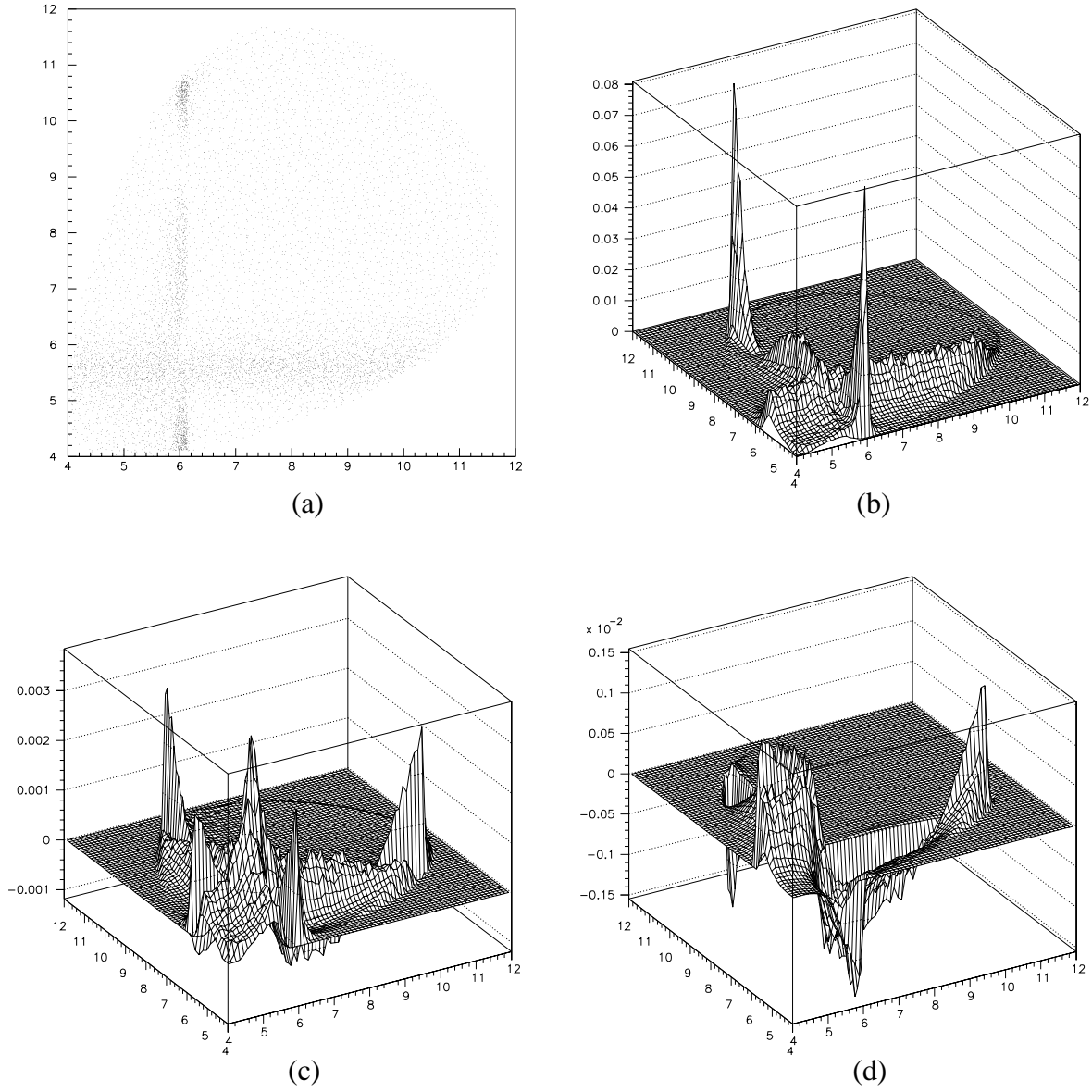


Figure 5-14. Dalitz plot $B_d \rightarrow D^+D^-\pi^0$ at $t = 0$ (5-14a,b) and terms in $\sin 2\beta$ (5-14c) and $\cos 2\beta$ (5-14d) at $\Delta mt = \frac{\pi}{2}$ and $\beta = \frac{\pi}{6}$.

decay modes. In Table 5-4 the Type II decays modes are given. The column PDG 1997 is obtained from rescaling of Cabibbo-allowed decays, through:

$$\mathcal{B}(\bar{B}_d \rightarrow D^+ D^-) \cong \tan^2 \theta_C \mathcal{B}(\bar{B}_d \rightarrow D_s^+ D^-) . \quad (5.79)$$

Besides $SU(3)$ symmetry, this amounts to assume also that the exchange diagram (Fig. 5-5b) is small. Table 5-5 lists the decay modes of Type III, penguin-dominated, namely $\bar{B}_d \rightarrow \phi \bar{K}(\bar{K}^*)$, $\eta' \bar{K}(\bar{K}^*)$, etc.

Table 5-3. Data on branching ratios for $\bar{B} \rightarrow \text{Charmonium } \bar{K}(\bar{K}^*)$ decay modes (Type I).

Decay Mode of \bar{B}_d^0 or B_u^-	Experimental Branching Ratio	
	PDG 1997 [32]	New Measurements
$J/\psi \bar{K}^0$	$(8.8 \pm 1.7) \times 10^{-4}$	$(8.5_{-1.2}^{+1.4} \pm 0.6) \times 10^{-4}$ [13]
$J/\psi K^-$	$(1.01 \pm 0.14) \times 10^{-3}$	$(1.02 \pm 0.08 \pm 0.07) \times 10^{-3}$ [13]
$J/\psi \pi^0$	$< 5.8 \times 10^{-5}$	
$J/\psi \pi^-$	$(5.1 \pm 1.6) \times 10^{-5}$	
$J/\psi \bar{K}^{*0}$	$(1.49 \pm 0.22) \times 10^{-3}$	$(1.32 \pm 0.17 \pm 0.17) \times 10^{-3}$ [13] $(1.78 \pm 0.14 \pm 0.29) \times 10^{-3}$ [34]
$J/\psi K^{*-}$	$(1.67 \pm 0.35) \times 10^{-3}$ $R_0 = 0.76 \pm 0.07$	$(1.41 \pm 0.23 \pm 0.24) \times 10^{-3}$ [13] $R_0 = 0.52 \pm 0.07 \pm 0.04$ [13] $R_\perp = 0.16 \pm 0.08 \pm 0.04$ [13]
$\psi' \bar{K}^0$	$< 8 \times 10^{-4}$	
$\psi' K^-$	$(6.9 \pm 3.1) \times 10^{-4}$	$(5.6 \pm 0.8 \pm 1.0) \times 10^{-4}$ [34]
$\psi' \bar{K}^{*0}$	$(1.4 \pm 0.9) \times 10^{-3}$	$(9.2 \pm 2.0 \pm 1.6) \times 10^{-4}$ [34]
$\psi' K^{*-}$	$< 3 \times 10^{-3}$	
$\chi_{c1} \bar{K}^0$	$< 2.7 \times 10^{-3}$	
$\chi_{c1} K^-$	$(1.0 \pm 0.4) \times 10^{-3}$	
$\chi_{c1} \bar{K}^*$	$< 2.1 \times 10^{-3}$	
$\eta_c \bar{K}$		
$\eta_c \bar{K}^*$		

Table 5-4. Data on branching ratios for Cabibbo-suppressed decays (Type II). (*) means that the value is rescaled from data on Cabibbo-allowed decays assuming $SU(3)$ symmetry and neglecting the exchange diagram.

Decay Mode of \bar{B}_d^0 or B_u^-	Experimental Branching Ratio	
	PDG 1997 [32]	New Measurements
$D^+ D^-$	$(3.9 \pm 1.5) \times 10^{-4}$ (*)	$< 1.2 \times 10^{-3}$ [35]
$D^0 D^-$	$(6.3 \pm 1.9) \times 10^{-4}$ (*)	
$D^0 \bar{D}^0$		
$D^+ D^{*-}$	$(4.8 \pm 2.4) \times 10^{-4}$ (*)	$< 1.8 \times 10^{-3}$ [35]
$D^0 D^{*-}$	$(4.4 \pm 1.9) \times 10^{-4}$ (*)	
$D^0 \bar{D}^{*0}$		
$D^{*+} D^-$	$(4.6 \pm 1.6) \times 10^{-4}$ (*)	$< 1.8 \times 10^{-3}$ [35]
$D^{*0} D^-$	$(5.8 \pm 2.4) \times 10^{-4}$ (*)	
$D^{*0} \bar{D}^0$		
$D^{*+} D^{*-}$	$(9.7 \pm 3.4) \times 10^{-4}$ (*)	$(5.3_{-3.7}^{+7.1} \pm 1.0) \times 10^{-4}$ [35] $(2.3_{-1.2}^{+1.9} \pm 0.4 \pm 0.2) \times 10^{-3}$ [36]
$D^{*0} D^{*-}$	$(1.3 \pm 0.5) \times 10^{-3}$ (*)	
$D^{*0} \bar{D}^{*0}$		

Table 5-5. Data on branching ratios for Penguin-dominated decays (Type III).

Decay Mode of \bar{B}_d^0 or B_u^-	Experimental Branching Ratio	
	PDG 1997 [32]	New Measurements
$\pi^+ K^-$	$< 1.7 \times 10^{-5}$	$(1.5_{-0.4}^{+0.5} \pm 0.1 \pm 0.1) \times 10^{-5}$ [37]
$\pi^+ \bar{K}^0$	$< 4.8 \times 10^{-5}$	$(2.3_{-1.0}^{+1.1} \pm 0.3 \pm 0.2) \times 10^{-5}$ [37]
$\pi^0 \bar{K}^0$	$< 4.0 \times 10^{-5}$	$< 4.1 \times 10^{-5}$ [37]
$\pi^0 K^-$	$< 1.4 \times 10^{-5}$	$< 1.6 \times 10^{-5}$ [37]
$\pi^0 \bar{K}^{*0}$	$< 2.8 \times 10^{-5}$	$< 2.0 \times 10^{-5}$ [38]
$\pi^0 K^{*-}$	$< 9.9 \times 10^{-5}$	$< 8.0 \times 10^{-5}$ [38]
$\eta \bar{K}^0$		$< 3.3 \times 10^{-5}$ [39]
ηK^-		$< 1.4 \times 10^{-5}$ [39]
$\eta \bar{K}^{*0}$		$< 3.0 \times 10^{-5}$ [39]
ηK^{*-}		$< 3.0 \times 10^{-5}$ [39]
$\eta' \bar{K}^0$		$(4.7_{-2.0}^{+2.7} \pm 0.9) \times 10^{-5}$ [39]
$\eta' K^-$		$(6.5_{-1.4}^{+1.5} \pm 0.9) \times 10^{-5}$ [39]
$\eta' \bar{K}^{*0}$		$< 3.9 \times 10^{-5}$ [39]
$\eta' K^{*-}$		$< 1.3 \times 10^{-4}$ [39]
$\rho^0 \bar{K}^0$	$< 3.9 \times 10^{-5}$	$< 3.0 \times 10^{-5}$ [38]
$\rho^0 K^-$	$< 1.9 \times 10^{-5}$	$< 1.4 \times 10^{-5}$ [38]
$\rho^0 \bar{K}^{*0}$	$< 4.6 \times 10^{-4}$	
$\rho^0 K^{*-}$	$< 9.0 \times 10^{-4}$	
$\omega \bar{K}^0$		$< 5.7 \times 10^{-5}$ [40]
ωK^-		$(1.5_{-0.6}^{+0.7} \pm 0.2) \times 10^{-5}$ [40]
$\omega \bar{K}^{*0}$		$< 2.3 \times 10^{-5}$ [40]
ωK^{*-}		$< 8.7 \times 10^{-5}$ [40]
$\phi \bar{K}^0$	$< 8.8 \times 10^{-5}$	$< 3.1 \times 10^{-5}$ [40]
ϕK^-	$< 1.2 \times 10^{-5}$	$< 0.5 \times 10^{-5}$ [40]
$\phi \bar{K}^*$		$< 2.2 \times 10^{-5}$ [40]
$\phi \bar{K}^{*0}$	$< 4.3 \times 10^{-5}$	$< 2.1 \times 10^{-5}$ [40]
ϕK^{*-}	$< 7.0 \times 10^{-5}$	$< 4.1 \times 10^{-5}$ [40]
$\gamma \bar{K}^{*0}$	$(4.0 \pm 1.9) \times 10^{-5}$	
γK^{*-}	$(5.7 \pm 3.3) \times 10^{-5}$	

5.2 Experimental Considerations for $\sin 2\beta$ Analyses

This section introduces and describes some general aspects of the analysis required to extract $\sin 2\beta$ from the data (see also Section 4.10). The determination of $\sin 2\beta$ is performed by fitting the time difference, $\Delta t = t_{CP} - t_{tag}$, in the decay in $\Upsilon(4S) \rightarrow B\bar{B}$, where one of two B mesons decays into particular CP eigenstates as described in the previous section and the other B decays into a mode whose b -quark flavor can be ascertained (the tag B). This measurement is made experimentally feasible by boosting the $\Upsilon(4S)$ and measuring decays in the lab frame, where the difference in the z positions is related to the time difference by $\gamma\beta c\Delta t = z_{CP} - z_{tag} = \Delta z$.

The physically measurable observable is the difference in lab z position, Δz , between the CP eigenstate and the other tagging B meson. Neglecting measurement errors, the Δz distribution will have the form

$$\Delta z = N e^{-\Gamma z |\Delta z|} [1 + a_f(\Delta z)], \quad (5.80)$$

where $a_f(\Delta z) = C_f \cos(\Delta m \Delta z) + S_f \sin(\Delta m \Delta z)$ and the coefficients C_f and S_f are functions of β (Section 5.1.1). In the simplest case such as $B^0 \rightarrow J/\psi K_S^0$ and $B^0 \rightarrow J/\psi K_L^0$, $C_f = 0$ and $S_f = \sin 2\beta$ and the extraction of $\sin 2\beta$ amounts to fitting the Δz distribution of the data for the parameter S_f in Eq. (5.80), appropriately smeared to account for experimental resolution.

In the analyses in the following sections, the aim was to determine the precision to which $\sin 2\beta$ can be measured with BABAR data. The precision on the measurement of $\sin 2\beta$ can be estimated from

$$\sigma_{\sin 2\beta} = \frac{\sigma(\sin 2\beta, \Delta m/\Gamma, \sigma_z)}{\sqrt{N_S} \sqrt{\epsilon_{tag} (1 - 2w)^2}} \frac{\sqrt{1 + N_B/N_S}}{1 + (A_B/A_S)(N_B/N_S)}, \quad (5.81)$$

where N_S (N_B) is the number of signal (background) events with CP asymmetry A_S (A_B), σ_z is the measurement error of the vertex, w is the misidentification rate of the B flavor tagging and ϵ_{tag} is the efficiency for finding the B flavor tag. The coefficient $\sigma(\sin 2\beta, \Delta m/\Gamma, \sigma_z)$ is obtained from tabulated values [41]. This represents the error for one event with no background and no uncertainty in the tag, denoted σ_0 throughout this book.

Hence the following analyses, to estimate $\sigma_{\sin 2\beta}$, for a particular value of $\sin 2\beta$, require:

- Number of reconstructed signal events, N_S
- Number of background events, N_B
- Δz vertex resolution, σ_z
- B mixing parameter, $\Delta m/\Gamma$
- Tagging factor, $\epsilon_{tag}(1 - 2w)^2$

Table 5-6. Assumptions in Chapter 5

$\int \mathcal{L} dt$	30 fb ⁻¹
$\sigma(ee \rightarrow \Upsilon(4S))$	1.05 nb
$\mathcal{B}(\Upsilon(4S) \rightarrow B^0 \bar{B}^0)$	0.5
$\sigma(ee \rightarrow q\bar{q})$	3.39 nb
$\epsilon_{\text{tag}}(1 - 2w)^2$	0.3 (Section 4.8.8)
$\sin 2\beta$	0.7
$\Delta m/\Gamma$	0.75

The analyses assume the values of these parameters as given in Table 5-6. Throughout this book, the term *usable sample* will be used for the number of events expected, including all branching fractions, but not including efficiencies.

In other analyses in this chapter, the extraction of $\sin 2\beta$ and determination of the estimated error, is more complex. The complications include mixed *CP* eigenstates and penguin corrections. The mixed *CP* eigenstates are unraveled by use of the angular distributions and the penguin corrections are applied by separating isospin states. These are explained and considered in their respective sections.

For full-reconstruction (Beta) analyses throughout this book, two types of Monte Carlo (MC) samples have been generated. Signal Monte Carlo was generated with the B meson decaying to the mode of interest and the \bar{B} meson decaying to all possible decay modes. Background Monte Carlo events were generated for both $q\bar{q}$ (Jetset 7.4) and $B\bar{B}$ (EvtGen) events (see Section 4.1.1). For the latter, both B mesons decay to all known B decay modes. The sample of 4.9 million $q\bar{q}$ events corresponds to a luminosity of 1.4 fb⁻¹. The sample of 2.3 million $B\bar{B}$ events corresponds to a luminosity of 2.2 fb⁻¹. Aslund and early Beta analyses have used other Monte Carlo samples.

5.3 Charmonium + Kaon modes

The decay modes $B^0, \bar{B}^0 \rightarrow J/\psi K_S^0(K_L^0), \psi' K_S^0(K_L^0)$ or $\chi_{1c} K_S^0(K_L^0)$, called Type I in Section 5.1.1, are color-suppressed and have the remarkable feature that $\sin 2\beta$ can be measured from the time-dependent asymmetry essentially without hadronic uncertainties, as has been discussed in detail in Section 5.1.2. This is because the tree and penguin contributions have the same weak phase up to small corrections.

5.3.1 $B^0 \rightarrow J/\psi K_s^0$

The combination of relatively large branching fractions, readily accessible final states with small backgrounds and negligible theoretical uncertainty have earned the decay $B^0 \rightarrow J/\psi K_s^0$ the name *gold-plated mode*. The aim of the analysis is to reconstruct the B meson through its decay products with good purity and efficiency, tag its flavor with the associated B and hence measure the time-dependent asymmetry from which $\sin 2\beta$ can be extracted.

Reconstructing the J/ψ through its decays to $\mu^+\mu^-$ and e^+e^- provides high efficiency and good background suppression. By reconstructing the K_s^0 through both charged ($\pi^+\pi^-$) and neutral ($\pi^0\pi^0$) decays good overall efficiency is maintained. In the charged decay the K_s^0 is identified as a pair of oppositely charged tracks with a vertex distinct from the interaction point while the neutral decays are identified as four neutral clusters in the calorimeter, which are consistent with being two π^0 s from a K_s^0 . Additional background suppression is achieved by exploiting the fact that the B^0 momentum is kinematically constrained in the rest frame of the $\Upsilon(4S)$ to be $p_{B^0}^* \sim 330$ MeV/c.

In one year of data taking at design luminosity, BABAR expects to collect 30 fb^{-1} of data. Using branching fractions and cross-sections measured by the CLEO collaboration [13] and noting that the BABAR trigger efficiency for these events is expected to be nearly 100%, ~ 1600 $B^0 \rightarrow J/\psi K_s^0$ events are expected to be recorded, with the J/ψ decaying into either a muon or an electron pair.

In order to estimate the precision which can be obtained on $\sin 2\beta$ from the time-dependent asymmetries, it is necessary to know the signal efficiency, background contamination and Δz resolution. These factors are examined in Sections 5.3.1.1–5.3.1.6. The methods of extracting $\sin 2\beta$ from the measured time dependent asymmetries are covered in detail in Section 4.10. All the results quoted in this section were obtained using the full BBSim simulation, a preliminary version of the BABAR reconstruction software and the software tools described in Chapter 4.

5.3.1.1 $J/\psi \rightarrow \ell^+\ell^-$ reconstruction and selection

In order to select $J/\psi \rightarrow \ell^+\ell^-$, all pairs of oppositely charged tracks in an event are considered. If the two tracks are consistent with the hypothesis that they originated from a common vertex and at least one of the two tracks is identified as either a muon or an electron, the invariant mass of the track pair is calculated at their vertex. Those pairs with an invariant mass within $70 \text{ MeV}/c^2$ of the J/ψ mass [32] are considered J/ψ candidates. The widths of the invariant-mass distributions of these candidates are dominated by detector effects. The width is $12 \text{ MeV}/c^2$ for the muon case and wider with a long tail towards lower invariant masses in the electron channel. The differences in efficiency and width between the electron and muon channels are due to bremsstrahlung by electrons, which occurs mainly in the beam pipe and beam support tube.

Much of the difference between the electron and muon decays can eventually be recovered by adding the bremsstrahlung photons which will often be measured in the calorimeter. For this reason in the study presented below, only the decay $J/\psi \rightarrow \mu^+ \mu^-$ is considered. The efficiency for reconstructing J/ψ in the muon channel was found to be $\sim 80\%$. Use of this number for both modes is expected to be slightly optimistic.

The B^0 decay vertex on the CP side is taken to be the decay vertex of the J/ψ . Its z coordinate is used in evaluating Δz . The distribution of the difference between the true and reconstructed Δz can be fitted with the sum of two Gaussian distributions. The narrow Gaussian has a width of $51 \mu\text{m}$ and there is a 5% admixture of a second Gaussian with a width of $150 \mu\text{m}$. For the tag vertex, improvements on the procedure discussed in Section 4.5.1.3 result in a narrow Gaussian with a width of $80 \mu\text{m}$ and a 20% admixture of a second Gaussian with a width of $280 \mu\text{m}$.

5.3.1.2 $K_s^0 \rightarrow \pi^+ \pi^-$ reconstruction

The decay $K_s^0 \rightarrow \pi^+ \pi^-$ is reconstructed by selecting all pairs of oppositely charged tracks which can be fitted to a common vertex and have an invariant mass within $13 \text{ MeV}/c^2$ of the nominal K_s^0 mass [32]. The reconstruction efficiency for the K_s^0 selection was found to be $\sim 75\%$.

5.3.1.3 $K_s^0 \rightarrow \pi^0 \pi^0$ reconstruction

Photon- and π^0 - Selection Criteria

The efficiency of this channel is highly dependent upon measuring the neutral calorimeter clusters (without an associated charged track) from the four photons from the two π^0 decays. The photons can have energies up to 2 GeV , but it is essential to maintain good photon detection efficiency down to 20 MeV .

The selection of π^0 mesons is complicated at high energy where the two photons from the π^0 have a small angular separation which can result in the photons entering adjacent crystals or even the same crystal. In such cases, the entire cluster is treated as a π^0 , and is subjected to the shower shape analysis, described in Section 4.4. These “merged” π^0 candidates are included with those constructed by the standard method of combining photons, as described below. A lower energy cutoff of 700 MeV is imposed on such merged π^0 candidates.

Event-Selection Criteria

In order to form π^0 candidates, pairs of neutral calorimeter clusters are combined. Only those having a shower shape that is consistent with being electromagnetic in origin are considered. To these are added those clusters which are consistent with being from a merged π^0 , to form a complete set of π^0 candidates. Where possible these are then combined to form K_s^0 candidates.

For the non-merged π^0 s, the invariant mass of the neutral cluster pair is required to lie in the range $100 \text{ MeV}/c^2 < m_{\pi^0} < 145 \text{ MeV}/c^2$. At this stage the invariant mass of the K_s^0 is required to be $380 \text{ MeV}/c^2 < m_{K_s^0} < 550 \text{ MeV}/c^2$. It is recognized that the invariant mass of both the π^0 s and the K_s^0 , formed for this purpose will necessarily be low since no account has been made for the finite lifetime of the K_s^0 . A correction for this using the direction information from the J/ψ proceeds as follows: the flight path of the K_s^0 is calculated using the reconstructed J/ψ momentum and the momentum of the B^0 meson, neglecting the small component of its momentum perpendicular to the beam axis. Points along the K_s^0 flight path are then considered from -2.0 to $5.0 K_s^0$ lifetimes in steps of $0.1 \tau_{K_s^0}$. At each point, the following procedure is adopted: if the two π^0 s constituting the candidate K_s^0 are not merged, the invariant mass of each cluster pair is calculated. The position at which the invariant mass is closest to the π^0 mass is then stored for possible K_s^0 combinations. $K_s^0 \rightarrow \pi^0\pi^0$ candidates are considered if the two times at which the best π^0 mass is found are within $3.0 \tau_{K_s^0}$ of each other, and the best π^0 masses lie within the range $110 \text{ MeV}/c^2 < m_{\pi^0} < 160 \text{ MeV}/c^2$. Restricting the difference in measured lifetime greatly reduces combinatorial background π^0 s, which will tend to be randomly distributed along the flight path. The cluster combinations from the genuine K_s^0 will tend to cluster around zero time difference. In addition, those candidates for which the best K_s^0 lifetime lie at either end of the range described above are rejected. Approximately two-thirds of the K_s^0 signal arises from these unmerged π^0 s.

If one of the two π^0 s constituting the candidate K_s^0 is a merged π^0 , then the invariant mass of the cluster pair constituting the other π^0 is formed at each point. Again, the position at which the mass is closest to the π^0 is kept, provided that it is in the range described above and that the lifetime is not at either extreme of the allowed range. Approximately one-third of the K_s^0 signal has one merged π^0 .

If both of the π^0 s constituting the candidate K_s^0 are merged, then the invariant mass of the π^0 pair is formed at each point, and compared to the K_s^0 mass. The point with the best K_s^0 mass is kept, provided that it does not lie at the extremes of the allowed range. A cut on the K_s^0 mass is not imposed at this point. The fraction of signal K_s^0 with two merged π^0 s is negligible with respect to the other two scenarios.

The K_s^0 decay length is now taken as the best point along the flight path as calculated in the appropriate method above and is used to re-calculate the K_s^0 mass. The resulting K_s^0 is restricted to have a mass in the range $440 \text{ MeV}/c^2 < m_{K_s^0} < 560 \text{ MeV}/c^2$ and a momentum, calculated in the rest frame of the B^0 meson, in the range $1.2 \text{ GeV}/c < p_{B^0}^* < 2.0 \text{ GeV}/c$. Efficiencies for this procedure are given in Table 5-7.

Machine-background suppression

While most events have few photons, there will be a significant number of low-energy showers produced by lost particles in PEP-II. The uncertainty on the number and energy spectrum of these machine background showers makes it difficult to predict their impact on the analysis backgrounds.

Table 5-7. Cuts used to select the decay $K_s^0 \rightarrow \pi^0\pi^0$ and the corresponding reconstruction efficiencies. All efficiencies were calculated using the full BBSim simulation and reconstruction chain

Cut	Efficiency
Overall $2\pi^0$ efficiency	37%
Wide K_s^0 cut $0.38 < m_K < 0.56$	76%
γ pairs make π^0 mass along K_s^0 flight path $-2.0 < \tau < 5.0$	99%
K_s^0 lifetime where π^0 s have correct mass $\Delta\tau < 3.0$	96%
Kaon mass from decay point $440 < M < 560$ MeV/ c^2	99%
Kaon mom in B rest frame $1.2 < p_{B^0}^* < 2.0$ GeV/ c	99%
Combined $K_s^0 \rightarrow \pi^0\pi^0$ efficiency	26%

Since most of these machine background showers have low energy, the impact on the selection efficiency can be studied as a function of a threshold for cluster production, as shown in Table 5-8.

Table 5-8. Efficiency for $K_s^0 \rightarrow \pi^0\pi^0$ detection as a function of calorimeter cluster threshold.

Minimum cluster energy detectable	Relative signal ϵ
20 MeV	100%
30 MeV	93%
40 MeV	86%
50 MeV	77%

5.3.1.4 B^0 reconstruction

B^0 candidates are formed by considering all possible combinations of previously reconstructed J/ψ and K_s^0 candidates. Before combining the J/ψ and K_s^0 , their masses are fitted to the nominal values. The B^0 candidate is then required to have a mass within 100 MeV/ c^2 of the nominal B^0 mass [32] and the momentum of the B^0 in the rest frame of the $\Upsilon(4S)$ is required to be in the range $200 < P_B < 500$ MeV/ c for the $\pi^0\pi^0$ channel and $140 < P_B < 450$ MeV/ c for the $\pi^+\pi^-$ channel. The global efficiencies for the full reconstruction are 60% for the $\pi^+\pi^-$ channel and 21% for the $\pi^0\pi^0$ channel.

5.3.1.5 Backgrounds

The rejection power afforded by demanding a J/ψ candidate in the signal is rather good, so that the dominant backgrounds are those which include a real J/ψ in the event. The following have been considered: i) $B^0 \rightarrow J/\psi X$; ii) semileptonic decays of b or c hadrons; and iii) $q\bar{q}$ continuum events. For this study very large samples of simulated background events of each type were generated. These studies place an upper limit of 6% for background events in both $\pi^+\pi^-$ and $\pi^0\pi^0$ modes.

5.3.1.6 CP reach

A summary of the numbers used in the analysis and the resulting uncertainty in $\sin 2\beta$ is given in Table 5-9.

Table 5-9. *CP reach for a 30 fb^{-1} data sample for the gold-plated mode. CP-mode efficiencies were derived from full BBSim simulation and reconstruction.*

	$K_s^0 \rightarrow \pi^+\pi^-$	$K_s^0 \rightarrow \pi^0\pi^0$
$\mathcal{B}(B^0 \rightarrow J/\psi K_s^0)$	4.25×10^{-4}	
$\mathcal{B}(J/\psi \rightarrow \ell^+\ell^-)$	0.12	
$\mathcal{B}(K_s^0 \rightarrow \pi\pi)$	0.686	0.314
Usable sample	1100	500
Reconstruction Efficiency	0.60	0.21
Number of reconstructed events per 30 fb^{-1}	660	110
Tag factor $\epsilon_{\text{tag}}(1 - 2w)^2$ (Section 4.8.8)	0.3	
N_B/N_S	0.06	0.06
σ_0	1.59	
$\delta(\sin 2\beta)$	0.12	0.30

5.3.2 $B^0 \rightarrow J/\psi K_L^0$

The study of the CP asymmetry in the channel $B^0 \rightarrow J/\psi K_L^0$ is an independent measurement of the angle β . Its importance goes beyond the increase in statistics. Since the K_s^0 and the K_L^0 are CP eigenstates of opposite sign, this channel provides also an excellent check of the systematics,

Table 5-10. Summary of the K_L^0 final states branching ratios and expected rates. The number of expected events is based on a $\sigma(\Upsilon(4S)) = 1.05 \text{ nb}^{-1}$, an integrated luminosity of $(\int \mathcal{L} dt = 30 \text{ fb}^{-1})$ and include the 12% branching fraction of the J/ψ decay to lepton pairs. The last three rows show the B^\pm decay to charmonium $K^{*\pm}$ as these are important backgrounds to all the K_L^0 channels.

Channel	Decay fractions (\mathcal{B} from Table 5-3)	# events
$B^0 \rightarrow J/\psi K_L^0$	4.25×10^{-4}	1600
$B^0 \rightarrow J/\psi K^{*0} (K^{*0} \rightarrow K_L^0 \pi^0)$	$1/3 \times 1/2 \times 13.2 \times 10^{-4}$	830
$B^0 \rightarrow \psi' K_L^0 (\psi' \rightarrow J/\psi \pi^+ \pi^-)$	$0.324 \times 3.5 \times 10^{-4}$	430
$B^0 \rightarrow \psi' K^{*0} (\psi' \rightarrow J/\psi \pi^+ \pi^-, K^{*0} \rightarrow K_L^0 \pi^0)$	$1/3 \times 1/2 \times 0.324 \times 14.0 \times 10^{-4}$	290
$B^0 \rightarrow \chi_{c1} K_L^0 (\chi_{c1} \rightarrow \gamma J/\psi)$	$0.273 \times 5.0 \times 10^{-4}$	520
$B^0 \rightarrow \chi_{c1} K^{*0} (\chi_{c1} \rightarrow \gamma J/\psi, K^{*0} \rightarrow K_L^0 \pi^0)$	$0.273 \times 1/3 \times 1/2 \times 14 \times 10^{-4}$	240
$B^\pm \rightarrow J/\psi K^{*\pm} (K^{*\pm} \rightarrow K_L^0 \pi^\pm)$	$2/3 \times 1/2 \times 14.1 \times 10^{-4}$	1780
$B^\pm \rightarrow \psi' K^{*\pm} (\psi' \rightarrow J/\psi \pi^+ \pi^-, K^{*\pm} \rightarrow K_L^0 \pi^\pm)$	$2/3 \times 1/2 \times 0.324 \times 14.0 \times 10^{-4}$	570
$B^\pm \rightarrow \chi_{c1} K^{*\pm} (\chi_{c1} \rightarrow \gamma J/\psi, K^{*\pm} \rightarrow K_L^0 \pi^\pm)$	$0.273 \times 2/3 \times 1/2 \times 14 \times 10^{-4}$	480

because its asymmetry should be equal in magnitude but opposite in sign compared with that of the $B^0 \rightarrow J/\psi K_S^0$ decay. For these reasons K_L^0 final states have been studied extensively from the very early stages of the BaBar experiment [42, 43], and updated and summarized in [44].

The expected event rates and branching ratios used for all the analyses involving K_L^0 in the final state are summarized in Table 5-10. Note that the various signals contaminate each other and therefore they are regarded as signal or background depending on the channel under study. Although the kinematics of the process is the same as that of $B^0 \rightarrow J/\psi K_S^0$, the analysis techniques are quite different because the K_L^0 momentum is not measured. Since there are fewer constraints, K_L^0 channels have a larger background than their K_S^0 counterparts. The analysis of the CP mode and backgrounds in this channel was done using the `Aslund` fast simulation, although, as will be seen later, a number of results concerning the signal are taken directly from the corresponding K_S^0 channel, in which the full `BBSim` reconstruction analysis chain was employed. In addition, the response of the BaBar detector to K_L^0 was parameterized in `Aslund` after a careful `BBSim` study, as summarized in Section 4.1.3.

The J/ψ is reconstructed through its leptonic decay into a pair of electrons or muons as described in Section 5.3.1.1, and its four-momentum ($\mathbf{p}_{J/\psi}, E_{J/\psi}$) is completely determined. For a $B^0 \rightarrow J/\psi K_L^0$ decay, the measured K_L^0 momentum must satisfy

$$M_{B^0}^2 = \left(E_{J/\psi} + \sqrt{p_{K_L^0}^2 + m_{K_L^0}^2} \right)^2 - |\mathbf{p}_{J/\psi} + \mathbf{p}_{K_L^0}|^2. \quad (5.82)$$

This equation has two solutions for $p_{K_L^0}$, but only one is positive, hence acceptable. A value for $\mathbf{p}_{K_L^0}$ is obtained from $p_{K_L^0}$ and the K_L^0 direction information measured in the IFR. Then, the momentum and the energy of the B^0 are simply the sum of those of the J/ψ and K_L^0 . The value of $p_{B^0}^*$ is then obtained by a Lorentz transformation, using the nominal values of the beam energies. If the assumption is correct, then $p_{B^0}^*$ must be monochromatic, apart from the spread in the CM total energy and the angular resolution in reconstructing the K_L^0 direction.

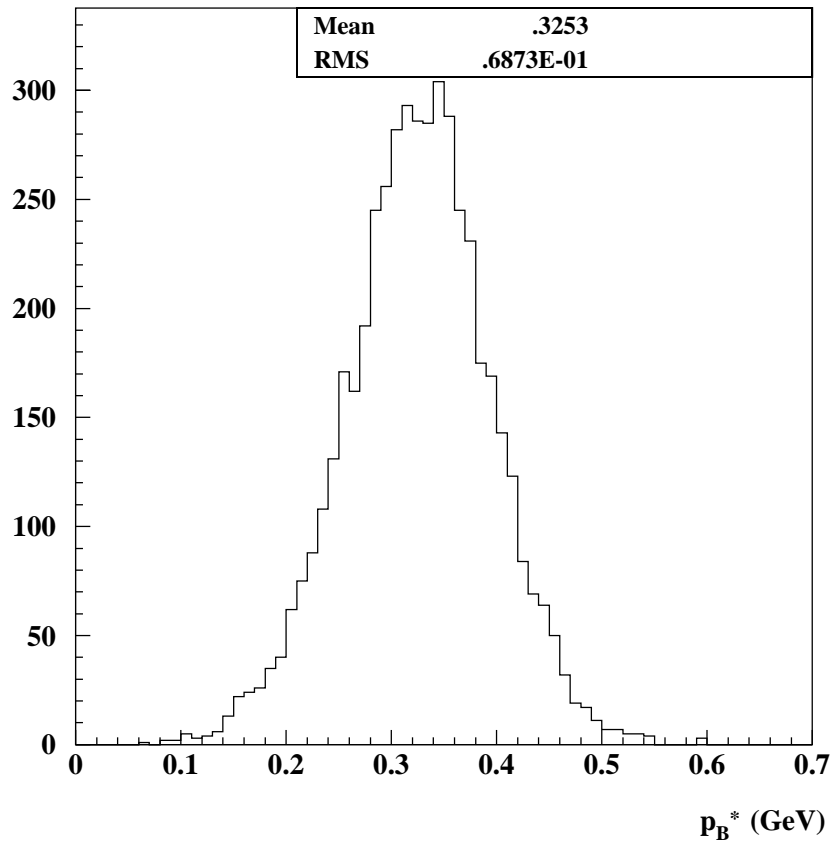


Figure 5-15. Distribution of $p_{B^0}^*$. The spread around the expected value (≈ 330 MeV/c) is due to beam-energy spread, momentum resolution and a 30 mrad resolution in the K_L^0 direction.

The distribution of $p_{B^0}^*$ with 30 mrad as the resolution in the K_L^0 direction measurement, is shown in Fig. 5-15. The peak is centered around the correct value $p_{B^0}^* \approx 330$ MeV/c; the r.m.s. is ≈ 69 MeV/c, with contributions from: the error in the K_L^0 direction measurement (≈ 51 MeV/c), the beam-energy spread (≈ 47 MeV/c, using 5.5 MeV and 2.5 MeV respectively for σ_{E_H} and σ_{E_L}), and the experimental resolution in the lepton momentum measurement (≈ 11 MeV/c). Improving the measurement of the K_L^0 direction would not result in a significant improvement of this channel, since the distribution of $p_{B^0}^*$ is limited by the spread in beam energies.

5.3.2.1 Event selection and efficiency

In the B^0 CM the J/ψ and the K_L^0 from the $B^0 \rightarrow J/\psi K_L^0$ decay are emitted back to back; since the component of the B^0 momentum transverse to the beam direction is very small, the difference in the azimuthal angle between the J/ψ and K_L^0 direction is also close to 180° , as shown in Fig. 5-16. This suggests a method to improve the background rejection: the K_L^0 direction in the xy plane should be opposite to the J/ψ , within a few hundred mr. In this analysis the direction of the K_L^0 has been required to be opposite to that of the J/ψ within 300 mr, resulting in substantial reduction of the background without affecting the signal significantly.

The event selection begins with all events where a J/ψ is identified in its decay into a lepton pair. A $\Delta\phi$ cut of 300 mr is applied around the direction opposite to the J/ψ to look for neutral clusters in the EMC and the IFR, following the criteria for K_L^0 identification described in Section 4.4.2, and in greater detail in [42, 44].

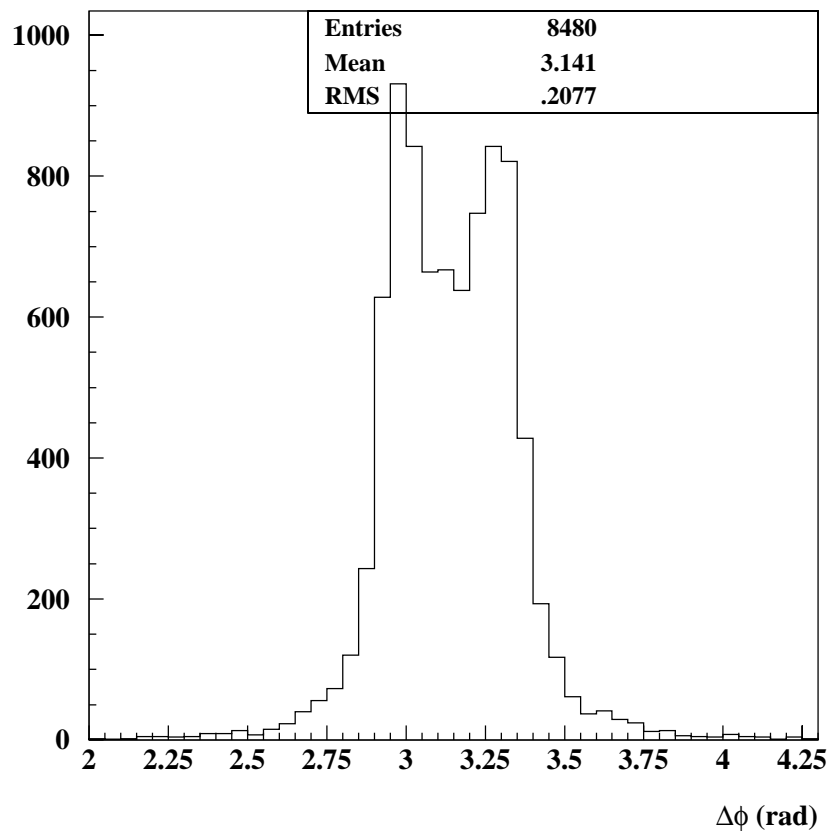


Figure 5-16. Distribution of the difference in azimuthal angle between the K_L^0 and the J/ψ . The dip at π is due to the $\sin^2 \theta^*$ angular distribution of the decay of the $\Upsilon(4S)$ to B mesons.

The quantity $p_{B^0}^*$ is calculated and a cut on this quantity, $p_{B^0}^* \leq 450 \text{ MeV}/c$, is finally applied. Of a sample of 10K Monte Carlo signal events a total of 4060 were correctly identified, giving 40.6% efficiency.

5.3.2.2 Backgrounds

The same analysis has been applied to other B^0 and B^+ decays which contain a J/ψ and a K_L^0 in the final state, since these are the dominant backgrounds. Among them, the most important processes are $B^0 \rightarrow J/\psi K^{*0}$, $B^+ \rightarrow J/\psi K^{*+}$, $B^0 \rightarrow \psi' X$, $B^0 \rightarrow \chi_{c1} X$. There is also combinatorial background due to accidental combinations of a J/ψ and a K_L^0 .

The $p_{B^0}^*$ distribution of the signal and its main background events, is shown in Fig. 5-17; the statistics correspond to one nominal year. The corresponding numbers of reconstructed events are summarized in Table 5-11.

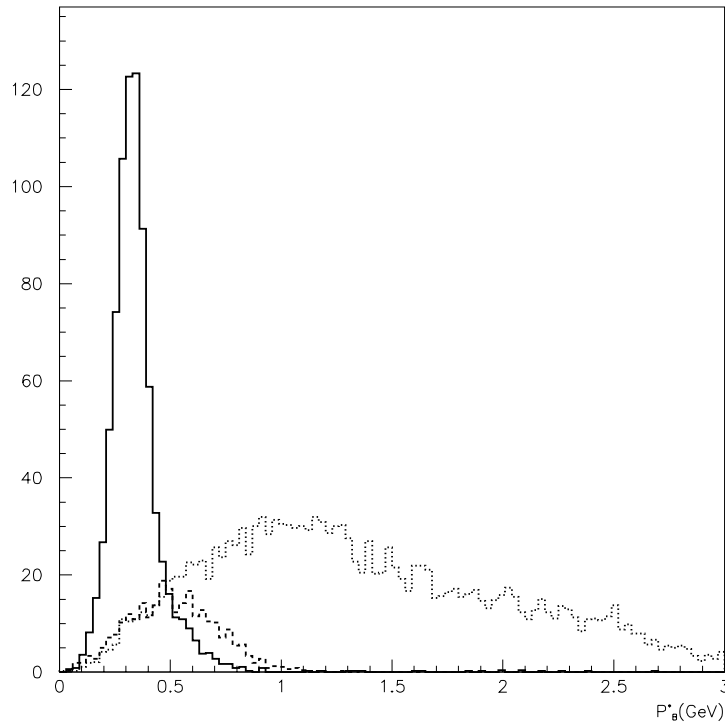


Figure 5-17. $p_{B^0}^*$ distribution for $J/\psi K_L^0$ (solid), $J/\psi K^{*0}$ (dashed) and combinatorial background (dotted).

Table 5-11. Summary of signal and background events selected applying the selection criteria optimized for the $B^0 \rightarrow J/\psi K_L^0$ decay described in the text. The analyses were performed with the Aslund fast simulation.

Process	Selection Efficiency	# Events Selected
$B^0 \rightarrow J/\psi K_L^0$	0.41	650
$B^0 \rightarrow J/\psi K^{*0}$	0.11	93
$B^\pm \rightarrow J/\psi K^{*\pm}$	0.12	210
$B^0 \rightarrow \psi' K_L^0$	0.032	14
$B^0 \rightarrow \chi_{c1} K_L^0$	0.062	32
Combinatorial		36

5.3.2.3 CP reach

A total of 650 signal events are expected with a background of 380 events, of which the largest contribution is from B^\pm decays. These events are expected to be reduced easily by removing those with at least one charged track associated with the J/ψ vertex and compatible with the $B^+ \rightarrow J/\psi K^{*+}$ ($K^{*+} \rightarrow K_L^0 \pi^+$) decay chain. No attempt has yet been made to do such a vertex analysis, but studies of this are planned. This background, unlike that due to K^{*0} , has zero CP asymmetry and therefore it affects the total statistical power of the measurement, but does not dilute the measured value (see Eq. (5.81)).

The effect on the measured asymmetry introduced by a CP asymmetric background is to introduce a term in the denominator of the error calculation as seen in Eq. (5.81). As the formula shows, if $Sign(A_B) = -Sign(A_S)$ then the error increases, as the measured asymmetry is diluted by the background. When they have the same sign, the error *decreases*, since in this case the background is actually measuring the same quantity, and therefore effectively increases the amount of signal.

Assuming a value of $\sin 2\beta=0.7$, a tagging factor of 0.30 (see Section 4.8.8), $\sigma_0 = 1.61$, and that the background has zero asymmetry, the precision achievable with the present analysis on $\sin 2\beta$ in 30 fb^{-1} would be $\delta(\sin 2\beta) = 0.15$.

If the asymmetry of the various background components is taken into account, this error is altered, according to Eq. (5.81). The combinatorial background, and that from $B^+ \rightarrow J/\psi K^{*+}$, have zero asymmetry, so there is no correction for them. The $B^0 \rightarrow \psi' K_L^0$ and $B^0 \rightarrow \chi_{c1} K_L^0$ backgrounds are expected to have the same asymmetry as the signal, and they therefore enter in the error calculation as signal. Since $J/\psi K^{*0}$ is not a pure CP state, an admixture of CP states was assumed [13], namely that 16% (84%) of it has the same (opposite) sign asymmetry with respect to that of the signal. Recalculating the error with this assumption, but considering only the effect of

same sign asymmetry background, leads to a reduction in $\delta(\sin 2\beta)$ or ~ 0.01 . Including also the opposite sign asymmetry background, increases $\delta(\sin 2\beta)$ by about 0.005, as evidently the effect of same sign and opposite sign background asymmetries compensate each other. The net effect is a negligible change in $\delta(\sin 2\beta)$.

A value for the Δz resolution equal to that used in the corresponding K_S^0 channel is assumed, since the determinations of the CP -side (see Section 4.10) and the tag-side (see Section 4.5.1.3) vertices are essentially the same in the two analyses.

5.3.3 $B^0 \rightarrow \psi' K_L^0$

The decay mode $B^0 \rightarrow \psi' K_L^0$ is expected to have the same asymmetry and almost the same branching ratio as $B^0 \rightarrow J/\psi K_L^0$, as indicated by the branching ratios measured in the case of the B^\pm decay.

The ψ' is reconstructed from the decay mode $\psi' \rightarrow J/\psi \pi^+ \pi^-$, which can be reconstructed with low background since there are four charged tracks coming from the vertex. However the number of events is reduced by a factor of three due to the $\psi' \rightarrow J/\psi \pi^+ \pi^-$ branching fraction. Another significant rate reduction compared with $B^0 \rightarrow J/\psi K_L^0$, is the lower K_L^0 detection efficiency in $B^0 \rightarrow \psi' K_L^0$ decays due to the lower K_L^0 momentum.

5.3.3.1 Event selection and efficiency

The selection criteria are the same as described in Section 5.3.2.1 for $B^0 \rightarrow J/\psi K_L^0$. After selecting a K_L^0 and a ψ' candidate, the K_L^0 momentum is calculated from the ψ' momentum and from the K_L^0 direction, assuming they are coming from a B decay. Consistency with $\Upsilon(4S) \rightarrow B\bar{B}$ decay is used as a constraint, requiring that the reconstructed center of mass B momentum has, within resolution, the expected value.

The efficiency for the signal was measured to be $\sim 27\%$ on a sample of 10K Aslund Monte Carlo events of the kind $B^0 \rightarrow \psi' K_L^0$, $\bar{B}^0 \rightarrow X$.

5.3.3.2 Backgrounds

Background decay modes for this decay are also similar to that for $B^0 \rightarrow J/\psi K_L^0$. The most significant are:

$$B^0 \rightarrow \psi' K^{*0} \quad (K^{*0} \rightarrow K_L^0 \pi^0) \quad (5.83)$$

$$B^\pm \rightarrow \psi' K^{*\pm} \quad (K^{*\pm} \rightarrow K_L^0 \pi^\pm) . \quad (5.84)$$

The background from $B^\pm \rightarrow \psi' K^{*\pm}$ events can be suppressed with a vertex analysis, as discussed in the previous section. Further background rejection may be achieved by removing all combinations of a ψ' , K_L^0 and π , consistent with the process $\psi' K^{*0}$. However the background reduction is not sufficient to offset the loss of efficiency. Conversely, due to the ψ' momenta being softer than that of the J/ψ , there is a larger combinatorial background expected from uncorrelated $\psi' K_L^0$ combinations in multi-hadronic events. Such events have a broad distribution up to $p_{B^0}^* \sim 2$ GeV/c.

The yields for 30 fb^{-1} , are shown in Fig. 5-18 as a function of $p_{B^0}^*$, and summarized in Table 5-12.

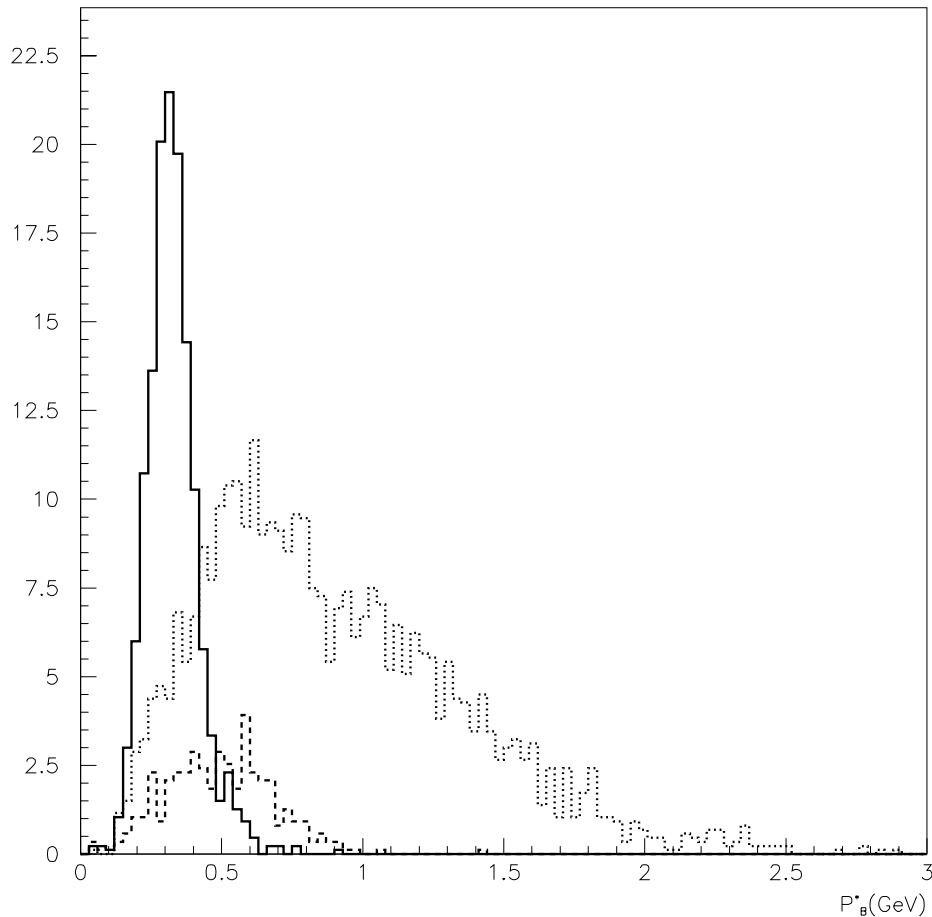


Figure 5-18. $p_{B^0}^*$ distribution for $\psi' K_L^0$ (solid), $\psi' K^{*0}$ (dashed) and combinatorial background (dot-dashed).

Table 5-12. Summary of signal and background events selected with the selection criteria optimized for the $B^0 \rightarrow \psi' K_L^0$ decay described in the text. The analysis was performed using the `ASlund` fast simulation.

Process	Selection Efficiency	# Events Selected
$B^0 \rightarrow \psi' K_L^0$	0.27	120
$B^0 \rightarrow \psi' K^{*0}$	0.06	17
$B^\pm \rightarrow \psi' K^{*\pm}$	0.056	32
$B^0 \rightarrow J/\psi K_L^0$	0.005	8
$B^0 \rightarrow \chi_{c1} K_L^0$	0.009	5
Combinatorial		34

5.3.3.3 CP reach

About 120 signal events are expected from the decay mode $B^0 \rightarrow \psi' K_L^0$, with a total background of 100 events. With the same assumptions for σ_0 and the tag factor as in the preceding section, and including in the signal all events with the same CP asymmetry as the signal, the error on $\sin 2\beta$ obtained is $\delta(\sin 2\beta) = 0.305$. Correcting for the asymmetric background, as discussed already in Section 5.3.2.3, the error becomes $\delta(\sin 2\beta) = 0.335$.

Reduction of the background for this channel is obviously very important for the $\sin 2\beta$ measurement.

5.3.4 $B^0 \rightarrow \chi_{c1} K_L^0$

The $B^0 \rightarrow \chi_{c1} K_L^0$ decay is expected to have similar asymmetry and branching ratio as for $B^0 \rightarrow J/\psi K_L^0$. The χ_{c1} is reconstructed from the $\chi_{c1} \rightarrow \gamma J/\psi$ decay. Taking into account all the appropriate branching ratios, the number of expected events is slightly larger than the aforementioned ψ' case, as can be seen in Table 5-10.

The analysis techniques are similar to those for $B^0 \rightarrow J/\psi K_L^0$, described in Section 5.3.2, except that in this case the χ_{c1} has first to be reconstructed from the J/ψ and a photon. Once the χ_{c1} four-momentum is obtained, it is used to determine the K_L^0 momentum and to reconstruct the B^0 . The photons from the radiative decay of the χ_{c1} are quite energetic, as can be seen from the energy spectrum shown in Fig. 5-19. The electromagnetic cluster energy is required to satisfy $E_{clust} \geq 250$ MeV. The invariant-mass distribution of the $\gamma J/\psi$ system is plotted in Fig. 5-20, after requiring $p_{B^0}^* \leq 450$ MeV/c. χ_{c1} candidates are selected by requiring $3.495 \leq M_{\gamma J/\psi} \leq$

3.525 GeV/c. The K_L^0 selection is similar to that described in Section 5.3.2.1. The efficiency for the signal was measured to be $\sim 28\%$ on a sample of 10K Aslund Monte Carlo events of the kind $B^0 \rightarrow \chi_{c1} K_L^0, \bar{B}^0 \rightarrow X$.

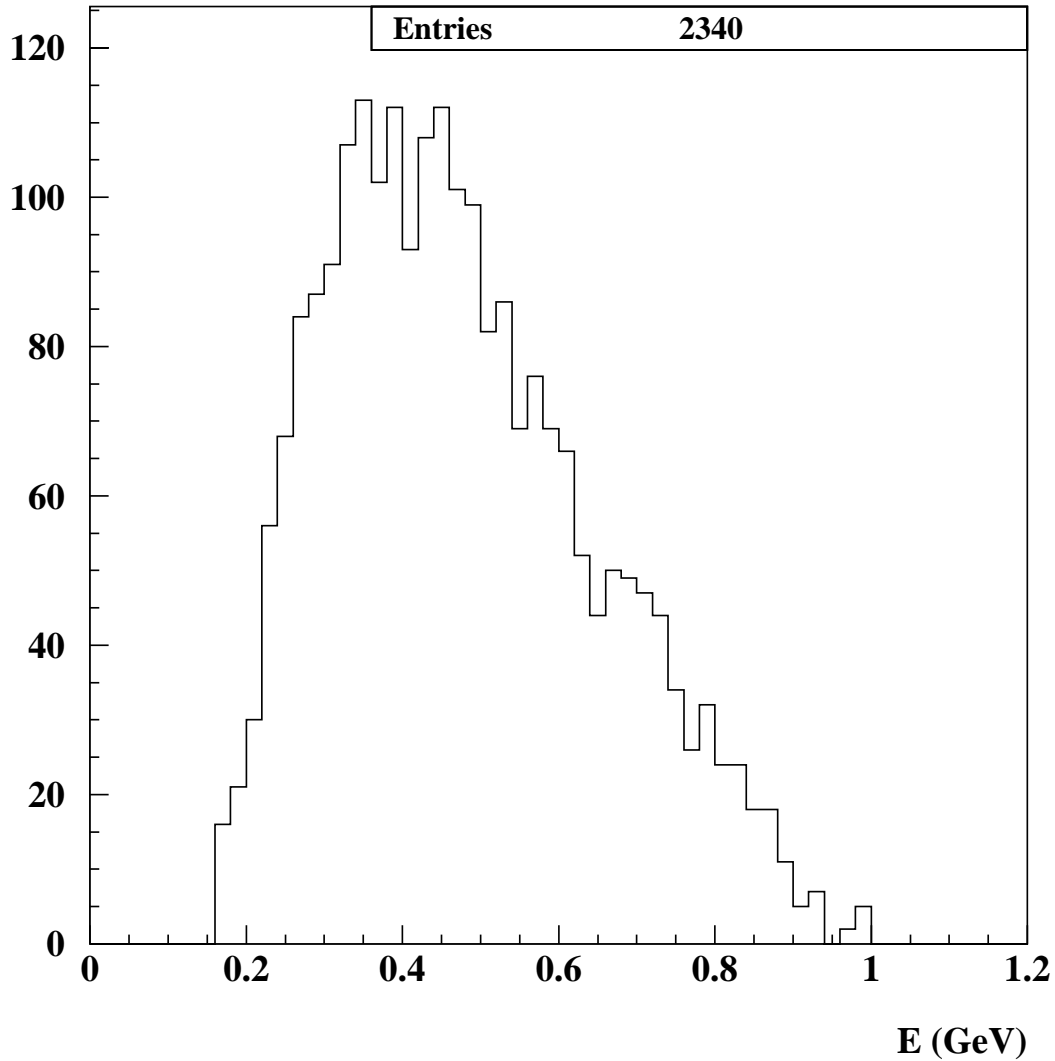


Figure 5-19. Distribution of photon energy from the decay $\chi_{c1} \rightarrow \gamma J/\psi$.

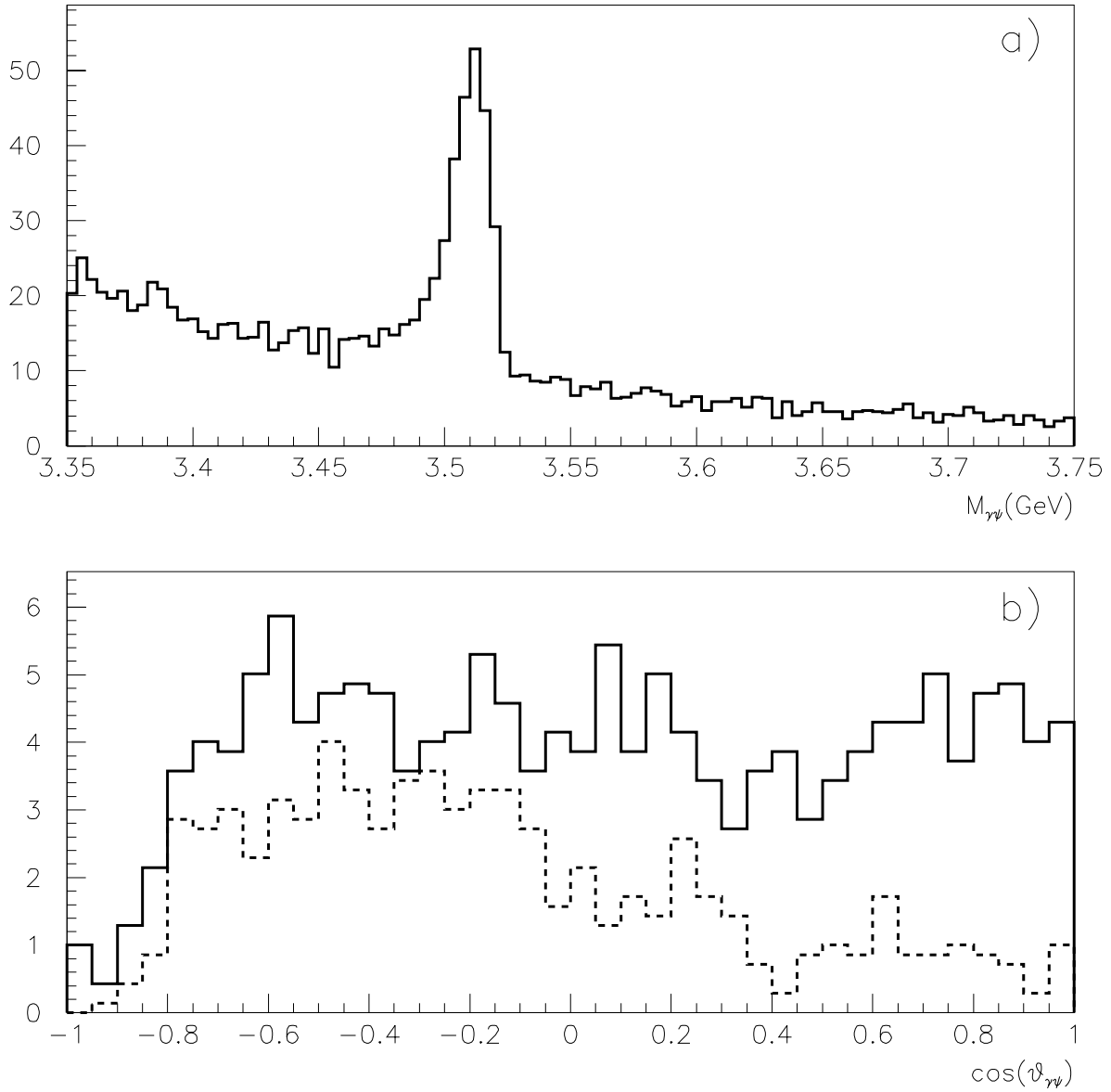


Figure 5-20. (a) $\gamma J/\psi$ invariant-mass distribution after the $p_{B^0}^* \leq 450$ MeV/c cut; (b) χ_{c1} decay and background (dashed) photon angular distribution in the χ_{c1} CM.

5.3.4.1 Backgrounds

The backgrounds for this channel are similar to those discussed in the previous sections. The largest contributions are expected from $B^0 \rightarrow \chi_{c1} K^{*0}$, $B^\pm \rightarrow \chi_{c1} K^{*\pm}$, $B^0 \rightarrow J/\psi K_L^0$, and combinatorial background as shown in Table 5-13.

Table 5-13. Summary of signal and background events selected applying the selection criteria optimized for the $B^0 \rightarrow \chi_{c1} K_L^0$ decay described in the text. The analysis was performed using the Aslund fast simulation.

Process	Selection Efficiency	# Events Selected
$B^0 \rightarrow \chi_{c1} K_L^0$	0.28	140
$B^0 \rightarrow \chi_{c1} K^{*0}$	0.068	16
$B^\pm \rightarrow \chi_{c1} K^{*\pm}$	0.065	31
$B^0 \rightarrow J/\psi K_L^0$	0.018	29
$B^0 \rightarrow \psi' K_L^0$	0.01	4
combinatorial		32

The angular distributions of the photon in the χ_{c1} CM is different for signal and background, as shown in Fig. 5-20b. This may be used to enhance the signal/background ratio, but was not exploited in the present analysis.

5.3.4.2 CP reach

About 140 signal events are expected from the decay $B^0 \rightarrow \chi_{c1} K_L^0$, with a total background of 110 events. Under the same assumptions made for the other K_L^0 channels, the error on $\sin 2\beta$ obtained is $\delta(\sin 2\beta) = 0.267$ (0.285) without (with) the correction for the asymmetric background. Further reduction in the backgrounds would substantially improve this error.

The results for $\sin 2\beta$ for all the K_L^0 channels are summarized in Table 5-14. Since these channels contaminate each other, it will be necessary to account for correlations when combining them.

5.4 Charmonium + K^{*0} Modes

The decay modes $B^0, \bar{B}^0 \rightarrow J/\psi K_{CP}^{*0}, \psi' K_{CP}^{*0}$ or $\chi_{1c} K_{CP}^{*0}$ (the subscript CP indicates a CP eigenstate such as $K_S^0 \pi^0$) are also Type I, as defined in Section 5.1.1. As in the modes B^0 ,

Table 5-14. CP reach for one standard year of data taking and $\sin 2\beta=0.7$ in the various K_L^0 modes. CP -mode efficiencies and background levels were calculated using the Aslund fast simulation. The Δz resolution was taken from the $J/\psi K_S^0$ analysis with full BBsim simulation.

	$B^0 \rightarrow J/\psi K_L^0$	$B^0 \rightarrow \psi' K_L^0$	$B^0 \rightarrow \chi_{c1} K_L^0$
$\mathcal{B}(X K_L^0)$ (see Table 5-10)	4.25×10^{-4}	1.134×10^{-4}	1.365×10^{-4}
$\mathcal{B}(J/\psi \rightarrow l^+ l^-)$	0.12		
Reconstruction Efficiency	0.41	0.27	0.28
# of signal events per 30 fb^{-1}	650	120	140
# of background events	380	100	110
# of CP symmetric background events	240	66	63
# of opposite CP background events	90	17	16
# of same CP background events	50	13	33
Δz resolution (see Section 5.3.1)	130 μm		
σ_0	1.61		
Tagging factor $\epsilon_{\text{tag}}(1 - 2w)^2$ (see Section 4.8.8)	0.30		
$\delta(\sin 2\beta)$	0.14	0.31	0.27
$\delta(\sin 2\beta)$ with CP -asymmetric background	0.15	0.34	0.28

$\bar{B}^0 \rightarrow$ Charmonium + Kaon, $\sin 2\beta$ can be measured from the time-dependent asymmetry without hadronic uncertainties, as has been discussed in detail in Section 5.1.2. However, for this purpose one needs to perform an angular analysis to separate the amplitudes of definite CP . The transversity analysis is a suitable tool for this, and has been described at length in Section 5.1.3 for the case $J/\psi K_{S\pi^0}^*$.

In this section the B^0 decays to the following final states are studied:

- $J/\psi K^{*0}, K^{*0} \rightarrow K_S^0 \pi^0, K_S^0 \rightarrow \pi^+ \pi^-$
- $J/\psi K^{*0}, K^{*0} \rightarrow K_S^0 \pi^0, K_S^0 \rightarrow \pi^0 \pi^0$
- $\psi' K^{*0}, \psi' \rightarrow \pi^+ \pi^- J/\psi, K^{*0} \rightarrow K_S^0 \pi^0, K_S^0 \rightarrow \pi^+ \pi^-$
- $\chi_{c1} K^{*0}, \chi_{c1} \rightarrow \gamma J/\psi, K^{*0} \rightarrow K_S^0 \pi^0, K_S^0 \rightarrow \pi^+ \pi^-$

For all four channels, only the leptonic decay of the J/ψ was considered. The branching ratios of the B^0 meson into these states are given in Table 5-3.

Samples of events for the three $J/\psi K^{*0}$ channels were produced with the `EvtGen` Monte Carlo generator taking into account the expected angular distribution described in Section 5.1.3. These events were analyzed after being passed through the full `BaBar` detailed simulation chain. The $\psi' K^{*0}$ and $\chi_{c1} K^{*0}$ channels were studied using a fast simulation procedure (`Aslund`). In all cases, the generated events were $\Upsilon(4S) \rightarrow B^0 \bar{B}^0$, with one B decaying to the CP channel under consideration and the other one to the full set of inclusive B decay modes.

The event selection is presented for all channels, but only the channel $J/\psi K^{*0}$, $K^{*0} \rightarrow K_s^0 \pi^0$, $K_s^0 \rightarrow \pi^+ \pi^-$ is considered in detail for the extraction of $\sin 2\beta$.

5.4.1 Event Selection

Since all of these final states contain a J/ψ , the event selection starts with the J/ψ reconstruction. The J/ψ has a nearly background-free signature and is used to determine the z coordinate of the decay vertex of the B^0 decaying into a CP eigenstate (z_{CP}). When a J/ψ candidate is found, the reconstruction of K_s^0 and π^0 candidates is further required. These are combined to form the K^{*0} candidate which is combined with the J/ψ , ψ' , or χ_{c1} to form a B meson candidate.

5.4.1.1 $J/\psi \rightarrow e^+e^-$, $\mu^+\mu^-$ selection

The J/ψ candidates are formed by combining all pairs of oppositely charged reconstructed tracks. No particle identification is required at this stage. Only pairs originating from a fitted common vertex are considered. The invariant mass is restricted to the range 2.9–3.15 GeV/c^2 ; the upper bound represents a $\sim 3\sigma$ cut ($\sigma \sim 13 \text{ MeV}/c^2$) around the J/ψ mass [32] whereas the lower bound is loosened to take into account radiative energy loss, which is particularly important for the electron mode. The J/ψ efficiency is 76%.

5.4.1.2 π^0 selection

The π^0 candidates are formed by combining pairs of neutral showers in the calorimeter with an energy greater than 25 MeV. The invariant mass of π^0 candidates is restricted to the range 0.110–0.150 GeV/c^2 . The π^0 detection efficiency is 40%.

5.4.1.3 $K_s^0 \rightarrow \pi^+\pi^-$ selection

Pairs of oppositely-charged tracks are combined to reconstruct the decay $K_s^0 \rightarrow \pi^+\pi^-$. Only track pairs with a decay distance in the xy plane greater than 1 mm are accepted. An invariant mass is calculated at this vertex and restricted to the range 0.486–0.510 GeV/ c^2 (the resolution is ~ 3.5 MeV/ c^2). The resulting efficiency is 61%.

5.4.1.4 $K_s^0 \rightarrow \pi^0\pi^0$ selection

$K_s^0 \rightarrow \pi^0\pi^0$ candidates are created by combining all π^0 pairs and requiring the invariant mass to be within the range 0.42–0.53 GeV/ c^2 . The efficiency for this decay mode is 18.8%.

5.4.1.5 $K^{*0} \rightarrow K_s^0\pi^0$ selection

K^{*0} candidates are created by combining pairs of π^0 and K_s^0 candidates. The invariant mass of the K^{*0} candidates is restricted to the range 0.70–1.10 GeV/ c^2 (0.74–0.96 GeV/ c^2) for the $K_s^0 \rightarrow \pi^+\pi^-$ ($K_s^0 \rightarrow \pi^0\pi^0$) channel. A smaller mass range is used for the $K_s^0 \rightarrow \pi^0\pi^0$ case in order to reduce the large combinatorial background coming from one or more wrong photons among the six needed for this decay. The invariant-mass distributions are shown for signal events in Fig. 5-21. The K^{*0} efficiencies are 23% and 9% for the charged and neutral decays of the K_s^0 respectively.

5.4.1.6 χ_{c1} selection

J/ψ candidates are combined with selected photons satisfying $0.15 < E_\gamma < 1.0$ GeV to form χ_{c1} candidates with a mass resolution of ~ 16 MeV/ c^2 . The invariant mass of the χ_{c1} is required to lie within the range 3.47–3.57 GeV/ c^2 . The χ_{c1} efficiency is 62%.

5.4.1.7 ψ' selection

J/ψ candidates are combined with all pairs of pions with opposite charge. A common vertex is required to be within 1 mm of the interaction point in the xy plane. The invariant mass of these ψ' candidates is restricted to the range 3.65–3.73 GeV/ c^2 (the resolution is ~ 14 MeV/ c^2). The ψ' efficiency is 52%.

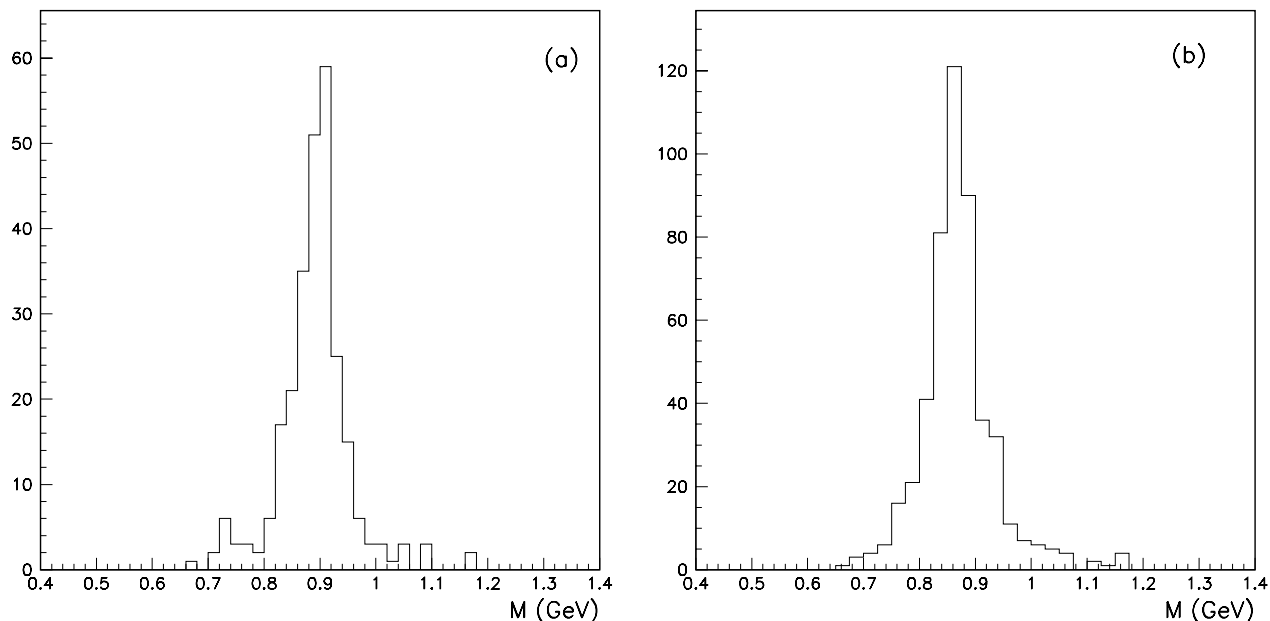


Figure 5-21. $K^{*0} \rightarrow K_S^0 \pi^0$ mass distribution for signal events for (a) $K_S^0 \rightarrow \pi^+ \pi^-$ and (b) $K_S^0 \rightarrow \pi^0 \pi^0$. The integrated luminosities correspond to (a) 50 fb^{-1} and (b) 250 fb^{-1} .

5.4.1.8 $B^0 \rightarrow J/\psi K^{*0}, K^{*0} \rightarrow K_S^0 \pi^0$ reconstruction

B^0 candidates are formed from selected pairs of J/ψ and K^{*0} . For the case $K^{*0} \rightarrow \pi^+ \pi^- \pi^0$ the B mass and $p_{B^0}^*$ are restricted to the range 5.21–5.34 GeV/c^2 and 0.25–0.43 GeV/c , respectively. The resulting total efficiency for this channel is $\sim 11\%$. Finally, a cut is applied on the helicity angle θ_1 (see Section 5.1.3), $\cos \theta_1 < 0.8$ (see Figure 5-22). This cut reduces the efficiency to 9.1% but reduces the combinatorial background from 40% to 15%. Expected numbers of selected and background events are summarized in Table 5-15.

For $K^{*0} \rightarrow 3\pi^0$, the B mass and $p_{B^0}^*$ are restricted to the ranges 5.15–5.31 GeV/c^2 and 0.20–0.45 GeV/c , respectively. In addition, the J/ψ and the K^* are required to be nearly back-to-back in the B rest frame, $\cos \theta_{\psi K^*} < -0.97$. The overall efficiency for this channel is $\sim 6\%$, but there is 15 times as much background as signal, so further improvement is needed to make this a viable analysis.

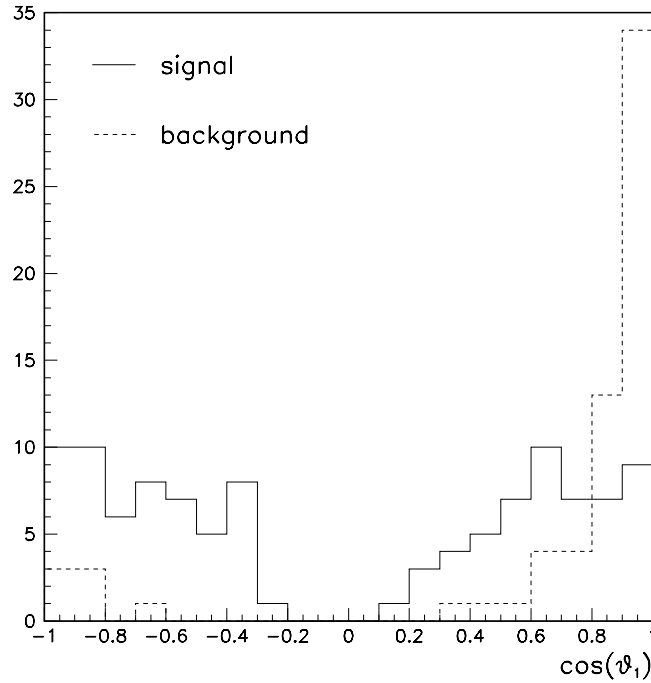


Figure 5-22. The distribution of $\cos \theta_1$ for signal (solid histogram) and background (dashed histogram).

Table 5-15. Expected numbers of signal and background events for the decay $B^0 \rightarrow J/\psi K^{*0}$. The analysis was performed using the full `BBsim` simulation and reconstruction chain.

	$K_S^0 \rightarrow \pi^+\pi^-$	$K_S^0 \rightarrow \pi^0\pi^0$
$\mathcal{B}(B^0 \rightarrow J/\psi K^{*0})$	1.32×10^{-3}	
$\mathcal{B}(J/\psi \rightarrow l^+l^-)$	0.12	
$\mathcal{B}(K^{*0} \rightarrow K_S^0\pi^0)$	0.167	
$\mathcal{B}(K_S^0 \rightarrow \pi^+\pi^-)$	0.686	0.314
# of produced events per 30 fb^{-1}	570	260
reconstruction efficiency	0.091	0.06
# of signal events per 30 fb^{-1}	51	16
N_B/N_S	0.18	15

5.4.1.9 $B^0 \rightarrow \chi_{c1} K^{*0}$ reconstruction

The B invariant mass is restricted to the range 5.21–5.35 GeV/ c^2 and the $p_{B^0}^*$ cut is the same as for $J/\psi K^{*0}$. The overall efficiency is $\sim 19\%$. Note that this number, obtained with fast simulation, is surely too optimistic. For comparison, the final efficiency obtained for $B^0 \rightarrow J/\psi K^{*0}$ with the same fast simulation procedure is $\sim 30\%$.

5.4.1.10 $B^0 \rightarrow \psi' K^{*0}$ reconstruction

The B invariant mass is restricted to the range 5.21–5.35 GeV/ c^2 . The overall efficiency, not including branching fractions is 12%, though again this is too optimistic.

5.4.1.11 Backgrounds

Backgrounds from $q\bar{q}$ and other $B\bar{B}$ decays have been considered. The backgrounds were found to be negligible for the $B^0 \rightarrow J/\psi K^{*0}$ analysis, though it is possible that some background might arise from decay modes not present in the $B\bar{B}$ Monte Carlo sample.

5.4.2 Measurement of $\sin 2\beta$ with the Decay $B^0 \rightarrow J/\psi K^{*0}$

In this section, the measurement of $\sin 2\beta$ using the transversity angular distributions of $B^0 \rightarrow J/\psi K^{*0}$ ($K_s^0 \rightarrow \pi^+\pi^-$) events is discussed. These events were selected as described in Section 5.4.1.8. From the time-dependent form of Eq. (5.39), $\sin 2\beta$ and R_\perp can be extracted simultaneously using an unbinned maximum likelihood fit. $\Delta z = z_{CP} - z_{\text{tag}}$ is determined using the J/ψ decay vertex for z_{CP} , and the tagging algorithm described in Section 4.5.1.3 for z_{tag} (the flavor of the tagging B is taken from the generator information, and the standard tagging efficiency, Section 4.8.8, is used at the end of the analysis).

CP mixture effects on the $\sin 2\beta$ resolution are considered by generating the events with different values of the transversity amplitudes in the model (detector smearing is ignored for this study). The $\sin 2\beta$ error, averaged over 20 experiments of 500 events each, is 0.09, for CP -even or CP -odd final states, but degrades to 0.19 when CP -even and CP -odd states are present in equal proportions. The measured CLEO values [13] of the transversity amplitudes tend to indicate that the CP -even eigenstates dominate, so events are generated with 100% CP -even longitudinal polarization ($A_\perp = A_\parallel = 0$). These events were reconstructed and the selection criteria described in Section 5.4.1 were applied.

The sample surviving the selection criteria is used to extract Δz and θ_{tr} . θ_{tr} smearing is found to be less than 1.5% over the whole acceptance region, so this effect is neglected in what follows.

Resolution on Δz can be described by the sum of two Gaussians distributions with widths similar to those for the $J/\psi K_s^0$ analysis described in Section 5.3.1. Using a sample of 759 signal events, an error on $\sin 2\beta$ of 0.065 is obtained, implying $\sigma_0 = 1.79$ (Eq. (5.81)). The value for σ_0 would decrease to 1.59 (as for the $J/\psi K_s^0$ analysis) if the CP mixture were known to be 100% and $\sin 2\beta$ were extracted with Δz only.

Using the numbers of expected signal and background events given in Table 5-15 and a tagging factor of 0.30 (Section 4.8.8), an error of 0.50 on the measurement of $\sin 2\beta$ with the decay $B^0 \rightarrow J/\psi K^{*0}$ is obtained, for an integrated luminosity of 30 fb^{-1} on the $\Upsilon(4S)$. Although the other modes appear to be feasible and will be considered in future analyses, their branching ratios and efficiencies are much smaller and thus the capability of measuring $\sin 2\beta$ with these modes has not yet been considered.

5.5 $D^+ D^-$, $D^* D$, and $D^* D^*$ Final States

The decay modes $B^0, \bar{B}^0 \rightarrow D\bar{D}, D\bar{D}^*, D^*\bar{D}, D^*\bar{D}^*$, that have been called Type II in Section 5.1.1, are Cabibbo suppressed and have color-allowed contributions. However, their branching ratios are not suppressed relative to the type I Charmonium+ $K(K^*)$ because of color. As was discussed in detail in Sections 5.1.2 and 5.1.4, these modes have a potentially important penguin contribution that, unlike the $\pi^+\pi^-$ case, cannot be extracted by isospin analysis. This penguin pollution is thus irreducible, but naïve estimates using factorization (Section 5.1.5) seem to indicate that it is small. In the case of $D^*\bar{D}^*$, angular analysis is, of course, necessary to measure $\sin 2\beta$ (up to penguins) without dilution, as discussed in detail in Section 5.1.3. Moreover, calculations using heavy-quark symmetry and factorization (Section 5.1.6) indicate that for the sum of ground state mesons $D\bar{D} + D\bar{D}^* + D^*\bar{D} + D^*\bar{D}^*$, one expects a CP asymmetry with small dilution and a gain in statistics of a factor of six relative to the golden mode $J/\psi K_s^0$. Section 5.1.7 points out the reasons for studying Dalitz plots of the type $D\bar{D}\pi$ or $D\bar{D}K_s^0$ via D^{**} s in order to measure $\text{sign}(\cos 2\beta)$, necessary to resolve one of the discrete ambiguities left by the measurement of $\sin 2\beta$.

5.5.1 Study of $B^0 \rightarrow D^+ D^-$

Due to the low value of the branching ratios for the decay of charged charmed mesons, six channels have been considered in the present analysis. These are shown in Table 5-16. The results from CLEO [35], based on an integrated luminosity of 3.1 fb^{-1} , did not show any evidence for a signal in the channel $B^0 \rightarrow D^+ D^-$; a 90% CL upper limit of 1.3×10^{-3} was obtained. Using the HQET hypothesis, the branching ratio for the decay $B^0 \rightarrow D^+ D^-$ can be predicted from that of the

Table 5-16. The branching ratio of the decay modes for D^+ used in this analysis. The branching ratios for the D^- modes are the same as for D^+ .

Mode	\mathcal{B} (%)
$D^+ \rightarrow K^- \pi^+ \pi^+$	9.1
$D^+ \rightarrow K^- \pi^+ \pi^+ \pi^0$	6.4
$D^+ \rightarrow \bar{K}^0 \pi^+$	2.74
$D^+ \rightarrow \bar{K}^0 \pi^+ \pi^0$	9.7
$D^+ \rightarrow \bar{K}^0 \pi^- \pi^+ \pi^+$	7.0
$D^+ \rightarrow \bar{K}^0 \pi^- \pi^+ \pi^+ \pi^0$	5.4

channel $B^0 \rightarrow D^+ D_s^-$ via the formula

$$\mathcal{B}(B^0 \rightarrow D^+ D^-) = (f_D/f_{D_s}) \tan^2 \theta_c \mathcal{B}(B^0 \rightarrow D_s^+ D^-), \quad (5.85)$$

where f_D and f_{D_s} are the decay constants for the D^\pm and D_s^\pm , respectively. The CLEO measurement [45] $\mathcal{B}(B^0 \rightarrow D_s^+ D^-) = 1.2 \pm 0.5\%$ leads to $\mathcal{B}(B^0 \rightarrow D^+ D^-) = 4.5 \times 10^{-4}$, which will be used in this section.

The Aslund fast simulation program was used throughout the analysis of the CP mode in this study.

5.5.1.1 Event shape cuts

Different variables were studied in order to extract the most powerful continuum background suppression cuts. Those chosen were applied in the early stages of the analysis as filter cuts. The initial study compared the methods using a variable called the separation, given by the formula [46]

$$s = \int_{-\infty}^{+\infty} \frac{[g^s(x) - g^b(x)]^2}{g^s(x) + g^b(x)}, \quad (5.86)$$

where g^s and g^b are the distributions of the variable x for the signal and background, respectively. Once s is computed for each discriminating variable, the methods with the largest separation are chosen. As discussed in Section 4.9.1, variables such as Fox-Wolfram moments, sphericity, thrust, and aplanarity can be used to distinguish B events of interest from $q\bar{q}$ background via the event shape. These quantities, and a clusterization algorithm have been studied for this decay mode.

The study was performed on samples of continuum events. The separation between $b\bar{b}$ events and each type of continuum background is displayed in Table 5-17. This study shows that the second-order Fox-Wolfram moment (H_2/H_0) is the variable which provides the best separation between

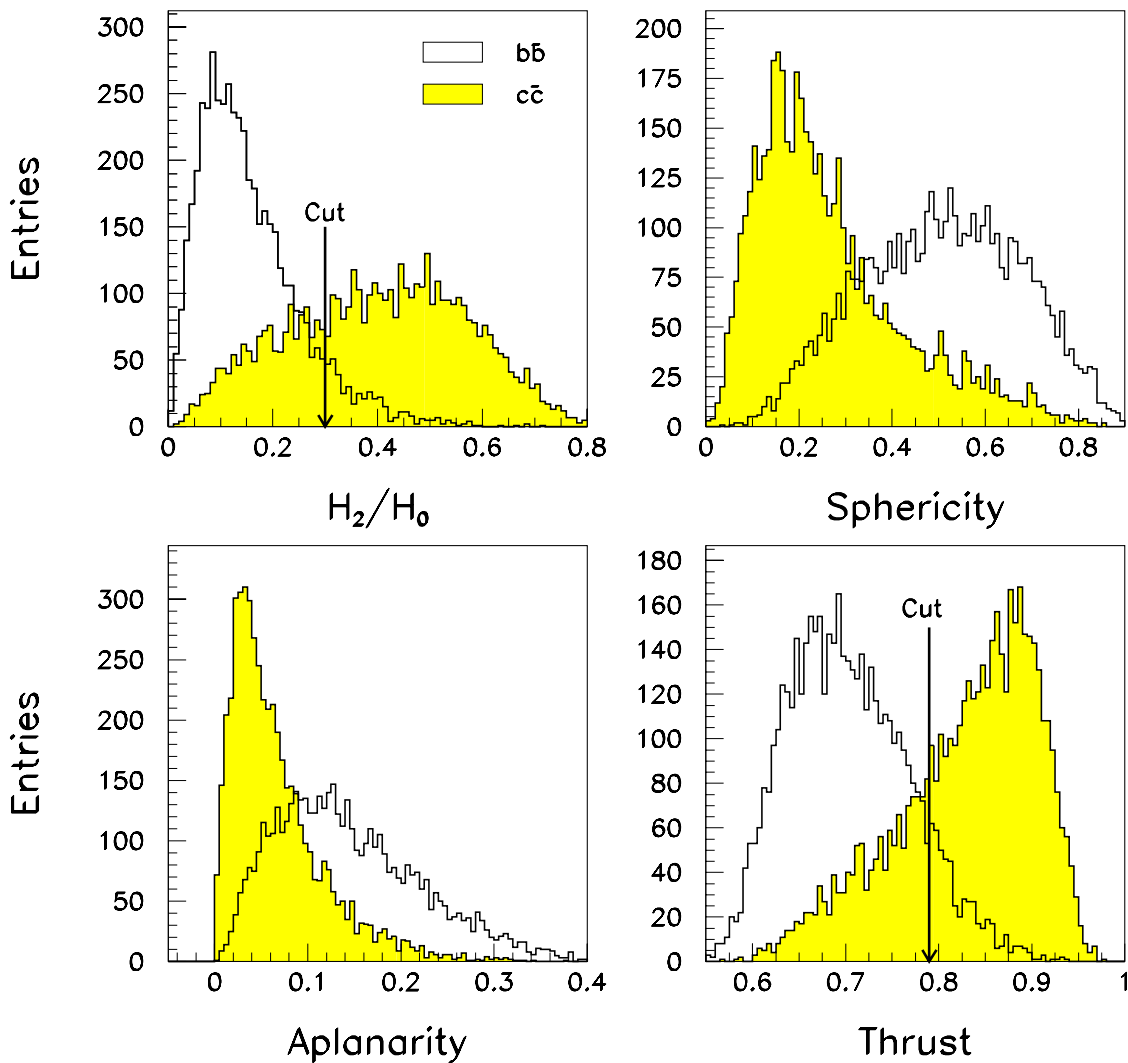


Figure 5-23. Four event-shape variables: the second order of Fox-Wolfram moment (top left), sphericity (top right), aplanarity (bottom left), and thrust (bottom right). There is good separation between $b\bar{b}$ events (open histogram) and $c\bar{c}$ events (shaded histogram). The cuts applied in the analysis are shown.

Table 5-17. The separation, as defined in the text, obtained between $b\bar{b}$ events and each type of the continuum background.

Variable	$b\bar{b}$.vs. $u\bar{u}$	$b\bar{b}$.vs. $d\bar{d}$	$b\bar{b}$.vs. $s\bar{s}$	$b\bar{b}$.vs. $c\bar{c}$
H_2/H_0	0.50 ± 0.09	0.46 ± 0.07	0.53 ± 0.10	0.56 ± 0.09
H_3/H_0	0.07 ± 0.05	0.09 ± 0.07	0.05 ± 0.05	0.06 ± 0.04
H_4/H_0	0.32 ± 0.09	0.31 ± 0.07	0.35 ± 0.09	0.27 ± 0.08
Thrust	0.48 ± 0.09	0.44 ± 0.08	0.51 ± 0.09	0.56 ± 0.09
Sphericity	0.42 ± 0.08	0.38 ± 0.06	0.45 ± 0.08	0.43 ± 0.08
Aplanarity	0.33 ± 0.08	0.33 ± 0.06	0.35 ± 0.08	0.30 ± 0.07
$D_{min}(d_{join} = 2.5)$	0.33 ± 0.07	0.30 ± 0.07	0.25 ± 0.07	0.28 ± 0.06
$D_{min}(d_{join} = 2.0)$	0.32 ± 0.06	0.29 ± 0.06	0.24 ± 0.06	0.26 ± 0.06
$D_{min}(d_{join} = 1.5)$	0.28 ± 0.05	0.24 ± 0.05	0.21 ± 0.05	0.25 ± 0.05
$T_{gen}(d_{join} = 2.5)$	0.47 ± 0.09	0.47 ± 0.09	0.50 ± 0.09	0.54 ± 0.09
$T_{gen}(d_{join} = 2.0)$	0.48 ± 0.08	0.47 ± 0.08	0.50 ± 0.08	0.53 ± 0.08
$T_{gen}(d_{join} = 1.5)$	0.39 ± 0.07	0.37 ± 0.07	0.39 ± 0.07	0.41 ± 0.07

signal and background (see Figure 5-23). A cut, $H_2/H_0 \leq 0.3$, allows rejection of 70% of the continuum while keeping 93% of the signal. A slight improvement can be made by adding the thrust variable, with a cut $T < 0.79$. Though these variables are highly correlated, use of both cuts reduces the background by 75% while keeping 91% of the signal. Further improvements could be obtained by combining all shape variables, for instance with a neural network.

$q\bar{q}$ background tends to have low multiplicity, so at least seven tracks were required in the event. All three cuts together reject 82% of the background while retaining 90% of the signal.

5.5.1.2 Particle identification

In order to identify charged kaons from D decays, the following simple algorithm was used. A track is considered a kaon if:

- The DIRC response is consistent with the kaon hypothesis (3σ) but inconsistent with the pion hypothesis (3σ), or
- The same criteria are satisfied for dE/dx if there is no DIRC response.

Table 5-18. The efficiency for the K_S^0 reconstruction found in the Aslund study after each step of the analysis.

Cut	ϵ (%)
Acceptance	74
Vertexing	95
Invariant mass	99
Combined	71

5.5.1.3 K_S^0 reconstruction

K_S^0 candidates were reconstructed from two charged tracks with opposite sign and vertexed with the YTOP package [47]. The vertex probability was required to satisfy $P(\chi^2) > 1\%$, and the fitted decay length of the K_S^0 candidate was required to be more than 3σ from 0. Finally, K_S^0 candidates were required to satisfy $|M_{\pi^-\pi^+} - M_{K_S^0}| \leq 3\sigma_{K_S^0}$, where the mass resolution, $\sigma_{K_S^0}$, is 2.0 MeV/ c^2 . The overall efficiency for K_S^0 reconstruction was found to be 71%, as seen in Table 5-18.

5.5.1.4 π^0 reconstruction

Electromagnetic clusters with an energy greater than 20 MeV were paired to form neutral pion candidates. The invariant mass distribution for the signal is a Gaussian with a low-mass tail, which reflects the presence of matter in front of the electromagnetic calorimeter and leakage out of the back of the calorimeter. Due to the tail effect, the position of the peak was shifted from the nominal π^0 mass at low π^0 momentum. This was corrected by rescaling the energy of the photons. The π^0 candidates were considered if they satisfied the requirement $|M_{\gamma\gamma} - M_{\pi^0}| \leq 3\sigma_{\gamma\gamma}$, where the π^0 mass resolution $\sigma_{\gamma\gamma}$ was 5.4 MeV/ c^2 . The π^0 efficiency at this point was 60%. In order to remove background photons, the requirement that $|\cos\theta^*| \leq 0.7$, was imposed, where θ^* is the decay angle. For the signal, the distribution of this variable is expected to be flat (before acceptance cuts) since the π^0 spin is zero. This cut removed one-third of the background while reducing the signal by 20%.

5.5.1.5 D^\pm reconstruction

Reconstruction of D^\pm mesons is performed by looping over tracks and K_S^0 and π^0 candidates, as applicable. In order to reduce CPU time, once one charmed meson is reconstructed, a cut is applied on the missing mass, $M_{\text{miss}}^2 = (P_{B^0} - P_{D_{\text{rec}}})^2$, where P_{B^0} and $P_{D_{\text{rec}}}$ are, respectively, the

Table 5-19. The reconstruction efficiency for charged D mesons, obtained using the `ASlund` fast simulation program.

Variable	$K^-\pi^+\pi^+$	$K^-\pi^+\pi^+\pi^0$	$K_S^0\pi^+$	$K_S^0\pi^+\pi^0$	$K_S^0\pi^+\pi^-\pi^+$	$K_S^0\pi^+\pi^-\pi^+\pi^0$
Total Efficiency (%)	60.5	33.2	56.4	31.0	42.0	23.5
σ_D (MeV/c ²)	4.3	8.1	4.7	10.9	3.5	6.2
\mathcal{B} (%)	9.1	6.4	1.4	4.9	3.5	6.2
$\epsilon \times \mathcal{B}$ (%)	5.5	2.1	0.5	1.0	1.0	0.4

reconstructed B^0 and D^\pm four-vectors. By performing the calculation in the center of mass and neglecting the B^0 momentum, the following is obtained

$$M_{\text{miss}} \simeq \sqrt{M_{B^0}^2 + M_{D_{\text{rec}}}^2 - 2E_{B^0}^* E_{D_{\text{rec}}}^*} . \quad (5.87)$$

The distribution of M_{miss} is a Gaussian centered at the D^\pm mass with a resolution of 180 MeV/c². This large resolution is due to the neglect of the B momentum in the above calculation. The cut, $1.2 < M_{\text{miss}} < 2.2$, is applied, which retains all signal and rejects a great deal of combinatoric background. A kinematic vertexing of the charged daughter particles of the D^\pm has also been performed. The D^\pm mass resolution is 4–10 MeV/c², depending on the number of π^0 mesons in the final state, as seen in Fig. 5-24 and Table 5-19. D candidates are taken to be those with a mass within 3σ of the nominal charged D mass. The total efficiency times \mathcal{B} for D^\pm reconstruction is 10.5%, as summarized in Table 5-19.

5.5.1.6 B^0 reconstruction

Once the list of charmed mesons has been obtained, opposite-charge pairs are combined. The B^0 momentum in the center of mass is required to satisfy $0.15 \leq p_{B^0}^* \leq 0.45$ GeV/c. The B mass distribution for events passing these cuts and with 0, 1, or 2 signal π^0 s is shown in Fig. 5-25. The two D mesons are required to be from the same vertex by requiring the probability of the combined vertex to be greater than 1%. If more than one B^0 has been reconstructed in the analysis, the one with the best vertex-fit probability is kept. The overall efficiency obtained in the B^0 reconstruction is $\sum \epsilon_i \times \mathcal{B}_i = 1.2\%$. The detailed results for the 21 combinations of decay channels are displayed in Table 5-20.

In order to study the performance of the vertex reconstruction, we have defined three categories depending on the number of charged tracks in the final state. The first category contains the modes which have 3 tracks in the final state for both D mesons. The second one has three tracks for one D and one track for the other one. The third category has one charged track for each D . The vertex probability for the three categories is flat for the signal (Fig. 5-26). This figure also shows the z vertex position, which has a resolution of 52 μm for all three classes.

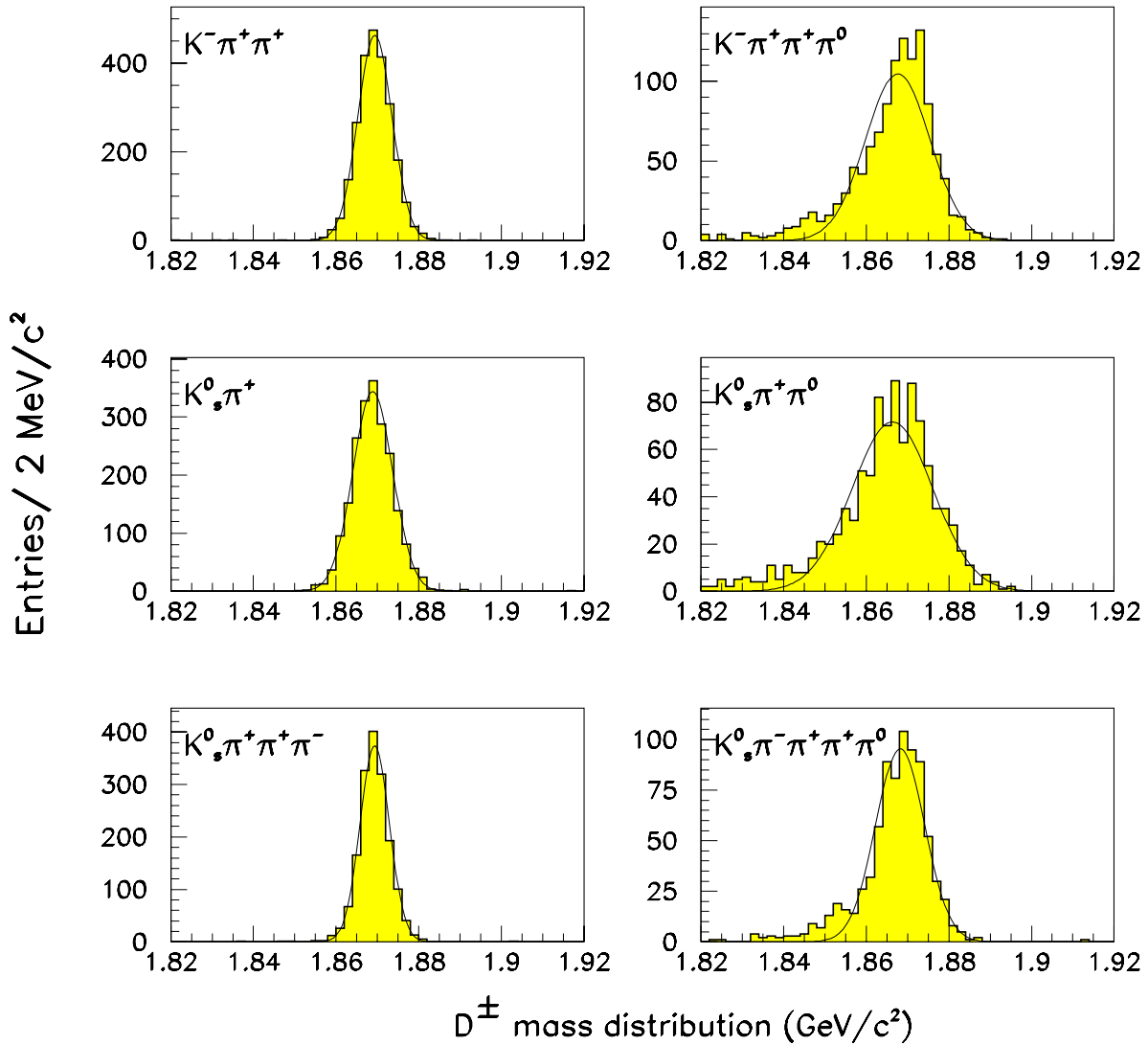


Figure 5-24. The D -mass distribution obtained in the six modes which are considered in the analysis. Those with a π^0 in the final state have larger mass resolution and a tail at lower mass. This does not affect the analysis because a D mass constraint is applied when the B^0 mesons are reconstructed.

Table 5-20. Relevant quantities for the various combinations of DD reconstruction. The upper number is the reconstruction efficiency for the mode, obtained using the Aslund fast simulation, the middle number is the branching ratio, and the lower number is the effective efficiency ($\epsilon \times \mathcal{B}$).

	$K\pi\pi$	$K\pi\pi\pi^0$	$K_S^0\pi$	$K_S^0\pi\pi^0$	$K_S^0\pi\pi^+\pi^-$	$K_S^0\pi\pi^+\pi^-\pi^0$
$K\pi\pi$	40% 0.83% 0.33%	20% 1.2% 0.24%	37% 0.17% 0.06%	18% 0.61% 0.11%	28% 0.44% 0.13%	14% 0.34% 0.05%
$K\pi\pi\pi^0$		11% 0.41% 0.04%	18% 0.12% 0.02%	9.1% 0.43% 0.04%	12% 0.31% 0.04%	6.4% 0.24% 0.02%
$K_S^0\pi$			32% 0.0086% 0.003%	18% 0.062% 0.01%	28% 0.044% 0.009%	12% 0.0034% 0.004%
$K_S^0\pi\pi^0$				9.5% 0.11% 0.01%	10% 0.16% 0.02%	5.1% 0.12% 0.006%
$K_S^0\pi\pi^+\pi^-$					15% 0.058% 0.009%	9.0% 0.089% 0.008%
$K_S^0\pi\pi^+\pi^-\pi^0$						6.1% 0.0034% 0.0002%

5.5.1.7 Background study

In order to evaluate the background in this analysis, large samples of $q\bar{q}$ and generic $b\bar{b}$ events have been used. The number of events for each type of background is shown in Table 5-21. The study shows that the background arises mainly from $b\bar{b}$ events and is concentrated in six decay combinations, five of which have two π^0 s:

$$\begin{aligned}
 D^+ &\rightarrow K^-\pi^+\pi^+\pi^0, & D^- &\rightarrow K^+\pi^-\pi^-\pi^0 \\
 D^+ &\rightarrow K^-\pi^+\pi^+\pi^0, & D^- &\rightarrow K_S^0\pi^-\pi^0 \\
 D^+ &\rightarrow K^-\pi^+\pi^+\pi^0, & D^- &\rightarrow K_S^0\pi^-\pi^+\pi^- \\
 D^+ &\rightarrow K^-\pi^+\pi^+\pi^0, & D^- &\rightarrow K_S^0\pi^-\pi^+\pi^-\pi^0 \\
 D^+ &\rightarrow K_S^0\pi^+\pi^0, & D^- &\rightarrow K_S^0\pi^-\pi^+\pi^-\pi^0 \\
 D^+ &\rightarrow K_S^0\pi^+\pi^+\pi^-\pi^0, & D^- &\rightarrow K_S^0\pi^-\pi^+\pi^-\pi^0
 \end{aligned}$$

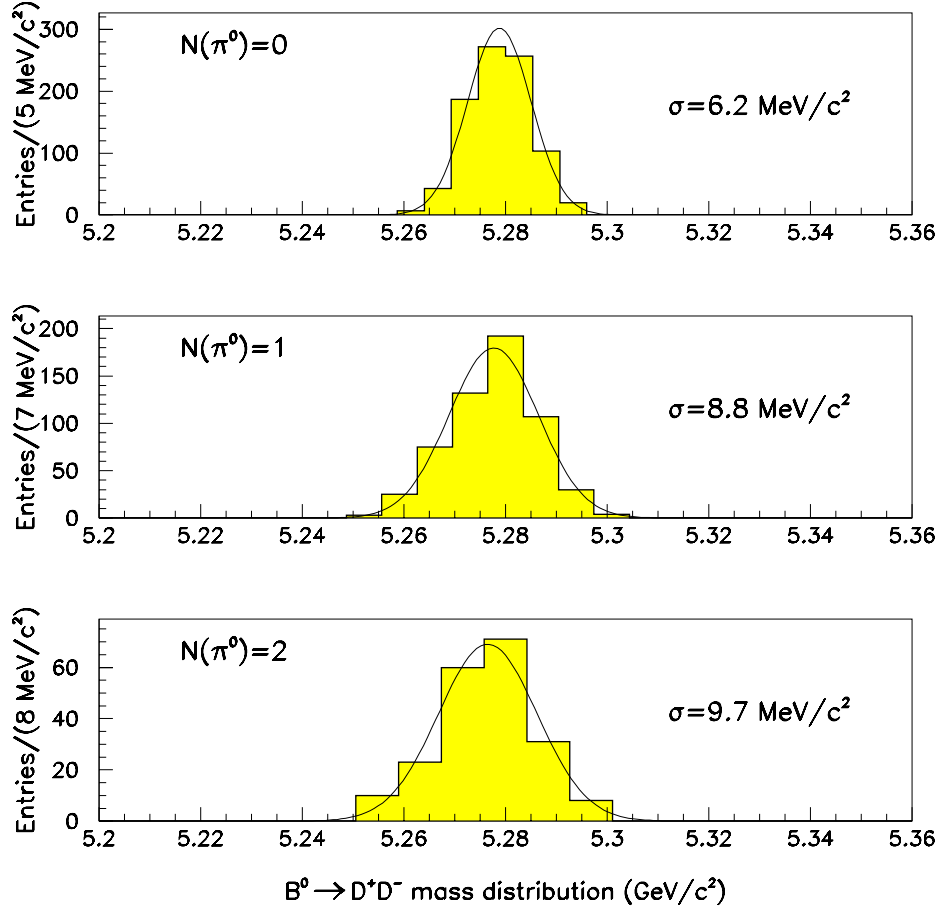


Figure 5-25. The mass distribution for the B^0 depending on the number of π^0 in the final state.

These modes are removed from the analysis, resulting in an efficiency loss of only 10%. After a 3σ B^0 mass cut, the signal to background ratio has been measured for each type of background to be

$$\frac{S}{B} = 5.7 |_{c\bar{c}}, 24.6 |_{u\bar{u}}, 7.4 |_{d\bar{d}}, 16.4 |_{s\bar{s}}, 0.42 |_{b\bar{b}}. \quad (5.88)$$

While the continuum background is relatively small ($N_B/N_S \sim 0.4$), the $b\bar{b}$ background is problematic, as can be seen in Fig. 5-27.

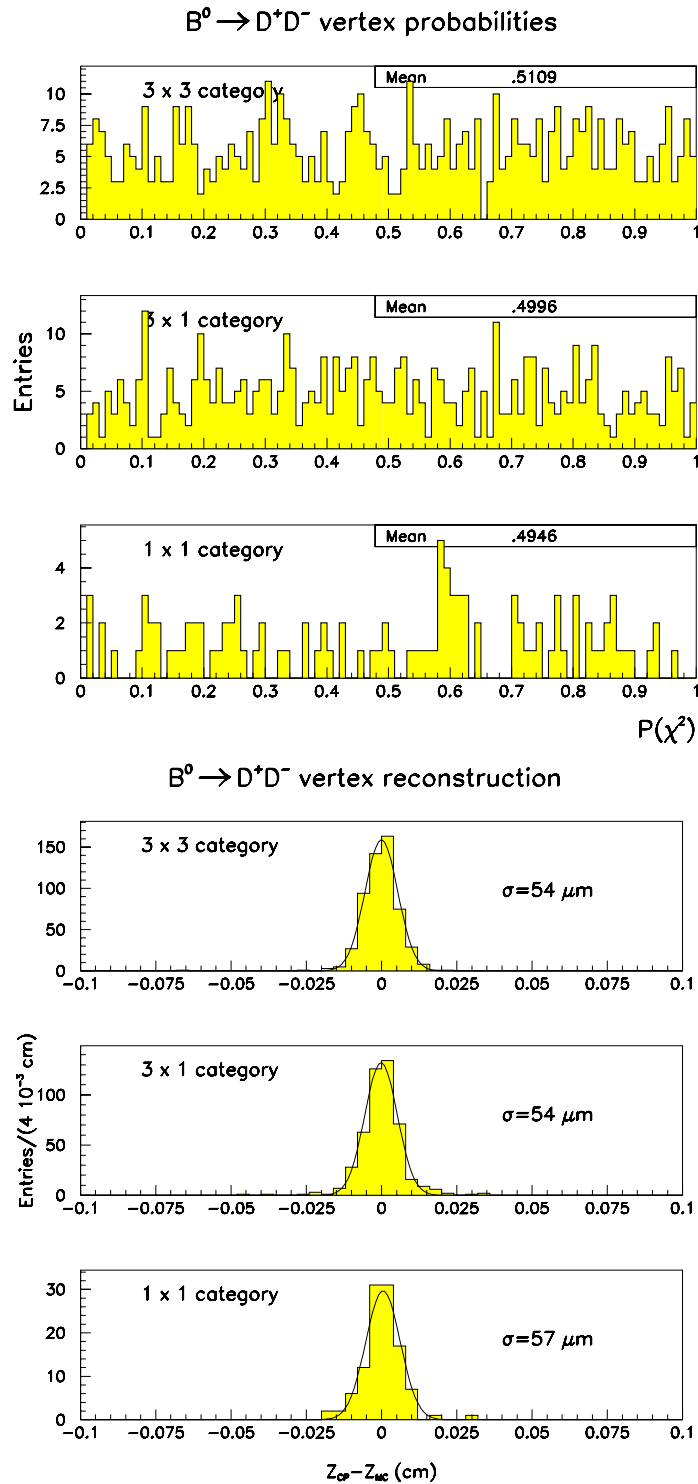


Figure 5-26. Plots on the top show the $D^+ D^-$ vertex probability for the three categories $N_1 \times N_2$, where N_1 and N_2 are the number of tracks in the final state for the two D decays. Plots on the bottom show the resolution for the z position of the B .

Table 5-21. The number of generated events for the background study.

Type of events	$b\bar{b}$	$c\bar{c}$	$u\bar{u}$	$d\bar{d}$	$s\bar{s}$
# events	2.2×10^6	3.6×10^6	3.9×10^6	4.1×10^6	3.9×10^6

Table 5-22. Summary of the expected results for the $B^0 \rightarrow D^+D^-$ analysis with an integrated luminosity of 30 fb^{-1} running on the $\Upsilon(4S)$. The analysis was performed using the `Aslund` fast simulation program.

$\mathcal{B}(B^0 \rightarrow D^+D^-)$	4.5×10^{-4}
Usable sample	610
Average reconstruction efficiency	0.24
Reconstructed signal events	140
N_B/N_S	2.8
Average CP vertex z resolution	$55 \mu\text{m}$

5.5.1.8 Final sample and conclusions

The summary of the results expected with an integrated luminosity of 30 fb^{-1} running on the $\Upsilon(4S)$ is shown in Table 5-22. The results are based on the `Aslund` fast simulation program. Studies with the full reconstruction program show that the mass and Δz resolutions are the same as found here. However the efficiency of this analysis is likely to decrease as a more realistic simulation is performed.

5.5.2 Study of $B^0 \rightarrow D^{*+}D^{*-}$

This vector-vector mode is a superposition of CP states due to the different possible helicity configurations of the final state. Experimentally, this means that in addition to reconstructing the decay $B^0 \rightarrow D^{*+}D^{*-}$ and tagging the event to determine the flavor of the B , the transversity angles of the final state must also be measured. Analyzing the distributions of transversity angles then allows the separation of the CP -even and CP -odd components of the final event sample.

The D^* mesons are identified by their decay $D^{*+} \rightarrow D^0\pi^+$. The D^0 mesons are reconstructed in four decay modes, involving one kaon (K^\pm or K_s^0) and one or more pions (charged or neutral), as shown in Table 5-23. Oppositely charged pairs of D^* are combined to form B^0 candidates and a tagging algorithm is then applied to identify the original flavor of the B^0 candidate.

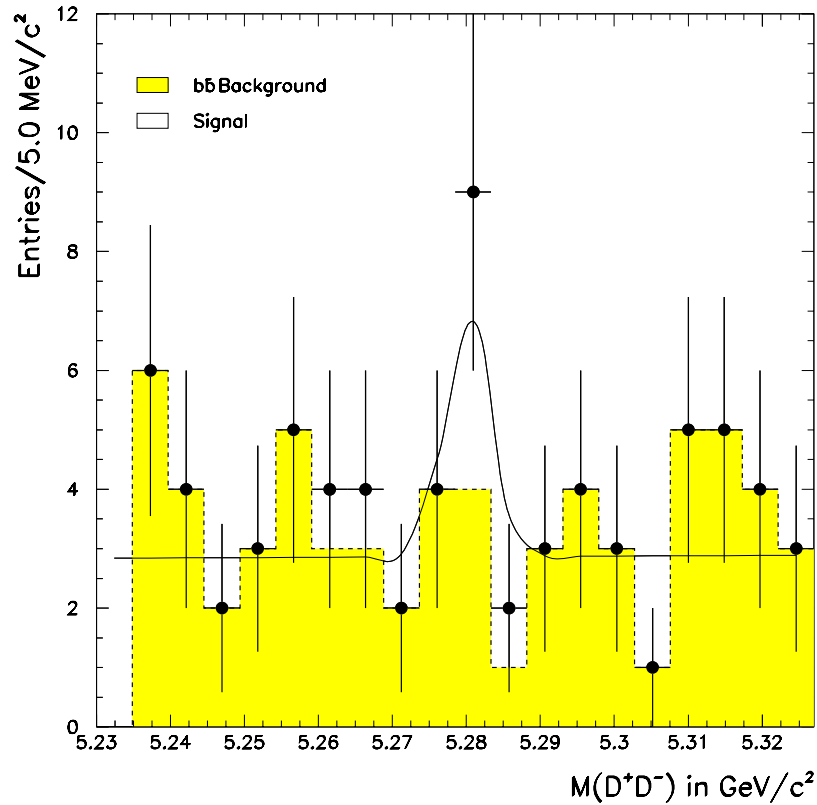


Figure 5-27. The B -mass distribution for 2.2×10^6 $\Upsilon(4S)$ events. The signal is constrained to the expected mass and width.

Table 5-23 lists the different modes studied and their branching ratios. The $B^0 \rightarrow D^{*+}D^{*-}$ branching ratio is not yet measured; an upper limit of $\mathcal{B}(B^0 \rightarrow D^{*+}D^{*-}) < 2.2 \times 10^{-3}$ at 90% confidence level is set by the CLEO-II collaboration [35]. The value used here to estimate the total number of reconstructed events in this channel is: $\mathcal{B}(B^0 \rightarrow D^{*+}D^{*-}) = 9.7 \times 10^{-4}$, corresponding to an estimate based on the measured $B^0 \rightarrow D_s^{*+}D^{*-}$ branching ratio [35].

The Monte Carlo simulation program used to produce the results presented for the $B^0 \rightarrow D^{*+}D^{*-}$ channel was the full `BBsim` simulation/reconstruction, except for studies of the CP -fitting program which were generally performed with a toy Monte Carlo.

Table 5-23. Branching ratios for decay modes used in the $B^0 \rightarrow D^{*+} D^{*-}$ study.

Decay Mode	\mathcal{B} (%)
$B^0 \rightarrow D^{*+} D^{*-}$	0.097
$D^{*+} \rightarrow D^0 \pi^+$	68.3 ± 1.4
$D^0 \rightarrow K^- \pi^+$	3.83 ± 0.12
$D^0 \rightarrow K^- \pi^+ \pi^0$	13.9 ± 0.9
$D^0 \rightarrow K^- \pi^+ \pi^- \pi^+$	7.5 ± 0.4
$D^0 \rightarrow K_S^0 \pi^+ \pi^-$	2.7 ± 0.2

5.5.2.1 General tools

In this section the general tools used to select B^0 candidates in the mode $B^0 \rightarrow D^{*+} D^{*-}$ are briefly summarized.

Charged particles are identified by reconstructing tracks in the silicon vertex tracker and the drift chamber. Particle identification of charged tracks has been discussed in detail previously (Section 4.3). Kaon candidates generally are required to be consistent with the kaon hypothesis, while all charged tracks are considered as pion candidates. For the low-background $D^0 \rightarrow K^- \pi^+$ mode, no PID requirement is made for the kaon.

Photons are identified as energy deposits (bumps) in the EMC. A track veto is applied to eliminate electron showers and charged hadrons that interact in the EMC. No selection is made on the photon (or π^0) momentum.

5.5.2.2 Event selection

Event selection is based on reconstructing the invariant mass of D^0 , D^* , and B^0 candidates. At a lower level, neutral pions and kaons are reconstructed in their decays to photons and charged pions, respectively. Charged and neutral particle candidates are combined to form the invariant mass of intermediate particles. Where relevant, a vertex is formed from charged tracks and a selection on the vertex probability is applied.

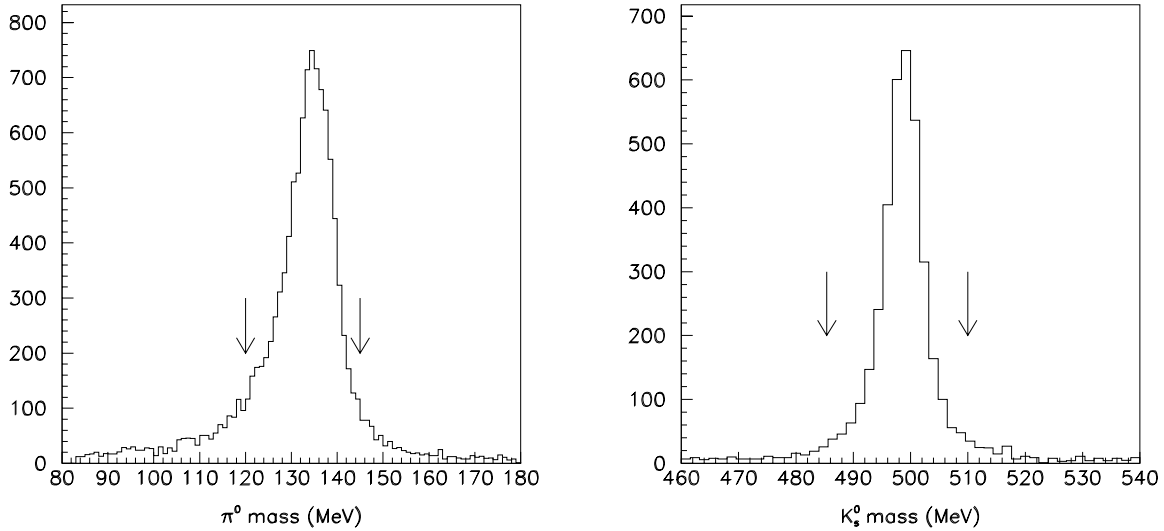


Figure 5-28. Reconstructed invariant mass of π^0 (left) and K_S^0 (right) candidates, using the full BBsim simulation and reconstructing chain.

5.5.2.3 π^0 selection

Neutral pions are reconstructed by combining all identified photons in an event. No selection is made on the photon (or π^0) momentum. All such candidates are then used for the $D^0 \rightarrow K^- \pi^+ \pi^0$ decay channel. The tail on the low-mass side of the distribution is accommodated by allowing the π^0 mass cuts to be asymmetric: $120 < m_{\pi^0} < 145 \text{ MeV}/c^2$. An efficiency of 42% is obtained for these π^0 s.

Figure 5-28 shows the reconstructed mass of π^0 candidates selected from B^0 decays.

5.5.2.4 K_S^0 selection

Oppositely charged pions are paired together to form $K_S^0 \rightarrow \pi^+ \pi^-$ candidates. The reconstructed K_S^0 mass is shown in Fig. 5-28, with arrows indicating the 3.5σ mass cut. The efficiency of this selection is 40%.

5.5.2.5 D^0 selection

The D^0 selection is characterized by the application of very few selection criteria. This is possible due to the low background that is encountered when there are two reconstructed D^* candidates in an event.

Charged and neutral kaons and pions were appropriately combined to form D^0 candidates in the four different channels as described in Table 5-23. Charged tracks were fit to a common vertex and the vertex probability was required to be greater than 1%. For the decay $D^0 \rightarrow K^- \pi^+$, for example, this cut removes about 25% of the background while retaining 94% of the signal.

For the decay mode $D^0 \rightarrow K^- \pi^+ \pi^0$ most of the rate is through the resonant states $\bar{K}^{*0} \pi^0$, $K^{*-} \pi^+$, and $K^- \rho^+$. This substructure is exploited to reduce the combinatorial background in this channel. For each of the possible resonances two quantities are calculated: the mass of the resonant particle and the *helicity angle*, defined as the angle between the scalar particle and one of the decay products of the vector particle calculated in the rest frame of the vector particle. The helicity angle is distributed as $\cos^2 \theta_H$ for resonant signal and approximately flat for background. A candidate is accepted if, for at least one of the three resonance hypotheses, the mass is within two standard deviations of the expected mass (both the natural width and experimental resolution were taken into account) *and* the helicity angle satisfies the condition $|\cos \theta_H| > 0.3$. This requirement removes 44% of the incorrect combinations while retaining 89% of the signal.

The reconstructed D^0 mass distributions for the four D^0 modes are shown in Fig. 5-29. These candidates were selected in simulated $B^0 \rightarrow D^{*+} D^{*-}$ decays. Table 5-24 reports the mass resolution σ_M obtained for each decay mode. The reconstructed mass is required to be within 2σ (3σ for the $K^- \pi^+$ case) of the nominal D^0 mass. The efficiency ϵ of the D^0 selection criteria (including all selection on charged and neutral pions and kaons) for D^0 arising from the CP mode under study are also shown in Table 5-24, together with $\epsilon \times \mathcal{B}$, where \mathcal{B} is the branching ratio of the D decay channel.

5.5.2.6 D^* selection

D^0 candidates are combined with charged pion candidates. For D^0 modes with a charged kaon, the flavor of the D^0 is unambiguous and these candidates are combined only with pions of opposite charge. For the D^0 modes with a K_S^0 in the final state, all charged pions are considered when forming D^* candidates.

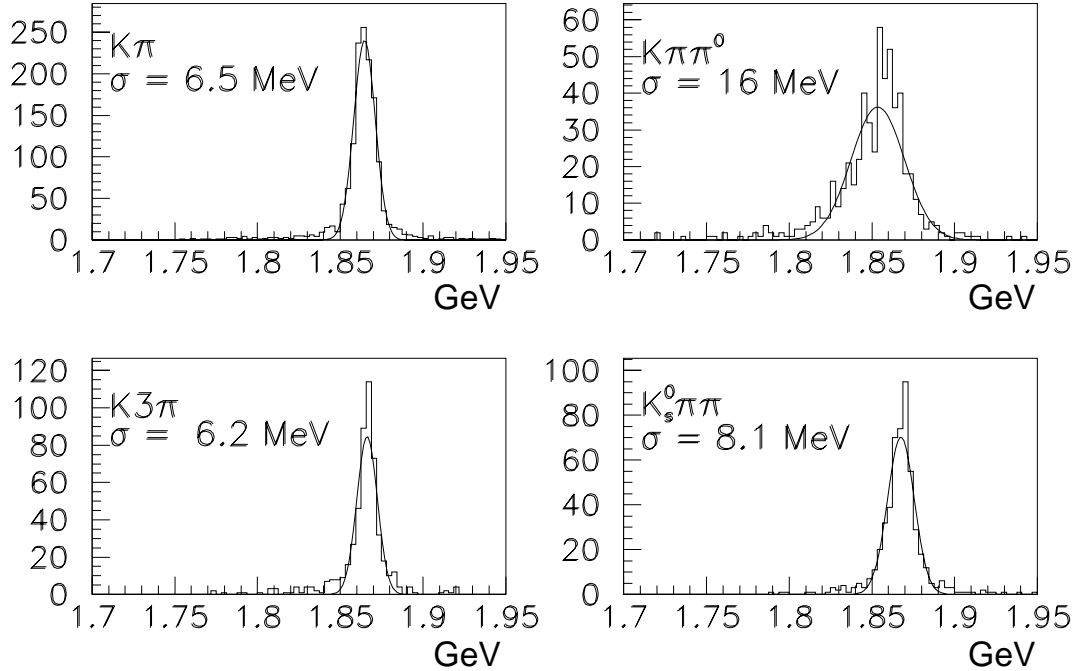


Figure 5-29. Reconstructed invariant-mass distribution of D^0 candidates for the decay modes of interest in this analysis.

Table 5-24. Mass resolution and efficiency (ϵ) for the D^0 decay modes. The analyses were performed using the full `BBsim` simulation and reconstruction.

Decay Mode	σ_M (MeV)	ϵ	$\epsilon \times \mathcal{B}$
$D^0 \rightarrow K^- \pi^+$	6.5	0.64	0.025
$D^0 \rightarrow K^- \pi^+ \pi^0$	16	0.17	0.024
$D^0 \rightarrow K^- \pi^+ \pi^- \pi^+$	6.2	0.34	0.026
$D^0 \rightarrow K_s^0 \pi^+ \pi^-$	8.1	0.33	0.006
Total			0.081

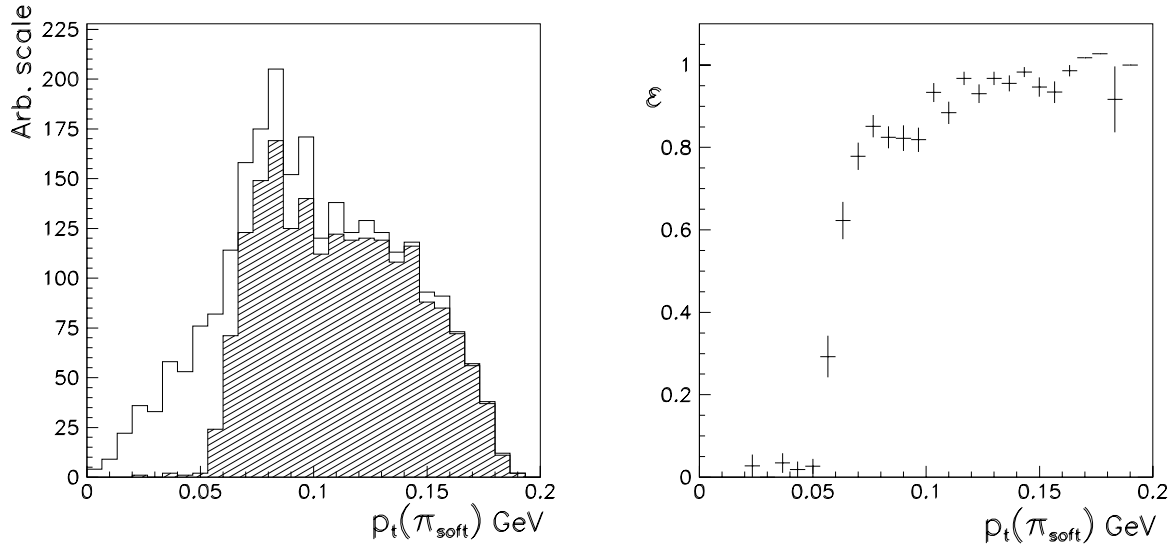


Figure 5-30. (left) Transverse momentum (p_T) of the slow pion in the D^* decay for events where the D^0 has been reconstructed from generated tracks (open histogram) and reconstructed tracks (shaded histogram); (right) soft pion reconstruction efficiency vs p_T .

The low Q -value of the $D^{*+} \rightarrow D^0 \pi^+$ decay means that very good resolution is obtained on the quantity $m_{D^*} - m_{D^0}$. A resolution of approximately $0.8 \text{ MeV}/c^2$ is obtained for this quantity, independent of the D^0 decay mode. $D^0 \rightarrow K^- \pi^+$ and $D^0 \rightarrow K_s^0 \pi^+ \pi^-$ candidates are accepted if $m_{D^*} - m_{D^0}$ is within $3 \text{ MeV}/c^2$ of the nominal value. A tighter cut of $2 \text{ MeV}/c^2$ is made for $D^0 \rightarrow K^- \pi^+ \pi^0$ and $D^0 \rightarrow K^- \pi^+ \pi^- \pi^+$ candidates, because of the larger background. The resolution can be improved somewhat by constraining the vertex position of the soft pion, but this technique was not employed in this study.

An important consideration of D^* reconstruction is the efficiency for reconstructing the slow pion. Figure 5-30 shows the transverse momentum distribution for soft pions in D^* decay in events where the D^0 was reconstructed. A significant number have $p_T < 100 \text{ MeV}/c$, which is the approximate cutoff for a track to reach the drift chamber. For these pions, it is necessary to perform stand-alone tracking in the silicon vertex tracker. Tracks with $p_T < 50 \text{ MeV}/c$ are not reconstructed at all. Also shown in Fig. 5-30 is the reconstruction efficiency for the soft pion as a function of its transverse momentum.

The efficiency for selecting a D^* , given a D^0 candidate, is $\sim 75\%$ for all D^0 decay modes, corresponding to the average efficiency for identifying the soft pion. The reduction in background obtained going from a D^0 selection to a D^* selection is illustrated in Fig. 5-31. The plot on the left shows the D^0 invariant-mass distribution obtained for a sample of generic $B^0 \bar{B}^0$ events. The plot

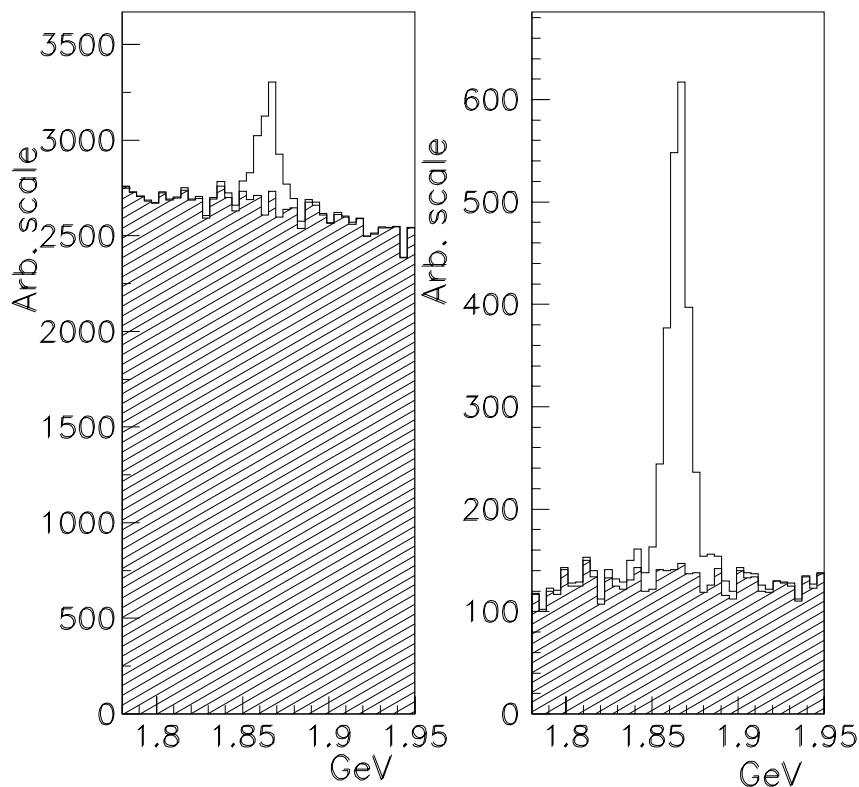


Figure 5-31. D^0 mass distribution without any D^* requirement (left) and requiring that the D originate from a D^* decay (right), clearly showing the reduction in background level.

on the right shows the same distribution with the additional requirement that the D^0 candidate be accompanied by a soft pion satisfying the $m_{D^*} - m_{D^0}$ cut.

5.5.2.7 B^0 selection

Oppositely charged D^* candidates selected in the same event are combined to form B^0 candidates. True B^0 mesons produced at the $\Upsilon(4S)$ have a narrow range of $p_{B^0}^*$. Fig. 5-32 shows the distribution of $p_{B^0}^*$ for $B^0 \rightarrow D^*+D^{*-}$ and background candidates. Most candidates are required to satisfy $0.2 < p_{B^0}^* < 0.45$ GeV/c. The upper limit was tightened to 0.38 GeV/c for candidates in the two decay combinations with high combinatoric backgrounds, where one D decayed to $K^-\pi^+\pi^-\pi^+$ and the other to either $K^-\pi^+\pi^0$ or $K^-\pi^+\pi^-\pi^+$.

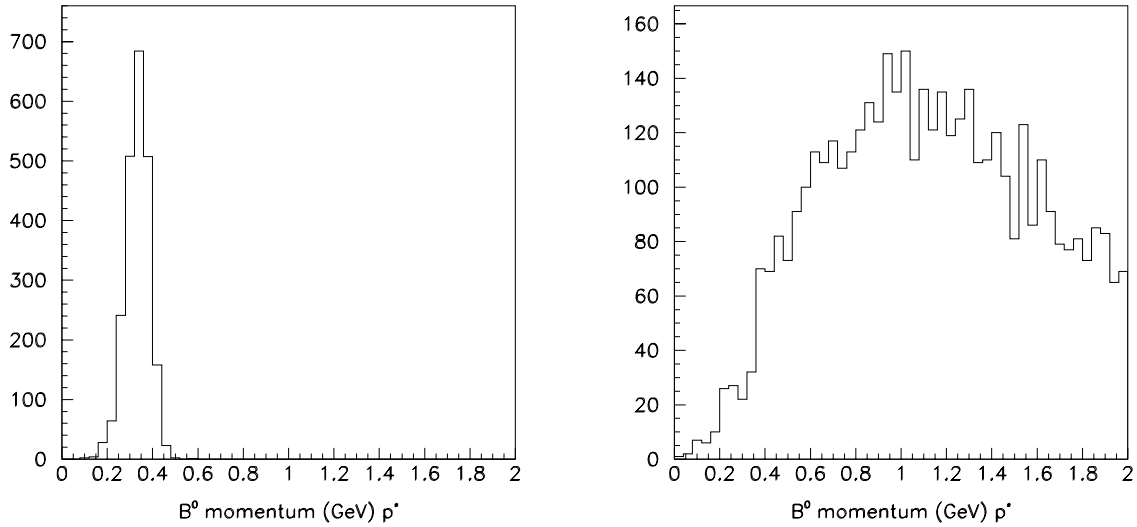


Figure 5-32. Distribution of $p_{B^0}^*$ for B^0 decays (top) and for background candidates (bottom).

The invariant-mass distribution of selected B^0 candidates is shown in Fig. 5-33, where the ten final states have been grouped into three categories, according to the number of π^0 mesons in the final state. A *signal region* is defined to be within 2.5σ of the nominal B^0 mass, where the resolutions given in Table 5-25 have been used. An *expanded signal region* is also defined. This is used to increase the effective statistics in the background studies described below. This region is five times wider than the signal region.

Table 5-26 shows the reconstruction efficiency for the ten final states, along with the expected number of events for an integrated luminosity of 30 fb^{-1} running on the $\Upsilon(4S)$. Details of this calculation are given below.

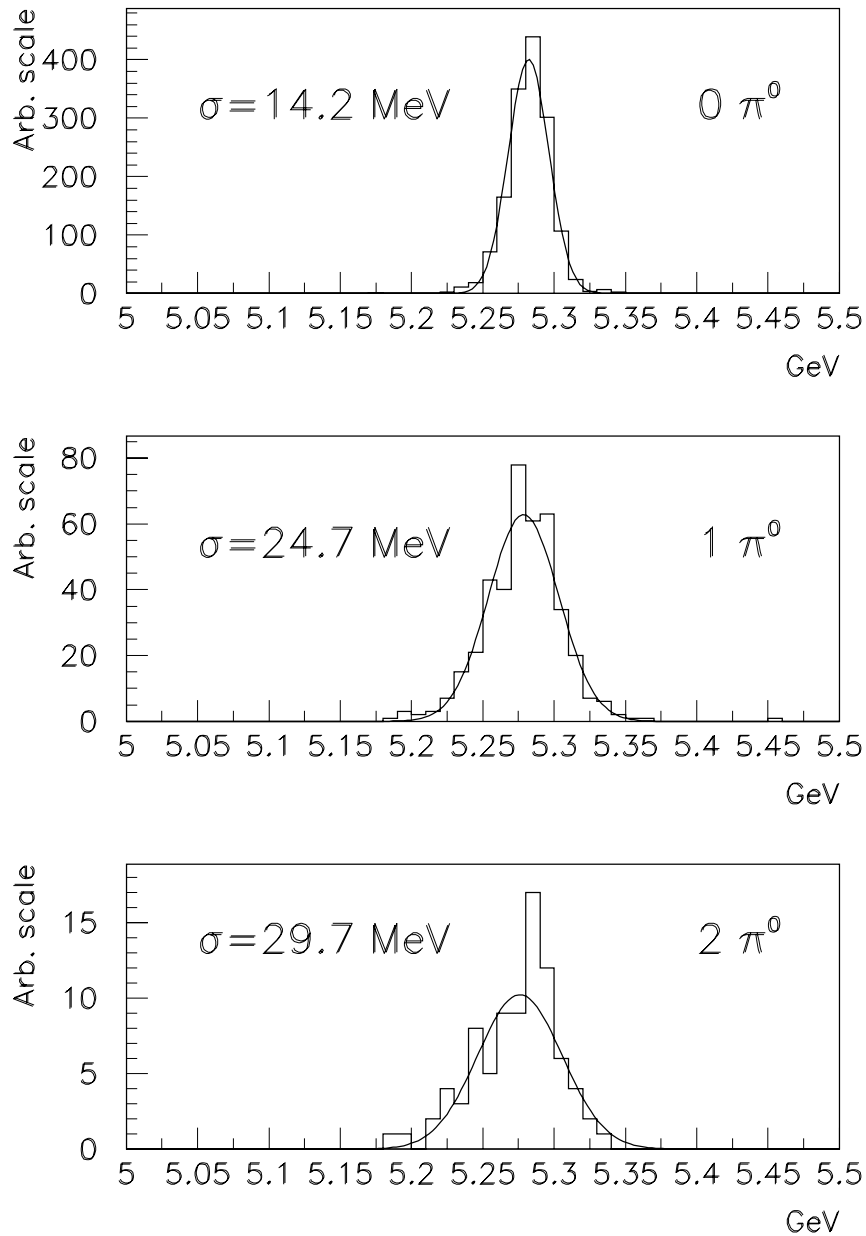


Figure 5-33. Invariant-mass distribution of B^0 candidates for final states with 0, 1 and $2 \pi^0$ s.

Table 5-25. Summary of B^0 resolutions grouped by number of π^0 s in the final state. These results were obtained with the full `BBSim` simulation and `BABAR` reconstruction code.

π^0 multiplicity	Mass Resolution (MeV)	Vertex Resolution (μm)	Fraction of final sample
0	14.2	66	0.48
1	24.7	102	0.39
2	29.7	136	0.13

Table 5-26. B^0 reconstruction efficiencies. The upper number in each cell is the efficiency, while the lower number is the number of events expected in 30 fb^{-1} . All results were obtained with the full `BBSim` simulation and the `BABAR` reconstruction.

	$K\pi$	$K\pi\pi^0$	$K(3\pi)$	$K_S^0\pi^+\pi^-$
$K\pi$	0.26 5.9	0.068 11.4	0.13 12.2	0.13 2.8
$K\pi\pi^0$		0.025 7.5	0.026 8.4	0.045 3.6
$K(3\pi)$			0.06 5.3	0.05 2.2
$K_S^0\pi^+\pi^-$				0.061 0.3

The decay position of the B^0 is determined by performing a vertex fit of the two D^0 candidates and the two soft pions. The possibility of determining the vertex directly from the D^* candidates, or with just the D^0 candidates (excluding the soft pions from the fit), was also studied, but both these options resulted in degraded vertex resolution. Figure 5-34 shows the vertex resolution of reconstructed B^0 candidates. The efficiency-weighted mean vertex resolution is $89 \mu\text{m}$.

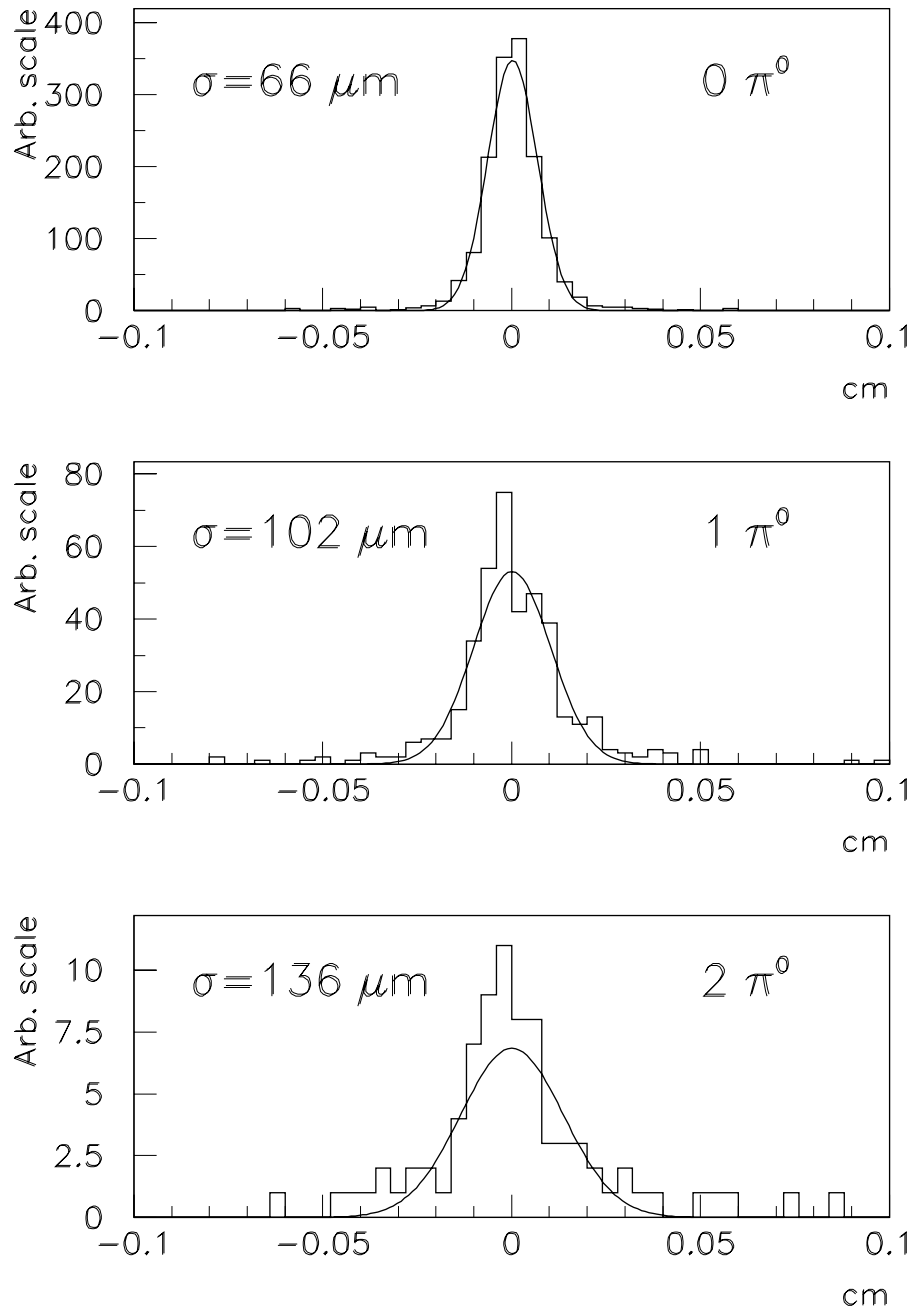


Figure 5-34. Difference in the z coordinate of the reconstructed vertex position and the true vertex position for B^0 candidates with 0, 1 and 2 π^0 s.

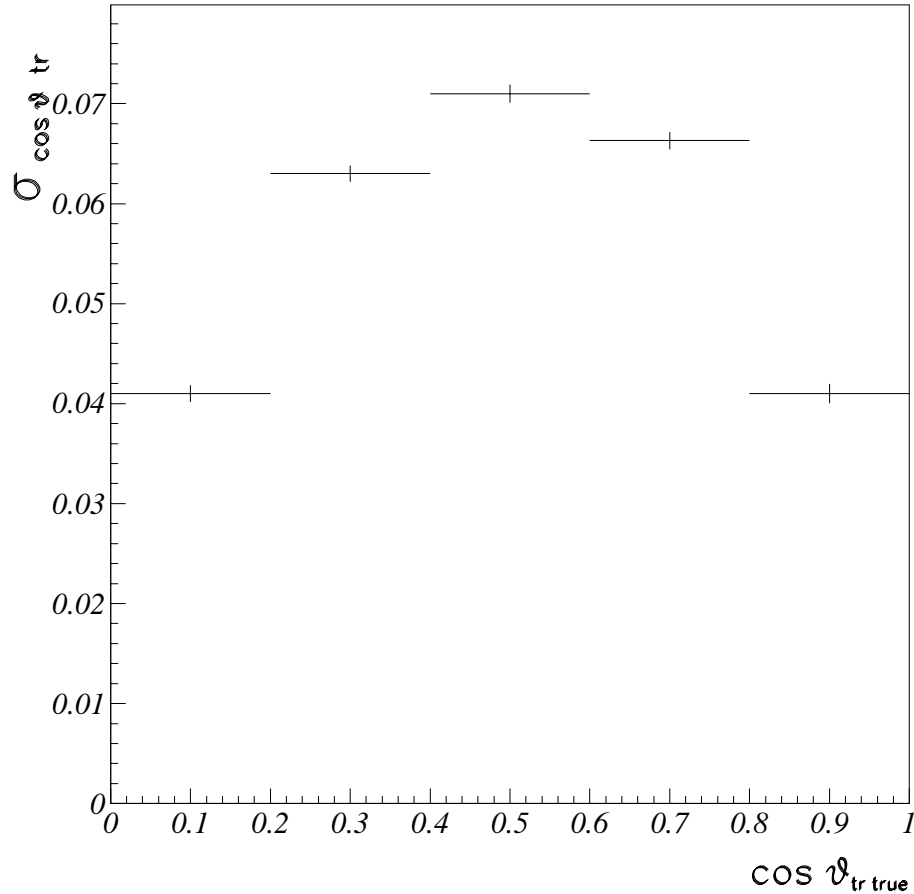


Figure 5-35. Resolution for the reconstructed transversity angle θ_{tr} as a function of $\cos \theta_{tr}$.

5.5.2.8 Reconstruction of angles

Once a B^0 candidate is fully reconstructed, it is straightforward to calculate decay angles in the transversity basis (see Section 5.1.3). The angular resolution was studied, and a significant dependence of the transversity angle, θ_{tr} , as a function of angle was found, as shown in Fig. 5-35. However the uncertainty in the angle measurement is negligible compared to the uncertainty in Δt as will be discussed with other realistic effects in Section 5.5.4.2. Figure 5-36 shows the B^0 reconstruction efficiency as a function of the three transversity angles. The small deviation from uniform acceptance is neglected when fitting the angular distributions.

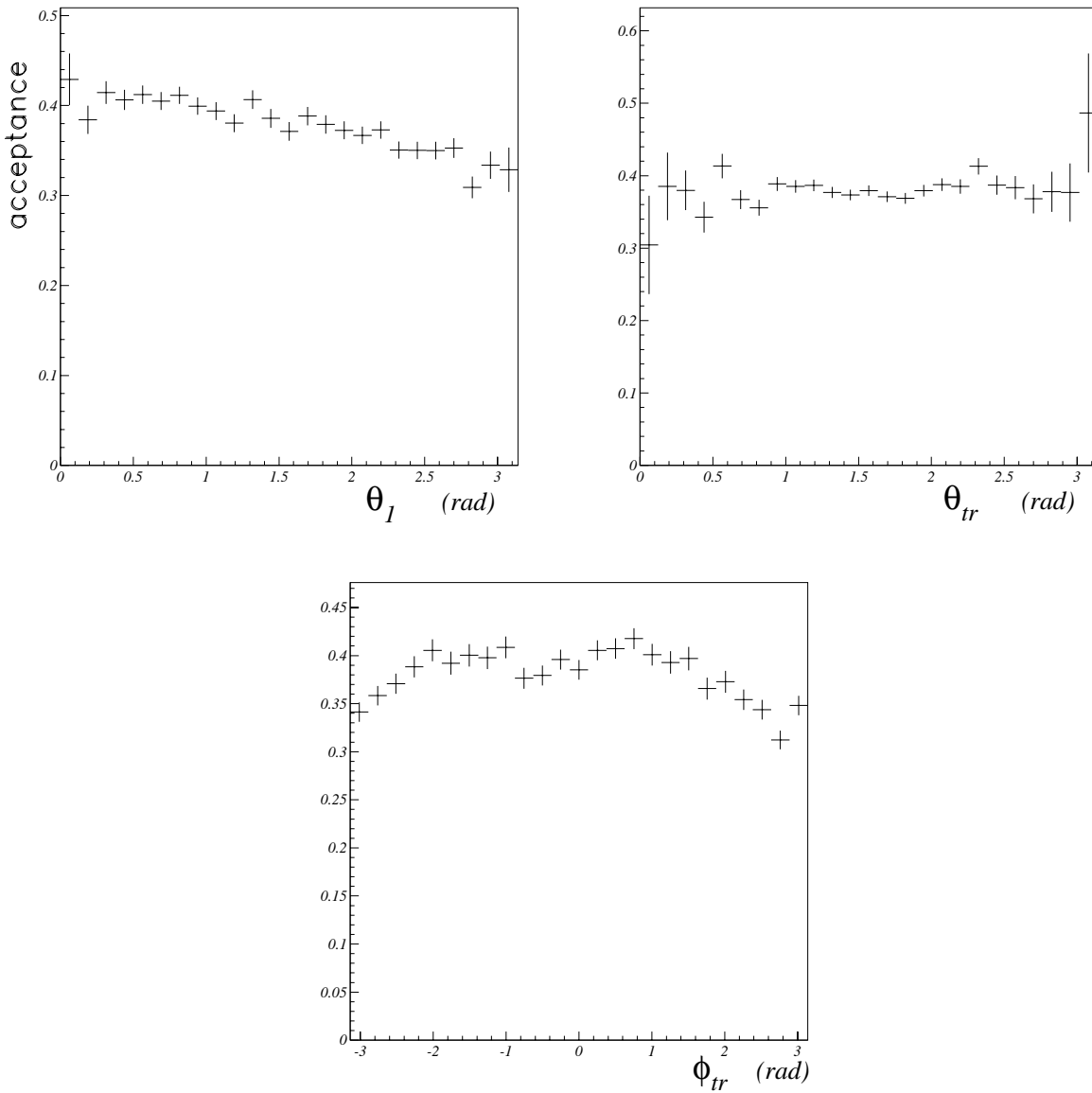


Figure 5-36. Angular acceptance for the three angles in the transversity frame: top left) angle θ_1 ; top right) angle θ_{tr} ; bottom) angle ϕ_{tr} . This figure was produced using the fast simulation (with all $D^0 \rightarrow K^- \pi^+$), hence the artificially high value of the average efficiency.

5.5.2.9 Backgrounds

Backgrounds are expected to be low for this channel, due to the low background in the D^* sample. In order to verify this expectation, samples of generic decays discussed in Section 5.2 were studied.

The background was studied separately for samples of $b\bar{b}$, $c\bar{c}$ and light-quark (uds) events. The background is expected to have a large component of correctly reconstructed D^* mesons, and therefore little background from uds events is expected. Pairs of real D^* s are produced in both $c\bar{c}$ and $b\bar{b}$ events, but most of these pairs fail the B^0 mass and momentum selection criteria. Figure 5-37 shows the scatter plot of the difference of the reconstructed B^0 invariant mass from the true B^0 mass (in sigma) versus $p_{B^0}^*$ for the three different samples. The boxes in the figures depict the signal region and the expanded signal region as defined above. Taking a mass window five times larger than nominal assumes that the shape of the background in this region is linear, although not necessarily flat. The fact that no light-quark or $c\bar{c}$ events are found in the expanded signal region indicates that few such background events would be expected in a 30 fb^{-1} sample. There are five $b\bar{b}$ events in the expanded region, suggesting a background of 14 events in a 30 fb^{-1} sample.

Most of the background events have one or two correctly reconstructed D^* mesons, implying that tightening the D^0 or D^* selection will not reduce the background levels dramatically. Slightly loosening the cuts demonstrates that the most serious background involves false candidates in the D^0 channels $K^-\pi^+\pi^0$ and $K^-\pi^+\pi^-\pi^+$. This is the motivation for the tighter selection criteria above when these modes are involved.

5.5.2.10 Final event sample

Table 5-27 summarizes the event sample obtained from a 30 fb^{-1} sample. The *usable sample* is the total number of events that decay into the decay modes analyzed, before any selection criteria are applied. It represents the number of events that would be reconstructed if the efficiency were 100% for all channels.

The number of signal events is calculated by combining the information from this table with the branching ratios from Table 5-23 and the efficiencies from Table 5-26. The yield from each of the ten channels is computed separately (see Table 5-26) and then summed. The average reconstruction efficiency quoted in Table 5-27 is simply the number of reconstructed events divided by the total sample. This efficiency is considerably smaller than for the previous $D^+ D^-$ analysis. While part of this loss is due to the efficiency for the slow pions, the remainder of the difference is due to the difference between the overly optimistic efficiency obtained from Aslund and the somewhat pessimistic values obtained here, since the reconstruction programs are still improving.

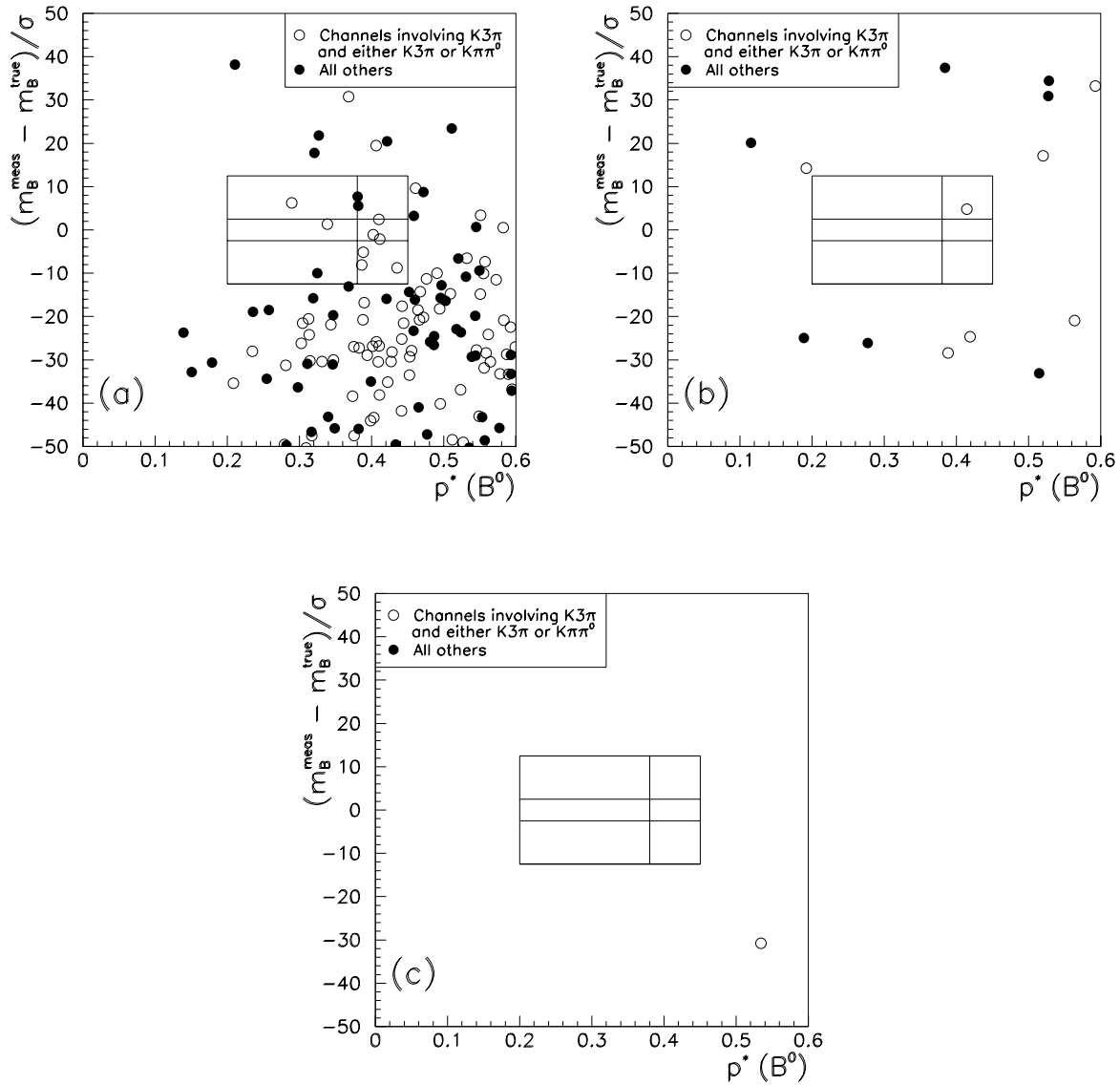


Figure 5-37. Difference of the measured invariant mass and the true B^0 mass (in sigma) plotted versus $p_{B^0}^*$ for B^0 candidates selected from background sources: a) $b\bar{b}$ events; b) $c\bar{c}$ events; c) uds events. Candidates in the two high-background combinations are shown as open circles and the rest are shown as filled circles.

Table 5-27. Summary for $B^0 \rightarrow D^{*+} D^{*-}$ for a 30 fb^{-1} sample. The full `BBSim` simulation and the `BABAR` reconstruction was used for this analysis.

$\mathcal{B}(B^0 \rightarrow D^{*+} D^{*-})$	9.7×10^{-4}
Usable sample	1140
Average reconstruction efficiency	0.053
Reconstructed signal events	60
Background events	14
Average CP vertex z resolution	$89 \mu\text{m}$

5.5.3 Estimates for the $D^* D$ Mode

This decay mode can have both $CP = +1$ and $CP = -1$ depending upon whether the wavefunction is symmetric or anti-symmetric. In this section it will be assumed to be $CP = +1$ since the heavy-quark symmetry prediction is that it is mostly $CP = +1$.

Using the D^\pm efficiency and background estimates from the $D^+ D^-$ analysis performed using the `Aslund` fast simulation, and the π^0 efficiency and vertex resolution from the $D^{*+} D^{*-}$ analysis, performed using the full `BBSim` simulation and the reconstruction, the CP resolution is estimated for the mode $D^\pm D^{*\mp}$. Assuming $\mathcal{B}(B^0 \rightarrow D^+ D^{*-}) = 4.8 \times 10^{-4}$, and an integrated luminosity of 30 fb^{-1} , a total of $\sim 15000 D^\pm D^{*\mp}$ events will be produced. 144 reconstructed events were found in the $D^+ D^-$ analysis. Requiring an additional slow π^0 would be expected to have an efficiency of $\sim 30\%$ (a guess based on numbers in the $D^{*+} D^{*-}$ study, Section 5.5.2), yielding an estimate of 43 $D^* D$ events observed in 30 fb^{-1} running at the $\Upsilon(4S)$. The signal to background rate from the $D^+ D^-$ analysis, Section 5.5.1, was 0.42 and the $D^\pm D^{*\mp}$ channel should be similar. The vertex resolution was determined to be 149 microns in the $D^{*+} D^{*-}$ analysis, and this estimate will be used to estimate the resolution of the $D^\pm D^{*\mp}$ channel. Assuming the $D^\pm D^{*\mp}$ channel is 100% $CP = +1$ allows CP fitting without the need of angular information. With these estimates, an uncertainty of 0.92 is obtained for $\sin 2\beta$. This may be improved with the inclusion of other final states.

Table 5-28. The fitted value of $\sin 2\beta$ for four event samples (background and the tagging uncertainties are not included).

Number of events	2416	239
$\sin 2\beta = 0.4$	0.42 ± 0.04	0.26 ± 0.11
$\sin 2\beta = 0.9$	0.94 ± 0.04	1.03 ± 0.12

5.5.4 Measurement of CP Asymmetries and Extraction of β

5.5.4.1 $B^0 \rightarrow D^+ D^-$

The extraction of $\sin 2\beta$ for this channel is straightforward since the $D^+ D^-$ final state is a pure CP eigenstate. The asymmetry is given by the formula

$$a(t) = \frac{\Gamma(B^0 \rightarrow D^+ D^-) - \Gamma(\bar{B}^0 \rightarrow D^+ D^-)}{\Gamma(B^0 \rightarrow D^+ D^-) + \Gamma(\bar{B}^0 \rightarrow D^+ D^-)} = \sin 2\beta \sin(\Delta mt). \quad (5.89)$$

In this study, both the forward-backward asymmetry, [48], and Kin, [49], methods for extracting $\sin 2\beta$ have been investigated. Both methods worked well and gave the same results. The method which uses the Kin variable is described here. In order to illustrate this method, a simple case is considered, without complications from background or vertex tagging, and where the B flavor is given by the charge of the lepton. The time-dependent rate for a B^0 tag is given by

$$R(\Delta z) = \Psi(\Delta z) \otimes G(\sigma_{det}, \Delta z), \quad (5.90)$$

where $\Psi(\Delta z) = e^{-\Gamma(z_{tag} + z_{CP})} [1 + \sin 2\beta \sin(\Delta m \Delta z)]$. The convolution with the Gaussian $G(\sigma_{det}, \Delta z)$ takes into account detector resolution. The Kin variable is

$$K \equiv \frac{R - \bar{R}}{R + \bar{R}}. \quad (5.91)$$

The values of $\langle K \rangle$ and $\langle K^2 \rangle$ are measured and the value and error of $\sin 2\beta$ are extracted:

$$\sin 2\beta = \frac{\langle K \rangle}{\langle K^2 \rangle}, \quad \sigma_{\sin 2\beta} = \frac{1}{\langle K^2 \rangle}. \quad (5.92)$$

The method has been applied to samples of events with $\sin 2\beta$ equal to 0.4 and 0.9. The fitted values are given in Table 5-28. The results in Fig. 5-38 and Table 5-28 show agreement between the generated and fitted values.

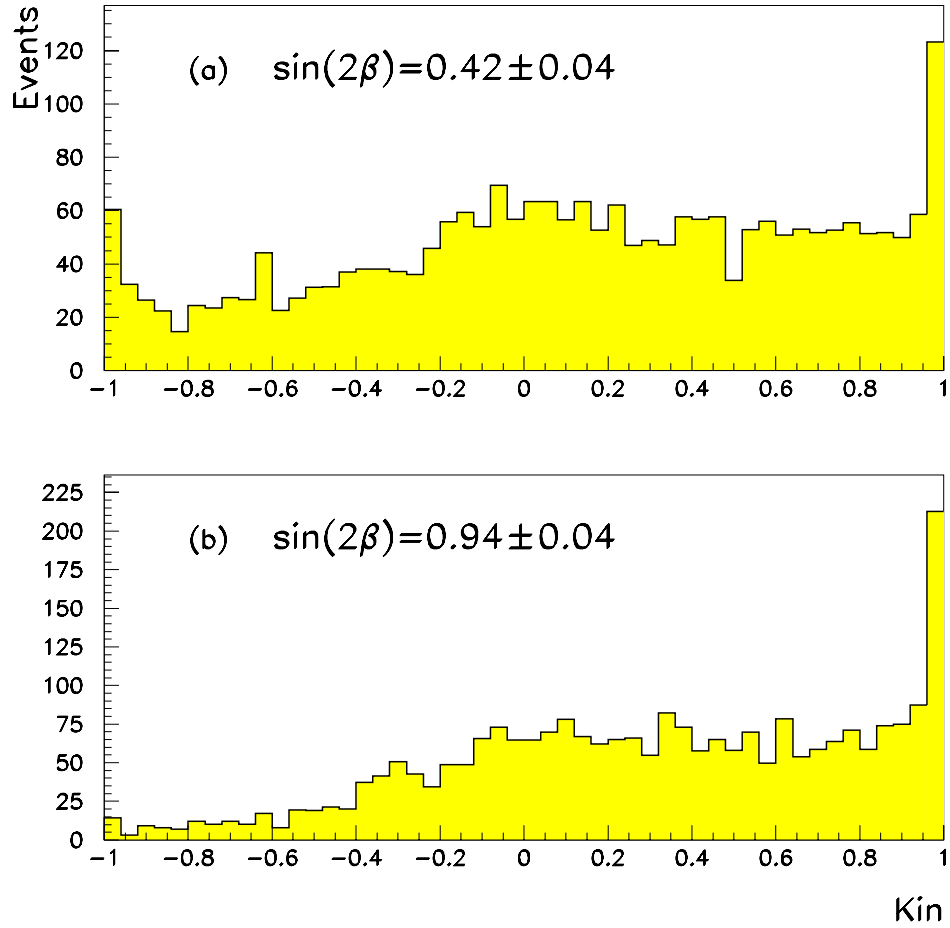


Figure 5-38. The Kin distribution for a large number of $B^0 \rightarrow D^+D^-$ events. (a) Events generated with $\sin 2\beta = 0.4$; and (b) $\sin 2\beta = 0.9$. The fitted values are shown on the plot.

In the more realistic case, where background and tagging are taken into account in the expression of the Kin , the double time expression of Eq. (1.41) takes the form

$$R(\Delta z, \text{tag}) = P_{\text{sig}} \times [P_{B^0} \times \Psi(\Delta z) \otimes G(\sigma_{\text{det}}, \Delta z) + P_{\bar{B}^0} \times \bar{\Psi}(\Delta z) \otimes G(\sigma_{\text{det}}, \Delta z)] + P_{\text{bkg}} \times \Phi(\Delta z), \quad (5.93)$$

where

- P_{sig} (P_{bkg}) is the probability that the event is signal (background) as determined by the Cornelius package ($P_{\text{sig}} + P_{\text{bkg}} = 1$).
- P_{B^0} ($P_{\bar{B}^0}$) is the probability that the event is a B^0 (\bar{B}^0) as determined by the Cornelius package ($P_{B^0} + P_{\bar{B}^0} = 1$).
- $\Phi(\Delta z)$ is the Δz distribution for the background.

Table 5-29. Error in the measurement of $\sin 2\beta$ in the decay mode $B^0 \rightarrow D^+ D^-$ for integrated luminosity of 30 fb^{-1} . The analysis was performed using the `Aslund` fast simulation.

$\mathcal{B}(B^0 \rightarrow D^+ D^-)$	4.5×10^{-4}
Usable sample	610
Average reconstruction efficiency	0.24
Reconstructed signal events	140
N_B/N_S	2.8
Δz resolution (narrow/wide)	63/189 μm
σ_0	1.59
Tag factor	0.3
$\sigma(\sin 2\beta)$	0.48

In this case, the Kin expression becomes

$$K = \frac{R - \bar{R}}{R + \bar{R}} = \underbrace{\frac{\Psi \otimes G - \bar{\Psi} \otimes G}{\Psi \otimes G + \bar{\Psi} \otimes G}}_{\text{'Ideal Kin'}} \times \underbrace{\frac{P_{B^0} - P_{\bar{B}^0}}{P_{B^0} + P_{\bar{B}^0}}}_{\text{Tagging effect}} \times \underbrace{\frac{1}{1 + \frac{2P_{\text{bkg}} \frac{\Phi}{\Psi + \bar{\Psi}}}{P_{\text{sig}}}}}_{\text{Background effect}} \quad (5.94)$$

Table 5-29 shows the summary of all relevant parameters in the extraction of the error in the measurement of $\sin 2\beta$ for our decay mode. The uncertainty expected is 0.48 with the fast simulation (`Aslund`). This error is likely to increase somewhat as the efficiency becomes more realistic.

5.5.4.2 $B^0 \rightarrow D^{*+} D^{*-}$

$D^{*+} D^{*-}$ is a vector-vector final state and thus, in principle, a mixture of CP -even and CP -odd states. As discussed in Section 5.1.3, in order to avoid the dilution of the measured asymmetries, an angular analysis can be performed to separate the two contributions. In this section, an unbinned Maximum Likelihood (ML) fit is described. This is based on combined time and angular distributions in the transversity basis.

The angular distribution in the transversity frame for the decay under study has already been given in Eq. (5.44). In order to write the complete probability distribution function, the time dependent

amplitudes are parameterized as

$$\begin{aligned}
A_{\parallel}(t) &= \mathcal{M}_{\parallel} e^{i\alpha_{\parallel}} e^{-imt-\Gamma t/2} \left[e^{i\beta} \cos\left(\frac{\Delta mt}{2}\right) + i e^{-i\beta} \sin\left(\frac{\Delta mt}{2}\right) \right] \\
A_{\perp}(t) &= \mathcal{M}_{\perp} e^{i\alpha_{\perp}} e^{-imt-\Gamma t/2} \left[-e^{i\beta} \cos\left(\frac{\Delta mt}{2}\right) + i e^{-i\beta} \sin\left(\frac{\Delta mt}{2}\right) \right] \\
A_0(t) &= \mathcal{M}_0 e^{i\alpha_0} e^{-imt-\Gamma t/2} \left[e^{i\beta} \cos\left(\frac{\Delta mt}{2}\right) + i e^{-i\beta} \sin\left(\frac{\Delta mt}{2}\right) \right],
\end{aligned} \tag{5.95}$$

where \mathcal{M}_i are the magnitudes of the amplitudes in the transversity basis and α_i are the strong phases ($i = 0, \parallel, \perp$).

The combined time and angular distribution can then be written as

$$\begin{aligned}
&\frac{d^3\Gamma(B^0(\bar{B}^0) \rightarrow D^{*+} D^{*-})}{d\cos\vartheta_1 d\cos\vartheta_{\text{tr}} d\phi_{\text{tr}}} = \frac{k}{4m_B^2} \frac{9}{8(2\pi)^2} e^{-\Gamma t} \\
&\{ \mathcal{M}_{\parallel}^2 (1 + (-) \sin 2\beta \sin(\Delta mt)) \sin^2 \vartheta_1 \sin^2 \vartheta_{\text{tr}} \sin^2 \phi_{\text{tr}} \\
&+ \mathcal{M}_{\perp}^2 (1 - (+) \sin 2\beta \sin(\Delta mt)) \sin^2 \vartheta_1 \cos^2 \vartheta_{\text{tr}} \\
&+ 2\mathcal{M}_0^2 (1 + (-) \sin 2\beta \sin(\Delta mt)) \cos^2 \vartheta_1 \sin^2 \vartheta_{\text{tr}} \cos^2 \phi_{\text{tr}} \\
&+ \mathcal{M}_{\perp} \mathcal{M}_{\parallel} \sin^2 \vartheta_1 \sin(2\vartheta_{\text{tr}}) \sin \phi_{\text{tr}} [\sin \alpha_{\parallel} \cos(\Delta mt) \\
&\quad + (-) \cos 2\beta \cos \alpha_{\parallel} \sin(\Delta mt)] \\
&+ \frac{1}{\sqrt{2}} \mathcal{M}_0 \mathcal{M}_{\parallel} \sin 2\vartheta_1 \sin^2 \vartheta_{\text{tr}} \sin(2\phi_{\text{tr}}) (1 \\
&\quad + (-) \sin 2\beta \sin(\Delta mt)) \cos(\alpha_{\parallel} - \alpha_0) \\
&+ \frac{1}{\sqrt{2}} \mathcal{M}_0 \mathcal{M}_{\perp} \sin 2\vartheta_1 \sin 2\vartheta_{\text{tr}} \cos \phi_{\text{tr}} [\sin \alpha_0 \cos(\Delta mt) \\
&\quad + (-) \cos 2\beta \cos \alpha_0 \sin(\Delta mt)] \} ,
\end{aligned} \tag{5.96}$$

where the $+(-)$ sign corresponds to the B^0 (\bar{B}^0) tag, and $\alpha_{\perp} = 0$ has been chosen by convention. The three amplitudes, \mathcal{M}_i , satisfy the equation:

$$\mathcal{M}_{\parallel}^2 + \mathcal{M}_0^2 + \mathcal{M}_{\perp}^2 = 1. \tag{5.97}$$

The definitions of the three angles ($\vartheta_1, \vartheta_{\text{tr}}, \phi_{\text{tr}}$) are given in Fig. 5-11.

The distribution of the polar transversity angle ϑ_{tr} is the observable that contains most of the information on the CP of the final state. In order to simplify the fit, the complete distribution given above can be integrated over the helicity angle ϑ_1 and the azimuthal transversity angle ϕ_{tr} , without losing the capability to disentangle the CP states. This simplified method will be referred to as *analysis in transversity*; it will be described below. However the smallest uncertainty on $\sin 2\beta$ is obtained using the complete angular and time information. While the *full angular analysis*, will be used to obtain the final result, both methods are described below.

The contribution of penguin diagrams to the decays under study can shift the measured value of β . This effect is discussed in Section 5.1.5, as a correction to be applied to the experimental determination, and is not taken into account in the following. Here, the possibility to perform a measurement in the case of an arbitrary CP mixture is stressed.

5.5.4.3 Transversity analysis for the extraction of $\sin 2\beta$

Integrating over the helicity angle ϑ_1 and the azimuthal transversity angle ϕ_{tr} , the time and angular distribution (Eq. (5.96)) becomes (up to a normalization constant)

$$g(t, \vartheta_{\text{tr}}) = \Gamma_+(t)(1 \pm a(t))\frac{3}{4} \sin^2 \vartheta_{\text{tr}} + \Gamma_-(t)(1 \mp a(t))\frac{3}{2} \cos^2 \vartheta_{\text{tr}}, \quad (5.98)$$

where the time dependent rates Γ_{\pm} , corresponding to $CP \pm 1$ states, are

$$\Gamma_+(t) = (\mathcal{M}_{\parallel}^2 + \mathcal{M}_0^2)e^{-\Gamma t} \text{ and } \Gamma_-(t) = \mathcal{M}_{\perp}^2 e^{-\Gamma t}, \quad (5.99)$$

and the time dependent asymmetry $a(t)$ is given by:

$$a(t) = \sin 2\beta \sin(\Delta mt). \quad (5.100)$$

One can then introduce a dilution factor K defined as:

$$K = \frac{\Gamma_+ - \Gamma_-}{\Gamma_+ + \Gamma_-} \quad (5.101)$$

that relates the observed diluted asymmetry to the asymmetry that would be measured in the case of pure CP eigenstates.

In each reconstructed $\overline{B}^0 \rightarrow D^{*+}D^{*-}$ event one can measure the transversity angle ϑ_{tr} and $\Delta t = t_{CP} - t_{\text{tag}}$. For a given measured tag, we will call this set of measurements $\overline{x} = \{\vartheta_{\text{tr}}, \Delta t\}$.

Using the ratio R_{\perp} as defined in Eq. (5.38) and the dilution factor K one can then express the relative rate of B^0 decay to $D^{*+}D^{*-}$ CP -even states as:

$$\frac{\Gamma_+}{\Gamma_+ + \Gamma_-} = (1 - R_{\perp}) = \frac{1}{2}(1 + K), \quad (5.102)$$

associated with an angular distribution of the type $\sin^2 \vartheta_{\text{tr}}$; for CP -odd states the corresponding relative rate is:

$$\frac{\Gamma_-}{\Gamma_+ + \Gamma_-} = R_{\perp} = \frac{1}{2}(1 - K) \quad (5.103)$$

and the transversity angle distribution is $\cos^2 \vartheta_{\text{tr}}$.

The probability distribution function for the maximum likelihood fit can then be written as:

$$F(\bar{x}; b, K) = \begin{cases} f(\bar{x}; b, K) = \frac{1}{2}(1+K)(1+a)\frac{3}{4}\sin^2\vartheta_{\text{tr}} + \\ \quad \frac{1}{2}(1-K)(1-a)\frac{3}{2}\cos^2\vartheta_{\text{tr}} & \text{for } B^0 \text{ tag} \\ \bar{f}(\bar{x}; b, K) = \frac{1}{2}(1+K)(1-a)\frac{3}{4}\sin^2\vartheta_{\text{tr}} + \\ \quad \frac{1}{2}(1-K)(1+a)\frac{3}{2}\cos^2\vartheta_{\text{tr}} & \text{for } \bar{B}^0 \text{ tag} , \end{cases} \quad (5.104)$$

where the parameter $b = \sin 2\beta$ appears in the time dependent asymmetry as

$$a(t) = b \sin(\Delta mt). \quad (5.105)$$

In the unbinned maximum likelihood fit the parameters b and K are determined by maximizing the log-likelihood function:

$$\log \mathcal{L} = \sum_{i=1}^n \log f(\bar{x}_i; b, K) + \sum_{i=1}^{\bar{n}} \log \bar{f}(\bar{x}_i; b, K) , \quad (5.106)$$

where n (\bar{n}) is the number of reconstructed events with a B^0 (\bar{B}^0) tag.

As a preliminary step in the study of the sensitivity of the transversity analysis, the properties of the maximum likelihood fit were studied with many Monte Carlo-generated distributions corresponding to experiments of typically 500 events each. Figure 5-39 shows the uncertainty in $\sin 2\beta$, averaged over 200 experiments of 500 events each as a function of the dilution factor K . As expected, the uncertainty increases for $K \sim 0$ where the mixing of CP -states is maximal.

In Fig 5-40 the distribution of the fitted values of b and K are shown for the (theoretically preferred) input values of $b = 0.7$ and $K = 0.88$, corresponding to a combination of eigenstates with 94% $CP = +1$ and 6% $CP = -1$.

5.5.4.4 Full angular analysis to extract $\sin 2\beta$

The full angular analysis will provide the most accurate measurement of β if sufficient data is available to determine all the parameters that are present in the theoretical distribution (Eq. (5.96)).

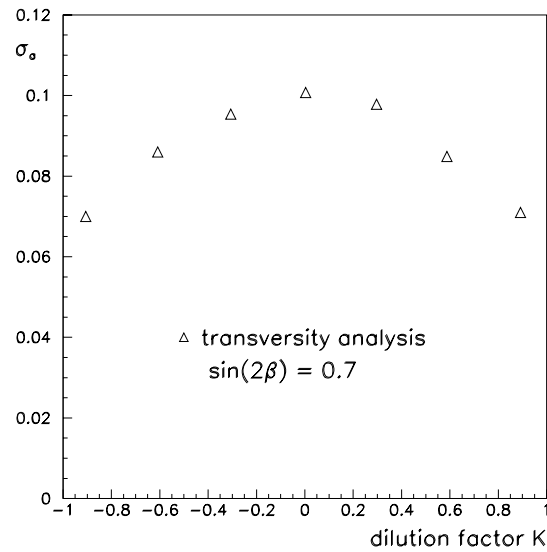


Figure 5-39. Uncertainty in $\sin 2\beta$ as a function of the K dilution factor for the case of $\sin 2\beta = 0.7$.

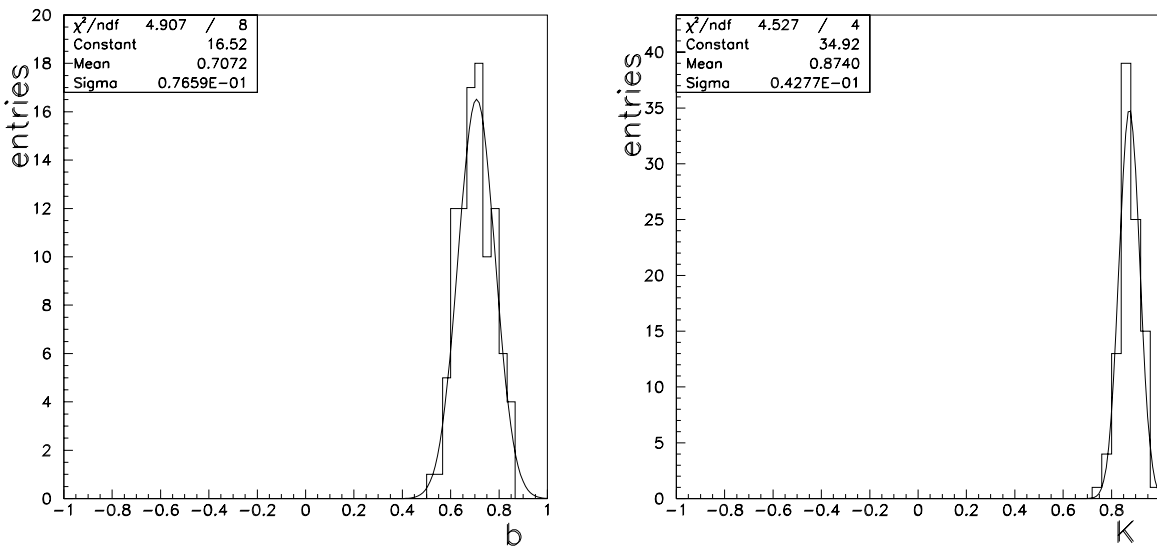


Figure 5-40. Distributions of the fit results for the parameters \hat{b} (left) and \hat{K} (right) obtained on a data sample generated with true value $b = 0.7$ and $K = 0.88$.

Five parameters must be evaluated in the fitting procedure: two of the three amplitudes \mathcal{M}_{\parallel} , \mathcal{M}_0 and \mathcal{M}_{\perp} , two strong phases α_{\parallel} and α_0 , and the β angle of the unitarity triangle. The five parameters, represented by a vector $\vec{\vartheta}$, are estimated by maximizing the log-likelihood function defined as:

$$\log \mathcal{L} = \sum_{i=1}^n \log f(\vec{x}_i; \vec{\vartheta}) + \sum_{i=1}^{\bar{n}} \log \bar{f}(\vec{x}_i; \vec{\vartheta}). \quad (5.107)$$

As before, n (\bar{n}) is the number of reconstructed events with a B^0 (\bar{B}^0) tag, and the probability distribution functions f and \bar{f} , defined up to a normalization constant by Eq. (5.96), are evaluated for each event at the measured values $\vec{x} = \{\vartheta_1, \vartheta_{\text{tr}}, \phi_{\text{tr}}, \Delta t\}$ for the given tag.

The sensitivity of the method in the simultaneous fit of $\sin 2\beta$ and the other four parameters was studied with Monte Carlo-generated samples of 500 events.

In Fig. 5-41 the resolution on $\sin 2\beta$ as a function of the dilution factor K is plotted for three different configurations of amplitudes, *i.e.*, for the CP -even transverse polarization equal to zero ($\mathcal{M}_{\parallel} = 0$), the longitudinal polarization equal to zero ($\mathcal{M}_0 = 0$), and the CP -even combination with equal amounts of \mathcal{M}_{\parallel} and \mathcal{M}_0 . Furthermore, Fig. 5-41 shows a comparison between the resolution achievable from a transversity analysis and from a full angular analysis. The improvement achieved using the full angular analysis is more significant for the case where the final state consists of a nearly equal mixture of CP -even and CP -odd states.

5.5.4.5 Realistic effects

The $\sin 2\beta$ uncertainty will increase due to non-zero background, errors in flavor tagging of the other B (mis-tagging), and nonperfect resolution on Δz and angle measurements. As described above, the background fraction is expected to be about 23% in the final sample. Using Eq. (5.81), an increase in the $\sin 2\beta$ uncertainty of a factor 1.12 is found. The increase due to flavor tagging is a factor of $1/\sqrt{0.3} = 1.8$.

The effect of the non-zero angular resolution is small compared to the temporal resolution and has been neglected. The Δz resolution is affected by vertex resolution of both the CP B and the tagging B . The resolutions obtained are $89 \mu\text{m}$ and $120 \mu\text{m}$, respectively, giving an uncertainty on Δz of $150 \mu\text{m}$. This resolution, for the case of the full angular analysis, gives $\sigma_0 = 1.70$.

5.5.4.6 CP Reach of the $B^0 \rightarrow D^{*+} D^{*-}$ Channel

The results of the previous sections may now be combined to estimate the expected uncertainty in $\sin 2\beta$ for a sample from 30 fb^{-1} running at the $\Upsilon(4S)$. Table 5-30 summarizes the relevant quantities. No study of systematic errors has yet been performed.

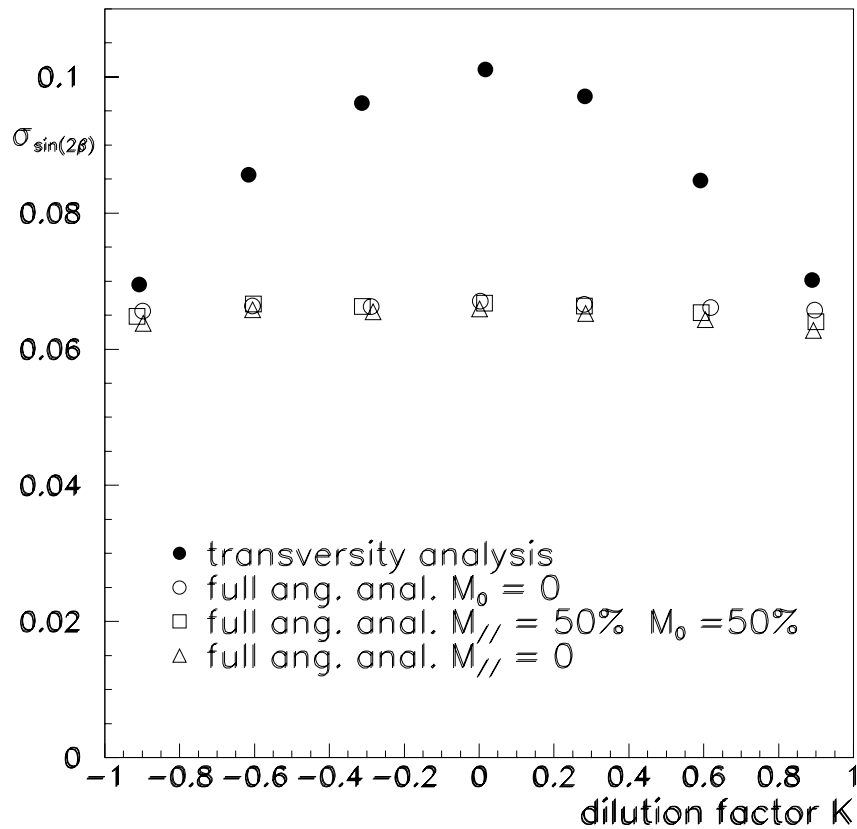


Figure 5-41. Resolution in $\sin 2\beta$ as a function of different combinations of amplitudes; a variation of the CP -odd M_{\perp} corresponds to a variation of the dilution factor K ; then for each value of K three combinations of CP -even are shown; the open circles correspond to $M_0 = 0$, the open squares to the $M_{\parallel} = 0$ and the triangles to a mixture of even parities, 50% M_0 and 50% M_{\parallel} . The filled circles correspond to the transversity analysis.

Table 5-30. Summary of $\sin 2\beta$ measurement with the $B^0 \rightarrow D^{*+}D^{*-}$ channel for an integrated luminosity of 30 fb^{-1} . The full `BBSim` simulation and the `BABAR` reconstruction was used for this analysis.

$\mathcal{B}(B^0 \rightarrow D^{*+}D^{*-})$	9.7×10^{-4}
Usable sample	1050
Average reconstruction efficiency	0.053
Number reconstructed	60
N_B/N_S	0.23
Δz resolution	$150 \mu\text{m}$
σ_0	1.7
Tag factor	0.3
$\sigma(\sin 2\beta)$	0.44

Improvements on the results presented here may be expected. Certain aspects of the analysis may be optimized, which will undoubtedly have the effect of reducing the overall error. Improvements to the π^0 and K_s^0 efficiencies will increase the number of reconstructed signal events, as will increasing the number of D^0 decay modes studied. Improved vertex/kinematic fitting will improve the mass resolution (reducing the background) and also the Δz resolution.

The combined result for $\sin 2\beta$ resulting from this and other measurements is presented in Table 5-38.

5.6 Penguin Modes

The decay modes $B^0, \bar{B}^0 \rightarrow \pi^0 K_s^0(K_L^0), \eta' K_s^0(K_L^0), \phi K_s^0(K_L^0), \dots$ (and the corresponding modes with K^*) that have been called Type III in Section 5.1.1, have dominant penguin contributions that could allow measurement of $\sin 2\beta$. The expected branching ratios are $\mathcal{O}(10^{-5})$. As discussed in detail in Section 5.1.2, in the pure-penguin modes $\phi K_s^0(K_L^0), \phi K_{CP}^{*0}$, there is contamination from other weak phases that is quite small, and these modes are then suitable to measure $\sin 2\beta$. However, in the modes of the type $\pi^0 K_s^0(K_L^0), \eta' K_s^0(K_L^0), \dots$ there are tree contributions that, although CKM suppressed, can pollute the determination of $\sin 2\beta$ (see Section 5.1.2). The mode $\eta' K_s^0$ is very interesting because the measured branching ratio at CLEO is rather large [37].

Estimation of the tree pollution on $\sin 2\beta$ using factorization (Section 5.1.5) seems to indicate that this mode is very encouraging.

Included in this section are examples of the various penguin modes that have been investigated: $B^0 \rightarrow \eta' K^0$ and $B^0 \rightarrow \phi K^{*0}$ in the K_s^0 channel and $B^0 \rightarrow \eta' K^0$ and $B^0 \rightarrow \phi K^0$ in the K_L^0 channel.

5.6.1 $B^0 \rightarrow \eta' K_s^0$

The $B^0 \rightarrow \eta' K_s^0$ analysis is rather similar to the $J/\psi K_s^0$ analysis discussed in Section 5.3.1. The full BBsim simulation and reconstruction is used and the K_s^0 finding is identical, except that only the $K_s^0 \rightarrow \pi^+\pi^-$ channel is used. For η' candidates the $\eta' \rightarrow \eta\pi^+\pi^-$ and $\eta' \rightarrow \rho^0\gamma$ decay channels are used. The $\eta' \rightarrow \eta\pi^+\pi^-$ analysis uses only the $\eta \rightarrow \gamma\gamma$ channel; because of lower efficiency, the $\eta \rightarrow \pi^+\pi^-\pi^0$ decay would increase the $\eta' \rightarrow \eta\pi^+\pi^-$ yield by only 30%. A preliminary filter with fairly loose mass cuts is used to obtain events for further study. In order to select a final sample, the following cuts are applied: $0.50 < m_\eta < 0.58$ GeV/ c^2 ; $0.3 < m_\rho < 0.9$ GeV/ c^2 ; $0.92 < m'_\eta < 0.98$ GeV/ c^2 ; $0.475 < m_{K_s} < 0.515$ GeV/ c^2 ; $5.20 < m_B < 5.35$ GeV/ c^2 and $0.20 < p_{B^0}^* < 0.45$ GeV/ c , where the notation for masses is clear and $p_{B^0}^*$ is the B momentum in the $\Upsilon(4S)$ center of mass. These cuts typically require quantities to be within three standard deviations of the nominal mean; the distributions for η' mass and B mass, before cuts, are shown in Fig. 5-42.

The numbers of Monte Carlo signal and $q\bar{q}$ background events which pass successive cuts are given in Table 5-31 and Table 5-32 for the $\eta' \rightarrow \eta\pi^+\pi^-$ and $\eta' \rightarrow \rho^0\gamma$ decay channels, respectively. The numbers for signal were obtained from a sample of 8000-signal Monte Carlo events and scaled to the expectations for a 30 fb^{-1} sample. These numbers reflect only the situation for events with the correct $B^0 \rightarrow \eta' K_s^0$ decay. With the present cuts, there are 12% (23%) additional combinations for the $\eta' \rightarrow \eta\pi^+\pi^-$ ($\eta' \rightarrow \rho^0\gamma$) samples which pass all cuts but are not from the correct B decay chain. Many of these are from events which have more than one combination of tracks and showers which pass the selection. While further study of events with multiple combinations is necessary, it is already known that about one-half of such events differ only in the photons in the event. Thus the vertex position of the CP decay is the same for such combinations since photons are not used to determine the vertex position.

The background numbers in Tables 5-31 and 5-32 are scaled from the full $q\bar{q}$ sample discussed in Section 5.2. The backgrounds are approximately an order of magnitude larger than for the comparable CLEO analyses since background suppression cuts have not been made. The use of tight event shape cuts, especially for the $\eta' \rightarrow \rho^0\gamma$ mode, should reduce the background to $\sim 10\%$ for the $\eta' \rightarrow \eta\pi^+\pi^-$ mode and $\sim 50\%$ for the $\eta' \rightarrow \rho^0\gamma$ mode. The $B\bar{B}$ background is expected to be negligible for both of these samples, confirmed by the fact that no events from the 2.2 fb^{-1} $B\bar{B}$ Monte Carlo sample passed our selection cuts.

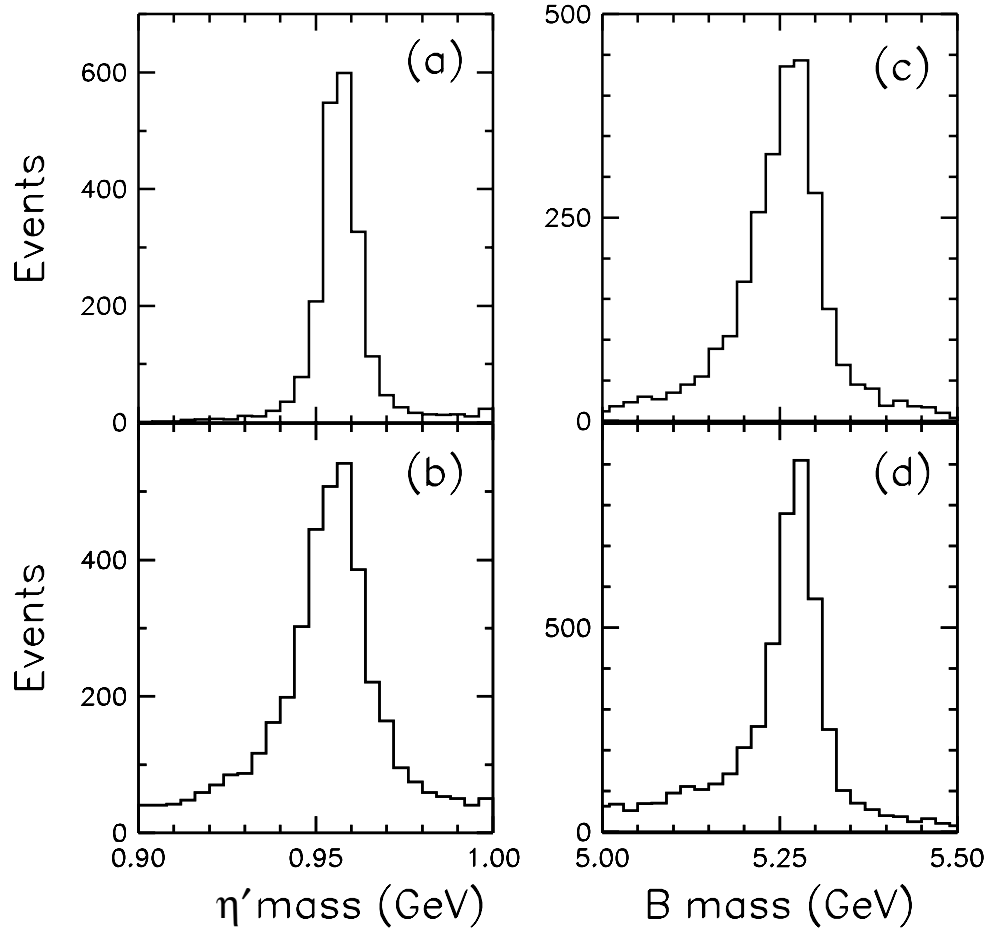


Figure 5-42. Distribution of η' mass for (a) $\eta' \rightarrow \eta\pi^+\pi^-$ and (b) $\eta' \rightarrow \rho^0\gamma$ decay channels. Distribution of B mass for (c) $\eta' \rightarrow \eta\pi^+\pi^-$ and (d) $\eta' \rightarrow \rho^0\gamma$ decay channels. All other cuts have been applied when making these distributions.

Table 5-31. Number of events and efficiency for signal and background events passing the $\eta' \rightarrow \eta\pi^+\pi^-$ selection criteria. Numbers in this table were derived from full BBsim simulation and reconstruction.

Cut	Signal		$q\bar{q}$ Background Events
	Events	Eff.	
None	89	1.00	101691000
Filter	35	0.40	887933
η mass	30	0.34	12839
η' mass	28	0.32	2255
K_s^0 mass	27	0.30	1253
B mass	21	0.24	167
$p_{B^0}^*$	20	0.23	21

Table 5-32. Number of events and efficiency for signal and background events passing the $\eta' \rightarrow \rho^0\gamma$ selection criteria. Numbers in this table were derived from full BBsim simulation and reconstruction.

Cut	Signal		$q\bar{q}$ Background Events
	Events	Eff.	
None	157	1.00	101691000
Filter	76	0.49	887933
ρ mass	71	0.46	717119
η' mass	64	0.41	232338
K_s^0 mass	61	0.39	110146
B mass	56	0.36	16450
$p_{B^0}^*$	55	0.35	1942

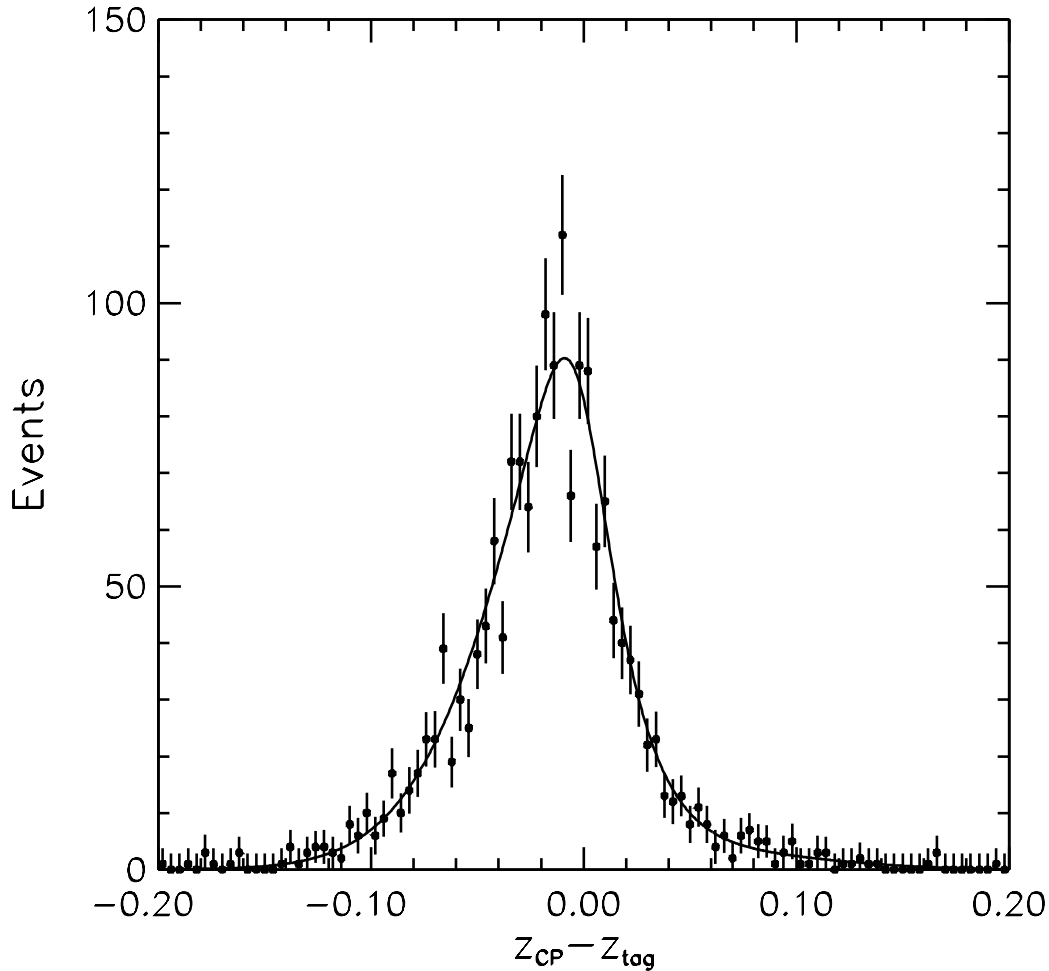


Figure 5-43. Distribution of $z_{CP} - z_{tag}$ for a sample of Monte Carlo $B^0 \rightarrow \eta' K_S^0$ events with $\eta' \rightarrow \rho\gamma$.

In order to determine $\sin 2\beta$ from the samples, $\Delta z = z_{CP} - z_{tag}$ is determined, as in Section 4.10. The z position of the CP vertex is determined from the charged tracks from the η' decay and the K_S^0 direction. The z position of the tag vertex is obtained with an algorithm similar to that discussed in Section 4.5.1.3, though with some improvements. The resolution is accounted for by a double-Gaussian (with the mean allowed to be non-zero to account for the effect of tracks from charm decays pulling the tag vertex) with parameters extracted from $\Delta z - \Delta z_{true}$. The Δz distribution for the $\eta' \rightarrow \rho^0\gamma$ sample with an input value of $\sin 2\beta = 0.7$ is shown in Fig. 5-43. The fitted value of $\sin 2\beta$ is 0.67 ± 0.04 , which leads to a value of $\sigma_0 = 1.8$, approximately the expected value given the effective resolution of $\sim 175 \mu\text{m}$. Minor quality cuts on the tag and CP vertices were needed to obtain these results. Improvements to the procedure for the location of the vertices, should enable us to achieve approximately the same resolution ($130 \mu\text{m}$) and σ_0 (1.59) as in the $J/\psi K_S^0$ analysis, since in both cases the resolution for the CP vertex is substantially smaller

Table 5-33. Efficiencies for the $B^0 \rightarrow \eta' K_L^0$ decay obtained with the `Aslund` fast simulation.

	$\epsilon(\eta' K_L^0)$	$\epsilon(\eta' K^{*0})$
	0.52	0.46
$p_{B^0}^* \leq 0.45$ (GeV/c)	0.42	0.13

than for the tag vertex. The charged tracks in the $\eta' \rightarrow \eta\pi^+\pi^-$ mode are scattered more due to their softer momentum spectrum. Hence, the resolution for this mode is expected to be larger, ($\sim 150 \mu\text{m}$), leading to $\sigma_0 \sim 1.70$. These and other numbers in this section are summarized below in Table 5-38.

5.6.2 Analysis of $B^0 \rightarrow \eta' K_L^0$

The decay $B^0 \rightarrow \eta' K_L^0$ has also been studied with the `Aslund` fast simulation. As mentioned already, the detection of both K^0 decay modes is important because the CP asymmetries have opposite signs and there is a substantial increase in statistics because of the large detection efficiency for high-energy K_L^0 mesons. On the other hand the overall branching ratio, $\mathcal{B}(B^0 \rightarrow \eta' K_L^0, \eta' \rightarrow \pi^+\pi^-\eta, \eta \rightarrow \pi^+\pi^-\pi^0, \pi^0 \rightarrow \gamma\gamma) \simeq 0.44 \times 0.62 \times 2.4 \times 10^{-5}$ [37, 50] is relatively low. This η' decay chain allows reconstruction of the B^0 vertex and it is more background free, due to the constraint on the η' and η masses than the decay $\eta' \rightarrow \rho\gamma$. Only the decays $\eta \rightarrow \pi^+\pi^-\pi^0$ and $\eta \rightarrow \gamma\gamma$ have been considered.

Selection criteria and background channels are the same as described in Section 5.3.2 for $B^0 \rightarrow J/\psi K_L^0$. The K_L^0 momentum is determined from the η' momentum and from the K_L^0 direction. Consistency with $\Upsilon(4S) \rightarrow B^0 \bar{B}^0$ decay is used as a constraint, requiring that the reconstructed center of mass B momentum has, within resolution, the expected value $p_{B^0}^* \sim 330$ MeV. The resolution on this momentum is dominated by the energy spread of the colliding beams and by the angular resolution in the K_L^0 direction as discussed in Section 5.3.2. Detection efficiencies are rather high, due to the high K_L^0 momenta, ranging from 1.5 GeV/c up to 4.4 GeV/c, with a flat distribution. The η' momentum distribution is rather independent of the η' mass.

After simple cuts, the detection efficiency is $\simeq 0.42$, as shown in Table 5-33.

Background arising from $B\bar{B}$ events are expected to be negligible as seen in the previous section. The background from $B \rightarrow \eta' K^*$ decays, which was important in Section 5.3.2, is expected to be only a few percent here because the branching fraction for the $B \rightarrow \eta' K^*$ decay is small compared to the $B^0 \rightarrow \eta' K_L^0$ decay (see Table 5-5), unlike the case for the $B^0 \rightarrow J/\psi K_L^0$ analysis. Background from an uncorrelated η' and a K_L^0 in a multihadronic event is also expected to be small.

Inclusive η' production has been simulated and it turns out that its contribution, due to the large difference in η' momentum, is negligible for $p_{B^0}^* \leq 450$ MeV/c.

The total yield of signal and background events expected from a 30 fb^{-1} sample, is shown in Fig. 5-44 as a function of $p_{B^0}^*$, with the K^* background normalized as in the $B^0 \rightarrow J/\psi K_L^0$ analysis (hence likely overestimated by about an order of magnitude). The most important background, from $q\bar{q}$ events, is not shown because the Monte Carlo samples were not available for this Aslund analysis. Suitable cuts such as those employed in the previous section should reduce the background to an acceptable level.

In conclusion $\simeq 87$ events are expected after these cuts from $B^0 \rightarrow \eta' K_L^0$ with an integrated luminosity of 30 fb^{-1} . Additional cuts to reduce $q\bar{q}$ background would be expected to decrease this level by about a factor of two.

5.6.3 Analysis of ϕK^*

This section presents an analysis of the mode $\bar{B}^0 \rightarrow \phi \bar{K}^{*0}$, where the ϕ decays to $K^+ K^-$, and the K^{*0} decays to a $K^+ \pi^-$. The current branching ratio limit for this mode is $\mathcal{B}(B^0 \rightarrow \phi K^{*0}) < 2.1 \times 10^{-5}$ [40]. If the true branching ratio is estimated to be $\mathcal{B}(B^0 \rightarrow \phi K^{*0}) = 1.0 \times 10^{-5}$ (close to the central value of the CLEO analysis), the $B^0 \rightarrow J/\psi K_S^0$ analysis can be used to estimate the number of events expected in one year of running. The two modes have the same number of charged tracks in the final state, so it has been assumed that they have the same geometrical acceptance and tracking efficiency. The branching ratios in the two modes are compared in Table 5-34. Although a factor of 40 is lost in the initial branching ratios, a factor of four is gained from the branching ratios of the daughters. If ~ 600 $B^0 \rightarrow J/\psi K_S^0$ events are expected for a 30 fb^{-1} sample, then ~ 60 $B^0 \rightarrow \phi K^{*0}$ events can be expected (this includes $\bar{B}^0 \rightarrow \phi \bar{K}^{*0}$ events). Note that this study looked only at the combinatoric background in $B^0 \rightarrow \phi K^{*0}$ events, and did not include background from continuum events.

Table 5-34. Comparison of the $B^0 \rightarrow \phi K^{*0}$ and $B^0 \rightarrow J/\psi K_S^0$ modes.

$\mathcal{B}(B^0 \rightarrow J/\psi K_S^0) = 4 \times 10^{-4}$	$\mathcal{B}(B^0 \rightarrow \phi K^{*0}) = 1 \times 10^{-5}$
$\mathcal{B}(J/\psi \rightarrow e^+ e^-, \mu^+ \mu^-) = 12\%$	$\mathcal{B}(\phi \rightarrow K^+ K^-) = 49\%$
$\mathcal{B}(K_S^0 \rightarrow \pi^+ \pi^-) = 69\%$	$\mathcal{B}(K^{*0} \rightarrow K^+ \pi^-) = 67\%$

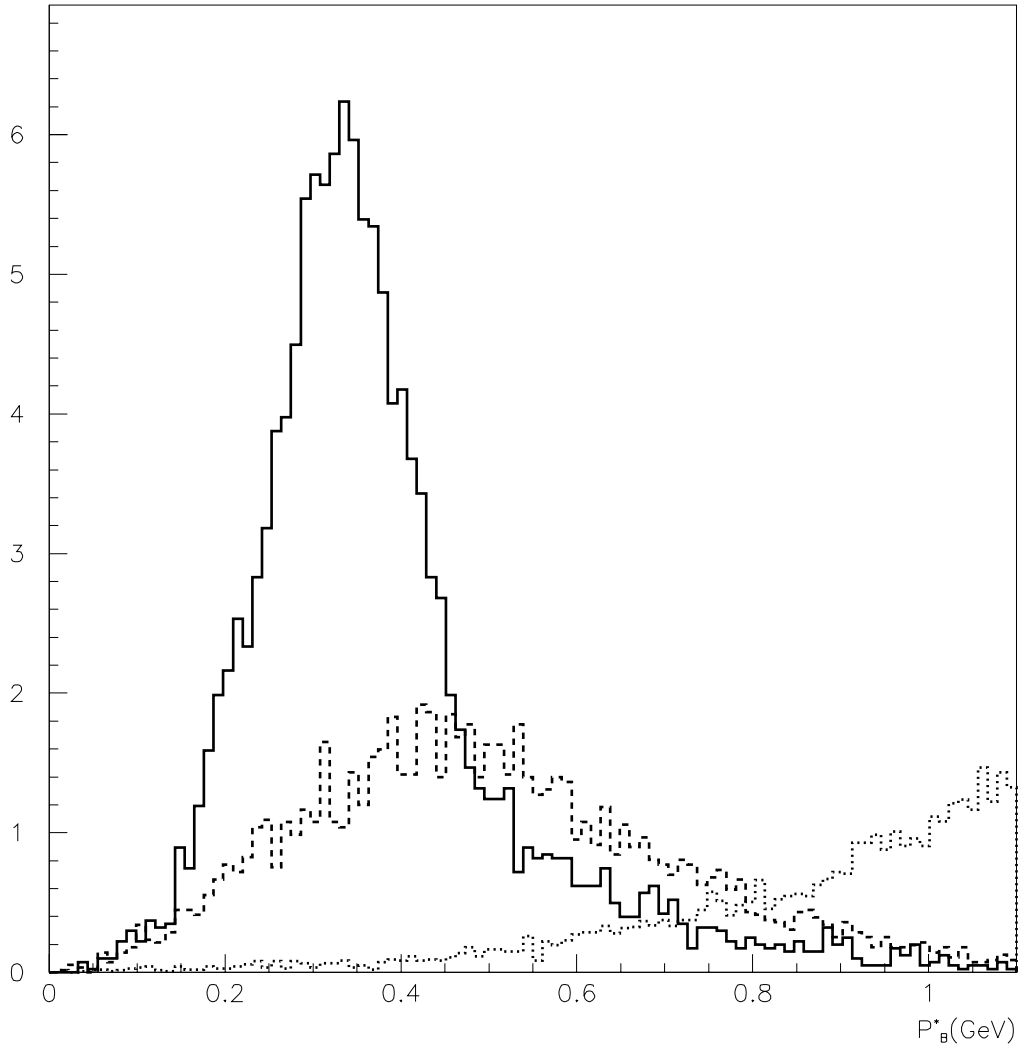


Figure 5-44. $p_{B^0}^*$ distribution for $\eta' K_L^0$ (solid histogram), $\eta' K^{*0}$ (dashed) and combinatorial background (dotted).

Table 5-35. *Phi-finding (reconstruction + identification) efficiency using different kaon selection criteria.*

Criterion	Mis-ID	Efficiency	S/B
loose	10%	0.50	45
tight	10%	0.59	31
$K \vee (\bar{e} \wedge \bar{\mu} \wedge \bar{p} \wedge \bar{\pi})$		0.73	19
... + DOCA cut		0.65	32

5.6.3.1 The ϕ selection

In order to reconstruct this channel, ϕ decays to K^+K^- are required, so the efficiency for finding charged kaons is an important contributor to the efficiency for finding ϕ s. Table 5-35 shows the efficiency of finding ϕ s for different methods of identifying kaons. In this table “criterion” and “mis-id” refer to parameters of the kaon selector code (`KaonParamSelector`); “efficiency” is the probability of correctly identifying a true ϕ , and “S/B” is the ratio of true to fake ϕ s.

At the time this analysis was performed, the kaon selector had significant inefficiencies, especially at low momentum (see Fig. 5-45). In order to maximize the number of kaon candidates, several other ways of creating kaon lists were explored, and the best method for this analysis was selected. This involved taking as kaons, all charged tracks that were not selected as electron, muon, or proton (using the tight selection criteria), nor selected as a pion (using the loose criteria), as well as any track identified as a kaon using the standard selector (`KaonParamSelector`) (with the tight criteria and a 10% mis-ID level, and all other cuts set to zero). As can be seen from Fig. 5-46, this enhanced the efficiency considerably. Even after making a cut on the distance of closest approach of the tracks, the efficiency is still larger than the standard kaon selection, and the signal-to-background is still large (see Table 5-35).

The ϕ candidates were selected by taking all pairs of oppositely-charged tracks that satisfied the kaon-ID criteria described above. In addition to the mass and momentum cuts listed in Table 5-36, these candidates were also required to pass a distance-of-closest-approach (DOCA) cut, where the DOCA is the distance of closest approach between the K^+ and K^- tracks. This cut reduced some of the candidates from combinatorial background. Figure 5-47 shows the DOCA between the K^+ and K^- tracks that form the ϕ .

98/01/20 08.25

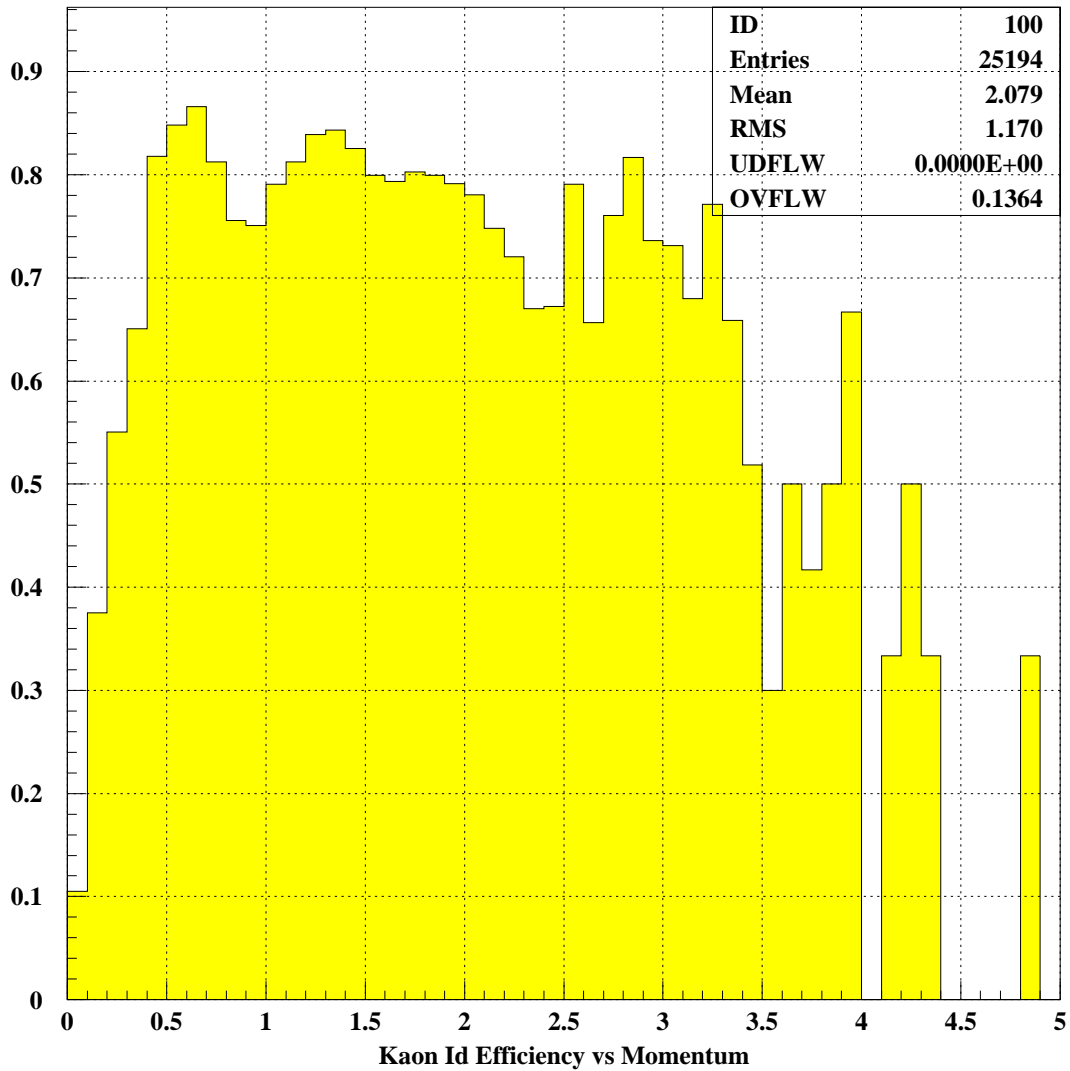


Figure 5-45. *Kaon particle ID efficiency using standard kaon lists.*

98/03/15 15.39

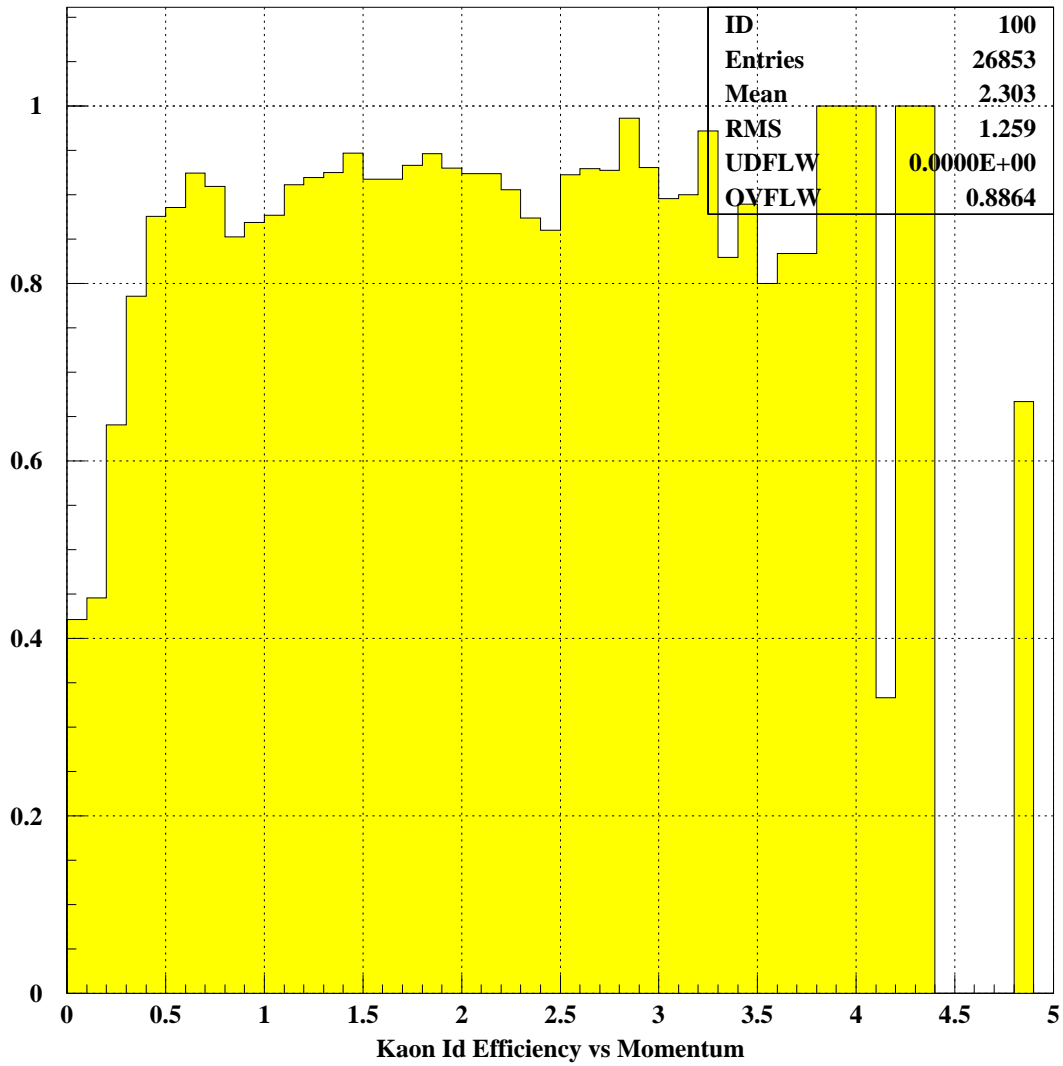


Figure 5-46. Kaon particle ID efficiency using all charged tracks that are not pions, electrons, muons, or protons.

98/03/02 17.10

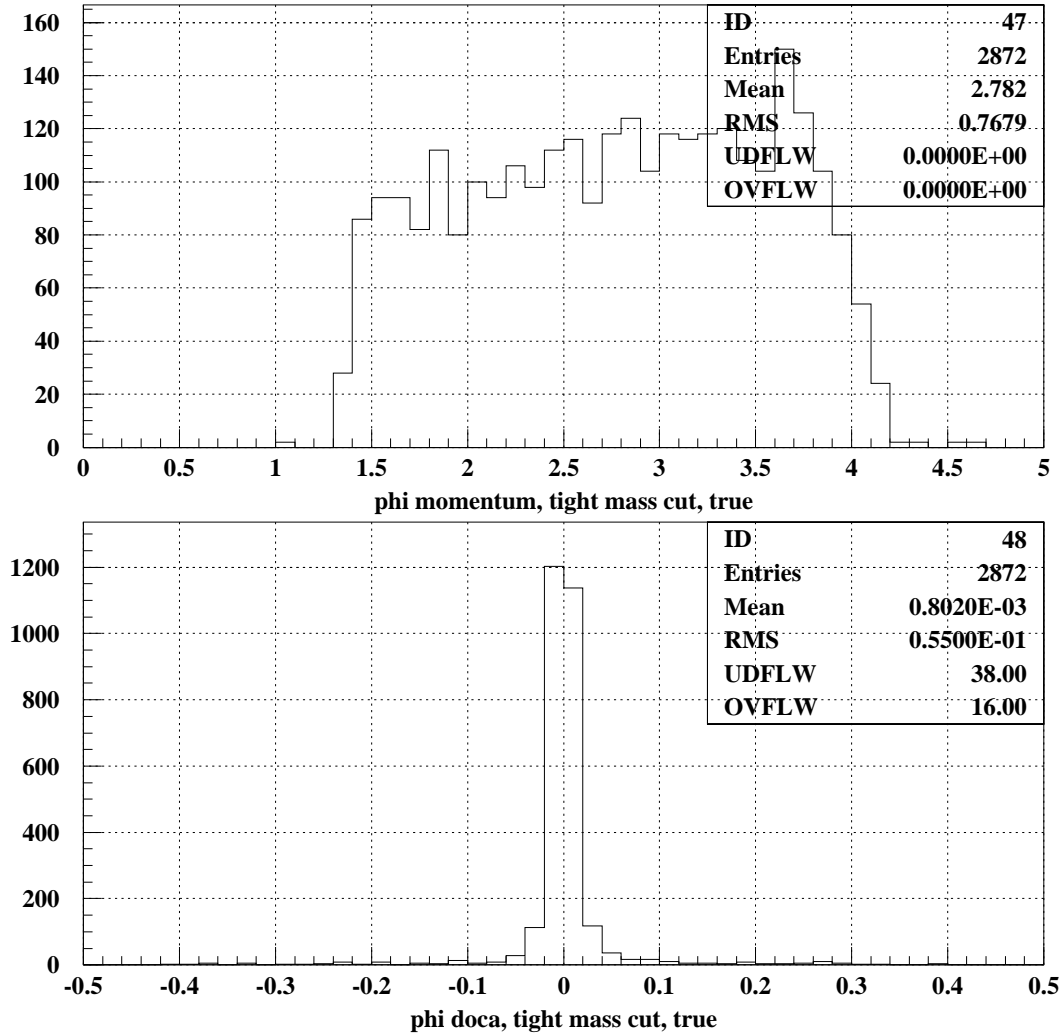


Figure 5-47. Momentum and DOCA for true ϕ candidates.

Table 5-36. Cuts used in the ϕK^* analysis.

Cut	Value
ϕ mass	$0.990 < M_{K^+K^-} < 1.050 \text{ GeV}/c^2$
DOCA	$d_{K^+K^-} < 400 \mu\text{m}$
ϕ momentum	$p_\phi > 1.30 \text{ GeV}/c$
K^* mass	$0.770 < M_{K^+\pi^-} < 1.00 \text{ GeV}/c^2$
DOCA	$d_{K^+\pi^-} < 400 \mu\text{m}$
K^* momentum	$p_{K^*} > 1.30 \text{ GeV}/c$
B^0 mass	$5.18 < M_{\phi K^*} < 5.40 \text{ GeV}/c^2$

5.6.3.2 The K^* selection

In this study, the decay mode $K^{*0} \rightarrow K^+\pi^-$ was reconstructed. This mode cannot exhibit CP violation, but it is simpler to study than $K^* \rightarrow K_S^0\pi^0$. Nevertheless, it provides an estimate of how well the $K^* \rightarrow K_S^0\pi^0$ mode can be measured. About a factor eight fewer events are expected in the $K^* \rightarrow K_S^0\pi^0$ mode, a factor of four coming from the branching fraction, and the rest coming from the smaller efficiency for K_S^0 and π^0 reconstruction.

In order to select $K^{*0} \rightarrow K^+\pi^-$ candidates, pairs of charged tracks were used, where one track satisfied the kaon-ID selection described above (and was not already used to make a ϕ), and the other track satisfied a pion-ID selection (the pion selector with loose cuts). The reconstructed K^* was required to satisfy the cuts described in Table 5-36.

5.6.3.3 Results

Table 5-36 lists all of the cuts that were used in this analysis. After these cuts, 1786 events remained from the original sample of 4000 $B^0 \rightarrow \phi K^{*0}$ events, giving an efficiency for these selection cuts of 45%. Application of $q\bar{q}$ background suppression cuts and the factor mentioned previously would suggest an efficiency of $\sim 20\%$ for the $K^* \rightarrow K_S^0\pi^0$ mode. The B^0 mass distribution is shown in Fig. 5-48 for signal and fake candidate events. Since the kaons have high momenta, the Δz resolution for this mode is expected to be similar to the $130 \mu\text{m}$ obtained for $B^0 \rightarrow J/\psi K_S^0$. The loss due to the angular analysis should be small, as for the $J/\psi K^*$ case.

98/03/02 17.13

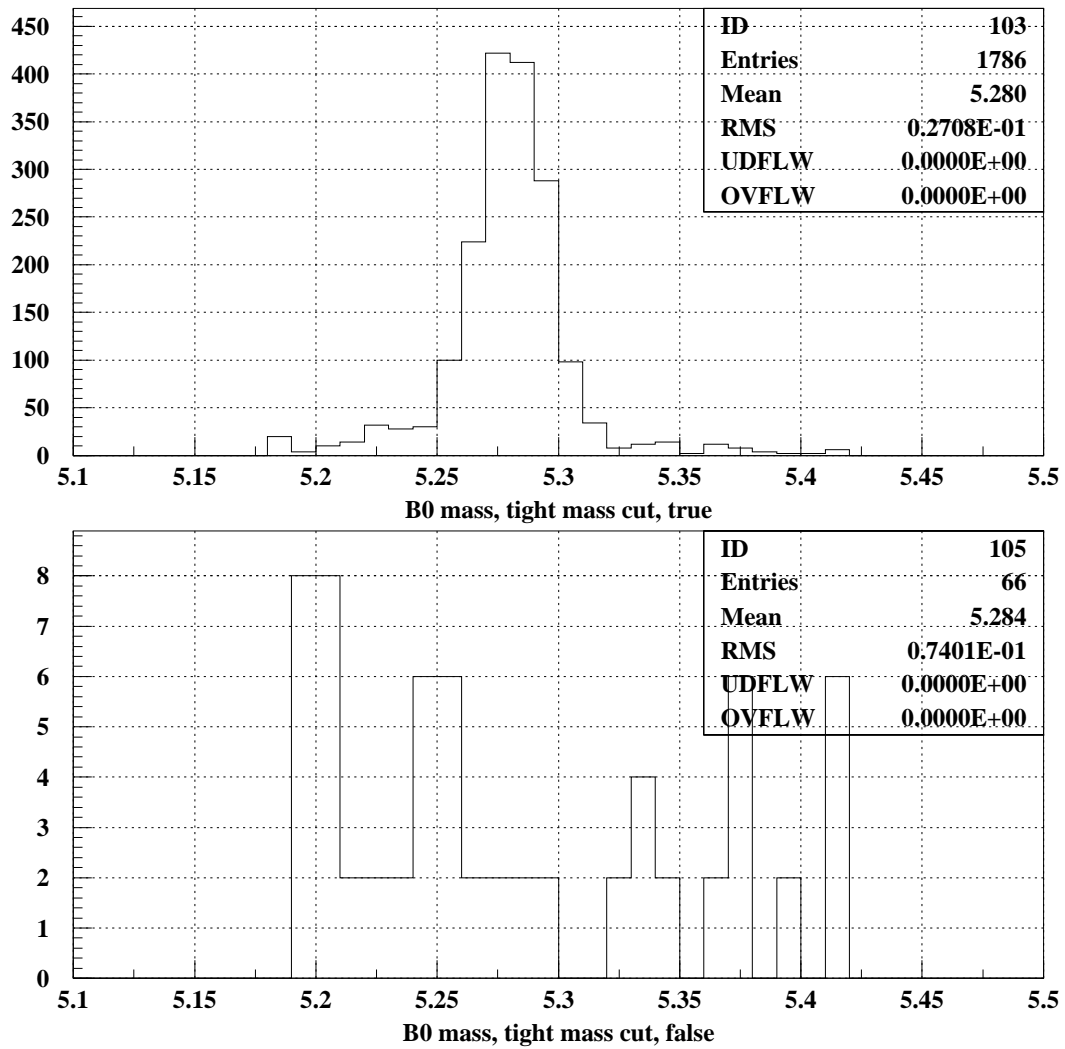


Figure 5-48. Reconstructed \bar{B}^0 mass from $B^0 \rightarrow \phi K^{*0}$ events, for both true and fake B s.

Table 5-37. Efficiencies for the $B^0 \rightarrow \phi K_L^0$ analysis obtained with analysis of the CP-mode and backgrounds in this channel was done the `Aslund` fast simulation.

	$\epsilon(\phi K_L^0)$	$\epsilon(\phi K^{*0})$
	0.66	0.54
$p_{B^0}^* \leq 0.45$ (GeV/c)	0.54	0.20
K^{*0} cuts	0.37	0.04

5.6.4 Estimates for $B \rightarrow \phi K_s^0$

The usable sample for the decay $B \rightarrow \phi K_s^0$, assuming $\mathcal{B}(B \rightarrow \phi K_s^0) = 0.65 \times 10^{-5}$ [51] and an integrated luminosity of 30 fb^{-1} , is ~ 100 events. Assuming the same geometrical acceptance and tracking efficiency as for the $J/\psi K_s^0$ decay, about 60 events are expected to pass loose cuts. Tighter cuts to reduce $q\bar{q}$ backgrounds would be expected to decrease this by about a factor of two. The z vertex resolution for the ϕ has been estimated to be ≈ 80 microns. As the Δz resolution will be limited by the recoiling B tag, the σ_0 for this mode will be similar to the 1.59 obtained for $J/\psi K_s^0$. Hence the error in $\sin 2\beta$, assuming there is little background, will be approximately 0.6.

5.6.5 Analysis of $B^0 \rightarrow \phi K_L^0$

The $B^0 \rightarrow \phi K_L^0$ process is expected to have a small branching ratio, $\mathcal{B}(B^0 \rightarrow \phi K_L^0, \phi \rightarrow K^+ K^-) \simeq 0.49 \times 0.65 \times 10^{-5}$, [51, 50]. The detection efficiency before cuts, however, is relatively large, as shown in Table 5-37, due to the high K_L^0 momenta, which range from 1.5 GeV/c up to 4.4 GeV/c (see Fig. 5-49). Selection criteria and backgrounds are similar to what has been described in Sections 5.3.2 and 5.6.2. All results in this section were obtained with the `Aslund` fast simulation.

For this channel, the backgrounds from $B \rightarrow \phi K^*$ are expected to be closer to that for the $B^0 \rightarrow J/\psi K_L^0$ decay than that for the $B^0 \rightarrow \eta' K_L^0$ decay since the branching fraction for $B \rightarrow \phi K^*$ is likely comparable to the branching fraction for $B^0 \rightarrow \phi K_L^0$. The analysis of these background channels follows the method employed previously. The momentum distribution of K_L^0 mesons from ϕK^* decays are also shown in Fig. 5-49. The low momentum K_L^0 decays can be eliminated with the usual requirement $p_{B^0}^* \leq 450 \text{ MeV/c}$.

Events from $B \rightarrow \phi K^*$ are rejected, if there is an additional pion such that the $K_L^0 \pi$ invariant mass and $p_{B^0}^*$ is consistent with the process $B \rightarrow \phi K^*$. This cut is optimized to increase the S/B ratio. The K^* background is reduced to $\sim 10\%$ as summarized in Table 5-37 and shown in Fig. 5-50;

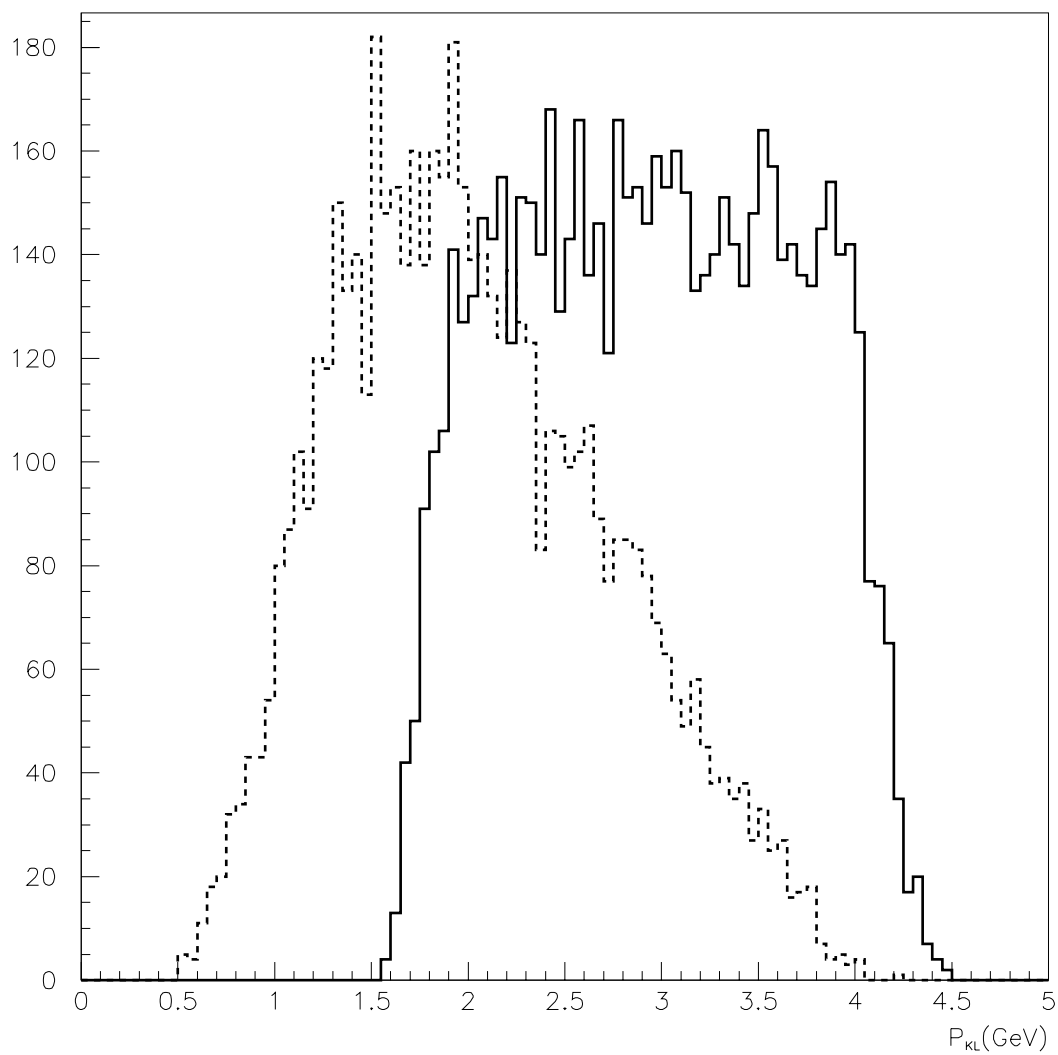


Figure 5-49. K_L^0 momentum distribution for ϕK_L^0 (solid) and ϕK^* (dashed) decays.

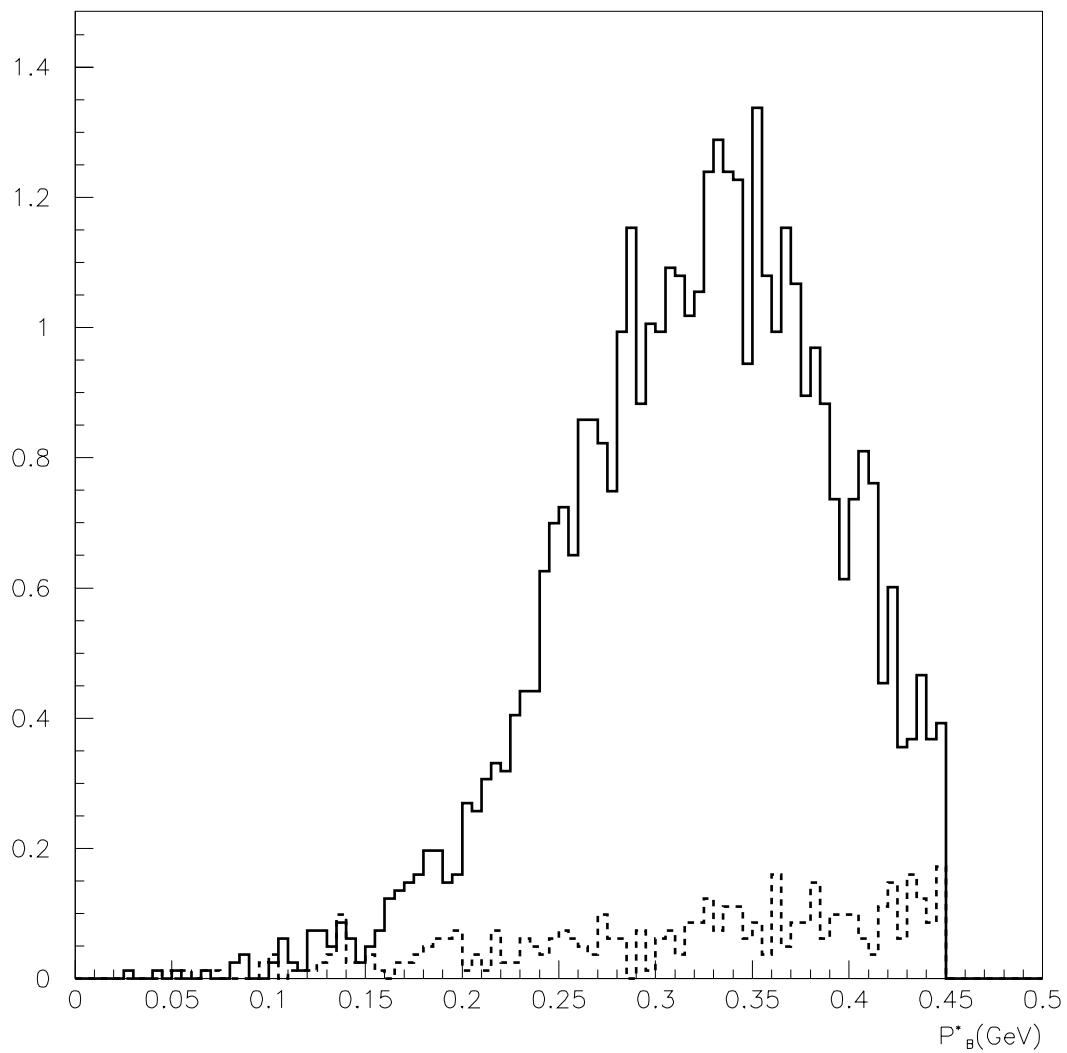


Figure 5-50. $p_{B^*}^*$ distribution for ϕK_L^0 (solid) and ϕK^{*0} (dashed) after all cuts.

the K^* to K_L^0 ratio was taken to be the same as for the $B^0 \rightarrow J/\psi K_L^0$ case. The loss of signal efficiency, could be reduced by requiring that the ϕ and the associated pion have a common vertex.

Combinatorial background is expected mostly at very high $p_{B^0}^*$, as is the case of $B \rightarrow J/\psi K_L^0 X$. While inclusive ϕ production is a factor of ~ 200 larger relative to signal than in the $B^0 \rightarrow J/\psi K_L^0$ case, the K_L^0 s from $B^0 \rightarrow \phi K_L^0$ are more energetic. Thus the detection efficiency will be higher and the combinatorial missing mass and background smaller. Furthermore, the combinatorial background is even more peaked at large $p_{B^0}^*$, than for $B^0 \rightarrow J/\psi K_L^0$. Inclusive ϕ production has been simulated and it is mostly due to $D\bar{D}_s^+$ production and decay. Identified D_s^+ channels account for $\simeq 50\%$ of the inclusive ϕ production and are consistent with the mean ϕ momentum $P_\phi \simeq 1.2$ GeV/c (see Fig. 5-51). The large difference in ϕ momentum is such that no events are expected to survive the requirement $p_{B^0}^* \leq 450$ MeV/c.

$\simeq 37$ $B^0 \rightarrow J/\psi K_L^0$ events are expected to pass these cuts, for an integrated luminosity of 30 fb^{-1} running at the $\Upsilon(4S)$. While $q\bar{q}$ background has not been simulated, it is likely that additional cuts will be required to suppress this background as discussed previously. Such cuts would lower the number of signal events, by $\sim 40\%$.

5.7 Summary and Conclusions

When measurements have been performed in several modes, it will be interesting to compare them, in order to verify that they are consistent with the same value of $\sin 2\beta$. If this is the case, it will also be interesting to combine them all, in order to obtain an overall value of $\sin 2\beta$. In this section, the errors from each of the Monte Carlo-based analyses are summarised. Following that, possible systematic errors are considered, and methods to deal with them are mentioned. Finally, there follows a brief summary.

5.7.1 Summary of Results

The results of the Monte Carlo-based analyses are listed in Table 5-38. The individual $\sin 2\beta$ errors for each mode were estimated using the dilution factor as determined from the Δz resolution, the number of reconstructed events for 30 fb^{-1} of data-taking at the $\Upsilon(4S)$, backgrounds if any, and the effective tagging factor. The $\sin 2\beta$ error is the one standard deviation error that would be obtained from a maximum likelihood fit. Note that the value of the error depends on the actual value of $\sin 2\beta$; a value of 0.7 was assumed here. The individual errors could be combined by simply adding them in quadrature, to estimate the total error on $\sin 2\beta$ obtained by combining all the measurements. In this case, this is not strictly possible, as there were two distinct approaches to the various analyses. However, it is clear that with 30 fb^{-1} of data-taking at the $\Upsilon(4S)$, the

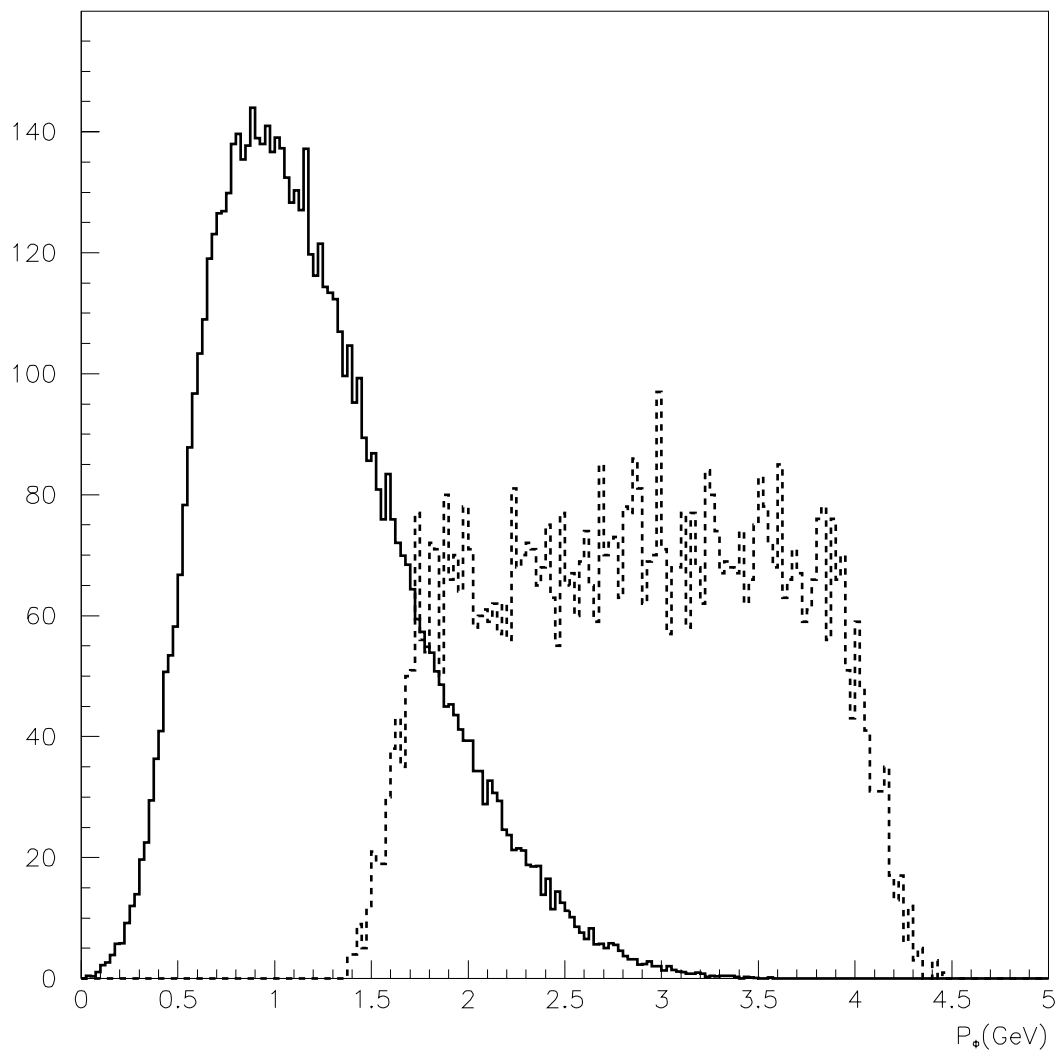


Figure 5-51. ϕ momentum distribution for combinatorial background (solid) and ϕK_L^0 (dashed), normalized to the same entries.

Table 5-38. Summary of $\sin 2\beta$ measurements assuming $\sin 2\beta=0.7$ for a 30 fb^{-1} sample.

Mode	\mathcal{B} (10^{-4})	Usable sample	Rec. eff.	N_S	N_B/N_S	$\sigma_{\Delta z}$ (μm)	σ_0	Tag factor	Error
$J/\psi(\ell^+\ell^-)K_S^0(\pi^+\pi^-)$	4.25	1100	0.60	660	0.06	130	1.59	0.3	0.12
$J/\psi(\ell^+\ell^-)K_S^0(\pi^0\pi^0)$	4.25	500	0.21	110	0.06	130	1.59	0.3	0.30
$J/\psi(\ell^+\ell^-)K_L^0$	4.25	1600	0.41	650	0.59	130	1.59	0.3	0.15*
$\psi'(\pi^+\pi^-\ell^+\ell^-)K_L^0$	3.5	430	0.27	120	0.83	130	1.59	0.3	0.34*
$\chi_{c1}(\gamma\ell^+\ell^-)K_L^0$	5.0	520	0.28	143	0.78	130	1.59	0.3	0.28*
$J/\psi(\ell^+\ell^-)K^{*0}(\pi^+\pi^-\pi^0)$	13.2	570	0.09	51	0.18	130	1.79	0.3	0.50
D^+D^- (6 D Modes)	4.5	610	0.24	140	2.80	130	1.59	0.3	0.48*
$D^{*+}D^{*-}$ (4 D Modes)	9.7	1050	0.05	60	0.23	150	1.70	0.3	0.44
$\phi(K^+K^-)K_L^0$	0.065	100	0.22	22	0.10	130	1.59	0.3	0.66*
$\phi(K^+K^-)K^{*0}(\pi^+\pi^-\pi^0)$	0.1	26	0.20	5	0.10	150	1.70	0.3	1.40*
$\eta'(\eta\pi^+\pi^-)K_S^0(\pi^+\pi^-)$	0.24	88	0.23	20	0.10	150	1.70	0.3	0.73
$\eta'(\rho\gamma)K_S^0(\pi^+\pi^-)$	0.24	160	0.35	55	0.90	130	1.59	0.3	0.56
$\eta'(\eta\pi^+\pi^-)K_L^0$	0.24	210	0.21	44	0.10	150	1.70	0.3	0.49*

* The efficiency for these modes is from an Aslund study, or is estimated from an incomplete analysis.

combined statistical error is likely to be on the order of 0.08. It is likely that this will dominate over the systematic errors and limit the precision.

Several remarks are in order concerning the results with the different modes. All the studies except for D^+D^- and the various K_L^0 channels used the full simulation and reconstruction to determine the reconstruction efficiencies. All the modes assumed an effective tagging efficiency of 0.3 and no loss in efficiency due to the vertex reconstruction of the recoiling B meson. The $B^0 \rightarrow J/\psi K_S^0$ and $B^0 \rightarrow \eta' K_S^0$ modes were analyzed with an actual fit to the Δz distribution to extract the dilution error and the other modes used a maximum likelihood estimator. The results of the actual fits agreed with the maximum likelihood estimate of the error.

The results show that the $J/\psi K_S^0$ and $J/\psi K_L^0$ modes are the most promising in terms of precision. These two measurements alone yield a precision of $\sigma(\sin 2\beta) = 0.09$ whereas all the others not including these two will yield worse precision. If $\sin 2\beta=0.7$, a three-standard-deviation measurement for CP violation requires an error of 0.23, which is possible with 5 fb^{-1} sample for the $J/\psi K_S^0$ and $J/\psi K_L^0$ modes or a 3 fb^{-1} sample with all of the modes studied here. Such samples

should surely be obtained in the first year of BABAR running. The mode $D^+ D^-$ will have substantial complications from penguin pollution and perhaps should be considered separately. Possible improvements to the combination of different modes would be to make a joint likelihood of all of the fits and extract nonsymmetric errors by integrating the likelihood, or to use the \mathcal{K} in variable.

5.7.2 Systematic Errors

Possible systematic errors are likely to include:

- Monte Carlo event-generator uncertainties:
 - B modeling (*e.g.*, semileptonic decays, rare backgrounds)
 - $q\bar{q}$ modeling (*e.g.*, charm- vs. light-quark ratios)
 - Modeling of specific CP -violating B decays
- Simulation uncertainties:
 - Uncertainties in the machine background modelling and imperfections in mixing them with the physics events
 - Digitization of the detector response
 - Imperfections in modelling hadronic interactions in the detector
- Reconstruction uncertainties:
 - Vertexing and tracking efficiencies
 - Vertex and drift chamber resolution
 - Particle identification efficiencies and mis-identifications
 - Uncertainties in the B flavor tagging effective efficiency
- Detector-performance uncertainties:
 - Tracking asymmetries in charge
 - Detector resolutions
 - Overlapping tracks
- Backgrounds:
 - Amount of background
 - Time distribution of background

- Experimental parameters uncertainties:
 - B lifetime, τ_B
 - B mixing, Δm_d

Although many effects cancel in CP -violating asymmetries, residual effects from the above sources contribute to effective dilutions, and possibly generate their own asymmetries. These can of course be corrected for, both on the basis of Monte Carlo simulations, and even better, on the basis of measurements of the effects in real data. It is the uncertainties in these corrections which lead to systematic uncertainties in the measured CP angles.

It should be possible that $q\bar{q}$ decays and various physics processes occurring in $\Upsilon(4S)$ decays can provide useful *in situ* measurements of resolutions and efficiencies. Such engineering measurements will be helpful to reduce possible systematic errors in the CP measurements. As the CP reach depends largely on the vertexing and the tagging, it is important to study these aspects carefully.

For vertexing, Monte Carlo studies have indicated that the Δz resolution is dominated by the resolution on the tagging vertex. Careful studies are required, both to optimise the vertexing on the tagging side, and to measure well the actual resolution there.

Determining effects due to tagging requires understanding the tagging efficiency and misidentification rates. These can be measured with real data, where a set of fully reconstructed B s can be used as a self-tagged sample, to measure the efficiency and misidentification of tagging on the other side of the event. Untangling mixing, and possibly vertexing between the two B s will require some effort to deconvolute the efficiency and misidentification rates.

5.7.3 Conclusion

The theoretical and experimental sides of measuring $\sin 2\beta$ in an asymmetric B factory have been extensively reviewed. The studies demonstrate that with a 30 fb^{-1} sample at the $\Upsilon(4S)$, a precision of ~ 0.08 could be achieved in the measurement of $\sin 2\beta$, which will provide crucial input to tests of the Standard Model description of CP violation.

References

- [1] On the unitarity triangle, see the review article by C. Jarlskog, in *CP Violation*, C. Jarlskog, Editor, World Scientific, Singapore (1987).
- [2] For recent updates of the constraints on the Standard Model parameters see M. Gronau, TECHNION-PH-97-17 (1997);
A. Ali and D. London, *Nucl. Phys. Proc. Suppl.* **54A**, 297 (1997).
- [3] A. B. Carter and A. I. Sanda, *Phys. Rev. D* **23**, 1567 (1981);
I. I. Bigi and A.I. Sanda, *Nucl. Phys.* **B193**, 85 (1981).
- [4] M. B. Gavela *et al.*, *Phys. Lett. B* **162**, 197 (1985);
I. I. Bigi and A. I. Sanda, *Nucl. Phys.* **B281**, 41 (1987).
- [5] I. I. Bigi *et al.*, in *CP violation*, C. Jarlskog, Editor, World Scientific, Singapore (1987).
- [6] Claudio O. Dib *et al.*, *Phys. Rev. D* **41**, 1522 (1990);
Y. Nir and H. R. Quinn, *Phys. Rev. D* **42**, 1473 (1990).
- [7] Y. Nir, Lectures presented at Theoretical Advanced Study Institute in Elementary Particle Physics, Boulder, Colorado, SLAC-PUB-5676 (1991);
Y. Nir and H. R. Quinn, in *B decays*, edited by S. Stone, SLAC-PUB-5643 (1991);
I. I. Bigi, *Proceedings of Les Rencontres de Physique de la Vallée d'Aoste*, La Thuile, March (1994), p.137.
- [8] D. London and A. Soni, *Phys. Lett. B* **407**, 61 (1997).
- [9] M. Ciuchini *et al.*, *Nucl. Phys.* **B501**, 3 (1998).
- [10] D. Atwood, M. Gronau and A. Soni, *Phys. Rev. Lett.* **79**, 185 (1997).
- [11] B. Kayser, in *Proceedings of the Workshop on B Factories and Related Physics Issues*, Blois, France (1989); *Proceedings of the International Workshop on Weak Interactions and Neutrinos*, Ginosar, Israel (1989); *Proceedings of the International Symposium on Fundamental Symmetries in Nuclei and Particles*, Pasadena (1989);
B. Kayser *et al.*, *Phys. Lett. B* **237**, 508 (1990).
- [12] W. Toki, "Double Momentum, *CP* Measurements and *CP* Moments," BaBar Note # 43, (1990);
I. Dunietz *et al.*, *Phys. Rev. D* **43**, 2193 (1991).
- [13] C. P. Jessop *et al.*, (CLEO Collaboration), *Phys. Rev. Lett.* **79**, 4533 (1997).

- [14] A. M. Dighe *et al.*, *Phys. Lett. B* **369**, 144 (1996);
J. L. Rosner, in *Proceedings of Les Rencontres de Physique de la Vallée d'Aoste*, La Thuile (1996), p. 219, DESY-96-062.
- [15] G. Kramer and W. F. Palmer, *Phys. Rev. D* **45**, 193 (1992).
- [16] R. Aleksan *et al.*, *Phys. Rev. D* **51**, 6235 (1995).
- [17] G. Michelon, "A Theoretical Review of the $B \rightarrow D^* \bar{D}^*$ Decay Channel," BaBar Note # 342, (1996).
- [18] A. I. Sanda and Z. Xing, *Phys. Rev. D* **56**, 6866 (1997).
- [19] R. Aleksan *et al.* (unpublished).
- [20] R. Aleksan *et al.*, *Nucl. Phys.* **B361**, 141 (1991).
- [21] R. Aleksan *et al.*, *Phys. Lett. B* **317**, 173 (1993).
- [22] D. Atwood and A. Soni, *Phys. Lett. B* **405**, 150 (1997).
- [23] Other calculations of the $\eta' \bar{K}$ rate using factorization are A. Datta, X.-G. He and S. Pakvasa, preprint UH-511-864-97 (1997);
N. G. Deshpande, B. Dutta and S. Oh, *Phys. Rev. D* **57**, 5723 (1998).
- [24] A. Ali and C. Greub, *Phys. Rev. D* **57**, 2996 (1998).
- [25] M. Beneke, G. Buchalla and I. Dunietz, *Phys. Lett. B* **393**, 132 (1997).
- [26] Y. Grossman and H. R. Quinn, *Phys. Rev. D* **56**, 7259 (1997).
- [27] A. E. Snyder and H. R. Quinn, *Phys. Rev. D* **48**, 2139 (1993).
- [28] J. Charles *et al.*, preprint LPTHE 97/70 (1997), to appear in *Phys. Lett.*
- [29] B. Kayser and D. London, talk presented by B. Kayser at the Orsay BaBar Workshop, June (1997);
B. Kayser, to appear in *Proceedings of the Moriond Workshop on Electroweak Interactions and Unified Theories*, Les Arcs, France, March (1997), hep-ph/9709382 .
- [30] N. Isgur and M. Wise, *Phys. Rev. D* **43**, 819 (1991).
- [31] M. Morénas *et al.*, *Phys. Rev. D* **56**, 5668 (1997); preprint LPTHE 97-23 (1997).
- [32] R. M. Barnett *et al.*, *Phys. Rev. D* **54**, 1 (1996) and 1997 off-year partial update for the 1998 edition available on the PDG WWW pages at URL:
<http://pdg.lbl.gov/>.

- [33] M. Athanas *et al.*, (CLEO Collaboration), *Phys. Rev. Lett.* **79**, 2208 (1997).
- [34] F. Abe *et al.*, (CDF Collaboration), *Phys. Rev. D* **58**, 072001 (1998).
- [35] D.M. Asner *et al.*, (CLEO Collaboration), *Phys. Rev. Lett.* **79**, 799 (1997).
- [36] R. Barate *et al.*, (ALEPH Collaboration), *Eur. Phys. Jour. C* **4**, 387 (1998).
- [37] R. Godang *et al.*, (CLEO Collaboration), *Phys. Rev. Lett.* **80**, 3456(1998).
- [38] A. Anastassov *et al.*, (CLEO Collaboration), CLEO CONF 97-24 and EPS97-334 (1997).
- [39] B. Behrens *et al.*, (CLEO Collaboration), *Phys. Rev. Lett.* **80**, 3710 (1998).
- [40] T. Bergfeld *et al.*, (CLEO Collaboration), *Phys. Rev. Lett.* **81**, 272 (1998).
- [41] F. Le Diberder, "Precision on CP Violation Measurements and Requirement on the Vertex Resolution," BaBar Note # 34, (1990).
- [42] R. Baldini-Ferroli *et al.*, "A Study of CP Violation in $B^0 \rightarrow J/\psi K_L^0$ using a Highly Segemented IFR," BaBar Note # 198, (1995).
- [43] R. Baldini-Ferroli *et al.*, "Further Study of $B^0 \rightarrow J/\psi K_L^0$," BaBar Note # 223, (1995).
- [44] R. Baldini-Ferroli *et al.*, BaBar Note in preparation.
- [45] D. Gibaut *et al.*, (CLEO Collaboration), *Phys. Rev. D* **53**, 4734 (1996).
- [46] Tagging group, "Basic formalism for the Tagging," Internal tagging note #1.
- [47] G. Lutz, "Topological Vertex Search in Collider Experiments," ALEPH 02-015 SOFTWR 92-003.
- [48] W. Toki, " CP Measurements from Forward-Backward Asymmetry of Decay Lengths," BaBar Note # 41, (1990).
- [49] See Section 4.10 and S. Versillé, "Simultaneous Handling of Tagging and Background Fighting," BaBar Note # 408, (1998).
- [50] F. Anulli *et al.*, BaBar Note in preparation.
- [51] R. Fleischer, *Z. Phys. C* **62**, 81 (1994).

This page was intentionally left blank.

Determinations of α and Direct CP Violation

6.1 Theoretical Background: The Role of Penguins and α -Extraction

Any mode with a contribution from $b \rightarrow du\bar{u}$ is a possible source of measurement of α . This chapter analyses the possibilities of extracting α in final states with two, three, and four final-state pions. It begins with some theoretical background. Section 6.1.1 reviews the methods for extracting the angle α of the unitarity triangle if penguin contributions can be ignored. In the BABAR Technical Design Report it was assumed that these methods would be sufficient and expected errors on α were determined under that assumption. However the determination of α is now expected to be complicated by the fact that penguin contributions may be large. In this case additional techniques, reviewed in Section 6.1.2, are needed to extract α cleanly. Several studies in this chapter explore the impact on the extraction of α of significant penguin contributions. In addition, in the presence of significant penguin contributions, the prospects for observing direct CP violation improve. Some expectations for such effects are discussed in Section 6.2.

The simulation work described in this chapter offers a view of both the opportunities and the difficulties in measuring α . Three themes emerge, (1) that the theoretical uncertainty on α is large in any analysis that does not include an isospin-based method to remove penguin pollution; (2) that analyses which do treat the full problem are difficult and will need several years of data taking before they can be expected to yield reliable answers; and (3) that efforts to test and improve theoretical model-dependent estimates of the various penguin and tree contributions are important because such methods may reduce the theoretical uncertainties in calculating penguin-induced shifts in α and thus provide the best determinations of alpha for some time to come. Refinement of models by comparison with data in many channels will be a significant part of the work of BABAR and should eventually contribute to significant reduction of theoretical uncertainties.

Finally some sample channels are studied as possible searches for direct CP violation in B decays. The results again indicate that, at least for these channels, a large data sample will be needed to yield well-controlled asymmetry measurements.

6.1.1 Extraction of α -Ignoring Penguins

The angle α can be obtained through measurements of CP -violating asymmetries involving final states which can be either CP eigenstates or not. If the state of interest is a CP eigenstate, it was shown in Chapter 1 how to relate an asymmetry to CKM parameters. If only a single weak-decay amplitude contributes to $B \rightarrow f_{CP}$, that is, if penguin contributions are negligible, then $|\bar{A}_{f_{CP}}/A_{f_{CP}}| = 1$, so that

$$a_{f_{CP}} = -\text{Im}\lambda_{f_{CP}} \sin(\Delta m_B t). \quad (6.1)$$

In this case $\lambda_{f_{CP}}$ is a pure phase, *i.e.*, $\text{Im}\lambda$ is one of the angles of the unitarity triangle. In particular, for the decay $B \rightarrow \pi\pi$, $\text{Im}\lambda_{\pi\pi} = \sin 2\alpha$.

The case where the final state f is not a CP eigenstate is considerably more complicated. There are four separate amplitudes for B^0 and \bar{B}^0 to decay to f and \bar{f} :

$$\begin{aligned} A(B^0 \rightarrow f) &\equiv A_f = |A_f|e^{i\theta_f}, \\ A(\bar{B}^0 \rightarrow f) &\equiv \bar{A}_f = |\bar{A}_f|e^{i\bar{\theta}_f}, \\ A(B^0 \rightarrow \bar{f}) &\equiv A_{\bar{f}} = |A_{\bar{f}}|e^{i\theta_{\bar{f}}}, \\ A(\bar{B}^0 \rightarrow \bar{f}) &\equiv \bar{A}_{\bar{f}} = |\bar{A}_{\bar{f}}|e^{i\bar{\theta}_{\bar{f}}}. \end{aligned} \quad (6.2)$$

The rates for the physical, time-evolved $B_{\text{phys}}^0(t)$ and $\bar{B}_{\text{phys}}^0(t)$ states to decay into f can then be written [1]

$$\begin{aligned} \Gamma(B_{\text{phys}}^0(t) \rightarrow f) &= e^{-\Gamma t} A^2 \times \\ &\quad \left\{ 1 + R \cos(\Delta m_B t) - D \sin(2\phi_M - \theta_f + \bar{\theta}_f) \sin(\Delta m_B t) \right\} \\ \Gamma(\bar{B}_{\text{phys}}^0(t) \rightarrow f) &= e^{-\Gamma t} A^2 \times \\ &\quad \left\{ 1 - R \cos(\Delta m_B t) + D \sin(2\phi_M - \theta_f + \bar{\theta}_f) \sin(\Delta m_B t) \right\} \end{aligned} \quad (6.3)$$

where ϕ_M is the phase of B^0 - \bar{B}^0 mixing, and

$$A^2 \equiv \frac{1}{2} (|A_f|^2 + |\bar{A}_f|^2), \quad R \equiv \frac{|A_f|^2 - |\bar{A}_f|^2}{|A_f|^2 + |\bar{A}_f|^2}, \quad D \equiv 2 \frac{|A_f||\bar{A}_f|}{|A_f|^2 + |\bar{A}_f|^2}. \quad (6.4)$$

Similarly, the rates for $B_{\text{phys}}^0(t)$ and $\bar{B}_{\text{phys}}^0(t)$ states to decay into \bar{f} are

$$\begin{aligned} \Gamma(B_{\text{phys}}^0(t) \rightarrow \bar{f}) &= e^{-\Gamma t} \bar{A}^2 \times \\ &\quad \left\{ 1 - \bar{R} \cos(\Delta m_B t) - \bar{D} \sin(2\phi_M + \bar{\theta}_{\bar{f}} - \theta_{\bar{f}}) \sin(\Delta m_B t) \right\} \\ \Gamma(\bar{B}_{\text{phys}}^0(t) \rightarrow \bar{f}) &= e^{-\Gamma t} \bar{A}^2 \times \\ &\quad \left\{ 1 + \bar{R} \cos(\Delta m_B t) + \bar{D} \sin(2\phi_M + \bar{\theta}_{\bar{f}} - \theta_{\bar{f}}) \sin(\Delta m_B t) \right\} \end{aligned} \quad (6.5)$$

where

$$\bar{A}^2 \equiv \frac{1}{2} (|A_{\bar{f}}|^2 + |\bar{A}_{\bar{f}}|^2), \quad \bar{R} \equiv \frac{|A_{\bar{f}}|^2 - |\bar{A}_{\bar{f}}|^2}{|A_{\bar{f}}|^2 + |\bar{A}_{\bar{f}}|^2}, \quad \bar{D} \equiv 2 \frac{|A_{\bar{f}}||\bar{A}_{\bar{f}}|}{|A_{\bar{f}}|^2 + |\bar{A}_{\bar{f}}|^2}. \quad (6.6)$$

CP conservation requires that

$$|A_{\bar{f}}| = |\bar{A}_f|, \quad |\bar{A}_{\bar{f}}| = |A_f|, \quad (6.7)$$

$$\sin(2\phi_M - \theta_f + \bar{\theta}_{\bar{f}}) = \sin(2\phi_M + \bar{\theta}_{\bar{f}} - \theta_{\bar{f}}). \quad (6.8)$$

CP violation occurs if any of these equalities is not satisfied.

The above expressions for the decays of $B_{\text{phys}}^0(t)$ and $\bar{B}_{\text{phys}}^0(t)$ to f and \bar{f} are completely general. However, when one assumes that each decay is dominated by a single weak amplitude (*i.e.*, that penguins and any new physics effects are negligible), the expressions simplify. In this case, the parameters in the amplitudes for the decays of B^0 and \bar{B}^0 to f and \bar{f} obey certain equalities which reflect their CP transformation relationships:

$$\begin{aligned} |A_{\bar{f}}| &= |\bar{A}_f|, & |\bar{A}_{\bar{f}}| &= |A_f|, \\ \theta_f &= \phi_{D_f} + \delta, & \bar{\theta}_{\bar{f}} &= -\phi_{D_f} + \delta, \\ \theta_{\bar{f}} &= \phi_{D_{\bar{f}}} + \delta', & \bar{\theta}_f &= -\phi_{D_{\bar{f}}} + \delta'. \end{aligned} \quad (6.9)$$

In the above, ϕ_{D_f} and $\phi_{D_{\bar{f}}}$ represent the weak-CKM phases of the decays of B^0 to f and \bar{f} respectively, while δ and δ' are the strong phases. With these equalities, the expressions in Eqs. (6.4) and (6.6) become very similar: $A^2 = \bar{A}^2$, $R = -\bar{R}$, $D = \bar{D}$. The above equalities give

$$\begin{aligned} \sin(2\phi_M - \theta_f + \bar{\theta}_{\bar{f}}) &= \sin(2\phi_M - \phi_{D_f} - \phi_{D_{\bar{f}}} - \Delta\delta), \\ \sin(2\phi_M + \bar{\theta}_{\bar{f}} - \theta_{\bar{f}}) &= \sin(2\phi_M - \phi_{D_f} - \phi_{D_{\bar{f}}} + \Delta\delta), \end{aligned} \quad (6.10)$$

where $\Delta\delta \equiv \delta - \delta'$. The CP -violating weak-CKM phase is given by the quantity $2\Phi \equiv 2\phi_M - \phi_{D_f} - \phi_{D_{\bar{f}}}$. From measurements of the time-dependent decay distributions one can obtain $S \equiv \sin(2\Phi + \Delta\delta)$ and $\bar{S} \equiv \sin(2\Phi - \Delta\delta)$, and from these one can extract $\sin^2 2\Phi$ up to a two-fold ambiguity:

$$\sin^2 2\Phi = \frac{1}{2} \left[1 + S\bar{S} \pm \sqrt{(1 - S^2)(1 - \bar{S}^2)} \right]. \quad (6.11)$$

The true value of $\sin^2 2\Phi$ is given by one of the signs on the right-hand side, while the other gives $\cos^2 \Delta\delta$. However, this discrete ambiguity can in principle be removed by comparison with other final states which have the same weak-phase 2Φ , but different strong phases. Note that, if the three different time-dependent terms (1, cos, sin) can be isolated with sufficient accuracy, it is not necessary to measure all four time-dependent rates $B_{\text{phys}}^0(t)$, $\bar{B}_{\text{phys}}^0(t) \rightarrow f, \bar{f}$. The measurement of one of the rates in Eq. (6.3) and one of the rates in Eq. (6.5) is sufficient to obtain the above phase information.

Thus, assuming penguins make negligible contributions, this technique can be used to extract the CP angle α : one must measure the decays of $B_{\text{phys}}^0(t)$ and $\bar{B}_{\text{phys}}^0(t)$ to such final states as $\rho^+ \pi^-$ or $a_1^+ \pi^-$. When penguins are significant these methods yield a quantity, denoted α_{eff} , which differs

from the true α by an unknown amount, which we will denote as $\kappa_f/2$. This quantity is channel-dependent because it depends on the ratio of tree-dominated to penguin-only contributions. Model-dependent calculations can be used to estimate this shift in α but significant theoretical uncertainty remains. Eventually, this uncertainty may be reduced by restricting the value of the penguin terms from other measurements, for example via the SU(3) relationships discussed below. As models become better tested by a variety of measurements the uncertainties that arise due to their application may also be reduced, even without the use of such SU(3) relationships. Eventually, however, one would like to be able to use model-independent methods that take the penguin contributions into account correctly. These are discussed below.

6.1.2 Extraction of α in the Presence of Penguins

In most cases there is in fact more than one weak-decay amplitude contributing to a decay, which can always be written as a tree-dominated plus a penguin-only term (see Section 1.5.2). In the channels of interest here, the weak-phase difference between these terms is α .

For the case where f is a CP eigenstate the amplitudes for $B \rightarrow f_{CP}$ and $\bar{B} \rightarrow f_{CP}$ can then be written as

$$\begin{aligned} A_{f_{CP}} &= T e^{i\phi_T} e^{i\delta_T} + P e^{i\phi_P} e^{i\delta_P} , \\ \bar{A}_{f_{CP}} &= T e^{-i\phi_T} e^{i\delta_T} + P e^{-i\phi_P} e^{i\delta_P} , \end{aligned} \quad (6.12)$$

where T , ϕ_T and δ_T (P , ϕ_P and δ_P) represent the magnitude, the weak phase and the strong phase of the tree-dominated (penguin-only) amplitude, respectively.

Now suppose that penguin contributions are non-negligible and that $\phi_T \neq \phi_P$. In this case it is clear from Eq. (6.12) that $\lambda_{f_{CP}}$ (Eq. (1.24)) depends on a function of tree and penguin parameters, so that it no longer cleanly measures a single CKM phase. Thus the presence of significant ‘‘penguin pollution’’ spoils the clean extraction of the angles of the unitarity triangle from CP -violating asymmetries. In general, the presence of non-negligible penguin contributions will also lead to direct CP violation (see Section 6.3), that is, $|\lambda_{f_{CP}}| \neq 1$. In the presence of direct CP violation, the time-dependent CP asymmetry contains a $\cos(\Delta m_B t)$ term, the coefficient of which can also be measured. However, this need not be the case. If the strong phases are equal, $\delta_T = \delta_P$, then $\lambda_{f_{CP}}$ is a pure phase (*i.e.*, $|\lambda_{f_{CP}}| = 1$). However, this phase depends on both tree and penguin parameters, so that there is still a shift in α due to penguin contributions, even though there is no direct CP violation.

Although the above discussion has been made for the case where the final state is a CP eigenstate, it applies equally well when the final state is not a CP eigenstate (*e.g.*, $\rho\pi$, $a_1\pi$, *etc.*). If penguin contributions are important in decays to such final states, then the CP asymmetries alone do not cleanly probe the angles of the unitarity triangle.

In fact, present experimental information suggests that penguin pollution may well be significant in $B^0 \rightarrow \pi^+\pi^-$. CLEO has observed the decay $B^0 \rightarrow \pi^-K^+$: they have $N_{K\pi} = 21.6_{-6.0}^{+6.8}$ events, which translates into a branching ratio of 1.5×10^{-5} [2]. For $B^0 \rightarrow \pi^+\pi^-$ they have $9.9_{-5.1}^{+6.0}$ events, leading to an upper limit of 1.5×10^{-5} [2]. While one cannot draw rigorous conclusions from these data, one can still make a back-of-the-envelope estimate as follows. The quantity of interest is a P/T , where

$$P \equiv A(B^0 \rightarrow \pi^+\pi^-)|_{\text{penguin}} , \quad T \equiv A(B^0 \rightarrow \pi^+\pi^-)|_{\text{tree}} . \quad (6.13)$$

This ratio can be written

$$\frac{P}{T} = \frac{A(B^0 \rightarrow \pi^-K^+)|_{\text{penguin}}}{T} \frac{P}{A(B^0 \rightarrow \pi^-K^+)|_{\text{penguin}}} , \quad (6.14)$$

This ratio can be estimated with the help of some assumptions. First, take the central values of the number of events at face value, so that the branching ratio for $B^0 \rightarrow \pi^+\pi^-$ is half that of $B^0 \rightarrow \pi^-K^+$. Second, assume that the observed events for $B^0 \rightarrow \pi^-K^+$ and $B^0 \rightarrow \pi^+\pi^-$ are due only to the $b \rightarrow s$ penguin and the $b \rightarrow u\bar{u}d$ tree amplitudes, respectively. This implies that

$$\frac{A(B^0 \rightarrow \pi^-K^+)|_{\text{penguin}}}{T} = \sqrt{2} . \quad (6.15)$$

The second term in Eq. (6.14) is the ratio of $b \rightarrow d$ and $b \rightarrow s$ penguins. This can be written

$$\frac{P}{A(B^0 \rightarrow \pi^-K^+)|_{\text{penguin}}} = \left| \frac{V_{td}}{V_{ts}} \right| \times \text{an SU(3)-breaking factor} . \quad (6.16)$$

The size of the SU(3)-breaking effects is not known. However, as a crude guess, take this factor to be roughly $f_\pi/f_K \sim 1/1.2$. The ratio of CKM matrix elements is constrained to be in the range [3]

$$0.15 \leq \left| \frac{V_{td}}{V_{ts}} \right| \leq 0.34 . \quad (6.17)$$

Putting all the factors together, gives

$$0.18 \leq \frac{P}{T} \leq 0.4 . \quad (6.18)$$

These numbers should not be taken literally, since they neglect both theoretical and experimental uncertainties other than the range of $\left| \frac{V_{td}}{V_{ts}} \right|$. However they show that the CLEO data suggests that penguins are likely to be significant in $B^0 \rightarrow \pi^+\pi^-$ and, by extension, in $B^0 \rightarrow \rho\pi$ and $a_1\pi$.

The tool to separate the tree and penguin contributions is isospin analysis. Isospin amplitudes $I_{\Delta I, I_f}$ can be labeled by the ΔI value of the b -quark decay and by the I_f of the final state, which includes the spectator quark. The key observation is that a gluon is pure $I = 0$, so that the dominant gluonic $b \rightarrow d$ penguins are pure $\Delta I = \frac{1}{2}$. On the other hand, the tree-level $b \rightarrow u\bar{u}d$ decays have both $\Delta I = \frac{3}{2}$ and $\Delta I = \frac{1}{2}$ components. Thus, if the $\Delta I = \frac{3}{2}$ piece can be isolated, then the tree

Table 6-1. Isospin decomposition for $B \rightarrow \pi\pi$, $B \rightarrow \pi K$ and $B \rightarrow \rho\pi$ in terms of the isospin amplitudes $A_{\Delta I, I_f}$, where ΔI and I_f are the isospin change of the transition and the final-state isospin, respectively. The CP -even part of $B \rightarrow \rho\rho$ decays follow the same pattern as $B \rightarrow \pi\pi$; $B \rightarrow \pi K^*$ and $B \rightarrow \rho K$ are analogous to $B \rightarrow \pi K$; $B \rightarrow a_1\pi$ is similar to $B \rightarrow \rho\pi$.

Channel	Decay Amplitudes
$\pi\pi$	$A(B^+ \rightarrow \pi^+\pi^0) = \frac{\sqrt{3}}{2}A_{3/2,2}$ $\frac{1}{\sqrt{2}}A(B^0 \rightarrow \pi^+\pi^-) = \frac{1}{\sqrt{12}}A_{3/2,2} - \sqrt{\frac{1}{6}}A_{1/2,0}$ $A(B^0 \rightarrow \pi^0\pi^0) = \frac{1}{\sqrt{3}}A_{3/2,2} + \sqrt{\frac{1}{6}}A_{1/2,0}$
πK	$A(B^+ \rightarrow \pi^0 K^+) = \frac{2}{3}A_{1,3/2} + \frac{1}{3}A_{1,1/2} - \sqrt{\frac{1}{3}}A_{0,1/2}$ $A(B^0 \rightarrow \pi^0 K^0) = \frac{2}{3}A_{1,3/2} + \frac{1}{3}A_{1,1/2} + \sqrt{\frac{1}{3}}A_{0,1/2}$ $\frac{1}{\sqrt{2}}A(B^+ \rightarrow \pi^+ K^0) = \frac{1}{3}A_{1,3/2} - \frac{1}{3}A_{1,1/2} + \sqrt{\frac{1}{3}}A_{0,1/2}$ $\frac{1}{\sqrt{2}}A(B^0 \rightarrow \pi^- K^+) = \frac{1}{3}A_{1,3/2} - \frac{1}{3}A_{1,1/2} - \sqrt{\frac{1}{3}}A_{0,1/2}$
$\rho\pi$	$A(B^+ \rightarrow \rho^+\pi^0) = \frac{1}{2}\sqrt{\frac{3}{2}}A_{3/2,2} - \frac{1}{2}\sqrt{\frac{1}{2}}A_{3/2,1} + \sqrt{\frac{1}{2}}A_{1/2,1}$ $A(B^+ \rightarrow \rho^0\pi^+) = \frac{1}{2}\sqrt{\frac{3}{2}}A_{3/2,2} + \frac{1}{2}\sqrt{\frac{1}{2}}A_{3/2,1} - \sqrt{\frac{1}{2}}A_{1/2,1}$ $A(B^0 \rightarrow \rho^+\pi^-) = \frac{1}{2}\sqrt{\frac{1}{3}}A_{3/2,2} - \frac{1}{2}A_{3/2,1} + \frac{1}{2}A_{1/2,1} - \sqrt{\frac{1}{6}}A_{1/2,0}$ $A(B^0 \rightarrow \rho^-\pi^+) = \frac{1}{2}\sqrt{\frac{1}{3}}A_{3/2,2} + \frac{1}{2}A_{3/2,1} - \frac{1}{2}A_{1/2,1} - \sqrt{\frac{1}{6}}A_{1/2,0}$ $A(B^0 \rightarrow \rho^0\pi^0) = \sqrt{\frac{1}{3}}A_{3/2,2} + \sqrt{\frac{1}{6}}A_{1/2,0}$

contribution, which contains the weak phase to be measured, is thereby isolated. Inclusion of the spectator quark then gives final isospin of 0 or 1 for the gluonic penguin contributions, but 0, 1 or 2 for the tree contributions. (Similar arguments apply to $b \rightarrow s$ penguins and $b \rightarrow u\bar{u}s$ tree amplitudes.)

Isospin analysis can be used for a variety of final states [4]–[5]: $\pi\pi$, $\rho\pi$, $a_1\pi$, $\rho\rho$, $K\pi$, $K^*\pi$, $K\rho$, *etc.* Isospin analysis for some final-state particle pairs will be discussed separately below. Table 6-1 lists the isospin amplitudes for all relevant channels for these states. Note that, in all cases, there is at least one isospin amplitude which can be reached only via tree diagrams: $A_{3/2,2}$ for $B \rightarrow \pi\pi$, $A_{1,3/2}$ for $B \rightarrow \pi K$, and $A_{3/2,2}$ and $A_{3/2,1}$ for $B \rightarrow \rho\pi$. Isolation of such isospin amplitudes allows the removal of penguin pollution. (Note: this statement is only true to the extent that electroweak penguins can be neglected [6] The effects of such contributions in the context of the various final states are discussed below.) Note also that the decay $B \rightarrow DD$ is not included in the list. This is because both tree and penguin diagrams correspond to $\Delta I = 1/2$ transitions. Thus, an isospin analysis cannot be used to remove penguin pollution in this case.

6.1.2.1 $B^0 \rightarrow \pi^+\pi^-$

In the absence of penguin contributions, the asymmetry in $B^0 \rightarrow \pi^+\pi^-$ measures $\sin 2\alpha$. However, penguins can contribute to this decay. Indeed, as was argued above, it appears that such penguin contributions are sizeable. Since the weak phase of the penguin diagram is different from that of the tree diagram, penguin pollution can affect the clean extraction of α from this process. An isospin analysis can be used to eliminate the penguin pollution in this case [4].

The isospin decomposition of the amplitudes $A^{+0} \equiv A(B^+ \rightarrow \pi^+\pi^0)$, $A^{+-} \equiv A(B^0 \rightarrow \pi^+\pi^-)$ and $A^{00} \equiv A(B^0 \rightarrow \pi^0\pi^0)$ is shown in Table 6-1. Note that because of Bose statistics the $J = 0$ two-pion state produced in B decay has no $I = 1$ contribution. Thus the three two-pion decay amplitudes depend only on two isospin amplitudes, hence there is one relationship,

$$\frac{1}{\sqrt{2}}A^{+-} + A^{00} = A^{+0}, \quad (6.19)$$

between them. Thus they form a triangle, as drawn in Fig. 6-1.

The amplitudes for the CP -conjugate processes $B^- \rightarrow \pi^-\pi^0$, $\bar{B}^0 \rightarrow \pi^+\pi^-$ and $\bar{B}^0 \rightarrow \pi^0\pi^0$ are obtained from the A amplitudes by simply changing the sign of the CKM phases; the strong phases remain the same. These amplitudes also form a triangle:

$$\frac{1}{\sqrt{2}}\bar{A}^{+-} + \bar{A}^{00} = A^{-0}. \quad (6.20)$$

The measurements of the total rates for $B^+ \rightarrow \pi^+\pi^0$ and $B^- \rightarrow \pi^-\pi^0$ yield $|A^{+0}|$ and $|A^{-0}|$, respectively. The measurement of the time-dependent decay rates for $B^0(t) \rightarrow \pi^+\pi^-$ and $\bar{B}^0(t) \rightarrow$

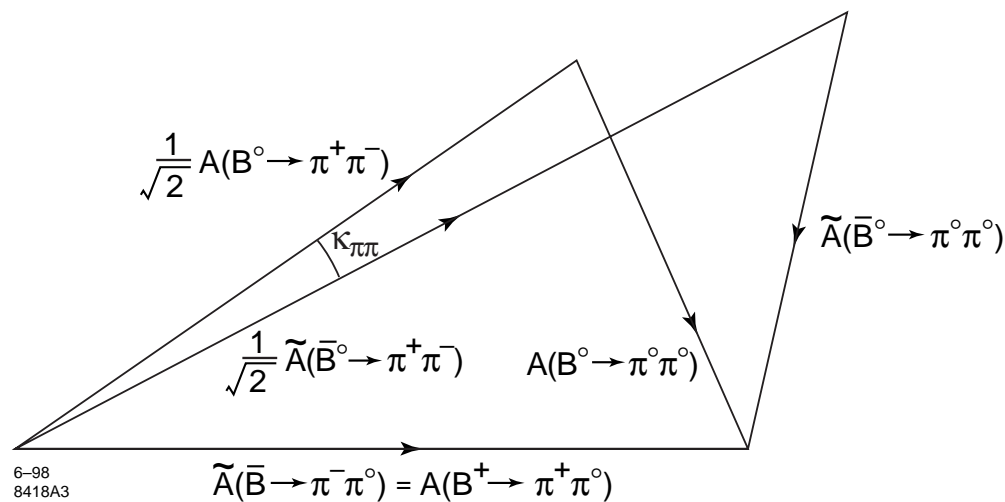


Figure 6-1. Isospin analysis of $B \rightarrow \pi\pi$ decays.

$\pi^+\pi^-$ allow the extraction of $|A^{+-}|$ and $|\bar{A}^{+-}|$ as well as the asymmetry which gives $\text{Im}\lambda_{\pi^+\pi^-}$. For the $\pi^0\pi^0$ final state, the time dependence will not be measurable at BABAR, but the time-independent rates still allow one to obtain $|A^{00}|$ and $|\bar{A}^{00}|$. The six magnitudes determine the shapes of two isospin triangles.

The key observation is that, since the penguin diagram is purely $\Delta I = 1/2$, the A^{+0} amplitude is fed solely from the tree diagram. This means that $|A^{+0}| = |\bar{A}^{-0}|$. In other words, the two triangles have a base in common. (However, due to the fact that both the tree and penguin diagrams contribute to the $I = 0$ final state, $|A^{+-}| \neq |\bar{A}^{+-}|$ and $|A^{00}| \neq |\bar{A}^{00}|$ in general.)

In fact, it is convenient to superimpose the triangles defined in Eqs. (6.19) and (6.20) by introducing

$$\tilde{A}^{ij} \equiv e^{2i\phi_T} \bar{A}^{ij} \quad (6.21)$$

and in particular,

$$\tilde{A}^{-0} \equiv e^{2i\phi_T} A^{-0} \quad (6.22)$$

where ϕ_T is the CKM phase of the tree diagram. Then $\tilde{A}^{-0} = A^{+0}$. From the resulting Fig. 6-1 one can determine the angle $\kappa_{\pi\pi}$ between A^{+-} and \tilde{A}^{+-} , up to a four-fold discrete ambiguity corresponding to the choice of orientation (above or below A^{+0}) of each of the triangles. Combined with the two-fold ambiguity that comes because only the sine of the angle $2\alpha + \kappa_{\pi\pi}$ is measured, this then leaves an eight-fold ambiguity in the value of α . Hence isospin analysis will reduce the uncertainty in α significantly only if the error on each possible choice of $\kappa_{\pi\pi}$ is small.

The CP asymmetry in $B^0 \rightarrow \pi^+\pi^-$ is given by

$$\text{Im}\lambda_{\pi^+\pi^-} = \text{Im} \left[e^{-2i\alpha} \frac{\tilde{A}^{+-}}{A^{+-}} \right]. \quad (6.23)$$

Thus the quantity \tilde{A}^{+-}/A^{+-} gives the penguin effect on the relationship between the angle α and the measured asymmetry. The two-triangle construction gives the magnitude and phase, $\kappa_{\pi\pi}$, of this quantity, so that α can in principle be extracted cleanly, even in the presence of penguins.

The experimental prospects for carrying out such an analysis are discussed in detail in Section 6.4. A crucial ingredient in the above analysis is the rate for $B^0 \rightarrow \pi^0\pi^0$. Present theoretical estimates put this branching ratio at $O(10^{-6})$ or even smaller, which would make its measurement very challenging. However, it should also be noted that these estimates all assume that color suppression is significant in B decays to light mesons and small penguins. It is known and experimentally confirmed that color suppression is important in the decays of B s to heavy mesons: for example, $\mathcal{B}(B^0 \rightarrow \Psi K^0)$ is only about 10% of $\mathcal{B}(B^0 \rightarrow D_s^+ D^-)$. However, color suppression does not hold for D decays to light mesons: for example,

$$\mathcal{B}(D^0 \rightarrow \pi^0\pi^0) \cong \mathcal{B}(D^0 \rightarrow \pi^+\pi^-)/2.$$

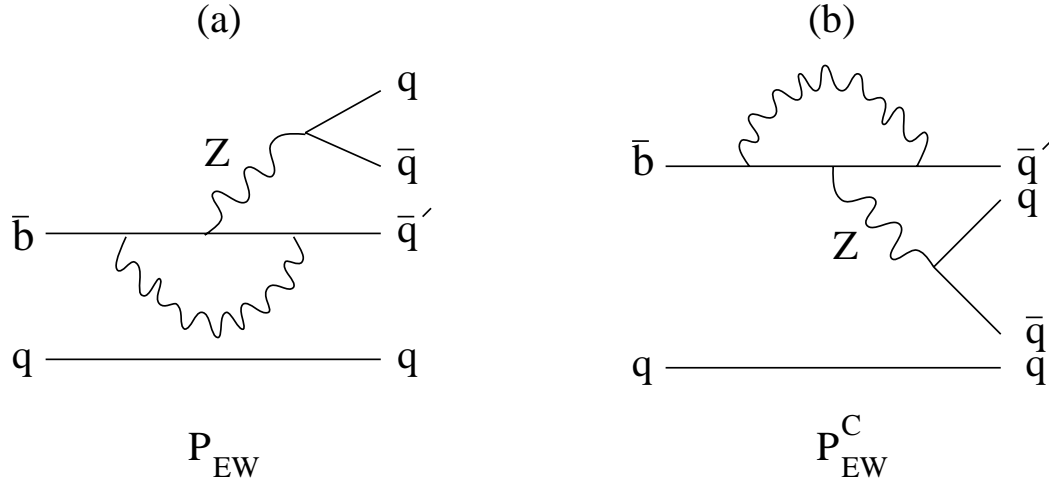


Figure 6-2. (a) Color-allowed Z -penguin, (b) Color-suppressed Z -penguin.

This could indicate that long-distance rescattering effects are large in such decays. If such large rescattering effects are also present in $B \rightarrow \pi\pi$, the branching ratio of $B^0 \rightarrow \pi^0\pi^0$ may be considerably larger than naive expectations, perhaps even as large as $\mathcal{B}(B^0 \rightarrow \pi^+\pi^-)/2$, and the isospin analysis could then yield more accurate results than those found in the study given below.

One potential problem from the theory side with the isospin method is the presence of electroweak penguins (EWP) [6]. The main EWP contributions to $B \rightarrow \pi\pi$ come from diagrams with virtual Z exchange (Fig. 6-2). Since the couplings of the Z contain both $I = 1$ and $I = 0$ terms, these contribute also to $\Delta I = \frac{3}{2}$, and their effects cannot be separated from tree contributions via isospin analysis. Fortunately, the effects of EWPs are expected to be small in this channel. Since both the W and the Z are color singlet particles, there are two contributions (color-allowed and color-suppressed) for each tree or electroweak-penguin quark diagram, which are defined by which quark lines go to which final hadron. Including both color-allowed and color-suppressed EWPs (Fig. 6-2), the $B \rightarrow \pi\pi$ amplitudes can be written [7].

$$\begin{aligned}
 A(B^+ \rightarrow \pi^+\pi^0) &= -\frac{1}{\sqrt{2}}(T + C + P_{EW} + P_{EW}^C), \\
 A(B^0 \rightarrow \pi^+\pi^-) &= -(T + P + E + \frac{2}{3}P_{EW}^C), \\
 A(B^0 \rightarrow \pi^0\pi^0) &= -\frac{1}{\sqrt{2}}(C - P - E + P_{EW}) + \frac{1}{3}P_{EW}^C.
 \end{aligned} \tag{6.24}$$

In the above, T , C , P , E , P_{EW} , and P_{EW}^C represent the color-allowed tree contribution, the color-suppressed tree contribution, the gluonic penguin, the exchange diagram, the color-allowed EWP contribution, and the color-suppressed EWP contribution, respectively. These various contributions are expected to obey roughly the following hierarchy:

$$\begin{aligned}
1 &: |T|, \\
\mathcal{O}(\bar{\lambda}) &: |C|, |P|, \\
\mathcal{O}(\bar{\lambda}^2) &: |E|, |P_{EW}| \\
\mathcal{O}(\bar{\lambda}^3) &: |P_{EW}^C|,
\end{aligned} \tag{6.25}$$

where $\bar{\lambda} \sim 20\%$. (Note that the factor $\bar{\lambda}$ is simply a size-counting factor which can come either from CKM factors, from color suppression, or from coupling constant ratio and loop counting.) The above amplitudes do indeed form the triangles of Eq. (6.19) and (6.20). However, the key point is that there are now two amplitudes, with different weak phases, which contribute to $B^+ \rightarrow \pi^+ \pi^0$ and likewise to its CP conjugate. Thus, the two triangles no longer have a common base. This is shown in Fig. 6-3. Therefore, due to the presence of EWPs, there is a theoretical uncertainty $\Delta\theta_f$ in the extraction of the angle $\kappa_{\pi\pi}$, which is the relative phase between the \tilde{A}^{+-} and A^{+-} amplitudes. This leads to an uncertainty in the determination of α [7]:

$$\Delta\alpha \approx \frac{1}{2}\Delta\theta_f \leq \left| \frac{P_{EW} + P_{EW}^C}{T + C} \right|. \tag{6.26}$$

It can however be seen from the above hierarchy that this uncertainty is small, at most $O(\bar{\lambda}^2) \sim 5\%$. Therefore the presence of electroweak penguins does not significantly affect the isospin analysis. (Note that this conclusion is largely independent of assumptions about the size of color suppression

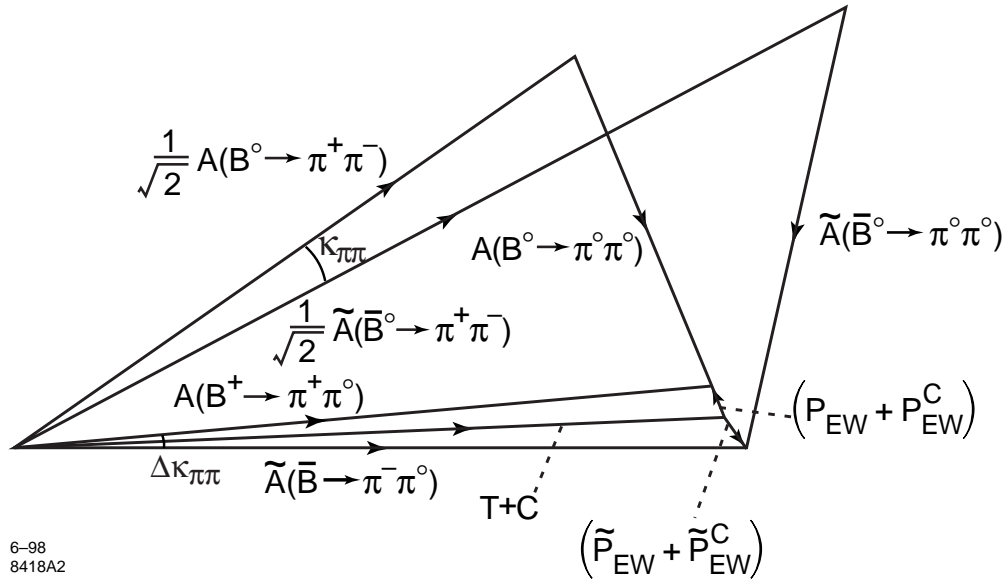


Figure 6-3. Isospin analysis of $B \rightarrow \pi\pi$ decays with the inclusion of electroweak penguins.

in $B \rightarrow \pi\pi$ decays. Even if the C (and P_{EW}^C) contributions turn out to be larger than expected, the uncertainty in α is still at most about 5%.)

6.1.2.2 $B^0 \rightarrow \rho\rho$

At first glance, the decays $B \rightarrow \rho\rho$ appear to be completely analogous to $B \rightarrow \pi\pi$. However, there is an important difference. Because the ρ is a vector meson, the $\rho\rho$ pair can be in a state of angular momentum $L = 0, 1$ or 2 . States of even and odd angular momentum correspond to states of even and odd CP , respectively. However, the sign of the CP asymmetry for a CP -even state will be opposite to that of a CP -odd state. Thus, if one does not separate the CP -odd component of the $\rho\rho$ final state from the CP -even component, there will be a dilution of the CP asymmetry due to a cancellation between these two components. This dilution factor is unknown since *a priori* there is no information about the relative sizes of the CP -even and CP -odd components. Thus it is not possible to extract α by simply measuring the asymmetry in $B \rightarrow \rho\rho$. This is independent of whether or not there is penguin pollution.

However, it is possible to separate out the even ($L = 0, 2$) and odd ($L = 1$) angular-momentum components of $\rho\rho$ through an angular analysis, as discussed in Section 5.1.3. Once this is done, then the $\rho^+\rho^-$ and $\rho^0\rho^0$ final states are CP eigenstates, and so can be used to probe the angle α . If penguins are unimportant, then all asymmetries measure $\pm \sin 2\alpha$, with the $+$ ($-$) sign corresponding to the CP -even (CP -odd) final state. Of course, here again penguin contributions may be important, so an isospin analysis is needed to remove the penguin pollution. For the CP -even components, which contain $I = 0$ and 2 , the analysis is identical to that developed above for $B \rightarrow \pi\pi$: the $I = 2$ amplitude, which is pure tree, can be isolated by measurements of the rates for $B^+ \rightarrow \rho^+\rho^0$, $B^0(t) \rightarrow \rho^+\rho^-$ and $B^0 \rightarrow \rho^0\rho^0$, along with their CP -conjugates. (As in the $\pi\pi$ case, electroweak-penguin contributions are expected to be small.) However, an isospin analysis will not work for the CP -odd components. Since these have $I = 1$ only, which can be fed by both the tree and the penguin diagrams, there is no way to remove the penguin pollution.

6.1.2.3 $B^0 \rightarrow \rho\pi$

As in the case of the $B \rightarrow \pi\pi$ modes, the $B \rightarrow \pi\pi\pi$ channels provide an independent means of extracting the CKM angle α [1, 8]. The full three-pion distribution contains both CP -odd and CP -even contributions, the ratios of which cannot be reliably calculated. Several hadronic resonances can contribute, and the nonresonant $B \rightarrow 3\pi$ decay may also play a significant role. However if two of the pions form a resonant state, the angular momentum is determined and hence CP -eigenstates can be made from combinations of different charge states, with the CP -eigenvalues specified by the spin of the resonance. In what follows, it is assumed that the resonant contributions are dominant and, among them, the $\rho(770)$ is the main one. Once the ρ -meson decays to two pions, the three decays $B^0 \rightarrow \rho^+\pi^-$, $B^0 \rightarrow \rho^-\pi^+$ and $B^0 \rightarrow \rho^0\pi^0$ all result in a $\pi^+\pi^-\pi^0$ final state.

Neutral B Dalitz-plot Analysis

As recognized by Snyder and Quinn [8], the decay to $\rho\pi$ provides enough observables to determine α in principle, even in the presence of penguins. The analysis of the time-dependent three-pion Dalitz plot including interference effects between the resonances offers three attractive features:

- From decays of neutral B s alone, it allows the determination of α , even in the presence of gluonic penguin contributions.
- It may resolve all the discrete phase ambiguities that remain after the traditional methods, with the single exception of $\alpha \rightarrow \alpha + \pi$.¹
- It may lead to the measurement of some QCD matrix elements, including those of penguin contributions. This will be useful in constraining and selecting models for use elsewhere.

The B^0 weak-decay amplitudes arise from “tree-dominated” contributions, for which the phase comes from $V_{ud}V_{ub}^*$ and from “penguin-only” contributions, for which the phase comes from $V_{td}V_{tb}^*$, and thus is the same as the Standard Model weak phase of the B^0 - \bar{B}^0 mixing. The only CP -violating phase in the problem is thus

$$\arg\left(\frac{V_{ud}V_{ub}^*}{V_{td}V_{tb}^*}\right) = \beta + \gamma \equiv \pi - \alpha, \quad (6.27)$$

where the last equality defines the quantity α .² The isospin decomposition for the various $B^0 \rightarrow \rho\pi$ decay amplitudes was shown in Table 6-1 [9]. There are four independent isospin amplitudes: $A_{3/2,2}$, $A_{3/2,1}$, $A_{1/2,1}$ and $A_{1/2,0}$, but only three linear combinations of them contribute to the neutral B decays. The penguins contribute only to the $\Delta I = 1/2$ amplitudes, so there are only two independent penguin amplitudes.³ It is convenient to incorporate the weak phase of the mixing

¹This ambiguity is irreducible (unless there is theoretical input to resolve it), thus its presence is to be understood everywhere in what follows.

²It is often said that one tests the Standard Model by testing the relationship $\alpha + \beta + \gamma = \pi$; in fact there are only two independent parameters defining the (scaled) Standard Model Unitarity triangle and one tests whether different ways of measuring these parameters give consistent results.

³If there are sizeable penguin contributions proportional to $V_{ud}V_{ub}^*$, as claimed by various authors [10], they can simply be absorbed into the tree amplitude, see Section 1.5.2. The essential point is that the contribution proportional to $V_{td}V_{tb}^*$ comes only from a $\Delta I = 1/2$ operator. This is true up to the small correction from electroweak-penguin contributions.

and write the amplitudes with the weak phases displayed explicitly as follows

$$\begin{aligned}
A(B^0 \rightarrow \rho^+ \pi^-) &\equiv A^{+-} = e^{-i\alpha} T^{+-} + P^{+-}, \\
A(B^0 \rightarrow \rho^- \pi^+) &\equiv A^{-+} = e^{-i\alpha} T^{-+} + P^{-+}, \\
A(B^0 \rightarrow \rho^0 \pi^0) &\equiv A^{00} = e^{-i\alpha} T^{00} + P^{00}, \\
q/p A(\bar{B}^0 \rightarrow \rho^+ \pi^-) &\equiv q/p \bar{A}^{+-} = e^{+i\alpha} T^{-+} + P^{-+}, \\
q/p A(\bar{B}^0 \rightarrow \rho^- \pi^+) &\equiv q/p \bar{A}^{-+} = e^{+i\alpha} T^{+-} + P^{+-}, \\
q/p A(\bar{B}^0 \rightarrow \rho^0 \pi^0) &\equiv q/p \bar{A}^{00} = e^{+i\alpha} T^{00} + P^{00},
\end{aligned} \tag{6.28}$$

where the isospin relationships given in Table 6-1 together with the $\Delta I = 1/2$ character of the penguin process give

$$P^{00} = -\frac{1}{2}(P^{+-} + P^{-+}). \tag{6.29}$$

In the theoretical parameterization given above, the six complex $B \rightarrow \rho\pi$ amplitudes are given by three complex tree amplitudes, plus two complex penguin amplitudes (from Eq. (6.29) to eliminate P^{00}) and the weak phase α . One can fix the strong phase of any one T or P to make the amplitude real by convention, so there are 10 parameters to be fit to the data (including the overall rate). The Dalitz-plot analysis in principal allows extraction of all these parameters.

With the notation of Eq. (6.28), dropping the exponential decay factor from the lifetime, the ρ -mediated $B \rightarrow 3\pi$ amplitude is given by:

$$\begin{aligned}
\mathcal{A}(t) = \cos(\Delta mt/2) &[f_+ A^{+-} + f_- A^{-+} + f_0 A^{00}] \\
&\pm i \sin(\Delta mt/2) [f_+ \bar{A}^{+-} + f_- \bar{A}^{-+} + f_0 \bar{A}^{00}],
\end{aligned} \tag{6.30}$$

where the \pm depends on the flavor of the tagged B . Here f_+ , for example, means the Breit-Wigner form for $\rho^+ \rightarrow \pi^+ \pi^0$. The Breit-Wigner form used here⁴ is

$$f(s) \propto \frac{\cos \theta_H}{s - m_\rho^2 + i\Pi(s)}, \tag{6.31}$$

where s is the square of the invariant mass of the putative ρ , and θ_H is the angle in the ρ rest frame between a decay pion direction and the line of flight of the ρ . The function Π is given by⁵

$$\Pi(s) = \frac{m_\rho^2}{\sqrt{s}} \left(\frac{p}{p_0} \right)^3 \Gamma_\rho(m_\rho^2), \tag{6.32}$$

⁴It is assumed that the most interesting part of the ρ strong decay is well-described by a Breit-Wigner. The precise form of this function is a source of a systematic uncertainty which has been investigated [11]. The form retained is the one used by ALEPH in their study of τ decays [12] where other resonant contributions ($\rho(1450)$ and $\rho(1700)$) were also taken into account. These are also considered for systematics studies (cf. [11]).

⁵The choice made for the function Π gives the proper threshold behavior for the width of the ρ and is consistent with elastic unitarity. The choice is not unique. One might ask that the p^3 dependence level off far from threshold, but this would be only a minor effect. Other overall dependence on s should be mild.

where $p = p(s) = \sqrt{s/4 - m_\pi^2}$ is the momentum of the daughter-pion in the ρ rest frame and $p_0 = p(m_\rho^2)$. In addition to the resonance form, the angular dependence of the ρ decay is included in the f_i . Angular momentum conservation requires the ρ to have zero helicity and thus the decay distribution is proportional to $\cos\theta_H$. The known phase variation over the Dalitz plot introduced by the Breit-Wigner form provides the means of disentangling the unknown phases in the amplitudes, both those introduced by the weak interactions and those arising from strong final-state interactions.

The time- and phase-space-dependent amplitude, Eq. (6.30), when squared, exhibits several contributions. For example, neglecting Penguin contributions for the sake of clarity, one can identify:

- a. Diagonal terms, *e.g.*, $|f_+ T^{+-}|^2$. These necessarily have no dependence on α and no phase dependence from the Breit-Wigner.
- b. Interference from two B^0 decays or two \bar{B}^0 decays to ρ s of different charges. These have no α dependence, but they show phase dependence from the Breit-Wigner factors and the strong phases of the various tree amplitudes.
- c. Interference between two different charged ρ s, one from B^0 and one from \bar{B}^0 . Here there is a phase dependence from the Breit-Wigner factors. Then the phase information comes from

$$\text{Im}(f_+ f_-^* e^{-2i\alpha}) = \text{Im}(f_+ f_-^*) \cos 2\alpha + \text{Re}(f_+ f_-^*) \sin 2\alpha \quad (6.33)$$

- d. Interference between a B^0 and a \bar{B}^0 decay to the same ρ . These have no phase-dependence from the Breit-Wigner (just an $|f|^2$), but a characteristic dependence

$$\sin(\Delta mt) \text{Im} \left[e^{\pm 2i\alpha} T T'^* \right] \quad (6.34)$$

where, for charged ρ s, the T and T' are different, but for neutral ρ s they are the same. Thus, for charged ρ s, there are terms proportional to $\sin(2\alpha + \delta)$ and $\sin(2\alpha - \delta)$ where δ is the strong-phase difference

$$\delta = \arg(T^{-+}(T^{+-})^*), \quad (6.35)$$

while for neutral ρ s the dependence is simply $\sin 2\alpha$.

Thus the interference between the various intermediate states contributing to the same three-pion kinematic region introduces a dependence on $\cos 2\alpha$ as well as on $\sin 2\alpha$. This then removes the $(\alpha, \pi/2 - \alpha)$ ambiguity in the value of α . Since the analysis fits both tree and penguin contributions it also removes any theoretical systematic uncertainty from our lack of ability to calculate the relative sizes and phases of these terms. The removal of these degeneracies and uncertainties could be an important step in the comparison of Standard Model predictions and B factory results. The interference terms are shown diagrammatically in Fig. 6-4. The strength of the interferences implies a correction to the amplitude-squared, whose phase-space variations⁶ are of the order of $\pm 10\%$, and which is significant even quite far from the ρ -band crossing region [11].

⁶In Ref. [8] a nonrelativistic Breit-Wigner is used. It yields significantly stronger interference effects.

Different Sources of Interferences:

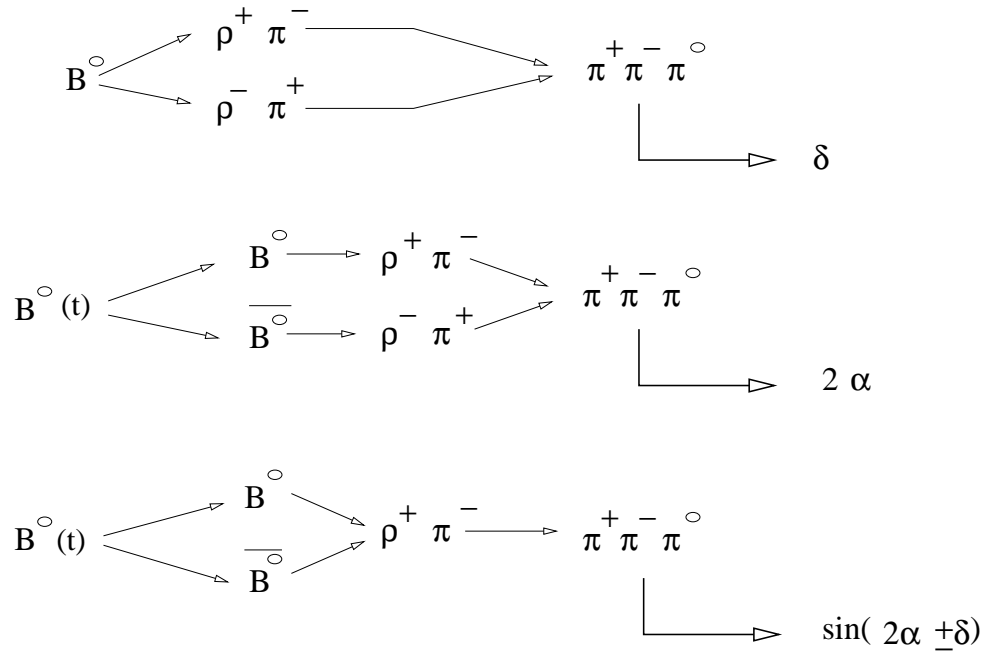


Figure 6-4. A representation of interference terms in $B \rightarrow \rho^\pm \pi^\mp$. The first diagram represents the term (b), the second (c), and the third (d): δ is the difference between the strong final-state-interaction phases for $B^0 \rightarrow \rho^+ \pi^-$ and $B^0 \rightarrow \rho^- \pi^+$. For $B \rightarrow \rho^0 \pi^0$ there is no such strong phase difference. Penguin effects are neglected in describing the α dependence here, but not in the full analysis.

There are a number of theoretical and experimental complications that need to be addressed to complete such an analysis

- **Higher resonances:** The assumption of ρ dominance has no strong theoretical basis. As is shown in Table 6-2 (which is not exhaustive) [13], there are many other higher resonances which can contribute to a 3π final state.⁷ Large values of such branching ratios would imply a contamination of events which should, however, be detectable by inspecting the Dalitz plots of the neutral and charged B decays.

⁷In principle, if one has enough information on these resonances, one can include them as well in the analysis. However, the increasing number of parameters necessary to describe the B -meson decay into higher resonances would make the fit impracticable unless very high statistics data were available.

Table 6-2. Potential $\pi\pi$ resonance candidates, X , that may be seen in $B^0 \rightarrow X\pi$. Only resonances with large branching ratios to $\pi\pi$ are shown [13].

Resonance (R)	$\mathcal{B}(R \rightarrow \pi\pi)$ (%)	Width (MeV)	$I^G(J^{PC})$	Remarks
$f_0(400 - 1200)$	dominant	600 to 1000	$0^+(0^{++})$	Non- $q\bar{q}$ candidate
$\rho(770)$	100	150.7 ± 1.2	$1^+(1^{--})$	Well-known
$f_0(980)$	(78.1 ± 2.4)	40 to 100	$0^+(0^{++})$	Odd shape
$f_2(1270)$	$(84.7^{+2.6}_{-1.2})$	185 ± 20	$0^+(2^{++})$	Well-known
$\rho_3(1690)$	(23.6 ± 1.3)	160 ± 10	$1^+(3^{--})$	High spin
$f_4(2050)$	(17.0 ± 1.5)	208 ± 13	$0^+(4^{++})$	High spin

- ρ shape uncertainties: The description of the $\rho(770)$ resonance used here, Eq. (6.31), makes the double assumption that $B^0 \rightarrow \rho^+\pi^-$ and $B^0 \rightarrow \rho^-\pi^+$ have the same ρ structure and that this structure is precisely known. This parameterization, while expected to be good, introduces some theoretical uncertainties.
- Nonresonant 3π : It is not possible to say anything reliable from theory on a nonresonant contribution. The simplest way to handle it is to fit it, by assuming that it is dominated by a flat component which can be measured in the center of the Dalitz plot (well outside the ρ bands). The uncertainties due to the precise parameterization of the ρ strong decay, and to the definition of the cuts used to reduce the contribution of higher resonances, will be reflected in variation of the fitted nonresonant contribution. For a recent illustration of these ideas in the non CP studies of the D and D_s systems, see for example [14]. The study of the Dalitz plots of both neutral and charged B decays may be helpful in understanding nonresonant contributions, if they turn out to be large.
- Electroweak penguins: In addition to the gluonic penguins, there are also Z^0 and photonic penguins which have a different isospin structure. Theoretical estimates of these terms are model-dependent [15], but suggest that they may not be negligible in the $\rho^0\pi^0$ channel, because of cancellations between the tree and gluonic penguin terms. A procedure to define a theoretical error on α induced by the electroweak penguins can be found in Ref. [15].

This “three-body” Dalitz-plot analysis requires fitting ten parameters and thus requires a substantial data set, as is discussed below in Section 6.5. When the data are limited, an alternative is to attempt an analysis that reduces the number of free parameters by making assumptions or approximations. These will be discussed in the experimental section on $\rho\pi$. The disadvantage of such analyses is that they do not resolve all the discrete ambiguities in α , and, more seriously, that they introduce theoretical systematic uncertainties which are difficult to quantify. As in the two-pion case how-

ever, it is likely that these more restricted approaches will be the only ones feasible for some time to come, and hence theoretical efforts to reduce the theoretical uncertainties will be important in controlling the errors on α .

Adding charged B decays

From the amplitudes in Table 6-1, one can write the charged B -decay amplitudes for $\rho\pi$ as,

$$\begin{aligned}\sqrt{2}A(B^+ \rightarrow \rho^+ \pi^0) &= e^{-i\alpha}T^{+0} + P^{+-} - P^{-+}, \\ \sqrt{2}A(B^+ \rightarrow \rho^0 \pi^+) &= e^{-i\alpha}(T^{+-} + T^{-+} + 2T^{00} - T^{+0}) - P^{+-} + P^{-+}.\end{aligned}\quad (6.36)$$

Note that there is a pentagonal relation between the three neutral and two charged B decay amplitudes

$$\sqrt{2} \left[A(B^+ \rightarrow \rho^+ \pi^0) + A(B^+ \rightarrow \rho^0 \pi^+) \right] = A^{+-} + A^{-+} + 2A^{00}.\quad (6.37)$$

The addition of the two charged channels $B^\pm \rightarrow \rho^\pm \pi^0, \pi^\pm \rho^0$ adds one more T -type amplitude. However, the $B^\pm \rightarrow \rho^\pm \pi^0$ channel has two π^0 s in the final state, and thus may be more difficult to measure (cf. Section 6.5.1.7). Without this channel, the inclusion of $B^\pm \rightarrow \rho^0 \pi^\pm$ rates in the analysis adds as many new parameters as new observables, thus in principal giving no new constraints. (Though an observation of direct CP -violation via a difference in the rates of two charge-conjugate channels would demonstrate that α is nonzero [11].) However the full three-charged-pion Dalitz plot distribution could give some valuable information on the isospin $I = 0, 1, 2$ resonant and/or nonresonant contributions and thus should also be considered as a cross-check of the neutral channel Dalitz-plot analysis. Once the two neutral pion amplitudes are measured then an analysis that fits the charged three-pion decay rates as well as the neutral Dalitz plot may better constrain the various fit parameters and should be pursued [15].

Pentagon analysis

A construction similar to the isospin triangle construction for $\pi\pi$ can be made in the $\rho\pi$ case, arising from the relationship Eq. (6.37) and its CP conjugate. The geometric figures to be constructed are pentagons rather than triangles. However, this analysis is equivalent to solving a number of higher-order algebraic equations for this system and hence the solution can be obtained only up to multiple discrete ambiguities [9, 5]. Given the effects of experimental errors and the multiple ambiguities, it is unlikely that such a phase-space-integrated (PSI) approach will give useful information with the kind of accuracy achievable at BABAR. Furthermore, if there were enough data to do such an analysis with small uncertainties, then the full 3π Dalitz-plot analysis would be also be possible. While the pentagon constructions rely on the measurement of *branching ratios*, that is, amplitudes *squared*, the Dalitz-plot analysis measures amplitudes and is *linearly* sensitive to the suppressed channels, *e.g.*, $\rho^0 \pi^0$. Hence it is expected that analyses based on the Dalitz-plot structure, rather than pentagon constructions will be the eventual method of choice to determine α from these channels.

6.1.2.4 $B^0 \rightarrow \pi K$

An isospin analysis can be performed for $B \rightarrow \pi K$ decays [16, 9]. By measuring the rates for $B^+ \rightarrow \pi^0 K^+$, $B^+ \rightarrow \pi^+ K^0$ and $B^0 \rightarrow \pi^- K^+$, along with the rates and CP asymmetry in $B^0 \rightarrow \pi^0 K_S$, it is possible in principle to remove the penguin pollution and measure α .

However, this analysis assumes that electroweak-penguin contributions are negligible. However CLEO data [2] suggest that electroweak penguins in $B \rightarrow \pi K$ are comparable to the corresponding tree contributions, unlike the $B \rightarrow \pi\pi$ and $B \rightarrow \rho\pi$ cases. This can be understood as follows. In the case of $B \rightarrow \pi K$ decays, there are contributions from both the $b \rightarrow u\bar{u}s$ tree amplitude and the $b \rightarrow s$ penguin amplitude. It is this latter penguin pollution which one seeks to remove. However, as discussed above in 6.1.2, CLEO results indicate that the $b \rightarrow s$ penguin amplitude may be about the same size as the $b \rightarrow u\bar{u}d$ tree amplitude. Thus the Cabibbo-suppressed $b \rightarrow u\bar{u}s$ tree amplitude is smaller by a factor of about 0.2 (the Cabibbo angle) than the $b \rightarrow s$ penguin amplitude. The $b \rightarrow s$ electroweak penguin is also suppressed, however, by about 0.2 relative to the $b \rightarrow s$ gluonic penguin. Thus, the $b \rightarrow s$ electroweak penguin and the $b \rightarrow u\bar{u}s$ tree amplitude, both of which contribute to $B \rightarrow \pi K$, are possibly roughly the same size. It therefore appears that electroweak-penguin contributions to $B \rightarrow \pi K$ are non-negligible, so that an isospin analysis is unlikely to successfully isolate a dominantly tree contribution in this case [7].

6.1.2.5 $B \rightarrow \pi\pi$, $B \rightarrow \pi K$, and flavor $SU(3)$

An additional method [17, 18] for obtaining α uses flavor $SU(3)$ symmetry [19] to relate $B \rightarrow \pi\pi$ to $B \rightarrow \pi K$ decays, which permits the removal of the penguin pollution in $B^0 \rightarrow \pi^+\pi^-$. Other similar methods involving flavor $SU(3)$, are discussed in Chapter 7.

The decays of interest are $B^0 \rightarrow \pi^+\pi^-$, $B^0 \rightarrow \pi^-K^+$, and $B^+ \rightarrow \pi^+K^0$. The amplitudes for these decays can be written

$$A_{\pi\pi} \equiv A(B^0 \rightarrow \pi^+\pi^-) = -(T + P) = \mathcal{T}e^{i\delta_T}e^{i\gamma} + \mathcal{P}e^{i\delta_P}e^{-i\beta}, \quad (6.38)$$

$$A_{\pi K} \equiv A(B^0 \rightarrow \pi^-K^+) = -(T' + P') = r_u\mathcal{T}e^{i\delta_T}e^{i\gamma} - \mathcal{P}'e^{i\delta_P}, \quad (6.39)$$

$$A_{\pi K}^+ \equiv A(B^+ \rightarrow \pi^+K^0) = P' = \mathcal{P}'e^{i\delta_P},$$

where $\mathcal{T} \equiv |T|$, $\mathcal{P} \equiv |P|$, and $\mathcal{P}' \equiv |P'|$. Here T and P represent respectively the color-allowed tree and penguin contributions for the $\Delta S = 0$ transitions, while their primed counterparts correspond to $\Delta S = 1$ processes. Unlike the $K\pi$ isospin analysis, channels with a final-state π^0 are not included here, and hence electroweak penguins are ‘‘color-suppressed’’ and are not expected to be a significant contribution. They are ignored in the analysis that follows. Three strong assumptions are essential in Eq. (6.38).

- Rescattering effects are small, otherwise the final equation receives a second contribution from rescattered tree diagrams (see further discussion in Chapter 7).
- The $b \rightarrow d$ penguin P is dominated by the t quark. Since long-distance effects may substantially enhance the u and c penguin contributions, this assumption may not be justified [20].
- The amplitudes T and T' are related simply by the ratio of their CKM matrix elements, with an $SU(3)$ breaking factor [21] of the ratio of K and π decay constants (*i.e.*, factorization is assumed). Factorization is unlikely to hold for penguin amplitudes, so \mathcal{P} and \mathcal{P}' are not related in a simple way. However the strong phase of the penguin diagram, δ_P , is assumed to be $SU(3)$ symmetric, so the same for both terms. While plausible, this assumption introduces some theoretical uncertainty.

With these assumptions one can obtain the following six quantities:

$$\begin{aligned}
A &\equiv \frac{1}{2} \left(|A_{\pi\pi}|^2 + |\bar{A}_{\pi\pi}|^2 \right) = \mathcal{T}^2 + \mathcal{P}^2 - 2\mathcal{T}\mathcal{P} \cos \delta \cos \alpha, \\
B &\equiv \frac{1}{2} \left(|A_{\pi\pi}|^2 - |\bar{A}_{\pi\pi}|^2 \right) = -2\mathcal{T}\mathcal{P} \sin \delta \sin \alpha, \\
C &\equiv \text{Im} \left(e^{2i\beta} A_{\pi\pi} \bar{A}_{\pi\pi}^* \right) = -\mathcal{T}^2 \sin 2\alpha + 2\mathcal{T}\mathcal{P} \cos \delta \sin \alpha, \\
D &\equiv \frac{1}{2} \left(|A_{\pi K}|^2 + |\bar{A}_{\pi K}|^2 \right) = r_u^2 \mathcal{T}^2 + \mathcal{P}'^2 - 2r_u \mathcal{T}\mathcal{P}' \cos \delta \cos \gamma, \\
E &\equiv \frac{1}{2} \left(|A_{\pi K}|^2 - |\bar{A}_{\pi K}|^2 \right) = 2r_u \mathcal{T}\mathcal{P}' \sin \delta \sin \gamma, \\
F &\equiv |A_{\pi K}^+|^2 = \mathcal{P}'^2.
\end{aligned} \tag{6.40}$$

These give six equations in six unknowns, so that one can solve for α , γ , \mathcal{T} , \mathcal{P} , \mathcal{P}' , and δ . However, because the equations are nonlinear, there are discrete ambiguities in extracting these quantities. In fact, a detailed study [18] shows that, depending on the actual values of the phases, there can be up to eight solutions. Many of these can be eliminated due to other information on the CKM phases, but still some ambiguity often remains.

Note that, if one relaxes any of the assumptions, the method breaks down because additional parameters are needed. Furthermore, even if the assumptions are correct, if $\delta = 0$, the quantities B and E vanish, so that one is left with four equations in five unknowns. In this case one must use additional assumptions to extract information about the CP phases. Thus, this is an interesting method for obtaining α with little or no penguin pollution, but it depends on several theoretical assumptions. If these assumptions can be justified (*e.g.*, via independent measurements), then this may become a useful way of measuring α cleanly.

6.2 Penguins and Direct CP Violation

Direct CP violation is an interesting and important manifestation of CP violation [22]. As a rule it is simpler to establish experimentally than indirect CP violation. It can occur in processes involving either charged or neutral B s. For all charged decays and for a few neutral decays (that are self-tagged), tagging “the other B ” is not necessary, which can translate into a reduction of a factor of about 5–10 in the number of B s needed. These advantages are offset by a serious disadvantage of direct CP violation: it is in general difficult to convert experimental observation of an asymmetry in a specific channel into a quantitative determination of the basic parameters of the Standard Model.

6.2.1 Varieties of Direct CP Violation

Direct CP violation arises from an explicit CP -odd phase in the $\Delta b = 1$ decay amplitude of the b quark. As a result, the comparison of b -decays to a specific final state with \bar{b} decays to the CP -conjugate final state can reveal CP violation. Since direct CP violation results from the presence of the CP -odd phase in the underlying ($\Delta b = 1$) Hamiltonian, it can show up in all types of B mesons [B_u, B_d, B_s, B_c]. This is in sharp contrast to indirect CP violation resulting from mixing and decay [23, 24], which necessarily requires mixing between neutral states: B^0 - \bar{B}^0 or B_s^0 - \bar{B}_s^0 . Such mixing results from $\Delta b = 2$ interactions, *i.e.*, they are second order in the usual $\Delta b = 1$ weak Hamiltonian and/or they involve $\Delta b = 2$ interactions from new physics.

For the CP -odd phase in the $\Delta b = 1$ effective Hamiltonian to manifest itself experimentally via direct CP violation, there must be interference between (at least) two ($\Delta b = 1$) amplitudes leading to the same final state. One can write:

$$A = |A_1| \exp[i(\delta_1 + \phi_1)] + |A_2| \exp[i(\delta_2 + \phi_2)]$$

where the δ s are the CP -even strong final-state rescattering phases, whereas the ϕ s are the CP -odd phases which in the Standard Model result from the single CP -odd phase present in the CKM matrix [25]. The corresponding amplitude for the CP -conjugate process has the form:

$$\bar{A} = |A_1| \exp[i(\delta_1 - \phi_1)] + |A_2| \exp[i(\delta_2 - \phi_2)].$$

The typical CP -violating observable is the *partial rate asymmetry* (PRA) defined as:

$$\begin{aligned} \alpha_{PRA} &= \frac{\mathcal{B}(B \rightarrow f) - \mathcal{B}(\bar{B} \rightarrow \bar{f})}{\mathcal{B}(B \rightarrow f) + \mathcal{B}(\bar{B} \rightarrow \bar{f})} \\ &= \frac{2|A_1||A_2| \sin \delta \sin \phi}{|A_1|^2 + |A_2|^2 + 2|A_1||A_2| \cos \delta \cos \phi}, \end{aligned} \quad (6.41)$$

where $\delta \equiv (\delta_1 - \delta_2)$ and $\phi \equiv (\phi_1 - \phi_2)$ are the CP -even and CP -odd phase differences between the amplitudes. Within the Standard Model, ϕ is a function of the angles of the unitarity triangle.

Equation (6.41) exhibits the central difficulty in dealing with direct CP violation. Although the asymmetry involves four unknowns (A_1, A_2, δ, ϕ), the measurements of only two branching ratios ($|A|$ and $|\bar{A}|$) are required to establish the existence of a PRA (*i.e.*, $\alpha_{PRA} \neq 0$). Thus the CP -odd phase (ϕ) that one wants cannot in general be deduced from a measurement of α_{PRA} without a separate knowledge of the strong-phase difference δ , and the amplitude ratio $|A_1/A_2|$. Theory is completely unreliable for predicting these quantities. This is especially so for exclusive reactions and probably true even for inclusive processes. So, while many model-dependent calculations have been done over the years to estimate PRAs in various modes, they should really be regarded as illustrative examples. As the branching fractions of more and more B decay modes become measured, it is quite likely that a few good phenomenological models of hadron dynamics will emerge which could eventually be used to deduce or at least constrain the phase ϕ from measurements of PRAs. In principle, there is also the possibility that, at least for some simple reactions (say two pseudoscalars, *e.g.*, $K\pi, \pi\pi, K\bar{K}$), the final-state phase shifts could be experimentally determined. Usually this is extremely difficult, but if it could be done, the weak phase might be deducible [26].

In some decay channels that are dominated by the presence of well-defined resonances, the strong phases may be determined from the masses and widths of the resonances. Some examples that have been discussed so far to illustrate this possibility are presented below [27, 28, 29, 30].

In addition to PRAs there are several other interesting CP -violating observables that can, and should be measured in order to understand fully the dynamics. It is useful to define the transformation T_N , the “naive” time reversal operator. This is defined to be the inversion of momenta and spins. It differs from the time-reversal operator (T) in quantum field theory which requires, in addition, the interchange of initial and final states. In general CP -odd observables can then be divided into two types:

1. The first type are CP -odd T_N -even observables. The simplest example is a PRA. Another interesting and important example is the energy asymmetry. In exclusive modes such asymmetries can occur when there are three or more particles in the final state. In inclusive reactions this means comparing the energy distribution of a particle in the final state with that of the corresponding antiparticle in the conjugate reaction.
2. The second type are CP -odd, T_N -odd observables. A simple example of this is the triple-correlation asymmetry, *e.g.*, $\mathbf{p}_1 \cdot (\mathbf{p}_2 \times \mathbf{p}_3)$, where p_1, p_2, p_3 are three linearly independent momenta in the final state. For exclusive reactions this requires at least four spinless mesons in the final state. When initial or final states involve particles with spin then T_N -odd (and also T_N -even) observables involving spin can also be defined. An important class of processes are B decays to two spin-one mesons, such as $B \rightarrow \phi K^*, B \rightarrow \phi\rho, B \rightarrow \omega K^*, \omega\rho$, *etc.* In

such cases the vector meson decays can give information about their spin orientation [31]. Another interesting case is when a τ -lepton is in the final state, say $B \rightarrow D\tau\nu_\tau$ [32, 33]. Then the transverse polarization asymmetry of the τ can be used as one of the three vectors in the product.

The T_N -even observables require the presence of a CP -even (C -even, P -even) strong phase which can originate from the absorptive part in a Feynman amplitude [34] and/or from the presence of resonances [27, 28, 29, 30] in the decay chain. When it originates from the perturbation-theory calculation of a Feynman amplitude such a phase is called the perturbative phase. Similarly, when resonances dominate the phase it is often called the resonant phase. T_N -odd observables are, on the other hand, driven by the real part of Feynman amplitudes. For these cases the CP -even phase is C -odd, P -odd and originates from the presence of a trace involving γ_5 , such as $Tr[\gamma_5 \not{p}_1 \not{p}_2 \not{p}_3 \not{p}_4]$, where p_1, p_2, p_3 , and p_4 are the four linear-independent 4-momenta. For this reason this phase is called the axial phase. A nonzero expectation value of a T_N -odd observable does not necessarily mean that CP is violated. To define observables which are manifestly CP -violating usually requires comparison of (T_N -odd) expectation values between the conjugate reactions [35].

The CPT theorem implies nontrivial and important restrictions on PRAs: absorptive parts of Feynman amplitudes that result from the scattering of a state onto itself cannot contribute to a PRA [36, 37, 38, 27]. As a result, PRA measurements do *not* represent exhaustive tests of CP . That is, even if all PRAs are identically zero it does not necessarily mean that the underlying theory is not CP -violating. Consider, as an explicit example, a two-Higgs-doublet model with natural flavor conservation. In such models flavor-diagonal interactions of neutral Higgs lead to CP violation [39]. Thus CP -violating vertices necessarily involve rescattering of states onto themselves. Consequently PRAs will not arise even though CP violation can manifest itself through all other observables. As an example, the energy asymmetry is an observable which is T_N -even (like PRAs) and is proportional to absorptive parts of Feynman amplitude. Such an asymmetry can, and in general will arise, through self-rescattering of quarks [40].

6.2.2 Illustrative Examples of Direct CP

The following few pages give some examples of direct CP violation that have been studied. The emphasis will be on calculations done in the last five years or so. This discussion focuses chiefly on modes with predicted branching ratios $\gtrsim 10^{-6}$ and asymmetries $\gtrsim 1\%$.

Asymmetries due to direct CP violation in inclusive processes, although somewhat challenging to measure, are expected to be relatively clean from a theoretical point of view. This is because notions of quark-hadron duality are likely to work best for inclusive reactions. Perturbation theory calculations for the inclusive reactions are, in fact, closest in spirit to the initial realization [34] that quantum corrections, in general, endow the amplitudes with an absorptive part. This absorptive part is essential for generating the asymmetries.

Table 6-3. Theoretical estimates of branching ratios and asymmetries for quark-level processes and other inclusive reactions.

Process	Reference(s)	\mathcal{B}	Asymmetry	Comments
$(b \rightarrow s)$				
$b \rightarrow sq\bar{q}$	[41]	$\sim 1\%$	$\sim (1 \pm 0.5)\%$	$q = u, d, s$
$B \rightarrow K, K^*(X)$	[43]	$\sim 1 \times 10^{-4}$	$\lesssim 15\%$	Energy Asymmetry
$(b \rightarrow d)$				
$b \rightarrow dq\bar{q}$	[41]	$\sim 0.5\%$	$\sim (2.0_{-1.0}^{+1.2})\%$	$q = u, d, s$
$b \rightarrow d\psi$	[44, 45]	$\sim 5 \times 10^{-4}$	$\sim 1\%$	
$B \rightarrow \eta'(\eta(1440))X_d$	[46]	$\sim 0(10^{-5})$	$\lesssim 12\%$	
$B \rightarrow f_0, f_2(X_d)$	[46]	$\sim "$	$"$	
$B \rightarrow K\bar{K}, \pi\pi(X_d)$	[46]	$\sim "$	$"$	

Table 6-3 gives a sample of inclusive processes. This contains quark-level asymmetries, in charmless final states, via $b \rightarrow sq\bar{q}$ (*i.e.*, $\Delta s = 1$) and $b \rightarrow dq\bar{q}$ (*i.e.*, $\Delta s = 0$), for $q = u, d, s$. In a recent study [41], CP asymmetries for $\Delta s = 1$ and $\Delta s = 0$ inclusive charmless final states were computed by a systematic use of the renormalization-group-improved perturbation theory by including the probable dominant contributions to next-to-leading order. These calculations give branching ratios and PRAs of around $\sim 1\%$. (See Table 6-3.) For earlier and comparable study see [42].

Another interesting recent study is of the energy asymmetry in the inclusive reaction $B \rightarrow KX$ [43]. Motivated by the recent CLEO observation[2] of $B \rightarrow \eta' + X_s$, estimated partial rate and energy asymmetries in such single-particle inclusive reactions, studied in Ref. 24, are also given in Table 6-3. Table 6-4 gives the estimated asymmetries in $B \rightarrow PP$ [47, 48], PV [47] and VV [49] where $P =$ pseudoscalar and $V =$ vector. Table 6-5 shows the asymmetries in electroweak-penguin processes. Note that different models can give significantly different numbers for both branching ratios and asymmetries. As an example, compare the $\rho\pi$ branching ratio given here to that used in the simulations in Section 6.5 from a different model calculation.

Table 6-4. Theoretical estimates of branching ratios and asymmetries for selected $B \rightarrow PP, PV$ and VV modes. [Note: except for the $K\pi$ case, where the result is due to long-distance effects, entries in this table are based on calculations that assume the absence of long-distance rescattering. Different models give significantly different numbers in some channels.]

Process	Reference	\mathcal{B}	Asymmetry
$B \rightarrow K^- K^0$	[48, 47]	$\sim 2 \times 10^{-6}$	$\sim 10\%$
$\rightarrow K^0 \bar{K}^0$	[48, 47]	$\sim 1 \times 10^{-6}$	$\sim 8\%$
$\rightarrow K^- \pi$	[48, 47]	$\sim 1 \times 10^{-5}$	$\sim 1\%$
	[50]	"	$\sim 20\%$
$\rightarrow K^- \phi$	[47]	$\sim 6 \times 10^{-6}$	$\sim 1\%$
$\rightarrow \pi^0 \rho^-$	[47]	$\sim 2 \times 10^{-5}$	$\sim 2\%$
$\rightarrow \pi^- \rho^0$	[47]	$\sim 2 \times 10^{-6}$	$\sim 2\text{--}10\%$
$\rightarrow \pi^- \omega$	[47]	$\sim 1.5 \times 10^{-6}$	$\sim 12\%$
$\rightarrow D^0 D^{*-}$	[47]	$\sim 5 \times 10^{-4}$	$\sim 0.6\%$
$\rightarrow \rho^- K^{*0}$	[49]	$\sim 1 \times 10^{-5}$	$\sim 0.6\%$
$\rightarrow \phi K^{*-}$	[49]	$\sim 1 \times 10^{-5}$	$\sim 0.6\%$
$\rightarrow \omega K^{*-}$	[49]	$\sim 3 \times 10^{-6}$	$\sim 28\%$
$\rightarrow \rho^0 K^{*-}$	[49]	$\sim 2 \times 10^{-6}$	$\sim 30\%$
$\rightarrow \rho^- \omega$	[49]	$\sim 2 \times 10^{-5}$	$\sim 4\%$
$\rightarrow D^{*-} D^{*0}$	[49]	$\sim 1 \times 10^{-3}$	$\sim 1\%$

Table 6-5. Theoretical estimate of branching ratio and asymmetry modes due to EW penguins [see also Table 6-6].

Process	References	\mathcal{B}	Asymmetry	Comments
$b \rightarrow s\gamma$	[51]	$\sim 2 \times 10^{-4}$.1–1%	
$b \rightarrow d\gamma$	[51]	$\sim 1 \times 10^{-5}$	1–10%	
$B \rightarrow K^*\gamma$	[52]	$\sim 4 \times 10^{-5}$	$\sim 1\%$	
$B \rightarrow \rho\gamma$	[52, 53]	$\sim 2 \times 10^{-6}$	$\lesssim 30\%$	
$b \rightarrow d\ell^+\ell^-$	[54, 55]	$\sim 5 \times 10^{-7}$	$\sim 3\%$	$1 < m_{\ell\ell}/\text{GeV} < 3$
$B \rightarrow \pi\ell^+\ell^-$	[54, 55]	$\sim 3 \times 10^{-8}$	"	"
$B \rightarrow \rho\ell^+\ell^-$	[54, 55]	$\sim 5 \times 10^{-8}$	"	"

Table 6-6. Examples of theoretical estimates of CP asymmetries in processes dominated by resonances.

Process	Ref.	\mathcal{B}	Asymmetry	Comments
$B \rightarrow K_i^*\gamma$	[27]	$\sim (1-5) \times 10^{-5}$	$\lesssim 8\%$	energy asymmetry
$K_i^* \rightarrow K\pi, K^*\pi, K\rho$	[27]		$\lesssim 3\%$	PRA
$B \rightarrow a_1/a_2\gamma \rightarrow 3\pi\gamma$	[28]	$\sim (1-5) \times 10^{-7}$	$\lesssim 10\%$	T_N -even, forward-backward asymmetry
			$\lesssim 10\%$	T_N -odd, triple correlation asymmetry
			$\lesssim 30\%$	T_N -even, optimal observable
			$\lesssim 20\%$	T_N -odd, optimal observable
$B \rightarrow h\pi$	[29]	$\sim 5 \times 10^{-7}$	$\sim 10\%$	$n_c = \rho\rho, K\bar{K}\pi, \pi\pi KK \dots$
$h = n_c, \chi_c^0$				$\chi_c^0 = \pi\pi, K\bar{K}, 4\pi \dots$
$B^\pm \rightarrow h^\pm \rho^0(\omega)$	[30]			
$h = \rho$		$\sim (1-2) \times 10^{-5}$	$\sim 9-30\%$	maximum asymmetry
$h = K^*$		$\sim 1 \times 10^{-5}$	$\sim 32-79\%$	in the region of
$h = \pi$		$\sim (2-7) \times 10^{-6}$	$\sim 17-48\%$	$M(\omega) \pm \Gamma(\omega)$

6.2.2.1 Long-distance rescattering effects on direct CP in $B \rightarrow K\pi$ -like modes

Recently there has been some discussion [56, 57, 58, 50] of the effects of soft physics on final-state (FS) rescattering phases and the consequences for direct CP violation in modes such as $B \rightarrow K\pi$. It is now recognized that direct CP violation in B decays has a very rich structure. (The presence of nontrivial final-state interaction phases and related direct CP -violating effects was discussed earlier in [42], but this work has not received much attention and the view that final-state-interaction effects are small has been widely held.) The important point is that the short-distance Hamiltonian, and in particular the penguin operators, are not the only source of direct CP violation in B decays. Whereas the penguin Hamiltonian (*e.g.*, in $b \rightarrow s$ transitions) has $\Delta I = 0$, long-distance (LD) rescattering effects represent a distinct source of CP violation, particularly in states that are mixtures of isospin such as $K\pi$.

Recall that the isospin operator intimately links the two charge states $\bar{K}^0\pi^-$ and $K^-\pi^0$ in B^- decays, and $\bar{K}^0\pi^0$ and $K^-\pi^+$ in \bar{B}^0 decays. Indeed, the CPT theorem places severe restrictions [50] on the PRA arising due to long-distance rescattering effects in such states related by the isospin operator: the PRA due to long-distance effects in $\bar{K}^0\pi^-$ must cancel exactly with that in $K^-\pi^0$; similarly, the PRA in $\bar{K}^0\pi^0$ must cancel with that in $K^-\pi^+$. A very important repercussion of this result is that the PRA caused by long-distance effects in $K^*\pi$ (or $K\rho$, or $Ka_1\dots$) cannot cancel with the PRA in $K\pi$. Thus each category of such final-state interactions provides an independent probe for searching for direct CP violation [50].

One is often tempted to assume that the B -meson mass (~ 5 GeV) is large enough that final-state rescattering effects will be negligible in such exclusive decay modes. Not only are there no good reasons to support such an assumption, Donoghue *et al.* [56, 59] have claimed, on very general grounds, that final-state rescattering phases due to soft physics do not vanish as $m_B \rightarrow \infty$. This has an important general consequence that it could improve the observability of direct CP in various exclusive modes. Specifically, for $B \rightarrow K\pi$, due to long-distance rescattering effects, PRAs of around $\sim 20\%$ (for $\sin\gamma = 1$) may be possible [50]. However, while enhancing direct CP asymmetries in B decays the presence of these long-distance rescattering effects also raises serious doubts about the validity of constraints on the angle γ [60] deduced by using the rates for $B^\pm \rightarrow K^0\pi^\pm$ and $B^0(\bar{B}^0) \rightarrow K^+\pi^-(K^-\pi^+)$, to the extent that the constraint is derived by explicitly assuming the absence of long-distance rescattering effects [57, 58, 50].

Two remarks are in order. First, most of the calculations of direct CP -violation asymmetries in exclusive hadronic channels, samples of which are given in Table 6-4, assume the absence of long-distance rescattering effects. If these effects are important for $K\pi$, as suggested in some of these studies [56, 57, 58, 50], then they are likely to be important in many other exclusive channels as well. Second, the PRAs due to these short- and long-distance effects are additive. As a result, in some modes the net asymmetries may be enhanced while in others they may be reduced due to cancellations.

6.3 Overview of the Experimental Studies

Early feasibility studies of the measurement of the angle α focused on the mode $B^0 \rightarrow \pi^+\pi^-$. This was partly motivated by the simple two-body topology of the decay and partly by the fact that it is a CP eigenstate. However, as was discussed in the theoretical introduction to this chapter, the presence of penguin effects can complicate the extraction of the angle α using the decay $B^0 \rightarrow \pi^+\pi^-$ alone. Therefore, in experimental studies it is crucial to use methods which enable the contribution of penguin diagrams to be disentangled from that of tree diagrams.

The theoretical basis of some of the proposed methods is discussed in the theoretical introduction, the most powerful being isospin-based analyses. The main message for experimental studies is that accurate measurement of the angle α in any channel requires information from several related decay modes, including charged B decays, which provide complementary information on the angle α and the penguin effects. The nature of this extended isospin-based analysis differs from channel to channel but in all cases will require large luminosity data samples to be carried out. Interim methods that constrain penguin effects by a combination of models and theory and comparison with many different modes will be important for some time to come.

It is thus expected that the correct solution for the angle α will arise from a comparison of the results from several modes. With this approach in mind, simulation studies have been performed for three classes of benchmark modes, all of which have the same underlying short-distance quark diagram structure. Modes with two, three or four pions in the final state are considered in Sections 6.4, 6.5, and 6.6 respectively. The studies of three-pion and four-pion modes are limited to the quasi-two-body states $\rho\pi$, $a_1\pi$, and $\rho\rho$.

A common feature of the benchmark modes is their expected low branching ratios, on the order of 10^{-5} or less. All are found also to have large backgrounds, both combinatorial background within signal events themselves and also those arising from continuum $q\bar{q}$ and generic $B\bar{B}$ events. The focus of the experimental studies is the identification of the background sources and methods to suppress them, and the performance of fits to extract the CP -violating asymmetry and other related parameters from the time evolution of the decays. The specific details of the analyses of the various decays are given in the following sections. For the two- and three-pion modes the experimental inputs for the possible isospin-based analyses are also examined.

6.4 B -Decay Modes with Two Pions

There are three $B \rightarrow \pi\pi$ decay modes: $B^0 \rightarrow \pi^+\pi^-$, $B^+ \rightarrow \pi^+\pi^0$ and $B^0 \rightarrow \pi^0\pi^0$ and the analogous decays of the \bar{B} . They are all important in the study of CP -violation. In this section, simulation studies of these modes using both the full `BBSim` simulation, and the fast simulation, `Aslund` are described.

In the absence of penguin effects, $\sin 2\alpha$ can be extracted from the analysis of the time evolution of the decays $B^0 \rightarrow \pi^+\pi^-$ and $\bar{B}^0 \rightarrow \pi^+\pi^-$ alone. However, in the more general case, one needs complementary information from all of the above modes in order to disentangle the penguin and tree effects. An important experimental issue in these channels is the suppression of events from continuum u -, d -, s -, c - quark production, which comprise the dominant background. Also, the recent results from the CLEO experiment indicate that the decays to $K\pi$ may be a substantial source of background, which presents a challenge to the particle identification capabilities of BABAR.

The following sections contain a description of the analyses used to determine the sensitivity of the BABAR experiment to the various relevant observables and the results of an isospin analysis which could be performed using these measurements.

6.4.1 The $\pi^+\pi^-$ Decay Mode

For this channel the observables are the coefficients of the $\sin \Delta m_d t$ and $\cos \Delta m_d t$ terms in the time evolution, in addition to the overall branching ratios of $B^0 \rightarrow \pi^+\pi^-$ and $\bar{B}^0 \rightarrow \pi^+\pi^-$. The branching ratio for this channel has not been measured, with the limit from CLEO currently 1.5×10^{-5} . A branching ratio of 1.2×10^{-5} has been assumed. This corresponds to ~ 380 events produced in 30 fb^{-1} running at the $\Upsilon(4S)$. The study reported here was done using Aslund's fast Monte Carlo simulation (Section 4.1.3). However, independent studies of the signal using the full BBSim simulation and the reconstruction software indicate that for such charged-only modes, the results are consistent.

Candidate $B^0 \rightarrow \pi^+\pi^-$ decays may be reconstructed simply by forming all pairs of oppositely charged tracks in the event and assuming they are pions in calculating the invariant mass. There are a number of possible sources of background.

6.4.1.1 Sources of background

The sources of background which were taken into account in this study were:

- **Continuum $q\bar{q}$ Production.** The combinatorial background produced by random combination of two tracks in events produced by nonresonant e^+e^- annihilation into light $q\bar{q}$ pairs; $\sim 10^8$ such events are expected for nominal annual luminosity. This is the largest source of background which survives the selection criteria. In general, the two tracks are in opposite jets, owing to the large invariant mass of the signal.
- $B^0 \rightarrow K^+\pi^-$. Using the CLEO result of 1.5×10^{-5} for the $K^+\pi^-$ branching ratio, there will be about 470 events of this kind per year. When the kaon is misidentified as a pion, this will show up as a background to the $\pi^+\pi^-$ channel. The reconstructed mass of the

B^0 is below the true value by $\sim 42 \text{ MeV}/c^2$. Since the mass resolution for $B^0 \rightarrow \pi^+\pi^-$ is about $22 \text{ MeV}/c^2$ at BaBar, there will be considerable overlap between the two channels using kinematics alone.

- **Combinatorial Background in Generic $\Upsilon(4S) \rightarrow B\bar{B}$ Events.** $\sim 3.15 \times 10^7$ events of this type are expected to be produced per year. Due to the kinematics of the two-body decay, this background was found to be negligible after preselection cuts. In particular, $\Upsilon(4S)$ events containing the decays $B^- \rightarrow \pi^+\pi^-\pi^-$ or $B^0 \rightarrow \pi^+\pi^-\pi^0$ were studied. No such events survived the kinematic cuts.
- **Combinatorial Background in the Signal Channel.** This was found to be insignificant, after the cuts which suppress the above backgrounds were made.

6.4.1.2 Background suppression

Many of the techniques used to reduce the background in this channel were summarized in Section 4.9. Here, details specific to this channel are given.

- **Kinematic Cuts:** The quantities which provide the most effective discrimination between signal and background are the mass of the B^0 candidate and its momentum in the $\Upsilon(4S)$ rest frame. The reconstructed mass distribution of the signal is shown in Fig. 6-5(a), with the mass distribution of $B^0 \rightarrow K^+\pi^-$ decays, treated as $B^0 \rightarrow \pi^+\pi^-$ candidates, superimposed. The invariant mass of the candidate is required to be within 2σ of the nominal B^0 mass, where σ , the resolution of the invariant mass, is about $22 \text{ MeV}/c^2$. The momentum of each pion candidate in the $\Upsilon(4S)$ rest frame, is also kinematically constrained for the signal, as is shown in Fig. 6-5(b). This is required to be in the range $2.46\text{--}2.82 \text{ GeV}/c^2$. The momentum of each B meson in the $\Upsilon(4S)$ rest frame is fixed by energy-momentum conservation to be $\sim 0.33 \text{ GeV}/c$. This translates into the range $0.17\text{--}0.42 \text{ GeV}/c$, once the widening of the distribution due to the beam energy spread is taken into account. The distributions for signal and $q\bar{q}$ background are shown in Fig. 6-5(c).
- **Particle ID:** The combinatorial background can be reduced by means of the particle identification system of BaBar. The DIRC and drift chamber dE/dx information, if available, are combined to form a χ^2 variable. In order to separate effectively the signal from the background (mainly $B^0 \rightarrow K^+\pi^-$) the following variable is used: $\Delta\chi^2 = \min(\chi^2(K, \pi) - \chi^2(\pi, \pi), \chi^2(\pi, K) - \chi^2(\pi, \pi))$ where $\chi^2(K, \pi)$, $\chi^2(\pi, K)$ and $\chi^2(\pi, \pi)$ are the overall χ^2 values for the $K\pi$, πK and $\pi\pi$ hypotheses, respectively. The distribution of this variable for the signal and background is shown in Figs. 6-6 (a) and (b), respectively.
- **Vertexing:** The vertexing capability of the BaBar tracking system is also used to reduce the combinatorial background. For a signal event the two pions are from the same vertex, so a fit to a common vertex is made for the two charged tracks; the χ^2 probability of this vertex is required to be greater than 0.01.

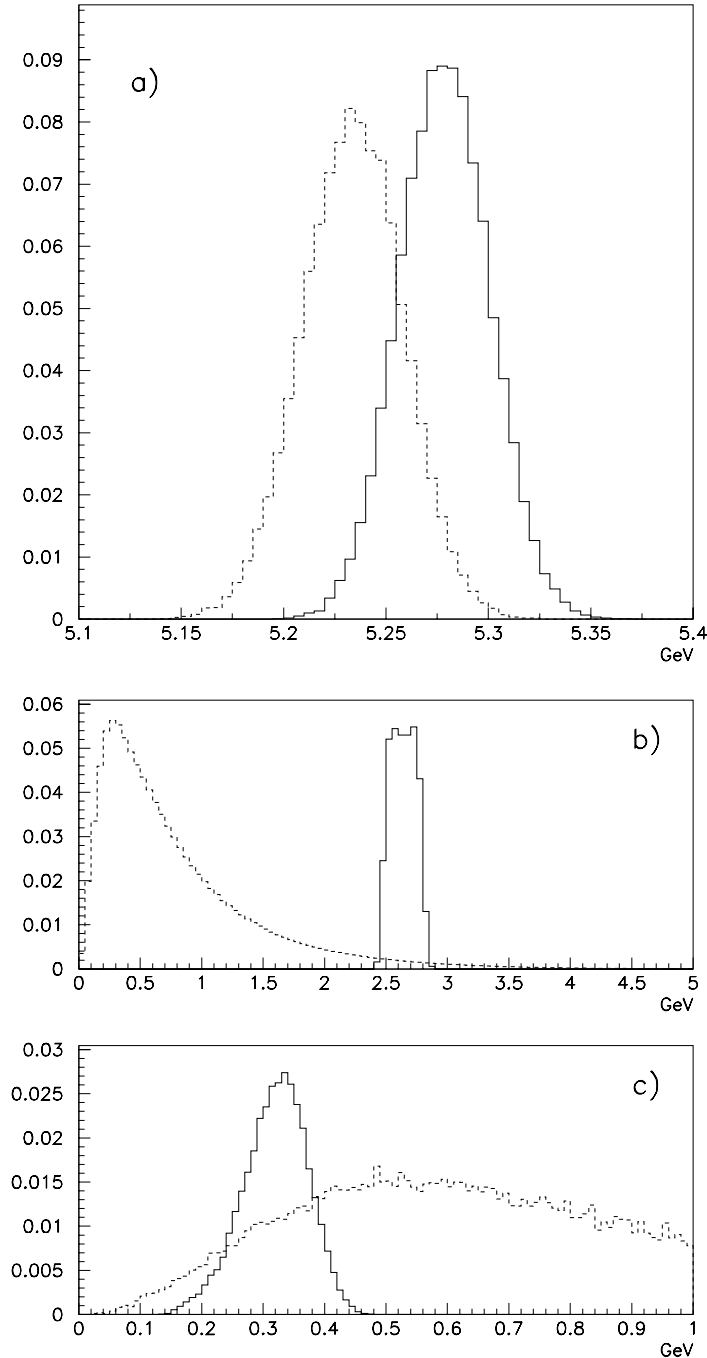


Figure 6-5. (a) The invariant mass of $B^0 \rightarrow \pi^+ \pi^-$ candidates for true $B^0 \rightarrow \pi^+ \pi^-$ decays (solid histogram) and for $B^0 \rightarrow K^+ \pi^-$ decays (dashed histogram); (b) momenta of pion candidates in the $\Upsilon(4S)$ rest frame for signal (solid histograms) and $q\bar{q}$ background (dashed histograms); and (c) momenta of B^0 candidates in the $\Upsilon(4S)$ rest frame (same key as (b)).

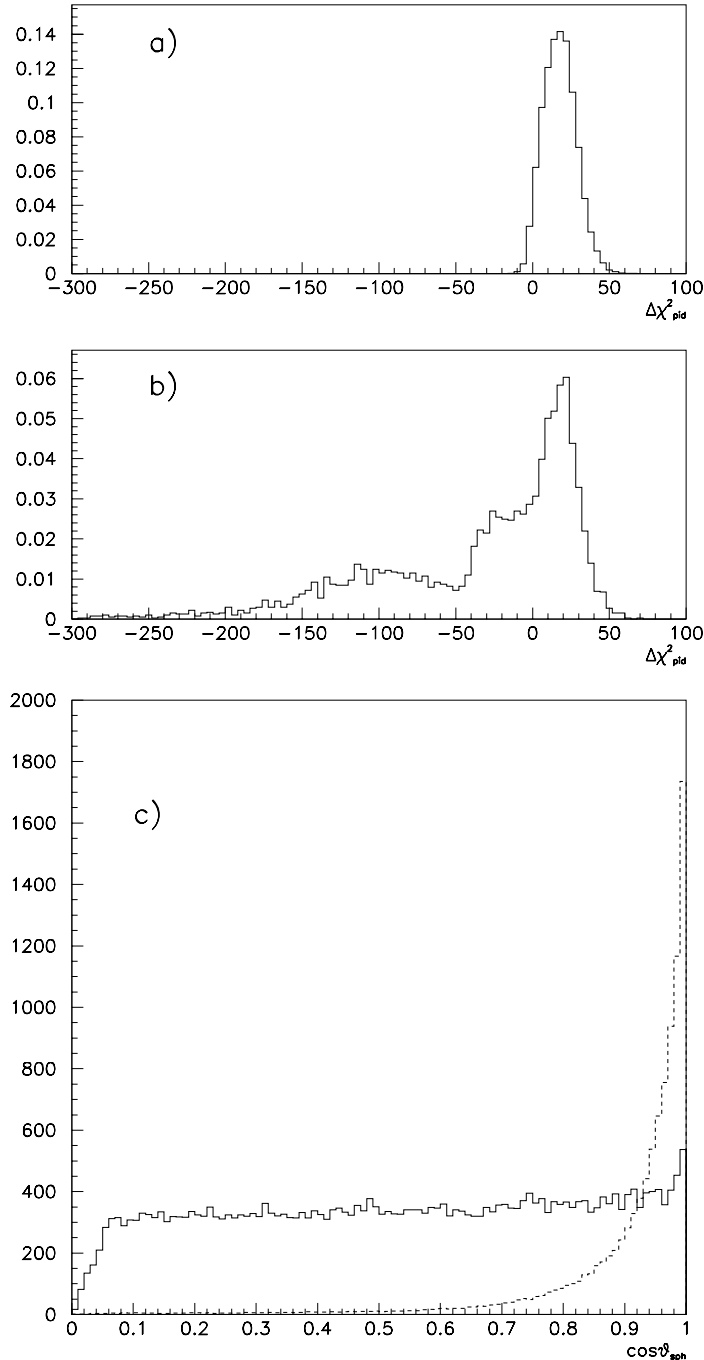


Figure 6-6. (a) Distribution of the particle identification variable $\Delta\chi^2$, defined in the text, for signal; (b) same for background events; and (c) absolute value of the cosine of the angle between the sphericity axis of the nonsignal tracks and the signal pion closest to it, calculated in the $\Upsilon(4S)$ rest frame for signal (solid histogram) and background events (dashed histogram).

- **Event Shape:** As explained in Section 4.9, the continuum background has a jet-like structure, while the signal is much more spherical. This difference is parameterized by the cosine of the angle between sphericity axis of the nonsignal tracks and the signal pion closest to it, calculated in the $\Upsilon(4S)$ rest frame, which can be seen in Fig. 6-6 (c). The B^0 candidate is required to have $|\cos \theta_{\text{sph}}| < 0.9$. Other shape variables, being strongly correlated to this variable, were not used.
- **Flavor-Tagging:** The tagging of the flavor of the B meson is determined using the `Cornelius` package, described in Section 4.7.2, for both leptons and kaons. This tagging information is essential for the time-dependent asymmetry measurement. The tagging also has the effect of improving the signal to background ratio for $q\bar{q}$ background, especially in the case of lepton tagging. The efficiency for signal events is 0.39 for the lepton tag and 0.23 for the kaon tag, while for background events it is 0.03 for the lepton tag and 0.22 for the kaon tag. The gain in the signal to noise ratio, in the lepton tag case, happens because the $q\bar{q}$ background produces fewer leptons in the final state.

Table 6-7 summarizes the efficiencies for the cuts described above, for both signal and background processes. The extraction of CP asymmetries for this mode is described in detail in Section 6.4.4.

Table 6-7. Efficiencies for each successive cut, for signal and backgrounds. The efficiencies for each row are computed after applying all the cuts in the previous rows. The final two rows are the number of events produced and the number surviving all cuts, respectively, for 30 fb^{-1} of integrated luminosity.

Cut	Efficiency		
	$\pi^+\pi^-$	$K^+\pi^-$	$q\bar{q}$
Kinematic cuts	0.75	0.37	5.1×10^{-5}
Event Shape	0.88	0.88	0.30
Particle ID	0.97	0.051	0.39
Vertexing	0.99	0.99	0.89
All cuts	0.63	0.017	5.3×10^{-6}
Flavor Tag (ℓ)	0.39	0.39	0.03
Flavor Tag (K)	0.23	0.23	0.22
Produced (30 fb^{-1})	380	470	10^8
Selected (ℓ)	93	3	15
Selected (K)	55	2	110

6.4.2 The $\pi^0\pi^0$ Decay Mode

Extraction of the decay rate for the process $B^0 \rightarrow \pi^0\pi^0$ will not be simple. There are two key complications which conspire to make this task a difficult one: the anticipated low branching fractions, and the experimental problems in background suppression and in reconstructing the $B^0 \rightarrow \pi^0\pi^0$ final state. Current knowledge of the branching ratio for this mode is limited to an upper bound of 9×10^{-6} from CLEO, and the theoretical predictions of order 10^{-6} , which are based on factorization models with color suppression effects. In constructing an all-neutral final state, the only information available is from the calorimeter clusters. This lack of information makes effective discrimination between signal and background particularly difficult.

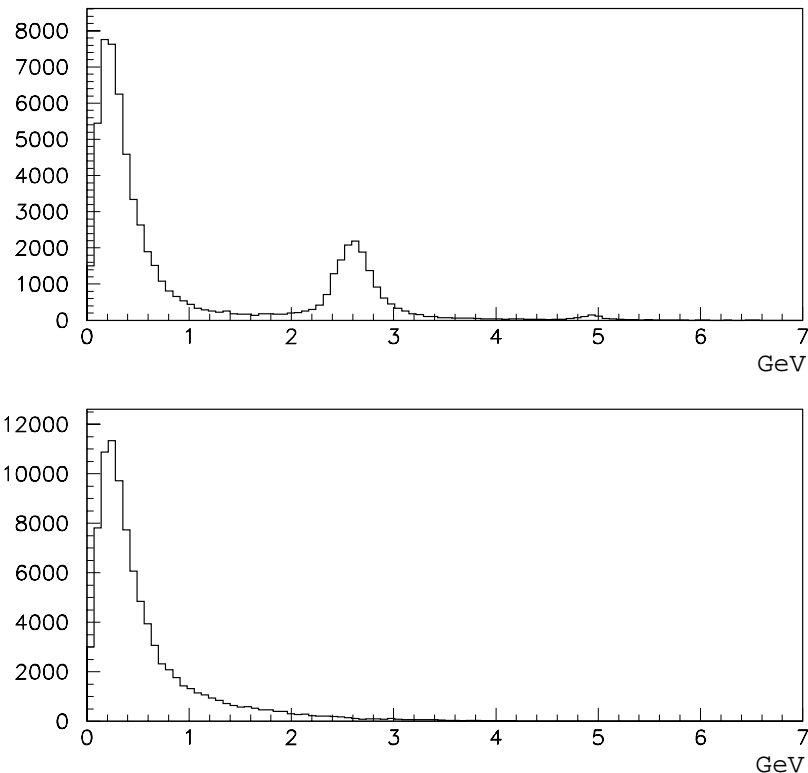


Figure 6-7. Distribution of the energy of the two clusters (E_t , defined in the text) for signal events (top) and background events (bottom). The simulations were done using the full `BBsim` simulation and the reconstruction software. The small peak near 0.4 GeV in the distribution for signal events is from random combinations of clusters that are not associated with the signal decay. The second peak near 2.7 GeV represents combinations in which one cluster is from the signal process and the other is not. The small peak near 5 GeV represents the case where both clusters are due to π^0 mesons from the signal process.

Since the π^0 mesons in this decay mode are energetic, the opening angle of the two photons is very small, and therefore they tend to overlap in the electromagnetic calorimeter. Such effects are known to be poorly simulated by the `Aslund` fast simulation program, so that the whole of this study (signal and background estimation) was done using the full `BBsim` simulation (Section 4.1.2) and the reconstruction software. These studies show that about 80% of the π^0 mesons from this process that enter the detector acceptance are seen as a single cluster in the electromagnetic calorimeter. For this reason an explicit reconstruction of the π^0 mass is not attempted in this analysis. B^0 candidates are reconstructed by forming pairs of electromagnetic clusters that are unmatched to charged tracks. By energy conservation, the sum of the energies of the clusters, boosted to the $\Upsilon(4S)$ rest frame, E_t , must be consistent with $M(\Upsilon(4S))/2$, where $M(\Upsilon(4S))$ is the mass of the $\Upsilon(4S)$. However, because of energy leakage in the calorimeter, the distribution of E_t has a mean value significantly different from this nominal value. The distribution of this quantity for signal and generic $q\bar{q}$ events is shown in Fig. 6-7. An energy window of $4.75 \text{ GeV} \leq E_t \leq 5.15 \text{ GeV}$ is used (the resolution on this quantity is approximately 100 MeV).

As in the case of the $B^0 \rightarrow \pi^+\pi^-$ mode, the dominant background is from the continuum processes $e^+e^- \rightarrow q\bar{q}$. A multivariate technique (based on a Genetic Algorithm, see Section 4.7) is used in order to optimize the cuts on kinematic and topological variables for background suppression. The algorithm fixes the cuts in such a way as to maximize the statistical significance, which is defined as

$$N_\sigma = \frac{\sqrt{N_S + N_B}}{N_S} \quad (6.42)$$

where N_S (N_B) is the number of signal (background) events in a sample surviving all cuts. The variables used (all computed in the $\Upsilon(4S)$ rest frame) are:

- Kinematic variables:
 - Momenta of the pion candidates, $|\mathbf{p}_\pi^*|$;
 - Momentum of the B candidate, $|\mathbf{p}_B^*|$;
 - The quantity

$$\chi_B^2 = \left(\frac{|p_\pi + p_\pi| - M_B}{\sigma_{m_B}} \right)^2 + \left(\frac{\sqrt{(M_{\Upsilon(4S)}/2)^2 - |\mathbf{p}_B^*|^2} - M_B}{\sigma_{beam}} \right)^2,$$

where σ_{m_B} and σ_{beam} are the width of the reconstructed B^0 candidate and the spread in the beam energy, respectively.

- Topological variables:
 - $\cos \theta_H$, where θ_H is the angle between the π^0 candidate with the highest momentum and the track closest to it;
 - Fox-Wolfram moments $H_{20} \equiv H_2/H_0$ and $H_{40} \equiv H_4/H_0$;

Table 6-8. Efficiencies for preselection and for each cut separately applied. The final two rows are the number of events produced and the number surviving all cuts, respectively, for 30 fb^{-1} of integrated luminosity. The number of signal events assumes a $\pi^0\pi^0$ branching ratio of 3×10^{-6} .

Cut	Efficiency	
	$\pi^0\pi^0$	Continuum
Preselection	0.47	2.2×10^{-3}
$ \mathbf{p}_{\pi_1^0} \geq 2.118 \text{ GeV}/c$	0.98	0.30
$ \mathbf{p}_{\pi_2^0} \leq 2.864 \text{ GeV}/c$	0.99	0.31
$0.190 \text{ GeV}/c \leq \mathbf{p}_B^* \leq 0.492 \text{ GeV}/c$	0.92	0.20
$\chi_B^2 \leq 2.39$	0.53	0.013
$H_{20} + H_{40} \geq 0.096$	0.52	0.046
All cuts	0.15	2.0×10^{-7}
Events Produced (30 fb^{-1})	95	10^8
Events Selected (30 fb^{-1})	14	20

Table 6-8 lists the cuts and the efficiencies for signal and background samples.

With these optimised efficiencies, ϵ_S and ϵ_B , for signal and background respectively, it is straightforward to show that (assuming no uncertainty on the knowledge of the background rate)

$$\sigma_B = \sqrt{\frac{\mathcal{B} + (\sigma_B \epsilon_B) / (\sigma_S \epsilon_S)}{\mathcal{L} \sigma_S \epsilon_S}}, \quad (6.43)$$

where σ_S and σ_B are the cross-sections for signal and background production respectively and \mathcal{L} is the integrated luminosity. The error in the branching ratio found from the above formula (as a fraction of the branching ratio itself) is shown in Fig. 6-8 as a function of the integrated luminosity for different assumptions for the branching fraction.

The branching ratio will be used below in an isospin analysis; the uncertainty limits the precision of the determination of α .

6.4.3 The $\pi^+\pi^0$ Decay Mode

As in the case of the $\pi^0\pi^0$ study (and for similar reasons), the simulation study of the $B^+ \rightarrow \pi^+\pi^0$ mode was performed using the full `BBsim` simulation and the reconstruction software. The genetic algorithm described for the $B^0 \rightarrow \pi^0\pi^0$ analysis was also used for the $B^+ \rightarrow \pi^+\pi^0$ mode. The

primary quantity of interest is the total decay rate, which is expected to be the same for $B^+ \rightarrow \pi^+\pi^0$ and $B^- \rightarrow \pi^-\pi^0$.

The cuts used for this mode, and the resulting efficiencies for signal and background events, are given in Table 6-9, where a branching ratio of 0.8×10^{-5} has been assumed. In Fig. 6-9 the relative error on the branching fraction as a function of the integrated luminosity is shown for different assumptions for the branching fraction.

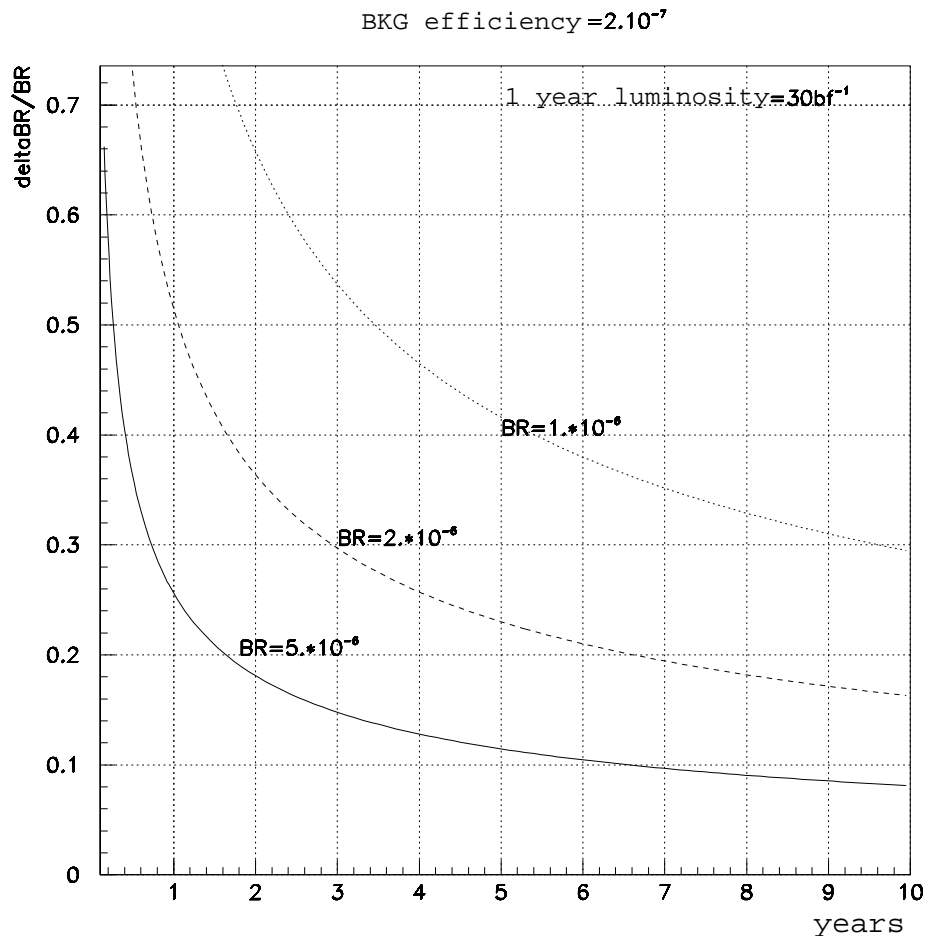


Figure 6-8. Relative error on the branching ratio as a function of the number of years of data taking (assuming 30 fb^{-1} per year), for $B^0 \rightarrow \pi^0\pi^0$, assuming different values for the branching ratio.

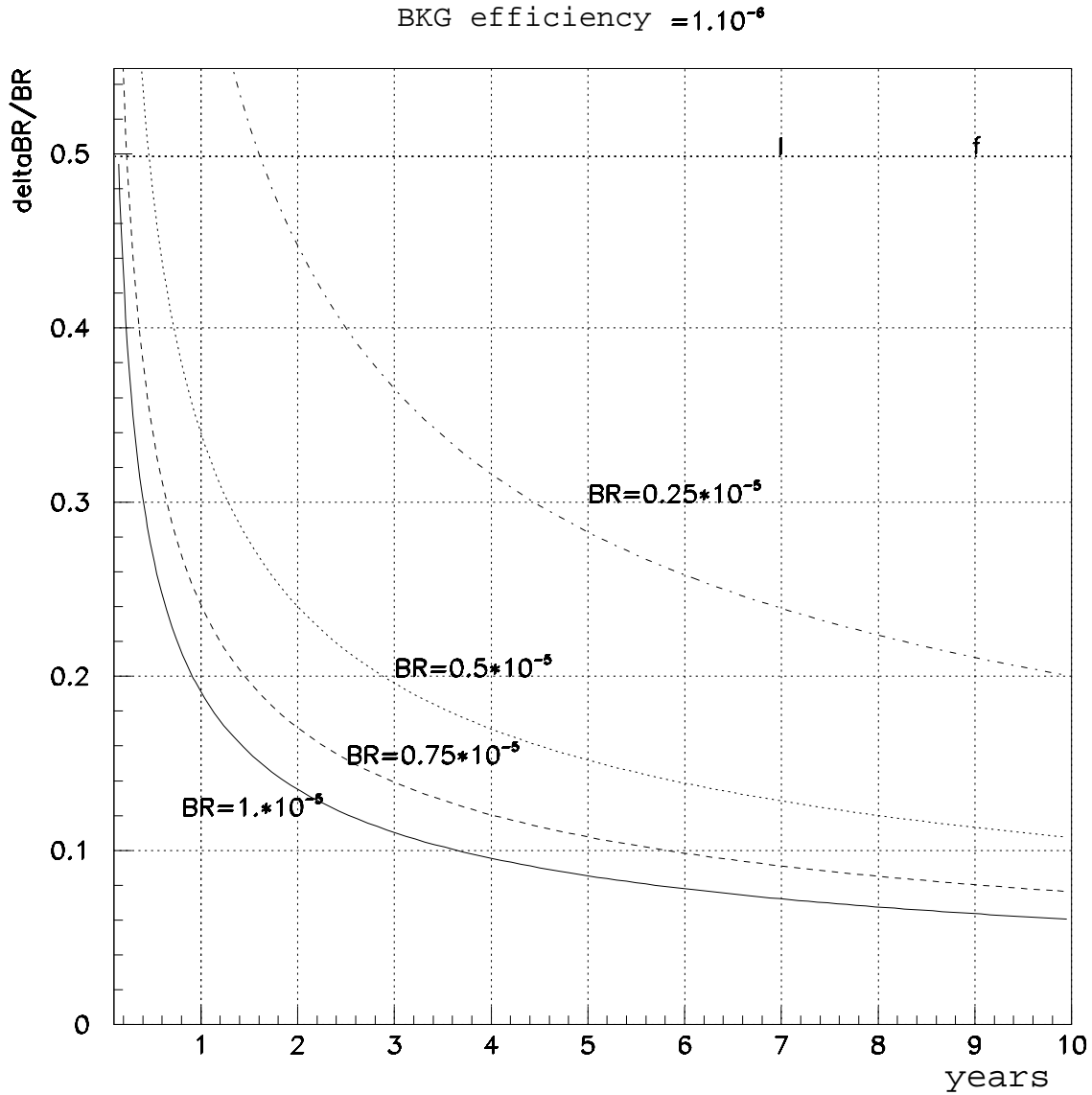


Figure 6-9. Relative error on the branching ratio as a function of the number of years of data taking (assuming 30 fb^{-1} per year), for $B^0 \rightarrow \pi^+ \pi^0$, assuming different values for the branching ratio.

Table 6-9. Efficiencies for preselection and for each cut separately applied. The final two rows are the number of events produced and the number surviving all cuts, respectively, for 30 fb^{-1} of integrated luminosity.

Cut	Efficiency	
	$\pi^+\pi^0$	Continuum
Preselection	0.63	3.7×10^{-3}
$ \mathbf{p}_{\pi^+} \geq 2.441 \text{ GeV}/c$	0.99	0.17
$ \mathbf{p}_{\pi^0} \leq 2.855 \text{ GeV}/c$	0.85	0.17
$0.190 \text{ GeV}/c \leq \mathbf{p}_B^* \leq 0.492 \text{ GeV}/c$	0.82	0.13
$\chi_B^2 \leq 3.55$	0.49	0.005
$\cos \theta_{\text{sph}} \leq 0.8$	0.78	0.15
$\cos \theta_H \leq 0.924$	0.72	0.40
All cuts	0.19	1.0×10^{-6}
Produced (30 fb^{-1})	250	10^8
Selected (30 fb^{-1})	48	100

6.4.4 Extraction of CP Asymmetries from the $B^0 \rightarrow \pi^+\pi^-$ Decay Mode

Information on CP violation for the mode $B^0 \rightarrow \pi^+\pi^-$ is contained in the time evolution of the decay, which, in the most general case (Eq. 6.3), is given by:

$$P(B^0 \rightarrow \pi^+\pi^-) \propto \exp(-|\Delta t|/\tau) (1 + a_{\text{sin}} \sin(\Delta m_d \Delta t) + a_{\text{cos}} \cos(\Delta m_d \Delta t)) , \quad (6.44)$$

where $\Delta t \simeq \Delta z/(\beta\gamma c)$ ($\beta\gamma \sim 0.56$) and Δz is the difference between the z coordinates of the two B^0 decays in the event. The parameter a_{sin} is analogous (but not equal) to the quantity $\sin 2\alpha$ obtained in the case of tree-dominated decays, and the parameter a_{cos} is a measure of direct CP violation. They also correspond to the parameters R and D in Eq. 6.3. Theoretical predictions are usually expressed in terms of the complex parameter $\lambda = \frac{q}{p} \frac{\bar{A}_f}{A_f}$ (see Eqs. 1.42 and 6.23). For the fit described here, the free parameters are the magnitude and phase of λ : $|\lambda|$ and $\arg \lambda \equiv 2\alpha_{\text{eff}}$. They are related to a_{sin} and a_{cos} by:

$$a_{\text{sin}} = \frac{-2|\lambda| \sin 2\alpha_{\text{eff}}}{1 + |\lambda|^2} \quad (6.45)$$

$$a_{\text{cos}} = \frac{1 - |\lambda|^2}{1 + |\lambda|^2} . \quad (6.46)$$

An unbinned, maximum-likelihood fit to the reconstructed Δt distribution is used to extract the parameters $|\lambda|$ and $2\alpha_{\text{eff}}$. In order to reconstruct Δt , it is necessary to estimate the z coordinates of the decay vertices of both the $B^0 \rightarrow \pi^+\pi^-$ candidate (z_{CP}) and the other B^0 (z_{tag}). In this section, the analysis of the time evolution of $B^0 \rightarrow \pi^+\pi^-$ decays is described, beginning with the technique used to estimate $\Delta z = z_{CP} - z_{\text{tag}}$.

6.4.4.1 Δz reconstruction

The z coordinate of the CP vertex comes directly from a fit of the candidate pion tracks to a common vertex. The average resolution on z_{CP} is $40 \mu\text{m}$. The Δz resolution is dominated by the error on the vertex of the tagging B^0 , which is not as easily determined in an unbiased manner. Two different methods of estimating z_{tag} have been studied:

- A vertex is formed using all the tracks in the event, excluding those of the B^0 candidate and those with a large impact parameter at the nominal interaction point (to remove K_S^0 daughters). The z coordinate of this vertex is a reasonable estimate of z_{tag} .
- z_{tag} is estimated using the z coordinate of the point of closest approach of the *tagging* track to the axis which is parallel to the z axis and passes through the $x - y$ projection of the CP vertex, where the tagging track is the candidate kaon or lepton track which has been used to tag the flavor of the other B^0 . Because the two B mesons are produced nearly at rest in the $\Upsilon(4S)$ rest frame, they decay along the same axis, to a very good approximation. The axis defined as described above is more accurate than the nominal z axis since the CP vertex is known to greater precision (about $40 \mu\text{m}$ in both x and y) than is the average beam spot position (about $150 \mu\text{m}$ in x and $6 \mu\text{m}$ in y).

The primary disadvantage of the first method is that the vertex contains a mixture of tracks which originate directly from the tagging B decay and tracks which originate from the subsequent charm decay. Thus, this vertex does not represent an unbiased estimate of the tagging B vertex. Corrections derived from Monte Carlo simulation must be applied to take into account this effect which entangles the charm lifetime with the tagging B decay time.

This problem is mitigated in the second method since only the tagging track is used. This track is preselected in a manner which favors particles coming directly from the tagging B decay, so there is less contamination from tertiary charm decays. In addition, the case where the tagging track comes from the charm decay can be taken into account in a rather straightforward manner without much reliance on Monte Carlo simulation, as will be demonstrated below. For these reasons, this second approach has been used here.

The Δt distribution of Eq. (6.44) is modified to take into account the experimental effects described above. The resolution on z_{CP} is accounted for by a simple Gaussian smearing of the idealized Δt

distribution. Two separate cases are considered in order to take into account properly the effects of the reconstructed z_{tag} :

- The case where the tagging track comes from the tagging B decay vertex (this is referred to as a primary track).
- The case where the tagging track comes from a D meson decay vertex (this is referred to as a secondary track).

The output of the `Cornelius` tagging package is used to assign to each tagging track i a probability, g_i , to be a primary track versus a secondary track. Simulation studies show that a tagging lepton track has a 50% probability to be a primary track, whereas a tagging kaon track has a 15% probability to be a primary track. A numerical convolution method is used to take into account the effect of using the CPB vertex to define the z axis for the tagging B decay and to take into account the effect of the charmed-meson decay length (for the case of secondary tracks only). Figure 6-10 shows the distributions of Δt , before and after experimental resolution convolutions, for primary and secondary leptons for two different choices of the CP violation parameters a_{sin} and a_{cos} .

6.4.4.2 The maximum-likelihood fit

The maximum likelihood fit used to extract the parameters $|\lambda|$ and $2\alpha_{\text{eff}}$ makes use of a probability density function, which is defined for each event i in the following manner:

$$\begin{aligned} \mathcal{P}(\Delta t_i, q_t, |\lambda|, 2\alpha_{\text{eff}}) = & f^{\text{sig}}[g_i \mathcal{P}_p^{\text{sig}}(\Delta t_i, q_t, |\lambda|, 2\alpha_{\text{eff}}) + \\ & (1 - g_i)(f_{ss} \mathcal{P}_s^{\text{sig}}(\Delta t_i, q_t, |\lambda|, 2\alpha_{\text{eff}}) + \\ & (1 - f_{ss}) \mathcal{P}_s^{\text{sig}}(\Delta t_i, -q_t, |\lambda|, 2\alpha_{\text{eff}})] + \\ & \sum_k f_k^{bg} \mathcal{P}_k^{bg}(\Delta t_i), \end{aligned} \quad (6.47)$$

where f^{sig} is the fraction of selected events that is signal; g_i is the probability that the tagging track is primary; $\mathcal{P}_p^{\text{sig}}(\Delta t_i, q_t, |\lambda|, 2\alpha_{\text{eff}})$ and $\mathcal{P}_s^{\text{sig}}(\Delta t_i, q_t, |\lambda|, 2\alpha_{\text{eff}})$ are the Δt distributions when the tagging particle is primary or secondary, respectively; f_k^{bg} and \mathcal{P}_k^{bg} are the fraction and the Δt distribution for the k -th source of background; f_{ss} is the fraction of tagging tracks that has the same sign of charge as the b quark in the tagging B (determined from Monte Carlo simulation); and q_t is the charge of the tagging track. The Δt distributions for the background processes are parameterized from Monte Carlo simulations. The Δt distribution of uds background is a Gaussian centered at zero, with a width given by the experimental resolution on Δt . For $c\bar{c}$ events, the Δt distribution is instead the convolution of the average charmed-meson lifetime with a Gaussian resolution function.

Table 6-10. Errors and correlations obtained from the fit to the *CP* parameters, using samples corresponding to 10, 30 and 90 fb⁻¹ of integrated luminosity. The samples were generated with $a_{\sin} = a_{\cos} = 0$ (no *CP* violation), which is the most conservative case.

	10 fb ⁻¹	30 fb ⁻¹	90 fb ⁻¹
$\delta \lambda $	0.58	0.33	0.19
$\delta 2\alpha_{\text{eff}}$	0.67	0.29	0.16
corr. ($ \lambda , 2\alpha_{\text{eff}}$)	0.28	0.19	0.12
δa_{\sin}	0.41	0.26	0.15
δa_{\cos}	0.39	0.29	0.18
corr. (a_{\sin}, a_{\cos})	0.35	0.20	0.12

The likelihood for a selected sample of events is the product of the probability density functions given by equation 6.47 for all the events in the sample. The fitted parameters $|\lambda|$ and $2\alpha_{\text{eff}}$ are those which maximize this likelihood. The fit was extensively tested by varying the size of the simulated data samples and by using a variety of values for $|\lambda|$ and $2\alpha_{\text{eff}}$ in generating the samples. In all cases, the fitted values of the *CP* parameters are normally distributed around the generated values. Table 6-10 gives the results of a fit using simulated samples corresponding to 10, 30 and 90 fb⁻¹ of integrated luminosity, generated in the most statistically conservative case, where $a_{\sin} = 0$ and $a_{\cos} = 0$.

6.4.4.3 $\kappa_{\pi\pi}$, the difference between 2α and $2\alpha_{\text{eff}}$

The observation of the time-dependent asymmetry, $A(t)$, in the presence of penguins, Eq. 6.44, enables the amplitudes of the sine and cosine terms, Eqs. (6.45) and (6.46), to be extracted with the resolutions quoted in Table 6-10. These in turn determine the complex parameter:

$$\lambda = |\lambda| e^{2i\alpha_{\text{eff}}} \equiv \frac{q \bar{A}}{p A} = \frac{e^{-i\alpha} T + P}{e^{+i\alpha} T + P} = e^{-2i\alpha} \frac{1 + |Z| e^{i(\delta + \alpha)}}{1 + |Z| e^{i(\delta - \alpha)}}, \quad (6.48)$$

where Eq. 6.12 has been used to expand the right-hand side, $Z = P/T$ is the ratio of the penguin amplitude P to the tree amplitude T , and $\delta = \delta_P - \delta_T$ is the difference in the strong phases of P and T . The experimental uncertainties in $|\lambda|$ and $2\alpha_{\text{eff}}$ are also given in the table.

It can be seen that in the limit as $|Z| \rightarrow 0$, the usual penguin-free limit, $|\lambda| \rightarrow 1$ and $\alpha_{\text{eff}} \rightarrow \alpha$ is recovered. In the general case, the equation represents corrections to this, of order $|Z|$, of unknown sign, and of magnitude dependent on the strong-phase difference δ . In fact it can be shown that the

Table 6-11. Theoretical central values and experimental resolution for the isospin analysis. The branching ratios are calculated in a model which gives: $\sin 2\alpha = -0.04$, $\sin 2\alpha_{\text{eff}} = 0.21$, [61]. The experimental errors are calculated for 90 fb^{-1} integrated luminosity.

\mathcal{B}_{av}	Central Value	Exp. Error(%)	Comments
$\pi^+\pi^-$	1.2×10^{-5}	6.0	Ref. [61]
$\pi^+\pi^0$	0.81×10^{-5}	14	Ref. [61]
$\pi^0\pi^0$	0.3×10^{-5}	21	Ref. [61]
$ \lambda_{+-} \sim \frac{ A^{+-} }{ A^{+0} }$	0.81	17	From CP Fit
$ \lambda_{00} \sim \frac{ A^{00} }{ A^{+0} }$	0.94	65	Flavor Tagging

maximum shift in 2α is $\simeq 2|Z|$, for $|Z| < 1$. This shift is the angle $\kappa_{\pi\pi}$ shown in Figs. 6-1 and 6-3, so named, because there are analogous shifts in other modes, of different values governed by the relative magnitudes and phases of their own tree and penguin amplitudes.

The shift in the angle α limits the available precision which can be obtained in its measurement. The relative magnitude of tree and penguin mechanisms is unknown at the time of writing, but is thought to be significant. In the next section, a study of the experimental possibilities for measuring $\kappa_{\pi\pi}$ using the isospin analysis is presented.

6.4.5 Isospin Analysis

This section studies the isospin analysis described in Section 6.1.2, which combines the information from the three 2π channels in order to estimate the effects of the penguin contribution and the uncertainty on the measurement of $\sin 2\alpha$.

As described in Section 6.1.2 and above, the effect of penguin diagrams can be characterized in terms of a shift in the value of $|\lambda_{+-}|$ and the shift, $\kappa_{\pi\pi} = 2\alpha_{\text{eff}} - 2\alpha$, these in turn depend on the ratio of the penguin to tree amplitudes and their strong-phase difference. The isospin analysis determines $\kappa_{\pi\pi}$ (with four-fold ambiguity), if the decay amplitudes and $\sin 2\alpha_{\text{eff}}$ are known. For this study, central values of the decay amplitudes, A^{+-} , A^{+0} , A^{00} , \bar{A}^{+-} , \bar{A}^{+0} and \bar{A}^{00} , were taken from the theoretical model analysis of [61]. They perform a full analysis of rare B decays, including the recent CLEO results on the branching ratios for $B \rightarrow K\pi$ and $B \rightarrow \pi\pi$, yielding predictions for the size of the penguin effects and average branching ratios of $B \rightarrow \pi\pi$. As an example, for an input value of $\sin 2\alpha = -0.04$, they predict $\sin 2\alpha_{\text{eff}} = 0.21$. In Table 6-11 the predictions for the central values Of the branching ratios are summarized, along with estimates of the ratio of decay amplitudes, $|\lambda_{+-}| \sim \frac{|A^{+-}|}{|A^{+0}|}$ and $|\lambda_{00}| \sim \frac{|A^{00}|}{|A^{+0}|}$. In addition, the measurement

errors on the branching ratios from Figs. 6-8 and 6-9 are shown. The experimental uncertainties on $|\lambda_{+-}|$ are known from the study of the time evolution of $B \rightarrow \pi^+\pi^-$. Since a time-dependence analysis is not feasible for the mode $B^0 \rightarrow \pi^0\pi^0$, the uncertainties on the decay amplitudes and the ratio $|\lambda_{00}|$ must be obtained from the time-integrated rates for the *joint decay* of $B^0\bar{B}^0$ pairs to $X_{\pm}\pi^0\pi^0$, where X_{\pm} is a *tagging* final state (X^+ tags a B^0 while X^- tags a \bar{B}^0). The joint decay branching ratio $\mathcal{B}(X_{\pm}; \pi^0\pi^0)$ is related to the partial rates by

$$\begin{aligned} \mathcal{B}(X_{\pm}; \pi^0\pi^0) = & \left(\frac{(\Gamma(B^0 \rightarrow \pi^0\pi^0) + \Gamma(\bar{B}^0 \rightarrow \pi^0\pi^0))}{2\Gamma_B} \mp \frac{1}{1+x_d^2} \frac{\Gamma(B^0 \rightarrow \pi^0\pi^0) - \Gamma(\bar{B}^0 \rightarrow \pi^0\pi^0)}{2\Gamma_B} \right) \\ & \times \sum_i \mathcal{B}(B_{\text{tag}} \rightarrow X_{\pm}^i), \end{aligned} \quad (6.49)$$

where $x_d = \Delta m/\Gamma_B$ and Γ_B is the total width of the neutral B meson, and $\mathcal{B}(B_{\text{tag}} \rightarrow X_{\pm}^i)$ is the branching ratio to the combined tagging modes. Since in the simulation study of the mode $B \rightarrow \pi^0\pi^0$, tagging was not applied, the branching ratios $\mathcal{B}(X_{\pm}; \pi^0\pi^0)$, and the corresponding uncertainties, were calculated from the simulation results on the experimental resolution of the average branching ratio for $B \rightarrow \pi^0\pi^0$, accounting in addition, for the effective tagging efficiency and the mistag rate. By inverting the two relations (6.49), $\Gamma(B^0 \rightarrow \pi^0\pi^0)$ and $\Gamma(\bar{B}^0 \rightarrow \pi^0\pi^0)$ can be extracted, and, by dividing by a common phase space factor, $|A^{ij}|$ and $|\bar{A}^{ij}|$ are obtained. The resolutions obtained on $|\lambda_{00}|$ and $|\lambda_{+-}|$ are given in Table 6-11.

In order to understand the influence of the predicted experimental resolutions on $|\lambda_{00}|$ and $|\lambda_{+-}|$, a Monte Carlo method was used to draw the isospin triangles, taking into account these uncertainties, for 90 fb^{-1} of BaBar data. In the example described above, with input values of $\sin 2\alpha = -0.04$ and $\sin 2\alpha_{\text{eff}} = 0.21$, the angle $\kappa_{\pi\pi}$ was determined with a four-fold ambiguity to be 0.2 rad., -0.2 rad., 0.7 rad. and -0.7 rad., with a root-mean-square spread of 0.6 rad. The distributions of these fitted values of $\kappa_{\pi\pi}$ are shown in Figs. 6-11. The large magnitude of the error seen in this analysis is mainly the result of the very poor statistics available with the branching ratio estimated for $B^0 \rightarrow \pi^0\pi^0$. With four solutions for $\kappa_{\pi\pi}$, and an additional factor of two in obtaining α from $\sin 2\alpha$, the method has a total of eight solutions for α . With such large errors, it is doubtful that this method will be useful for many years to come.

Another possible method for bounding the effect of penguin diagrams in the limit of a small branching ratio has been suggested by Grossman and Quinn, [62]. This bound can be obtained using only the measured rate of $\mathcal{B}(B^{\pm} \rightarrow \pi^{\pm}\pi^0)$ and an upper bound on the combined rate $\mathcal{B}(B^0 \rightarrow \pi^0\pi^0) + \mathcal{B}(\bar{B}^0 \rightarrow \pi^0\pi^0)$. In this approach no b tagging is required.

In Fig. 6-12 limits for the $\kappa_{\pi\pi}$ confidence level interval $[-\overline{\kappa_{\pi\pi}}, +\overline{\kappa_{\pi\pi}}]$ are displayed as a function of the upper limit on

$$B^{00} = \frac{\mathcal{B}_{\text{av}}(B^0 \rightarrow \pi^0\pi^0)}{\mathcal{B}(B^+ \rightarrow \pi^+\pi^0)}. \quad (6.50)$$

Possible values for $\kappa_{\pi\pi}$ are not only within this interval but also in $[\pi - \overline{\kappa_{\pi\pi}}, \overline{\kappa_{\pi\pi}}]$ and $[-\pi, -\pi + \overline{\kappa_{\pi\pi}}]$. It can be seen that this method also leads to very poor limits on α .

6.4.6 α without $B^0 \rightarrow \pi^0 \pi^0$?

As was seen in the last section, although theoretically clean, the isospin analysis in $B \rightarrow \pi\pi$ is likely to be undermined by the expected smallness of the branching ratio in the $B^0 \rightarrow \pi^0 \pi^0$ mode: although the measurement of $\sin(2\alpha + \kappa_{\pi\pi})$ is likely to be reasonably precise, the uncertainty in the measurement of the correction, $\kappa_{\pi\pi}$, could suffer from a large statistical error. In this section, another method is presented, which seeks to obtain information on the true α , without relying on the $B^0 \rightarrow \pi^0 \pi^0$ mode. Though theoretically less clean, it is conceivable that it could provide a phenomenologically interesting bound on α , with far lower luminosity.

Referring back to Eq. (6.48), it can be seen that it represents two constraints on the unknowns $|Z|$, δ and α . If one more constraint could be found, then α could be determined, up to a finite number of ambiguities. As was discussed in Section 6.1.2, the recent observation of $B^0 \rightarrow K^\pm \pi^\mp$ and $B^0 \rightarrow \pi^+ \pi^-$ events at CLEO [2] indicates that penguins are not negligible in such modes. As was shown there, taking the current central values of the CLEO results at face value (and, for now, ignoring their measurement error, and theoretical uncertainties), leads to a striking estimate of $|Z|$, Eq. (6.18):

$$0.18 < |Z| < 0.40 . \quad (6.51)$$

If this range could be taken seriously, it could be used as a constraint to solve Eq. (6.48) and to bound α and δ . In fact, the experimental errors on the branching ratios $\mathcal{B}(B^0 \rightarrow K^\pm \pi^\mp)$ and $\mathcal{B}(B^0 \rightarrow \pi^+ \pi^-)$ are today very significant and, when taken into account properly, expand the allowed ranges of Eq. (6.51) dramatically (in fact, it is not currently possible to put an upper bound on $|Z|$). However, by the time that BABAR has recorded enough $B^0 \rightarrow \pi^+ \pi^-$ events to measure the time-dependent asymmetry, the experimental errors on these quantities will be negligible, and only the theoretical uncertainties will be an issue.

The rest of this section summarizes the results of a study of the precision in the determination of α by such methods. First it is necessary to examine briefly the possible bounds on $|Z|$. The argument presented in Section 6.1.2, simply makes an order-of-magnitude estimate about the value of $|Z|$, based on an (assumed) exact knowledge of SU(3) breaking and ignoring experimental errors. Chapter 7, and references therein, on the other hand, discuss in detail, the possible ways of bounding penguin amplitudes using SU(3) symmetry. Here, it is assumed that an unspecified method has been used for bounding $|Z|$, and a range of putative resulting central values and uncertainties have been explored. For a more detailed discussion of the possibilities for such constraints see [63].

As a first guess estimate, the method of Section 6.1.2.5 can be used, but modified by assuming that the SU(3) breaking factor has an uncertainty, and is given (say) by 1.0 ± 0.3 . Here, the present central values of the CLEO branching ratios for $\mathcal{B}(B^0 \rightarrow K^\pm \pi^\mp)$ and $\mathcal{B}(B^0 \rightarrow \pi^+ \pi^-)$ will be assumed. The experimental errors on them will be considered negligible, as will be the case by the

time the asymmetry in $B^0 \rightarrow \pi^+\pi^-$ is measured. Then, the allowed range of $|Z|$ becomes:

$$0.15 < |Z| < 0.62 . \quad (6.52)$$

Clearly, the central value could change up or down from the one used here, so this range is just used for illustrative purposes. In addition, as models are refined, and tested by comparison with measurements in many channels, the model dependence in estimates of $|P/T|$ without reference to SU(3) relationships may decrease to the point where the range given by such estimates is even smaller than this.

For any given pair of measured values (a_{\cos}, a_{\sin}) , Eqs. (6.45), (6.46) and (6.48) can be solved for α and δ as a function of $|Z|$ within this range. The resulting range of values of α represents its measurement. The solution is a mapping of a point in the space of possible values of (a_{\cos}, a_{\sin}) onto a locus (or loci) in the solution space of (α, δ) . Ambiguities (mirror solutions) mean that the mapping is, in general, a one-to-many mapping and the topology of the solution can depend strongly on the values of (a_{\cos}, a_{\sin}) (or equivalently, the “true” values of α and δ). It is possible to get no solution at all, which would indicate a violation of the assumed bounds on $|Z|$ (presumably an interesting outcome in itself), although measurement errors could cause this also.

A toy Monte Carlo was used to generate many pairs of experimental values, (a_{\cos}, a_{\sin}) , according to each of several initial (test) values of $(\alpha, \delta, |Z|)$. The mock experimental results were generated for each set of test parameters, according to a two-dimensional Gaussian distribution with widths given by the experimental errors tabulated in Table 6-10 for 90 fb^{-1} integrated BABAR luminosity at the $\Upsilon(4S)$. For each pair (a_{\cos}, a_{\sin}) , Eqs. (6.45), (6.46) and (6.48) were solved numerically for the values of the initial parameters (α, δ) .

Some example distributions of the true and “measured” values of α and δ are shown in Fig. 6-13 (a) and (b). The broadening of the loci in the (α, δ) space into bands is caused by the experimental resolution, factored in via the Gaussian smearing of the experimental quantities. The range of values of α is constrained with respect to the full range of possible values. Furthermore, it can be seen that any future constraints on the allowed range of δ would help restrict it further. The kind of resolution obtainable for α can be seen from the projections of the scatter plots onto the α axis, as seen in Figs. 6-13 c) and d). The widths here get a contribution from the slopes of the loci in the (α, δ) plane as well as from the resolution in the observed quantities. In Fig. 6-13 c), the peak is close to the true value of α , but in the latter, the true value corresponds to the smaller peak. The two figures shown are “typical.” They were generated with the “true” values of (α, δ) shown in the plots, and a “true” value of $|Z| = 0.3$. The solutions were obtained using many trial values of $|Z|$ in the range specified by Eq. (6.52).

Eq. (6.48) has a symmetry under the transformations $\alpha \rightarrow \alpha + \pi, \delta \rightarrow \delta + \pi$, which results in the repeating of the pattern of solutions in diagonally opposite quadrants of the full (α, δ) space. This symmetry is the only exact symmetry of the equations, and results in the method having two degenerate sets of solutions for α , separated by π , which is why the figures are plotted only for $0 < \alpha < \pi$.

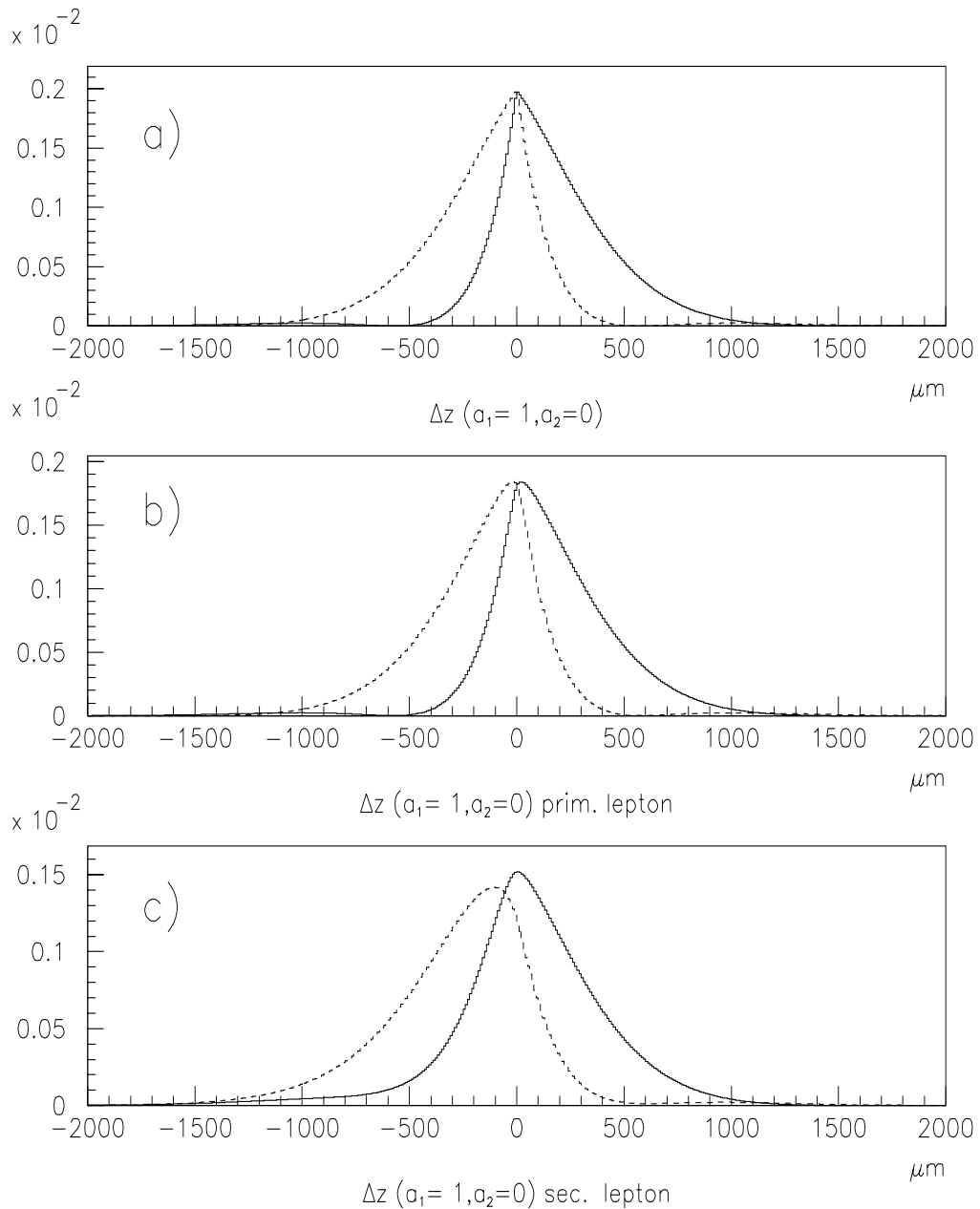


Figure 6-10. Underlying physics function: (a) true difference between CP and tag vertex; (b) primary leptons; (c) secondary leptons for $a_{\sin} = 1$ ($a_{\sin} = -1$ dotted) and $a_{\cos} = 0$.

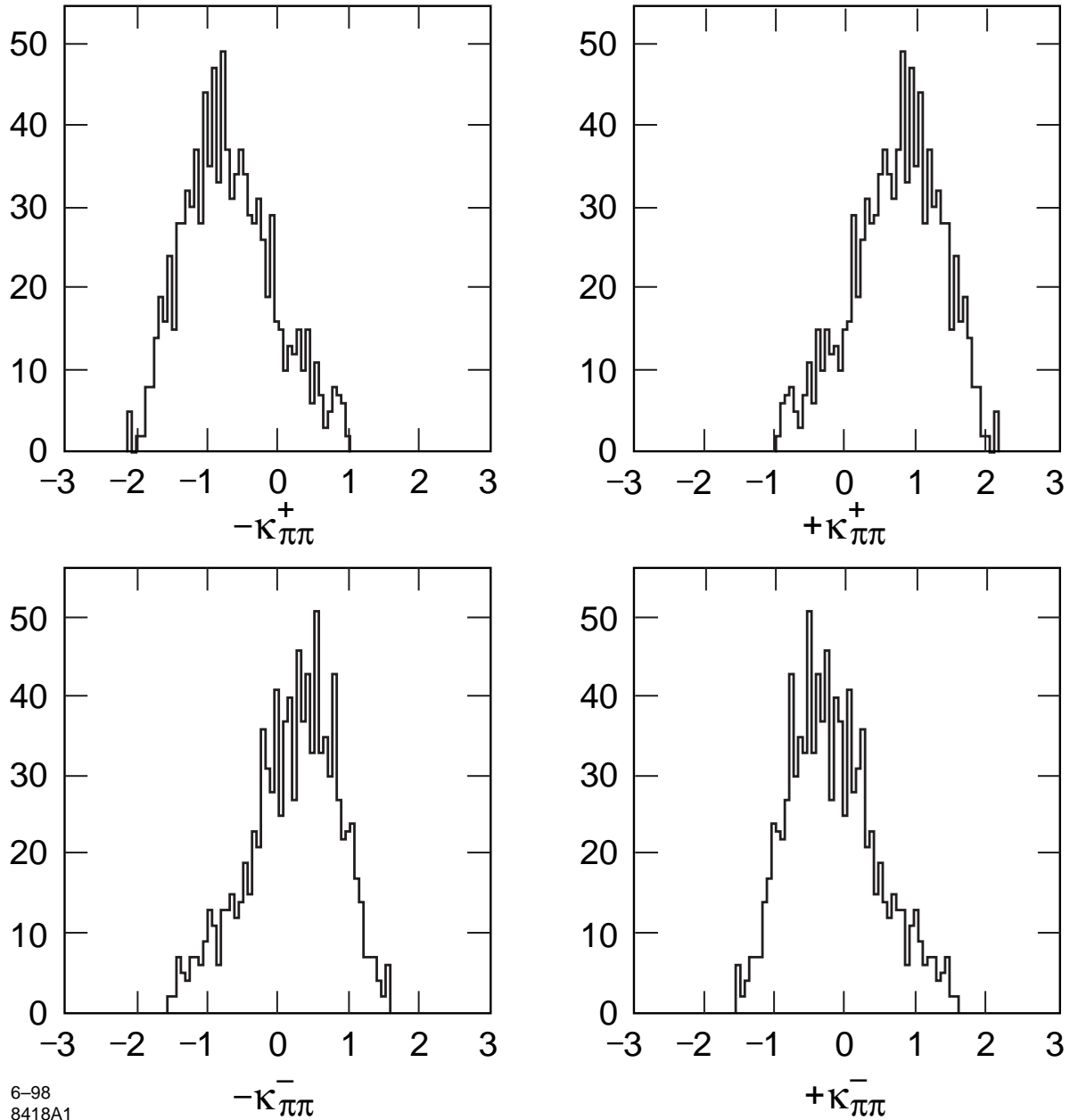


Figure 6-11. Distributions of $\kappa_{\pi\pi}$, the shift in 2α due to penguin effects, for toy Monte Carlo samples. The four plots represent the four-fold ambiguity arising from the isospin analysis. Each plot has an rms width of ~ 0.6 rad.

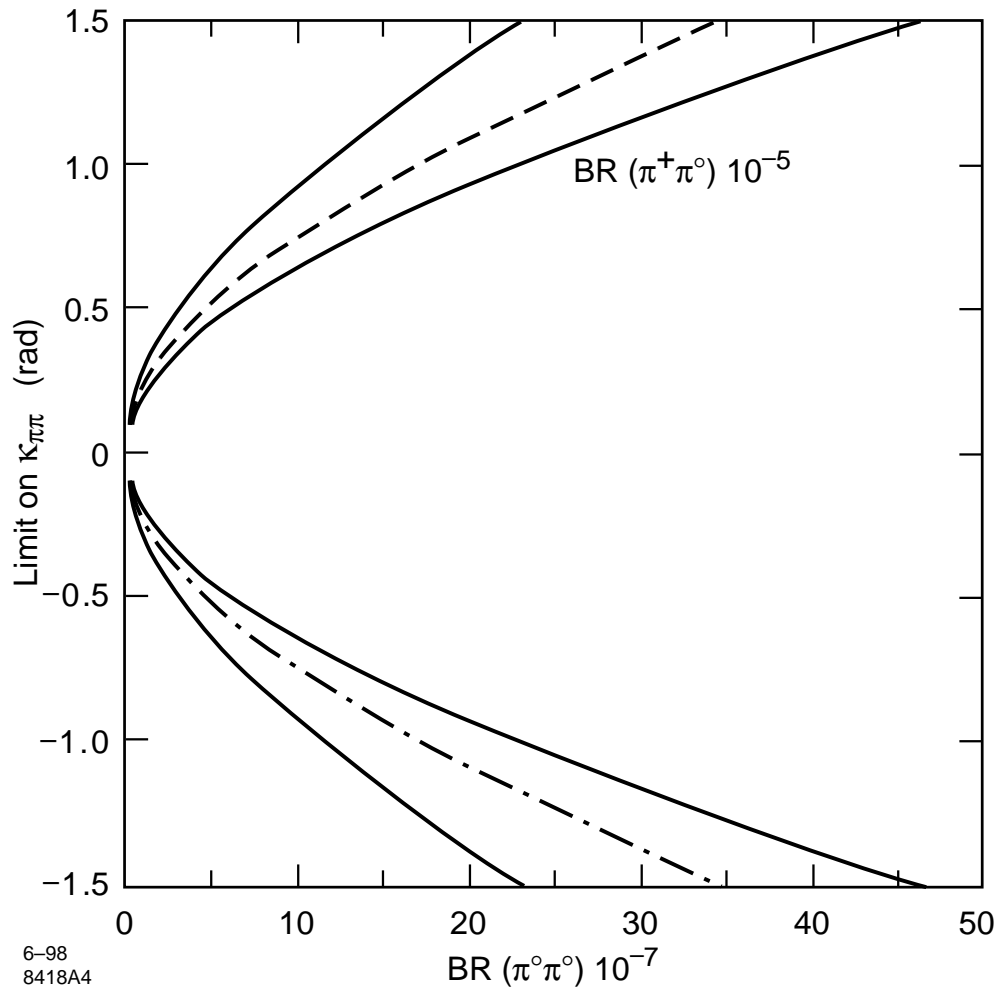


Figure 6-12. Limits for the $\kappa_{\pi\pi}$ confidence level interval $[-\overline{\kappa_{\pi\pi}}, +\overline{\kappa_{\pi\pi}}]$ versus the upper limit on B^{00} (horizontal scale 10^{-7}). The three curves displayed refer to $\mathcal{B}(B^+ \rightarrow \pi^+\pi^0) = 1 \times 10^{-5}$, 0.75×10^{-5} and 0.5×10^{-5} .

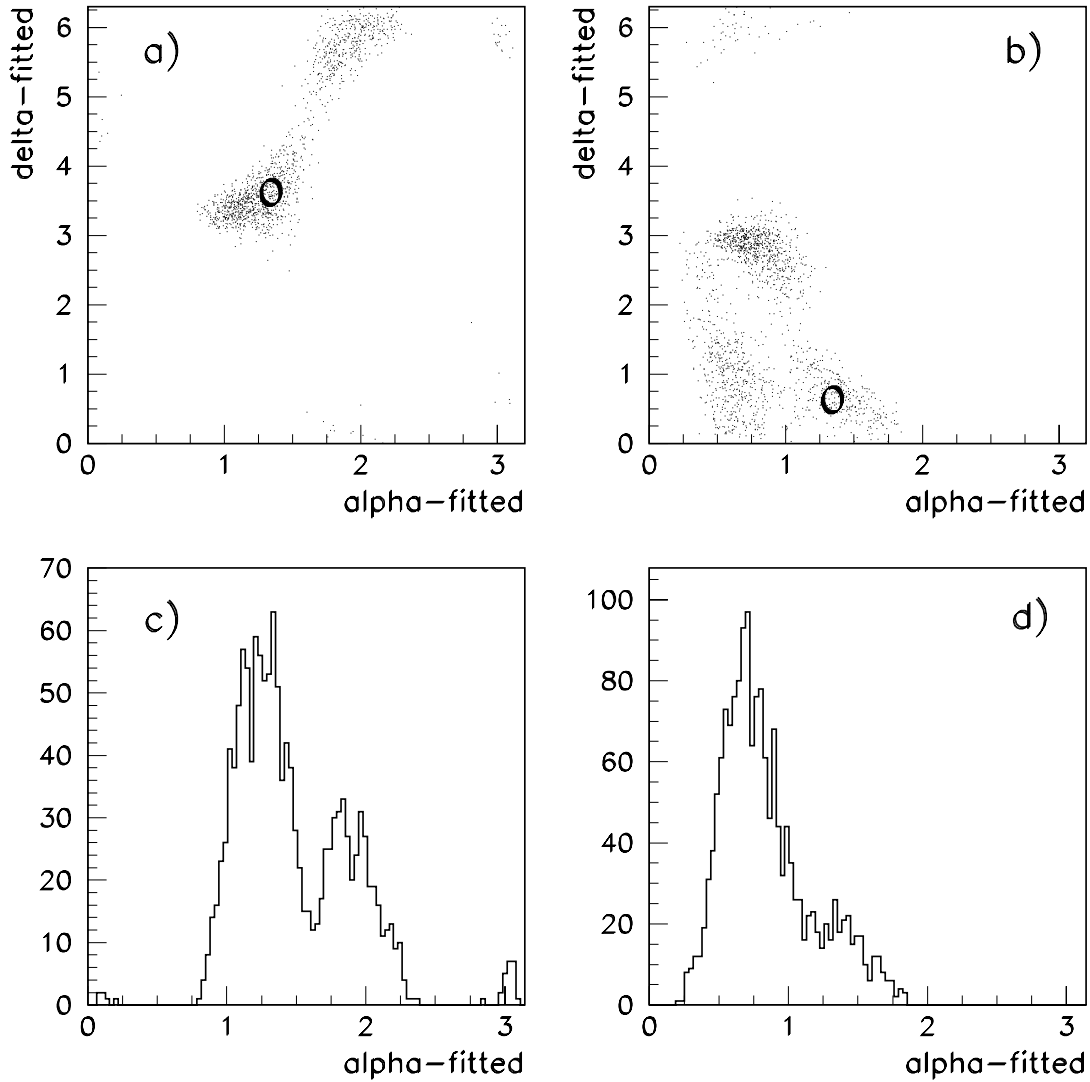


Figure 6-13. Scatter plots of extracted values of α and δ for two pairs of “true” values, which are indicated by the “O” characters in the figures.

It has been found that the typical widths of the “measured” values of α are dominated by the experimental resolution (at 90 fb^{-1}), for values of $|Z| \ll 1$, but start to get smeared more significantly for $|Z| \gtrsim 0.5$. If $|Z| \gg 1$, *i.e.*, $B \rightarrow \pi\pi$ is dominated by penguin diagrams, then both asymmetries’ amplitudes, Eq. (6.45), (6.46), become very small and difficult to measure. They vanish in the limit $|Z| \rightarrow \infty$, because the penguin weak phase cancels with the one from mixing.

This method is limited by theoretical uncertainties in the *a priori* knowledge of the factor $|Z| = |P/T|$ and breaks down if the central value of $|Z|$ gets close to unity. Comparison of model calculations and measurements to study penguin effects in many channels will eventually limit the theoretical uncertainties, and in that case this approach may give the best knowledge of α for some time to come.

6.4.7 Conclusions

The power of the BABAR detector to isolate signals for $B^0 \rightarrow \pi^+\pi^-$ decays and their CP -violating asymmetries has been reviewed, together with a number of methods of interpreting them in terms of the angle α of the unitarity triangle. Observation of CP violation in this channel can be established if either a_{\cos} or a_{\sin} differ significantly from zero, but translation of such an observation into a value for α requires the further considerations discussed below.

The recent discovery of significant penguin effects in these kinds of modes makes their interpretation much more difficult than thought earlier. Significant penguin amplitudes however may lead to larger than expected branching ratios for $B^0 \rightarrow \pi^0\pi^0$. With present estimates for this rate the statistical uncertainty on the measurement of this quantity, together with the large multiplicity of solutions inherent in the method make improvement in the knowledge of α via isospin analysis of two-pion channels, at best, a doubtful proposition.

Future efforts to reduce the theoretical uncertainties in the ratio $|P/T|$ may be the best hope for an accurate value of α from the two-pion channel. Such efforts will be dependent on tests of models in a great variety of channels. Measuring these will be an important aspect of the BABAR experimental program.

6.5 B Decay Modes with Three Pions

Decays of B^0 or \bar{B}^0 to three pions via the $\rho\pi$ channel are studied in this section. The feasibility of the entire $B \rightarrow \rho\pi \rightarrow 3\pi$ analysis depends on the number of events and their distribution among the three ρ bands, the strength of the penguin contributions compared to those of the trees, and the size of the interference effects. In order to estimate these and to provide input for the Monte Carlo generators, the relevant QCD matrix elements have been evaluated within the factorization assumption, together with some model and/or phenomenological ansätze to estimate the contributing form factors. The sensitivity of the analysis also depends on the presence of final-state interaction phases. Clearly once data exist, analyses will be less model-dependent, but it is

Table 6-12. $B \rightarrow \rho\pi$ amplitudes used in these studies. The Small Penguins amplitudes were derived from theoretical models. The Large Penguin set enhances penguin contributions and has also been used in studies because of the evidence that penguins are important in $B \rightarrow K\pi$.

Mode	Small Penguins	Large Penguins	No Penguins
$\rho + i\eta$	0.05+i0.36	0.05+i0.36	0.05+i0.36
α	1.35	1.35	1.35
T^{+-}	1.00	1.00	1.00
T^{-+}	0.47	0.47	0.47
T^{00}	0.14	0.14	0.14
T^{+0}	1.09	1.09	1.09
P^{+-}	-0.09	$-0.20 e^{-0.5i}$	0.00
P^{-+}	0.01	$0.15 e^{2.0i}$	0.00

worth briefly discussing here the assumptions that were used in modeling these modes. The main ingredients are [15]:

- The factorization of the nonleptonic matrix elements has been assumed. They are expressed as the product of two matrix elements of weak currents, *i.e.*, form factors.
- The heavy-to-light $B \rightarrow \pi(\rho)$ form factors⁸ are estimated from $D \rightarrow K(K^*)$ Fermilab data [13, 64] and $SU(3)$ and heavy-quark symmetries [65, 66].

The set of amplitudes labeled “Small Penguins” in Table 6-12 is obtained from this model calculation. The set of amplitudes called “Large Penguins” is obtained from the Small Penguins amplitudes by simply increasing the penguin amplitudes, taking into account indications from CLEO data on $K\pi$ and $\pi\pi$ that penguin terms are significant [2]. Indeed, the very small value for P^{-+} predicted by the factorization model (Small Penguins set) comes from a cancellation between terms of different signs and is quite unstable. Somewhat randomly chosen strong phases have been included in the penguin amplitudes, reflecting our ignorance of final-state interactions.⁹ The behaviour of this set is typical of what is seen with other phase choices. A set of amplitudes without penguins, but with the same value of α , has also been defined. In Table 6-12, $T^{+-} = 1$ has been set by convention. The full model calculation provides an absolute normalization, leading to the predicted branching ratios shown in Table 6-13.

⁸In order to estimate the contribution of other resonances, the $B \rightarrow f_0(980) (f_2(1270))$ form factors are estimated from the quark model and/or $D \rightarrow f_0(f_2)K$ data [15].

⁹Even in the $1/N_c \rightarrow 0$ limit, such phases between penguin and tree amplitudes are $\mathcal{O}(1)$.

Table 6-13. Branching ratios for B decays predicted by the same model that gives the amplitudes in Table 6-12. The three sets of amplitudes yield the same overall branching ratio (5.5×10^{-5}) for the average over the six processes B^0 and $\bar{B}^0 \rightarrow \rho\pi$. The significant increase of the $B^0 \rightarrow \rho^0\pi^0$ branching ratio predicted by the Large Penguins set is due in large part to the final-state interaction phases assumed for the penguin amplitudes.

Mode	Small Penguins	Large Penguins	No Penguins
$B^0 \rightarrow \rho^+\pi^-$	4.4×10^{-5}	3.4×10^{-5}	4.4×10^{-5}
$B^0 \rightarrow \rho^-\pi^+$	1.0×10^{-5}	0.5×10^{-5}	1.0×10^{-5}
$B^0 \rightarrow \rho^0\pi^0$	0.1×10^{-5}	0.4×10^{-5}	0.1×10^{-5}
$\bar{B}^0 \rightarrow \rho^+\pi^-$	1.0×10^{-5}	1.7×10^{-5}	1.0×10^{-5}
$\bar{B}^0 \rightarrow \rho^-\pi^+$	4.4×10^{-5}	4.9×10^{-5}	4.4×10^{-5}
$\bar{B}^0 \rightarrow \rho^0\pi^0$	0.1×10^{-5}	0.1×10^{-5}	0.1×10^{-5}
$B^+ \rightarrow \rho^+\pi^0$	2.6×10^{-5}	2.7×10^{-5}	2.7×10^{-5}
$B^+ \rightarrow \rho^0\pi^+$	1.1×10^{-5}	0.9×10^{-5}	1.0×10^{-5}
$B^- \rightarrow \rho^-\pi^0$	2.6×10^{-5}	2.4×10^{-5}	2.7×10^{-5}
$B^- \rightarrow \rho^0\pi^-$	1.1×10^{-5}	1.2×10^{-5}	1.0×10^{-5}

The number of neutral B mesons produced in a canonical year of running (30 fb^{-1}) is 3.2×10^7 , leading to 1700 decays of B^0 or \bar{B}^0 to $\rho\pi$ (The TDR [67] assumed similar branching ratios). Reconstruction efficiency, tagging, and backgrounds reduce this to an equivalent number of perfect events near 100 (cf. Table 6-18 and Section 6.5.2.3, Results for 30 fb^{-1}). The large variation among the branching ratios for the different $\rho\pi$ channels and the strong angular dependence of the polarized ρ decay leads to the Dalitz plot shown in Fig. 6-14.

It should be stressed that these values are only indicative. In particular, the small branching ratios for the $\rho^0\pi^0$ channels are a consequence of a cancellation between different terms, and are very sensitive to the precise value of phases, V_{td} etc. This cancellation is particularly unfortunate because this channel is important for the analysis [11, 15]. Moreover for this channel the tree is color-suppressed whereas the electroweak-penguin contribution is color-allowed and thus may be significant, thereby spoiling the (critical) relation Eq. (6.29). For further discussion, see below and Refs. [11, 15].

6.5.1 Event Selection

As in the $B \rightarrow \pi\pi$ case, this channel suffers from a huge background compared with the small number of expected signal events. There are several sources of background: combinatorial back-

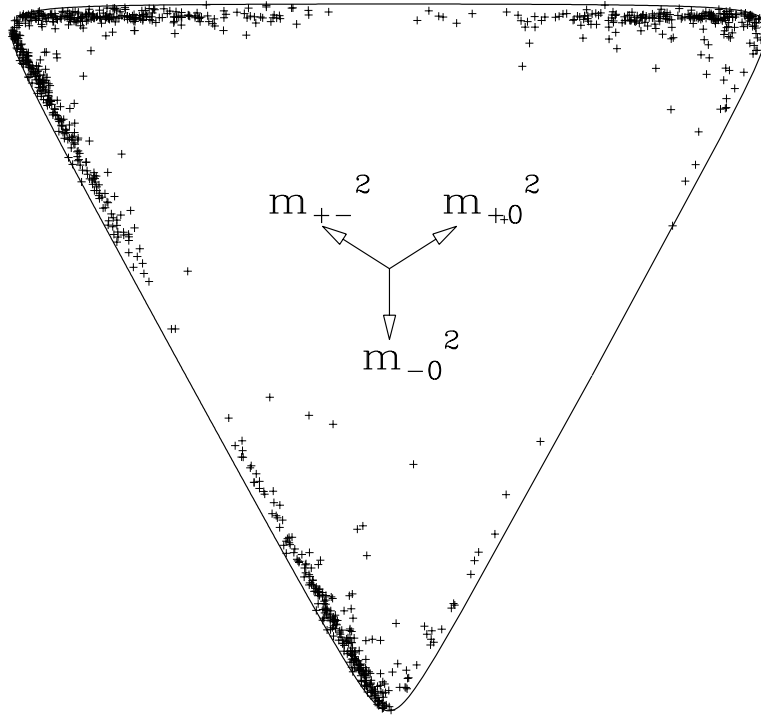


Figure 6-14. A Dalitz plot showing 1200 $B \rightarrow \rho\pi$ events, generated with the Small Penguins set of amplitudes. The $\rho^0\pi^0$ band is noticeably depleted. The events are concentrated at the ends of the ρ bands because of the longitudinal polarization of the ρ (cf. Eq. (6.31)).

ground within the signal events, background from B decays to similar channels (such as $B \rightarrow K\pi\pi$), combinatorial background from generic $B\bar{B}$ and, most importantly, continuum $q\bar{q}$ events. The event selection presented here does not treat the full three-body Dalitz plot, but instead focuses on the three ρ bands where a better signal to background ratio can be obtained.

In addition to selecting $B^0 \rightarrow \rho^+\pi^-$ candidates, the estimated selection efficiencies for the signal can be verified by measuring the branching ratios for several similar channels with known branching ratios, with exactly the same event selection. For this purpose, the following decays can be used: $B^0 \rightarrow D^-\pi^+ \rightarrow \pi^-\pi^0\pi^+$, $B^+ \rightarrow \bar{D}^0\pi^+ \rightarrow K^+\pi^-\pi^+$ and $B^+ \rightarrow \bar{D}^0\pi^+ \rightarrow \pi^+\pi^-\pi^+$. The branching ratios are similar to those expected for $\rho\pi$ [13]. Thus, in addition to the ρ bands, D bands are included in the preselection for both neutral and charged B s. The cuts are chosen large enough (about $1 \text{ GeV}/c^2$) to keep both the signal and a significant fraction of background. Further experimental cross-checks for the selection efficiency can be made by measuring the background level in regions close to, but outside, the ρ bands. A study of the $K\pi\pi$ channels which present a particular background is presented in Section 6.5.1.4; preselection criteria do not include particle identification and thus retain events from such channels as well as the three-pion events. Studies of similar three body channels in charged B decays will also be helpful.

Table 6-14. Mass cuts and signal efficiencies for B -decay products.

	Allowed Range (GeV/ c^2)	Signal Efficiency
π^0	Detect γs	75%
π^0	$0.10 < M_{\gamma\gamma} < 0.17$	99%
ρ^0	Detect $\pi^+\pi^-$	81%
ρ^0	$0.35 < M_{\pi^+\pi^-} < 1.20$	99%
ρ^\pm	Detect $\pi^\pm\pi^0$	68%
ρ^\pm	$0.35 < M_{\pi^\pm\pi^0} < 1.20$	99%

The analysis was performed with the `Aslund` fast simulation. The `BBsim` full simulation was used to evaluate the effect of particle identification with more realism. The event selection was carried out in two stages. In the first stage, a set of preselection cuts was applied for the purpose of reducing the background while keeping the signal efficiency essentially unaffected. In the second stage, a set of more stringent cuts was applied, in order to increase the background rejection to a sufficient level, but with some loss in signal efficiency. This factorization of the problem facilitates optimization of the analysis in the second stage.

6.5.1.1 Preselection of events

The variables used for these preliminary cuts are the masses of the B candidate decay products and the mass and momentum (in the $\Upsilon(4S)$ rest frame) of the B candidate. The continuum background is reduced by a factor of ~ 200 by the following cuts:

- **π^0 mass:** $\pi^0 s$ are formed in `Aslund` by combining all pairs of photon candidates. The mass resolution is $5.4 \text{ MeV}/c^2$ for $\pi^0 s$ coming from ρ decay, and $8.3 \text{ MeV}/c^2$ for $\pi^0 s$ coming from B decay. The cuts used and the signal efficiencies are shown in Table 6-14.
- **ρ mass:** ρ candidates are reconstructed by forming all appropriately charged pairs of pions. No particle identification is applied at this stage: the charged pion candidates are simply taken to be all the charged tracks in the event. The cuts used and the signal efficiencies are shown in Table 6-14.
- **B mass and momentum:** The B candidates are reconstructed by forming all opposite-sign combinations of ρ and π which give an invariant mass compatible with the B mass. The B is produced nearly at rest in the $\Upsilon(4S)$ rest frame, so a cut on the B momentum, $p_{B^0}^*$, decreases the background substantially without affecting the signal significantly. The values of the B

Table 6-15. Preselection efficiencies (in percent) and B -mass resolutions for the true signals.

	$\rho^\pm \pi^\mp$	$\rho^0 \pi^0$	$\pi^+ \pi^- \pi^0$ (NR)
All particles detected	65	67	65
π, ρ selection	98	97	27
$5.17 < M_{\rho\pi} < 5.37$ GeV/ c^2 and $0.12 < p_{B^0}^* < 0.52$ GeV/ c	95	90	93
Total efficiency	60	58	16
$\sigma(M_B)$ (MeV/ c^2)	26	35	27

candidate cuts, the signal efficiencies and the B candidate mass resolutions are summarized in Table 6-15. The mass resolution for the $\rho^0 \pi^0$ channel is larger than that of $\rho^\pm \pi^\mp$ because of the high-energy π^0 in this mode. Also included in this table are the results obtained for the nonresonant (NR) three-pion decay of the B^0 , generated according to phase space, which is selected roughly equally in the $\rho^+ \pi^-$, $\rho^- \pi^+$ and $\rho^0 \pi^0$ channels.

The mass distributions of π^0 candidates for $\rho^+ \pi^-$ signal and continuum events after all preselection cuts are shown in Fig. 6-15. The B candidate mass distributions for the $\rho^+ \pi^-$ channel are shown in Fig. 6-16 for signal and continuum background. It should be noted that an important combinatorial background is present within signal events, which can be seen from Fig. 6-16. It is due to wrong low-energy photons from the other B or from machine background. For each pre-selected true signal combination in the $\rho^\pm \pi^\mp$ ($\rho^0 \pi^0$) channel, there are also 1.4 (0.3) false combinations in the same ρ band, and 0.65 (0.25) in the other two.¹⁰

6.5.1.2 Alternative preselection

The preselection method for reconstructing B^0 s relies on the efficient reconstruction of π^0 s. However, it is possible to undertake the entire preselection without the need to reconstruct π^0 s by using only the charged pions in the event. This is advantageous, since the status of BABAR charged-track reconstruction is quite advanced. The tracking efficiency cuts off at $p_t \simeq 50$ MeV/ c , which is comparable to the detection energy threshold for neutral pions. However the charged-track efficiency is close to 100% efficient within the acceptance, while the π^0 reconstruction efficiency varies from 80% at 2 GeV/ c^2 to as little as 60% below 200 MeV/ c^2 [67].

¹⁰The signal combinatorial background may be reduced by about a factor of two by requiring that the energy of each photon is greater than 50 MeV; this reduces the signal by 10%.

This preselection method exploits the fact that B mesons are produced with small velocity in the $\Upsilon(4S)$ rest frame ($\beta_B \simeq 0.064$). Pairs of oppositely charged particles are formed, with the requirement of a two-track vertex χ^2 probability larger than 1%. The method uses the quantity $\mu_{\pi\pi} = E_{\pi^0}^* + E_{\pi^+\pi^-}/\gamma_B$, where $E_{\pi^+\pi^-}$ is the total energy of the pair in the $\Upsilon(4S)$ rest frame, and $E_{\pi^0}^* = (m_B^2 - m_{\pi\pi}^2 + m_{\pi^0}^2)/2m_B$ is the expected π^0 energy in the B meson decay frame. For the signal, $\mu_{\pi\pi}$ is a nonbiased estimator of the B meson mass m_B . At a given value of $m_{\pi\pi}$, the distribution is flat with width $\beta_B p^*$ where p^* is the momentum of the π^0 in the B rest frame ($p^* \simeq E_{\pi^0}^*$). Applying a cut centered on the B mass and linear in $m_{\pi\pi}^2$ is very efficient for signal. The efficiency of the preselection is 76% for $\rho^+\pi^-$ events including acceptance effects, with no internal combinatorial background. Since the tracking efficiency and acceptance are largely independent of momentum, this preselection does not bias the Dalitz plot.

It is also possible to estimate all the topological variables that enter the list for the multivariate analysis (see next section) without detecting the π^0 . In order to determine the final position of selected events in the Dalitz plot, a well-measured π^0 direction is still needed, which will decrease the efficiency, but this requirement may be postponed until after the background-fighting process.

6.5.1.3 Multivariate background rejection

After preselection, the background still dominates by a factor ~ 400 (cf. Table 6-18). Unfortunately there is no variable left for which a cut to reduce background does not also reduce the signal. There are, however, a number of other discriminating variables available. In order to optimize their use, the remainder of the background rejection which is needed is done with multivariate analysis techniques which were discussed in Section 4.9.

The most powerful discriminating variable is $\cos\theta_{\text{sph}}^{\rho\pi}$, the cosine of the angle between the sphericity axis of the rest of the event and the ρ or π , whichever is closer to it. A cut at 0.9, 0.8 or 0.7 on this quantity reduces the continuum background, by a factor of 3.5, 8 or 15, respectively, while reducing signal by only 12%, 23%, or 34%. The idea is to apply a multivariate analysis in order to reduce the background, while keeping a reasonable efficiency for signal. In this analysis, selections based on cuts, the linear method and a neural network were used, for comparison [68].

Ten discriminating variables were used to separate signal and continuum background:

- $\cos\theta_{\text{sph}}^{\rho\pi}$, defined above
- $\cos\theta_{\text{sph}}^B$, a similar quantity defined for the reconstructed B direction,
- R_2^{ev} , the normalized Fox-Wolfram second moment for the whole event,
- R_2^{tag} , the same quantity calculated for the rest of the event,
- $\sum P_{t/B}$, the sum of transverse momenta of the rest of the event with respect to the B direction,
- χ_m^2 , a χ^2 formed from the masses of all reconstructed particles,

- M_B ,
- $p_{B^0}^*$,
- M_ρ , and
- $\sum P_\pi^*$, the algebraic sum of the three pion momenta.

Many of these variables were introduced in Section 4.9. The first five are topological, while the last five characterize the quality of the CP candidate. Particle identification was not used in the multivariate analysis, its use being postponed to a later stage of the analysis.

Figure 6-17 shows the effect of a cut at 0.9 on the neural network output, for both the signal and the continuum background, as a function of $\cos \theta_{\text{sph}}^{\rho\pi}$. This illustrates one of the advantages of multivariate analyses, which allow the selection of events even in a variable-range dominated by background, resulting in improved signal efficiency.

Figure 6-18 shows the efficiency for the continuum background obtained as a function of the efficiency for the signal for the three techniques considered here (cuts, linear multivariate analysis, neural network). For a rejection factor of 10^5 for continuum background in the $\rho^+\pi^-$ channel these three methods have corresponding signal efficiencies of 31.5%, 32.6%, and 37.6% respectively (these correspond to a cut with a value of 0.94 in the neural network output). These results do not depend very much on the channel studied. For a fixed rejection factor for continuum background, the selection based on the neural network gives the best efficiency for the signal, and will be used in the rest of this section.

As already mentioned, there is also combinatorial background present in signal events. A separate multivariate analysis was performed (with similar variables), optimized to reduce this background. This resulted in a further loss of about 10% of the signal, while effectively eliminating the combinatorial background.

In order to see how all of the above cuts affect the Dalitz plot, Fig. 6-19 illustrates how the efficiency for the signal varies as a function of the Dalitz-plot variables. Each plot is a projection of one of the three ρ bands onto the corresponding side of the Dalitz plot. The efficiency is rather flat except for a decrease at the ends of the ranges, which correspond to the production of a soft charged or neutral pion. This reduction is largely due to the combinatorial background rejection cut.

6.5.1.4 Background from other B -decay channels: particle identification cuts

The $B^0 \rightarrow \pi^+\pi^-\pi^0$ mode can also suffer backgrounds from other B decay processes, leading to final states with one π^0 and two charged particles including one or two kaons. The focus here is on the $B^0 \rightarrow K^+\pi^-\pi^0$ final state which can be reached from $B^0 \rightarrow K^+\rho^-$, $B^0 \rightarrow K^{*+}\pi^-$ with $K^{*+} \rightarrow K^+\pi^0$, and $B^0 \rightarrow K^{*0}\pi^0$ with $K^{*0} \rightarrow K^+\pi^-$. The branching ratios for the $K\pi\pi$ modes

Table 6-16. The branching ratios for the $K\pi\pi$ modes predicted for the three sets of amplitudes considered for the $B^0 \rightarrow \pi\pi\pi$ analysis.

Mode	Small Penguins	Large Penguins	No Penguins
$B^0 \rightarrow K^{*+}\pi^-$	1.1×10^{-5}	3.0×10^{-5}	0.2×10^{-5}
$B^0 \rightarrow K^+\rho^-$	0.8×10^{-6}	2.3×10^{-5}	0.8×10^{-6}
$B^0 \rightarrow K^{*0}\pi^0$	0.4×10^{-5}	1.8×10^{-5}	0.1×10^{-7}
$\bar{B}^0 \rightarrow K^{*-}\pi^+$	1.1×10^{-5}	4.7×10^{-5}	0.2×10^{-5}
$\bar{B}^0 \rightarrow K^-\rho^+$	0.8×10^{-6}	3.9×10^{-5}	0.8×10^{-6}
$\bar{B}^0 \rightarrow K^{*0}\pi^0$	0.4×10^{-5}	1.7×10^{-5}	0.1×10^{-7}
$B^+ \rightarrow K^{*+}\pi^0$	0.6×10^{-5}	1.5×10^{-5}	0.1×10^{-5}
$B^+ \rightarrow K^+\rho^0$	0.7×10^{-6}	1.1×10^{-5}	0.7×10^{-6}
$B^+ \rightarrow K^{*0}\pi^+$	0.7×10^{-5}	3.5×10^{-5}	0
$B^- \rightarrow K^{*-}\pi^0$	0.6×10^{-5}	2.4×10^{-5}	0.1×10^{-5}
$B^- \rightarrow K^-\rho^0$	0.7×10^{-6}	2.1×10^{-5}	0.7×10^{-6}
$B^- \rightarrow K^{*0}\pi^-$	0.7×10^{-5}	3.5×10^{-5}	0

predicted for the three sets of amplitudes considered for the $B^0 \rightarrow \pi\pi\pi$ analysis are given in Table 6-16. The Large Penguins set leads to $K\pi\pi$ branching ratios above the currently available upper limits [69]. Therefore, its prediction cannot be taken at face value. However, it clearly indicates that the level of $K\pi\pi$ background (and especially $K\rho$ background) is very sensitive to penguin contributions.

None of the topological cuts designed to fight the dominant continuum background contribute to reduce this background, since these are genuine B decays: $K^+\pi^-\pi^0$ events are expected to survive the selection stage with essentially the same efficiency as the 3π signal. Kinematic separation is more difficult to exploit than in the $\pi\pi$ case. Even though $K\pi\pi$ events peak slightly below the mass of the B in the $\pi\pi\pi$ mass plot, the actual shift (of the order of $50 \text{ MeV}/c^2$) and width depend on the kaon momentum spectrum, in other words, on the position of the candidate in the Dalitz Plot. Besides, the mass peak for the signal is broader and exhibits a low-mass tail. Therefore, the reduction of the $K\pi\pi$ background relies mostly on Particle Identification (PID).

By combining individual PID information as provided by the different subsystems, one defines a discriminating variable $\sigma_{\pi/K}$ which characterizes the charged pair. A null value would indicate that the particle of the pair most likely to be a kaon has equal probability to be a pion. A positive value favors the $\pi\pi$ hypothesis against any of the $K\pi$ and πK hypotheses. When this variable is included in the multivariate analysis, it improves significantly the signal efficiency for a given rejection level of the continuum combinatorial background (by roughly 20% at a rejection of 10^5),

Table 6-17. Efficiency of selected and tagged events from *B* or \bar{B} events (not summed).

	$\rho^\pm \pi^\mp$	$\rho^0 \pi^0$
Signal	21 %	21 %
$\pi^+ \pi^- \pi^0$ (NR)	2.0 %	1.5 %
$B\bar{B}$	10^{-6}	$< 10^{-6}$
Continuum	3×10^{-6}	3×10^{-6}
Signal combinatorial / Signal	0.11	0.05

This is because about one-third of selected continuum events otherwise would contain at least one kaon. However, subsequent PID cuts still have to be applied to further reduce the $K\pi\pi$ background to an acceptable level.

The discriminating power of the $\sigma_{\pi/K}$ variable depends on the number of particles of the pair reaching the DIRC. In the case of two-body *B* decays ($\pi^+\pi^-$ and $K^+\pi^-$), the two particles are kinematically almost fully correlated: it is very unlikely that both particles escape DIRC detection. The presence of a π^0 in the final state greatly reduces this correlation. Furthermore, the kinematical aspects depend on the π^0 spectrum, and thus on the resonance structure of the final state. Events are classified into three categories according to the number of particles which reach the DIRC. For instance, the fraction of $\rho^+\pi^-$ events in the first category (two particles in the DIRC acceptance) is 68%, there are 27% in the second (only one in the DIRC acceptance) and 5% in the third (none in the DIRC acceptance). For candidates of the first category, purity is limited essentially by kaon decays in flight occurring before the DIRC.

The study of $K\pi\pi$ event rejection was performed with full simulation, reconstruction and preliminary versions of PID combining algorithms, as described in Section 4.3.1, on the sample of events surviving the alternative preselection based on charged tracks only. For a PID cut with an efficiency of 95%, 75% of $K^{*+}\pi^-$ events and 80% of $K^+\rho^-$ events are rejected. The rejection probability reaches 90% and 97% respectively for candidates of the first category. While soft kaons from K^* decays are difficult to reject from PID alone, the energy for such events is ~ 300 MeV below the expected value, so they can easily be rejected with an energy cut.

The selection efficiency for $K\pi\pi$ events with the PID cuts is 4–5%, to be compared with the values given in Table 6-17 for the signal and other backgrounds. For the branching ratios of the Small Penguins set (cf. Tables 6-13,6-16) the $K\pi\pi$ background is 3% with PID cuts alone. It reaches 30% for the Large Penguins set, however, as remarked above, some values given by this set for $K\pi\pi$ channels are already excluded by experimental upper limits.

6.5.1.5 Time (Δz) resolution and tagging

The following steps describe the remainder of the analysis.

- **Δz determination:** The B vertices are reconstructed by using a kinematical fitter (based on `FitVer` see Section 4.5.2) for the CP -side and an impact parameter method for the tag-side (Section 4.5.1.3). The resolutions (widths of the narrow Gaussian in a double-Gaussian fit) obtained on z_{CP} , z_{tag} and $\Delta z = z_{\text{tag}} - z_{CP}$ are respectively 30, 63 and 82 μm . The selection procedure described above does not affect the Δz distribution.

It is worth noting here that, as for any B -decay channel, the discrimination between continuum background events and B -decay events could in principle be further enhanced by performing a cut in Δz , since background events cluster at small Δz whereas B -decay events (particularly those that are important for determining the coefficient of $\sin(\Delta mt)$) extend to larger Δz values. Such a cut is, however, not needed, since fits use Δz values and fit to different shapes in Δz for signal and background events. The background to signal ratio varies from one value of Δz to another, so the overall background numbers reported here appear worse than is actually the case for most of the range.

- **Tagging:** The standard method of tagging, *i.e.*, Cornelius, is applied. This gives an additional factor of two in continuum background rejection since the fraction of tagged events is 58% for signal events and 30% for continuum events. However, the tagging is not perfect; this is not accounted for in the above tagging efficiency but the effect of wrong tags is included in estimating the number of “perfectly tagged events” (cf. Sections 4.8 and 6.5.2.3).

6.5.1.6 Summary of results for neutral B modes

Table 6-17 gives the efficiencies for the signal and the main backgrounds for each of the three ρ bands after the final selection including tagging. Table 6-18 gives the expected number of signal and background candidates from generic $B\bar{B}$, continuum and $K\pi\pi$ events at the various stages of the selection, for an integrated luminosity of 30 fb^{-1} . In the case of generic $B\bar{B}$ events, relevant exclusive final states, such as the signal, and $B \rightarrow K\pi\pi$ events were explicitly excluded from the generator. Other sources of background, such as downfeed from 4π ($a_1\pi$ and $\rho\rho$), have been studied and were found to make negligible contributions. For the charged ρ bands, the overall background over signal ratio is $B \simeq 2$. If $\rho^0\pi^0$ has a branching ratio at the level of 10^{-6} , the signal to noise ratio will be about 0.01; the direct production of $\rho^0\pi^0$ events well apart from the charged ρ bands will not be seen.¹¹ However, such events are not essential for the analysis; the interference effects in the overlap region of the bands can still be significant enough to yield results.

¹¹Applying a tighter cut on the neural network output would achieve an efficiency of 11% after tagging with a background less than 5×10^{-7} . The signal to noise ratio would still be very small, ~ 0.03 for these cuts with the same $\rho^0\pi^0$ branching ratio.

Table 6-18. Number of signal and background events in the charged ρ bands for the neutral B decays at the various stages of the selection for an integrated luminosity of $30 fb^{-1}$. The branching ratios of the Small Penguin set of Table 6-16 are used, where the final state includes a charge kaon. Generation of the generic $B\bar{B}$ sample explicitly excluded the 3π and $K\pi\pi$ exclusive modes. The $\rho^0\pi^0$ signal is overwhelmed by background because of its low branching ratio. The nonresonant $B \rightarrow 3\pi$ background is not shown because its branching ratio is uncertain.

	$\rho^+\pi^-$ and $\rho^-\pi^+$	$B\bar{B}$	Continuum	$K\pi\pi$
Produced	1.7×10^3	3.2×10^7	1.0×10^8	2.1×10^2
Preselected	1.0×10^3	1.3×10^3	3.9×10^5	1.2×10^2
Selected	6.1×10^2	2.2×10^2	4.0×10^3	7.6×10^1
PID	6.0×10^2	1.1×10^2	2.0×10^3	15
Tagged	3.5×10^2	6.3×10^1	5.9×10^2	9

6.5.1.7 Charged B modes

For the charged modes $B^\pm \rightarrow \rho^\pm\pi^0$ or $\rho^0\pi^\pm$, the preselection analysis follows the same strategy as for the neutral modes. Nearly all of the detectable signal remains after the preselection cuts for the $\rho^0\pi^\pm$ channel and $\sim 77\%$ remains for the $\rho^\pm\pi^0$ channel. At this level only a rejection factor of about 400 is obtained in each channel for the continuum background.

In order to fight the remaining high background the same approach has been used as for the neutral modes. The main results on B -mass resolution and efficiencies are given in Table 6-19. The efficiencies correspond to a rejection factor of 10^{-5} for the $q\bar{q}$ events.

The worsening in the resolution and the efficiencies obtained for the $B^\pm \rightarrow \rho^\pm\pi^0$ channel is due to the presence of the two π^0 s in the final state. If the background rejection is increased to a level of 10^6 to obtain better sensitivity, the $\rho^\pm\pi^0$ ($\rho^0\pi^\pm$) efficiency is 14% (29%). Furthermore, in the charged modes Δz may be used to reject additional background, since no time-dependent fit is needed. Rejecting candidates with $|\Delta z| < 200 \mu\text{m}$, keeps 62% (54%) of signal events and 27% (15%) of continuum events in the $\rho^\pm\pi^0$ ($\rho^0\pi^\pm$) channel.

Table 6-20 gives the expected numbers of signal events and background candidates from generic $B\bar{B}$ and continuum events at the last stage of the selection, for an integrated luminosity of $30 fb^{-1}$. Taken at face value, these numbers would lead to a $\sim 10\%$ precision measurement of each branching ratio within three years of data-taking.

Table 6-19. B mass resolution and selection efficiencies (ϵ) in the $\rho\pi$ charged modes for a 10^{-5} rejection in background.

	$\rho^+\pi^0$	$\rho^0\pi^+$
$\sigma(M_B)$ (MeV/ c^2)	45.	20.
ϵ - preselection		
Signal	0.45	0.74
ϵ - NN selection		
Signal	0.22	0.48
$B\bar{B}$	2×10^{-6}	$< 10^{-6}$
Continuum	10^{-5}	10^{-5}
Signal Combinatorial / Signal	0.22	0.05

6.5.2 Analysis

Several obstacles stand in the way of completing the full Dalitz-plot analysis of these modes. First, the small branching ratios mean that there will be limited statistics for some time to come. Second, the problem of low statistics will be exacerbated by backgrounds from several sources. Third, both because of the near “mirror” solutions discussed below, and also because many parameters are to be fitted, there may be several local minima of χ^2 , leading to ambiguous results.

Ultimately, these issues need to be explored in a complete simulation. Results reported here are based on simplified Monte Carlo calculations in which backgrounds have been included as

Table 6-20. Number of signal and continuum background events for the charged B decays for 30 fb^{-1} using the tight selection with a continuum background rejection factor of 10^6 , and applying a $|\Delta z| < 200 \mu\text{m}$ cut. At this last stage of the selection, the generic $B\bar{B}$ background contributes about 10 events in each channels. The expected background from $K\pi\pi$ events is typically of a few events. However, the Large Penguins set predicts a residual background to $\rho^0\pi^\pm$ from $K\pi\pi$ comparable to the signal yield.

	$\rho^\pm\pi^0$	continuum	$\rho^0\pi^\pm$	Continuum
Produced	8.2×10^2	1.0×10^8	3.5×10^2	1.0×10^8
Selected (tight)	70	30	60	15

suggested by studies with the `Aslund` simulation, as described in the previous section.¹² The results are sensitive to the choice of input amplitudes, to their phases and to the relative amounts of tree and penguin amplitudes. Despite these limitations, the current study is a significant advance on the work done for the TDR [67], in which the effects of penguins were ignored. Not surprisingly, the conclusions here are more modest.

The parameterization of Eq. (6.28) uses the fact that the penguin contribution has a purely $\Delta I = 1/2$ character. In this treatment the two parameters of P^{00} are effectively replaced by α .¹³

When fitting for penguins as well as for α , the contributions from $\rho^0\pi^0$ are essential. To see this, take as the independent quantities α and the four complex amplitudes A^{-+} , \overline{A}^{+-} , \overline{A}^{-+} and $T_2 = T^{00} + (T^{+-} + T^{-+})/2$, and set $A^{+-} = 1$.¹⁴ Then one can write

$$\begin{aligned} A^{00} &= e^{-i\alpha}T_2 - (A^{+-} + A^{-+})/2 \\ \overline{A}^{00} &= e^{i\alpha}T_2 - (\overline{A}^{+-} + \overline{A}^{-+})/2 \end{aligned} \quad (6.53)$$

Without any knowledge of the $\rho^0\pi^0$ contributions, the number of unknowns is greater than the number of observables and α remains undetermined. Note, however, that a fit to data in all three $\rho\pi$ bands with an unobservably small signal in the $\rho^0\pi^0$ channel can still give information on α because it requires cancellations between the T_2 term and the $A^{\pm\mp}$ terms in Eq. 6.53, and because of small effects in the interference regions with the $\rho^{\pm}\pi^{\mp}$ channels. This interference effect can be detected in the fits even when the signal-to-background ratio in the $\rho^0\pi^0$ band is quite small. (If data from all the charged B decays to $\rho\pi$ channels are also available the sensitivity of the analysis to the $\rho^0\pi^0$ modes is reduced [11].)

6.5.2.1 Alternative approaches

Since with few events it will be difficult to perform the full nine-parameter analysis, it is of interest to consider alternative possible analyses. These analyses regard the penguins as small effects, either by ignoring them or by using estimated bounds on their size to limit their influence on the analysis. A variety of alternative simplifications can be considered [15]:

- (a) To measure only the amplitudes of the four neutral- B charged- ρ channels and use a constraint taken from theory on the relative size of tree and penguin terms. Even though in the full

¹²A preliminary `BBSim` study, not reported here, indicates that both signal selection-efficiencies and background rejection factors may be significantly overestimated by the `Aslund` simulation, as expected.

¹³This procedure neglects electroweak penguins, which may be significant in the $\rho^0\pi^0$ channel. Cancellations between tree and penguin contributions are found in the model calculation leading to a small amplitude. A model-independent approach based on a ten-parameter fit together with a simple parameterization of electroweak-penguin effects can be found in [11, 15].

¹⁴This gives nine independent parameters. The tenth, as counted in Section 6.1.2.3, is the overall rate, which does not impact this analysis and is hence scaled out, as reflected in the arbitrary definition of the magnitude of A^{+-} .

analysis the penguin contributions mask the presence of α in the amplitudes for the charged ρ s, a seven-parameter description (the four complex amplitudes T^{+-} , T^{-+} , P^{\pm} , P^{\mp} , and α minus one free phase and one free magnitude), can be augmented by a single constraint, taken from data and/or models, to allow the extraction of α . The theoretical uncertainties arising from the constraint can be evaluated using phenomenological assumptions and/or model-calculations.

- (b) To assume both charged and neutral ρ bands to be available and to ignore penguin contributions.¹⁵ This analysis uses a five-parameter fit to the Dalitz-plot distributions, (the three complex amplitudes T^{+-} , T^{-+} , T^{00} , and α minus one free phase and one free magnitude).
- (c) To assume the interference with the neutral ρ channel to be negligible and to assume this channel is too weak to provide reliable fits. In this case, one must also neglect penguin contributions. This analysis uses a three-parameter fit (the two complex amplitudes T^{+-} , T^{-+} , and α , minus one free phase and one free magnitude), but still retains a full description of the resonance structure of the 3π final state and interference effects between the two charged channels. It thus depends on the assumed ρ shape and on a precise understanding of detector effects.
- (d) To ignore the detailed event kinematics and apply a Phase Space Integrated (PSI, or quasi-two-body) analysis and again a three-parameter fit. This analysis, by integrating the ρ bands rather than using the angular distributions, has less ability to discriminate between mirror solutions (discussed in the following section) and to discriminate against backgrounds, but is also less dependent on the details of the assumed ρ shape than the Dalitz-plot treatments outlined above. This method has been studied and is discussed in some detail in Section 6.5.2.3.
- (e) To ignore, in addition, all interference effects and to perform the three-parameter fit of the simple two-body analysis [1, 67].¹⁶

Methods (b)–(e) drop penguin terms, and thus implicitly assume there are no direct CP violations; observation of any such effects would indicate that there are significant penguin contributions and thus that such methods are not satisfactory. Even if no direct CP violation is seen, the results of all such methods will include a penguin-induced shift in the measured value of α compared to the actual value. The size of this shift depends on the size and strong phase of the penguin amplitudes, and estimates of it are model dependent. In order to stress this theoretical uncertainty, the value of α extracted via such an analysis will be denoted α_{eff} .¹⁷

¹⁵Alternatively, it may be assumed that they are known from other channels such as $K^*\pi$ or $K\rho$.

¹⁶In practice, after integration over phase-space the residual interference contribution is weak. Thus, the PSI and two-body analyses yield very similar results.

¹⁷The existence of such a shift is studied in Section 6.5.2.4, where errors as large as 0.2 in $\sin 2\alpha$ are encountered when fits ignoring penguins are performed.

6.5.2.2 Mirror solutions

Multiple minima of the Likelihood function complicate all parameter-fitting methods. Consider first the ambiguities that occur in the two-body analysis when penguins terms are assumed to be negligible, interference effects between different ρ bands are neglected, and there is no information on the $\rho^0\pi^0$ channel (*i.e.*, method e above). In that case some of the minima are related by parameter redefinitions and have exactly the same value of the likelihood. These are here referred to as “mirror solutions”. The fit determines $\sin(2\alpha + \delta)$ and $\sin(2\alpha - \delta)$, where δ is the difference between the strong final-state-interaction phases for $B^0 \rightarrow \rho^+\pi^-$ and $B^0 \rightarrow \rho^-\pi^+$ (cf. Eq. (6.35) and Eq. (6.11)). Given this information, the parameters α and δ cannot be unambiguously determined; the discrete ambiguities are summarized in Table 6-21. The eight minima are exactly degenerate in this simplified treatment, see for example Section 6.5.2.3.

Table 6-21. *The eight degenerate solutions (α', δ') obtained by measuring only the charged- ρ states in the absence of penguins when only $\rho^\pm\pi^\mp$ are observed and interference between different ρ bands is ignored. The true solution is (α, δ) .*

(α', δ')	$\sin 2\alpha'$	$\cos 2\alpha'$
(α, δ)	$\sin 2\alpha$	$\cos 2\alpha$
$(\pi/4 - \delta/2, \pi/2 - 2\alpha)$	$\cos \delta$	$\sin \delta$
$(\pi/2 + \alpha, \pi + \delta)$	$-\sin 2\alpha$	$-\cos 2\alpha$
$(3\pi/4 - \delta/2, 3\pi/2 - 2\alpha)$	$-\cos \delta$	$-\sin \delta$
$(\pi/4 + \delta/2, -\pi/2 + 2\alpha)$	$\cos \delta$	$-\sin \delta$
$(\pi/2 - \alpha, -\delta)$	$\sin 2\alpha$	$-\cos 2\alpha$
$(3\pi/4 + \delta/2, -3\pi/2 + 2\alpha)$	$-\cos \delta$	$\sin \delta$
$(-\alpha, \pi - \delta)$	$-\sin 2\alpha$	$\cos 2\alpha$

The full three-body analysis is sensitive to $\sin 2\alpha$ and $\cos 2\alpha$, thus even with vanishing penguin contributions some of these degeneracies are lifted by interferences between ρ s of different charges and $\rho^0\pi^0$ events. In the presence of penguins the mirror solutions are not precisely degenerate and their locations are not dependent solely on δ . Nevertheless, a number of local minima of the Likelihood function are expected. Depending on the values of the parameters (α , δ and penguin amplitudes) several of the mirror solutions may have a likelihood close to that of the true solution when the statistics are limited. At sufficiently high statistics, these degeneracies are lifted (except for some special values of parameters).

The full analysis is further hampered by the large number of correlated parameters, and hence the difficulty of fully searching the parameter space for alternate minima. A procedure to ensure that

the fit finds all such solutions, including the known mirror solutions of the simplified case, has been developed and is described in [11]. In order to clarify the extraction of α , the approach advocated in [70] may be used.

6.5.2.3 Phase-space integrated analysis

In this approach one distinguishes four types of events: B^0 (or \bar{B}^0) tag with a 3π final state categorized in the $\rho^+\pi^-$ (or $\rho^-\pi^+$) channel. With penguins dropped, the time-dependent amplitude Eq. (6.30) becomes

$$\begin{aligned} \mathcal{A}(t) = & \cos(\Delta mt/2)[f_+e^{-i\alpha}T^{+-} + f_-e^{-i\alpha}T^{-+}] \\ & \pm i \sin(\Delta mt/2)[f_+e^{i\alpha}T^{-+} + f_-e^{i\alpha}T^{+-}] \end{aligned} \quad (6.54)$$

where the \pm sign before the sine term depends on the sign of the tag, and $+ - (-+)$ denotes the tree amplitudes for final states $\rho^+\pi^- (\rho^-\pi^+)$. In order to find the decay rate to these final states, it is necessary to square the amplitude, and integrate over the available phase space.

In this PSI analysis, the association of a particular 3π final state to a given channel is a matter of experimental definition based on the event kinematics. Selection functions, denoted by s^\pm , are defined to be equal to one when the kinematics of a 3π final state is such that the event is associated with the $\rho^\pm\pi^\mp$ channel, and equal to zero elsewhere. The choice of region where s^\pm are nonzero is somewhat arbitrary and can be varied to optimize the treatment; the two functions are related by interchange of the momenta of the two charged pions. One can then define the quantities

$$G = \int d\Phi s^+ |f_+|^2, \quad B = \int d\Phi s^+ |f_-|^2, \quad U = \int d\Phi s^+ f_+ f_-^* \quad (6.55)$$

where $d\Phi$ indicates an integration over the full phase space (Dalitz plot). The notations stand for Good association, Bad association, and Undefined association.

These quantities depend only on the assumed Breit-Wigner form (cf. Eq. 6.31) and on the experimental algorithm used to select events.¹⁸ Therefore, they can be evaluated by Monte Carlo integration. From these values, a dilution factor d and two interference terms I_i and I_r can be formed [71]:

$$d = \frac{G - B}{G + B}, \quad I_i = \text{Im} \frac{2U}{G + B}, \quad I_r = \text{Re} \frac{2U}{G + B}. \quad (6.56)$$

The observable time distribution of \bar{B}^0 tagged events associated to the $\rho^\pm\pi^\mp$ channel is given by (omitting the exponential factor):

$$\mathcal{E}^\pm(t) \propto (1 \pm a) \left(1 - a_{\cos}^\pm \cos(\Delta mt) - a_{\sin}^\pm \sin(\Delta mt) \right), \quad (6.57)$$

¹⁸The quantities B and U could be made vanishingly small by choice of the selection functions, but at the cost of reducing the efficiency of the selection procedure and removing all information from interference effects.

where (neglecting penguins), the coefficients can be written in terms of the quantities defined above and the unknown parameters α_{eff} , R and δ :

$$a = 0 \quad , \quad (6.58)$$

$$a_{\text{cos}}^{\pm} = \mp \frac{dR + DI_i \sin \delta}{1 + DI_r \cos \delta} \quad , \quad (6.59)$$

$$a_{\text{sin}}^{\pm} = \frac{\sin 2\alpha_{\text{eff}}[D \cos \delta + I_r] \pm \cos 2\alpha_{\text{eff}}[dD \sin \delta - RI_i]}{1 + DI_r \cos \delta} \quad . \quad (6.60)$$

Here, $D = \sqrt{1 - R^2}$ with R defined by

$$R = \frac{|T^{+-}|^2 - |T^{-+}|^2}{|T^{+-}|^2 + |T^{-+}|^2} \quad , \quad (6.61)$$

and δ is the relative strong phase between T^{+-} and T^{-+} , Eq. (6.35). For B^0 tagged events, the signs in front of the a_{cos} and a_{sin} coefficients are reversed. The values of the a , a_{cos}^{\pm} and a_{sin}^{\pm} observables in the three reference scenarios are given in Table 6-22.

Table 6-22. Values of the a , a_{cos}^{\pm} and a_{sin}^{\pm} coefficients predicted in the three reference scenarios (the value $\delta = 0$ was used here). The values of d , I_i and I_r were calculated using realistic experimental values for the s^{\pm} selection functions (cf. Table 6-23). The slight difference between the a_{sin}^{\pm} coefficients in the No Penguins scenario arises because of interference effects. (cf. Eq. (6.59-6.60)).

	Small Penguins	Large Penguins	No Penguins
a	-5×10^{-3}	-0.05	0
a_{cos}^{+}	-0.58	-0.32	-0.59
a_{cos}^{-}	0.58	0.79	0.59
a_{sin}^{+}	0.25	0.07	0.30
a_{sin}^{-}	0.32	0.13	0.37

The relations $a = 0$ (Eq. 6.58) and $a_{\text{cos}}^{+} = -a_{\text{cos}}^{-}$ (Eq. 6.59) are consequences of neglecting the penguin contribution. These relations no longer hold if penguin terms are present and $\sin 2\alpha \neq 0$. In particular, evidence that these relations are violated would indicate direct CP violation.

In practice, even for a crude choice of the s^{+} selection function, both the dilution factor d and the interference term I give corrections at the level of a few percent (cf. Table 6-23), which may appear

Table 6-23. Examples of the evaluation of the dilution factor d and the interference terms I_r and I_i as obtained in two cases: using a perfect detector and using the `Aslund` simulation of the `BaBar` detector. The differences observed between the perfect and `Aslund` values are mostly due to combinatorial background within signal events.

	d	I_r	I_i
perfect	0.98	0.01	-0.04
<code>Aslund</code>	0.95	0.03	-0.06

small compared to the statistical accuracy¹⁹ for a_{\cos}^+ and a_{\sin}^+ expected for a low statistics analysis. However, the relationship between α_{eff} and the a_{\cos}^{\pm} and a_{\sin}^{\pm} terms may be affected significantly by d , I_r and I_i , depending on the value of δ and R . Therefore, a quasi-two-body analysis must check the stability of the values obtained for α_{eff} with respect to variations of the s^{\pm} selection function designed to reduce/enhance the values of these coefficients.²⁰

In order to illustrate the actual capabilities of `BaBar`, in low-statistics regimes, analyses were performed in the framework of the PSI approach. It was assumed that the $\rho^0\pi^0$ events would be too scarce to be useful. The aim was to measure the model-independent five observables, a , a_{\cos}^{\pm} and a_{\sin}^{\pm} (cf. Eq. (6.57)). For such measurements, the loss of precision due to imperfect tagging, residual background, and vertex resolution have been the subject of several previous studies [72]. The experimental resolutions²¹ for the a , a_{\cos} and a_{\sin} determinations can be shown [71] to be:

$$\sigma_a \simeq \frac{1}{\sqrt{\epsilon_a(N^+ + N^-)}} \quad , \quad \sigma_{a_{\cos}^{\pm}} \simeq \frac{1}{\sqrt{\epsilon_{\cos}N^{\pm}}} \quad , \quad \sigma_{a_{\sin}^{\pm}} \simeq \frac{1}{\sqrt{\epsilon_{\sin}N^{\pm}}} \quad , \quad (6.62)$$

where N^{\pm} is the number of signal events associated to the $\rho^{\pm}\pi^{\mp}$ channel (before tagging) and ϵ_a , ϵ_{\cos} and ϵ_{\sin} are effectively selection efficiencies:

$$\epsilon_a \simeq 0.20 = (1 + \eta_a B_0)^{-1} \quad , \quad (6.63)$$

$$\epsilon_{\cos} \simeq 0.07 = \frac{2}{3} S^2 (1 + \eta_{\cos} B)^{-1} e^{-(\sigma_t x_d)^2} \quad , \quad (6.64)$$

$$\epsilon_{\sin} \simeq 0.05 = \frac{1}{3} S^2 (1 + \eta_{\sin} B)^{-1} e^{-(\sigma_t x_d)^2} \quad , \quad (6.65)$$

¹⁹There is a subtlety here: not only are the measurements of a_{\cos}^+ and a_{\sin}^+ subject to statistical fluctuations, but their true values themselves depend on the analyzed sample and are thus also subject to statistical fluctuations. However, the statistical fluctuations of the true a_{\cos}^+ and a_{\sin}^+ values are negligible compared to the statistical fluctuations on their measurements and, thus, they can be safely ignored [71].

²⁰For instance, since the small value of the I_i integral results from an averaging of positive and negative contributions, one may consider a choice of s^{\pm} which yields $I_i = 0$, by construction.

²¹The formulae given here for a , a_{\cos} and a_{\sin} omit a^2 , $(a_{\cos}^{\pm})^2$ and $(a_{\sin}^{\pm})^2$ dependence, since these quantities are all small; the exact form was used in the Monte Carlo analysis. The a coefficient is measured without tagging.

where S^2 accounts for the imperfect tagging; it is the absolute separation defined in Sec. 4.8 ($S^2 = 0.3$). The next factor accounts for the residual background: $B_0 \simeq 4$ is the background over signal ratio before tagging, and $B \simeq 2$ is the background over signal ratio after tagging (cf. Table 6-18). The quantities $\eta_a \simeq 1$, $\eta_{\cos} \simeq 1$ and $\eta_{\sin} \simeq 0.5$ stem from the differences in the time distribution and in the tagging response [73] for background and signal events. (The latter value reduces the impact of background on the determination of a_{\sin}^{\pm} .) The exponential factor accounts for the limited vertex resolution ($\sigma_t x_d = \sigma_{\Delta z} \Delta m / \beta \gamma c \simeq 0.35$). It leads to a negligible correction.

Results for 30 fb^{-1} : One nominal year of data-taking on the $\Upsilon(4S)$ (defined as 30 fb^{-1}) would yield a total number of signal events, before tagging (see Table 6-18) $N^+ + N^- \simeq 600$ (with about 2200 background events), hence about $0.58 \times 600 \simeq 350$ tagged events (with about 700 background events). The number of perfectly tagged events is $S^2 \times 600 \simeq 180$ and the effective number of perfectly tagged and background-free events is about $180 / (1 + \eta_{\sin} B) \simeq 100$.

With these initial statistics the goal of the analysis is essentially limited to a search for CP violation in the data. There are three signals that would indicate CP violation:

$$a \neq 0 \quad (6.66)$$

$$a_{\cos}^+ + a_{\cos}^- \neq 0 \quad (6.67)$$

$$a_{\sin}^+ + a_{\sin}^- \neq 0 \quad (6.68)$$

For each of these, the possible significance of a nonzero value for the measurement can be expressed in terms of χ^2 -like variables:

$$\chi_a^2 = \frac{a^2[\text{meas}]}{\sigma_a^2}, \quad \chi_{\cos}^2 = \frac{(a_{\cos}^+[\text{meas}] + a_{\cos}^-[\text{meas}])^2}{\sigma_{a_{\cos}^+}^2 + \sigma_{a_{\cos}^-}^2}, \quad \chi_{\sin}^2 = \frac{(a_{\sin}^+[\text{meas}] + a_{\sin}^-[\text{meas}])^2}{\sigma_{a_{\sin}^+}^2 + \sigma_{a_{\sin}^-}^2} \quad (6.69)$$

(where [meas] indicates the measured value of the quantity) or, for a combined measure of CP -violation, their sum²², or alternatively, the quantity $N_{\sigma}[CP]$ [70]²³ can be used. The expected sensitivities to CP violation turn out to be similar in the three reference scenarios, as shown in Table 6-24.²⁴ It is seen that, in the Large Penguins reference scenario, direct CP violation could be established from the a_{\cos}^{\pm} observables (cf. Tables 6-22 and 6-25), whereas a nonzero value of the a coefficient would only be barely measurable. Thus, in the Large Penguins reference scenario, for one year of data-taking, one expects from the a , a_{\cos}^{\pm} and a_{\sin}^{\pm} measurements a total $\chi^2 = 6.6$ which corresponds to a demonstration of CP violation at the 90% confidence level.²⁵

²²The correlations between the a , a_{\cos} and a_{\sin} measurements are weak, thus the three χ^2 can be directly added.

²³The expression of the \mathcal{K} in variable in the quasi-two-body approach may be found in [70, 71].

²⁴The expected χ^2 for the difference of any quantity x from zero is obtained from $\langle \chi_x^2 \rangle = 1 + (\langle x \rangle / \sigma_x)^2$. The results shown in Table 6-24 are obtained from Tables 6-22 and 6-25, scaling the latter values by three to reflect the ratio of the running times. The results of these simple calculations have been confirmed by Monte Carlo simulations.

²⁵However, it is easy to build other scenarios where CP violation would be difficult to demonstrate. An example is provided by a No-penguins reference scenario with a strong-phase $\delta \simeq \pi/2$.

Table 6-24. Expected values of the three χ^2 s with one year of data-taking at nominal luminosity in the various reference scenarios (for $\alpha = 1.35$, $\sin 2\alpha = 0.43$). Non-zero χ_a^2 and/or χ_{\cos}^2 indicate direct CP violation.

Scenario	$\langle \chi_a^2 \rangle$	$\langle \chi_{\cos}^2 \rangle$	$\langle \chi_{\sin}^2 \rangle$
Small Penguins	1	1	3.4
Large Penguins	1.3	4.0	1.3
No Penguins	1	1	4.3

The distribution of events in the \mathcal{K}_{in} variable (Section 4.10.5) is a tool that may be used to display CP violation graphically, which is demonstrated by any asymmetry of the distribution. The example shown in Fig. 6-20 is obtained using the Small Penguin scenario. The accumulation at small \mathcal{K}_{in} values corresponds to events either intrinsically irrelevant for CP violation or where tagging information is poor. Detector effects and backgrounds tend to shrink the distribution to small values, which explains why no events reach the extreme values $\mathcal{K}_{in} = \pm 1$. Events with sizeable \mathcal{K}_{in} values (e.g., $|\mathcal{K}_{in}| > 0.1$) give significant information on CP violation. These events must be thoroughly understood to establish the observation of CP violation.

Results obtainable with 90 fb^{-1} : From the numbers of events estimated above, scaled to three years of data taking, the errors on the measured values of the a , a_{\cos}^{\pm} and a_{\sin}^{\pm} coefficients are estimated²⁶ and given in Table 6-25.

Table 6-25. Estimated errors on the measurements of the a , a_{\cos}^{\pm} and a_{\sin}^{\pm} coefficients. The quoted errors correspond to 90 fb^{-1} ($N^+ + N^- \simeq 1800$) and depend only weakly on the input values of the parameters.

Parameter	a	a_{\cos}^+	a_{\cos}^-	a_{\sin}^+	a_{\sin}^-
Error	0.05	0.11	0.11	0.15	0.15

Constraints on α_{eff} may be derived from the measurements of the a_{\cos}^{\pm} and a_{\sin}^{\pm} coefficients by using the approximate expressions of Eq. (6.59-6.60) which ignore penguin contributions. If χ_a^2 or χ_{\cos}^2 are large, direct CP violation can be established, but in this case penguin contributions cannot consistently be ignored and the extraction of the actual value of α requires further inputs. However, note that small values for χ_a^2 and χ_{\cos}^2 do not guarantee that $\alpha_{\text{eff}} = \alpha$.

²⁶The actual values obtained from Monte Carlo simulation are reproduced well by the approximate expressions of Eq. (6.62).

The values taken by the a , a_{\cos}^{\pm} and a_{\sin}^{\pm} coefficients in the three reference scenarios were given in Table 6-22. The residual effect of interference is weak in the PSI analysis, so that the analysis cannot distinguish between the various mirror solutions (cf. Table 6-21). Figure 6-21 shows an example, for two different levels of statistics (30 fb^{-1} and 90 fb^{-1}), of the χ^2 as a function of α_{eff} :

$$\chi^2(\alpha_{\text{eff}}) = \frac{(\bar{a}_{\cos} - \bar{a}_{\cos}[\text{meas}])^2}{\sigma_{\bar{a}_{\cos}}^2} + \frac{(a_{\sin}^+ - a_{\sin}^+[\text{meas}])^2}{\sigma_{a_{\sin}^+}^2} + \frac{(a_{\sin}^- - a_{\sin}^-[\text{meas}])^2}{\sigma_{a_{\sin}^-}^2}, \quad (6.70)$$

where \bar{a}_{\cos} is the difference $a_{\cos}^+ - a_{\cos}^-$. At each α_{eff} value a fit is performed in order to locate the minimum of the χ^2 with respect to R and δ . The values of the a_x at the minimum thus found are used to determine the values of $\chi^2(\alpha_{\text{eff}})$ shown in Figure 6-21. The translation of the χ^2 value in terms of confidence level is straightforwardly obtained using a number of degree of freedom $n_{\text{dof}} = 1$. The chosen example uses the Small Penguins set. For an integrated luminosity of 90 fb^{-1} , CP violation is established from χ_{\sin}^2 at about a three-sigma level, while, due to a statistical fluctuation, $\chi_a^2 = 3.5$ indicates that there might be significant penguin contributions, although this is not the case. Two pairs of mirror solutions are very close and are not resolved. Since the χ^2 behavior near the six apparent minima is not parabolic, (especially for the 30 fb^{-1} sample), it is unwise to express the analysis result in terms of a set of values of α with errors. It is better to use confidence levels [11] as a function of α_{eff} as shown here.

The important limitations due to the multiple mirror solutions, dictate that the capabilities of BABAR for this mode should not be summarized by the resolution on $\sin 2\alpha_{\text{eff}}$, but by the resolutions on the a_{\cos}^{\pm} and a_{\sin}^{\pm} coefficients of Table 6-22. These model-independent coefficients yield multiple solutions for the quantity α_{eff} . Furthermore, the shift of α_{eff} from the true α cannot be assessed easily and estimation of this shift introduces model-dependence and thus theoretical uncertainties (see however [15] and [63]).²⁷ Thus a quasi-two-body analysis of $\rho\pi$, by itself, cannot set significant constraints on α , even when significant CP violation is indeed visible.

Experimental cross-checks: Two experimental cross-checks should be made. The first cross-check can be applied even for the 30 fb^{-1} analysis. One uses the background to probe CP -violating effects that the detector or the analysis might induce. For instance the analysis can be repeated using side-bands or multiply charged candidates or off-resonance data (cf. Section 6.5.1.1). It must be verified that no CP violation is observed in such samples. The second cross-check concerns the 90 fb^{-1} analysis. One can use the Δz distributions of events selected before and after tagging to determine the background-to-signal ratio from the analyzed events themselves. For example, from a naive likelihood analysis based on a 90 fb^{-1} sample, one may expect the background-to-signal ratio before and after tagging to be determined as $B_0 = 4 \pm 0.3$ and $B = 2 \pm 0.25$ respectively, if the background distribution is about twice as sharp in Δz as the signal distribution and if the

²⁷Of course, in the present exercise, the true values of the theoretical parameters are known, and the measurement biases can be quoted: $\sin 2\alpha_{\text{eff}} - \sin 2\alpha = -0.06$ and $+0.13$ for the Small Penguins and Large Penguins sets respectively. These numerical values only give a very rough idea of how large the theoretical uncertainties might be.

shape of its distribution is known. Such a precision on B would be sufficient since the systematic effects on the a_{\sin}^{\pm} coefficients ($\Delta_{\sin} \simeq a_{\sin}^{\pm} \Delta B / (1 + \eta_{\sin} B)$) would be smaller than the statistical uncertainty.

6.5.2.4 Fitting for α and penguins: studies of the three-body analysis

The full three-body analysis pioneered by Snyder and Quinn [8] holds the prospect of determining α from the data, even in the presence of penguin contributions. How well this can be accomplished depends on the extent and purity of the data. Studies of this method were made with a simple Monte Carlo to address three specific questions:

- How well is the true solution separated from mirror solutions?
- How big an error is likely to be introduced by ignoring penguin contributions?
- How much does the background degrade the measurement of α ?

Distinguishing the true solution from mirrors

Even though the addition of penguins and interference effects lifts the degeneracies between the minima of the Likelihood function, with finite data there is always the chance that a near-mirror solution, not the true solution, will have the lower χ^2 . With the input amplitudes considered and $\alpha = 1.35$, the most dangerous mirror solution occurs for $\alpha' = \pi/2 - \alpha$. To study this, multiple samples of 300, 600, and 1200 events were generated. For each such experiment α is determined twice with `Minuit`, once beginning near the true α and once beginning near the mirror solution. The χ^2 for each ($\chi_{\text{true}}^2, \chi_{\text{mirror}}^2$) was noted and the better solution was identified. By taking 100 experiments of each kind one obtains the mean difference in χ^2 :

$$\Delta\chi^2 = \chi_{\text{true}}^2 - \chi_{\text{mirror}}^2 \quad (6.71)$$

and the variation in $\Delta\chi^2$ (see also [70]). The results are in Table 6-26.

From Table 6-26, using Gaussian statistics, one expects that, with 300 events, about 72% of the time the correct α is picked. With 600 and 1200 events, this rises to 81% and 91%, respectively. (However, one should remember that in any analysis that does not include penguin effects, these two minima will always be indistinguishable.) In an actual analysis, one would not simply select a given minimum, the output information is the value of the best χ^2 against α , for all values of α . The point of this study is to estimate how many events are needed in order to achieve a statistically meaningful and reliable separation of the correct value of α from the near-mirror values by this method.

Table 6-26. *The difference, $\Delta\chi^2 = \chi_{\text{true}}^2 - \chi_{\text{mirror}}^2$, between the likelihood at α and that at $\pi/2 - \alpha$, averaged over 100 experiments. The rms variation away from this mean is shown, as well. The mean separation is expected to grow as N , the number of events. The rms variation is expected to grow as \sqrt{N} . At 300 and 600 events the separation is less than 1σ , while by 1200 it is more than 1σ . No backgrounds are included.*

Events	$\Delta\chi^2$	$\sigma(\Delta\chi^2)$
300	-2.13	3.54
600	-5.22	5.81
1200	-10.7	7.90

Error introduced by ignoring penguins

A possible means of analyzing a small data set is to ignore the penguin amplitudes and thus reduce the number of parameters to be fitted. The error introduced in this way will depend on the magnitudes of the penguin amplitudes and their phases. This was studied in two ways. First, the Large Penguins amplitudes were used. Since these amplitudes have ad hoc strong-interaction phases, this study might not be representative. Therefore, a second study was done with strong-interaction phases introduced in a random way.

For each of the three sample sizes (300, 600, and 1200 events), 100 independent samples were generated with the Large Penguin amplitudes. Each sample was analyzed both with penguins (nine-parameter fit) and without penguins (five-parameter fit). In each case, `Minuit` was run with three different starting points, the true α (1.35), $\pi/2 - \alpha$ and $\pi/4$. The last was chosen because it is a mirror solution in the case of zero strong-interaction phases and no penguins (cf. Table 6-21). The χ^2 s obtained for the three fits were compared and the one with the lowest χ^2 value was taken as the best solution. Thus for each of the 300 data samples, six `Minuit` fits were done. The best fit with penguins and the best fit without penguins were each retained. The results are shown in Fig. 6-22 and Table 6-27.²⁸

The improvement as the number of events increase is quite clear in Fig. 6-22. Looking in more detail, it can be seen that the analysis with penguins makes fewer mistakes than the analysis without penguins, that is, it picks $\pi/2 - \alpha$ less often. In addition, it can be seen that there is also a systematic bias in the result without penguins. This is displayed quantitatively in Table 6-27. The smaller spread in the results when the analysis is done without penguins is an obvious consequence of there being fewer parameters to fit. The increased precision is illusory since the systematic bias overwhelms this apparent advantage.

²⁸In an actual analysis the full χ^2 versus α plot is the “result,” not just the value of α corresponding to the the lowest χ^2 .

Table 6-27. Sample studies of the determination of $\sin 2\alpha$ by fitting α itself along with all the amplitudes. Both fits with and without penguins are considered. The Monte Carlo data were generated with the large penguin amplitudes for $\alpha = 1.35$ ($\sin 2\alpha = 0.43$). The column labeled % indicates how often the α choice closest to the input value was identified.

# events	Generated	Penguins			No penguins		
		$\langle \sin 2\alpha \rangle$	$\sigma(\sin 2\alpha)$	%	$\langle \sin 2\alpha_{\text{eff}} \rangle$	$\sigma(\sin 2\alpha_{\text{eff}})$	%
300	0.432	0.34	0.27	73	0.19	0.16	76
600	0.432	0.38	0.20	89	0.20	0.12	81
1200	0.432	0.39	0.11	95	0.19	0.06	90

Since strong-interaction phases will remain unknown, an additional study was made of the error $\sin(2\alpha_{\text{eff}}) - \sin(2\alpha)$ introduced by ignoring penguins. The magnitudes of the input amplitudes were taken from the Large Penguins set. For each trial the amplitudes were given randomly-chosen strong phases and data generated. Then two fits for the parameters, including α were made, one including and one excluding penguins from the analysis (though always using penguins in generating the events). To remove spurious sources of error (such as selection of a mirror solution), many events were generated in each of 100 trials. The results are shown in Table 6-28. The analysis with penguins performs as expected. The typical error introduced in $\sin 2\alpha$ by ignoring penguins is roughly 0.10. (In the study that used the model-assigned phases of the Large Penguin amplitudes the shift turned out to be about twice this, a perfectly consistent result.)

Clearly this result depends on the magnitudes of the Large Penguin reference amplitudes. It is worth remembering that the actual penguin amplitudes may be even larger than the Large Penguin amplitudes used here (see for instance the last column of Table 6-28). Similar errors can be expected to limit studies that ignore penguin amplitudes in the two- or four-pion decay channels. It is possible that, with further data on many rare decays, measurements and models will combine to give well-constrained results for the ratio of magnitudes of tree and penguin amplitudes. In this case simulations such as that presented here can be used to estimate the expected magnitude of the shift $|\sin(2\alpha_{\text{eff}}) - \sin(2\alpha)|$. In combination with fits to low statistics data that extract $\sin(2\alpha_{\text{eff}})$, this may provide the best estimates for the allowed range of values of α that can be made (until such time as sufficient data are available to carry out the full analysis including penguin contributions). The implication of this study is that the range will possibly be quite large.

Inclusion of background

The idealized three-body treatment can be made more realistic by introducing simulated backgrounds. In addition to the $\rho\pi$ final state, one expects some amount of nonresonant 3π in addition to background from continuum events. The nonresonant background is assumed to be distributed

Table 6-28. The mean values of α and $\sin 2\alpha$ and their variations determined from 100 experiments, each with many events. Each experiment had fixed values of the tree and penguin amplitudes. Different experiments had different phase relations between different amplitudes as explained in the text. The magnitudes of tree amplitudes for final states with $I = 0, 1,$ and 2 were taken from the Large Penguin set. Penguin amplitudes even larger than these appear quite possible.

	Events	$\langle\alpha\rangle$	$\langle\sin 2\alpha\rangle$	$\sigma(\alpha)$	$\sigma(\sin 2\alpha)$
With penguins	1000	1.35	0.436	0.046	0.082
	2000	1.35	0.426	0.030	0.054
	6000	1.34	0.437	0.016	0.028
Without penguins	1000	1.36	0.411	0.063	0.116
	2000	1.36	0.406	0.063	0.115
	6000	1.35	0.416	0.054	0.099

uniformly across the Dalitz plot with the same size as the signal, and thus fairly sparse in the region of the ρ . The nonresonant background has the exponential decay time characteristic of B decays.

Because the continuum events are dominantly two-jet, there is a tendency for two of the pions to have a small invariant mass. This means that these continuum background events will tend to accumulate near the boundary of the Dalitz plot. The continuum events are therefore modeled by Breit-Wigner-like distributions on top of the ρ Breit-Wigner.²⁹ The results drawn from the present study do not depend significantly on the details of the background simulation³⁰ [15].

The Monte Carlo events generated with such added background contributions were analyzed with the ratios of the nonresonant background to the signal and the continuum background to the signal as free parameters. Thus the number of parameters to be fitted by `Minuit` was increased from nine to eleven. To study how the presence of background degrades the resolution for α , experiments of 400, 600 and 1200 signal events were generated. The continuum within the ρ bands was taken to be from 2 to 7 times the signal. The spreads were determined by running 100 experiments in each instance.

The fits with only 400 or 600 signal events showed some variability. The difficulty of working with such a small data sample is apparent in Fig. 6-23. This figure represents a single experiment, viewed first without any background then with continuum background included with a background over signal ratio of two. In this last instance, much of the range of α is less than four units of χ^2

²⁹This is a worst-case scenario, other distributions for the background shape, which will be determined by fits to off-resonance data, will make it easier to separate background and signal events.

³⁰For example, the continuum u, d, s events that are mistakenly called 3π will typically have small values of Δz . Their distribution is described either by the sum of two Gaussians with widths $100 \mu\text{m}$ and $200 \mu\text{m}$, with 80% of the events in the narrower distribution and 20% in the wider, or, by a single exponential of effective lifetime $0.4\tau_B$.

Table 6-29. *The dependence of the uncertainty σ_α on the extent of the backgrounds. The nonresonant background was taken to be uniform across the Dalitz plot. The continuum background is concentrated at the periphery of the Dalitz plot as described in the text. In all instances, 100 experiments were simulated. Accordingly, the rms error on σ should be about 10%. It is not possible to determine from these limited samples how much is gained by reducing the continuum-to-signal ratio from 7.2 to 3.6. The continuum background levels considered here reflect early results from a preliminary `BBSim` study, which are more pessimistic than the `Aslund` results reported above. Further work on background fighting may well reduce the backgrounds below the levels considered in this table.*

Signal Events	Nonresonant Events	Continuum Events	$\sigma(\alpha)$
1200	0	0	0.06
1200	1200	0	0.07
1200	1200	4200	0.13
1200	1200	8600	0.12

removed from the minimum. Of course, different samples of events would lead to different features in detail, but the lesson is clear and unsurprising. It is difficult to fit 8, 9, or 10 parameters with a few hundred data points, especially in the presence of background. A comparison of Fig. 6-23 with the results given earlier for the PSI study Fig. 6-21 (after three years of data taking) shows that, even with backgrounds, the multi-parameter fit excludes a greater range of α values because it removes a number of the mirror solutions. It is interesting to note that this occurs even though the signal for $\rho^0\pi^0$ events is much smaller than background and could not be isolated. However the effect of its interference with the $\rho^\pm\pi^\mp$ bands does significantly constrain the parameters even in this situation.

With 1200 events, the situation is much improved, as shown in Table 6-29. Roughly speaking, the background adds about 0.10 to the error in α , taken in quadrature. What is clear is that the backgrounds significantly degrade the result that can be achieved in their absence. With effective background fighting, a 1200-event signal sample might be expected to determine α to ± 0.10 . Figure 6-24 shows a single 1200-event experiment with various backgrounds added. While this particular example is exceptionally clean in its identification of the true solution and the near mirror, it reflects the more general feature that a 1200-event signal sample allows a good determination of α .

The presence of background will diminish the ability to distinguish the true solution from mirror solutions. This is shown in Table 6-30, which may be compared to Table 6-26. Here nonresonant background equal to the signal and continuum background 2.4 times the signal have been included. Assuming Gaussian statistics, one expects to pick the right α 70%, 77%, and 83% of the time for 300, 600, and 1200 signal events.

Table 6-30. The difference, $\Delta\chi^2 = \chi_{\text{true}}^2 - \chi_{\text{mirror}}^2$, between the likelihood at α and that at $\pi/2 - \alpha$, averaged over 100 experiments. The rms variation away from this mean is also shown. Here nonresonant background equal to the signal and continuum background 2.4 times the signal have been included. At 300 and 600 events the separation is less than 1σ , while by 1200 it is more than 1σ . The results are somewhat worse than without backgrounds (See Table 6-26).

Events	$\Delta\chi^2$	$\sigma(\Delta\chi^2)$
300	-1.60	3.10
600	-2.80	3.88
1200	-5.33	5.72

6.5.3 Conclusion

In the first few years of running the analysis of three-pion channels will be carried out in the framework of a No-Penguin analysis. Measurements of α will thus be subject to significant theoretical uncertainties, and the values obtained should be referred to as α_{eff} . When performed in the quasi two-body approach, the analysis will not be able to distinguish between the eight-fold α_{eff} ambiguity inherent in a non CP -eigenstate analysis. Even analyses such as the phase-space-integrated approach described above, which retains some information from interference effects, will have difficulty in distinguishing many of the multiple minima. It is expected that CP violation can be established at the 3σ level within the first few years of data taking at nominal luminosity.³¹

Methods such as these, which suppress penguin contributions in parameterizing the data, cannot be used to give an accurate value of α unless supplemented by theoretical models which can help determine the shift between the measured α_{eff} and the true α . The situation here is similar to that for two- and four-pion channels. Systematic work to limit the theoretical uncertainties arising from such methods is needed and will improve the information available from any of these channels.

Eventually, the $B \rightarrow \pi\pi\pi$ channels in principle offer the possibility of extracting the angle α with no ambiguity or penguin uncertainties. This ambitious goal would necessitate several years of data taking, given current branching ratio estimates. Further it must be hoped that the underlying amplitudes do not conspire to yield quasi-degenerate mirror-solutions, that the $\rho(770)$ contribution is fairly dominant in the three-pion Dalitz plot, and that the $\rho^0\pi^0$ contribution is large enough, both so that its impact on the parameter fitting is sufficient and so that electroweak penguins do not spoil the isospin relation which is at the core of the analysis. Further study and actual measurements of these channels will clarify these points.

³¹The luminosity needed depends of course on the actual value of α and on the tree and penguin amplitudes.

The charged B decays to three-pion channels can also be measured. As for the neutral B channels, the major problem is low rates and large background effects, particularly for the channels with two neutral pions. It will require several years of data collection to acquire samples large enough to use these channels, in combination with the neutral B channels, to improve the extraction of α . The inclusion of these channels reduces the sensitivity to the expected low rate in the $\rho^0\pi^0$ channels and provides a number of cross-checks on the effects of other resonances and of backgrounds. It will be an important part of the eventual analysis.

With sufficient data and sufficient experience in background fighting the three-pion channels hold out the best hope for an eventual measurement of α which resolves most of the ambiguities inherent in the simpler treatments and correctly treats the impact of penguin effects (or beyond Standard Model contributions) in a model-independent way. These channels, with one or two π^0 s in the final state, will be quite difficult to study in a hadronic environment, so it is important for BaBar to persist in efforts to make and improve measurements of them.

6.6 B -Decay Modes with Four Pions

6.6.1 Overview

This section describes the results of a study of two benchmark modes, $B \rightarrow a_1\pi$ and $B \rightarrow \rho\rho$, both of which result in four pions in the final state. On the whole, analysis of these channels is somewhat more complex than that of the two-pion and three-pion modes, as one has to deal with a much larger combinatorial background level. Complications also arise from interference of the various modes that make up the four-pion final states, from the fact that some of these modes are not CP eigenstates (e.g., $a_1^+\pi^-$), and in the $\rho\rho$ channel from the presence of both CP -odd and CP -even components in the final states. However, these drawbacks are somewhat compensated if the branching ratios are much larger than for $B \rightarrow \pi\pi$, as expected. The following sections review the predictions for the branching ratios of the four-pion modes, followed by descriptions of the simulation studies of the two benchmark modes $B \rightarrow a_1\pi$ and $B \rightarrow \rho\rho$, providing a first order assessment of the experimental issues involved in extracting CP violation in these modes.

6.6.1.1 Comments on the branching ratio for the four-pion modes

At this time, there is no experimental measurement of the branching ratio of B mesons into four-pion final states. Theoretical calculations of the branching ratios for the exclusive $B \rightarrow a_1\pi$ and $B \rightarrow \rho\rho$ have been made within the framework of the factorization model, by Bauer, Stech and Wirbel (BSW) (Table 6-31). These rates, and in particular the ratio of the branching ratios, are sensitive to final-state scattering, which, as the authors point out, is not taken into account in

Table 6-31. Theoretical predictions of BSW for the branching ratios of the modes $B \rightarrow a_1\pi$ and $B \rightarrow \rho\rho$ in the factorization model.

Decay Mode	\mathcal{B} (%)	\mathcal{B} for $ V_{ub}/V_{cb} =0.08$
$B^0 \rightarrow a_1^- \pi^+$	$0.59 V_{ub}/V_{cb} ^2$	3.8×10^{-5}
$B^0 \rightarrow a_1^0 \pi^0$	$0.0069 V_{ub}/V_{cb} ^2$	4.4×10^{-7}
$B^0 \rightarrow \rho^+ \rho^-$	$0.45 V_{ub}/V_{cb} ^2$	2.9×10^{-5}
$B^0 \rightarrow \rho^0 \rho^0$	$0.01 V_{ub}/V_{cb} ^2$	6.4×10^{-7}

these calculations. For example, according to BSW the branching ratios of the color mixed modes $B^0 \rightarrow \rho^0 \rho^0$ and $B^0 \rightarrow a_1^0 \pi^0$ are suppressed compared to the decays $B^0 \rightarrow \rho^+ \rho^-$, and $B^0 \rightarrow a_1^- \pi^+$. Final-state scattering effects, however, tend to cancel the suppression and raise the branching ratios of the color suppressed modes.

A rough estimate of the overall branching ratio for the $B \rightarrow 4\pi$ channel also can be obtained from the mean multiplicity of final-state particles in B decays combined with the transition rate for $b \rightarrow u$. The $b \rightarrow u$ transition accounts for approximately 1% of B meson decays. The measured mean particle multiplicity of B decay final states is 8.25. If a Poisson multiplicity distribution is assumed, this leads to a probability of 5% for the occurrence of a four-pion final state. This suggests a branching ratio of approximately 5×10^{-4} for the $B \rightarrow 4\pi$ final states, which includes nonresonant $B \rightarrow 4\pi$ as well as the various resonant two and three body modes, $B \rightarrow a_1\pi$, $B \rightarrow \rho\rho$, and $B \rightarrow \rho\pi\pi$. In the absence of more solid information on the branching ratios, this guess-timate is used to set the scale for the branching ratios of benchmark modes in the simulation studies. Branching ratios of 10^{-4} are assumed for each of the benchmark modes, $B \rightarrow a_1\pi$ ($a_1^+ \pi^-$, $a_1^- \pi^+$, and $a_1^0 \pi^0$ combined), and $B \rightarrow \rho\rho$ ($\rho^+ \rho^-$ and $\rho^0 \rho^0$ combined). The sensitivity of the results to changes in the branching ratios are discussed, and the results for the case of BSW predictions are presented.

6.6.2 The $a_1\pi$ Decay Modes

In order to extract a measurement of $\sin 2\alpha$ using the decays of B mesons into $a_1\pi$, one must measure the amplitudes and CP asymmetries (for the case of neutral B decays) for each of the five possible $B \rightarrow a_1\pi$ decay channels: $B^0 \rightarrow a_1^+ \pi^-$, $B^0 \rightarrow a_1^- \pi^+$, $B^0 \rightarrow a_1^0 \pi^0$, $B^+ \rightarrow a_1^+ \pi^0$ and $B^+ \rightarrow a_1^0 \pi^+$. A branching ratio of 6×10^{-5} is assumed for the sum of the $B^0 \rightarrow a_1^+ \pi^-$ and $B^0 \rightarrow a_1^- \pi^+$ channels and 3×10^{-5} is assumed for the other three a_1 channels. For background channels of relevance here, we have assumed branching ratios of 10^{-4} for $\rho\rho$, $\rho\pi\pi$ and 4π nonresonant. The division of this into each of the possible charged states of these modes is assumed to be equal. As

will be described in greater detail later in this section, each channel contains a final state with at least two charged pions, which means that one is able to employ vertexing to estimate the parent B vertex in all cases. Using these branching fractions, only ~ 1000 of each of the above decays are expected to be produced for 30 fb^{-1} of integrated luminosity.

In addition to the signal channels discussed above, the following sources of background have been considered:

- **Combinatorial Background within Signal Events:** This consists of combinatorial background within events containing one of the signal decays. This arises when one or more of the tracks or reconstructed π^0 mesons from a signal decay is combined with products of the other B decay to form a candidate which passes all of the cuts. Unlike other combinatorial backgrounds, these events tend to produce a broad peak in the 4π invariant mass distribution near the B meson mass. Hereafter this background will be referred to as SCB (Signal Combinatorial Background).
- **$B\bar{B}$ Background:** This consists of combinatorial background in generic $\Upsilon(4S) \rightarrow B\bar{B}$ decays. For each 30 fb^{-1} of integrated luminosity, 31.5 million $B\bar{B}$ events are produced.
- **Continuum Background:** This is combinatorial background in $e^+e^- \rightarrow q\bar{q}$ events, where $q = u, d, s$ or c . Approximately 100 million of these types of events are produced for an integrated luminosity of 30 fb^{-1} .
- **Physics Background:** This background is from B decays into states which have the same four-pion final-state signature as one of the signal modes. Particular attention must be paid to this background since it includes decays into CP eigenstates, such as $B \rightarrow \rho\rho$, which exhibit time-dependent asymmetries that must be taken into account. As will be shown later, cuts have been devised to specifically reduce this type of background.

The rest of this section will be divided into three parts: B^0 decays, charged B decays and extraction of the CP asymmetries and amplitudes. The analysis [74] was performed on data samples of Monte Carlo-simulated signal and background events, generated using the `ASLUND` fast Monte Carlo code.

6.6.2.1 B^0 decays

Each of the decays $B^0 \rightarrow a_1^+ \pi^-$, $B^0 \rightarrow a_1^- \pi^+$ and $B^0 \rightarrow a_1^0 \pi^0$, manifests a CP asymmetry which must be extracted by fitting the relevant Δt distributions, where $\Delta t \cong \Delta z / (\gamma\beta c)$ and $\gamma\beta \approx 0.56$. For the analysis described in this section, it is assumed that a single amplitude dominates each decay mode. The $a_1^0 \pi^0$ mode is a CP eigenstate with time dependence

$$P(B^0(\bar{B}^0) \rightarrow a_1^0 \pi^0) \propto e^{-|\Delta t|/\tau} [1 \pm a_0 \sin(\Delta m_d \Delta t)], \quad (6.72)$$

where τ is the B^0 lifetime, Δm_d is the $B^0 \leftrightarrow \bar{B}^0$ oscillation frequency and a_0 is the CP asymmetry. The Δt distributions for the $a_1^\pm \pi^\mp$ mode are not simple because it is not a CP eigenstate. The distributions can be described by

$$\begin{aligned} P(B^0(\bar{B}^0) \rightarrow a_1^+ \pi^-) &\propto e^{-|\Delta t|/\tau} [1 \mp R \cos(\Delta m_d \Delta t) \pm D a_1 \sin(\Delta m_d \Delta t)] \\ P(B^0(\bar{B}^0) \rightarrow a_1^- \pi^+) &\propto e^{-|\Delta t|/\tau} [1 \pm R \cos(\Delta m_d \Delta t) \pm D \bar{a}_1 \sin(\Delta m_d \Delta t)], \end{aligned} \quad (6.73)$$

where a_1 and \bar{a}_1 are the CP asymmetries for the two decays, R is given by

$$R = \frac{[\Gamma(B^0 \rightarrow a_1^- \pi^+) - \Gamma(B^0 \rightarrow a_1^+ \pi^-)]}{[\Gamma(B^0 \rightarrow a_1^- \pi^+) + \Gamma(B^0 \rightarrow a_1^+ \pi^-)]}, \quad (6.74)$$

and D is a dilution factor, related to R according to $D = \sqrt{1 - R^2}$.

The goal of the analysis of the B^0 decays is to measure the three asymmetries, a_0 , a_1 and \bar{a}_1 , which contain information about $\sin 2\alpha$. In fact, in the absence of penguin diagrams: $a_0 = \sin 2\alpha$, $a_1 = \sin(2\alpha + \delta)$ and $\bar{a}_1 = \sin(2\alpha - \delta)$, where δ is the difference in the strong-interaction phases for the $B^0 \rightarrow a_1^+ \pi^-$ and $B^0 \rightarrow a_1^- \pi^+$ decays. Even in the presence of penguin diagrams, it may be possible to utilize an isospin-based analysis to extract an unbiased measurement of $\sin 2\alpha$ using the $a_1 \pi$ decays alone. In that case, one must also measure the relative amplitudes of each of the three B^0 decays, as well as the relative amplitudes of the charged B decays, which is achieved by measuring the branching fractions and the quantity R .

The decay $B^0 \rightarrow a_1^\pm \pi^\mp$, with $a_1^\pm \rightarrow \rho^0 \pi^\pm$ and $\rho^0 \rightarrow \pi^+ \pi^-$, is the cleanest signal channel to reconstruct due to the four charged pions in the final state. In addition to the all-charged final state, there are states containing one or more π^0 mesons. For the $B^0 \rightarrow a_1^\pm \pi^\mp$ decays, the a_1^\pm can decay to $\rho^\pm \pi^0$, with the ρ^\pm subsequently decaying to $\pi^\pm \pi^0$, thus creating a final state with two π^0 mesons. These decays involve the same amplitudes and asymmetries as the all-charged final state, so events reconstructed in this topology can be simply added to the all-charged sample to enhance the statistics. In the decay $B^0 \rightarrow a_1^0 \pi^0$, the a_1^0 decays to either $\rho^+ \pi^-$ or $\rho^- \pi^+$, with equal probabilities, and the ρ^\pm decays to $\pi^\pm \pi^0$. The final state of this decay is always $\pi^+ \pi^- \pi^0 \pi^0$.

The first step in reconstructing B^0 candidates is to form appropriate neutral combinations of four-pion candidates for each event. One then associates the pion candidates with the a_1 and ρ decays. A variety of cuts are employed to reduce the backgrounds. These cuts include kinematic cuts, particle identification, vertex quality, and flavor tagging, the effects of which are summarized in Tables 6-32 and 6-33.

Kinematic cuts: The so-called bachelor pion which comes directly from the B^0 decay has a momentum in the B^0 rest frame in the range 2.2 – 2.7 GeV/ c , which is much higher than the momenta of the other pions in the decay. The distribution of reconstructed momentum, boosted into the B^0 rest frame, for the bachelor pion and for the other three pions in the decay is shown in Fig. 6-25. The π^\pm or the π^0 with the highest momentum in the rest frame of the four-pion

Table 6-32. Efficiencies for each successive cut, for signal and backgrounds, for the all-charged final state. The efficiencies for each row are computed after applying all the cuts in the previous rows. The final two rows are the number of events produced and the number surviving all cuts, respectively, for a 30 fb^{-1} sample.

Cut	Efficiency						
	$a_1^\pm \pi^\mp$	SCB	$\rho^0 \rho^0$	$\rho^0 \pi^+ \pi^-$	$\pi^+ \pi^+ \pi^- \pi^-$	$B\bar{B}$	Continuum
Kinematic cuts	0.37	-	0.013	0.051	0.016	2.3×10^{-5}	5.0×10^{-5}
Particle ID	0.64	-	0.65	0.64	0.61	0.047	0.25
Vertex quality	0.83	-	0.83	0.83	0.83	0.39	0.57
Flavor Tag	0.59	-	0.59	0.59	0.59	0.53	0.32
Events Produced (30 fb^{-1})	945	-	1575	1050	1575	31.5×10^6	10^8
Events Selected (30 fb^{-1})	112	7	7	17	8	7	230

Table 6-33. Efficiencies of signal and backgrounds for B^0 modes containing π^0 mesons in the final state. The quantities in parentheses and square brackets are the numbers of events produced and selected, respectively, for a 30 fb^{-1} sample.

Mode	Signal effic. (evts. prod.) [evts. sel.]	SCB Bkgd. effic. (evts. prod.) [evts. sel.]	Physics Bkgd. effic. (evts. prod.) [evts. sel.]	$B\bar{B}$ effic. (evts. prod.) [evts. sel.]	Continuum effic. (evts. prod.) [evts. sel.]
$B^0 \rightarrow a_1^\pm \pi^\mp$ ($a_1^\pm \rightarrow \rho^\pm \pi^0$)	0.065 (1890) [123]	- (-) [30]	0.0049 (5250) [26]	1.1×10^{-6} (31.5×10^6) [35]	7.8×10^{-6} (10^8) [780]
$B^0 \rightarrow a_1^0 \pi^0$	0.070 (1015) [72]	- (-) [14]	0.0043 (5250) [23]	1.3×10^{-6} (31.5×10^6) [41]	9.7×10^{-6} (10^8) [970]

combination and the correct charge for the given signal channel is assumed to be the bachelor pion and this momentum is required to be greater than $2.3 \text{ GeV}/c$.

The remaining three-pion candidates are then assumed to be from the a_1 decay and the invariant mass of the combination is required to be in the range $0.7\text{--}1.8 \text{ GeV}/c^2$ ($M(a_1) = 1.23 \text{ GeV}/c^2$, $\Gamma = 0.400 \text{ GeV}$). From this three-pion combination there are two possible ways to form a ρ candidate and it is required that the invariant mass of at least one of the combinations be in the

range $0.5\text{--}1.0\text{ GeV}/c^2$. In order to reduce background from $B^0 \rightarrow \rho\rho$ decays, the candidate is rejected if two distinct ρ^0 candidates can be formed from the four-pion candidates.

The most effective cuts are those on the invariant mass and momentum of the B^0 candidate in the $\Upsilon(4S)$ rest frame, $M(B^0)$ and $p_{B^0}^*$, respectively. The invariant mass is required to be within 2.5σ ($\sigma = 17\text{ MeV}/c^2$) of the nominal B^0 mass, $5.280\text{ GeV}/c^2$, and the momentum is required to be in the range $0.175 - 0.425\text{ GeV}/c$. Each of these cuts is about 98% efficient for signal and rejects continuum and generic $B\bar{B}$ backgrounds by factors of about 25.

The continuum background is further reduced with event-shape cuts as described in Section 4.9.1. Cuts at $R_2 < 0.55$ and $|\cos\theta_{\text{thr}}| < 0.8$ are required.

Particle ID: The particle identification capabilities of the BABAR detector are also employed to reduce the combinatorial backgrounds. All charged tracks in the B^0 candidate are required to be consistent (within 2σ) with the pion hypothesis for both DIRC and dE/dx measurements and to be at least 3σ from the kaon hypothesis using the DIRC alone. Only tracks for which DIRC measurements are available are subjected to these cuts.

Vertex quality: For a signal event, all the charged tracks of the B^0 candidate originate from a common vertex. The position of this vertex is determined from a fit, for which the confidence level is required to be greater than 1%. The position of the vertex of the other B meson in the event is also needed. It is estimated by fitting to a common vertex all the tracks in the event, excluding the tracks of the B^0 candidate and all other tracks with impact parameters transverse to the beam direction, measured at the point of closest approach to the nominal interaction point, greater than 1 mm. The exclusion of tracks with large impact parameters primarily removes decay products of K_s^0 mesons. The confidence level of this vertex is also required to be greater than 1%. The coordinates of the two vertices are used to reconstruct Δz . The Δz resolution is modeled by the sum of two Gaussians, with widths of $85\text{ }\mu\text{m}$ (75%) and $235\text{ }\mu\text{m}$ (25%). The difference between the reconstructed and true Δz from Monte Carlo-simulated events is displayed in Fig. 6-26 along with the fit to two Gaussians.

Flavor tagging: The neural network of the Cornelius package, described elsewhere in this document, is used to tag the flavor of the other B meson in the event, using both kaons and leptons. Since the tagging efficiency for signal events is 59% and for continuum events it is 32%, nearly a factor of two is gained in the signal-to-background ratio by applying the flavor tag.

Cuts specific to channels with π^0 mesons: The π^0 candidates are reconstructed from pairs of EMC clusters unassociated with charged tracks and are required to have energy above 150 MeV and invariant mass in the range $123\text{--}147\text{ MeV}/c^2$. The invariant mass of the B^0 candidate is required to be within 2.5σ of the nominal B^0 mass, where $\sigma = 24\text{ MeV}/c^2$ for the $B^0 \rightarrow a_1^\pm \pi^\mp$ channel and $\sigma = 30\text{ MeV}/c^2$ for the $B^0 \rightarrow a_1^0 \pi^0$ channel.

6.6.2.2 B^+ decays

The decay $B^+ \rightarrow a_1^+ \pi^0$ has a final state with three π^0 mesons ($a_1^+ \rightarrow \rho^+ \pi^0$ and $\rho^+ \rightarrow \pi^+ \pi^0$) and one with a single π^0 ($a_1^+ \rightarrow \rho^0 \pi^+$ and $\rho^0 \rightarrow \pi^+ \pi^-$). Only the latter decay has been considered since the $3\pi^0$ final state is expected to have a much larger background and much lower reconstruction efficiency. The other B^+ decay considered is $B^+ \rightarrow a_1^0 \pi^+$, which always results in a final state with a single π^0 ($a_1^0 \rightarrow \rho^\pm \pi^\mp$ and $\rho^\pm \rightarrow \pi^\pm \pi^0$).

The only quantities which need to be measured from these charged B decays are the branching fractions, which can be used to provide information about penguin-mediated decays and are inputs to an isospin analysis

All of the decay modes considered above are reconstructed in a manner analogous to that described in the previous section, and the same cuts are used. Two cuts, in particular, are very important in the final selection of the charged B decays:

- A significant increase in the signal-to-background ratio for B^+ decays is obtained by cutting on the reconstructed Δz . For signal events, the two B vertices are well separated and the Δz distribution has an RMS around 250 μm , which roughly corresponds to the B lifetime. The continuum events, on the other hand, are very peaked around $\Delta z = 0$. The Δz distributions for signal and continuum events are displayed in Fig. 6-27. A cut requiring $|\Delta z| < 170 \mu\text{m}$ is applied, which has an efficiency of 58% for signal events and only 13% for the continuum events (after all other cuts have been applied).
- Flavor tagging, although not essential for the analysis of the charged B decays, is very useful in discriminating against continuum background because it preferentially selects events containing B meson decays. As for the neutral B case, the tagging efficiency is about 60% for signal events and 30% for continuum events.

Table 6-34 lists the reconstruction efficiencies, expected sample sizes, and backgrounds for the two B^+ decays.

6.6.2.3 Comparison with full simulation for $B^0 \rightarrow \pi^+ \pi^- \pi^+ \pi^-$

A study of the all-charged mode was performed [75] using the full simulation of the BABAR detector (BBSim) and the current version of the reconstruction code. This study was limited to the all-charged mode because the reconstruction of neutral particles is presently in a less reliable state. Table 6-35 summarizes the results of this study for the efficiencies of the signal and background processes. The signal efficiency is similar to that given in Table 6-32 but the background levels are substantially higher.

Table 6-34. Efficiencies of signal and backgrounds for B^+ modes. The quantities in parentheses and square brackets are the numbers of events produced and selected, respectively, for 30 fb^{-1} of integrated luminosity.

Mode	Signal effic. (evts. prod.) [evts. sel.]	SCB Bkgd. effic. (evts. prod.) [evts. sel.]	Physics Bkgd. effic. (evts. prod.) [evts. sel.]	$B\bar{B}$ effic. (evts. prod.) [evts. sel.]	Continuum effic. (evts. prod.) [evts. sel.]
$B^+ \rightarrow a_1^+ \pi^0$ ($a_1^+ \rightarrow \rho^0 \pi^+$)	0.044 (508) [23]	- (-) [3]	0.0012 (6300) [8]	4.1×10^{-7} (31.5×10^6) [13]	8.9×10^{-7} (10^8) [89]
$B^+ \rightarrow a_1^0 \pi^+$	0.042 (945) [43]	- (-) [5]	0.0025 (6300) [16]	5.2×10^{-7} (31.5×10^6) [16]	9.8×10^{-7} (10^8) [98]

Table 6-35. Effect of cuts on signal and background, using the full simulation.

Cut	Surviving events			
	$a_1 \pi$	$B\bar{B}$	light-quark	$c\bar{c}$
Simulated events	5000	2.0×10^6	2.8×10^6	1.6×10^6
B Candidates	7026	1565	39460	10010
p_{fast}	5521	343	23612	5798
m_B	2796	46	2154	592
m_{a_1}	2772	46	2086	556
m_ρ	2267	29	1300	339
p_B	2088	22	766	206
$B_{CP} \chi^2 > 0.01$	1774	8	477	90
$B_{tag} \chi^2 > 0.01$	1509	6	440	80
$R_2 < 0.55$	1318	5	217	38
$ \cos \theta_{thr} < 0.8$	1094	4	168	29
Tagging	698	2	20	16
Combinatorial	607	2	20	16
Overall effic.	0.12	1.0×10^{-6}	7×10^{-6}	1.0×10^{-5}

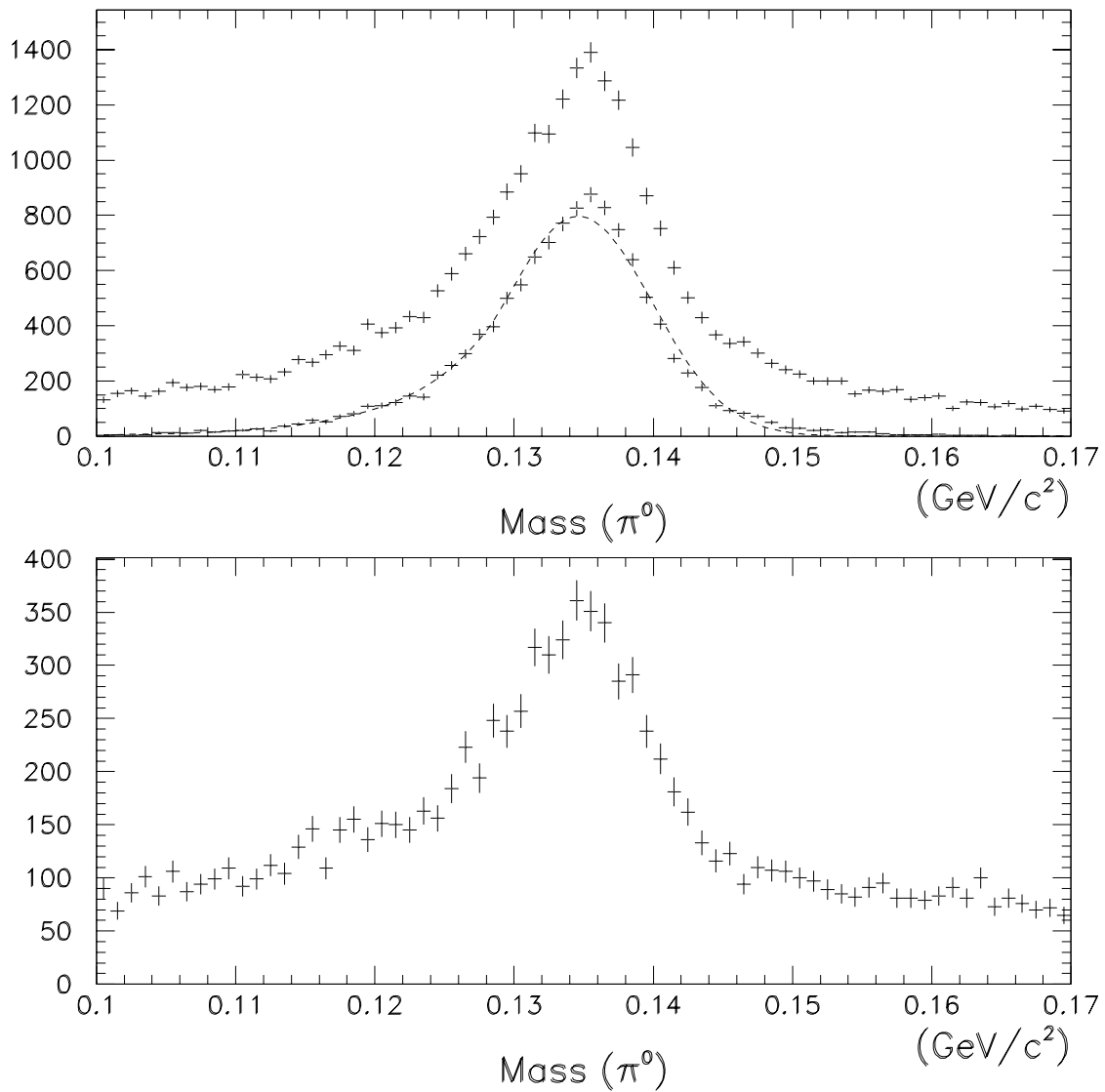


Figure 6-15. Distributions of the reconstructed π^0 mass for signal events (top) and continuum events (bottom). The fitted histogram in the top plot corresponds to the true signal, the remainder is combinatorial within signal events.

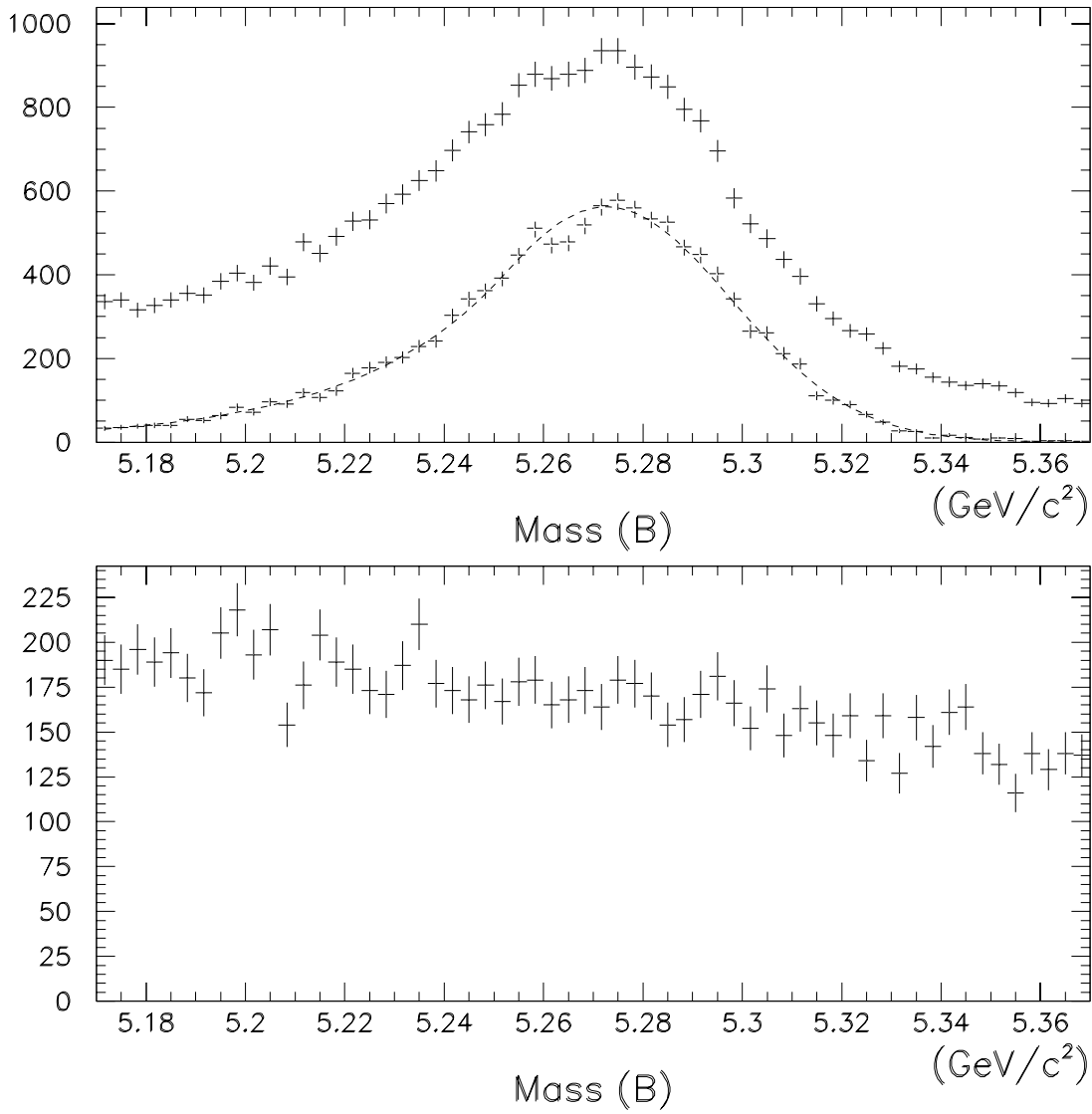


Figure 6-16. Distributions of mass of the reconstructed B for signal events (top) and continuum events (bottom). The fitted histogram in the top plot corresponds to the true signal, the remainder is combinatorial within signal events.

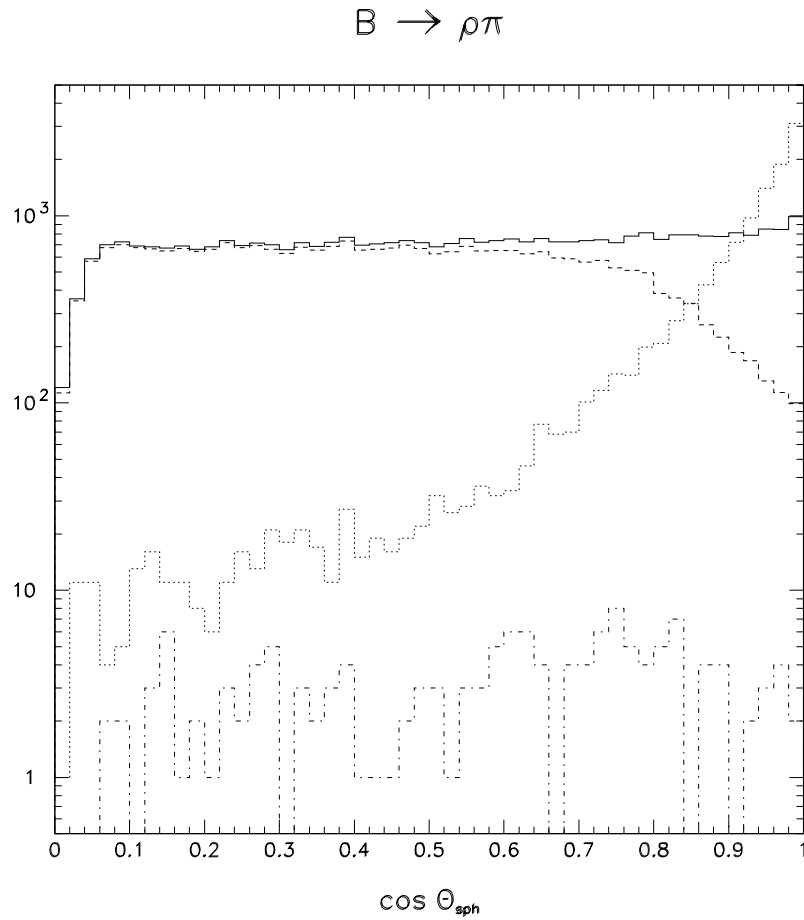


Figure 6-17. Distributions of the cosine of the angle between the sphericity axis of the rest of the event and the B decay axis, $\cos \theta_{\text{sph}}^{\rho\pi}$, for signal before (solid) and after (dashed) cutting on the neural network output at 0.9. The continuum background is shown before (dotted) and after (dot-dashed) the neural net cut.

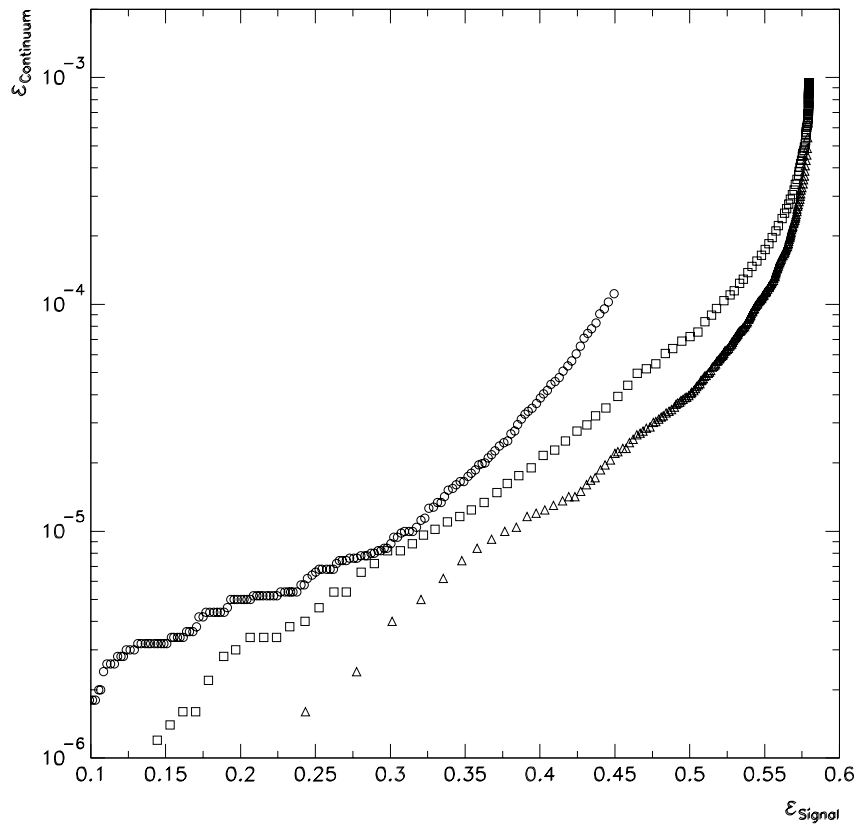


Figure 6-18. Efficiency for continuum background versus efficiency for signal for neural network (triangles), linear method (squares) and simple cuts (circles).

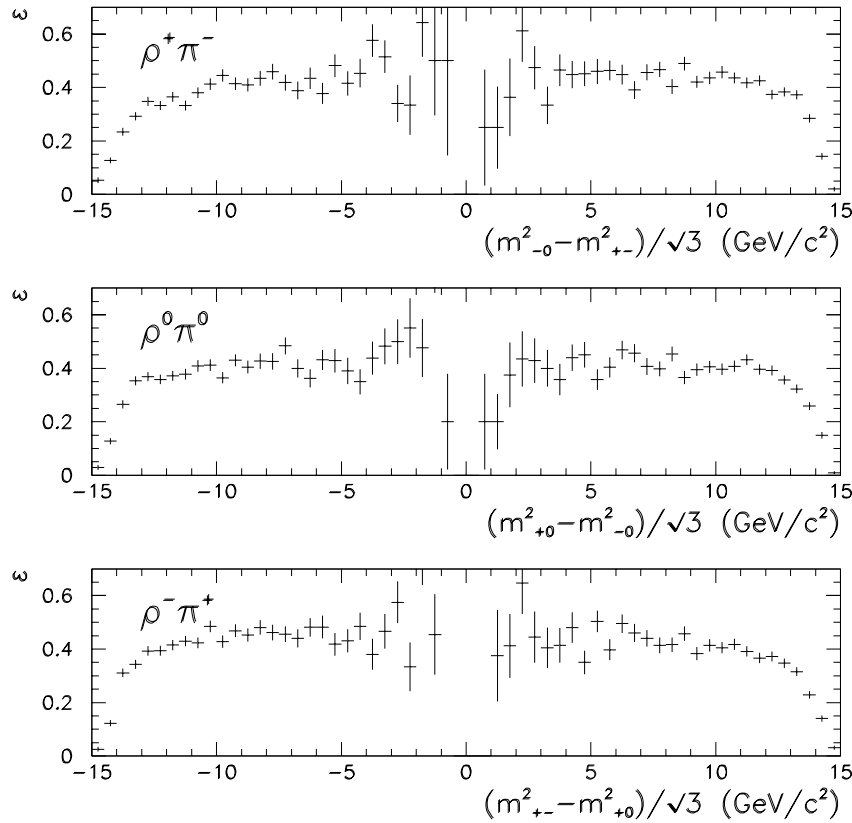


Figure 6-19. Efficiency for signal as a function of the three Dalitz-plot coordinates : $\rho^+\pi^-$ band (top), $\rho^0\pi^0$ band (center) and $\rho^-\pi^+$ band (bottom). The large error bars near 0 are due to the fact that the center of each ρ band is depleted because of the ρ polarization (cf. Eq. 6.31). The drop in efficiency at the edges of the ranges is mainly due to the cut which reduces the combinatorial background.

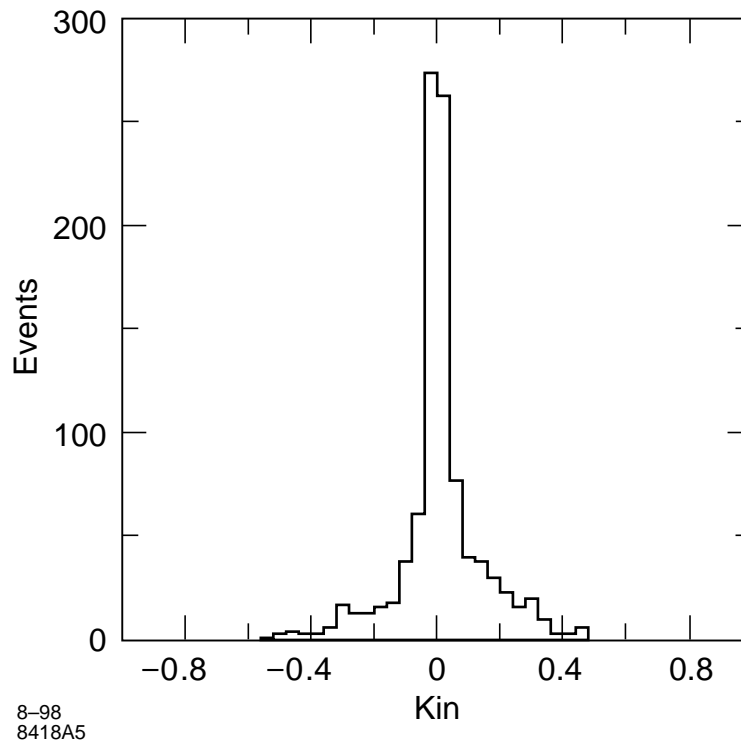


Figure 6-20. Distribution of the \mathcal{K}_{in} variable for a total sample of ~ 1000 tagged events (corresponding to a $\sim 90 \text{ fb}^{-1}$ sample) analyzed in the framework of the quasi-two-body approach for the Small Penguins set. *CP* violation is established from the asymmetry of the distribution. For most of the events the \mathcal{K}_{in} value is close to zero, hence they do not carry information on *CP* violation: for 34% of the events $|\mathcal{K}_{in}| > 0.1$, and among them 60% are signal events.

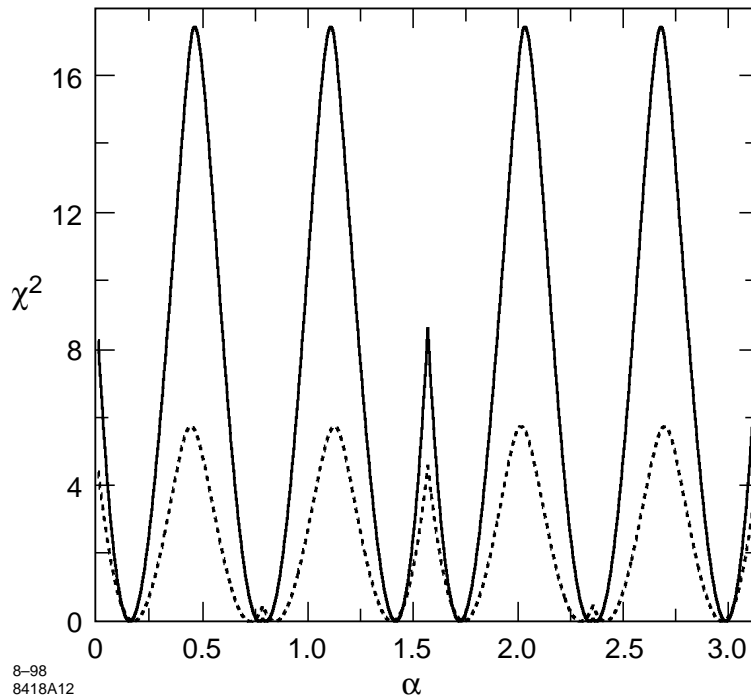


Figure 6-21. An example of χ^2 (Eq. (6.70)) minimized with respect to R and δ , as a function of α_{eff} for 30 fb^{-1} (dashed) and 90 fb^{-1} (solid) samples. The example uses the Small-Penguin set. Because the penguin contributions are unknown, α_{eff} is a model-dependent conventional quantity. The only model-independent conclusion which may be drawn from this χ^2 is that the value reached at $\alpha_{\text{eff}} = 0$ establishes CP violation.

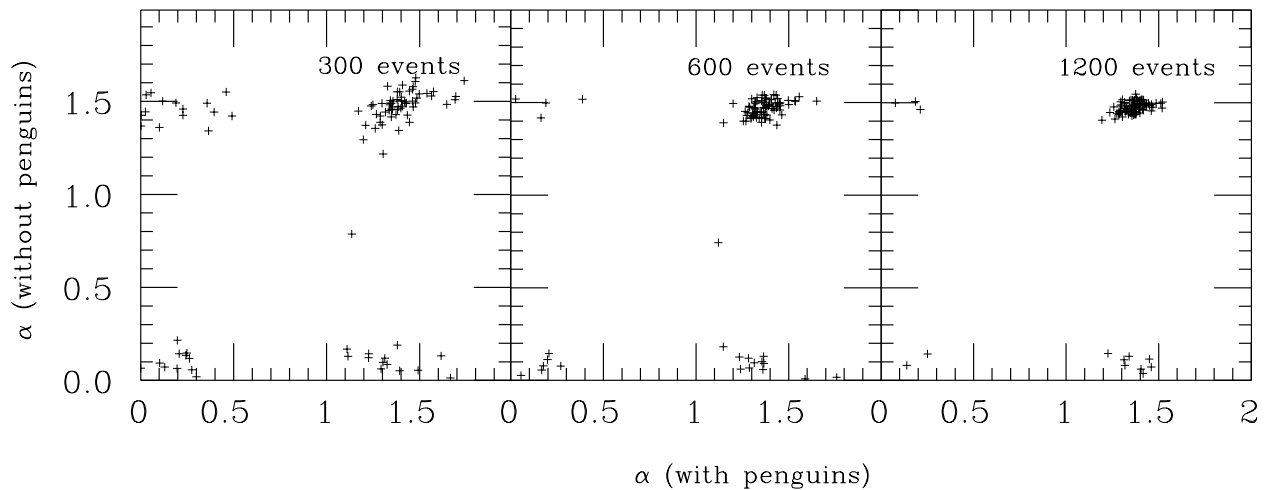


Figure 6-22. Scatter plots showing α extracted with and without penguins. There are 100 experiments each of the data sample of 300, 600, and 1200 events. The results cluster near the true α (1.35) and $\pi/2 - \alpha = 0.224$. The analysis with penguins chooses the correct α more often than the analysis without penguins does. While the distribution is narrow for the analysis without penguins, the result shows a bias, due to the model-dependent shift in α by penguin contributions. (cf. Table 6-27).

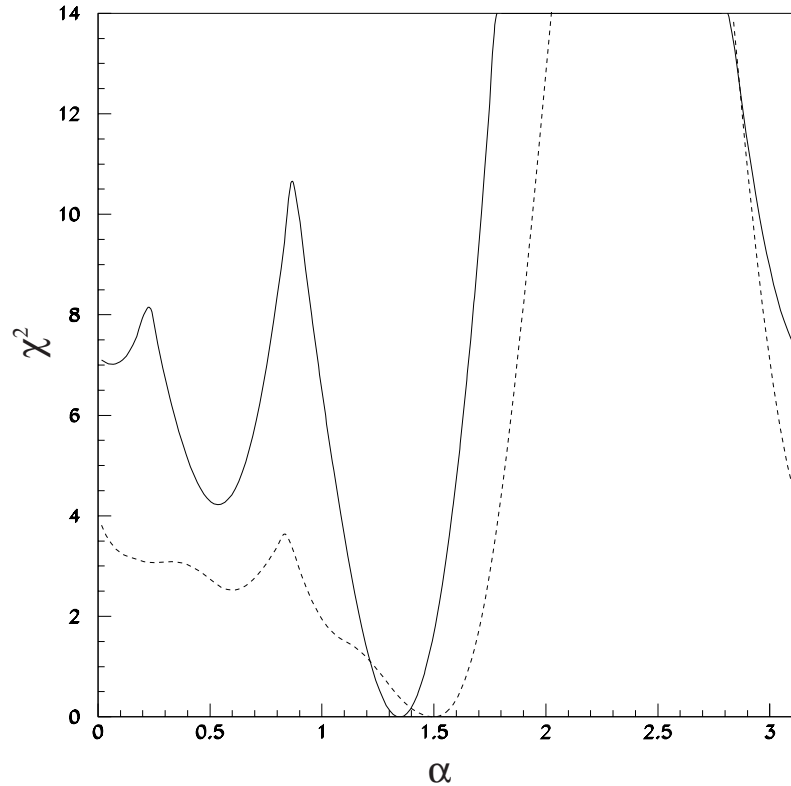


Figure 6-23. χ^2 ($-2 \ln \mathcal{L}$) as a function of α with 600 signal events: with no background (solid) and with 1200 continuum events (dotted). The events were generated with the Large Penguins amplitude set. The “true” (generated) value of α was 1.35. The solid curve is obtained from a set of eight-parameter fits performed at each α value to locate the minimum of the χ^2 and to probe for mirror solutions. The dotted curve is obtained from similar fits, but with the continuum background over signal ratio as an additional parameter.

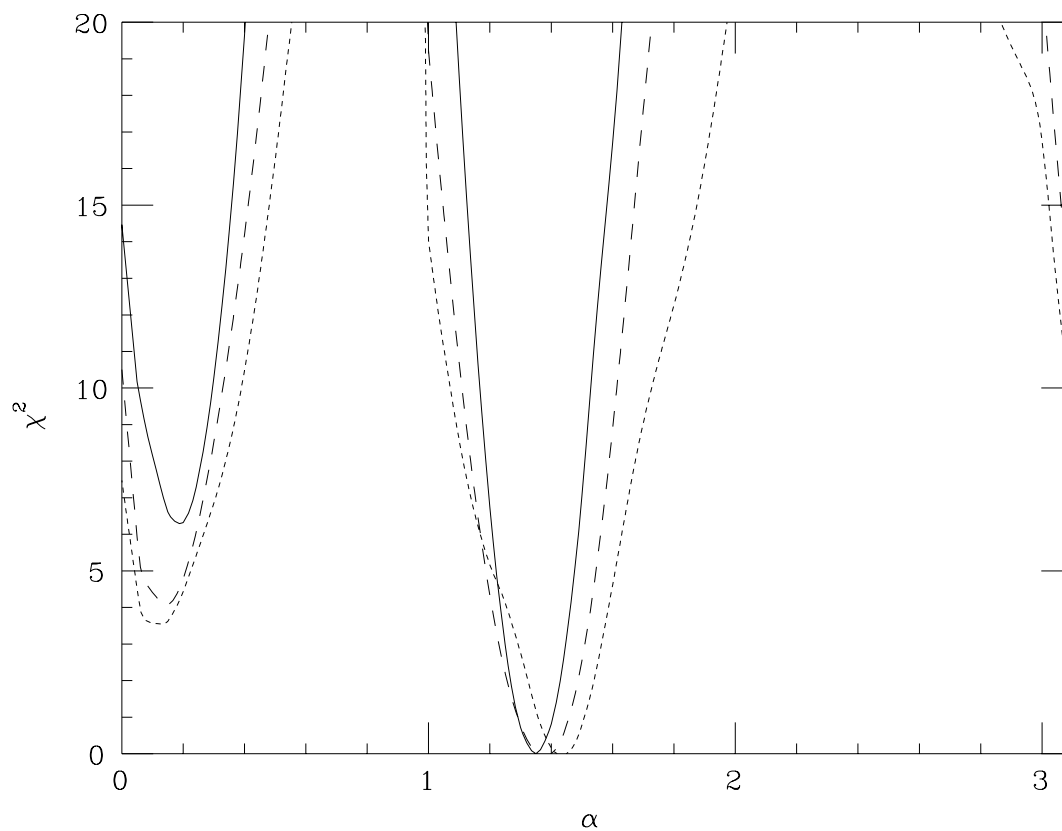


Figure 6-24. Scan in α with 1200 events: with no background (solid), with 1200 nonresonant events (dashed), with 4200 continuum events as well (dotted). The Large Penguin amplitudes were used, with $\alpha = 1.35$.

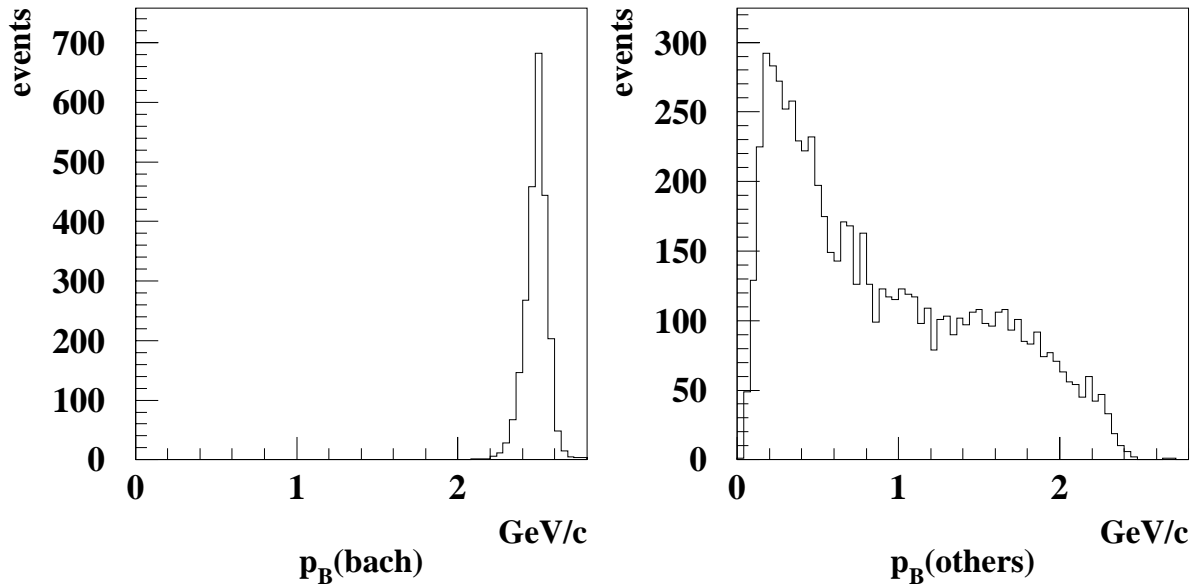


Figure 6-25. Distribution of momentum in the B^0 rest frame of (a) the bachelor pion from the B^0 decay, (b) the remaining pions in the decay.

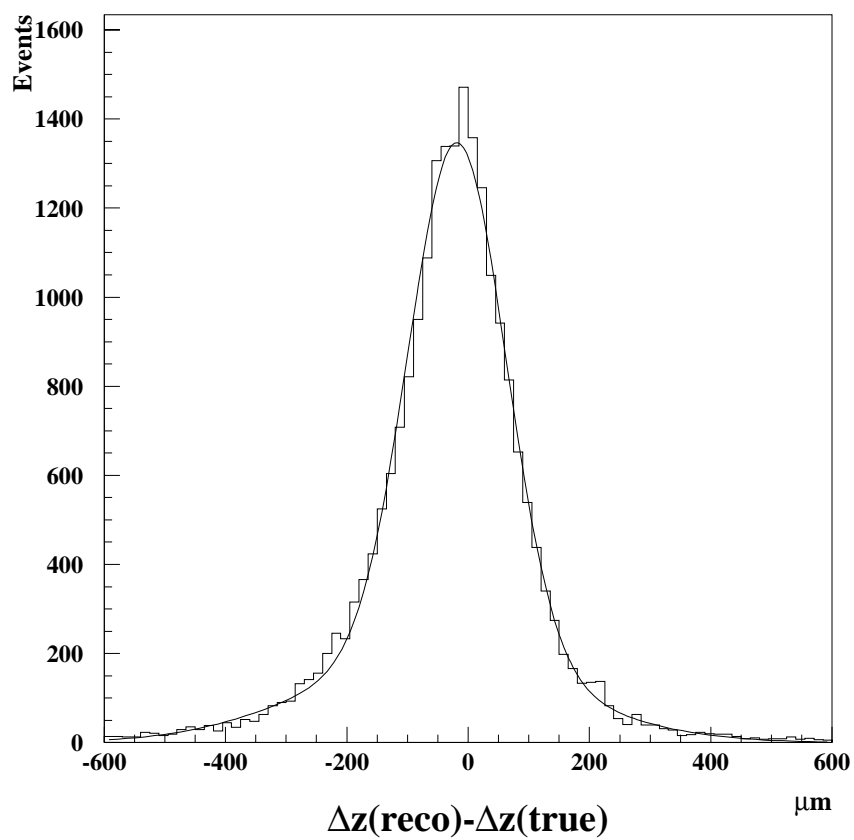


Figure 6-26. Aslund distribution of the difference between the reconstructed and true Δz for Monte Carlo simulated $B^0 \rightarrow a_1^\pm \pi^\mp$ decays. The fit function is a sum of two Gaussians as described in the text.

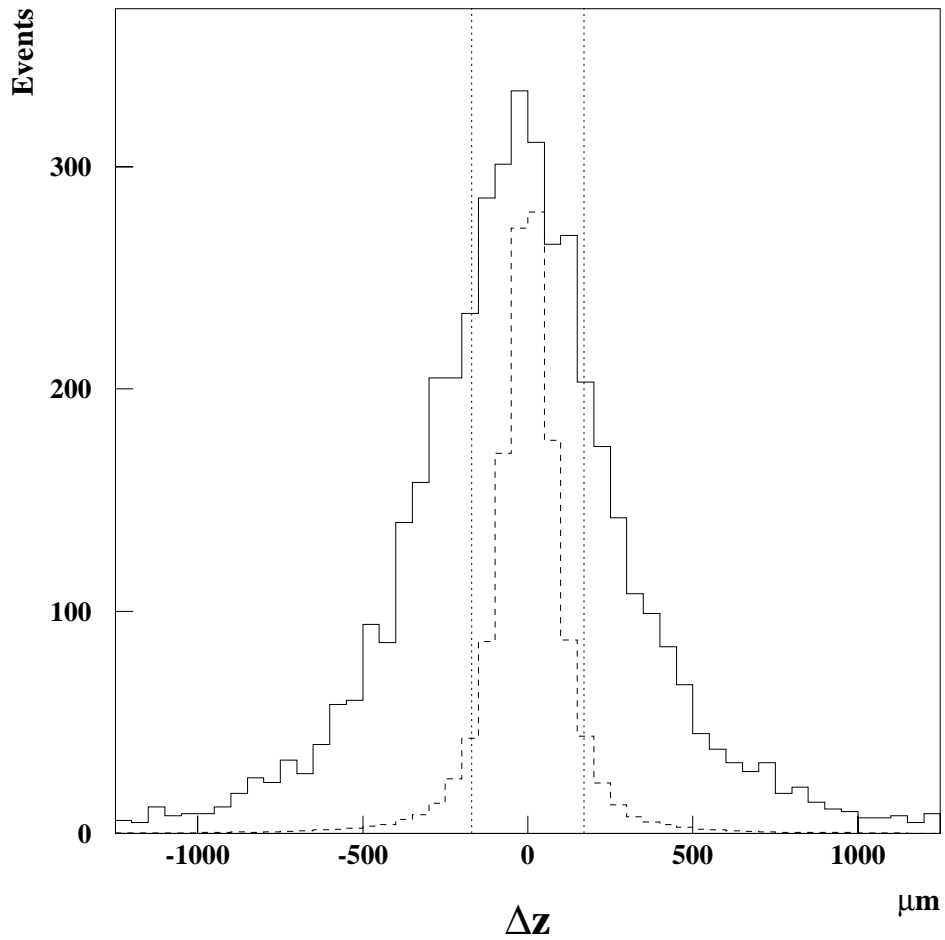


Figure 6-27. Distribution of reconstructed Δz for charged B decays (solid histogram) and continuum events (dashed histogram), with arbitrary normalizations. The area between the dotted lines is rejected by a cut on $|\Delta z|$.

6.6.2.4 Extraction of the *CP* asymmetries and decay amplitudes

As described in Section 6.6.2.1, each of the three B^0 decays has its own distinct time evolution. For the $B^0 \rightarrow a_1^0 \pi^0$ decay, there is a single asymmetry, a_0 , which can be extracted from the Δt distributions. For the $B^0 \rightarrow a_1^\pm \pi^\mp$ decays, there are two asymmetries, a_1 and \bar{a}_1 , as well as the parameter R . The observed asymmetry in the time-integrated rates to $a_1^- \pi^+$ and $a_1^+ \pi^-$, R_{obs} , is related to R by

$$R = \frac{1 + (\Delta m_d \tau)^2}{2P_{\text{tag}} - 1} R_{\text{obs}}, \quad (6.75)$$

where P_{tag} is the probability that the *B* flavor has been correctly tagged.

The asymmetries are extracted using an unbinned maximum likelihood fit. The probability density function for each event i is a sum of signal and background terms:

$$\begin{aligned} \mathcal{P}(\Delta t_i) = & f^s [\eta_i \mathcal{P}_{B^0}(\Delta t_i, \zeta) + (1 - \eta_i) \mathcal{P}_{\bar{B}^0}(\Delta t_i, \zeta)] \\ & + \sum_j f_j^b \mathcal{P}_j^b(\Delta t_i), \end{aligned} \quad (6.76)$$

where: f^s is the fraction of events which are signal; η_i is the probability that the decay is that of a B^0 , as opposed to a \bar{B}^0 ; \mathcal{P}_{B^0} and $\mathcal{P}_{\bar{B}^0}$ are the probability density functions for B^0 and \bar{B}^0 decays, respectively; ζ represents the fit quantities (a_0 or a_1 , \bar{a}_1 and R , depending on the decay mode); f_j^b are the fractions of events comprised by each of the backgrounds discussed above; and \mathcal{P}_j^b are the probability density functions for each of the backgrounds. The functions \mathcal{P}_{B^0} and $\mathcal{P}_{\bar{B}^0}$ are derived from the convolution of the distributions in equations 6.72 and 6.73 with resolution functions represented by the sum of two Gaussians. The background functions, \mathcal{P}_j^b , are empirical parameterizations of the distributions of Δt for Monte Carlo-simulated samples of each type of background. The B^0 tag probability, η_i , is derived from the output of the `Cornelius` neural network.

The likelihood is the product of the probability density functions, described by Eq. 6.76, of all the events in a given sample. The $a_1^+ \pi^-$ and $a_1^- \pi^+$ events are combined in a single fit since they are related by a common value for the fit parameter R . The $a_1^\pm \pi^\mp$ fit has three free parameters: a_1 , \bar{a}_1 and R , where R is given a Gaussian constraint around the value calculated from the measured R_{obs} . The $a_1^0 \pi^0$ sample has a_0 as the only fit parameter.

The fits were performed on Monte Carlo-simulated samples representing luminosities of 30, 90, 120, 150, and 300 fb^{-1} . For each luminosity, signal samples were generated with seven different values of the fit parameters in order to estimate the variation of the errors for different values of the parameters. For the $a_1^\pm \pi^\mp$ sample, events were generated using parameters given in Table 6-36.

For the $a_1^0 \pi^0$ sample, events were generated with $a_0 = 0.5$, $a_0 = -0.8$ and $a_0 = 0.2$. Only small differences were found in the sizes of the errors for the different cases. The addition of the mode $B^0 \rightarrow a_1^\pm \pi^\mp$, with $a_1^\pm \rightarrow \rho^\pm \pi^0$, to the all-charged mode was found to improve the errors on

Table 6-36. The parameter sets used for CP -fitting studies.

Sample	2α	δ	R	a_1	\bar{a}_1
A	0	0	0	0	0
B	0	0	0.6	0	0
C	0.100	0	0.6	0.100	0.100
D	0.100	$3\pi/4$	0.6	0.633	-0.774
E	-0.200	0.5	0.6	0.296	-0.644
F	0.800	0.2	-0.6	0.841	0.565
G	0.524	0	0	0.500	0.500

the asymmetries by a negligible amount, so it is not used in the final fit. Its very poor signal-to-background ratio gives it a small statistical weight, relative to the all-charged mode, with a potential for large systematic uncertainties. Figure 6-28a shows the errors on the asymmetries as a function of luminosity for the two decay modes $B^0 \rightarrow a_1^\pm \pi^\mp \rightarrow \pi^+ \pi^- \pi^+ \pi^-$ and $B^0 \rightarrow a_1^0 \pi^0 \rightarrow \pi^+ \pi^- \pi^0 \pi^0$ for a representative subsample of the fit scenarios described in Table 6-36. The errors on R were found to be independent of the choice of parameters. Figure 6-28b shows the errors on R as a function of luminosity.

The flavor tagging used in this analysis is known to be optimistic, which leads to somewhat smaller statistical uncertainties on the fitted quantities than would be expected for real data. The effect of more realistic tagging can be accounted for by simply scaling the uncertainties by the factor $0.35/0.30 = 1.17$, which is the ratio of “effective tagging efficiencies” ($\epsilon(1 - 2\eta)^2$, where ϵ is the efficiency for tagging an event and η is the global mistag probability) for the overly optimistic simulation and a more realistic assumption (see equation 4.62 and the discussion following it for a description of the dependence of the error on the effective tagging efficiency).

In this simple case where one amplitude dominates each decay (no penguins), the asymmetries are related to the CP -violating phase 2α in the following manner:

$$a_0 = \sin 2\alpha, \quad a_1 = \sin(2\alpha + \delta) \text{ and } \bar{a}_1 = \sin(2\alpha - \delta), \quad (6.77)$$

where δ is the phase introduced by the strong interaction. The angle 2α can be extracted from a_1 and \bar{a}_1 with an eight-fold ambiguity:

$$\sin^2 2\alpha = \frac{1}{2} \left[1 + a_1 \bar{a}_1 \pm \sqrt{(1 - a_1^2)(1 - \bar{a}_1^2)} \right]. \quad (6.78)$$

The amplitudes for all of the relevant B^0 and B^+ decays are determined from the observed number of signal events in each mode. The actual values of the amplitudes are not needed for the isospin

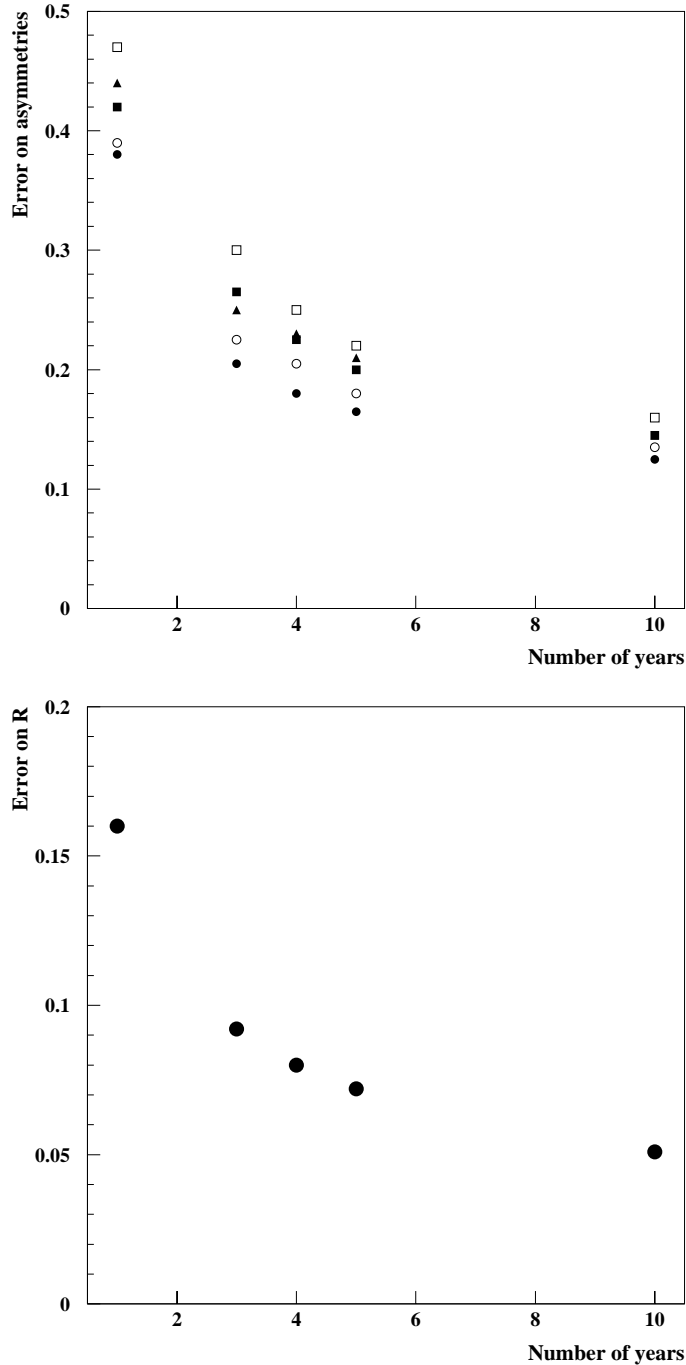


Figure 6-28. (a) Errors on the asymmetries as a function of integrated luminosity. The open circles are for scenario A, the solid squares are for scenario E, the solid triangles are for scenario F, the solid circles are for scenario G and the open squares are for the $a_1^0 \pi^0$ mode with $a_0 = 0.50$., (b) Errors on the parameter R as a function of integrated luminosity.

analysis, since an arbitrary normalization can be used. The quantities of interest are the sizes of the amplitudes relative to each other. The time-integrated number of events for the $a_1^+ \pi^-$ (f) and $a_1^- \pi^+$ (\bar{f}) are related to the amplitudes according to the following expressions:

$$N(B^0 \rightarrow f) + N(\bar{B}^0 \rightarrow f) \propto (|A_f|^2 + |\bar{A}_f|^2) \quad \text{and} \quad (6.79)$$

$$N(B^0 \rightarrow \bar{f}) + N(\bar{B}^0 \rightarrow \bar{f}) \propto (|A_{\bar{f}}|^2 + |\bar{A}_{\bar{f}}|^2), \quad (6.80)$$

where the amplitudes are as defined in Chapter 1. Under the assumption $|\bar{A}_{\bar{f}}| = |A_f| \equiv A$ and $|\bar{A}_f| = |A_{\bar{f}}| \equiv \bar{A}$, the sum of all the above decays is $N_{a_1^\pm \pi^\mp} \propto 2(A^2 + \bar{A}^2)$. Since $\bar{A}^2/A^2 = (1 + R')/(1 - R')$, where R' is defined to be $R/(1 + x_d^2)$ and $x_d = \Delta m_d \tau$, one can derive:

$$\bar{A}^2 \propto \frac{N_{a_1^\pm \pi^\mp}}{2} \frac{1 + R'}{2} \quad \text{and} \quad A^2 = \frac{1 - R'}{1 + R'} \bar{A}^2. \quad (6.81)$$

The fractional errors on the amplitudes are 16% for A and 11% for \bar{A} , for 30 fb^{-1} , and scale like $\sqrt{\mathcal{L}_{int}}$, where \mathcal{L}_{int} is the integrated luminosity.

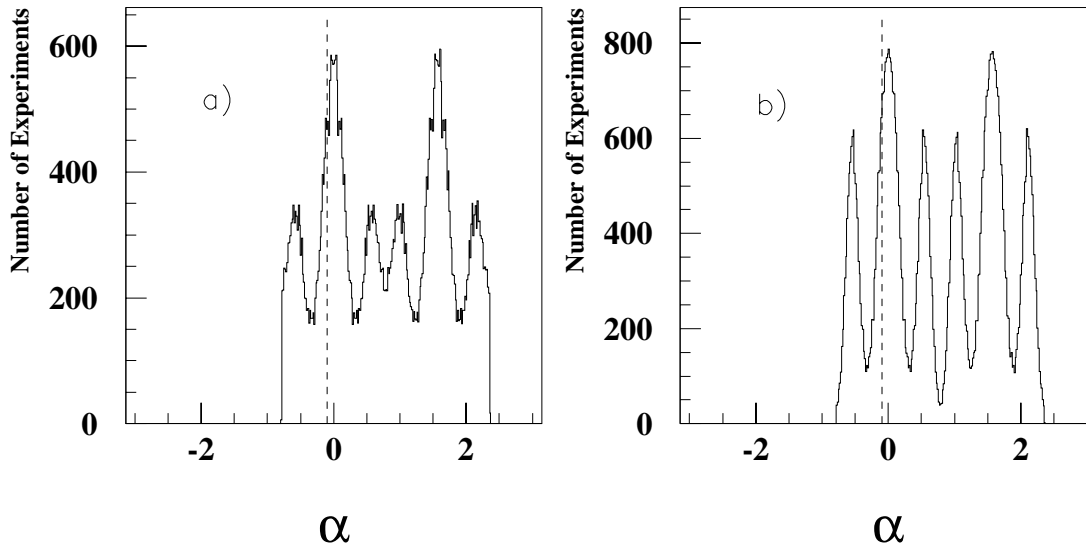


Figure 6-29. Distribution of extracted values of α for many toy Monte Carlo simulations with true $\alpha = -0.1$ and $\delta = 0.5$. The assumed errors on the observed asymmetries are those for 30 fb^{-1} and 90 fb^{-1} of integrated luminosity, for plots a) and b), respectively. The dashed line is at the true value of α .

As discussed earlier in this section, the angle α can be extracted from the measured values of a_1 and \bar{a}_1 from equation 6.78, with an eight-fold ambiguity. In order to get an idea of the uncertainty on the

measurement of α using the $a_1^\pm \pi^\mp$ mode alone, thousands of values of a_1 and \bar{a}_1 were generated, using the central values given by parameter set E in Table 6-36 and allowing for Gaussian smearing, where the widths of the Gaussians are given by the expected errors on a_1 and \bar{a}_1 . For each set of “observed” asymmetries, the eight solutions for α were calculated. Figure 6-29 displays the resulting distributions of α assuming 30 fb^{-1} and 90 fb^{-1} of integrated luminosity. For parameter set E, the true value of α is -0.1 , which is shown in the figures by the dashed lines. In theory, the measured uncertainties on the eight possible values of α are given by the widths of the peaks in Figure 6-29. However, it is clear that for poor statistics many of the solutions become merged. The ability to extract information about α from multiple channels will hopefully allow one to eliminate these discrete ambiguities.

6.6.3 The $\rho\rho$ Decay Modes

The $B \rightarrow \rho\rho$ decays involve three possible modes, $B^0 \rightarrow \rho^0\rho^0$, $B^0 \rightarrow \rho^+\rho^-$ and $B^+ \rightarrow \rho^+\rho^0$. These modes result in final states with four charged pions, two charged and two neutral pions, and three charged and one neutral pion, respectively. Since all of these contain at least two charged particles, as in the case of the $a_1\pi$ modes, the B vertex can be determined for all final states. Consequently, both neutral B decays, $B^0 \rightarrow \rho^0\rho^0$ and $B^0 \rightarrow \rho^+\rho^-$, can be used to measure CP asymmetries. Since $\rho\rho$ is a vector-vector state, its decay can proceed via S , P or D waves. Hence, there is the possibility of both longitudinal ($\lambda = 0$) and transverse ($\lambda = \pm 1$) polarization for the ρ meson. The longitudinal mode is CP -even, while the transverse mode has both CP -even and CP -odd components. The longitudinal state is believed to be dominant [66]. This was supported by early measurements from CLEO in other vector-vector channels. However, a recent angular analysis of the ψK^* mode by CLEO indicates that the transverse state may be more important than previously thought [76].

The general formalism for angular analysis introduced in Section 5.1.3 shows that the $B^0 \rightarrow \rho\rho$ decay is described by three amplitudes: longitudinal (A_0), CP -even transverse (A_{\parallel}), and CP -odd transverse (A_{\perp}). The time evolution for these is given by:

$$\begin{aligned} A_0(\Delta t) &= A_0(0)e^{-im\Delta t} e^{-|\Delta t|/2\tau} \left(\cos \frac{\Delta m_d \Delta t}{2} + i\eta\lambda_0 \sin \frac{\Delta m_d \Delta t}{2} \right) \\ A_{\parallel}(\Delta t) &= A_{\parallel}(0)e^{-im\Delta t} e^{-|\Delta t|/2\tau} \left(\cos \frac{\Delta m_d \Delta t}{2} + i\eta\lambda_{\parallel} \sin \frac{\Delta m_d \Delta t}{2} \right) \\ A_{\perp}(\Delta t) &= A_{\perp}(0)e^{-im\Delta t} e^{-|\Delta t|/2\tau} \left(\cos \frac{\Delta m_d \Delta t}{2} - i\eta\lambda_{\perp} \sin \frac{\Delta m_d \Delta t}{2} \right), \end{aligned} \quad (6.82)$$

where $\eta = 1$ for $\rho\rho$. The three parameters, λ_0 , λ_{\parallel} and λ_{\perp} , are in general different from one another.

However, they are equal if penguins are negligible.³² This result is true even in the presence of penguins if factorization is assumed. The angular dependence takes the general form given in Section 5.1.3. Introducing explicitly the time dependence into the latter, the time-dependent decay rate of $B^0 \rightarrow \rho\rho$ is obtained as a function of the transversity angle θ_{tr} , defined in the $\rho^+\rho^-$ ($\rho^0\rho^0$) channel as the angle in the ρ^+ (ρ^0) rest frame between the line of flight of the π^+ coming from one of the ρ mesons and the normal to the decay plane of the other ρ meson in the decay:

$$P = \frac{e^{-|\Delta t|/\tau}}{2\tau} \left[\frac{3}{4}(1 - R_{\perp}) \sin^2 \theta_{\text{tr}} (1 - a \sin(\Delta m_d \Delta t)) + \frac{3}{2} R_{\perp} \cos^2 \theta_{\text{tr}} (1 + a \sin(\Delta m_d \Delta t)) \right]. \quad (6.83)$$

A fit to the experimental distribution yields the fraction of CP -odd component R_{\perp} and the CP asymmetry a , which is simply $\sin 2\alpha$ in the no-penguin approximation.

The branching fraction for each of the three $\rho\rho$ modes is small. As explained in Section 6.6.1.1, it is assumed to be of the order of 5×10^{-5} , which is still optimistic compared to the BSW prediction (see Table 6-31). The number of expected signal events is therefore relatively small (1575 events for a 30 fb^{-1} sample). Consequently, background will be a problem. As in the case of $B \rightarrow a_1\pi$ and the $B \rightarrow 2\pi$ and $B \rightarrow 3\pi$ channels, there are several sources of background: continuum events, generic $B\bar{B}$ events, physics background, and combinatorial background in signal events. As will be shown below, the dominant contribution comes from the continuum. The studies [68] described in this section were performed using Aslund fast Monte Carlo-simulated events.

6.6.3.1 Reconstruction and preselection

Since an important aspect of this analysis is background suppression, two approaches were explored: 1) a simple cut method, and 2) a neural network-based multi-variate analysis. The purpose of the neural network analysis was to explore the optimal use of the cut variables for background separation. As a starting point for both analyses, a loose preselection of events was applied to the data. The π^0 candidates are reconstructed as a combination of two photons with an invariant mass in the range $0.10 < M_{\gamma\gamma} < 0.17 \text{ GeV}/c^2$. Candidate ρ mesons must satisfy $0.35 < M_{\pi\pi} < 1.20 \text{ GeV}/c^2$. Since each ρ candidate originates from a two-body decay, its momentum in the $\Upsilon(4S)$ rest frame is restricted to the range $2.25 < P_{\rho}^* < 2.85 \text{ GeV}/c$. Finally, B candidates are reconstructed by forming all possible $\rho\rho$ combinations that satisfy $5.17 < M_{\rho\rho} < 5.37 \text{ GeV}/c$ and $0.12p_{B^0}^* < 0.52 \text{ GeV}/c$, where $p_{B^0}^*$ is the magnitude of the momentum of the B candidate in the $\Upsilon(4S)$ rest frame.

Table 6-37 gives the efficiencies of this preselection and the reconstructed B -mass resolution in the various signal channels. The results get worse when channels with more π^0 s are considered.

³²This is certainly not true in $B \rightarrow \rho\rho$ decays. However the analysis during the first years of data taking will probably be done with this approximation, since an analysis taking into account penguins will require far more data.

Table 6-37. Efficiencies in percent and mass resolutions in MeV/c^2 in the three channels for longitudinal (L) and transverse (T) polarization.

	$\rho^0\rho^0$ (L)	$\rho^0\rho^0$ (T)	$\rho^+\rho^0$ (L)	$\rho^+\rho^0$ (T)	$\rho^+\rho^-$ (L)	$\rho^+\rho^-$ (T)
All particles detected	64.8	72.2	57.4	64.0	50.0	57.1
Reconstruction	99.8	99.9	97.7	98.5	96.0	96.8
M_B and P_B^*	100.	100.	95.6	96.1	88.3	90.5
Total	64.7	72.1	53.6	60.6	42.4	50.0
$\sigma(M_B)$	17.	13.5	23.	21.5	32.5	32.5

Table 6-38. Cuts on masses (in GeV/c^2) and B momentum (in GeV/c).

	$\rho^0\rho^0$	$\rho^+\rho^0$	$\rho^+\rho^-$
π^0	-	$0.12 < M_{\gamma\gamma} < 0.15$	
ρ	$0.60 < M_{\pi\pi} < 0.95$		
B	$5.235 < M_{\rho\rho} < 5.325$	$5.21 < M_{\rho\rho} < 5.33$	$5.18 < M_{\rho\rho} < 5.34$
B	$0.15 < p_{B^0}^* < 0.45$		

Longitudinal polarization is also less favorable than transverse polarization because the decay of the ρ produces mainly a high-energy pion and a low-energy pion (less likely to be detected) in the former case and two medium-energy pions in the latter case.

6.6.3.2 Background fighting

At this stage, the background-to-signal ratio is still close to 1000 to 1. As discussed in the previous section, two approaches were used to further reduce the background. For the simple cut method the criteria listed in Table 6-38 are imposed. In addition, each photon is required to have at least 50 MeV of energy and each charged particle to have a greater probability to be identified as a pion than as a kaon. Finally, the cosine of the angle between the sphericity axis of the rest of the event and the ρ which is closer to it must be less than 0.8.

In the multivariate analysis, the following eleven discriminating variables are used to separate signal and continuum background:

- The cosine of the sphericity axis of the rest of the event with the ρ which is closer to it.
- The cosine of the sphericity axis of the rest of the event with the reconstructed B direction.

- The ratio of the second Fox-Wolfram moment divided by the zeroth moment for the whole event.
- The above quantity for the tagging B only.
- The sphericity of the event.
- The algebraic sum of transverse momentum with respect to the B direction of the rest of the event.
- The mass χ^2 defined as $\chi^2 = \sum (\frac{M^{\text{rec}} - M^{\text{true}}}{\sigma_M})^2$, where the sum runs over all reconstructed particles (B , ρ mesons and π^0 mesons, if any).
- The B momentum in the $\Upsilon(4S)$ rest frame.
- The π/K separation of the charged track in the B candidate which is most likely to be a kaon.
- The larger mass of the two ρ candidates.
- $\cos \theta_H$, with θ_H the angle of the pion from the ρ decay in the ρ rest frame, with respect to the line of flight of the ρ in the B rest frame (for longitudinal polarization this has a $\cos^2 \theta_H$ distribution).

A second multivariate analysis is performed to discriminate between signal and signal combinatorial. Cutting on the two neural network outputs rather than only on the signal/continuum discriminating output permits reduction of the signal combinatorial by more than a factor two for essentially the same efficiencies on signal and continuum.

The effect of the selection will be given for the longitudinally polarized signal, which is more difficult to extract from the background. Figure 6-30 shows the rejection obtained for the continuum in this case, as a function of the efficiency for the signal for both cut and neural-network methods.

Table 6-39 gives the continuum background efficiencies with simple cuts and with the multivariate analysis using neural networks for the same efficiencies on the signal. It shows that the multivariate analysis somewhat improves the background rejection, especially in modes with π^0 mesons. Therefore, for the remainder of this section the results are presented only for the neural network analysis.

Table 6-40 gives the efficiencies for the signal and the background processes, and the expected number of events after the final selection, assuming a branching ratio of 5×10^{-5} , for an integrated luminosity of 30 fb^{-1} . Included in the table are contaminations from various sources of physics background. Some of these background processes can be problematic for a CP analysis, as these events may originate from B decays with different CP asymmetries. Fortunately this background is not dominant.

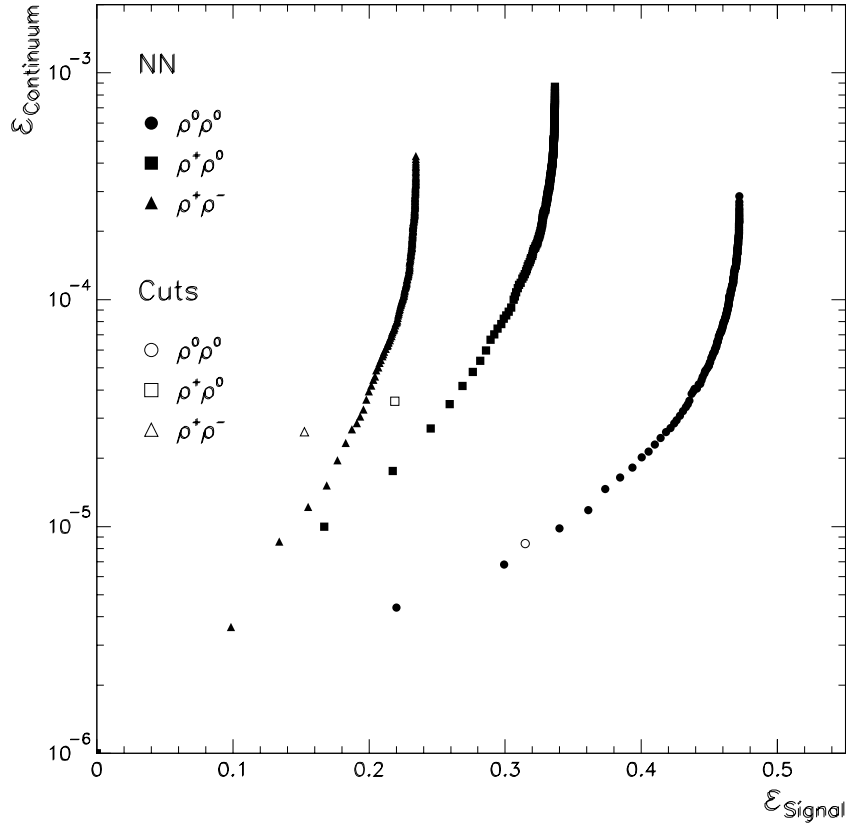


Figure 6-30. Efficiency for continuum events as a function of the signal efficiency for $\rho^0\rho^0$ (circles), $\rho^+\rho^0$ (squares) and $\rho^+\rho^-$ (triangles) channels. The filled symbols are for cutting at different values of the neural network output (signal/continuum discrimination), and the open symbols are for the simple cut analysis.

6.6.3.3 Tagging and vertexing

Cornelius is used for tagging, as described in the $a_1\pi$ section. Vertexing is done using an impact parameter method. The resolutions obtained (width of the narrow Gaussian) are respectively 31, 36 and 42 μm for the determination of z_{CP} in the $\rho^0\rho^0$, $\rho^+\rho^0$, and $\rho^+\rho^-$ channels. In all cases the resolution is dominated by the $\sim 120 \mu\text{m}$ expected for the tag vertex.

Table 6-39. Comparison of continuum background rejection obtained with the cut approach and the neural network approach for the same efficiency of selection on the signal.

	$\rho^0 \rho^0$	$\rho^+ \rho^0$	$\rho^+ \rho^-$
ϵ_{Signal}	0.315	0.219	0.153
$\epsilon_{q\bar{q}}^{cuts}$	0.85×10^{-5}	3.6×10^{-5}	2.6×10^{-5}
$\epsilon_{q\bar{q}}^{NN}$	0.75×10^{-5}	1.8×10^{-5}	1.2×10^{-5}

Table 6-40. Efficiencies of signal and backgrounds. The quantities in square brackets are the numbers of selected events for an integrated luminosity of 30 fb^{-1} .

	Signal	SCB	$a_1\pi$	$\rho\pi\pi$	4π	$B\bar{B}$	Continuum
Produced	1575	-	5×945	8×1050	4×1575	31.5×10^6	10^8
$\rho^0 \rho^0$	0.315 [496]	- [47]	0.004 [18]	0.004 [31]	0.003 [20]	0.7×10^{-5} [220]	0.75×10^{-5} [750]
$\rho^+ \rho^0$	0.219 [345]	- [70]	0.011 [51]	0.008 [71]	0.0025 [16]	1.9×10^{-5} [600]	1.8×10^{-5} [1800]
$\rho^+ \rho^-$	0.153 [241]	- [79]	0.007 [33]	0.007 [55]	0.001 [8]	0.4×10^{-5} [126]	1.2×10^{-5} [1200]

6.6.3.4 Decay amplitudes and extraction of CP asymmetries

With the above estimates of the signal and background yields, one can determine the resolutions of the decay amplitudes from $\frac{\sqrt{S+B}}{S}$, where S is the number of signal events and B is the number of background events for a given luminosity. Figure 6-31 shows the resolution for the decay amplitudes for the three modes as a function of the branching fraction for 30 fb^{-1} of integrated luminosity.

For a branching fraction of 5×10^{-5} , the amplitude $B^0 \rightarrow \rho^0 \rho^0$ can be measured in one year with a precision better than 10%. However, for the branching fraction of 6.4×10^{-7} predicted by the BSW model, there is no hope to see a $\rho^0 \rho^0$ signal. With a time-integrated angular analysis, one can also extract the longitudinal component and the CP -odd transverse component, as described above. For one year of data taking, these fractions can be measured with an absolute precision better than 10%.

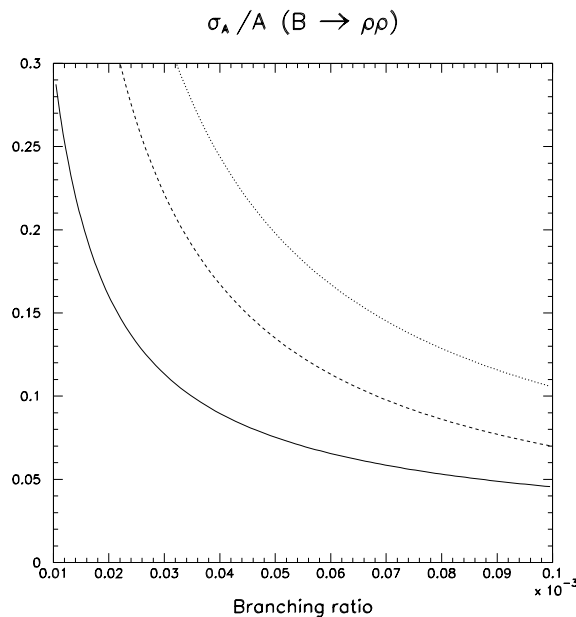


Figure 6-31. Amplitude resolution (σ_A/A) for $\rho^0\rho^0$ (solid line), $\rho^+\rho^0$ (dashed line) and $\rho^+\rho^-$ (dotted line).

For the extraction of the CP asymmetries, the unbinned maximum likelihood method described in the $a_1\pi$ section was employed. If the decay is dominated by longitudinal polarization (CP even), the Δt distribution is

$$P(B^0(\bar{B}^0) \rightarrow \rho\rho) \propto \frac{e^{-|\Delta t|/\tau}}{2\tau} [1 \pm a_0 \sin(\Delta m_d \Delta t)]. \quad (6.84)$$

In the absence of penguins, the coefficient a_0 corresponds to $\sin 2\alpha$. Figure 6-32a shows the resolution obtained on a_0 as a function of the integrated luminosity.

Allowing a transverse polarization component results in a degradation of the resolution of the CP asymmetry. In this case, the coefficient of the $\sin(\Delta m \Delta t)$ term obtained in the previous method is no longer simply $\sin 2\alpha$. There is an additional dilution factor $(1 - 2R_\perp)$, where R_\perp is the fraction of the CP -odd component. The angular analysis, described in the introduction of this section, is performed to extract simultaneously the CP asymmetry a ($\sin 2\alpha$ in the no-Penguin approximation) and R_\perp . Figure 6-32b shows the resolution on the CP asymmetry (a) as a function of the CP -odd component R_\perp , in the case of $\rho^0\rho^0$, for an integrated luminosity of 100 fb^{-1} . The resolution degrades by a factor of 1.6 for a value of $R_\perp = 0.5$.

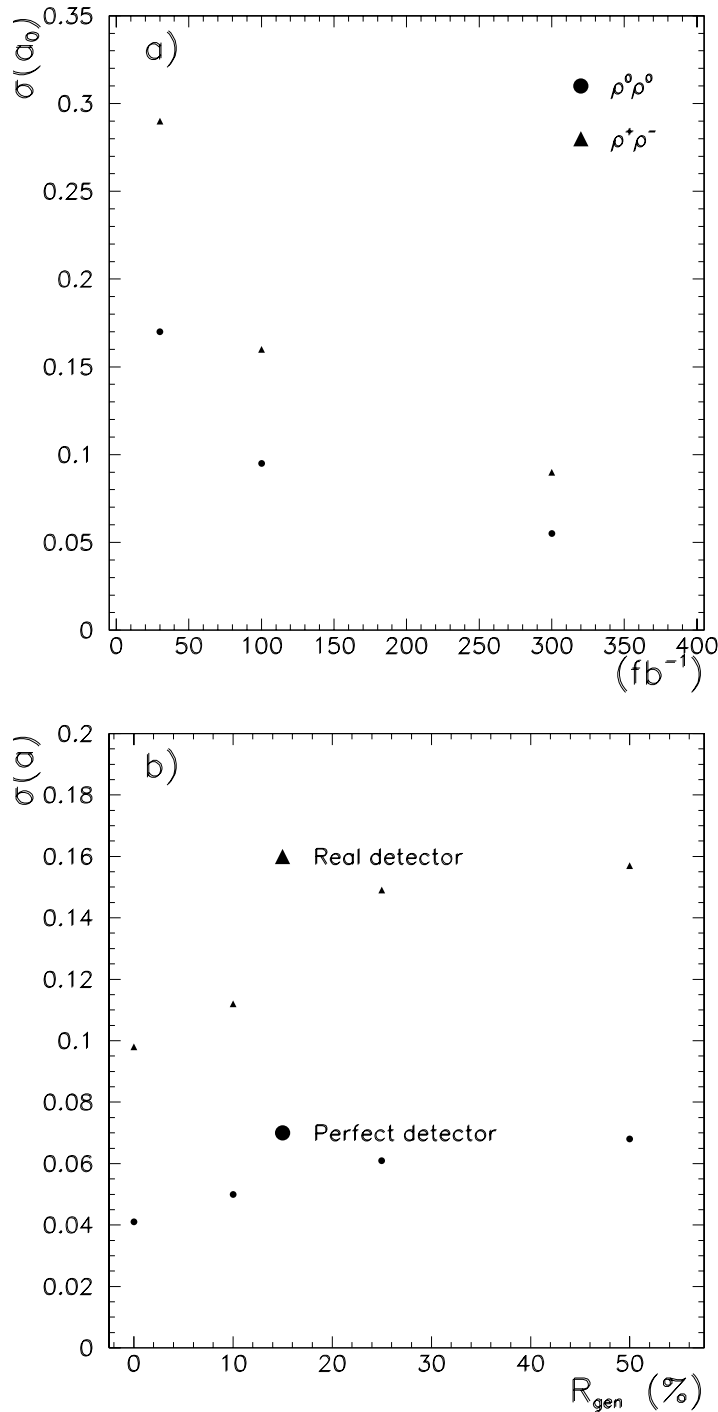


Figure 6-32. (a) Uncertainty in the CP asymmetry a_0 as a function of the integrated luminosity for $\rho^0\rho^0$ (circles) and $\rho^+\rho^-$ (triangles); (b) uncertainty in α for a 100 fb^{-1} sample as a function of the value of R_{\perp} used in the generation for a perfect detector (circles) and the Aslund $B\bar{A}B\bar{A}R$ simulation (triangles).

6.6.4 Summary and Conclusion for Four-Pion Channels

The results of the simulation studies are summarized in Tables 6-32 and 6-40 for the modes $B \rightarrow a_1\pi$, and $B \rightarrow \rho\rho$. Since these studies have been carried out with the `Aslund` fast simulation program, and that there is little experimental or theoretical information on the branching ratios of these modes, one should use extreme caution in the use and interpretation of these numbers. Nonetheless, for modes involving charged particles only, the comparison with studies of the full simulation of `BaBar` and the current reconstruction programs indicate that the background level predicted by the fast simulation studies is within a factor of two of the `Aslund` results. With this in mind, one can conclude that at least in modes involving only charged tracks, the task of extracting a signal from background is not insurmountable — signal-to-background ratios (S/N) of 1/2 can be obtained in both $B \rightarrow a_1\pi$, and $B \rightarrow \rho\rho$. At this level of S/N ratio, with a 30 fb^{-1} sample, unbinned maximum likelihood fits to the Δt distributions yield a statistical error of 0.4 for the CP asymmetry for the mode $B \rightarrow a_1\pi$ ($\mathcal{B} = 6 \times 10^{-5}$), and 0.15 for the mode $B \rightarrow \rho^0\rho^0$ ($\mathcal{B} = 5 \times 10^{-5}$). For the modes involving π^0 mesons, preliminary results from full simulation studies show that the background level is significantly higher than that which is predicted by the fast simulation studies. Therefore, further caution should be taken there, and these results should only be used as a first indication of the experimental conditions.

Penguin effects: The simulation studies and the fits to the data were performed using the time evolution relation for dominance of one weak amplitude. In the presence of penguins, one needs to perform an isospin analysis, which in the case of $B \rightarrow a_1\pi$, would involve measuring the rates and asymmetries of the charged B modes as well as the rate of the B^0 decays. These quantities form a pentagon in the complex plane. While such an analysis may be feasible at a mature state of the experiment, it is not warranted at early stages of the experiment, when statistical errors dominate the uncertainties. As an example, Fig. 6-33, shows the shift (error) in the angle α which results from ignoring the presence of a penguin diagram in the amplitude, as a function of the ratio of penguin-to-tree amplitude (P/T) and the difference in the strong phase of the two diagrams. For moderate values of P/T (e.g., 0.2) and a strong-phase difference $(\delta_p - \delta_t) = 0.5$, $\Delta\alpha \approx 0.15$ is obtained, corresponding to an error of approximately 0.3 on $\sin 2\alpha$, as compared with the statistical error of 0.4 for 30 fb^{-1} . Eventually, theory may be able to restrict the range of P/T in which case the range of the shift in α from these effects can be limited.

In conclusion, these studies indicate that extraction of signal and ultimately CP information from the $B \rightarrow 4\pi$ modes, while difficult, is feasible. As was discussed in the introduction, the CP studies in the B system, in general, and extraction of the angle α , in particular, require complementary information from various decay processes. It has been shown that such information can be obtained from the 4π decays of the B .

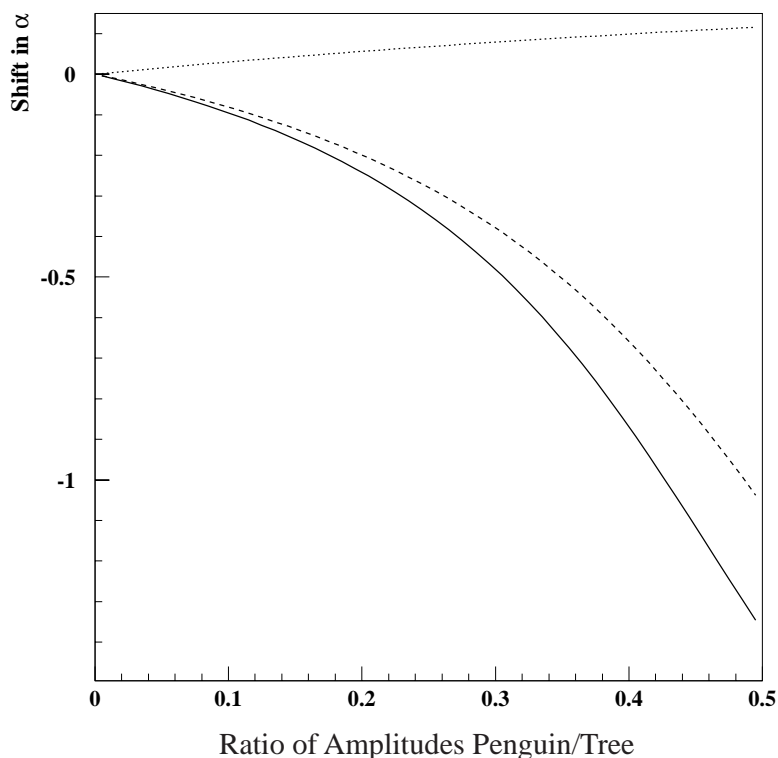


Figure 6-33. Shift in the angle α due to the effect of ignoring the presence of a penguin diagram, as a function of the ratio of penguin-to-tree amplitude. The plots are made with $\alpha = 0.4$. The solid curve is for a strong-phase difference between the penguin and tree diagrams of 0, the dashed curve is for a strong-phase difference of 0.5 and the dotted line is for a strong-phase difference of 2.0.

6.7 Conclusions

The results of the simulation studies of the neutral and charged B decays into two, three and four-pion final states are summarized in Table 6-41. These results, which consist of the expected uncertainties of the observables from the various modes for an integrated luminosity of 30 fb^{-1} , must be viewed only as indicative since the branching ratios are not known and the BABAR reconstruction software is still in a preliminary stage. Furthermore, as discussed in detail above, the relationship between $\sin 2\alpha$ and the CP observables a_{\cos} and a_{\sin} , is model- and channel-dependent and is therefore subject to important theoretical uncertainties. Hence, no additional information can be obtained by combining the raw (penguin untreated) information from various channels, other than improving the χ^2 -reliability of a demonstration that CP -violation occurs. It is found that, with reasonable estimates of penguin size, based on the CLEO $K\pi$ observations, the shift in the extracted value of $\sin 2\alpha$ in an analysis that ignores penguins can be of order 0.1 to

Table 6-41. Summary of the studies of the two-, three- and four-pion final states. Note that at this point there is very limited information on the branching ratios, those given here represent plausible choices used in in the simulation studies. The selection efficiency, ϵ , includes the impact of tagging. For the $\rho\rho$ channel, the effect of the transverse polarization is not included in the numbers presented here. Note that for channels that are not CP eigenstates, such as $\rho^+\pi^-$ a nonzero value for $a_{\sin}^{+-} + a_{\sin}^{-+}$ is needed to demonstrate CP violation, a nonzero value for a single channel is not sufficient.)

f	B_{tot}	ϵ	N_{tot}	B/S	$\delta a_{\cos}(f)$	$\delta a_{\sin}(f)$
$\pi^+\pi^-$	1.0×10^{-5}	0.39	135	0.9	0.29	0.26
$\pi^0\pi^0$	3.0×10^{-6}	0.15	14	2.5	-	-
$\pi^+\pi^0$	8.0×10^{-6}	0.19	50	2.0	-	-
$\rho^+\pi^- + \rho^-\pi^+$	5.4×10^{-5}	0.21	350	2	0.19	0.26
$\rho^0\pi^0$	1.0×10^{-6}	0.21	7	50	-	-
$\rho^0\pi^+$	1.1×10^{-5}	0.16	30	0.3	-	-
$\rho^+\pi^0$	2.6×10^{-5}	0.09	40	0.3	-	-
$a_1^+\pi^- + a_1^-\pi^+$	6.0×10^{-5}	0.12	124	1.7	0.23	0.34
$a_1^0\pi^0$	3.0×10^{-5}	0.07	72	13.3	-	0.47
$a_1^+\pi^0$	3.0×10^{-5}	0.042	43	3.0	-	-
$a_1^0\pi^+$	3.0×10^{-5}	0.044	23	4.6	-	-
$\rho^+\rho^-$	5.0×10^{-5}	0.15	263	5.3	-	0.28
$\rho^0\rho^0$	5.0×10^{-5}	0.22	377	6.7	-	0.17

0.3, depending on the model and the channel. These large and uncertain shifts make the type of analysis discussed in the TDR insufficient for the accurate determination of α . However despite the difficulty in extracting the actual value of α any observation of CP violation in these channels would be interesting and would indicate a nonzero-value for α . At this level of result the CP -eigenstate modes $\pi\pi$ have the advantage that any asymmetry is a direct indication of CP -violation.

A procedure must be devised to evaluate the penguin effects. Until such time as the statistics are sufficient that a full isospin-based analysis that treats penguin effects correctly yields good results for one or more channels, there will be a theoretical uncertainty in the actual value of α coming from such effects. In order to limit this uncertainty a multi-channel study of many penguin-related effects will be needed. The values of the a_{\cos} terms, measurements of branching ratios and asymmetries for charged B decays, and evaluations of the size of the penguin contributions from measurements of branching ratios for many rare decay channels will all contribute to such studies. As a better understanding of the magnitudes of penguin contributions in a variety of channels is

developed through these studies, theoretical constraints on the magnitude of the possible penguin-induced shifts in the channels studied here will be refined. These will be valuable in determining the allowed range of values for α .

Eventually, the aim will be to carry out a more complete isospin-based analysis, such as have been studied here for the two and three-pion channels. The message from these studies is that very large data samples must be accumulated before these studies can yield good results. As an example, in the two-pion section an isospin analysis was presented for one set of input parameters (extracted from a theoretical analysis of the existing CLEO results on rare B decays (for $\sin 2\alpha = -0.04$ and $\sin 2\alpha_{\text{eff}} = 0.21$) and with experimental resolution of observables corresponding to an integrated luminosity of 90 fb^{-1}). This analysis indicates that for this scenario, the phase shift, $\Theta = 2\alpha_{\text{eff}} - 2\alpha$, can be determined (with a four-fold ambiguity) with an uncertainty of $0.6(\text{Rad})$, yielding the value of α with multiple ambiguities and a wide range about each minimum. The message of this study is that, unless the $B \rightarrow \pi^0\pi^0$ branching ratio is somewhat higher than this model predicts, it will be very difficult to achieve good restrictions on the true value of α from an isospin analysis in this channel. The conclusion of the three-pion Dalitz-plot analysis is a little more encouraging. With a data sample of 1000 fully tagged and reconstructed events, and even with significant backgrounds the analysis is able to determine the unshifted α and to rule out most of the alternative solutions. At most one alternate minimum of the likelihood function (rather than the eight of the analysis neglecting penguins and interference effects) is found to lie within a $\Delta\chi^2$ range of five of the true minimum. This analysis also will be improved if the suppression of the $\rho^0\pi^0$ channel is not as large as the (model-dependent) estimates suggest. Further improvements in background suppression may also significantly improve the result, as will the inclusion of data from charged B decays to $\rho\pi$ channels. For the $\rho\rho$ channels one can in principle carry out an isospin analysis similar to that for $\pi\pi$, but only after angular analysis is used to isolate the even-spin contributions. While the branching ratio to these channels is expected to be larger than for $\pi\pi$ the requirement of angular analysis of the ρ decays will mean that larger data samples are needed. No study of the feasibility of this analysis has yet been made. For $a_1\pi$ the isospin structure is similar to that for $\rho\pi$. An isospin-based analysis to determine the unshifted value of α is in principle possible if charged B channels are measured as well as the neutral ones, although the overlap region of the resonance bands are smaller than in the $\rho\pi$ case because of the higher dimensional four-pion phase space, which will reduce the impact of interference effects. Preliminary studies of all relevant channels were made here, these indicate that further work on background reduction methods will be needed to obtain good values for α via an isospin analysis of these channels.

In conclusion, the accurate determination of α will require the accumulation of a large luminosity data sample. From the above studies one may draw the conclusion that a vigorous effort must be pursued to explore more thoroughly the experimental feasibility of analyses that correctly treat penguin effects. The $\rho\pi$ Dalitz-plot analysis appears at present to be the most hopeful. Even though these analyses are difficult at an $\Upsilon(4S)$ B -Factory, they may be even more so at a hadronic B factory, where, despite higher rates, the need to observe low-branching-ratio channels involving only hadrons, including π^0 s, makes them very challenging.

6.8 Charged B Decays and Direct CP Violation

A striking consequence of CP -non-conservation is that the rate for the decay of a particle into a definite final state can be different from that for the corresponding charge-conjugate decay. Such partial-rate asymmetries (PRA) are predicted for many charged B decays, and, if observed, could be the first evidence for CP violation involving non-neutral systems. Such asymmetries are examples of direct CP violation. The observable asymmetry can be defined as

$$A_m = \frac{N(B^+ \rightarrow f) - N(B^- \rightarrow \bar{f})}{N(B^+ \rightarrow f) + N(B^- \rightarrow \bar{f})} \quad (6.85)$$

which is proportional to the CP asymmetry of the signal $A_m = A_s N_S / (N_S + N_B)$, where N_S and N_B are the numbers of signal and background events, respectively. Model predictions of CP -violating asymmetries (\mathcal{O} 0.1-1%) exist for many channels (see for example Section 6.2); for some of them the branching fractions in the corresponding channels range from 10^{-4} to 10^{-6} , giving rates which should be accessible with the statistics of BABAR.

In this section the results of a study of two benchmark modes are described: $B^- \rightarrow \eta h^-$ (where h can be either K or π) and $B^- \rightarrow D^- D^0$. Theoretical predictions, based on several models, suggest that these modes have the largest value of the product $\mathcal{B} \times A_m^2$, which is the relevant quantity governing the observability of an asymmetry. The channels with D mesons have a large branching ratio, but a small asymmetry, while the opposite is true for the η channel. Many other channels can be used to search for direct CP violation; these studies are simply given as examples. However, since the benchmark channels studied here involve both charged and neutral particles in the final state and cover a wide range of topologies, selection criteria similar to those developed here can be applied in other cases, to estimate the efficiency and, with some caution, also the background.

The statistical error on the asymmetry of the signal can be estimated as

$$\delta A_s = \sqrt{\frac{(1 - A_m^2)(1 + F_{B/S})}{N_S}}, \quad (6.86)$$

where N_S is the observed number of signal events and $F_{B/S}$ is the background to signal ratio. The number of $B\bar{B}$ pairs needed to claim that an asymmetry A in a channel f is different from zero by n_σ standard deviations, assuming $A \ll 1$, is

$$N_{B\bar{B}} > n_\sigma^2 \frac{1}{\epsilon A_s^2 \mathcal{B}(B \rightarrow f)} (1 + F_{B/S}), \quad (6.87)$$

where ϵ is the selection efficiency for the channel f . In order to quote the sensitivity of BABAR in the benchmark channels, some assumption for both the CP asymmetry and the branching fraction must be made; for the theoretical input used, see Section 6.2; this study estimates the efficiency, the signal to background ratio, and the systematic errors. All the simulations reported in this section were performed with the Aslund parameterized fast Monte Carlo simulation.

6.8.1 $B^- \rightarrow \eta h^-$

The branching fraction for $B^- \rightarrow \eta\pi^-$ is estimated to be $\sim 0.5 \times 10^{-5}$, with an asymmetry of the order of 10%. The η is searched for in the channels $\eta \rightarrow \gamma\gamma$ and $\eta \rightarrow \pi^+\pi^-\pi^0$. In these channels the acceptance is expected to be fairly large because the final states have low multiplicity.

For the $\eta \rightarrow \gamma\gamma$ mode, the η candidates are reconstructed from pairs of clusters in the electromagnetic calorimeter not associated with charged tracks. In order to reduce accelerator related background, photons are required to have an energy greater than 40 MeV. This removes about 90% of the fake combinations, keeping 98% of the signal. A fit to the Gaussian core of the distribution gives a mass resolution of 13 MeV/ c^2 . The η is required to be within 3σ of the nominal value; this selection criterion keeps 97% of the signal. The average η momentum is 3 GeV/ c and the opening angle of the two photons is generally rather small: the average cosine of the opening angle is in fact 0.85 for signal events. This feature is exploited by requiring that the cosine of the opening angle is greater than 0 for the η candidate.

For the $\eta \rightarrow 3\pi$ channel, the π^0 is reconstructed from clusters in the calorimeter with energy greater than 40 MeV, and not associated with charged tracks. The π^0 candidate is required to have an invariant mass in the range 115–147 MeV/ c^2 ; this is not symmetric around the nominal value due to the characteristic low-mass tail. The Gaussian core of the invariant mass distribution has a width of 4.7 MeV. The charged tracks are required to have a probability of being a pion greater than 2%, in order to reduce the combinatorial background. B^- candidates are obtained by combining the η and the remaining pion candidates. If the η is reconstructed in the 3π channel, a fit to the common vertex of the three charged pions from the B^- candidate is performed, and the χ^2 probability is required to be greater than 2%.

The selection criteria that are most effective in reducing the background are those related to the decay kinematics in the $\Upsilon(4S)$ frame: the momentum and the invariant mass of the B^- . The invariant mass is required to be within 2.5σ of the nominal B^- mass and the momentum is required to be in the range 0.175–0.425 GeV/ c .

The main source of background arises from light quarks produced in the continuum: about half of this contains a real η . Background from $B\bar{B}$ decays is negligible. The continuum background has a jet-like shape, while the signal is more spherical. These topologies can be discriminated using the ratios of the Fox-Wolfram moments, H_2/H_0 and H_4/H_0 (calculated in the $\Upsilon(4S)$ frame), as described in Section 4.9. In addition, the sphericity angle, θ_{sph} (see Section 4.9), is also used. The signal candidate is required to have $|\cos \theta_{\text{sph}}| < 0.9$.

After this selection, the reconstruction efficiency, including the η branching ratio, is 45%. Assuming a branching ratio for the signal of 0.5×10^{-5} , 70 signal events are expected in 30 fb^{-1} with 190 background events. The expected statistical error on the asymmetry is $\delta A_m = 0.23$.

6.8.2 $B^- \rightarrow D^- D^0$

The reconstruction of this channel is similar to that for the $B^0 \rightarrow D^+ D^-$ decay described in Section 5.5. Only channels having a branching ratio greater than 10% and not more than one π^0 in the final state are included here; the decay channels are listed in the Table 6-42. In order to reduce combinatorial background, the information from the DIRC and the dE/dx in the central tracking chamber are combined into a χ^2 which is used to calculate the probability of a given mass hypothesis. Candidate π and K mesons are required to have a probability greater than 2%. If a track is consistent with both hypotheses, or if the particle identification information is not available, the track is used for both π and K candidates.

Table 6-42. Selected D^- and D^0 decay channels.

D^0 decay	\mathcal{B}	D^- decay	\mathcal{B}
$K^+ \pi^-$	0.040	$K^+ \pi^- \pi^-$	0.091
$K^+ \pi^- \pi^0$	0.138	$K^+ \pi^- \pi^- \pi^0$	0.064
$K_s^0 \pi^+ \pi^-$	0.026	$K_s^0 \pi^-$	0.014
$K_s^0 \pi^+ \pi^- \pi^0$	0.049	$K_s^0 \pi^- \pi^0$	0.049
$K^+ \pi^+ \pi^- \pi^-$	0.081	$K_s^0 \pi^+ \pi^- \pi^-$	0.035
$K^+ \pi^+ \pi^- \pi^- \pi^0$	0.043	$K_s^0 \pi^+ \pi^- \pi^- \pi^0$	0.027

The criteria used to select the π^0 are the same as described in Section 6.8.1. K_s^0 mesons are reconstructed only in the $K_s^0 \rightarrow \pi^+ \pi^-$ channel. The two charged tracks are fitted to a common vertex and the χ^2 probability is required to be greater than 2%.

The masses of the two D mesons are required to be within 3σ of the nominal value. The vertex fit for the D daughters is required to have a χ^2 probability greater than 2%. In addition, the cosine of the angle between the two D s is required to be less than -0.1 . The mass resolutions and reconstruction efficiencies for all decay channels are summarized in Table 6-43.

In the selection of the B candidate, the most effective cuts are the momentum of the B in the $\Upsilon(4S)$ frame, and the invariant mass of the candidates. If more than one B candidate per event survives the cuts, that with the smaller value of the quantity

$$\chi_M^2 = \frac{(m_{D^0}^{\text{reco}} - m_{D^0}^{\text{true}})^2}{\sigma_{m_{D^0}}^2} + \frac{(m_{D^-}^{\text{reco}} - m_{D^-}^{\text{true}})^2}{\sigma_{m_{D^-}}^2} \quad (6.88)$$

Table 6-43. Mass resolutions and reconstruction efficiencies of the D^- and D^0 decay channels used in this analysis.

D^0 decay mode	σ_m^D (MeV/c ²)	Eff. (%)	D^- decay mode	σ_m^D (MeV/c ²)	Eff. (%)
$K^+\pi^-$	5.2	77	$K^+\pi^-\pi^-$	4.4	69
$K^+\pi^-\pi^0$	13.0	52	$K^-\pi^+\pi^-\pi^0$	9.6	40
$K_s^0\pi^+\pi^-$	5.3	50	$K_s^0\pi^-$	6.0	58
$K_s^0\pi^+\pi^-\pi^0$	10.0	29	$K_s^0\pi^-\pi^0$	11.9	37
$K^+\pi^+\pi^-\pi^-$	3.5	56	$K_s^0\pi^+\pi^-\pi^-$	5.2	43
$K^+\pi^+\pi^-\pi^-\pi^0$	9	33	$K_s^0\pi^+\pi^-\pi^-\pi^0$	6.1	25

is retained. The background is mainly from other $B\bar{B}$ decays and from $c\bar{c}$ events from the continuum; the latter is greatly reduced using event shape cuts: the sphericity of the events is computed and is required to be greater than 0.1.

The number of background event surviving the cuts is 190 $B\bar{B}$ events and 90 $c\bar{c}$, in 30 fb⁻¹ collected at the $\Upsilon(4S)$ peak. The overall reconstruction efficiency, including the branching ratio of the D mesons is $\epsilon = 2.8\%$. Assuming $\mathcal{B}(B^- \rightarrow D^- D^0) = 6.3 \times 10^{-4}$ (see Table 5-4), an sample of 560 signal events can be expected, leading to a statistical error on the asymmetry, $\delta A_m = 0.05$.

6.8.3 Outlook

These preliminary studies indicate that for the modes in question, and by extension, for other multibody modes, the direct CP -violating asymmetries predicted by the Standard Model calculations will be difficult to observe. In particular such searches will require more sophisticated background-fighting techniques than developed in these preliminary studies. It should not be forgotten however that models beyond the Standard Model can yield significantly larger direct CP violations (see Chapter 13). Thus, systematic searches for such effects should be carried out in any channel where the combined branching ratios, and efficiencies are large enough to achieve a CP asymmetry sensitivity of $\sim 10\%$.

References

- [1] R. Aleksan *et al.*, *Nucl. Phys.* **B361**, 141 (1991).
- [2] R. Godang *et al.*, (CLEO Collaboration), *Phys. Rev. Lett.* **80**, 3456 (1998).
- [3] A. Ali and D. London, *Nucl. Phys. Proc. Suppl.* **54A** 297 (1997).
- [4] M. Gronau and D. London, *Phys. Rev. Lett.* **65**, 3381 (1990).
- [5] M. Gronau, *Phys. Lett. B* **265**, 389 (1991);
L. Lavoura, *Mod. Phys. Lett. A* **7**, 1553 (1992).
- [6] R. Fleischer, *Z. Phys. C* **62**, 81 (1994); *Phys. Lett. B* **321**, 259 (1994); *Phys. Lett. B* **332**, 419 (1994);
N. G. Deshpande and X.-G. He, *Phys. Rev. Lett.* **74**, 26 (1995).
- [7] M. Gronau *et al.*, *Phys. Rev. D* **52**, 6374 (1995).
- [8] H. R. Quinn and A. E. Snyder, *Phys. Rev. D* **48**, 2139 (1993).
- [9] H. J. Lipkin *et al.*, *Phys. Rev. D* **44**, 1454 (1991).
- [10] M. Ciuchini *et al.*, *Nucl. Phys.* **B512**, 3 (1998) and references therein.
- [11] S. Versillé and F. Le Diberder, *B_{ABAR} Note # 429*, note in preparation.
- [12] R. Barate *et al.*, (ALEPH Collaboration), *Z. Phys. C* **76**, 15 (1997).
- [13] R. M. Barnett *et al.*, *Phys. Rev. D* **54**, 1 (1996).
- [14] P. L. Frabetti *et al.*, (E687 Collaboration), *Phys. Lett. B* **407**, 79 (1997).
- [15] R. N. Cahn, J. Charles, F. Le Diberder and S. Versillé, *B_{ABAR} Note # 430*, note in preparation.
- [16] Y. Nir and H. R. Quinn, *Phys. Rev. Lett.* **67**, 541 (1991).
- [17] M. Gronau and J. L. Rosner, *Phys. Rev. Lett.* **76**, 1200 (1996);
A. S. Dighe, M. Gronau and J. L. Rosner, *Phys. Rev. D* **54**, 3309 (1996).
- [18] A.S. Dighe and J. L. Rosner, *Phys. Rev. D* **54**, 4677 (1996).

- [19] D. Zeppenfeld, *Z. Phys. C* **8**, 77 (1981);
M. Savage and M. Wise, *Phys. Rev. D* **39**, 3346 (1989); *Phys. Rev. D* **40**, 3127(E) (1989);
L. L. Chau *et al.*, *Phys. Rev. D* **43**, 2176 (1991);
J. Silva and L. Wolfenstein, *Phys. Rev. D* **49**, 1151 (1994);
T. Hayashi, M. Matsuda and M. Tanimoto, *Phys. Lett. B* **323**, 78 (1994);
M. Gronau *et al.*, *Phys. Rev. D* **50**, 4529 (1994).
- [20] R. Fleischer, *Phys. Lett. B* **341**, 205 (1994);
A. J. Buras and R. Fleischer, *Phys. Lett. B* **341**, 379 (1995).
- [21] M. Gronau *et al.*, *Phys. Rev. D* **52**, 6356 (1995).
- [22] Y. Nir and H. Quinn, *Ann. Rev. Nucl. Part. Sci.* **43**, 211 (1992).
- [23] A. B. Carter and A. I. Sanda, *Phys. Rev. Lett.* **45**, 952 (1980); *Phys. Rev. D* **23**, 1567 (1981).
- [24] I. I. Bigi and A. I. Sanda, *Nucl. Phys.* **B193**, 45 (1981).
- [25] M. Kobayashi and T. Maskawa, *Prog. Th. Phys.* **49**, 652 (1973).
- [26] O. Hernandez *et al.*, *Phys. Lett. B* **333**, 500 (1994).
- [27] D. Atwood and A. Soni, *Z. Phys. C* **64**, 241 (1994).
- [28] D. Atwood and A. Soni, *Phys. Rev. Lett.* **74**, 220 (1995).
- [29] G. Eilam, M. Gronau and R. Mendel, *Phys. Rev. Lett.* **74**, 4984 (1995);
N. Deshpande *et al.*, *Phys. Rev. D* **52**, 5354 (1995).
- [30] R. Enomoto and M. Tanabashi, *Phys. Lett. B* **386**, 413 (1996).
- [31] G. Valencia, *Phys. Rev. D* **39**, 3339 (1989);
G. Kramer, W. F. Palmer and H. Simma, *Nucl. Phys.* **B428**, 77 (1994).
- [32] D. Atwood, G. Eilam and A. Soni, *Phys. Rev. Lett.* **71**, 492 (1993).
- [33] R. Garisto, *Phys. Rev. D* **51**, 1107 (1995).
- [34] M. Bander, D. Silverman and A. Soni, *Phys. Rev. Lett.* **43**, 242 (1979).
- [35] For explicit examples of how this is done, see *e.g.*, Ref. 7 and 11.
- [36] J. M. Gerard and W. S. Hou, *Phys. Rev. D* **43**, 2909 (1991).
- [37] L. Wolfenstein, *Phys. Rev. D* **43**, 151 (1991).
- [38] H. Simma, G. Eilam and D. Wyler, *Nucl. Phys.* **B352**, 367 (1991).

- [39] W. Bernreuther, T. Schroder and T. N. Pham, *Phys. Lett. B* **279**, 389 (1992).
- [40] G. Valencia and A. Soni, *Phys. Lett. B* **263**, 517 (1991);
C. Schmidt and M. Peskin, *Phys. Rev. Lett.* **69**, 410 (1992).
- [41] A. Lenz, U. Nierste and G. Ostermaier, hep-ph/9802202. See also Refs. 15, 17 and 21.
- [42] N. G. Uraltsev, “FSI Phases and CP Asymmetries in Beauty: QCD Point of View,” in *Proceedings of 7th Meeting of the Division of Particles and Fields of the APS (DPF 92)*, Batavia, IL 10–14 November (1992); C. H. Albright *et al.*, eds. World Scientific, Singapore (1993), Vol. 1, p. 855.
- [43] T. Browder *et al.*, *Phys. Rev. D* **57**, 6829 (1998).
- [44] J. M. Soares, *Phys. Rev. D* **52**, 242 (1995).
- [45] X.-G. He and A. Soni, *Phys. Lett. B* **391**, 456 (1997).
- [46] D. Atwood and A. Soni, in preparation.
- [47] G. Kramer, W.F. Palmer and H. Simma, *Z. Phys. C* **66**, 429 (1995).
- [48] R. Fleischer, *Z. Phys. C* **58**, 483 (1993); *Z. Phys. C* **62**, 81 (1994).
- [49] G. Kramer, W. F. Palmer and H. Simma, *Nucl. Phys.* **B428**, 77 (1994).
- [50] D. Atwood and A. Soni, *Phys. Rev. D* **58**, 036005 (1998).
- [51] J. M. Soares, *Nucl. Phys.* **B367** (1991).
- [52] C. Greub, H. Simma and D. Wyler, *Nucl. Phys.* **B434**, 39 (1995).
- [53] G. Eilam, A. Ioannissian and R. R. Mendel, *Z. Phys. C* **71**, 95 (1996).
- [54] F. Kruger and L.M. Sehgal, *Phys. Lett. B* **380**, 199 (1996).
- [55] F. Kruger and L. M. Sehgal, *Phys. Rev. D* **55**, 2799 (1997); *Phys. Rev. D* **56**, 5452 (1997).
- [56] J. F. Donoghue *et al.*, *Phys. Rev. Lett.* **77**, 2178 (1996).
- [57] M. Neubert, *Phys. Lett. B* **424**, 152 (1998).
- [58] A. Falk *et al.*, *Phys. Rev. D* **57**, 4290 (1998).
- [59] L. Wolfenstein, *Phys. Rev. D* **52**, 537 (1995).
- [60] R. Fleischer and T. Mannel, *Phys. Rev. D* **57** 2752 (1998);
A. J. Buras, R. Fleischer and T. Mannel, hep-ph/9711262.

- [61] M. Ciuchini *et al.*, *Nucl. Phys.* **B501**, 271 (1997)
- [62] Y. Grossmann and H. R. Quinn, *Phys. Rev. D* **58**, 017504 (1998).
- [63] J. Charles, hep-ph/9806468 (1998).
- [64] E. M. Aitala *et al.*, *Phys. Rev. Lett.* **80**, 1393 (1998).
- [65] R. Aleksan *et al.*, *Phys. Rev. D* **51**, 6235 (1995).
- [66] R. Aleksan *et al.*, *Phys. Lett. B* **356**, 95 (1995).
- [67] *Technical Design Report*, (BaBar Collaboration), SLAC-Report-372 (1995).
- [68] A. Gaidot and G. Vasseur, “Background Fighting in the $B \rightarrow n\pi$ Analyses,” BaBar Note # 425, (1998).
- [69] A. Anastassov *et al.*, (CLEO Collaboration), CLEO CONF 97-24 and EPS97-334 (1997).
- [70] S. Versillé and F. Le Diberder, “The KIN Variable,” BaBar Note # 406, (1998); “The KIN Variable and CP Thinking Revisited,” BaBar Note # 421, (1998).
- [71] S. Versillé and F. Le Diberder, BaBar Note # 428, note in preparation.
- [72] F. Le Diberder, “Precision on CP Violation Measurements and Requirement on the Vertex Resolution,” BaBar Note # 34, (1990);
 W. Toki, “Parametrization of Decay Length Distributions with Errors,” BaBar Note # 35, (1990);
 A. Snyder, “ CP Extraction Tool,” BaBar Note # 188, (1994);
 A. Snyder, “ CP Reach Estimates for the TDR,” BaBar Note # 219, (1995);
 P.S. Marrocchesi, “An Unbinned Maximum Likelihood Analysis of CP Violation,” BaBar Note # 257, (1995); and Tagging Note;
 P.F. Harrison, “Study of $B^0 \rightarrow J/\psi K_S^0$ and $B^0 \rightarrow \rho^\pm \pi^\mp$,” BaBar Note # 218, (1996).
- [73] S. Versillé, “Simultaneous Handling of Tagging and Background Fighting,” BaBar Note # 408, (1998).
- [74] C. Dallapiccola and A. Jawahery, “Analysis of $B^0 \rightarrow a_1 \pi$ Decays,” BaBar Note # 434, (1998).
- [75] A. Forti, F. Lanni and F. Palombo, “Measurement of the CKM Alpha Angle in the Processes $B_d^0 \rightarrow a_1^\pm \pi^\mp \rightarrow \pi^+ \pi^- \pi^+ \pi^-$,” BaBar Note # 423, (1998).
- [76] C. P. Jessop *et al.*, (CLEO Collaboration), *Phys. Rev. Lett.* **79**, 4533 (1998).

Methods of Measuring γ

7.1 Introduction and Motivation for Measuring γ

This chapter presents methods to determine the angle γ of the unitarity triangle. At present, this triangle can only be constrained indirectly through semileptonic $b \rightarrow c \ell \bar{\nu}$, $b \rightarrow u \ell \bar{\nu}$ decays, $B^0-\bar{B}^0$ mixing and the parameter ε_K describing indirect CP violation in the neutral kaon system. The latter observable requires a non-zero value of γ . Such indirect methods typically result in a large allowed range, *e.g.*, [1]

$$41^\circ \lesssim \gamma \lesssim 134^\circ. \quad (7.1)$$

The studies presented in this chapter deal with *direct* measurements of γ , which are usually regarded as being very difficult from an experimental point of view.

Possible new physics contributions to $B_{d,s}^0-\bar{B}_{d,s}^0$ mixing are among the preferred mechanisms for physics beyond the Standard Model to manifest itself in CP -violating asymmetries of neutral B meson decays [2, 3]; the effect of such new physics cancels in the sum of α and β determined from $B_d \rightarrow \pi^+\pi^-$ and $B_d \rightarrow \psi K_S^0$, respectively. A detailed discussion of this issue is given in Chapter 13. Consequently, such new physics will not affect the unitarity relation

$$\alpha + \beta + \gamma = 180^\circ, \quad (7.2)$$

although the triangle may not be that given by Standard Model constraints. However other effects can change the various quantities which, in the Standard Model, measure the 3rd angle γ . Hence γ should be measured in a variety of ways, to check whether one consistently finds the same result. There are indeed several methods to accomplish this task, and they are expected to be affected differently by new physics.

7.2 An Overview of Methods for Extracting γ

During recent years, several methods to obtain information on the CKM angle γ , to constrain or even to extract it have been proposed. These strategies can be classified in various ways. For example, some of them are theoretically clean, some suffer from hadronic uncertainties, some use

B_s decays — which will not be accessible to the BaBar experiment for the first years of running — and some methods appear simply to be unfeasible. The studies summarized in this chapter are rather selective, and are focused on those methods which appear most promising at the present time. They include strategies to determine γ using the following tools:

- Triangle relations among decay amplitudes (general discussion of experimental errors in Section 7.3).
- $B^\pm \rightarrow DK^\pm$ and related decays (Section 7.4).
- Amplitude relations among $B_{u,d} \rightarrow \pi K$ decays (Section 7.5).
- Partial reconstruction of $B_d \rightarrow D^{(*)}\pi$ decays to extract $\sin(2\beta + \gamma)$ (Section 7.6).
- $B_s-\bar{B}_s$ mixing (Section 7.7).

Although methods employing B_s mesons require BaBar to operate at the $\Upsilon(5S)$ resonance, these methods are discussed briefly in Section 7.7.

The techniques discussed in Section 7.4 use pure tree decays, which receive no penguin contributions at all and originate from $\bar{b} \rightarrow \bar{u} c \bar{s}$ and $\bar{b} \rightarrow \bar{c} u \bar{s}$ quark-level transitions. The prototype of this method was proposed by Gronau and Wyler [4] and employs the decays $B^+ \rightarrow D^0 K^+$, $B^+ \rightarrow \bar{D}^0 K^+$, $B^+ \rightarrow D_\pm^0 K^+$ and their charge conjugates, where D_\pm^0 denotes a CP eigenstate of the neutral D meson system with CP eigenvalue ± 1 . Using such CP eigenstates, which are detected for instance through $D_+^0 \rightarrow \pi^+ \pi^-$, $K^+ K^- \dots$, it is straightforward to derive simple relations among the corresponding decay amplitudes. The relations are *exact* and can be represented in the complex plane as two triangles. Since the difference in CP -violating weak phase between the $B^+ \rightarrow \bar{D}^0 K^+$ and the $B^+ \rightarrow D^0 K^+$ amplitudes is proportional to $e^{2i\gamma}$, these triangles allow a determination of γ . Since the corresponding amplitude relations are exact and the decays employed in this method are pure tree decays, this approach is *theoretically clean* and does not suffer from hadronic uncertainties. Another important feature of these methods is that they are unaffected by a large class of new-physics effects, *i.e.*, by any new contribution to $B^0-\bar{B}^0$ mixing as well as any new penguin-like contribution. Unfortunately the triangles are expected to be very “squashed.” Moreover one has to deal with additional experimental problems [5], so that this approach is very difficult from a practical point of view. Recently variants have been proposed by Atwood, Dunietz and Soni [5]. These methods and their experimental feasibility are the subject of Section 7.4. Since “triangles” among decay amplitudes play an important role for the extraction of γ and will show up at several places throughout this chapter, a general discussion of the propagation of experimental errors in generic “triangle methods” is given in Section 7.3.

In contrast to the theoretically clean strategies for measuring γ using $B^\pm \rightarrow DK^\pm$ and related decays, methods employing amplitude relations among $B_{u,d} \rightarrow \pi\pi$, πK decays [6, 7] (for a review, see [8]) are complicated by several inputs affecting the theoretical cleanliness. Both the $SU(2)$ and

$SU(3)$ flavor symmetries can be used to relate amplitudes of nonleptonic B decays [9]. While the $SU(2)$ isospin symmetry relating up and down quarks is nearly exact, $SU(3)$ is badly broken, so there are significant theoretical uncertainties [10]. Another problem is related to possible long-distance contributions to QCD penguins with internal charm and up quarks, which may affect some of these methods considerably [11]. Interestingly, also electroweak (EW) penguins [12] have an important impact on some strategies and have been discussed extensively in the recent literature [13, 14]. Since the ratio $\alpha/\alpha_s = \mathcal{O}(10^{-2})$ of the QED and QCD couplings is very small, one would expect that electroweak penguins should play a minor role in comparison with QCD penguins. If the top quark were not heavy, that would indeed be the case. However, the Wilson coefficient of one electroweak-penguin operator increases strongly with the top-quark mass, so that these contributions cannot be neglected [12]. As far as the determination of the CKM angle γ from amplitude relations based on flavor symmetries is concerned, electroweak penguins lead in general to very complicated geometrical constructions, *i.e.*, not just to simple triangles, but for instance to amplitude quadrangles [14], whose experimental feasibility is questionable.

The studies of such strategies, summarized in Section 7.5, focus on a simple approach to obtain information on γ with the help of the branching ratios for the decays $B^+ \rightarrow \pi^+ K^0$, $B^0 \rightarrow \pi^- K^+$ and their charge conjugates that was proposed in [15] (see also [8, 16, 17]). In these decays, electroweak penguins contribute only in “color-suppressed” form and are expected to be considerably less important than in the strategies mentioned in the previous paragraph. Using the $SU(2)$ isospin symmetry of strong interactions to relate the QCD penguin contributions to these decays, one can derive simple relations between the $B^+ \rightarrow \pi^+ K^0$ and $B^0 \rightarrow \pi^- K^+$ decay amplitudes, which probe the CKM angle γ . In order to present the basic idea, a discussion is given that at first neglects the electroweak-penguin contributions, as well as certain final state interaction effects, which have received a lot of attention in the recent literature [18, 19] (see also [16]). In this case, simple triangle relations are obtained between the $B^+ \rightarrow \pi^+ K^0$, $B^0 \rightarrow \pi^- K^+$ decay amplitudes and the color-allowed $\bar{b} \rightarrow \bar{u} u \bar{s}$ “tree” amplitude T' contributing to the latter decay. If $|T'|$ could be fixed by using an additional input, one could extract γ from this approach, which is — from a geometrical point of view — very similar to the $B^\pm \rightarrow DK^\pm$ method. Since it requires only time-independent measurements of branching ratios at the $\mathcal{O}(10^{-5})$ level, the $B_{u,d} \rightarrow \pi K$ approach is, in contrast with strategies of the $B^\pm \rightarrow DK^\pm$ method, promising for future B -physics experiments [16, 17]. In fact, the CLEO collaboration has recently reported the first experimental observation of these decays [20].

The crucial theoretical difference between the $B_{u,d} \rightarrow \pi K$ and $B^\pm \rightarrow DK^\pm$ methods is, however, that the former approach gives a value of γ that suffers from some model dependence, in particular, due to the need to fix $|T'|$. Another theoretical limitation is the neglect of electroweak penguins and rescattering effects, which may also affect the value of $|T'|$ significantly, thereby making the theoretical uncertainty hard to control [19]. Thus an accurate measurement of the modes $B^+ \rightarrow \pi^+ K^0$ and $B^0 \rightarrow \pi^- K^+$ provides phenomenologically interesting *theoretical constraints* on γ , though not a precision measurement. The combined branching ratios for $B_d \rightarrow \pi^\mp K^\pm$ and $B^\pm \rightarrow \pi^\pm K$, which have been measured recently for the first time by the CLEO collaboration [20], imply

a range for γ , which takes the form

$$0^\circ \leq \gamma \leq \gamma_0 \quad \text{or} \quad 180^\circ - \gamma_0 \leq \gamma \leq 180^\circ, \quad (7.3)$$

where γ_0 can be determined from data. This may be able to provide information complementary to the presently allowed range (7.1) that is implied by the usual “indirect” fits of the unitarity triangle. Consequently, such constraints on γ are of particular phenomenological interest. However, a result inconsistent with these constraints would lead one to question the assumptions of their derivation, particularly those related to final-state interactions, before concluding that there must be beyond-Standard-Model effects. As was pointed out in [21], if the ratio R of the combined $B_d \rightarrow \pi^\mp K^\pm$ and $B^\pm \rightarrow \pi^\pm K$ branching ratios is found experimentally to be smaller than one, a maximal value of γ_0 can be obtained, which does not depend on the magnitude of the “tree” amplitude T' , the quantity that introduces the major theoretical uncertainty into the determination of γ as sketched in the previous paragraph. Rescattering effects can be taken into account completely in these constraints with the help of experimental data on $B^+ \rightarrow K^+ \bar{K}^0$, and the theoretical accuracy is mainly limited by electroweak-penguin effects [19] and $SU(3)$ assumptions. These constraints on γ will be discussed in detail in Section 7.5.

In Section 7.6, it is shown how the partial reconstruction of $B_d \rightarrow D^{(*)\pm} \pi^\mp$ decays may be used to extract $\sin(2\beta + \gamma)$ [22].¹ Although the expected CP asymmetries are small, the decay rates are large and one can reconstruct the $D^{(*)\pm} \pi^\mp$ final states inclusively with a good efficiency and modest backgrounds. Taking both effects into account, one finds a sensitivity that is comparable to that expected for other determinations of α for a given luminosity. From a theoretical point of view, the approach with $B_d \rightarrow D^{(*)\pm} \pi^\mp$ decays [22], which are caused by $b \rightarrow c \bar{u} d$ ($\bar{b} \rightarrow \bar{u} c \bar{d}$) quark-level transitions, is very similar to an approach to determine γ from the time evolution of $B_s \rightarrow D_s^\pm K^\mp$ decays [23]. The important differences are that in the case of $B_d \rightarrow D^{(*)\pm} \pi^\mp$, one decay path is doubly Cabibbo-suppressed, and that the $B^0 - \bar{B}^0$ mixing phase enters, which can be determined from decays of the type $B_d \rightarrow \psi K_s^0$ (the $B_s - \bar{B}_s$ mixing phase is very small within the Standard Model). As a first approximation, one may use “factorization” to estimate the corresponding hadronic matrix elements. Since the $B_d \rightarrow D^{(*)\pm} \pi^\mp$ modes are color-allowed tree decays receiving no penguin contributions at all, the factorization hypothesis may work reasonably well in this case [24]. Performing more involved analyses, the corresponding hadronic uncertainties can be eliminated in principle, yielding a theoretically clean value of $2\beta + \gamma$, up to discrete ambiguities. The details of this method will be discussed in Section 7.6. A brief presentation of similar strategies which use the time evolution of $B_s \rightarrow D_s^\pm K^\mp$ transitions is given in Section 7.7; this section also presents a brief look at other interesting B_s decays.

¹This quantity can be interpreted equally well as $\sin(\beta - \alpha)$.

7.3 Experimental Errors in Extracting γ from Triangles

In the methods for measuring γ described in the following sections, decays whose amplitude A_3 can be expressed as the sum of two contributions A_1 and A_2 are considered:

$$A_3 = A_1 + A_2 = A_1 + |A_2|e^{i\gamma}e^{i\delta} \quad (7.4)$$

Such relations between amplitudes are represented geometrically by a triangle construction in the complex plane. If A_1 and A_2 are the two amplitudes which contribute to a given decay, and if the decay has been chosen such that A_2 has a relative CKM phase γ and a relative strong-phase δ with respect to A_1 , the situation can be presented as shown in Fig. 7-1. \bar{A}_1 and \bar{A}_2 are the corresponding

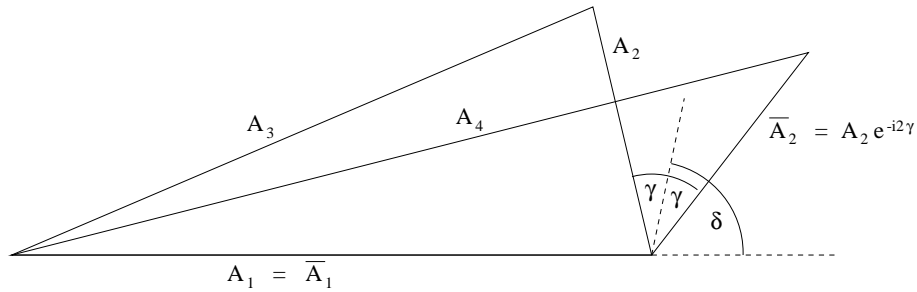


Figure 7-1. Generic Triangle for γ Measurement

amplitudes for the \bar{B} , where the overall phase convention has been selected such that $\bar{A}_1 = A_1$. In addition, since $|\bar{A}_2| = |A_2|$, one finds

$$A_4 = \bar{A}_1 + \bar{A}_2 = A_1 + |A_2|e^{-i\gamma}e^{i\delta}. \quad (7.5)$$

The variable δ is the difference in the strong phases for the two amplitudes and A_3 and A_4 are the two total amplitudes for the decays of the B and \bar{B} respectively. Direct CP violation manifests itself in the magnitudes of A_3 and A_4 being unequal, if the strong-phase δ is different from zero. There are 4 parameters in total for the two triangles corresponding to B and \bar{B} ; these are taken to be $|A_1|$, $|A_2|$, γ and δ .

Explicit examples of this type of construction are given in Section 7.4.1, where, for instance, $A_3 = A(B^+ \rightarrow D^0_+ K^+)$ and $A_4 = A(B^- \rightarrow D^0_+ K^-)$, and in Section 7.5.2, where $A_3 = A(B^0 \rightarrow \pi^- K^+)$ and $A_4 = A(\bar{B}^0 \rightarrow \pi^+ K^-)$.

In the simplest case, the experimentally measured quantities are the magnitudes of the four amplitudes A_1 , A_2 , A_3 and A_4 . Hence, $|A_1|$ and $|A_2|$ are measured directly, but γ and δ need to be calculated from the values of the $|A_i|$. Simple geometry gives (modulus symbols are dropped between here and Eq. (7.12))

$$\cos(\delta + \gamma) = \frac{(A_3^2 - A_1^2 - A_2^2)}{2A_1A_2} \equiv B_3 \quad (7.6)$$

$$\cos(\delta - \gamma) = \frac{(A_4^2 - A_1^2 - A_2^2)}{2A_1A_2} \equiv B_4. \quad (7.7)$$

The resulting error on γ is calculated from

$$\frac{\partial\gamma}{\partial B_3} = \frac{-1}{2\sqrt{1 - B_3^2}} = \frac{-1}{2\sin(\delta + \gamma)}, \quad (7.8)$$

$$\frac{\partial\gamma}{\partial B_4} = \frac{1}{2\sqrt{1 - B_4^2}} = \frac{1}{2\sin(\delta - \gamma)} \quad (7.9)$$

and the derivatives for the B_i with respect to the A_i :

$$\frac{\partial B_3}{\partial A_1} = \frac{-(A_3^2 + A_1^2 - A_2^2)}{2A_1^2A_2}, \quad \frac{\partial B_3}{\partial A_2} = \frac{-(A_3^2 - A_1^2 + A_2^2)}{2A_1A_2^2}, \quad \frac{\partial B_3}{\partial A_3} = \frac{A_3}{A_1A_2}, \quad \frac{\partial B_3}{\partial A_4} = 0 \quad (7.10)$$

$$\frac{\partial B_4}{\partial A_1} = \frac{-(A_4^2 + A_1^2 - A_2^2)}{2A_1^2A_2}, \quad \frac{\partial B_4}{\partial A_2} = \frac{-(A_4^2 - A_1^2 + A_2^2)}{2A_1A_2^2}, \quad \frac{\partial B_4}{\partial A_3} = 0, \quad \frac{\partial B_4}{\partial A_4} = \frac{A_4}{A_1A_2}. \quad (7.11)$$

The error on γ is

$$\sigma_\gamma^2 = \sum_i \left(\frac{\partial\gamma}{\partial A_i} \right)^2 \sigma_{A_i}^2, \quad \frac{\partial\gamma}{\partial A_i} = \left(\frac{\partial\gamma}{\partial B_3} \right) \left(\frac{\partial B_3}{\partial A_i} \right) + \left(\frac{\partial\gamma}{\partial B_4} \right) \left(\frac{\partial B_4}{\partial A_i} \right). \quad (7.12)$$

Note that for values of $\delta \sim \pm\gamma$, either $\frac{\partial\gamma}{\partial B_3}$ or $\frac{\partial\gamma}{\partial B_4}$ becomes very large so the error determined in this way becomes infinite. This corresponds to the case where one of the two triangles has no height, *i.e.*, $|A_1| + |A_2| = |A_3|$ (or $|A_4|$). However, in this case, the CP asymmetry between $|A_3|$ and $|A_4|$ is relatively large for a given γ and therefore easier to observe. Figure 7-2 illustrates the dependence of the uncertainty in γ on the value of δ and the amplitude ratio $|A_2|/|A_1|$. The relative errors on the amplitudes have been set to typical values which appear later in this chapter, specifically $\sigma_{A_i}/A_i = 0.05$ is used for these figures. In the first plot $|A_2|/|A_1| = 0.5$ is assumed, in the second $\delta = 0^\circ$. It is seen that the error is a strong function of δ if no constraint is imposed.

Also included in the figure are numerical estimations of the error, which explicitly take into account the constraint that the triangles must be closed. The numerically estimated error is still large for $\gamma \simeq \delta$ although significantly reduced from the “naive” analytic value. While the strong-phase values are unknown for many decays, it seems that small values of δ are favored, while γ is known to be greater than 40° ; hence it seems likely that this unfavorable situation will not occur. In any case, a four-fold ambiguity in the determination of γ is unavoidably present, due to the four possible orientations of the two triangles relative to the base A_1 .

In more complicated cases, it may be that one of the common amplitudes is not experimentally accessible; to be definite, assume $|A_2|$ is not directly measurable. In this case, having only three experimental measurables $|A_1|$, $|A_3|$ and $|A_4|$, will not allow the four parameters including δ and

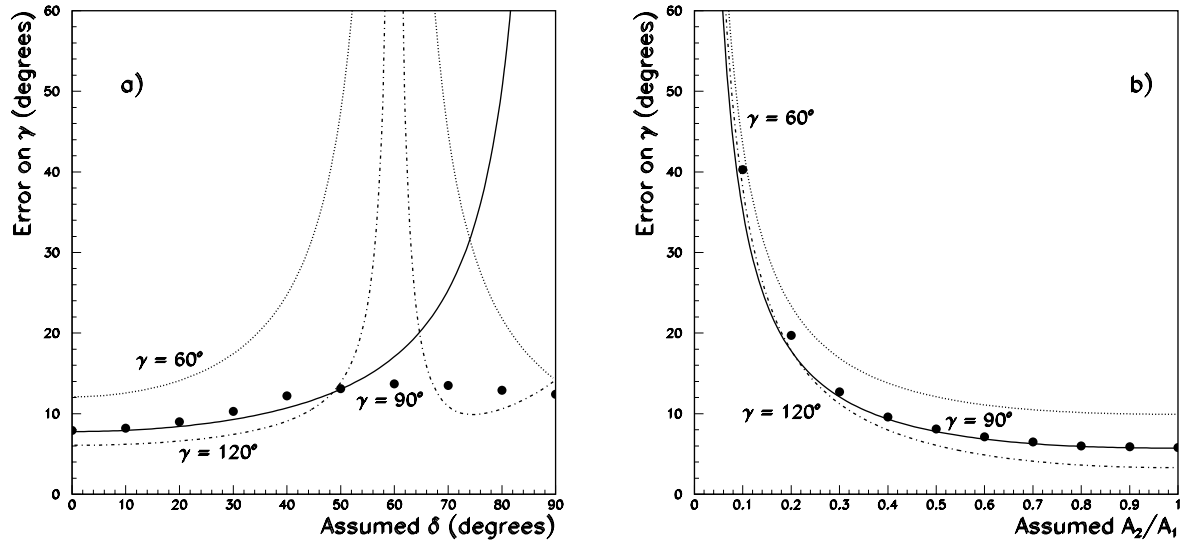


Figure 7-2. Error on γ as a function of (a) the strong-phase δ and (b) the amplitude ratio $|A_2|/|A_1|$. In (a), a value of $A_2/A_1 = 0.5$ was used. For (b), a value of $\delta = 0^\circ$ was used. The lines show the error calculated from the equations given in the text while the points show a numerical estimate of the error for the case of $\gamma = 90^\circ$.

γ to be determined. However, if another process can be found which has the same magnitudes of the amplitudes $|A_1|$ and $|A_2|$, but a different strong-phase $\delta_2 \neq \delta \equiv \delta_1$, then

$$A'_3 = A_1 + |A_2|e^{i\gamma}e^{i\delta_2} \quad (7.13)$$

$$A'_4 = A_1 + |A_2|e^{-i\gamma}e^{i\delta_2}. \quad (7.14)$$

Measurements of $|A_1|$, $|A'_3|$ and $|A'_4|$ for this process will allow both pairs of triangles to be completely determined. There are again three measurements for the second process, of which one (A_1) is not an independent value. Hence, the total number of measured quantities for the two processes is five, which allows the determination of the five unknown parameters, A_1 , A_2 , γ , δ_1 and δ_2 . Thus, A_2 , although not directly measurable in either process, can be calculated from these measurements. Note that, this method results in large errors if γ is close to either δ_1 or δ_2 , or if $\delta_1 \sim \delta_2$, since the two sets of measurements become redundant. Because small values of the strong phases may be favored (*i.e.*, $\delta_1 \sim \delta_2 \sim 0$), this method may not be feasible.

Clearly, this method of considering more processes can be extended to an arbitrary number of measurements. Each new process considered adds two independent measured quantities, but only one unknown (the strong phase). Hence, with three or more processes, the system becomes overconstrained, allowing a cross-check to be made of the results. However, as before, nothing is gained if the strong phases are equal. The requirement that the amplitudes have the same magnitude

in the different processes is a major constraint and the only case considered here where this could be applied is for $B^+ \rightarrow D^{(*)0} K^+$ decays, where the different processes correspond to different $D^{(*)0}$ decay modes. In that case, the triangles needed for the γ measurement are made from the amplitudes for the B^+ decays only, but the experimental measurements are of the products of the amplitudes for both the B^+ and $D^{(*)0}$ decays, where the B^+ part is clearly independent of the $D^{(*)0}$ decay mode.

7.4 Methods Using $B \rightarrow DK$ Decays

During recent years, relations among amplitudes of nonleptonic B decays have been very popular in developing strategies for extracting angles of the unitarity triangle, in particular for γ . There are both *exact* and *approximate* relations. The latter are based on flavor symmetries of strong interactions in combination with certain dynamical assumptions and are the subject of Section 7.5. The exact relations will be discussed in this section.

7.4.1 Theoretical Framework

7.4.1.1 A method using $B^\pm \rightarrow DK^\pm$ decays

Applying an appropriate CP phase convention to simplify the following discussion, the CP eigenstates $|D_\pm^0\rangle$ of the neutral D meson system with CP eigenvalues ± 1 are given by

$$|D_\pm^0\rangle = \frac{1}{\sqrt{2}} (|D^0\rangle \pm |\bar{D}^0\rangle), \quad (7.15)$$

so that the $B^\pm \rightarrow D_\pm^0 K^\pm$ transition amplitudes can be expressed as [4]

$$\sqrt{2}A(B^+ \rightarrow D_+^0 K^+) = A(B^+ \rightarrow D^0 K^+) + A(B^+ \rightarrow \bar{D}^0 K^+) \quad (7.16)$$

$$\sqrt{2}A(B^- \rightarrow D_+^0 K^-) = A(B^- \rightarrow \bar{D}^0 K^-) + A(B^- \rightarrow D^0 K^-). \quad (7.17)$$

These relations, which are exact, can be represented as two triangles in the complex plane. Taking into account that the $B^+ \rightarrow DK^+$ decays originate from $\bar{b} \rightarrow \bar{u} c \bar{s}$ and $\bar{b} \rightarrow \bar{c} u \bar{s}$ quark-level transitions (see Fig. 7-3) yields

$$A(B^+ \rightarrow D^0 K^+) = e^{i\gamma} \lambda |V_{cb}| R_b |a| e^{i\Delta_a} = e^{2i\gamma} A(B^- \rightarrow \bar{D}^0 K^-) \quad (7.18)$$

$$A(B^+ \rightarrow \bar{D}^0 K^+) = \lambda |V_{cb}| |A| e^{i\Delta_A} = A(B^- \rightarrow D^0 K^-), \quad (7.19)$$

where $R_b = \frac{1-\lambda^2/2}{\lambda} \left| \frac{V_{ub}}{V_{cb}} \right|$ measures one side of the unitarity triangle. The quantities $|a|$, $|A|$ are magnitudes of hadronic matrix elements of current-current operators, and Δ_a , Δ_A denote the

corresponding CP -conserving strong phases. Consequently, the modes $B^+ \rightarrow D^0 K^+$ and $B^+ \rightarrow \bar{D}^0 K^+$ exhibit no CP -violating effects. However, if $\gamma \neq 0$, one finds

$$|A(B^+ \rightarrow D^0 K^+)| \neq |A(B^+ \rightarrow \bar{D}^0 K^+)|. \quad (7.20)$$

Observation of such a CP -violating effect would rule out superweak scenarios in an unambiguous way.

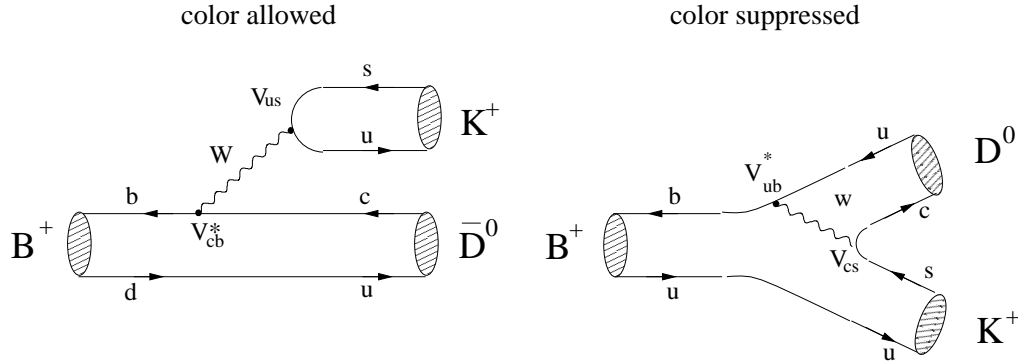


Figure 7-3. The leading-order Feynman Diagrams contributing to the decays $B^+ \rightarrow \bar{D}^0 K^+$ and $B^+ \rightarrow D^0 K^+$.

Combining all these considerations, the triangle relations (7.16) and (7.17), which are depicted in Fig. 7-4, can be used to extract γ by measuring only the rates of the six processes. This approach was proposed by Gronau and Wyler [4]. It is theoretically clean and suffers from no hadronic uncertainties. As can be seen easily from Fig. 7-4, this method works also for vanishing CP -conserving strong phases in the $B^\pm \rightarrow DK^\pm$ modes. Although there would be no CP violation in $B^\pm \rightarrow D^0 K^\pm$ in this case, the extraction of γ is still possible. Unfortunately the amplitude triangles are expected to be very squashed ones since $B^- \rightarrow \bar{D}^0 K^-$ is both color- and CKM-suppressed with respect to $B^- \rightarrow D^0 K^-$:

$$\frac{|A(B^- \rightarrow \bar{D}^0 K^-)|}{|A(B^- \rightarrow D^0 K^-)|} = R_b \frac{|a|}{|A|} \approx 0.36 \frac{a_2}{a_1} \approx 0.08. \quad (7.21)$$

Here a_1 and a_2 are the usual phenomenological color-factors [25]. $SU(3)$ flavor symmetry allows the corresponding branching ratios to be estimated from the measured value, $\mathcal{B}(B^- \rightarrow D^0 \pi^-) = (5.3 \pm 0.5) \times 10^{-3}$ [26]; one finds $\mathcal{B}(B^- \rightarrow D^0 K^-) \approx 4 \times 10^{-4}$ and $\mathcal{B}(B^- \rightarrow \bar{D}^0 K^-) \approx 2 \times 10^{-6}$.

While the former branching ratio can be measured using conventional methods, the latter suffers from considerable experimental problems. If $\mathcal{B}(B^- \rightarrow \bar{D}^0 K^-)$ is measured using hadronic decays of the \bar{D}^0 , e.g., through $\bar{D}^0 \rightarrow K^+ \pi^-$, one has to deal with large interference effects of $\mathcal{O}(1)$ with the D^0 channel, e.g., $B^- \rightarrow K^- D^0 [\rightarrow K^+ \pi^-]$, as has been shown recently [5]. Consider as an example the decay $\bar{D}^0 \rightarrow K^+ \pi^-$ exhibiting the branching ratio $\mathcal{B}(\bar{D}^0 \rightarrow K^+ \pi^-) = 3.9 \times 10^{-2}$ [26]. Thus the total rate for the decay chain $B^- \rightarrow K^- [\bar{D}^0 \rightarrow K^+ \pi^-]$ will be of $\mathcal{O}(10^{-7})$.

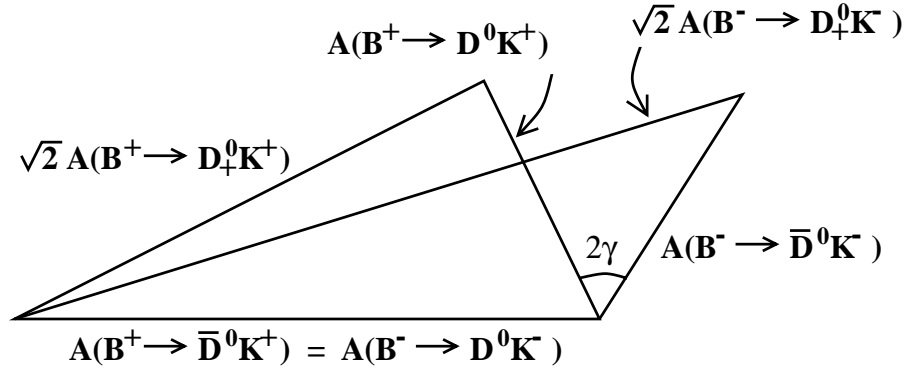


Figure 7-4. Triangle relations among $B^\pm \rightarrow DK^\pm$ decay amplitudes.

Although doubly Cabibbo-suppressed, the D^0 may also decay into a $K^+\pi^-$ final state, where $\mathcal{B}(D^0 \rightarrow K^+\pi^-) \approx 3 \times 10^{-4}$ [26]. Taking into account that the primary decay $B^- \rightarrow K^- D^0$ has a branching ratio of 4×10^{-4} , the decay chain $B^- \rightarrow K^- [D^0 \rightarrow K^+\pi^-]$ also has a total branching ratio of $\mathcal{O}(10^{-7})$. Since both decay chains give the same final state, there will be $\mathcal{O}(1)$ interference effects between the two channels. All possible hadronic tags of the \bar{D}^0 in the decay $B^- \rightarrow \bar{D}^0 K^-$ will be similarly affected by such interference effects. This serious problem can in principle be avoided by using the semileptonic decay $\bar{D}^0 \rightarrow \ell^- \bar{\nu}_\ell X_s$ to tag the \bar{D}^0 . However, there will be huge backgrounds, for instance from $B^- \rightarrow \ell^- \bar{\nu}_\ell X_c$, which are $\mathcal{O}(10^6)$ larger and may be difficult to control [5]. Another problem that CP eigenstate decays of the neutral D system $D^0_+ \rightarrow \pi^+\pi^-, K^+K^-, \dots$ are experimentally challenging since the corresponding $\mathcal{B} \times (\text{detection efficiency})$ is expected to be at most of $\mathcal{O}(1\%)$. Therefore the original Gronau–Wyler method [4] will unfortunately be very difficult in practice.

7.4.1.2 A method using $B_d \rightarrow DK^*$ decays

A variant of the determination of γ discussed above was proposed by Dunietz [27]. It uses the decays $B^0 \rightarrow D^0_+ K^{*0}$, $B^0 \rightarrow \bar{D}^0_+ K^{*0}$, $B^0 \rightarrow D^0_+ K^{*0}$ and their charge conjugates. Since these modes are “self-tagging” through $K^{*0} \rightarrow K^+\pi^-$, no time-dependent measurements are needed in this method, although neutral B_d decays are involved. Compared to the Gronau–Wyler approach [4], both $B^0 \rightarrow \bar{D}^0_+ K^{*0}$ and $B^0 \rightarrow D^0_+ K^{*0}$ are color-suppressed, *i.e.*,

$$\frac{|A(B^0 \rightarrow D^0_+ K^{*0})|}{|A(B^0 \rightarrow \bar{D}^0_+ K^{*0})|} \approx R_b \frac{a_2}{a_2} \approx 0.36. \quad (7.22)$$

Consequently the amplitude triangles are probably not as squashed as in the $B^\pm \rightarrow DK^\pm$ case. The corresponding branching ratios are expected to be of $\mathcal{O}(10^{-5})$. Unfortunately, one also has to deal with the difficulties of detecting the neutral D meson CP eigenstate D^0_+ .

7.4.1.3 Another method using $B^\pm \rightarrow DK^\pm$ decays

Another method has been proposed [5] to overcome the problems discussed in the previous section. In this approach, the decay chains $B^- \rightarrow K^- D^0 [\rightarrow f]$ and $B^- \rightarrow K^- \bar{D}^0 [\rightarrow f]$, with f denoting a doubly Cabibbo-suppressed (Cabibbo-favored) non- CP -final eigenstate of D^0 (\bar{D}^0), were considered. In this method, one *makes use of* the large interference effects discussed above which spoil the hadronic tag of the \bar{D}^0 in the original Gronau–Wyler method. Examples of such decays are the final states $f = K^+ \pi^-$, $K \pi \pi$. Here, in contrast to the case of $B^- \rightarrow D^0_+ K^-$, both contributing decay amplitudes should be of comparable size, and potentially large CP -violating asymmetries proportional to the rate difference $\mathcal{B}(B^+ \rightarrow K^+[\bar{f}]) - \mathcal{B}(B^- \rightarrow K^-[f])$ are expected. Since several hadronic final states f of neutral D mesons with different strong phases can be considered, measurement of the small branching ratio $\mathcal{B}(B^- \rightarrow K^- \bar{D}^0)$, is not required in order to extract γ . Following Ref. [5], the relevant formulae can be written as

$$d(K, f_i) = a(K) c(f_i) + b(K) c(\bar{f}_i) + 2\sqrt{a(K)b(K)c(f_i)c(\bar{f}_i)} \cos(\zeta_i + \gamma) \quad (7.23)$$

$$\bar{d}(K, f_i) = a(K) c(f_i) + b(K) c(\bar{f}_i) + 2\sqrt{a(K)b(K)c(f_i)c(\bar{f}_i)} \cos(\zeta_i - \gamma), \quad (7.24)$$

where

$$a(K) \equiv \mathcal{B}(B^- \rightarrow K^- D^0), \quad b(K) \equiv \mathcal{B}(B^- \rightarrow K^- \bar{D}^0), \quad c(f) \equiv \mathcal{B}(D^0 \rightarrow f) \quad (7.25)$$

$$c(\bar{f}_i) \equiv \mathcal{B}(D^0 \rightarrow \bar{f}_i), \quad d(K, f_i) \equiv \mathcal{B}(B^- \rightarrow K^-[f_i]), \quad \bar{d}(K, f_i) \equiv \mathcal{B}(B^+ \rightarrow K^+[\bar{f}_i]), \quad (7.26)$$

and ζ_i denotes a CP -conserving strong rescattering phase (consisting both of strong B and D decay phases) and i labels a specific final state f_i . Since CP violation in the D system is very tiny within the Standard Model, $\mathcal{B}(D^0 \rightarrow f_i) = \mathcal{B}(\bar{D}^0 \rightarrow \bar{f}_i)$. In general, each possible final state f_i will have a different value of ζ_i . Choosing two different final states f_1 and f_2 , gives a set of four equations corresponding to (7.23) and (7.24) for $i = 1, 2$. Assuming that $a(K)$ and the D^0 branching ratios $c(f_i)$ and $c(\bar{f}_i)$ will be known accurately by the time $d(K, f_i)$ and $\bar{d}(K, f_i)$ are measured, these four equations determine the four unknowns γ , ζ_1 , ζ_2 and $b(K)$. It is interesting to note that one also obtains the value of the branching ratio $b(K)$, which spoiled the original Gronau–Wyler method, as a by-product. These equations will be nondegenerate if either $c(f_1)/c(\bar{f}_1) \neq c(f_2)/c(\bar{f}_2)$ or $\zeta_1 \neq \zeta_2$, which will occur if both f_1 and f_2 are not CP eigenstates, or if f_1 is a CP eigenstate and f_2 is not. The experimental feasibility studies discussed in the following subsection, focus on this variant of the Gronau–Wyler method. To summarize briefly the major problems of this approach: it involves small “total” branching ratios at the 10^{-7} level or even smaller, many channels have to be measured and an accurate determination of the relevant D branching ratios is essential. The limitations arising from these problems will become clearer in the following subsection.

7.4.2 Experimental Feasibility Studies

The previous section describes the extraction of the CKM angle γ from the amplitudes for $B \rightarrow D^0 K$ decays. The actual experimental measurements are of the combined rates for $B \rightarrow D^0 K$ and the subsequent D^0 decay, meaning the magnitude of the amplitude product $A_B A_D$. The D^0 amplitude must be known or measured. There is an additional strong (non- CP -violating) phase from the D^0 ; however, as the strong phase for the B decay is unknown and must be determined experimentally, the D^0 phase simply adds to this and so does not effect the measurement method. Note, several as yet unmeasured Cabibbo-suppressed D^0 decay branching ratios are used in this study; prospects for their estimation are discussed in Section 12.1.4. It is assumed in the following that they have been measured with an accuracy such that their contribution to the error on γ is negligible.

The differences between the charged and neutral B decays to $D^0 K$ mean that different experimental approaches need to be taken in the two cases. To set the scene, Table 7-1 lists the assumptions used for the branching ratios of the relevant decay modes for this study. Some of these are known and the rest are thought to be reasonable estimates.

For B^0 , the K will only be self-tagging (and hence not require further analysis of the other B in the event) in the case of $K^{*0} \rightarrow K^+ \pi^-$. The decay $B^0 \rightarrow D^{*0} K^{*0}$ occurs in a mixture of orbital angular momentum states and so would require a spin decomposition. Since this requires a larger sample statistically, then this approach is neglected here and only $B^0 \rightarrow D^0 K^{*0}$ and $\bar{D}^0 K^{*0}$ decays are considered. As previously explained, these are both color-suppressed decays and the branching ratios are expected to be $\sim 10^{-6}$ – 10^{-5} . It is sufficient to measure the rate when the D^0 or \bar{D}^0 decays through a Cabibbo-allowed decay, such as $D^0 \rightarrow K^- \pi^+$, where the interference from the doubly Cabibbo-suppressed decay of the other mode is relatively small ($\lesssim 1\%$). Hence, both the amplitudes A_1 and A_2 of the relevant triangle, defined in Section 7.3, are determined directly from the data for the B^0 . The remaining amplitudes, A_3 for the B decay and A_4 for the \bar{B} , need to be measured from a decay with a substantial asymmetry. A decay such as $K^- \pi^+$ is not useful, for the reasons outlined above; one of the two decays is doubly Cabibbo-suppressed and so gives a small interference. However, D^0 decays such as $K_s^0 \pi^0$ are attractive since they have equal rates from both the D^0 and the \bar{D}^0 and so give sizable interference.

The B^+ decays to $D^0 K^+$ are quite different. Here, all K modes are self-tagging as the sign of the K determines the sign of the B . Hence, K^+ , $K^{*+} \rightarrow K_s^0 \pi^+$ and $K^{*+} \rightarrow K^+ \pi^0$ are all in principle usable. In addition, in order to avoid a spin analysis, any combination except $D^{*0} K^{*+}$ is acceptable. However, in contrast with the B^0 case, the rates for $B^+ \rightarrow \bar{D}^0 K^+$ and $B^+ \rightarrow D^0 K^+$ are expected to be very different, as the latter is both color and CKM suppressed; the expected rates are $\sim 10^{-4}$ and 10^{-6} , respectively. Hence, to measure A_1 is straightforward by measuring the $B^+ \rightarrow \bar{D}^0 K^+$ rate with the \bar{D}^0 to a Cabibbo-allowed decay such as $\bar{D}^0 \rightarrow K^+ \pi^-$. However, for $B^+ \rightarrow D^0 K^+$, the Cabibbo-allowed decays of the D^0 are comparable to the doubly Cabibbo-suppressed decays from the \bar{D}^0 and so a clean determination of A_2 is not possible with

Table 7-1. Assumed branching ratios for $B \rightarrow DK$ decays.

Mode	Branching ratio
$B^+ \rightarrow \bar{D}^0 K^+$	4×10^{-4}
$B^+ \rightarrow D^0 K^+$	2×10^{-6}
$B^+ \rightarrow \bar{D}^0 K^{*+}$	12×10^{-4}
$B^+ \rightarrow D^0 K^{*+}$	6×10^{-6}
$B^+ \rightarrow \bar{D}^{*0} K^+$	4×10^{-4}
$B^+ \rightarrow D^{*0} K^+$	2×10^{-6}
$B^0 \rightarrow \bar{D}^0 K^{*0}$	9×10^{-6}
$B^0 \rightarrow D^0 K^{*0}$	3×10^{-6}
$D^{*0} \rightarrow D^0 \pi^0$	0.62
$D^{*0} \rightarrow D^0 \gamma$	0.38
$D^0 \rightarrow K^- \pi^+$	0.038
$D^0 \rightarrow K^- \pi^+ \pi^0$	0.14
$D^0 \rightarrow K^- \pi^+ \pi^+ \pi^-$	0.075
$D^0 \rightarrow K^+ \pi^-$	3×10^{-4}
$D^0 \rightarrow K^+ \pi^- \pi^0$	1×10^{-3}
$D^0 \rightarrow K^+ \pi^- \pi^+ \pi^-$	6×10^{-4}
$D^0 \rightarrow K_s^0 \pi^0$	0.011
$D^0 \rightarrow K_s^0 \pi^+ \pi^-$	0.027
$D^0 \rightarrow K_s^0 \pi^0 \pi^+ \pi^-$	0.050

hadronic decays of the D^0 . In principle, the semileptonic decay modes such as $D^0 \rightarrow \mu^+ \nu_\mu K^-$ can cleanly determine A_2 as no interference from the \bar{D}^0 is possible. However, experimentally this is difficult due to the very low combined branching ratio ($\sim 10^{-7}$) coupled with the lack of any mass constraint because of the neutrino. Hence, the B^+ is a case where the magnitude of A_2 probably needs to be left as a parameter to be determined by measuring two (or more) triangles, as described in Section 7.3. For the modes to be used to measure A_3 and A_4 , then the large difference in the D^0 and \bar{D}^0 decay amplitudes means the overall amplitudes of a doubly Cabibbo-suppressed \bar{D}^0 decay and a Cabibbo-allowed D^0 decay are similar and so give a significant interference effect. Therefore, decays such as $K^- \pi^+$ are used.

The preliminary study presented here was based on the `Aslund` simulation. For charged $K^{(*)}$, the states K^\pm and $K^{*\pm} \rightarrow K_s^0 \pi^\pm$ and $K^\pm \pi^0$ were used. Here and in all cases below, only the

$K_S^0 \rightarrow \pi^+\pi^-$ decay mode was used. For the neutral B , the $K^{*0} \rightarrow K^+\pi^-$ mode was used. K^\pm candidates were selected from information from the DIRC and dE/dx in the drift chamber. K_S^0 candidates were selected from all pairs of oppositely-charged pion candidates, for which the invariant mass at the vertex position was between 0.480 and 0.515 GeV/c^2 . Candidate π^0 's were formed from all pairs of clusters in the calorimeter. The invariant mass of the pair was required to be between 0.12 and 0.15 GeV/c^2 . Finally, $K^{*\pm}$ and K^{*0} candidates were required to have invariant masses between 0.8 and 1.0 GeV/c^2 . The efficiency for selecting a K^\pm was 77%, a $K^{*\pm}$ was 19% and a K^{*0} was 61%, including the branching ratios of the subsequent decays.

The D^0 candidates were reconstructed in the following modes; $K^\pm\pi^\mp$, $K^\pm\pi^\mp\pi^0$, $K^\pm\pi^\mp\pi^+\pi^-$, $K_S^0\pi^0$, $K_S^0\pi^+\pi^-$ and $K_S^0\pi^0\pi^+\pi^-$. The cuts to select the K^\pm , K_S^0 and π^0 candidates are described above. The D^0 invariant mass resolution was found to be 5-10 MeV/c^2 and the D^0 candidates were required to have a mass between 1.84 and 1.89 GeV/c^2 . Before being used further, all accepted D^0 candidates were constrained to the measured D^0 mass of 1.8645 GeV/c^2 . The total efficiency for reconstructing a D^0 was estimated to be 6%.

The D^{*0} selection used these reconstructed D^0 candidates (except the K_S^0 modes) with either a π^0 or a photon. All clusters in the calorimeter were considered as photon candidates and D^{*0} candidates were formed from all combinations of a D^0 and a π^0 or photon with an invariant mass between 2.005 and 2.010 GeV/c^2 (for the π^0 decay) or 2.000 and 2.015 GeV/c^2 (for the photon decay). The D^{*0} candidates were constrained to have a mass of 2.0067 GeV/c^2 before being used to reconstruct a B^+ candidate.

In order to form B^0 candidates, all combinations of K^{*0} with any D^0 candidates were used, giving a total of six combinations, as listed in Table 7-2. The B^0 invariant mass for one of these modes, the decay $D^0 \rightarrow K^-\pi^+$, is shown in Fig. 7-5, where the mass resolution is found to be $\sigma_{m_B} \simeq 10 \text{ MeV}/c^2$. The B^0 candidate formed was required to have a mass between 5.25 and 5.32 GeV/c^2 and momentum in the center-of-mass of between 200 and 450 MeV/c . The resulting B^0 reconstruction efficiencies are given in Table 7-2, where the efficiency is given for

Table 7-2. Efficiencies in percent for $B^0 \rightarrow D^0 K^{*0}$ channels.

B^0 Decay	D^0 Decay	K^{*0} decay	Efficiency (%)
$D^0 K^{*0}$	$K^-\pi^+$	$K^+\pi^-$	46
$D^0 K^{*0}$	$K^-\pi^+\pi^0$	$K^+\pi^-$	28
$D^0 K^{*0}$	$K^-\pi^+\pi^+\pi^-$	$K^+\pi^-$	36
$D^0 K^{*0}$	$K_S^0\pi^0$	$K^+\pi^-$	14
$D^0 K^{*0}$	$K_S^0\pi^+\pi^-$	$K^+\pi^-$	20
$D^0 K^{*0}$	$K_S^0\pi^+\pi^-\pi^0$	$K^+\pi^-$	16

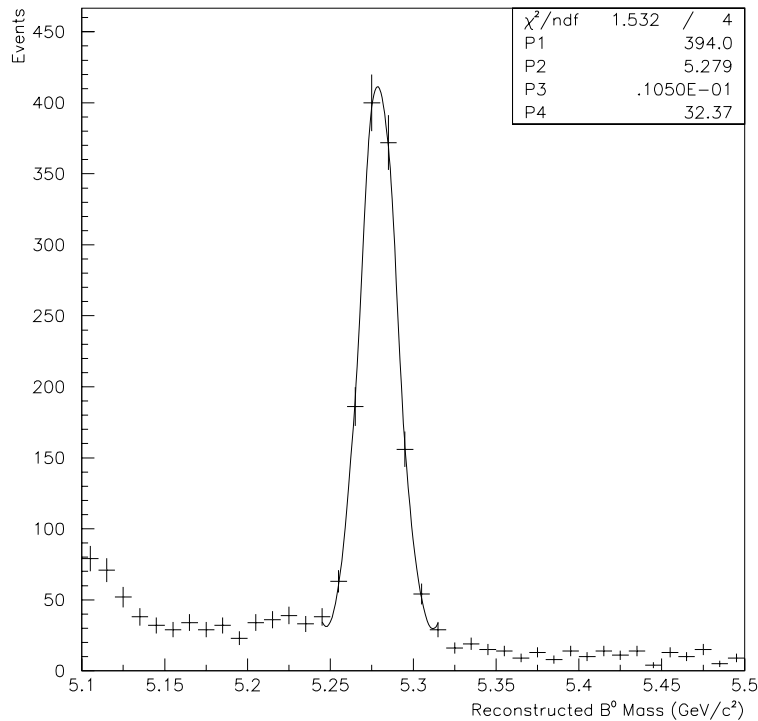


Figure 7-5. Invariant mass peak for $B^0 \rightarrow D^0 K^{*0}$, with $D^0 \rightarrow K^- \pi^+$ and $K^{*0} \rightarrow K^+ \pi^-$.

the case where all the subsequent decays to the given channels are specified. The efficiencies for the equivalent Cabibbo-suppressed D^0 decays are taken to be the same as for the Cabibbo-allowed decays. The overall efficiency for selecting a B^0 is approximately the product of the efficiencies for the D^0 and K^{*0} candidates.

The cuts applied were very loose, as the signals are expected to have small branching ratios. In order to give some feeling for the uncertainty in the efficiencies, the analysis was redone with `BBsim` and full reconstruction for the decay chain $B^0 \rightarrow D^0 K^{*0}$, $D^0 \rightarrow K^- \pi^+$, $K^{*0} \rightarrow K^+ \pi^-$. This yielded an efficiency of 23%, which indicates the above figures may be optimistic at the level of a factor of two, though the reconstruction code is still being improved.

B^+ candidates were formed from all combinations of a K^+ with a $D^{(*)0}$ or a K^{*+} with a D^0 , where the D^0 decayed to a K^\pm state. The resulting 15 final states are listed in Table 7-3. The B^+ candidate formed was required to satisfy the same cuts as in the case of the B^0 candidate. The resulting B efficiencies are shown in Table 7-3, where again, the efficiencies are mainly determined from the efficiencies for the $D^{(*)0}$ and K .

A nominal BABAR year provides an integrated luminosity of 30 fb^{-1} , which yields ~ 32 million $B\bar{B}$ events, assumed to be divided equally between charged and neutral B s. The resulting numbers of identified B^0 events per year at design luminosity is given in Table 7-4. For the channels with

Table 7-3. Efficiencies in percent for $B^+ \rightarrow D^{(*)0} K^{(*)+}$ channels.

B^+ decay	$D^{(*)0}$ decay	K^{*+} decay	Efficiency (%)
$D^0 K^+$	$D^0 \rightarrow K^- \pi^+$		53
$D^0 K^+$	$D^0 \rightarrow K^- \pi^+ \pi^0$		38
$D^0 K^+$	$D^0 \rightarrow K^- \pi^+ \pi^+ \pi^-$		43
$D^0 K^{*+}$	$D^0 \rightarrow K^- \pi^+$	$K^+ \pi^0$	34
$D^0 K^{*+}$	$D^0 \rightarrow K^- \pi^+ \pi^0$	$K^+ \pi^0$	22
$D^0 K^{*+}$	$D^0 \rightarrow K^- \pi^+ \pi^+ \pi^-$	$K^+ \pi^0$	23
$D^0 K^{*+}$	$D^0 \rightarrow K^- \pi^+$	$K_S^0 \pi^+$	16
$D^0 K^{*+}$	$D^0 \rightarrow K^- \pi^+ \pi^0$	$K_S^0 \pi^+$	12
$D^0 K^{*+}$	$D^0 \rightarrow K^- \pi^+ \pi^+ \pi^-$	$K_S^0 \pi^+$	13
$D^{*0} K^+$	$D^{*0} \rightarrow D^0 \pi^0, D^0 \rightarrow K^- \pi^+$		25
$D^{*0} K^+$	$D^{*0} \rightarrow D^0 \pi^0, D^0 \rightarrow K^- \pi^+ \pi^0$		12
$D^{*0} K^+$	$D^{*0} \rightarrow D^0 \pi^0, D^0 \rightarrow K^- \pi^+ \pi^+ \pi^-$		18
$D^{*0} K^+$	$D^{*0} \rightarrow D^0 \gamma, D^0 \rightarrow K^- \pi^+$		53
$D^{*0} K^+$	$D^{*0} \rightarrow D^0 \gamma, D^0 \rightarrow K^- \pi^+ \pi^0$		28
$D^{*0} K^+$	$D^{*0} \rightarrow D^0 \gamma, D^0 \rightarrow K^- \pi^+ \pi^+ \pi^-$		38

significant interference effects, the values $\delta = 0^\circ$ and $\gamma = 90^\circ$ are used. It should be remembered that at least one decay mode from each of the three sections of this table must be measured to yield the amplitudes needed to reconstruct the triangle.

Preliminary studies suggest that the main background contribution is from continuum events, particularly $c\bar{c}$ events, which contain real $D^{(*)0}$ particles. Background from $B\bar{B}$ events is relatively small, despite also containing a large number of $D^{(*)0}$ s. For example, one possible contribution is from $D^{*0} \pi^\pm$, where the π^\pm is misidentified as a K^\pm and so is reconstructed as a $D^0 K^\pm$ candidate with approximately the right B mass. However, although $\mathcal{B}(B^+ \rightarrow D^{*0} \pi^+)$ is an order of magnitude greater than $\mathcal{B}(B^+ \rightarrow D^0 K^+)$, the particle identification systems of BaBar should be able to reject all but a few percent of the kaons, reducing this background to tolerable levels. With the cuts listed above, the background is at least an order of magnitude larger than the signals given in Table 7-4 for any of the decay modes. It is not clear that the background can be reduced sufficiently for this measurement to be feasible if the branching ratios in Table 7-1 are realistic. However, it is interesting to calculate what the errors on the angle γ would be in the absence of background, given the above efficiencies. This is done below assuming a total integrated luminosity of 300 fb^{-1} . A “central” value of $\delta = 0^\circ$ and $\gamma = 90^\circ$ has been used. Only the

Table 7-4. Events per nominal BaBar year for $B^0 \rightarrow D^0 K^{*0}$ channels.

B^0 decay	D^0 decay	K^{*0} decay	Number of events/year
$D^0 K^{*0}$	$K^- \pi^+$	$K^+ \pi^-$	1.6
$D^0 K^{*0}$	$K^- \pi^+ \pi^0$	$K^+ \pi^-$	3.6
$D^0 K^{*0}$	$K^- \pi^+ \pi^+ \pi^-$	$K^+ \pi^-$	2.5
$\bar{D}^0 K^{*0}$	$K^+ \pi^-$	$K^+ \pi^-$	0.6
$\bar{D}^0 K^{*0}$	$K^+ \pi^- \pi^0$	$K^+ \pi^-$	1.2
$\bar{D}^0 K^{*0}$	$K^+ \pi^- \pi^+ \pi^-$	$K^+ \pi^-$	0.9
$(D^0/\bar{D}^0)K^{*0}$	$K_S^0 \pi^0$	$K^+ \pi^-$	0.2
$(D^0/\bar{D}^0)K^{*0}$	$K_S^0 \pi^+ \pi^-$	$K^+ \pi^-$	0.7
$(D^0/\bar{D}^0)K^{*0}$	$K_S^0 \pi^+ \pi^- \pi^0$	$K^+ \pi^-$	1.1

case of the B^0 will be considered, as the B^+ measurement has many more free parameters. The amplitude A_1 is measured from the Cabibbo-allowed \bar{D}^0 decays; this provides a relative error on A_1 , $\sigma_{A_1}/A_1 = 0.04$. Similarly, A_2 is measured from the Cabibbo-allowed decays of D^0 , with $\sigma_{A_2}/A_2 = 0.06$. The total amplitudes A_3 and A_4 are directly measured using the $K_S^0 n\pi$ final states; the events from these different decays cannot be simply combined as the strong phase could be different for each. For the decay $K_S^0 \pi^+ \pi^- \pi^0$, which yields the most accurate value for γ , the relative error would be $\sigma_{A_3}/A_3 = 0.15$, with the same value for A_4 since the two amplitudes are equal for $\delta = 0^\circ$ and $\gamma = 90^\circ$. The resulting error on γ is then $\sigma_\gamma = 14^\circ$. The other two modes, $K_S^0 \pi^0$ and $K_S^0 \pi^+ \pi^-$, give $\sigma_\gamma = 26^\circ$ and $\sigma_\gamma = 16^\circ$, respectively. As described in Section 7.3, the value of the error depends strongly on the assumed values not only of γ but also of the strong-phase difference, δ . The error is clearly also a function of the assumed branching ratios as listed in Table 7-1, although this dependence is less sensitive for reasonable variations.

The B^+ case requires at least two decay modes to be measured with different strong phases; there are many variables in such combined measurements. As pointed out in Section 7.3, if the strong phases are almost equal, then the resulting error on γ will be very large. As this is theoretically the most favored situation, no explicit values for σ_γ will be given here. However, it can be seen from the tables in this section that the numbers of events for B^+ will be similar to B^0 , at least for the interference modes which dominate the statistical error. Therefore, if the strong phases do turn out to have a reasonably large difference, both from each other and from γ , then errors on γ of approximately the same size would be expected.

More optimistic numbers were recently found by the BELLE collaboration [28], at least partly due to their use of a much larger branching ratio for the $B^0 \rightarrow \bar{D}^0 K^{*0}$ decay.

7.5 Methods Using Flavor Symmetries

The previous section dealt with amplitude relations that are valid exactly. The relations used in this section arise from flavor symmetries of strong interactions and certain dynamical assumptions.

7.5.1 Theoretical Framework

In a series of interesting papers [6, 7], Gronau, Hernández, London and Rosner (GHLR) pointed out that the $SU(3)$ flavor symmetry of strong interactions [9] can be combined with certain dynamical assumptions, *e.g.*, neglect of annihilation topologies to derive amplitude relations among B decays into $\pi\pi$, πK and $K\bar{K}$ final states. Such relations provide an important tool for determining both weak phases of the CKM matrix and strong final-state interaction phases. To this end, only the corresponding branching ratios have to be measured.

In order to review this approach, consider the “state of the art” available about four years ago, when these relations were proposed. At that time it was assumed that electroweak penguins play a very minor role in nonleptonic B decays and consequently their contributions were not taken into account. Within that approximation, the decay amplitudes for $B \rightarrow \pi\pi, \pi K, K\bar{K}$ transitions can be represented in the limit of an exact $SU(3)$ flavor symmetry in terms of five reduced matrix elements. This decomposition can also be performed in terms of diagrams. At the quark level one finds six different topologies of diagrams contributing to $B \rightarrow \pi\pi, \pi K, K\bar{K}$ that show up in the corresponding decay amplitudes only as five independent linear combinations [6, 7]. These six topologies include also three non-spectator diagrams, *i.e.*, annihilation processes, where the decaying b quark interacts with its partner anti-quark in the B meson. However, for dynamical reasons, these three contributions are expected to be suppressed relative to the others and thus should play a minor role. Consequently, neglecting these diagrams, three topologies of diagrams suffice to represent the transition amplitudes of B decays into $\pi\pi$, πK and $K\bar{K}$ final states. To be specific, these diagrams, which are shown in Fig. 7-6, describe “color-allowed” and “color-suppressed” current–current, *i.e.*, “tree,” processes T (T') and C (C'), respectively, and QCD penguins P (P'). The unprimed amplitudes denote strangeness-preserving decays, whereas the primed amplitudes indicate strangeness-changing transitions [6, 7].

Consider the decays $B^+ \rightarrow \pi^+\pi^0, \pi^+K^0, \pi^0K^+$, *i.e.*, the “original” GRL method [6], as an example. Neglecting both electroweak penguins, which will be discussed in more detail below, and the dynamically suppressed non-spectator contributions mentioned above, GHLR found

$$\begin{aligned}\sqrt{2}A(B^+ \rightarrow \pi^+\pi^0) &= -(T + C) \\ A(B^+ \rightarrow \pi^+K^0) &= P' \\ \sqrt{2}A(B^+ \rightarrow \pi^0K^+) &= -(T' + C' + P')\end{aligned}\tag{7.27}$$

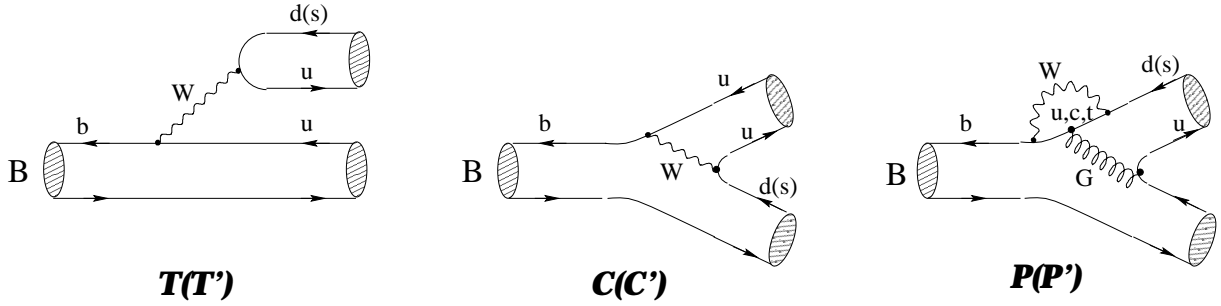


Figure 7-6. Diagrams contributing to $B \rightarrow \pi\pi, \pi K, K\bar{K}$ decays.

with

$$T = |T| e^{i\gamma} e^{i\delta_T}, \quad C = |C| e^{i\gamma} e^{i\delta_C}. \quad (7.28)$$

Here δ_T and δ_C denote CP -conserving strong phases. $SU(3)$ flavor symmetry allows the strangeness-changing amplitudes T' and C' to be obtained from the strangeness-preserving ones:

$$\frac{T'}{T} \approx \frac{C'}{C} \approx \lambda \frac{f_K}{f_\pi} \equiv r_u, \quad (7.29)$$

where f_K and f_π take into account factorizable $SU(3)$ breaking corrections. It is an easy exercise to combine the decay amplitudes given in (7.27) appropriately to derive the relations

$$\sqrt{2} A(B^+ \rightarrow \pi^0 K^+) + A(B^+ \rightarrow \pi^+ K^0) = r_u \sqrt{2} A(B^+ \rightarrow \pi^+ \pi^0) \quad (7.30)$$

$$\sqrt{2} A(B^- \rightarrow \pi^0 K^-) + A(B^- \rightarrow \pi^- \bar{K}^0) = r_u \sqrt{2} A(B^- \rightarrow \pi^- \pi^0), \quad (7.31)$$

which can be represented as two triangles in the complex plane. If one measures the branching ratios for the corresponding six decays, these triangles can easily be constructed. Their relative orientation is usually fixed by assuming $A(B^+ \rightarrow \pi^+ K^0) = A(B^- \rightarrow \pi^- \bar{K}^0)$. The origin of this relation is as follows: a generic $\bar{b} \rightarrow \bar{s}$ QCD penguin amplitude P' , which governs the ‘‘penguin’’ decay $B^+ \rightarrow \pi^+ K^0$, can be expressed as

$$P' = \left[1 - \Delta P' + \lambda^2 R_b e^{i\gamma} \right] e^{-i\pi} |V_{cb}| |P'_{tu}| e^{i\delta'_{tu}} \quad (7.32)$$

with

$$\Delta P' = \frac{P'_c - P'_u}{P'_t - P'_u}, \quad P'_{tu} \equiv |P'_{tu}| e^{i\delta'_{tu}} = P'_t - P'_u, \quad (7.33)$$

where P'_q denotes strong $\bar{b} \rightarrow \bar{s}$ QCD penguin amplitudes with internal q quarks [11, 29]. Unless certain final state interaction effects play an important role, thereby leading to $\Delta P'$ close to one, the highly CKM suppressed $e^{i\gamma}$ term in (7.32) can be neglected. In this case, there is no CP -violating weak phase present in the $\bar{b} \rightarrow \bar{s}$ QCD penguin amplitude, and

$$A(B^+ \rightarrow \pi^+ K^0) = A(B^- \rightarrow \pi^- \bar{K}^0). \quad (7.34)$$

Figure 7-7 gives an example of a rescattering process affecting this relation. In model calculations using Regge phenomenology to estimate such final state interactions (see, for instance, [30]), one typically finds contributions of the $e^{i\gamma}$ term in (7.32) at the level of 10%, which would lead to direct CP -violating asymmetries in $B^+ \rightarrow \pi^+ K^0$ of the same order of magnitude. Also annihilation topologies may be enhanced considerably through rescattering effects [31]. This issue has been discussed in several recent papers [19, 32]. It is unclear at present to what extent $B \rightarrow \pi K$ decays are affected by such rescattering processes.

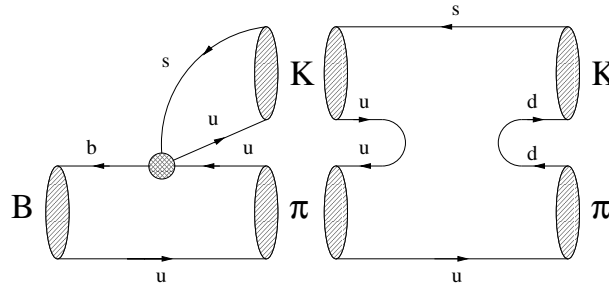


Figure 7-7. An example of a rescattering contribution to the decay $B^+ \rightarrow \pi^+ K^0$ arising from $B^+ \rightarrow \{\pi^0 K^+\} \rightarrow \pi^+ K^0$. The shaded circle represents insertions of the usual current–current operators $Q_{1,2}^u$.

With the assumption of (7.34), the triangles corresponding to (7.30) and (7.31) allow a determination of γ , as can be seen in Fig. 7-8. From a geometrical point of view, this “original” GRL approach [6] is very similar to the $B^\pm \rightarrow DK^\pm$ construction [4] shown in Fig. 7-4. Furthermore, it also involves only charged B decays and therefore neither time-dependent measurements nor tagging are required. In comparison with the Gronau–Wyler method [4], the major advantage of the GRL strategy appears to be that all branching ratios are expected to be of the same order of magnitude $\mathcal{O}(10^{-5})$, *i.e.*, the corresponding triangles are not squashed ones, and that the difficult-to-measure CP eigenstate D_+^0 is not required.

Unfortunately, things are not that simple and — despite its attractiveness — the general GHLR approach [6, 7] to extract CKM phases from $SU(3)$ amplitude relations suffers from theoretical limitations. As discussed above, an important limitation is related to final state interactions, such as those shown in Fig. 7-7. Another more obvious limitation is that the amplitude relations are not valid exactly, as, *e.g.*, (7.16) or (7.17), but suffer from $SU(3)$ -breaking corrections [10]. While factorizable $SU(3)$ breaking can be included straightforwardly through certain meson decay constants or form factors (*e.g.*, (7.29)), nonfactorizable $SU(3)$ -breaking corrections cannot be described in a reliable quantitative way at present. In certain strategies to extract γ — an example is given below — another limitation arises from theoretical uncertainty in contributions from $\bar{b} \rightarrow \bar{d}$ QCD penguin topologies with internal up- and charm-quark exchanges [11]. With notation similar to (7.32) and (7.33), a generic $\bar{b} \rightarrow \bar{d}$ QCD penguin amplitude P can be written as

$$P = \left[e^{-i\beta} - \frac{1}{R_t} \Delta P \right] |V_{td}| |P_{tu}| e^{i\delta_{tu}}, \quad (7.35)$$

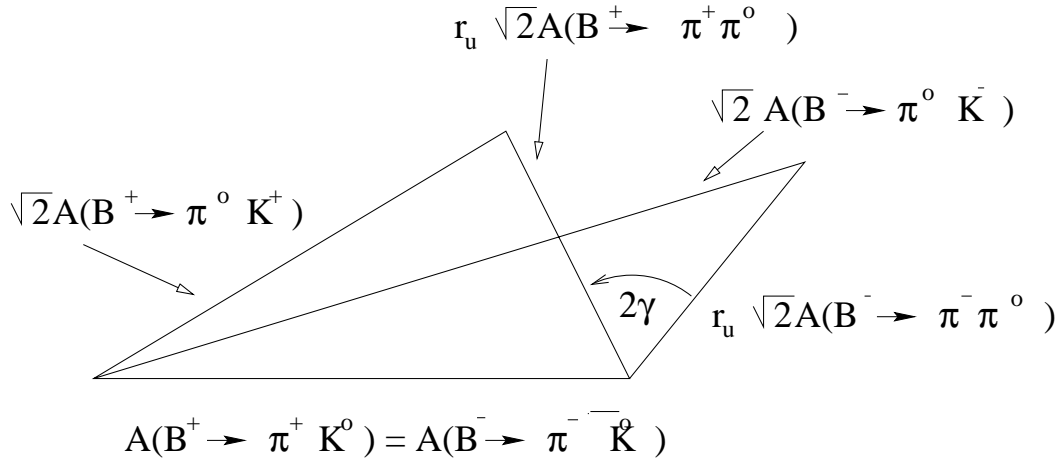


Figure 7-8. Naïve $SU(3)$ triangle relations among $B^+ \rightarrow \pi^+ \pi^0, \pi^+ K^0, \pi^0 K^+$ and charge-conjugate decay amplitudes neglecting electroweak-penguin contributions.

which is very different from the $\bar{b} \rightarrow \bar{s}$ case given in (7.32). The crucial point is that QCD penguin topologies with internal up and charm-quark exchanges affect the phase structure of this amplitude strongly. In particular, the simple relation

$$P = e^{-i\beta} e^{i\delta_P} |P|, \quad (7.36)$$

which would hold if the $\bar{b} \rightarrow \bar{d}$ penguin amplitude were dominated by internal top quarks, may receive large corrections so that P is no longer proportional to the CP -violating phase factor $e^{-i\beta}$ [11].

Remarkably, electroweak penguins [12], which have been neglected in the discussion above, also have a very important impact on some $SU(3)$ constructions, particularly on the “original” GRL method to determine γ . This approach is even *spoiled* by these contributions [13, 14]. The color-allowed “tree” amplitude T' is highly CKM-suppressed by $\lambda^2 R_b \approx 0.02$. Consequently, one expects that the QCD penguin amplitude P' plays the dominant role and that T' and the color-allowed electroweak-penguin amplitude P'_{EW} , which contributes to $B^+ \rightarrow \pi^0 K^+$, are equally important:

$$\left| \frac{T'}{P'} \right| = \mathcal{O}(0.2), \quad \left| \frac{P'_{EW}}{T'} \right| = \mathcal{O}(1). \quad (7.37)$$

In the presence of electroweak penguins, the construction shown in Fig. 7-8 is modified as sketched in Fig. 7-9. If the electroweak-penguin contributions were not there, triangles could be constructed by measuring only the corresponding branching ratios. However, since the electroweak penguins are as important as the T' amplitude and are completely unknown, this construction is unfortunately spoiled by their contributions. A detailed discussion of the issue of electroweak penguins in nonleptonic B decays and strategies for extracting CKM phases is beyond the scope of this discussion. Several solutions have been proposed to solve this “electroweak-penguin problem” (for a recent review, see [8]). Since most of these strategies are quite complicated and appear to be

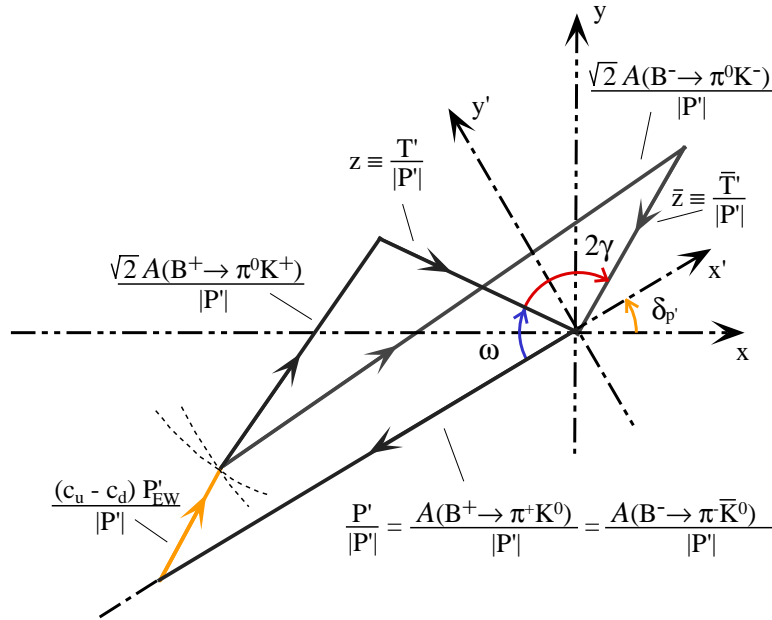


Figure 7-9. The $SU(3)$ triangle relations among $B^+ \rightarrow \pi^+\pi^0, \pi^+K^0, \pi^0K^+$ and charge-conjugate decay amplitudes, which correspond to the “original” GRL construction, in the presence of electroweak-penguin contributions.

very challenging from an experimental point of view, the studies presented here focus on a much simpler approach, which was proposed in [15] and will be the subject of the next subsection.

7.5.2 A Simple Strategy for Extracting γ

The main role in this subsection is played by the decays $B^+ \rightarrow \pi^+K^0, B^0 \rightarrow \pi^-K^+$ and their charge conjugates, originating at lowest order from the diagrams shown in Fig. 7-10. For these transitions, electroweak penguins contribute only in “color-suppressed” form. To simplify the presentation of the basic idea of this approach, electroweak penguins, as well as certain final state interaction effects (see, for instance, Fig. 7-7) which may affect (7.34) sizeably, are first neglected. These contributions are discussed in more detail later.

From Eq. (7.34) and the $SU(2)$ isospin symmetry of strong interactions to relate the QCD penguin contributions, the corresponding decay amplitudes can be written in the GHLR notation [7] as

$$\begin{aligned}
 A(B^+ \rightarrow \pi^+K^0) &= P' = A(B^- \rightarrow \pi^- \bar{K}^0) \\
 A(B^0 \rightarrow \pi^-K^+) &= -(P' + T') \\
 A(\bar{B}^0 \rightarrow \pi^+K^-) &= -(P' + e^{-2i\gamma} T').
 \end{aligned}
 \tag{7.38}$$

These relations can be represented in the complex plane as shown in Fig. 7-11. Here (a) corresponds to $A(B^+ \rightarrow \pi^+ K^0) = P' = A(B^- \rightarrow \pi^- \bar{K}^0)$, (b) to $A(B^0 \rightarrow \pi^- K^+)$, (c) to $A(\bar{B}^0 \rightarrow \pi^+ K^-)$, and the dashed lines (d) and (e) to the color-allowed “tree” amplitudes T' and $e^{-2i\gamma} T'$, respectively. The dotted lines (f)–(h) are discussed below. From a geometrical point of view, this construction is very similar to the “original” GRL approach [6]. The major difference is related to the electroweak-penguin contributions, which spoil the GRL strategy, as was discussed above [13, 14].

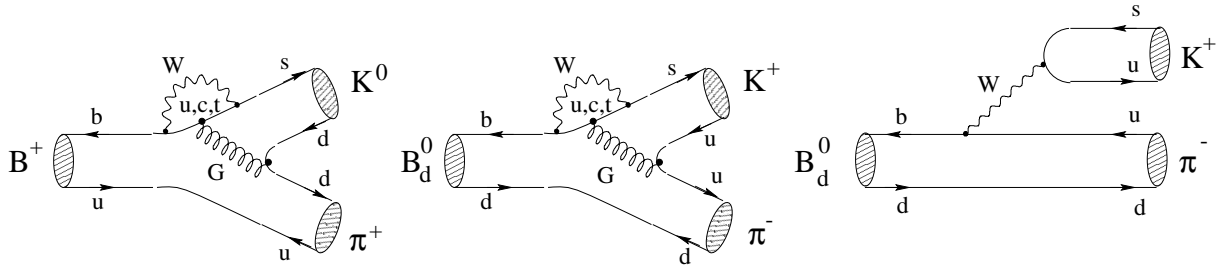


Figure 7-10. The lowest order Feynman diagrams contributing to $B^+ \rightarrow \pi^+ K^0$ and $B^0 \rightarrow \pi^- K^+$.

Such $B_{u,d} \rightarrow \pi K$ decays were also considered in [33]. There it was shown that, by combining their branching ratios appropriately with the CP -violating observables of a time-dependent measurement of $B^0 \rightarrow \pi^+ \pi^-$ and by assuming that the weak phase of the $\bar{b} \rightarrow \bar{d}$ QCD penguin amplitude is given by β (see (7.36)), a simultaneous extraction of α and γ may become possible. One of the major problems of this approach is, that the latter assumption, corresponding to top-quark dominance of QCD penguins, may fail [11].

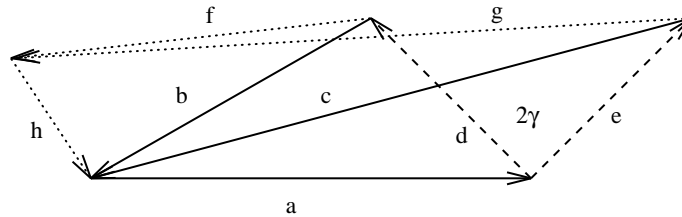


Figure 7-11. $SU(2)$ isospin relations among $B^+ \rightarrow \pi^+ K^0$, $B^0 \rightarrow \pi^- K^+$ and charge conjugates. The labels are explained in the text.

In the following discussion, a different way of combining the information provided by the branching ratios of the $B_{u,d} \rightarrow \pi K$ modes listed above is the focus. If the length $|T'|$ of the dashed lines (d) and (e) in Fig. 7-11 could be fixed, one could then extract γ with the help of the construction shown in this figure. An approximate way to fix this amplitude is to neglect color-suppressed current–current operator contributions to $B^+ \rightarrow \pi^+ \pi^0$ and to use the $SU(3)$ flavor symmetry to relate the color-allowed current–current amplitude of that decay to T' :

$$|T'| \approx \lambda \frac{f_K}{f_\pi} \sqrt{2} |A(B^+ \rightarrow \pi^+ \pi^0)|. \quad (7.39)$$

Another approach to obtain information on $|T'|$ is to use a model calculation. The factorization assumption gives

$$|T'|_{\text{fact}} = \frac{G_F}{\sqrt{2}} \lambda |V_{ub}| a_1 \left(M_{B_d}^2 - M_\pi^2 \right) f_K F_{B\pi}(M_K^2; 0^+), \quad (7.40)$$

where $F_{B\pi}$ is a quark-current form factor. $|V_{ub}|$ has been measured by CLEO to be $(3.2 \pm 0.8) \times 10^{-3}$. Data from $\bar{B}^0 \rightarrow D^{(*)+} \pi^-$ and $\bar{B}^0 \rightarrow D^{(*)+} \rho^-$ decays imply $a_1 = 1.06 \pm 0.03 \pm 0.06$ [34]. Using the form factor $F_{B\pi}(M_K^2; 0^+) = 0.3$, as obtained in the BSW model [35], one has

$$|T'|_{\text{fact}} = a_1 \times \left[\frac{|V_{ub}|}{3.2 \times 10^{-3}} \right] \times 7.8 \times 10^{-9} \text{ GeV}. \quad (7.41)$$

As pointed out in [16, 17], semileptonic $B^0 \rightarrow \pi^- l^+ \nu_l$ decays also may play an important role in fixing $|T'|$, providing a measurement of the relevant form factor.

Following these lines, it is possible to extract an *approximate* value of γ by measuring only $\mathcal{B}(B^+ \rightarrow \pi^+ K^0) = \mathcal{B}(B^- \rightarrow \pi^- \bar{K}^0)$, $\mathcal{B}(B^0 \rightarrow \pi^- K^+)$, and $\mathcal{B}(\bar{B}^0 \rightarrow \pi^+ K^-)$. Note that the neutral B_d decays are self-tagging modes so that no time-dependent measurements are needed. This strategy is very simple from a geometrical point of view — just triangle constructions — and promising from an experimental point of view since all branching ratios are of the same order of magnitude $\mathcal{O}(10^{-5})$ (for interesting recent feasibility studies, see [16, 17]). The CLEO collaboration has recently reported the first observation of the corresponding decays [20]. These results are discussed further below

The values for γ obtained this way are not exact, as already noted, but suffer from some model-dependence, related in particular to the fact that $|T'|$ has to be fixed. Closer examination shows that T' is not just a simple color-allowed “tree” amplitude — in that case factorization would probably work reasonably well [24] — but actually has a rather complex structure due to final state interaction effects [29]. In particular, it also receives contributions from penguin-like and annihilation topologies due to some subtleties of the isospin symmetry of strong interactions in relating the decays $B^+ \rightarrow \pi^+ K^0$ and $B^0 \rightarrow \pi^- K^+$. These contributions (a detailed discussion is beyond the scope of this presentation) may shift $|T'|$ significantly from its “factorized” value (7.41). Thus, the theoretical uncertainty of this quantity is hard to control if rescattering processes should in fact play an important role [19].

Interestingly, the combined branching ratios for $B^0 \rightarrow \pi^- K^+$ and $B^+ \rightarrow \pi^+ K^0$ allow one to *constrain* the CKM angle γ without any information on $|T'|$, provided the ratio R of these combined branching ratios is found experimentally to be smaller than one [21]. The construction shown in Fig. 7-11 provides even more information. Consider in addition the amplitude relations

$$\sqrt{2} A(B^+ \rightarrow \pi^0 K^+) = - [P' + T' + (c_u - c_d) P'_{\text{EW}}] \quad (7.42)$$

$$\sqrt{2} A(B^- \rightarrow \pi^0 K^-) = - [P' + e^{-2i\gamma} T' + (c_u - c_d) P'_{\text{EW}}], \quad (7.43)$$

where $c_u = +2/3$, $c_d = -1/3$ denote the up- and down-quark charges, and color-suppressed “tree” and electroweak-penguin amplitudes have been neglected [15]. The dotted lines (f) and (g) corresponding to $\sqrt{2} A(B^+ \rightarrow \pi^0 K^+)$ and $\sqrt{2} A(B^- \rightarrow \pi^0 K^-)$, respectively, allow a determination of the dotted line (h) denoting the color-allowed $\bar{b} \rightarrow \bar{s}$ electroweak-penguin amplitude $(c_u - c_d)P'_{EW}$. electroweak penguins are — in contrast to QCD penguins — clearly dominated by internal top-quark exchanges. Thus, the $\bar{b} \rightarrow \bar{d}$ electroweak-penguin amplitude $(c_u - c_d)P_{EW}$ is related in the limit of an exact $SU(3)$ flavor symmetry to the corresponding $\bar{b} \rightarrow \bar{s}$ amplitude through the simple relation

$$(c_u - c_d)P_{EW} = -\lambda R_t e^{-i\beta} (c_u - c_d)P'_{EW}, \quad (7.44)$$

and can be determined from the constructed $(c_u - c_d)P'_{EW}$ amplitude [36]. The knowledge of electroweak-penguin amplitudes is interesting for several reasons. For example, Eq. (7.44), in principle, allows correction for the expected small electroweak-penguin uncertainties in the determination of α from $B \rightarrow \pi\pi$ isospin triangles [15, 36]. Moreover, the experimentally determined $\bar{b} \rightarrow \bar{s}$ electroweak-penguin amplitude P'_{EW} provides information on the question of whether the neglect of the color-suppressed electroweak-penguin contributions to $B^0 \rightarrow \pi^- K^+$ and $B^+ \rightarrow \pi^+ K^0$ is really justified. Also, there are several scenarios for physics beyond the Standard Model where electroweak penguins receive significant contributions; such a measurement provides a test of these scenarios (see Chapter 13).

7.5.3 Constraints from Combined $B_{u,d} \rightarrow \pi K$ Branching Ratios

At present, experimental data on $B_{u,d} \rightarrow \pi K$ decays is starting to become available. The CLEO collaboration has recently published the first results for these modes [20]. So far, however, only results for the *combined* branching ratios

$$\mathcal{B}(B^\pm \rightarrow \pi^\pm K) \equiv \frac{1}{2} \left[\mathcal{B}(B^+ \rightarrow \pi^+ K^0) + \mathcal{B}(B^- \rightarrow \pi^- \bar{K}^0) \right] \quad (7.45)$$

$$\mathcal{B}(B_d \rightarrow \pi^\mp K^\pm) \equiv \frac{1}{2} \left[\mathcal{B}(B^0 \rightarrow \pi^- K^+) + \mathcal{B}(\bar{B}^0 \rightarrow \pi^+ K^-) \right] \quad (7.46)$$

are available with large experimental uncertainties:

$$\mathcal{B}(B^\pm \rightarrow \pi^\pm K) = (2.3_{-1.0}^{+1.1} \pm 0.3 \pm 0.2) \times 10^{-5} \quad (7.47)$$

$$\mathcal{B}(B_d \rightarrow \pi^\mp K^\pm) = (1.5_{-0.4}^{+0.5} \pm 0.1 \pm 0.1) \times 10^{-5}. \quad (7.48)$$

Therefore it is not yet possible to extract a value for γ by using the triangle construction [15, 16] discussed in the previous subsection. However, as was pointed out in [21], from these combined branching ratios one can derive *constraints* on γ , which are of the form

$$0^\circ \leq \gamma \leq \gamma_0 \quad \text{or} \quad 180^\circ - \gamma_0 \leq \gamma \leq 180^\circ, \quad (7.49)$$

and are hence complementary to the range (7.1) for γ arising from the usual indirect fits of the unitarity triangle. The quantity γ_0 in (7.49) depends both on the ratio

$$R \equiv \frac{\mathcal{B}(B_d \rightarrow \pi^\mp K^\pm)}{\mathcal{B}(B^\pm \rightarrow \pi^\pm K)} = \frac{\mathcal{B}(B^0 \rightarrow \pi^- K^+) + \mathcal{B}(\bar{B}^0 \rightarrow \pi^+ K^-)}{\mathcal{B}(B^+ \rightarrow \pi^+ K^0) + \mathcal{B}(B^- \rightarrow \pi^- \bar{K}^0)} \quad (7.50)$$

of the combined branching ratios, and on the amplitude ratio

$$r \equiv \frac{|T'|}{|P'|} \quad (7.51)$$

of the current–current and penguin operator contributions to $B_d \rightarrow \pi^\mp K^\pm$. Neglecting contributions both from rescattering processes (see, *e.g.*, Fig. 7-7) and from color-suppressed electroweak penguins, one finds [21]

$$\gamma_0 = \arccos \left(\frac{1-R}{2r} + \frac{1}{2} r \right). \quad (7.52)$$

Thus, in order to constrain γ , one must not only determine R , but also fix the ratio r of $|T'|$ and $|P'|$. While $|P'|$ can be measured straightforwardly through the $B^+ \rightarrow \pi^+ K^0$ branching ratio, $|T'|$ introduces the same problems and model dependences as in Section 7.5.2. From Fig. 7-12, where the dependence of γ_0 on the amplitude ratio r for various values of R is shown, one sees, however, that this is actually only the case for $R \geq 1$. If R is found to be smaller than one, γ_0 takes

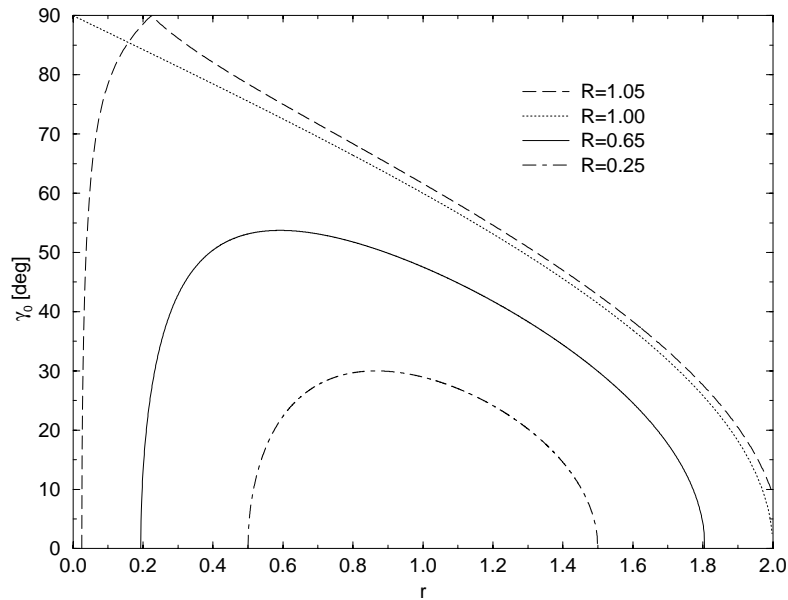


Figure 7-12. The dependence of γ_0 on r for various values of R .

a *maximal* value γ_0^{\max} that is independent of r and is only a function of the measurable ratio R of combined $B_{u,d} \rightarrow \pi K$ branching ratios [21]:

$$\gamma_0^{\max} = \arccos \sqrt{1 - R}. \quad (7.53)$$

In the future, this constraint may become interesting to reduce the allowed region for the apex of the unitarity triangle in the ρ - η plane. See also Ref. [37] for further discussion.

In a recent paper [19], a comprehensive analysis of constraints on γ arising from the observables of $B_{u,d} \rightarrow \pi K$ decays was performed. A general parametrization of the $B^+ \rightarrow \pi^+ K^0$ and $B^0 \rightarrow \pi^- K^+$ decay amplitudes was given, taking into account both rescattering and electroweak-penguin effects. Moreover, generalized constraints on γ were derived, making use not only of the ratio R of combined branching ratios defined in (7.50), but also of the “pseudo-asymmetry”

$$A_0 \equiv \frac{\mathcal{B}(B^0 \rightarrow \pi^- K^+) - \mathcal{B}(\bar{B}^0 \rightarrow \pi^+ K^-)}{\mathcal{B}(B^+ \rightarrow \pi^+ K^0) + \mathcal{B}(B^- \rightarrow \pi^- \bar{K}^0)}. \quad (7.54)$$

It can be shown that R takes a *minimal* value, which is given by the expression

$$R_{\min} = \kappa \sin^2 \gamma + \frac{1}{\kappa} \left(\frac{A_0}{2 \sin \gamma} \right)^2, \quad (7.55)$$

where κ takes into account rescattering and electroweak-penguin effects [19] ($\kappa = 1$ without these contributions). Figure 7-13, shows the dependence of R_{\min} on γ , *i.e.*, $\kappa = 1$, and various values of A_0 . If R is measured to be smaller than one, or if it should become possible to obtain an experimental upper limit $R_{\text{exp}}^{\max} < 1$, a range of γ near 90° would be excluded. With any nonvanishing experimental result for A_0 , an interval around $\gamma = 0^\circ$ and 180° can also be ruled out, while the impact on the excluded region around 90° is rather small, as can be seen in Fig. 7-13.

Measured values of R and A_0 would fix contours in the γ - r plane. Neglecting rescattering and electroweak-penguin effects, one finds

$$r = \sqrt{R - 1 + 2 \cos^2 \gamma \pm 2 \cos \gamma \sqrt{R - \sin^2 \gamma - \frac{A_0^2}{4 \sin^2 \gamma}}}. \quad (7.56)$$

As an example, Figure 7-14 shows the contours corresponding to the value, $R = 0.65$, and various values of A_0 . If r could be fixed, γ could be determined up to a four-fold ambiguity, as can be seen in Fig. 7-14. For $R < 1$, the allowed range for γ can also be read off from the corresponding contours.

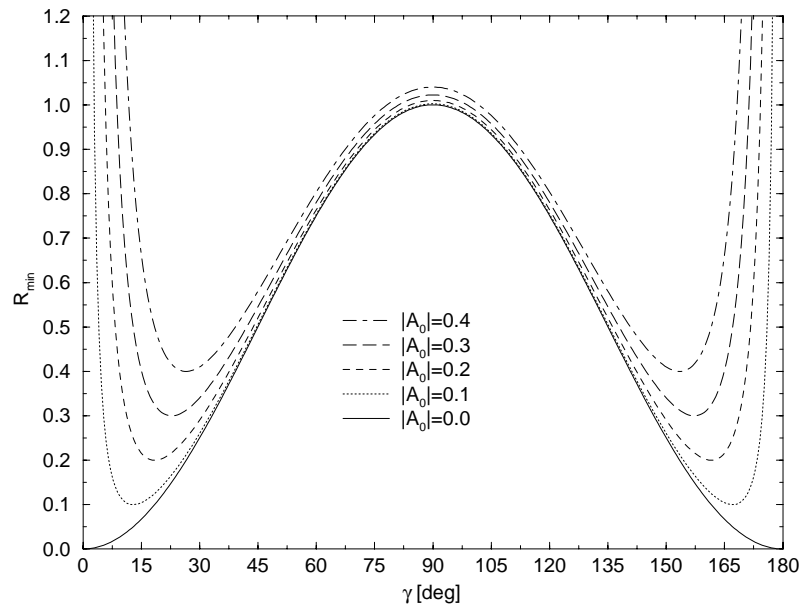


Figure 7-13. The dependence of R_{\min} on the CKM angle γ for various values of the pseudo-asymmetry A_0 , where rescattering and electroweak-penguin effects are neglected.

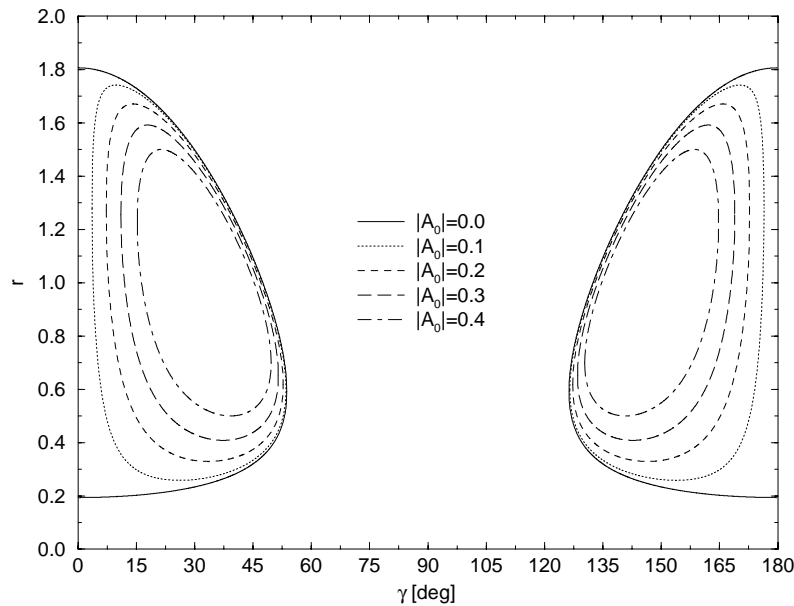


Figure 7-14. The dependence of r on the CKM angle γ for $R = 0.65$ and for various values of the pseudo-asymmetry A_0 , where rescattering and electroweak-penguin effects are neglected.

The impact of contributions from rescattering processes and electroweak penguins has been discussed in great detail in [19]. A measurement of direct CP violation in the mode $B^+ \rightarrow \pi^+ K^0$ would lead to a first experimental constraint on the “strength” of the rescattering effects. Model calculations using Regge phenomenology give $\mathcal{O}(10\%)$ [30] (for other arguments suggesting sizeable CP violation in this decay, see *e.g.*, Refs. [31, 32, 38]). The contributions from such rescattering processes can be included *completely* in the contours in the γ - r plane—and therefore also in the constraints on γ —with the help of the decay $B^+ \rightarrow K^+ \bar{K}^0$, which is related to $B^+ \rightarrow \pi^+ K^0$ by interchanging all d and s quarks, *i.e.*, through the U spin of the $SU(3)$ flavor symmetry. Interestingly, rescattering effects may enhance the combined $B^\pm \rightarrow K^\pm K$ branching ratio by a factor of $\mathcal{O}(10)$ from its short-distance value, $\mathcal{O}(10^{-6})$, so that this channel may be promising from an experimental point of view [19]. The present upper limit from the CLEO collaboration [20] is given by $\mathcal{B}(B^\pm \rightarrow K^\pm K) < 2.1 \times 10^{-5}$.

Although the decay $B^+ \rightarrow K^+ \bar{K}^0$ determines the shift of the contours in the γ - r plane due to rescattering processes, it unfortunately does not show how to take into account these effects in the determination of γ . The latter requires, in contrast to the constraints on γ , some knowledge of r . This quantity, as discussed previously, may be affected considerably by final-state interactions.

For the electroweak penguins, model calculations using factorization to deal with hadronic matrix elements typically give contributions at the 1% level in the case of $B^+ \rightarrow \pi^+ K^0$ and $B^0 \rightarrow \pi^- K^+$ decays, where electroweak penguins contribute only in “color-suppressed” form. This treatment of electroweak penguins may underestimate their importance [16, 31]. An improved theoretical description of the electroweak-penguin amplitude which affects the isospin relations (7.38) between $B^+ \rightarrow \pi^+ K^0$ and $B^0 \rightarrow \pi^- K^+$ has been presented in [19], clarifying also the notion of “color-suppressed” electroweak penguins. This approach does not use questionable assumptions, such as factorization, and only makes use of the general structure of the electroweak-penguin operators and of the isospin symmetry of strong interactions to relate the hadronic matrix elements corresponding to $B^+ \rightarrow \pi^+ K^0$ and $B^0 \rightarrow \pi^- K^+$ transitions. This analysis shows that the importance of electroweak penguins is closely related to the ratio of certain “effective” color factors $a_2^{\text{eff}}/a_1^{\text{eff}}$. Using $|a_2^{\text{eff}}|/|a_1^{\text{eff}}| = 0.25$ gives an enhancement of the relevant electroweak-penguin amplitude by a factor of three with respect to the factorized result. A first step towards constraining this electroweak-penguin amplitude through experimental data is provided by the mode $B^+ \rightarrow \pi^+ \pi^0$. The formulae derived in [19] include the electroweak-penguin contributions in a completely general way, which will be important once a better understanding of color-suppression and rescattering effects in $B_{u,d} \rightarrow \pi K$ decays has been developed.

Although the decays $B^+ \rightarrow \pi^+ K^0$, $B^0 \rightarrow \pi^- K^+$ and their charge conjugates will probably not allow a precision measurement of γ , they are expected to provide a very fertile ground to constrain this CKM angle. An accurate measurement of these modes, as well as of $B^\pm \rightarrow K^\pm K$, is therefore an important goal of the BaBar experiment. Further work is needed to investigate the theoretical errors introduced by the various assumptions in the methods discussed, and to devise methods that limit those errors. This is an active area of theoretical study at present.

7.5.4 Experimental Feasibility Studies

This section contains a discussion of the experimental feasibility of the method outlined in Sections 7.5.2 and 7.5.3, selected among the several approaches proposed in this literature to determine the unitarity angle γ using flavor symmetry.

This particular method relates the penguin amplitude P' , determined by measuring the branching ratio $\mathcal{B}(B^+ \rightarrow \pi^+ K^0) = \mathcal{B}(B^- \rightarrow \pi^- \bar{K}^0)$, with the amplitudes obtained from $\mathcal{B}(B^0 \rightarrow \pi^- K^+)$ and $\mathcal{B}(\bar{B}^0 \rightarrow \pi^+ K^-)$, as shown in Fig. 7-8. Underlying theoretical assumptions are SU(2) symmetry and negligible color-suppressed electroweak penguins. For a determination of γ using the two-triangles approach, however, the knowledge of the sides of length $|T'|$ is required: for this one has to rely on theoretical calculations or on an approximate SU(3) based relationship between $|T'|$ and $\mathcal{B}(B^\pm \rightarrow \pi^\pm \pi^0)$.

The following feasibility study concentrates on the determination of γ in the original approach based on the two triangular relations (Eqs. 7.30 and 7.31), assuming that a reasonable estimate of r can be obtained, for instance from the measurement of $\mathcal{B}(B^\pm \rightarrow \pi^\pm \pi^0)$. This method requires the measurement of the decay rates for $B \rightarrow \pi K$ and $B \rightarrow \pi\pi$ for charged and neutral B mesons, in several different charge combinations. The theoretical expectations for these branching fractions are now beginning to have experimental confirmation; recent results from the CLEO collaboration [20], summarized in Table 7-5, show that these decay modes are well within the reach of BaBar.

Table 7-5. Branching ratios and limits from CLEO. Decay modes are listed according to their correspondence with the amplitudes A_i in the triangular relations, as described in Section 7.3.

Amplitude	Mode	$\epsilon(\%)$	Yield	Signif	$\mathcal{B}(\times 10^{-5})$	UL($\times 10^{-5}$)
$ A_1 $	$K^0 \pi^\pm$	12	$9.2^{+4.3}_{-3.8}$	3.2σ	$2.3^{+1.1}_{-1.0} \pm 0.3 \pm 0.2$	4.0
$ A_2 $	$\pi^\pm \pi^0$	37	$11.3^{+6.3}_{-5.2}$	2.8σ	$0.9^{+0.6}_{-0.5}$	2.0
$ A_3 , A_4 $	$K^\pm \pi^\mp$	44	$21.6^{+6.8}_{-6.0}$	5.6σ	$1.5^{+0.5}_{-0.4} \pm 0.1 \pm 0.1$	

In the first part of this subsection an overview is presented of the efficiencies and backgrounds expected in BaBar for the relevant decay modes. Most of these results are extrapolations from more detailed analyses performed on two-body hadronic decay modes for the extraction of the α unitarity angle, discussed in Section 6.4. The second part of this subsection describes the determination of the expected sensitivity to γ as a function of the accumulated luminosity, using the triangular relations described in Section 7.3 and 7.5.2. Finally some comments are given on the expected theoretical errors of the method.

7.5.4.1 Event selection and backgrounds

Criteria for selecting the following two-body hadronic decays were studied: $B \rightarrow K^\pm \pi^\mp$, corresponding to the amplitudes A_3 and A_4 in the triangular analysis; and $B^\pm \rightarrow K^0 \pi^\pm$ and $\pi^\pm \pi^0$, corresponding to amplitudes A_1 (\bar{A}_1) and A_2 (\bar{A}_2), respectively.

The reconstruction of K^\pm and π^\pm candidates requires charged tracks with good particle identification. K_S^0 mesons are reconstructed from the $K_S^0 \rightarrow \pi^+ \pi^-$ decay, with pairs of oppositely-charged tracks from a common vertex, within an invariant mass window. Candidate π^0 mesons are formed selecting clusters in the electromagnetic calorimeter, not matched with charged tracks, and evaluating their energy and momentum as discussed in Section 6.4.

Two-body decay candidates $K_S^0 \pi^\pm$, $\pi^\pm \pi^0$ and $K^\pm \pi^\mp$ are selected with both kinematic and event-shape variables as described in Section 6.4, where summaries of the selection efficiencies are given. Preliminary background estimates were obtained using the As1 und fast simulation of the detector.

As reported in Section 6.4, the main background contribution is from continuum events. A careful tuning of the kinematic and event-shape selection criteria should reduce backgrounds to the levels in Table 7-6.

Table 7-6. *Expected signal to background ratio N_S/N_B for the selected decays; the assumed branching ratios \mathcal{B} and the efficiencies for signal (ϵ_S) and background (ϵ_B) are also given.*

Amplitude	Mode	$\mathcal{B}(10^{-5})$	ϵ_S	ϵ_B	N_S/N_B
$ A_1 $	$K^0 \pi^\pm$	1.0	0.32	2.6×10^{-6}	$\simeq 1/1$
$ A_2 $	$\pi^\pm \pi^0$	0.5	0.18	2.0×10^{-6}	$\simeq 1/2$
$ A_3 , A_4 $	$K^\pm \pi^\mp$	1.0	0.58	4.0×10^{-6}	$\simeq 1/2$

7.5.4.2 Experimental errors on γ

The lengths of the sides of the triangles in Fig. 7-15 are proportional to the magnitudes of the amplitudes A_1 , A_2 , A_3 , and A_4 of the decay processes listed in Tables 7-5 and 7-6. The common base corresponds to $A_1 = \bar{A}_1$, and two of the other sides have equal lengths ($|A_2| = |\bar{A}_2|$). The different lengths of sides A_3 and A_4 correspond to a CP asymmetry in the rates of the modes $B^0 \rightarrow K^+ \pi^-$ and $\bar{B}^0 \rightarrow K^- \pi^+$. Any given set of measured side lengths implies a four-fold ambiguity in the determination of γ , as indicated in the figure.

After collecting an integrated luminosity of 100 fb^{-1} , corresponding to approximately three years of data collection with nominal PEP-II luminosity, the expected relative errors on the amplitudes

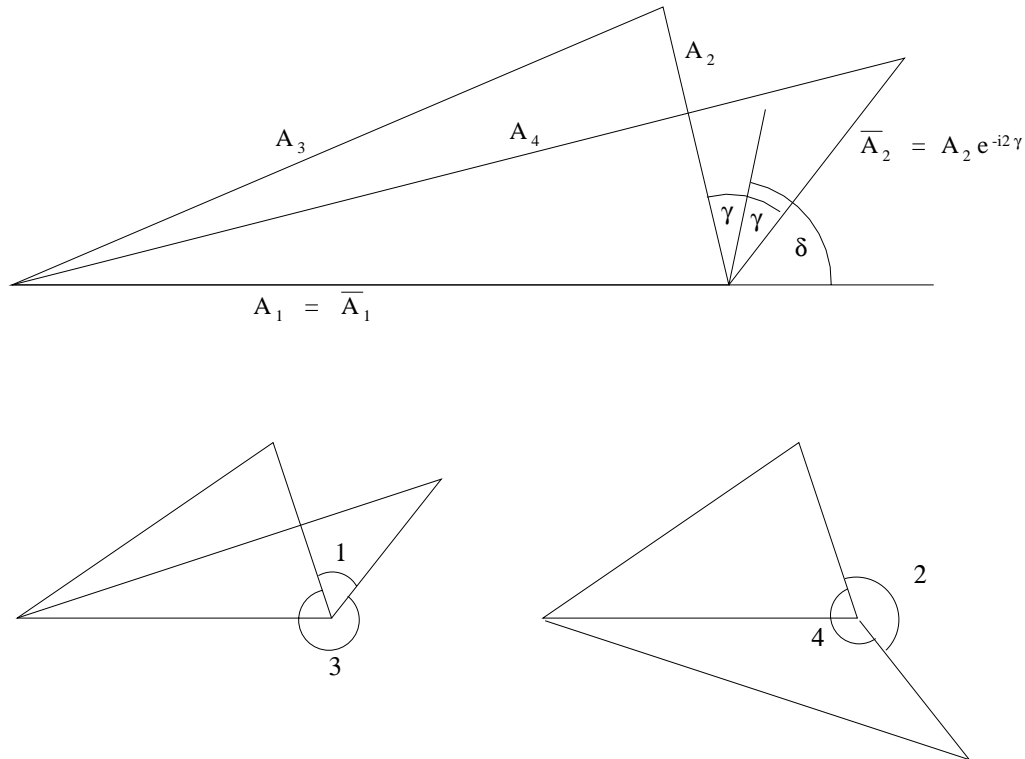


Figure 7-15. Triangular relations between the four amplitudes A_1 , A_2 , A_3 and A_4 : the four-fold ambiguity in the determination of 2γ is indicated by the four solutions labeled 1, 2, 3 and 4 for a given set of measured magnitudes of the amplitudes.

$|A_i|$ can be related to the total number of observed events N_i and the corresponding estimated number of background events B_i :

$$\frac{\sigma_{A_i}}{A_i} = \frac{1}{2} \frac{\sigma_{\Gamma_i}}{\Gamma_i} = \frac{1}{2} \frac{\sqrt{N_i}}{N_i - B_i}. \quad (7.57)$$

According to Table 7-6, they will be $\sigma_{A_1}/A_1 \simeq 4.4\%$, $\sigma_{A_2}/A_2 \simeq 7.6\%$, and $\sigma_{A_3}/A_3 \simeq \sigma_{A_4}/A_4 \simeq 4.2\%$, where the possibility of averaging two measurements for both $|A_1|$ and $|A_2|$ has been taken into account.

The corresponding errors can be propagated to the measurement of the angle γ , as described in Section 7.3. Uncertainties in the determination of efficiencies are neglected here; the effect of the theoretical uncertainty in the estimate of $|A_2| = |T'|$ is discussed separately in the following subsection.

As discussed in Section 7.3, the error on γ depends on the shape of the triangles for fixed errors on their sides. In particular, the error is larger for $\delta \simeq \gamma$ (at least one degenerate “flat” triangle) and for small $r = |T'|/|P'| \simeq |A_2|/|A_1|$ (“squashed” triangles). The numerical error propagation was therefore repeated for three values of γ (60° , 90° , 120°) varying δ in the range between 0° and 100° .

For $r = |A_2|/|A_1|$ the values 0.2 and 0.3 were used; the lower value is preferred by the arguments given in [16], where the rate of $B \rightarrow \pi l \nu$ is used to estimate $|T'|$ and the rate of $B^+ \rightarrow K^0 \pi^+$ to estimate $|P'|$.

Figure 7-16(a) shows the result of the numerical error propagation for $\gamma = 90^\circ$, $r = |A_2|/|A_1| = 0.3$, and δ varying between 0° and 100° : when the two solutions γ_1 and γ_2 become degenerate, the errors get larger, as discussed in Section 7.3. The error on the good solution $\gamma_1 = 90^\circ$ is $\sigma_\gamma = 12^\circ$ for the specific set of conditions shown in Fig. 7-16(b) ($\gamma = 90^\circ$, $\delta = 20^\circ$, $r = |A_2|/|A_1| = 0.3$) and can be as small as 10° for $\delta = 0^\circ$. The corresponding errors increase to $\sigma_\gamma = 19^\circ$ and $\sigma_\gamma = 17^\circ$ if a smaller $r = |A_2|/|A_1| = 0.2$ is assumed. The error becomes significantly larger than 20° if the strong-phase shift δ is allowed to assume values larger than $\sim 50^\circ$.

7.5.4.3 Theoretical uncertainties

As discussed in the previous sections, these simple triangular relations should be modified if color-suppressed electroweak-penguin contributions and rescattering effects turn out not to be negligible.

Moreover, factorization and SU(3) symmetry are assumed when estimating the amplitude $|A_2| \simeq |T'|$ from $\mathcal{B}(B^\pm \rightarrow \pi^\pm \pi^0)$ and $\Gamma(B^0 \rightarrow \pi^- l^+ \nu_l)$. A corresponding additional theoretical uncertainty of 10-20% [16] on the determination of the $|A_2|$ side may spoil the determination of γ , depending on the shape of the triangles, particularly if the strong-phase δ is large. However, the $B \rightarrow \pi K$ modes retain their interest because a substantial direct CP asymmetry would be observed in this case.

In either case, rather stringent constraints on γ may be accessible, as discussed in Section 7.5.3, controlling rescattering effects by measurements of $\mathcal{B}(B^\pm \rightarrow K^\pm K)$.

7.6 Partial Reconstruction of $B_d \rightarrow D^{(*)\pm}\pi^\mp$ Decays to Extract $\sin(2\beta + \gamma)$

This section discusses the extraction of $\sin(2\beta + \gamma)$ from partially reconstructed $B_d \rightarrow D^{(*)\pm}\pi^\mp$ decays [22]. This method can equally well be considered a measurement of $\sin(\beta - \alpha)$. Although the expected CP asymmetries are small, the decay rates are large and the $D^{(*)\pm}\pi^\mp$ final states can be reconstructed inclusively with good efficiency and relatively low background. Before turning to the experimental aspects, the theoretical framework of this approach will be considered.

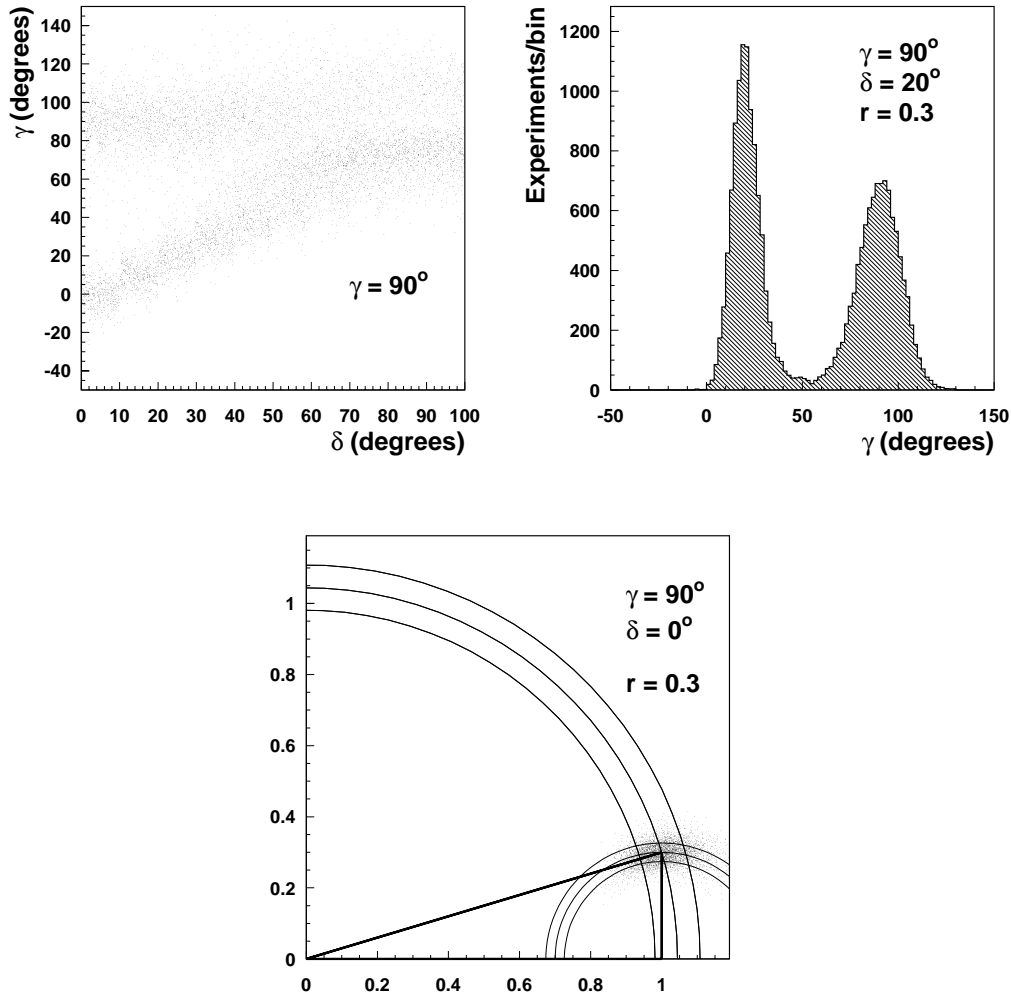


Figure 7-16. (a) Distributions of the solutions γ_1 and γ_2 when $\gamma = 90^\circ$, δ varies between 0 and 100° and the amplitudes are measured with the errors estimated in the text ($\int L dt \simeq 100 \text{ fb}^{-1}$). (b) Distribution of the two solutions γ_1 and γ_2 , for a specific set of conditions: $\gamma = 90^\circ$, $\delta = 20^\circ$ and $r = |A_2|/|A_1| = 0.3$: the rms for the “good” solution $\gamma_1 \simeq 90^\circ$ is $\sigma_\gamma = 12^\circ$. (c) Representation of the triangular relation, normalized to the base $|A_1|$, when $\gamma = 90^\circ$, $\delta = 0^\circ$ and $r = |A_2|/|A_1| = 0.3$; the error bands correspond to the errors estimated for an integrated luminosity $\int L dt \simeq 100 \text{ fb}^{-1}$: $\sigma_{A_1}/A_1 \simeq 4.4\%$, $\sigma_{A_2}/A_2 \simeq 7.6\%$, $\sigma_{A_3}/A_3 \simeq \sigma_{A_4}/A_4 \simeq 4.2\%$ (see text).

7.6.1 Theoretical Framework

Exclusive B_d decays caused by $\bar{b} \rightarrow \bar{u} c \bar{d}$ ($b \rightarrow c \bar{u} d$) quark-level transitions are pure tree decays receiving no penguin contributions. Their transition amplitudes can be expressed as hadronic matrix elements of low-energy effective Hamiltonians having the structure [8]:

$$\mathcal{H}_{\text{eff}}(\bar{B}^0 \rightarrow f) = \frac{G_F}{\sqrt{2}} \bar{v} [\bar{O}_1 \mathcal{C}_1(\mu) + \bar{O}_2 \mathcal{C}_2(\mu)] \quad (7.58)$$

$$\mathcal{H}_{\text{eff}}(B^0 \rightarrow f) = \frac{G_F}{\sqrt{2}} v^* [O_1^\dagger \mathcal{C}_1(\mu) + O_2^\dagger \mathcal{C}_2(\mu)]. \quad (7.59)$$

Here f denotes a final state with valence-quark content $c\bar{d}d\bar{u}$, for example $D^{*+} \pi^-$, and the relevant CKM factors take the form

$$\bar{v} \equiv V_{ud}^* V_{cb} = \left(1 - \frac{1}{2} \lambda^2\right) A \lambda^2, \quad v \equiv V_{cd}^* V_{ub} = -A \lambda^4 R_b e^{-i\gamma}, \quad (7.60)$$

where the Wolfenstein parametrization has been used and \bar{O}_k and O_k denote current–current operators that are given by

$$\begin{aligned} \bar{O}_1 &= (\bar{d}_\alpha u_\beta)_{V-A} (\bar{c}_\beta b_\alpha)_{V-A}, & \bar{O}_2 &= (\bar{d}_\alpha u_\alpha)_{V-A} (\bar{c}_\beta b_\beta)_{V-A}, \\ O_1 &= (\bar{d}_\alpha c_\beta)_{V-A} (\bar{u}_\beta b_\alpha)_{V-A}, & O_2 &= (\bar{d}_\alpha c_\alpha)_{V-A} (\bar{u}_\beta b_\beta)_{V-A}. \end{aligned} \quad (7.61)$$

The Wilson coefficient functions $\mathcal{C}_1(\mu)$ and $\mathcal{C}_2(\mu)$ have been calculated at NLO [39].

CP transformations can be performed by using

$$(CP)|B^0\rangle = e^{i\phi_{CP}(B_d)}|\bar{B}^0\rangle \quad (7.62)$$

$$(CP)O_k^\dagger(CP)^\dagger = O_k \quad (7.63)$$

and

$$\begin{aligned} &\langle f | O_1^\dagger(\mu)\mathcal{C}_1(\mu) + O_2^\dagger(\mu)\mathcal{C}_2(\mu) | B^0 \rangle \\ &= \langle f | (CP)^\dagger(CP) [O_1^\dagger(\mu)\mathcal{C}_1(\mu) + O_2^\dagger(\mu)\mathcal{C}_2(\mu)] (CP)^\dagger(CP) | B^0 \rangle \\ &= e^{i\phi_{CP}(B_d)} \langle \bar{f} | O_1(\mu)\mathcal{C}_1(\mu) + O_2(\mu)\mathcal{C}_2(\mu) | \bar{B}^0 \rangle. \end{aligned} \quad (7.64)$$

The relevant amplitudes are then

$$A(\bar{B}^0 \rightarrow f) \equiv \langle f | \mathcal{H}_{\text{eff}}(\bar{B}^0 \rightarrow f) | \bar{B}^0 \rangle = \frac{G_F}{\sqrt{2}} \bar{v} \bar{M}_f \quad (7.65)$$

$$A(B^0 \rightarrow f) \equiv \langle f | \mathcal{H}_{\text{eff}}(B^0 \rightarrow f) | B^0 \rangle = e^{i\phi_{CP}(B_d)} \frac{G_F}{\sqrt{2}} v^* M_{\bar{f}} \quad (7.66)$$

where the strong hadronic matrix elements are

$$\overline{M}_f \equiv \langle f | \overline{O}_1(\mu) \mathcal{C}_1(\mu) + \overline{O}_2(\mu) \mathcal{C}_2(\mu) | \overline{B}^0 \rangle \quad (7.67)$$

$$M_{\overline{f}} \equiv \langle \overline{f} | O_1(\mu) \mathcal{C}_1(\mu) + O_2(\mu) \mathcal{C}_2(\mu) | \overline{B}^0 \rangle. \quad (7.68)$$

Consequently, the observable $\lambda(B_d \rightarrow f)$, which was defined in Chapter 1 and contains essentially all the information needed to evaluate the mixing-induced and direct CP -violating asymmetries, is given by

$$\lambda(B_d \rightarrow f) = \frac{q}{p} \frac{A(\overline{B}^0 \rightarrow f)}{A(B^0 \rightarrow f)} = -e^{-i\phi_M^{(d)}} \frac{\overline{v}}{v^*} \frac{\overline{M}_f}{M_{\overline{f}}} = -e^{-i(2\beta+\gamma)} \frac{1}{\lambda^2 R_b} \frac{\overline{M}_f}{M_{\overline{f}}}, \quad (7.69)$$

where the phase convention $\phi_M^{(d)} = 2\beta$ is used. The additional convention-dependent phase $\phi_{CP}(B_d)$ is canceled by the one introduced through the $B^0-\overline{B}^0$ mixing phase [8]. An analogous calculation yields

$$\lambda(B_d \rightarrow \overline{f}) = -e^{-i\phi_M^{(d)}} \frac{v}{v^*} \frac{M_{\overline{f}}}{\overline{M}_f} = -e^{-i(2\beta+\gamma)} \lambda^2 R_b \frac{M_{\overline{f}}}{\overline{M}_f}. \quad (7.70)$$

If one measures the corresponding CP asymmetries, both $\lambda(B_d \rightarrow f)$ and $\lambda(B_d \rightarrow \overline{f})$ can be determined up to discrete ambiguities and allow a *theoretically clean* determination of $2\beta + \gamma$ from

$$\lambda(B_d \rightarrow f) \lambda(B_d \rightarrow \overline{f}) = e^{-2i(2\beta+\gamma)}. \quad (7.71)$$

Since 2β , *i.e.*, the $B^0-\overline{B}^0$ mixing phase, can be determined from CP violation in decays such as $B^0 \rightarrow J/\psi K_s^0$, one can extract γ from (7.71). It is interesting to note that this approach is still possible if $B^0-\overline{B}^0$ mixing receives sizeable CP -violating new-physics contributions, since it is unlikely that the $B_d \rightarrow D^{(*)\pm} \pi^\mp$ decay amplitudes are affected strongly by physics beyond the Standard Model (for a detailed discussion, see Chapter 13).

7.6.2 The Experimental Approach

The $\overline{B}^0 \rightarrow D^{*+} \pi^-$ decay was noted by Sachs [40] and studied by others [41, 42] as a possible CP violation mode. Even in the absence of $B^0-\overline{B}^0$ mixing, the decay modes $\overline{B}^0 \rightarrow D^{*+} \pi^-$ and $\overline{B}^0 \rightarrow D^{*-} \pi^+$ are both possible, the latter through a doubly-Cabbibo suppressed (DCS) decay. $B^0-\overline{B}^0$ mixing then causes interference and so gives an asymmetry in each case. In principle, either decay mode can give an independent measurement of $\sin(2\beta + \gamma)$ but, as shown above, combining the two asymmetries allows cancellation of the hadronic parts of the matrix elements. Since the selection of $D^{*+} \pi^-$ and $D^{*-} \pi^+$ are identical, the charge conjugate state is implied throughout the following.

The decay chain $\bar{B}^0 \rightarrow D^{*+} \pi^-; D^{*+} \rightarrow D^0 \pi^+$ has a low efficiency if the two pions and the D^0 daughters are all reconstructed. Estimates of the efficiency for full reconstruction for this mode indicate that it would not be useful for measuring the CKM angles. However, the CLEO collaboration has performed a partial reconstruction [43] of this mode, where the D^0 daughters are ignored and yet there is still sufficient information from the two pions to determine fully the kinematics of the decay. In 3.1 fb^{-1} of data, the yield of $D^* \pi$ events in the partial reconstruction is ~ 2600 events. This is an order of magnitude larger than the 248 events found in the same data with CLEO's full reconstruction [44] analysis. The higher efficiency from partial reconstruction is enough to provide interesting sensitivity to $\sin(2\beta + \gamma)$ provided the information from the two pions is sufficient to separate signal from background. In this section, a detailed description of the partial reconstruction technique will be given, and the error on $\sin(2\beta + \gamma)$ attainable in BABAR will be estimated.

In order to fully describe the kinematics of the $\bar{B}^0 \rightarrow D^{*+} \pi^-$ decay, 20 parameters are required: four for each four-vector of the five particles: B , D^* , π_f , D , and π_s . Energy-momentum conservation can be applied twice, in the $B \rightarrow D^* \pi_f$ and $D^* \rightarrow D \pi_s$ decays, yielding eight equations. The masses of the five particles can be assumed, and the center-of-mass energy of the $e^+ e^-$ collisions can be used to obtain the magnitude of the three-momentum of the initial B . The six free parameters that remain describe the kinematics of the decay sequence. These can be thought of as six angles: two that describe the B direction, two that describe the direction of the π_f in the B rest frame (θ_f^*, ϕ_f^*), and two that describe the direction of the π_s in the D^* rest frame (θ_s^*, ϕ_s^*). The six angles are evaluated from the measurement of the three components of the π_f momentum and the three components of the π_s momentum.

The angles that provide effective discrimination between signal and background are θ_f^* and θ_s^* , for which the explicit expressions are:

$$\cos \theta_f^* = \frac{-\beta_B(E_f^* - E_{D^*}^*)}{2P_f^*} + \frac{|\mathbf{p}_f|^2 - |P_{D^*}|^2}{2\gamma_B^2 \beta_B M_B P_f^*} \quad \text{and} \quad (7.72)$$

$$\cos \theta_s^* = \frac{-\beta_{D^*}(E_s^* - E_D^*)}{2P_s^*} + \frac{|\mathbf{p}_s|^2 - |P_D|^2}{2\gamma_{D^*}^2 \beta_{D^*} M_{D^*} P_s^*}, \quad (7.73)$$

where: E_f^* , $E_{D^*}^*$ and P_f^* are the energy and momentum of the π_f and D^* in the B center-of-mass; and E_s^* , E_D^* and P_s^* are the energy and momentum of the π_s and D in the D^* center-of-mass; $\gamma_{B(D^*)}$, $\beta_{B(D^*)}$ and $M_{B(D^*)}$ are the Lorentz factor, the velocity and the mass of the $B(D^*)$ in the lab frame. The magnitude of the D^* and D momenta in the lab frame, $|P_{D^*}|$ and $|P_D|$, are determined by applying energy-momentum conservation in the decay chain. These formulæ relate the measured pion momenta to the center-of-mass decay angles assuming that the pions were produced in a $\bar{B}^0 \rightarrow D^{*+} \pi^-$ decay. For signal, the magnitudes of these cosines will tend to fall in the physical region (less than 1.0), though detector resolution can cause this limit to be exceeded somewhat. The signal is uniform in $\cos \theta_f^*$ (because the B has spin 0), and is distributed as $\cos^2 \theta_s^*$ (because the D^* has helicity 0), before consideration of detector acceptance, efficiency,

and resolution. Backgrounds are capable of producing pions with momenta that are physically inconsistent with the assumption of $\bar{B}^0 \rightarrow D^{*+} \pi^-$ production; the reconstructed center-of-mass angles are often in the nonphysical region, $|\cos \theta^*| > 1$. The variables $\cos \theta_f^*$ and $\cos \theta_s^*$ tend to depend linearly on $|\mathbf{p}_f|$ and $|\mathbf{p}_s|$ once the dependence of $|P_{D^*}|$ and $|P_D|$ on these variables is included.

The angle between the plane of the $B \rightarrow D^* \pi_f$ decay and the plane of the $D^* \rightarrow D \pi_s$ decay, $\phi = \phi_f^* - \phi_s^*$, is reconstructed in the following manner. In the lab frame, the D^* direction must lie on a small cone of angle α_f around the direction *opposite* to the π_f , as shown in Fig. 7-17. The D^* must *also* lie on a second small cone of angle α_s around the direction of the π_s . The expressions for these angles are:

$$\cos \alpha_f = \frac{M_B^2 - M_{D^*}^2 - M_\pi^2}{2 |P_{D^*}| |\mathbf{p}_f|} - \frac{1}{\beta_{D^*} \beta_f} \quad \text{and} \quad \cos \alpha_s = -\frac{M_{D^*}^2 + M_\pi^2 - M_D^2}{2 |P_{D^*}| |\mathbf{p}_s|} + \frac{1}{\beta_{D^*} \beta_s}, \quad (7.74)$$

where the momenta and velocities are measured in the lab frame. The decay kinematics limit $\alpha_f \leq 0.14$ and $\alpha_s \leq 0.28$. Intersection of these two cones determines the D^* directions to within the quadratic ambiguity. For both solutions

$$\cos \phi = \frac{\cos \delta - \cos \alpha_f \cos \alpha_s}{\sin \alpha_f \sin \alpha_s}, \quad (7.75)$$

where δ is the angle between \mathbf{p}_s and the direction opposite to \mathbf{p}_f . For most signal events $|\cos \phi| < 1$, *i.e.*, a “physical” value. For the limiting cases $|\cos \phi| \rightarrow 1$ the two D^* solutions collapse to one, where the pions and the D^* lie in a plane. The pions are closer to (further from) back-to-back for $\cos \phi = 1$ ($\cos \phi = -1$). Signal events with imperfect measurement of the pion momenta, as well as background events, can result in $|\cos \phi| > 1$.

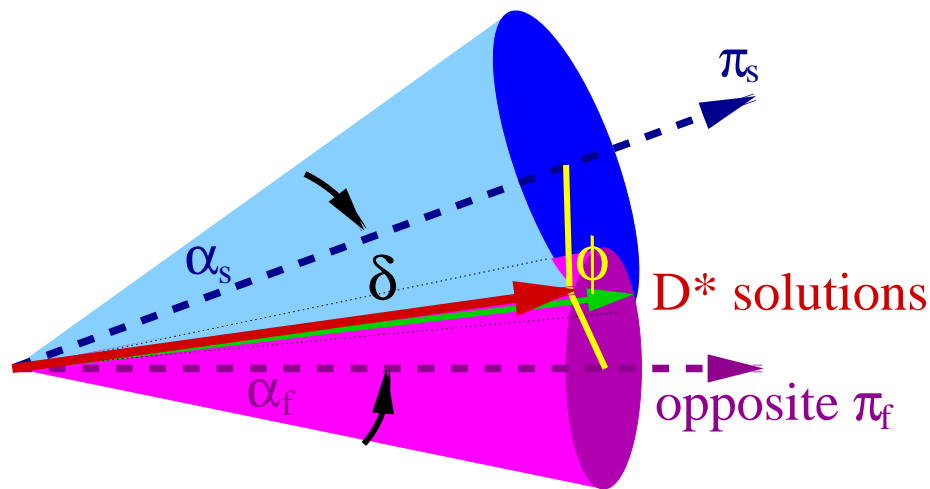


Figure 7-17. The cones of possible D^* solutions around each pion direction.

The CLEO analysis resulted in a measurement [43] of the branching ratio of $\bar{B}^0 \rightarrow D^{*+} \pi^-$. Candidate events were required to satisfy a global event shape requirement which suppresses continuum background. The variables $\cos \theta_f^*$, $\cos \theta_s^*$ and $\cos \phi$ were reconstructed for all combinations of two charged pions with opposite sign. Candidate combinations were required to satisfy a cone overlap requirement of $|\cos \delta - \cos \alpha_f \cos \alpha_s| < \sin \alpha_f \sin \alpha_s + 0.02$, which allows for detector resolution. A two-dimensional fit was then performed with the variables $\cos \theta_f^*$ and $\cos \theta_s^*$ to separate signal from background. This analysis resulted in $2612 \pm 102 D^{*+} \pi^-$ events reconstructed out of a sample of $(3.27 \pm 0.06) \times 10^6 B\bar{B}$ pairs produced. This corresponds to a reconstruction efficiency of 42%. The $\cos \theta_s^*$ distribution obtained is shown in Fig. 7-18, both before and after background subtraction. The $\bar{B}^0 \rightarrow D^{*+} \pi^-$ branching fraction determined in the partial reconstruction is consistent with the value determined in a separate, full reconstruction analysis. Even though the backgrounds are higher in the partial reconstruction than in the full reconstruction, the measurement of the branching fraction in the former is the more precise.

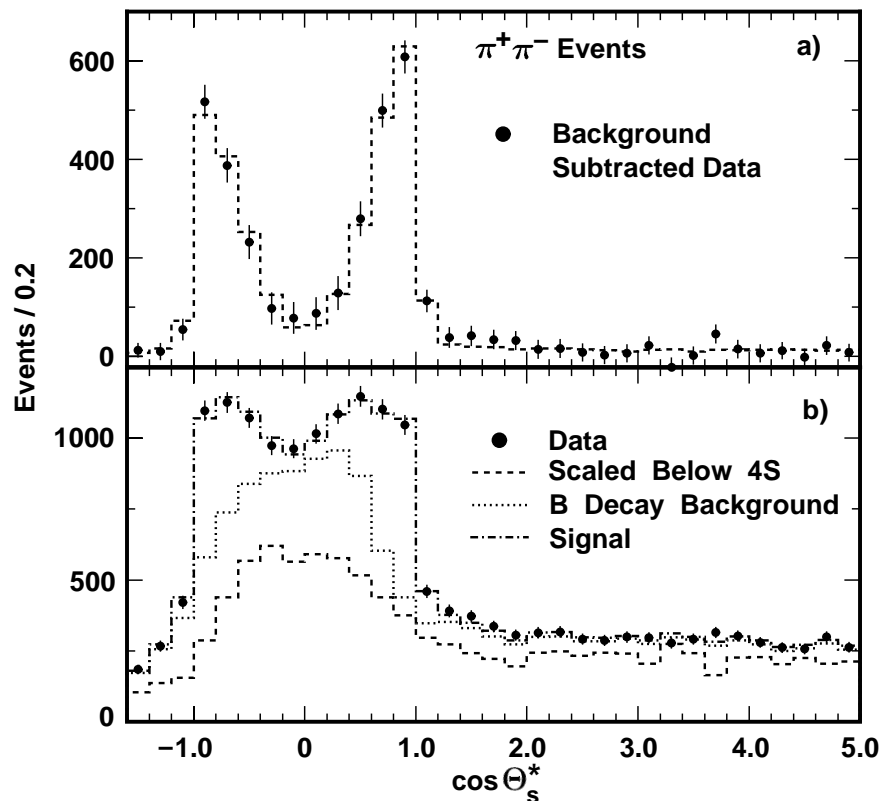


Figure 7-18. The $\cos \theta_s^*$ distribution of $\pi^+ \pi^-$ combinations in the CLEO II data. The distribution after background subtraction is shown in a) and the distribution before background subtraction in b). The $\cos^2 \theta_s^*$ distribution expected for signal is clearly visible.

This technique could be applied at BaBar by first boosting into the rest frame of the $\Upsilon(4S)$, and then performing an identical analysis. In order to use this partial reconstruction technique to measure $\sin(2\beta + \gamma)$ at BaBar, it would also be necessary to tag the flavor of the other B . There are, however, two issues which should be noted. First, the presence of a lepton tag has the benefit of reducing the backgrounds in the partial reconstruction. The $\cos \theta_s^*$ distribution of $D^*\pi$ events, after requiring the presence of a lepton tag, but before background subtraction, is shown in Fig. 7-19. Comparing this to Fig. 7-18b, it can be seen that the signal to background ratio changes from 1:4 to 3:1, an improvement of an order of magnitude, albeit at the expense of a significant amount of signal. Second, as described above, $D^*\pi$ is really two distinct final states; $D^{*+}\pi^-$ and $D^{*-}\pi^+$. This means that the events can be split into two samples by comparing the charge of the lepton tag with the charge of the fast pion. It is useful to define right-sign (wrong-sign) events to be those in which the two particles have the opposite (same) charge. Since both decay modes are present in the absence of $B^0-\bar{B}^0$ mixing, the nomenclature is slightly misleading; the right-sign combination corresponds to the leading decay mode and the wrong-sign to the doubly-Cabbibo-suppressed mode.

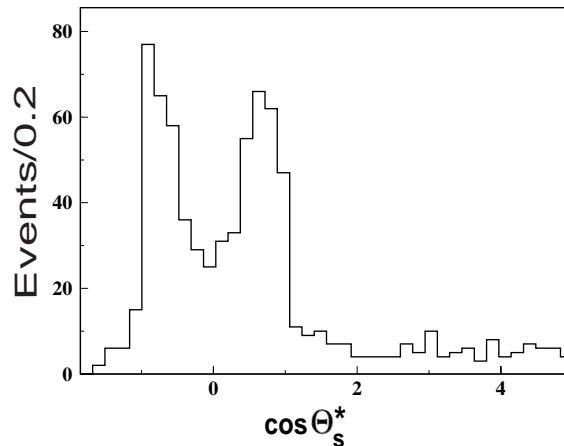


Figure 7-19. The $\cos \theta_s^*$ distribution of $\pi^+\pi^-$ combinations in the CLEO II data after requiring the presence of a lepton tag.

The information extracted from these samples is enhanced by a fit to the decay time distribution of the events as they provide additional information about the CP -violating asymmetry. The decay time distributions of the two samples are quite different and are dependent on x_d , which describes the strength of the $B^0-\bar{B}^0$ mixing. The distribution of events versus decay time is shown in Fig. 7-20 for right-sign and wrong-sign events, along with their charge conjugates. The size of the asymmetry has been exaggerated for effect, and the scale for wrong-sign events has been expanded so that the larger asymmetry is visible.

One consequence of this difference in time evolution is that the asymmetry in the right-sign and wrong-sign events is different. The asymmetry in the wrong-sign events is a factor of 4.7 larger

than in the right-sign events. However, the actual numbers of right-sign to wrong-sign events differ by the same factor. Since the significance of an asymmetry measurement is proportional to the asymmetry divided by the square root of the number of events, (A/\sqrt{N}) , the wrong-sign sample actually has a greater statistical significance than the right-sign sample, by a factor of 2.2. An interesting benefit from this effect is that it provides a useful experimental cross-check on certain systematic errors. An asymmetry that arises from a systematic error in tagging efficiencies will have the same magnitude in both samples, while an asymmetry from CP violation will show the ratio of 4.7 between right- and wrong-sign samples.

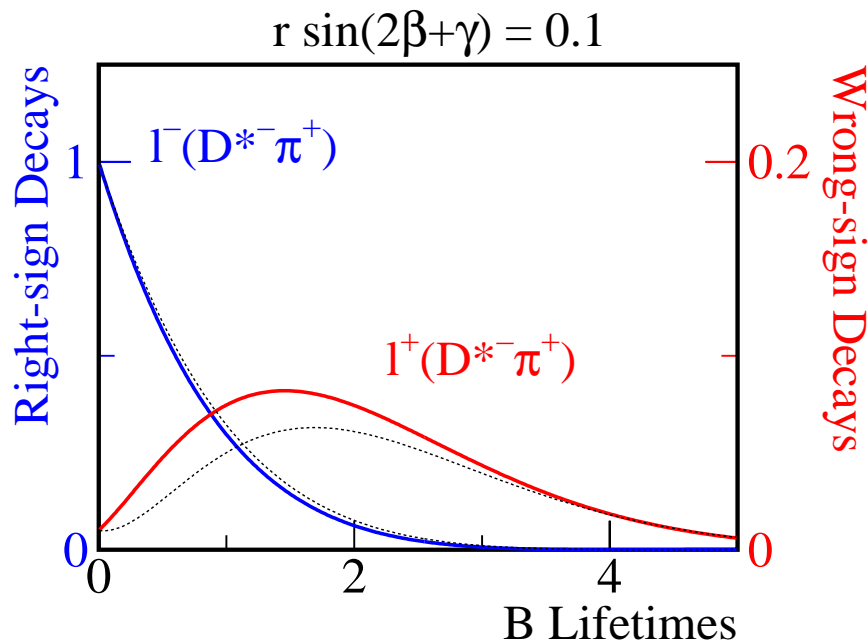


Figure 7-20. The time distributions for right-sign (highest curve) and wrong-sign (middle curve) events. In each case the dashed black line shows the time evolution of the charge-conjugate state.

In order to calculate the error on $\sin(2\beta + \gamma)$ that could be achieved at BABAR in this mode with 30 fb^{-1} of data-taking at the $\Upsilon(4S)$, the branching fractions and signal-to-background levels determined in the CLEO analysis are used, along with the assumptions of the BABAR Technical Design Report (TDR) where relevant. For comparison, the error on $\sin 2\beta$ from $J/\psi K_S^0$ is also estimated with the same assumptions. The results of the estimates are shown in Table 7-7 and the numbers in that table are described below.

The total number of $D^* \pi$ and $J/\psi K_S^0$ events were determined assuming 30 fb^{-1} of data-taking at the $\Upsilon(4S)$, and multiplying by the branching fraction, reconstructible fraction, and reconstruction efficiency. It was assumed that the reconstruction efficiency for partial reconstruction of $\bar{B}^0 \rightarrow D^{*+} \pi^-$ is the same as for $B \rightarrow \pi \pi$, as they are dominated by geometrical acceptance. The actual efficiencies achieved in CLEO for each mode are shown in parentheses. Not all of these events will

Table 7-7. the estimate of the error on the measurement of $\sin(2\beta + \gamma)$ from $D^*\pi$ compared to the estimate of the error on the measurement of $\sin 2\beta$ from $J/\psi K_s^0$.

Quantity	$D^*\pi$		$J/\psi K_s^0$
Branching Fraction	2.8×10^{-3}		0.425×10^{-3}
Reconstructible fraction	0.68		0.08
Reconstruction efficiency	0.60 (0.42)		0.60 (0.35)
# events	36000		660
tagging efficiency (TDR)	0.86		0.86
# tagged events	31000		570
	right-sign wrong-sign		
# tagged events	25600	5400	570
Max. Asym. (inc. dilution)	0.0083	0.039	0.30
$\sigma(\sin(\phi))$, Counting	0.75	0.37	0.14
Fit Benefit (Cramer-Rao)	0.63	0.67	0.82
$\sigma(\sin(\phi))$, Time Fit	0.47	0.25	0.12
$\sigma(\sin(\phi))$, Combined	0.22		0.12

have tagging information however. According to the TDR, 86% of events will have some sort of tagging information from either lepton or kaon tags. This factor was used to determine the number of events with tagging information. Events that are mistagged will dilute the observed asymmetry, and this effect was included when computing the dilution.

The predicted asymmetry is proportional to $\sin(2\beta + \gamma)$. However, since the two interfering amplitudes are unequal in magnitude, there is an additional suppression factor, r , in the asymmetry. This suppression is given by the ratio of the amplitudes of the DCS decay, $\bar{B}^0 \rightarrow D^{*-}\pi^+$, and the Cabbibo-favored decay, $\bar{B}^0 \rightarrow D^{*+}\pi^-$. One finds $r \approx 0.025$ from the magnitudes of the appropriate CKM matrix elements and estimates of hadronic factors [45, 46]. For the purposes of this study, the maximum value of the sine of the relevant angle in each case was assumed. Hence, a maximum asymmetry was determined by assuming that $\sin(2\beta + \gamma) = 1$, $r = 0.025$ and integrating the time evolution curves. The dilution due to mistags and Δz measurement errors was taken from the TDR and included in the calculation of the maximum asymmetry. The error on $\sin(2\beta + \gamma)$ was estimated using the expected maximum asymmetry, the predicted number of events, and assuming a signal to background ratio of 1:4. This was used, rather than the 3:1 quote above with a lepton tag, as the tag enhancement is already factored in to the TDR tagging quality to some extent. This was a simple counting analysis and no fit to the time distribution was done. The resulting error on

$\sin(2\beta + \gamma)$ in $D^*\pi$ was estimated to be around 0.3, a factor of 3 higher than the error on $\sin 2\beta$ from $J/\psi K_S^0$.

As previously stated, a fit to the time distribution of the decays will increase the significance of the result. The Cramer-Rao theorem [47] gives a general limit on the amount of information which can be extracted from a sample. For this analysis, it was assumed that the information that could be extracted from a fit to the time distributions was optimized at this limit. However, in order to do this, some assumptions had to be made about the amount and kind of backgrounds that can be expected for this mode. As mentioned, a signal to background ratio of 1:4 was used, where the background is expected to be dominated by continuum events. The remaining background is mainly B decays of the form $B \rightarrow D^*(n\pi)$, which have the same dependence on $\sin(2\beta + \gamma)$ as $D^*\pi$, although they have different hadronic factors. It was assumed that these modes would have a negligible impact on the measurement, and they were ignored. It was also assumed that the continuum background was peaked at a proper time of zero, with a width composed of a narrow Gaussian of $50\mu\text{m}$ and a broad Gaussian of $250\mu\text{m}$, where the ratio of events is 5:1 between the narrow and wide Gaussians. The error on $\sin(2\beta + \gamma)$ which would be obtained after fitting was found to be 0.22, about twice as large as the error on $\sin 2\beta$.

This estimate makes some assumptions that should be re-examined in detail with a full Monte Carlo analysis. First, the background assumptions which were used neglected the effect of tagging on the background levels. The background suppression from lepton tags should be re-evaluated using the BABAR Monte Carlo. The effect of kaon tags on the background levels should also be determined. Second, for this type of analysis one must take into account the fact that mistags tend to convert right-sign to wrong-sign events and vice versa. The fit to the time evolution diagram should provide a handle on this effect since mistagged events retain their parent time distribution. However, a complete analysis of this effect remains to be done.

In conclusion, it has been shown that the mode $B \rightarrow D^*\pi$ has the potential to provide interesting information about the phases of the CKM matrix if a partial reconstruction technique is used to give increased statistics. Along with $J/\psi K_S^0$ and $\pi^+\pi^-$ this mode will give a third constraint on the vertex of the CKM triangle. This overconstraint opens the possibility that the measurements will disagree and indicate the presence of new physics.

7.7 Strategies to Determine γ from B_s Decays

In the B_s system, very rapid $B_s-\bar{B}_s$ oscillations are expected because of the large mixing parameter $x_s \equiv \Delta m_{B_s} \tau_{B_s} \gtrsim 15$. Consequently, in order to keep track of these oscillations, an excellent vertex resolution system is needed and experimental studies of CP violation in B_s decays are regarded as being very difficult. Since strategies using B_s decays require PEP-II to operate at the $\Upsilon(5S)$ resonance, the BABAR experiment will not be in a position to make use of such methods in the near

future. Nevertheless, to complete this review, this chapter includes a brief discussion of methods to determine γ from measurements made with the B_s system.

The transition $B_s \rightarrow \rho^0 K_s^0$ appears frequently in the literature as a tool for extracting γ (for a detailed discussion, see, *e.g.*, [8]). It is a B_s decay into a final CP eigenstate with eigenvalue -1 (similar to the case of the $B_d \rightarrow \pi^+ \pi^-$ mode) caused by the quark-level process $\bar{b} \rightarrow \bar{u} u \bar{d}$. Consequently, the phase structure of the corresponding decay amplitude is analogous to that of $B_d \rightarrow \pi^+ \pi^-$, and since the weak $B_s - \bar{B}_s$ mixing phase is very small (the usual convention) within the Standard Model, $B_s \rightarrow \rho^0 K_s^0$ probes the CKM angle γ . Although the penguin contributions are expected to be of the same order of magnitude in these decays, their importance is enhanced considerably in the case of $B_s \rightarrow \rho^0 K_s^0$, since the corresponding tree amplitude is expected to be color-suppressed by a phenomenological color-suppression factor $a_2 \approx 0.2$. Therefore, a meaningful determination of γ from the mixing-induced CP asymmetry arising in $B_s \rightarrow \rho^0 K_s^0$ appears not to be possible. Further, the branching ratio for this decay is expected to be of $\mathcal{O}(10^{-7})$, which makes its experimental investigation very difficult. One should keep in mind, however, that $B_s \rightarrow \rho^0 K_s^0$ may be in better shape to provide information about γ , if color suppression is found to fail for this transition. A recent model calculation of $B_s \rightarrow \rho^0 K_s^0$ within a perturbative framework can be found, *e.g.*, in [48].

Interestingly, there are other B_s decays that *do* allow meaningful extractions of γ . Several of these strategies are *theoretically clean*. A key role in this respect is played by methods making use of the time evolution of exclusive B_s decays originating from $\bar{b} \rightarrow \bar{u} c \bar{s}$ and $b \rightarrow c \bar{u} s$ quark-level transitions. Decays such as $B_s \rightarrow D_s^\pm K^\mp$ [23] and $B_s \rightarrow D \phi$ [49, 50] are pure tree decays, *i.e.*, receive no penguin contributions. From a theoretical point of view, these decays are very similar to the $B_d^0 \rightarrow D^{(*)\pm} \pi^\mp$ modes discussed in the previous section, and allow us (in principle) to extract the observables $\lambda(B_s \rightarrow f)$ and $\lambda(B_s \rightarrow \bar{f})$ (see Chapter 1). The important difference is that both decay paths are equally CKM-suppressed in the B_s case, and the $B_s - \bar{B}_s$ mixing phase is tiny within the Standard Model. These facts mean that in this case, the observables take the same forms as in Eqs. (7.69) and (7.70), with the simple replacements of $\lambda^2 R_b$ by R_b , and of 2β by the tiny B_s mixing phase. However, in order to extract these observables from the corresponding time-dependent decay rates, it is crucial to resolve the rapid $\Delta m_{B_s} t$ oscillations, which is an experimental challenge.

An alternative route to study CP violation in the B_s system may be provided by the expected sizeable width difference $\Delta\Gamma_s \equiv \Gamma_H^{(s)} - \Gamma_L^{(s)}$ between the mass eigenstates B_s^H (“heavy”) and B_s^L (“light”) [51]. This width difference originates from CKM-allowed $b \rightarrow c \bar{c} s$ decays that are common to both B_s and \bar{B}_s and may be as large as $\mathcal{O}(20\%)$ of the average B_s decay width [52]. Because of the width difference $\Delta\Gamma_s$, which is studied in more detail in Chapter 11, *untagged* data samples of nonleptonic B_s meson decays, where one does not distinguish between initially present B_s or \bar{B}_s mesons, may play an important role to explore CP violation. In such untagged B_s decay rates, the rapid oscillatory $\Delta m_{B_s} t$ terms cancel, so that the time evolution is simply governed by

two exponentials [51]. Several strategies have recently been proposed to extract CKM phases from such untagged B_s decays [51, 53], for example from $B_s \rightarrow K^{(*)} \bar{K}^{(*)}$ modes.

Finally, it is worth noting that the B_s system also provides interesting probes for physics beyond the Standard Model. One of the most important decays in this respect is $B_s \rightarrow \psi \phi$, which is the B_s counterpart of the mode $B^0 \rightarrow \psi K_S^0$. Since to a good approximation the decay amplitude of this channel does not involve a CP -violating weak phase and since moreover the Standard Model B_s - \bar{B}_s mixing phase is very small, the CP -violating effects in this transition are tiny within the framework of the Standard Model. Consequently, a future measurement of sizeable CP violation in the decay $B_s \rightarrow \psi \phi$ would be a striking signal for a new-physics contribution to B_s - \bar{B}_s mixing. This study is a promising one for B physics experiments at hadron machines.

7.8 Summary of Results and Overall γ Reach

A clean measurement of the angle γ of the unitarity triangle is very desirable but not easy. Possibly the best tools to extract γ are measurements of time-dependent asymmetries in B_s decays: experiments at the B factories are not likely to have access to these decays in the near future. However, the studies presented in this chapter indicate that useful information on γ will indeed be obtained by BaBar in several different ways.

Time-dependent asymmetries in $B \rightarrow D^{*\pm} \pi^\mp$ decays are related to $\sin(2\beta + \gamma)$ in a theoretically clean way. The experimental challenge is to observe effects that are expected to be at the few percent level. A preliminary analysis, performed on CLEO data, shows that an inclusive partial reconstruction technique can be used to give increased statistics. An extrapolation of these results, with some assumptions on dilution factors in BaBar, predicts an error on $\sin(2\beta + \gamma)$ approximately twice as large as the error expected on $\sin 2\beta$ in the $J/\psi K_S^0$ channel for the same integrated luminosity.

A promising approach, although theoretically not as clean, is the study of the rates of the $B \rightarrow K^\pm \pi^\mp$ and $K^0 \pi^\pm$ modes. Neglecting rescattering effects and color suppressed electroweak-penguin diagrams, triangular relations between penguin and tree decay amplitudes can be deduced. Additional assumptions on factorization and SU(3) symmetry breaking are necessary to relate one of the sides of the triangles (the tree amplitude) to the measured branching ratio of the $\pi^0 \pi^\pm$ decay mode. Depending on the shape of the triangles (*i.e.*, on the values of γ , the strong-phase difference δ and the ratio r of tree and penguin amplitudes), a statistical error σ_γ in the range $10^\circ - 20^\circ$ can be achieved with an integrated luminosity of 100 fb^{-1} , corresponding to about three years of BaBar running. The theoretical uncertainty in estimating the tree amplitude will amplify this error. However, there are ways to constrain the allowed range of γ significantly, avoiding this additional uncertain theoretical input.

Finally, methods using $B^\pm \rightarrow DK^\pm$ and $B \rightarrow DK^*$ decays were considered. In particular, a new method exploiting the interplay of color suppressed/allowed B decay amplitudes interfering with Cabibbo allowed/doubly suppressed D decay amplitudes was studied. From a theoretical point of view, these methods are free of penguin contributions and do not suffer from hadronic uncertainties. However, at the nominal PEP-II initial luminosity, only a few events per year will be collected in the different decay modes, if realistic values for color suppressed branching ratios are assumed. In order to reach a sensitivity in the range $\sigma_\gamma \simeq 10^\circ - 20^\circ$ an integrated luminosity of the order of 300 fb^{-1} will be needed.

References

- [1] A. J. Buras, TUM-HEP-299-97 (1997), hep-ph/9711217; Invited Plenary Talk given at the 7th International Symposium on Heavy Flavor Physics, Santa Barbara, California, 7-11 July (1997), to appear in the proceedings.
- [2] Y. Nir and D. Silverman, *Nucl. Phys.* **B345**, 301 (1990).
- [3] Y. Nir, Lectures presented in the 20th SLAC Summer Institute, SLAC-PUB-5874 (1992); Y. Nir and H.R. Quinn, *Ann. Rev. Nucl. Part. Sci.* **42**, 211 (1992).
- [4] M. Gronau and D. Wyler, *Phys. Lett. B* **265**, 172 (1991).
- [5] D. Atwood, I. Dunietz and A. Soni, *Phys. Rev. Lett.* **78**, 3257 (1997).
- [6] M. Gronau, J. L. Rosner and D. London, *Phys. Rev. Lett.* **73**, 21 (1994).
- [7] O. F. Hernández *et al.*, *Phys. Lett. B* **333**, 500 (1994); M. Gronau *et al.*, *Phys. Rev. D* **50**, 4529 (1994).
- [8] R. Fleischer, *Int. Jour. Mod. Phys.* **A12**, 2459 (1997).
- [9] D. Zeppenfeld, *Z. Phys. C* **8**, 77 (1981); M. Savage and M. B. Wise, *Phys. Rev. D* **39**, 3346 (1989); [E: *Phys. Rev. D* **40** 3127 (1989)]; L. L. Chau *et al.*, *Phys. Rev. D* **43**, 2176 (1991); B. Grinstein and R. F. Lebed, *Phys. Rev. D* **53**, 6344 (1996).
- [10] M. Gronau *et al.*, *Phys. Rev. D* **52**, 6356 (1995).
- [11] A. J. Buras and R. Fleischer, *Phys. Lett. B* **341**, 379 (1995); R. Fleischer, *Phys. Lett. B* **341**, 205 (1994); M. Ciuchini *et al.*, *Nucl. Phys.* **B501**, 271 (1997); *Nucl. Phys.* **B512**, 3 (1998).
- [12] R. Fleischer, *Z. Phys. C* **62**, 81 (1994); *Phys. Lett. B* **321**, 259 (1994); *Phys. Lett. B* **332**, 419 (1994).
- [13] N.G. Deshpande and X.-G. He, *Phys. Rev. Lett.* **74**, 26 (1995); [E: *ibid.*, p. 4099].
- [14] M. Gronau *et al.*, *Phys. Rev. D* **52**, 6374 (1995).
- [15] R. Fleischer, *Phys. Lett. B* **365**, 399 (1996).
- [16] M. Gronau and J. L. Rosner, *Phys. Rev. D* **57**, 6843 (1998).
- [17] F. Würthwein and P. Gaidarev, CALT-68-2153 (1997), hep-ph/9712531.

- [18] L. Wolfenstein, *Phys. Rev. D* **52**, 537 (1995);
J. F. Donoghue *et al.*, *Phys. Rev. Lett.* **77**, 2178 (1996);
B. Blok and I. Halperin, *Phys. Lett. B* **385**, 324 (1996);
B. Blok, M. Gronau and J. L. Rosner, *Phys. Rev. Lett.* **78**, 3999 (1997).
- [19] R. Fleischer, CERN-TH/98-60 (1998), hep-ph/9802433.
- [20] R. Godang *et al.*, (CLEO Collaboration), *Phys. Rev. Lett.* **80**, 3456 (1998).
- [21] R. Fleischer and T. Mannel, *Phys. Rev. D* **57**, 2752 (1998).
- [22] R.G. Sachs, Enrico Fermi Institute Report, EFI-85-22 (1985) (unpublished);
I. Dunietz and R.G. Sachs, *Phys. Rev. D* **37**, 3186 (1988); [E: *Phys. Rev. D* **39** 3515 (1989)];
I. Dunietz, FERMILAB-PUB-97/384-T (1997), *Phys. Lett. B* **427**, 179 (1998).
- [23] R. Aleksan, I. Dunietz and B. Kayser, *Z. Phys. C* **54**, 653 (1992).
- [24] J. D. Bjorken, *Nucl. Phys. B Proc. Suppl.* **11**, 325 (1989);
SLAC-PUB-5389 (1990), published in *Proceedings of the SLAC Summer Institute* (1990), p. 167.
- [25] For a recent discussion, see M. Neubert and B. Stech, CERN-TH/97-99 (1997), hep-ph/9705292, to appear in *Heavy Flavours II*, eds. A. J. Buras and M. Lindner, World Scientific, Singapore (1998).
- [26] C. Caso *et al.*, Particle Data Group, *Eur. Phys. Jour. C* **3**, 1 (1998).
- [27] I. Dunietz, *Phys. Lett. B* **270**, 75 (1991).
- [28] BELLE Progress Report, KEK Progress Report 96-1 (1996).
- [29] A. J. Buras, R. Fleischer and T. Mannel, CERN-TH/97-307 (1997), hep-ph/9711262.
- [30] A. F. Falk *et al.*, *Phys. Rev. D* **57**, 4290 (1998).
- [31] M. Neubert, *Phys. Lett. B* **424**, 152 (1998).
- [32] J.-M. Gérard and J. Weyers, UCL-IPT-97-18 (1997), hep-ph/9711469.
- [33] M. Gronau and J. L. Rosner, *Phys. Rev. Lett.* **76**, 1200 (1996);
A. S. Dighe, M. Gronau and J. L. Rosner, *Phys. Rev. D* **54**, 3309 (1996);
A. S. Dighe and J. L. Rosner, *Phys. Rev. D* **54**, 4677 (1996).
- [34] T. E. Browder, in *Proceedings of the XXVIII International Conference on High Energy Physics – ICHEP96*, Warsaw, Poland, July (1996), eds. Z. Ajduk and A.K. Wroblewski, World Scientific, Singapore (1997) p. 1139.

- [35] M. Bauer, B. Stech and M. Wirbel, *Z. Phys. C* **34**, 103 (1987); *Z. Phys. C* **29**, 637 (1985).
- [36] A. J. Buras and R. Fleischer, *Phys. Lett. B* **365**, 390 (1996).
- [37] Y. Grossman *et al.*, *Nucl. Phys.* **B511**, 69 (1998).
- [38] D. Atwood and A. Soni, *Phys. Rev. D* **58**, 036005 (1998).
- [39] G. Buchalla, A. J. Buras and M. E. Lautenbacher, *Rev. Mod. Phys.* **68**, 1125 (1996) and references therein.
- [40] R. G. Sachs, Report No. EFI-85-22, Chicago (1985), unpublished;
R. G. Sachs, *The Physics of Time Reversal*, The University of Chicago Press, Chicago, IL, (1987), pp. 257-261; the analogous decays $B^0 \rightarrow D^\mp \pi^\pm$ are discussed.
- [41] I. I. Bigi and A. I. Sanda, *Nucl. Phys.* **B281**, 41 (1987).
- [42] Z. Xing, *Phys. Lett. B* **364**, 55 (1995).
- [43] G. Brandenburg *et al.*, (CLEO Collaboration), *Phys. Rev. Lett.* **80**, 2762 (1998).
- [44] B. Barish *et al.*, contribution to the 1997 European Physical Society meeting, Jerusalem, preprint CLEO CONF 97-01 (1997) (unpublished).
- [45] M. Bauer, B. Stech, and M. Wirbel, *Z. Phys. C* **29**, 639 (1985).
- [46] M. Neubert and B. Stech, CERN-TH/97-99, (1997), to appear in *Heavy Flavours II*, edited by A. J. Buras and M. Linder World Scientific, Singapore (1997), hep-ph/9705292.
- [47] W. T. Eadie *et al.*, *Statistical Methods in Experimental Physics*, North-Holland, New York (1971), p. 131.
- [48] B.F.L. Ward, UTHEP-98-0201 (1998).
- [49] M. Gronau and D. London, *Phys. Lett. B* **253**, 483 (1991).
- [50] R. Aleksan, B. Kayser and D. London, National Science Foundation preprint NSF-PT-93-4 (1993), hep-ph/9312338.
- [51] I. Dunietz, *Phys. Rev. D* **52**, 3048 (1995).
- [52] A. J. Buras, W. Slominski and H. Steger, *Nucl. Phys.* **B245**, 369 (1984);
M. B. Voloshin *et al.*, *Sov. J. Nucl. Phys.* **46**, 112 (1987);
A. Datta, E. A. Paschos and U. Türke, *Phys. Lett. B* **196**, 382 (1987); *Nucl. Phys.* **B311**, 35 (1988);
R. Aleksan *et al.*, *Phys. Lett. B* **316**, 567 (1993);
M. Beneke, G. Buchalla and I. Dunietz, *Phys. Rev. D* **54**, 4419 (1996).

- [53] R. Fleischer and I. Dunietz, *Phys. Rev. D* **55**, 259 (1997); *Phys. Lett. B* **387**, 361 (1996);
R. Fleischer, CERN-TH/97-281 (1997), hep-ph/9710331.

Semileptonic B Decays and the Extraction of $|V_{cb}|$ and $|V_{ub}|$

This chapter describes BaBar's potential to determine the two CKM matrix elements $|V_{cb}|$ and $|V_{ub}|$ using semileptonic decays of B mesons. These determinations rely strongly on theoretical support. Therefore, the first five sections of the chapter describe the present status of the theory connecting the observed rates of exclusive and inclusive decays with the matrix elements. Section 8.5 summarizes the estimates of the theoretical uncertainties in the determinations of $|V_{cb}|$ and $|V_{ub}|$. Section 8.6 gives an introduction to common features of the four experimental determinations presented in the following four sections. The last section summarizes the estimates of both theoretical and experimental errors.

8.1 Exclusive Semileptonic B Decays to Charmed Mesons

8.1.1 Heavy-Quark Symmetry

The properties of hadronic bound states composed of a heavy quark and other light constituents are characterized by a large separation of length scales. The size of such systems is determined by the QCD scale, $R_{\text{had}} \sim 1/\Lambda_{\text{QCD}} \sim 1 \text{ fm}$, and thus the typical momenta exchanged between the heavy and light constituents are of order Λ_{QCD} . The heavy quark is surrounded by a most complicated, strongly interacting cloud of gluons and light quarks or antiquarks. On the other hand, the Compton wavelength of the heavy quark, $\lambda_Q \sim 1/m_Q$, is much smaller than the size of the hadron, and thus to resolve the quantum numbers of the heavy quark would require a hard probe. The soft gluons exchanged between the heavy quark and the light constituents can only resolve distances much larger than λ_Q . Therefore, the light degrees of freedom are blind to the flavor (mass) and spin of the heavy quark. They experience only its color field, which extends over distances large compared with $1/m_Q$. Therefore, in the limit $m_Q \rightarrow \infty$, hadronic systems which differ only in the flavor or spin quantum numbers of the heavy quark have the same configuration of their light degrees of freedom [1]–[4]. The resulting spin-flavor symmetry provides relations between the properties of such particles as the heavy mesons B , D , B^* , and D^* , or the heavy baryons Λ_b and Λ_c . These are only approximate relations, since the masses of the bottom and charm quarks are not infinite. The

symmetry-breaking corrections can be organized in a systematic expansion in powers of $\alpha_s(m_Q)$ and $1/m_Q$, using the formalism of the heavy-quark effective theory (HQET) [5]–[7].¹

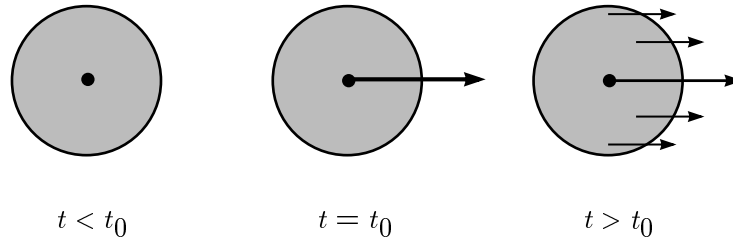


Figure 8-1. Elastic transition induced by an external heavy-quark current

Heavy-quark symmetry implies relations between the weak decay form factors of heavy hadrons [11], which are of particular interest for the analysis of exclusive semileptonic decays of the type $H_b \rightarrow H_c \ell \bar{\nu}$. From a theoretical point of view, these processes are simple enough to allow for a reliable, quantitative description based on first principles of QCD. Consider the elastic scattering of a B meson, $\bar{B}(v) \rightarrow \bar{B}(v')$, induced by a vector current coupled to the b quark. Before the action of the current, the light degrees of freedom inside the B meson orbit around the heavy quark, which acts as a static source of color. On average, the b quark and the B meson have the same velocity v . The action of the current is to replace instantaneously (at time $t = t_0$) the color source by one moving at a velocity v' , as indicated in Fig. 8-1. If $v = v'$, nothing happens, since the light degrees of freedom have no way to realize that there was a current acting on the heavy quark. If the velocities are different, however, the light constituents suddenly find themselves interacting with a moving color source. Soft gluons have to be exchanged to rearrange them so as to form a B meson moving at velocity v' . This rearrangement leads to a form-factor suppression, reflecting the fact that, as the velocities become more and more different, the probability for an elastic transition decreases. The important observation is that, in the limit $m_b \rightarrow \infty$, the form factor can only depend on the Lorentz boost $\gamma = v \cdot v' \geq 1$ connecting the rest frames of the initial- and final-state mesons. Thus, in this limit a dimensionless probability amplitude $\xi(v \cdot v')$ describes the transition. It is sometimes called the “Isgur-Wise function” [11]. In the HQET, which provides the appropriate framework for taking the limit $m_b \rightarrow \infty$, the hadronic matrix element describing the scattering process can thus be written as

$$\frac{1}{m_B} \langle \bar{B}(v') | \bar{b}_{v'} \gamma^\mu b_v | \bar{B}(v) \rangle = \xi(v \cdot v') (v + v')^\mu. \quad (8.1)$$

Here b_v and $b_{v'}$ are the velocity-dependent heavy-quark fields of the HQET. It is important that the function $\xi(v \cdot v')$ does not depend on m_b . The factor $1/m_B$ on the left-hand side compensates for a trivial dependence on the heavy-meson mass due to the usual relativistic normalization of meson states. The function $\xi(v \cdot v')$ is nothing but the elastic form factor of a heavy meson, and current

¹See also [8]. Other related work uses the method of direct nonrelativistic expansion of QCD [9, 10]. –Editors

conservation implies that it is normalized to unity at zero momentum transfer, corresponding to the “zero-recoil” point where $v \cdot v' = 1$, *i.e.*, $\xi(1) = 1$. This is in accordance with the intuitive argument that the probability for an elastic transition is unity if there is no velocity change.

The heavy-quark flavor symmetry can be used to replace the bottom quark in the final-state meson with a charm quark, thereby turning the B meson into a D meson. Then the scattering process turns into a weak decay process. In the heavy-quark limit, the replacement $b_{v'} \rightarrow c_{v'}$ is a symmetry transformation, under which the strong interactions are invariant. Hence, the matrix element

$$\frac{1}{\sqrt{m_B m_D}} \langle D(v') | \bar{c}_{v'} \gamma^\mu b_v | \bar{B}(v) \rangle = \xi(v \cdot v') (v + v')^\mu \quad (8.2)$$

is still determined by the same function $\xi(v \cdot v')$. This is interesting, since in general the matrix element of a flavor-changing current between two pseudoscalar mesons is described by two form factors,² $F_1(q^2)$ and $F_0(q^2)$. It follows that, in the heavy-quark limit, these form factors are no longer independent, but they must obey the relation

$$F_1(q^2) = \left[1 - \frac{q^2}{(m_B + m_D)^2} \right]^{-1} F_0(q^2) = \frac{m_B + m_D}{2\sqrt{m_B m_D}} \xi(v \cdot v'), \quad (8.3)$$

where the momentum transfer q is related to the variable $v \cdot v'$ through $q^2 = m_B^2 + m_D^2 - 2m_B m_D v \cdot v'$. Thus, the flavor symmetry relates two *a priori* independent form factors to one and the same function. Moreover, the normalization of the Isgur-Wise function at $v \cdot v' = 1$ now implies a nontrivial normalization of the form factors at the point of maximum momentum transfer, $q_{\text{max}}^2 = (m_B - m_D)^2$. The heavy-quark spin symmetry leads to additional relations among weak decay form factors. It can be used to relate matrix elements involving vector mesons to those involving pseudoscalar mesons, because a vector meson with longitudinal polarization is related to a pseudoscalar meson by a rotation of the heavy-quark spin. Hence, the spin-symmetry transformation $c_{v'}^\uparrow \rightarrow c_{v'}^\downarrow$ relates $\bar{B} \rightarrow D$ with $\bar{B} \rightarrow D^*$ transitions. Now this is even more remarkable, since in general four form factors, $V(q^2)$ for the vector current, and $A_i(q^2)$ with $i = 0, 1, 2$ for the axial current, are required to parameterize the $\bar{B} \rightarrow D^*$ matrix elements. In the heavy-quark limit, they obey the relations

$$V(q^2) = A_0(q^2) = A_2(q^2) = \left[1 - \frac{q^2}{(m_B + m_{D^*})^2} \right]^{-1} A_1(q^2) = \frac{m_B + m_{D^*}}{2\sqrt{m_B m_{D^*}}} \xi(v \cdot v'). \quad (8.4)$$

Equations (8.3) and (8.4) summarize the relations imposed by heavy-quark symmetry on the weak decay form factors describing the semileptonic decay processes $\bar{B} \rightarrow D \ell \bar{\nu}$ and $\bar{B} \rightarrow D^* \ell \bar{\nu}$. These relations are model-independent consequences of QCD in the limit where $m_b, m_c \gg \Lambda_{\text{QCD}}$.

²In this chapter, the conventions of Bauer, Stech and Wirbel [12] are adopted for the semileptonic decay form factors.

In terms of the recoil variable $w = v \cdot v'$, the differential semileptonic decay rates in this limit become [13]

$$\begin{aligned} \frac{d\Gamma(\bar{B} \rightarrow D \ell \bar{\nu})}{dw} &= \frac{G_F^2 |V_{cb}|^2}{48\pi^3} (m_B + m_D)^2 m_D^3 (w^2 - 1)^{3/2} \xi^2(w), \\ \frac{d\Gamma(\bar{B} \rightarrow D^* \ell \bar{\nu})}{dw} &= \frac{G_F^2 |V_{cb}|^2}{48\pi^3} (m_B - m_{D^*})^2 m_{D^*}^3 \sqrt{w^2 - 1} (w + 1)^2 \\ &\quad \times \left(1 + \frac{4w}{w + 1} \frac{m_B^2 - 2w m_B m_{D^*} + m_{D^*}^2}{(m_B - m_{D^*})^2} \right) \xi^2(w). \end{aligned} \quad (8.5)$$

These expressions receive symmetry-breaking corrections, since the masses of the heavy quarks are not infinite. Perturbative corrections of order $\alpha_s^n(m_Q)$, where $m_Q = m_b$ or m_c , can be calculated order by order in perturbation theory. A more difficult task is to control the nonperturbative power corrections of order $(\Lambda_{\text{QCD}}/m_Q)^n$. The HQET provides a systematic framework for analyzing these corrections [7, 14, 15].³ An important result obtained in this way is that the leading (first-order) $1/m_Q$ corrections to the $\bar{B} \rightarrow D^* \ell \bar{\nu}$ decay rate vanish at zero recoil (known as Luke's theorem). A similar statement is, however, not true for the decay $\bar{B} \rightarrow D \ell \bar{\nu}$ [17].

Expressions similar to Eq. (8.5) can also be derived for the semileptonic decays of other heavy hadrons, such as the baryon decay $\Lambda_b \rightarrow \Lambda_c \ell \bar{\nu}$, or B -meson decays into excited charm mesons. Since the configuration of light degrees of freedom involved in these transitions is different from that in the ground-state mesons, new ‘‘Isgur-Wise functions’’ will appear in these expressions. For the case of $\bar{B} \rightarrow D^{**} \ell \bar{\nu}$ decays, this will be discussed in more detail in Section 8.1.5.

8.1.2 Determination of $|V_{cb}|$

A model-independent determination of the element $|V_{cb}|$ of the Cabibbo-Kobayashi-Maskawa matrix can be obtained by measuring the recoil spectrum of D^* mesons produced in $\bar{B} \rightarrow D^* \ell \bar{\nu}$ decays [13]. In the heavy-quark limit, the differential decay rate for this process has been given in (8.5). In order to allow for corrections to that limit, it can be written

$$\begin{aligned} \frac{d\Gamma(\bar{B} \rightarrow D^* \ell \bar{\nu})}{dw} &= \frac{G_F^2}{48\pi^3} (m_B - m_{D^*})^2 m_{D^*}^3 \sqrt{w^2 - 1} (w + 1)^2 \\ &\quad \times \left(1 + \frac{4w}{w + 1} \frac{m_B^2 - 2w m_B m_{D^*} + m_{D^*}^2}{(m_B - m_{D^*})^2} \right) |V_{cb}|^2 \mathcal{F}^2(w), \end{aligned} \quad (8.6)$$

where the hadronic form factor $\mathcal{F}(w)$ coincides with the Isgur-Wise function up to small symmetry-breaking corrections. The idea is to measure the product $|V_{cb}| \mathcal{F}(w)$ as a function of w , and to

³See also [8, 16]—*Editors*

extract $|V_{cb}|$ from an extrapolation of the data to the zero-recoil point $w = 1$, where the B and the D^* mesons have a common rest frame. At this kinematic point, heavy-quark symmetry allows us to calculate the normalization of the form factor, $\mathcal{F}(1)$, with small and controlled theoretical errors.

The general structure of the symmetry-breaking corrections to the form factor at zero recoil is

$$\mathcal{F}(1) = \eta_A \eta_{\text{QED}} \left(1 + 0 \times \frac{\Lambda_{\text{QCD}}}{m_Q} + \text{const} \times \frac{\Lambda_{\text{QCD}}^2}{m_Q^2} + \dots \right) \equiv \eta_A \eta_{\text{QED}} (1 + \delta_{1/m^2}), \quad (8.7)$$

where η_A is a short-distance correction arising from the finite QCD renormalization of the flavor-changing axial current at zero recoil, $\eta_{\text{QED}} \approx 1.007$ accounts for QED corrections (in leading logarithmic order) [18], and δ_{1/m^2} parameterizes second-order (and higher) power corrections. The absence of first-order power corrections at zero recoil is a consequence of Luke's theorem [14]. The one-loop expression for η_A has been known for a long time [2]:

$$\eta_A = 1 + \frac{\alpha_s(M)}{\pi} \left(\frac{m_b + m_c}{m_b - m_c} \ln \frac{m_b}{m_c} - \frac{8}{3} \right). \quad (8.8)$$

An optimization of the scale in the running coupling constant, using the BLM prescription [19], gives $M \approx 0.51\sqrt{m_c m_b}$ [20]. With this choice, the above result is an excellent approximation to the exact two-loop expression for η_A , which gives the value [21, 22]

$$\eta_A = 0.960 \pm 0.007, \quad (8.9)$$

where the error is taken to be the size of the two-loop correction.⁴ The analysis of the power corrections is more difficult, since it cannot rely on perturbation theory. Three approaches have been discussed: in the ‘‘exclusive approach,’’ all $1/m_Q^2$ operators in the HQET are classified and their matrix elements estimated, leading to $\delta_{1/m^2} = -(3 \pm 2)\%$ [15, 26]; the ‘‘inclusive approach’’ has been used to derive the bound $\delta_{1/m^2} < -3.5\%$, and to estimate that $\delta_{1/m^2} = -(7 \pm 3)\%$ [27]; the ‘‘hybrid approach’’ combines the virtues of the former two to obtain a more restrictive lower bound on δ_{1/m^2} , leading to $-8\% < \delta_{1/m^2} < -3\%$ [28]. This result has been confirmed, using a similar approach, in Ref. [29].⁵ Combining this value with the results for η_A and η_{QED} given above yields

$$\mathcal{F}(1) = 0.913 \pm 0.007 \pm 0.024 \pm 0.011 \quad (8.10)$$

for the normalization of the hadronic form factor at zero recoil. The first error accounts for the remaining perturbative uncertainty, while the second one reflects the uncertainty in the calculation

⁴The calculations of [23] suggest that higher-order terms lead to a larger uncertainty in η_A , ± 0.03 . Note however that technical differences in definitions in various calculations lead to differences as to which parameter is assigned certain parts of the higher-order uncertainties. See also [24, 25] –*Editors*

⁵The ‘‘exclusive approach’’ has also been referred to as the ‘‘symmetry approach’’; matrix elements in this approach are estimated in a nonrelativistic quark model. Earlier estimates with this approach gave $\delta_{1/m^2} = -(2 \pm 1)\%$, the number quoted above is an updated estimate by the same authors. The ‘‘inclusive approach’’ is also known as the ‘‘dynamical approach’’ and is based on sum rules [10]. The lower bounds of [28, 29] are disputed in [30, 25]. –*Editors*

of $1/m_Q^2$ corrections. The third error gives an estimate of higher-order power corrections obtained by taking 20% of the central value for δ_{1/m^2} , corresponding to a suppression by an additional factor of Λ_{QCD}/m_c . Adding the theoretical uncertainties in quadrature gives $\mathcal{F}(1) = 0.913 \pm 0.027$, whereas adding them linearly to be conservative leads to $\mathcal{F}(1) = 0.913 \pm 0.042$. Thus, the corrections to the heavy-quark limit amount to a moderate decrease of the form factor by about 9%. Note that, from a theoretical point of view, the definition of “perturbative” and “nonperturbative” contributions to $\mathcal{F}(1)$ in (8.7) is intrinsically ambiguous and scheme-dependent. Only the sum of all contributions is a meaningful quantity. Therefore, it was an important result when the short- and long-distance contributions to $\mathcal{F}(1)$ were calculated in a different scheme based on the Wilsonian operator product expansion. When corrected for QED effects, the result $\mathcal{F}(1) = 0.91 \pm 0.06$ obtained from such an analysis [24] is in good agreement with the value quoted above.⁶

In principle, a determination of $|V_{cb}|$ can also be done using the recoil spectrum measured in $\bar{B} \rightarrow D \ell \bar{\nu}$ decays. However, both from a theoretical and from an experimental point of view, the accuracy that can be achieved is less than in the decays $\bar{B} \rightarrow D^* \ell \bar{\nu}$ described above. Nevertheless, such an analysis would provide an interesting consistency check. Generalizing (8.5), the recoil spectrum in $\bar{B} \rightarrow D \ell \bar{\nu}$ decays can be written as

$$\frac{d\Gamma(\bar{B} \rightarrow D \ell \bar{\nu})}{dw} = \frac{G_F^2 |V_{cb}|^2}{48\pi^3} (m_B + m_D)^2 m_D^3 (w^2 - 1)^{3/2} V_1^2(w), \quad (8.11)$$

where the vector form factor $V_1(w)$ coincides with the Isgur-Wise function up to symmetry-breaking corrections. Unlike the form factor $\mathcal{F}(w)$ discussed above, the function $V_1(w)$ is not protected against $1/m_Q$ corrections at zero recoil [17]; still, these corrections are numerically small since they must vanish in the limit $m_b = m_c$, in which the vector current is conserved. An explicit calculation using the QCD sum-rule approach gives $V_1(1)/\mathcal{F}(1) = 1.08 \pm 0.06$ [31], and thus $V_1(1) = 0.99 \pm 0.07$.

For either decay, the extrapolation of the differential decay rate to the zero-recoil point introduces some systematic uncertainties at present. Because of the phase-space suppression, few events occur close to $w = 1$. In order to reduce the theoretical uncertainty it would therefore help to have constraints on the shape of the functions $\mathcal{F}(w)$ and $V_1(w)$. Since the range of w values accessible in the decays $\bar{B} \rightarrow D^{(*)} \ell \bar{\nu}$ is rather small ($1 < w < 1.6$), the interest is mainly in constraining the first few parameters in an expansion around $w = 1$, e.g.,

$$\mathcal{F}(w) = \mathcal{F}(1) \left[1 - \hat{\rho}^2 (w - 1) + \hat{c} (w - 1)^2 + \dots \right]. \quad (8.12)$$

The shape of the form factor is highly constrained by analyticity and unitarity requirements [32]–[34]. This is discussed in more detail below. In the long run, the statistics of the experimental

⁶The estimates of [24, 25] find an uncertainty of order ± 0.015 from higher-order corrections to $\mathcal{F}(1)$. In [27] the value of approximately 10% for reduction of the form factor at the origin was first obtained. These sum-rule-based approaches introduce a somewhat different definition of the short-distance factor, thereby avoiding some of the theoretical uncertainties associated with η_A [25, 24, 30]. Despite these differences in detail, the final estimates are now quite similar, as noted above. –Editors

results close to zero recoil will be such that these theoretical constraints will not be crucial to get a precision measurement of $|V_{cb}|$. They will, however, enable strong consistency checks.

Bounds on the slope parameter $\hat{\rho}^2$ can also be derived from a sum rule expressing the fact that, in the heavy-quark limit, the inclusive sum of the probabilities for decays into hadronic states is equal to the probability for the free quark transition. Expanding the resulting sum rule around the zero-recoil point, and denoting by ρ^2 the slope parameter of the Isgur-Wise function, one finds the Bjorken sum rule [36]–[38]

$$\rho^2 = \frac{1}{4} + \sum_m |\tau_{1/2}^{(m)}(1)|^2 + 2 \sum_n |\tau_{3/2}^{(n)}(1)|^2 > \frac{1}{4}, \quad (8.13)$$

where the functions $\tau_j(w)$ are the analogues of the Isgur-Wise function for B decays into p -wave charm mesons (see Section 8.1.5). Voloshin has derived another sum rule involving the form factors for these transitions [39], which can be combined with the Bjorken sum rule to obtain an upper bound for the slope parameter ρ^2 , which is approximately $\rho^2 < 0.75$. Because of theoretical uncertainties in the calculation of higher-order corrections to these sum rules, as well as to the relation between the slope of the Isgur-Wise function and that of the physical form factor $\mathcal{F}(w)$ entering the semileptonic decay rate, one should relax the bounds when translating them into an allowed region for the slope parameter $\hat{\rho}^2$. A conservative range of allowed values is $0.2 < \hat{\rho}^2 < 1.1$ [40], in good agreement with the range obtained from the dispersive bounds to be discussed below.⁷

8.1.3 Dispersive Bounds and Unitarity Constraints on Form Factors

Dispersive methods can be used to derive rigorous, model-independent constraints on exclusive semileptonic, radiative, or elastic form factors. The derivations are based on first principles: the analyticity properties of two-point functions of local current operators and the positivity of the corresponding spectral functions. Analyticity relates integrals of the hadronic spectral functions to the behavior of QCD two-point functions in the deep Euclidean region via dispersion relations. Positivity guarantees that the restriction of the sum over hadronic states, which contribute to the spectral function, to the states involved in the decays of interest is bounded above by the full spectral function. The constraints on the relevant form factors, given their specific analyticity properties, then follow from this bound. The beauty of these techniques is that they can be supplied with information about the form factors, such as their values or derivatives at different points, to make the constraints more restrictive. They also have the advantage of yielding optimal constraints on the form factor, given the information fed into them.

⁷Higher-order power and perturbative corrections to these sum rules, and additional sum rules, were derived in Refs. [10, 30, 41]. –*Editors*

The history of these techniques goes back quite far, before the advent of QCD. In one of the first applications, bounds on the value and the derivatives of the form factors for $\bar{K} \rightarrow \pi \ell \bar{\nu}$ decays were obtained [42]. Later, the dispersive constraints were combined with the operator product expansion, thus making the method fully rigorous [43]. After the discovery of heavy-quark symmetry, the technique was applied to B mesons, to constrain the slope and curvature of the Isgur-Wise function given its normalization at zero-recoil [44]. Similar techniques have since been applied to two different situations. The first concerns exclusive $b \rightarrow c$ decays, where the goal is to constrain the parametrization used to extrapolate the experimental data for the differential decay rate to the zero-recoil point. The second concerns exclusive $b \rightarrow q$ decays, where q is a light quark. Here, the recoil energy of the light final-state hadron can range from 0 up to a few GeV, requiring one to understand the underlying QCD dynamics from a nonperturbative regime to a semi-perturbative one. Thus, calculations of the form factors over the full kinematic range are usually highly model-dependent. The goal, then, is to use the dispersive constraints to extrapolate (or interpolate) form factors to kinematic regions where they cannot be calculated reliably. Some approaches along these lines will be discussed in more detail in Section 8.2.2.

Here the focus is on applications to $b \rightarrow c$ transitions. These decays are simpler to study theoretically than heavy-to-light decays, because their kinematic range is much smaller and heavy-quark symmetry provides a normalization of the relevant form factors at zero recoil. The application of the dispersive bound techniques, however, is more difficult because the form factors have many sub-threshold singularities that must be accounted for: below the $B^{(*)}D^{(*)}$ thresholds, there are various B_c meson poles and $B_c h$ cuts, where h is a light hadron with appropriate quantum numbers. In Refs. [32], the dispersive techniques were applied to the $\bar{B} \rightarrow D^{(*)} \ell \bar{\nu}$ form factors, and few-parameter descriptions of the corresponding differential decay rates were obtained.

A slightly different approach was taken in Refs. [33, 34],⁸ where the dispersive techniques were used to provide bounds on and correlations between the slope and curvature parameters $\hat{\rho}^2$, \hat{c} , *etc.* entering the expansion (8.12) of the form factor $\mathcal{F}(w)$ around zero recoil, as well as between the parameters ρ_1^2 , c_1 , *etc.* in the corresponding expansion of the form factor $V_1(w)$. The allowed regions for the slope and curvature parameters are strongly correlated. In the most recent analysis [34], full use is made of the heavy-quark spin symmetry in the ground state doublets (B, B^*) and (D, D^*) , including the dominant $1/m_Q$ and radiative corrections. Simple one-parameter descriptions of the form factors $\mathcal{F}(w)$ and $V_1(w)$ are obtained, which are accurate to better than 2% over the full semileptonic domain. For $V_1(w)$, for instance, the result is

$$\frac{V_1(w)}{V_1(1)} \approx 1 - 8\rho_1^2 z + (51.\rho_1^2 - 10.)z^2 - (252.\rho_1^2 - 84.)z^3,$$

$$\text{with } z = \frac{\sqrt{w+1} - \sqrt{2}}{\sqrt{w+1} + \sqrt{2}}. \quad (8.14)$$

⁸A critique of this approach is found in [30, 35]. –*Editors*

The only parameter, the slope ρ_1^2 at zero recoil, is constrained by the dispersive bounds to lie in the interval $-0.17 < \rho_1^2 < 1.51$. To exhibit the possible behavior predicted by this parametrization, Fig. 8-2 shows $V_1(w)$ versus w , for a selection of equally-spaced values of ρ_1^2 covering the allowed domain. The width of the bands shows the total theoretical uncertainty. A similar parametrization is obtained for the form factor $\mathcal{F}(w)$.

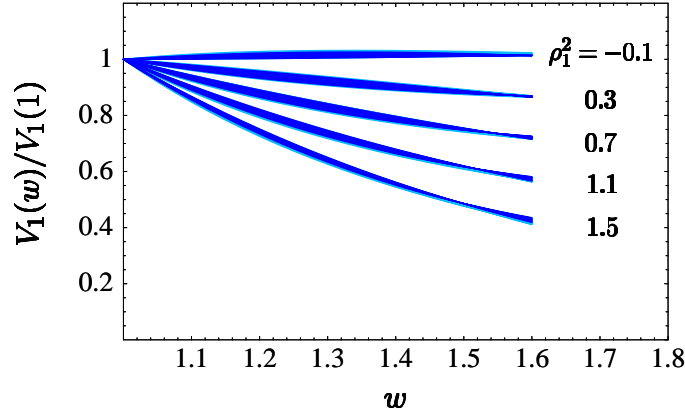


Figure 8-2. The form factor $V_1(w)$ for a selection of equally spaced values of the slope parameter ρ_1^2 [34].

8.1.4 Tests of Heavy-Quark Symmetry

The heavy-quark symmetry relations between semileptonic form factors play a crucial role in the model-independent determination of $|V_{cb}|$. They receive symmetry-breaking corrections, which can be estimated using the HQET. The extent to which these relations hold can be tested experimentally by comparing the different form factors describing the decays $\bar{B} \rightarrow D^{(*)}\ell\bar{\nu}$ at the same value of w . When the lepton mass is neglected, the differential decay distributions in $\bar{B} \rightarrow D^*\ell\bar{\nu}$ decays can be parametrized by three helicity amplitudes, or equivalently by three independent combinations of form factors. A good choice for three such quantities should be inspired by the heavy-quark limit [7]. One thus selects a single reference form factor, which, up to symmetry-breaking corrections, coincides with the Isgur-Wise function, and then introduces two form-factor ratios

$$\begin{aligned} R_1(w) &= \left[1 - \frac{q^2}{(m_B + m_{D^*})^2} \right] \frac{V(q^2)}{A_1(q^2)}, \\ R_2(w) &= \left[1 - \frac{q^2}{(m_B + m_{D^*})^2} \right] \frac{A_2(q^2)}{A_1(q^2)}, \end{aligned} \quad (8.15)$$

in such a way that in the heavy-quark limit $R_1 = R_2 = 1$, independently of w (or q^2). It is a complicated task to extract these ratios from experimental data. However, HQET-based calculations

suggest that the w -dependence of the form-factor ratios is rather mild and, to a good approximation, can be neglected [31]. With this assumption, the CLEO Collaboration has extracted R_1 and R_2 from an analysis of the angular distributions in $\bar{B} \rightarrow D^* \ell \bar{\nu}$ decays, finding that $R_1 = 1.18 \pm 0.32$ and $R_2 = 0.71 \pm 0.23$ [45]. The HQET gives an essentially model-independent prediction for the symmetry-breaking corrections to R_1 , whereas the corrections to R_2 are somewhat model-dependent [7]:

$$\begin{aligned} R_1 &\approx 1 + \frac{4\alpha_s(m_c)}{3\pi} + \frac{\bar{\Lambda}}{2m_c} \approx 1.3 \pm 0.1, \\ R_2 &\approx 1 - \kappa \frac{\bar{\Lambda}}{2m_c} \approx 0.8 \pm 0.2, \end{aligned} \quad (8.16)$$

with $\kappa \approx 1$ from QCD sum rules [31]. Here $\bar{\Lambda} \approx 500$ MeV is the light-quark contribution to the mass of a ground-state heavy meson. The experimental data confirm the theoretical prediction that $R_1 > 1$ and $R_2 < 1$, although the errors are still large. In the future, precise measurements of form-factor ratios will provide very sensitive tests of the pattern of symmetry-breaking corrections in the heavy-quark expansion.

Heavy-quark symmetry can also be tested by comparing the form factor $\mathcal{F}(w)$ in $\bar{B} \rightarrow D^* \ell \bar{\nu}$ decays with the corresponding form factor $\mathcal{G}(w)$ governing $\bar{B} \rightarrow D \ell \bar{\nu}$ decays. In the heavy-quark limit, both form factors are given by the same function of w . A precise measurement of their ratio would provide information about the size of symmetry-breaking corrections away from zero recoil.

8.1.5 B Decays to p -Wave Charm Mesons

Semileptonic B decays into p -wave charm mesons are the most important source of background events polluting the measurement of the $\bar{B} \rightarrow D^* \ell \bar{\nu}$ decay rate. Ultimately, one would like to understand these processes and be able to model them in a reliable way. A better understanding of such decays is desirable also with respect to identifying the decay modes which, together with $\bar{B} \rightarrow D^{(*)} \ell \bar{\nu}$, saturate the inclusive semileptonic width of B mesons. Present data suggest that the sum of all (resonant or nonresonant) decays $\bar{B} \rightarrow D^{(*)} \pi \ell \bar{\nu}$ account for about 20% of the total semileptonic width [46].

In the heavy-quark limit, hadrons containing a single heavy quark can be classified not only by their total spin J , but also by the angular momentum j of their light degrees of freedom [47]–[49]. Hadrons corresponding to the same j belong to degenerate doublets under the heavy-quark spin symmetry. Therefore, the four charm meson states D^{**} corresponding, in the constituent quark model, to the orbital angular momentum $l = 1$ can be classified in two doublets: (D_0, D_1^*) have $j = \frac{1}{2}$ and $J^P = (0^+, 1^+)$, whereas (D_1, D_2^*) have $j = \frac{3}{2}$ and $J^P = (1^+, 2^+)$. The relations between this classification and the quark-model p -wave states can be found, *e.g.*, in Refs. [50, 51]. The charm meson state with $J^P = 2^+$ has been observed and is denoted by $D_2^*(2460)$. To a good

approximation, the observed $J^P = 1^+$ state $D_1(2420)$ can be identified with the HQET state D_1 ($j = \frac{3}{2}$), even though a small admixture of the $j = \frac{1}{2}$ component D_1^* is present in the physical state since the charm-quark mass is not infinite. Both states are narrow ($\Gamma \sim 20$ MeV), since their strong decays proceed through d-wave transitions. Their two-body hadronic widths are given in terms of a single coupling constant, which can be determined experimentally [52]. The doublet (D_0, D_1^*) corresponding to $j = \frac{1}{2}$ has not been observed yet. These states can decay through s -wave pion emission and are thus expected to be rather broad. The coupling constant governing the two-body hadronic transitions can be computed, *e.g.*, using QCD sum rules, with the result $\Gamma(D_0 \rightarrow D^+ \pi^-) \approx 180$ MeV and $\Gamma(D_1^{*0} \rightarrow D^{*+} \pi^-) \approx 165$ MeV [53]. The mixing angle between D_1 and D_1^* has been estimated to be about 16° [53, 54].

Experimental data on semileptonic B decays into p -wave charm resonances are at present rather limited. With some assumptions, the ALEPH Collaboration finds [46]

$$\mathcal{B}(\bar{B} \rightarrow D_1 \ell \bar{\nu}) = (0.73 \pm 0.17)\%, \quad \mathcal{B}(\bar{B} \rightarrow D_2^* \ell \bar{\nu}) < 0.7\% \quad (95\% \text{ CL}). \quad (8.17)$$

The CLEO Collaboration has reported [55]

$$\mathcal{B}(\bar{B} \rightarrow D_1 \ell \bar{\nu}) = (0.56 \pm 0.15)\%, \quad \mathcal{B}(\bar{B} \rightarrow D_2^* \ell \bar{\nu}) < 0.8\% \quad (90\% \text{ CL}). \quad (8.18)$$

Below, the theoretical predictions for semileptonic and some hadronic B decays into the narrow p -wave charm resonances D_1 and D_2^* are discussed in more detail.

8.1.5.1 Theoretical framework

The theoretical description of semileptonic decays involves the hadronic matrix elements of vector and axial vector currents between heavy meson states. For B decays into the narrow p -wave states D_1 and D_2^* , these matrix elements can be parametrized by a set of eight form factors, $f_i(w)$ ($i = V_1, V_2, V_3, A$) and $f_j(w)$ ($j = A_1, A_2, A_3, V$). In terms of these functions, the differential semileptonic decay rates are given by

$$\begin{aligned} \frac{d\Gamma(\bar{B} \rightarrow D_1 \ell \bar{\nu})}{dw} &= \frac{G_F^2 |V_{cb}|^2 m_B^5}{48\pi^3} r_1^3 \sqrt{w^2 - 1} \left\{ \left[(w - r_1) f_{V_1} + (w^2 - 1) (r_1 f_{V_2} + f_{V_3}) \right]^2 \right. \\ &\quad \left. + 2(1 - 2wr_1 + r_1^2) \left[f_{V_1}^2 + (w^2 - 1) f_A^2 \right] \right\}, \\ \frac{d\Gamma(\bar{B} \rightarrow D_2^* \ell \bar{\nu})}{dw} &= \frac{G_F^2 |V_{cb}|^2 m_B^5}{72\pi^3} r_2^3 (w^2 - 1)^{3/2} \left\{ \left[(w - r_2) k_{A_1} + (w^2 - 1) (r_2 k_{A_2} + k_{A_3}) \right]^2 \right. \\ &\quad \left. + \frac{3}{2} (1 - 2wr_2 + r_2^2) \left[k_{A_1}^2 + (w^2 - 1) k_V^2 \right] \right\}, \end{aligned} \quad (8.19)$$

where $r_1 = m_{D_1}/m_B$ and $r_2 = m_{D_2^*}/m_B$. It may be useful (if experimentally feasible) to separate the contributions corresponding to the different helicity states of the D_1 and D_2^* mesons. They

are associated with a characteristic dependence on the angle between the charged lepton and the charm meson in the rest frame of the virtual W boson. The corresponding expressions for the double-differential decay rates can be found in Ref. [56].

In the heavy-quark limit, all form factors are proportional to a universal function $\tau_{3/2}(w)$, where the subscript indicates the spin $j = \frac{3}{2}$ of the light constituents in the p -wave states. At tree level,

$$\begin{aligned}\sqrt{2} f_{V_1}(w) &= (w^2 - 1) \tau_{3/2}(w), & k_{A_1}(w) &= \sqrt{3} (w + 1) \tau_{3/2}(w), \\ \sqrt{2} f_{V_2}(w) &= 3 \tau_{3/2}(w), & k_{A_2}(w) &= 0, \\ \sqrt{2} f_{V_3}(w) &= (2 - w) \tau_{3/2}(w), & k_{A_3}(w) &= -\sqrt{3} \tau_{3/2}(w), \\ \sqrt{2} f_A(w) &= (w + 1) \tau_{3/2}(w), & k_V(w) &= \sqrt{3} \tau_{3/2}(w).\end{aligned}\quad (8.20)$$

In this limit, the matrix elements of the weak currents vanish at $w = 1$, reflecting the fact that the ground-state B meson is orthogonal to the p -wave D^{**} states. An important observation is that the leading $1/m_Q$ corrections at zero recoil can be calculated in a model-independent way in terms of the masses of charm-meson states [56]. The expressions for the form factors in the presence of $1/m_Q$ corrections are rather complicated; however, all model-independent information can be incorporated if the result for the form factor $f_{V_1}(w)$ in (8.20) is modified according to [57]

$$\sqrt{2} f_{V_1}(w) = (w + 1)(w - 1 + 2\delta) \tau_{3/2}(w), \quad \delta = \frac{m_{D_1} - m_D}{m_D} \approx 0.29, \quad (8.21)$$

so that $f_{V_1}(1)$ no longer vanishes. Numerically, this is quite a large effect. There are many other sources of $1/m_Q$ corrections; however, they do not yield contributions at zero recoil. Since the physical range of w values is restricted between 1 and about 1.3, it is likely that these other corrections will have a sub-dominant effect.

8.1.5.2 Theoretical predictions

In order to calculate the total semileptonic rates, an ansatz is required for the form factor $\tau_{3/2}(w)$. It is sufficient to adopt a linear approximation, $\tau_{3/2}(w) \approx \tau_{3/2}(1) [1 - \rho_{3/2}^2 (w - 1)]$, since the accessible range of w values is small. Higher-order terms can be taken into account partially by re-expressing the results for the decay rates obtained in linear approximation through values of the function $\tau_{3/2}(w)$ at intermediate points. In that way, one obtains [57]

$$\begin{aligned}\Gamma(\bar{B} \rightarrow D_1 \ell \bar{\nu}) &\approx (0.016 + 0.069\delta + 0.117\delta^2) \times [\tau_{3/2}(1.23)]^2 \text{ ps}^{-1} \\ &\approx 0.046 \times [\tau_{3/2}(1.23)]^2 \text{ ps}^{-1}, \\ \Gamma(\bar{B} \rightarrow D_2^* \ell \bar{\nu}) &\approx 0.021 \times [\tau_{3/2}(1.21)]^2 \text{ ps}^{-1}.\end{aligned}\quad (8.22)$$

These results do not include $1/m_Q$ corrections, except those proportional to the quantity δ , which are kinematically enhanced and specific for $\bar{B} \rightarrow D_1$ transitions. From the analysis of power

corrections for $\bar{B} \rightarrow D^{(*)} \ell \bar{\nu}$ decays it is known that the remaining $1/m_Q$ corrections tend to be spin-independent and thus may be expected to cancel, to a large extent, in ratios of decay rates. Therefore, an accuracy of about 20% can be expected in the prediction for the ratio of the two decay rates:

$$R_{**} = \frac{\Gamma(\bar{B} \rightarrow D_2^* \ell \bar{\nu})}{\Gamma(\bar{B} \rightarrow D_1 \ell \bar{\nu})} = \frac{1.31}{1 + 4.39\delta + 7.40\delta^2} \left(\frac{\tau_{3/2}(1.21)}{\tau_{3/2}(1.23)} \right)^2 \approx 0.48, \quad (8.23)$$

where $\rho_{3/2}^2 = 1.5 \pm 0.5$ is assumed to estimate the form-factor difference, which is a small effect. Note that the corrections proportional to δ are very important and change the result $R_{**}^\infty \approx 1.3$ obtained in the heavy-quark limit to a value significantly lower than unity [56]. Although the experimental errors are still large, the data in (8.17) and (8.18) support this prediction.

The present data on the branching ratio for the decay $\bar{B} \rightarrow D_1 \ell \bar{\nu}$ can be used to determine the value of the function $\tau_{3/2}(w)$ at an intermediate point. One finds $\tau_{3/2}(1.23) \approx 0.26$, which, under the assumption that $\rho_{3/2}^2 \approx 1.5$, translates to $\tau_{3/2}(1) \approx 0.4$. The leading $1/m_Q$ corrections parametrized by δ substantially reduce the value of $\tau_{3/2}(1)$ from the result obtained in the strict heavy-quark limit. The value determined here is in broad agreement with theoretical predictions, as discussed below.

A reliable theoretical determination of the universal function $\tau_{3/2}(w)$, and of the corresponding function $\tau_{1/2}(w)$ entering the description of B decays into the broad p -wave states D_0 and D_1^* , requires nonperturbative techniques, such as lattice gauge theory, QCD sum rules, or QCD-inspired quark models. The main difference with respect to the calculation of the Isgur-Wise form factor $\xi(w)$ is that the normalization of the form factors $\tau_j(w)$ at zero recoil is not predicted by any symmetry argument. So far, the functions $\tau_{3/2}(w)$ and $\tau_{1/2}(w)$ have been calculated using QCD sum rules and constituent quark models. A collection of results is shown in Table 8-1. Using these parameters one can compute the branching ratios, the distributions in the invariant mass of the lepton pair, the lepton-energy- spectrum, *etc.* In particular, one can predict the branching ratios for

Table 8-1. Predictions for the normalization and slope parameters of the functions $\tau_{3/2}(w)$ and $\tau_{1/2}(w)$. Only central values are quoted. The two sets of parameters from Ref. [58] refer to two choices of the inter-quark potential.

$\tau_{3/2}(1)$	$\rho_{3/2}^2$	$\tau_{1/2}(1)$	$\rho_{1/2}^2$	Method	Ref.
0.28	0.9	0.25	0.4	QCD Sum Rules	[59]
0.31	2.8	0.31	2.8	Quark Model	[37]
0.66	1.9	0.41	1.3	Quark Model	[60]
0.54	1.5	0.22	0.8	Quark Model	[58]
0.51	1.4	0.06	0.7	Quark Model	[58]

the decays into the broad p -wave states D_0 and D_1^* with $j = \frac{1}{2}$, which have not yet been observed experimentally. Although the theoretical uncertainties are large, it can be concluded that these branching ratios do not exceed a few times 10^{-3} .

The analysis of semileptonic B decays into p -wave charm states is a basic step for the study of the D^{**} production in nonleptonic B decays, in the factorization approximation [61, 62] and beyond [57]. This is important in the light of the BaBar experimental program on CP violation, since B decays into $D^{**}\bar{D}$ final states represent interesting processes as far as the determination of the angle β of the unitarity triangle is concerned. Here the discussion is restricted to hadronic two-body decays with a pion in the final state, which are related in a model-independent way to the corresponding semileptonic decays at $q^2 = 0$ [63]. For the case of decays into p -wave charm mesons, the relation reads [57]

$$\frac{\Gamma(\bar{B} \rightarrow D^{**}\pi^-)}{d\Gamma(\bar{B} \rightarrow D^{**}\ell\bar{\nu})/dq^2\Big|_{q^2=0}} \approx 6\pi^2 f_\pi^2 |V_{ud}|^2 |1 + \delta_{\text{nf}}|^2, \quad (8.24)$$

where the quantity $\delta_{\text{nf}} = \mathcal{O}(1/N_c)$ parameterizes nonfactorizable contributions to the decay amplitudes, which are color suppressed. The semileptonic rates at $q^2 = 0$ can be calculated using the HQET, as described above. With some rather mild assumptions, it is then possible to derive theoretical predictions for the following two ratios [57]:

$$\begin{aligned} R_{\pi\ell} &= \frac{\Gamma(\bar{B} \rightarrow D_1\pi^-)}{\Gamma(\bar{B} \rightarrow D_1\ell\bar{\nu})} \approx (0.20 \pm 0.06) |1 + \delta_{\text{nf}}|^2, \\ R_{\pi\pi} &= \frac{\Gamma(\bar{B} \rightarrow D_2^*\pi^-)}{\Gamma(\bar{B} \rightarrow D_1\pi^-)} \approx 0.35 \left| \frac{1 + \delta_{\text{nf}}(D_2^*)}{1 + \delta_{\text{nf}}(D_1)} \right|^2. \end{aligned} \quad (8.25)$$

The first prediction is in good agreement with the measurement $R_{\pi\ell} = 0.21 \pm 0.08$ obtained by combining data reported by the CLEO Collaboration [55, 64]. The second prediction, when combined with the experimental value for $\mathcal{B}(\bar{B} \rightarrow D_1\pi^-)$, implies that

$$\mathcal{B}(\bar{B} \rightarrow D_2^*\pi^-) \approx 0.35 \mathcal{B}(\bar{B} \rightarrow D_1\pi^-) \approx 4 \times 10^{-4}, \quad (8.26)$$

which is about a factor of five lower than the current central value reported by the CLEO Collaboration [64].

8.2 Exclusive Semileptonic B Decays to Light Mesons and Determination of $|V_{ub}|$

Since their discovery, the exclusive semileptonic decay modes $\bar{B} \rightarrow \pi\ell\bar{\nu}$ and $\bar{B} \rightarrow \rho\ell\bar{\nu}$ have been used to extract a value of the element $|V_{ub}|$ of the Cabibbo-Kobayashi-Maskawa matrix. The theoretical description of these heavy-to-light ($b \rightarrow u$) decays is, unfortunately, more model-dependent

than that for $b \rightarrow c$ transitions, because heavy-quark symmetry does not help to normalize the relevant hadronic form factors. A variety of calculations for such form factors exists, based on lattice gauge theory, QCD sum rules, perturbative QCD, or quark models. With few exceptions, the results for $|V_{ub}|$ obtained by confronting these predictions with experimental data lie in the range $|V_{ub}| = (2.5\text{--}4.5) \times 10^{-3}$, which is in agreement with the (strongly model-dependent!) values obtained from the endpoint region of the lepton-energy spectrum in inclusive semileptonic decays. In view of the importance of a precise knowledge of the quark mixing parameters and their impact on studies of CP violation, a more accurate determination of $|V_{ub}|$ with controlled theoretical uncertainties is most desirable.

On the theoretical side, large efforts are being made to develop more reliable methods to determine the form factors for heavy-to-light transitions. The most promising approaches aim at combining several methods, each of which have a limited range of applicability. Some of these developments are described in more detail below. Some others are discussed in Refs. [65, 66]. Ultimately, a reliable determination of $|V_{ub}|$ will emerge from a combination of such (and maybe other) approaches.

8.2.1 Heavy-to-Light Form Factors from Lattice QCD

Potentially, lattice gauge theory can provide calculations of hadronic matrix elements based on first principles. As such, it may offer the most rigorous tool to control the hadronic physics relevant to the determination of $|V_{ub}|$. Several groups have calculated heavy-to-light form factors using lattice simulations (see Refs. [67, 68] for recent reviews). Here some representative results obtained for the semileptonic form factors relevant to $\bar{B} \rightarrow \pi \ell \bar{\nu}$ and $\bar{B} \rightarrow \rho \ell \bar{\nu}$ decays are discussed, as well as for the form factors of the decay $\bar{B} \rightarrow K^* \gamma$, which are related by heavy-quark and light-flavor symmetries to the $\bar{B} \rightarrow \rho$ form factors.

Although heavy-quark symmetry is less predictive for heavy-to-light decays than for heavy-to-heavy ones, it does give useful scaling laws for the form factors, as the mass of the heavy quark varies at fixed value of $w = v \cdot v'$. They can be used to extrapolate lattice calculations performed with quark masses around m_c to the b -quark mass. Moreover, the heavy-quark spin symmetry relates the $\bar{B} \rightarrow V$ matrix elements of the weak current (where V is a light vector meson) with the corresponding matrix elements of magnetic moment operators, thereby relating $\bar{B} \rightarrow \rho \ell \bar{\nu}$ and $\bar{B} \rightarrow K^* \gamma$ decays up to $SU(3)$ -breaking effects [69, 70].

In order to control discretization errors in lattice simulations, it is necessary that the three-momenta of the B , π and ρ mesons be small in lattice units. Therefore, the form factors can only be determined at large momentum transfer, corresponding to small recoil. Future experiments will be able to compare the lattice form-factor calculations directly with experimental data at large q^2 . A proposal in this direction, which may serve as an example of a possible strategy to extract $|V_{ub}|$, was made by the UKQCD Collaboration [71]. They parameterize the differential decay rate for

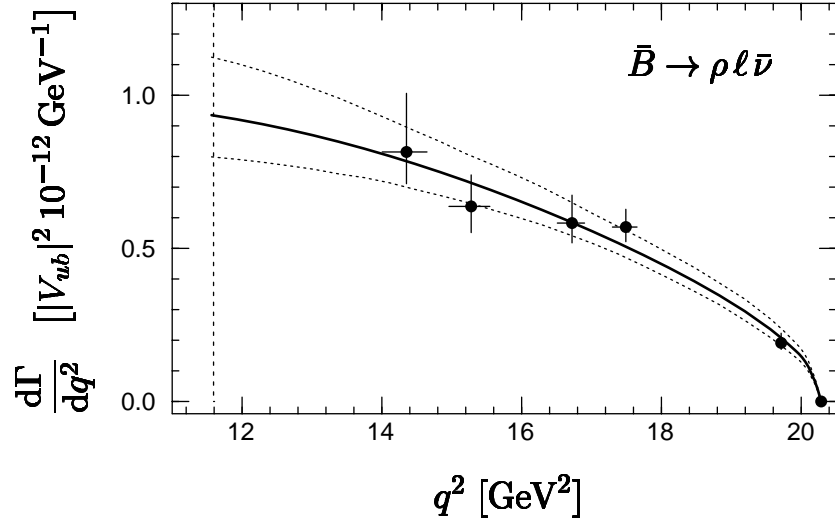


Figure 8-3. Example of a lattice prediction for the differential decay rate as a function of q^2 for the semileptonic decay $\bar{B} \rightarrow \rho \ell \bar{\nu}$ [71]. The points are measured lattice data, whereas the solid curve is a fit using (8.27). The dashed curves show the variation from the statistical errors in the fit parameters. The vertical dotted line marks the charm endpoint.

$\bar{B} \rightarrow \rho \ell \bar{\nu}$ near q_{\max}^2 by

$$\frac{d\Gamma(\bar{B} \rightarrow \rho \ell \bar{\nu})}{dq^2} = 10^{-12} \frac{G_F^2 |V_{ub}|^2}{192\pi^3 m_B^3} q^2 \lambda^{1/2}(q^2) a^2 [1 + b(q^2 - q_{\max}^2)], \quad (8.27)$$

where $\lambda(q^2) = (m_B^2 + m_\rho^2 - q^2)^2 - 4m_B^2 m_\rho^2$. The constants

$$a = 4.6_{-0.3}^{+0.4} \pm 0.6 \text{ GeV}, \quad b = (-8_{-6}^{+4}) \times 10^{-2} \text{ GeV}^2 \quad (8.28)$$

are determined from the lattice calculations. The result for a incorporates a systematic error dominated by the uncertainty ascribed to discretization errors and would lead to an extraction of $|V_{ub}|$ with less than 10% statistical error and about 12% systematic error from the theoretical input. The prediction for the differential decay rate $d\Gamma/dq^2$ is presented in Fig. 8-3.

Derivation of the full q^2 -dependence of the form factors from the lattice data involves a large extrapolation from the high q^2 values, where present-day lattice calculations can produce reliable results, all the way to $q^2 = 0$. The situation is even worse for the radiative decay $\bar{B} \rightarrow K^* \gamma$, which occurs at $q^2 = 0$. An interesting approach to this extrapolation problem has been suggested, and applied to $\bar{B} \rightarrow \pi \ell \bar{\nu}$ decays, in Ref. [72]. Using dispersion relations constrained by UKQCD lattice results at large values of q^2 and kinematic constraints at $q^2 = 0$, one can derive tight bounds on the values of the relevant form factor $F_1(q^2)$ in the entire kinematic region. More generally,

lattice-constrained parameterizations of heavy-to-light form factors, which are consistent with heavy-quark scaling relations, kinematic constraints and dispersive bounds, have been used to derive simple, few-parameter descriptions of semileptonic form factors [73]. The same method has also been applied to the rare radiative decay $\bar{B} \rightarrow K^* \gamma$ [74]. Potentially, these dispersive analyses can provide model-independent results, which will improve as the error bars on the lattice data decrease, and as the kinematic range covered by lattice calculations is extended.

8.2.2 Dispersive Bounds on Heavy-to-Light Form Factors

Some aspects of the dispersive bounds used to constrain the shape of semileptonic form factors have already been discussed in Section 8.1.3. This section focuses on how dispersion relations may be used to aid the extraction of $|V_{ub}|$ from $\bar{B} \rightarrow \pi \ell \bar{\nu}$ decays [75, 76]. The application of dispersive-bound techniques is particularly clean in this case, since the only dynamical singularity below the $B\pi$ threshold is the B^* pole.

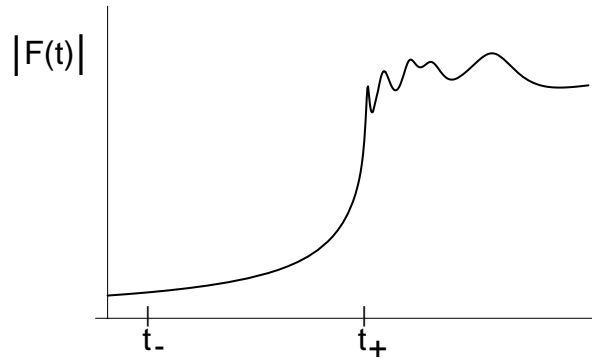


Figure 8-4. The magnitude of a generic form factor $F(t)$ as a function of momentum transfer $t = q^2$. The pair-production threshold t_+ and the semileptonic endpoint t_- are shown schematically.

The physical principle behind the dispersive technique can be illustrated with the help of Fig. 8-4, which shows the typical behavior of a $\bar{B} \rightarrow H \ell \bar{\nu}$ form factor $F(t)$ that has been analytically continued beyond the maximum momentum transfer, $t_- = (m_B - m_H)^2$, accessible in semileptonic decays. H is a generic meson such as a D or π . Crossing symmetry implies that in the region $t \geq t_+ = (m_B + m_H)^2$ the form factor describes the production of BH pairs. The point of the figure is that the functional form of $F(t)$ in the semileptonic region $t \leq t_-$ is largely determined by its behavior in the unphysical region $t_- < t < t_+$ and the pair-production region $t \geq t_+$.

It turns out [32] that the relative amount a form factor can vary over the semileptonic region $0 \leq t \leq t_-$ is controlled by the parameter

$$z_{\max} = \left(\frac{\sqrt{m_B} - \sqrt{m_H}}{\sqrt{m_B} + \sqrt{m_H}} \right)^2. \quad (8.29)$$

Table 8-2. Maximal velocity transfers and z_{\max} for some semileptonic decays

Decay Mode	$v \cdot v'_{\max}$	z_{\max}	Decay Mode	$v \cdot v'_{\max}$	z_{\max}
$D \rightarrow K^* \ell \bar{\nu}$	1.3	0.033	$\bar{B} \rightarrow D^* \ell \bar{\nu}$	1.5	0.056
$D \rightarrow K \ell \bar{\nu}$	2.0	0.10	$\bar{B} \rightarrow D \ell \bar{\nu}$	1.6	0.064
$D \rightarrow \rho \ell \bar{\nu}$	1.4	0.048	$\bar{B} \rightarrow \rho \ell \bar{\nu}$	3.5	0.20
$D \rightarrow \pi \ell \bar{\nu}$	6.8	0.33	$\bar{B} \rightarrow \pi \ell \bar{\nu}$	19	0.52

The square roots lead to remarkably small numbers for some decays, as can be seen from Table 8-2. To see how z_{\max} enters the parameterizations of form factors, note that in the pair-production region perturbative QCD can be used to describe the inclusive rate of production of all hadrons with BH quantum numbers. This calculation in turn serves to bound the rate of production of BH pairs, and thus to bound the form factor $|F(t)|$ in the region $t \geq t_+$. Schematically,

$$\int_{t_+}^{\infty} dt [\text{perturbative } W \rightarrow X_{bh} \text{ rate}] \geq \int_{t_+}^{\infty} dt [\text{exclusive } W \rightarrow BH \text{ rate}], \quad (8.30)$$

where X_{bh} represents all hadronic states with BH quantum numbers. The left-hand side of this equation is calculable in QCD, whereas the right-hand side involves the square of the form factor $F(t)$. In the unphysical region $t_- < t < t_+$, $F(t)$ will not be a smooth function because of the contributions from resonances below the pair-production threshold. These resonances can be accounted for by introducing a function $P(t)$ that has unit magnitude in the pair-production region and depends only on the masses of the sub-threshold resonances. This leads to a bound of the type

$$\int_{t_+}^{\infty} dt |\phi(t)P(t)F(t)|^2 \leq 1, \quad (8.31)$$

where ϕ incorporates the perturbative and phase-space information in the pair-production region, P incorporates phenomenological information in the unphysical region, and the product $\phi P F$ is smooth for $t < t_+$.

In order to turn (8.31) into a useful constraint in the semileptonic region, one constructs a function $z(t)$ whose powers form an orthonormal basis in the integration region. Expanding $\phi P F$ in powers of z and substituting the result into (8.31) then gives

$$F(t) = \frac{1}{\phi(t)P(t)} \sum_{k=0}^{\infty} a_k z^k(t) \quad (8.32)$$

with unknown expansion coefficients obeying $\sum_k |a_k|^2 \leq 1$. Explicit formulae for ϕ and P for a variety of form factors can be found in Refs. [32, 34, 75, 76]. The variable $z(t)$ is given by

$$z(t) = \frac{t_0 - t}{(\sqrt{t_+ - t} + \sqrt{t_+ - t_0})^2}, \quad (8.33)$$

where t_0 is a free parameter that can be chosen for convenience. The significance of the parameter z_{\max} introduced in (8.29) is that, in general, $|z(t)| \leq z_{\max}$ for any t corresponding to semileptonic decay, *i.e.*, $0 \leq t \leq t_-$. In fact, by choosing an optimal value of t_0 , one typically finds $|z(t)| \lesssim \frac{1}{2}z_{\max}$. This, together with the upper bound on the sum of squares of the expansion coefficients a_k , justifies the truncation of the series (8.32) after the first few terms. How many terms are needed for a given level of accuracy has to be decided case by case. For instance, in the case of $\bar{B} \rightarrow D^{(*)}\ell\bar{\nu}$ decays the small value of z_{\max} allows each of the six form factors to be parameterized, to an accuracy of 3% or better, in terms of its normalization at zero recoil and one unknown fit coefficient [32, 34]. For $\bar{B} \rightarrow \pi\ell\bar{\nu}$ transitions, on the other hand, $z_{\max} \approx \frac{1}{2}$ would seem to require a large number of fit coefficients for any degree of accuracy.

There are two possibilities to reduce the number of coefficients needed. The first is to include on the right-hand side of (8.30) the contribution of $B^*\pi$ states in addition to $B\pi$. Tighter bounds on the first few coefficients a_k can then be obtained by relating the $\bar{B}^* \rightarrow \pi\ell\bar{\nu}$ and $\bar{B} \rightarrow \pi\ell\bar{\nu}$ form factors near zero recoil using heavy-quark symmetry. The second possibility is to weight the integrals in (8.30) more heavily near t_+ by taking higher moments, that is, by inserting additional powers of $1/t^n$ in the integrands. This allows one to decrease the allowed range for the first few coefficients a_k by roughly a factor of two.

To some extent, how well the $\bar{B} \rightarrow \pi\ell\bar{\nu}$ form factor can be described using, say, three fit coefficients depends on what it actually looks like. To get a rough idea, assume that $F_1(t)$ is known at three points and takes the values $F_1(0) = 0.5$, $F_1(21 \text{ GeV}^2) = 1.7$ and $F_1(t_-) = 6.0$. This determines a_0 , a_1 and a_2 . Varying the remaining parameters over their allowed ranges gives an envelope of the allowed parameterizations. In this example, a three-coefficient parameterization describes $F_1(t)$ over the entire kinematic range with an accuracy of about 15%.

8.2.3 Heavy-to-Light Form Factors from Light-Cone Sum Rules

QCD sum rules provide another tool for calculating nonperturbative quantities such as hadronic form factors. However, although they are rooted in QCD, it is not possible in practice to avoid making several assumptions which introduce some model-dependence in this approach.

In exclusive decays of B mesons involving only light quarks in the final state the decay products typically have a large energy, up to $E \approx \frac{1}{2}m_B \approx 2.5 \text{ GeV}$ at maximum recoil in the B rest frame. This could potentially upset the operator product expansion adopted in QCD sum-rule calculations [77], since contributions of operators of high dimension are accompanied by powers of Em_b/M^2 ,

where $M^2 \sim m_b \Lambda$ (with $\Lambda \sim 1$ GeV) is the Borel parameter. A remedy is provided by the light-cone sum-rule approach [78]–[80], in which the operator product expansion is organized according to the twist of the operators rather than their dimension. This allows, in a certain approximation, the resumming of an infinite series of contributions proportional to $(Em_b/M^2)^n$, using results on the asymptotic behavior of exclusive processes at large momentum transfer. Whether this approach is superior to the standard approach is not clear, *a priori*, since in many decays the maximum energy is not very large. There are indications that for D decays both methods are equally applicable and yield comparable results, whereas for energetic two-body decays of B mesons, such as $\bar{B} \rightarrow \pi \ell \bar{\nu}$ and $\bar{B} \rightarrow \rho \ell \bar{\nu}$, the light-cone sum rules are superior.

Semileptonic B decays have attracted most of the attention, especially the simplest of them, $\bar{B} \rightarrow \pi e \bar{\nu}$ (see Refs. [81]–[85] for some recent analyses). The hadronic matrix element is parametrized by two form factors, $F_1(t)$ and $F_0(t)$, where $t = (p - p')^2$ is the square of the momentum transfer. Only $F_1(t)$ is important for the semileptonic decay $\bar{B} \rightarrow \pi e \bar{\nu}$. The results for this decay are well established; a recent prediction is quoted in Table 8-3. Results of the traditional sum rules and the light-cone approach are in good agreement. Both methods predict a t -dependence of the form factor which is similar to vector-meson dominance. A simple parametrization, which gives an excellent description of the sum-rule results, is

$$F(t) = \frac{F(0)}{1 + a_F t/m_B^2 + b_F t^2/m_B^4}. \quad (8.34)$$

The differential $B \rightarrow \pi e \bar{\nu}$ decay rate is shown in the left plot of Fig. 8-5. The longitudinal form factor $F_0(t)$, which can be measured in the decay $\bar{B} \rightarrow \pi \tau \bar{\nu}_\tau$, has been calculated in Refs. [83, 85].

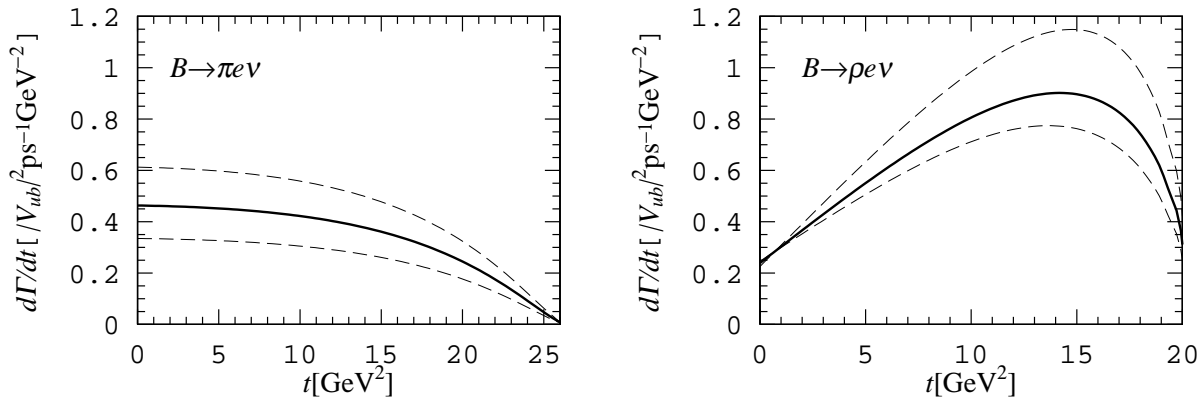


Figure 8-5. Sum-rule predictions for the differential rates in $\bar{B} \rightarrow \pi e \bar{\nu}$ [85] and $\bar{B} \rightarrow \rho e \bar{\nu}$ [86] decays, with estimated theoretical errors

Semileptonic $\bar{B} \rightarrow \rho e \bar{\nu}$ decays have been controversial for some time, with a considerable dispersion of results. The differential decay rate is described by three form factors: $A_1(t)$, $A_2(t)$ and $V(t)$. They were recently re-examined in [86], with the conclusion that the existing three-point

Table 8-3. Form-factor predictions from light-cone sum rules with functional t -dependence fitted to (8.34)

Form Factor	Ref.	$F(0)$	a_F	b_F
$F_1^{B \rightarrow \pi}$	[85]	0.27 ± 0.05	-1.50	0.52
$F_0^{B \rightarrow \pi}$	[85]	0.30 ± 0.05	-0.84	0.03
$A_1^{B \rightarrow \rho}$	[86]	0.27 ± 0.05	-0.42	-0.29
$A_2^{B \rightarrow \rho}$	[86]	0.28 ± 0.05	-1.34	0.38
$V^{B \rightarrow \rho}$	[86]	0.35 ± 0.07	-1.51	0.47

sum rules are not reliable, and the light-cone approach is more appropriate in this case. It is found that all three form factors rise with t , contrary to some of the earlier predictions. The results are summarized in Table 8-3, and the resulting differential decay rate is shown in the right-hand plot of Fig. 8-5.

There exists a rich variety of rare B decays induced by flavor-changing neutral currents, which also involve heavy-to-light transition form factors. Of these, the decay $\bar{B} \rightarrow K^* \gamma$ has received the most attention. Calculations exist both within the three-point and light-cone sum-rule framework, although one may argue that the light-cone approach is superior in this case [86, 87]. Other decays studied are $\bar{B} \rightarrow \rho \gamma$, $\bar{B} \rightarrow \omega \gamma$, $\bar{B}_s \rightarrow K^* \gamma$, and $\bar{B}_s \rightarrow \phi \gamma$ [87]. Also the $\bar{B} \rightarrow K^* \ell^+ \ell^-$ and $\bar{B} \rightarrow K \ell^+ \ell^-$ decay form factors have been calculated [88, 89].

The behavior of the heavy-to-light decay form factors in the heavy-quark limit has been subject to numerous discussions. At small recoil, the quark-mass dependence of form factors is given by HQET, and the QCD sum rules obey these scaling laws explicitly. However, at large recoil HQET is not applicable and the b -quark mass dependence has to be studied using different methods [90]–[92]. One finds that heavy-to-light form factors generically scale as $m_b^{-3/2}$ at maximum recoil. The form factors calculated by the light-cone sum rules have the expected behavior, while for usual three-point sum rules the heavy-quark limit at maximum recoil does not exist. However for realistic values of the b -quark mass it is important to recognize that these scaling laws have to be applied with great caution (see, *e.g.*, the discussion in [87]).

The question of how to quantify the theoretical uncertainties of the QCD sum-rule method is a difficult one. It is argued by most sum-rule practitioners that at present the most elaborate calculations of heavy-to-light form factors have an accuracy of about 15–30%, which translates into an uncertainty of order 30–60% in the decay rates. As far as the sum rule parameters are concerned, the main sources of errors are the high sensitivity to the b -quark mass and the uncertainty in the value of the B -meson decay constant f_B . A typical strategy is to consider ratios of sum rules, in which the dependence on m_b and f_B is reduced. On the theoretical side, significant uncertainties

are due to uncalculated radiative corrections. Taking them into account is relatively straightforward, but tedious. In the context of the light-cone sum rules, first results on the radiative corrections to the form factor $F_1(t)$ in $\bar{B} \rightarrow \pi \ell \bar{\nu}$ decays have become available very recently [93, 94]. Another source of uncertainties are higher-twist contributions, which so far have only been studied for the $\bar{B} \rightarrow \pi e \bar{\nu}$ form factor. Their estimate for other decays requires as a preliminary step a systematic study of light-cone distributions of vector mesons (and photons) beyond the leading twist. By working out radiative and higher-twist corrections to the sum rules, it should be possible to increase the accuracy and reliability of the predictions considerably.⁹

8.2.4 Using Semileptonic D Decays and Dispersive Bounds to Extract $|V_{ub}|$

Heavy-quark symmetry can be used to predict the $\bar{B} \rightarrow \pi \ell \bar{\nu}$ form factor $F_1(t)$ over a limited kinematic range, if the corresponding form factor in the charm decay $D \rightarrow \pi \ell \bar{\nu}$ is measured. In the heavy-quark limit, the two form factors obey the relation [69]

$$F_1^{B \rightarrow \pi}(t_B) = \sqrt{\frac{m_D}{m_B}} F_1^{D \rightarrow \pi}(t_D). \quad (8.35)$$

This equality holds when the form factors are evaluated at equal velocity transfer, *i.e.*, with $v_B \cdot v_\pi = v_D \cdot v_\pi$, or equivalently when

$$t_B = m_B(m_B - m_D) + m_\pi^2 \left(1 - \frac{m_B}{m_D}\right) + \frac{m_B}{m_D} t_D. \quad (8.36)$$

The decay spectrum for $D \rightarrow \pi \ell \bar{\nu}$ over the entire kinematic range $0 \leq t_D \leq (m_D - m_\pi)^2$ can thus be used to predict the spectrum for $\bar{B} \rightarrow \pi \ell \bar{\nu}$ over the range $18 \text{ GeV}^2 < t_B \leq (m_B - m_\pi)^2$.

This prediction invokes heavy-quark symmetry at the charm scale, so it should be accurate to about 30%. Some of the symmetry-breaking corrections, in particular the short-distance ones, can be calculated. As for the long-distance corrections, one may hope to learn more about their typical size from other decays like $\bar{B} \rightarrow D^* \ell \bar{\nu}$. If $SU(3)$ flavor symmetry is assumed in addition to heavy-quark symmetry, one can relate the $\bar{B} \rightarrow \pi \ell \bar{\nu}$ spectrum to that of the decay $D \rightarrow K \ell \bar{\nu}$, which has already been measured. The theoretical uncertainties entering such relations are, however, even larger [96]. In principle, a higher precision can be reached by taking a double-ratio of form factors, in which the leading $SU(3)$ and $1/m_Q$ corrections cancel [97], such as

$$\frac{F_1^{B \rightarrow \pi}}{F_1^{D \rightarrow \pi}} \cdot \frac{F_1^{D \rightarrow K}}{F_1^{B \rightarrow K}} = 1 + \mathcal{O}\left(\frac{\Lambda_{\text{QCD}}}{m_c} \cdot \frac{m_s}{\Lambda_\chi}\right), \quad (8.37)$$

if it proves possible to make these challenging experimental measurements. A similar double-ratio can be used to relate the $\bar{B} \rightarrow \rho$ and $\bar{B} \rightarrow K^*$ form factors with their counterparts in the charm sector [98].

⁹It has been pointed out to us by the authors that recent work has made progress in this direction, see [95].—Editors

Alternatively, lattice simulations can be used to predict the form factor $F_1(t)$ from first principles. Because of restrictions on the masses of the quarks that can be realistically simulated, however, present-day simulations can only cover a limited kinematic range close to zero recoil. Hence, a similar situation to that described above arises. Whether information on the form factor comes from combining heavy-quark symmetry with information extracted from charm decays or from lattice simulations, the region of phase space in $\bar{B} \rightarrow \pi \ell \bar{\nu}$ decays that can be directly accessed theoretically is limited to about a third of the allowed range. Fortunately, there are rigorous methods based on dispersion relations that allow predictions for form factors obtained in a limited kinematic region to extend over a much wider range. These techniques have been described in Section 8.2.2.

8.3 Inclusive Semileptonic $b \rightarrow c$ Decays

Inclusive decay rates determine the probability for the decay of a particle into the sum of all possible final states with a given set of global quantum numbers. An example is provided by the inclusive semileptonic decay rate of the B meson, $\Gamma(\bar{B} \rightarrow X \ell \bar{\nu})$, where the final state consists of a lepton-neutrino pair accompanied by any number of hadrons. From a theoretical point of view, inclusive decays of hadrons containing a heavy quark offer two advantages [100]–[109]: first, bound-state effects related to the initial state (such as the “Fermi motion” of the heavy quark inside the hadron [107, 108]) can be accounted for in a systematic way using the heavy-quark expansion; secondly, when the final state consists of a sum over many hadronic channels this eliminates bound-state effects related to the properties of individual hadrons.¹⁰ This second feature is based on the hypothesis of quark-hadron duality, which is an important concept in QCD phenomenology. The assumption of duality is that cross sections and decay rates, which are defined in the physical region (*i.e.*, the region of time-like momenta), are calculable in QCD after a “smearing” or “averaging” procedure has been applied [110]. In semileptonic decays, it is the integration over the lepton and neutrino phase space that provides a smearing over the invariant hadronic mass of the final state (so-called global duality). For nonleptonic decays, on the other hand, the total hadronic mass is fixed, and it is only the fact that one sums over many hadronic states that provides any averaging (so-called local duality). Local duality is a stronger assumption than global duality. It is important to stress that quark-hadron duality cannot yet be derived from first principles; still, it is a necessary assumption for many applications of QCD.

Using the optical theorem,¹¹ the inclusive decay width of a hadron H_b containing a b quark can be written as

$$\Gamma(H_b \rightarrow X) = \frac{1}{m_{H_b}} \text{Im} \langle H_b | \mathbf{T} | H_b \rangle, \quad (8.38)$$

¹⁰For early work on inclusive decays see [99], and on Fermi motion, see the first paper of [101] –*Editors*

¹¹The method discussed in the following paragraphs was introduced in [101]. –*Editors*

where the transition operator \mathbf{T} is given by

$$\mathbf{T} = i \int d^4x T \{ \mathcal{L}_{\text{eff}}(x), \mathcal{L}_{\text{eff}}(0) \}, \quad (8.39)$$

and \mathcal{L}_{eff} is the effective weak Lagrangian. The leading contributions to the transition operator are shown in Fig. 8-6. The large mass of the b quark means that the momenta flowing through the internal propagator lines are large. It is thus possible to construct an operator product expansion for the two-point function \mathbf{T} , where it is represented as a series of local operators containing the b -quark fields. The operator with the lowest dimension is $\bar{b}b$; it arises from contracting the internal lines in the first diagram. The only gauge-invariant operator with dimension four is $\bar{b} i \not{D} b$; however, the equations of motion imply that this operator can be replaced by $m_b \bar{b}b$. The first operator with a different structure has dimension five and contains the gluon field-strength tensor. Finally, from dimension six on, a large number of new operators appear. For dimensional reasons, the matrix elements of these operators are suppressed by inverse powers of the b -quark mass. Thus, any inclusive decay rate may be written in the form [101]–[104]

$$\Gamma(H_b \rightarrow X_f) = \frac{G_F^2 m_b^5}{192\pi^3} \left\{ c_3^f \langle \bar{b}b \rangle_H + c_5^f \frac{\langle \bar{b} g_s \sigma_{\mu\nu} G^{\mu\nu} b \rangle_H}{m_b^2} + \dots \right\}, \quad (8.40)$$

where the prefactor arises from the loop integrations, c_n^f are calculable short-distance coefficient functions (which also contain the relevant CKM matrix elements) depending on the quantum numbers f of the final states, and $\langle O \rangle_H$ are the (normalized) forward matrix elements of local operators, written using the short-hand notation

$$\langle O \rangle_H = \frac{1}{2m_{H_b}} \langle H_b | O | H_b \rangle. \quad (8.41)$$

These matrix elements, which contain all the long-distance contributions, can be systematically expanded in powers of $1/m_b$ using HQET. For the particular case of B mesons ($H_b = B$), the result is [15, 101, 103]

$$\begin{aligned} \langle \bar{b}b \rangle &= 1 + \frac{\lambda_1 + 3\lambda_2}{2m_b^2} + \mathcal{O}(1/m_b^3), \\ \frac{\langle \bar{b} g_s \sigma_{\mu\nu} G^{\mu\nu} b \rangle}{m_b^2} &= \frac{6\lambda_2}{m_b^2} + \mathcal{O}(1/m_b^3), \end{aligned} \quad (8.42)$$

where λ_1 and λ_2 parameterize the matrix elements of the heavy-quark kinetic energy and chromomagnetic interaction inside the B meson, respectively. The same parameters appear in the heavy-quark expansion of meson masses. Introducing the spin-averaged masses $\bar{m}_B = \frac{1}{4}(m_B + 3m_{B^*})$ and $\bar{m}_D = \frac{1}{4}(m_D + 3m_{D^*})$, one finds

$$\begin{aligned} m_b - m_c &= (\bar{m}_B - \bar{m}_D) \left(1 + \frac{(-\lambda_1)}{2\bar{m}_B \bar{m}_D} + \dots \right), \\ m_{B^*}^2 - m_B^2 &= 4\lambda_2 + \dots, \end{aligned} \quad (8.43)$$

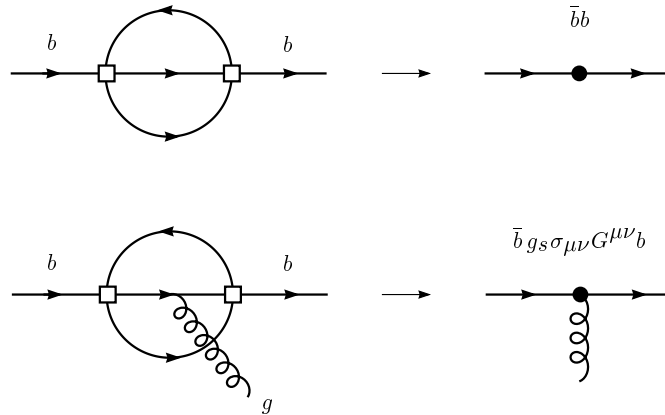


Figure 8-6. Perturbative contributions to the transition operator \mathbf{T} (left), and the corresponding operators in the operator product expansion (right). The open squares represent a four-fermion interaction of the effective weak Lagrangian \mathcal{L}_{eff} , while the black circles represent local operators in the $1/m_b$ expansion.

where the ellipses represent higher-order terms in the heavy-quark expansion. From the second relation, it follows that $\lambda_2 \approx 0.12 \text{ GeV}^2$. The kinetic-energy parameter λ_1 , on the other hand, is given in terms of a difference of quark masses and cannot be determined from hadron spectroscopy. Extracting this parameter from data involves some theoretical subtleties, which will be addressed later in Section 8.3.2. Various model approaches have been used to obtain values for λ_1 . However, since λ_1 is not a physical quantity, it is hard to compare the results from different methods. The range of predictions obtained from a variety of methods is $0.1 \text{ GeV}^2 < -\lambda_1 < 0.6 \text{ GeV}^2$ [111].¹²

Inserting the results (8.42) into (8.40) yields

$$\Gamma(\bar{B} \rightarrow X_f) = \frac{G_F^2 m_b^5}{192\pi^3} \left\{ c_3^f \left(1 + \frac{\lambda_1 + 3\lambda_2}{2m_b^2} \right) + c_5^f \frac{6\lambda_2}{m_b^2} + \dots \right\}. \quad (8.44)$$

The main result of the heavy-quark expansion for inclusive decay rates is the observation that the free quark decay (*i.e.*, the parton model) provides the first term in a systematic $1/m_b$ expansion [100].¹³ For dimensional reasons, the corresponding rate is proportional to the fifth power of the b -quark mass. The nonperturbative corrections, which arise from bound-state effects inside the B meson, are suppressed by at least two powers of the heavy-quark mass, *i.e.*, they are of relative order $(\Lambda_{\text{QCD}}/m_b)^2$. The absence of first-order power corrections is a consequence of the equations of motion, as there is no independent gauge-invariant operator of dimension four that could appear in the operator product expansion. The fact that bound-state effects in inclusive decays are strongly

¹²For a more technical discussion of these points see [24, 25]. In the OPE approach, the quantities λ_1, λ_2 are replaced by μ_π^2, μ_G^2 where the definition of the former is chosen to avoid some of the unphysical ambiguities of λ_1 [10, 30]. –Editors

¹³For related earlier work see [99]. –Editors

suppressed explains *a posteriori* the success of the parton model in describing such processes [112]–[114].

In the case of the inclusive semileptonic decay rate for $\bar{B} \rightarrow X_c \ell \bar{\nu}$ transitions, the short-distance coefficients appearing in (8.44) are given by

$$\begin{aligned} c_3^{\text{SL}}(x) &= |V_{cb}|^2 \left\{ 1 - 8x + 8x^3 - x^4 - 12x^2 \log x + \mathcal{O}(\alpha_s) \right\}, \\ c_5^{\text{SL}}(x) &= -|V_{cb}|^2 (1 - x)^4. \end{aligned} \quad (8.45)$$

where $x = (m_c/m_b)^2$. The corrections of order α_s to the leading term in the operator product expansion can be found in [115]. Also, the corresponding expressions for the case of a heavy τ lepton are known [116]–[118]. Finally, the expression for the $\bar{B} \rightarrow X_u \ell \bar{\nu}$ decay rate is obtained by setting $x \rightarrow 0$ and replacing $|V_{cb}|$ with $|V_{ub}|$. In order to determine $|V_{cb}|$ using the above prediction for the total semileptonic rate requires taking into account QCD radiative corrections, which in turn requires fixing a precise definition of the heavy-quark mass m_b . This will be discussed in more detail in the next section. The nonperturbative corrections, on the other hand, are very small, and therefore the theoretical uncertainty in the value of λ_1 is not a limiting factor.¹⁴ In order to determine $|V_{ub}|$ from inclusive charmless decays it is necessary to perform cuts that are optimized to discriminate the small $b \rightarrow u$ signal from the background arising from the much larger yield of $b \rightarrow c$ decays. Therefore, on the theoretical side there is a need to study the differential decay distributions in different kinematic variables, such as the lepton energy or the invariant hadronic mass in the final state. The heavy-quark expansion applies to such differential distributions as well. However, it turns out that the relevant mass scales in the operator product expansion are provided by the energy release to the hadronic final state and its invariant mass, in addition to the mass of the heavy quark. In close analogy with deep-inelastic scattering, the hadronic tensor depends on the Lorentz-invariants $\sqrt{Q^2}$ and $v \cdot Q$ (where Q is the total momentum of the final-state hadrons, and v the B -meson velocity), and one has to distinguish various regions of phase space depending on the values of these variables. In most of the phase space both variables are of order m_b , and the operator product expansion is performed in the way outlined above. The corresponding expressions for differential inclusive rates start with the corresponding free-quark distributions, and bound-state corrections are described as previously in terms of the two parameters λ_1 and λ_2 . An example is provided by the tree-level result for the lepton-energy spectrum in $\bar{B} \rightarrow X_u \ell \bar{\nu}$ decays, which at order $1/m_b^2$ reads [103, 104]¹⁵

$$\begin{aligned} \frac{1}{\Gamma} \frac{d\Gamma(\bar{B} \rightarrow X_u \ell \bar{\nu})}{dy} &= \left\{ 2y^2(3 - 2y) + \frac{y^2}{3} (16y - 9) \frac{\lambda_1}{m_b^2} + y^2(39 - 8y) \frac{\lambda_2}{m_b^2} \right\} \Theta(1 - y) \\ &\quad - \frac{\lambda_1 + 33\lambda_2}{3m_b^2} \delta(1 - y) - \frac{\lambda_1}{3m_b^2} \delta'(1 - y), \end{aligned} \quad (8.46)$$

where δ' denotes the derivative of the delta function, and $y = 2E_\ell/m_b$ is the rescaled energy of the charged lepton. In most of the phase space the spectrum is given by a smooth function, with

¹⁴This uncertainty limits the accuracy of the calculation only via the dependence on $m_b - m_c$ [27, 30]. –Editors

¹⁵See also [101]. –Editors

small nonperturbative corrections governed by the parameters λ_1 and λ_2 . However, the theoretical prediction becomes ill-behaved close to the endpoint of the spectrum where singularities appear. This can be traced back to the fact that close to the endpoint the operator product expansion breaks down, since higher-order terms become as important as the leading ones. It is described below how a reasonable result can be obtained by resumming an infinite set of terms in a twist expansion. In order to interpret the theoretical result (8.46) as it stands, one needs to “smear” it over a sufficiently large energy interval. Then the endpoint singularities are smoothed out, and the result can be compared with experimental data.

Close to the endpoint of the lepton spectrum, there is a kinematic region where the variable Q^2 (*i.e.*, the hadronic invariant mass of the final state) becomes small, of order $\Lambda_{\text{QCD}} m_b$, whereas $v \cdot Q$ is still of order m_b . Then terms of order $(v \cdot Q/Q^2)^n$ are formally all of the same magnitude, and the operator product expansion breaks down. The way out is to resum these terms using the twist expansion familiar from deep-inelastic scattering. The result can be expressed in terms of a “distribution function” $f(k_+)$ [107]–[109], a nonperturbative object analogous to the light-cone distribution functions for the quarks. The shape function gives the distribution of the light-cone projection k_+ of the heavy-quark momentum in the B meson,

$$f(k_+) = \frac{1}{2m_B} \langle B(v) | \bar{b}_v \delta(k_+ - iD_+) b_v | B(v) \rangle, \quad (8.47)$$

where D_+ is the light cone component of the covariant derivative of QCD, which is defined with the help of a light-like vector $n_+ = (1, 0, 0, 1)$ as the scalar product $D_+ = n_+ \cdot D$. This function is non-vanishing for values $\infty < k_+ \leq \bar{\Lambda}$, where $\bar{\Lambda} = m_B - m_b$ is the binding energy. The moments,

$$A_n = \int dk_+ k_+^n f(k_+) = \frac{1}{2m_B} \langle B(v) | \bar{b}_v (iD_+)^n b_v | B(v) \rangle, \quad (8.48)$$

are given in terms of the matrix elements of higher-dimensional operators in the HQET. The normalization of the distribution function gives $A_0 = 1$, $A_1 = 0$ by the equations of motion, and $A_2 = -\frac{1}{3}\lambda_1$, meaning that the width of the function is proportional to the heavy-quark kinetic energy. Indeed, the effects accounted for by the distribution function are related to the “Fermi motion” of the heavy quark inside the meson. If $d\Gamma_{\text{parton}}(m_b)$ denotes any differential decay rate in the parton model, the corresponding rate corrected for Fermi motion is given by the convolution [109].¹⁶

$$d\Gamma = \int dk_+ f(k_+) d\Gamma_{\text{parton}}(m_b + k_+). \quad (8.49)$$

If one were to look into the endpoint region with an even finer resolution than $Q^2 \sim \Lambda_{\text{QCD}} m_b$, no model-independent description of the spectrum could be obtained. The rate is dominated by single hadron states or resonances, and the appropriate description would be to sum over these exclusive states individually.

¹⁶See also [108]. –Editors

8.3.1 Determination of $|V_{cb}|$

The inclusive decays $\bar{B} \rightarrow X \ell \bar{\nu}$ are dominated by final states involving charm particles, and hence the total rate for these processes is very sensitive to the value of $|V_{cb}|$. At first sight, a precise calculation of inclusive decay rates seems to be limited by their strong dependence on the b -quark mass, and also by the appearance of large radiative corrections at higher orders in α_s , which indicate a sizable scale-dependence. However, a detailed investigation shows that it is nevertheless possible to obtain $|V_{cb}|$ with relatively small theoretical uncertainties.

The dependence of the total semileptonic rate on the b -quark mass is less strong than is suggested by the m_b^5 factor in (8.44). This becomes apparent if one introduces the variables m_b and $m_b - m_c$ instead of m_b and m_c . From the theoretical point of view, this has the advantage that these new variables have uncorrelated theoretical uncertainties: m_b is determined by the value of $\bar{\Lambda}$, whereas the difference $m_b - m_c$ depends on the value of λ_1 . In terms of the new parameters, and in the vicinity of $m_c/m_b \approx 0.3$, the decay rate behaves as $\Gamma_{\text{SL}} \propto m_b^{2.3} (m_b - m_c)^{2.7}$ [119].¹⁷ From (8.43), it follows that $m_b - m_c = 3.40 \pm 0.03 \pm 0.03 \text{ GeV}/c^2$, where the first error reflects the uncertainty in the value of λ_1 , whereas the second one accounts for unknown higher-order corrections in the heavy-quark expansion. An uncertainty of $60 \text{ MeV}/c^2$ in this mass difference translates into an uncertainty of 5% in the semileptonic rate. Also, an uncertainty of $100 \text{ MeV}/c^2$ in the value of m_b translates into an uncertainty of 5% in the rate. There have been attempts to extract a rather precise value for the pole mass m_b from Υ spectroscopy [121]–[124]. The most recent analysis yields the range $4.74 \text{ GeV}/c^2 < m_b < 4.87 \text{ GeV}/c^2$ for the pole mass defined at two-loop order in perturbation theory [124]. The difference between the one- and two-loop pole masses is about $250 \text{ MeV}/c^2$.¹⁸ Since only partial calculations of the $\mathcal{O}(\alpha_s^2)$ corrections to the semileptonic rate exist (see below), there is an ambiguity in which definition to use. Below, an uncertainty of $100 \text{ MeV}/c^2$ is assigned to the value of m_b . However, it is also indicated how final error estimate would change if a smaller uncertainty were assumed.

The next issue to discuss is that of the perturbative corrections to the semileptonic rate. The short-distance coefficient $c_3^{\text{SL}}(x)$ in (8.44) is known exactly to order α_s . In the $\overline{\text{MS}}$ renormalization scheme, and with an on-shell definition of the heavy-quark mass, one finds that the $\mathcal{O}(\alpha_s)$ corrections reduce the leading-order prediction for the rate by 12%. Unfortunately, only partial results exist for the $\mathcal{O}(\alpha_s^2)$ corrections. The terms of order $\beta_0 \alpha_s^2$, where β_0 is the first coefficient of the β function, have been calculated and found to decrease the rate further by about 6% [128]. Recently, the exact $\mathcal{O}(\alpha_s^2)$ corrections have been computed to the differential decay rate $d\Gamma/dq^2$ at the two kinematic points where $q^2 = 0$ and $q^2 = (m_b - m_c)^2$ [22, 129]. At these two values, corrections were found to be dominated by the terms of order $\beta_0 \alpha_s^2$. In view of these results, one can assume that those terms do indeed provide an accurate approximation for the full $\mathcal{O}(\alpha_s^2)$ corrections. To

¹⁷For earlier work see [120]. –Editors

¹⁸This large difference is expected [125, 126, 127]. One can, however, achieve power-like accuracy for the decay rates using running masses and fits based on Υ spectroscopy, as is discussed later. –Editors

be conservative, an error the size of the last computed term, *i.e.*, 6%, is assigned. This treatment is supported by an all-order resummation of the leading $\beta_0^{n-1}\alpha_s^n$ terms, which yields a further decrease of the decay rate by 7% from the terms with $n \geq 3$ [130].

There is a variety of different methods to estimate the theoretical error associated with the truncation of the perturbative series for the semileptonic rate, two of which have been discussed above: to take the size of the last computed term, or to consider the magnitude of higher-order terms in a certain approximation scheme. However, the values of the expansion coefficients also depend on the renormalization scheme used to define the heavy-quark mass. For instance, if one were to use the running mass in the $\overline{\text{MS}}$ scheme, $\overline{m}_b(m_b)$, instead of the pole mass, one would find a much larger correction at order α_s , whereas the next-order coefficient would turn out to be somewhat smaller. A certain class of large higher-order terms in the scheme based on the on-shell definition of m_b is associated with an intrinsic infrared ambiguity in the definition of the pole mass [127, 126]. Effectively, those terms can be eliminated when a value of m_b is extracted from another observable (such as the spectrum of \mathcal{T} resonances) and then used in the prediction for the semileptonic rate [131, 30].¹⁹ Care must be taken that in this process the same definitions and approximations are adopted in the two calculations. Elimination of scheme-dependent parameters, such as m_b , in favor of other observables may result in a better-behaved perturbative series. An example of this approach is discussed below. What remains, however, are genuine higher-order corrections, which are as yet uncalculated.²⁰

Based on these remarks, it follows that from a comparison of the theoretical expression for the inclusive $\overline{B} \rightarrow X_c \ell \overline{\nu}$ decay rate with experimental data, a fairly model-independent extraction of $|V_{cb}|$ is possible. From a theoretical point of view, this method is quite different from the determination based on the recoil spectrum in the exclusive decay $\overline{B} \rightarrow D^* \ell \overline{\nu}$, described in Section 8.1.2. In the exclusive method, the main uncertainty comes from the estimate of power corrections of order $1/m_c^2$. Short-distance corrections, on the other hand, are small and well under control. In the inclusive method, the genuine power corrections are of order $1/m_b^2$ and thus very small, whereas short-distance corrections are larger. In addition, there are uncertainties related to the explicit appearance of the heavy-quark masses. There is also an element of uncertainty related to the assumption of global quark-hadron duality, which underlies the theoretical description of inclusive decay rates. Both the small changes in the value of m_b , and the truncation error of the perturbative series, translate into an uncertainty that scales as $1/m_b$. Taking the average of the (consistent) central values for the semileptonic rate from [130] and [30], the final result for $|V_{cb}|$ reads

$$|V_{cb}| = \xi_{\text{th}} \left(\frac{\mathcal{B}(\overline{B} \rightarrow X_c \ell \overline{\nu})}{10.5\%} \right)^{1/2} \left(\frac{1.6 \text{ ps}}{\tau_B} \right)^{1/2}, \quad (8.50)$$

¹⁹See also [120, 121, 132]. –Editors

²⁰In calculations using the Wilson running-mass prescription and fitting this parameter from \mathcal{T} spectroscopy, it is found that the effect of higher-order terms is better controlled than in the pole-mass methods discussed above [25, 120, 133]. Such calculations have recently been done. It is found that the impact of higher-order terms is about 2% in the value of V_{cb} [30, 120, 134]. –Editors

where τ_B is the B -meson lifetime, and

$$\xi_{\text{th}} = 0.0400\eta_{\text{QED}} (1 \pm 0.030 \pm 0.024 \pm 0.025 \pm 0.012), \quad (8.51)$$

where $\eta_{\text{QED}} \approx 1.007$ is the same QED correction as in the exclusive case. The different theoretical uncertainties account for higher-order perturbative corrections, the dependence on the mass difference $m_b - m_c$, the dependence on the b -quark mass, and unknown $1/m_b^3$ corrections, respectively. The effects of terms of order $1/m_b^3$ have been estimated in [30]. The uncertainty in the value of the bound-state correction involving the parameter λ_1 in (8.44) is below 1% and has been absorbed into the last error quoted above. Adding the theoretical uncertainties in quadrature gives $\xi_{\text{th}} = 0.0403 \pm 0.0019$, whereas adding them linearly, to be conservative, leads to $\xi_{\text{th}} = 0.0403 \pm 0.0037$. If the more optimistic error estimates $\Delta(m_b - m_c) = 40 \text{ MeV}/c^2$ and $\Delta m_b = 50 \text{ MeV}/c^2$ are used, the errors in these numbers reduce to 0.0015 and 0.0024, respectively.²¹

Another possibility for the determination of $|V_{cb}|$ has been suggested in Ref. [131]. This method refers not only to the total semileptonic rate, but also uses moments of the hadronic invariant mass spectrum as an experimental input. In this way, all dependences on quantities that have intrinsic ambiguities or scheme-dependences (like the heavy-quark pole mass and the kinetic energy λ_1) may be eliminated, at the price of using additional input of data. Defining the moments of the hadronic mass spectrum as

$$\langle (s_H - \bar{m}_D^2)^n \rangle = \frac{1}{\Gamma_{\text{SL}}} \int ds \frac{d\Gamma_{\text{SL}}}{ds} (s - \bar{m}_D^2)^n, \quad (8.52)$$

one obtains, *e.g.*,

$$\langle (s_H - \bar{m}_D^2) \rangle = m_B^2 \left[0.051 \frac{\alpha_s}{\pi} + 0.23 \frac{\bar{\Lambda}}{m_B} \left(1 + 0.43 \frac{\alpha_s}{\pi} \right) + 0.26 \frac{\bar{\Lambda}^2}{m_B^2} + 1.01 \frac{\lambda_1}{m_B^2} - 0.31 \frac{\lambda_2}{m_B^2} \right], \quad (8.53)$$

where $\alpha_s = \alpha_s(m_b)$. This relation can be used to eliminate the quantity $\bar{\Lambda}$ (*i.e.*, the dependence on the b -quark mass) in the rewritten expression for the total semileptonic rate,

$$\Gamma_{\text{SL}} = \frac{G_F^2 |V_{cb}|^2 m_B^5}{192\pi^3} \times 0.369 \left[1 - 1.54 \frac{\alpha_s}{\pi} - 1.65 \frac{\bar{\Lambda}}{m_B} \left(1 - 0.87 \frac{\alpha_s}{\pi} \right) - 0.95 \frac{\bar{\Lambda}^2}{m_B^2} - 3.18 \frac{\lambda_1}{m_B^2} + 0.02 \frac{\lambda_2}{m_B^2} \right], \quad (8.54)$$

²¹For details of this method from the perspective of its proponents, who favor also the Wilson running-mass definition, and for further references see [25, 30]. These authors estimate that the remaining uncertainties are at the few percent level, and may be further reduced after detailed study of semi-leptonic B decays into excited D -states.
–Editors

in favor of additional experimental input. In principle, one could go further and use another moment to eliminate the dependence on the parameter λ_1 , as well. However, in practice, higher moments will be more sensitive to violations of local quark-hadron duality and introduce an additional element of theoretical uncertainty in this approach. More accurate expressions for the hadronic mass moments, which include $\mathcal{O}(\alpha_s^2)$ and $1/m_B^3$ corrections, along with an estimate of the theoretical uncertainties, can be found in Ref. [135], where the effect of an experimental cutoff imposed on the energy of the charged lepton is also investigated.

8.3.2 Aspects of Inclusive B Decays

In addition to the extraction of $|V_{cb}|$ and $|V_{ub}|$, inclusive semileptonic (and rare) B decays provide information on the structure of the B meson itself. This information is available when one studies inclusive observables which reflect kinematic distributions in the decay. Analysis of a particular observable, such as a moment of some kinematic quantity, typically yields restrictions on hadronic parameters such as $\bar{\Lambda}$ and λ_1 . The requirement of consistency between results obtained from analyses of different quantities allows one to test the accuracy of the theoretical expressions, which are only available at some fixed order in α_s and $1/m_b$, and even to examine underlying theoretical assumptions such as quark-hadron duality.

Only observables that are sufficiently inclusive are calculable using the operator product expansion. At a minimum, the observable must integrate over enough kinematic variables so as to smear out any sensitivity to individual resonances in the hadronic final states. In addition, technical features of the expansion may require additional smearing for the theoretical calculation to make sense. For example, the differential distribution $d\Gamma/dE_\ell$ in the semileptonic decay $\bar{B} \rightarrow X_c \ell \bar{\nu}$ is calculable for all values of E_ℓ not too close to the endpoint, where a few resonances dominate the spectrum. Hence, one can either use the spectrum itself, or integrals of the form $\int dE_\ell E_\ell^n d\Gamma/dE_\ell$, in the comparison between theory and experiment. By contrast, consider the invariant mass s_H of the inclusive hadronic final state, which is measurable if the four-momentum of the neutrino can be reconstructed. Here the differential distribution $d\Gamma/ds_H$ is not calculable for each individual value of s_H , as it is directly sensitive to the structure of resonances in the final state. Only integrals of this spectrum are sufficiently inclusive to yield useful information.

As an example, consider the first moment of the hadronic mass spectrum given in (8.53). The theoretical expression for this quantity depends on $\bar{\Lambda}$, λ_1 , λ_2 , and α_s . This expression refers to a fully inclusive measurement; if the reconstruction of the neutrino requires additional experimental cuts, the coefficients in the expansion are modified [135]. Since λ_2 and α_s are known, a measurement of the first moment allows one to constrain the values of $\bar{\Lambda}$ and λ_1 . The inclusion of higher-order perturbative corrections, *e.g.*, the terms proportional to $\beta_0 \alpha_s^2$, not only improves the accuracy of this constraint, but also changes the identity of the quantities $\bar{\Lambda}$ and λ_1 . The situation is similar to perturbative QCD, where a two-loop calculation of some observable such as a jet-shape variable both improves the theoretical accuracy by reducing the renormalization-scale dependence of the

result and also changes the value of α_s , which is extracted from experiment as a quantity defined by one-loop renormalization-group running to a quantity defined by the renormalization group at two loops. These two quantities are generally not the same. In the case of $\bar{\Lambda}$, *e.g.*, inclusion of the $\beta_0\alpha_s^2$ terms changes the extracted $\bar{\Lambda}$ from $\bar{\Lambda}_{\text{one-loop}}$ to $\bar{\Lambda}_{\text{two-loop}}$ (assuming that other two-loop corrections are negligible). These two quantities are different, and if a comparison is made with a value of $\bar{\Lambda}$ extracted from some other analysis, the same definition must be used in both cases.

The hadronic invariant mass moments $\langle (s_H - \bar{m}_D^2)^n \rangle$ have the nice feature that they start at order α_s and $\bar{\Lambda}$ in the operator product expansion.²² However, they are somewhat difficult to measure experimentally. A more accessible quantity is the energy of the charged lepton. Moments of the lepton-energy spectrum in the decay $\bar{B} \rightarrow X_c \ell \bar{\nu}$ may be defined as

$$M_n(E_1, E_2) = \frac{\int_{E_1}^{E_{\text{max}}} dE_\ell E_\ell^n (d\Gamma/dE_\ell)}{\int_{E_2}^{E_{\text{max}}} dE_\ell (d\Gamma/dE_\ell)}, \quad (8.55)$$

where $E_{1,2}$ are arbitrary lower cuts on the lepton energy. In general, the smaller these cuts can be made, the more reliable is the theoretical analysis. Explicit expressions for $R_1 = M_1(1.5 \text{ GeV}, 1.5 \text{ GeV})$ and $R_2 = M_0(1.7 \text{ GeV}, 1.5 \text{ GeV})$ are provided in Ref. [137]; those for $M_n(0, 0)$ with $n = 1, \dots, 5$ are given in Ref. [138]. The convergence of these expressions rapidly becomes poorer as n increases. Various higher-order corrections to the moments have been analyzed in Refs. [139, 140].

Finally, one can extract information on $\bar{\Lambda}$ and λ_1 from the photon-energy spectrum in the rare decays $\bar{B} \rightarrow X_s \gamma$. Since in this case the value of E_γ fully determines the hadronic invariant mass s_H , only integrals of the spectrum $d\Gamma/dE_\gamma$ are sufficiently inclusive to be insensitive to nonperturbative resonance effects. Moments of the form

$$M_n(E_0) = \frac{\int_{E_0}^{E_{\text{max}}} dE_\gamma E_\gamma^n (d\Gamma/dE_\gamma)}{\int_{E_0}^{E_{\text{max}}} dE_\gamma (d\Gamma/dE_\gamma)} \quad (8.56)$$

are studied in Ref. [141]. It is also possible to extract information about hadronic parameters from a study of the photon spectrum itself [107, 142, 143].²³ In this case, in the region in E_γ which is dominated by resonances, it is necessary to perform a smearing over a sufficiently wide energy range. The precise nature of this smearing will depend on the shape of the spectrum that is observed.

8.4 $|V_{ub}|$ from Inclusive Semileptonic $b \rightarrow u$ Decays

In the past, the traditional way to determine $|V_{ub}|$ has been to use the endpoint region of the charged-lepton energy spectrum in $\bar{B} \rightarrow X_u \ell \bar{\nu}$ decays, applying a lower cut on E_ℓ to eliminate

²²For a derivation see [136]. –Editors

²³See also [108]. –Editors

the background from $\bar{B} \rightarrow X_c \ell \bar{\nu}$ transitions. This cut implies that only a very narrow window $\Delta E \approx 350$ MeV is left, and in order to extract $|V_{ub}|$, a large extrapolation is unavoidable. As a result this method is very sensitive to model uncertainties. A more reliable extraction of $|V_{ub}|$ must exploit better discriminators between $b \rightarrow u$ and $b \rightarrow c$ transitions, which may use vertex information combined with a cut on the hadronic invariant mass (or energy) of the final state [144]–[149]. Calculation of the fraction of events surviving such a cut is more reliable than in the case of a cut on the charged-lepton energy. Despite significant experimental difficulties, this strategy appears to be more attractive than the conventional method. Eventually, it may lead to a precise determination of $|V_{ub}|$ with controlled theoretical uncertainties.

An obvious advantage of extracting $|V_{ub}|$ from a measurement of the hadronic invariant mass spectrum in the region below the charm threshold rather than from the endpoint region of the charged-lepton energy spectrum is that most of the $\bar{B} \rightarrow X_u \ell \bar{\nu}$ decays are expected to have hadronic invariant mass $\sqrt{s_H}$ below m_D , while only a small fraction of these decays have lepton energies in the endpoint region. Both the invariant mass region below the charm threshold and the endpoint region of the lepton spectrum receive contributions from hadronic final states with invariant masses that range up to m_D . However, for the electron endpoint region the contribution of states with mass near m_D is kinematically suppressed. In fact, models suggest that the electron endpoint region is dominated by contributions from the π and ρ states. On the other hand, many final states contribute to the hadronic invariant mass spectrum below the charm threshold, without any preferential weighting towards the lowest-mass states. Consequently, it is much more likely that the first few terms in the operator product expansion will provide a more accurate description of $\bar{B} \rightarrow X_u \ell \bar{\nu}$ decays in the region $s_H < m_D^2$ than in the endpoint region of the lepton spectrum. A modest cut on the lepton energy, which will probably be required experimentally for the direct measurement of s_H via the neutrino reconstruction technique, does not destroy this conclusion. Note that the $\bar{B} \rightarrow X_u \ell \bar{\nu}$ decay rate in the invariant mass region $s_H < m_D^2$ is likely to be less sensitive to nonperturbative effects than is the rate in the hadron energy (defined in the B rest frame) region $E_H < m_D$, because the requirement $E_H < m_D$ cuts out more of the phase space for states with mass near m_D than for the lower mass states. Thus, from a theoretical point of view a cut on the hadronic invariant mass [144, 148, 149] is a better discriminator against charm background than a cut on hadronic energy [146, 147].

The spectrum $d\Gamma/ds_H$ is sensitive to nonperturbative effects related to the Fermi motion of the heavy quark inside the B meson [107, 108]. According to (8.49), these effects can be taken into account by convoluting the parton model result for the hadronic mass distribution with the distribution function $f(k_+)$. The result obtained in this way can be compared with experimental data provided these have been averaged over a sufficiently wide interval to smear out local resonance structures.

In order to extract $|V_{ub}|$, the relevant question is which fraction of all $\bar{B} \rightarrow X_u \ell \bar{\nu}$ decays have s_H below a certain value M_{\max}^2 . This fraction is measured by the function

$$\Phi(M_{\max}) = \frac{1}{\Gamma_{\text{SL}}} \int_0^{M_{\max}^2} ds_H \frac{d\Gamma_{\text{SL}}}{ds_H}. \quad (8.57)$$

Unlike the hadronic mass spectrum itself, the function $\Phi(M_{\max})$ is an inclusive quantity, that is insensitive to fine details in the shape of the distribution function $f_+(k_+)$. As long as the threshold M_{\max} is sufficiently large, the result for $\Phi(M_{\max})$ is mainly sensitive to the value of the b -quark mass and, to a lesser extent, to the kinetic energy parameter λ_1 . A theoretical prediction for this function has been obtained in Ref. [148] by adopting the following simple ansatz for the distribution function:

$$f(k_+) = N \theta(1-x) e^{cx} (1-x)^a [1 + b(1-x)], \quad x = \frac{k_+}{\Lambda}, \quad (8.58)$$

with the parameters N, a, b, c chosen such that the first three moments of $f(k_+)$ satisfy the relations mentioned after (8.48). The result is shown in Fig. 8-7, where only m_b is varied with all other parameters kept fixed. The resulting theoretical uncertainty in the calculation of $\Phi(M_{\max})$, which directly translates into an uncertainty in the value of $|V_{ub}|$ extracted using this approach, strongly depends on the value of the threshold M_{\max} . First estimates yield $\delta|V_{ub}|/|V_{ub}| \approx 10\%$ for $M_{\max} = m_D$, and $\delta|V_{ub}|/|V_{ub}| \approx 20\%$ for $M_{\max} = 1.5 \text{ GeV}/c^2$ [148, 149]. For the theory underlying this measurement to be reliable, it is very important that the cut M_{\max} be as large as is experimentally feasible. For M_{\max} much below $1.5 \text{ GeV}/c^2$ radiative and nonperturbative corrections are less well controlled. This method is challenging, but ultimately it should be superior to the endpoint method. With what precision one will be able to extract $|V_{ub}|$ will depend on its experimental feasibility, for example, on the value of M_{\max} that can be attained.

8.5 Theory Summary

In the preceding sections, the theoretical basis for precise measurements of the parameters $|V_{cb}|$ and $|V_{ub}|$ of the Cabibbo-Kobayashi-Maskawa matrix has been discussed. Accurate values of these quantities are a necessary input for many analyses that will be pursued at BABAR. Both parameters can be measured in the semileptonic decays of B mesons, using both exclusive and inclusive decay modes. The theoretical tools that allow a precise description of these processes rely on heavy-quark symmetry and the operator product expansion.

The two most precise ways to extract $|V_{cb}|$ are (a) the measurement of the recoil spectrum in $\bar{B} \rightarrow D^* \ell \bar{\nu}$ decays, and (b) the measurement of the inclusive semileptonic branching ratio of B mesons. In the first case, heavy-quark symmetry, Luke's theorem and sum-rule estimates help to calculate

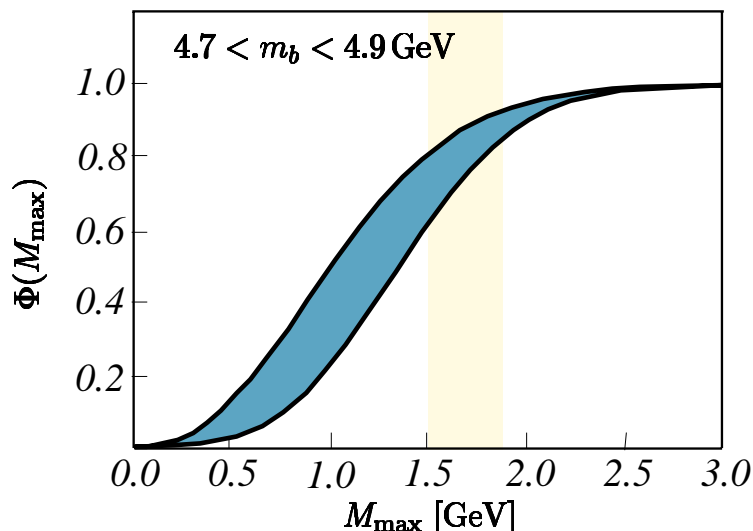


Figure 8-7. Theoretical prediction for the fraction of $\bar{B} \rightarrow X_u \ell \bar{\nu}$ events below a threshold M_{\max} obtained by varying m_b between 4.7 and 4.9 GeV/ c^2 , with fixed α_s and λ_1 [148].

the normalization of the semileptonic form factor at zero recoil. Dispersive constraints on the shape of the form factor eliminate most of the systematic uncertainty arising from the extrapolation of the measured spectrum to zero recoil. In the second case, experimental information on gross features of the decay distributions, such as moments of the hadronic mass spectrum, help to reduce the sensitivity of the theoretical prediction to the values of the heavy-quark masses. At present, both methods have theoretical uncertainties of a few per cent, and it is realistic to expect that combining them, a theoretical precision of 3% on the value of $|V_{cb}|$ will be obtained. Looking a few years ahead, anticipating further progress in the theoretical understanding of heavy-flavor transitions, one can hope that ultimately an accuracy of 1% may be reached.

On the contrary, there is at present no “best way” to determine $|V_{ub}|$. Rather, a cocktail of various analyses and consistency checks will be the strategy to follow. The analysis of the exclusive modes $\bar{B} \rightarrow \pi \ell \bar{\nu}$ and $\bar{B} \rightarrow \rho \ell \bar{\nu}$ may combine information from lattice QCD, dispersive constraints, heavy-quark symmetry and scaling relations, and QCD sum rules. As for inclusive semileptonic decays, it seems most promising to concentrate on measurements of the hadronic invariant mass distribution, combined with vertex information and a weak cut on the lepton energy. To what extent such an analysis is feasible remains to be seen. With present theoretical tools, it seems a realistic goal to reach a precision of 10% on $|V_{ub}|$. An optimistic hope for the long-term future, counting again on significant theoretical progress, is to achieve an accuracy of 5%.

8.6 Studying Semileptonic Decays with the BABAR Detector

8.6.1 The Experimental Environment

The only sources of prompt leptons at the $\Upsilon(4S)$ resonance are direct charm production and $B\bar{B}$ events, with about equal cross sections. In $B\bar{B}$ events, the momentum of the lepton is used to separate primary from secondary (cascade) leptons, and $b \rightarrow cl\nu$ decays from $b \rightarrow ul\nu$ decays. Figure 8-8 shows the momentum spectrum for the primary leptons from $b \rightarrow cl\nu$ decays. Electrons with momentum as low as 0.6 GeV/c will be identified cleanly using the electromagnetic calorimeter and the IFR will be efficient for identifying muons down to about 0.7 GeV/c. For muons and electrons, the rate of hadrons faking leptons should be quite low, and the dominant backgrounds will usually be due to real leptons from competing semileptonic decay modes.

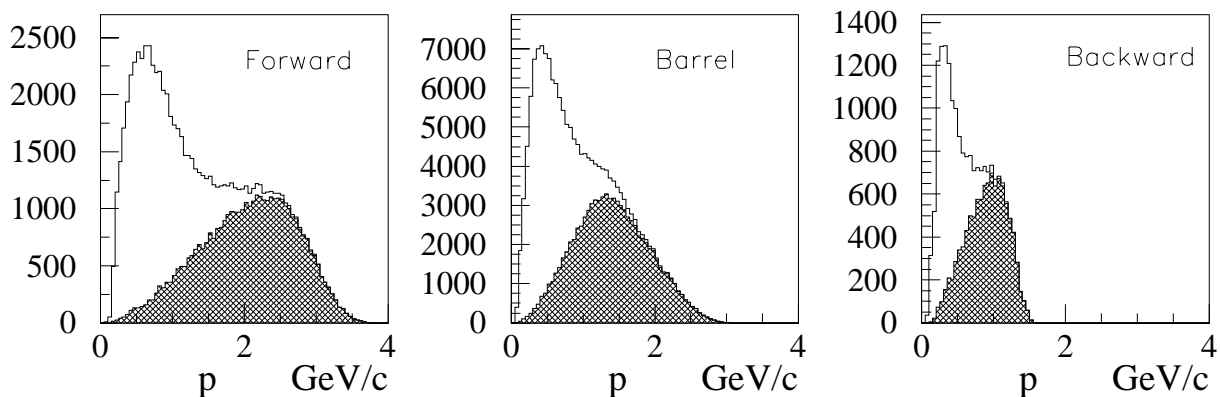


Figure 8-8. Momentum distribution of primary and secondary muons from B decay in (a) the forward endcap, (b) the barrel, and (c) the backward endcap regions. The shaded part of the histogram refers to primary decay muons.

8.6.2 Semileptonic Event Generators

In Section 4.1.1, a general description of the event generators used in the studies were discussed. Here, some particular features relevant to semileptonic decays are described.

The list of exclusive final state hadrons used in modeling the process $b \rightarrow cl\nu$ includes the D , D^* , the four P -wave states, the radially excited D and D^* , and nonresonant $D^{(*)}\pi$. All of these decays, except the nonresonant $D^{(*)}\pi$, are modeled according to the ISGW2 model, primarily because it gives explicit predictions for many final states. The sum of branching fractions for the decay modes

included is 10.4%, which is close to the measured B semileptonic branching fraction at the $\Upsilon(4S)$. The lepton-energy spectrum produced is somewhat softer than observed.

Similarly, the $b \rightarrow u\ell\nu$ transitions are modeled using the ISGW2 model for a long list of exclusive final states. This list includes the π , η , ω , and ρ which are of particular interest in the exclusive measurements, but also the a_1 , b_1 , a_0 , a_2 , $\rho(2S)$, η' , ρ' , π' , and f_0 . The sum of the branching ratios for all the $b \rightarrow u\ell\nu$ transitions is about 0.1%.

There are a number of models that predict the hadronic form factors for various semileptonic decay modes. The event generator uses these form factors to generate the distributions of the lepton energy and q^2 , and the associated decay distributions for the final state meson. All correlations in the decay are correctly handled, but no final state (electromagnetic) radiation is included. $B \rightarrow X\tau\bar{\nu}_\tau$ decays are also generated. The polarization of the τ and the resulting angular distributions are handled correctly.

In order to study the model-dependence of specific exclusive semileptonic decays, models other than the ISGW2 default model are available. The ISGW, KS, WSB, and Ball models can be used for $\pi\ell\nu$ and $\rho\ell\nu$, and a parameterization of HQET predictions is available for $D^{(*)}\ell\nu$.

8.6.3 Reconstruction of the Other B

The detailed study of $|V_{ub}|$ semileptonic decays is particularly challenging because of the huge background due to the semileptonic B decays into a charm final state that occurs one hundred times more frequently. One way to reduce this background is to reconstruct the other B in the event. The nature of this reconstruction of the “other B ” depends on whether one is analyzing exclusive or inclusive semileptonic decays.

It is possible to measure $|V_{ub}|$ by studying one of the simpler exclusive decays, such as $B \rightarrow \pi\ell\nu$ or $B \rightarrow \rho\ell\nu$. In this case one assumes that all the other particles in the event are due to the second B , and that the energy and momentum are those of the undetected neutrino:

$$p_\nu = p_{CM} - (p_l + p_\rho + p_B) \quad (8.59)$$

where p_B is the four momentum of all other particles. The background can be reduced strongly by requiring that the reconstructed mass and energy of the B decaying semileptonically be consistent with the kinematics of the event. This method has been used extensively by the CLEO collaboration [150]. The main limitation is that if a single track is missed from the other B decay, the event is lost. The main advantage is that a large fraction of all B decay modes can be included.

For reasons detailed in the theoretical section, there are advantages to reconstructing the charmless semileptonic B decays inclusively. In this case, one must use a different strategy to separate the suppressed decays from the dominant $b \rightarrow c\ell\nu$ decays. As is discussed below, the proposal is to

use the mass of the hadronic system in the semileptonic decay to separate charmless decays. The problem is how to identify which particles come from which B meson. The surest way to do this is to reconstruct fully the second B in one of a number of exclusive channels. In this case, one knows that all of the other detected particles form the hadronic system in the semileptonic decay, making it possible to reconstruct the mass of that system.

Thus, in one case, an exclusive semileptonic decay mode is considered and the other B is reconstructed inclusively. In the other case, the semileptonic decays are considered inclusively, while exclusive decays of the other B are reconstructed. In both cases, it is necessary to reconstruct all the decay products. Therefore the two methods put a premium on detector hermiticity, both for charged and neutral particles, and on good energy and momentum reconstruction. Both methods use the following cuts to reduce the fraction of events with an undetected particle:

- The total charge is required to be zero, which rejects events in which one track escaped detection,
- No additional lepton is allowed in the event, and
- The mass of the neutrino, obtained from the missing momentum and energy in the event, must be compatible with zero.

The crucial figure of merit for the final event sample available with this method is the fraction of events with one B meson fully and exclusively reconstructed. In order to estimate this fraction, the method outlined in [151] for the study of the decay $B \rightarrow D\bar{D}$ was followed. This consists of a simple parametrization of the efficiency according to the number of charged and neutral particles. The decay modes considered were of the type $B \rightarrow D^{(*)}X$, where X is π , ρ , or $\pi^+\pi^+\pi^-$, and decay modes of the D mesons with up to one π^0 in the final state. The modes considered for the D^+ and D^0 are listed in Tables 8-4 and 8-5. The efficiency per charged track was taken to be 87% and for π^0 s it was taken to be 62%. Only decays of D^{*0} into $D^0\pi^0$ and of D^{*+} into $D^0\pi^+$ were considered.

Table 8-4. Efficiency for D^0 reconstruction

Mode	Branching Fraction (%)	Efficiency (%)	$\epsilon \times Br$ (%)
$K^-\pi^+$	4.0	77	3.1
$K^-\pi^+\pi^0$	13.8	48	6.6
$K^-\pi^+\pi^+\pi^-$	8.1	55	4.4
Total	21.8		14.1

Table 8-5. Efficiency for D^+ reconstruction

Mode	Branching Fraction (%)	Efficiency (%)	$\epsilon \times Br$ (%)
$K^- \pi^+ \pi^+$	9.1	67	6.0
$K^- \pi^+ \pi^+ \pi^0$	6.4	42	2.7
Total	15.5		8.7

Table 8-6. Efficiency for B^+ reconstruction

Mode	Branching Fraction (%)	Efficiency (%)	$\epsilon \times Br(10^{-3})$
$\bar{D}^0 \pi^+$	0.55	12.2	0.7
$\bar{D}^0 \rho^+$	1.35	7.6	1.0
$\bar{D}^0 \pi^+ \pi^+ \pi^-$	1.10	9.2	1.0
$\bar{D}^{*0} \pi^+$	0.52	4.8	0.2
$\bar{D}^{*0} \rho^+$	1.68	2.7	0.5
$\bar{D}^{*0} \pi^+ \pi^+ \pi^-$	0.94	3.6	0.3
Total	6.14		3.7

Table 8-7. Efficiency for B^0 reconstruction

Mode	Branching Fraction (%)	Efficiency (%)	$\epsilon \times Br(10^{-3})$
$D^- \pi^+$	0.29	7.6	0.2
$D^- \rho^+$	0.81	4.7	0.4
$D^- \pi^+ \pi^+ \pi^-$	0.80	5.7	0.5
$D^{*-} \pi^+$	0.26	7.1	0.2
$D^{*-} \rho^+$	0.74	4.4	0.3
$D^{*-} \pi^+ \pi^+ \pi^-$	0.76	5.4	0.4
Total	3.66		2.0

From Tables 8-6 and 8-7, it can be concluded that the fraction of $B\bar{B}$ events where one of the two B meson is completely reconstructed is 5.7×10^{-3} . This is higher than the fraction actually reconstructed by the CLEO experiment, 1.2×10^{-3} [152]. Some improvement with respect to CLEO should be expected at BABAR, due to the superior particle identification capabilities and the precise tracking and vertex information from the vertex detector, both of which should help considerably in reducing the combinatorial background. On the other hand, additional cuts may be needed for the high-multiplicity D decay modes to reduce the backgrounds sufficiently.

8.7 Measuring $|V_{cb}|$ Using HQET in Exclusive Decays

The most precise measurements of $|V_{cb}|$ using exclusive decays comes from analysis of the decay mode $\bar{B} \rightarrow D^* \ell^- \bar{\nu}$. There are a number of reasons for this. Experimentally, the backgrounds in this mode are much smaller than for the other decay that might be used, $\bar{B} \rightarrow D \ell^- \bar{\nu}$. In addition to combinatoric background from fake D mesons, $\bar{B} \rightarrow D \ell^- \bar{\nu}$ has substantial feed-down from $\bar{B} \rightarrow D^* \ell^- \bar{\nu}$. Finally, the rate for $\bar{B} \rightarrow D \ell^- \bar{\nu}$ is suppressed at high q^2 by the kinematic factor p_D^3 , where p_D is the momentum of the D in the B rest frame, because it is a p -wave decay. Although it is important to test HQET and to study the form factor shape for $\bar{B} \rightarrow D \ell^- \bar{\nu}$, the best exclusive measurement of $|V_{cb}|$ should continue to come from $\bar{B} \rightarrow D^* \ell^- \bar{\nu}$.

As discussed in the theoretical section on $|V_{cb}|$, the best way to extract the CKM matrix element from the experimental data is to measure the rate near zero recoil, or $q^2 = q_{max}^2$. The standard analysis consists of converting the differential decay rate into $\mathcal{F}(w)|V_{cb}|$ and then plotting that as a function of w . A fit to this distribution is then used to find the intercept at $w = 1$, $\mathcal{F}(1)|V_{cb}|$.

Presently, this quantity is determined about equally well by the LEP experiments and by CLEO. The CLEO result is

$$\mathcal{F}(1)|V_{cb}| = 0.0351 \pm 0.0019(\text{stat}) \pm 0.0020(\text{syst}).$$

A recent review by DiCiaccio of the experimental situation gave an average value of 0.0343 ± 0.0016 . Assuming from theoretical estimates the value $\mathcal{F}(1) = 0.91 \pm 0.03$, DiCiaccio calculated

$$|V_{cb}| = 0.0376 \pm 0.0018(\text{exp}) \pm 0.0012(\text{th}).$$

Clearly there is room for improvement in this number at BABAR. Assuming the same acceptance and efficiency, the statistical error for an integrated luminosity of 30 fb^{-1} would be ± 0.006 . One could reasonably expect to reduce the systematic error to about the same level.

8.8 Measuring $|V_{ub}|$ Using Exclusive Decays

In studying the rare exclusive $b \rightarrow ul\nu$ transitions the biggest challenge is to reduce the backgrounds from the much more abundant $b \rightarrow cl\nu$ decays. There is also a substantial background from nonresonant $c\bar{c}$ production. Measurements of exclusive $b \rightarrow ul\nu$ transitions have focused on the decays $B \rightarrow \pi l\nu$, $B \rightarrow \rho l\nu$, and $B \rightarrow \omega l\nu$. These are expected to be the exclusive channels with the largest branching ratios, and they are also the simplest to reconstruct. In the vector final states the charged lepton is produced with a hard energy spectrum. Thus, a requirement of a lepton above ~ 2 GeV/ c is efficient, while it rejects a large fraction of the $b \rightarrow cl\nu$ background. The $B \rightarrow \pi l\nu$ final state does not have a hard lepton-energy spectrum and it is therefore necessary to use a larger range of lepton energies for this decay. However, the charged pion final state does not suffer from combinatorial problems, which do affect the channel with the ρ .

CLEO has used a strategy to suppress the background from $b \rightarrow cl\nu$ events in which the energy and momentum of the neutrino is estimated from the missing energy and momentum of the event. This requires detection of all decay products of the second B meson in the event. A series of event selection criteria were designed to select events in which this requirement is well fulfilled.

- Events with a non-zero net charge indicate that additional charged particles are missing and are therefore rejected.
- Events with additional leptons are rejected since most leptons are produced in semileptonic decays and therefore indicated the presence of another, undetected, neutrino.
- A neutrino candidate reconstructed close to the beam axis is rejected since it is often due to lost particles along the beam pipe.
- The invariant mass of the reconstructed neutrino is required to be consistent with zero.
- When estimating the total energy and momentum using information from the calorimeter, special care has to be taken to reject as much of the hadronic split-offs and back splashes as possible.

After this selection of neutrino candidates, the analysis is relatively straightforward. A beam-energy-constrained B mass is constructed from the lepton, meson, and neutrino candidate in the event. It is also required that $\Delta E = E_\nu + E_\ell + E_X - E_{\text{beam}}$ is consistent with zero, where E_{beam} is the energy of the meson candidate. The signal is a peak at the B -mass in the beam-energy-constrained mass.

CLEO has searched for the decays $B^0 \rightarrow \pi^- \ell^+ \nu$, $B^+ \rightarrow \pi^0 \ell^+ \nu$, $B^0 \rightarrow \rho^- \ell^+ \nu$, $B^+ \rightarrow \rho^0 \ell^+ \nu$, and $B^+ \rightarrow \omega \ell^+ \nu$ (the charge conjugated modes are also included and $\ell = e$ or μ) in 2.66 fb^{-1}

(2.84×10^6 $B\bar{B}$ pairs). They measured the following branching fractions [150]

$$\begin{aligned}\mathcal{B}(B^0 \rightarrow \pi^- \ell^+ \nu) &= (1.8 \pm 0.4 \pm 0.3 \pm 0.2) \times 10^{-4}, \\ \mathcal{B}(B^0 \rightarrow \rho^- \ell^+ \nu) &= (2.5 \pm 0.4_{-0.7}^{+0.5} \pm 0.5) \times 10^{-4}\end{aligned}$$

where the errors are statistical, systematic, and model-dependent, respectively. With a large model-dependence these measurements give an estimate of

$$|V_{ub}| = (3.3 \pm 0.2_{-0.4}^{+0.3} \pm 0.7) \times 10^{-3}. \quad (8.60)$$

A study of measuring these decays at BABAR was first carried out in the fast parameterized Aslund Monte Carlo. This study indicated that the BABAR experiment would be able to do these measurements quite well. With selection criteria that were similar to those used by CLEO, a similar reconstruction efficiency was obtained while the estimated background levels were significantly lower. Accurate modeling of the backgrounds needs a complete detector simulation. The efficiency for reconstructing all decay products of the other B is about 7%. However, when migrating to the full simulation the performance was severely degraded. This is largely understood as problems with not yet well enough developed tools for handling hadronic split-offs and track matching in the calorimeter.

Assuming that BABAR will be able to reach the same efficiency and cleanliness as CLEO for reconstructing these semileptonic decays using the neutrino reconstruction technique, the statistical uncertainty in these branching fraction measurements will be around 5% for 30 fb^{-1} .

Improvements over CLEO are expected due to the improved performance in particle identification, *i.e.*, $K - \pi$ separation and muon identification, and also in improved vertexing, which will help to reduce the combinatorial background. The increase in statistics should also allow a reduction of the systematic error, which is dominated by the simulation of the inclusive reconstruction of the neutrino candidate. The size of these event samples should also allow studies of the dynamics, which will reduce the model-dependence of the branching fraction measurements by allowing a study of the distribution of events in the Dalitz plot.

8.9 Measuring $|V_{cb}|$ with Inclusive Decays

In view of the continuing discrepancy between the inclusive semileptonic decay fractions $\mathcal{B}(B \rightarrow \ell \nu X)$, as measured at the $\Upsilon(4S)$ and at the Z^0 , it is highly desirable to get a precision measurement of this fraction with BABAR soon. Since it is one of the main sources for $|V_{cb}|$, it should even be measured more than once with increasing precision in the process of accumulating luminosity.

The fraction \mathcal{B} is determined by integrating $d\mathcal{B}/dp$ over a momentum range as wide as possible and by then extrapolating to all momenta in B decays. There is no principal difference in

choosing p either in the BABAR lab frame or in the $\Upsilon(4S)$ or B meson rest frame. For mastering the main backgrounds, it is convenient to use $p = p^*$ in the $\Upsilon(4S)$ frame. Since electrons will cover a wider measurable p^* range than muons, we limit the discussion here to $\mathcal{B}(B \rightarrow e\nu X)$. A precise measurement requires precise knowledge of the electron detection efficiency $\eta_e(p^*)$ including trackfinding and electron identification, precise normalization $d\mathcal{B}(B \rightarrow e\nu X)/dp^* = dN(B \rightarrow e\nu X)/dp^*/N(B)$, and precise evaluation of all contributing backgrounds. The main backgrounds are

1. Electrons from non- $B\bar{B}$ events,
2. Secondary electrons from $B \rightarrow D \rightarrow e$,
3. Misidentified hadrons,
4. Electrons from $B \rightarrow \psi X$ with $J/\psi = J/\psi$ or $\psi(2S) \rightarrow e^+e^-$,
5. γ conversion or $\pi^0 \rightarrow \gamma e^+e^-$ if only one electron of the pair is detected, and
6. Cascade electrons from $B \rightarrow \tau \rightarrow e$.

To master the first two backgrounds, BABAR should not begin with a “fully inclusive” search for $e\nu X$ events, but rather should start its efforts with the “state of the art” as presented by ARGUS in 1993 [154] and CLEO in 1996 [153]. In these two analyses, electrons are tagged by requiring a second lepton with selected p^* , either e or μ , in the same event. If originating from the second B meson in the $\Upsilon(4S)$ decay, the charge of this lepton tags the origin of the selected electron; opposite sign ℓ^\mp tags indicate primary e^\pm and same sign ℓ^\pm tags indicate secondary e^\pm from B meson decays. The charge correlation is diluted by $B^0-\bar{B}^0$ oscillations in a precisely known way:

$$\frac{dN(e^\pm\ell^\mp)}{dp^*} = N(\text{tag}) \cdot \eta_e(p^*) \cdot \left[(1 - \chi) \frac{d\mathcal{B}(B \rightarrow e\nu X)}{dp^*} + \chi \frac{d\mathcal{B}(B \rightarrow D \rightarrow e\nu X)}{dp^*} \right], \quad (8.61)$$

$$\frac{dN(e^\pm\ell^\pm)}{dp^*} = N(\text{tag}) \cdot \eta_e(p^*) \cdot \left[\chi \frac{d\mathcal{B}(B \rightarrow e\nu X)}{dp^*} + (1 - \chi) \frac{d\mathcal{B}(B \rightarrow D \rightarrow e\nu X)}{dp^*} \right], \quad (8.62)$$

where $N(\text{tag}) = N(B) \cdot \eta_{\text{tag}}$ is the number of selected lepton tags to be determined separately, and $\chi = f_0 \cdot \chi_0$ where f_0 is the fraction of $B^0\bar{B}^0$ in $\Upsilon(4S)$ decays and the well-known $B^0\bar{B}^0$ oscillation strength is $\chi_0 = 0.175 \pm 0.016$ [155].

After all background subtractions, now including backgrounds in the tag leptons, this set of linear equations can be solved for $d\mathcal{B}(B \rightarrow e\nu X)/dp^*$ and $d\mathcal{B}(B \rightarrow D \rightarrow e\nu X)/dp^*$; the CLEO results

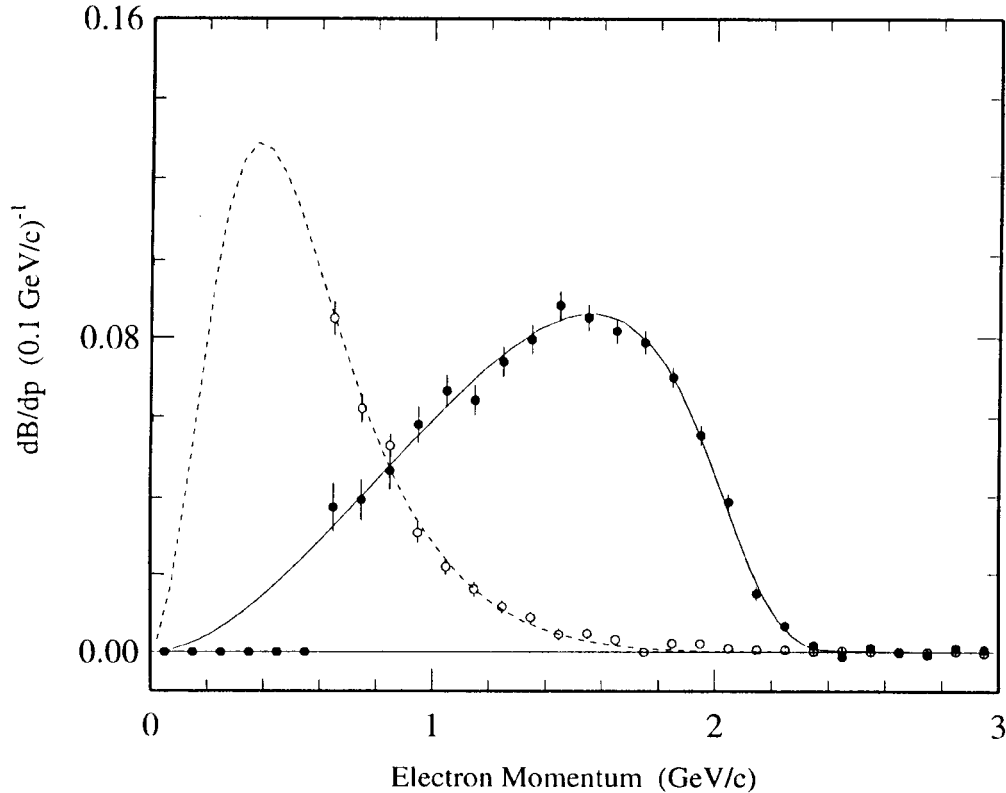


Figure 8-9. The CLEO results [153] on the momentum spectra of primary and secondary electrons from B meson decays.

are shown in Fig. 8-9. Table 8-8 gives the main properties of the two lepton-tag experiments. In the following, an estimate is given for the performance of BaBar with $\mathcal{L} = 30 \text{ fb}^{-1}$ from the same method with better optimized selection criteria. After a few years of running, more refined tags with vertex information and eventually full B meson reconstruction will be able to determine $\mathcal{B}(B \rightarrow \ell \nu X)$ with smaller systematic error, and to separate into $\mathcal{B}(B^0 \rightarrow \ell \nu X)$ and $\mathcal{B}(B^+ \rightarrow \ell \nu X)$. These refinements will, however, not be discussed here.

Improvements in the lepton tag measurement at BaBar will obviously come from statistics, but there will also have to be improvements in the systematics of the measurement. For an integrated luminosity of 30 fb^{-1} (25 fb^{-1} on the $\Upsilon(4S)$ and 5 fb^{-1} in the continuum), the statistical error on $\mathcal{B}(B \rightarrow e \nu X)$ is estimated to be ± 0.005 . It is expected that at BaBar it will be possible to identify electrons down to a lab momentum of $0.5 \text{ GeV}/c$. The identification efficiency and the misidentification probability for pions and Kaons cannot be determined with absolute reliability

Table 8-8. The main features of the determination of $\mathcal{B}(B \rightarrow e\nu X)$ using lepton tags, in the two previous experiments and in BABAR.

	ARGUS [154]	CLEO [153]	BABAR Estimate
$\mathcal{L}(\Upsilon(4S))$	0.25/fb	2.06/fb	25/fb
$\mathcal{L}(\text{continuum})$	0.10/fb	0.96/fb	5/fb
$N(B\bar{B})$	0.2 M	2.0 M	27 M
e momentum range	$p^* > 0.6 \text{ GeV}/c$		$p^* > 0.3 \text{ GeV}/c$
Tags	e and μ with $1.4 \text{ GeV}/c < p^* < 2.3 \text{ GeV}/c$		
η_{tag}	0.14	0.123	0.1
N_{tag}	30 K	246 K	2.7 M
$N(e^\pm \ell^\mp)$	956	9938	125 K
background	45%	32%	$\sim 30\%$
$N(e^\pm \ell^\pm)$	798	5319	70 K
background	65%	45%	$\sim 40\%$
$\sigma_{\text{stat}}(\mathcal{B})/\mathcal{B}$	5.0%	1.6%	0.5%
$\sigma_{\text{syst}}(\mathcal{B})/\mathcal{B}$	4.0%	4.3%	2.0%

from Monte Carlo simulation. When data become available, radiative Bhabha events will be used to determine the the efficiency, and K_s^0 and D^0 decays will be used for the misidentification probabilities.

The systematic errors on these two quantities as a function of electron momentum are the most important, because they dominate the systematic error of the result. Table 8-9 summarizes the contributions to the systematic error in the two previous experiments and the estimate for BABAR with 30 fb^{-1} . The moving $\Upsilon(4S)$ frame will be of advantage for BABAR for two reasons; the minimum of p_e^* will be much lower than the minimum of $p_e(\text{lab})$ and it is expected that $p_e^*(\text{min}) \approx 0.3 \text{ GeV}/c$ — and different $p_e(\text{lab})$ will contribute to the same p_e^* . The latter will help to perform a variety of cross checks in determining the electron ID efficiency η_e , ending eventually in a systematic error around 1% on η_e , which still dominates the systematic error of the result.

To conclude, it is expected that $\mathcal{B}(B \rightarrow e\nu X)$ will be determined with systematic errors of $\pm 0.005 \pm 0.020$ or even slightly smaller after extended studies on electron identification efficiencies and misidentification probabilities.

Table 8-9. Contributions to the relative systematic error on $\mathcal{B}(B \rightarrow e\nu X)$. In the ARGUS list, the track efficiency (*) is combined with the electron ID efficiency. In the CLEO list, the two errors on the fake electrons (**) are combined.

	ARGUS [154]	CLEO [153]	BaBAR Estimate
$N_{\text{tag}}(\text{syst})$	0.8%	1.2%	0.6%
$\chi(\text{stat and syst})$	2.0%	1.1%	0.6%
Faked e (opposite sign)	0.8%	2.1%	0.4%
Faked e (like sign)	0.2%	(**)	0.1%
e from the same B	0.6%	0.7%	0.5%
Other bg in e sample	1.5%	1.5%	1.0%
Track efficiency	(*)	1.0%	0.5%
e ID efficiency	3.2%	2.0%	1.0%
Wrong sign tags	0.7%	0.5%	0.3%
momentum extrapolation	1.0%	0.6%	0.3%
quadratic sum	4.4%	3.9%	2.0%
quoted	4%	4.1%	

8.10 Measuring $|V_{ub}|$ with Inclusive Decays

A possible way to select charmless semileptonic events is to require that the invariant mass of the hadronic system accompanying the lepton and the neutrino is below the charm threshold [144]. This has the advantage that it gives access to a much larger fraction of these events than the selection based on the lepton-energy spectrum, or even the method based on exclusive decays. Therefore, at least potentially, this method allows for a measurement of $|V_{ub}|$ with a reduced model-dependence. In addition, the systematic error of a measurement based on this method will have little correlation with that of other methods.

Although this idea can be applied to other classes of events [156], we have focused on events where one of the B mesons has been completely reconstructed in an exclusive mode. The task of isolating $|V_{ub}|$ semileptonic events is then relatively easy and proceeds through the following steps:

- A high-energy lepton is selected, thereby rejecting most of the events with a cascade lepton.

- Some technical cuts reject events where some particles are undetected (total charge imbalance, presence of an additional lepton).
- The missing momentum and energy in the event are assigned to the neutrino. Its squared invariant mass is required to be below $0.5 \text{ GeV}/c^2$ (Fig. 8-10) and its momentum should not point towards the forward beam direction ($\cos\theta_\nu < 0.8$) to reject events with particles lost in the beam-pipe region.
- A cut is placed on the invariant mass of the hadronic system M_X , thereby rejecting most of the semileptonic decays to charm (Fig. 8-11).

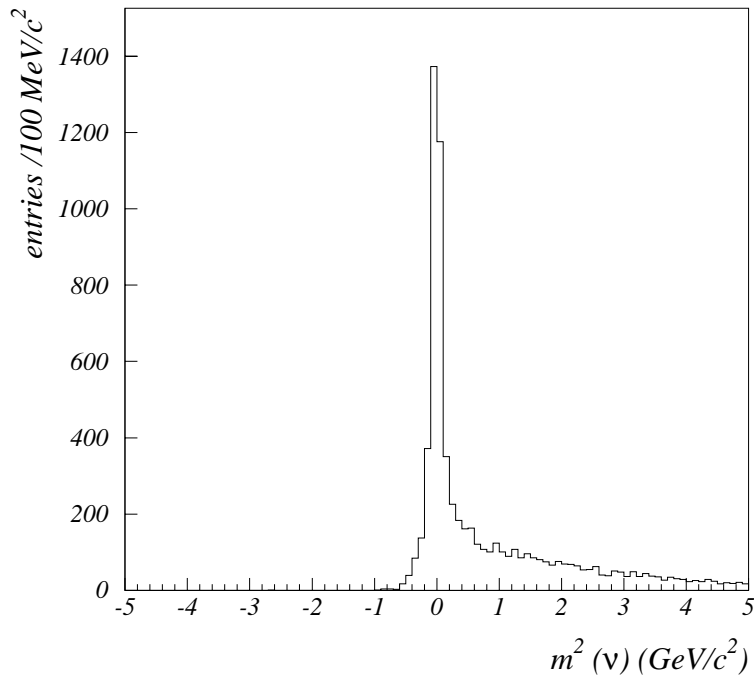


Figure 8-10. Distribution of m_ν^2 for B semileptonic decays. The tail on the positive side is due to events where some particles beside the neutrino escaped detection.

All these steps have been performed on the data produced by the fast simulation program `Aslund`. The efficiency of selecting signal events is $\sim 30\%$ while, with a cut on M_X at 1.7 GeV , the signal-background ratio is ≈ 5 , for the background coming from the other B semileptonic decays. It is expected that the sample of selected events will be ~ 120 per 30 fb^{-1} , for an efficiency of full exclusive reconstruction of $5.7 \sim 10^{-3}$ per $B\bar{B}$ event. Even considering a lower performance for

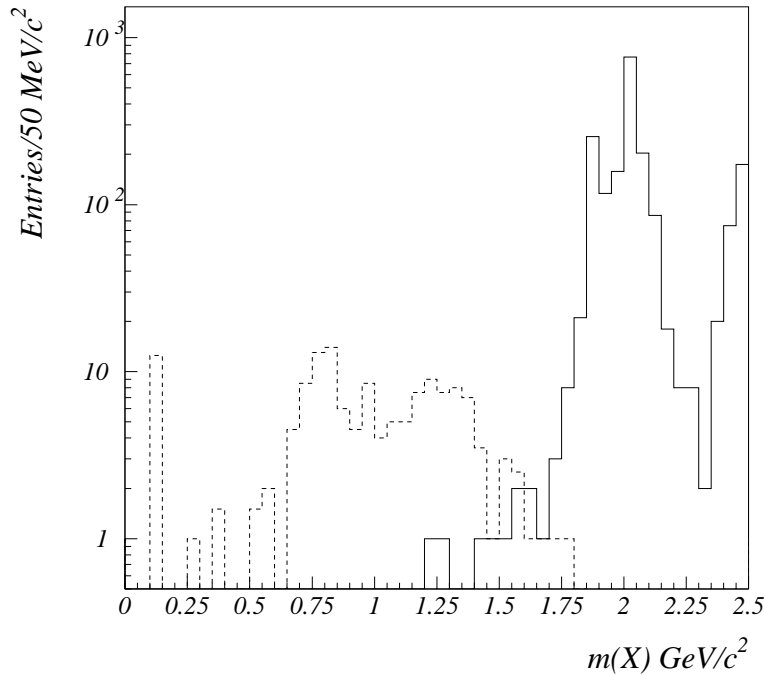


Figure 8-11. Distribution of m_X , the mass of the hadronic system recoiling against the lepton and neutrino, in events where the second B meson has been exclusively reconstructed. The dashed histogram is for charmless semileptonic transitions, the other for decays to charm.

the exclusive reconstruction algorithm, a signal sample of the order of 10^2 events can be expected over the full data size of 100 fb^{-1} .

In order to convert this rate into a measurement of $|V_{ub}|$, it is necessary to take into account the efficiency of the cut on M_X , which is of the order of 90 % for $M_X < 1.7 \text{ GeV}/c^2$ with a systematic error that should not exceed the fraction that is rejected [149]. Even allowing for a substantial (100 %) uncertainty in the leakage from the charm into the signal region, which is 20 % of the signal, it is concluded that a measurement of $|V_{ub}|$ at the 15 % level is at least possible using this method.

There is one additional handle to reduce the background from the dominant semileptonic decay to charm hadronic states. Using the information from the vertex detector, one can require that all of the tracks from the candidate semileptonic decay come from the same vertex, without evidence of the vertex separation expected from the charm lifetime.

8.11 Conclusions

Large data sets will be obtained at BABAR that can be used for the determination of $|V_{cb}|$ and $|V_{ub}|$. With 30 fb^{-1} , the experimental errors on $|V_{cb}|$ are estimated to be ± 0.0006 (1.5%) and ± 0.0004 (1.0%) from exclusive $B \rightarrow D^* \ell \nu$ and inclusive $B \rightarrow \ell \nu X$ decays, respectively. The theoretical uncertainties are of comparable size for both methods and are of the order of a few percent. If the two results agree, a realistic estimate of the combined theoretical uncertainty is ± 0.0012 (3%), leading to a BABAR result of

$$|V_{cb}| = \dots \pm 0.0004 \pm 0.0012 (\pm 1\% \pm 3\%) \quad (8.63)$$

after a few years of running, where the first error is experimental (statistical and systematic) and the second is from theory. The estimate of the theoretical uncertainty is based on present theoretical tools. A decrease in this uncertainty to a level of 1% will require new theoretical ideas.

For $|V_{ub}|$, expectations are more modest. With 30 events/fb, BABAR will be able to determine the decay fractions of $B \rightarrow \pi \ell \nu$, $B \rightarrow \rho \ell \nu$, and $B \rightarrow \omega \ell \nu$ with statistical errors around 6%, giving $|V_{ub}|$ with statistical errors around 3%. Systematic errors should be of the same order, and averaging the three decay modes leads to an estimate of $\pm 2.5\%$ for the experimental error on $|V_{ub}|$. Inclusive decays will not reach the same precision experimentally. They will, however, be extremely important because they have completely different theoretical uncertainties. These are estimated to be about 10% for both methods, based on present theoretical technology. Thus, BABAR could reach

$$|V_{ub}| = \dots \pm 0.0001 \pm 0.0004 (\pm 2.5\% \pm 10\%) \quad (8.64)$$

after a few years of running. Again, new theoretical approaches could decrease the theoretical uncertainties to a level of 5%.

References

- [1] E. V. Shuryak, *Phys. Lett. B* **93**, 134 (1980); *Nucl. Phys.* **B198**, 83 (1982).
- [2] J. E. Paschalis and G. J. Gounaris, *Nucl. Phys.* **B222**, 473 (1983);
F. E. Close, G. J. Gounaris and J. E. Paschalis, *Phys. Lett. B* **149**, 209 (1984).
- [3] S. Nussinov and W. Wetzel, *Phys. Rev. D* **36**, 130 (1987).
- [4] M. B. Voloshin and M. A. Shifman, *Yad. Fiz.* **45**, 463 (1987) [*Sov. J. Nucl. Phys.* **45**, 292 (1987)]; *Yad. Fiz.* **47**, 801 (1988) [*Sov. J. Nucl. Phys.* **47**, 511 (1988)].
- [5] E. Eichten and B. Hill, *Phys. Lett. B* **234**, 511 (1990); *Phys. Lett. B* **243**, 427 (1990).
- [6] H. Georgi, *Phys. Lett. B* **240**, 447 (1990).
- [7] M. Neubert, *Phys. Rep.* **245**, 259 (1994).
- [8] S. Balk, J. G. Körner and D. Pirjol, *Nucl. Phys.* **B428**, 499 (1994).
- [9] W. E. Caswell and G. P. Lepage, *Phys. Lett. B* **167**, 437 (1986);
G. P. Lepage *et al.*, *Phys. Rev. D* **46**, 405 (1992).
- [10] I. I. Bigi *et al.*, *Phys. Rev. D* **52**, 196 (1995).
- [11] N. Isgur and M. B. Wise, *Phys. Lett. B* **232**, 113 (1989); *Phys. Lett. B* **237**, 527 (1990).
- [12] M. Wirbel, B. Stech and M. Bauer, *Z. Phys. C* **29**, 637 (1985);
M. Bauer, B. Stech and M. Wirbel, *Z. Phys. C* **34**, 103 (1987).
- [13] M. Neubert, *Phys. Lett. B* **264**, 455 (1991).
- [14] M. E. Luke, *Phys. Lett. B* **252**, 447 (1990).
- [15] A. F. Falk and M. Neubert, *Phys. Rev. D* **47**, 2965 and 2982 (1993).
- [16] M. Voloshin and M. Shifman, *Yad. Fiz.* **47**, 801 (1988); [*Sov. J. Nucl. Phys.* **47**, 511 (1988)].
- [17] M. Neubert and V. Rieckert, *Nucl. Phys.* **B382**, 97 (1992).
- [18] A. Sirlin, *Nucl. Phys.* **B196**, 83 (1982).
- [19] S. J. Brodsky, G. P. Lepage, and P. B. Mackenzie, *Phys. Rev. D* **28**, 228 (1983);
G. P. Lepage and P. B. Mackenzie, *Phys. Rev. D* **48**, 2250 (1993).
- [20] M. Neubert, *Phys. Lett. B* **341**, 367 (1995).

- [21] A. Czarnecki, *Phys. Rev. Lett.* **76**, 4124 (1996).
- [22] A. Czarnecki and K. Melnikov, *Nucl. Phys.* **B505**, 65 (1997).
- [23] N. G. Uraltsev, *Mod. Phys. Lett.* **A10**, 1803 (1995).
- [24] N. Uraltsev, *Nucl. Phys.* **B491**, 303 (1997);
A. Czarnecki, K. Melnikov and N. Uraltsev, *Phys. Rev. D* **57** 1769 (1998).
- [25] N. Uraltsev, “Heavy Flavour Physics: A Probe of Nature’s Grand Design,” in *Proceedings of the International School of Physics Enrico Fermi, Varenna, July 7–18 (1997)*, hep-ph/9804275.
- [26] T. Mannel, *Phys. Rev. D* **50**, 428 (1994).
- [27] M. Shifman, N. G. Uraltsev and A. Vainshtein, *Phys. Rev. D* **51**, 2217 (1995).
- [28] M. Neubert, *Phys. Lett. B* **338**, 84 (1994).
- [29] C. G. Boyd and I. Z. Rothstein, *Phys. Lett. B* **395**, 96 (1997).
- [30] I. Bigi, M. Shifman and N. Uraltsev, *Ann. Rev. Nucl. Part. Sci.* **47**, 591 (1997).
- [31] M. Neubert, *Phys. Rev. D* **46**, 3914 (1992);
Z. Ligeti, Y. Nir and M. Neubert, *Phys. Rev. D* **49**, 1302 (1994).
- [32] C. G. Boyd, B. Grinstein and R. F. Lebed, *Phys. Lett. B* **353**, 306 (1995); *Nucl. Phys.* **B461**, 493 (1996); *Phys. Rev. D* **56**, 6895 (1997);
C. G. Boyd and R. F. Lebed, *Nucl. Phys.* **B485**, 275 (1997).
- [33] I. Caprini and M. Neubert, *Phys. Lett. B* **380**, 376 (1996).
- [34] I. Caprini, L. Lellouch and M. Neubert, Preprint CERN-TH/97-91 (1997) [hep-ph/9712417].
- [35] N. G. Uraltsev, *Acta Phys. Polon.* **B28**, 755 (1997).
- [36] J. D. Bjorken, “Results and Perspectives in Particle Physics,” in *Proceedings of the 4th Rencontres de Physique de la Vallée d’Aoste, La Thuile, Italy (1990)*, ed. M. Greco (Editions Frontières, Gif-sur-Yvette, (1990), p. 583; “Gauge Bosons and Heavy Quarks,” in *Proceedings of the 18th SLAC Summer Institute on Particle Physics, Stanford, California (1990)*, ed. J. F. Hawthorne, SLAC Report No. 378 (1991), p. 167.
- [37] N. Isgur and M. B. Wise, *Phys. Rev. D* **43**, 819 (1991).
- [38] J. D. Bjorken, I. Dunietz and J. Taron, *Nucl. Phys.* **B371**, 111 (1992).
- [39] M. B. Voloshin, *Phys. Rev. D* **46**, 3062 (1992).

- [40] C. G. Boyd *et al.*, *Phys. Rev. D* **55**, 3027 (1997).
- [41] A. Czarnecki, K. Melnikov and N. Uraltsev, *Phys. Rev. Lett.* **80**, 3189 (1998).
- [42] S. Okubo and I.-F. Shih, *Phys. Rev. D* **4**, 2020 (1971).
- [43] C. Bourrely, B. Machet and E. de Rafael, *Nucl. Phys.* **B189**, 157 (1981).
- [44] E. de Rafael and J. Tarón, *Phys. Lett. B* **282**, 215 (1992); *Phys. Rev. D* **50**, 373 (1994).
- [45] J. E. Duboscq *et al.*, (CLEO Collaboration), *Phys. Rev. Lett.* **76**, 3898 (1996).
- [46] D. Buskulic *et al.*, (ALEPH Collaboration), *Z. Phys. C* **73**, 601 (1997).
- [47] N. Isgur and M. B. Wise, *Phys. Rev. Lett.* **66**, 1130 (1991).
- [48] H. D. Politzer, *Phys. Lett. B* **250**, 128 (1990).
- [49] A. F. Falk, *Nucl. Phys.* **B378**, 79 (1992).
- [50] J. L. Rosner, *Comm. Nucl. Part. Phys.* **16**, 109 (1986).
- [51] S. Balk *et al.*, *Z. Phys. C* **59**, 283 (1993).
- [52] A. F. Falk and M. Luke, *Phys. Lett. B* **292**, 119 (1992).
- [53] P. Colangelo *et al.*, *Phys. Rev. D* **52**, 6422 (1995).
- [54] U. Kilian, J. G. Körner and D. Pirjol, *Phys. Lett. B* **288**, 360 (1992).
- [55] A. Anastassov *et al.*, (CLEO Collaboration), *Phys. Rev. Lett.* **80**, 4127 (1998).
- [56] A. K. Leibovich *et al.*, *Phys. Rev. Lett.* **78**, 3995 (1997); *Phys. Rev. D* **57**, 308 (1998).
- [57] M. Neubert, *Phys. Lett. B* **418**, 173 (1998).
- [58] V. Morenas *et al.*, *Phys. Rev. D* **56**, 5668 (1997).
- [59] P. Colangelo, G. Nardulli and N. Paver, *Phys. Lett. B* **293**, 207 (1992).
- [60] A. Wambach, *Nucl. Phys.* **B434**, 647 (1995).
- [61] P. Colangelo, F. De Fazio and G. Nardulli, *Phys. Lett. B* **303**, 152 (1993).
- [62] G. Lopez Castro and J. H. Munoz, *Phys. Rev. D* **55**, 5581 (1997).
- [63] J. D. Bjorken, *Nucl. Phys. B Proc. Suppl.* **11**, 325 (1989).

- [64] J. Gronberg *et al.*, (CLEO Collaboration), Conference report CLEO CONF 96-25 (1996), contributed paper to the 28th International Conference on High Energy Physics (ICHEP 96), Warsaw, Poland, July (1996).
- [65] G. Burdman and J. Kambor, *Phys. Rev. D* **55**, 2817 (1997).
- [66] B. Stech, *Phys. Lett. B* **354**, 447 (1995).
- [67] J. M. Flynn and C. T. Sachrajda, SHEP-97-20, to appear in *Heavy Flavours II*, eds. A. J. Buras and M. Linder (World Scientific, Singapore) (1997) [hep-lat/9710057].
- [68] H. Wittig, OUTP-97-59-P, “Heavy Flavor Physics—A Probe of Nature’s Grand Design,” to appear in *Proceedings of the International School of Physics “Enrico Fermi,”* Varenna, Italy, July (1997) [hep-lat/9710088].
- [69] N. Isgur and M. B. Wise, *Phys. Rev. D* **42**, 2388 (1990).
- [70] P. A. Griffin, M. Masip and M. McGuigan, *Phys. Rev. D* **42**, 5751 (1994).
- [71] J. M. Flynn *et al.*, (UKQCD Collaboration), *Nucl. Phys.* **B461**, 327 (1996).
- [72] L. Lellouch, *Nucl. Phys.* **B479**, 353 (1996).
- [73] L. Del Debbio *et al.*, (UKQCD Collaboration), *Phys. Lett. B* **416**, 392 (1998).
- [74] D. Becirevic, Preprint LPTHE-Orsay 97/16 (1997) [hep-ph/9707271].
- [75] C. G. Boyd, B. Grinstein and R. F. Lebed, *Phys. Rev. Lett.* **74**, 4603 (1995).
- [76] C. G. Boyd and M. J. Savage, *Phys. Rev. D* **56**, 303 (1997).
- [77] M. A. Shifman, A. I. Vainshtein and V. I. Zakharov, *Nucl. Phys.* **B147**, 385 and 448 (1979).
- [78] I. I. Balitsky, V. M. Braun and A.V. Kolesnichenko, *Nucl. Phys.* **B312** 509 (1989).
- [79] V. M. Braun and I. E. Filyanov, *Z. Phys. C* **44**, 157 (1989).
- [80] V. L. Chernyak and I. R. Zhitnitsky, *Nucl. Phys.* **B345**, 137 (1990).
- [81] P. Ball, *Phys. Rev. D* **48**, 3190 (1993).
- [82] N. Paver and Riazuddin, *Phys. Lett. B* **320**, 364 (1994).
- [83] P. Colangelo and P. Santorelli, *Phys. Lett. B* **327**, 123 (1994).
- [84] V. M. Belyaev *et al.*, *Phys. Rev. D* **51**, 6177 (1995).

- [85] A. Khodjamirian and R. Rückl, in *Heavy Flavors II*, eds. A. J. Buras and M. Linder, World Scientific, Singapore (1998), p. 345, hep-ph/9801443.
- [86] P. Ball and V. M. Braun, *Phys. Rev. D* **55**, 5561 (1997).
- [87] A. Ali, V. M. Braun and H. Simma, *Z. Phys. C* **63**, 437 (1994).
- [88] P. Colangelo *et al.*, *Phys. Rev. D* **53**, 3672 (1996).
- [89] T. M. Aliev, A. Ozpineci and M. Savci, *Phys. Rev. D* **56**, 4260 (1997);
T. M. Aliev *et al.*, *Phys. Lett. B* **400**, 194 (1997).
- [90] V. L. Chernyak and A. R. Zhitnitsky, *JETP Lett.* **25**, 510 (1977); *Yad. Fiz.* **31**, 1053 (1980);
V. L. Chernyak, V. G. Serbo and A. R. Zhitnitsky, *JETP Lett.* **26**, 594 (1977); *Sov. J. Nucl. Phys.* **31**, 552 (1980).
- [91] A. V. Efremov and A. V. Radyushkin, *Phys. Lett. B* **94**, 245 (1980); *Teor. Mat. Fiz.* **42**, 147 (1980).
- [92] G. P. Lepage and S. J. Brodsky, *Phys. Lett. B* **87**, 359 (1979); *Phys. Rev. D* **22**, 2157 (1980).
- [93] A. Khodjamirian, R. Rückl, S. Weinzierl and O. Yakovlev, *Phys. Lett. B* **410**, 275 (1997).
- [94] E. Bagan, P. Ball and V. M. Braun, *Phys. Lett. B* **417**, 154 (1998).
- [95] P. Ball, hep-ph/9802394, to appear in *Journal of High Energy Physics*;
P. Ball and V. M. Braun, hep-ph/9805422, to appear in *Phys. Rev. D*.
- [96] A. F. Falk and B. Grinstein, *Nucl. Phys.* **B416**, 771 (1994).
- [97] B. Grinstein, *Phys. Rev. Lett.* **71**, 3067 (1993);
C. G. Boyd and B. Grinstein, *Nucl. Phys.* **B442**, 205 (1995).
- [98] Z. Ligeti and M. B. Wise, *Phys. Rev. D* **53**, 4937 (1996);
Z. Ligeti, I. W. Stewart and M. B. Wise, *Phys. Lett. B* **240**, 359 (1998).
- [99] M. Voloshin and M. Shifman, *Yad. Fiz.* **41**, 187 (1985); [*Sov. J. Nucl. Phys.* **41**, 120 (1985)];
ZhETF **91**, 1180 (1986); [*Sov. Phys.-JETP* **64**, 698 (1986)].
- [100] J. Chay, H. Georgi and B. Grinstein, *Phys. Lett. B* **247**, 399 (1990).
- [101] I. I. Bigi, N. G. Uraltsev and A. I. Vainshtein, *Phys. Lett. B* **293**, 430 (1992); [*Phys. Lett. B* **297**, 477(E) (1993)];
B. Blok and M. Shifman, *Nucl. Phys.* **B399**, 441 and 459 (1993);
I. I. Bigi *et al.*, in *Proceedings of the Annual Meeting of the Division of Particles and Fields of the APS*, Batavia, Illinois, (1992), eds. C. Albright *et al.*, World Scientific, Singapore (1993), p. 610.

- [102] I. I. Bigi *et al.*, *Phys. Rev. Lett.* **71**, 496 (1993).
- [103] A.V. Manohar and M. B. Wise, *Phys. Rev. D* **49**, 1310 (1994).
- [104] B. Blok *et al.*, *Phys. Rev. D* **49**, 3356 (1994); [*Phys. Rev. D* **50**, 3572(E) (1994)].
- [105] M. Luke and M. J. Savage, *Phys. Lett. B* **321**, 88 (1994);
A. F. Falk, M. Luke and M. J. Savage, *Phys. Rev. D* **49**, 3367 (1994).
- [106] T. Mannel, *Nucl. Phys.* **B413**, 396 (1994); *Rep. Prog. Phys.* **60**, 1113 (1997).
- [107] M. Neubert, *Phys. Rev. D* **49**, 3392 and 4623 (1994).
- [108] I. I. Bigi *et al.*, *Int. J. Mod. Phys. A* **9**, 2467 (1994); *Phys. Lett. B* **328**, 431 (1994).
- [109] T. Mannel and M. Neubert, *Phys. Rev. D* **50**, 2037 (1994).
- [110] E. C. Poggio, H. R. Quinn and S. Weinberg, *Phys. Rev. D* **13**, 1958 (1976).
- [111] M. Neubert, *Nucl. Phys. B Proc. Suppl.* **59**, 101 (1997).
- [112] A. Ali and I. Pietarinen, *Nucl. Phys.* **B154**, 519 (1979).
- [113] G. Altarelli *et al.*, *Nucl. Phys.* **B208**, 365 (1982).
- [114] C. H. Jin, W. F. Palmer and E. A. Paschos, *Phys. Lett. B* **329**, 364 (1994);
A. Bareiss and E. A. Paschos, *Nucl. Phys.* **B327**, 353 (1989).
- [115] Y. Nir, *Phys. Lett. B* **221**, 184 (1989).
- [116] A. F. Falk *et al.*, *Phys. Lett. B* **326**, 145 (1994).
- [117] S. Balk *et al.*, *Z. Phys. C* **64**, 37 (1994).
- [118] L. Koyrakh, *Phys. Rev. D* **49**, 3379 (1994).
- [119] M. Neubert, *Int. J. Mod. Phys. A* **11**, 4173 (1996).
- [120] N. Uraltsev, *Int. J. Mod. Phys. A* **11**, 515 (1996).
- [121] M. B. Voloshin, *Int. J. Mod. Phys. A* **10**, 2865 (1995).
- [122] M. Jamin and A. Pich, *Nucl. Phys.* **B507**, 334 (1997).
- [123] J. H. Kühn, A. A. Penin and A. A. Pivovarov, Preprint TTP-98-01 [hep-ph/9801356].
- [124] A.H. Hoang, Preprint UCSD-PTH-98-02 [hep-ph/9803454].

- [125] I. I. Bigi and N. G. Uraltsev, *Phys. Lett. B* **321**, 412 (1994).
- [126] M. Beneke and V. M. Braun, *Nucl. Phys.* **B426**, 301 (1994).
- [127] I. I. Bigi *et al.*, *Phys. Rev. D* **50**, 2234 (1994).
- [128] M. Luke, M. J. Savage and M. B. Wise, *Phys. Lett. B* **343**, 329 (1995); *Phys. Lett. B* **345**, 301 (1995).
- [129] A. Czarnecki and K. Melnikov, *Phys. Rev. Lett.* **78**, 3630 (1997); *Phys. Rev. D* **56**, 7216 (1997).
- [130] P. Ball, M. Beneke, and V. M. Braun, *Phys. Rev. D* **52**, 3929 (1995).
- [131] A. F. Falk, M. Luke and M. J. Savage, *Phys. Rev. D* **53** 2491 (1996); *Phys. Rev. D* **53** 6316 (1996).
- [132] M. Beneke, V. M. Braun and V. I. Zakharov, *Phys. Rev. Lett.* **73**, 3058 (1994).
- [133] K. Melnikov and A. Yelkhovski, TTP-98-17, hep-ph/9805270.
- [134] A. Czarnecki and K. Melnikov, TTP-98-14, hep-ph/9804215.
- [135] A. F. Falk and M. Luke, *Phys. Rev. D* **57**, 424 (1998).
- [136] I. Bigi and N. Uraltsev, *Nucl. Phys.* **B423**, 33 (1994).
- [137] M. Gremm *et al.*, *Phys. Rev. D* **77**, 20 (1996).
- [138] M. Voloshin, *Phys. Rev. D* **51**, 4934 (1995).
- [139] M. Gremm and I. Stewart, *Phys. Rev. D* **55**, 1226 (1997).
- [140] M. Gremm and A. Kapustin, *Phys. Rev. D* **55**, 6924 (1997).
- [141] A. Kapustin and Z. Ligeti, *Phys. Lett. B* **355**, 318 (1995).
- [142] R. D. Dikeman, M. Shifman and N. G. Uraltsev, *Int. J. Mod. Phys.* **A11**, 571 (1996).
- [143] H. Li and H.-L. Yu, *Phys. Rev. D* **55**, 2833 (1997).
- [144] V. Barger, C. S. Kim and R.J.N. Phillips, *Phys. Lett. B* **251**, 629 (1990).
- [145] J. Dai, *Phys. Lett. B* **333**, 212 (1994).
- [146] A. O. Bouzas and D. Zappala, *Phys. Lett. B* **333**, 215 (1994).
- [147] C. Greub and S.-J. Rey, *Phys. Rev. D* **56**, 4250 (1997).

- [148] R.D. Dikeman and N.G. Uraltsev, *Nucl. Phys.* **B509**, 378 (1998);
I. Bigi, R.D. Dikeman and N. Uraltsev, *Eur. Phys. Jour. C* **4**, 453 (1998)
- [149] A. F. Falk, Z. Ligeti and M. B. Wise, *Phys. Lett. B* **406**, 225 (1997).
- [150] J. P. Alexander *et al.*, (CLEO Collaboration), *Phys. Rev. Lett.* **77**, 5000 (1996).
- [151] “Technical Design Report,” (BABAR Collaboration), pp. 62, (1995).
- [152] M. Athanas *et al.*, (CLEO Collaboration), *Phys. Rev. Lett.* **73**, 3503 (1994); [*Phys. Rev. Lett.* **74**, 3090(E) (1995)].
- [153] B. Barish *et al.*, (CLEO Collaboration), *Phys. Rev. Lett.* **76**, 1570 (1996).
- [154] H. Albrecht *et al.*, (ARGUS Collaboration), *Phys. Lett. B* **318**, 397 (1993).
- [155] R. M. Barnett *et al.*, *Phys. Rev. D* **54**, 1 (1996).
- [156] M. Zito, “Measuring V_{ub} with Inclusive Methods,” BABAR note in preparation.

This page was intentionally left blank.

Rare B Decays within the Standard Model

Rare B decays are an important testing ground of the Standard Model and offer a complementary strategy in the search for new physics by probing the indirect effects of new interactions in higher order processes. In particular, the probing of loop-induced couplings can provide a means of testing the detailed structure of the Standard Model at the level of radiative corrections where the Glashow–Iliopoulos–Maiani cancellations are important. The recent observation of radiative B decays by CLEO has provided bounds on the CKM ratio $|V_{ts}/V_{cb}|$ as well as powerful constraints on new physics. Most classes of models which induce large effects in flavor-changing neutral current (FCNC) decays also affect B_d^0 – \bar{B}_d^0 mixing. Should BABAR observe CP violation in the B system that is inconsistent with the Standard Model, measurements of, or even bounds on, many of the rare decay modes discussed in this chapter may help elucidate the origin of the new phenomena.

This chapter examines the purely leptonic decays, $B_d \rightarrow \ell^+ \ell^-$, $\ell \bar{\nu}_\ell$ and the FCNC $b \rightarrow s(d) + X$ transitions. The small branching fractions associated with these decays demand the high luminosity and separated B vertices available at PEP-II and the improved reconstruction techniques of BABAR for accurate measurements of these modes. Note that some of these decays have larger branching fractions than the benchmark rare hadronic B decays such as $B^0 \rightarrow \pi^+ \pi^-$, which are discussed in other chapters.

For each decay the theoretical construction is delineated and then the experimental analysis techniques are discussed. In this chapter the theory is limited to the Standard Model. The chapter concludes by describing a model-independent test for new physics which may appear in the loop-mediated channels. Discussions of the effects of specific models of physics beyond the Standard Model can be found in Chapter 13.

9.1 Leptonic Decays

The leptonic decays of the B meson provide a classic means to determine the decay constant f_B and also offer probes for physics beyond the Standard Model. The purely leptonic channel, $B \rightarrow \ell \ell'$, is helicity suppressed and cleanly calculable within the Standard Model. The charged B decay modes ($\ell' = \nu_\ell$) proceed through the W -boson annihilation graph (displayed in Fig. 9-1), and the neutral channels ($\ell' = \bar{\ell}$) are mediated by a set of electroweak penguin and box diagrams. The photon emission in the radiative decays $B \rightarrow \ell \ell' \gamma$ removes the helicity suppression governing

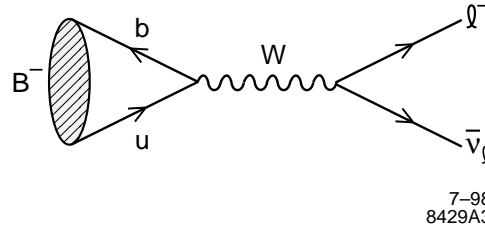


Figure 9-1. Annihilation diagram which mediates the decay $B \rightarrow \ell \nu_\ell$.

the purely leptonic modes and thus yields, in principle, larger rates for the radiative channels. However, the radiative leptonic decays suffer from uncertainties in the associated long-distance physics and hence do not provide as clean a determination of f_B .

The most general non-derivative effective four-fermion interaction involving a b quark, a $q = d, s, u$ or c quark, and a pair of leptons ℓ and ℓ' can be written in the form

$$\mathcal{H}_{\text{eff}}^{qb} = -G_F \sum_a (\bar{q} \Gamma_a b) (\bar{\ell} [C_a \Gamma_a + C'_a \Gamma_a \gamma_5] \ell'), \quad (9.1)$$

where $\Gamma_a = \{I, \gamma_5, \gamma^\mu, \gamma^\mu \gamma_5, \sigma^{\mu\nu}\}$, with $a = \{S, P, V, A, T\}$ being the standard basis of operators of the Clifford algebra. In (9.1) the Fermi constant G_F is factored out so that all the coefficients C_a and C'_a are dimensionless. The rare B decays $B^- \rightarrow l \bar{\nu}_l$, $B \rightarrow l^+ l^-$ and $B \rightarrow X \nu \bar{\nu}$ depend only on a subset of these operators [1, 2, 3] due to the fact that several matrix elements of the quark operators vanish for purely leptonic B decays.

Purely leptonic B decays have yet to be observed experimentally. Present upper limits on the branching fractions for the various channels are summarized in the table at the end of the chapter. Note that the CDF and D^0 bounds on B_s and $B_d \rightarrow \mu^+ \mu^-$ are already competitive with the CLEO constraints on $B_d \rightarrow \ell^+ \ell^-$. The channels with muons or electrons are strongly helicity suppressed and require samples of B mesons significantly larger than have been accumulated so far. Channels with τ leptons have larger branching ratios, but the presence of additional missing neutrinos makes the detection of these decays very difficult due to large backgrounds from other B decays. The addition of a radiated photon to any of these purely leptonic decays increases the branching fractions by about an order of magnitude, but does not significantly improve the background situation.

Finally, note that the lepton flavor-violating decays, $B_d \rightarrow e\mu, e\tau, \mu\tau$, are forbidden in the Standard Model. Observation of these processes would thus provide an unambiguous signal for the existence of new physics. CLEO has established limits [4] on these channels of $< 5.9 \times 10^{-6}$, $< 5.3 \times 10^{-4}$, $< 8.3 \times 10^{-4}$, respectively.

9.1.1 $B \rightarrow \ell \nu_\ell$

9.1.1.1 Theoretical framework

In the Standard Model the $B^+ \rightarrow \ell^+ \nu_\ell$ decay of heavy charged mesons is of particular interest, due to its sensitivity to both the meson decay constants and the CKM matrix elements V_{qb} , with the case $q = u$ being relevant for BaBar. The decay is described by the effective Hamiltonian (9.1) with $\ell' = \nu_\ell$, and proceeds through the annihilation diagram. The general amplitude for this decay involves the set of matrix elements $\langle 0 | \bar{u} \Gamma_a b | B \rangle$. They vanish for the parity-even operators $\Gamma_S = I$ and $\Gamma_V = \gamma^\mu$ due to the pseudoscalar nature of the B meson. The tensor operator $\Gamma_T = \sigma_{\mu\nu}$ is antisymmetric in the Lorentz indices, and hence its matrix element must also vanish since the only available four-vector is the momentum p_B^μ of the B meson. Therefore, only the matrix elements of the pseudoscalar and axial-vector operators contribute. They are given by the partial conserved axial current relations

$$\begin{aligned} \langle 0 | \bar{u} \gamma^\mu \gamma_5 b | B^+ \rangle &= i f_B p_B^\mu, \\ \langle 0 | \bar{u} \gamma_5 b | B^+ \rangle &= -i f_B \frac{m_B^2}{m_b + m_u} \simeq -i f_B \frac{m_B^2}{m_b}. \end{aligned} \quad (9.2)$$

Assuming massless neutrinos, the general amplitude for the $B^- \rightarrow l \bar{\nu}_\ell$ decay reads

$$\mathcal{A}^{\ell\nu} = i f_B m_B G_F \left[(C_A^{\ell\nu} - C_A^{\ell\nu'}) \frac{m_\ell}{m_B} - (C_P^{\ell\nu} - C_P^{\ell\nu'}) \frac{m_B}{m_b} \right] (\ell\nu), \quad (9.3)$$

yielding the helicity suppressed branching fraction

$$\mathcal{B}(B^+ \rightarrow \ell^+ \nu) = \frac{G_F^2}{16\pi} f_B^2 \tau_B m_B m_\ell^2 \left[1 - \frac{m_\ell^2}{m_B^2} \right]^2 \left| (C_A^{\ell\nu} - C_A^{\ell\nu'}) - \frac{m_B}{m_\ell} (C_P^{\ell\nu} - C_P^{\ell\nu'}) \right|^2, \quad (9.4)$$

where the approximation $m_B/m_b \simeq 1$ has been made. In the Standard Model $C_P^{\ell\nu} = C_P^{\ell\nu'} = 0$ and $[C_A^{\ell\nu} - C_A^{\ell\nu'}]_{\text{SM}} = -\sqrt{2} V_{ub}$, which simplifies the above expression to

$$\mathcal{B}(B^+ \rightarrow \ell^+ \nu) = \frac{G_F^2 |V_{ub}|^2}{8\pi} f_B^2 \tau_B m_B m_\ell^2 \left[1 - \frac{m_\ell^2}{m_B^2} \right]^2. \quad (9.5)$$

Numerically, the predictions for this mode are somewhat imprecise due to the present uncertainties in the values of f_B and V_{ub} :

$$\mathcal{B}(B^+ \rightarrow \ell^+ \nu) = \mathcal{B}_{SM} \left[\frac{\tau_B}{1.66 \text{ps}} \right] \left[\frac{f_B}{180 \text{MeV}} \right]^2 \left[\frac{V_{ub}}{0.0035} \right]^2, \quad (9.6)$$

with

$$\begin{aligned} \mathcal{B}_{SM} &= 6.9 \times 10^{-12}, & \ell &= e, \\ &= 2.9 \times 10^{-7}, & \ell &= \mu, \\ &= 6.6 \times 10^{-5}, & \ell &= \tau, \end{aligned} \quad (9.7)$$

using the central value of $f_B = 180$ MeV as calculated by lattice gauge theory (see Appendix A). Once V_{ub} has been more precisely measured in semileptonic decays as discussed in Chapter 8, the $\tau\nu$ and $\mu\nu$ channels may be used to experimentally determine the B -meson decay constant and validate the lattice results.

The possibility that new physics can be constrained by these decays has been explored in different models and will be discussed in Chapter 13.

9.1.1.2 Experimental considerations: $B^+ \rightarrow \mu^+\nu_\mu$

The decay $B^+ \rightarrow \mu^+\nu$ is helicity suppressed with respect to $B^+ \rightarrow \tau^+\nu$ by a factor of 225. However, unlike the tau, the muon does not decay before detection, so the B decay is reconstructed as a two-body decay with a monochromatic muon momentum in the B rest frame with a central value of 2.645 GeV/ c . All the other visible particles in the event must be compatible with being produced by the decay of the other B meson. In the recent CLEO publication [5] of branching ratio limits for $B^+ \rightarrow \tau^+\nu$ ($< 2.2 \times 10^{-3}$ at the 90% confidence level) and $B^+ \rightarrow \mu^+\nu$ ($< 2.1 \times 10^{-5}$), their limit on $f_b|V_{ub}|$ from $B^+ \rightarrow \mu^+\nu$ is less than a factor of two worse than the one from $B^+ \rightarrow \tau^+\nu$. Since their $B^+ \rightarrow \tau^+\nu$ analysis contains 968 background events, about one-third from continuum and the rest from semileptonic B decays, whereas their $B^+ \rightarrow \mu^+\nu$ analysis has only 3 background events, one would expect the limit on $B^+ \rightarrow \mu^+\nu$ to fall faster than that for $B^+ \rightarrow \tau^+\nu$. In some ways, $B^+ \rightarrow \mu^+\nu$ is the most tantalizing of all the rare decays discussed in this chapter. At the upper end of its predicted Standard Model range, there would be ~ 10 of these events in 30 fb $^{-1}$ of running at the $\Upsilon(4S)$, and at the lower end, there would be ~ 10 decays in an *entire* 10 year data sample (~ 300 fb $^{-1}$).

Backgrounds from the main B decay modes are small, since true muons from semileptonic $b \rightarrow c\mu\nu$ decays cut off at 2.3 GeV/ c . There are also few pions and kaons that can fake muons above this momentum by decay or punchthrough. The largest source of background from B decays is $b \rightarrow u\mu\nu$, since the endpoint of the muon spectrum falls under the $B \rightarrow \mu\nu$ signal (Fig. 9-2). The worst background is from $B \rightarrow \pi^0\mu\nu$, which has a branching ratio of $\sim 1 \times 10^{-4}$, about 300 times bigger than the signal from $B^+ \rightarrow \mu^+\nu$.

The largest background in the CLEO analysis is from continuum background, where a charged hadron fakes a muon, or a real high-momentum muon comes from (for example) a charm semileptonic decay. This is combined with large missing momentum which can result from neutral hadrons, an additional neutrino or a detection inefficiency. The finely segmented IFR system should give BaBar excellent muon identification and pion rejection capabilities at these high energies. It can also be used to veto neutral hadrons. However, the level of sophistication needed from the IFR reconstruction for this analysis is still being developed, so the question of muon identification is deferred to future studies. In this analysis, it is assumed that the muon-finding efficiency is close to 100% for these hard muons, and the pion rejection fraction is left as a free

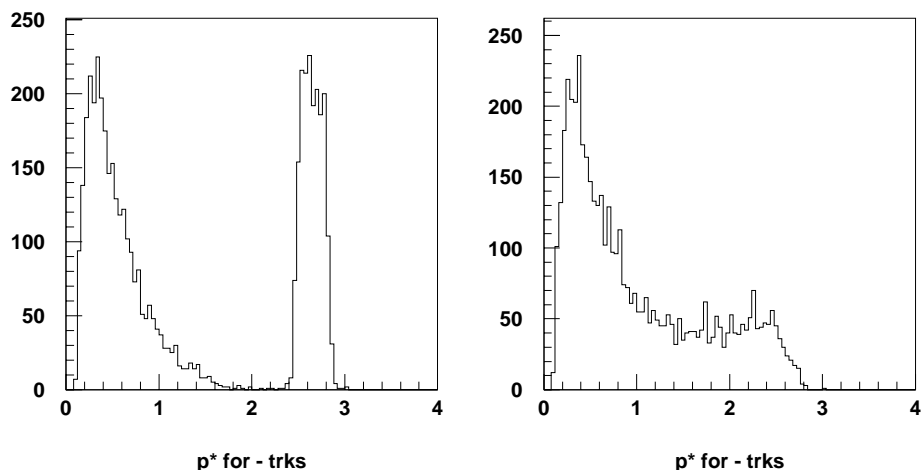


Figure 9-2. Momentum (GeV/c) in the $\Upsilon(4S)$ rest frame for all negative tracks in 2000 $B^+ B^-$ events where a) the B^- decays into $\mu^- \nu$ and b) the B^- decays into $\pi^0 \mu^- \nu$. The tracks from the (generic) B^+ are retained to show the clean separation of tracks from generic B decays and the monochromatic μ^- from $B^- \rightarrow \mu^- \nu$.

parameter. The CLEO analysis has been repeated in a `BBsim` reconstruction [6] which uses full charged-particle tracking in the drift chamber. Tracking in the silicon vertex detector should be added in the final analysis to improve the hermiticity and the track momentum resolution. Photons are not dealt with by full reconstruction in the calorimeter, but by using a parameterized smearing similar to that in `Aslund`. Photons outside the acceptance of the CsI calorimeter and with $E < 20$ MeV are deleted, and the remaining photons are smeared in E , θ , and ϕ . The results of this analysis depend very little on whether or not photon smearing is turned on. A perfect match between charged tracks and clusters has been assumed, although it is known that the results of this sort of “neutrino-reconstruction” analysis depend very much on accurate charged track-cluster matching in the calorimeter. The match is being developed as part of the full reconstruction, but was not in place for the forward calorimeter when this study was performed. Other problems with the present analysis are the lack of treatment of additional clusters arising from machine backgrounds, from hadronic interactions in the calorimeter (“splitoffs”), and from the reflection of energy at the surface of the calorimeter (“albedo”). Such clusters are usually dealt with using a cluster shape analysis. It is anticipated that such an algorithm will be developed in time for use in this kind of analysis with real data.

With the full `BBsim` simulation, the CLEO analysis was repeated as exactly as possible on a sample of $2K B^+ \rightarrow X, B^- \rightarrow \mu^- \nu$. Due to the forward/backward asymmetry of the `BaBar` detector, the requirement: $-0.77 < \cos \theta_{MISS} < +0.94$. was made. The rest of the CLEO analysis can be summarized as

$$n > 3, 2.545 \leq p_\mu^* \leq 2.745, M > 5.23, -2 \leq \Delta E \leq 0.5, |\cos \theta_{\mu-thrust}| < 0.7,$$

and $R_2 < 0.3$ (p^* , M and δE are in GeV). Our reconstruction efficiency with these cuts is 10.4%, while CLEO has $13 \pm 1\%$. A very similar Aslund analysis [7] finds an efficiency of 14%.

For the continuum background, the Aslund analysis, which assumes perfect lepton ID, sees no events in 10^6 $q\bar{q}$ events. The reconstruction analysis was repeated (with no lepton ID) on 10K BBsim $q\bar{q}$ events; none passed the CLEO cuts. Assuming a pion fake rate of 1% (roughly the estimate used for the BABAR TDR), there would be no background observed in 10^6 $q\bar{q}$ events, although one event survives to the last cut, so some background is not far away. CLEO sees 0.33 ± 0.11 continuum background events per 10^6 $q\bar{q}$ events, which is consistent with this study.

For the reconstruction analysis, the primary B decay background, $B^+ \rightarrow \pi^0 \mu^+ \nu$, was examined in detail. A sample of 2K BBsim events of this type were generated and reconstructed as above. Three events were observed after all the cuts, for an efficiency of 0.15%. Using the measured CLEO branching ratio of 0.9×10^{-4} for $B^+ \rightarrow \pi^0 \mu^+ \nu$, their expected number of background events can be converted to an efficiency of 0.20%, consistent with the results of this study. However, it should be noted that the CLEO number is for an inclusive sample of $b \rightarrow u\ell\nu$, whereas it has been assumed here that $B^+ \rightarrow \pi^0 \mu^+ \nu$ is the dominant background. It needs to be checked whether $B^+ \rightarrow \rho^0 \mu^+ \nu$ or other $b \rightarrow u\mu\nu$ channels contribute significantly.

Either simple $\sqrt{\mathcal{L}}$ scaling, or slightly more detailed arguments put forward in [7], indicate that a 90% confidence level upper limit of $\sim 4 \times 10^{-6}$ should be obtained for the branching ratio for $B^+ \rightarrow \mu^+ \nu$ after a “nominal” first year of 30 fb^{-1} data taking at the $\Upsilon(4S)$, and that the eventual upper limit would be $\sim 1 \times 10^{-6}$ after 300 fb^{-1} . While a CLEO-type analysis will continue to put interesting limits on $f_B^2 |V_{ub}|^2$, it is clear that better separation between signal and background will be needed if BABAR hopes to observe $B^+ \rightarrow \mu^+ \nu$.

In performing the CLEO analysis on the BABAR BBsim data, several possibilities for improving the analysis were observed. The $n > 3$ (event multiplicity) cut reduces the signal more than the backgrounds considered. If backgrounds from $e^+e^- \rightarrow \tau^+\tau^-$ events prove negligible this cut can be changed to $n > 1$. The p_μ^* signal is symmetric around 2.645 for signal, whereas the backgrounds are falling as p_μ^* increases. Either an asymmetric cut of $2.545 \leq p_\mu^* \leq 2.795$ should be adopted, or a likelihood fit should be used. Using the direction of the other B with respect to the μ in the $\mu\nu$ rest frame allows a one-sided cut to be used, $\cos \theta_{\mu-B^+} < 0.7$. With these minor changes to the CLEO analysis, it was possible to increase the signal efficiency by 50%, while keeping the backgrounds unchanged. There are other possible cuts to consider *e.g.*, on missing mass squared (mm^2), on p_{MISS}^* , and $m_{\ell\nu}$. These were explored and look promising. The Aslund analysis was able to tighten up the ΔE distribution with a simple missing mass-squared constraint of $mm^2 = 0$. Since there are significant correlations between the variables, this is an analysis where Neural Net methods might help substantially.

9.1.1.3 Experimental considerations: $B^+ \rightarrow \tau^+ \nu_\tau$

Two studies of $B^- \rightarrow \tau^- \bar{\nu}$ have been performed using `Aslund`[7, 8] and a CLEO-style analysis [5] in which a single, identified lepton is required which is assumed to come from the τ decay. The rest of the event is then required to be consistent with a hadronic decay of the other B in which all the energy is reconstructed. These studies show that `BaBar` should be able to set a 90% confidence level upper limit of $2 - 3 \times 10^{-4}$ on the branching ratio with the “nominal” first year’s data sample of $\sim 30 \text{ fb}^{-1}$. This is somewhat surprising, as simple $\sqrt{\mathcal{L}}$ scaling of the background-dominated CLEO limit would suggest an achievable upper limit of 6×10^{-4} .

The improved sensitivity is probably due to a lack of realism in the `Aslund` simulation. Tracking efficiency, neutral reconstruction and particle identification are all known to be handled optimistically, leading to an underestimate of the number of background events. The ΔE distribution in [8] differs from the CLEO one in [5]), and a much tighter ΔE cut is used than in the CLEO analysis [7]. This almost completely suppresses the continuum and $B\bar{B}$ backgrounds while reducing the signal efficiency by a factor of ~ 4.5 . The results of these `Aslund` studies need verifying with the full `BBSim` simulation and reconstruction.

It is probably best to assume that with a CLEO-style analysis, the upper limit `BaBar` will achieve with 30 fb^{-1} is between 3 and 6×10^{-4} . The current best upper limit of $< 5.7 \times 10^{-4}$ (90% confidence level) is from the L3 collaboration [9]. This measurement uses their entire LEP I data sample, and so will not be substantially improved before `BaBar` begins reporting results.

It is possible that hadronic tau decays such as $\pi^+ \nu$ could be included in the analysis. Due to the polarization of the τ , the π^+ tends to follow the τ^+ direction [8]. The possibility of using partial reconstruction of the other B when it decays into $D^{(*)0} \ell \nu$ has also been considered [8]. This topology is currently excluded from the CLEO analysis, and more work is needed to show that it will not introduce an unacceptable level of background.

About a third of the background events that CLEO sees are from continuum $q\bar{q}$ events. CLEO needs a significant amount of off-resonance data ($\sim \frac{1}{2}$ of their amount of Υ_{4S} data) just to subtract this background. Simply scaling from CLEO, ~ 4000 continuum events would be expected to pass a CLEO-style analysis in 30 fb^{-1} of data. It is important to look for improvements in continuum rejection, such as tightening the ΔE cut [7].

The number of $B^+ \rightarrow \tau^+ \nu$ decays expected in a 30 fb^{-1} data sample is ~ 1500 . Even at the *lower* end of the Standard Model range there will still be ~ 500 events in the data sample. Thus it is possible to imagine a measurement in the first year with a sophisticated enough analysis that exploits the advantages that `BaBar` has over CLEO II for this measurement. For example, CLEO states that 83% of the $B\bar{B}$ background has $> 500 \text{ MeV}$ of missing energy due to neutral hadrons (primarily K_L^0), while only 14% of the signal events do. The fine segmentation of the IFR has been shown to be efficient in identifying high-momentum K_L^0 mesons [10]. What needs to be studied is the combined efficiency of the IFR and the EMC for tagging events which have a K_L^0 of

any momentum which could have carried away > 500 MeV of energy. Note that the momentum spectrum of K_L^0 mesons from generic B decays is quite soft.

Another feature of the $B\bar{B}$ background is that it comes mostly from events in which at least one B decays semileptonically. These events have a much richer vertex structure (2 B vertices, 2 D vertices) than signal events (1 B vertex and 1 D vertex with the candidate lepton excluded). Both analyses have looked at fitting all tracks from the recoiling B candidate to a single vertex and cutting on the vertex probability (see Fig. 9-3). The conclusion is that this will reduce $B\bar{B}$ background with respect to the signal by about a factor of four.

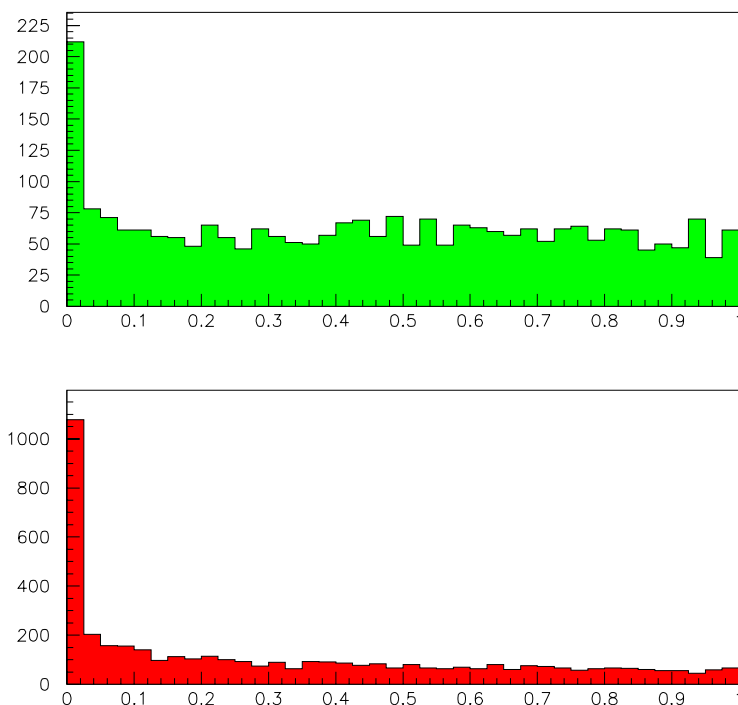


Figure 9-3. Vertex χ^2 probability, for all tracks excluding the candidate lepton, for a) $B^+ \rightarrow \tau^+ \nu$ events and b) $B\bar{B}$ background events.

9.1.2 $B^0 \rightarrow \ell^+ \ell^-$

9.1.2.1 Theoretical framework

The purely leptonic neutral B decays are described by the effective Hamiltonian in Eq. (9.1) with $\ell = \ell' = e, \mu$, or τ , and $q = d$ being relevant for BaBar. These transitions proceed through electroweak penguin diagrams with Z exchange (and in principle, Higgs boson exchange) as well

as W box diagrams. Electromagnetic current conservation forbids the contribution of the photon exchange penguin diagram for on-shell leptons in the final state. Recent analyses of this decay can be found in [2, 11, 12].

For on-shell leptons, $p_B^\mu (\bar{\ell} \gamma_\mu \ell) = (p_{\ell^+}^\mu + p_{\ell^-}^\mu) (\bar{\ell} \gamma_\mu \ell) = 0$, and hence the contribution of the axial-vector operator $\langle 0 | \bar{d} \gamma^\mu \gamma_5 b | B \rangle$ vanishes when contracted with the leptonic vector current. The parity-even and tensor operators also vanish as discussed above. The resulting most general form of the $B_d \rightarrow l^+ l^-$ amplitude is then

$$\mathcal{A}^{\ell\bar{\ell}} = iG_F f_{B_d} m_B \left[\left(C_P^{\ell\bar{\ell}} - \frac{2m_\ell}{m_B} C_A^{\ell\bar{\ell}} \right) (\bar{\ell} \gamma_5 \ell) + C_P^{\ell\bar{\ell}'} (\bar{\ell} \ell) \right], \quad (9.8)$$

and the corresponding branching ratio reads

$$\mathcal{B}(B_d \rightarrow l^+ l^-) = \frac{G_F^2}{8\pi} f_B^2 \tau_B m_B^3 \sqrt{1 - \frac{4m_\ell^2}{m_B^2}} \left[\left| C_P^{\ell\bar{\ell}} - \frac{2m_\ell}{m_B} C_A^{\ell\bar{\ell}} \right|^2 + \left(1 - \frac{4m_\ell^2}{m_B^2} \right) \left| C_P^{\ell\bar{\ell}'} \right|^2 \right]. \quad (9.9)$$

In the Standard Model, $C_P^{\ell\bar{\ell}'}$ and $C_P^{\ell\bar{\ell}}$ arise from penguin diagrams with physical and unphysical neutral scalar exchange, and are suppressed by a factor of $(m_b/M_W)^2$ [11]. The decay rate is then determined by the coefficient

$$\left[C_A^{\ell\bar{\ell}} \right]_{\text{SM}} = \frac{\alpha V_{tb} V_{td}^*}{\sqrt{8} \pi \sin^2 \theta_w} Y(x_t), \quad (9.10)$$

where $x_t \equiv m_t^2/m_W^2$, $\sin^2 \theta_w$ is the weak mixing angle, and the function $Y(x)$ is given by $Y(x) = Y_0(x) + \frac{\alpha_s}{4\pi} Y_1(x)$ at next-to-leading order (NLO). At leading order [13]

$$Y_0(x) = \frac{x}{8} \left[\frac{x-4}{x-1} + \frac{3x}{(x-1)^2} \ln x \right], \quad (9.11)$$

while the expression for the next-to-leading order term $Y_1(x)$ can be found in [12]. Numerically, $Y(x_t) \approx 1.03 \cdot Y_0(x_t)$. The NLO branching fraction for the Standard Model is then given by

$$\begin{aligned} \mathcal{B}(B_d \rightarrow l^+ l^-) &= (8.4 \times 10^{-8}) \frac{m_\ell^2}{m_B^2} \left[\frac{\tau_B}{1.55 \text{ ps}} \right] \left[\frac{f_B}{180 \text{ MeV}} \right]^2 \left[\frac{|V_{td}|}{0.004} \right]^2 \\ &\times \sqrt{1 - \frac{4m_\ell^2}{m_B^2}} \left[Y_0^2(x_t) + \frac{\alpha_s}{2\pi} Y_0(x_t) Y_1(x_t) \right], \end{aligned} \quad (9.12)$$

resulting in

$$\begin{aligned} \mathcal{B}(B_d \rightarrow e^+ e^-) &= 2.6 \times 10^{-15}, \\ \mathcal{B}(B_d \rightarrow \mu^+ \mu^-) &= 1.1 \times 10^{-10}, \\ \mathcal{B}(B_d \rightarrow \tau^+ \tau^-) &= 3.1 \times 10^{-8}. \end{aligned} \quad (9.13)$$

These numerical results show that these decays are too rare to be observed at BaBar unless they are significantly enhanced by new physics.

9.1.2.2 Experimental considerations

The feasibility of searching for $B^0 \rightarrow \ell^+ \ell'^-$, where ℓ'^- may or may not be the same type of charged lepton as ℓ^+ , was studied using `ASLUND` for the case of an integrated luminosity of 30 fb^{-1} at `BABAR` [14]. For $\ell^+ \ell^- = ee, \mu\mu$, or $e\mu$, `BABAR`'s 90% confidence level upper limits on branching ratios should be $\mathcal{B}(B^0 \rightarrow \ell^+ \ell^-) < 5.0 \times 10^{-7}$. The signatures for these decays are two high-momentum leptons corresponding to monochromatic lepton momenta of $2.645 \text{ GeV}/c$ in the rest frame of the B meson. This is a remarkably clean signature, and should not be background limited at `BABAR`. The limits are expected to scale approximately as \mathcal{L} from the `CLEO` limits, [4], which are $< 5.9 \times 10^{-6}$ for all three modes, and this is what is observed in our studies.

For the $\ell^+ \ell^- = e\tau$ or $\mu\tau$ case, the `BABAR` upper limit should be $\mathcal{B}(B^0 \rightarrow \ell^+ \ell^-) < 4.3 \times 10^{-5}$. The signature here is one monochromatic lepton, corresponding to $2.645 \text{ GeV}/c$ in the B rest frame, and either another, lower momentum lepton, or a pion with the additional constraint that it come from a two-body decay of a polarized τ lepton. The current `CLEO` limits [4] are $< 5.3 \times 10^{-4}$ and $< 8.3 \times 10^{-4}$, respectively.

There is as yet no experimental upper limit on $B^0 \rightarrow \tau^+ \tau^-$. A possible signature is two low-momentum leptons plus a large missing energy, with the rest of the event being consistent with a fully reconstructed hadronic B decay. This is essentially an extension of the $B \rightarrow \tau\nu$ analysis with the addition of a lepton from the other τ . The `BABAR` sensitivity to this decay was found to be $\mathcal{B}(B^0 \rightarrow \tau^+ \tau^-) < 2.0 \times 10^{-3}$.

All of the expected upper limits for the decays $B \rightarrow ee, \mu\mu$ and $\tau\tau$ are significantly above the Standard Model predictions, even with the full `BABAR` data sample of 300 fb^{-1} . Thus, their interest lies in placing constraints on new physics (see Chapter 13). The Fermilab collider experiments will undoubtedly set better limits on $B^0 \rightarrow \mu^+ \mu^-$, and can also search for $B_s \rightarrow \mu^+ \mu^-$ which has a larger branching fraction in the Standard Model, and may even be observable (see Table 9-8 at end of chapter). The current best limits are 1.6×10^{-6} for the B^0 decay, and 8.4×10^{-6} for the B_s decay, both from `CDF` [15].

9.1.3 $B \rightarrow \ell\nu\gamma, \ell^+ \ell^- \gamma$

9.1.3.1 Theoretical framework: $B \rightarrow \ell\nu\gamma$

Radiative leptonic modes, although suppressed by an additional factor of α , are not helicity suppressed, due to the presence of the photon [16]. Naively, one would expect the corresponding branching fractions to scale as

$$R^\ell \equiv \frac{\mathcal{B}(B \rightarrow \ell\bar{\nu}_\ell\gamma)}{\mathcal{B}(B \rightarrow \ell\bar{\nu}_\ell)} \simeq \alpha \left(\frac{m_B}{m_\ell} \right)^2. \quad (9.14)$$

This would imply that $B^- \rightarrow \mu^- \bar{\nu}_\mu \gamma$ has a branching fraction enhanced by a factor of 20 with respect to the purely leptonic mode, or $\mathcal{B}(B^- \rightarrow \mu^- \bar{\nu}_\mu \gamma) \simeq \text{few} \times 10^{-6}$. Due to the lack of dependence on the lepton mass, the muon and electron radiative modes are expected to have similar rates; the τ mode is smaller due to phase space suppression. This expected enhancement over the helicity suppressed two-body decays suggests that this channel may be used as an alternative to extract V_{ub} and/or measure f_B . More detailed inspection reveals a complexity underlying these decay modes due to long-distance contributions. The only contributions not suppressed by helicity in the Standard Model involve the coupling of the B meson to a photon and an off-shell $J^P = 1^\pm$ meson containing a b quark, as shown in Fig. 9-4. Helicity suppression is absent here, since the hadron coupling to the lepton pair via the weak current has spin one.¹ The size of each depicted

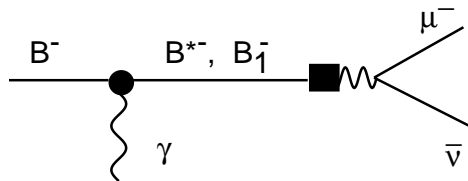


Figure 9-4. Pole contributions to $B \rightarrow \mu \bar{\nu}_\mu \gamma$.

pole contribution is governed by a $B - \gamma$ coupling and the weak annihilation amplitude of the pole into a lepton pair, *i.e.*, its decay constant. These additional unknowns add theoretical uncertainties to these modes not present in the purely leptonic case. It is possible, however, to estimate these quantities in model calculations, assuming a small number of resonances saturates the rate. In [16] the contributions of the B^* and the two lowest lying axial-vector mesons B_1 and B_1' were taken into account. Estimating the $BB_i\gamma$ couplings and the ratio of the axial-vector to vector decay constants in a non-relativistic quark model gives $R^\mu \simeq (1 - 20)$, corresponding to $\mathcal{B}(B \rightarrow \mu \bar{\nu}_\mu \gamma) \simeq (10^{-7} - 10^{-6})$. The uncertainties in this case arise from various sources, including relativistic corrections and form-factor suppression in photonic couplings, and are always related to quantities that are not calculable in perturbation theory, since they are due to hadronic effects. Thus in these modes, an accurate assessment of the rates is rather model dependent. Other attempts to compute the decay rates for these modes yield similar results. In Refs. [17, 18] the rate is estimated using light cone sum rules; the result obtained in [17] gives $R^\mu \simeq 19$, while in [18] the branching ratio is estimated to be $\mathcal{B}(B \rightarrow \ell \bar{\nu}_\ell \gamma) \simeq 2 \cdot 10^{-6}$. A non-relativistic quark model is adopted in [19], yielding $\mathcal{B}(B \rightarrow \ell \bar{\nu}_\ell \gamma) \simeq 3.5 \times 10^{-6}$. Finally, the relativistic potential model in [20] predicts $\mathcal{B}(B \rightarrow \ell \bar{\nu}_\ell \gamma) \simeq 0.9 \times 10^{-6}$. All these results suggest that the rate for these channels is indeed an order of magnitude larger than the purely leptonic mode. However, large uncertainties remain, and it is possible that the radiative leptonic modes have rates only just above the purely leptonic channels.

¹This is why simple Bremsstrahlung contributions are still helicity suppressed: they do not flip the heavy meson spin.

Although the uncertainties coming from hadronic physics limit the ability to extract interesting quantities like V_{ub} and f_B , a detailed experimental study of these modes may result in a better understanding of the underlying hadronic physics. The characteristics of the photon spectrum are quite dependent on the hadronic modeling. In the models employed in Refs. [16, 19, 20], the spectrum has a parabolic shape, which peaks at a photon energy in the range $E_\gamma = 1.3 - 1.5$ GeV, with the exact value varying between the different models. Conversely, in [18] the spectrum is asymmetric and peaks at $E_\gamma = 0.8$ GeV. Such asymmetry is attributed to the inclusion of the non-perturbative resonance contributions, which are prevalent in the sum rule approach. On the other hand, the lepton spectrum in radiative leptonic decays is expected to be very hard. In [19] it is stressed that its shape is different from the analogous spectrum in the decay chain $B \rightarrow \tau\nu$, $\tau \rightarrow \ell\nu\nu$, which represents a possible background to the radiative process considered here.

9.1.3.2 Theoretical framework: $B \rightarrow \ell^+\ell^-\gamma$

The radiative leptonic decays involving flavor-changing neutral-current vertices such as $B_q \rightarrow \ell^+\ell^-\gamma$ ($q=s,d$) possess similar properties to those discussed above for the charged transitions [16]. Hence, a potentially large enhancement in $B_q \rightarrow \mu^+\mu^-\gamma$, approximately one order of magnitude with respect to the purely muonic mode, is to be expected and branching ratios for the electronic mode $B_q \rightarrow e^+e^-\gamma$ are again anticipated to be similar to those for the muonic channels. The long-distance structure of these neutral modes is related by isospin to that of the charged decays discussed above, and is then determined by the sum over the same pole contributions. What makes these decay modes particularly interesting is the fact that they are induced by short-distance FCNC interactions, forbidden at tree level in the Standard Model. This suggests the possibility of using these decays as Standard Model tests, as well as a constraint on its various extensions.

The short-distance structure of these decays is slightly different from that of the $B_q \rightarrow \ell^+\ell^-$ case. The photonic penguin diagram, which does not contribute to the purely leptonic case, is present in $B_q \rightarrow \ell^+\ell^-\gamma$. Furthermore, of the leading one-loop annihilation diagrams which contribute to $B_q \rightarrow \ell^+\ell^-\gamma$, those in which the photon is radiated off an internal W -boson or top-quark will result in higher dimension operators and can therefore be neglected. Hence, the short-distance structure of these decay modes is similar to that of $b \rightarrow q\ell^+\ell^-$, which will be studied in detail later in this chapter. The short-distance amplitude then depends on the Wilson coefficient C_7^{eff} , corresponding to the magnetic dipole operator, as well as C_9^{eff} and C_{10} , which arise mainly from the off-shell photon contributions as well as from Z penguin and box diagrams. (These coefficients and operators are defined and discussed in Section 9.3.) In principle, measurements of these coefficients can thus be obtained from these transitions, independently from observations of $b \rightarrow s\gamma$ and $b \rightarrow s\ell^+\ell^-$. However, the ubiquitous hadronic uncertainties complicate the task of extracting the interesting short-distance information. Here, the uncertainties arise in the hadronic matrix elements of the operators \mathcal{O}_7 , \mathcal{O}_9 and \mathcal{O}_{10} . These quantities cannot be obtained from first-principle calculations other than lattice gauge theory computations. Model calculations in the constituent

quark model [21] and light cone QCD sum rules [22] give estimates of $\mathcal{B}(B_s \rightarrow \ell^+ \ell^- \gamma) \simeq (2 - 5) \times 10^{-9}$ and $\mathcal{B}(B_d \rightarrow \ell^+ \ell^- \gamma) \simeq (3 - 6) \times 10^{-10}$, for $\ell = e, \mu$. These results do not reflect a large enhancement over the purely leptonic modes, which have only slightly smaller branching ratios. The theoretical uncertainty inherent to these calculations is unfortunately quite large.

An interesting possibility to reduce the theoretical uncertainties in these modes and turn them into stringent constraints on the Standard Model, involves combining both the $B \rightarrow \ell^+ \ell^- \gamma$ and the $B \rightarrow \ell^- \bar{\nu}_\ell \gamma$ decay modes [23]. The basic idea is that the long-distance contributions in both channels are essentially the same. The main obstacle is that the Lorentz structure of the matrix elements is different for $B \rightarrow \ell^+ \ell^- \gamma$, due to the presence of the operator \mathcal{O}_7 . Although the operators \mathcal{O}_9 and \mathcal{O}_{10} can be related to the effective operator mediating the transitions entering in the charged mode $B \rightarrow \ell \nu_\ell \gamma$, this is not the case with the magnetic dipole operator \mathcal{O}_7 , which introduces new and independent hadronic quantities. It is possible, however, to relate the hadronic matrix element of \mathcal{O}_7 to those of the radiative charged mode by making use of heavy-quark spin symmetry relations [24]. Once these relations are implemented, it can be shown that the short- and long-distance pieces factorize in $B \rightarrow \ell^+ \ell^- \gamma$. This factorization is valid in the limit where $(\Delta_i)/m_B \ll 1$, with Δ_i being the excitation energy of the i -th pole above the ground state m_B , for all poles that contribute significantly. This approximation holds since contributions from highly excited states, with larger Δ_i , are strongly suppressed by form-factor effects. The approximate factorization of long- and short-distance contributions implies that the long-distance pieces cancel in the ratio

$$R_{0+} \equiv \frac{\mathcal{B}(B \rightarrow \ell^+ \ell^- \gamma)}{\mathcal{B}(B \rightarrow \ell \nu_\ell \gamma)}, \quad (9.15)$$

leaving R_{0+} exclusively dependent on short-distance quantities. One obtains [23]

$$R_{0+} \simeq \alpha^2 \left| \frac{V_{tb}^* V_{tq}}{V_{ub}} \right|^2 \left\{ |2C_7^{\text{eff.}} + C_9^{\text{eff.}}|^2 + |C_{10}|^2 \right\}, \quad (9.16)$$

with $q = (s, d)$. In general, the ratios of any quantities derived from the Dalitz plot (*e.g.*, photon or lepton momentum distributions) will give the same cancellation. By combining experimental information on both types of radiative leptonic decays, it is possible to make reliable predictions within a controlled approximation and hence test the Standard Model.

9.1.3.3 Experimental considerations: $B^+ \rightarrow \mu^+ \nu \gamma$

The decay $B \rightarrow \mu \nu \gamma$ is characterized by the relatively high energy of the detected decay products, the muon and the photon. Neglecting the muon mass, the following phase-space constraints hold:

$$p_\mu \leq \frac{m_B}{2}, \quad (9.17)$$

$$p_\gamma \leq \frac{m_B}{2}, \quad (9.18)$$

$$p_\mu + p_\gamma \geq \frac{m_B}{2}. \quad (9.19)$$

Figure 9-5 shows the distribution of the muon and photon momenta for the signal and the B^+B^- and $B^0\bar{B}^0$ backgrounds.

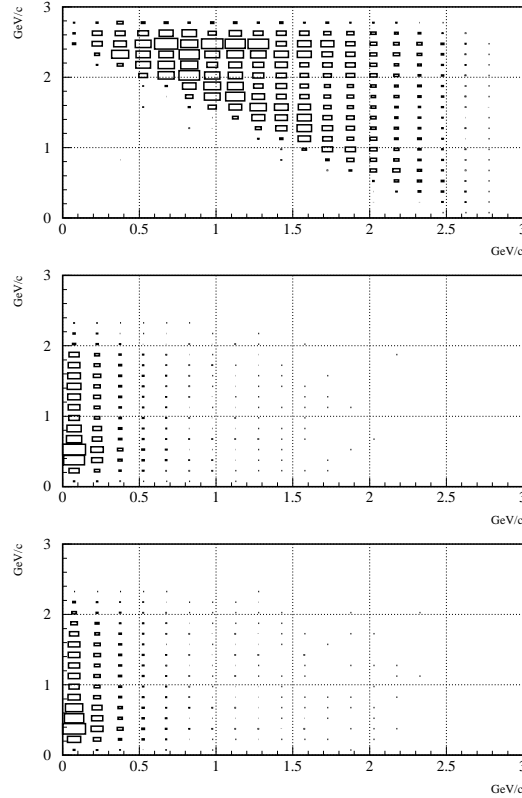


Figure 9-5. Momentum of the muon versus momentum of the photon for the signal and the backgrounds B^+B^- and $B^0\bar{B}^0$.

The low expected branching ratio ($\sim 10^{-6}$) requires a very high rejection of the backgrounds. The missing neutrino reduces the number of constraints that can be applied to the signal events. In the approximation that the B meson decays at rest in the center-of-mass frame, the neutrino momentum vector can be reconstructed as the opposite of the total momentum vector of the $\mu\gamma$ pair, and the reconstructed B mass has the spectrum shown in Fig. 9-6.

Relativistic kinematics requires that the following relation holds in the laboratory frame:

$$E_\nu^2 = p_B^2 + |\mathbf{p}_\mu + \mathbf{p}_\gamma|^2 - 2p_B|\mathbf{p}_\mu + \mathbf{p}_\gamma|\cos\theta' \quad (9.20)$$

$$= (E_B - E_\mu - E_\gamma)^2, \quad (9.21)$$

where θ' is the angle of the vector $\mathbf{p}_\mu + \mathbf{p}_\gamma$ with respect to the B direction. Since the B meson momentum vector in the laboratory frame is approximately directed along the beam axis, θ' can be

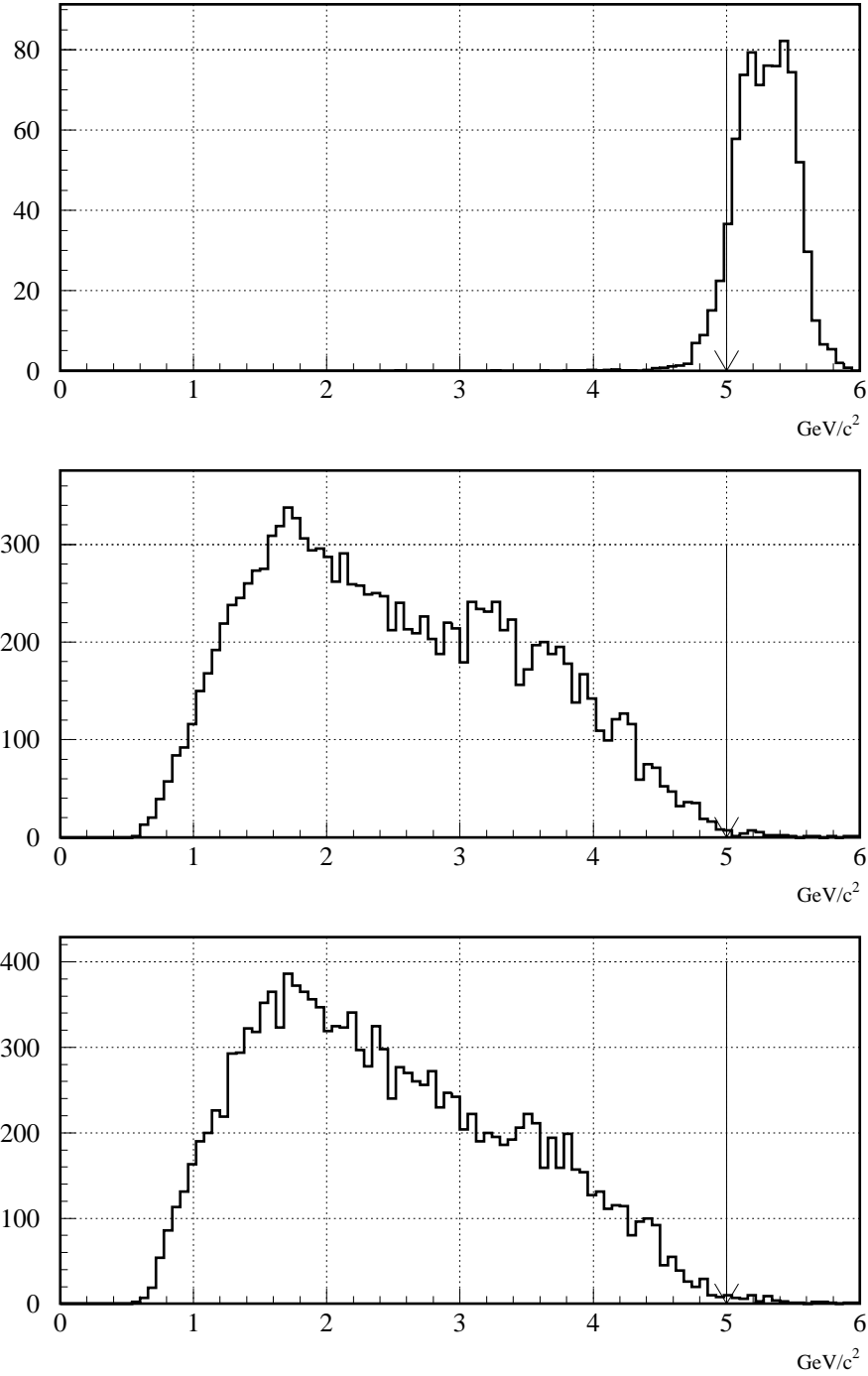


Figure 9-6. Reconstructed B mass for the signal and the backgrounds B^+B^- and $B^0\bar{B}^0$.

approximated by the polar angle θ of the vector $\mathbf{p}_\mu + \mathbf{p}_\gamma$. The variable D is defined as:

$$D = \cos \theta - \frac{p_B^2 + |\mathbf{p}_\mu + \mathbf{p}_\gamma|^2 - (E_B - E_\mu - E_\gamma)^2}{2p_B |\mathbf{p}_\mu + \mathbf{p}_\gamma|}, \quad (9.22)$$

where p_B is the average B momentum. D should be close to zero for the signal, but not for the background, as shown in Fig. 9-7.

A study [25] carried out using `ASLUND`, which also includes more kinematical variables and π^0 rejection, shows that a possible level of rejection of the $B\bar{B}$ background is $\sim 4 \times 10^{-7}$, while keeping an overall signal efficiency around 15–20%. An analysis published by CLEO [26] shows that the $q\bar{q}$ contribution to the total background is much smaller than the $B\bar{B}$ contribution.

The CLEO analysis has put the following limits at 90% confidence level:

$$\mathcal{B}(B \rightarrow \mu\nu\gamma) < 5.3 \times 10^{-5}, \quad \mathcal{B}(B \rightarrow e\nu\gamma) < 2.0 \times 10^{-4}.$$

Our study shows that BABAR should be sensitive to a signal with a branching ratio of 10^{-6} at the 5σ level with a data sample of 100fb^{-1} .

9.1.3.4 Experimental considerations: $B^0 \rightarrow \mu^+\mu^-\gamma$

No Monte Carlo study has yet been made to determine the sensitivity of BABAR to the decay $B^0 \rightarrow \mu^+\mu^-\gamma$. The kinematics should be the same as those described above for $B^+ \rightarrow \mu^+\nu\gamma$, except that the ν is replaced by a charged muon. This will *substantially* reduce the background, and it is likely that this decay can be made background-free. Under this assumption a limit of $\mathcal{B}(B^0 \rightarrow \mu^+\mu^-\gamma) < 5.0 \times 10^{-7}$ can be obtained at the 90% confidence level from a sample of 30fb^{-1} . Even with a data sample of 300fb^{-1} , the upper limit would still be a factor of ~ 10 above the Standard Model prediction.

9.2 $b \rightarrow s(d) + X$ Transitions

Flavor-changing neutral current decays involving $b \rightarrow s$ or $b \rightarrow d$ transitions have received much attention in recent years. They occur only at loop level in the Standard Model and hence provide an excellent probe of new indirect effects by yielding information on the masses and couplings of the virtual particles running in the loops. Within the Standard Model they have relatively large rates for loop processes due to the massive internal top-quark and the CKM structure of the contributing penguin and box diagrams. Due to the heavy B mass, long-distance effects are expected to be less important than in rare D or K meson decays, and hence the rare B transitions are essentially short-distance dominated.

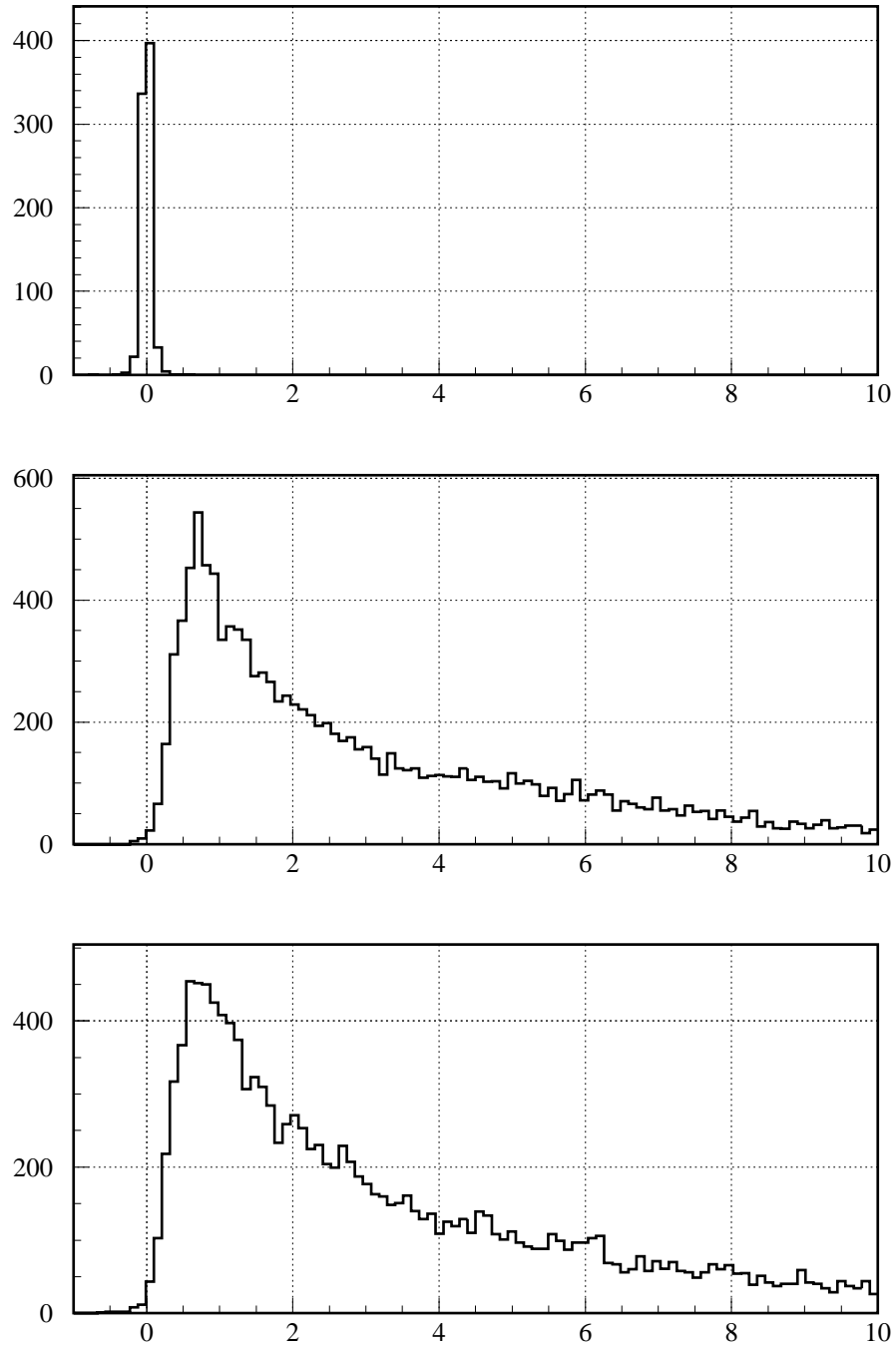


Figure 9-7. *Distribution of the variable D .*

The effective field theory for $b \rightarrow s(d)$ transitions is universal for all the channels discussed here; the salient features are briefly reviewed here. The one-loop processes which mediate flavor-changing neutral currents can be classified as electromagnetic, weak, or gluonic penguin diagrams and box diagrams. Samples of these classes of diagrams are displayed in Fig. 9-8. The operator product expansion gives the effective Hamiltonian governing these processes (see also Chapters 1, 2 and Appendix A). The conventional form used in the rare decay literature is

$$H_{eff} = -\frac{4G_F}{\sqrt{2}}V_{tb}V_{tq}^* \sum_{i=1}^{10} C_i(\mu)\mathcal{O}_i \quad , \quad (9.23)$$

where the \mathcal{O}_i are local renormalized operators built with light fields and $V_{tq}^*V_{tb}$ are elements of the Cabibbo-Kobayashi-Maskawa matrix with $q = s, d$. The C_i represent the corresponding Wilson coefficients and contain the relevant short-distance physics. They are evaluated perturbatively at the electroweak scale, where matching conditions are imposed, and then evolved down to the scale $\mu \sim m_b$ via the renormalization group equations (RGE). The solution to the RGE requires the knowledge of the anomalous dimension matrix to a given order in α_s . The operators of dimension less than or equal to four are renormalizable and contribute only to redefine couplings and fields of the light sector, according to the decoupling theorem. The operators of dimension greater than 4 are suppressed by powers of $1/M_W^2$. In the sum (9.23) one needs to consider only operators of dimension 5 and 6; these must contain two quarks fields and a photon, Z/W , or gluon field, and for dimensional reasons can have at most two derivatives. Other properties of the operators include the correct flavor change $\Delta b = -\Delta s = -\Delta d = -1$ and invariance under the unbroken color and electromagnetic gauge interactions.

Note that the above effective Hamiltonian is defined with *opposite* sign and a different overall numerical factor to that presented in Eq. (1.116) and in Appendix A. As stated above, this convention is customary in the rare decay literature, and is employed here to avoid confusion in determining the relative signs and numerical factors when including the long-distance contributions (various pieces of which appear in several sources in the literature).

The basis of local operators that is most often used is obtained from the more general set of gauge-invariant dimension-five and -six local operators with up to three external gauge bosons by applying the QED and QCD equations of motion [27]. The current-current operators, \mathcal{O}_1 and \mathcal{O}_2 , and the four-fermion penguin operators, \mathcal{O}_{3-6} , are as delineated in Appendix A for $b \rightarrow d$ transitions, and with the replacement of d by s for $b \rightarrow s$ processes. In our convention, the magnetic and chromomagnetic dipole operators, \mathcal{O}_7 and \mathcal{O}_8 , respectively, are

$$\begin{aligned} \mathcal{O}_7 &= \frac{e}{16\pi^2} \bar{q}_\alpha \sigma^{\mu\nu} (m_b R + m_q L) b_\alpha F_{\mu\nu} \quad , \\ \mathcal{O}_8 &= \frac{g_s}{16\pi^2} \bar{q}_\alpha \sigma^{\mu\nu} (m_b R + m_q L) t_{\alpha\beta}^a b_\beta G_{\mu\nu}^a \quad , \end{aligned} \quad (9.24)$$

where α and β are color indices, and the chiral structure is specified by the projectors $L, R = (1 \mp \gamma_5)/2$. $F_{\mu\nu}$ and $G_{\mu\nu}^a$ denote the QED and QCD field strength tensors, and e and g_s represent

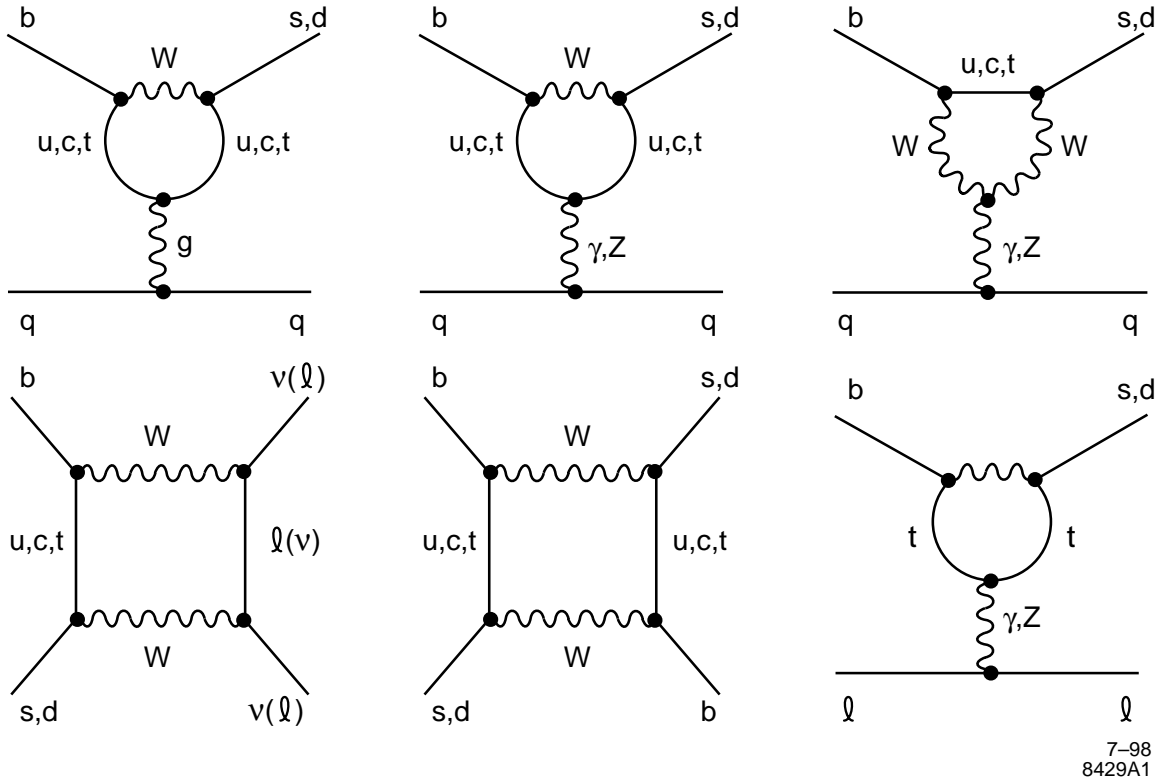


Figure 9-8. Sample one-loop Feynman diagrams which mediate flavor-changing neutral current decays.

7-98
8429A1

the electromagnetic and strong coupling constants. Note that these operators are defined to contain a mass factor. The remaining electroweak penguin operators, which are relevant for $b \rightarrow s\ell^+\ell^-$, are of order G_F^2 and can be written as

$$\begin{aligned} \mathcal{O}_9 &= \frac{\alpha}{4\pi} \bar{q}_\alpha \gamma^\mu L b_\alpha \bar{\ell} \gamma_\mu \ell, \\ \mathcal{O}_{10} &= \frac{\alpha}{4\pi} \bar{q}_\alpha \gamma^\mu L b_\alpha \bar{\ell} \gamma_\mu \gamma_5 \ell. \end{aligned} \tag{9.25}$$

A detailed review of this effective Hamiltonian (9.23) and its QCD corrections is given in Ref. [28]

A brief summary of the present experimental status and main theoretical features of each decay mode is presented here. Further discussion of the theoretical formalism and experimental considerations relevant for B_{BAR} are given in the following subsections.

The inclusive decay $B \rightarrow X_s \gamma$, where X_s is a strange hadronic state, is of particular interest. The branching ratio has been measured by the CLEO collaboration to be [29]:

$$\mathcal{B}(B \rightarrow X_s \gamma) = (3.15 \pm 0.35 \pm 0.41) \times 10^{-4}, \tag{9.26}$$

and there is also a very recent preliminary result from the ALEPH collaboration [30]

$$\mathcal{B}(B \rightarrow X_s \gamma) = (3.38 \pm 0.74 \pm 0.85) \times 10^{-4}. \quad (9.27)$$

As usual, in the above, the first error is statistical and the second is systematic. The theoretical description of the inclusive decay $B \rightarrow X_s \gamma$ is particularly clean, since it corresponds to the partonic weak decay $b \rightarrow s \gamma$. Short-distance perturbative QCD corrections introduce large logarithms of the form $\alpha_s^n(\mu) \log^m(\mu/M)$ ($m \leq n$), where α_s is the strong coupling, M is a large scale ($M = \mathcal{O}(m_t)$ or $\mathcal{O}(m_W)$) and μ is the renormalization scale. By using the RGE, the large logarithms are resummed order by order and the coefficients of the effective Hamiltonian can be calculated at the relevant scale for B decays, $\mu \sim \mathcal{O}(m_b)$. It is well known that the perturbative QCD corrections are important in this decay, enhancing the rate by a factor of 2–3, and that the theoretical prediction is sensitive to the choice of scale μ . A complete next-to-leading order (NLO) calculation of these corrections has been computed recently and will be discussed thoroughly below. The expected Standard Model branching fraction is in complete agreement with the experimental observations. It is interesting to note that this prediction would not be compatible with the observation, even within the current large experimental errors, if the QCD corrections were not so large.

The original observation of a FCNC decay by CLEO was a signal for the exclusive decay $B \rightarrow K^* \gamma$ [31]. In 1.4 fb^{-1} of data taken on the $\Upsilon(4S)$, there were 13 events on a background of two events, consistent with a branching ratio of $\mathcal{B}(B \rightarrow K^* \gamma) \sim 5 \times 10^{-5}$. It is more challenging for theory to predict the rate for the exclusive channel than the inclusive one, since this requires an accurate knowledge of the relevant hadronic form factors. These are poorly determined, with expectations for $B \rightarrow K^* \gamma$ between 6% and 40% of the inclusive rate, as compared to the measured fractional rate of $(18 \pm 6)\%$.

Decays of the type $B \rightarrow X_d \gamma$ are Cabibbo suppressed in the Standard Model by a factor $|V_{td}/V_{ts}|^2$ relative to $B \rightarrow X_s \gamma$. The expected branching ratio is thus $\mathcal{O}(10^{-5})$ [32]. At present there are only upper limits from CLEO [33] on the exclusive channels $B \rightarrow \rho \gamma, \omega \gamma$. In principle, these decays may be used to extract information on $|V_{td}|$ (see [34] for a review), however various theoretical uncertainties complicate this possibility. These include long-distance contributions, which are expected to be more important in $b \rightarrow d \gamma$, as well as the additional CKM factors from the light quark loops (both c - and u -quark loops), which have comparable size of $\mathcal{O}(\lambda^3)$ to the heavy-quark loops.

The inclusive rare B decays $B \rightarrow X_s \ell^+ \ell^-$ and $B \rightarrow X_d \ell^+ \ell^-$ ($\ell = e, \mu, \tau$) receive short-distance contributions from electromagnetic and Z penguin diagrams as well as W box diagrams and long-distance contributions from the resonant processes $B \rightarrow X_s (c\bar{c})_{res} \rightarrow X_s \ell^+ \ell^-$ and from $c\bar{c}$ continuum intermediate states. After the resonant backgrounds have been eliminated by suitable cuts in the dilepton invariant-mass spectrum, the decays are dominated by the quark-level process $b \rightarrow s \ell^+ \ell^-$ which has been calculated to NLO in perturbation theory. Additional nonperturbative effects are suppressed by Λ_{QCD}^2/m_b^2 and have been computed in the literature.

Information on the contributing short-distance physics can be extracted from measurements of the various kinematic distributions associated with the final-state lepton pair, such as the lepton pair invariant-mass distribution, the lepton pair forward-backward asymmetry, and the tau polarization asymmetry. Measurement of these distributions require the high statistics samples available at PEP-II. By combining the di-electron and di-muon modes, CLEO [35] has given a bound on the inclusive channel of $\mathcal{B}(b \rightarrow s\ell^+\ell^-) < 4.2 \times 10^{-5}$; DØ [36] obtains a similar constraint on the $\mu\mu$ channel alone. Limits [15, 37] on the exclusive channels $B \rightarrow K/K^*\ell^+\ell^-$ are in the range $(1 - 2) \times 10^{-5}$.

The decay $B \rightarrow X_s\nu\bar{\nu}$ proceeds through Z penguin and W box diagrams and is quite clean theoretically. Measurement of this process would help to determine the size of Z penguin effects in rare B hadronic decays. The limit from ALEPH [38] on this channel is $\mathcal{B}(B \rightarrow X_s\nu\bar{\nu}) < 7.7 \times 10^{-4}$.

This section also includes a discussion of the hadronic FCNC process $b \rightarrow sg$, which introduces the chromomagnetic dipole operator. This operator could give a large contribution to rare hadronic decays involving a K or a ϕ in the final state. There is speculation that this process could be enhanced significantly compared to the Standard Model prediction of an inclusive rate of $\sim .2\%$ [39]. The experimental study of $b \rightarrow sg$ uses the endpoints of the inclusive K and ϕ momentum spectra. It is also interesting in this context to look for large direct CP -violating asymmetries in exclusive decays such as $B \rightarrow K\pi$.

9.2.1 $B \rightarrow X_s\gamma, X_d\gamma$

9.2.1.1 Theoretical framework: inclusive decays

In calculating the inclusive rate, it is customary to use the following approximate equality

$$\mathcal{B}(B \rightarrow X_s\gamma) \equiv \frac{\Gamma(B \rightarrow X_s\gamma)}{\Gamma(B \rightarrow X_c e \bar{\nu}_e)} \mathcal{B}(B \rightarrow X_c e \bar{\nu}_e) \simeq \frac{\Gamma(b \rightarrow s\gamma)}{\Gamma(b \rightarrow c e \bar{\nu}_e)} \mathcal{B}(B \rightarrow X_c e \bar{\nu}_e), \quad (9.28)$$

as the uncertainties due to the CKM matrix elements and the m_b^5 dependence on the b quark mass cancel in the ratio. The parton level widths are calculated in the spectator model including corrections for short-distance QCD effects. Support for the use of the spectator model in inclusive decays comes from the $1/m_b$ expansion of heavy-quark effective theory [40, 41], where the leading order corresponds to an expansion up to $1/m_b$ terms, and the first corrections appear at the $\mathcal{O}(1/m_b^2)$ level.

Since $B \rightarrow X_s\gamma$ is a magnetic dipole transition, at leading order (LO) one obtains [27, 42, 43]

$$\mathcal{B}(B \rightarrow X_s\gamma) = \frac{|V_{ts}^* V_{tb}|^2}{|V_{cb}|^2} \frac{6\alpha}{\pi f(z)} |C_7^{(0)\text{eff}}(\mu)|^2 \mathcal{B}(B \rightarrow X_c e \bar{\nu}_e), \quad (9.29)$$

where

$$f(z) = 1 - 8z^2 + 8z^6 - z^8 - 24z^4 \ln z, \quad \text{with} \quad z = \frac{m_c}{m_b} \quad (9.30)$$

is the phase space factor in the semileptonic b -decay.

The full calculation at LO of the anomalous dimension matrix is now a well established procedure. The main problem has been the evaluation of the two-loop diagrams that mix the operators ($O_1 \dots O_6$) with the operators (O_7, O_8). The effect of these diagrams has been found to be very large. It should not be surprising that two-loop diagrams are already present at the LO in the QCD corrections, since the lowest order of this weak decay is at one loop at order α_s^0 . The effective coefficient $C_7^{(0)\text{eff}}(\mu)$ can be written as

$$C_7^{(0)\text{eff}}(\mu) = \eta^{\frac{16}{23}} C_7^{(0)}(M_W) + \frac{8}{3} \left(\eta^{\frac{14}{23}} - \eta^{\frac{16}{23}} \right) C_8^{(0)}(M_W) + C_2^{(0)}(M_W) \sum_{i=1}^8 h_i \eta^{a_i}, \quad (9.31)$$

where the expressions for h_i and a_i can be found in, *e.g.*, Buras *et al.*, [44], and the coefficients at the matching scale are [13]

$$\begin{aligned} C_2^{(0)}(M_W) &= 1, \\ C_7^{(0)}(M_W) &= \frac{3x_t^3 - 2x_t^2}{4(x_t - 1)^4} \ln x_t + \frac{-8x_t^3 - 5x_t^2 + 7x_t}{24(x_t - 1)^3}, \\ C_8^{(0)}(M_W) &= \frac{-3x_t^2}{4(x_t - 1)^4} \ln x_t + \frac{-x_t^3 + 5x_t^2 + 2x_t}{8(x_t - 1)^3}, \end{aligned} \quad (9.32)$$

with the definitions

$$\eta = \frac{\alpha_s(m_W)}{\alpha_s(\mu)}, \quad x_t = \frac{m_t^2}{m_W^2}. \quad (9.33)$$

Equation (9.31) illustrates the effects of the QCD corrections at leading order. In the absence of QCD, $\eta = 1$ and $C_7^{(0)\text{eff}}(\mu) = C_7^{(0)}(M_W)$. If $m_t = 170$ GeV, $\mu = 5$ GeV and $\alpha_s(m_Z) = 0.118$ one obtains

$$\begin{aligned} C_7^{(0)\text{eff}}(\mu) &= 0.695 C_7^{(0)}(M_W) + 0.085 C_8^{(0)}(M_W) - 0.158 C_2^{(0)}(M_W) \\ &= 0.695 (-0.193) + 0.085 (-0.096) - 0.158 = -0.300. \end{aligned} \quad (9.34)$$

Thus the inclusion of the QCD corrections lead to a large contribution from the term proportional to $C_2^{(0)}(M_W)$, which arises from the two-loop diagrams. These corrections enhance the rate by a factor of ~ 2 .

A troublesome feature of the expression (9.31) is that the branching fraction (9.29) changes by $\pm 25\%$ if μ is varied by a factor of 2 in both directions around $m_b \simeq 5$ GeV [44]. This introduces a large uncertainty in the theoretical prediction. A strong motivation to perform a NLO order analysis was to reduce this dependence on μ . The calculation of the perturbative QCD corrections

involves several steps, requiring corrections to both the Wilson coefficients and the matrix elements of the operators in Eq. (9.23) in order to ensure a scheme-independent result. The two-loop mixing among the operators $\mathcal{O}_1 \dots \mathcal{O}_6$ was the first NLO effect to be calculated [45]. The two-loop mixing among \mathcal{O}_7 and \mathcal{O}_8 has also been computed [46], and recently the calculation of the mixing between the operators $(\mathcal{O}_1 \dots \mathcal{O}_6)$ and the operators $(\mathcal{O}_7, \mathcal{O}_8)$ was completed [47]. This mixing involves three-loop contributions at NLO, since they are already a two-loop effect at LO. Apart from the anomalous dimension matrix, the other ingredients necessary for a full NLO calculation are: the $O(\alpha_s)$ corrections to the matching conditions $C_7(M_W)$ and $C_8(M_W)$ [48, 49]; the one-loop matrix elements $\langle s\gamma g | \mathcal{O}_i | b \rangle$ [44, 50] corresponding to the QCD bremsstrahlung corrections; and the two-loop corrections to $\langle s\gamma | \mathcal{O}_i | b \rangle$ [51].

After employing an explicit lower cut on the photon energy in the gluon bremsstrahlung correction, *i.e.*,

$$\Gamma(B \rightarrow X_s \gamma) = \Gamma(b \rightarrow s\gamma) + \Gamma(b \rightarrow s\gamma g)^{E_\gamma > (1-\delta)E_\gamma^{max}}, \quad (9.35)$$

where $E_\gamma^{max} = m_b/2$, the complete NLO analysis gives

$$\mathcal{B}(B \rightarrow X_s \gamma) = \frac{|V_{ts}^* V_{tb}|^2}{|V_{cb}|^2} \frac{6\alpha}{\pi f(z)\kappa(z)} F |D^{\text{eff}}|^2 \mathcal{B}(B \rightarrow X_c e \bar{\nu}_e). \quad (9.36)$$

Here, $|D^{\text{eff}}|^2$ corresponds to the quantity $|D|^2 + A$ in Refs. [47, 52] and takes on the central value $|D^{\text{eff}}| = 0.373$ for $m_t = 175 \text{ GeV}/c^2$ and $\alpha_s = 0.118$. The factor $F = m_b^2(m_b)/m_{b,pole}^2 = 1 - 8\alpha_s(m_b)/3\pi$ arises from the mass factor present in the magnetic dipole operator and $\kappa(z)$ represents the NLO QCD correction to the semileptonic decay [53]. This yields the branching fraction [47]:

$$\mathcal{B}(B \rightarrow X_s \gamma) = (3.28 \pm 0.22 \text{ (scale)} \pm 0.25 \text{ (par)}) \times 10^{-4} = (3.28 \pm 0.33) \times 10^{-4}, \quad (9.37)$$

where the first error originates from the scale uncertainty and the second error from the uncertainties in the values of the input parameters $\alpha_s(M_Z)$, $\mathcal{B}(B \rightarrow X_c e \nu_e)$ and m_c/m_b . A similar numerical result has been obtained by [51]. These predictions should be compared with those of [52], who find

$$\mathcal{B}(B \rightarrow X_s \gamma) = (3.48 \pm 0.13 \text{ (scale)} \pm 0.28 \text{ (par)}) \times 10^{-4} = (3.48 \pm 0.31) \times 10^{-4}. \quad (9.38)$$

The authors in [52] find that the NLO scale uncertainties are roughly a factor 1.5-2.0 smaller than the scale uncertainties reported in [47, 51], while they agree on the parametric uncertainties. The estimate in [52] includes the theoretical uncertainties related to the choice of the high-energy matching scale $\mu_W = (M_W)$ and the scale $\mu_t = (m_t)$ at which the running top-quark mass is defined. These uncertainties have not been taken into account in [47, 49, 51, 54]. Comparing these results, it can be observed that in spite of the smaller scale uncertainties the final results in [47, 51, 52] are compatible, due to the parametric uncertainties which dominate the theoretical error at present.

In addition, the two-loop electroweak corrections have recently been computed [55], where fermion and photonic loop effects are found to reduce the inclusive branching fraction by $\sim (8 \pm 2)\%$. Taking the value from 9.38, this leads to the prediction $\mathcal{B}(B \rightarrow X_s \gamma) = (3.28 \pm 0.30) \times 10^{-4}$.

Non-perturbative corrections due to long-distance effects are another source of theoretical error. For the $B \rightarrow X_s \gamma$ decay, the leading power corrections in $1/m_b^2$ and $1/m_c^2$ have been calculated and are generally estimated to be less than $\sim 5\%$ [41, 56, 57, 58, 59, 60]. A further reduction of both the theoretical and the experimental errors can be expected in the forthcoming years, which should lead to improvements in the constraints on new physics effects in these decays.

The dependence of the inclusive branching fraction on the CKM parameters can be written as

$$\frac{|V_{ts}^* V_{tb}|^2}{|V_{cb}|^2} = |V_{tb}|^2 \left(1 - \frac{|V_{td}|^2 - |V_{ub}|^2}{|V_{cb}|^2} \right) = 0.95(1 + 0.10\rho), \quad (9.39)$$

in the Wolfenstein parameterization and taking $|V_{cb}| = 0.039 \pm 0.003$. Comparing the full NLO QCD plus two-loop electroweak-corrected branching fraction to the CLEO data yields [55]

$$\rho = -1.7 \pm 1.9, \quad (9.40)$$

which is not yet competitive with the constraints from B semileptonic decay, $B^0 - \bar{B}^0$ mixing and ϵ'/ϵ . Alternatively, $B \rightarrow X_s \gamma$ may be used to determine V_{ts} ; Ali [61] finds

$$|V_{ts}| = 0.033 \pm 0.007, \quad (9.41)$$

taking [62] $|V_{cb}| = 0.0393 \pm 0.0028$ and $|V_{tb}| = 0.55 \pm 0.15$. However, some caution needs to be applied in obtaining bounds on CKM elements from loop processes, due to the possibility of new physics participating in the loops.

Measurement of the inclusive rate for $B \rightarrow X_s \gamma$ is performed by searching for events in the high-energy region of the photon energy spectrum, outside the region populated by radiative $b \rightarrow c q \bar{q}$ decays. A good theoretical description of the spectral shape is essential in order to perform a fit to the spectrum and extrapolate to the total decay rate. Earlier calculations of the photon spectrum are given in Ref. [50], while a recent NLO analysis in HQET has been performed in Ref. [63]. The shape of the spectrum is dominated by QCD dynamics and is insensitive to contributions from new physics.

Since the quark-level process is a two-body decay, it yields a trivial photon energy spectrum, a discrete line. The physical spectrum is obtained by convoluting the perturbative QCD corrections, such as those arising from gluon radiation, $b \rightarrow s \gamma + g$, with the non-perturbative effects of hadronization. The inclusion of the gluon emission results in a typical Bremsstrahlung spectrum shape, peaking near both end-points due to soft gluon and soft photon singularities. The collinear singularities at $E_\gamma \rightarrow 0$ are regulated by the strange quark mass, but still contain large logarithms of the form $\alpha_s \log(m_b^2/m_s^2)$. These logarithms can be resummed to all orders [64], thereby smoothing

the singular collinear $m_s \rightarrow 0$ limit result. The soft gluon divergence at $E_\gamma \rightarrow E_\gamma^{max}$ can be treated by the isolation and exponentiation of the leading behavior in terms of the form $\alpha_s(\mu)^m \log^{2n}(1-x)$ with $m \leq n$. A full NLO resummation of these Sudakov logarithms has yet to be performed. The leading non-perturbative effect arises from the residual interaction of the b quark inside the B meson and is described by including Fermi motion effects. These effects comprise the dominant source of theoretical error in the photon energy distribution. The Fermi motion can be consistently included in the heavy-quark expansion by resumming the leading-twist corrections into the universal shape function which governs the light-cone momentum distribution of the heavy quark inside the B meson. The physical decay distribution is then obtained by convoluting the parton model spectra with this function. The largest source of error in this procedure arises from the imprecisely known value of the b quark mass. From the NLO QCD analysis of Kagan and Neubert [63], including these improved bound state treatments, an extrapolation factor of $K_{2.2} = 0.78_{-0.11}^{+0.09}$ is found. This factor relates the total branching fraction to that determined in the lab with the cut $E_\gamma > 2.2$ GeV, as employed by CLEO. Using this factor Kagan and Neubert find that the extrapolation of the CLEO measurement to the total branching fraction results in

$$\mathcal{B}(B \rightarrow X_s \gamma) = (2.62 \pm 0.60_{-0.30}^{+0.37}) \times 10^{-4}, \quad (9.42)$$

where the first error is experimental and the second denotes the theoretical uncertainties.

The CKM suppressed radiative mode, $B \rightarrow X_d \gamma$, populates the high energy region of the photon energy spectrum. $B \rightarrow X_s \gamma$ provides the largest background source for this channel. Observation of this suppressed mode hence requires that the hadronic X_d system recoiling against the photon does not contain strange hadrons. While difficult, this may be feasible by summing all the relevant exclusive final states as has been done by CLEO in their measurement of $B \rightarrow X_s \gamma$.

The procedure for computing the $B \rightarrow X_d \gamma$ branching fraction mirrors that presented above for $B \rightarrow X_s \gamma$. The complete set of operators is given by Eq. (9.23) with the substitutions [32, 65]

$$\begin{aligned} \mathcal{O}_1 &\rightarrow -\frac{V_{cb}V_{cs}^*}{V_{tb}V_{ts}^*}(\bar{d}_\alpha c_\beta)_{V-A}(\bar{c}_\beta b_\alpha)_{V-A} - \frac{V_{ub}V_{us}^*}{V_{tb}V_{ts}^*}(\bar{d}_\alpha u_\beta)_{V-A}(\bar{u}_\beta b_\alpha)_{V-A}, \\ \mathcal{O}_2 &\rightarrow -\frac{V_{cb}V_{cs}^*}{V_{tb}V_{ts}^*}(\bar{d}_\alpha c_\alpha)_{V-A}(\bar{c}_\beta b_\beta)_{V-A} - \frac{V_{ub}V_{us}^*}{V_{tb}V_{ts}^*}(\bar{d}_\alpha u_\alpha)_{V-A}(\bar{u}_\beta b_\beta)_{V-A}, \end{aligned} \quad (9.43)$$

and the remaining operators \mathcal{O}_{3-8} are defined as for $B \rightarrow X_s \gamma$ with the obvious replacement $s \rightarrow d$. Note that in this case, the CKM factors are implicitly contained in the operators $\mathcal{O}_{1,2}$. The matching conditions for and the RGE evolution of the Wilson coefficients as well as the evaluation of the operator matrix elements are as described above for $B \rightarrow X_s \gamma$. In addition, it has been explicitly verified [51, 66] that the rate and E_γ spectrum are free of mass singularities, *i.e.*, there are no spurious enhancements of the form $\alpha_{em}\alpha_s \log(m_u^2/m_c^2)$, and hence the limit $m_u \rightarrow 0$ may be taken safely.

A NLO analysis has recently been performed in Ref. [67] predicting the Standard Model range $6.0 \times 10^{-6} \leq \mathcal{B}(B \rightarrow X_d \gamma) \leq 2.6 \times 10^{-5}$, where the NLO corrections are found to increase the branching fraction by 10% over the leading order value. Most of the uncertainty in this prediction is due to the imprecisely known CKM factors, while the errors associated with the renormalization scale and remaining input parameters is only $\sim 10\%$. Estimates for the long-distance contribution from intermediate u-quarks in the penguin, which are expected to be small even though they are not CKM suppressed, have been included in this result. The theoretical errors, including the $1/m_b^2$ and $1/m_c^2$ corrections, tend to cancel in the ratio,

$$0.017 \leq \frac{\mathcal{B}(B \rightarrow X_d \gamma)}{\mathcal{B}(B \rightarrow X_s \gamma)} \leq 0.074, \quad (9.44)$$

evaluated here at NLO [67], where the range in values is completely attributed to the CKM factors and the small u-quark loop contribution. Since the inclusive modes are relatively free of long-distance contributions, this ratio would provide a clean determination of $|V_{td}/V_{ts}|$.

Finally, the direct CP violation asymmetry could potentially be large in $B \rightarrow X_d \gamma$. At leading order the asymmetry lies in the range [67] $a_{CP} = (7 - 35)\%$, where the residual theoretical uncertainty due to the scale dependence and the values of the input parameters (other than the CKM elements) is estimated to be $\Delta a_{CP} = 17\%$. The full NLO corrections to this quantity have yet to be computed as the CP -odd numerator in this asymmetry is suppressed by an extra order of α_s , *i.e.*, it starts at order $\alpha_s(m_b)(\alpha_s^n \log^n(M_W/m_b))$.

9.2.1.2 Theoretical framework: exclusive radiative decays

Exclusive radiative decays have a distinctive signature which makes them experimentally accessible. In principle, they can provide information on the CKM elements $V_{ts,td}$. Unfortunately, these transitions are plagued with theoretical uncertainties associated with the hadronic matrix elements and with long-distance contributions. In the end, the experimental determination of the rates for these modes may only be used to select amongst the various hadronization models, rather than testing the underlying theory.

At the quark level, the short-distance contribution to these decays is described by the magnetic dipole operator, as detailed in the previous section for the inclusive case. The transition matrix element for the exclusive process $B \rightarrow V + \gamma$, where $V = K^*, \rho, \omega$, can be written in terms of the form factors

$$\begin{aligned} \langle V(p) | \bar{\psi} \sigma_{\mu\nu} q^\nu (1 + \gamma_5) b | B(p_B) \rangle &= 2i \epsilon_{\mu\nu\rho\sigma} \epsilon^{*\nu} p_B^\rho p^\sigma T_1(q^2) \\ &+ \left[\epsilon_\mu^* (m_B^2 - m_V^2) - (\epsilon^* \cdot q)(p_B + p)_\mu \right] T_2(q^2) \\ &+ (\epsilon^* \cdot q) \left[q_\mu - \frac{q^2}{m_B^2 - m_V^2} (p_B + p)_\mu \right] T_3(q^2), \end{aligned} \quad (9.45)$$

Table 9-1. Form factor predictions in various models.

Ref.	$T_1^{B \rightarrow K^*}(0)$	$\frac{T_1^{B \rightarrow K^*}(0)}{T_1^{B \rightarrow \rho}(0)}$	$\mathcal{B}(B \rightarrow K^* \gamma)(\times 10^{-5})$	R_{K^*}
[68] LCSR	0.32 ± 0.05	1.32 ± 0.1	4.8 ± 1.5	0.16 ± 0.05
[71] LCSR	0.31 ± 0.04	1.14 ± 0.02	4.45 ± 1.13	0.16 ± 0.05
[72] LCSR	0.38 ± 0.06	1.33 ± 0.13	--	0.20 ± 0.06
[73] lattice	$0.10 \pm 0.01 \pm 0.3$	--	--	$0.060 \pm 0.012 \pm 0.034$
[69] lattice	$0.16_{-0.01}^{+0.02}$	--	--	$0.16_{-0.03}^{+0.04}$

where ϵ^* represents the polarization vector of the vector meson, $q = p_B - p$, and ψ stands for the light field s or d . The signs are defined such that the form factors are positive. For the on-shell matrix element, *i.e.*, $q^2 = 0$, the coefficient of T_3 vanishes and it can be shown that $T_2(0) = -iT_1(0)$. Hence in the physical cases of interest here, the decay widths can be expressed in terms of a single form factor

$$\Gamma(B \rightarrow V + \gamma) = \frac{\alpha G_F^2}{32\pi^4} |V_{tb} V_{t\psi}^*|^2 (m_b^2 + m_\psi^2) m_B^3 \left(1 - \frac{m_V^2}{m_B^2}\right)^3 |C_7^{(0)eff}(m_b)|^2 |T_1^{B \rightarrow V}(q^2 = 0)|^2, \quad (9.46)$$

and the branching fraction is computed by scaling to the semileptonic rate as usual. These form factors have been estimated using a wide variety of techniques [68]–[69]; a sampling of some recent predictions using light-cone sum rules and lattice gauge theory are given in Table 9-1. Note that these calculations are actually performed for non-zero values of q^2 and then extrapolated to $q^2 = 0$ using plausible assumptions such as the pole dominance approximation. The resulting value of $\mathcal{B}(B \rightarrow K^* \gamma)$ is in good agreement with the CLEO data for all models displayed in Table 9-1.

A good test of the model dependence of the form factors is provided by the ratio of rates for the exclusive to inclusive decays,

$$R_{K^*} = \frac{\mathcal{B}(B \rightarrow K^* \gamma)}{\mathcal{B}(B \rightarrow X_s \gamma)} = 4 \left(\frac{m_B}{m_b}\right)^3 \left(1 - \frac{m_{K^*}^2}{m_B^2}\right)^3 |T_1(q^2 = 0)|^2. \quad (9.47)$$

As shown in Table 9-1, most recent computations agree well with the CLEO data [31] for this ratio, which is $R_{K^*} = (18 \pm 6)\%$. Earlier estimates, *before* the CLEO observation of $B \rightarrow K^* \gamma$, ranged from $R_{K^*} = (1 - 98)\%$! Hence, the data sample has already been used to distinguish between theoretical models. Veseli and Olsson [70] also estimate the ratio for $B \rightarrow K_2^*(1430) \gamma$ to inclusive $b \rightarrow s \gamma$ decays to be $(6.2 \pm 2.9)\%$.

From Eq. (9.46) above, it appears that the ratio

$$\frac{\Gamma(B \rightarrow \rho\gamma)}{\Gamma(B \rightarrow K^*\gamma)} = \Phi \frac{|T_1^{B \rightarrow \rho}(0)|^2 |V_{td}|^2}{|T_1^{B \rightarrow K^*}(0)|^2 |V_{ts}|^2}, \quad (9.48)$$

where Φ is a phase space factor,

$$\Phi = \frac{(m_b^2 + m_d^2) (1 - m_\rho^2/m_B^2)^3}{(m_b^2 + m_s^2) (1 - m_{K^*}^2/m_B^2)^3}, \quad (9.49)$$

ratio of form factors, also shown in Table 9-1, can in principle be more accurately determined than each by itself, since several theoretical uncertainties cancel in the ratio. The form factor ratio then depends only on SU(3) breaking effects. This expression for the ratio of rates assumes that the short-distance physics is dominant. This is essentially the case for $B \rightarrow K^*\gamma$, where long-distance effects have been estimated [60, 59, 57] to be not more than $\simeq 5\%$. This is also borne out by the fact that the recent theoretical estimates of R_{K^*} are consistent with experiment. However, the long-distance contributions to $B \rightarrow \rho\gamma$ can be large [74]–[75] and have the potential to destroy the validity of this ratio.

The long-distance effects in $B \rightarrow \rho\gamma$ originate from several sources, all of which involve different CKM matrix elements than the short-distance piece. Initial studies [57, 74, 76] applied the vector meson dominance model and examined the decay $B \rightarrow \rho V^*$, where V^* represents an off-shell neutral vector meson such as $\rho^0, \omega, \phi, \psi$, with subsequent conversion of the vector meson to a photon. This transition is depicted in Fig. 9-9(a). The results from this approach vary, but the general consensus yields a contribution of order $\lesssim 10\%$ of the short-distance rate. The uncertainties present in this method arise from the fact that the effective $VV^*\gamma$ couplings are only measured at the V^* mass and must be scaled to zero, and that only the the transverse part of this coupling can contribute to the photon transition.

A second long-distance contribution arises from the weak annihilation diagram, similar to that of Fig. 9-1 with final-state quarks instead of leptons and with a possible photon bremsstrahlung from every charged leg. Earlier perturbative estimates [74, 77] showed that this contribution could be substantial for the charged $B^\pm \rightarrow \rho^\pm\gamma$ modes, but these estimates are uncertain due to problems associated with the direct photon emission from the almost on-shell propagation of the light spectator quark. More recent calculations [78] have employed light-cone QCD sum rules. In this approach the annihilation contributions are dominantly induced by the four fermion operators $\mathcal{O}_{1,2}$. Using factorization, the amplitude for the charged decay mode can then be written in terms of two form factors,

$$\begin{aligned} \mathcal{A}_{LD} = & -\frac{eG_F}{\sqrt{2}} V_{ub} V_{ud}^* \left(C_2 + \frac{C_1}{N_c} \right) m_\rho \epsilon_\mu^{(\gamma)} \epsilon_\nu^{(\rho)} \\ & \times \left\{ -2i [g^{\mu\nu} (q \cdot p_B) - p_M^\mu q^\nu] F_1^{LD}(q^2) + 2\epsilon^{\mu\nu\alpha\beta} p_{B\alpha} q_\beta F_2^{LD}(q^2) \right\}. \end{aligned} \quad (9.50)$$

These form factors are evaluated via the light-cone sum rules and found to be roughly equal to each other in magnitude. The ratio of long- to short-distance amplitudes can then be written as

$$\frac{\mathcal{A}_{LD}}{\mathcal{A}_{SD}} = R_{L/S}^{B^\pm \rightarrow \rho^\pm \gamma} \frac{V_{ub} V_{ud}^*}{V_{tb} V_{td}^*}, \quad (9.51)$$

where $R_{L/S}^{B^\pm \rightarrow \rho^\pm \gamma}$ is evaluated to be -0.30 ± 0.07 . This results in a 10 – 20% contribution to $\mathcal{B}(B^\pm \rightarrow \rho^\pm \gamma)$ from the weak annihilation diagram. The effect is anticipated to be less severe in the neutral channel due to the smaller electric charge of the d -quark and color suppression. Estimates give $R_{L/S}^{B^0 \rightarrow \rho^0 \gamma} \simeq R_{L/S}^{B^0 \rightarrow \omega \gamma} = 0.05$, and thus this approach asserts that long-distance physics is not expected to contaminate the neutral channels.

A third source of long-distance contributions arises from final-state interactions, where the B decays into some intermediate state, such as $\rho^0 \rho^0$ and $\rho^+ \rho^-$ in B^0 decay, which then undergoes soft-rescattering into the final-state $\rho \gamma$. This mechanism is depicted in Fig. 9-9(b). The magnitude of the $\rho \rho \rightarrow \rho \gamma$ soft-rescattering contribution to $B^0 \rightarrow \rho^0 \gamma$ is found [75] to be roughly 8%. This result differs from the QCD sum rule calculation in that the neutral channels are sizeably affected.

One measure of the size of the long-distance component of these exclusive modes is to determine the deviation from the isospin relation

$$\Gamma(B^+ \rightarrow \rho^+ \gamma) = 2\Gamma(B^0 \rightarrow \rho^0 \gamma) = 2\Gamma(B^0 \rightarrow \omega \gamma), \quad (9.52)$$

which holds for the short-distance contributions only. The degree of isospin violation is found [78, 75] to be quite sensitive to the value of the Wolfenstein CKM parameter ρ .

Although the size of these long-distance interactions is somewhat uncertain at present, they constitute a potential source of serious error in the extraction of V_{td} . However, measurement of the exclusive radiative modes can be used to gather information on the various approaches to the theoretical modeling of the form factors and the validity of the factorization approximation. This

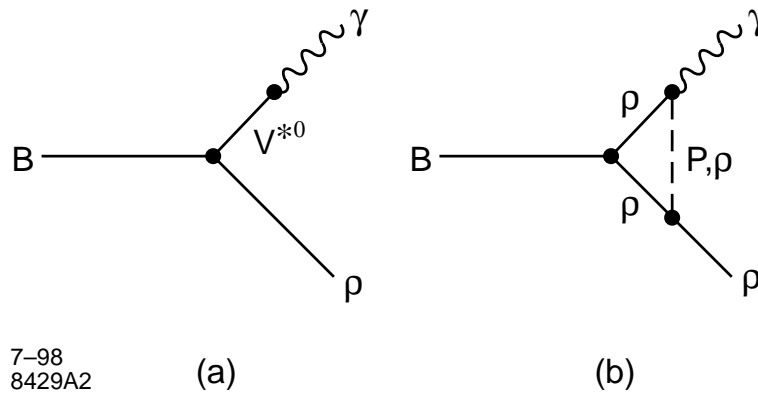


Figure 9-9. (a) Vector Meson Dominance and (b) Final-State Interaction contributions to the decay $B \rightarrow \rho \gamma$.

in turn, can be applied to other modes, such as $B \rightarrow \pi\pi$, where the evaluation of the relative sizes of the contributing tree and penguin amplitudes are subject to the same theoretical uncertainties. As is discussed in Chapter 6, the accuracy with which α can be determined will be limited by such uncertainties for some time to come, so measurements that can be used to reduce them will be important.

9.2.1.3 Experimental considerations

The simplest way to measure an inclusive rate is to ignore the hadronic products of the $s(d)$ quark, and search for an excess of events with a high energy gamma. To establish a signal for $b \rightarrow s\gamma$ it is necessary to understand the backgrounds from other processes which are quite large. Note that only the dominant $b \rightarrow s$ transition can be measured by this method, since there is no way of distinguishing between the s and d channels without reconstructing the hadronic part of the decay.

The CLEO collaboration reported two $b \rightarrow s\gamma$ analyses [29]. The first of these studied the inclusive gamma spectrum. The large background from continuum processes was measured by running for a third of the time off the $\Upsilon(4S)$ resonance. This continuum background was scaled and subtracted, and dominates the statistical error on the measurement. If BABAR wishes to perform a similar analysis it will have to run for a significant fraction of time below the $\Upsilon(4S)$ resonance, which may not be desirable. The recent ALEPH result [30] also studies the inclusive gamma spectrum, but uses topological vertex cuts to reduce the backgrounds. The remaining backgrounds are modeled by standard Monte Carlo generators and are then subtracted. A significant part of the uncertainty in their result comes from the reliability of the Monte Carlo models, both for the signal and for the background.

The second CLEO analysis reconstructs a large fraction of the possible hadronic final states associated with the s quark, estimates the efficiency for the inclusive signal, and then takes the sum to be a measurement of the inclusive rate. This appears to be a better approach to the measurement of the inclusive rate. With the good particle identification of the BABAR DIRC system it should be possible to make separate measurements of the $b \rightarrow s$ and $b \rightarrow d$ channels. By reconstructing exclusive final states the continuum backgrounds are reduced to an acceptable level. There are difficulties with using high multiplicity hadronic final states which have lower reconstruction efficiencies, and which have large backgrounds from $b \rightarrow c$ decays. This limits the ability to reconstruct all possible final states, introducing a model-dependence into the result.

The experimental difficulties in measuring the inclusive rate $b \rightarrow s\gamma$ are mostly associated with the detection of the high energy photon. In the CLEO detector the $\Upsilon(4S)$ is produced at rest, and $b \rightarrow s\gamma$ is a quasi two-body process giving an almost monochromatic photon with an energy of 2.45 ± 0.25 GeV. The smearing results from the Fermi motion of the quarks in the B meson, the small B meson momentum, and the effects of gluon bremsstrahlung which lead to a low-energy tail [50]. In BABAR the $\Upsilon(4S)$ is boosted in the lab frame. The photons have to be measured up to a maximum energy of 4 GeV in the forward endcap calorimeter, and there is a correlation between

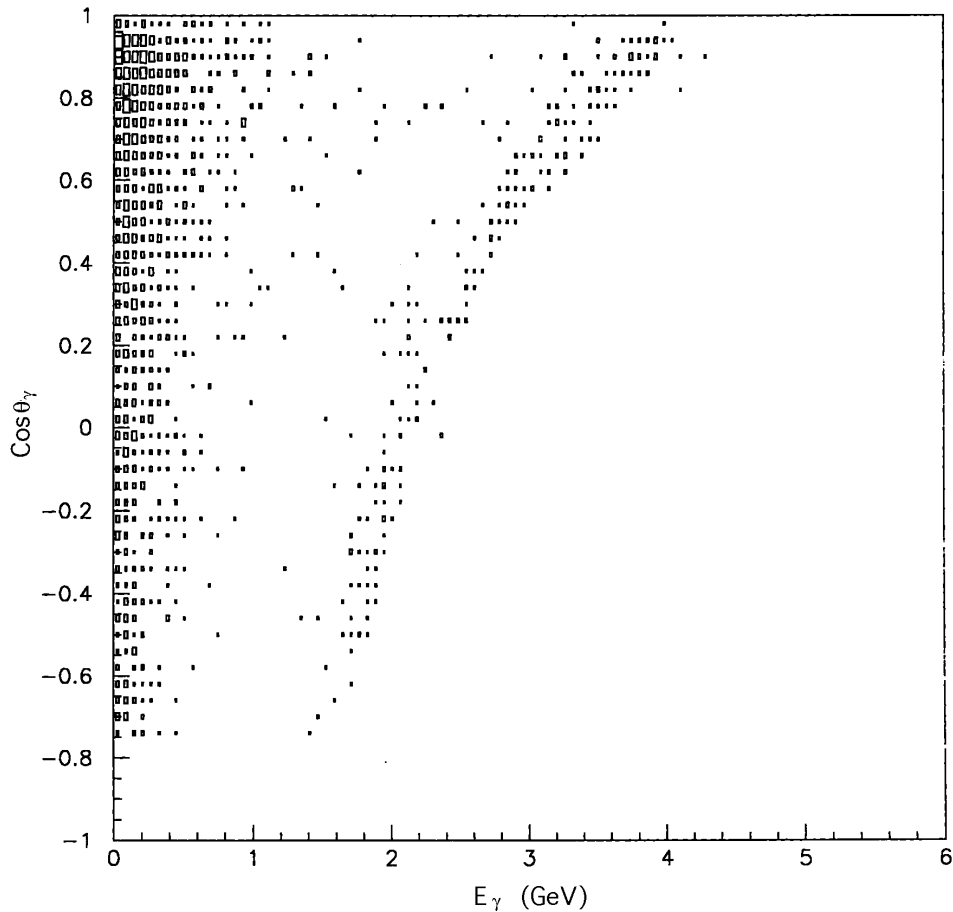


Figure 9-10. Photon lab angle versus energy.

the energy and the theta direction of the photon (see Fig. 9-10). By boosting back into the $\Upsilon(4S)$ rest frame the original spectrum is recovered, but with a photon energy resolution that depends on the laboratory angle.

The photon energy resolution is expected to be in the range 1.2 to 1.5%, corresponding to 30-50 MeV. This is small compared to the smearing effects discussed above, but it is large compared to the resolution on the reconstructed energy of the hadronic system that makes up the rest of an exclusive $b \rightarrow s\gamma$ decay. The B invariant-mass resolution, and hence the level of the background, is determined primarily by the photon energy resolution. It is important that the calorimeter is accurately calibrated, and that this resolution function is well understood.

A preliminary study of $B^0 \rightarrow K^{*0}(\rho^0)\gamma$ in Aslund shows that the resolution on the B invariant mass is $\sigma(M_B) = 41 \text{ MeV}/c^2$, and the resolution on the B momentum in the $\Upsilon(4S)$ rest frame is $\sigma(p_B) = 52 \text{ MeV}/c$. (see Fig. 9-11). These numbers are very similar to the resolutions obtained

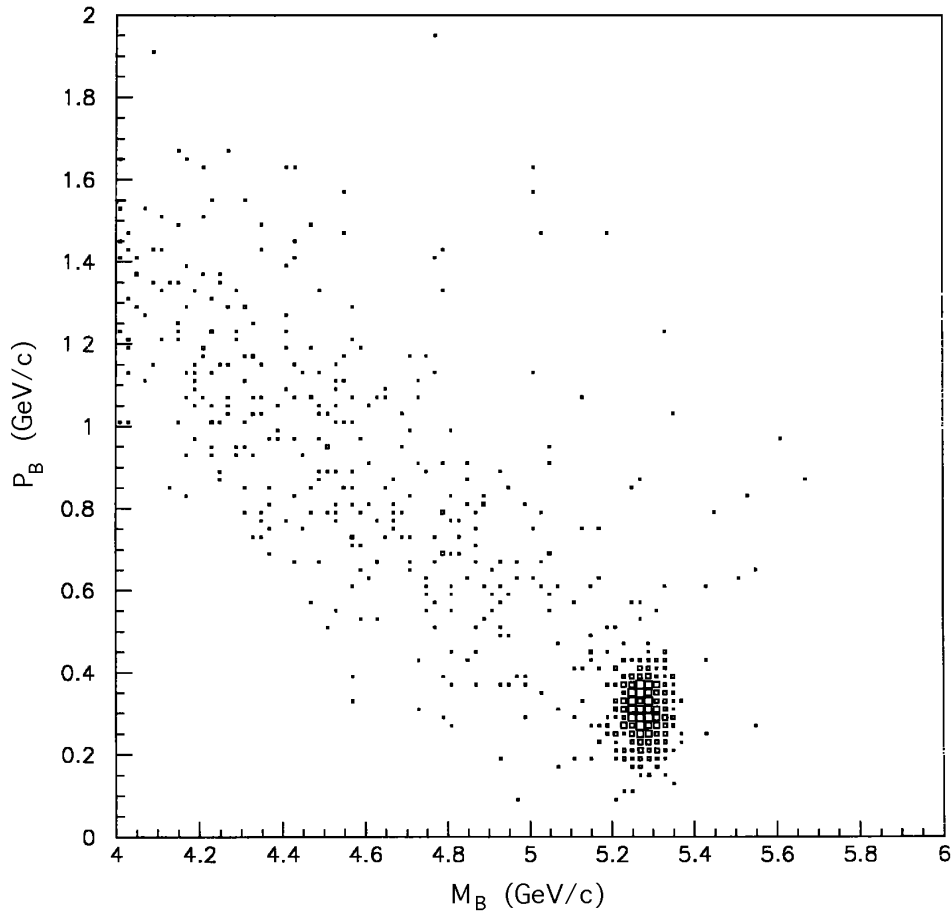


Figure 9-11. B momentum versus invariant mass.

in the CLEO detector in spite of the fact that BABAR has to measure higher energy photons. The calorimeter response is rather naively modeled in `Aslund`, and it is desirable that this study should be repeated with a full simulation and reconstruction. Since this analysis is very sensitive to the energy resolution of the high-energy photon, it is necessary to include beam backgrounds, and to have an accurate shower energy calibration.

There are three types of background that need to be suppressed:

- Initial State Radiation (ISR) where the process $e^+e^- \rightarrow q\bar{q}$ occurs after the radiation of the high-energy photon.
- Continuum jets ($q\bar{q}$) in which the high-energy photon comes from the decays of π^0 and η mesons or from final-state radiation.
- B meson decays ($B\bar{B}$) in which the high-energy photon comes from π^0 or η decays or from other radiative decays. There are contributions from $b \rightarrow c$, $b \rightarrow u$ and $b \rightarrow sg$ decays.

At energies above the $b \rightarrow s\gamma$ signal region, the ISR contribution is the only significant one. Below the signal region the $B\bar{B}$ backgrounds from $b \rightarrow c$ decays dominate. In the signal region all three backgrounds have to be considered, with the $B\bar{B}$ background falling to zero at the endpoint of the $b \rightarrow s\gamma$ spectrum.

The CLEO inclusive analysis used a large number of shape variables to suppress the continuum ISR and $q\bar{q}$ backgrounds. These variables were eventually combined into a neural net approach to give the most effective discrimination between signal and background events. This type of analysis should be redone for the BABAR detector. Additional suppression of the continuum backgrounds may be possible using vertex constraints as was done in the ALEPH analysis, although the short B decay length and the fact that a lot of energy is taken away by a neutral make this an unfavorable channel for such a cut.

The photons from the $q\bar{q}$ and $B\bar{B}$ backgrounds come primarily from the decays of π^0 and η mesons. There are two ways of dealing with this background, both of which depend on detecting the second photon from the decay. The simplest thing to do is to apply a veto to the high-energy photon if it can be combined with another photon to form a π^0 or η . This costs efficiency for the signal, particularly if there are large beam-associated backgrounds, since the decays are very asymmetric and the second photon is typically very low in energy. There are also problems at the highest energies with the merging of the two photons to form a single cluster. Studies of the use of shape variables to distinguish merged clusters from single photons are in progress.

An alternative approach is to retain the reconstructed π^0 and η samples and use them to model the expected contribution of high-energy photons from these decays. This effectively replaces the π^0 and η spectra generated by the Monte Carlo with the spectra measured in data. To do this accurately it is necessary to understand the π^0 and η reconstruction efficiencies, however, it should be noted that symmetric decays of high-energy mesons can be used to measure the spectrum as well as the asymmetric decays that give rise to the background photons. A study of this approach should be made with realistic beam backgrounds, and with a calibrated calorimeter.

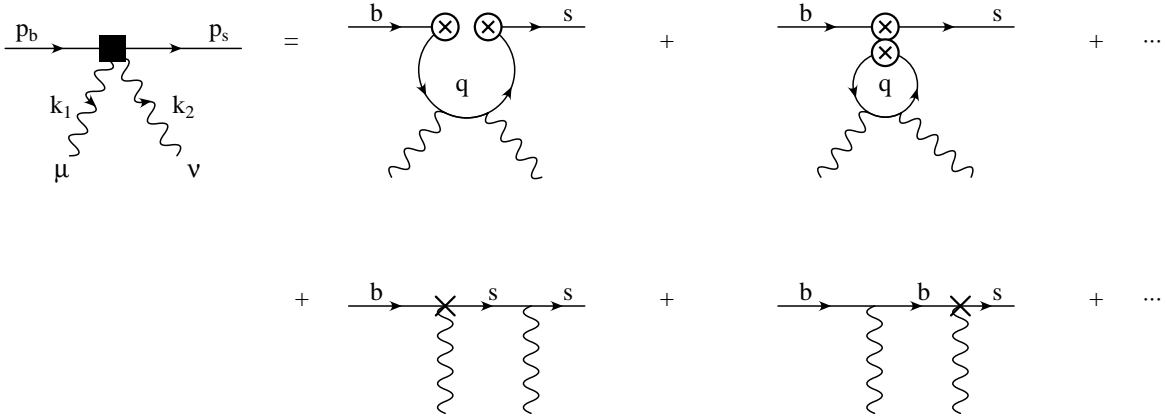


Figure 9-12. Possible insertions of the operators O_i [81]. In the 1PI diagrams q indicates a generic virtual quark. The double circled cross vertices represent the two possible insertions of the operators O_1, \dots, O_6 , depending on their flavor, chiral, and color structure; the cross vertices stand for the insertion of O_7 .

9.2.2 $B \rightarrow X_s \gamma \gamma$

The decay process $B \rightarrow X_s \gamma \gamma$ can also be studied in the well established framework of electroweak effective Hamiltonians described in Eq. (9.23). The basis of local operators coincide identically with that used for the transition $B \rightarrow X_s \gamma$, and the reader is therefore referred to that Section 9.2.1 for more details on both the structure of the local operators and the behavior of the Wilson coefficients. Recall that the coefficients $C_i(\mu)$ are process-independent and that their renormalization is determined only by the basis of operators $\{O_i\}$.

The amplitude for the quark-level process $b \rightarrow s \gamma \gamma$ was first determined in Refs. [48, 79, 80], and the leading order QCD corrections are computed in [81, 82]. The amplitude can be expressed in the form

$$A = -\frac{ie^2 G_F}{\sqrt{2}\pi^2} V_{tb} V_{ts}^* \sum_{i=1}^7 C_i(\mu) \bar{u}_s(p_s) T_i^{\mu\nu} u_b(p_b) \epsilon_\mu(k_1) \epsilon_\nu(k_2) , \quad (9.53)$$

where $\epsilon_\mu(k_1)$ and $\epsilon_\nu(k_2)$ are the polarization vectors of the two photons and the convention on momenta is as in Fig. 9-12. $T_i^{\mu\nu}$ denotes the tensor structure of the transition amplitude induced by the operator O_i ; their explicit form can be found for example in [81]. The different $T_i^{\mu\nu}$ are obtained inserting the operators O_i into the Feynman diagrams of Fig. 9-12. Note that both one-particle reducible (1PR) and one-particle irreducible (1PI) diagrams contribute to the process.

The inclusive decay $B \rightarrow X_s \gamma \gamma$ can be studied to a very good approximation in terms of the quark level decay $b \rightarrow s \gamma \gamma$ [83]. In order to obtain the total rate into two hard photons one has to place suitable kinematical cuts. Two hard photons can be isolated if one demands that their energy is not too small and that they are not collinear to each other and to the outgoing s -quark. Indeed the

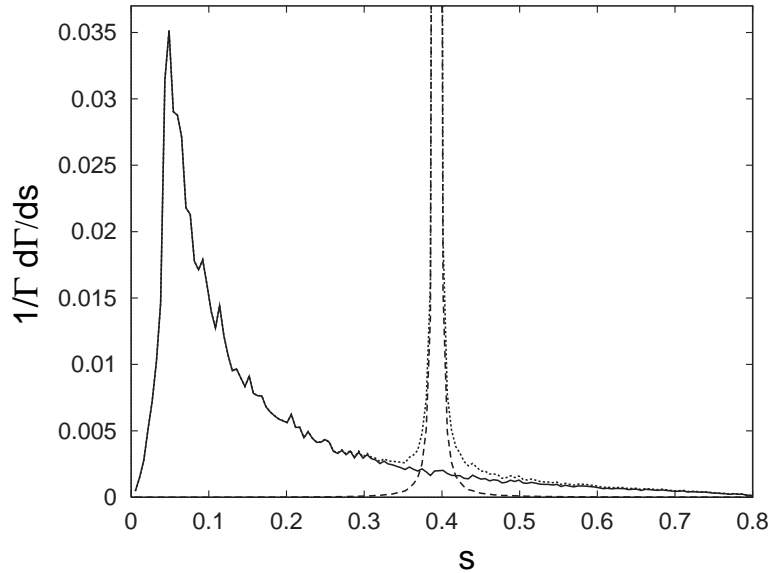


Figure 9-13. The invariant-mass distribution of the two photons in the presence of the η_c resonance, normalized to the total rate $\Gamma_{\text{tot}} = 5.7 \times 10^{-7}$, as obtained for $m_s = 0.5 \text{ GeV}/c^2$. The curves are the distributions for pure non-resonant (solid), pure resonant (dashed) and the total (dot-dashed). The resonance peak is truncated in order to show the relevance of the different contributions both inside and outside the resonance region.

total rate and the relevance of each different contribution (1PR,1PI) depends on the kinematical cuts imposed. In the absence of QCD corrections, the branching ratio into hard photons is about 1×10^{-7} in the Standard Model [80]. QCD corrections, however, enhance the rate by a factor of $\simeq 2 - 2.5$ [81]. The main source of theoretical uncertainty arises from the scale dependence and it is around $25 - 30\%$, as is the case for $B \rightarrow X_s \gamma$ at LO.

Another source of uncertainties in the expected branching fraction arises from the effects of long-distance contributions. In fact, in the region of invariant mass of the two photons near $s \simeq 4m_c^2/m_b^2$, the rate is dominated by the η_c resonance, which subsequently decays into two photons, *i.e.*, $B \rightarrow \eta_c X_s \rightarrow X_s \gamma \gamma$. In order to estimate the effect of these contributions, a resonant amplitude is added to the short-distance amplitude and one can then determine its influence on the invariant-mass distribution, $d\Gamma/ds$, away from the resonance peak. As shown in Fig. 9-13, the effect of the resonance is very well localized around the peak and is practically negligible in the regions $0.0 \leq s \leq 0.3$ and $s \geq 0.5$. Cutting around the resonance and including only these two regions in the perturbative calculation reduces the branching ratio by at most 14% [81]. The impact of the long-distance contribution can be further reduced by using a model calculation of the η_c -photon-photon coupling where the vertex form factor $f(q^2)$ is drastically suppressed when q^2 , the invariant mass of the two photons, is smaller than $m_{\eta_c}^2$ [84].

A useful probe of the dynamics of the inclusive decay is given by the forward-backward asymmetry [80]

$$A_{\text{FB}} = \frac{\Gamma(\cos \theta_{s\gamma} \geq 0) - \Gamma(\cos \theta_{s\gamma} < 0)}{\Gamma(\cos \theta_{s\gamma} \geq 0) + \Gamma(\cos \theta_{s\gamma} < 0)}, \quad (9.54)$$

where $\theta_{s\gamma}$ is the angle between the s quark and the softer photon. The main effects of the QCD corrections tend to cancel in the ratio and hence they do not significantly change the value of A_{FB} , increasing it by no more than 15%. The asymmetry is thus found to be 0.78 (with LO QCD corrections) [81]. Furthermore A_{FB} is practically insensitive to the choice of scale in the LO Wilson coefficients.

This decay has also been studied in some extensions of the Standard Model, in particular in Two-Higgs Doublet models [80] and in SUSY [85]. The effects of both models on this transition are quite restricted after the constraints from the measurement of $B \rightarrow X_s \gamma$ (which are discussed in Chapter 13) are imposed. However, measurement of A_{FB} could yield additional information on the existence of new physics.

At the exclusive level, many interesting channels can be studied. The first calculations of the exclusive modes $B_s \rightarrow \eta(\eta')\gamma\gamma$ and $B \rightarrow K\gamma\gamma$ have been performed very recently, by using a cascade mechanism for both the 1PI and the 1PR contributions [86], however difficulties arise from the unknown relative phase between the 1PR and the 1PI amplitudes.

Another interesting decay induced by the $b \rightarrow s\gamma\gamma$ is the $B_s \rightarrow \gamma\gamma$ exclusive mode, which may be studied if PEP-II has future runs on the $\Upsilon(5S)$. Here, the final state contains CP -odd and CP -even states, allowing one to study CP -violating effects.

9.2.3 $B \rightarrow X_s ll, X_d ll$

9.2.3.1 Theoretical framework: inclusive decays

The dominant contribution to $B \rightarrow X_s \ell^+ \ell^-$ comes from the partonic process $b \rightarrow s \ell^+ \ell^-$, which can be calculated in perturbation theory [87] via the effective Hamiltonian in Eq. (9.23). This formalism leads to the decay amplitude (neglecting the strange quark mass),

$$\begin{aligned} \mathcal{A}(B \rightarrow X_s \ell^+ \ell^-) = & \frac{\sqrt{2}G_F\alpha}{\pi} V_{tb}V_{ts}^* \left[C_9^{eff} \bar{s}_L \gamma_\mu b_L \bar{\ell} \gamma^\mu \ell + C_{10} \bar{s}_L \gamma_\mu b_L \bar{\ell} \gamma^\mu \gamma_5 \ell \right. \\ & \left. - 2C_7^{(0)eff} m_b \bar{s}_L i\sigma_{\mu\nu} \frac{q^\nu}{q^2} b_R \bar{\ell} \gamma^\mu \ell \right], \end{aligned} \quad (9.55)$$

where q^2 represents the momentum transferred to the lepton pair.

This yields the differential branching fraction (neglecting $\mathcal{O}(m_s^2/m_b^2)$ terms)

$$\begin{aligned} \frac{d\mathcal{B}(B \rightarrow X_s \ell^+ \ell^-)}{d\hat{s}} = \mathcal{B}(B \rightarrow X \ell \bar{\nu}) \frac{\alpha^2}{4\pi^2} \frac{|V_{tb}V_{ts}^*|^2}{|V_{cb}|^2} \frac{(1-\hat{s})^2}{f(z)\kappa(z)} \left[1 - \frac{4x}{\hat{s}}\right]^{1/2} \left\{ \left[|C_9^{eff}|^2 - |C_{10}|^2\right] 6x \right. \\ \left. + \left[|C_9^{eff}|^2 + |C_{10}|^2\right] \left[(\hat{s} - 4x) + \left(1 + \frac{2x}{\hat{s}}\right)(1 + \hat{s}) \right] \right. \\ \left. + 12C_7^{(0)eff} \operatorname{Re} C_9^{eff} \left(1 + \frac{2x}{\hat{s}}\right) + \frac{4|C_7^{(0)eff}|^2}{\hat{s}} \left(1 + \frac{2x}{\hat{s}}\right)(2 + \hat{s}) \right\}, \end{aligned} \quad (9.56)$$

with $x \equiv m_\ell^2/m_b^2$ which is relevant for the case $\ell = \tau$ [88], and $\hat{s} \equiv (p_{\ell^+} + p_{\ell^-})^2/m_b^2$ is the scaled momentum transfer. The rate has been scaled to that for B semileptonic decay, with the definitions of z , $f(z)$ and $\kappa(z)$ given in Section 9.2.1. There are four contributions to this quantity, arising from the modulus squared of C_9^{eff} , C_{10} , $C_7^{(0)eff}$ and from the interference of $C_7^{(0)eff}$ with C_9^{eff} . C_9^{eff} contains contributions from physics at the weak scale (including m_t dependence) and from renormalization group evolution between M_W and $\mu \approx m_b$. In addition C_9^{eff} is defined to incorporate the contributions from the $b \rightarrow s\ell^+\ell^-$ matrix elements of \mathcal{O}_{1-6} (hence the superscript ‘effective’), which involve loops with charm- and light-quark flavors. C_{10} is a function only of the top-quark mass. $C_7^{(0)eff}$ is the same coefficient that appears in $B \rightarrow X_s \gamma$ decay; its main effect on $B \rightarrow X_s \ell^+ \ell^-$ is through the interference with C_9^{eff} , which is a sizable contribution. The piece proportional to $|C_7^{(0)eff}|^2$ is comparatively small, except for very low values of \hat{s} . The dominant terms in the branching fraction are those from $|C_9^{eff}|^2$ and $|C_{10}|^2$, which have about the same magnitude for $m_t \approx 175$ GeV.

The NLO analysis for this decay has been performed in [43, 89], where it is stressed that a scheme-independent result can only be obtained by including the leading and next-to-leading logarithmic corrections to $C_9(\mu)$, while retaining only the leading logarithms in the remaining Wilson coefficients. The residual leading μ dependence in $C_9(\mu)$ is cancelled by that contained in the matrix element of \mathcal{O}_9 . The combination yields an effective value of C_9 given by

$$C_9^{eff}(\mu, \hat{s}) = C_9(\mu)\eta(\hat{s}) + Y(\hat{s}). \quad (9.57)$$

$Y(\hat{s})$ is the one-loop matrix element of \mathcal{O}_9 , which incorporates the contributions from the charm and light quark loops as mentioned above. The expression for this quantity can be found in [89, 90]. $\eta(\hat{s}) = 1 + \alpha_s(\mu)\omega(\hat{s})/\pi$, where the function $\omega(s)$ is given in [28, 89], represents the single gluon corrections to this matrix element. In the naive dimensional regularization (NDR) scheme

$$C_9(\mu) = P_0 + \frac{Y_0(x_t)}{\sin^2 \theta_w} - 4Z(x_t) + P_E E(x_t), \quad (9.58)$$

where $Y_0(x_t)$ is given in Eq. (9.11), $P_{0,E}$, $E(x_t)$ can be found in [89], and

$$Z(x) = \frac{x}{4} \left[\frac{x-6}{2(x-1)} + \frac{3x+2}{2(x-1)^2} \ln x - \frac{x(19x-25)}{36(x-1)^3} + \frac{x(5x^2-2x-6)}{18(x-1)^4} \ln x - \frac{4}{9} \ln x \right]. \quad (9.59)$$

The effective value for $C_7^{(0)eff}(\mu)$ is as defined in Eq. (9.31). The operator \mathcal{O}_{10} does not renormalize and hence its corresponding coefficient

$$C_{10}(\mu) = -\frac{Y_0(x_t)}{\sin^2 \theta_w} \quad (9.60)$$

does not depend on the value of μ (except for the μ dependence associated with the definition of the top-quark mass). The numerical estimates, in the NDR scheme, for these coefficients are then (taking $m_b^{pole} = 4.87$ GeV/ c^2 , $m_t^{phys} = 175$ GeV/ c^2 , and $\alpha_s = 0.118$)

$$C_9(\mu = m_b^{-m_b/2}) = 4.21_{-0.40}^{+0.31}, \quad C_{10}(\mu) = -4.55. \quad (9.61)$$

$B \rightarrow X_s \ell^+ \ell^-$ also receives large long-distance contributions from the tree-level processes $B \rightarrow K^{(*)} \psi^{(\prime)}$ followed by $\psi^{(\prime)} \rightarrow \ell^+ \ell^-$. These pole contributions can be incorporated into the lepton pair invariant-mass spectrum following the prescription in Ref. [91], where both on- and off-shell vector mesons are considered by employing a Breit-Wigner form for the resonance propagator. This produces an effective $(\bar{s}_L \gamma_\mu b_L)(\bar{\ell} \gamma_\mu \ell)$ interaction which can be incorporated into C_9^{eff} via the addition of

$$\frac{-3\pi}{\alpha^2 m_b^2} \sum_{V_i=J/\psi, \psi'} \frac{M_{V_i} \Gamma(V_i \rightarrow \ell^+ \ell^-)}{(\hat{s} - M_{V_i}^2/m_b^2) + i\Gamma_{V_i} M_{V_i}/m_b^2}. \quad (9.62)$$

The relative sign between the short- and long-distance terms was once a source of controversy, but can be explicitly determined via the analyses presented in Ref. [92].

The resulting differential branching fraction, with and without the long-distance resonance contributions, is presented in Fig. 9-14. The small cusp in the partonic result at $\hat{s} = 4m_c^2/m_b^2$ originates from intermediate $c\bar{c}$ pairs and is the perturbative ‘remnant’ of intermediate $c\bar{c}$ resonances. The residual dependence on the renormalization scale μ at NLO is quite moderate and is typically below $\pm 6\%$ (for $2.5 \text{ GeV} \leq \mu \leq 10 \text{ GeV}$). It is clear that the pole contributions dominate the branching fraction near the J/ψ and ψ' peaks, and that there is significant interference between the dispersive part of the resonance and the short-distance contributions. However, suitable $\ell^+ \ell^-$ invariant-mass cuts can eliminate the resonance contributions, and observations away from these peaks cleanly separate out the short-distance physics. This divides the spectrum into two distinct regions [90], (i) low-dilepton mass, $4x \leq \hat{s} \leq M_{\psi'}^2/m_b^2 - \delta$, and (ii) high-dilepton mass, $M_{\psi'}^2/m_b^2 + \delta \leq \hat{s} \leq \hat{s}_{max}$, where δ is to be matched to an experimental cut. The integrated branching fractions (without the pole contributions) for $\ell = e, \mu, \tau$ are presented in Table 9-2 for both the total and high-dilepton mass regions of \hat{s} . Note that the branching fraction for $B \rightarrow X_s \tau^+ \tau^-$ is comparable to that for $\ell = e, \mu$ in the clean \hat{s} region above the ψ' resonance.

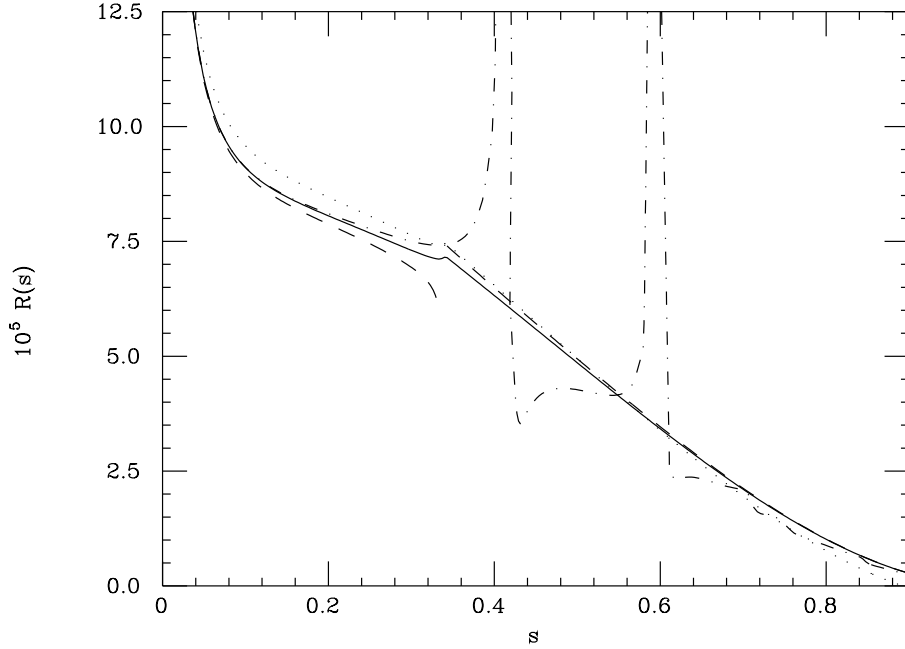


Figure 9-14. Dilepton invariant-mass spectrum of $B \rightarrow X_s e^+ e^-$ normalized to the semileptonic rate: partonic result (full line), partonic result + $\mathcal{O}(\Lambda_{QCD}^2/m_b^2)$ corrections (dotted line), partonic result + $\mathcal{O}(\Lambda_{QCD}^2/m_c^2)$ corrections (dashed line), partonic result + factorizable resonance contributions (dash-dotted line). These results have been obtained for $\mu = m_b = 4.8 \text{ GeV}/c^2$ and $m_c = 1.4 \text{ GeV}/c^2$.

Other interesting observables that can be studied in $B \rightarrow X_s \ell^+ \ell^-$ decays are the lepton forward-backward (A_{FB}) [93] and the left-right (LR) polarization [88, 94] asymmetries. The former can be defined as

$$A(\hat{s})_{FB} = \frac{\int_0^1 dz d^2 \mathcal{B} / dz d\hat{s} - \int_{-1}^0 dz d^2 \mathcal{B} / dz d\hat{s}}{\int_0^1 dz d^2 \mathcal{B} / dz d\hat{s} + \int_{-1}^0 dz d^2 \mathcal{B} / dz d\hat{s}}, \quad (9.63)$$

where $z \equiv \cos \theta$ with θ being the angle between the momentum of the B meson (or outgoing s -quark) and the ℓ^+ in the dilepton center-of-mass frame. As shown in [95] $A(\hat{s})_{FB}$ is identical to the energy asymmetry introduced in [96]. The NLO perturbative result for $A(\hat{s})_{FB}$ is given by

$$A(\hat{s})_{FB} = -\frac{3(1 - 4x/\hat{s})^{1/2} C_{10} [\mathcal{R}e C_9^{eff} \hat{s} + 2C_7^{(0)eff}]}{D}, \quad (9.64)$$

where D is the expression in curly brackets in Eq. (9.56) and x is defined above. The tau polarization asymmetry is

$$P_\tau(\hat{s}) \equiv \frac{dB_{\lambda=-1} - dB_{\lambda=+1}}{dB_{\lambda=-1} + dB_{\lambda=+1}}, \quad (9.65)$$

Table 9-2. Integrated branching fractions for $B \rightarrow X_s l^+ l^-$ for the total and high-dilepton mass regions.

ℓ	$4x \leq \hat{s} \leq 1$	$0.6 \leq \hat{s} \leq 1$
e	$(6.25_{-0.93}^{+1.04}) \times 10^{-6}$	5.8×10^{-7}
μ	$(5.73_{-0.78}^{+0.75}) \times 10^{-6}$	5.8×10^{-7}
τ	$(3.24_{-0.54}^{+0.44}) \times 10^{-7}$	2.5×10^{-7}

where $d\mathcal{B}$ represents the differential $B \rightarrow X_s \tau^+ \tau^-$ branching fraction. The spin projection operator is represented as $(1 + \gamma_5 \not{s})/2$, with the normalized dot product being defined as $\hat{s} \cdot \hat{p} = \lambda = \pm 1$ with the $-(+)$ sign corresponding to the case where the spin polarization is anti-parallel (parallel) to the direction of the τ^- momentum. This corresponds to the usual definition of a polarization asymmetry, given in terms of couplings, *i.e.*, $(L - R)/(L + R)$, in the massless case. This asymmetry is calculated to be

$$P_\tau(\hat{s}) = \frac{-2[1 - 4x/\hat{s}]^{1/2} C_{10} [\text{Re} C_9^{eff}(1 + 2\hat{s}) + 6C_7^{(0)eff}]}{D}. \quad (9.66)$$

The forward-backward and polarization asymmetries are displayed as a function of \hat{s} in Fig. 9-15. Both asymmetries are sensitive to the relative signs between $C_7^{(0)eff}$ and C_9^{eff} and provide a powerful probe for new physics. However, the LR asymmetry is not likely to be observed in the early stages of the B -factory.

The parton-level results for the lepton pair invariant-mass distribution and asymmetries receive nonperturbative corrections from higher orders in the heavy-quark ($1/m_b$) expansion. The leading effects of this type arise at $\mathcal{O}(\Lambda_{QCD}^2/m_b^2)$. They have been investigated most recently in [95] (see [41] for earlier work on this subject). From the results of [95] one can derive

$$\delta_{1/m_b^2} \frac{d\mathcal{B}}{d\hat{s}} = \frac{3\lambda_2}{2m_b^2} \left(\frac{\alpha^2}{4\pi^2} \left| \frac{V_{ts}}{V_{cb}} \right|^2 \frac{1}{f(z)\kappa(z)} \left[(1 - 15\hat{s}^2 + 10\hat{s}^3)(|C_9^{eff}|^2 + |C_{10}|^2) - \right. \right. \quad (9.67)$$

$$\left. \left. (6 + 3\hat{s} - 5\hat{s}^3) \frac{4|C_7^{(0)eff}|^2}{\hat{s}} - (5 + 6\hat{s} - 7\hat{s}^2) 4C_7^{(0)eff} \text{Re} C_9^{eff} \right] + \frac{g(z)}{f(z)} \frac{d\mathcal{B}}{d\hat{s}} \right),$$

where $\lambda_2 = (M_{B^*}^2 - M_B^2)/4$ and $g(z) = 3 - 8z^2 + 24z^4 - 24z^6 + 5z^8 + 24z^4 \ln z$. The contribution proportional to $g(z)$ arises from the corresponding correction to the normalizing rate $\Gamma(B \rightarrow X_c e \nu)$. The correction due to the b -quark kinetic energy is the same for $\Gamma(B \rightarrow X_s l^+ l^-)$ and $\Gamma(B \rightarrow X_c e \nu)$ and therefore cancels in the ratio. The relative magnitude of this correction decreases from +4% to about -5% as the variable \hat{s} is increased from 0.1 to 0.7; this is shown in

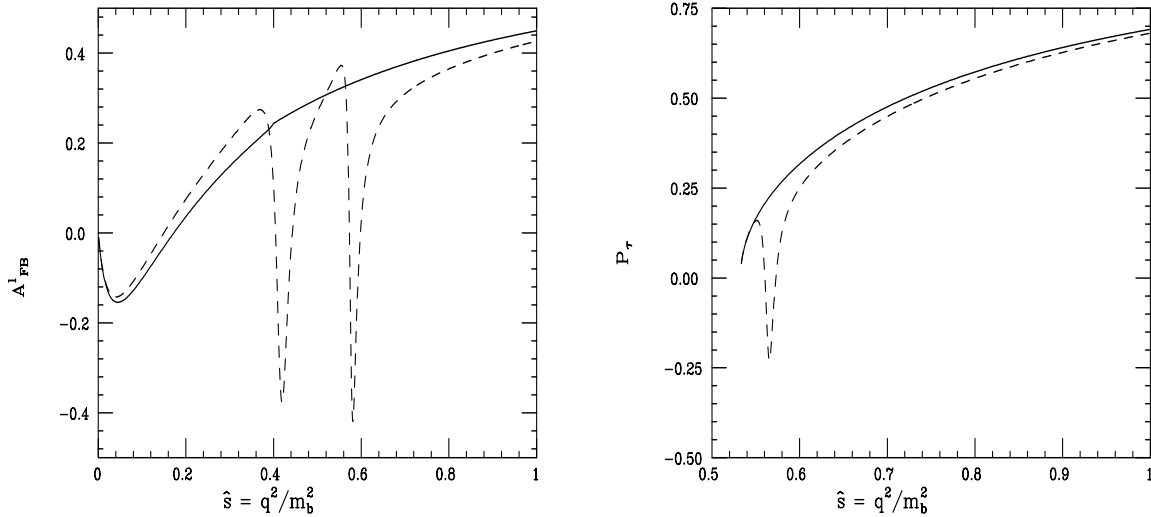


Figure 9-15. Lepton forward-backward ($\ell = e$) and tau polarization asymmetry with and without the long-distance resonance contributions.

Fig. 9-14. The correction from $\Gamma(B \rightarrow X_c e \nu)$ contributes a constant +3% to this. The (negative) correction becomes much larger beyond $\hat{s} = 0.7$ and the expansion eventually breaks down in the endpoint region. Similarly, these $\mathcal{O}(\Lambda_{QCD}^2/m_b^2)$ corrections to A_{FB} amount to a few percent up to $\hat{s} = 0.6$ and diverge in the limit $\hat{s} \rightarrow 1$.

In addition to higher order terms in the $1/m_b$ expansion, $B \rightarrow X_s \ell^+ \ell^-$ decays are affected by long-distance corrections related to $c\bar{c}$ intermediate states. These originate from the nonperturbative interactions of the $c\bar{c}$ pair in the process $B \rightarrow X_s c\bar{c} \rightarrow X_s \ell^+ \ell^-$. If the dilepton invariant mass is near to a $J^{PC} = 1^{--}$ $c\bar{c}$ -resonance (Ψ, Ψ', \dots) this effect is very large and shows up as a peak in the distribution (see Fig. 9-14). However, as discussed above this background can be eliminated by suitable kinematical cuts. The estimation of the long-distance effects away from the resonance regions is a more delicate problem.

Nonperturbative contributions generated by $c\bar{c}$ intermediate states have been widely discussed in the literature by means of phenomenological resonance-exchange models [94, 93, 95, 97]. These approaches are useful near the resonance peaks, but their validity outside this region is certainly less reliable. Indeed, the shape of the resonance tails far from the peaks is not under control. Moreover, a double-counting problem is introduced by the simultaneous use of quark and hadronic degrees of freedom. Nevertheless, within this framework it is worthwhile to mention the approach of [94], which incorporates $\sigma(e^+e^- \rightarrow c\bar{c}\text{-hadrons})$ data using a dispersion relation. This method has the advantage of avoiding the double counting problem but has the disadvantage of only including the *factorizable* contributions due to resonance exchanges.

A more systematic and model-independent estimate of $c\bar{c}$ long-distance effects far from the resonance region, based on a heavy-quark expansion in inverse powers of the charm-quark mass, has been recently presented in [98] (see also [99]). This approach, originally proposed in [58, 59] to evaluate similar effects in $B \rightarrow X_s \gamma$ decays, has the advantage of dealing only with partonic degrees of freedom. In this framework the leading nonperturbative corrections to both the rate and the asymmetries turn out to be $\mathcal{O}(\Lambda_{QCD}^2/m_c^2)$. They originate from the effective $\bar{s}b$ -photon-gluon vertex (induced by charm loops), where the gluon is soft and couples to the light cloud surrounding the b quark inside the B meson. The corresponding matrix elements can be related to the strength of the chromomagnetic interaction of the b quark inside the meson and thus are known both in magnitude and in sign. The explicit correction is given by

$$\delta_{1/m_c^2} \frac{d\mathcal{B}}{d\hat{s}} = -\frac{8\lambda_2}{9m_c^2} C_2 \left\{ \frac{\alpha^2}{4\pi^2} \left| \frac{V_{ts}}{V_{cb}} \right|^2 \frac{(1-\hat{s})^2}{f(z)\kappa(z)} \operatorname{Re} \left[F(\hat{s}) \left(C_7^{(0)eff} \frac{1+6\hat{s}-\hat{s}^2}{\hat{s}} + C_9^{eff}(2+\hat{s}) \right) \right] \right\}, \quad (9.68)$$

where the functions $F(\hat{s})$ can be found in [98]. This correction is expected to be the dominant long-distance effect for small values of the dilepton invariant mass ($\hat{s} < 0.2$), however, the relative magnitude of this effect is very small (at the one or two percent level), as shown in Fig. 9-14. Higher-order terms become more important near the $c\bar{c}$ threshold, where the description in terms of partonic degrees of freedom is clearly inadequate. An estimate [98] of the higher-order terms shows that the leading corrections should provide a reliable approximation of the effect up to $\hat{s} = 3m_c^2/m_b^2 \approx 0.25$. Moreover, the $\mathcal{O}(\Lambda_{QCD}^2/m_c^2)$ calculation should also be reliable above the resonance region ($\hat{s} > 0.7$) where the effect is again quite small.

The hadronic invariant-mass and energy spectra in $B \rightarrow X_s \ell^+ \ell^-$ have recently been studied in [100]. Here the leading order perturbative QCD and $1/m_b^2$ power corrections have been computed using HQET techniques and an improved Fermi motion model which takes the B -meson wave function effects into account. The corrections are found to be small over most of the hadronic energy spectrum. However, the $1/m_b$ expansion fails near the lower kinematic endpoint and at the $c\bar{c}$ threshold. The hadronic invariant-mass spectrum is found to be only reliably calculable over a limited range $M_H > \bar{\Lambda} m_B$ in the heavy-quark expansion where $\bar{\Lambda} \simeq m_B - m_b$.

The theoretical treatment of $B \rightarrow X_s \ell^+ \ell^-$ is reasonably well under control, particularly in the region of small dilepton invariant mass. For $\hat{s} < 0.25$ the dominant uncertainty is from the scale dependence of the perturbative result and is of the order of few percent. Due to the appearance of the resonance peaks and due to the breakdown of the $1/m_b$ expansion for $\hat{s} \rightarrow 1$, somewhat larger uncertainties are expected for $\hat{s} > 0.25$. The ratio of decay distributions $d\mathcal{B}/d\hat{s}(B \rightarrow X_d \ell^+ \ell^-)/d\mathcal{B}/d\hat{s}(B \rightarrow X_s \ell^+ \ell^-)$ can be used [101] to extract the ratio of CKM elements $|V_{td}|/|V_{ts}|$ with an estimated theoretical uncertainty of 15%.

CP violation can occur in the inclusive mode $B \rightarrow X_d \ell^+ \ell^-$ due to the simultaneous presence of different CKM phases in the $u\bar{u}$ - and $c\bar{c}$ -loop contributions and different dynamical phases. The results of [102] show that a CP asymmetry of $(2-5)\%$ is possible for dilepton invariant masses

below the J/ψ resonance. In addition, a determination of the CP angle γ may be possible, with some associated theoretical uncertainty.

9.2.3.2 Theoretical framework: exclusive decays

The investigation of the rare exclusive decays $B \rightarrow K^{(*)}\ell^+\ell^-$ is experimentally more tractable than the inclusive case, but suffers more theoretical uncertainties related to the values of the $B \rightarrow K^{(*)}$ hadronic matrix elements. The relevant matrix elements of the effective Hamiltonian governing the exclusive transitions can be parametrized in terms of form factors as follows:

$$\begin{aligned}
\langle K(p') | \bar{s} \gamma_\mu b | B(p) \rangle &= (p + p')_\mu F_1(q^2) + \frac{m_B^2 - m_K^2}{q^2} q_\mu (F_0(q^2) - F_1(q^2)) , \\
\langle K(p') | \bar{s} i \sigma_{\mu\nu} q^\nu b | B(p) \rangle &= \left[(p + p')_\mu q^2 - (m_B^2 - m_K^2) q_\mu \right] \frac{F_T(q^2)}{m_B + m_K} , \\
\langle K^*(p', \epsilon) | \bar{s} \gamma_\mu (1 - \gamma_5) b | B(p) \rangle &= \epsilon_{\mu\nu\alpha\beta} \epsilon^{*\nu} p^\alpha p'^\beta \frac{2V(q^2)}{m_B + m_{K^*}} \\
&\quad - i \left[\epsilon_\mu^* (m_B + m_{K^*}) A_1(q^2) - (\epsilon^* \cdot q)(p + p')_\mu \frac{A_2(q^2)}{(m_B + m_{K^*})} \right. \\
&\quad \left. - (\epsilon^* \cdot q) \frac{2m_{K^*}}{q^2} (A_3(q^2) - A_0(q^2)) q_\mu \right] , \tag{9.69} \\
\langle K^*(p', \epsilon) | \bar{s} \sigma_{\mu\nu} q^\nu \frac{(1 + \gamma_5)}{2} b | B(p) \rangle &= i \epsilon_{\mu\nu\alpha\beta} \epsilon^{*\nu} p^\alpha p'^\beta 2 T_1(q^2) \\
&\quad + \left[\epsilon_\mu^* (m_B^2 - m_{K^*}^2) - (\epsilon^* \cdot q)(p + p')_\mu \right] T_2(q^2) \\
&\quad + (\epsilon^* \cdot q) \left[q_\mu - \frac{q^2}{m_B^2 - m_{K^*}^2} (p + p')_\mu \right] T_3(q^2) .
\end{aligned}$$

Here, $q = p - p'$ is the momentum transferred to the lepton pair, $F_1(0) = F_0(0)$, $A_3(q^2) = \frac{m_B + m_{K^*}}{2m_{K^*}} A_1(q^2) - \frac{m_B - m_{K^*}}{2m_{K^*}} A_2(q^2)$, $A_3(0) = A_1(0)$, and $T_1(0) = iT_2(0)$. The value of $T_1(0)$, which is estimated, *e.g.*, in [103], determines the exclusive $B \rightarrow K^* \gamma$ decay rate as discussed above. The various observables in $B \rightarrow K^{(*)}\ell^+\ell^-$, such as the differential decay rate, the angular lepton asymmetry and the lepton polarization asymmetry, depend not only on the normalization of the form factors at vanishing momentum transfer, but also on their q^2 dependence in the range $q^2 = M_\ell^2 - (M_B - M_{K,K^*})^2$. These form factors have been estimated by lattice QCD (for large q^2) [104], QCD sum rules [105], light-cone sum rules [106] and quark models [107, 108]. In Table 9-3 various predictions for the $B \rightarrow K^{(*)}\ell^+\ell^-$ branching fractions are collected, taking $V_{ts} = 0.04$ and neglecting the long-distance resonance contributions from the process $B \rightarrow K^{(*)}\psi^{(n)}$, with the subsequent decay $\psi^{(n)} \rightarrow \ell^+\ell^-$.

Table 9-3. Predictions for the branching fractions of the exclusive decays $B \rightarrow K^* \ell^+ \ell^-$ in various models.

Ref.	$\mathcal{B}(B \rightarrow K \ell^+ \ell^-)$	$\mathcal{B}(B \rightarrow K^* e^+ e^-)$	$\mathcal{B}(B \rightarrow K^* \mu^+ \mu^-)$
[104]		1.15×10^{-6}	1.15×10^{-6}
[105]	3×10^{-7}	1×10^{-6}	1×10^{-6}
[107]	$(6.2 \pm 1.3) \times 10^{-7}$	$(2.1 \pm 0.7) \times 10^{-6}$	$(1.5 \pm 0.6) \times 10^{-6}$
[93]	$(5.9 \pm 2.2) \times 10^{-7}$	$(3.4 \pm 1.3) \times 10^{-6}$	$(2.2 \pm 0.9) \times 10^{-6}$
[106]	$(2.45 \pm 0.7) \times 10^{-7}$		0.95×10^{-6}
[108]	0.5×10^{-6}		1.4×10^{-6}

The prediction of [105] for the invariant-mass-squared distribution of the lepton pair for the decay $B \rightarrow K \ell^+ \ell^-$ is displayed in Fig. 9-16, with and without the long-distance pole contributions. A comparison between the results of [105] and [107] is also shown in the figure. Analogously, various model expectations [104, 105, 107] for the same quantity in the case of $B \rightarrow K^* \ell^+ \ell^-$ is presented in Figure 9-17, where the curve including long-distance effects is superimposed over that for the short-distance contributions for the model from Ref. [105].

The lepton forward-backward asymmetry in $B \rightarrow K^* \ell^+ \ell^-$ can provide important information, since it is sensitive to the relative sign of the coefficient C_7 in the effective Hamiltonian as discussed above. This asymmetry is displayed in Fig. 9-18, where the three curves refer to the results of [104, 105, 107].

While these model calculations of exclusive decay modes provide useful estimates of the decay rates and distributions, it is clear that the theoretical uncertainties associated with them are large enough to hamper the use of these modes as meaningful tests of the short-distance structure of the Standard Model or its extensions. Inspection of Table 9-3 shows that while various models agree on the order of magnitude of the branching ratio, uncertainties of factors of four to five are present. Clearly, most extensions of the Standard Model not presently ruled out by other measurements can only produce deviations that cannot be resolved by these ambiguous expectations. Thus, in order to turn these modes into stringent tests of the Standard Model, reliable predictions within controlled approximations are needed. An example of this approach, is the model-independent analysis of the processes $B \rightarrow K^* \ell^+ \ell^-$ and $B \rightarrow \rho \ell^+ \ell^-$ proposed in [109]. In the limit $m_b \rightarrow \infty$, it is possible to derive relations among the form factors F_T, T_i and F_i, V, A_i [24], that allow the expression of the $B \rightarrow (K^*, \rho) \ell^+ \ell^-$ amplitudes in terms of the form-factors entering in the semileptonic process $B \rightarrow \rho \ell \nu$. These relations are valid over the entire physical region for B decays. Thus, employing experimental information on the semileptonic transition (and neglecting $SU(3)$ corrections in the K^* case), it is possible to reliably predict the dilepton mass distribution, lepton asymmetry and overall decay rate of the various exclusive transitions. The $SU(3)$ corrections in the case of $B \rightarrow$

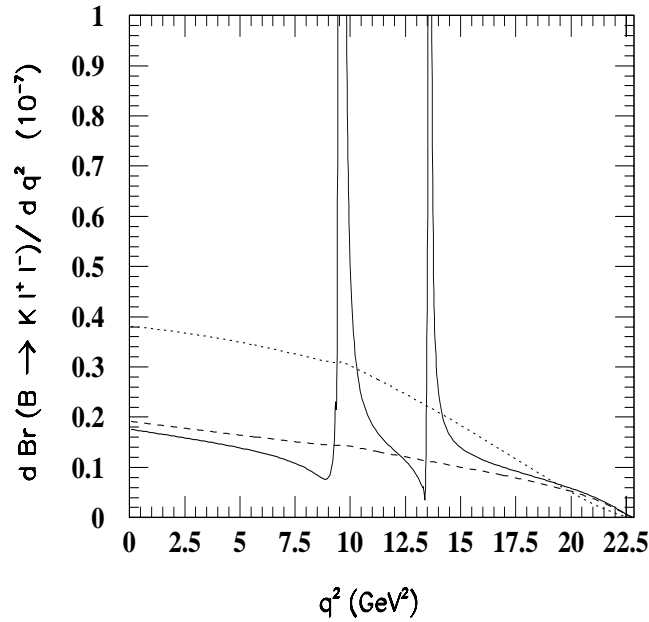


Figure 9-16. Invariant-mass-squared distribution of the lepton pair for the decay $B \rightarrow K \ell^+ \ell^-$. The dashed and dotted lines refer to the short-distance contribution only, computed using the form factors in [105] and [107], respectively. The solid curve refers to both short- and long-distance contributions according to [105].

$K^* \ell^+ \ell^-$, which is expected to be the dominant mode, are small as long as the recoil energy of the K^* is above 1 GeV [23]. In this region, e.g., dilepton masses *below* the J/ψ and ψ' resonances, the validity of the heavy-quark relations of [24] is thus ensured.

An additional model-independent constraint can be derived from the zero of the forward-backward asymmetry for leptons, A_{FB} , in the $B \rightarrow (K^{(*)}, \rho) \ell^+ \ell^-$ decays. This asymmetry depends on the short-distance coefficients $C_7^{(0)eff}$, C_9^{eff} and C_{10} as described in the previous section on the inclusive modes. If the asymmetry vanishes at some value of $m_{\ell\ell}^2$, as is the case in the Standard Model, the location of this zero is independent of the value of C_{10} [23]. In the exclusive case, it is possible to write the condition for this asymmetry zero such that its only dependence on hadronic form-factors is through the ratio of the vector to the axial-vector form-factors, $R_V \equiv V(s_0)/A_1(s_0)$, where s_0 represents the value of $m_{\ell\ell}^2$ for which A_{FB} vanishes. This ratio can be measured in the semileptonic mode $B \rightarrow \rho \ell \nu$. Since the vanishing condition is not very sensitive to R_V [23], a highly precise measurement of R_V is not necessary in order to obtain an accurate prediction of the location of the asymmetry zero. For example, in the Standard Model the values of $C_7^{(0)eff}$ and C_9^{eff} imply the occurrence of this zero at about $m_{\ell\ell}^2 \simeq 4 \text{ GeV}^2/c^2$, rather independently of the model used to compute R_V . Shifts in these Wilson coefficients, induced by new physics contributions, could

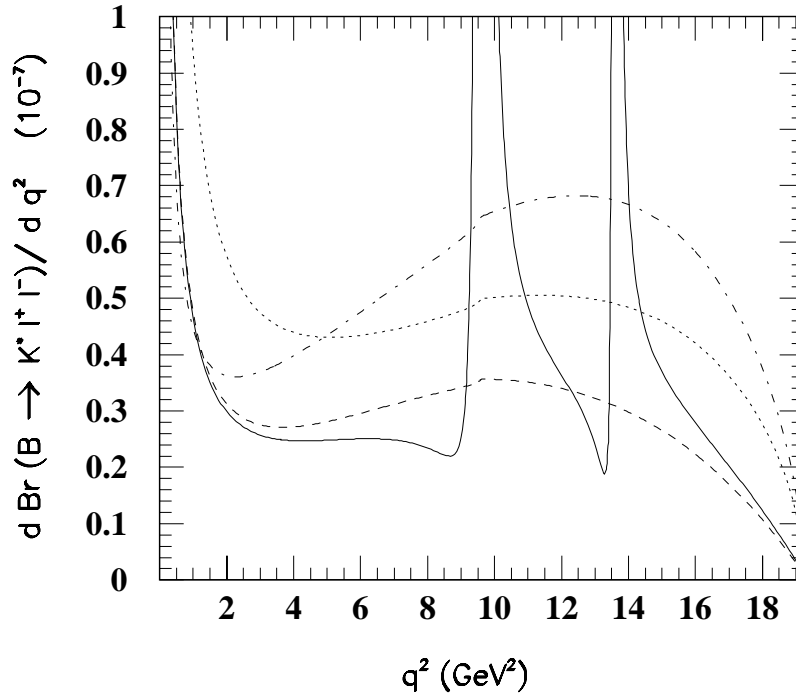


Figure 9-17. Invariant-mass-squared distribution of the lepton pair for the decay $B \rightarrow K^* \ell^+ \ell^-$. The dashed, dotted, and dashed-dotted curves correspond to the short-distance contribution only, using the form factors in [105], [107], and [104], respectively. The long-distance contributions are shown for the model of [105].

drastically change² the value of s_0 . In this way, the determination of the value of s_0 provides a test of the physics encoded in the short-distance coefficients, with small theoretical uncertainties.

9.2.3.3 Experimental considerations: $B \rightarrow K^{(*)} \mu^+ \mu^-$

There have been two Aslund-based Monte Carlo studies [110, 111] of the feasibility of detecting the decays $B \rightarrow K^*(892) \mu^+ \mu^-$ and $B^+ \rightarrow K^+ \mu^+ \mu^-$ at BaBar. The branching ratios expected for these modes are less than or equal to 10^{-6} so the expected number of signal events is small, and a huge factor is needed for the background rejection. As described in detail in the following, most of the experimental issues for detecting this decay are associated with the background rejection, which has been estimated using fast simulation in order to obtain sufficiently large statistics.

Events have been generated according to three-body phase space, and according to the models of [95] and [112], which give predictions for the invariant-mass distribution for the lepton pair and their angular distribution with respect to the decaying B . The J/ψ and ψ' resonances and long-

²For instance, if $C_7^{(0)eff}$ has the opposite sign to the Standard Model prediction, then A_{FB} does not have a zero.

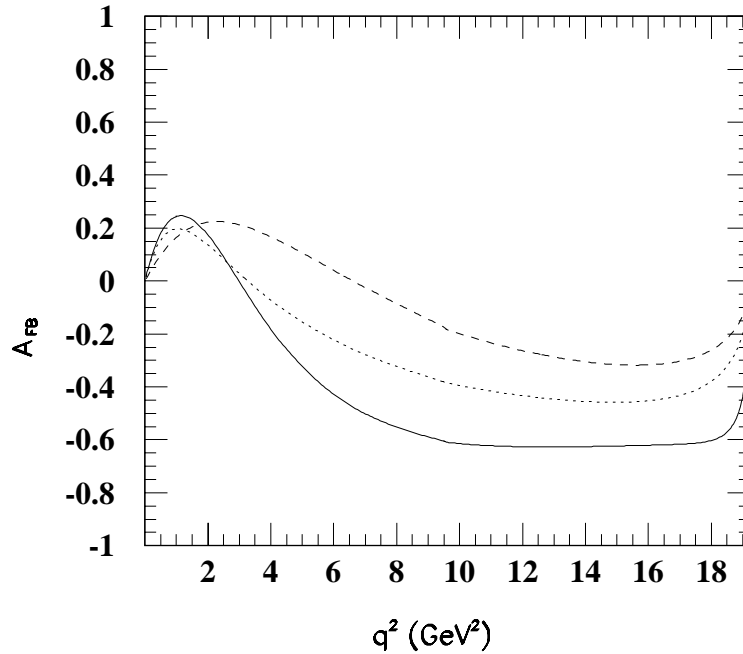


Figure 9-18. Lepton pair forward-backward asymmetry in the decay $B \rightarrow K^* \ell^+ \ell^-$; the three curves correspond to the results of [105] (continuous line), [107] (dashed line) and [104] (dotted line).

distance effects are not included in the generator, since it is assumed that these are negligible after suitable lepton invariant-mass cuts have been applied (Fig. 9-19).

Samples of $\approx 50,000$ signal events have been used to evaluate the acceptance. The decay modes considered are $B^+ \rightarrow K^{*0} \mu^+ \mu^-$ (with $K^{*0} \rightarrow K^+ \pi^-$), $B^+ \rightarrow K^{*+} \mu^+ \mu^-$ (with $K^{*+} \rightarrow K^+ \pi^0$ and $K_s^0 \pi^+$) and $B^+ \rightarrow K^+ \mu^+ \mu^-$. A requirement of two muons identified in the Instrumented Flux Return (IFR), is imposed, and also the presence of a suitable combination of identified neutral and charged pions and kaons, in order to reconstruct a B decay candidate.

The fast simulation package uses parameterized response functions for both muon and hadron identification. The geometrical acceptance of the IFR is 90%, and the average detection efficiency for a muon is 85%. The pion contamination has been modeled as a constant value in the range 2–5% for all momenta. The reconstruction efficiency for charged particles is modeled as 95% based on studies using the detailed Monte Carlo package `BBsim`. Charged-particle identification is provided by parametrized outputs from the DIRC and the drift chamber dE/dx . A track is positively identified as a particular hadron if the χ^2 probability for that hypothesis is greater than 2%. The efficiencies for π and K identification are 98% and 92% respectively. The probability that a pion is misidentified as a kaon is 5%, and the $\pi \rightarrow K$ contamination is 17%.

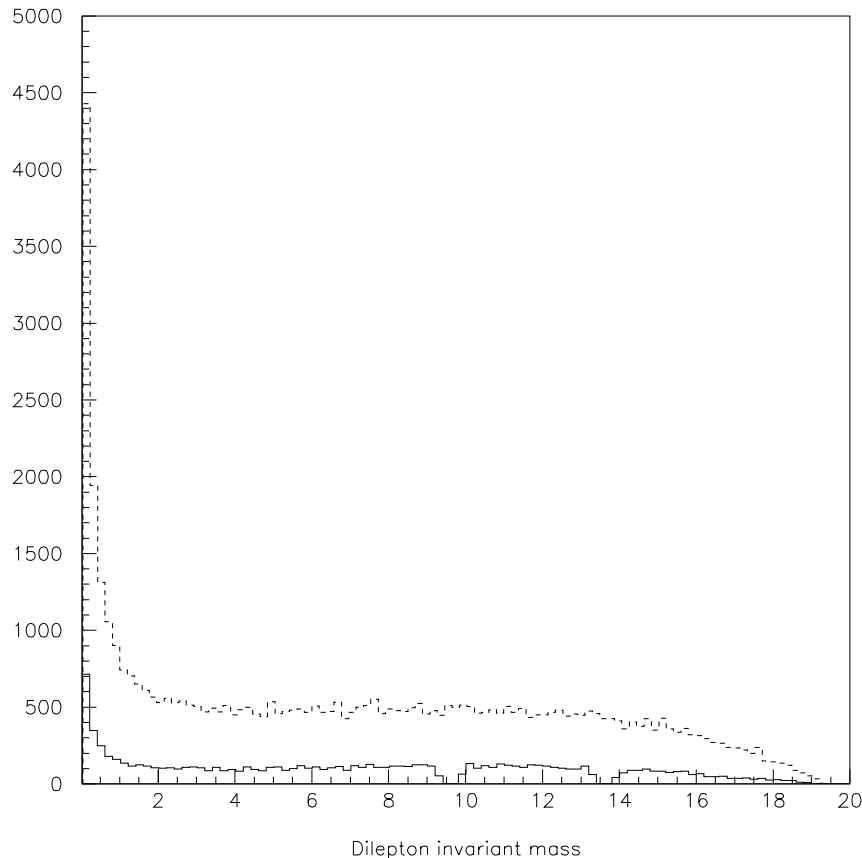


Figure 9-19. *Invariant-mass distribution of the generated and reconstructed lepton pair. The J/ψ and ψ' cuts are evident. Long-distance effects are not included in this plot.*

Neutral pions are reconstructed from pairs of neutral clusters in the electromagnetic calorimeter. The clusters are required to have more than 50 MeV of energy to reduce the combinatorial background by a factor of two. The invariant mass of the pair is required to be in the range $0.120 \text{ GeV}/c^2 < M(\gamma\gamma) < 0.144 \text{ GeV}/c^2$. The efficiency for finding a π^0 is 60% (Fig. 9-20).

The K_s^0 candidates are looked for by forming all possible pairs of opposite-sign charged tracks which have been identified as pions. The fast simulation unfortunately does not properly handle tracks originating from secondary vertices displaced from the beam axis. For this study the decay length of the K_s^0 has been forced to be no greater than 2.0 cm. It is assumed that this is not an important bias, but this needs checking with a full simulation and reconstruction. The invariant mass of the pairs is required to be within 18 MeV/ c^2 of the nominal mass, and the χ^2 probability that the two pions come from the same vertex has to be larger than 2%. The vertex is required

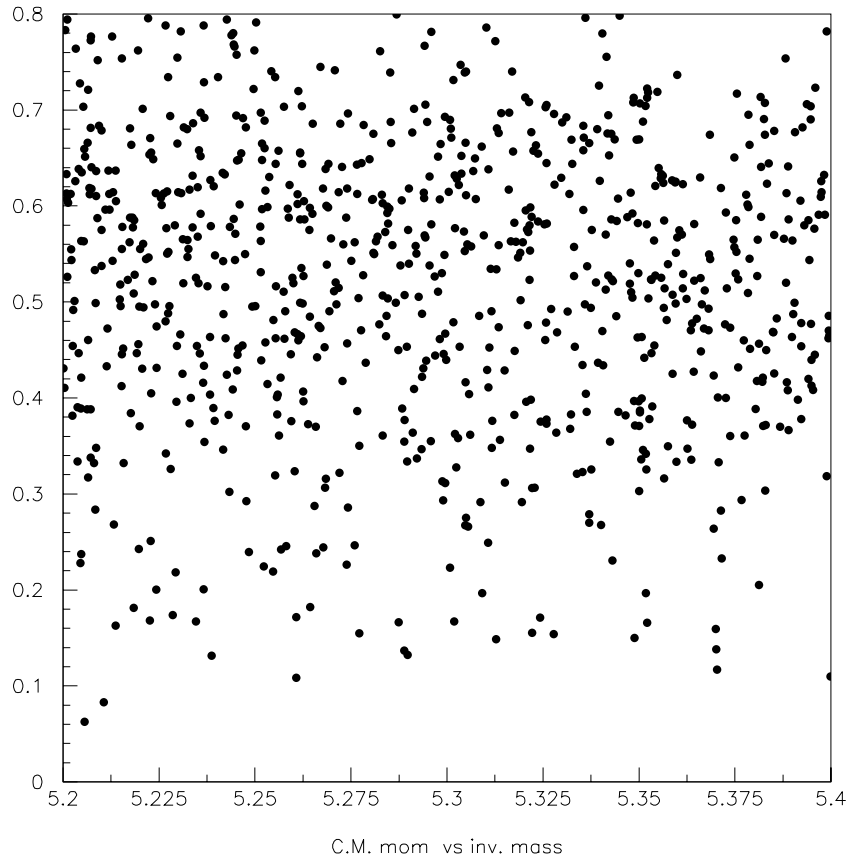


Figure 9-20. *C.M. momentum vs. invariant mass for background $c\bar{c}$ events with two identified muons in the IFR.*

to be more than $960\mu m$ from the beam axis (three times the impact parameter resolution). The efficiency for finding a K_s^0 is 63%.

The K^{*0} is reconstructed from a charged kaon and a pion $\approx 40\%$ of the times (this includes branching ratio, hadron identification and a tight invariant mass cut). The K^{*+} is reconstructed with a similar efficiency by combining a K^+ with a π^0 candidate or a K_s^0 candidate with a charged pion. In both cases the invariant mass of the combination is required to be within $60 \text{ MeV}/c^2$ of the K^{*} mass.

The B candidate formed from the $K^{(*)}$ and the muon pair is required to have an invariant mass, M_I , and a beam constrained mass, M_B , within 2σ of the nominal B mass. The resolution on M_I varies between $14 \text{ MeV}/c^2$ and $22 \text{ MeV}/c^2$ according to the mode considered. The resolution on M_B is $3 \text{ MeV}/c^2$.

The background sources for this channel can be classified as:

- B meson decays
- Continuum events with leptons (mostly $c\bar{c}$ events)
- Continuum events without leptons (mostly light $q\bar{q}$ events)

It might be anticipated that B and D semileptonic decays would be the source of most of the background, but with the assumed muon fake rate of 2–5% the third type of background also needs to be considered.

Both analyses have generated large background samples consisting of $\approx 10^8$ cc events, $\approx 3 \times 10^7$ $B^0\bar{B}^0$ events, and $\approx 2.5 \times 10^7$ light-quark events. An additional sample of 3.3×10^7 cc events was generated with π misidentification set at 5% to test the dependence of the background on the assumed fake rate.

The largest single background comes from B decays to $J/\psi K^{(*)}$ or $\psi' K^{(*)}$ followed by the J/ψ and ψ' decay into $\mu^+\mu^-$. These decays can be rejected by cuts on the invariant mass of the lepton pair. In one of the analyses a wider cut has been made covering the region $9.0 \text{ GeV}^2 < s_{\mu\mu} < 14.35 \text{ GeV}^2$. It is argued that this is required to remove the region of interference between graphs containing virtual J/ψ s and graphs containing the FCNC loop [95].

The distribution of the continuum background events as a function of B invariant mass, M_I , and beam-constrained mass, M_B , is rather uniform. Without additional cuts the continuum background is between 7 and 20 times the signal depending on the channel. Most of this background comes from $c\bar{c}$ events in which there is a D meson decaying semileptonically and a second μ coming from the misidentification of a π . The events in which both the D mesons decay semileptonically are only 20% of the total continuum background.

In order to reduce the continuum background cuts have applied on event-shape variables evaluated in the center-of-mass frame of the $\Upsilon(4S)$:

- Sphericity (S)
The sphericity of the event is computed using all charged and neutrals clusters. S is between 0 (perfectly jet-like event) and 1 (perfectly spherical event). For a $B\bar{B}$ event S tends to be large and for a $q\bar{q}$ event it is small.
- $|\cos(\theta_S)|$
The angle between the sphericity axis of the B candidate and the sphericity axis of the rest of the event is θ_S . $|\cos(\theta_S)|$ has an almost flat distribution for signal events, but is peaked at 1 for the background.

A two-dimensional cut is applied in the plane S versus $|\cos(\theta_{ss})|$. Note that for signal events S and $\cos(\theta_{ss})$ are almost uncorrelated whereas they are strongly correlated for continuum events.

Table 9-4. Efficiency and rejection factor after the cuts.

Mode	Signal	$q\bar{q}$	$B\bar{B}$	N_S	N_{qq}	N_{bb}
$K^+\pi^-\mu\mu$	0.114	7.6×10^{-9}	0.2×10^{-7}	3.9	1.4	1.3
$K^+\pi^0\mu\mu$	0.038	9.3×10^{-9}	1.1×10^{-7}	1.3	1.7	7.4
$K^+\mu\mu$	0.224	1.4×10^{-8}	0.9×10^{-7}	2.3	2.5	5.9
$K^0\pi^+\mu\mu$	0.028	3.2×10^{-9}	3.9×10^{-8}	1.0	0.6	2.7

A further reduction in the continuum background can be obtained by requiring that the charged tracks forming the candidate come from a common vertex. In the case of charm background the charged tracks, in particular the muons, come from different D decays and are separated in space. The same is true for $B\bar{B}$ events where the muons originate from two semileptonic B decays. A vertex fit was performed with four tracks in the K^{*0} mode and with three tracks in the other modes. The tool used for the vertexing is based on the Kalman Filter [113]. The χ^2 probability of the vertex fit is required to be larger than 2%.

The signal efficiencies and background rejection factors from one of the studies are summarized in Table 9-4. The rejection factors have been determined by relaxing the cuts on M_I and M_B to study the effect of the other cuts.

The second study did not apply shape and vertex cuts to reduce the continuum background, and has slightly larger backgrounds. In this analysis there were no background events from the light quark sample. From the $B^0\bar{B}^0$ sample there was one event which is a double semileptonic decay of the B pair. The $c\bar{c}$ sample yielded 15 events, of which seven are double semileptonic decays, six are single semileptonic decay with a misidentified π , and two are doubly misidentified pions.

The results of these studies demonstrate that after one year of running at nominal luminosity ($3 \times 10^{33} \text{cm}^{-2}\text{sec}^{-1}$) a handful of signal events should be observed, with a signal to background ratio of about 1:1. This encourages us to believe that a branching ratio measurement can be made using a few years of data. Whether it is possible to obtain information on the lepton pair invariant-mass spectrum and forward-backward asymmetry requires further study using larger background samples, of the order of at least 10^8 events, and a better parametrization of the detector response.

9.2.4 $B \rightarrow X_s \nu \bar{\nu}$

9.2.4.1 Theoretical framework

The decay $B \rightarrow X_q \nu \bar{\nu}$ ($q = s, d$) was thoroughly studied in [3]. Under the single assumption that neutrinos are purely left-handed and effectively massless, the general amplitude has the remarkably simple form

$$\mathcal{A}^{q\nu\bar{\nu}} = G_F \left[C_L^{q\nu\bar{\nu}} (\bar{q}_L \gamma_\mu b_L) (\bar{\nu}_L \gamma^\mu \nu_L) + C_R^{q\nu\bar{\nu}} (\bar{q}_R \gamma_\mu b_R) (\bar{\nu}_L \gamma^\mu \nu_L) \right]. \quad (9.70)$$

In terms of the coefficients in (9.1) $C_{L,R}$ can be written as $C_{L,R} = [(C_V - C'_V) \pm (C_A - C'_A)]/4$. Summing over the three undetected neutrino flavors, the branching ratio (again normalized to the semileptonic decay) reads

$$\frac{\mathcal{B}(b \rightarrow X_q \nu \bar{\nu})}{\mathcal{B}(b \rightarrow X_c e \bar{\nu})} = \frac{3 \left(|C_L^{q\nu\bar{\nu}}|^2 + |C_R^{q\nu\bar{\nu}}|^2 \right) \bar{\eta}}{8 |V_{cb}|^2 f_{PS}(z_c) \kappa(z_c)}, \quad (9.71)$$

where $z, f(z), \kappa(z)$ are defined as usual (see Section 9.3.1). The factor $\bar{\eta} = \kappa(0) \approx 0.83$ represents the QCD correction to the matrix element of the $B \rightarrow X_q \nu \bar{\nu}$ transition [28].

In the Standard Model, the decay proceeds via W box and Z penguin diagrams which induce only the left-handed operator, while $C_R^{q\nu\bar{\nu}} = 0$. The corresponding coefficient reads

$$\left[C_L^{q\nu\bar{\nu}} \right]_{\text{SM}} = \frac{\sqrt{2} \alpha V_{tb}^* V_{tq}}{\pi \sin^2 \theta_W} X(x_t), \quad (9.72)$$

where $x_t = m_t^2/m_W^2$, $X(x) = X_0(x) + \frac{\alpha_s}{4\pi} X_1(x)$ and at leading order [13]

$$X_0(x) = \frac{x}{8} \left[\frac{2+x}{x-1} + \frac{3x-6}{(x-1)^2} \ln x \right]. \quad (9.73)$$

The QCD correction $X_1(x)$ can be found in [12]. Numerically $X(x_t) \approx 0.985 \cdot X_0(x_t)$.

Explicit expressions for the $1/m_b^2$ and α_s corrections to this decay can be found in [3, 12, 28, 114]. In contrast to the previous decays in this section, the theoretical predictions for $B \rightarrow X_q \nu \bar{\nu}$ are remarkably free from uncertainties. All the parameters entering in (9.71) and (9.72) are known with good accuracy; there are no long-distance effects and QCD corrections are small [3]. In fact, the main theoretical uncertainty comes from the precise value of m_t ! The Standard Model prediction for the branching ratio is $\mathcal{B}(B \rightarrow X_q \nu \bar{\nu}) = (4.1_{-1.0}^{+0.8}) \times 10^{-5} |V_{tq}/V_{ts}|^2$. It is worth noticing that in the ratio $\mathcal{B}(B \rightarrow X_d \nu \bar{\nu})/\mathcal{B}(B \rightarrow X_s \nu \bar{\nu})$ the uncertainties related to $\mathcal{B}(B \rightarrow X_c l \bar{\nu})$ and $|V_{cb}|$ cancel, allowing in principle for a very clean determination of $|V_{td}|/|V_{ts}|$.

A preliminary 90% confidence level limit on this decay, which is only one order of magnitude above the $B \rightarrow X_s \nu \bar{\nu}$ Standard Model rate, was recently obtained by the ALEPH Collaboration [115]

$$\mathcal{B}(B \rightarrow X \nu \bar{\nu}) < 7.7 \times 10^{-4}. \quad (9.74)$$

The exclusive decays $B \rightarrow K^{(*)} \nu \bar{\nu}$ are characterized by the absence of long-distance contributions, and by the fact that the effective Hamiltonian is represented in Standard Model by only one operator. Various predictions for the branching ratios are collected in Table 9-5. Missing energy distributions, using three point QCD sum rules results, are shown in Figs. 9-21, 9-22 [105].

Table 9-5. Branching Fraction predictions for the exclusive decays $B \rightarrow K^{*} \nu \bar{\nu}$ in various theoretical models.

Ref.	$\mathcal{B}(B \rightarrow K \sum_i \nu_i \bar{\nu}_i)$	$\mathcal{B}(B \rightarrow K^* \sum_i \nu_i \bar{\nu}_i)$
[105]	$(5.1 \pm 0.8) \times 10^{-6}$	$(2.4 \pm 0.6) \times 10^{-6}$
[107]	$(7.6 \pm 1.6) \times 10^{-6}$	$(1.9 \pm 0.7) \times 10^{-5}$
[93]	$(4.7 \pm 2.3) \times 10^{-6}$	$(1.6 \pm 0.8) \times 10^{-5}$

9.2.4.2 Experimental considerations

A search for the decays $B \rightarrow K^{(*)} \nu \bar{\nu}$ has been studied [116] using the `Aslund` fast simulation and fully reconstructed data from the `BBsim` simulation. These decays are distinguishable by the large amount of “missing” energy carried off by the neutrino pair. This characteristic is more pronounced by the fact that the neutrino pair occasionally carries very little invariant mass as well. Hence, the signal $K^{(*)}$ tends to have a high value of energy in the $B/\Upsilon(4S)$ rest frames. Additional distinctions are based upon requiring that the remainder of the event is consistent with a B decay.

Candidates for the signal modes are reconstructed through the following channels:

- $B^0 \rightarrow K_s^0 \nu \bar{\nu}, K_s^0 \rightarrow \pi^+ \pi^-$
- $B^0 \rightarrow K^{*0} \nu \bar{\nu}, K^{*0} \rightarrow K^- \pi^+$
- $B^- \rightarrow K^- \nu \bar{\nu},$ (no secondary decay)
- $B^- \rightarrow K^{*-} \nu \bar{\nu}, K^{*-} \rightarrow K_s^0 \pi^-, K_s^0 \rightarrow \pi^+ \pi^-$

Each of the exclusive signal decay modes have been studied with 3 million generated `Aslund` events and 600 thousand generated `BBsim` events. Charged kaon candidates were identified by

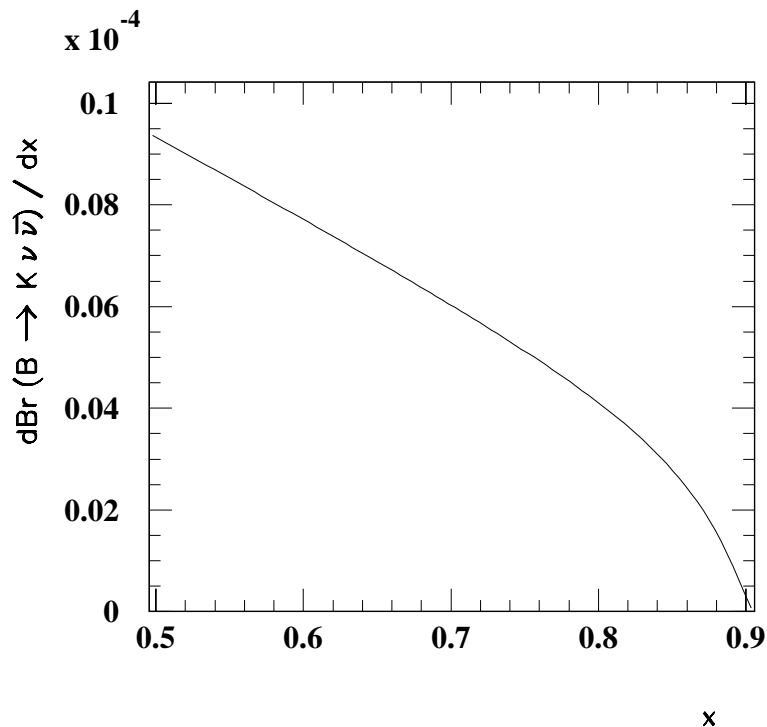


Figure 9-21. Missing energy distribution for the decay $B \rightarrow K \nu \bar{\nu}$ [105].

a consistency, from the product of the silicon vertex detector, drift chamber, and DIRC detector consistencies, of greater than 0.02. Charged pion candidates were similarly identified. The K_s^0 candidates were reconstructed from all pairs of oppositely charged pion candidates by first applying a loose mass cut ($400 \text{ MeV}/c^2 \leq M_{\pi\pi} \leq 600 \text{ MeV}/c^2$) to the invariant mass of the pair before fitting the tracks to a common vertex. The invariant mass of the fitted tracks was then required to be within $480 \text{ MeV}/c^2 \leq M_{\pi\pi} \leq 516 \text{ MeV}/c^2$, and the K_s^0 candidate vertex position and momentum vector were required to satisfy the relation $(x \times p_x + y \times p_y) / (p_x^2 + p_y^2) > 1 \text{ cm}/\text{GeV}/c$. The K^{*0} candidates were reconstructed from all pairs of oppositely charged kaon and pion candidates by fitting to a common vertex and requiring the vertex consistency be greater than 0.02 and the invariant mass be within $50 \text{ MeV}/c^2$ of the nominal K^* mass. The K^{*-} candidates were similarly reconstructed from charged pion candidates and previously reconstructed K_s^0 candidates. The center-of-mass energy of the $K^{(*)}$ candidate was required to be greater than 2.4 GeV (note the kinematic limit is $M_B/2 + M_{K^{(*)}}^2/2M_B$). The trajectory must also point away from the beamline ($-0.8 \leq \cos \theta \leq 0.8$).

Once the signal channel is selected, the remainder of the event is required to meet several criteria which categorize it as consistent with the decay of the other B in the event. The total four-momentum of the remainder of the event is constructed from the sum of all reconstructed tracks

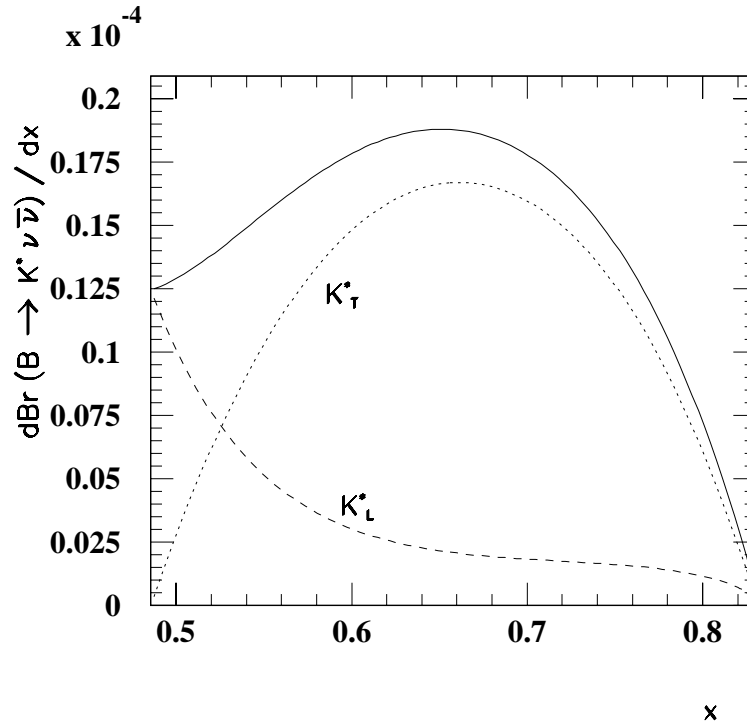


Figure 9-22. Missing energy distribution for the decay $B \rightarrow K^* \nu \bar{\nu}$; the dashed curve corresponds to a transversely polarized K^* , the dotted curve to a longitudinally polarized K^* [105].

and calorimeter clusters which do not match any track with a consistency of at least 1%. The energy in the center-of-mass frame must satisfy $3.2 \text{ GeV} \leq E \leq 5.6 \text{ GeV}$. The thrust axis of the remainder of the event is also formed and compared to the trajectory of the signal $K^{(*)}$. This angle measured in the center-of-mass system must satisfy $-0.8 \leq \cos \theta \leq 0.8$. Furthermore, the square of the missing mass (assuming the remainder of the event originated from a B decay) was required to be greater than $-0.5 \text{ GeV}/c^2$.

Table 9-6 summarizes the efficiencies for each of the above criteria as applied to signal and background (both $b\bar{b}$ and $q\bar{q}$) for each of the exclusive channels considered. The numbers appearing in parentheses are those taken from the `Aslund` simulation, which in some cases may better represent the actual efficiency because of known defects in the vertex reconstruction code at the time of this analysis. Given the anticipated luminosity and production cross-sections the expected number of events for each channel can be calculated. These numbers are listed for the backgrounds in Table 9-6. Their corresponding contribution to statistical uncertainty in the branching ratio measurements is displayed. Systematic uncertainties in the estimated background level will also degrade those channels with especially high background numbers (denoted by an asterisk in the branching ratio uncertainty estimate). Reaching below the 10^{-4} exclusive branching ratio level appears difficult in these modes with two neutrinos.

Table 9-6. Summary of efficiencies for signal and background for each exclusive channel, as discussed in the text.

Cuts	Candidates per Generated Event		
	Signal	$b\bar{b}$	$q\bar{q}$
$B^- \rightarrow K^- \nu \bar{\nu}$			
K^- ID	(.90)	1.24 (.10)	.908 (.775)
Signal Mode Cuts	(.10)	7.10×10^{-4}	1.35%
Other B Cuts	(8.0%)	$\leq 6 \times 10^{-6}$ (4×10^{-6})	3.8×10^{-4} (1.7×10^{-4})
Num Evts / $30 fb^{-1}$		(200)	34k
$\sigma_B(\text{bkg})$	8×10^{-5}		
$B^0 \rightarrow K_s^0 \nu \bar{\nu}$			
K_s^0 ID	(.46)	2.54% (.20)	2.71% (.25)
Signal Mode Cuts	(6.6%)	1×10^{-4}	7.2×10^{-4}
Other B Cuts	(3.8%)	$\leq 6 \times 10^{-6}$ ($\leq 2 \times 10^{-6}$)	2×10^{-5} (4.2×10^{-5})
Num Evts / $30 fb^{-1}$		(120)	1.8k
$\sigma_B(\text{bkg})$	4×10^{-5}		
$B^- \rightarrow K^{*-} \nu \bar{\nu}$			
K^{*-} ID	(.16)	1.43×10^{-3} (.47)	1.40×10^{-3} (.13)
Signal Mode Cuts	(3.5%)	2×10^{-5}	8.4×10^{-5}
Other B Cuts	(2.1%)	$\leq 6 \times 10^{-6}$ (6×10^{-6})	$\leq 3 \times 10^{-6}$ (4×10^{-5})
Num Evts / $30 fb^{-1}$		(360)	(3.6k)
$\sigma_B(\text{bkg})$	1×10^{-4}		
$B^0 \rightarrow K^{*0} \nu \bar{\nu}$			
K^{*0} ID	(.39)	7.3% (.63)	6.3% (.29)
Signal Mode Cuts	(8.5%)	3.9×10^{-3}	5.3×10^{-3}
Other B Cuts	(5.2%)	6×10^{-6}	4×10^{-5} (1.2×10^{-4})
Num Evts / $30 fb^{-1}$		(2.4k)	(11k)
$\sigma_B(\text{bkg})$	7×10^{-5}		

9.2.5 $B \rightarrow X_s + \text{Gluon}$

9.2.5.1 Theoretical framework

The subject of QCD loop-induced charmless B decays is a murky one, both computationally and experimentally. The various contributions to inclusive gluonic penguins can in principal be classified according to the different kinematic regions of gluon momentum. These are (i) $q^2 = 0$ (light-like), corresponding to direct $b \rightarrow sg$ where the emitted gluon is on-shell, (ii) $q^2 > 0$ (time-like), where the off-shell gluon subsequently branches into quark or gluon pairs or where two gluons are emitted, *i.e.*, $b \rightarrow sq\bar{q}$, sgg , and (iii) $q^2 < 0$ (space-like), corresponding to the process $b\bar{q} \rightarrow s\bar{q}$. In reality gluons are not directly observed, and these regions are separated by some typical hadronic mass scale of order Λ_{QCD} .

To lowest order, these subprocesses can be described by the gauge invariant bsg three-point function

$$\Gamma_\mu^a = \frac{g_s G_F}{4\sqrt{2}\pi^2} V_{ib} V_{is}^* \bar{s} t^a \left[F_1^i(q^2 \gamma_\mu - q_\mu \not{q}) L - F_2^i i\sigma_{\mu\nu} q^\nu (m_s L + m_b R) \right] b, \quad (9.75)$$

where $t^a = \lambda^a/2$ with λ^a being the Gell-Mann matrices. At lowest order, the charge radius form factor is given by

$$F_1^t(x) = \frac{x^3 + 11x^2 - 18x}{12(x-1)^3} + \left[\frac{2}{3(x-1)} - \frac{4x^3 - 3x^2 - 4x}{6(x-1)^4} \right] \ln x, \quad (9.76)$$

with the usual definition $x = m_i^2/M_W^2$. For $i = u, c$ the external momentum dependence must be treated more carefully since $m_{u,c} < m_b/2$ resulting in

$$F_1^i(q^2) = -4 \int_0^1 dx x(1-x) \ln \left[\frac{m_i^2 - q^2 x(1-x)}{M_W^2} \right]. \quad (9.77)$$

Clearly, absorptive parts occur when $q^2 > 4m_i^2$, *i.e.*, when quark level on-shell $\bar{u}u, \bar{c}c$ intermediate states rescatter via a single gluon, giving rise to CP asymmetries [117, 118]. F_2 is related to the chromomagnetic dipole moment Wilson coefficient given in Eq. (9.32) by $F_2(x) = -2C_8^{(0)}(M_W)$. When the gluon goes on-shell, *i.e.*, $q^2 \rightarrow 0$, the F_1 contribution vanishes and only the dipole moment form factor contributes. However, for the time-like and space-like subprocesses both F_1 and F_2 participate.

The time-like subprocesses give the largest loop-induced contribution to charmless B decays. This may seem surprising at first as this subprocess is higher order in α_s compared to the light-like case. However the charge radius form factor F_1 contains large logarithms which dominate the GIM suppressed F_2 and compensate for the higher order. A partial QCD-corrected rate for $b \rightarrow sq\bar{q}$ was computed some time ago in terms of this form factor language [119, 120] with

$$\langle \mathcal{H} \rangle = \frac{G_F}{\sqrt{2}} \left[\frac{\alpha_s}{8\pi} \sum_{i=u,c} V_{ib} V_{is}^* \left(F_1^t(x_t) - F_1^i(q^2) + \frac{2}{3} \ln \frac{m_b^2}{M_W^2} \right) \right] \langle P \rangle. \quad (9.78)$$

Here, $P = \mathcal{O}_4 + \mathcal{O}_6 - (\mathcal{O}_3 + \mathcal{O}_6)/N_c$, the QCD corrections have been approximated by evaluating α_s at $\mu = m_b$, and the F_2 contributions have been neglected. This results in an inclusive branching fraction of $\sim 1\%$. A careful treatment of the subprocess $b \rightarrow sgg$ was performed to lowest order in [79] with the result that its contribution to charmless B decays is smaller with $\mathcal{B}(b \rightarrow sgg) \sim 0.1\%$. The space-like subprocess $b\bar{q} \rightarrow s\bar{q}$ is also found [119, 120] to be numerically insignificant with $\mathcal{B} \sim 0.1\%$.

The NLO QCD corrections to the time-like transitions were computed in terms of the operator product expansion in [45]. The effective Hamiltonian can be written as

$$\begin{aligned} \mathcal{H}_{eff} = & \frac{G_F}{\sqrt{2}} (V_{ub}V_{us}^*[C_1\mathcal{O}_1^u + C_2\mathcal{O}_1^u] \\ & + V_{cb}V_{cs}^*[C_1\mathcal{O}_1^c + C_2\mathcal{O}_1^c] - V_{tb}V_{ts}^* \sum_{i=3}^6 C_i\mathcal{O}_i) + h.c. . \end{aligned} \quad (9.79)$$

The resulting expressions for the partial widths for $b \rightarrow sq\bar{s}$ (note that the case of $q = s$ must include identical particle effects) are rather lengthy and can be found in Fleischer [118]. The corresponding rates for the loop-induced semi-inclusive modes are $\mathcal{B}(b \rightarrow sdd, su\bar{u}) \simeq 4 \times 10^{-3}$ and $\mathcal{B}(b \rightarrow ss\bar{s}) \simeq 3 \times 10^{-3}$. The NLO corrections are found to increase the branching fractions by 10 – 15% over the result from Eq. (9.78) above.

Computation of the loop-induced contributions to the corresponding exclusive decay modes requires evaluation of the relevant hadronic matrix elements. Here, the factorization approach is usually applied [121]. This is discussed in other sections of this book and will not be repeated here.

The light-like transition $B \rightarrow X_s$ plus an on-shell gluon is mediated by the chromomagnetic dipole operator \mathcal{O}_8 , which is given in Eq. (9.24). The leading order QCD corrections to the on-shell decay mirror those presented above for the radiative process $B \rightarrow X_s\gamma$. The effective coefficient $C_8^{(0)eff}(\mu)$ can be written as

$$\begin{aligned} C_8^{(0)eff}(\mu) = & C_8(M_W)\eta^{14/23} + C_2(M_W) \left(-0.0571\eta^{-0.8994} + 0.0873\eta^{-0.4230} \right. \\ & \left. + 0.0209\eta^{0.1456} - 0.9135\eta^{0.4086} + 0.8623\eta^{14/23} \right) , \end{aligned} \quad (9.80)$$

where $C_{2,8}^{(0)}(M_W)$ and η are defined in Eq. (9.32). The branching fraction is given by the expression (9.29) with the substitutions $\alpha \rightarrow \alpha_s$ and $7 \rightarrow 8$ and is found numerically [39] to be $\mathcal{B}(b \rightarrow sg) = (1.57 \pm 0.15_{-0.59}^{+0.86} \pm 0.23) \times 10^{-3}$, for $m_t = 175$. Here, the first error corresponds to varying the values of the input parameters ($m_t, m_c, \mathcal{B}(B \rightarrow X\ell\nu)$) within their allowed ranges, the second to varying $m_b/2 < \mu < 2m_b$, and the last to uncertainties in the determination of α_s . The full NLO corrections have yet to be computed, and until this step is complete, a full NLO prediction, which would significantly decrease the scale dependence, is not available.

There is a possibility that $\mathcal{B}(b \rightarrow sg)$ is enhanced to $\sim 10\%$ by new physics that contributes to the $\Delta B = 1$ chromomagnetic dipole operators. In many models enhanced $b \rightarrow sg$ is associated with

generation of particular combinations of quark masses or CKM mixing angles via new dynamics at TeV scales [122]. The chirality flip inherent in new contributions to the dipole operators and to quark mass matrices has a common origin, leading to direct correlations between the two. There are several known examples in which this connection can be realized without violating FCNC bounds [122]: radiatively induced quark masses at one-loop via exchange of gluinos and squarks, or via exchange of new charge $-1/3$ vectorlike quarks and neutral scalars, and dynamically generated quark masses in technicolor models with techniscalars. Note that constraints following from the measurement of $\mathcal{B}(b \rightarrow s\gamma)$ rule out enhanced $b \rightarrow sg$ via one-loop exchange of Higgs doublets and top quark. A detailed discussion of $b \rightarrow s\gamma$ in supersymmetric models of enhanced $b \rightarrow sg$ can be found in Ref. [123]. Models of quark substructure with $\mathcal{O}(\text{TeV})$ compositeness scales would be natural candidates to consider since gluon emission by an exchanged preon participating in quark mass generation would also lead to new dipole operator contributions.

Some phenomenological consequences of enhanced $b \rightarrow sg$ for B decays are a decrease in the average charm multiplicity, a decrease in the semileptonic branching ratio [124], and an increase in the kaon yields. There exist some hints for all three of these outcomes in the present world data sample; details are given in [125, 126, 127]. Hence it is worthwhile to consider placing constraints on this decay. The challenge is to define what is meant by this decay from an experimental point of view.

One technique of setting bounds on $B \rightarrow X_s g$ is by measurement of the charmless B branching ratio. Updated inclusive B to charmed-hadron flavor-blind branching ratios used to obtain the B decay charm multiplicity at the $\Upsilon(4S)$ are given in [126]. For the D/D_s yields an average of the ARGUS, CLEO 1.5 and CLEO measurements [128] can be used. The charmed-baryon and charmonium yields are those recently used by the CLEO collaboration [129]. The resulting world-average B decay charm multiplicity at the $\Upsilon(4S)$ is

$$n_c^{\text{exp}} = 107.9 \pm 4.8\%. \quad (9.81)$$

Using only the recent CLEO D/D_s yields [129] rather than the world averages gives $n_c = 111.8 \pm 5.3\%$.

The flavor-specific inclusive charmed-hadron branching ratios [130] are combined with the inclusive charmonium yield to obtain

$$\mathcal{B}^{\text{exp}}(\bar{B} \rightarrow X_{c\bar{s}}) = 19.5 \pm 3.5\%. \quad (9.82)$$

Using only the recent CLEO D/D_s yields gives $\mathcal{B}(\bar{B} \rightarrow X_{c\bar{s}}) = 21.3 \pm 3.6\%$, which is consistent with NLO QCD predictions. It is important to note that $\mathcal{B}(\bar{B} \rightarrow X_{c\bar{u}d})$ can also be determined purely experimentally by combining flavor-blind and flavor-specific charmed-hadron yields [125, 126], giving

$$\mathcal{B}^{\text{exp}}(B \rightarrow X_{c\bar{u}d}) = 45.5 \pm 6.6\%. \quad (9.83)$$

The result using only the CLEO D/D_s yields is essentially the same. It will be shown below that this is also in good agreement with NLO predictions. Similarly, one finds

$$\mathcal{B}(\bar{B} \rightarrow X_{c\bar{u}d} \rightarrow DX/D_sX) = 41.0 \pm 6.2\%, \quad (9.84)$$

which is used to normalize estimates of kaon production via non-perturbative $s\bar{s}$ pair production (from the hadronic remnants of the B), subsequently called “ $s\bar{s}$ popping.”

The charm multiplicity and $\mathcal{B}(\bar{B} \rightarrow X_{c\bar{c}s})$ can be used to bound $\mathcal{B}(\bar{B} \rightarrow X_{sg})$ via the relation

$$n_c = 1 + \mathcal{B}(B \rightarrow X_{c\bar{c}s}) - \mathcal{B}(B \rightarrow X_{no\ charm}). \quad (9.85)$$

The above determinations of n_c and $\mathcal{B}(B \rightarrow X_{c\bar{c}s})$ give

$$\mathcal{B}(B \rightarrow X_{no\ charm}) = 11.6 \pm 5.9\%. \quad (9.86)$$

Using only the recent CLEO D/D_s yields gives $9.5 \pm 6.4\%$. For comparison, a recent NLO analysis [131] gives $\mathcal{B}(B \rightarrow X_{no\ charm}) = 1.5 \pm 0.4\%$ in the Standard Model. Bounds on $\mathcal{B}(B \rightarrow X_{sg})$ follow by subtracting $\approx 1\%$ to account for $b \rightarrow u$ transitions. This is a potential hint for enhanced $b \rightarrow sg$, although it is also consistent with no $b \rightarrow sg$ at the 2σ level. In the error bars approximately $\pm 3.4\%$ is due to uncertainties in the D decay branching fractions, *i.e.*, $D^0 \rightarrow K\pi$, $D^+ \rightarrow K^+\pi\pi$, and $D_s \rightarrow \phi\pi$. The remaining errors will be considerably reduced at the B factories, so that this method will provide an important measurement of the charmless branching ratio.

9.2.5.2 Kaon counting

It is possible to check whether the potentially large charmless yield is due to $b \rightarrow s$ transitions by comparing the measured flavor-blind [62] and flavor-specific [132] inclusive $\bar{B} \rightarrow KX$ branching ratios with the kaon yields from intermediate charmed states [125, 126]. The latter are divided into two classes: kaon yields which are essentially determined by experiment and those which have to be estimated. For example, the largest known contributions are decays of intermediate D/D_s , which have been obtained by combining inclusive $\bar{B} \rightarrow DX/D_sX$ and PDG $D/D_s \rightarrow KX$ branching ratios. Sizable 4.4σ and 5.6σ excesses remain in the total K^- and K^+/K^- yields, respectively, compared to known contributions.

The most important contribution to be estimated is $s\bar{s}$ popping in $\bar{B} \rightarrow X_{c\bar{u}d}$, leading to final states of the form $DK\bar{K}X$ and $D_s\bar{K}X$.³ The additional kaon yields per $\bar{B} \rightarrow X_{c\bar{u}d} \rightarrow DX/D_sX$ decay have been estimated using a `Jetset 7.4` [133] string fragmentation model for $B \rightarrow X_{c\bar{u}d}$. The total probability of $s\bar{s}$ popping in such decays is found to be $\approx 14 \pm 3\%$. Crude but generous estimates for kaon production from Λ_c , Ξ_c and charmonium decays make up the rest.

³ $s\bar{s}$ popping in other processes, *e.g.*, $\bar{B} \rightarrow \Lambda_c X$ or $\bar{B} \rightarrow X_{c\bar{c}s}$, can be safely neglected due to small rates for these processes or phase space suppression.

Including the above estimates gives [%]

$$\begin{aligned}
\mathcal{B}(\bar{B} \rightarrow K^- X) - \mathcal{B}(\bar{B} \rightarrow X_c \rightarrow K^- X) &= 16.8 \pm 5.6, 15.2 \pm 5.8 \\
\mathcal{B}(\bar{B} \rightarrow K^+ X) - \mathcal{B}(\bar{B} \rightarrow X_c \rightarrow K^+ X) &= 1.2 \pm 4.2, 0.8 \pm 4.2 \\
\mathcal{B}(\bar{B} \rightarrow K^+/K^- X) - \mathcal{B}(\bar{B} \rightarrow X_c \rightarrow K^+/K^- X) &= 17.8 \pm 5.3, 15.8 \pm 5.7 \\
\mathcal{B}(\bar{B} \rightarrow K^0/\bar{K}^{*0} X) - \mathcal{B}(\bar{B} \rightarrow X_c \rightarrow K^0/\bar{K}^0 X) &= 4.6 \pm 6.9, 2.9 \pm 7.2.
\end{aligned} \tag{9.87}$$

The second set of numbers is obtained using only the recent CLEO $B \rightarrow DX/D_s X$ branching ratios. A 3σ K^- excess is seen. The K^- excess is also reflected in the 3σ total charged kaon excess. The K^0/\bar{K}^0 result is consistent with either no kaon excess, or sizable kaon excess.

Such kaon excesses are consistent with expectations from enhanced $b \rightarrow sg$, as discussed later. Alternatively, if the excesses are due to underestimates of kaon yields then the most likely culprit is $s\bar{s}$ popping. It is important to note that this can be determined at the B factories via measurements of $\mathcal{B}(\bar{B} \rightarrow DK\bar{K}X)$ and $\mathcal{B}(\bar{B} \rightarrow D_s\bar{K}X)$. A measurement of the additional kaon spectra in these decays is also extremely important since this is one of the largest uncertainties in determining the Standard Model inclusive kaon spectra. About 90% of the uncertainty in the charged kaon excesses in Eq. (9.87) is due to measurements of $\mathcal{B}(B \rightarrow KX)$, $\mathcal{B}(B \rightarrow DX)$, and $\mathcal{B}(D \rightarrow KX)$. The first two of these will be known much more precisely at the B factories.

9.2.5.3 n_c and $\mathcal{B}(B \rightarrow X_{cl\nu_\ell})$

In Fig. 9-23 predictions of the Standard Model and models with enhanced $b \rightarrow sg$ for n_c , $\mathcal{B}(\bar{B} \rightarrow X_{c\bar{c}s})$, $\mathcal{B}(\bar{B} \rightarrow X_{c\bar{u}d})$, and $\mathcal{B}(B \rightarrow X_{cl\nu_\ell})$ are compared with their measured values at the $\Upsilon(4S)$. For the measured semileptonic branching ratio [134]

$$\mathcal{B}^{\text{exp}}(B \rightarrow X_{cl\nu_\ell}) = 10.23 \pm 0.39, \tag{9.88}$$

is used, which is the average of the nearly model-independent ARGUS and CLEO dilepton charge correlation measurements [135]. The theoretical inputs include full on-shell scheme NLO QCD corrections [136], and $\mathcal{O}(1/m_b^2)$ HQET corrections [137] to the tree-level $b \rightarrow c$ parton model decay widths. NLO scheme-independent corrections to the $\Gamma(b \rightarrow c\bar{c}s)$ penguin contributions are also included. The remaining scheme-dependent corrections should be an order of magnitude smaller. The $b \rightarrow u$ transitions have also been taken into account to NLO [136], but the penguin $b \rightarrow s$ transitions have been neglected. As in Ref. [138] the quark pole masses are varied in the range $4.6 < m_b < 5.0$ and $0.25 < m_c/m_b < 0.33$, and the renormalization scale from $m_b/4 < \mu < m_b$.

According to Figs. 9-23a,c,e, n_c^{exp} is lower than the Standard Model range for all μ , but $\mathcal{B}^{\text{exp}}(B \rightarrow X_{c\bar{c}s})$ and $\mathcal{B}^{\text{exp}}(B \rightarrow X_{c\bar{u}d})$ are consistent with the Standard Model ranges. In particular, there is no indication that the discrepancy in n_c is due to poor theoretical control over hadronic decays, e.g., large deviations from local parton-hadron duality, beyond the sources of uncertainty already

considered above. $\mathcal{B}^{\text{exp}}(B \rightarrow X_{c\ell\nu_\ell})$ is consistent with the Standard Model range at low values of μ . Note, however, that whereas a low renormalization scale appears to be justified for the semileptonic decay widths [139]; this may not be the case for the hadronic decays [126].

Figures 9-23b,d,f use $\mathcal{B}(\bar{B} \rightarrow X_{sg}) \approx 10\%$. With this value, n_c becomes consistent with experiment, $\mathcal{B}^{\text{exp}}(B \rightarrow X_{c\bar{c}s})$ and $\mathcal{B}^{\text{exp}}(B \rightarrow X_{c\bar{u}d})$ remain consistent with experiment, and $\mathcal{B}^{\text{exp}}(B \rightarrow X_{c\ell\nu_\ell})$ can now be reproduced at larger values of μ , *i.e.*, without requiring large perturbative or non-perturbative QCD corrections.

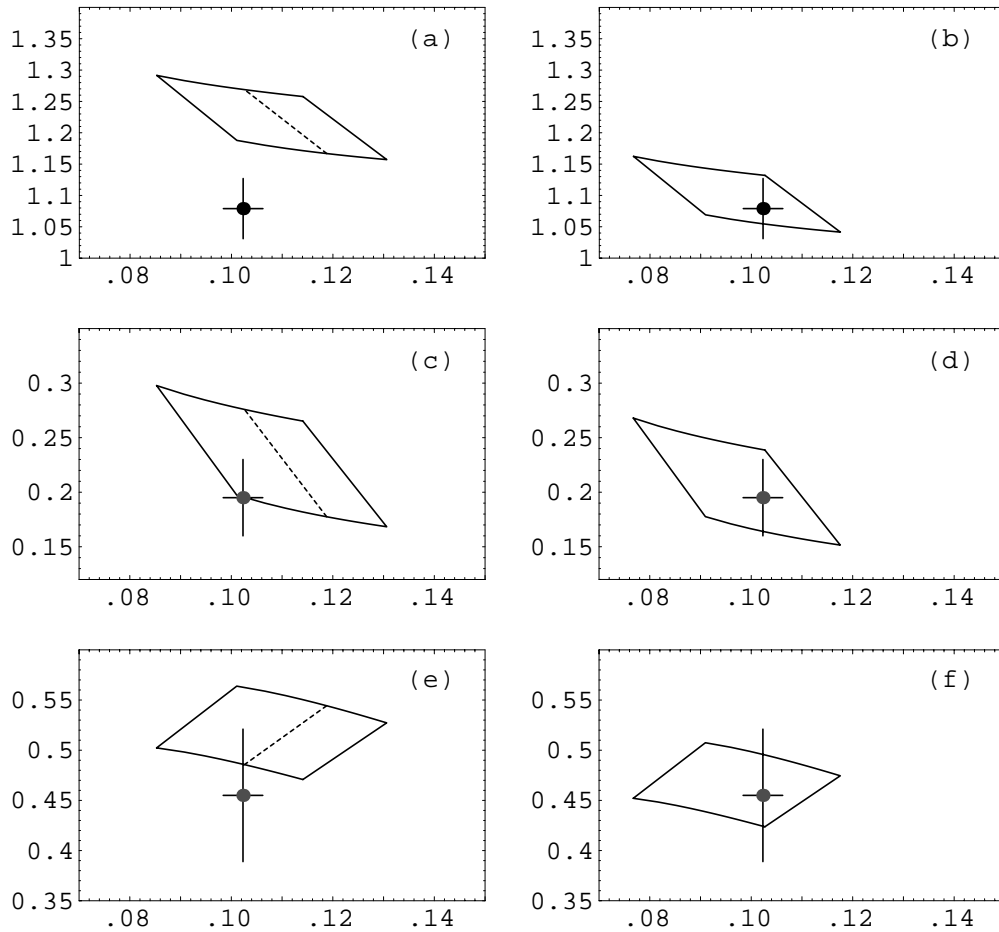


Figure 9-23. SM NLO predictions ($\alpha_s(M_Z) = .117$) for (a) n_c , (c) $\mathcal{B}(B \rightarrow X_{c\bar{c}s})$, (e) $\mathcal{B}(B \rightarrow X_{c\bar{u}d})$ vs. $\mathcal{B}(B \rightarrow X_{c\ell\nu_\ell})$. The impact of $\mathcal{B}(b \rightarrow sg) = 10\%$ is shown in (b), (d), (f), respectively. Left (right) borders are for $\mu = m_b/4$ ($\mu = m_b$). Dashed lines are for $\mu = m_b/2$. Bottom (top) borders are for $m_b = 5.0$, $m_c/m_b = 0.33$ ($m_b = 4.6$, $m_c/m_b = 0.25$) in (a)–(d). This is reversed in (e) and (f). The crosses are the experimentally determined ranges at the $\Upsilon(4S)$.

9.2.5.4 K and ϕ production from $B \rightarrow X_{sg}$

The main contribution of enhanced $b \rightarrow sg$ to K and ϕ production is fragmentation via soft $q\bar{q}$ popping. In the b quark rest frame the gluon and s quark emerge back to back with energy $m_b/2$. In the string picture a string connects the s and spectator quarks and the gluon is a kink in the string which carries energy and momentum [133]. The ensuing fragmentation is modeled [125] using a Jetset 7.4 Monte Carlo with recent DELPHI tunings [140]. The same tunings accurately reproduce the K and ϕ spectra observed in the e^+e^- continuum near the Υ resonances [141]. The large energy release in this decay leads to high-multiplicity final states, or soft K and ϕ momentum spectra.

The number of kaons per $\bar{B} \rightarrow X_{sg}$ decay produced in Monte-Carlo [125] is 0.67 (K^-), 0.19 (K^+), 0.62 (\bar{K}^0), and 0.15 (K^0). As an example of the impact of enhanced $b \rightarrow sg$ on the charged kaon excesses, note that for $\mathcal{B}(\bar{B} \rightarrow X_{sg}) \sim 15\%$ the observed inclusive kaon yields can all be accounted for at the 1σ level.

Hard $q\bar{q}$ fragmentation of the gluon becomes important at large K and ϕ momenta. In this case the decay $b \rightarrow sg^* \rightarrow sq\bar{q}$ can be described by an effective four-quark operator. The corresponding contribution to fast K or ϕ production can be estimated using factorization [142], *i.e.*, the meson is formed from the primary quarks in the decay. This mechanism will also be important when discussing direct CP violation.

9.2.5.5 Semi-inclusive K and ϕ momentum spectra

In Fig. 9-24 inclusive K_s momentum spectra (in the $\Upsilon(4S)$ rest frame) generated by the $\bar{B} \rightarrow X_{sg}$ and (SLD tuned) CLEO $\bar{B} \rightarrow X_c$ Monte Carlos are compared with the measured spectrum [132]. In the $b \rightarrow sg$ Monte Carlo the b and spectator quark momenta are modeled using the Gaussian distribution of Ref. [143], with $p_F = 250$ MeV/c. Parton showers are also included. For those momenta where most $b \rightarrow sg$ kaons are produced the expected ratio of signal to Standard Model background is $\approx 1 : 5 - 1 : 10$. Clearly, resolving the presence of enhanced $b \rightarrow sg$ at these momenta *directly* would be a very difficult task. A vertexing veto of charm would have to be extremely efficient to significantly enhance the $b \rightarrow sg$ component. Perhaps the relative back-to-back geometry of signal events versus the more spherical geometry of background events could help discriminate between the two.

A promising strategy is to search for kaons from enhanced $b \rightarrow sg$ at higher momenta, *e.g.*, $p_K \gtrsim 1.8$ GeV/c.⁴ According to Fig. 9-24b the ratio of enhanced $b \rightarrow sg$ signal to Standard Model background in this region is expected to be $\sim 1 : 1$. Although branching ratios are reduced to the

⁴A significant kaon signal at still higher momenta, *e.g.*, above 2.1 GeV/c, where the background from intermediate charm states is highly suppressed would provide an unambiguous signal for charmless $b \rightarrow s$ transitions. Unfortunately, because of very large theoretical uncertainties above 2.1 GeV/c [125] it would be very difficult to

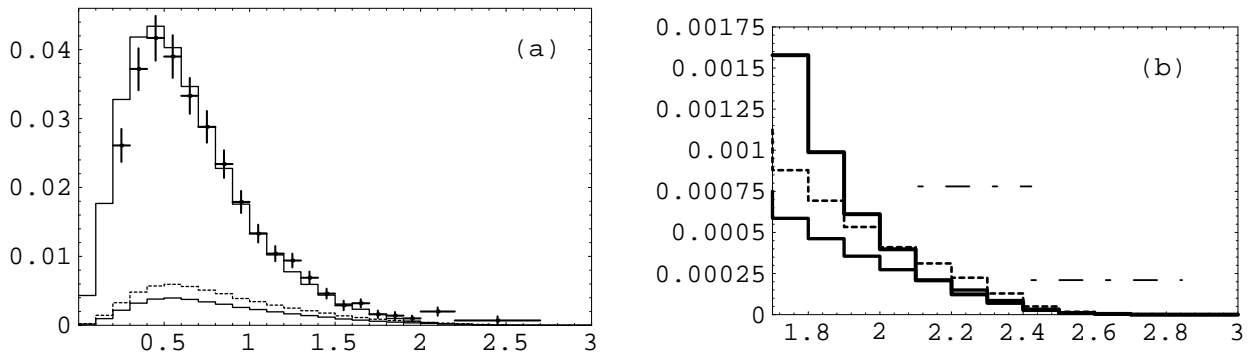


Figure 9-24. $\mathcal{B}(B \rightarrow K_s X)$ vs. p_{K_s} [GeV/c]. Branching ratios are for 0.1 GeV/c bins except CLEO upper limits. (a) ARGUS data (crosses), SLD/CLEO Monte Carlo (upper solid), Monte Carlo for $\mathcal{B}(\bar{B} \rightarrow X_{sg}) = 10\%$ (lower solid) and 15% (dashed). (b) fast kaon spectra: CLEO 90% CL UL's for $2.11 < p_{K_s} < 2.42$, $2.42 < p_{K_s} < 2.84$ (dot - dashed), SLD Monte Carlo (thick solid), Monte Carlo for $\mathcal{B}(\bar{B} \rightarrow X_{sg}) = 10\%$ (solid), 15% (dashed).

10^{-3} level, high statistics analysis will be possible at the B factories. In principle, the background can be determined experimentally with little theoretical input. For example, the dominant $B \rightarrow D \rightarrow K$ contributions can be obtained directly by folding measured $B \rightarrow DX$ and MARK III $D \rightarrow KX$ inclusive momentum spectra. Of course, the D spectra will be determined to very high precision at the B factories. Furthermore, the poorly known $s\bar{s}$ popping and $B \rightarrow D_s \rightarrow K$ contributions should be much softer and are unlikely to contribute significantly. In addition, a vertexing veto of charm of modest efficiency, which should certainly be available at BABAR, would significantly enhance the $b \rightarrow sg$ component above 1.8 GeV/c. The SLD Collaboration is in fact carrying out such an analysis for high p_T K^\pm production [145].

It is important to use an essentially model-independent procedure when searching for new physics in the kaon spectra. The high-momentum search advocated above satisfies this criterion since it minimizes the need to model Standard Model background. On the other hand, fitting the entire measured spectra with Monte Carlo $B \rightarrow X_{sg}$ and $B \rightarrow X_c$ components kept free is too model-dependent at the present time to reach definitive conclusions. This is especially true since the shapes of the two components are not expected to differ dramatically over a wide range of momenta, as indicated in Figs. 9-24 and 9-25. Of course, once more precise knowledge of the Standard Model spectra is available, particularly the $s\bar{s}$ popping and $D_s \rightarrow K$ components, this will be a more reliable technique. The DELPHI Collaboration has been pursuing such a strategy [146].

determine whether the origin is purely due to Standard Model penguins or intervention of enhanced $b \rightarrow sg$, unless the signal is close to the current bound [144].

Finally, Fig. 9-25 compares the inclusive ϕ momentum spectrum generated by the $B \rightarrow X_{sg}$ Monte Carlo to the measured spectrum in the $\Upsilon(4S)$ rest frame [147]. x is the scaled momentum variable, $x \equiv p_\phi/p_{beam}$. For $\mathcal{B}(B \rightarrow X_{sg}) \approx 10\%$, the ϕ yield is predicted to account for about 16% of the total ϕ yield. However, fast ϕ production is essentially consistent with the 90% confidence level CLEO upper limit [148] in Fig. 4b. As in the case of K production, a signal beyond the $B \rightarrow D$ end point would be indicative of charmless b decays but would be unlikely to place a useful constraint on $\mathcal{B}(b \rightarrow sg)$ because of large theoretical uncertainties. The Monte Carlo $b \rightarrow sg$ spectrum is much broader than the measured spectrum and therefore considerably harder than the Standard Model spectrum, so there should be significant distortion if $b \rightarrow sg$ is enhanced. In principle, such a test is possible at the B factories. Unfortunately, there is not enough currently known about $D/D_s \rightarrow \phi$ decays to reliably estimate the Standard Model spectrum.

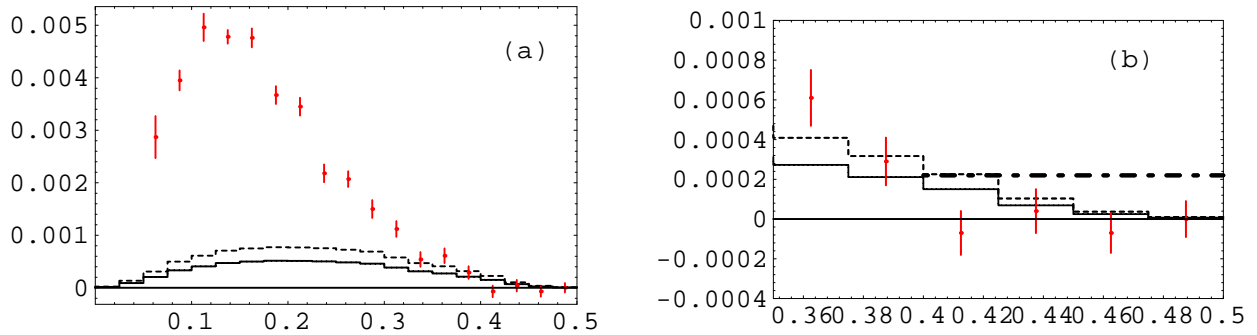


Figure 9-25. $\mathcal{B}(B \rightarrow \phi X)$ vs. x . Branching ratios are for 0.025 bins in x , except the CLEO upper limit. (a) CLEO data and Monte Carlo for $\mathcal{B}(B \rightarrow X_{sg}) = 10\%$ (solid), 15% (dashed). (b) same as (a) with CLEO 90% confidence level upper limit for $0.4 < x < 0.5$ (dot-dashed) included.

9.2.5.6 CP violation

Enhanced dipole operator coefficients can carry new CP -violating weak phases. Furthermore, for $\mathcal{B}(b \rightarrow sg) \sim 10\%$ the dipole amplitudes for rare hadronic decays are of same order as the Standard Model amplitudes [126]. Since the strong interaction phases associated with the two amplitudes must in general differ, their interference can lead to large CP asymmetries. Factorization model results for $B^\pm \rightarrow \phi K^\pm$, $B \rightarrow \phi X_s$ and $B^\pm \rightarrow K^0 \pi^\pm$ will be presented here. In the Standard Model the leading contributions to these decays are due to the penguin $b \rightarrow s\bar{s}s$ and $b \rightarrow s\bar{d}d$ transitions, respectively. In the absence of soft final state interactions the expected CP -violating asymmetries in these modes are $\sim 1\%$ [118], so that they are thought to be particularly well suited for new physics searches.

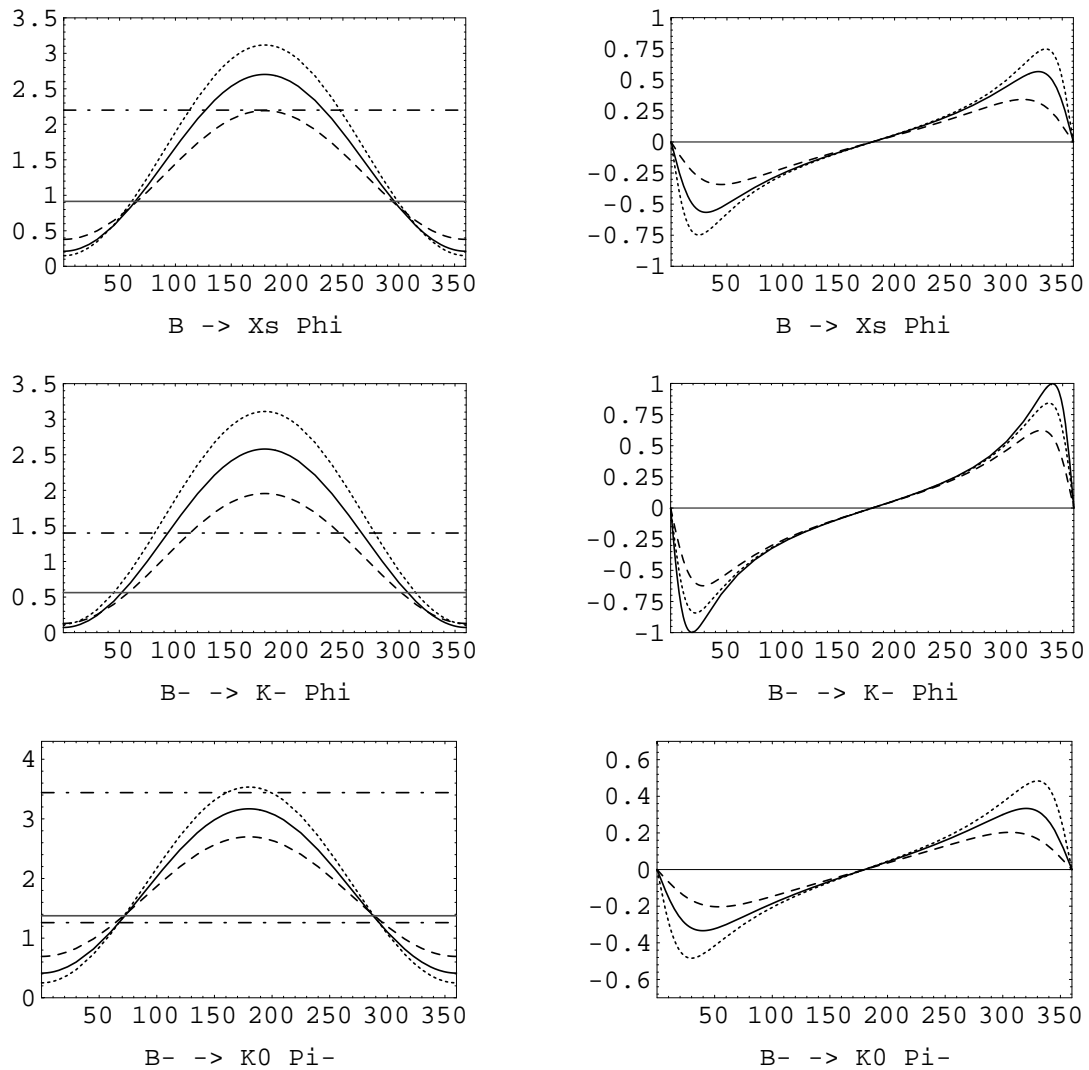


Figure 9-26. $10^4 \mathcal{B}(B \rightarrow \phi X_s)$, $10^5 \mathcal{B}(B^\pm \rightarrow \phi K^\pm)$, and $10^5 \mathcal{B}(B^\pm \rightarrow K^0 \pi^\pm)$ vs. θ_{11} and corresponding direct CP asymmetries vs. θ_{11} for $\mathcal{B}(b \rightarrow sg) \approx 15\%$ (dotted curves), 10% (solid curves), 5% (dashed curves). Horizontal solid lines are Standard Model branching ratio estimates. Horizontal dot-dashed lines are CLEO branching ratio upper limits for $B \rightarrow \phi K, \phi X_s$ and measured interval for $B^\pm \rightarrow K^0 \pi^\pm$.

The dipole operators

$$O_{11} = \frac{g_s}{32\pi^2} m_b(\mu) \bar{s} \sigma_{\mu\nu} R t^a b G_a^{\mu\nu}, \quad O'_{11} = \frac{g_s}{32\pi^2} m_b(\mu) \bar{s} \sigma_{\mu\nu} L t^a b G_a^{\mu\nu} \quad (9.89)$$

are included in the factorization model by allowing the gluon to go off-shell and turn into a quark-antiquark pair. The dipole operator Wilson coefficients can be parametrized as⁵

$$c_{11} = -|c_{11}| e^{i\theta_{11}}, \quad c'_{11} = -|c'_{11}| e^{i\theta'_{11}}. \quad (9.90)$$

For economy, only results with $c'_{11} = 0$ are presented. Strong phases originating at NLO from $c\bar{c}$ rescattering [149] have been taken into account in the Standard Model penguin amplitudes using the NLO scheme-independent effective Wilson coefficient formalism of Refs. [118, 150].

In Fig. 9-26 rare decay branching ratios with enhanced $b \rightarrow sg$ (averaged over CP conjugate modes) are compared to CLEO measurements [148, 151, 152] and Standard Model predictions. The large dependence on θ_{11} confirms that there can be substantial destructive or constructive interference between the penguin and dipole amplitudes. Given the large uncertainties in the factorization model estimates it is clear that the experimental constraints can be satisfied for a significant range of θ_{11} , even if $\mathcal{B}(b \rightarrow sg) \approx 15\%$. The general case where both O_{11} and O'_{11} are enhanced is even less constrained. Note that the direct CP asymmetries can easily exceed 20%. This is more than an order of magnitude larger than naive Standard Model estimates which do not take soft final state interactions into account. Moreover, even if there were no strong interaction phases, hence no direct CP asymmetries, large effects would still be seen by comparing time-dependent CP asymmetries for $B \rightarrow \psi K_s$ and $B \rightarrow \phi K_s$ [153].

9.2.5.7 Conclusion

There are two novel features of radiative B decays which can arise in models with enhanced $b \rightarrow sg$ and which are accessible at the B factories. It has been pointed out [154] that new chromomagnetic dipole operator-mediated graphs in which the spectator quark radiates a photon can lead to large isospin violation in $B \rightarrow K^* \gamma$. In particular, rate asymmetries between the $K^{*-} \gamma$ and $K^{*0} \gamma$ final states could exceed 50%, compared to only a few % in the standard model. In models in which enhanced dipole operators are associated with generation of V_{ub} the $b \rightarrow d\gamma$ transition can be enhanced [122] so that, for example, $\mathcal{B}(B \rightarrow \rho\gamma)$ could be an order of magnitude larger than in the Standard Model.

It is remarkable that enhanced $b \rightarrow sg$ can evade all existing rare B decay constraints. To summarize, there are two experimental hints for enhanced $b \rightarrow sg$, a 2σ deficit in charm counting and a 3σ deficit in kaon counting. Significantly improved precision in charm and kaon counting will require a reduction in uncertainties in the absolute D/D_s branching scales. Improved precision

⁵In the Standard Model $c_{11} \approx -.3$, and c'_{11} is a factor m_s/m_b smaller hence negligible.

in kaon counting will also require an experimental determination of the amount of $s\bar{s}$ popping in B decays via future measurements of $\mathcal{B}(\bar{B} \rightarrow DK\bar{K}X)$ and $\mathcal{B}(\bar{B} \rightarrow D_s\bar{K}X)$. There are also well-known hints for something new from comparison of NLO Standard Model predictions for the charm multiplicity and semileptonic branching ratio with measurements at the $\Upsilon(4S)$. All these things are only hints, because there are large theoretical uncertainties in the relevant predictions. Unfortunately, improved theoretical precision poses a difficult challenge.

A promising direct search strategy is the search for high-momentum kaon excesses in B decays, *e.g.*, $p_K \gtrsim 1.8$ GeV/ c . A `Jetset 7.4` analysis indicates that for $\mathcal{B}(b \rightarrow sg) \sim 10\%$ the corresponding $B \rightarrow KX$ branching ratios are of order 10^{-3} . The Standard Model background at these momenta is of same order and is dominated by kaon yields from intermediate D^0/D^+ decays, which can be determined experimentally. In addition, new weak phases in the chromomagnetic dipole operator coefficients can lead to large CP violation. For example, direct CP -violating asymmetries in $B^\pm \rightarrow \phi K^\pm$ and $B^\pm \rightarrow K^0\pi^\pm$ can easily exceed 20%. In the absence of final state interactions small $\sim 1\%$ asymmetries are expected for these decays in the Standard Model.

At the present time, despite several interesting hints, compelling evidence for or against the enhanced $b \rightarrow sg$ hypothesis is lacking. Direct searches and related measurements at the B factories should resolve this issue.

9.2.5.8 Experimental considerations

Several previous experiments have attempted $b \rightarrow sg$ searches using the method described above, but they have all been limited in one way or another. CLEO lacks particle ID, but has studied the K_s spectrum. The analysis has been limited by continuum background, however. ARGUS has looked at the charged kaon spectrum, but in addition to continuum background, they also had to contend with low statistics. At the Z^0 , SLD and Delphi have used their Cherenkov detectors to study the charged kaon spectrum, but have been limited by lack of knowledge of the B boost. Delphi has placed a preliminary limit of $\mathcal{B}(b \rightarrow sg) < 4\%$, but their result is new and somewhat controversial. SLD has observed a 2.5σ excess of kaons with high momentum transverse to the B flight direction. SLD, however, is limited by statistics.

BaBar should essentially remove all of these limitations. The statistics, will, of course, be ample and the particle ID provided by the DIRC will allow study of the charged kaon spectrum. The DIRC particle ID should be sufficient to suppress mis-ID backgrounds since in the SLD analysis, with somewhat worse π/K separation, mis-ID accounts for only about 25% of the background. BaBar will still have to contend with continuum background, and this will probably form the bulk of the work that will be needed.

This analysis has not yet really begun. But, it seems clear that BaBar is uniquely suited to determine, once and for all, whether $b \rightarrow sg$ is greatly enhanced over Standard Model predictions or not.

9.3 Model-Independent Test of the Standard Model

A powerful and model-independent test of the Standard Model is provided by the simultaneous experimental determination of the magnitudes and signs of the Wilson coefficients which contribute to the flavor-changing neutral current transitions discussed in this chapter. In some ways a determination of the Wilson coefficients via a global fitting procedure in rare B decays is similar to the searches for new physics in precision electroweak measurements through the use of the oblique parameters S, T, U [155]. In general there are three ways new physics can affect such a global fit to the coefficients: (i) the numerical values for the coefficients are found to agree with Standard Model expectations with a good χ^2 ; in this case new physics is either decoupled or doesn't exist. (ii) A quality fit is obtained, but the fit values of the coefficients deviate from Standard Model expectations. (iii) The χ^2 value for the best parameter fit is found to be very large and cannot be explained by an under estimation of systematic uncertainties. It is this latter case which indicates the existence of additional non-Standard Model operators, *e.g.*, right-handed operators.

Measurements of $\mathcal{B}(B \rightarrow X_s \gamma)$ alone constrain the magnitude, but not the sign, of $C_7^{eff}(\mu)$. The coefficients at the matching scale can be written in the form $C_i(M_W) = C_i^{SM}(M_W) + C_i^{new}(M_W)$, where $C_i^{new}(M_W)$ clearly represents the contributions from new interactions. Due to operator mixing, $B \rightarrow X_s \gamma$ then limits the possible values for $C_i^{new}(M_W)$ for $i = 7, 8$. These bounds are summarized in Fig. 9-27. Here, the solid bands correspond to the constraints obtained from the current CLEO measurement, taking into account the variation of the renormalization scale $m_b/2 \leq \mu \leq 2m_b$, as well as the allowed ranges of the other input parameters. The dashed bands represent the constraints when the scale is fixed to $\mu = m_b$. Note that large values of $C_8^{new}(M_W)$ are allowed even in the region where $C_7^{new}(M_W) \simeq 0$. Experimental bounds on the decay $b \rightarrow sg$ are needed to constraint C_8 .

Measurement of the kinematic distributions associated with the final-state lepton pair in $B \rightarrow X_s l^+ l^-$ as well as the rate for $B \rightarrow X_s \gamma$ allows for the determination of the sign and magnitude of all the Wilson coefficients for the contributing operators in a model-independent fashion [90, 88, 156]. Here, a Monte Carlo analysis is performed in order to ascertain how much quantitative information will be obtainable at future B -factories. For the process $B \rightarrow X_s l^+ l^-$, the lepton pair invariant-mass distribution and forward-backward asymmetry for $\ell = e, \mu, \tau$, and the tau polarization asymmetry for $B \rightarrow X_s \tau^+ \tau^-$ are considered. Recall that the asymmetries have the form $A(\hat{s}) \sim C_{10}(\text{Re } C_9^{eff} f_1(\hat{s}) + C_7^{eff} f_2(\hat{s}))$, and hence are sensitive probes of the Wilson coefficients. Monte Carlo “data” is generated, assuming that the Standard Model is realized, by dividing the lepton pair invariant-mass spectrum into nine bins. Six of the bins are taken to be in the low dilepton invariant-mass region below the J/ψ resonance (in order to take advantage of the larger statistics), with $0.02 \leq \hat{s} \leq 0.32$ and a bin width of $\Delta \hat{s} = 0.05$. The region near $q^2 = 0$ has been cut in order to remove the photon pole. The high $M_{\ell^+ \ell^-}$ region above the ψ' pole is divided into three bins, corresponding to $0.6 \leq \hat{s} \leq 0.7$, $0.7 \leq \hat{s} \leq 0.8$, and $0.8 \leq \hat{s} \leq 1.0$. The number

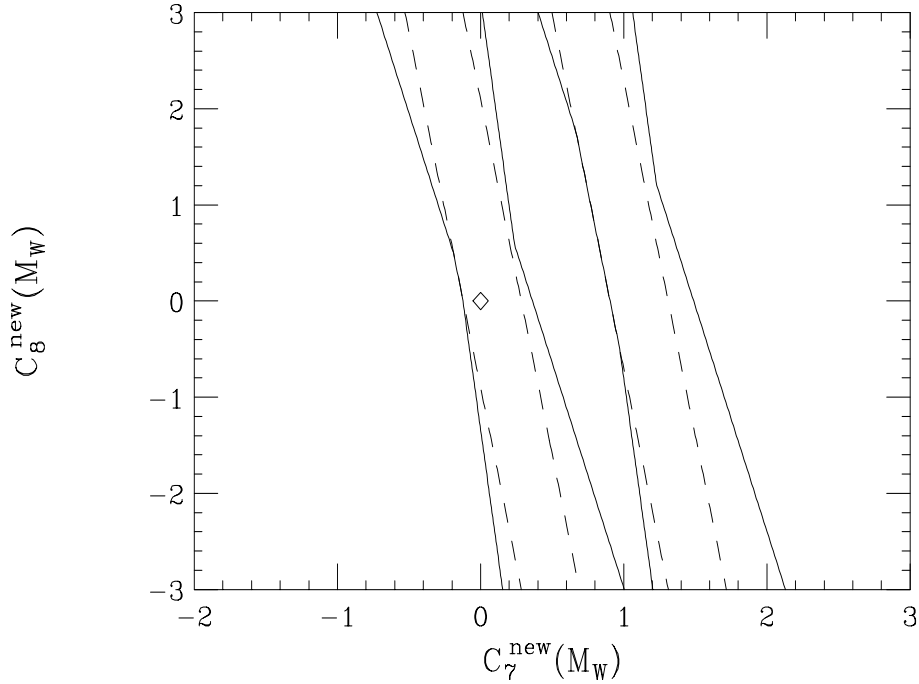


Figure 9-27. Bounds on the contributions from new physics to $C_{7,8}$. The region allowed by the CLEO data corresponds to the area inside the solid diagonal bands. The dashed bands represent the constraints when the renormalization scale is set to $\mu = m_b$. The diamond at the position $(0,0)$ represents the standard model.

of events per bin is calculated as usual via

$$N_{bin} = \mathcal{L} \int_{\hat{s}_{min}}^{\hat{s}_{max}} \frac{d\Gamma(B \rightarrow X_s l^+ l^-)}{d\hat{s}} d\hat{s}, \quad (9.91)$$

and the average value of the asymmetries in each bin is

$$\langle A \rangle_{bin} = \frac{\mathcal{L}}{N_{bin}} \int_{\hat{s}_{min}}^{\hat{s}_{max}} A \frac{d\Gamma(B \rightarrow X_s l^+ l^-)}{d\hat{s}} d\hat{s}. \quad (9.92)$$

The “data” is statistically fluctuated using a normalized Gaussian distributed random number procedure, where the statistical errors are given by $\delta N = \sqrt{N}$ and $\delta A = \sqrt{(1 - A^2)/N}$. The errors in each bin are expected to be statistics dominated and hence systematic errors are neglected here. For $B \rightarrow X_s \gamma$, the “data” is again statistically fluctuated for the inclusive rate. However, in this case, the statistical precision will eclipse the possible systematic and theoretical accuracy; thus a flat 10% error is assumed in the determination of the branching fraction in anticipation of future theoretical and experimental improvements. A three dimensional χ^2 fit to the coefficients $C_{7,9,10}(\mu)$ is performed, employing the usual prescription

$$\chi_i^2 = \sum_{bins} \left(\frac{Q_i^{obs} - Q_i^{SM}}{\delta Q_i} \right)^2, \quad (9.93)$$

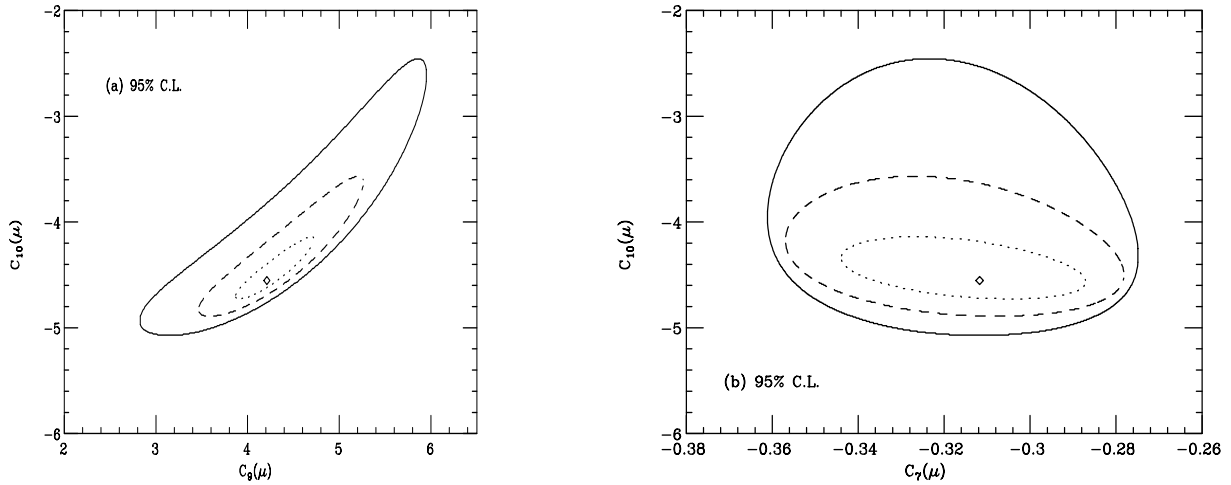


Figure 9-28. The 95% confidence level projections in the (a) $C_9 - C_{10}$ and (b) $C_7^{eff} - C_{10}$ planes, where the allowed regions lie inside of the contours. The solid, dashed, and dotted contours correspond to 3×10^7 , 10^8 , and 5×10^8 $B\bar{B}$ pairs. The Standard Model prediction is labeled by the diamond.

for each observable quantity Q_i . This procedure is repeated for three values of the integrated luminosity, 3×10^7 , 10^8 , and 5×10^8 $B\bar{B}$ pairs. The 95% confidence level allowed regions as projected onto the $C_9(\mu) - C_{10}(\mu)$ and $C_7^{eff}(\mu) - C_{10}(\mu)$ planes are depicted in Figs. 9-28(a-b), where the diamond represents the expectations in the Standard Model. The determinations are seen to be relatively poor for 3×10^7 $B\bar{B}$ pairs and that higher statistics are required in order to focus on regions centered around the Standard Model. Clearly, C_9 and C_{10} are highly correlated, whereas C_7^{eff} and C_{10} are not. The χ^2 values are found to be good with $\chi^2 = 22.3/25$ degrees of freedom for the large luminosity case. Note that the sign, as well as the magnitude, of all the coefficients including C_7^{eff} can now be determined. The effects of an extended operator basis on this fit procedure is discussed in Chapter 13 and [157].

9.4 Summary

The theoretical description of the short-distance physics mediating rare decay modes of the B meson is well in hand. The next-to-leading order QCD corrections have been computed for essentially every channel. For inclusive decays the theoretical uncertainties are at the 10 – 15% level. For exclusive channels the uncertainties in hadronic matrix elements dominate the predictions.

The radiative decays, $B \rightarrow X_s \gamma$ and $B \rightarrow K^* \gamma$, should be well measured with a nominal year's data sample of 30 fb^{-1} . These branching fractions are a few $\times 10^{-4}$ and $\times 10^{-5}$, respectively, which is no longer rare at the BaBar design luminosity. Improvement of the systematic error on the inclusive $B \rightarrow X_s \gamma$ measurement, and an attempt to describe the inclusive rate as the sum of the exclusive channels, are both interesting topics made accessible by BaBar's vertex detector and particle identification.

Measurements of $B \rightarrow (\rho, \omega) \gamma$ and $b \rightarrow d \gamma$ appear to require more data. However, the sum of the $\rho(\omega) \gamma$ exclusive modes is 1/10 of the $K^* \gamma$ ones (see Table 9-8), and our canonical year's sample is ~ 20 times what it took CLEO to find $K^* \gamma$, so observation of these channels should be pursued aggressively. While long-distance effects do complicate the extraction of $|\frac{V_{td}}{V_{ts}}|$, the measurement of the inclusive rate $b \rightarrow d \gamma$ is an important one which requires the excellent particle identification of BaBar. These channels are also a very promising place to look for large CP -violating effects predicted within the Standard Model.

Measurements of the branching fractions for $B^+ \rightarrow \ell^+ \nu$ and $\ell^+ \nu \gamma$ will require very large data samples (100 to 300 fb^{-1}), and some significant advances in background rejection. $B^+ \rightarrow \mu^+ \nu$ seems more promising than $B^+ \rightarrow \tau^+ \nu$.

$B \rightarrow K^{(*)} \ell^+ \ell^-$ and $b \rightarrow s \ell^+ \ell^-$ should be observable within a few years. These channels really become interesting when the lepton pair invariant-mass and forward-backward asymmetry can be measured. This will require a very large data sample.

$b \rightarrow s \nu \bar{\nu}$ may be accessible if background problems can be resolved. In addition to its physics interest, it is a possible background to the search for $B^+ \rightarrow \tau^+ \nu$.

The possibility of a large branching ratio for $b \rightarrow s g$ may not be resolved before BaBar turns on, in which case measurements of charm and kaon production are required, as well as studies of possible excesses in K and ϕ spectra at the kinematic limit for B decays.

Table 9-7. Standard Model predictions and the present experimental bound [62] for the branching fractions of the B^- leptonic decay modes, assuming $f_B = 180 \text{ MeV}$ and taking the central value [62] of the CKM matrix element V_{ub} .

Mode	Experimental Bound	SM Prediction
$e^- \bar{\nu}_e$	$< 1.5 \times 10^{-5}$ (CLEO)	6.9×10^{-12}
$\mu^- \bar{\nu}_\mu$	$< 2.1 \times 10^{-5}$ (CLEO)	2.9×10^{-7}
$\tau^- \bar{\nu}_\tau$	$< 5.7 \times 10^{-4}$ (L3)	6.6×10^{-5}

Table 9-8. Standard Model predictions for the branching fractions for various rare B meson decays with $f_{B_d} = 180$ MeV. Also shown are the current experimental limits [62].

Decay Mode	Experimental Limit	B_{SM}
$B_d^0 \rightarrow e^+e^-$	$< 5.9 \times 10^{-6}$ (CLEO)	2.6×10^{-15}
$B_d^0 \rightarrow \mu^+\mu^-$	$< 1.6 \times 10^{-6}$ (CDF)	1.1×10^{-10}
$B_d^0 \rightarrow \tau^+\tau^-$	—	3.1×10^{-8}
$B^0 \rightarrow e^\pm\mu^\mp$	$< 5.9 \times 10^{-6}$ (CLEO)	0
$B^0 \rightarrow e^\pm\tau^\mp$	$< 5.3 \times 10^{-4}$ (CLEO)	0
$B^0 \rightarrow \mu^\pm\tau^\mp$	$< 8.3 \times 10^{-4}$ (CLEO)	0
$B_d^0 \rightarrow \gamma\gamma$	$< 3.9 \times 10^{-5}$ (L3)	1.0×10^{-8}
$B \rightarrow X_s + \gamma$	$(3.15 \pm 0.35 \pm 0.41) \times 10^{-4}$ (CLEO)	$(3.28 \pm 0.30) \times 10^{-4}$
$B \rightarrow K^* + \gamma$	$(4.2 \pm 0.8 \pm 0.6) \times 10^{-5}$ (CLEO)	$(4.45 \pm 1.13) \times 10^{-5}$
$B \rightarrow X_d + \gamma$	—	$(1.6 \pm 1.0) \times 10^{-5}$
$B^0 \rightarrow \rho^0\gamma$	$< 3.9 \times 10^{-5}$ (CLEO)	$(0.65 \pm 0.35) \times 10^{-6}$
$B^0 \rightarrow \omega^0\gamma$	$< 1.3 \times 10^{-5}$ (CLEO)	$(0.65 \pm 0.35) \times 10^{-6}$
$B^- \rightarrow \rho^-\gamma$	$< 1.1 \times 10^{-5}$ (CLEO)	$(1.5 \pm 1.1) \times 10^{-6}$
$B \rightarrow X_s + e^+e^-$	$< 5.7 \times 10^{-5}$ (CLEO)	$(6.25_{-0.93}^{+1.04}) \times 10^{-6}$
$B \rightarrow X_s + \mu^+\mu^-$	$< 5.8 \times 10^{-5}$ (CLEO)	$(5.73_{-0.78}^{+0.75}) \times 10^{-6}$
$B \rightarrow X_s + \tau^+\tau^-$	—	$(3.24_{-0.54}^{+0.44}) \times 10^{-7}$
$B^0 \rightarrow K^0 ee/\mu\mu$	$< 1.5/2.6 \times 10^{-4}$ (CLEO)	$(5.0 \pm 3.0)/(3.0 \pm 1.8) \times 10^{-7}$
$B^- \rightarrow K^- ee/\mu\mu$	$< 1.2/0.9 \times 10^{-5}$ (CLEO)	$(5.0 \pm 3.0)/(3.0 \pm 1.8) \times 10^{-7}$
$B^0 \rightarrow K^{*0} ee/\mu\mu$	$< 1.6/2.5 \times 10^{-5}$ (CLEO/CDF)	$(2.0 \pm 1.0)/(1.25 \pm 0.62) \times 10^{-6}$
$B^- \rightarrow K^{*-} ee/\mu\mu$	$< 6.9/11 \times 10^{-4}$ (CLEO)	$(2.0 \pm 1.0)/(1.25 \pm 0.62) \times 10^{-6}$
$B^+ \rightarrow K^+ e^\pm\mu^\mp$	$< 1.2 \times 10^{-5}$ (CLEO)	0
$B^0 \rightarrow K^{*0} e^\pm\mu^\mp$	$< 2.7 \times 10^{-5}$ (CLEO)	0
$B \rightarrow X_s + \nu\bar{\nu}$	$< 7.7 \times 10^{-4}$ (ALEPH)	$(4.1_{-1.0}^{+0.8}) \times 10^{-5}$

References

- [1] D. Guetta and E. Nardi, *Phys. Rev. D* **58**, 012001 (1998).
- [2] Y. Grossman, Z. Ligeti and E. Nardi, *Phys. Rev. D* **55**, 2768 (1997).
- [3] Y. Grossman, Z. Ligeti and E. Nardi, *Nucl. Phys.* **B465**, 369 (1996); *Nucl. Phys.* **B480**, 753(E) (1996).
- [4] R. Ammar *et al.*, (CLEO Collaboration), *Phys. Rev. D* **49**, 5701 (1994).
- [5] M. Artuso *et al.*, (CLEO Collaboration), *Phys. Rev. Lett.* **75**, 785 (1995).
- [6] S. Wagner, <http://www.slac.stanford.edu/stevew/munu.html>
- [7] S. Yang, "A Search for $B \rightarrow \ell\nu$ at BaBAR," BaBAR Note # 393, (1997).
- [8] M. Carpinelli, <http://www.pi.infn.it/mca/btau.html>
- [9] M. Acciarri *et al.*, (L3 Collaboration), *Phys. Lett. B* **396**, 327 (1997).
- [10] Section 8.3.3, BaBAR Technical Design Report, SLAC-R-95-457, and references therein.
- [11] W. Skiba and J. Kalinowski, *Nucl. Phys.* **B404**, 3 (1993).
- [12] G. Buchalla and A. J. Buras, *Nucl. Phys.* **B400**, 225 (1993).
- [13] T. Inami and C. S. Lim, *Prog. Th. Phys.* **65**, 297 (1981); 1772(E).
- [14] S. Yang, "A Search for B to Two Charged Leptons at BaBAR," BaBAR Note # 394, (1997).
- [15] F. Abe *et al.*, (CDF Collaboration), *Phys. Rev. Lett.* **76**, 4675 (1996).
- [16] G. Burdman, T. Goldman and D. Wyler, *Phys. Rev. D* **51**, 111 (1995).
- [17] A. Khodjamirian, G. Stoll and D. Wyler, *Phys. Lett. B* **358**, 129 (1995).
- [18] G. Eilam, I. Halperin and R. R. Mendel, *Phys. Lett. B* **361**, 137 (1995).
- [19] D. Atwood, G. Eilam and A. Soni, *Mod. Phys. Lett. A* **11**, 1061 (1996).
- [20] P. Colangelo, F. De Fazio and G. Nardulli, *Phys. Lett. B* **386**, 328 (1996); *Phys. Lett. B* **372**, 331 (1996).
- [21] G. Eilam, G. D. Lu and D. X. Zhang, *Phys. Lett. B* **391**, 461 (1997).
- [22] T. M. Aliev, A. Öspineci and M. Savci, *Phys. Rev. D* **55**, 7059 (1997).

- [23] G. Burdman, *Phys. Rev. D* **57**, 4254 (1998).
- [24] N. Isgur and M. B. Wise, *Phys. Rev. D* **42**, 2388 (1990);
G. Burdman and J. F. Donoghue, *Phys. Lett. B* **270**, 55 (1991).
- [25] G. De Nardo and L. Lista, “Study of the Rare Decay $B \rightarrow \mu\mu\gamma$,” BaBar Note # 396, (1997).
- [26] T. E. Browder *et al.*, (CLEO Collaboration), *Phys. Rev. D* **56**, 11 (1997).
- [27] B. Grinstein, R. Springer and M. B. Wise, *Nucl. Phys.* **B339**, 269 (1990);
H. Simma, *Z. Phys. C* **61**, 67 (1994).
- [28] G. Buchalla, A. J. Buras and M. E. Lautenbacher, *Rev. Mod. Phys.* **68**, 1125 (1996).
- [29] M. S. Alam *et al.*, (CLEO Collaboration), *Phys. Rev. Lett.* **74**, 2885 (1995). For the result from an updated analysis, see T. Skwarnicki, talks given at XXIXth International Conference on High Energy Physics, Vancouver, Canada, July (1998).
- [30] R. Barate *et al.*, (ALEPH Collaboration), *Phys. Lett. B* **429**, 169 (1998);
M. Williams, private communication.
- [31] R. Ammar *et al.*, (CLEO Collaboration), *Phys. Rev. Lett.* **71**, 674 (1993).
- [32] A. Ali and C. Greub, *Phys. Lett. B* **287**, 191 (1992).
- [33] S. Anderson *et al.*, (CLEO Collaboration), CLEO-CONF-96-06 (1996).
- [34] A. Ali, *Nucl. Phys. Proc. Suppl.* **59**, 86 (1997); *Acta Phys. Polon.* **B27**, 3529 (1996).
- [35] S. Glenn *et al.*, (CLEO Collaboration), *Phys. Rev. Lett.* **80**, 2289 (1998).
- [36] S. Abachi *et al.*, (D0 Collaboration), FERMILAB-CONF-96/253-E.
- [37] R. Balest *et al.*, (CLEO Collaboration), in *Proceedings of the 27th International Conference on High Energy Physics*, Glasgow, Scotland, (1994), eds. P. J. Bussey and I. Knowles (IOP, London (1995)).
- [38] H. Kroha, (ALEPH Collaboration) in *Proceedings of the 28th International Conference on High Energy Physics*, Warsaw, Poland 1996, eds. Z. Ajduk and A. K. Wroblewski, World Scientific, Singapore (1997).
- [39] A. Kagan, presented at 7th International Symposium on Heavy Flavor Physics, Santa Barbara, CA, July 1997;
M. Ciuchini *et al.*, *Phys. Lett. B* **334**, 137 (1994).
- [40] I. Bigi *et al.*, in *Proceedings of the DPF meeting of APS*, World Scientific, Singapore (1993), p. 610.

- [41] A. Falk, M. Luke, M.J. Savage, *Phys. Rev. D* **49**, 3367 (1994).
- [42] S. Bertolini *et al.*, *Phys. Rev. Lett.* **59**, 180 (1987);
N. G. Deshpande *et al.*, *Phys. Rev. Lett.* **59**, 183 (1987);
R. Grigjanis *et al.*, *Phys. Lett. B* **213**, 355 (1988); *Phys. Lett. B* **286**, 413(E) (1992);
G. Cella *et al.*, *Phys. Lett. B* **248** 181 (1990);
M. Ciuchini *et al.*, *Phys. Lett. B* **316**, 127 (1993); *Nucl. Phys.* **B421**, 41 (1994);
G. Cella *et al.*, *Phys. Lett. B* **325**, 227 (1994); *Nucl. Phys.* **B431**, 417 (1994).
- [43] M. Misiak, *Nucl. Phys.* **B393**, 23 (1993); *Nucl. Phys.* **B439**, 461(E) (1995).
- [44] A. Ali, and C. Greub, *Z. Phys. C* **60**, 433 (1993);
A. J. Buras *et al.*, *Nucl. Phys.* **B424**, 374 (1994).
- [45] G. Altarelli *et al.*, *Nucl. Phys.* **B187**, 461 (1981);
A. J. Buras and P.H. Weisz, *Nucl. Phys.* **B333**, 66 (1990);
A. J. Buras *et al.*, *Nucl. Phys.* **B370**, 69 (1992); *Nucl. Phys.* **B400**, 37 (1993);
A. J. Buras, M. Jamin and M. E. Lautenbacher, *Nucl. Phys.* **B408**, 209 (1993);
M. Ciuchini *et al.*, *Phys. Lett. B* **301**, 263 (1993); *Nucl. Phys.* **B415**, 403 (1994).
- [46] M. Misiak and M. Münz, *Phys. Lett. B* **344**, 308 (1995).
- [47] K.G. Chetyrkin, M. Misiak, and M. Münz, *Phys. Lett. B* **400**, 206 (1997).
- [48] G.-L. Lin, J. Liu and Y.-P. Yao, *Phys. Rev. Lett.* **64**, 1498 (1990); *Phys. Rev. D* **42**, 2314 (1990).
- [49] C. Greub and T. Hurth, *Phys. Rev. D* **56**, 2934 (1997).
- [50] A. Ali, and C. Greub, *Z. Phys. C* **49**, 431 (1991); *Phys. Lett. B* **259**, 182 (1991); *Phys. Lett. B* **361**, 146 (1995);
N. Pott, *Phys. Rev. D* **54**, 938 (1996).
- [51] C. Greub, T. Hurth and D. Wyler, *Phys. Lett. B* **380**, 385 (1996); *Phys. Rev. D* **54**, 3350 (1996);
C. Greub and T. Hurth, (1996) hep-ph/9608449.
- [52] A. Buras, A. Kwiatkowski and N. Pott, *Phys. Lett. B* **414**, 157 (1997);
M. Ciuchini *et al.*, *Nucl. Phys.* **B527**, 21 (1998).
- [53] N. Cabibbo and L. Maiani, *Phys. Lett. B* **79**, 109 (1978);
Y. Nir, *Phys. Lett. B* **221**, 184 (1989).
- [54] K. Adel and Y. P. Yao, *Mod. Phys. Lett. A* **8**, 1679 (1993); *Phys. Rev. D* **49**, 4945 (1994).
- [55] A. Czarnecki and W. J. Marciano, *Phys. Rev. Lett.* **81**, 277 (1998).

- [56] G. Eilam *et al.*, *Phys. Rev. D* **53**, 3629 (1996);
J. M. Soares, *Phys. Rev. D* **53**, 241 (1996);
Z. Ligeti, L. Randall and M. B. Wise, *Phys. Lett. B* **402**, 178 (1997);
A. K. Grant *et al.*, *Phys. Rev. D* **56**, 3151 (1997).
- [57] N.G. Deshpande, X.-G. He, and J. Trampetic, *Phys. Lett. B* **367**, 362 (1996).
- [58] M. B. Voloshin, *Phys. Lett. B* **397**, 275 (1997).
- [59] A. Khodjamirian *et al.*, *Phys. Lett. B* **402**, 167 (1997).
- [60] E. Golowich and S. Pakvasa, *Phys. Rev. D* **51**, 1215 (1995).
- [61] A. Ali, to appear in *Proceedings of the First APCTP Workshop: Particle Physics Phenomenology*, October (1997), Seoul, South Korea, hep-ph/9801270.
- [62] R. M. Barnett *et al.*, *Phys. Rev. D* **54**, 1 (1996).
- [63] A. L. Kagan and M. Neubert, hep-ph/9805303.
- [64] A. Kapustin, Z. Ligeti, and H. D. Politzer, *Phys. Lett. B* **357**, 653 (1995).
- [65] G. Ricciardi, *Phys. Lett. B* **355**, 313 (1995).
- [66] M. Abud, G. Ricciardi, and G. Sterman, hep-ph/9712346.
- [67] A. Ali, H. Asatrian, and C. Greub, *Phys. Lett. B* **429**, 87 (1998).
- [68] A. Ali, V.M. Braun and H. Simma, *Z. Phys. C* **63**, 437 (1994).
- [69] L. Del Debbio *et al.*, *Phys. Lett. B* **416**, 392 (1998) ; K.C. Bowler *et al.*, (UKQCD Collaboration), *Phys. Rev. D* **51**, 4955 (1995).
- [70] S. Veseli and M.G. Olsson, *Phys. Lett. B* **367**, 309 (1996).
- [71] S. Narison, *Phys. Lett. B* **327**, 354 (1994).
- [72] P. Ball and V.M. Braun, hep-ph/9805422;
P. Ball, hep-ph/9308244.
- [73] C. Bernard, P. Hsieh, and A. Soni, *Phys. Rev. Lett.* **72**, 1402 (1994).
- [74] D. Atwood, B. Blok, and A. Soni, *Int. J. Mod. Phys. A***11**, 3743 (1996).
- [75] J. F. Donoghue, E. Golowich, and A. A. Petrov, *Phys. Rev. D* **55**, 2657 (1997).
- [76] H.-Y. Cheng, *Phys. Rev. D* **51**, 6228 (1995);
J. Milana, *Phys. Rev. D* **53**, 1403 (1996).

- [77] G. Eilam, A. Ioannissian, and R. R. Mendel, *Z. Phys. C* **71**, 71 (1996).
- [78] A. Ali and V. M. Braun, *Phys. Lett. B* **359**, 223 (1995).
- [79] H. Simma and D. Wyler, *Nucl. Phys.* **B344**, 283 (1990);
J. Liu and Y.P. Yao, *Phys. Rev. D* **41**, 2147 (1990);
S. Herrlich and J. Kalinowski, *Phys. Lett. B* **381**, 501 (1992).
- [80] L. Reina, G. Ricciardi and A. Soni, *Phys. Lett. B* **396**, 231 (1997) .
- [81] L. Reina, G. Ricciardi, and A. Soni, *Phys. Rev. D* **56**, 5805 (1997) .
- [82] C.-H. V. Chang, G.-L. Lin, and Y.-P. Yao, *Phys. Lett. B* **415**, 395 (1997);
G. Hiller and E. O. Iltan, *Phys. Lett. B* **409**, 425 (1997).
- [83] I. I. Bigi, in *Proceedings of the 1994 International Workshop on B-Physics*, Nagoya, p. 391,
eds. A.I. Sanda and S. Suzuki, World Scientific (1994), and references therein.
- [84] M. R. Ahmady, E. Kou, and A. Sugamoto, (1997) hep-ph/9708347.
- [85] S. Bertolini and J. Matias, *Phys. Rev. D* **57**, 4197 (1998).
- [86] P. Singer and D-X. Zhang, *Phys. Rev. D* **56**, 4274 (1997).
- [87] B. Grinstein, M. J. Savage and M. B. Wise, *Nucl. Phys.* **B319**, 271 (1989).
- [88] J. Hewett, *Phys. Rev. D* **53**, 4964 (1996).
- [89] A.J. Buras and M. Münz, *Phys. Rev. D* **52**, 186 (1995).
- [90] A. Ali, G. F. Giudice, and T. Mannel, *Z. Phys. C* **67**, 417 (1995).
- [91] N.G. Deshpande, J. Trampetic, and K. Panrose, *Phys. Rev. D* **39**, 1461 (1989);
C. S. Lim, T. Morozumi, and A. I. Sanda, *Phys. Lett. B* **218**, 343 (1989).
- [92] A. I. Vainshtein *et al.*, *Yad. Fiz.* **24**, 820 (1976) [*Sov. J. Nucl. Phys.* **24**, 427 (1976)];
P. J. O'Donnell and H. K. Tung, *Phys. Rev. D* **43**, R2076 (1991).
- [93] A. Ali, T. Mannel and T. Morozumi, *Phys. Lett. B* **273**, 505 (1991).
- [94] F. Krüger and L. M. Sehgal, *Phys. Lett. B* **380**, 199 (1996).
- [95] A. Ali *et al.*, *Phys. Rev. D* **55**, 4105 (1997).
- [96] P. Cho, M. Misiak and D. Wyler, *Phys. Rev. D* **54**, 3329 (1996).
- [97] M. R. Ahmady, *Phys. Rev. D* **53**, 2843 (1996);
C.-D. Lü and D.-X. Zhang, *Phys. Lett. B* **397**, 279 (1997).

- [98] G. Buchalla, G. Isidori and S. J. Rey, *Nucl. Phys.* **B511**, 594 (1998).
- [99] J.-W. Chen, G. Rupak and M. J. Savage, *Phys. Lett. B* **410**, 285 (1997).
- [100] A. Ali and G. Hiller, hep-ph/9803407 and hep-ph/9803428.
- [101] C. S. Kim, T. Morozumi, and A. I. Sanda, *Phys. Rev. D* **56**, 7240 (1997).
- [102] F. Kruger and L. M. Sehgal, *Phys. Rev. D* **55**, 2799 (1997); *Phys. Rev. D* **56**, 5452 (1997);
L. T. Handoko, *Phys. Rev. D* **57**, 1776 (1998).
- [103] C. A. Dominguez, N. Paver and Riazuddin, *Phys. Lett. B* **214**, 459 (1988);
T. M. Aliev, A. A. Ovchinnikov and V. A. Slobodenyuk, *Phys. Lett. B* **237**, 569 (1990);
N. Paver and Riazuddin, *Phys. Rev. D* **45**, 978 (1992);
P. Colangelo *et al.*, *Phys. Lett. B* **317**, 183 (1993).
- [104] C. Allton *et al.*, (APE Collaboration), *Phys. Lett. B* **345**, 513 (1995); *Phys. Lett. B* **365**, 275 (1996);
K. Bowler *et al.*, (UKQCD Collaboration), *Nucl. Phys.* **B447**, 425 (1995); *Phys. Rev. D* **51**, 4955 (1995);
L. Del Debbio *et al.*, (UKQCD Collaboration), *Phys. Lett. B* **416**, 392 (1998).
- [105] P. Colangelo *et al.*, *Phys. Rev. D* **53**, 3672 (1996); *Phys. Lett. B* **395**, 338 (1997).
- [106] T. M. Aliev, A. Özpineci and M. Savci, *Phys. Rev. D* **56**, 4260 (1997);
T. M. Aliev *et al.*, *Phys. Lett. B* **400**, 194 (1997).
- [107] D. Melikhov, N. Nikitin and S. Simula, *Phys. Lett. B* **410**, 290 (1997).
- [108] W. Jaus and D. Wyler, *Phys. Rev. D* **41**, 3405 (1990);
C. Q. Geng and C. P. Kao, *Phys. Rev. D* **54**, 5636 (1996).
- [109] G. Burdman, *Phys. Rev. D* **52**, 6400 (1995).
- [110] F. Ferrarotto, F. Ferroni, and M. Rotondo, “ Search for $B \rightarrow s\mu^+\mu^-$ at BaBar Performed with Aslund,” BaBar Note # 432, (1998).
- [111] D. Falciari and M. Piccolo, “ Experimental Study of the Decay $B^0 \rightarrow K^{*0}\mu^+\mu^-$,” BaBar Note # 391, (1997).
- [112] P. Colangelo, private communication.
- [113] C. Greub, private communication.
- [114] A. F. Falk, M. Luke, and M. J. Savage, *Phys. Rev. D* **53**, 2491 (1996).

- [115] H. Kroha, (ALEPH Collaboration), in *Proceedings of the 28th International Conference on High Energy Physics*, Warsaw, Poland, July (1996), eds. Z. Ajduk and A. K. Wroblewski, World Scientific, Singapore (1997).
- [116] M. Weaver, <http://www.slac.stanford.edu/weaver/snunu.html>.
- [117] J. M. Gerard and W. S. Hou, *Phys. Lett. B* **253**, 478 (1991); *Phys. Rev. D* **43**, 2909 (1991).
- [118] R. Fleischer, *Z. Phys. C* **58**, 483 (1993); *Z. Phys. C* **62**, 81 (1994).
- [119] B. Guberina, R. D. Peccei, and R. Rückl, *Phys. Lett. B* **90**, 169 (1981);
B. Guberina, *Fizika* **16**, 49 (1984);
W. A. Ponce, *Phys. Rev. D* **23**, 1134 (1981).
- [120] W. S. Hou, A. Soni, and H. Steger, *Phys. Rev. Lett.* **59**, 1521 (1987);
W. S. Hou, *Nucl. Phys.* **B308**, 561 (1988).
- [121] N. G. Deshpande and J. Trampetic, *Phys. Rev. D* **41**, 895 (1990);
A. Deandrea *et al.*, *Phys. Lett. B* **320**, 170 (1993).
- [122] A. L. Kagan, *Phys. Rev. D* **51**, 6196 (1995).
- [123] M. Ciuchini, E. Gabrielli, and G. F. Giudice, *Phys. Lett. B* **388**, 353 (1996); *Phys. Lett. B* **393**, 489(E) (1997).
- [124] B. G. Grzadkowski and W.-S. Hou, *Phys. Lett. B* **272**, 383 (1991).
- [125] A. L. Kagan and J. Rathsman, hep-ph/9701300.
- [126] A. Kagan, talks given at the Second International Conference on *B* Physics and *CP* Violation, Honolulu, Hawaii, March (1997), and at the Seventh International Symposium on Heavy Flavor Physics, Santa Barbara, California, July (1997).
- [127] P. Drell, talk given at the 18th International Symposium on Lepton Photon Interactions, Hamburg, Germany, July (1997), hep-ex/9711020.
- [128] H. Albrecht *et al.*, (ARGUS Collaboration), *Z. Phys. C* **52**, 353 (1991).
- [129] D. Bortoletto *et al.*, (CLEO Collaboration), *Phys. Rev. D* **45**, 21 (1992);
L. Gibbons *et al.*, (CLEO Collaboration), *Phys. Rev. D* **56**, 3783 (1997).
- [130] S. Glenn *et al.*, (CLEO Collaboration), CLEO CONF 97-27 (1997);
X. Fu *et al.*, (CLEO Collaboration), CLEO-CONF 95-11 (1995);
D. Cinabro *et al.*, (CLEO Collaboration), CLEO-CONF 94-8 (1994).
- [131] A. Lenz, U. Nierse and G. Ostermaier, *Phys. Rev. D* **56**, 7228 (1997).

- [132] H. Albrecht *et al.*, (ARGUS Collaboration), *Z. Phys. C* **62**, 371 (1994);
M. S. Alam *et al.*, (CLEO Collaboration), *Phys. Rev. Lett.* **58**, 1814 (1987);
I. Dunietz, FERMILAB-PUB-94-163-T (1994), hep-ph/9409355.
- [133] T. Sjostrand, *Comput. Phys. Commun.* **82**, 74 (1994).
- [134] J. D. Richman, plenary talk at the ICHEP Conference, Warsaw, Poland (1996), hep-ex/9701014.
- [135] H. Albrecht *et al.*, (ARGUS Collaboration), *Phys. Lett. B* **318**, 397 (1993);
B. Barish *et al.*, (CLEO Collaboration), *Phys. Rev. Lett.* **76**, 1570 (1996).
- [136] E. Bagan *et al.*, *Nucl. Phys.* **B432**, 3 (1994); *Phys. Lett. B* **351**, 546 (1995); *Phys. Lett. B* **342**, 362 (1995); *Phys. Lett. B* **374**, 363(E) (1996).
- [137] I. Bigi *et al.*, *Phys. Lett. B* **323**, 408 (1994).
- [138] M. Neubert and C. T. Sachrajda, *Nucl. Phys.* **B483**, 339 (1997).
- [139] P. Ball, M. Beneke, and V. M. Braun, *Phys. Rev. D* **52**, 3929 (1995).
- [140] K. Hamacher and M. Weierstall, (DELPHI Collaboration), DELPHI 95-80 (1995).
- [141] H. Albrecht *et al.*, (ARGUS Collaboration), *Z. Phys. C* **44**, 547 (1989); *Z. Phys. C* **41**, 557 (1989).
- [142] N. G. Deshpande, X.-G. He and J. Trampetic, *Phys. Lett. B* **377**, 161 (1996).
- [143] G. Altarelli *et al.*, *Nucl. Phys.* **B208**, 365 (1982).
- [144] M. Artuso *et al.*, (CLEO Collaboration), CLEO CONF 96-18 (1996).
- [145] M. Daoudi, (SLD Collaboration), talk given at the EPS meeting, Jerusalem, August (1997).
- [146] M. Battaglia and P. M. Kluit, (DELPHI Collaboration), DELPHI 97-80 CONF 66.
- [147] J. P. Alexander *et al.*, (CLEO Collaboration), CLEO-CONF 95-3 (1995).
- [148] K. W. Edwards *et al.*, CLEO-CONF-95-8 (1995).
- [149] M. Bander, D. Silverman, and A. Soni, *Phys. Rev. Lett.* **43**, 242 (1979).
- [150] N. G. Deshpande and X.-G. He, *Phys. Lett. B* **336**, 471 (1994).
- [151] J. Smith, (CLEO Collaboration), talk given at the 1997 Aspen Winter Conference on Particle Physics.

-
- [152] J. Alexander, (CLEO Collaboration), talk given at the Second International Conference on *B* Physics and *CP* Violation, Honolulu, Hawaii, March (1997).
- [153] Y. Grossman and M. Worah, *Phys. Lett. B* **395**, 241 (1997).
- [154] A. A. Petrov, *Phys. Rev. D* **399**, 172 (1997).
- [155] M. Peskin and T. Takeuchi, *Phys. Rev. Lett.* **65**, 964 (1990); *Phys. Rev. D* **46**, 381 (1992).
- [156] J. L. Hewett and J. D. Wells, *Phys. Rev. D* **55**, 5549 (1997).
- [157] T.G. Rizzo, hep-ph/9802401.

Hadronic B Meson Decays

The two previous chapters have treated semileptonic B decays and rare B decays, respectively. This chapter describes theoretical ideas and experimental information on generic hadronic B meson decays. Hadronic decays are generally a topic where direct QCD calculations give only limited information. However simulations of generic B decays are essential to experiment, and the extraction of theoretically interesting parameters also often depends on the simulation inputs. This chapter therefore reviews the situation from the theoretical perspective, and also discusses the generator input used in BABAR simulation. General parameterizations, for example in terms of helicity amplitudes, can be used for many exclusive decays, but rely on measurements or theoretical models to fix the parameters. Any simulation generator is an evolving system; wherever possible, inputs based on measurement replace theoretical models as such data become available. However there are inevitably theory- and model-dependent inputs to the simulation. The uncertainty (sometimes called the “theoretical error”) introduced into any result by this dependence needs to be studied, and is often ill-defined. Typically it is estimated by looking at the range of values obtained by using a variety of models for input. Since certain assumptions are common to all models, this procedure is not rigorously justifiable, but it is usually the best one can do. One should however be wary of treating the range of values so obtained as if it is a statistical (Gaussian distributed) error.

There is some hope that the large b -quark mass, and in particular its large difference from lighter quark masses makes predictions for B decays somewhat more reliable than for charmed-meson decays, as the asymptotic freedom of QCD may govern certain aspects of the decays. Quasi-two-body decays, namely any decays to two particles or resonances, can be treated by approaches based on the assumption of factorization. These are discussed in Section 10.1. Section 10.2 discusses the theory of final-state interactions, which are neglected in the factorization approximation. These effects can have a marked impact on a number of theoretical predictions (see for example the discussion in 7.5.3 and [1]) and are currently an active area of theoretical discussion. In Section 10.3, relations between various decays that can be obtained by combining heavy-quark perturbation theory and chiral perturbation theory for the emission of soft pseudoscalar particles (π s and K s) are discussed. Section 10.4 presents approaches to many-body channels. One approach here is to apply QCD fragmentation methods to the fast-moving quarks produced in the decay of a b quark. This approach, other theoretical tools, and the experimental inputs, used to develop a generator that describes generic B decays as completely as possible, are discussed in this section. Finally, Section 10.5 discusses exclusive decays to baryons.

10.1 Exclusive Hadronic Decays: The Factorization Ansatz in Nonleptonic Decays of Heavy Mesons

There are many ways that the quarks produced in a nonleptonic weak decay can arrange themselves into hadrons. The final state is linked to the initial state by complicated trees of gluon and quark interactions, pair production, and loops. These make the theoretical description of nonleptonic decays difficult. However, since the products of a B meson decay are quite energetic, it is possible that the complicated QCD interactions are less important and that the two-quark pairs of the currents in the weak Hamiltonian, Eq. 2.6, coalesce individually into the final-state mesons without further exchanges of gluons. The “color transparency” argument [2] suggests that a quark-antiquark pair remains a state of small size (on the QCD scale) with a correspondingly small chromomagnetic moment until it is far from the other decay products.

Color transparency is the basis for the *factorization hypothesis*, in which amplitudes factorize into products of two current matrix elements. This ansatz is widely used in heavy-quark physics, as it is almost the only way to treat hadronic decays. Its validity, however, is not demonstrated by any quantitative theoretical argument, and there can be instances where this approach is not applicable. The most obvious cases are those in which the final state is chosen in such a way that the quark pair of one of the currents does not correspond to a final state particle. Whether factorization “works,” therefore, depends on the particular decay considered. Surprisingly, it seems to be applicable in many cases. It has been used mainly in hadronic two-body decays [3, 4], but it may also be applicable to certain multibody decays [5].

Figure 10-1 illustrates the diagrams by which hadronic B^0 and B^+ decays are often assumed to proceed. The light quark in the B -meson is a spectator, that is, it participates in the decay only through gluon exchanges. Decays where the spectator is involved in the weak process are usually much less frequent. Mesons are colored singlets, and for this reason, diagrams (b) and (d) are suppressed relative to (a) and (c) by a factor $1/N_c$, where N_c is the number of colors: in the latter, the color index of the second quark line (top) is free and thus runs over all colors, while in the former, all final quarks must have the same color. Therefore one expects (b) and (d) (color-suppressed) to give smaller contributions than (a) and (c) (color-enhanced). In general, the two types of diagrams give different final states, but as seen from the figure, in B^+ decays there can be interference between (c) and (d).

When gluon exchanges between the quarks are added, the color structure of the effective four-fermion interaction is modified and an additional effective neutral-current contribution arises with the same $V - A$ structure as the charged current matrix element from pure W exchange. Furthermore, since m_b is much smaller than m_W , the weak interactions can be represented via effective four-quark interactions. One obtains, after partial summation of the leading QCD contributions,

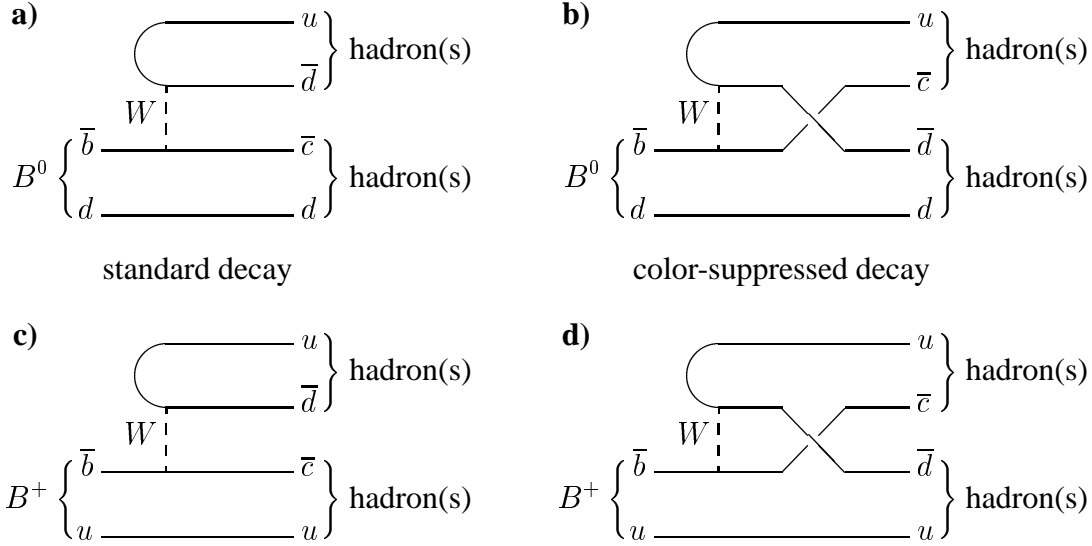


Figure 10-1. Some diagrams for hadronic B^0 (a,b) and B^+ (c,d) decays. Diagrams (b,d) are often called color-suppressed since they can only lead to stable hadrons if the colors of the combined quarks match appropriately. Diagrams (a) and (b) for B^0 decays lead to different final states, while diagrams (c) and (d) for B^+ decays can lead to the same hadronic final state and interfere.

the two four-Fermi interaction operators $O_1 = O_I$ and $O_2 = O_{II}$ in the total weak Hamiltonian given in Eq. 2.6:

$$\mathcal{H}_{\text{eff}} = \frac{4G_F}{\sqrt{2}} V_{cb} V_{ud}^* [C_1(\mu) O_1(\mu) + C_2(\mu) O_2(\mu)],$$

$$O_1 = \left(\bar{c}_i \gamma_\mu \frac{1 - \gamma_5}{2} b_i \right) \left(\bar{d}_j \gamma^\mu \frac{1 - \gamma_5}{2} u_j \right),$$

$$O_2 = \left(\bar{c}_i \gamma_\mu \frac{1 - \gamma_5}{2} b_j \right) \left(\bar{d}_j \gamma^\mu \frac{1 - \gamma_5}{2} u_i \right). \quad (10.1)$$

Here, Roman indices represent the color of each quark participating in the process and the $C_i(\mu)$ are the (Wilson) coefficients. Here μ is a momentum scale, typically $\mu \approx m_b$. At this value, $C_1(\mu) = 1.13$ and $C_2(\mu) = -0.29$. Without QCD corrections, $C_1 = 1$, $C_2(\mu) = 0$, and O_1 is the conventional four-Fermi interaction operator. (Note, however that the corresponding matrix elements can not be evaluated at the high scale $\mu \approx m_b$ as discussed in Chapter 2, and hence these results must be used, in combination with calculations of higher order QCD corrections, to determine the coefficients at the lower scale appropriate for the matrix elements, approximations made in this evaluation lead to theoretical uncertainties and residual unphysical scale dependence in the results.)

Both operators contribute to the two decay types in Fig. 10-1. From the color structures, it can be seen that O_1 enters (a), (c) unsuppressed, but there is a factor $1/N_C$ for (b) and (d). For O_2 ,

the situation is the opposite. Thus it can be seen that the effective coupling strength is $a_1 = C_1 + \frac{1}{N_c}C_2$ for the color-enhanced modes and $a_2 = C_2 + \frac{1}{N_c}C_1$ for the color-suppressed modes. More elaborate extensions of this simple picture are presented in the following sections. In the following discussion the scale dependence of the operator coefficients is not explicitly indicated.

In order to see how factorization is applied, consider the effective Hamiltonian (10.1) for B decays to a final state containing one charmed quark, where the coefficients C_1 and C_2 are taken at the scale $\mu = m_b$. While the scale dependence would cancel in a complete calculation, the choice of μ is often crucial, given the present low-order calculations. Although the representation above is natural (C_2 vanishes in the absence of strong interactions in the standard model), it is somewhat arbitrary, since the effective Hamiltonian can be transformed into the sum of two different operators by a Fierz transformation, which is a purely algebraic operation. One possibility is to write the Hamiltonian as the sum of the operator O_1 introduced above and the octet operator $O^{(8)}$ defined by

$$O^{(8)} = \left(\bar{c}_i \gamma_\mu \frac{1 - \gamma_5}{2} \frac{\lambda_{ij}^a}{2} b_j \right) \left(\bar{d}_k \gamma^\mu \frac{1 - \gamma_5}{2} \frac{\lambda_{kl}^a}{2} u_l \right), \quad (10.2)$$

where λ^a , with $a = 1 \dots 8$, indicates the Gell-Mann matrices. Of course, the corresponding Wilson coefficients are changed; the first coefficient changes from C_1 to $C_1 + C_2/N_c$, and the coefficient of the operator $O^{(8)}$ is $2C_2$. In other words, one tries to choose the two operators in such a way that the contribution of one of them to the decay in question is very small and can be neglected. In the example above the contribution of the octet operator is usually neglected, since no color singlet state can be produced by factorizing out currents which are octets in the color space. The validity of any factorization-based result clearly depends on the scale at which it is applied, since the approximation does not give any scale dependence to the matrix elements. Hence a residual scale dependence and a corresponding theoretical uncertainty appears in results calculated using this approximation. Table 10-1 shows the values of the Wilson coefficients at the scale $m_b = 4.8 \text{ GeV}/c$.

Table 10-1. Values of the Wilson coefficients at the scale $m_b = 4.8 \text{ GeV}/c^2$, both at leading (LO) and next-to-leading (NLO) order (from [4]).

$\alpha_s(m_Z)$	$C_1^{\text{LO}}(m_b)$	$C_2^{\text{LO}}(m_b)$	$C_1^{\text{NLO}}(m_b)$	$C_2^{\text{NLO}}(m_b)$
0.115	1.102	-0.239	1.124	-0.273
0.118	1.108	-0.249	1.132	-0.286
0.121	1.113	-0.260	1.140	-0.301

Continuing with the above example of the simplest weak transition that converts an initial-state b quark to a final-state c quark and a pair of light quarks, consider the color-allowed decay $\bar{B} \rightarrow D^+ \pi^-$.

The algebraic procedure outlined above yields for the matrix elements

$$\begin{aligned}
\mathcal{A}(B(p_B) \rightarrow D(p_D)\pi(q)) &= \\
&-i\frac{4G_F}{\sqrt{2}}V_{cb}V_{ud}^*\left\{\left(C_1 + \frac{1}{N_c}C_2\right)\langle\pi D|\bar{c}\gamma_\mu\frac{1-\gamma_5}{2}b\bar{d}\gamma^\mu\frac{1-\gamma_5}{2}u|B\rangle\right. \\
&\quad \left.+ 2C_2\langle\pi D|\bar{c}\gamma_\mu\frac{1-\gamma_5}{2}\frac{\lambda^a}{2}b\bar{d}\gamma^\mu\frac{1-\gamma_5}{2}\frac{\lambda^a}{2}u|B\rangle\right\} \\
&= -i\frac{4G_F}{\sqrt{2}}V_{cb}V_{ud}^*\left\{\left(C_1 + \frac{1}{N_c}C_2\right)\mathcal{M}_1 + 2C_2\mathcal{M}_8\right\}. \tag{10.3}
\end{aligned}$$

A Fierz identity for the Dirac matrices

$$(\bar{\psi}_1\psi_2)_{V-A}(\bar{\psi}_3\psi_4)_{V-A} = (\bar{\psi}_1\psi_4)_{V-A}(\bar{\psi}_3\psi_2)_{V-A}, \tag{10.4}$$

and the completeness relation for the color matrices

$$\delta_{ii}\delta_{kj} = 2\frac{\lambda_{ij}^a\lambda_{kl}^a}{2} - \frac{1}{N_c}\delta_{ij}\delta_{kl}, \tag{10.5}$$

were used to bring the second operator into the desired form. The matrix elements \mathcal{M}_1 , \mathcal{M}_2 , and \mathcal{M}_8 are

$$\begin{aligned}
\mathcal{M}_1 &= \langle\pi D|O_1|B\rangle = \langle\pi D|\bar{c}_i\gamma_\mu\frac{1-\gamma_5}{2}b_i\bar{d}_k\gamma^\mu\frac{1-\gamma_5}{2}u_k|B\rangle \\
\mathcal{M}_2 &= \langle\pi D|O_2|B\rangle = \langle\pi D|\bar{c}_i\gamma_\mu\frac{1-\gamma_5}{2}b_k\bar{d}_k\gamma^\mu\frac{1-\gamma_5}{2}u_i|B\rangle \\
\mathcal{M}_8 &= \langle\pi D|O^{(8)}|B\rangle = \langle\pi D|\bar{c}_i\gamma_\mu\frac{1-\gamma_5}{2}\frac{\lambda_{ij}^a}{2}b_j\bar{d}_k\gamma^\mu\frac{1-\gamma_5}{2}\frac{\lambda_{kl}^a}{2}u_l|B\rangle, \tag{10.6}
\end{aligned}$$

where color indices are written explicitly. In factorization, where one separates currents by inserting the vacuum state and disregards any QCD interactions between them, the matrix element \mathcal{M}_1 would be given by $\langle D|\bar{c}\gamma_\mu\frac{1-\gamma_5}{2}b|B\rangle\langle\pi|\bar{d}\gamma^\mu\frac{1-\gamma_5}{2}u|0\rangle$. One therefore writes the complete matrix element as

$$\mathcal{A} = -i\frac{4G_F}{\sqrt{2}}V_{cb}V_{ud}^*a_1^{\text{eff}}\langle D|\bar{c}\gamma_\mu\frac{1-\gamma_5}{2}b|B\rangle\langle\pi|\bar{d}\gamma^\mu\frac{1-\gamma_5}{2}u|0\rangle, \tag{10.7}$$

where the coefficient a_1^{eff}

$$a_1^{\text{eff}} = \left(C_1 + \frac{1}{N_c}C_2\right)(1 + \epsilon_1(\mu)) + 2C_2\epsilon_8(\mu), \tag{10.8}$$

and the quantities ϵ_1 , ϵ_8 are given by

$$\begin{aligned}
\epsilon_1(\mu) &= \frac{\mathcal{M}_1}{\langle D|\bar{c}\gamma_\mu\frac{1-\gamma_5}{2}b|B\rangle\langle\pi|\bar{d}\gamma^\mu\frac{1-\gamma_5}{2}u|0\rangle} - 1 \\
\epsilon_8(\mu) &= \frac{\mathcal{M}_8}{\langle D|\bar{c}\gamma_\mu\frac{1-\gamma_5}{2}b|B\rangle\langle\pi|\bar{d}\gamma^\mu\frac{1-\gamma_5}{2}u|0\rangle}. \tag{10.9}
\end{aligned}$$

The coefficient a_1^{eff} is independent of the scale μ , since all the dependence in the various terms must cancel. The quantities ϵ_1, ϵ_8 measure, respectively, the deviation of the singlet matrix element from the factorized form, and the admixture of the octet operator. Obviously, they take different values depending on the decay considered. In the following a_1 is often written, instead of a_1^{eff} , especially in the factorization approximation.

Processes such as this one, which are governed in this approximation by the coefficient a_1 , are here denoted as ‘‘Type I,’’ often called ‘‘color allowed’’ transitions. Type I $b \rightarrow c$ transitions correspond essentially to the decays where the spectator quark in the B meson becomes the spectator quark in a D meson, that is, processes such as $\bar{B}^0 \rightarrow D^+$ and $B^- \rightarrow D^0$. Similarly, $b \rightarrow c$ transitions corresponding to decays where the spectator quark in the B meson cannot become part of a D meson are called ‘‘Type II’’ or ‘‘color forbidden’’ transitions. Type II transitions include the decays $\bar{B}^0 \rightarrow D^0$. For these, one writes the analogous equation to (10.7) as

$$\mathcal{A} = -i \frac{4G_F}{\sqrt{2}} V_{cb} V_{ud}^* a_2^{\text{eff}} \langle \pi | \bar{u} \gamma_\mu \frac{1-\gamma_5}{2} b | B \rangle \langle D | \bar{d} \gamma_\mu \frac{1-\gamma_5}{2} c | 0 \rangle, \quad (10.10)$$

where the coefficient a_2^{eff} is

$$a_2^{\text{eff}} = \left(C_2 + \frac{1}{N_c} C_1 \right) (1 + \tilde{\epsilon}_1(\mu)) + 2C_1 \tilde{\epsilon}_8(\mu). \quad (10.11)$$

The quantities $\tilde{\epsilon}_1(\mu)$ and $\tilde{\epsilon}_8(\mu)$ are now defined as:

$$\begin{aligned} \tilde{\epsilon}_1(\mu) &= \frac{\mathcal{M}_2}{\langle \pi | \bar{u} \gamma_\mu \frac{1-\gamma_5}{2} b | B \rangle \langle D | \bar{d} \gamma_\mu \frac{1-\gamma_5}{2} c | 0 \rangle} - 1 \\ \tilde{\epsilon}_8(\mu) &= \frac{\mathcal{M}_8}{\langle \pi | \bar{u} \gamma_\mu \frac{1-\gamma_5}{2} b | B \rangle \langle D | \bar{d} \gamma_\mu \frac{1-\gamma_5}{2} c | 0 \rangle}. \end{aligned} \quad (10.12)$$

Factorization in Type II processes is not very reliable. The coefficient $2C_1$ multiplying $\tilde{\epsilon}_8$ is much larger than the $(C_2 + C_1/N_c)$ factor, due to the cancellation between the C_2 and C_1/N_c terms. However, as discussed below, the approach of Bauer, Stech, and Wirbel (hereafter, BSW [3]), which is related to factorization, can work for Type-II decays.

Finally, decays governed by a combination of a_1 and a_2 are known as ‘‘Type III’’ processes. Here, the D meson’s spectator quark can come either from the B meson or from the quark pair produced in the b decay. One example of a Type III process is the decay $B^- \rightarrow D^0$.

The values of the C_1, C_2 coefficients are given in Table 10-1 for a scale $\mu = m_b$, which seems appropriate for b decays. They yield

$$a_1 \sim 1, \quad a_2 \sim 0.1. \quad (10.13)$$

The near cancellation of C_2 and C_1/N_c , in a_2 makes the perturbative scale dependence a sensitive issue in Type II processes; these are the most difficult ones to handle theoretically and they may acquire large nonfactorizable contributions. As will be explained later, the diagrams of Class III play

an important role in understanding the QCD dynamics in nonleptonic heavy-meson decay, and, in particular, in extracting the information on the magnitude and sign of the effective constant a_2 .

In the factorization ansatz, each current in the operators develops separately into a physical state. Thus, when the effective Hamiltonian is written as the sum of O_1 and O_8 , the octet part does not contribute, so $\epsilon_8 = 0$. Note that such an approximation breaks the “duality” (“equivalence”) of the quark and hadron description of the amplitudes [5], since neglecting the octet contribution corresponds to omitting different contributions in the quark and hadron pictures.

In the second step, corresponding to setting $\epsilon_1 = 0$, the matrix elements of the currents are represented *approximately* by products of physical quantities, such as decay constants and form factors. This introduces a scale uncertainty since these physical quantities are scale-independent, and thus the scale dependence of the Wilson coefficient of the singlet operator O_1 cannot be matched. This approximation can at most hold at one particular scale, the factorization scale, a quantity which is in general different for all decays. Note also that in this approximation, the constant a_1 is taken to be universal, *i.e.*, process-independent. The failure to reproduce the known renormalization group dependence of the matrix elements reflects the purely phenomenological nature of the factorization ansatz.

The two-quark matrix elements appearing in Eq. (10.7) are well known from the studies of semileptonic transitions. They are conventionally parameterized as

$$\begin{aligned}\langle \pi | \bar{d} \gamma^\mu \gamma_5 u | 0 \rangle &= -i\sqrt{2} F_\pi q^\mu, \\ \langle D | \bar{c} \gamma_\mu b | B \rangle &= f_+(q^2) (p_B + p_D)_\mu + f_-(q^2) q_\mu.\end{aligned}\quad (10.14)$$

Some other parameterizations often used in the literature are as follows:

$$\langle V | (\bar{q}q)_{V-A} | 0 \rangle = \epsilon^\mu m_V f_V \quad (10.15)$$

$$\langle P | (\bar{b}q)_{V-A} | B \rangle = \left(p_B^\mu + p_P^\mu - \left(\frac{m_B^2 - m_P^2}{q^2} \right) q^\mu \right) F_1(q^2) + \left(\frac{m_B^2 - m_P^2}{q^2} \right) q^\mu F_0(q^2), \quad (10.16)$$

$$\begin{aligned}\langle V | (\bar{b}q)_{V-A} | B \rangle &= - \left[(m_B + m_V) \eta^{*\mu} A_1(q^2) - \frac{\eta^* \cdot q}{m_B + m_V} (p_B^\mu + p_V^\mu) A_2(q^2) \right. \\ &\quad \left. - 2m_V \frac{\eta^* \cdot q}{q^2} q^\mu (A_3(q^2) - A_0(q^2)) - 2i\epsilon^{\mu\nu\rho\sigma} \frac{\eta_{*\nu} p_{B\rho} p_{V\sigma}}{m_B + m_V} V(q^2) \right] \quad (10.17)\end{aligned}$$

Here $q_\mu = (p_B + p_D)_\mu$ is the momentum transfer, which in this case satisfies $q^2 = m_\pi^2$. This yields the amplitude

$$\mathcal{A} = -G_F V_{cb} V_{ud}^* \left(C_1 + \frac{1}{N_c} C_2 \right) F_\pi f_+(q^2) (m_B^2 - m_D^2). \quad (10.18)$$

Further refinements are possible. One can show that in the heavy-quark limit there is only one form factor in Eq. (10.14). It can be parameterized by the usual Isgur-Wise function $\xi(v \cdot v')$, where $v \cdot v' = (m_B^2 + m_D^2 - m_\pi^2)/(2m_B m_D)$,

$$\mathcal{A} = -G_F V_{cb} V_{ud}^* \left(C_1 + \frac{1}{N_c} C_2 \right) F_\pi \xi(v \cdot v') \sqrt{\frac{m_B + m_D}{4m_B m_D}} (m_B^2 - m_D^2), \quad (10.19)$$

which leads to the decay rate

$$\Gamma = |\mathcal{A}|^2 |p_1| / (8\pi m_B^2), \quad (10.20)$$

where $|p_1| = [(m_B^2 - (m_\pi + m_D)^2)(m_B^2 - (m_\pi - m_D)^2)]^{1/2} / (2m_B)$. The Isgur-Wise function is normalized as $\xi(1) = 1$ and can be studied in semileptonic decays of the B meson at different values of $v \cdot v'$ (see Chapter 8). If the gluon exchanges between the light-quark pair and the rest of the hadronic system are included, new nonfactorizable corrections to the amplitude \mathcal{A} can arise. This results in additional contributions to Eq. (10.7) from the octet part of the matrix element (last line of Eq. (10.3)). Obviously, a more quantitative estimate of these contributions is needed. This is considered later, after a discussion of the heuristic BSW approximation.

There are many applications of the formalism illustrated in this section. These include studies of the decay $B \rightarrow DD_s$, although there are two complications here which must be considered, but turn out to be numerically unimportant. The first complication is associated with the effect of the penguin operators. Since the decay amplitude produces a $c\bar{c}$ pair in the final state, the penguin operators also contribute. As shown below, the penguins are suppressed by small values of the Wilson coefficients. Another complication is associated with the fact that one can no longer discard terms proportional to $q^2 \simeq m_{D_s}^2$. Thus, even in the heavy-quark limit, this decay amplitude is proportional to *two* form factors instead of one. The effective Hamiltonian is now given by

$$\begin{aligned} \mathcal{H}_{\text{eff}} &= \frac{4G_F}{\sqrt{2}} V_{cb} V_{cs}^* \left[C_1(\mu) O_1(\mu) + C_2(\mu) O_2(\mu) - \sum_{i=3}^6 C_i(\mu) O_i(\mu) \right], \\ O_1 &= \bar{c}_i \gamma_\mu \frac{1 - \gamma_5}{2} b_i \bar{s}_j \gamma^\mu \frac{1 - \gamma_5}{2} c_j, \quad O_2 = \bar{c}_i \gamma_\mu \frac{1 - \gamma_5}{2} b_j \bar{s}_j \gamma^\mu \frac{1 - \gamma_5}{2} c_i \\ O_3 &= \bar{s}_i \gamma_\mu \frac{1 - \gamma_5}{2} b_i \bar{c}_j \gamma^\mu \frac{1 \mp \gamma_5}{2} c_j, \quad O_4 = \bar{s}_i \gamma_\mu \frac{1 - \gamma_5}{2} b_j \bar{c}_j \gamma^\mu \frac{1 \mp \gamma_5}{2} c^i, \end{aligned} \quad (10.21)$$

where $C_i \sim 10^{-2}$ for $i = 3..6$. Here, the unitarity relation for the CKM matrix elements was used and the term proportional to V_{ub} was neglected. Following the procedure outlined above, the decay amplitude can be written as

$$\mathcal{A}(B^- \rightarrow D^0 D_s) = A_{\text{tree}} + A_{\text{peng}}, \quad (10.22)$$

where A_{tree} and A_{peng} are defined as

$$\begin{aligned} A_{\text{tree}} &= -G_F V_{cb} V_{cs}^* a_1 F_{D_s} f_+(m_{D_s}^2) (m_B^2 - m_D^2) \left[1 + \frac{f_-(m_{D_s}^2)}{f_+(m_{D_s}^2)} \frac{m_{D_s}^2}{m_B^2 - m_D^2} \right], \\ A_{\text{peng}} &= \frac{1}{a_1} \left(a_4 - 2a_6 \frac{m_{D_s}^2}{(m_b - m_c)(m_c + m_s)} \right) A_{\text{tree}}. \end{aligned} \quad (10.23)$$

Here $a_6 = C_6^4 + C_3^3 / N_c \sim 10^{-2} - 10^{-1}$ and nonfactorizable contributions were completely neglected. The decay rate $\Gamma = |\mathcal{A}(B^- \rightarrow D^0 D_s)|^2 |p_1| / (8\pi m_B^2)$, where $|p_1| = [(m_B^2 - (m_{D_s} + m_D)^2)(m_B^2 - (m_{D_s} - m_D)^2)]^{1/2} / (2m_B)$, can be obtained readily. It is clear that the inclusion

of the penguin operators does not significantly modify the prediction for the decay rate, but is essential for evaluation of direct CP -violating asymmetries. The smallness of the “penguin pollution” makes this decay mode useful for the observation of mixing-induced CP -violating effects. There is, however, a conceptual difference in the evaluation of the $B \rightarrow D\pi$ and $B \rightarrow DD$ decays which is associated with the small energy release in $B \rightarrow DD$ decay. This implies that the color transparency argument of [2] is not applicable to this decay mode (this is a common problem for *any* decay governed by the $b \rightarrow c\bar{c}s$ quark subprocess). A more theoretically sound argument is needed to justify the factorization of these decay amplitudes and the neglect of the octet contribution.

10.1.1 The BSW Approach

In the phenomenological BSW approach [3], the constants a_1 and a_2 are not calculated perturbatively. They are considered to be free parameters and are fitted using data from one or several decays. This procedure ensures that, for the decays used in the fit, all of the unaccounted pieces are automatically absorbed. The point is that the a_1 and a_2 values obtained are now taken to apply *universally* to all decays. That is, the universality hypothesis assumes that the nonfactorizable parts are the same for the decays used in the fit as for any other decays studied. Predictions based on the BSW approach are correct only if this is true. This hypothesis is not justified by any theoretical arguments and, in fact, these nonfactorizable terms can be rather different in different decays.

In order to denote the effective nature of these coefficients and their process-dependence, they are often complemented with additional subscripts, such as $a_1^{\text{eff}}|_{DD_s}$, which denotes the effective a_1 obtained for the decays $\bar{B} \rightarrow D^{(*)}D_s^{(*)-}$, *etc.* The constants a_1, a_2 are obtained by fitting formulae such as (10.19) to the decay amplitudes, replacing $(C_1 + C_2/N_c)$ by the free parameter a_1 , and using the best values for the necessary form factors and decay constants from various sources (heavy-quark symmetry, lattice, sum rules) (see Chapter 8). In a recent analysis by Neubert and Stech [4], two models were used for the form factors, which each yield a value for the effective coefficients (one of which is shown in square brackets). The difference in the two results can be taken as a minimal estimate of the theoretical uncertainty.

From the class of decays $\bar{B}^0 \rightarrow D^{(*)+}h^-$, where h^- is a light meson ($h = \pi, \rho$ or a_1), one finds

$$a_1^{\text{eff}}|_{Dh} = 1.08 \pm 0.04 \quad [0.98 \pm 0.04]. \quad (10.24)$$

The coefficient a_1 can also be determined from the decays $\bar{B} \rightarrow D^{(*)}D_s^{(*)-}$, which are characterized by quite different decay kinematics. In principle, it would be interesting to investigate whether the resulting value is different in the two cases, *i.e.*, whether there is an observable process-dependence of the phenomenological parameter. In practice, this cannot be done because of the large uncertainties in the values of the decay constants of charm mesons. From a fit to the data, one finds

$$a_1^{\text{eff}}|_{DD_s} = 1.10 \pm 0.07 \pm 0.17 \quad [1.05 \pm 0.07 \pm 0.16], \quad (10.25)$$

where the second error accounts for the uncertainty in $f_{D_s^{(*)}}$. In both cases, (10.24) and (10.25), the data support the theoretical expectation that a_1^{eff} is close to unity (see (10.13)).

A value for the parameter $|a_2^{\text{eff}}|$ (but not the relative sign between a_2^{eff} and a_1^{eff}) can be obtained from the Class II decays $\bar{B} \rightarrow \bar{K}^{(*)} J/\psi$ and $\bar{B} \rightarrow \bar{K}^{(*)} \psi'$. From a fit to the six measured branching ratios, one extracts

$$|a_2^{\text{eff}}|_{K\psi} = 0.21 \pm 0.01 \quad [0.29 \pm 0.01]. \quad (10.26)$$

This result is even more strongly dependent on the model chosen for the form factors. This is not surprising, since Class II decays involve heavy-to-light transition matrix elements (see Ref. [4] and Chapter 8 for a discussion of form factors).

A determination of a_2^{eff} from decays with rather different kinematics is possible by considering the Class III transitions $B^- \rightarrow D^{(*)0} h^-$ with $h = \pi$ or ρ . Moreover, because of the interference of the a_1 and a_2 amplitudes, these decays are sensitive to the relative sign of the QCD coefficients. From the theoretical point of view, it is useful to normalize the branching ratios to those of the corresponding \bar{B}^0 decays, which are Class I transitions. The theoretical predictions for these ratios are of the form

$$\frac{\text{B}(B^- \rightarrow D^{(*)0} h^-)}{\text{B}(\bar{B}^0 \rightarrow D^{(*)+} h^-)} = \frac{\tau(B^-)}{\tau(\bar{B}^0)} \left[1 + 2x_1 \frac{a_2^{\text{eff}}}{a_1^{\text{eff}}} + x_2^2 \left(\frac{a_2^{\text{eff}}}{a_1^{\text{eff}}} \right)^2 \right], \quad (10.27)$$

where x_1 and x_2 are process-dependent parameters depending on the ratio of some hadronic form factors and decay constants ($x_1 = x_2$ except for the decay $B^- \rightarrow D^{*0} \rho^-$). The ratios of branching fractions on the left-hand side are taken from recent CLEO data reported in Ref. [6]. By performing a fit to the data, one extracts the ratio $a_2^{\text{eff}}/a_1^{\text{eff}}$ for each channel. The results are collected in Table 10-2, where the second error results from the uncertainty in the lifetime ratio [7] $\tau(B^-)/\tau(\bar{B}^0) = 1.06 \pm 0.04$. Taking the average, and using (10.24), gives

$$\begin{aligned} \left. \frac{a_2^{\text{eff}}}{a_1^{\text{eff}}} \right|_{Dh} &= 0.21 \pm 0.05 \quad [0.31 \pm 0.08], \\ a_2^{\text{eff}}|_{Dh} &= 0.23 \pm 0.05 \quad [0.30 \pm 0.08]. \end{aligned} \quad (10.28)$$

The value of a_2^{eff} is in remarkably good agreement with that obtained in (10.26).

The magnitude and, in particular, the positive sign of a_2^{eff} (which coincides with the sign of the perturbative value $C_1 + C_2/3$) are important for the theoretical interpretation of the results. In nonleptonic B decays the two parameters a_1^{eff} and a_2^{eff} have the same sign, meaning that the corresponding amplitudes interfere constructively. This is in contrast to the situation encountered in D meson decays, where a similar analysis yields [3]

$$a_1^{\text{eff}}|_{\text{charm}} = 1.10 \pm 0.05, \quad a_2^{\text{eff}}|_{\text{charm}} = -0.49 \pm 0.04, \quad (10.29)$$

indicating a strong destructive interference. Since most D decays are (quasi) two-body transitions, this effect is responsible for the observed lifetime difference between D^+ and D^0 mesons [8],

Table 10-2. Ratios of nonleptonic decay rates of charged and neutral B mesons [6], and the corresponding values for $a_2^{\text{eff}}/a_1^{\text{eff}}$.

Experimental Ratios	Predictions for x_i	$a_2^{\text{eff}}/a_1^{\text{eff}}$
$\frac{\text{B}(B^- \rightarrow D^0 \pi^-)}{\text{B}(\bar{B}^0 \rightarrow D^+ \pi^-)} = 1.73 \pm 0.25$	1.127 [0.729]	$0.24 \pm 0.08 \pm 0.02$ [0.38 \pm 0.13 \pm 0.03]
$\frac{\text{B}(B^- \rightarrow D^0 \rho^-)}{\text{B}(\bar{B}^0 \rightarrow D^+ \rho^-)} = 1.19 \pm 0.24$	0.587 [0.450]	$0.10 \pm 0.18 \pm 0.03$ [0.13 \pm 0.24 \pm 0.04]
$\frac{\text{B}(B^- \rightarrow D^{*0} \pi^-)}{\text{B}(\bar{B}^0 \rightarrow D^{*+} \pi^-)} = 1.64 \pm 0.28$	1.361 [0.886]	$0.18 \pm 0.08 \pm 0.02$ [0.27 \pm 0.12 \pm 0.03]
$\frac{\text{B}(B^- \rightarrow D^{*0} \rho^-)}{\text{B}(\bar{B}^0 \rightarrow D^{*+} \rho^-)} = 1.71 \pm 0.36$	$x_1 = 0.759$ [0.646] $x_2 = 0.813$ [0.675]	$0.35 \pm 0.17 \pm 0.03$ [0.41 \pm 0.20 \pm 0.04]

$\tau(D^+)/\tau(D^0) = 2.55 \pm 0.04$. In B decays on the other hand, the majority of transitions proceed into multibody final states, and moreover, there are many B^- decays (such as those involving two charm quarks in the final state) where no interference can occur. The relevant scale for multibody decay modes may be significantly lower than m_b , leading to destructive interference. Therefore, the observed constructive interference in the two-body modes is not in conflict with the fact that $\tau(B^-) > \tau(\bar{B}^0)$.

The values of a_2^{eff} extracted from $\bar{B} \rightarrow \bar{K}^{(*)} J/\psi$ and $\bar{B} \rightarrow D^{(*)} h$ decays in (10.26) and (10.28) indicate that nonuniversal contributions (at the scale $\mu = m_b$) are small in these processes. Writing (for a definition of ξ and ϵ see below)

$$\begin{aligned} a_2^{\text{eff}}|_{KJ/\psi} &= C_2(m_b) + \xi_{KJ/\psi} C_1(m_b) = 0.21 \pm 0.01, \\ a_2^{\text{eff}}|_{Dh} &= C_2(m_b) + \xi_{Dh} C_1(m_b) = 0.23 \pm 0.05, \end{aligned} \quad (10.30)$$

with conservative errors, and combining these with the values of the Wilson coefficients given in Table 10-1, gives

$$\begin{aligned} \xi_{K\psi} &= 0.44 \pm 0.05, & 2\epsilon_8^{(BK,\psi)}(m_b) &= 0.11 \pm 0.05, \\ \xi_{Dh} &= 0.46 \pm 0.05, & 2\epsilon_8^{(BD,h)}(m_b) &= 0.13 \pm 0.05. \end{aligned} \quad (10.31)$$

Hence, within errors there is no experimental evidence for a process dependence of the value of ξ .

The predictions of the BSW approach, refined by Neubert and Stech [4] are listed in Tables 10-3, 10-4, and 10-5 for several two-body decays. Although there are discrepancies with the experiments, the errors are still too large to dismiss the BSW approach. It is important to measure these decays as accurately as possible to detect deviations from the BSW approach (universality of the coefficients) and from simple factorization.

Table 10-3. Branching ratios (in percent) for Class-I nonleptonic \bar{B}^0 decays in the model described in [4]. The last column shows the world average experimental results [6, 9].

\bar{B}^0 Modes	NS Model	$a_1^{\text{eff}} = 0.98$ $a_2^{\text{eff}} = 0.29$	Experimental Average
Class I			
$D^+\pi^-$	$0.318 a_1^2$	0.30	$0.31 \pm 0.04 \pm 0.02$
D^+K^-	$0.025 a_1^2$	0.02	
D^+D^-	$0.037 a_1^2 (f_D/200)^2$	0.03	
$D^+D_s^-$	$1.004 a_1^2 (f_{D_s}/240)^2$	0.96	$0.74 \pm 0.22 \pm 0.18$
$D^+\rho^-$	$0.778 a_1^2$	0.75	$0.84 \pm 0.16 \pm 0.07$
D^+K^{*-}	$0.041 a_1^2$	0.04	
D^+D^{*-}	$0.032 a_1^2 (f_{D^*}/230)^2$	0.03	
$D^+D_s^{*-}$	$0.830 a_1^2 (f_{D_s^*}/275)^2$	0.80	$1.14 \pm 0.42 \pm 0.28$
$D^+a_1^-$	$0.844 a_1^2$	0.81	
$D^{*+}\pi^-$	$0.296 a_1^2$	0.28	$0.28 \pm 0.04 \pm 0.01$
$D^{*+}K^-$	$0.022 a_1^2$	0.02	
$D^{*+}D^-$	$0.023 a_1^2 (f_D/200)^2$	0.02	
$D^{*+}D_s^-$	$0.603 a_1^2 (f_{D_s}/240)^2$	0.58	$0.94 \pm 0.24 \pm 0.23$
$D^{*+}\rho^-$	$0.870 a_1^2$	0.84	$0.73 \pm 0.15 \pm 0.03$
$D^{*+}K^{*-}$	$0.049 a_1^2$	0.05	
$D^{*+}D^{*-}$	$0.085 a_1^2 (f_{D^*}/230)^2$	0.08	
$D^{*+}D_s^{*-}$	$2.414 a_1^2 (f_{D_s^*}/275)^2$	2.32	$2.00 \pm 0.54 \pm 0.49$
$D^{*+}a_1^-$	$1.217 a_1^2$	1.16	$1.27 \pm 0.30 \pm 0.05$
$\pi^+\pi^-$	$50.0 a_1^2 V_{ub} ^2$		
$\pi^+\rho^- + \rho^+\pi^-$	$176.9 a_1^2 V_{ub} ^2$		

Table 10-4. Branching ratios (in percent) for Class-II nonleptonic \bar{B}^0 decays in the model described in[4]. Here $\theta = 20^\circ$ is used for the η - η' mixing angle. Upper limits are at the 90% confidence level.

\bar{B}^0 Modes	NS Model	$a_1^{\text{eff}} = 0.98$ $a_2^{\text{eff}} = 0.29$	Experimental Average
Class II			
$\bar{K}^0 J/\psi$	$0.800 a_2^2$	0.07	0.075 ± 0.021
$\bar{K}^0 \psi'$	$0.326 a_2^2$	0.03	< 0.08
$\bar{K}^{*0} J/\psi$	$2.518 a_2^2$	0.21	0.153 ± 0.028
$\bar{K}^{*0} \psi'$	$1.424 a_2^2$	0.12	0.151 ± 0.091
$\pi^0 J/\psi$	$0.018 a_2^2$	0.002	< 0.006
$\rho^0 J/\psi$	$0.050 a_2^2$	0.004	< 0.025
$\pi^0 D^0$	$0.084 a_2^2 (f_D/200)^2$	0.007	< 0.033
$\pi^0 D^{*0}$	$0.116 a_2^2 (f_{D^*}/230)^2$	0.010	< 0.055
$\rho^0 D^0$	$0.078 a_2^2 (f_D/200)^2$	0.007	< 0.055
$\rho^0 D^{*0}$	$0.199 a_2^2 (f_{D^*}/230)^2$	0.017	< 0.117
ωD^0	$0.081 a_2^2 (f_D/200)^2$	0.007	< 0.057
ωD^{*0}	$0.203 a_2^2 (f_{D^*}/230)^2$	0.017	< 0.120
ηD^0	$0.058 a_2^2 (f_D/200)^2$	0.005	< 0.033
ηD^{*0}	$0.073 a_2^2 (f_{D^*}/230)^2$	0.006	< 0.050

Table 10-5. Branching ratios (in percent) for nonleptonic B^- decays in the model described in [4].

B^- Modes	NS Model	$a_1^{\text{eff}} = 0.98$ $a_2^{\text{eff}} = 0.29$	Experimental Average
Class I			
$D^0 D^-$	$0.039 a_1^2 (f_D/200)^2$	0.04	
$D^0 D_s^-$	$1.069 a_1^2 (f_{D_s}/240)^2$	1.03	$1.36 \pm 0.28 \pm 0.33$
$D^0 D^{*-}$	$0.034 a_1^2 (f_{D^*}/230)^2$	0.03	
$D^0 D_s^{*-}$	$0.883 a_1^2 (f_{D_s^*}/275)^2$	0.85	$0.94 \pm 0.31 \pm 0.23$
$D^{*0} D^-$	$0.025 a_1^2 (f_D/200)^2$	0.02	
$D^{*0} D_s^-$	$0.642 a_1^2 (f_{D_s}/240)^2$	0.62	$1.18 \pm 0.36 \pm 0.29$
$D^{*0} D^{*-}$	$0.091 a_1^2 (f_{D^*}/230)^2$	0.09	
$D^{*0} D_s^{*-}$	$2.570 a_1^2 (f_{D_s^*}/275)^2$	2.47	$2.70 \pm 0.81 \pm 0.66$
Class II			
$K^- J/\psi$	$0.852 a_2^2$	0.07	0.102 ± 0.014
$K^- \psi'$	$0.347 a_2^2$	0.03	0.070 ± 0.024
$K^{*-} J/\psi$	$2.680 a_2^2$	0.23	0.174 ± 0.047
$K^{*-} \psi'$	$1.516 a_2^2$	0.13	< 0.30
$\pi^- J/\psi$	$0.038 a_2^2$	0.003	0.0057 ± 0.0026
$\rho^- J/\psi$	$0.107 a_2^2$	0.009	< 0.077
Class III			
$D^0 \pi^-$	$0.338 [a_1 + 0.729 a_2 (f_D/200)]^2$	0.48	$0.50 \pm 0.05 \pm 0.02$
$D^0 \rho^-$	$0.828 [a_1 + 0.450 a_2 (f_D/200)]^2$	1.02	$1.37 \pm 0.18 \pm 0.05$
$D^0 a_1^-$	$0.898 [a_1 + 0.317 a_2 (f_D/200)]^2$	1.03	
$D^{*0} \pi^-$	$0.315 [a_1 + 0.886 a_2 (f_{D^*}/230)]^2$	0.48	$0.52 \pm 0.08 \pm 0.02$
$D^{*0} \rho^-$	$0.926 [a_1^2 + 0.456 a_2^2 (f_{D^*}/230)^2$ $+ 1.292 a_1 a_2 (f_{D^*}/230)]$	1.26	$1.51 \pm 0.30 \pm 0.02$
$D^{*0} a_1^-$	$1.296 [a_1^2 + 0.128 a_2^2 (f_{D^*}/230)^2$ $+ 0.269 a_1 a_2 (f_{D^*}/230)]$	1.36	$1.89 \pm 0.53 \pm 0.08$

10.1.2 Phenomenology of Nonfactorizable Contributions

Since it is known that the factorized result of Eq. (10.7) is altered by QCD, one should investigate the nonfactorizable effects and attempt to calculate the quantities ϵ_1 and ϵ_8 introduced earlier. The expected decrease of experimental errors will eventually enable one to test these calculations and the quantitative understanding of QCD that they represent. Note that in the presence of a sizable octet contribution, the parameters a_1^{eff} and a_2^{eff} defined in (10.8) and (10.11) are not universal.

It can be shown that ϵ_1 is of order $1/N_c^2$, and therefore it is usually neglected. Defining

$$\xi = \frac{1}{N_c} + 2\epsilon_8, \quad (10.32)$$

one can write

$$a_1^{\text{eff}} = C_1 + \xi C_2. \quad (10.33)$$

Here ξ is an additional parameter which one must fit to get agreement with experiment. The factorization approximation corresponds to $\xi = 1/N_c \simeq 0.3$.

The situation is more complicated in the case where the decay rate is not dominated by a single amplitude. This occurs in some Class II decays, for instance, where the tree-level amplitude can be suppressed if it depends on CKM matrix elements which have small values and the penguin amplitude may contribute at a comparable level. Additional complications arise in the case of decays involving particles with spin in the final state [10]. It has been shown [10, 11] that nonfactorizable corrections are *different* for different helicity amplitudes.

In order to gain a complete understanding of the hadronic (two-body) decays and of the octet contributions which break factorization, additional QCD-based methods must be found. Some of the available results are discussed below. In particular, sum-rule calculations [12] seem to shed some light on this issue. Other model calculations exist but may yield only order-of-magnitude estimates. Unfortunately, no systematic treatment exists and only scattered results are available.

10.1.3 Towards an Understanding of Factorization. Departures from Factorization

As emphasized above, a complete theoretical treatment of hadronic decays is not close at hand. There are, however, attempts to “understand” the factorization ansatz. These are reviewed briefly below.

In the definition of the effective couplings a_1^{eff} and a_2^{eff} , there are terms proportional to $1/N_c$ which come from the Fierz reordering of one of the operators. Furthermore, in a_2^{eff} there is the term proportional to $2C_1$, which is of similar magnitude in model calculations. It was noticed some

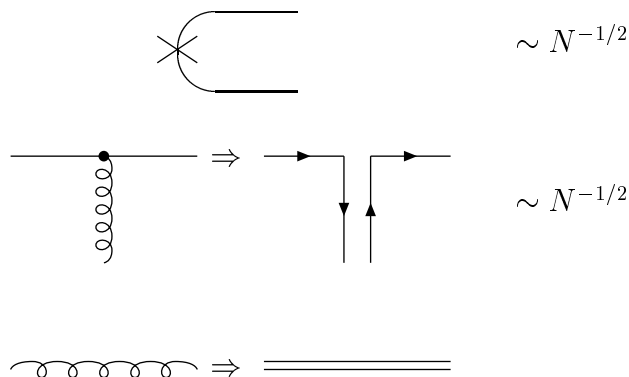


Figure 10-2. Feynman rules in the large N_c limit.

time ago that the omission of the contribution of the Fierz-transformed current (which scales like $1/N_c$) significantly improves the agreement between theoretical predictions and experimental measurements of $D^0 \rightarrow K^0 \pi^0$ [13]. The $1/N_c$ suppressed amplitudes can be dropped in the so-called “large N_c ” limit. The argument is similar for the B meson decays, due to the energy independence of the $1/N_c$ expansion. It turns out that QCD with $N_c = 3$ is in many respects a large N_c theory. There are also indications that the nonfactorizable contribution proportional to $2C_1$ in a_2^{eff} partly cancels the $1/N_c$ term [14].

The bookkeeping of the large N_c theory is most easily done in terms of the so-called topological Feynman diagrams (Fig. 10-2). Since the number of colors is extended to N_c , the gauge group of QCD is no longer $SU(3)$ but $SU(N_c)$. In this limit the physics of meson decays simplifies considerably and the leading contribution can be easily identified. This is achieved by redrawing the relevant Feynman diagrams using the following graphical rules [15]:

1. A meson is represented by its valence quark content.
2. Each gluon is represented by a double line.
3. A factor of N_c is associated with each closed-quark loop.
4. A factor of $1/\sqrt{N_c}$ is assigned to each quark-gluon vertex.
5. A factor of $1/\sqrt{N_c}$ is assigned to each quark-meson vertex.

Using this set of rules, it is easy to isolate the leading contributions to nonleptonic B decays. For example, because of the different number of closed-quark loops, the weak rescattering diagrams are sub-leading with respect to Type-I diagrams. This has implications for those decays which are manifestly governed by the weak annihilation amplitudes, as there are always other decay channels which can scatter into the channel of interest. These decay channels are *coupled*; for instance, final state interactions can convert a $D^+ D^-$ state to a $\pi^+ \pi^-$ one [16], so amplitudes calculated in the

factorization approximation are modified. Neglecting final state rescattering contributions and retaining only the leading terms in the $1/N_c$ expansion, implies for the effective QCD constants, $a_1 = C_1 > 0$ and $a_2 = C_2 < 0$. $1/N_c$ arguments are much more subtle when applied to baryons, since a baryon is itself made of N_c quarks.

The first attempt to put the factorization approximation on a solid theoretical base was made in [17] (see also [18]). The authors considered the limit of a large energy transfer to the light quarks

$$E = v \cdot q = \frac{m_b^2 - m_c^2}{2m_b}, \quad (10.34)$$

which scales as m_b , as $m_b \rightarrow \infty$. Here v is the velocity of the decaying heavy quark, $p_b = m_b v + k$, and q is the momentum transferred to the light-quark pair. As seen from Eq. (10.34), in this limit, the energy scales as the heavy-quark mass. By proposing a Large-Energy Effective Theory as an extension of Heavy-Quark Effective Theory and by making use of a convenient gauge condition, the authors could prove factorization applies for the physical amplitude dominated by collinear quarks. However, this approach does not clarify how the pair of collinear quarks hadronizes into the pion.

10.1.3.1 Perturbative studies

Another problem is the numerical estimate of the size of nonfactorizable corrections. These can originate from either perturbative or nonperturbative effects. Consider first perturbative contributions. Here, one is trying to account for gluon exchanges by treating them perturbatively, since $\alpha_s(m_b) \simeq 0.21$ is still a reasonably small quantity. Some of the perturbative QCD corrections have already been taken into account in the derivation of \mathcal{H}_{eff} , but there remain the effects in the matrix elements.

For the $B \rightarrow \pi D$ decays treated before, these have been evaluated in [19], where the Brodsky-Lepage perturbative QCD framework was employed. In this approach, the mesons are described by quark-antiquark (and gluon) wave functions which are used to calculate the matrix elements. The perturbative QCD corrections to the decay can be summarized by the convolution of a wave function with a ‘‘hard’’ amplitude T representing the exchange of large-momentum gluons, proportional to $\alpha_s(m_b)$.

$$\begin{aligned} \langle H_c(v') \pi^-(q) | O_j(m_b) | H_b(v) \rangle = & \\ & \frac{1}{4} \langle H_c(v') | \bar{h}_v^c h_v^b | H_b(v) \rangle m_b (1-r) \int_0^1 dx T_j^S(x, r, m_b) \phi(x) \\ & + \frac{1}{4} \langle H_c(v') | \bar{h}_v^c \gamma_5 h_v^b | H_b(v) \rangle m_b (1+r) \int_0^1 dx T_j^P(x, r, m_b) \phi(x). \end{aligned} \quad (10.35)$$

The $h_{v^{(i)}}^q$ are the heavy-quark velocity-dependent fields. At the leading (zeroth) order in $\alpha_s(m_b)$, the hard rescattering amplitudes are given by

$$T_1^S(x, r, m_b) = T_1^P(x, r, m_b) = 1, \quad T_8^S(x, r, m_b) = T_8^P(x, r, m_b) = 0, \quad (10.36)$$

and $r = m_c/m_b$ is fixed as $m_b \rightarrow \infty$. Here $\phi(x)$ is a pion distribution function normalized as

$$\int_0^1 dx \phi(x) = f_\pi / 2\sqrt{N_c}, \quad (10.37)$$

where f_π is the pion decay constant. Clearly, the T_8 amplitudes vanish in leading order since a gluon exchange is needed to rearrange the colors. As a consequence, the matrix element of interest is factorizable in the leading order in $\alpha_s(m_b)$, *i.e.*, when the QCD interactions are switched off. In order to illustrate the QCD effect, consider the ratio of $\Gamma(B^0 \rightarrow D^+\pi^-)$ and $\Gamma(B^0 \rightarrow D^{*+}\pi^-)$, which can be written as

$$\frac{\Gamma(\bar{B}^0 \rightarrow D^+\pi^-)}{\Gamma(\bar{B}^0 \rightarrow D^{*+}\pi^-)} = \left| \frac{\int_0^1 dx T_1^S(x, r, m_b)\phi(x) + (C_2/C_1) \int_0^1 dx T_8^S(x, r, m_b)\phi(x)}{\int_0^1 dx T_1^P(x, r, m_b)\phi(x) + (C_2/C_1) \int_0^1 dx T_8^P(x, r, m_b)\phi(x)} \right|^2. \quad (10.38)$$

Expanding in the strong coupling, gives

$$\begin{aligned} \frac{\Gamma(\bar{B}^0 \rightarrow D^+\pi^-)}{\Gamma(\bar{B}^0 \rightarrow D^{*+}\pi^-)} &\simeq 1 + 2Re \int_0^1 dx (T_1^S(x, r, m_b) - T_1^P(x, r, m_b))\phi(x) \\ &\quad + 2\frac{C_2}{C_1}Re \int_0^1 dx (T_8^S(x, r, m_b) - T_8^P(x, r, m_b))\phi(x), \end{aligned} \quad (10.39)$$

with the following expression for the gluon exchange in T_8 ,

$$T_8^S(x, r, m_b) - T_8^P(x, r, m_b) = -\frac{\alpha_s(m_b)}{9\pi} \left\{ rI[x(1-r^2)] + \frac{1}{r}I\left[(1-x)\left(1-\frac{1}{r^2}\right)\right] \right\}, \quad (10.40)$$

where

$$I[z] = \frac{1}{(1-z)} \left(\frac{z \log z}{1-z} + 1 \right). \quad (10.41)$$

The singlet corrections are proportional to $T_1^S(x, r, m_b) - T_1^P(x, r, m_b)$ and have been studied in the context of semileptonic B decays. They do not contribute any new nonfactorizable corrections and numerically change the ratio Eq. (10.39) by approximately 10%.

On the other hand, the octet contributions are responsible for the corrections to the factorization result of Eq. (10.7). From Eq. (10.40) one sees that they are numerically small, not exceeding $0.1\alpha_s(m_b)/\pi$. This small correction is typical for perturbative effects. In order to estimate the range of possible values, it is instructive to study the wave-function dependence of this nonfactorizable contribution. Although the overall correction turns out to be relatively small, the result strongly depends on the value of r and on the form chosen for the pion wave function; it grows significantly

if one changes from the asymptotic wave function $\phi_\pi \sim x(1-x)$ to the Chernyak-Zhitnitsky one with $\phi_\pi \sim x(1-x)(1-2x)$. Moreover, since the ratio Eq. (10.39) is a sum of terms of comparable magnitude but different signs, even the overall sign of the correction is uncertain; the correction turns negative for smaller values of r . One must note that although the value of the perturbative correction is unstable, the uncertainty associated with it is rather small and does not exceed 5%. It would of course be desirable to extend these calculations to other situations, but it seems that perturbative effects cannot account for possibly large deviations from factorization.

10.1.3.2 Nonperturbative contributions

Sum rules provide a useful tool for studying QCD effects, including the important nonperturbative ones (see Appendix D). An important step towards the theoretical description of nonperturbative nonfactorizable corrections was made in [21]. The authors considered a specific small velocity (SV) limit where $m_b - m_c \sim \text{const}$. This implies a different scaling of (10.34), $E \sim \text{const}$ as $m_b \rightarrow \infty$. It turns out that this limit is theoretically “clean” for the application of the QCD sum rule method and provides a theoretical justification of the “rule of discarding $1/N_c$ corrections” [13] on dynamical grounds. Consider the correlator

$$A^\beta = - \int d^4x e^{iqx} \langle D | T \{ \mathcal{H}_8(x), \pi^\beta(0) \} | B \rangle, \quad (10.42)$$

where $\pi^\beta = \bar{u}\gamma^\beta\gamma^5 d$ is the interpolating axial current that annihilates the pion, and $\mathcal{H}_8(x)$ is an octet part of the interaction Hamiltonian.

As in the usual QCD sum rule calculation, the correlator Eq. (10.42) is evaluated in Euclidean space, both phenomenologically

$$A^\beta = M_{nf} \frac{f_\pi q^\beta}{q^2} + \dots, \quad (10.43)$$

and theoretically, applying short-distance OPE to the right hand side of Eq. (10.42),

$$A^\beta = i \frac{1}{4\pi^2} \frac{q^\alpha q^\beta}{q^2} \langle D | \bar{c}\gamma_\mu\gamma_5 \bar{G}_{\alpha\mu} b | B \rangle + \dots. \quad (10.44)$$

Equating Eqs. (10.43) and (10.44) one finds for the nonfactorizable contributions

$$r_{nf} \equiv 2\epsilon_8 = - \frac{m_{\sigma H}^2}{4\pi^2 f_\pi^2} \simeq - \frac{1}{N_c}, \quad (10.45)$$

with $m_{\sigma H}^2 = 3(m_{B^*}^2 - m_B^2)/4$, which, as can be seen from Eq. (10.32), numerically implies a partial cancellation of the $1/N_c$ suppressed factorizable amplitude and a nonfactorizable one. Unfortunately, the actual B decays are at the borderline of the kinematic limit which justifies the formalism, bringing large uncertainties into the estimation of the matrix elements. Note that as

for the phenomenological estimate, the nonfactorizable corrections are case-by-case dependent. A similar analysis was performed for the color-suppressed $B^0 \rightarrow \pi^0 D^0$ decay [14], which reached a similar conclusion: the nonfactorizable corrections partially cancel $1/N_c$ -suppressed factorizable amplitudes, *i.e.*, $a_2 \simeq C_2 < 0$.

An alternative approach, using four-point sum rules [20], was earlier applied to investigate nonfactorizable effects in charmed decays. It also has been applied to determine nonfactorizable effects in the decay $B^0 \rightarrow J/\psi K_S^0$ [12]. Consider an effective Hamiltonian for this color-suppressed decay with a singlet and an octet operator,

$$\begin{aligned}\mathcal{H}_{\text{eff}} &= \frac{4G_F}{\sqrt{2}} V_{cb} V_{cs}^* \left[\left(C_2 + \frac{C_1}{N_c} \right) (\mu) O^{(1)}(\mu) + 2C_1(\mu) O^{(8)}(\mu) \right], \\ O^{(1)} &= \bar{c}_i \gamma_\mu \frac{1 - \gamma_5}{2} c_i \bar{s}_j \gamma^\mu \frac{1 - \gamma_5}{2} b_j, \\ O^{(8)} &= \bar{c}_i \gamma_\mu \frac{1 - \gamma_5}{2} \frac{\lambda_{ij}^a}{2} b_j \bar{s}_k \gamma^\mu \frac{1 - \gamma_5}{2} \frac{\lambda_{kl}^a}{2} b_l,\end{aligned}\tag{10.46}$$

where now $a_2^{\text{naive}} = (C_2 + C_1/N_c)(\mu) \simeq 0.155$ at the scale $\mu \sim m_b$, while at the scale $\mu \sim m_b/2$ it is ~ 0.08 .

One can compare these results with the values given earlier for a_2 in the BSW framework (recall $a_2 \sim (C_2 + C_1/N_c)$). The BSW approach, where only the first operator is retained with a factorized matrix element, yields $a_2 \sim 0.31 \pm 0.02$, which is not inconsistent with the estimates of a_2 made earlier. Since this value is considerably larger than the naive value $a_2^{\text{naive}} = (0.0 - 0.155)$, factorization must be badly violated in this decay. In Ref. [12], the octet contribution is determined using a sum rule involving a four-point correlation function. Since this operator is multiplied by the large Wilson coefficient C_1 , it is expected that its contribution is substantial. Indeed, these authors find an increase of the effective a_2 coupling which, however, is not quite sufficient to reproduce the experimental value. Moreover, the sign of a_2 is preferably negative in contrast to the former results.

Departing from the small velocity limit introduces new operators each contributing at the same order of magnitude to the amplitude under consideration. These can be resummed in the limit $E \sim m_b$ as $m_b \rightarrow \infty$ [22]. The idea is to study the propagation of the light quarks emerging to form the final hadron while passing through the (perturbative or nonperturbative) gluonic fields present in the decay. Interestingly, results can be obtained which are independent of the nature of the gluonic fields and, at leading order, of the hadronic wave function. The light-quark pair produced at $x = 0$ interacts strongly with the background gluonic field while escaping from the production point and hadronizing into the pion. Since the energy transferred to the quark pair is large, it is not necessary that the hadronization occur at $x \sim 0$. As a result, it is not sufficient to take the operators of the lowest dimension in the Operator Product Expansion (OPE). Instead, one must sum up a whole series of operators by introducing a set of “generating (distribution) functions” which incorporate this infinite series of matrix elements. Heavy-quark symmetry is then used to

restrict the form of the matrix elements enough that useful statements can be made. In principle, the generating functions could be modeled or perhaps fixed by other measurements. However, at the leading order in $q^2 = 0, x^2 \sim 0$ the color octet matrix element vanishes due to cancellations and factorization holds [22].

10.1.4 Tests of Factorization

As discussed in the previous sections, factorization allows one to express the matrix element of a given four-quark operator as the product of two matrix elements of color-singlet currents. One may test the deviations of experimental results from predictions based on factorization and, in some cases, extract certain physical quantities, such as meson decay constants or form factors. Factorization tests are interesting because of the insight they shed on strong dynamics. However, because of the uncontrolled nature of the ansatz, the use of factorization for the direct extraction of form factors and decay constants is not very reliable.

The first test involves making a direct comparison of branching ratios (R -test). Once the total matrix element for a hadronic decay is factorized, the amplitude in a particular region of phase space in a related semileptonic decay can be obtained by replacing one of the matrix elements by the corresponding leptonic quantity. For any Type-I decay, one finds

$$R_h^{(*)} = \frac{\Gamma(B^0 \rightarrow D^{(*)} h^-)}{d\Gamma(B^0 \rightarrow D^{(*)} l^- \nu)/dq^2|_{q^2=m_h^2}} = 6\pi^2 f_h^2 |a_1|^2 |V_{ij}|^2 X_h^{(*)}, \quad (10.47)$$

where the semileptonic differential decay rate is evaluated at $q^2 = m_h^2$. Here f_h is the decay constant of the meson h , and V_{ij} is the appropriate CKM matrix element (depending on the flavor quantum numbers of the meson h). One example is $h = \pi$, where $V_{ij} = V_{ud}$. The constant $X_\pi^{(*)}$ was evaluated in [23] and found to be

$$X_\pi = \frac{(m_B^2 - m_D^2)^2}{(m_B^2 - (m_D + m_\pi)^2)(m_B^2 - (m_D - m_\pi)^2)} \frac{|F_0(m_\pi^2)|^2}{|F_1(m_\pi^2)|^2},$$

$$X_\pi^* = (m_B^2 - (m_D + m_\pi)^2)(m_B^2 - (m_D - m_\pi)^2) \frac{|A_0(m_\pi^2)|^2}{m_\pi^2 \sum_{i=0,\pm} |H_i(m_\pi^2)|^2}, \quad (10.48)$$

where F and A_0 are form factors.

The helicity amplitudes $H_0(q^2)$ and $H_\pm(q^2)$ are defined in Ref. [4]. Numerically, $X_\pi \simeq 1.001$ and $X_\pi^* \simeq 0.994$. Taking the Heavy Quark Limit, $X_\pi \simeq X_\pi^* = 1$, one finds

$$R_\pi = R_\pi^* = 6\pi^2 f_\pi^2 |a_1|^2 |V_{ud}|^2 \simeq \left(\frac{a_1}{1.12}\right)^2 \times 1.23 \text{ GeV}^2. \quad (10.49)$$

Experiment gives $R_\pi^* = (1.21 \pm 0.43) \text{ GeV}^2$, which is in excellent agreement with Eq. (10.49). This implies $a_1^{\text{eff}} = 1.11 \pm 0.10$, in good agreement with previous values. Further improvements in the measurements would test the assumptions with better precision.

An even cleaner test of factorization is obtained when (10.48) is evaluated for a vector or pseudovector meson, in which case one has exactly [24]

$$X_V = X_V^* = 1. \quad (10.50)$$

Since the lepton pair created by the $(V - A)$ current carries spin one, its production is kinematically equivalent to that of a (pseudo)vector particle with four-momentum q_μ . For a ρ meson in the final state, for instance,

$$R_\rho = R_\rho^* = 6\pi^2 f_\rho^2 |a_1^{\text{eff}}|^2 |V_{ud}|^2 \approx |a_1^{\text{eff}}|^2 \times 2.48 \text{ GeV}^2, \quad (10.51)$$

which can be compared with the experimental value $R_\rho^* = 2.92 \pm 0.71 \text{ GeV}^2$. This gives $a_1^{\text{eff}} = 1.09 \pm 0.13$, again in good agreement with the expectation based on factorization. In principle, Eqs. (10.48) and (10.51) offer the possibility for four independent determinations of the parameter a_1^{eff} . Good agreement among the extracted values supports the validity of the factorization approximation in B decays. At the present level of accuracy this agreement already indicates that there is little room for final state interactions to affect the magnitude of the considered decay amplitudes (which is not always the case for Type-II decays).

It is interesting to note that if the factorization approximation holds for Type-I decays, and if the coefficient a_1 is known with enough precision, then Eqs. (10.47) and (10.48) can be used to extract the decay constants of various mesons. This has been exploited in Ref. [4] for D mesons.

Given the argument that the lepton pair in the semileptonic decay and the spin-1 meson in the hadronic decay are equivalent, it follows that (10.47) is valid separately for longitudinal and transverse polarization of the D^* meson in the final state. Thus, the polarization of the D^* meson produced in the nonleptonic decay $\bar{B}^0 \rightarrow D^{*+} V^-$ should be equal to the polarization in the corresponding semileptonic decay $\bar{B} \rightarrow D^* \ell \bar{\nu}$ at $q^2 = m_V^2$. However, in order to turn this prediction into a test of the factorization hypothesis, one would have to determine the polarization of the D^* meson with high precision. This is because in both the semileptonic and nonleptonic cases, the D^* polarization at the points $q^2 = 0$ and $q^2 = q_{\text{max}}^2$ is determined by kinematics alone to be 100% longitudinal and 1/3 longitudinal, respectively. This shows that for a stringent test of the factorization hypothesis at small q^2 , one must determine the transverse polarization contribution with a small relative error. In the heavy-quark limit, the ratio of transverse to longitudinal polarization at some fixed q^2 is simply given by

$$\frac{\Gamma_T}{\Gamma_L} = \frac{4q^2(m_B^2 + m_{D^*}^2 - q^2)}{(m_B - m_{D^*})^2[(m_B + m_{D^*})^2 - q^2]}. \quad (10.52)$$

Including the leading symmetry-breaking corrections to this result [25, 26], one obtains the numbers shown in Table 10-6. For the polarization of the D^* meson in the decay $\bar{B}^0 \rightarrow D^{*+} \rho^-$, the CLEO Collaboration finds [9] $\Gamma_T/\Gamma_{\text{tot}} = (7 \pm 5 \pm 5)\%$, in agreement with the prediction of 12% transverse polarization for the semileptonic decay at $q^2 = m_\rho^2$. However, in order for this test to be sensitive to deviations from factorization, the experimental uncertainty will have to be reduced

substantially. The situation may be more favorable in the decay $\bar{B}^0 \rightarrow D^{*+} D_s^*$, where the predicted transverse polarization is 48%, which will permit, one hopes, a measurement with smaller relative uncertainties.

Table 10-6. Theoretical predictions for the ratio $\Gamma_T/\Gamma_{\text{tot}}$ at fixed q^2 , where $\Gamma_{\text{tot}} = \Gamma_T + \Gamma_L$.

q^2	0	m_ρ^2	$m_{a_1}^2$	$m_{D_s^*}^2$	q_{max}^2
$\Gamma_T/\Gamma_{\text{tot}}$	0	0.12 ± 0.01	0.26 ± 0.02	0.48 ± 0.01	2/3

There are also factorization tests involving the color-suppressed Type-II decays. As mentioned, the nonfactorizable terms are proportional to the large Wilson coefficient C_1 , and therefore cannot be neglected. Nevertheless, if universality is assumed, as advocated in the BSW picture, specific predictions can be made and checked.

One of these decays is $B \rightarrow J/\psi K^*$ which is of major interest for CP violation measurements. The vector-vector decay $B^0 \rightarrow J/\psi K^{*0}$, with $K^{*0} \rightarrow K_s^0 \pi^0$, is a mixture of CP -even and CP -odd eigenstates since it can proceed via an S -, P -, or D -wave decay. If one CP eigenstate dominates or if the two CP eigenstates can be separated, this decay can be used to measure the angle β of the unitarity triangle in a manner similar to that in which the CP -odd eigenstate decay $B^0 \rightarrow J/\psi K_s^0$ is used.

Several phenomenological models predict the longitudinal polarization fraction in $B \rightarrow J/\psi K^*$ decays, denoted Γ_L/Γ , and the ratio of vector to pseudoscalar meson production, $R_\psi \equiv \mathcal{B}(B \rightarrow J/\psi K^*)/\mathcal{B}(B \rightarrow J/\psi K)$ [3, 23, 27, 28, 29]. Additional information about the validity of factorization can be obtained from measuring the decay amplitude phases, since any nontrivial phase differences indicate final state interactions and the breakdown of factorization [30]. A recent CLEO collaboration publication [31] presented a complete angular analysis and an update of the branching fractions for $B \rightarrow J/\psi K^{*0}$. They measured five quantities including $\Gamma_L/\Gamma = 0.52 \pm 0.07 \pm 0.04$ and $R_\psi = 1.45 \pm 0.20 \pm 0.17$. The data on the relative phases $\phi(A_\perp)$ and $\phi(A_\parallel)$ with respect to $\phi(A_0)$ indicates that the amplitudes are relatively real, and that final state interactions are not present at a significant level.

From the effective Hamiltonian (10.1) with the Wilson coefficients C_1 and C_2 , the decay amplitude for $B \rightarrow J/\psi P(V)$ can be written as (see (10.10))

$$\begin{aligned} \mathcal{A}(B(p_B) \rightarrow P(V)(p_{P(V)})J/\psi(q)) &= \\ &= \frac{4G_F}{\sqrt{2}} V_{cb}^* V_{cs} \left[\left(C_2 + \frac{1}{N_c} C_1 \right) \langle P(V)J/\psi | O_1 | B \rangle + 2C_1 \langle P(V)J/\psi | O^{(8)} | B \rangle \right]. \end{aligned} \quad (10.53)$$

As before, the matrix elements are split into a factorizable part and a remainder. Since now there are spins involved, instead of one matrix element, there are several form factors. Instead of using

the ϵ s introduced earlier, one can denote the nonfactorizable terms by a subscript NF and write

$$\begin{aligned}\langle P(V)J/\psi | O_1 | B \rangle &= \langle J/\psi | (\bar{c}c)_{V-A} | 0 \rangle \langle P(V) | (\bar{b}s)_{V-A} | B \rangle + \langle P(V)J/\psi | O^{(1)} | B \rangle_{NF}, \\ \langle P(V)J/\psi | O^{(8)} | B \rangle &= \langle P(V)J/\psi | O^{(8)} | B \rangle_{NF}.\end{aligned}\quad (10.54)$$

The factorizable parts are given by Eqs. (10.15)-(10.17) with momenta implicitly defined in (10.54). The nonfactorizable ones are

$$\begin{aligned}\langle PJ/\psi | O^{(1,8)} | B \rangle_{NF} &= 2(\epsilon \cdot p_B) m_\psi f_\psi F_1^{(1,8)NF}(q^2) \\ \langle VJ/\psi | O^{(1,8)} | B \rangle_{NF} &= - \left\{ (m_B + m_V)(\epsilon \cdot \eta^*) A_1^{(1,8)NF}(q^2) - 2 \frac{(\epsilon \cdot p_B)(\eta^* \cdot p_B)}{m_B + m_V} A_2^{(1,8)NF}(q^2) \right. \\ &\quad \left. - 2i \frac{\epsilon_{\mu\nu\rho\sigma} \epsilon^\mu \eta^{*\nu} p_B^\rho p_V^\sigma}{m_B + m_V} V^{(1,8)NF}(q^2) \right\} m_\psi f_\psi.\end{aligned}\quad (10.55)$$

The polarization vectors ϵ^μ and η^μ correspond to the two vector mesons J/ψ and V , respectively.

Substituting Eqs. (10.54)-(10.55) into the decay amplitude (10.53), one can calculate decay rates for the processes $B \rightarrow P(V)J/\psi$ and polarization for the $B \rightarrow VJ/\psi$ process. The decay widths for each process are

$$\begin{aligned}\Gamma(B \rightarrow PJ/\psi) &= \frac{G_F^2 m_B^5}{32\pi} |V_{cb}|^2 |V_{cs}|^2 \left(C_2 + \frac{1}{N_c} C_1 \right)^2 \left(\frac{f_\psi}{m_B} \right)^2 k^3(t^2) \left| F_1(m_\psi^2) \right|^2 \left| 1 + \frac{2C_1 \chi_{F_1}}{C_2 + C_1/N_c} \right|^2, \\ \Gamma(B \rightarrow VJ/\psi) &= \frac{G_F^2 m_B^5}{32\pi} |V_{cb}|^2 |V_{cs}|^2 \left(C_2 + \frac{1}{N_c} C_1 \right)^2 \left(\frac{f_\psi}{m_B} \right)^2 \left| A_1(m_\psi^2) \right|^2 k(t^2) t^2 (1+r)^2 \sum_{\lambda\lambda} H_{\lambda\lambda},\end{aligned}\quad (10.56)$$

where $\lambda\lambda$ sums over the vector mesons helicities: 00, ++ and --. The symbol χ_{F_1} is defined as

$$\chi_{F_1} = \frac{1}{F_1(m_\psi^2)} \left[F_1^{(8)NF}(m_\psi^2) + \frac{1}{2C_1} \left(C_2 + \frac{1}{N_c} C_1 \right) F_1^{(1)NF}(m_\psi^2) \right], \quad (10.57)$$

and the dimensional parameters r, t, k are

$$r = \frac{m_{P(V)}}{m_B}, \quad t = \frac{m_\psi}{m_B}, \quad k(t^2) = \sqrt{(1-r^2-t^2)^2 - 4r^2 t^2}. \quad (10.58)$$

The *longitudinal* and *transverse* polarizations for the decay $B \rightarrow VJ/\psi$, are given by

$$\begin{aligned}H_L = H_{00} &= \left[a \left(1 + \frac{2C_1 \chi_{A_1}}{C_2 + C_1/N_c} \right) - bx \left(1 + \frac{2C_1 \chi_{A_2}}{C_2 + C_1/N_c} \right) \right]^2, \\ H_T = H_{++} + H_{--} &= 2 \left[\left(1 + \frac{2C_1 \chi_{A_1}}{C_2 + C_1/N_c} \right)^2 + c^2 y^2 \left(1 + \frac{2C_1 \chi_V}{C_2 + C_1/N_c} \right)^2 \right],\end{aligned}\quad (10.59)$$

where χ_{A_1} , χ_{A_2} , and χ_V , are defined as in (10.57), when F_1 is replaced, respectively, by A_1 , A_2 , and V . In (10.59) the dimensionless parameters

$$a = \frac{1 - r^2 - t^2}{2rt}, \quad b = \frac{k^2(t^2)}{2rt(1+r)^2}, \quad c = \frac{k(t^2)}{(1+r)^2} \quad (10.60)$$

were introduced. Their numerical values for the processes $B \rightarrow J/\psi K(K^*)$ are given as $a = 3.165$, $b = 1.308$, $c = 0.436$. Furthermore x , y , and z are defined by

$$x = \frac{A_2^{BK^*}(m_\psi^2)}{A_1^{BK^*}(m_\psi^2)}, \quad y = \frac{V^{BK^*}(m_\psi^2)}{A_1^{BK^*}(m_\psi^2)}, \quad z = \frac{F_1^{BK}(m_\psi^2)}{A_1^{BK^*}(m_\psi^2)}. \quad (10.61)$$

The longitudinal polarization fraction Γ_L/Γ and the ratio R_ψ are defined as

$$\frac{\Gamma_L}{\Gamma} \equiv \frac{\Gamma(B \rightarrow J/\psi K^*)_L}{\Gamma(B \rightarrow J/\psi K^*)} = \frac{H_L}{H_L + H_T}, \quad (10.62)$$

$$R_\psi \equiv \frac{\Gamma(B \rightarrow J/\psi K^*)}{\Gamma(B \rightarrow J/\psi K)} = 1.08 \frac{(H_L + H_T)}{z^2 |1 + \frac{2C_1 \chi_{F_1}}{C_2 + C_1/N_c}|^2}. \quad (10.63)$$

Finally the parity-odd (P -wave) transverse polarization measured in the transversity basis [31, 32] is given by

$$|P_\perp|^2 = \frac{|A_\perp|^2}{|A_0|^2 + |A_\parallel|^2 + |A_\perp|^2} = 2c^2 y^2 \frac{\left(1 + \frac{2C_1 \chi_{F_1}}{C_2 + C_1/N_c}\right)^2}{(H_L + H_T)}. \quad (10.64)$$

Strict factorization would imply that all the quantities χ are equal to zero. Since this is not tenable for Type-II decays, for simplicity *universality* is assumed, $\chi_{F_1} = \chi_{A_1} = \chi_{A_2} = \chi_V = \chi$. In this case, the nonfactorizable terms only affect the coefficient a_2 ,

$$C_2 + \frac{1}{N_c} C_1 \longrightarrow a_2^{\text{eff}} = C_2 + \xi C_1, \quad \xi = \frac{1}{N_c} + 2\chi. \quad (10.65)$$

Note, however, that the ratios Γ_L/Γ , R_ψ , and $|P_\perp|^2$ are in fact independent of the value of χ , as for the strict factorization ansatz [3].

For comparison with experiment, several phenomenological models of form factors are considered:

1. The BSW model [3] in which $B \rightarrow K(K^{(*)})$ form factors are first evaluated at $q^2 = 0$ and then extrapolated to finite q^2 using a monopole type q^2 -dependence for all form factors F_1 , A_1 , A_2 , and V .

2. The modified BSW model (called BSW II here) [23], takes the values of the form factors at $q^2 = 0$ as in BSW I but uses a monopole form factor for A_1 and a dipole form factor for $F_1, A_2,$ and V .
3. The nonrelativistic quark model by Isgur *et al.* (ISGW)[27] with exponential q^2 dependence for all form factors.
4. The model of Casalbuoni *et al.* and Deandrea *et al.* (CDDFGN)[28] in which the normalization at $q^2 = 0$ is obtained in a model that combines heavy-quark symmetry with chiral symmetry for light pseudoscalar degrees of freedom and also introduces light vector degrees of freedom. Here all form factors are extrapolated with monopole behavior.

Several authors have derived the $B \rightarrow K(K^*)$ form factors from experimentally measured $D \rightarrow K(K^*)$ form factors at $q^2 = 0$, using the Isgur-Wise scaling laws based on the SU(2) heavy-quark symmetry [33], which relate B and D form factors at q^2 near q_{max}^2 .

1. The $B \rightarrow K(K^*)$ form factors are calculated in Ref. [34] by assuming a constant for A_1 and A_2 , a monopole type form factor for F_1 , and dipole type for V .
2. An ansatz proposed in Ref. [29], which relies on “soft” Isgur-Wise scaling laws and a monopole type for A_1 and a dipole type for A_2, V, F_1 .
3. For Ref. [35], they are computed by advocating a monopole extrapolation for F_1, A_0, A_1 , a dipole behavior for A_2, V , and an approximately constant value for F_0 .

Table 10-7 summarizes the predictions of $\Gamma_L/\Gamma, R_\psi$ and $|P_\perp|^2$ resulting from the use of the various form factor models mentioned above. The factorization approach is used and the absence of inelastic final state interactions is assumed.

Gourdin *et al.* [36] also have suggested that the ratio $R_{\eta_c} = \mathcal{B}(B \rightarrow \eta_c K^*)/\mathcal{B}(B \rightarrow \eta_c K)$ would provide a good test of the factorization hypothesis in Type-II decays. Using the Particle Data Group [8] value for $\mathcal{B}(B^+ \rightarrow K^+ J/\psi) = (1.02 \pm 0.14)\%$, one expects $\mathcal{B}(B^+ \rightarrow K^+ \eta_c) = (1.14 \pm 0.31) \times 10^{-3}$ (a value consistent with this was recently reported by CLEO [37]). Other decay rate ratios in modes with charmonium mesons may also be used to test universality [10, 34, 38].

Finally, yet another test [40] is possible. Consider the matrix element corresponding to the product of two currents. These currents can, in general, produce only $0^-, 1^-$ and 1^+ states from the vacuum, but not 0^+ and 2^+ states. Only if the current is not conserved (*e.g.*, a $\bar{c}\gamma_\mu d$ current) can 0^+ be produced, since it is directly related to the divergence. This implies immediately that in the factorization approximation, certain two-body decays with 2^+ and 0^+ mesons have a vanishing decay rate.

Table 10-7. Experimental data and theoretical predictions for Γ_L/Γ , R_ψ , and $|P_\perp|^2$.

	Γ_L/Γ	R_ψ	$ P_\perp ^2$
CLEO II(96)[31]	$0.52 \pm 0.07 \pm 0.04$	$1.45 \pm 0.20 \pm 0.17$	$0.16 \pm 0.08 \pm 0.04$
BSW I [3]	0.57	4.23	0.09
BSW II [23]	0.36	1.61	0.24
ISGW [27]	0.07	1.72	0.52
CDDFGN [28]	0.36	1.50	0.30
JW [39]	0.44	2.44	
Orsay [29]	0.45	2.15	0.25
Keum [34]	0.59 ± 0.07	1.74 ± 0.38	0.14 ± 0.05
CT [35]	0.56	1.84	0.16

A partial list of these “forbidden” decays is:

$$\begin{aligned}
 \text{Type I: } & \bar{B}^0 \rightarrow D^+ a_2^-, \quad \bar{B}^0 \rightarrow D_{s(2+)}^{*-} D^+ \\
 & \bar{B}^0 \rightarrow D^+ a_0^-, \quad B^- \rightarrow D_{s(2+)}^{*-} \\
 \text{Type II: } & \bar{B}^0 \rightarrow D^{*0} \pi^0 \\
 & \bar{B}^0 \rightarrow \chi_0^c \bar{K}^0, \quad \bar{B}^0 \rightarrow \chi_2^c \bar{K}^0 \\
 & B^- \rightarrow \chi_0^c K^-, \quad B^- \rightarrow \chi_2^c K^-
 \end{aligned}$$

In Type-III decays, the decay $B^- \rightarrow D^{*0} \pi^-$ has a factorizable contribution proportional to a_1 , and since the a_2 component is forbidden by current conservation, the amplitude equals that of the Type-I decay $\bar{B}^0 \rightarrow D^{*+} \pi^-$.

10.1.5 Factorization in Multibody Decays

The theoretical treatment of multibody decays is still in its infancy. However, as these decays are expected to have sizable branching ratios and to be an important background to specific CP studies, it is important to make at least qualitative estimates for branching ratios, angular distributions, *etc.* The literature on this subject is rather limited; here the paper by Reader and Isgur [5] is followed.

One possible way to estimate the rates of multibody processes with several pions is to use heavy quark chiral perturbation theory. The applicability of this theory is limited to low-energy pions, it is discussed in Section 10.3

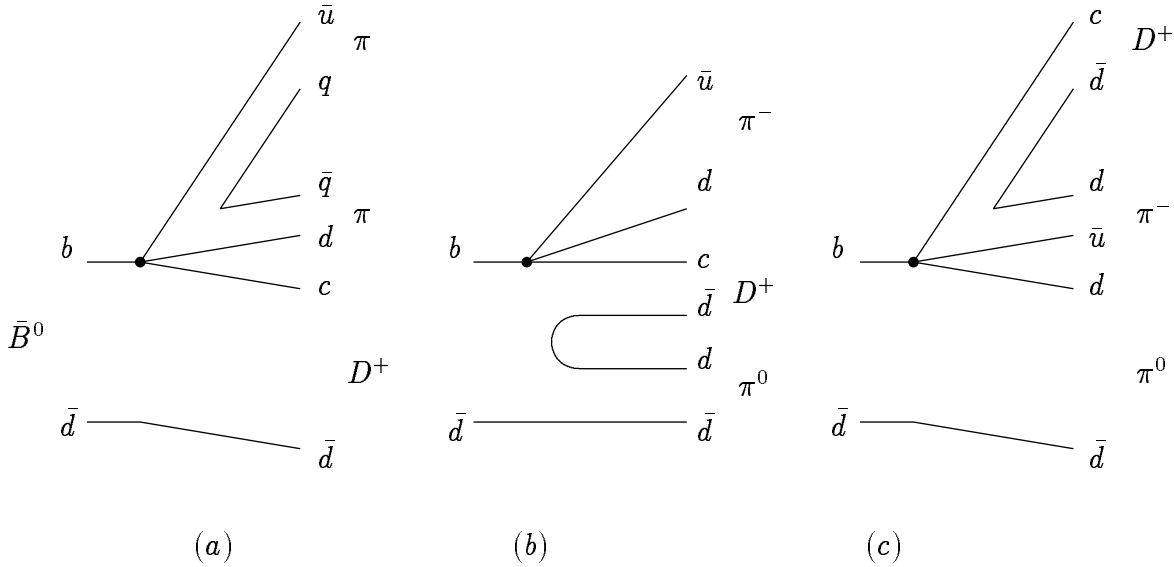


Figure 10-3. Color-allowed (a) and (b) and color-suppressed (c) diagrams for $\bar{B}^0 \rightarrow D^+ \pi^- \pi^0$. Only (a) contributes to $\bar{B}^0 \rightarrow D^+ K^- K^0$.

Another alternative is to use factorization. Although this has been mainly applied to two-body decays of the B meson, it might also be a suitable framework for describing multibody decays. However, the situation is more involved. Since the weak (four-Fermi) interaction generates only three quarks, at least one of the quark pairs in a multi body decay has to be pair produced via gluons. This can usually happen in many ways. Consider as an example the decay $\bar{B}^0 \rightarrow D^+ \pi^- \pi^0$. The color preferred contribution (mainly O_1) comes in two ways: the first current, $\bar{c}b$ (together with the spectator \bar{d} quark) can either produce a D^+ or a $D^+ \pi^0$ pair while the other current generates the remaining particle(s)¹ (Fig. 10-3). While both contributions factorize, there is no way to assess their relative size. In order to overcome this problem, one might look at decays where one of the topologies cannot occur. One possibility includes decays to some specific final states containing strange-quark pairs.

Consider the decay $\bar{B}^0 \rightarrow D^+ K^- \bar{K}^0$. It can proceed only through the diagram where the $\bar{c}b$ current produces the D^+ and the other current the kaon pair (see Fig. 10-3). The factorizable contribution for $\bar{B}^0 \rightarrow D^+ \pi^- \pi^0$ is

$$\begin{aligned} \mathcal{A}(\bar{B}^0 \rightarrow D^+ \pi^- \pi^0) = & (-i)G_F V_{cb} V_{ud}^* a_1 m_B^2 \times \\ & \left\{ 2f_+^D(s_{13})F_-^{\pi\pi} [1 - \mu_D - \mu_{23} - 2\mu_{13}] + 2f_+^D(s_{13})F_+^{\pi\pi} [1 - \mu_D] + 2f_-^D(s_{13})F_+^{\pi\pi} \mu_{23} \right. \\ & \left. - F_\pi S(0) [1 - \mu_{13}] - F_\pi P(0) [1 - 2\mu_{23} - \mu_{13}] \right\} + A_2(\bar{B}^0 \rightarrow D^+ \pi^- \pi^0), \end{aligned} \quad (10.66)$$

¹In addition, there is also a color-suppressed combination, where the $D^+ \pi^-$ are produced by one term and π^+ by the other.

with $A_2(\bar{B}^0 \rightarrow D^+ \pi^- \pi^0)$ being a color-suppressed combination,

$$A_2(\bar{B}^0 \rightarrow D^+ \pi^- \pi^0) = (-i)G_F V_{cb} V_{ud}^* a_1 m_B^2 \times \left\{ f_+^\pi(s_{12}) F_+^{D\pi} + f_-^\pi(s_{12}) F_+^{D\pi} [1 + \mu_D - \mu_{23} - \mu_{13}] + f_+^\pi(s_{12}) F_-^{D\pi} \mu_D \right\}. \quad (10.67)$$

This is to be compared to $A(\bar{B}^0 \rightarrow D^+ K^- \bar{K}^0)$, for which only three terms contribute [cf. Eq. (10.66)],

$$\mathcal{A}(\bar{B}^0 \rightarrow D^+ K^- \bar{K}^0) = (-i)G_F V_{cb} V_{ud}^* a_1 m_B^2 \times \left\{ f_+^D(s_{13}) F_-^{KK} [1 - \mu_D - \mu_{23} - \mu_{13}] + f_+^D(s_{13}) F_+^{KK} [1 - \mu_D] + f_-^D(s_{13}) F_+^{KK} \mu_{23} \right\}, \quad (10.68)$$

where form factors defined in Eq (10.14) were used in addition to

$$\begin{aligned} \langle P_1 P_2 | \bar{u} \Gamma_\mu d | 0 \rangle &= \sqrt{2} F_-^{P_1 P_2} (k_1 - k_2)_\mu + \sqrt{2} F_+^{P_1 P_2} (k_1 + k_2)_\mu, \\ \langle P_D P_2 | \bar{c} \Gamma_\mu b | B \rangle &= -i \left\{ S(p_1 + k_2)_\mu + P(p_D - k_2)_\mu + R(p_B - p_D - k_2)_\mu + iH \epsilon_{\mu\nu\alpha\beta} p_B^\nu p_D^\alpha k_2^\beta \right\}. \end{aligned} \quad (10.69)$$

The invariant variables $s_{12} = (p_B - k_2)^2$, $s_{23} = (p_B - p_D)^2$, $s_{13} = (p_B - k_1)^2$, with $s_{12} + s_{23} + s_{13} = m_B^2 + m_D^2$ and $\mu_{ik} = s_{ik}/m_B^2$ have been used in these equations.

Thus, unless the final state is carefully chosen, factorization does not seem a very useful concept. Only if there are no gluons exchanged and the produced pair “stays within” the color singlet flow of one of the current quark pairs, is factorization applicable. This implies in general that there are only limited kinematical regions of validity, for instance where there are intermediate resonances, and thus the multibody decay is a quasi two-body decay.

In Ref. [5] the decays $B \rightarrow D + n\pi$ are considered. The effective Hamiltonian is split according to Eq. (10.1). The various rates are calculated using a resonance model where the final state is generated by a sum of possible D (or D^* , D^{**}) and multi pion (ρ , a_1 , *etc.*) resonances in an obvious way. The results, which depend on model input, are shown in Tables 10-8 and 10-9. Various improvements can be made, but they are beyond the scope of this discussion.

10.2 The Role of Final State Interactions in B Decays

The decay of a heavy hadron produces quarks in the final state. These quarks interact strongly, and these QCD interactions continue after the weak transition takes place and after hadron formation. As a result, developing an understanding of *final state rescatterings* or *final state interactions* (FSI) is an important part of understanding the physics of nonleptonic b -decays.

Final state rescatterings can be extremely important. They can crucially affect the decay amplitudes; changing their sizes and even their dependence on CKM matrix elements. This is an

Table 10-8. Theoretical predictions and experimental values for various three-body decays described in the text.

Decay	via $D\rho$		via D_2^*		via D_0^*		Total	
	Th.	Exp.	Th.	Exp.	Th.	Exp.	Th.	Exp.
$\bar{B}^0 \rightarrow D^+ \pi^- \pi^0$.55	$.88 \pm .62$.02	-	.01	-	.59	-
$\bar{B}^0 \rightarrow D^0 \pi^- \pi^+$	0	$< .06$.04	$< .04$.02	$< .01$.07	$< .70$
$B^- \rightarrow D^0 \pi^- \pi^0$.55	1.32 ± 0.62	.02	-	.01	-	.59	-
$B^- \rightarrow D^+ \pi^- \pi^-$	0	-	.04	$< .40$.02	$< .48$.07	$< .70$

Decay	via $D^* \rho$		via D_2^*	via $D_1^{\frac{3}{2}}$	via $D_1^{\frac{1}{2}}$	Total	
	Th.	Exp.	Theor.			Th.	Exp.
$\bar{B}^0 \rightarrow D^{*+} \pi^- \pi^0$.69	$.70 \pm .44$.01	.03	.01	.75	$1.80 \pm .66$
$\bar{B}^0 \rightarrow D^{*0} \pi^- \pi^+$	0	-	.02	.07	.02	.11	-
$B^- \rightarrow D^{*0} \pi^- \pi^0$.69	$1.01 \pm .70$.01	.03	.01	.75	-
$B^- \rightarrow D^{*+} \pi^- \pi^-$	0	-	.02	.07	.02	.11	$.24 \pm .18$

important effect as one tries to pin down the angles α , β and γ from the mixing-decay mechanism (see chapters 5,6,7). The effect most obviously dependent on FSI is direct CP violation (CP violation in decay), a difference in the rates of a B -meson decay with the charge-conjugated process. The asymmetries depend on both a weak phase (from CKM matrix elements) and a strong rescattering phase. This strong phase is provided by the FSI. Any nonvanishing asymmetry requires two different final states produced by different weak amplitudes which can mix with each other by a strong-interaction rescattering. Thus, FSI must occur to give any direct CP asymmetries, furthermore the size of these asymmetries can only be interpreted in terms of fundamental parameters if these FSI phases are calculable.

FSI occur both at the quark and at the hadronic level. It is impossible to separate these two effects cleanly and to avoid double counting of effects. These are often described as “short-” and “long-distance” effects, respectively, but the separation is not rigorously made. In the following discussion, the two effects and their relationship are described, but these issues are not resolved.

Final state interactions arise as a consequence the fact that there are multiple interacting states of a given isospin. Unitarity of the full S -matrix, $S^\dagger S = 1$ gives some constraints that can be useful.

Table 10-9. Theoretical predictions and experimental values for various four-body decays described in the text.

Decay	via Da_1		via $D_2^*\rho$	via $D_0^*\rho$	via $D\rho\pi$	via $D\pi\pi\pi$	Total	
	Th.	Exp.	Theor.		Expt.		Th.	Exp.
$\bar{B}^0 \rightarrow D^+ \pi^- \pi^0 \pi^0$.19	-	.05	.03	-	-	.27	-
$\bar{B}^0 \rightarrow D^+ \pi^- \pi^- \pi^+$.19	$.30 \pm .17$	0	0	$.11 \pm .10$	$.39 \pm .31$.21	$.80 \pm .28$
$\bar{B}^0 \rightarrow D^0 \pi^0 \pi^- \pi^+$	0	-	.10	.05	-	-	.15	-
$B^- \rightarrow D^0 \pi^- \pi^0 \pi^0$.19	-	.05	.03	-	-	.27	-
$B^- \rightarrow D^0 \pi^- \pi^- \pi^+$.19	$.22 \pm .18$	0	0	$.42 \pm .32$	$.51 \pm .42$.21	$1.15 \pm .39$
$B^- \rightarrow D^+ \pi^0 \pi^- \pi^-$	0	-	.10	.05	-	-	.15	-

Decay	via D^*a_1		via $D_2^*\rho$ $D_1^{\frac{3}{2}}\rho$ $D_1^{\frac{1}{2}}\rho$			via $D^*\rho\pi$ $D^*\pi\pi\pi$		Total	
	Th.	Exp.	Theor.			Expt.		Th.	Exp.
$\bar{B}^0 \rightarrow D^{*+} \pi^- \pi^0 \pi^0$.27	-	.02	.06	.03	-	-	.40	-
$\bar{B}^0 \rightarrow D^{*+} \pi^- \pi^- \pi^+$.27	$.90 \pm .44$	0	0	0	$.68 \pm .40$	$.00 \pm .00$.29	-
$\bar{B}^0 \rightarrow D^{*0} \pi^0 \pi^- \pi^+$	0	-	.04	.13	.06	-	-	.22	-
$B^- \rightarrow D^{*0} \pi^- \pi^0 \pi^0$.27	-	.02	.06	.03	-	-	.40	-
$B^- \rightarrow D^{*+} \pi^- \pi^- \pi^+$.27	-	0	0	0	-	-	.29	-
$B^- \rightarrow D^{*+} \pi^- \pi^- \pi^0$	0	-	.04	.13	.06	-	-	.22	$1.80 \pm .92$

The \mathcal{T} -matrix, defined by $\mathcal{S} = 1 + i\mathcal{T}$, obeys the equation (optical theorem):

$$Disc \mathcal{T}_{B \rightarrow F} \equiv \frac{1}{2i} [\langle F | \mathcal{T} | B \rangle - \langle F | \mathcal{T}^\dagger | B \rangle] = \frac{1}{2} \sum_I \langle F | \mathcal{T}^\dagger | I \rangle \langle I | \mathcal{T} | B \rangle, \quad (10.70)$$

where $Disc$ denotes the dispersive part (in theories without CP violation it is often referred to as the imaginary part, but when the Lagrangian contains complex coefficients this is a misnomer). Using CPT in the form

$$\langle \bar{F} | \mathcal{T} | \bar{B} \rangle^* = \langle \bar{B} | \mathcal{T}^\dagger | \bar{F} \rangle = \langle F | \mathcal{T}^\dagger | B \rangle \quad (10.71)$$

this can be transformed into the more intuitive form

$$\langle \bar{F} | \mathcal{T} | \bar{B} \rangle^* = \sum_I \langle F | \mathcal{S}^\dagger | I \rangle \langle I | \mathcal{T} | B \rangle. \quad (10.72)$$

Here, the states $|I\rangle$ represent all possible final states (including $|F\rangle$ itself) which can be reached from the state $|B\rangle$ by the weak transition matrix \mathcal{T} . The right hand side of Eq. (10.72) can then be viewed as a weak decay of $|B\rangle$ into $|I\rangle$ followed by a strong rescattering of $|I\rangle$ into $|F\rangle$. Thus, $\langle F|\mathcal{S}^\dagger|I\rangle$ may be identified as a CP -conserving FSI rescattering of particles. Notice that if $|I\rangle$ is an eigenstate of \mathcal{S} with a phase $e^{2i\delta}$, then

$$\langle \bar{I}|\mathcal{T}|\bar{B}\rangle^* = e^{-2i\delta_I} \langle I|\mathcal{T}|B\rangle, \quad (10.73)$$

which implies equal rates for the charge conjugated decays and hence no CP asymmetry. Therefore, at least two different states with equal quantum numbers must exist which can be connected by strong rescattering (for example states with different numbers of particles or states with different particle charges but the same total charge and isospin) Eq. (10.73) implies also

$$\langle \bar{I}|\mathcal{T}|\bar{B}\rangle = e^{i\delta} T_I \langle I|\mathcal{T}|B\rangle = e^{i\delta} T_I^*. \quad (10.74)$$

The matrix elements T_I are assumed to be the “bare” decay amplitudes, which have no rescattering phases and which are calculated, for example, in the factorization approximation [2, 13, 17, 21, 22]. This implies that the transition matrix elements between charge-conjugated states are just the complex conjugates of each other. Eq. (10.74) is known as Watson’s theorem [41]. Thus in (10.74), one finds, instead of 2δ that would arise for a full rescattering of in states to out states, only the phase δ because the amplitudes refer to the transition of the B meson to the final states.

Thus final state interactions provide not only the absorptive phases of the amplitudes, but also affect their magnitudes as well because they relate to the mixings of various intermediate channels $|I\rangle$ available. (Recall that \mathcal{S} must connect the different states $|I\rangle$ and $|F\rangle$; so these should not be eigenstates.) Therefore, the separation of each amplitude into “bare” and “FSI” parts in Eq. (10.74) is quite *ad hoc*. The mathematical procedure for finding the “correct” functions $A^{(0)}(s)$ is known as the Omnès problem [42]. In the case of the one-channel (elastic) process, consisting of two masses m_1 and m_2 , one looks for the functions which are analytic in s , the two particle invariant momentum squared, except for a cut $(m_1 + m_2)^2 < s < \infty$ if s is real and $s < (m_1 + m_2)^2$, and for which $e^{-i\delta(s)} A^{(0)}(s)$ is real if s is real and $s > (m_1 + m_2)^2$. The solution is given by

$$A^{(0)}(s) = P(s)D^{-1}(s) = P(s) \exp\left(\frac{s}{\pi} \int_{4m^2}^{\infty} \frac{dt}{t} \frac{\delta(s)}{t - s - i\epsilon}\right), \quad (10.75)$$

where $P(s)$ is a polynomial of s , $D^{-1}(s)$ is the Omnès function, and $\lim_{s \rightarrow \infty} \delta(s) = \text{finite}$; $\lim_{s \rightarrow \infty} |A^{(0)}(s)|/s \rightarrow 0$. Equation (10.75) could be used, for instance, in the decay $B \rightarrow D\pi$ if $\delta(s)$, if the $D\pi$ scattering phase were known for sufficiently many points of the invariant mass squared (s). In principle, the procedure can probably be generalized to a multichannel problem, as appropriate in B decays; however, this is a complicated problem. It has been partly solved for decays of the form $K \rightarrow 3\pi$ or $\eta \rightarrow 3\pi$ [43]. There is not even a partial treatment along these lines available for B decays, the discussion here relies directly on Eqs. (10.70, 10.74). However, this brings in the uncertainty of whether or not to use quark or hadronic states.

The treatment of this problem in the following is based on [46], which gives a perturbative description for the rescattering. Consider a block diagonal S -matrix, one can divide each block into two sets, A and B (the result can be generalized to the case of many sets) and write the S -matrix as

$$S = S_0 + S_1, \quad (10.76)$$

where S_0 describes the “elastic” $A(B)$ to $A(B)$ transition and S_1 is responsible for the “inelastic” off-diagonal transitions. Now assume S_1 is proportional to a *small* parameter ϵ . Working always to first order in the ϵ , gives:

$$\begin{aligned} S_{0\alpha\alpha} &= e^{2i\delta_\alpha}, & S_{0\beta\beta} &= e^{2i\delta_\beta}, \\ S_{1\alpha\beta} &= 2i\epsilon_{\alpha\beta}e^{i(\delta_\alpha+\delta_\beta)}, & \epsilon_{\alpha\beta} &= \epsilon_{\beta\alpha}, \end{aligned} \quad (10.77)$$

where unitarity and time reversal invariance have been used. Here a basis spanned by the eigenstates of S_0 : A_α, B_β is chosen. This leads to a set of solutions of (10.70, 10.74):

$$\langle \bar{A}_\alpha | \mathcal{T} | \bar{B} \rangle = e^{i\delta_\alpha} \left\{ T_\alpha + \sum_\beta i\epsilon_{\alpha\beta} T_\beta \right\} \quad (10.78)$$

and similarly for B_β . Here, of course, T_β is the “bare amplitude”:

$$T_\beta = (\langle \bar{B}_\beta | \mathcal{T} | \bar{B} \rangle)^{\text{bare}} \quad (10.79)$$

etc.

After these general comments, now consider a CP -violating rate asymmetry, defined as

$$a_{CP} = \frac{\Delta_f}{\Gamma_{B \rightarrow f} + \Gamma_{\bar{B} \rightarrow \bar{f}}}, \quad \Delta_f = \Gamma_{B \rightarrow f} - \Gamma_{\bar{B} \rightarrow \bar{f}}. \quad (10.80)$$

The asymmetries can easily be obtained:

$$\begin{aligned} \Delta_\alpha &= 4 \sum_\beta \mathcal{I}m(T_\alpha^* T_\beta) \epsilon_{\alpha\beta} \\ \Delta_\beta &= 4 \sum_\alpha \mathcal{I}m(T_\beta^* T_\alpha) \epsilon_{\alpha\beta} \quad , \end{aligned} \quad (10.81)$$

or inclusively (summing over all possible states $\alpha(\beta)$)

$$\Delta_A = -\Delta_B = 4 \sum_{\alpha\beta} \mathcal{I}m(T_\alpha^* T_\beta) \epsilon_{\alpha\beta}, \quad (10.82)$$

where the first identity follows from CPT invariance.

It is clear from Eqs. (10.81, 10.82) that direct CP violation can occur if two amplitudes with different CP -violating weak phases interfere.

In the literature it is commonly stated that in order to obtain a nonvanishing asymmetry, two amplitudes with different weak *and* strong phases must contribute. In the present discussion, it is seen that this can only occur if there are two weak transition amplitudes (with different weak phases) each of which creates a different superposition of states $|I\rangle$ which mix via FSI with the final state of interest. Clearly this requires that there are at least two different possible states created in the weak decay which undergo strong transitions into each other. The strong phase is then nothing but the absorptive part due to the occurrence of the *physical* intermediate states $|B_\beta\rangle$ and arises when summing over the intermediate states as in Eq. (10.81). (In the summation, one sums over all the states, for instance over all allowed momenta of a given set of particles, all charge configurations etc.)

The final state rescatterings of high-energy particles may be divided into “soft” and “hard” scattering. Soft scattering occurs primarily in the forward direction. The transverse momentum is limited, having a distribution which falls exponentially on a scale of order $0.5 \text{ GeV}/c$. Soft scattering is probably best described via hadronic rather than quark states as it is a long-range process. At a higher transverse momentum one encounters the region of hard scattering, which falls only as a power of the transverse momentum. Collisions involving hard scattering are interpreted as interactions between the point-like hadronic constituents, the quarks and gluons of QCD.

As an example, consider the phase generated in the “penguin loop” involving a charmed quark. In the language of the present discussion, the weak process is $b \rightarrow c\bar{c}s$. The $c\bar{c}$ then annihilate (“rescatter”) into a $u\bar{u}$ pair. Integration over all intermediate $c\bar{c}$ momenta yields a phase for the amplitude of $b \rightarrow u\bar{u}s$. The quarks then group themselves into hadrons, say K and π . On the other hand, the tree-level process $b \rightarrow u\bar{u}s$ also produces the same final state without this phase. The process may be viewed also in another way. The decay $b \rightarrow c\bar{c}s$ gives rise to decays such as $B \rightarrow \bar{D}_s D$. The quark rescattering can be replaced now by hadronic processes like $\bar{D}_s D \rightarrow \pi \bar{K}$. These rescatterings are considered soft rescatterings and are usually described as interactions of the asymptotic states of QCD, that is of mesons or baryons. It should be clear from this example that the two rescattering mechanisms — soft and hard — cannot be really separated. The hope is that in certain processes one of them dominates.

The possibility of the hard rescattering on the quark level was noticed (see above) by Bander, Silverman and Soni [44] (see also Refs. [45, 46, 47]) in nonleptonic B decays into charmless final states. As mentioned, there are two different pathways to reach a given final state: the first proceeds through the Cabibbo-suppressed tree diagram $b \rightarrow u\bar{u}s$, the other produces a Cabibbo-favored final state *via* $b \rightarrow c\bar{c}s$ tree-level process, with subsequent final state rescattering of the two charmed quarks into two up quarks (penguin diagram). Since the energy release in b -decay is of the order $m_b > 2m_c$, the rescattered c quarks can go on-shell. In addition, $c\bar{c}$ annihilation involves a large energy release (*i.e.*, creates a hard gluon), and therefore the use of a one-gluon perturbative QCD description can be justified.

The absorptive FSI parts arise in penguin decays as follows. The penguin diagram is usually described by two form factors, the Inami-Lim functions $F_{1,2}$ describing the internal (charm, *etc.*)

quark loop. F_2 is dropped hereafter as being numerically small. For each quark flavor i , the leading contribution to F_1^i comes from the integral

$$F_1^i(m_i^2, Q^2) = -4 \int_0^1 dx x(1-x) \ln \left[\frac{m_i^2}{M_W^2} - \frac{Q^2}{M_W^2} x(1-x) \right] = -4 \left[\frac{1}{6} \ln \frac{m_i^2}{M_W^2} + \Pi\left(\frac{Q^2}{m_i^2}\right) \right]. \quad (10.83)$$

The explicit form for $\Pi(\frac{Q^2}{m_i^2})$ is given by:

$$\begin{aligned} \mathcal{R}e \Pi(x) = & -\frac{1}{6} \left(\frac{5}{3} + \frac{4}{x} - \left[1 + \frac{2}{x} \right] \left\{ \left[1 - \frac{4}{x} \right]^{\frac{1}{2}} \ln \left(\frac{1 + \sqrt{1 - 4/x}}{1 - \sqrt{1 - 4/x}} \right) \theta \left(1 - \frac{4}{x} \right) \right. \right. \\ & \left. \left. + 2 \left[\frac{4}{x} - 1 \right]^{\frac{1}{2}} \operatorname{arccot} \left(\left(\frac{4}{x} - 1 \right)^{\frac{1}{2}} \right) \theta \left(\frac{4}{x} - 1 \right) \right\} \right), \end{aligned} \quad (10.84)$$

$$\mathcal{I}m \Pi(x) = -\frac{\pi}{6} \left[1 + \frac{2}{x} \right] \left[1 - \frac{4}{x} \right]^{\frac{1}{2}} \theta \left(1 - \frac{4}{x} \right). \quad (10.85)$$

Here, Q^2 is the invariant momentum squared of the emitted $u\bar{u}$ pair. One observes from (10.85) that $\Pi(Q^2/m_i^2)$ develops an imaginary part for $Q^2 > 4m_i^2$ when internal quarks go on their mass shells, signaling CP violation; the asymmetry is proportional to the imaginary part. The presence of the tree-level diagram is not a necessary condition, and CP -violating effects may also occur in purely penguin transitions, such as $b \rightarrow \bar{s}ss$. The formalism is parallel to the one described above, with the difference that the interference occurs among penguin diagrams with different quark flavors. The theoretical problem with pure penguin modes is that the rescattering among light quarks of different flavors is not always a short-distance process. Moreover, since the perturbative QCD calculation of the CP asymmetry involves corrections up to α_s^2 , one must include all possible diagrams to maintain unitarity and gauge invariance [47, 48, 49].

Since Q^2 is not a direct observable, it is not clear how to translate this result into an observable effect. In exclusive transitions the quarks are distributed (hadronize) according to some wave function and there is no model-independent approach available. Using the factorization approximation and adopting a specific model for the meson form factors, one can calculate the values of a_{CP} using the procedure described above [47, 50, 51], but results are model-dependent. Moreover the treatment of the rescattering itself is purely perturbative, including even those kinematic regions where this approach is not clearly justified.

As noted, the rescattering of the charm quarks could possibly be better described with ‘‘hadronic’’ language. In the case of the exclusive transitions, one might expect that the final state phases are not exhausted by their perturbative values, but they should be dominated by soft, nonperturbative effects. Although soft hadronic interactions generally cannot be computed from first principles, there is a wealth of experimental studies [8] and accurate high energy phenomenology [52] as a basis to investigate the behavior of soft final state phases. One way to generate FSI by soft

processes is to use “resonance-background interference,” where FSI phases arise because of s -channel resonances and the phase shifts have a characteristic peaked behavior. An example is the decay $B^+ \rightarrow \pi^+\pi^-\pi^+$ which can proceed through the decay chain $B^+ \rightarrow \xi_{c0}\pi^+$ with subsequent decay $\xi_{c0} \rightarrow \pi^+\pi^-$ [53, 54]. The asymmetry is then proportional to an interference of this mechanism with an unpeaked background decay. The asymmetries in this case are of course peaked around the resonance.

In the kaon system, the low-energy effective theory of strong interactions can be used to estimate FSI phase differences. In the D system, where the center of mass energy is too large to apply low-energy effective theory, final state rescattering has been studied assuming the dominance of intermediate resonances: the strong interaction amplitude is parameterized in terms of the couplings of the resonance to the interacting particles, and of the decay rate of the resonance [55].

In the B system, where the density of the resonances available is large due to the increased energy, a different approach must be employed. One can use, for example, the fact that the b -quark mass is large compared to the QCD scale. Then, in the context of soft FSI in B decays, it is worth investigating the issue on the leading-order behavior of soft final-state phases in the $m_b \rightarrow \infty$ limit. The common perception is that they should become less and less important as the mass of the decaying quark becomes heavier. This can be shown to be true for the *hard* rescattering part, since “the final state particles emerge at such high momenta that they do not have a chance to rescatter.” However, one has to take into account the fact that soft scattering actually increases with energy.

One can investigate this point by considering first the *elastic* channel, and demonstrating that elastic rescattering does not disappear in the limit of large m_B . Since the unitarity of the S -matrix requires that the inelastic channels are indeed the dominant contributors to soft rescattering, such contributions have to share a similar behavior in the heavy-quark limit. The elastic channel is convenient because of the optical theorem which connects the forward (imaginary) invariant amplitude \mathcal{M} to the total cross-section,

$$\text{Im } \mathcal{M}_{f \rightarrow f}(s, t = 0) = 2k\sqrt{s}\sigma_{f \rightarrow \text{all}} \sim s\sigma_{f \rightarrow \text{all}}, \quad (10.86)$$

where s is the squared center-of-mass energy and t is the squared-momentum transfer. The asymptotic total cross-sections are known experimentally to increase slowly with energy. All known cross-sections can be parameterized by the form [56]:

$$\sigma(s) = X \left(\frac{s}{s_0} \right)^{0.08} + Y \left(\frac{s}{s_0} \right)^{-0.56}, \quad (10.87)$$

where $s_0 = \mathcal{O}(1) \text{ GeV}^2$ is a typical hadronic scale. Thus, the imaginary part of the forward elastic scattering amplitude (10.86) increases asymptotically as $s^{1.08}$.

Considering only the imaginary part of the amplitude, and building in the known exponential fall-off of the elastic cross-section in t ($t < 0$) [57] by writing

$$i\mathcal{I}m \mathcal{M}_{f \rightarrow f}(s, t) \simeq i\beta_0 \left(\frac{s}{s_0}\right)^{1.08} e^{bt}, \quad (10.88)$$

one can calculate the contribution of the imaginary part of the elastic amplitude to the unitarity relation for a final state $f = a + b$ with kinematics $p'_a + p'_b = p_a + p_b$ and $s = (p_a + p_b)^2$:

$$\begin{aligned} \mathcal{D}isc \mathcal{M}_{B \rightarrow f} &= \\ &= \frac{1}{2} \int \frac{d^3 p'_a}{(2\pi)^3 2E'_a} \frac{d^3 p'_b}{(2\pi)^3 2E'_b} (2\pi)^4 \delta^{(4)}(p_B - p'_a - p'_b) \left(-i\beta_0 \left(\frac{s}{s_0}\right)^{1.08} e^{b(p_a - p'_a)^2} \right) \mathcal{M}_{B \rightarrow f} \\ &= -\frac{1}{16\pi} \frac{i\beta_0}{s_0 b} \left(\frac{m_B^2}{s_0}\right)^{0.08} \mathcal{M}_{B \rightarrow f}, \end{aligned} \quad (10.89)$$

where $t = (p_a - p'_a)^2 \simeq -s(1 - \cos\theta)/2$, and $s = m_B^2$.

One can refine the argument further, since the phenomenology of high-energy scattering is well accounted for by the Regge theory [57]. Scattering amplitudes are described by the exchanges of Regge trajectories (families of particles of differing spin) which lead to elastic amplitudes of the form

$$\mathcal{M}_{f \rightarrow f} = \xi \beta(t) \left(\frac{s}{s_0}\right)^{\alpha(t)} e^{i\pi\alpha(t)/2}, \quad (10.90)$$

with $\xi = 1$ for charge conjugation $C = +1$ and $\xi = i$ for $C = -1$. Each trajectory is described by a straight line:

$$\alpha(t) = \alpha_0 + \alpha' t. \quad (10.91)$$

The leading trajectory for high energy scattering is the Pomeron, having $C = +1$, $\alpha_0 \simeq 1.08$ and $\alpha' \simeq 0.25 \text{ GeV}^{-2}$. Notice that, since

$$\left(\frac{s}{s_0}\right)^{\alpha(t)} = \left(\frac{s}{s_0}\right)^{\alpha_0} e^{\alpha' \ln(s/s_0) t}, \quad (10.92)$$

the exponential fall-off in t in Eq. (10.88) is connected with the slope α' , and the effective slope parameter b increases logarithmically with s . Since α_0 is near unity, the phase of the Pomeron-exchange amplitude is seen from Eq. (10.90) to be almost purely imaginary. One can also include several nonleading trajectories; their net effect is represented by a second term in (10.87) and, as a consequence, they vanish as $1/m_B$ in the infinite heavy-quark mass limit. Taking into account the momentum dependence of the residue function, and evaluating the corresponding integrals at $s = m_B^2 \simeq 25 \text{ GeV}^2$, the Pomeron contribution in $B \rightarrow \pi\pi$ turns out to be:

$$\mathcal{D}isc \mathcal{M}_{B \rightarrow \pi\pi} |_{\text{Pomeron}} = -i\epsilon \mathcal{M}_{B \rightarrow \pi\pi}, \quad \epsilon \simeq 0.21. \quad (10.93)$$

From this numerical result and from the nature of its derivation, one can conclude that additional individual soft FSI are not vanishingly small. Moreover, other final states should have elastic rescattering effects of comparable size. However, of chief significance is the naive expected weak dependence of ϵ on m_B — the $(m_B^2)^{0.08}$ factor in the numerator is attenuated by the $\ln(m_B^2/s_0)$ dependence in the effective value of b (compare Eqs. (10.88), (10.92)).

The analysis of the elastic channel suggests that, at high energies, FSI phases are mainly generated by inelastic effects. At a physical level, this conclusion immediately follows from the fact that the high-energy cross-section is mostly inelastic. It is also plausible at the analytic level, given that the Pomeron elastic amplitude is almost purely imaginary. Since the study of elastic rescattering has yielded a \mathcal{T} -matrix element $\mathcal{T}_{ab \rightarrow ab} = 2i\epsilon$, *i.e.*, $\mathcal{S}_{ab \rightarrow ab} = 1 - 2\epsilon$, and since the constraint of unitarity of the \mathcal{S} -matrix implies that the off-diagonal elements are $\mathcal{O}(\sqrt{\epsilon})$, with ϵ approximately $\mathcal{O}(m_B^0)$ in powers of m_B and numerically $\epsilon < 1$, then the inelastic amplitude must also be $\mathcal{O}(m_B^0)$ and of magnitude $\sqrt{\epsilon} > \epsilon$. There is another argument, utilizing the form of the final state unitarity relations, which also shows that inelastic effects are required to be present. In the limit of T invariance for the weak interactions, the discontinuity $\mathcal{D}isc \mathcal{M}_{B \rightarrow f}$ is a real number (up to irrelevant rephasing invariance of the B state). The factor of i obtained in the elastic rescattering in Eq. (10.93) must be compensated by the inelastic rescattering in order to make the total real. Therefore, the presence of inelastic effects is seen to be necessary.

Inelastic final state interactions can contribute to CP -violating asymmetries at leading order in m_B . Since the strong phase is generated by inelastic channels, the relevant pathways would involve $B \rightarrow f$ directly or $B \rightarrow$ “multibody” followed by the inelastic rescattering, “multibody” $\rightarrow f$. Depending on the dynamics of weak decay matrix elements, these may pick up different weak phases. As an example, consider the final state $f = K^- \pi^0$, which can be generated either by a standard W exchange or by the penguin diagram, involving different weak phases ϕ_w and ϕ_n , respectively [46]. For the strong rescattering, one must also consider a channel to which $K^- \pi^0$ scatters inelastically, here called $K n \pi$ (although one can generate this asymmetry by a hard rescattering $D_s D \rightarrow K^- \pi^0$, the emphasis here is on the soft physics). The W -exchange and penguin amplitudes will contribute with different weight to $K \pi$ and $K n \pi$, so that in the absence of final-state interactions one expects:

$$\begin{aligned} \mathcal{M}(B^- \rightarrow K^- \pi) &= |A_1| e^{i\phi_1} = A_1^w e^{i\phi_w} + A_1^p e^{i\phi_p} \\ \mathcal{M}(B^- \rightarrow K^- n \pi) &= |A_n| e^{i\phi_n} = A_n^w e^{i\phi_w} + A_n^p e^{i\phi_p}, \end{aligned} \quad (10.94)$$

with $\phi_1 \neq \phi_n$ and an obvious notation for W exchange and penguin amplitudes. Representing the strong rescattering by the two channel model [58], gives for B and \bar{B} decays

$$\begin{aligned} \mathcal{M}(B^- \rightarrow K^- \pi) &= |A_1| e^{i\phi_1} + i\sqrt{\epsilon} |A_n| e^{i\phi_n} \\ \mathcal{M}(B^+ \rightarrow K^+ n \pi) &= |A_1| e^{-i\phi_1} + i\sqrt{\epsilon} |A_n| e^{-i\phi_n}. \end{aligned} \quad (10.95)$$

This leads to a CP -violating decay-rate asymmetry

$$\Gamma(B^- \rightarrow K^- \pi^0) - \Gamma(B^+ \rightarrow K^+ \pi^0) \sim \sqrt{\epsilon} |A_1| |A_n| \sin(\phi_n - \phi_1). \quad (10.96)$$

This can yield an asymmetry as large as $a_{CP} \simeq 0.2$.

Final state interactions can modify the decay amplitudes, violating the expected hierarchy of amplitudes in the absence of rescattering. For example, it is expected that the amplitudes that do not involve spectator quarks (such as color-allowed and color-suppressed tree-level amplitudes or penguin amplitudes) dominate over the diagrams involving spectator quarks (*e.g.*, weak annihilation or weak rescattering amplitudes). In many cases, large amplitudes might contribute to the processes involving spectator quarks through the final state rescattering [59, 60]. It must be stressed that although the predictive power of available methods is limited and most of the numerical estimates are based on the two-body rescattering diagrams, some conclusions can still be reached. Using the Regge-based analysis [58] it is possible to show [60] that the rescattering from the dominant channel leads to a suppression of order $\lambda \sim 0.2$ compared to $f_B/m_B \sim \lambda^2$ obtained from the naive quark diagram estimate. Soft FSI manifest themselves even more dramatically in the processes where the contribution from the tree-level operators is mixing, *e.g.*, $B^\pm \rightarrow \pi^\pm K$. For instance, they might induce large ($a_{CP} \simeq 0.2$) CP -violating asymmetries (usually associated with potential New Physics contributions), or spoil certain relations constraining CKM angles [61, 1]. However, in the case of nonleptonic B decays to charmed mesons ($B \rightarrow KD$, $B \rightarrow \pi D^*$, $B \rightarrow \rho D$) the application of the Regge theory suggests that FSI phases are small; provided that the Pomeron coupling to the charm quark is suppressed in comparison with the coupling to the light quarks [62].

Another class of the processes affected by FSI are the radiative decays of B mesons, which provide valuable information on the structure of the CKM matrix. In the case of $B \rightarrow K^* \gamma$, the process is dominated by the short-distance penguin amplitude, related to the single CKM matrix element V_{ts} [63]; on the other hand, the extraction of V_{td} from $B \rightarrow \rho \gamma$ is hampered by uncertainties related to certain long-distance effects [64] and to the contribution of the two-body on-shell hadron rescattering with subsequent conversion of one of the hadrons into the photon. This contribution could be sizable [65].

It is possible that the values of strong phase differences in various decay channels will be experimentally accessible. This could be the case, for example, for the decay mode $B_d^0 \rightarrow \pi^+ \pi^-$, where a time-dependent analysis would allow the extraction from experimental data of the weak phase α and the strong phase shift δ (up to certain discrete ambiguities), and allow a test of various theoretical predictions [66].

10.3 Heavy-Quark Chiral Perturbation Theory

In the heavy-quark limit of QCD the interactions of the heavy quark Q are simplified because of a new set of symmetries not manifestly present in the full QCD. This fact is usually used in the construction of the new effective theory where the heavy-quark mass goes to infinity ($m_Q \gg \Lambda_{QCD}$) with its four-velocity fixed. The spin-flavor symmetry group of this new theory with N heavy quarks is $SU(2N)$ because the interactions of the heavy quarks are independent of their spins and flavors. This fact is widely used in the description of the semileptonic decays of B mesons to D and D^* mesons where heavy-quark symmetry allows a parameterization of the decay amplitudes in terms of the single Isgur-Wise function (See Ref. [67] and Chapter 8 for an overview).

Similarly, the chiral symmetry of QCD constrains the interactions of pions and kaons at low energy. This approximate symmetry arises because the masses of the light quarks u, d, s are well below the scale $\Lambda_{QCD} \sim 300 \text{ MeV}$ which governs nonperturbative QCD. At low energies, the approximate $SU(3)_L \times SU(3)_R$ chiral symmetry of QCD is spontaneously broken down to its $SU(3)_V$ subgroup. The Goldstone theorem then gives rise to the octet of the Goldstone bosons which are essentially identified with the light octet of pions, kaons and eta. The effective theory of heavy and light mesons is based on the assumption that the energy release in the reactions among pions and kaons (and possibly photons) is small and allows a controlled expansion in terms of derivatives and quark mass insertions.

It is clear that while in most cases of heavy meson or baryon decays the energy release is rather large, there is always a part of the phase space where the momentum of the produced pions or kaons is small. This is the case in semileptonic decays of B -flavored mesons to pions and nonleptonic multibody B decays. Thus a consistent description of the heavy to light weak transitions, not available in HQET alone, is possible in the combined-heavy quark and chiral-symmetry limit (see Ref. [68, 69, 70]).

In order to write a heavy-quark chiral Lagrangian and to establish notations, recall that the pseudo-Goldstone bosons are incorporated in a 3×3 unitary matrix [71]

$$U = \exp\left(i\frac{2\lambda^a\phi^a}{F}\right), \quad \frac{\lambda^a}{\sqrt{2}}\phi^a = \begin{pmatrix} \frac{1}{\sqrt{2}}\pi^0 + \frac{1}{\sqrt{6}}\eta & \pi^+ & K^+ \\ \pi^- & -\frac{1}{\sqrt{2}}\pi^0 + \frac{1}{\sqrt{6}}\eta & K^0 \\ K^- & \bar{K}^0 & -\frac{2}{\sqrt{3}}\eta \end{pmatrix}. \quad (10.97)$$

Here $F = 0.093 \text{ GeV}$ is the pseudoscalar decay constant at lowest order in chiral expansion. In order to build a Lagrangian satisfying the desired transformation properties, one must consider how this field changes under the QCD symmetry transformations. Under chiral $SU(3)_L \times SU(3)_R$, the field U transforms as

$$U \rightarrow LUR^\dagger, \quad (10.98)$$

where $L(R)$ belongs to $SU(3)_L(SU(3)_R)$. It is also convenient to introduce the field ξ : $U = \xi\xi$ with

$$\xi \rightarrow L\xi V^+ = V\xi R^\dagger, \quad (10.99)$$

with V from $SU(3)_V$. Because the heavy quark is a singlet under the light-quark flavor symmetry, the heavy-hadron multiplet transforms as

$$H \rightarrow VH \quad (10.100)$$

under unbroken $SU(3)_V$. The role of the first excitation of the $B(D)$ meson, the $B^*(D^*)$, deserves comment. As the mass of the heavy quark increases, this particle becomes degenerate with the ground state meson, since $m_B - m_{B^*} = \mathcal{O}(1/m_b)$. Therefore, it must be explicitly included in the description. The superfield formalism [72] (see also [73]) in which the B and the B^* are incorporated into a 4×4 matrix serves this purpose:

$$H = \frac{1 + \not{v}}{2} \left(B_\mu^* \gamma^\mu - B \gamma_5 \right), \quad v^\mu B_\mu^* = 0. \quad (10.101)$$

In order to build an effective Lagrangian, a covariant derivative is needed. Since V is a position-dependent matrix, the covariant derivative is defined as

$$D_\mu = \partial_\mu + iV_\mu, \quad V_\mu = -\frac{1}{2}i \left(\xi^\dagger \partial_\mu \xi + \xi \partial_\mu \xi^\dagger \right), \\ D_\mu H \rightarrow V D_\mu H \quad (10.102)$$

An axial current A_μ is introduced analogously:

$$A_\mu = -\frac{1}{2}i \left(\xi^\dagger \partial_\mu \xi - \xi \partial_\mu \xi^\dagger \right), \quad A_\mu \rightarrow V A_\mu V^\dagger. \quad (10.103)$$

These are all the components necessary to build an effective Lagrangian invariant under both the chiral and heavy-quark symmetries [68, 69, 70]

$$\mathcal{L} = -i \text{Tr} \bar{H} v \cdot D H - g \text{Tr} \bar{H} \gamma_\mu \gamma_5 A^\mu H + \dots, \quad (10.104)$$

with $\bar{H} = \gamma^0 H^\dagger \gamma^0$. The normalization of the heavy hadron fields is chosen such that they have (mass) dimension $3/2$. This Lagrangian is useful in the processes where two heavy mesons and an arbitrary number of light pseudoscalars are involved, *e.g.*, $B \rightarrow D n \pi$. An example, is the rate for the strong decays of excited B^* states such as $B^*(5732)$ to $B\pi$ whose rate is given by

$$\Gamma(B^* \rightarrow B\pi) = \frac{1}{12\pi} \frac{g^2}{F^2} |\mathbf{p}_\pi|^3 \quad (10.105)$$

and which allows a qualitative estimate of the value for g . Similar estimates are possible for strong decays of higher excitations of heavy mesons [74].

There are many applications of the heavy-quark chiral perturbation theory in B meson decays. It is not difficult to extend the strong Lagrangian discussed above to the weak transitions. The matrix element of the current $J_\mu^h = \bar{q}\gamma_\mu(1 + \gamma_5)b$ transforms as $(\bar{3}_L, 1_R)$ under $SU(3)_L \times SU(3)_R$ and is therefore given by

$$J_\mu^h = i \frac{F_B}{\sqrt{2m_B}} \text{Tr} \gamma_\mu(1 + \gamma_5) H \xi^\dagger \quad (10.106)$$

where the coefficient is fixed by the definition of the B -meson decay constant. Then, the total weak current J_μ consists of all the usual terms (light quarks, leptons) plus J_μ^h , and the decay Lagrangian is simply

$$\mathcal{L}_{eff} = -\frac{G_F}{\sqrt{2}} \xi_q J_\mu J^\mu \quad (10.107)$$

where ξ_q denotes the appropriate factors of CKM matrix elements.

As a simple example, take the semileptonic decay $B \rightarrow \pi l \nu$. The relevant hadronic matrix element is

$$\langle \pi | \bar{u}\gamma_\mu(1 + \gamma_5)b | B \rangle = f_+(p_B + p_\pi)_\mu + f_-(p_B - p_\pi)_\mu. \quad (10.108)$$

The heavy-quark chiral expansion formulae (10.104) and (10.107) yield for the form factor

$$f_+ \simeq -\frac{gF_B m_B}{2F(v \cdot p_\pi + \Delta)}, \quad (10.109)$$

where $\Delta = m_{B^*} - m_B \simeq 50 \text{ MeV}/c^2$. The expressions (10.107, 10.104) can be used to estimate semileptonic or hadronic B decays with many pions in the final state, such as $B \rightarrow 3\pi$. These are required for estimates of the background to CP searches using decays such as $B \rightarrow \pi\rho$. However, the high pion momenta in large areas of the phase space for such decays make such estimates untrustworthy; a more serious attempt would require additional considerations, a combination of HQChPT and phenomenological descriptions, or perhaps modeling of the process.

An improvement is possible if the decays can be modeled as proceeding via one or several intermediate resonances. For instance, the semileptonic decay $B \rightarrow \pi l \nu$ can proceed through an intermediate step where the B decays first to a B^* and a π , and the B^* decays leptonically. If this route is dominant, a good representation of the decay is possible. Equally, multibody decays to several pions, such as $B \rightarrow 3\pi$ can be treated this way. The problem is that the method works only for limited regions of phase space, and therefore no systematic investigation has been undertaken. It is however extremely useful for studies of direct CP -violating effects on the appropriate portions of the available phase space. For instance, heavy-quark chiral-perturbation theory can be used to estimate the resonance-background CP -violating asymmetries in $B \rightarrow \pi\pi\pi$ vs. $B \rightarrow \chi_0\pi \rightarrow \pi\pi\pi$ [54] as the interference occurs in the region where the momentum of one of the pions is soft.

A similar formalism can be applied to semileptonic and nonleptonic D decays as well as to rare decays of the type $B \rightarrow Kl^+l^-$.

This procedure fixes the semileptonic form factor at low values of the pion momentum. The use of the perturbative QCD at higher values and the application of dispersion relation techniques constrain the behavior of the semileptonic form factor over virtually the whole range of the pion momenta in $B \rightarrow \pi l \nu$ [75]. It has also been noted that an “effective” model for the semileptonic and nonleptonic D decays can be constructed, based on the fact that the relatively low mass of the D meson allows for zero-recoil values of the form factors, fixed by the chiral predictions, to be successfully extrapolated from the zero-recoil point by assuming a pole-like structure of the form factors using “full propagators” instead of the HQET ones [76] (cf. (10.109)).

10.4 Inclusive Properties of B Meson Decays

While D meson decays into hadrons proceed almost completely via two-body decays involving resonances, the much heavier B mesons decay into multiple hadrons most of the time, giving rise to an innumerable number of exclusive final states. It then becomes highly desirable to describe these exclusive decays in terms of their common properties and make predictions in terms of inclusive and semi-inclusive decays. These predictions can then be compared to experimental measurements of the inclusive properties of B meson decays. At the $\Upsilon(4S)$, exclusive pairs of charged or neutral B mesons are produced almost at rest. What is measured are the combined properties of B^0 and B^+ decays unless special efforts are made. This isodoublet is denoted in the following by the generic name B meson.

A natural extension of these studies is the investigation of B^0 , \bar{B}^0 , B^+ and B^- separately or in pairs, via charge and angular correlations between two particles in an event, and, more straightforwardly, via events where one B meson is fully reconstructed. This latter method does not suffer from model dependence in the interpretation of the data, but requires a large data sample and will provide useful results only at the B factories.

10.4.1 Fully Integrated Rates

Invoking quark-hadron duality one expects that total widths and other fully integrated rates can be treated theoretically with decent accuracy. Such a program has been undertaken most recently through Heavy-Quark Expansions (HQE); for a critical review of the literature see [77] and for a discussion specifically of beauty and charm widths see [78]. The basic idea is the following: analogous to the treatment of $e^+e^- \rightarrow \text{hadrons}$ one describes the transition rate to an inclusive final-state f through the imaginary part of a forward scattering operator evaluated to second order in the weak interactions [79, 80]:

$$\hat{T}(Q \rightarrow f \rightarrow Q) = i \text{Im} \int d^4x \{ \mathcal{L}_W(x) \mathcal{L}_W^\dagger(0) \}_T, \quad (10.110)$$

where $\{ \}$ denotes the time-ordered product and \mathcal{L}_W the effective weak Lagrangian at the parton level. For a sufficiently high-energy release in the decay the *nonlocal* operator product in Eq. (10.110) can, through an operator product expansion (OPE), be expressed as an infinite sum of *local* operators O_i of increasing dimension with coefficients \tilde{c}_i containing higher and higher powers of $1/m_Q$; a *short-distance* mass must be used here for the heavy quarks. The width for a hadron H_Q containing the heavy quark, Q , is then obtained by taking the expectation value of \hat{T} for the state H_Q :

$$\langle H_Q | \hat{T} | H_Q \rangle \propto \Gamma(H_Q \rightarrow f) = G_F^2 |CKM|^2 \sum_i \tilde{c}_i^{(f)} \langle H_Q | O_i | H_Q \rangle, \quad (10.111)$$

where CKM denotes the appropriate CKM matrix elements. Through order $1/m_Q^3$ it takes the following form:

$$\begin{aligned} \Gamma(H_Q \rightarrow f) = \frac{G_F^2 m_Q^5}{192\pi^3} |CKM|^2 & \left[c_3^f \langle H_Q | \bar{Q}Q | H_Q \rangle + c_5^f \frac{\langle H_Q | \bar{Q}i\sigma \cdot GQ | H_Q \rangle}{m_Q^2} \right. \\ & \left. + \sum_i c_{6,i}^f \frac{\langle H_Q | (\bar{Q}\Gamma_i q)(\bar{q}\Gamma_i Q) | H_Q \rangle}{m_Q^2} + \mathcal{O}(1/m_Q^4) \right]. \end{aligned} \quad (10.112)$$

Equation (10.112) represents a master equation for a host of different inclusive heavy-flavor decays: semileptonic, nonleptonic and radiative transitions, CKM-favored or -suppressed, *etc.* They can all be calculated through an OPE; the only difference lies in the operator \mathcal{L}_W . Since that operator has a simpler structure for semileptonic than for nonleptonic transitions one might expect a faster convergence for the former than the latter expansion. Yet *a priori* there is little reason for a qualitative difference here.

There are two leading classes of nonleptonic beauty decays, namely $\Gamma(b \rightarrow c\bar{u}d)$ and $\Gamma(b \rightarrow c\bar{c}s)$. One finds

$$\Gamma_{NL}(B^0) \simeq \Gamma_{\text{decay}}(B; b \rightarrow c\bar{u}d) + \Gamma_{\text{decay}}(B; b \rightarrow c\bar{c}s) \quad (10.113)$$

$$\Gamma_{NL}(B^-) \simeq \Gamma_{NL}(B^0) + \Delta\Gamma_{PI}(B^-) \quad (10.114)$$

where

$$\begin{aligned} \Gamma_{\text{decay}}(B; b \rightarrow c\bar{u}d) = \frac{3G_F^2 m_b^5}{192\pi^3} |V_{cb}V_{ud}|^2 \langle B | \bar{b}b | B \rangle \times \\ \left[\frac{A_0}{3} I_0(x, 0, 0) + \frac{\langle \mu_G^2 \rangle_B}{m_b^2} \left(x \frac{d}{dx} - 2 \right) I_0(x, 0, 0) - \frac{4}{3} A_2 \frac{\langle \mu_G^2 \rangle_B}{m_b^2} I_2(x, 0, 0) \right] \end{aligned} \quad (10.115)$$

$$\begin{aligned} \Gamma_{\text{decay}}(B; b \rightarrow c\bar{c}s) = \frac{3G_F^2 m_b^5}{192\pi^3} |V_{cb}V_{cs}|^2 \langle B | \bar{b}b | B \rangle \times \\ \left[\frac{A_0}{3} \rho_{c\bar{c}} I_0(x, x, 0) + \frac{\langle \mu_G^2 \rangle_B}{m_b^2} \left(x \frac{d}{dx} - 2 \right) I_0(x, x, 0) - \frac{4}{3} A_2 \frac{\langle \mu_G^2 \rangle_B}{m_b^2} I_2(x, x, 0) \right] \end{aligned} \quad (10.116)$$

where $x = \frac{m_s^2}{m_b^2}$. The phase space factors I_0 and I_2 are defined as

$$\begin{aligned} I_0(x, 0, 0) &= (1 - x^2)(1 - 8x + x^2) - 12x^2 \log x \\ I_2(x, 0, 0) &= (1 - x)^3 \end{aligned} \quad (10.117)$$

$$\begin{aligned} I_0(x, x, 0) &= v(1 - 14x - 2x^2 - 12x^3) + 24x^2(1 - x^2) \log \frac{1+v}{1-v} \\ I_2(x, x, 0) &= v\left(1 + \frac{x}{2} + 3x^2\right) - 3x(1 - 2x^2) \log \frac{1+v}{1-v}, \end{aligned} \quad (10.118)$$

with $v = \sqrt{1 - 4x}$. The quantities A_0 , A_2 and $\rho_{c\bar{c}}$ denote the QCD radiative corrections:

$$A_2 = (c_+^2 - c_-^2) = 4C_1C_2, \quad A_0 = (c_-^2 + 2c_+^2)J = (3C_1^2 + 3C_2^2 + 2C_1C_2)J \quad (10.119)$$

with J denoting the subleading logarithms. The nonperturbative corrections through order $1/m_b^2$ enter through two quantities:

- The chromomagnetic moment

$$\langle \mu_G^2 \rangle_B \equiv \langle B | \bar{b} \frac{\vec{\sigma}}{2} \cdot G b | B \rangle \quad (10.120)$$

which can be determined reliably from the hyperfine splitting

$$\langle \mu_G^2 \rangle_B \simeq \frac{3}{4}(M_{B^*}^2 - M_B^2) \simeq 0.37 \text{ GeV}^2 \quad (10.121)$$

- The expectation value

$$\langle B | \bar{b} b | B \rangle \simeq 1 - \frac{\langle \mathbf{p}_b^2 \rangle}{2m_b^2} + \frac{1}{2} \frac{\langle \mu_G^2 \rangle_B}{m_b^2} \quad (10.122)$$

where $\langle \mathbf{p}_b^2 \rangle$ is the average kinetic energy of the b quark inside the B meson and is estimated to be $\sim 0.4\text{--}0.5 \text{ GeV}^2$.

A lifetime difference arises in order $1/m_b^3$

$$\begin{aligned} \Delta\Gamma_{PI}(B^-) &= \frac{G_F^2 m_b^5}{8\pi} |V_{cb}V_{ud}|^2 \frac{f_B^2}{M_B^2} \kappa^{-4} \times \\ &\left[(c_+^2 - c_-^2) \kappa^{9/2} + \frac{c_+^2 + c_-^2}{3} - \frac{1}{9} (\kappa^{9/2} - 1)(c_+^2 - c_-^2) \right] \end{aligned} \quad (10.123)$$

with κ reflecting hybrid renormalization

$$\kappa \equiv \left[\frac{\alpha_S(\mu_{had}^2)}{\alpha_S(m_b^2)} \right]^{1/b}, \quad b = 11 - \frac{2}{3}n_F, \quad (10.124)$$

leading to the prediction that the lifetime of charged B mesons exceeds that for neutral ones by several percent. One should note here the absence of nonperturbative corrections of order $1/m_b$. Strictly speaking the expansion parameter is the inverse of the energy release, rather than $1/m_b$; therefore the result for $\Gamma(\overline{B} = [b\overline{q}] \rightarrow c\overline{u}d\overline{q})$ has to be viewed as intrinsically suspect since in it the energy release is not much larger than ordinary hadronic scales. Together with $\Gamma_{SL}(B)$, one can then predict the lifetime ratios among beauty hadrons, their semileptonic branching ratios, $\mathcal{B}_{SL}(B)$, and the charm content in the final state, n_c .

The predictions of the lifetime ratios for B_d^0 and B_u^+ are in good agreement with present data: $\frac{\tau(B^+)}{\tau(B^0)} = 1.07 \pm 0.04$, and there is no longer a clearcut discrepancy between predictions and data for $\mathcal{B}_{SL}(B)$ and n_c .

It is possible that problems might (re)surface once more accurate data become available on $\tau(B^+)/\tau(B^0)$ and n_c . The important point to note in any evaluation is that HQE predictions are deduced from QCD proper rather than from merely a model ansatz. Thus, a failure of these predictions would be an important result.

This is exemplified by the discrepancy between the expected and the presently observed beauty baryon lifetime, where the expected value relative to the B^0 lifetime

$$\left. \frac{\tau(\Lambda_b)}{\tau(B^0)} \right|_{HQE} \simeq 0.90 - 0.95 \quad (10.125)$$

is significantly larger than the world average measurements:

$$\left. \frac{\tau(\Lambda_b)}{\tau(B^0)} \right|_{WA} = 0.77 \pm 0.05 . \quad (10.126)$$

There is a lively debate on this issue in the theoretical literature, where four positions are advocated:

- (i) A violation of so-called local quark-hadron duality generating contributions of order $1/m_b$ has been established.
- (ii) Such a violation can actually be predicted which limits the numerical reliability of HQE results for nonleptonic, but not for semileptonic rates, since a weaker form of quark-hadron duality suffices for the latter.
- (iii) There is no principal or qualitative distinction in the validity of quark-hadron duality in semileptonic and nonleptonic decays, but there are larger pre-asymptotic corrections for the widths of baryons than mesons that have not been brought under theoretical control yet due to the more complex structure of hadrons.
- (iv) Wait for an upward movement of the measurements.

The foreseeable future will show whether position (iv) is vindicated. If position (iii) is closest to the truth, then the predictions for the B meson lifetimes basically stay as quoted above. Positions (i) and (ii) on the other hand would have serious consequences for $\tau(B)$ as well making the present success of the HQE prediction a coincidence. Further insights will be gained from more precise measurements of the lifetimes of charm-strange baryons and from ongoing theoretical work.

Without belittling the theoretical uncertainties, it seems fair to state that these total widths can now be described with decent accuracy within a theoretical rather than merely phenomenological framework. More accurate data will yield further valuable lessons for hadronization in QCD.

10.4.2 Semi-inclusive Transitions

The two extreme regimes, of two-body modes on the one hand and total rates on the other, represent — for very different reasons — the areas where the most reliable theoretical tools for understanding nonleptonic transitions are available. There is strong theoretical as well as experimental motivation to go beyond those regimes, *i.e.*, to analyze semi-inclusive and genuine multibody channels. Unfortunately theory can provide little quantitative guidance there: on the one hand the specifics of hadronization are essential in shaping the amplitudes, on the other the complexity of the final state is considerably higher than for the two-body modes. The concept of factorization can be defined in several inequivalent ways, the most straightforward one is described in Section 10.1.5. One is forced to rely on phenomenological prescriptions. However, some further help can be derived from theory beyond the provision of just the overall normalization of the fully integrated rates.

10.4.3 Charm Production and Charm Counting

The dominant B -decay modes proceed via the spectator tree diagram, and commonly involve the $b \rightarrow c$ transition. Only a small fraction ($\sim 2|V_{ub}|^2/|V_{cb}|^2 \approx 1\%$) of decays proceed through $b \rightarrow u$. Therefore, 0.99 charm quarks per B decay from $b \rightarrow c$ are expected. In addition, the virtual W in the loop can produce a $\bar{c}s$ or $\bar{c}d$ pair, which accounts for another ~ 0.2 charm quarks, resulting in a total $n_c \approx 1.2$. A more precise number can be calculated on the quark level using the QCD operator-product expansion. However, the results of these calculation vary with the values of unknown parameters such as the quark masses or the renormalization scale, and allow therefore a wide range of possible c -quark multiplicities. Thereby the value of n_c becomes related to other inclusive properties, such as the total semileptonic branching fraction and the ratio of B -mesons lifetimes.

The multiplicity of charmed mesons is listed in Table 10-10. Although these numbers have reached a satisfactory experimental precision, they have fluctuated during the last few years. One reason is the change in results on charmed-hadron branching fractions which still contribute significantly

Table 10-10. *Charmed-meson multiplicities: experimental product branching fractions and values rescaled to current values of D branching fractions [8]. The last error of the multiplicity is always due to the D branching fractions. A best guess is indicated in **bold** typeface.*

Particle	$\langle n \rangle \mathcal{B}$	$\langle n \rangle$	Experiment
$D^0 \rightarrow K^- \pi^+$	$0.0194 \pm .0015 \pm .0025$	$0.502 \pm 0.038 \pm 0.065 \pm 0.018$	ARGUS 91 [81]
	$0.0233 \pm .0012 \pm .0014$	$0.602 \pm 0.032 \pm 0.035 \pm 0.022$	CLEO 92 [82]
	$0.0251 \pm .0006 \pm .0007$	$0.644 \pm 0.014 \pm 0.020 \pm 0.023$	CLEO 96 [83]
	$0.0243 \pm .0008$	$0.625 \pm 0.021 \pm 0.023$	average
$D^+ \rightarrow K^- \pi^+ \pi^+$	$0.0209 \pm .0027 \pm .0040$	$0.230 \pm 0.030 \pm 0.044 \pm 0.018$	ARGUS 91 [81]
	$0.0226 \pm .0030 \pm .0018$	$0.249 \pm 0.033 \pm 0.020 \pm 0.019$	CLEO 92 [82]
	$0.0216 \pm .0008 \pm .0008$	$0.237 \pm 0.009 \pm 0.009 \pm 0.018$	CLEO 96 [83]
	$0.0217 \pm .0011$	$0.238 \pm 0.012 \pm 0.018$	average
$D^{*+} \rightarrow (K^- \pi^+) \pi^+$	$0.0071 \pm .0006 \pm .0012$	$0.269 \pm 0.023 \pm 0.046 \pm 0.011$	ARGUS 91 [81]
	$0.00556 \pm .00031 \pm .00050$	$0.211 \pm 0.012 \pm 0.019 \pm 0.009$	CLEO 92 [82]
	$0.00655 \pm .00034^a$	$0.248 \pm 0.013 \pm 0.014 \pm 0.010$	CLEO 96 [83]
	$0.00634 \pm .00029$		average
$D^{*+} \rightarrow (K^- \pi^+ \pi^+) \pi^0$	$0.00639 \pm .00054$	$0.229 \pm 0.019 \pm 0.014 \pm 0.026$	CLEO 96 [83]
$D^{*+} \rightarrow D^+ \pi^0 + D^0 \pi^+$		$0.239 \pm 0.011 \pm 0.014 \pm 0.009$	CLEO 96 [83]
		$0.234 \pm 0.013 \pm 0.009$	average
$D^{*0} \rightarrow (K^- \pi^+) \pi^0$	$0.00620 \pm .00031$	$0.259 \pm 0.013 \pm 0.019 \pm 0.015$	CLEO 96 [83]
$D_s^+ \rightarrow \phi \pi^+$	$0.00306 \pm .00047$	$0.085 \pm 0.013 \pm 0.021$	CLEO 90 [84]
	$0.00292 \pm .00039 \pm .00031$	$0.081 \pm 0.011 \pm 0.009 \pm 0.020$	ARGUS 92 [85]
	$0.00424 \pm .00014 \pm .00030$	$0.118 \pm 0.004 \pm 0.009 \pm 0.029$	CLEO 96 [86]
	0.00384 ± 0.00028	$0.100 \pm 0.007 \pm 0.025$	average

^a For $x > 0.15$: 0.00570 ± 0.00021 , extrapolation from $D^+ \pi^0$ mode: $+0.00085 \pm 0.00027$.

to the total error. For example, the $D^0 \rightarrow K^- \pi^+$ decay branching fraction has changed from $(5.4 \pm 0.4)\%$ in 1986 to $(3.86 \pm 0.14)\%$ in 1996. The most reliable value has been obtained by CLEO. This one measurement dominates the present number; therefore, a second independent measurement of similar precision is highly desired. The multiplicities in Table 10-10 have been rescaled to $\mathcal{B}(D^0 \rightarrow K^- \pi^+) = 0.0386 \pm 0.0014$, $\mathcal{B}(D^+ \rightarrow K^- \pi^+ \pi^+) = 0.091 \pm 0.007$, $\mathcal{B}(D^{*+} \rightarrow D^0 \pi^+) = 0.683 \pm 0.014$, $\mathcal{B}(D^{*+} \rightarrow D^+ \pi^0) = 0.306 \pm 0.025$, $\mathcal{B}(D^{*0} \rightarrow D^0 \pi^0) = 0.619 \pm 0.029$, and $\mathcal{B}(D_s \rightarrow \phi \pi^+) = 0.036 \pm 0.009$ [8].

The results for the production of vector mesons are also included in Table 10-10. D -meson momentum spectra are shown in Fig. 10-4, D_s spectra in Fig. 10-5, and D^* spectra in Fig. 10-6. All scales are renormalized to the world average multiplicities given in Table 10-10, except the D^0 and D_s multiplicities where the most recent CLEO II results are used (as listed in Table 10-10, normalized to world average D branching fractions). The D_s spectrum has a pronounced soft

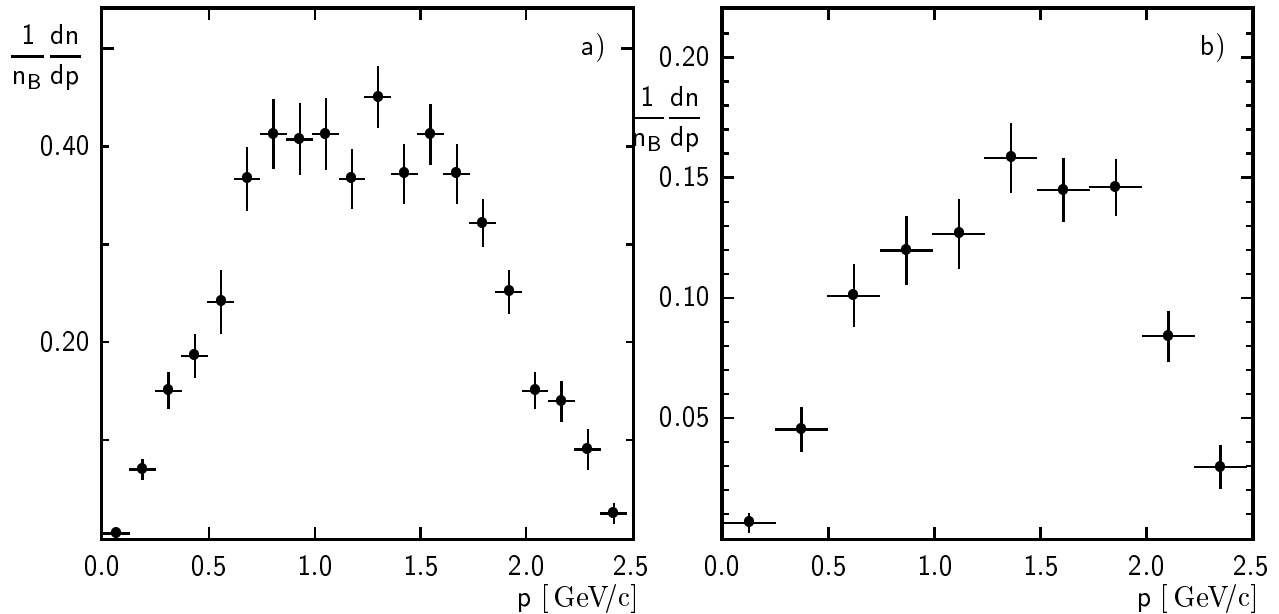


Figure 10-4. Inclusive momentum distribution of (a) D^0 and \bar{D}^0 mesons (normalized to $\langle n \rangle = 0.644$) and (b) D^\pm mesons in $\Upsilon(4S)$ decays [83]. Only statistical errors are shown.

component in addition to a two-body-like peak. This may be taken as an indication that not all D_s^+ mesons are produced from $W^+ \rightarrow c\bar{s}$, but some may contain the c quark from $b \rightarrow c$.

The relationship of D meson flavor to that of the parent B has been derived from D lepton charge correlations by CLEO [88]. While these correlations had been used previously to measure the $B\bar{B}$ mixing probability, with the availability of a precise value for this from the time-dependent analyses at LEP, one can now use this flavor analysis to deduce the effectiveness of flavor tags. If the ratio

$$\frac{\mathcal{B}(B \rightarrow DX)}{\mathcal{B}(B \rightarrow \bar{D}X)} = 0.100 \pm 0.026 \pm 0.016$$

is the same for neutral and charged B mesons, it corresponds to a “wrong” sign fraction of $(9.1 \pm 2.6)\%$ for all D mesons which would provide a “wrong” tag, or a dilution factor $D_t = 0.82 \pm 0.05$. The spectra of these D mesons are expected to differ, so that the momentum could serve as a discriminating variable to increase the tagging separation obtained with reconstructed D mesons. Two *caveats* should be noted: first, the ratio for D^* mesons will differ, since the vector to pseudoscalar ratio is not the same for the dominant production mechanism in different flavor-correlated channels. Second, due to this fact the actual dilution for D^\pm and neutral D mesons can differ also.

These correlations give for the first time information on the amount of D mesons from the $b \rightarrow c\bar{s}(d)$ process (“upper vertex” charm production). The $\bar{c}d$ could produce D^- or D^{*-} directly, while $\bar{c}s$ requires a quark-antiquark pair from the vacuum in addition, and can produce charged and neutral D mesons with equal probability. A known process of the latter kind is the $D_s^{**} \rightarrow DK$

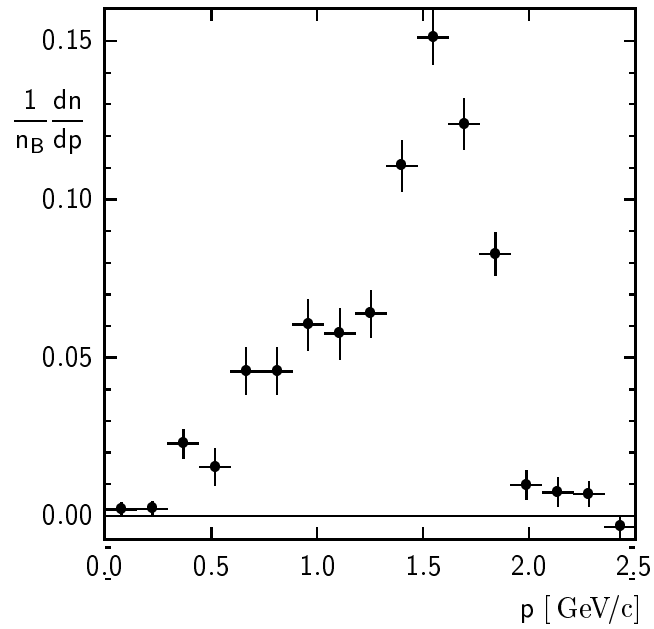


Figure 10-5. Inclusive momentum distribution of D_s^\pm mesons in $\Upsilon(4S)$ decays [86]. Only statistical errors are shown.

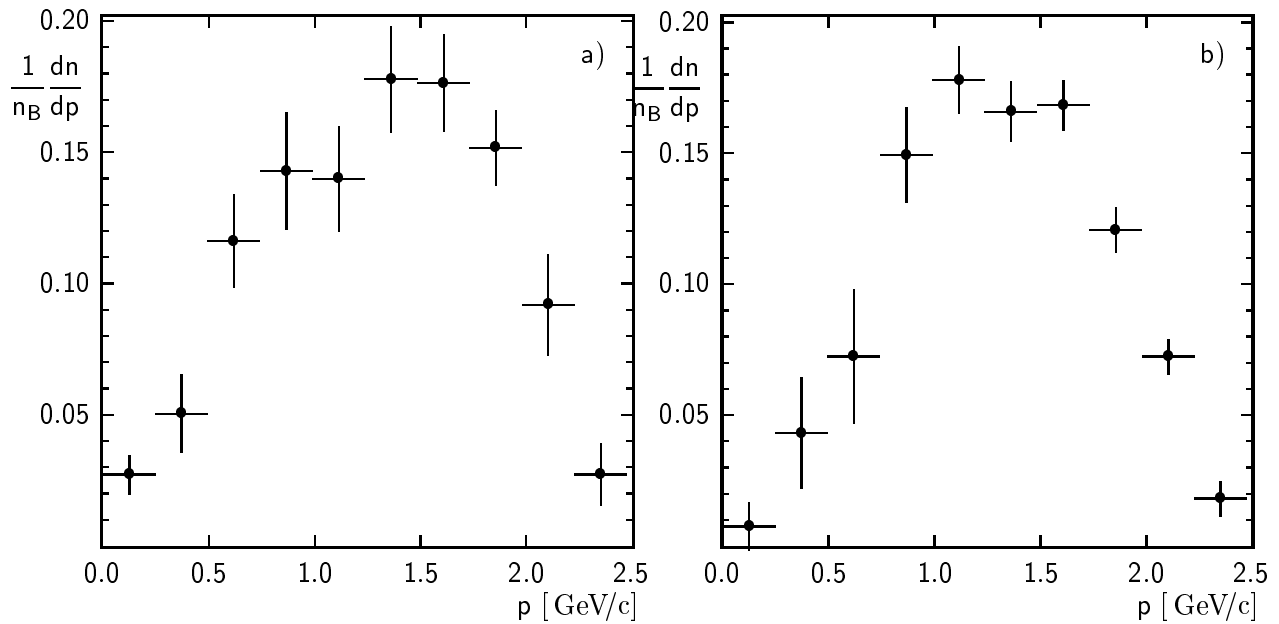


Figure 10-6. Inclusive momentum distribution of (a) D^{*0} and \bar{D}^{*0} mesons and (b) $D^{*\pm}$ mesons in $\Upsilon(4S)$ decays [83]. Only statistical errors are shown.

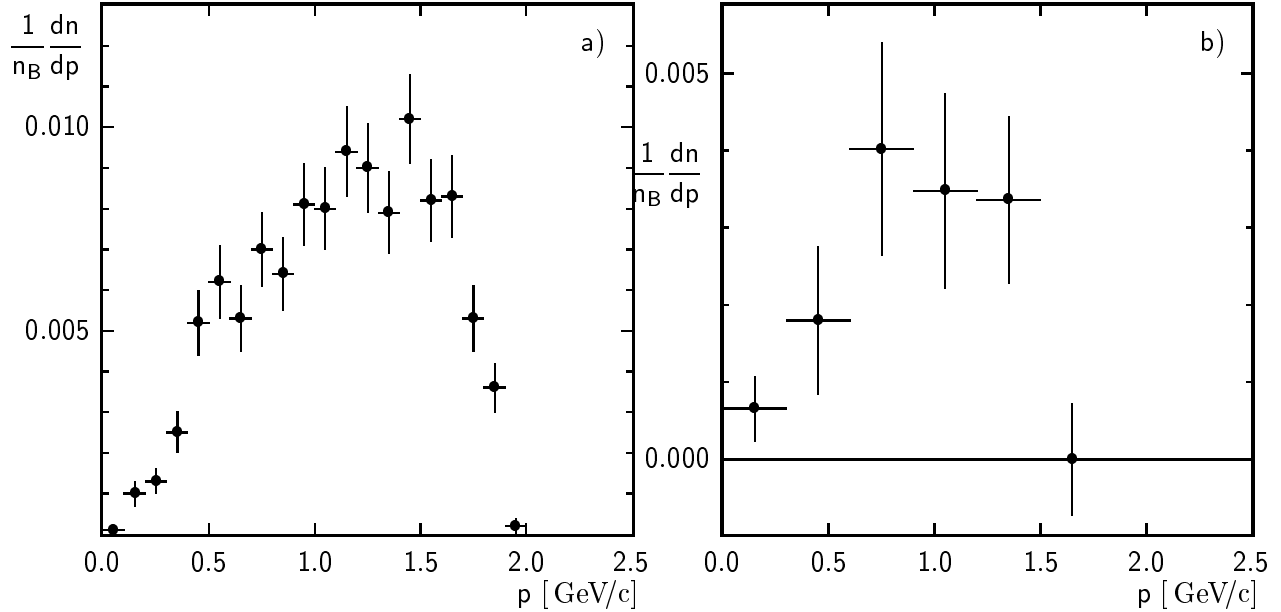


Figure 10-7. Inclusive momentum distribution of (a) J/ψ mesons and (b) χ_{c1} mesons in $\Upsilon(4S)$ decays [87].

decay, but nonresonant production is also possible. More detailed studies at BABAR, including information on the lifetime difference to separate flavor changes from mixing, will shed more light on these mechanisms.

Complementing HQE with additional assumptions on how chiral symmetry and duality are implemented, the authors in Ref. [89] infer the (somewhat surprising) result that at most half of the decays driven by $b \rightarrow c\bar{c}s$ contain a D_s in the final state. They find

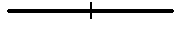

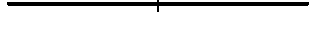

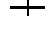
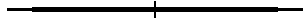


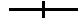
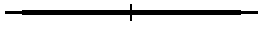

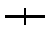
$$\Gamma(\bar{B} \rightarrow \bar{D}K + X) \geq \frac{1}{2}\Gamma(\bar{B} \rightarrow c\bar{c}s\bar{q}), \quad (10.127)$$

which is supported by the data.

Charmonium states have been observed by ARGUS, Crystal Ball and CLEO. All results are summarized in Table 10-11, rescaled to the best estimate of $\mathcal{B}(J/\psi \rightarrow l^+l^-)$. Results for inclusive J/ψ production have also been obtained at LEP [90, 91]. However, since they correspond to a mixture including B_s mesons and beauty baryons, they can not be merged with results on the $\Upsilon(4S)$. The missing states can be estimated from theoretical predictions of the ratios [96] to be $\langle n(\eta_c) \rangle \approx 0.006$ and $\langle n(h_c) \rangle \approx 0.002$, adding to a total of $\langle n(c\bar{c}\text{-onium}) \rangle = 0.027 \pm 0.003$.

The total number of c and \bar{c} quarks from B decays can be obtained by adding up all the charmed and charmonium states that decay into light flavors. These are the charged and neutral D and D_s mesons listed in Table 10-10; the charmed baryons Λ_c and the Ξ_c isodoublet listed in Table 10-15 (the Ω_c can be neglected due to its two s quarks); and charmonium states below the open charm threshold (from Table 10-11, subtracting the decay fractions into lower charmonium) which

Table 10-11. Inclusive branching ratios to charmonium states rescaled to $\mathcal{B}(J/\psi \rightarrow l^+l^-) = (6.02 \pm 0.19)\%$.

	$\mathcal{B} [\%]$	Experiment
$B \rightarrow J/\psi X$		
	$1.34 \pm 0.24 \pm 0.04$	CLEO 86 [92]
	$1.23 \pm 0.27 \pm 0.04$	ARGUS 87 [93]
	$1.28 \pm 0.44 \pm 0.04$	Crystal Ball 90 [94]
	$1.11 \pm 0.05 \pm 0.04$	CLEO II 95 [87]
	1.12 ± 0.05	average
$B \rightarrow \psi' X$ incl. $(0.57 \pm 0.04)J/\psi$		
	$0.50 \pm 0.18 \pm 0.12$	ARGUS 87 [93]
	$0.36 \pm 0.09 \pm 0.13$	CLEO [9]
	$0.34 \pm 0.04 \pm 0.03$	CLEO II 95 [87]
	0.35 ± 0.05	average
$B \rightarrow \chi_{c1} X$ incl. $(0.273 \pm 0.016)J/\psi$		
	$1.20 \pm 0.40 \pm 0.23$	ARGUS 91 [95]
	$0.39 \pm 0.06 \pm 0.04$	CLEO II 95 [87]
	0.41 ± 0.07	average
$B \rightarrow \chi_{c2} X$ incl. $(0.135 \pm 0.011)J/\psi$		
	$0.25 \pm 0.10 \pm 0.03$	CLEO II 95 [87]

account for two c quarks. The D branching fractions are still an important part of the uncertainty of this sum. For example, $\mathcal{B}(D_s \rightarrow \phi\pi^+) = (3.6 \pm 0.9)\%$ is used, but previous measurements have resulted in numbers as low as 2% which would imply almost double the D_s multiplicity. Similarly, smaller uncertainties apply to the other mesons. Surprisingly, some product branching fractions given in Table 10-10 have also increased over time. Therefore, the sum from the average of all measurements and the sum using only CLEO II data are listed side by side in Table 10-12. The weak tendency to a higher sum from more recent measurements may indicate a movement in the direction of the result predicted by theory.

10.4.4 Production of Light Hadrons

The charged multiplicity in B decays is $5.45 \pm 0.03 \pm 0.12$ which includes K_s^0 and Λ decay products [9, 97]. CLEO finds about the same number of photons, $\langle n_\gamma \rangle = 5.00 \pm 0.26 \pm 0.25$.

Table 10-12. Charm counting in B decays from average $\Upsilon(4S)$ data and from CLEO II data (N_c denotes charmed baryons).

	Average	CLEO II	“Best guess”
$B \rightarrow D^0 X$	0.625 ± 0.031	0.644 ± 0.034	0.644 ± 0.034
$B \rightarrow D^+ X$	0.238 ± 0.022	0.237 ± 0.022	0.238 ± 0.022
$B \rightarrow D_s X$	0.100 ± 0.026	0.118 ± 0.031	0.118 ± 0.031
$B \rightarrow N_c X$	0.070 ± 0.005	0.059 ± 0.022	0.070 ± 0.005
$2 \times B \rightarrow (\psi \dots) X$	0.054 ± 0.006	0.052 ± 0.006	0.054 ± 0.006
sum	1.09 ± 0.05	1.11 ± 0.06	1.12 ± 0.05

The production of light flavor (u, d, s) hadrons in B decays is at the very end of the decay chain, and can therefore not be predicted from theory. A simple model to describe inclusive B decays starts with two or four quarks according to QCD predictions, and uses a fragmentation model to produce the final state composition. Monte Carlo event generators are based on this ansatz, and inclusive data are important input to tune these programs. The light hadrons test the combined effect of B decays and subsequent charmed hadron decays. This means that the branching fractions and decay models used for D and D_s mesons, and also for Λ_c and Ξ_c baryons, have a significant influence on the light meson and baryon spectra.

A list of light-meson multiplicities is given in Table 10-13. Although these numbers sometimes appear in the literature as “branching fractions,” they are in fact average multiplicities, including multiple particles in the same event, as decay products from the same B meson. These numbers are determined by measuring inclusive yields on the $\Upsilon(4S)$, and subtracting the continuum contribution by using data taken at center-of-mass energies below the $B\bar{B}$ threshold.

These analyses give inclusive momentum distributions on the $\Upsilon(4S)$, which are close to the distributions expected in the B rest system, since the boost of a B meson is only $\beta\gamma = 0.06$. These spectra are therefore more useful for checking models of inclusive B decays used in Monte Carlo event generators, than are spectra obtained in $b\bar{b}$ jet events. Figure 10-8 shows the spectrum of charged pions, which are the most abundant particles in B decays. The measurement [98] is dominated by systematics rather than statistics, because it relies sensitively on the understanding of dE/dx and time-of-flight distributions used to separate pions from electrons, kaons, and protons. The distributions of these parameters overlap substantially in the high-momentum region, and the particle types can only be separated by a fit of the data to these distributions.

The same procedure leads to the inclusive charged kaon spectrum shown in Fig. 10-9a. In addition, the faint crosses show a kaon spectrum obtained independently by reconstructing kaons that decay within the ARGUS drift chamber, and can be identified by the kink in their tracks. This method suffers from poor statistics, but due to completely different systematics is a valuable consistency check. Direct $b \rightarrow s$ decays via penguin diagrams are expected to produce a hard kaon spec-

Table 10-13. Light-meson multiplicities in B decays. These numbers are obtained as one-half of the mean number of produced particles per $\Upsilon(4S)$ decay. A best guess is indicated in **bold** typeface.

Particle	$\langle n \rangle$	Experiment
π^\pm	3.585 \pm 0.025 \pm 0.070 ^a	ARGUS 92 [98]
	4.105 \pm 0.025 \pm 0.080 ^b	ARGUS 92 [98]
K^\pm	0.85 \pm 0.07 \pm 0.09	CLEO 87 [99]
	0.775 \pm 0.015 \pm 0.025	ARGUS 92 [98]
$B \rightarrow K^+ X$	0.66 \pm 0.05 \pm 0.07	CLEO 87 [99]
	0.613 \pm 0.01 \pm 0.04	ARGUS 92 [98, 100]
$B \rightarrow K^- X$	0.19 \pm 0.05 \pm 0.02	CLEO 87 [99]
	0.162 \pm 0.01 \pm 0.04	ARGUS 92 [98, 100]
K^0/\bar{K}^0	0.63 \pm 0.06 \pm 0.06	CLEO 87 [99]
	0.642 \pm 0.011 \pm 0.042	ARGUS 92 [100]
η	0.176 \pm 0.011 \pm 0.012	CLEO 96 [101]
η'	< 0.15 (90%CL)	ARGUS 93 [102]
	0.031 \pm 0.006 \pm 0.006 ^c	CLEO 96 [103]
ρ^0	0.208 \pm 0.042 \pm 0.032	ARGUS 94 [104]
ω	< 0.81 (90%CL)	ARGUS 94 [104]
$K^{*\pm}$	0.182 \pm 0.054 \pm 0.024	ARGUS 94 [104]
	0.146 \pm 0.016 \pm 0.020	ARGUS 94 [104]
ϕ	0.023 \pm 0.006 \pm 0.005	CLEO 86 [105]
	0.0390 \pm 0.0030 \pm 0.0035	ARGUS 94 [104]
^a without K_s^0 and Λ decay products		
^b incl. K_s^0 and Λ decay products		
^c for $0.10 < x_p < 0.39$		

trum. Both K^\pm and K^0 (Fig. 10-9b) momentum distributions are interesting in this respect. The present data show no substantial excess, so no quantitative statement can be made within present knowledge of the details of spectator decays.

BA \bar{B} AR will be able to redo these measurements using the DIRC for particle identification. This particle identification system will be able to separate pions from kaons with much less overlap, which leads to a significant reduction in systematic errors. The performance can be verified with the help of reconstructed $D^0 \rightarrow K^- \pi^+$, which may be separated from the background either by requiring a well-separated vertex, or by tagging with $D^{*+} \rightarrow D^0 \pi^+$ production. After a small period of data taking at the $\Upsilon(4S)$ and below the $B\bar{B}$ threshold, results with substantially improved errors can be obtained.

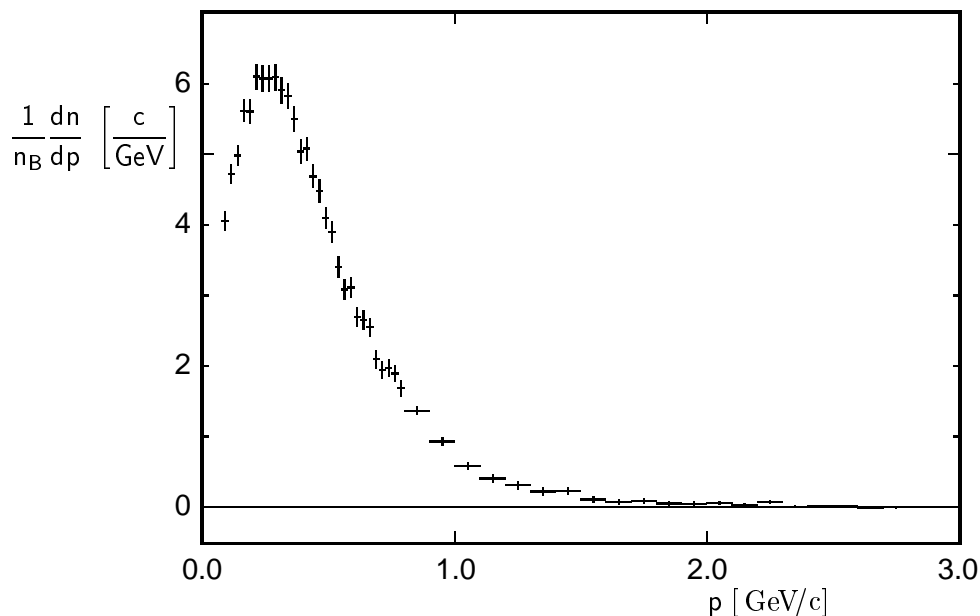


Figure 10-8. Inclusive momentum distribution of charged pions in $\Upsilon(4S)$ decays [98]. Pions from K^0 and Λ decays are subtracted. Only statistical errors are shown.

The correlations between kaon charge (strangeness) and B flavor (beauty) have been investigated by CLEO [99] and ARGUS [100], by investigating kaon-lepton charge correlations. Since this analysis has not yet been repeated with a tagged B sample, the rates given are for a mixture of charged and neutral B mesons, and their assignment to an individual type is based on simple Monte Carlo models. The true experimental information is summarized in Table 10-14, and is a most unbiased test for an inclusive B decay model. These data are the basis on which to estimate the performance of B flavor tagging via charged kaons. Using the ARGUS data, and assuming an equal correlation for charged and neutral B mesons, one finds that charged kaons as B flavor tags have a dilution factor of $D_t = 0.59 \pm 0.08$.

The spectra of flavor-neutral mesons such as π^0 or η are not sensitive to the B flavor, but provide useful information on the reliability of Monte Carlo models. The η spectrum from CLEO is shown in Figure 10-10a.

Table 10-14. Kaon multiplicities in $B\bar{B}$ events with a lepton on the $\Upsilon(4S)$.

	CLEO [99]	ARGUS [100]
$BB \rightarrow l^+\nu, K^+X$	$0.54 \pm 0.07 \pm 0.07$	$0.594 \pm 0.021 \pm 0.056$
$BB \rightarrow l^+\nu, K^-X$	$0.10 \pm 0.05 \pm 0.02$	$0.086 \pm 0.011 \pm 0.044$
$BB \rightarrow l^+\nu, K_s^0X$	$0.195 \pm 0.03 \pm 0.02$	$0.226 \pm 0.019 \pm 0.028$

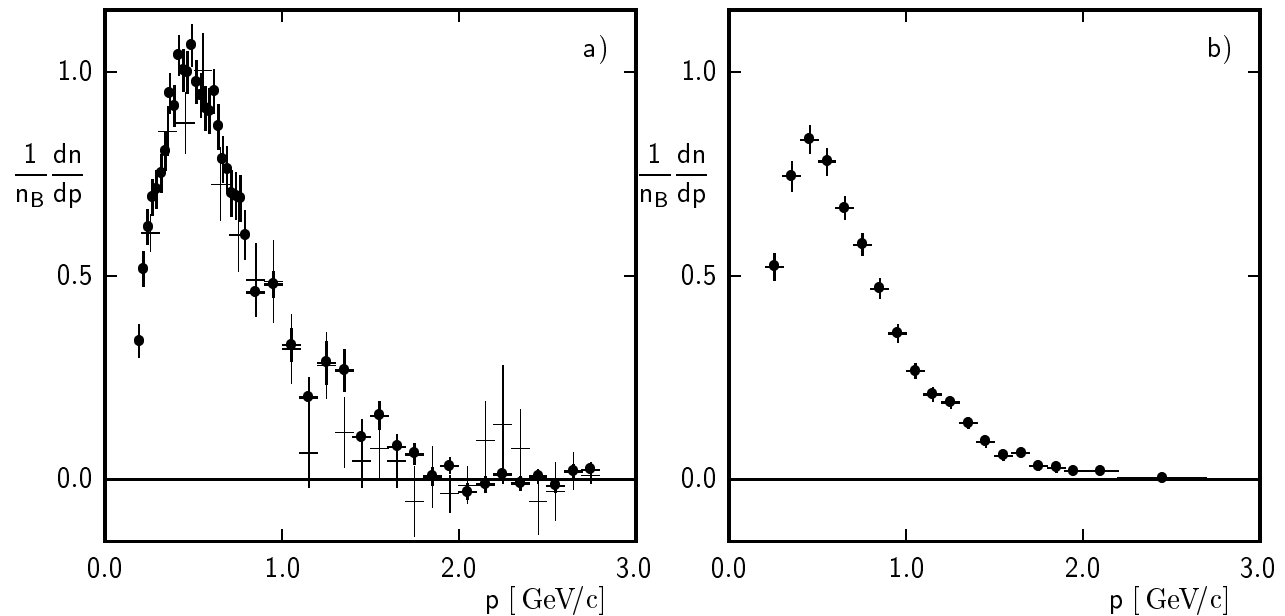


Figure 10-9. (a) Inclusive momentum distribution of charged kaons in $\Upsilon(4S)$ decays [98]. The thin crosses are reconstructed from K^\pm decays in the detector. (b) Inclusive momentum distribution of neutral kaons in $\Upsilon(4S)$ decays [100]. Only statistical errors are shown.

The production rates of some light flavor resonances is also shown in Table 10-13. The spectra of charged and neutral K^* mesons are shown in Fig. 10-10b. These data can be substantially improved with BaBar data.

10.5 B Meson Decays to Baryons

B mesons are heavy enough to decay into baryons. These decays could proceed via two-body decays to a baryon-antibaryon pair, with subsequent decays of baryon resonances to ground states, or via multibody decays. A parton model ansatz has been invoked some time ago [106] to suggest in a semi-quantitative way that a substantial fraction of B meson decays lead to a baryon-antibaryon pair in the final state. This has been borne out by the data.

When the B -meson decays into baryons, at least one additional quark pair has to be generated besides those created in the b -quark decay. The three quarks and three antiquarks can then combine in many ways. Hence decays into baryons are difficult to describe theoretically and there exists only a rudimentary literature. Furthermore, with limited experimental b -flavor-tagging capability, there are often ambiguities in identifying baryons or antibaryons from a B decay, and this then requires taking into account even more production mechanisms. In order to simplify the discussion, the decays of b (rather than \bar{b}) quarks will always be considered in what follows.

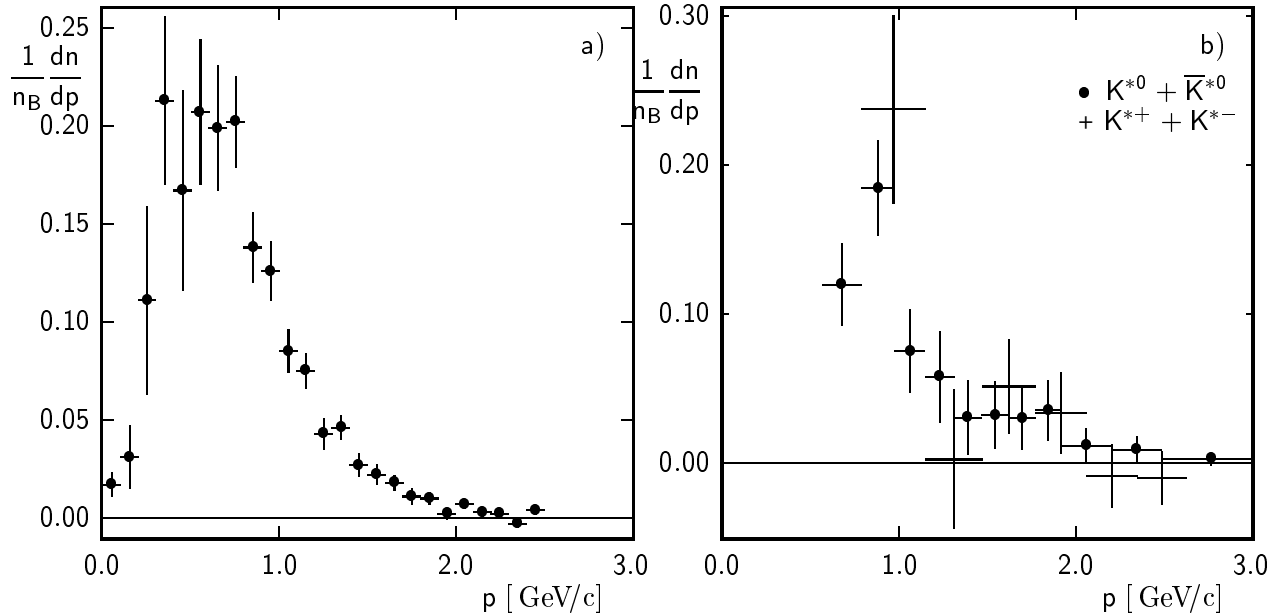


Figure 10-10. Inclusive momentum distribution (a) of η mesons [101], and (b) of K^{*0} and $K^{*\pm}$ mesons in $\Upsilon(4S)$ decays [104]. Only statistical errors are shown.

One usually distinguishes several contributions which are illustrated in Fig. 10-11. The basic mechanism is a tree-level four-fermion interaction for a $b \rightarrow c$ transition. This can be replaced by $b \rightarrow u$ or by a penguin graph in an obvious way.

The first mechanism is disintegration of the excited $c\bar{q}$ state from the $b \rightarrow c$ transition and the spectator quark into a baryon anti-baryon pair ($+ \geq 0$ mesons) with “external” W -emission, where the emitted W transforms into a lepton and neutrino as in graph (a) or to mesons. This requires at least two quark-antiquark pairs produced from the vacuum. The accompanying meson(s) from the hadronization of the W have little phase space, hence $W^- \rightarrow \bar{c}(\bar{u})s$ is suppressed. This mechanism would produce semileptonic decays to baryons even with an advantage in the available phase space, but only small upper limits have been observed: $\mathcal{B}(B \rightarrow \bar{p}Xl^+\nu) < 0.16\%$ (90%CL) [107] and $\mathcal{B}(B \rightarrow \bar{\Lambda}_c X l^+ \nu) / \mathcal{B}(B \rightarrow \Lambda_c / \bar{\Lambda}_c X) < 0.05$ (90%CL) [108].

A very similar process works for “internal exchange” graphs where the emitted W boson interacts with the spectator quark in the B meson shown as graph (d).

Another process is the recombination of all four quarks in a spectator decay into a baryon-antibaryon pair ($+ \geq 0$ mesons), using one additional quark-antiquark pair from the vacuum. These are the “internal emission” graphs (b) and (c). Process (b) is the most favorable process given the available phase space.

Process (e) is the very unlikely decay of the virtual W into a baryon-antibaryon pair ($+ \geq 0$ mesons). This, too, requires at least two quark-antiquark pairs produced from the vacuum.

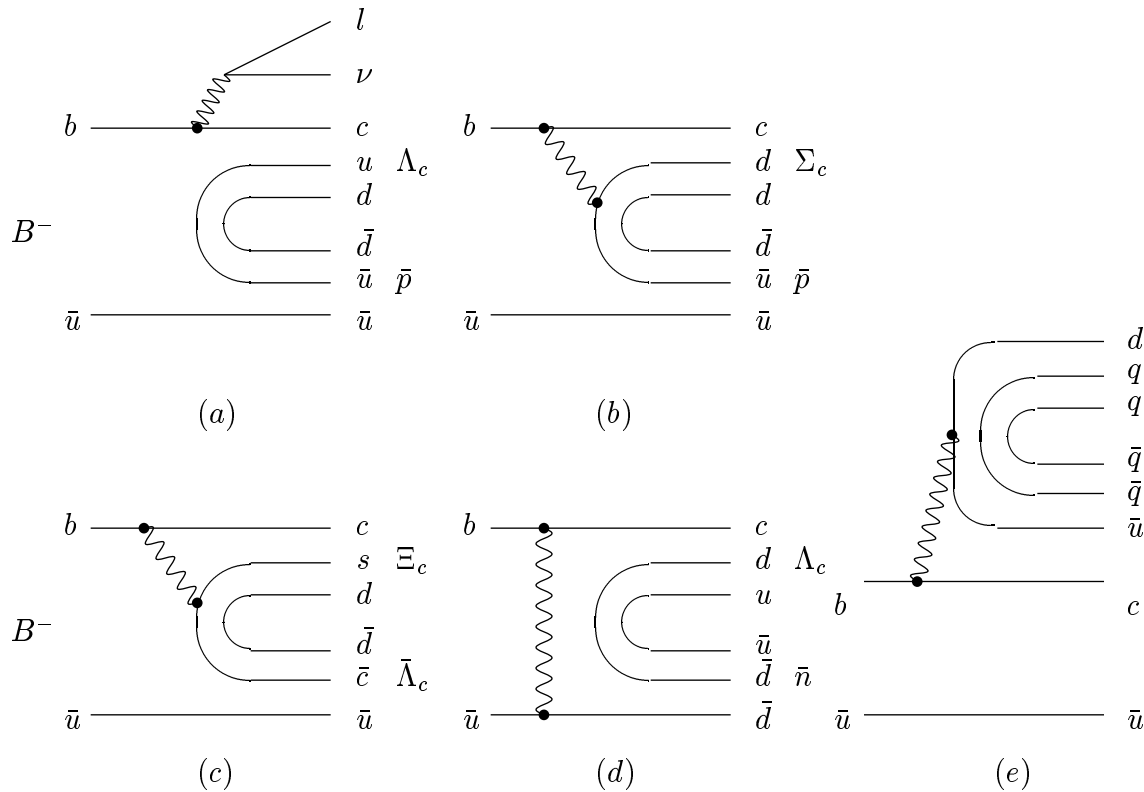


Figure 10-11. Various topologies of baryonic decay modes of B -meson. (a) Semileptonic baryonic decay; (b) Internal $\bar{u}d$ emission; (c) Internal $\bar{c}s$ emission; (d) Weak Annihilation topology; (e) baryon production from W .

Note that certain decays are only possible through one or the other mechanism. For instance, the decays into a doubly-charged charmed baryon containing two u quarks only proceeds through internal exchange graphs or when many pairs are produced from the vacuum. This implies that various production mechanisms can possibly be studied and distinguished by selecting appropriate decay channels. Channels where both four-fermion and penguin decays contribute suggest possible studies of direct CP violation in baryonic B decays.

The dominant decays are those induced by a $b \rightarrow c$ transition. Depending on whether the W boson transforms into a $\bar{u}d$ (or leptons) or a $\bar{c}s$ pair, either one or two charmed baryons are generated. The two cases can be distinguished, if appropriate tagging is possible. Most processes strongly favor light quarks over s quarks as additional valence partners, while (b) and (c) allow an s quark from $W^- \rightarrow \bar{c}(\bar{u})s$. The suppressed $b \rightarrow u$ transition leads to the final states including only “ordinary” baryons, such as protons, neutrons and Δ baryons, as will baryon production from $W^- \rightarrow \bar{u}d$ decay. Finally, penguin decays can yield more exotic final states, such as $p\Lambda$,

Table 10-15. Baryon multiplicities in *B* decays. These numbers are obtained as half of the mean number of produced particle per $\Upsilon(4S)$ decay. A best guess is indicated in **bold** typeface.

Particle/Pair	$\langle n \rangle$	Experiment
p/\bar{p}	$0.055 \pm 0.005 \pm 0.0035^a$	ARGUS 92 [98]
	$0.056 \pm 0.006 \pm 0.005^a$	CLEO 92 [109]
	0.055 ± 0.005^a	average
	$0.080 \pm 0.005 \pm 0.005^b$	ARGUS 92 [98]
	$0.080 \pm 0.005 \pm 0.003^b$	CLEO 92 [109]
	0.080 ± 0.005^b	average
$\Lambda/\bar{\Lambda}$	$0.042 \pm 0.005 \pm 0.006$	ARGUS 89 [110]
	$0.038 \pm 0.004 \pm 0.006$	CLEO 92 [109]
	0.040 ± 0.005	average
$\Xi^-/\bar{\Xi}^+$	0.0028 ± 0.0014	ARGUS 89 [110]
	$0.0027 \pm 0.0005 \pm 0.0004$	CLEO 92 [109]
$p\bar{p}$	$0.025 \pm 0.002 \pm 0.002^b$	ARGUS 89 [110]
	$0.024 \pm 0.001 \pm 0.004^b$	CLEO 92 [109]
$\Lambda\bar{p}/\bar{\Lambda}p$	$0.023 \pm 0.004 \pm 0.003^b$	ARGUS 89 [110]
	$0.029 \pm 0.005 \pm 0.005^b$	CLEO 92 [109]
$\Lambda\bar{\Lambda}$	< 0.009 (90% <i>CL</i>)	ARGUS 89 [110]
	< 0.005 (90% <i>CL</i>)	CLEO 92 [109]
“ $\Lambda_c/\bar{\Lambda}_c$ ”	0.076 ± 0.014	ARGUS 89 [110]
	$0.064 \pm 0.008 \pm 0.008$	CLEO 92 [109]
^a without Λ decay products		
^b incl. Λ decay products		

Since baryons are quite heavy and have to be produced in pairs, even the spectra of the baryons at the end of the decay chain, *i.e.*, protons or Λ hyperons, can tell something about the underlying decay mechanisms. They have been observed by ARGUS and CLEO, and the data are shown in Fig. 10-12. More direct decay products are Λ_c , Σ_c or Ξ_c baryons. The baryon multiplicities are listed in Table 10-15. While the proton and Λ data are well under control, the average number of charmed baryons has a pronounced uncertainty due to the unknown absolute scale of their exclusive branching fractions into the reconstructed final states.

The total fraction of baryon-antibaryon pairs in *B* meson decays can be estimated from the number of protons and Λ hyperons, assuming that an equal number of neutrons is produced for the protons

which are not from Λ decay. This leads to a fraction

$$f_{N\bar{N}} = \frac{2\langle n_{p,\bar{p},\text{no } \Lambda} \rangle + \langle n_{\Lambda,\bar{\Lambda}} \rangle}{2} = 0.075 \pm 0.008$$

of events with baryons. Including a better guess from baryon-antibaryon and baryon-lepton correlations, a fit to ARGUS data gives [111]

$$f_{N\bar{N}} = 0.068 \pm 0.005 \pm 0.003$$

The true branching fraction will most probably be in between these two estimates, and a measurement of antineutron production (*e.g.*, in the BABAR EMC and IFR) could be very helpful in determining this number.

The numbers of Λ_c baryons given in Table 10-15 are based on the assumption that the majority of baryonic B decays proceed via a Λ_c as the carrier of the c quark. For all processes in Fig. 10-11, the assumption that one Λ_c baryon (or its antiparticle) is among the decay products is a good approximation; for process (e) this is true only for $W^- \rightarrow \bar{c}s(d)$. The momentum spectrum of the baryons is shown in Fig. 10-13a.

From the total numbers of Λ_c baryons, the scale of Λ_c branching fractions can then be obtained as $\mathcal{B}(\Lambda_c^+ \rightarrow pK^- \pi^+) = (4.1 \pm 0.3 \pm 0.8)\%$ [109, 111].

This assumption still holds for cascades from other charmed-baryon states, for example, the Σ_c baryons observed by CLEO [112], the scale of which depend on the scale of the Λ_c branching fractions:

$$\begin{aligned} \mathcal{B}(B \rightarrow \Sigma_c^{++} X) \mathcal{B}(\Lambda_c \rightarrow pK^- \pi^+) &= (2.1 \pm 0.8 \pm 0.7) \cdot 10^{-4} \\ \mathcal{B}(B \rightarrow \Sigma_c^+ X) \mathcal{B}(\Lambda_c \rightarrow pK^- \pi^+) &= (2.3 \pm 0.8 \pm 0.7) \cdot 10^{-4} \\ \mathcal{B}(B \rightarrow \Sigma_c^0 X) \mathcal{B}(\Lambda_c \rightarrow pK^- \pi^+) &< 4.8 \cdot 10^{-4} \text{ (90\% CL)} \end{aligned}$$

However, CLEO has recently found a substantial fraction of Ξ_c baryons [113] which do not decay via the Λ_c state:

$$\begin{aligned} \mathcal{B}(B \rightarrow \Xi_c^0 X) \mathcal{B}(\Xi_c^0 \rightarrow \Xi^- \pi^+) &= (1.44 \pm 0.48 \pm 0.21) \cdot 10^{-4} \\ \mathcal{B}(B \rightarrow \Xi_c^+ X) \mathcal{B}(\Xi_c^+ \rightarrow \Xi^- \pi^+ \pi^+) &= (4.53 \pm 0.96 \pm_{0.65}^{0.85}) \cdot 10^{-4} \end{aligned}$$

The absolute branching fraction of B mesons to these states are very uncertain due to the unknown Ξ_c branching fractions. Therefore, the normalization of their spectra in Fig. 10-13b is only a guess.

Both charmed- and stable-baryon spectra are surprisingly soft, indicating that either the exclusive baryon-antibaryon pair is not the favored final state, or that there is a dominant contribution from $b \rightarrow c\bar{c}s$ via process (c) with two heavy charmed baryons, which would occupy the low region

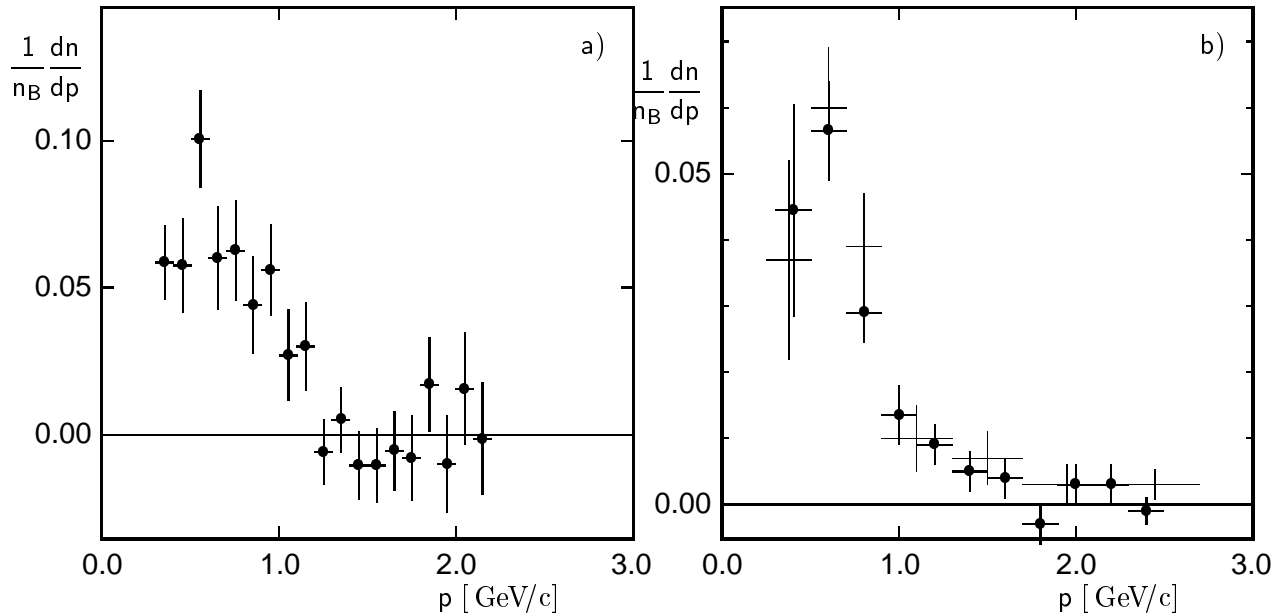


Figure 10-12. Inclusive momentum distribution of (a) protons [98] and (b) Λ baryons from CLEO [109] and ARGUS (thin crosses, [110]). Protons from Λ decays are subtracted in (a). Only statistical errors are shown.

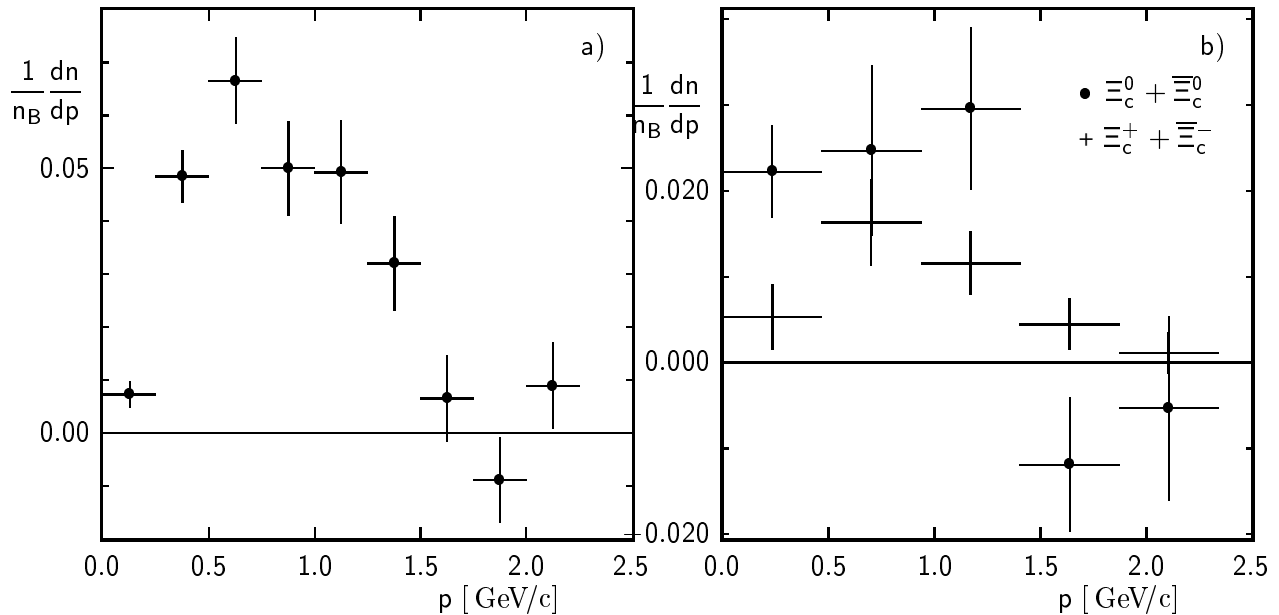


Figure 10-13. Inclusive momentum distribution of (a) Λ_c baryons [114] and (b) Ξ_c^0 and Ξ_c^+ baryons from CLEO [113] Only statistical errors are shown. The absolute scales are very uncertain, especially in (b), due to ignorance of charmed-baryon branching fractions.

Table 10-16. *Inclusive B/\bar{B} decays to leptons + baryons*

$\frac{\bar{B} \rightarrow \bar{\Lambda}, B \rightarrow l^+}{\bar{B} \rightarrow \Lambda, B \rightarrow l^+}$	0.55 ± 0.22 < 0.14 (90%CL) $0.43 \pm 0.09 \pm 0.07$	ARGUS 92 [111] CLEO 92 [109] CLEO 96 [115]
$\frac{\bar{B} \rightarrow \bar{\Lambda}_c^-, B \rightarrow l^+}{\bar{B} \rightarrow \Lambda_c^+, B \rightarrow l^+}$	$0.19 \pm 0.13 \pm 0.04$	CLEO 96 [115]

in the momentum distributions due to the limited phase space available. The production of Ξ_c baryons may indicate either $s\bar{s}$ pairs produced from the vacuum, or the presence of process (c).

Our ignorance of the relative weight of the different production processes and of the absolute branching fractions of Λ_c and Ξ_c baryons makes it hard to make further progress on both items. However, the correlation of the s quark and the c quark with the B flavor can shed further light on the first one, thereby helping with the second question, too. Process (a) yields from a b quark only c , and equal numbers of s and \bar{s} . Process (e) yields a dominance of s over \bar{s} from the primary quarks, and only c from b . “Internal” emission graphs yields a dominance of c over \bar{c} from (b), and of s over \bar{s} from (c). These correlations can be explored with baryon-lepton correlation measurements in $B\bar{B}$ events at the $\Upsilon(4S)$. Experimental results on lepton Λ correlations are given in Table 10-16.

The more interesting data are those on charmed-baryon correlations with leptons, where first results are also given in Table 10-16. Although the errors are still large, the presence of the “wrong” charm flavor together with the soft spectra seems to indicate that processes (b) and (c) are contributing significantly to the production of baryons.

Further experimental results on charmed baryon flavor correlations with respect to the parent B meson will be an interesting topic for BABAR studies. These may eventually reveal the secrets of baryon pair creation in the weak decays of heavy mesons.

10.5.1 Exclusive Decays to Baryons

Baryon number conservation implies that the final state should contain at least one baryon-anti-baryon pair. Since baryons are in general relatively heavy, it seems reasonable to assume that decays with many additional mesons are suppressed by the phase space limitations. Furthermore, in the internal emission picture additional mesons require extra quark-antiquark pairs. Therefore, the exclusive and inclusive baryon decays might not be too different in rates, maybe by factors of order ten, and exclusive decays are expected at rates of a few tenths percent. Comparing decays with Λ_c to those with Σ_c , much can be learned about the production mechanism.

Table 10-17. Branching ratios for baryonic *B* decays.

Decay Mode	$\mathcal{B}_{CZ} \times 10^{-5}$ [116]	$\mathcal{B}_{BD} \times 10^{-5}$ [117]	$\mathcal{B}_{JLYOPR} \times 10^{-5}$ [118]
$B \rightarrow p\bar{p}$	0.16	0.4 – 3.8	0.7
$B \rightarrow N\bar{N}$	0.05 – 0.2	0.4 – 3.8	~ 1
$B \rightarrow \Lambda_c^+ \bar{p}$	40	170 – 190	~ 100
$B \rightarrow \bar{\Lambda}_c \Xi_c$	100	120 – 180	–
$B \rightarrow \bar{p}\Delta^{++}$	0.04	0.001 – 0.012	32

Several authors [116, 117, 118] have attempted to calculate exclusive decays rates. The results are model-dependent and vary quite drastically. In particular, certain models favor decays with specific final-state baryons such as the Δ [118], which are not particularly enhanced in others. Some of the theoretical predictions are presented in Table 10-17 along with recent limits from CLEO [119].

Considering first decays with charmed baryons, it is desirable to understand the production mechanisms. From the existing data [108], it seems that the external production mechanism with leptons is rather suppressed, since at most 5% of the charmed baryon decays have a lepton. Therefore, internal emission plays a dominant role in baryon production in *B* decays. It was proposed [120] that the situation where the *W* produces a $\bar{c}s$ pair contributes significantly to the charmed baryons. However, further experiments [115] indicated that although there is a slight enhancement in the $B \rightarrow \Lambda_c \bar{\Xi}_c$ channel, this is not the case because no significant amount of \bar{c} have been seen. Furthermore, it is widely assumed that the contribution of the internal exchange graph (d) is not significant, since its amplitude is proportional to the small decay constant f_B because the *B* meson is annihilated. Therefore, it may be concluded that the internal emission with the $\bar{u}d$ pair (b) dominates the single charmed baryon prediction.

The next class of decays includes a pair of a charmed and anticharmed baryon, originating from internal emission with a $\bar{c}s$ pair. Here, the problem is whether the $\bar{c}c$ modes (such as the J/ψ) dominate this quark diagram. In order to estimate the baryonic part, one uses the fact that decays with a *D* pair make up about a tenth of those with one *D*. It seems reasonable to take $0.1 \times 6\% = 0.006$ as a typical branching ratio for these decays. Again, final-state particle identification is highly desirable.

The most interesting decays are those without charm, since they can also contribute to *CP* violation studies. Taking $|V_{ub}/V_{cb}|^2 \sim 10^{-2}$, it may be expected that the total inclusive baryonic rate is around $0.01 \times 6\% \sim 10^{-3}$. This is considerably larger than the sum of expected quasi-two-body meson modes ($\pi\pi, \rho\pi, a_1\pi$). Thus, even if the exclusive decays make up only 10% of the inclusive one (see above), baryonic decays still might be comparable to mesonic decays.

Generators that include baryon production are necessary both for the B -decay channels and for the simulation of continuum backgrounds. Given the lack of definitive theoretical predictions, such generators necessarily contain parameters which must be adjusted to fit data as baryonic channels are detected.

10.5.2 CP Violation in Baryonic Decays

It is questionable whether baryonic decays are useful for CP violation studies because of the many amplitudes involved. Indeed, a baryonic final state in general is not a CP eigenstate. The reason for this is the fact that the CP transformation flips the helicity of the state. Therefore, formation of the usual CP -violating asymmetries of the B and \bar{B} decays would not reveal clean information about weak phases of the CKM matrix. The baryonic final state ($p\bar{p}$) can be cast into the form of the linear combinations of the states $|p, 1/2; \bar{p}, 1/2\rangle$ and $|p, -1/2; \bar{p}, -1/2\rangle$ that are CP eigenstates

$$|p\bar{p}; CP = \pm\rangle = \frac{1}{\sqrt{2}} (|p, 1/2; \bar{p}, 1/2\rangle \pm |p, -1/2; \bar{p}, -1/2\rangle) , \quad (10.128)$$

but since the ratio of the two states is not known, the resulting CP asymmetry is not free of hadronic uncertainties. The decay rate is given by

$$\Gamma(B \rightarrow p\bar{p}) = (A_+^2 + A_-^2)e^{-\Gamma t} \left(1 - \frac{A_+^2 - A_-^2}{A_+^2 + A_-^2} \sin \phi_w \sin \Delta mt \right) , \quad (10.129)$$

where A_{\pm} are the amplitudes for B decay to one of the CP eigenstates. The explicit factor $(A_+^2 - A_-^2)/(A_+^2 + A_-^2)$ persists in the asymmetry and not only spoils a clean determination of the weak phase but also decreases the asymmetry itself. In principle, in the case of unstable baryons such as Λ , angular distributions of the decay products can be analyzed to separate the different helicity contributions, just as in the vector-vector two-meson decays described in Section 5.1.3. In such cases asymmetries can be written for baryonic B decays to the states of definite angular momentum exploiting the fact that the baryon-antibaryon state in the S or P wave is in fact an eigenstate of CP (with opposite CP signs for S and P waves) and thus would become independent of hadronic models in cases where only a single weak phase occurs in the production amplitudes. However it is not likely to have sufficient data in any clean channel to perform such an analysis.

Some of the possible signals of CP violation in B decays to baryonic final states require moving B mesons to extract the time-dependent terms and thus exploit unique capabilities of asymmetric B factories not available for CLEO. The analysis of any such signal has many unavoidable theoretical complications, but will add to the overall picture of B decay and hence should be searched for wherever branching ratios are sufficiently large to make such a search feasible.

References

- [1] M. Neubert, *Phys. Lett. B* **424**, 152 (1998).
- [2] J. D. Bjorken, “Gauge Bosons and Heavy Quarks” in *Proceedings of SLAC SSI*, ed. Jane F. Hawthorne, Stanford, California, SLAC, (1991). See also Preprint SLAC-PUB-5389 (1990); *Nucl. Phys. B Proc. Suppl.* **11**, 325 (1989).
- [3] M. Bauer, B. Stech, and M. Wirbel, *Z. Phys. C* **29**, 637 (1985); *Z. Phys. C* **34**, 103 (1987).
- [4] M. Neubert and B. Stech, CERN-TH/97-099 (1997), to appear in *Heavy Flavours II*, ed. by A. J. Buras and M. Lindner, World Scientific, Singapore, hep-ph/9705292.
- [5] C. Reader and N. Isgur, *Phys. Rev. D* **47**, 1007 (1993).
- [6] J. L. Rodriguez, in *Proceedings of the 2nd International Conference on B Physics and CP Violation*, Honolulu, Hawaii, March (1997), p. 124.
- [7] J. D. Richman, preprint UCSB-HEP-97-01 (1997), to appear in *Proceedings of the 28th International Conference on High-Energy Physics (ICHEP 96)*, Warsaw, Poland, July (1996) [hep-ex/9701014].
- [8] R. M. Barnett *et al.*, *Phys. Rev. D* **54**, 1 (1996).
- [9] T. E. Browder, K. Honscheid, and D. Pedrini, *Ann. Rev. Nucl. Part. Sci.* **46**, 395 (1996).
- [10] H.-Y. Cheng, *Phys. Lett. B* **395**, 345 (1997);
M. Gourdin, Y. Y. Keum, and X. Y. Pham, *Phys. Rev. D* **52**, 1597 (1995).
- [11] H.-Y. Cheng, *Phys. Lett. B* **335**, 428 (1994);
J. M. Soares, *Phys. Rev. D* **51**, 3518 (1995).
- [12] A. Khodjamirian and R. Rückl, in *Heavy Flavours II*, eds. A.J. Buras and M. Lindner (World Scientific, Singapore) p.345 (1998).
- [13] A. J. Buras, J.-M. Gerard, and R. Rückl, *Nucl. Phys.* **B268**, 16 (1986).
- [14] I. Halperin, *Phys. Lett. B* **349**, 548 (1995).
- [15] G. 't Hooft, *Nucl. Phys.* **B72**, 461 (1974);
E. Witten, *Nucl. Phys.* **B160**, 57 (1979).
- [16] A. A. Petrov, Ph.D. thesis, University of Massachusetts (1997), unpublished.
- [17] M. J. Dugan and B. Grinstein, *Phys. Lett. B* **255**, 583 (1991).

- [18] U. Aglietti, *Phys. Lett. B* **292**, 285 (1992).
- [19] P. D. Politzer and M. B. Wise, *Phys. Lett. B* **257**, 399 (1991);
G. D. Haas and M. Youssefmir, *Phys. Lett. B* **272**, 391 (1991);
C. E. Carlson and J. Milana, *Phys. Lett. B* **301**, 237 (1993).
- [20] B. Blok and M. Shifman, *Sov. J. Nucl. Phys.* **45**, 135 (1987).
- [21] B. Blok and M. Shifman, *Nucl. Phys.* **B389**, 534 (1993).
- [22] J. F. Donoghue and A. A. Petrov, *Phys. Lett. B* **393**, 149 (1997).
- [23] M. Neubert, *et al.*, in *Heavy Flavours*, eds. A.J. Buras and M. Lindner, World Scientific, Singapore (1992), p. 286.
- [24] V. Rieckert, *Phys. Rev. D* **47**, 3053 (1993).
- [25] M. Neubert, *Nucl. Phys.* **B371**, 149 (1992); *Phys. Rev. D* **46**, 2212 (1992).
- [26] V. Rieckert, Ph.D. thesis, University of Heidelberg (1994), unpublished.
- [27] N. Isgur *et al.*, *Phys. Rev. D* **39**, 799 (1989);
N. Isgur and D. Scora, *Phys. Rev. D* **40**, 1491 (1989).
- [28] R. Casalbuoni *et al.*, *Phys. Lett. B* **292**, 371 (1992); *Phys. Lett. B* **299**, 139 (1993);
A. Deandrea *et al.*, *Phys. Lett. B* **318**, 549 (1993).
- [29] R. Aleksan *et al.*, *Phys. Rev. D* **51**, 6235 (1995).
- [30] J. G. Kroner and G. R. Goldstein, *Phys. Lett. B* **89**, 105 (1979).
- [31] C. P. Jessop *et al.*, (CLEO Collaboration), *Phys. Rev. Lett.* **79**, 4533 (1997).
- [32] A. S. Dighe *et al.*, *Phys. Lett. B* **369**, 144 (1996).
- [33] N. Isgur and M. B. Wise, *Phys. Rev. D* **42**, 2388 (1990).
- [34] Y. Y. Keum, in *Proceedings of the APCTP-ICTP Joint International Conference '97*, Seoul, Korea; APCTP-97-23 (1997).
- [35] H.-Y. Cheng and B. Tseng, *Phys. Rev. D* **51**, 6259 (1995).
- [36] M. Gourdin, Y. Y. Keum, and X. Y. Pham, *Phys. Rev. D* **51**, 3510 (1995).
- [37] S. Chan *et al.*, (CLEO Collaboration), CONF 98-24, paper contributed to ICHEP98.
- [38] Y. Y. Keum, Ph.D. thesis, Université Pierre et Marie Curie (Pais VI) (1996), unpublished.

- [39] W. Jaus, *Phys. Rev. D* **41**, 3394 (1990);
W. Jaus and D. Wyler, *Phys. Rev. D* **41**, 3405 (1990);
M. Neubert, *Phys. Lett. B* **418**, 173 (1998).
- [40] A. Khodjamirian, private communication. The vanishing of certain amplitudes in factorization has also been noted before, *e.g.*, by M. Neubert.
- [41] K.M. Watson, *Phys. Rev.* **88**, 1163 (1952).
- [42] R. Omnès, *Nuo. Cim.* **8**, 1244 (1958). See: G. Barton, *Introduction to dispersion relation techniques in field theories*, Benjamin, New York (1965).
- [43] N. Khuri and S. Treiman, *Phys. Rev. D* **119**, 1115 (1960);
J. Kambor *et al.*, *Nucl. Phys.* **B465**, 215 (1996).
- [44] M. Bander, D. Silverman, and A. Soni, *Phys. Rev. Lett.* **43**, 242 (1979).
- [45] I. I. Bigi *al.*, in “*CP Violation*,” C. Jarlskog, ed. World Scientific, Singapore (1988).
- [46] L. Wolfenstein, *Phys. Rev. D* **43**, 151 (1991).
- [47] J.-M. Gerard and W.-S. Hou, *Phys. Rev. D* **43**, 2909 (1991).
- [48] Yu. Dokshitzer and N. Uraltsev, *JETP Lett.* **52** (10), 1109 (1990).
- [49] A. E. Blinov, V. A. Khoze, and N. G. Uraltsev, *Int. J. Mod. Phys. A* **4**, 1933 (1989); [*Sov. Phys. JETP* **70**, 32 (1990)].
- [50] L.-L. Chau and H.-Y. Cheng, *Phys. Rev. Lett.* **59**, 958 (1987).
- [51] G. Kramer, W. Palmer, and H. Simma, *Z. Phys. C* **66**, 429 (1995) and *Nucl. Phys.* **B428**, 77 (1994);
H. Simma *et al.*, *Phys. Lett. B* **272**, 395 (1991); *Nucl. Phys.* **B352**, 367 (1991).
- [52] P. V. Landshoff, in *QCD – 20 Years Later*, World Scientific, Singapore (1993).
- [53] G. Eilam, M. Gronau, and R. R. Mendel, *Phys. Rev. Lett.* **74**, 4984 (1995);
- [54] N. G. Deshpande *et al.*, *Phys. Rev. D* **52**, 5354 (1995).
- [55] F. Buccella, A. Pugliese and M. Lusignoli, *Phys. Lett. B* **379**, 249 (1996).
- [56] A. Donnachie and P.V. Landshoff, *Phys. Lett. B* **296**, 227 (1992).
- [57] P.D.B. Collins, *Introduction to Regge Theory and High Energy Physics*, Cambridge University Press, Cambridge, England (1977).

- [58] J. F. Donoghue *et al.*, *Phys. Rev. Lett.* **77**, 2178 (1996).
- [59] B. Blok and I. Halperin, *Phys. Lett. B* **385**, 324 (1996).
- [60] B. Blok, M. Gronau, and J. L. Rosner, *Phys. Rev. Lett.* **78**, 3999 (1997).
- [61] R. Fleischer and T. Mannel, *Phys. Rev. D* **57**, 2752 (1998);
A. F. Falk *et al.*, *Phys. Rev. D* **57**, 4290 (1998);
D. Atwood and A. Soni, *Phys. Rev. D* **58**, 360 (1998).
- [62] N. G. Deshpande and C.O. Dib, *Phys. Lett. B* **319**, 313 (1993);
H. Zheng, *Phys. Lett. B* **356**, 107 (1995);
G. Nardulli and T.N. Pham, *Phys. Lett. B* **391**, 165 (1997).
- [63] P. Colangelo *et al.*, *Z. Phys. C* **45**, 575 (1990);
A. Khodjamirian *et al.*, *Phys. Lett. B* **402**, 167 (1997).
- [64] A. Khodjamirian, G. Stoll, and D. Wyler, *Phys. Lett. B* **358**, 129 (1995);
A. Ali and V. M. Braun, *Phys. Lett. B* **359**, 223 (1995).
- [65] J. F. Donoghue, E. Golowich, and A. A. Petrov, *Phys. Rev. D* **55**, 2657 (1997).
- [66] P. S. Marrocchesi and N. Paver, *Int. J. Mod. Phys. A* **13**, 251 (1998).
- [67] N. Isgur and M. Wise, *Phys. Lett. B* **232**, 113 (1989); *Phys. Lett. B* **237**, 527 (1990).
- [68] G. Burdman and J. F. Donoghue, *Phys. Lett. B* **280**, 287 (1992).
- [69] M. B. Wise, *Phys. Rev. D* **45**, 2188 (1992).
- [70] T.-M. Yan, *et al.*, *Phys. Rev. D* **46**, 1148 (1992).
- [71] J. F. Donoghue, E. Golowich, and B. R. Holstein, *Dynamics of the Standard Model*, Cambridge University Press, Cambridge, England (1992).
- [72] H. Georgi, TASI-91 lectures, Preprint HUTP-91-A 031 (1991).
- [73] A. F. Falk, *Nucl. Phys.* **B378**, 79 (1992).
- [74] A. F. Falk and M. Luke, *Phys. Lett. B* **292**, 119 (1992).
- [75] G. Burdman and J. Kambor, *Phys. Rev. D* **55**, 2817 (1997).
- [76] B. Bajc, S. Fajfer, and R. J. Oakes, *Phys. Rev. D* **53**, 4957 (1996);
B. Bajc *et al.*, *Phys. Rev. D* **56**, 7207 (1997).
- [77] For a critical review of the literature, see: I. I. Bigi, M. Shifman and N. G. Uraltsev, *Ann. Rev. Nucl. Part. Sci.* **47**, 591 (1997).

- [78] For a detailed discussion and references to earlier work, see: G. Bellini, I. I. Bigi and P. J. Dornan, *Phys. Rep.***289**, 1 (1997).
- [79] M. Shifman and M. Voloshin, *Sov. J. Nucl. Phys.* **41**, 120 (1985).
- [80] I. I. Bigi, N. G. Uraltsev and A. Vainshtein, *Phys. Lett. B* **293**, 430 (1992); *Phys. Lett. B* **297**, 477(E) (1993);
B. Blok and M. Shifman, *Nucl. Phys.* **B399**, 441, 459 (1993).
- [81] H. Albrecht *et al.*, (ARGUS Collaboration), *Z. Phys. C* **52**, 353 (1991).
- [82] D. Bortoletto *et al.*, (CLEO Collaboration), *Phys. Rev. D* **45**, 21 (1992).
- [83] L. Gibbons *et al.*, (CLEO Collaboration), *Phys. Rev. D* **56**, 3783 (1997).
- [84] D. Bortoletto *et al.*, (CLEO Collaboration), *Phys. Rev. Lett.* **64**, 2117 (1990).
- [85] H. Albrecht *et al.*, (ARGUS Collaboration), *Z. Phys. C* **54**, 1 (1992).
- [86] D. Gibaut *et al.*, (CLEO Collaboration), *Phys. Rev. D* **53**, 4734 (1996).
- [87] R. Balest *et al.*, (CLEO Collaboration), *Phys. Rev. D* **52**, 2661 (1995).
- [88] T. E. Coan *et al.*, (CLEO Collaboration), *Phys. Rev. Lett.* **80**, 1150 (1998).
- [89] B. Blok, M. Shifman and N. G. Uraltsev, *Nucl. Phys.* **B494**, 237 (1997).
- [90] D. Buskulic *et al.*, (ALEPH Collaboration), *Phys. Lett. B* **295**, 396 (1992).
- [91] M. Acciarri *et al.*, (L3 Collaboration), plb407, 351 (1997).
- [92] M.S. Alam *et al.*, (CLEO Collaboration), *Phys. Rev. D* **34**, 3279 (1986).
- [93] H. Albrecht *et al.*, (ARGUS Collaboration), *Phys. Lett. B* **199**, 451 (1987).
- [94] W.S. Maschmann *et al.*, (Crystal Ball Collaboration), *Z. Phys. C* **46**, 555 (1990).
- [95] H. Albrecht *et al.*, (ARGUS Collaboration), *Phys. Lett. B* **277**, 209 (1992).
- [96] J. Kühn *et al.*, *Z. Phys. C* **5**, 117 (1980);
J. Kühn and R. Rückl, *Phys. Lett. B* **135**, 477 (1984);
P. A. Rączka, *Phys. Rev. D* **46**, 3699 (1992).
- [97] H. Albrecht *et al.*, (ARGUS Collaboration), *Z. Phys. C* **54**, 13 (1992).
- [98] H. Albrecht *et al.*, (ARGUS Collaboration), *Z. Phys. C* **58**, 191 (1993).
- [99] M.S. Alam *et al.*, (CLEO Collaboration), *Phys. Rev. Lett.* **58**, 1814 (1987).

- [100] H. Albrecht *et al.*, (ARGUS Collaboration), *Z. Phys. C* **62**, 371 (1994).
- [101] Y. Kubota *et al.*, (CLEO Collaboration), *Phys. Rev. D* **53**, 6033 (1996).
- [102] H. Albrecht *et al.*, (ARGUS Collaboration), *Z. Phys. C* **58**, 199 (1993).
- [103] CLEO Collaboration, CLEO CONF 96-18 (1996), contributed paper pa05-73 to the 28th International Conference on High Energy Physics, Warsaw 96.
- [104] H. Albrecht *et al.*, (ARGUS Collaboration), *Z. Phys. C* **61**, 1 (1994).
- [105] D. Bortoletto *et al.*, (CLEO Collaboration), *Phys. Rev. Lett.* **56**, 800 (1986).
- [106] I. I. Bigi, *Phys. Lett. B* **106**, 510 (1981).
- [107] H. Albrecht *et al.*, (ARGUS Collaboration), *Phys. Lett. B* **249**, 359 (1990).
- [108] G. Bonvicini *et al.*, (CLEO Collaboration), *Phys. Rev. D* **57**, 6604 (1998).
- [109] G. Crawford *et al.*, (CLEO Collaboration), *Phys. Rev. D* **45**, 752 (1992).
- [110] H. Albrecht *et al.*, (ARGUS Collaboration), *Z. Phys. C* **42**, 519 (1989).
- [111] H. Albrecht *et al.*, (ARGUS Collaboration), *Z. Phys. C* **56**, 1 (1992).
- [112] M. Procaro *et al.*, (CLEO Collaboration), *Phys. Rev. Lett.* **73**, 1472 (1995).
- [113] B. Barish *et al.*, (CLEO Collaboration), *Phys. Rev. Lett.* **79**, 3599 (1997).
- [114] M. Athanas *et al.*, (CLEO Collaboration), CLEO-CONF 94-2, submitted to International Conference on High Energy Physics, Glasgow, Scotland, Jul 20-27, (1994).
- [115] R. Ammar *et al.*, (CLEO Collaboration), *Phys. Rev. D* **55**, 13 (1997).
- [116] V. L. Chernyak and I. R. Zhitnitsky, *Nucl. Phys.* **B345**, 137 (1990).
- [117] P. Ball and H.G. Dosch, *Z. Phys. C* **51**, 445 (1991).
- [118] M. Jarfi *et al.*, *Phys. Rev. D* **43**, 1599 (1991).
- [119] T. E. Coan *et al.*, (CLEO Collaboration), Cornell Preprint CLNS-98-1583 (1998).
- [120] I. Dunietz *et al.*, *Phys. Rev. Lett.* **73**, 1075 (1994).

11.1 Overview

Previous chapters have demonstrated why a factory is needed to do CP -violation physics in B -meson decays. Before the B -production line is in a steady state, running at the desired pace, it can produce significant B -meson physics. These measurements can be compared with previous experiments in the field, and, given the different detector capabilities at BABAR, they will have different systematic errors, and will doubtless bring new insights. In some cases, because of new features in the BABAR setup, breakthroughs can be expected. In addition, some present-day puzzles in B physics simply cry out for new data. Last but not least, the physics reachable after one year of operation will help understand the detector and provide solid ground for the long term CP -violation physics.

This chapter focuses on two main topics that can be investigated at the $\Upsilon(4S)$. First, B_d mixing will be studied through flavor oscillations, a new feat at an e^+e^- machine running at threshold. Section 11.2.2 deals with that subject. The second topic is the measurement of B_d and B^+ lifetimes. There again, the boost at the asymmetric B factory allows such a study for the first time at the $\Upsilon(4S)$ (see Section 11.3.4). More precise data than currently available are awaited. These will help sort out non-spectator hadronic decay mechanisms. Both subjects are introduced theoretically in Sections 11.2 and 11.3.

Section 11.4 summarizes bottomonium spectroscopy. The properties of the $\Upsilon(4S)$ and their implications on B pair production are first described. Then, new measurements at PEP-II are discussed. The studies presented here have found that, with the luminosity of PEP-II, radiative decays from the $\Upsilon(4S)$ to bound bottomonium states are accessible. This genuine non- CP b -physics topic is treated in Section 11.4, together with bottomonium physics.

Finally, in Section 11.5, more speculative studies on B_s mesons are presented. They are for a more distant future if any, so not much emphasis has been put on them. The $\Upsilon(5S)$ is the place of choice on the machine energy scale to produce B_s . A prototype of partial B_s reconstruction methods is presented in Section 11.5.2. A sketch of a method to look for two lifetime components in the B_s system is explained in Section 11.5.3.

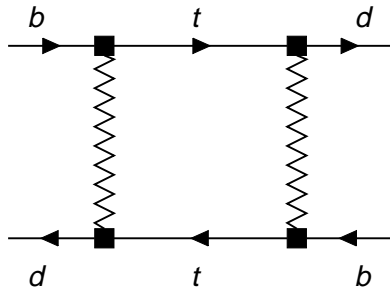


Figure 11-1. Box diagram describing B^0 - \bar{B}^0 -mixing. The zigzag lines denote W -bosons or charged Higgs bosons.

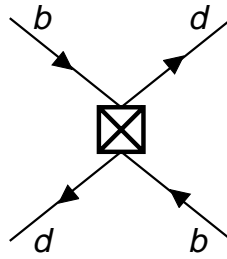


Figure 11-2. Local $\Delta B = 2$ four-quark operator.

11.2 The Determination of Δm_B

11.2.1 Theory of B^0 - \bar{B}^0 Mixing

The general formalism which describes B^0 - \bar{B}^0 mixing was presented in Section 1.2. The 2×2 matrix H governing the time evolution in Eq. (1.8) was decomposed into a Hermitian part M and an anti-Hermitian part $i\Gamma/2$. Equations (1.13), (1.14), and (1.28) show how the mass and width differences of the physical eigenstates B_H and B_L are related to M_{12} and Γ_{12} . This section elucidates how M_{12} and Γ_{12} are calculated from the fundamental parameters of the Standard Model Lagrangian, to express M_{12} and Γ_{12} in terms of CKM elements, quark masses, *etc.* The next section is devoted to the mass difference; the section following it covers the width difference of the neutral B eigenstates.

11.2.1.1 The B_H - B_L mass difference

In order to calculate the B_H - B_L mass difference, Δm_B , one needs to obtain M_{12} , see Eq. (1.28). The transition of a \bar{B}^0 into a B^0 changes the bottom quantum number B by two units and is therefore forbidden at the tree level in the Standard Model. The lowest order contribution to M_{12} arises from the box diagram depicted in Fig. 11-1. The matrix element is roughly proportional to the masses of the two internal quark lines, so that the box diagrams in which one or both top quarks are replaced by up or charm quarks are negligible compared to the one with two top quarks.

Is it sufficient to calculate the box diagram to find M_{12} ? No! Calculations based on Fig. 11-1 treat the b and \bar{d} quarks as free particles and therefore ignore the strong interaction. The virtual W and top travel over short distances of the order $\hbar c/M_W$. The asymptotic freedom property of

QCD makes quarks behave like free particles at short distances, and Fig. 11-1 provides the correct physical picture in this regime. Further short-distance QCD correction can be calculated within perturbation theory by dressing the box diagrams in all possible ways with gluons. At longer distances of order $\hbar c/m_b$, however, the $|\Delta B| = 2$ transition appears to arise from a pointlike four-fermion interaction shown in Fig. 11-2. Pictorially this four-quark interaction is obtained by shrinking the box in Fig. 11-1 to a point. Most importantly QCD effects associated with long-distance hadronic scales of order $\hbar c/\Lambda_{QCD}$ can no longer be described by the exchange of gluons and quarks. Instead they are described by nonperturbative forces, which bind the quarks into B mesons. The best method of calculating such binding effects is by lattice QCD. Consequently the correct inclusion of QCD effects requires the clear separation of short- and long-distance physics. The theoretical tool for this is the *operator product expansion*, which has been explained in detail in Section 2.1 (see also Appendix A). The aim is to derive a low-energy Hamiltonian, $H^{|\Delta B|=2}$, which reproduces the Standard Model amplitude M_{12} for $B^0-\bar{B}^0$ mixing correctly for energies of order m_b or less:

$$M_{12} = \frac{\langle B^0 | H^{|\Delta B|=2} | \bar{B}^0 \rangle}{2m_B} \left[1 + O\left(\frac{m_b^2}{M_W^2}\right) \right]. \quad (11.1)$$

The result is of the form is

$$H^{|\Delta B|=2} = \frac{G_F^2}{16\pi^2} (V_{tb}V_{td}^*)^2 C^{|\Delta B|=2}(m_t, M_W, \mu) Q(\mu) + h.c. \quad (11.2)$$

Here,

$$Q = \bar{d}\gamma_\nu (1 \Leftrightarrow \gamma_5) b \bar{d}\gamma^\nu (1 \Leftrightarrow \gamma_5) b \quad (11.3)$$

is the local $|\Delta B| = 2$ operator depicted in Fig. 11-2. All the short-distance physics is contained in the *Wilson coefficient*, $C^{|\Delta B|=2}$. $G_F^2/16\pi^2$ and the CKM elements are factored out by convention, so that $C^{|\Delta B|=2}$ is real. One can interpret the right hand side of Eq. (11.2) as a local four-quark interaction with coupling strength $(G_F^2/16\pi^2) (V_{tb}V_{td}^*)^2 C^{|\Delta B|=2}(m_t, M_W, \mu)$. The Wilson coefficient depends only on the heavy masses m_t and M_W and the renormalization scale μ . Since $H^{|\Delta B|=2}$ does not depend on the unphysical scale μ , the μ -dependence between $C^{|\Delta B|=2}$ and Q cancel. However in practice the calculation of such matrix elements between physical observables involves approximations, which render the theoretical predictions μ -dependent. It is common practice, though not rigorously defensible, to use the remaining μ -dependence over some “reasonable” range of μ to estimate the theoretical uncertainty.

The crucial point in calculating the coefficient $C^{|\Delta B|=2}$ is that any Wilson coefficient is independent of the nature of the external states. One needs to adjust $C^{|\Delta B|=2}$ in Eq. (11.2) such that Eq. (11.1) holds. Fortunately $C^{|\Delta B|=2}$ is the same whether one takes B mesons as external states on both sides of Eq. (11.1) or free quarks. The evaluation of M_{12} in the Standard Model for free quarks to lowest order in α_s is easy. It is simply the calculation of the box diagram in Fig. 11-1. Likewise it is simple to calculate the operator matrix element $\langle Q \rangle$ for free quarks, so that one

can find $C^{|\Delta B|=2}(m_t, M_W, \mu)$ by comparing the two results. This procedure is called a *matching* calculation. It can be done to any desired order in α_s by including QCD radiative corrections to the box diagram and to $\langle Q \rangle$. Already the correction of order α_s^1 requires the cumbersome calculation of two-loop diagrams. The result for $C^{|\Delta B|=2}(m_t, M_W, \mu)$ contains logarithms of the form $\alpha_s \ln(\mu/M_W)$. This *leading logarithm* appears repeatedly in all orders α_s^n , $n = 1, 2, \dots$, as $\alpha_s^n \ln^n(\mu/M_W)$. For a perturbative result to be reliable, higher order corrections must be small. Hence one originally chooses μ close to M_W . The hadronic matrix element of $Q(\mu)$, as discussed in Chapter 2, can only be calculated for $\mu = \mathcal{O}(m_b)$ or less! In order to predict $\langle B^0 | H^{|\Delta B|=2} | \bar{B}^0 \rangle$ one therefore needs to know $C^{|\Delta B|=2}(m_t, M_W, \mu)$ for $\mu = \mathcal{O}(m_b)$. This is accomplished with the help of the *renormalization group* (RG). The RG-improved Wilson coefficient contains the large logarithm $\alpha_s^n \ln^n(\mu/M_W)$, $n = 1, 2, \dots$, summed to all orders in perturbation theory. The result reads

$$C^{|\Delta B|=2}(m_t, M_W, \mu) = M_W^2 S \left(\frac{m_t^2}{M_W^2} \right) \eta_B b_B(\mu) \quad (11.4)$$

Here $S(x)$ is the result of the box diagram calculation,

$$S(x) = x \left[\frac{1}{4} + \frac{9}{4} \frac{1}{1 \leftrightarrow x} \Leftrightarrow \frac{3}{2} \frac{1}{(1 \leftrightarrow x)^2} \right] \Leftrightarrow \frac{3}{2} \left[\frac{x}{1 \leftrightarrow x} \right]^3 \ln x. \quad (11.5)$$

(In Eq. (1.104) $M_W^2 S$ has been denoted by $m_t^2 f_2$.) The coefficients η_B and b_B in Eq. (11.4) comprise the short-distance QCD corrections. In leading order they read

$$\begin{aligned} \eta_B &= [\alpha_s(M_W)]^{6/23} \\ b_B(\mu) &= [\alpha_s(\mu)]^{-6/23}. \end{aligned} \quad (11.6)$$

The exponent $6/23$ is composed of the two ingredients governing the RG evolution: The *anomalous dimension* of the operator Q and the QCD β -function. By expanding $\eta_B b_B(\mu)$ in terms of $\alpha_s(\mu)$ one may reproduce the summed leading logarithms $\alpha_s^n \ln^n(\mu/M_W)$.

This *leading-log approximation* has some severe drawbacks that render leading-order predictions too inaccurate for high-precision experiments like BaBar. For example, the result for the box diagram, Eq. (11.5), contains two physical scales, M_W and m_t . Hence one is equally entitled to sum $\alpha_s \ln(\mu/m_t)$ instead of $\alpha_s \ln(\mu/M_W)$. This would replace $\alpha_s(M_W)$ by $\alpha_s(m_t)$ in Eq. (11.6), and would change the result numerically. This scale ambiguity, however, is reduced, if one extends the calculation to the NLO, which involves two-loop corrections to the box diagrams and to the anomalous dimensions entering (11.6). Including the NLO corrections in the theoretical prediction, the expressions in Eq. (11.6) are modified by factors of the form $1 + \mathcal{O}(\alpha_s)$. Then they not only contain the leading logarithms summed to all orders, but also the next-to-leading logarithms $\alpha_s^{n+1} \ln^n(\mu/M_W)$, $n = 1, 2, \dots$

Another shortcoming of the leading-log result in Eq. (11.6) concerns the proper use of quark masses. Two popular definitions of the quark mass are related as

$$m_{\text{pole}}^{(1)} = m(m) \left[1 + \frac{\alpha_s(m)}{\pi} \frac{4}{3} \right] \quad (11.7)$$

Here $m_{\text{pole}}^{(1)}$ is the *one-loop pole mass* measured at Fermilab and $m(\mu)$ is the running $\overline{\text{MS}}$ mass. In Eq. (11.7) the relation between the two definitions of the mass is given for $\mu = m$. For the top quark, the two definitions differ by 7–8 GeV. Leading-order results are not sensitive to the mass definition, and one may use either one in Eq. (11.5), thereby introducing uncertainty in the theoretical prediction. This problem is cured by using the NLO result. The NLO calculation has been carried out in [1] yielding

$$\eta_B = 0.55. \quad (11.8)$$

When using NLO results, one must use the correct definition of m_t in $S(m_t^2/M_W^2)$ multiplying η_B in Eq. (11.4). The value in Eq. (11.8) corresponds to the use of the $\overline{\text{MS}}$ mass $m_t(m_t) = (167 \pm 5)$ GeV.

Now the calculation of the hadronic matrix element of $Q(\mu)$ is needed. The result is parameterized as

$$\langle B^0 | Q(\mu) | \overline{B}^0 \rangle = \frac{8}{3} B_B(\mu) f_B^2 m_B^2 = \frac{8}{3} \frac{\hat{B}_B}{b_B(\mu)} f_B^2 m_B^2. \quad (11.9)$$

In the vacuum-saturation approximation described in Section 2.3.3, $B_B(\mu) = 1$. The unphysical μ -dependence must cancel between $b_B(\mu)$ in Eq. (11.4) and $\langle Q(\mu) \rangle$ in Eq. (11.9). Hence, in an exact calculation, \hat{B}_B does not depend on μ . Actual values for \hat{B}_B from lattice calculations are tabulated in Table C-2 and are summarized in Eq. (C.20). The present situation for $\hat{B}_B f_B^2$ is summarized in Eq. (C.21), while the result from QCD sum rules can be found in Eqs. (D.31) and (D.36). Inserting Eqs. (11.4) and (11.9) into Eq. (11.1) gives the result for Δm_B :

$$\Delta m_B = 2 |M_{12}| = \frac{G_F^2}{6\pi^2} \eta_B m_B \hat{B}_B f_B^2 M_W^2 S \left(\frac{m_t^2}{M_W^2} \right) |V_{tb} V_{td}^*|^2. \quad (11.10)$$

In order to calculate M_{21} instead of M_{12} , the quark lines are simply reversed in Fig. 11-1. The result is the same, except that $V_{tb} V_{td}^*$ is replaced by $V_{tb}^* V_{td}$. Hence, $M_{21} = M_{12}^*$, as required by the hermiticity of M , because $S(x)$ in Eq. (11.5) is real. This is not the case in the width difference calculation, which is discussed in the following paragraph. Notice also that the phase of M_{12} , which is responsible for the mixing-induced CP violation, can be calculated without hadronic uncertainty from Eqs. (11.1) and (11.2): $\arg M_{12} = 2\beta$. This would not be the case, however, if there were a second operator with a different CKM structure contributing to Eq. (11.2).

The mass difference for the two eigenstates of the B_s meson involves the diagram of Fig. 11-1 with d replaced by s . The result differs from the one in Eq. (11.10) in that $|V_{td}|^2 m_B \hat{B}_B f_B^2$ is

replaced by $|V_{ts}|^2 m_{B_s} \hat{B}_{B_s} f_{B_s}^2$. The ratio $\Delta m_B/\Delta m_{B_s}$ can be predicted more cleanly than Δm_B and Δm_{B_s} individually, because the ratio $\hat{B}_B f_B^2/(\hat{B}_{B_s} f_{B_s}^2)$ can be calculated more reliably than each of the hadronic parameters separately (see (C.23)). The measurement of Δm_{B_s} will therefore precisely determine $|V_{td}/V_{ts}|$ from $\Delta m_{B_d}/\Delta m_{B_s}$.

How does new physics affect the prediction in Eq. (11.10)? New particles are heavy and therefore they affect the Wilson coefficients rather than the hadronic matrix elements. Yet if there were new physics contributions to M_{12} , they would probably not only modify $C^{|\Delta B|=2}$, but also generate additional operators. For example, the coefficient of the operator $\bar{d}(1+\gamma_5)b\bar{d}(1+\gamma_5)b$ is zero in the Standard Model, but not in its supersymmetric extensions. New physics scenarios will be discussed in Chapter 13.

This section closes by reviewing the contrast between $B^0-\bar{B}^0$ and $K^0-\bar{K}^0$ mixing. Recall that the key information available today on *CP* violation stems from the measurement of ϵ_K , which describes *CP* violation in $K^0-\bar{K}^0$ mixing. The corresponding box diagrams substitute an *s* quark for the *b* quark in the external lines. The boxes with internal *u* and *c* quarks become important, and one encounters three QCD coefficients instead of one. These coefficients have been calculated in the NLO in [1, 2].

11.2.1.2 The B_H - B_L width difference

The width difference was given in Eq. (1.13) as

$$\Delta\Gamma_B = \Gamma_H \Leftrightarrow \Gamma_L = \frac{1}{2m_B} \left[\sum_f |\langle f|H^{|\Delta B|=1}|B_H\rangle|^2 \Leftrightarrow \sum_f |\langle f|H^{|\Delta B|=1}|B_L\rangle|^2 \right]. \quad (11.11)$$

Here, the sum is over all final states *f* into which B_H or B_L can decay. The decays are triggered by the $|\Delta B| = 1$ Hamiltonian introduced in Chapter 1. $|B_H\rangle$ and $|B_L\rangle$ are expressed in terms of $|B^0\rangle$ and $|\bar{B}^0\rangle$. With Eqs. (1.9) and (1.10), one finds from Eq. (11.11)

$$\Delta\Gamma_B = \Leftrightarrow \frac{2}{m_B} \text{Re} \left[pq^* \sum_f \langle \bar{B}^0|H^{|\Delta B|=1}|f\rangle \langle f|H^{|\Delta B|=1}|B^0\rangle \right]. \quad (11.12)$$

In Eq. (11.12), non-zero contributions come only from those final states *f*, into which both the B^0 and the \bar{B}^0 can decay. The following modifications use the approximations of Section 1.2.3, which exploit the fact that $\Delta\Gamma_B \ll \Delta m_B$. Then Eqs. (1.11) and (1.29) imply that $|p|^2 = |q|^2 = 1/2$, and one can thus eliminate *p* and *q* from Eq. (11.12):

$$\Delta\Gamma_B = \frac{\text{Re} \left[M_{12}^* \sum_f \langle B^0|H^{|\Delta B|=1}|f\rangle \langle f|H^{|\Delta B|=1}|\bar{B}^0\rangle \right]}{m_B |M_{12}|}. \quad (11.13)$$

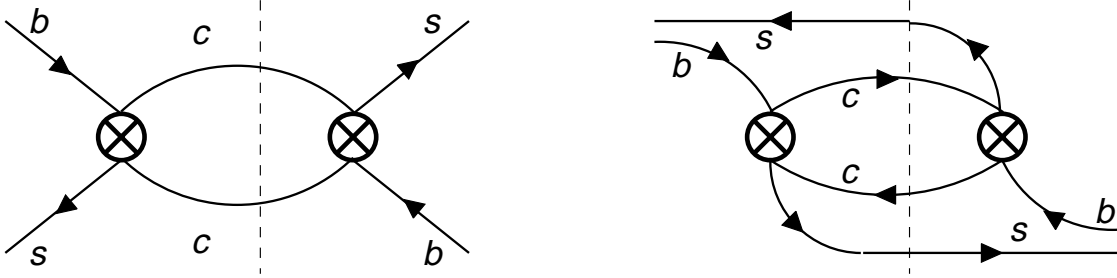


Figure 11-3. Diagrams determining $\Delta\Gamma_{B_s}$. Only the CKM favored contribution is shown. The left-hand diagram is the weak annihilation diagram and the right-hand one is the spectator interference diagram. The dashed line indicates the cut through the final state.

$\Delta\Gamma_B$ can now be calculated directly from Eq. (11.13). It is instructive to compare the direct derivation above with the result in Eq. (1.28), in order to understand the connection between $\Delta\Gamma_B$ and Γ_{12} . The underlying principle is the *optical theorem* which states that

$$\Gamma_{21}^* = \Gamma_{12} = \frac{1}{2m_B} \left[\sum_f \langle B^0 | H^{|\Delta B|=1} | f \rangle \langle f | H^{|\Delta B|=1} | \bar{B}^0 \rangle \right]. \quad (11.14)$$

Inserting Eq. (11.14) into Eq. (11.13) yields the expression found earlier in Eq. (1.28). Γ_{12} is called the *absorptive part* of the $B^0-\bar{B}^0$ mixing amplitude. In the Standard Model, Γ_{12} is related to box diagrams with internal u and c quarks. The corresponding analogues of the heavy box function $S(x)$ in Eq. (11.5) have a non-zero imaginary part, which contributes to the anti-Hermitian part $i\Gamma_{12}$ of the mixing matrix H in Eq. (1.8). Equation (11.14) makes it clear that this imaginary part is related to real intermediate states, which are kinematically accessible in B -meson decays.

In the effective theory describing B decays in terms of $H^{|\Delta B|=1}$, the desired absorptive part is calculated from the diagram in Fig. 11-3, which is obtained from the corresponding box diagram by shrinking the W lines to a point. One can view Fig. 11-3 either as a contribution to the $B^0-\bar{B}^0$ mixing amplitude, and recall that the imaginary part of the loop function contributes to Γ_{12} , or one can divide the diagram by a “cut” through the light quark lines and interpret the part on the left-hand side of the cut as the decay amplitude $\langle f | H^{|\Delta B|=1} | \bar{B}^0 \rangle$ and likewise the part on the right hand side as $\langle f | H^{|\Delta B|=1} | B^0 \rangle^* = \langle B^0 | H^{|\Delta B|=1} | f \rangle$. The sum over f in Eq. (11.14) corresponds to the integration over the $c \leftrightarrow \bar{c}$ phase space.

All of the discussion presented so far applies to the width difference for both the B_d and the B_s systems. The CKM-favored contribution to $\Delta\Gamma_{B_s}$ depicted in Fig. 11-3 involves the CKM factor $(V_{cb}V_{cs}^*)^2$, while the dominant diagrams for $\Delta\Gamma_B$ involve a CKM factor which is smaller by two powers of the Wolfenstein parameter λ . In fact $\Delta\Gamma_B$ may be too small to be detected. Therefore only $\Delta\Gamma_{B_s}$ is discussed in the following. The diagrams in Fig. 11-3 yield [3, 4, 5]

$$\Gamma_{12} = \Leftrightarrow \frac{G_F^2}{24\pi m_{B_s}} (V_{cb}V_{cs}^*)^2 m_b^2 \sqrt{1 \Leftrightarrow 4z} \left[\left((1 \Leftrightarrow z)K_1 + \frac{1}{2}(1 \Leftrightarrow 4z)K_2 \right) \langle B_s^0 | Q | \bar{B}_s \rangle \right. \\ \left. + (1 + 2z)(K_1 \Leftrightarrow K_2) \langle B_s^0 | Q_S | \bar{B}_s \rangle \right]. \quad (11.15)$$

Here $z = m_c^2/m_b^2$, and

$$K_1 = 3C_1^2 + 2C_1C_2, \quad K_2 = C_2^2$$

are combinations of Wilson coefficients from $H^{|\Delta B|=1}$. In addition to the operator Q in Eq. (11.3) (with \bar{d} replaced by \bar{s}), one now encounters a second operator, Q_S , and thereby another B -factor $B_S(\mu)$:

$$Q_S = \bar{s}(1 + \gamma_5)b \bar{s}(1 + \gamma_5)b, \quad \langle B^0 | Q_S | \bar{B}^0 \rangle = \Leftrightarrow f_{B_S}^2 m_{B_S}^2 \frac{5}{3} B_S(\mu). \quad (11.16)$$

Comparing Eq. (11.15) with Eq. (11.10) shows that Γ_{12} is smaller than M_{12} by a factor of order m_b^2/m_t^2 , which predicts that $\Delta\Gamma_{B_s} \ll \Delta m_{B_s}$. There cannot be a sizable contribution from new physics to Γ_{12} , because the decays $B^0, \bar{B}^0 \rightarrow X_{c\bar{c}}$ arise at the tree level in the Standard Model. Furthermore, the coefficients C_1 and C_2 are fairly well determined by the experimental information from various hadronic B -decays, leaving little room for nonstandard contributions. If there is also no new physics in M_{12} , one can simplify Eqs. (1.28) and (1.29) further to

$$\Delta\Gamma_{B_s} = 2\Gamma_{12}, \quad p = \Leftrightarrow q = \pm \frac{1}{\sqrt{2}}, \quad (11.17)$$

because the phases of all the CKM elements involved can be rotated away (up to small corrections of higher order in λ). This simplification occurs because in the Standard Model, CP violation is negligible in the B_S mass and decay matrix, so that $|B_H\rangle$ and $|B_L\rangle$ are CP eigenstates.

The short-distance QCD corrections to Γ_{12} in Eq. (11.11) are known in the NLO [4, 6]. Compared to M_{12} , there is a further source of relevant corrections here: Γ_{12} receives corrections of order Λ_{QCD}/m_b [5]. Both contributions reduce the value of Γ_{12} in Eq. (11.15) considerably.

A further assumption was made in the derivation of Eq. (11.15): in the sum over the final states in Eq. (11.14), quark states rather than hadron states were used. This assumes the validity of local quark-hadron duality, a concept which is discussed in Section 2.2. Physically, this means that the effect of the hadronization process cancels out in the sum over a sufficient number of hadronic final states $|f\rangle$, even though these states all have the same energy, m_{B_s} . At present, duality is tested in various inclusive observables in B decays and no experimental evidence for duality violation in B -meson widths has yet been found. On the other hand, duality violations in the width difference may be larger than in the average B_s width, Γ_{B_s} , because there are fewer final states contributing to $\Delta\Gamma_{B_s}$ than to Γ_{B_s} . One indication that the result may be reliable is that the earlier theoretical analysis in Ref. [7], where a sum over exclusive final states was performed and a numerical result for $\Delta\Gamma_{B_s}$ was found which is consistent with that in Ref. [5].

11.2.2 Measurement of Δm_B

The mass difference Δm_B between the two mass eigenstates of the $(B^0 \bar{B}^0)$ system may be measured by comparing the rate as a function of time for pairs of neutral B mesons to decay with the same b -flavor sign with the rate to decay with the opposite flavor sign, using the following time-dependent asymmetry:

$$\mathcal{A}(\Delta t) = \frac{N(B^0 \bar{B}^0)(\Delta t) \Leftrightarrow (N(B^0 B^0)(\Delta t) + N(\bar{B}^0 \bar{B}^0)(\Delta t))}{N(B^0 \bar{B}^0)(\Delta t) + (N(B^0 B^0)(\Delta t) + N(\bar{B}^0 \bar{B}^0)(\Delta t))} = \cos(\Delta m_B \cdot \Delta t), \quad (11.18)$$

where Δt is the difference between the two neutral B decay times. The simplest way to determine the b flavor [8] of the decaying neutral B is to use leptons as tagging particles. By counting the number of “like-sign” events $(l^+l^+) + (l^-l^-)$ and “unlike-sign” events (l^+l^-) , a measurement of Δm_B may be extracted through the asymmetry:

$$A_{\Delta m_B}(|\Delta t|) = \frac{N(l^+l^-) \Leftrightarrow (N(l^+l^+) + N(l^-l^-))}{N(l^+l^-) + (N(l^+l^+) + N(l^-l^-))}. \quad (11.19)$$

The probability to get a direct lepton (muon or electron) from a $(b \rightarrow c)$ transition is around 20%. The dilepton events useful for this analysis represent 4% of the $\Upsilon(4S) \rightarrow B^0 \bar{B}^0$. In terms of statistics, the dilepton tagging at BABAR is more efficient than the semi-exclusive tagging performed at the ARGUS [9] and CLEO[10] experiments. Moreover, this dilepton approach with a time-dependent asymmetry is radically different from the usual dilepton methods developed at the $\Upsilon(4S)$ [10], which allow only the measurement of $\chi_d = x_d^2/(2 \cdot (1 + x_d^2))$ with $x_d = \Delta m_B/\Gamma$. With only one year of data taking at nominal luminosity, this simple and robust approach can lead to a relative accuracy of about 1% in Δm_B , whereas the current world average (essentially due to LEP results) has an accuracy of $\sim 4\%$ [11]. In addition, the study of the asymmetry permits the measurement of the ratio $R = (b_+^2 f_{+-})/(b_0^2 f_{00})$ (where b_+ and b_0 are respectively the semileptonic branching fraction of charged and neutral B mesons, and f_{+-}/f_{00} is the production ratio of charged and neutral B meson pairs at the $\Upsilon(4S)$).

Beyond the measurement of Δm_B , the specific study of like-sign events (l^+l^+) and (l^-l^-) may show for the first time that the neutral $B^0 B^0$ and $\bar{B}^0 \bar{B}^0$ pairs cannot decay at the same time in the $\Upsilon(4S)$ frame, which constitutes a test of the EPR [12, 13] correlations predicted by quantum mechanics in the $(B^0 \bar{B}^0)$ system. Moreover, the comparison of the number of (l^+l^+) and (l^-l^-) pairs probes T (or CP) violation in mixing.

This subsection is exclusively devoted to the Δm_B measurement. The method used to identify and select the lepton pairs is first described, then that for determining the difference between the two B -decay times. The accuracy of the measurements that can be achieved with one year of data-taking at the nominal luminosity is then discussed. This analysis has been performed both with the BABAR fast Monte Carlo (ASLUND + perfect particle ID) and with BBSIM with a full reconstruction of the tracks and a preliminary version of particle ID (earlier than that described in Section 4.3).

11.2.2.1 Identification of leptonic tracks

In this study of the mixing parameter Δm_B , the flavor of the B meson is determined by the sign of the direct leptons produced in the ($b \rightarrow c$) transition. The cascade leptons are not included because the Δz resolution for these leptons is very bad. This contrasts with the flavor tagging performed for a CP analysis, where both direct and reverse-sign leptons are used. Here, the typical momentum of direct leptons which tag the flavor is rather high (above 800 MeV). Hence the identification of the electrons is essentially based on the calorimeter and that of the muons on the IFR. At lower momenta, this identification may be augmented by the dE/dx and the DIRC information.

With the list of particles identified as leptons by the preliminary version of the particle ID tools package used, the efficiency of lepton identification obtained with `BBsim` events was relatively low (around 40%), with a rather large contamination due to pions. However, these pions look like cascade leptons, and are greatly suppressed by the tools developed to separate the direct and cascade leptons.

11.2.2.2 Selection of dilepton events

A selection is made to discriminate the direct leptons produced in the ($b \rightarrow c$) transitions from the cascade leptons produced in the decays of the c quark. This separation is obtained with the following discriminating variables:

- P_1^* , the momentum in the $\Upsilon(4S)$ center-of-mass system (CMS) of the first lepton in the event particle list.
- P_2^* , the second lepton momentum in the $\Upsilon(4S)$ CMS.
- P_{miss} , the missing momentum of the event in the $\Upsilon(4S)$ CMS.
- E_{tot} , the total energy of the event in the $\Upsilon(4S)$ CMS. The total energy is computed by summing the energy measured by the calorimeter for the neutral tracks with the energy calculated from measured momentum for charged tracks assuming they are pions.
- N_{ch} , the number of charged tracks.
- V_{12}^x , the difference between the x positions for each lepton at the point of closest approach to the origin (mean beam position) in the transverse plane.
- V_{12}^y , the difference between the y positions for each lepton at the point of closest approach to the origin in transverse plane.
- θ_{lep} , the angle between the two leptons in the $\Upsilon(4S)$ CMS.

The first two variables P_1^* and P_2^* are very powerful discriminants between direct and cascade leptons and the last variable θ_{lep} efficiently removes direct-cascade leptonic pairs coming from the same neutral B and rejects γ -conversions. One can also extract information from the other variables. In order to combine all the information, a multidimensional nonlinear treatment is performed using an Artificial Neural Network (ANN). The neural network architecture chosen (8:8:2) is a multilayer perceptron with back-propagation updating composed of three layers. The first layer is composed of eight neurons (one for each discriminating variable). Then there is a hidden layer with eight neurons, and the output layer is designed with two outputs (one for each lepton). The ANN is trained with `Aslund` events in order to have the following outputs ($1 \Leftrightarrow 1$, $1 \Leftrightarrow 0$, $0 \Leftrightarrow 1$, $0 \Leftrightarrow 0$) for the leptonic pair configurations (direct \Leftrightarrow direct, direct \Leftrightarrow cascade, cascade \Leftrightarrow direct, cascade \Leftrightarrow cascade) respectively (see Fig. 11-4).

For fully reconstructed `BBsim` events, the discriminating variables V_{12}^x and V_{12}^y are not very effective, therefore a simpler NN (6:6:2) without these two variables is used.

Identical cuts are applied to the ANN output for each lepton candidate. Figure 11-5 compares the performance of a traditional approach based on a cut on the $(P_1^*, P_2^*, \theta_{lep})$ variables and an ANN approach.

In terms of mistag probability (η)¹ and efficiency (ε), the ANN approach is always better. The optimum for the sensitivity ($\propto 1/(\sqrt{\varepsilon}) \cdot (1 \Leftrightarrow 2\eta)$) is obtained for a cut on ANN outputs above 0.8 ($\varepsilon = 45\%$ and $\eta = 13\%$) for the `Aslund` events. For the fully reconstructed `BBsim` events the optimum is about the same (ANN output > 0.75). However, the mistag probability is slightly higher ($\eta = 14\%$) because of the pion contamination (8% of the pairs), and the total efficiency (NN + particle ID) decreases to $\varepsilon = 22\%$.

This selection, based on ANN, is also efficient against continuum background. After a cut at 0.75 on the ANN output, the ratio of continuum background over signal is equal to 7.5%. In addition, a cut on the ratio of Fox-Wolfram parameters $H_2/H_0 > 0.35$ reduces the continuum background to 2.5% with an efficiency of 90% for the signal.

11.2.2.3 Validity of the boost approximation

In `BaBar`, the Δt time difference is usually taken to be equal to $\Delta z / (\langle \beta\gamma \rangle c)$, with $\langle \beta\gamma \rangle = 0.557$. This approximation neglects the B meson motion in the $\Upsilon(4S)$ rest frame. Numerically, the B^0 momentum in the $\Upsilon(4S)$ rest frame is very small (340 MeV), but this approximation introduces a systematic shift in the determination of Δm_B which is not negligible for a 1% measurement of Δm_B [14]. In this dilepton study, the inclusive approach does not permit an exact determination of

¹This mistag probability, η , is defined as the probability that a $B^0\bar{B}^0$ pair is tagged as a B^0B^0 or a $\bar{B}^0\bar{B}^0$ pair. Note that this mistag probability differs from that, w (the probability that a B^0 is tagged as a \bar{B}^0) used in the tagging section, Section 4.8. However $\eta \simeq 2w$.

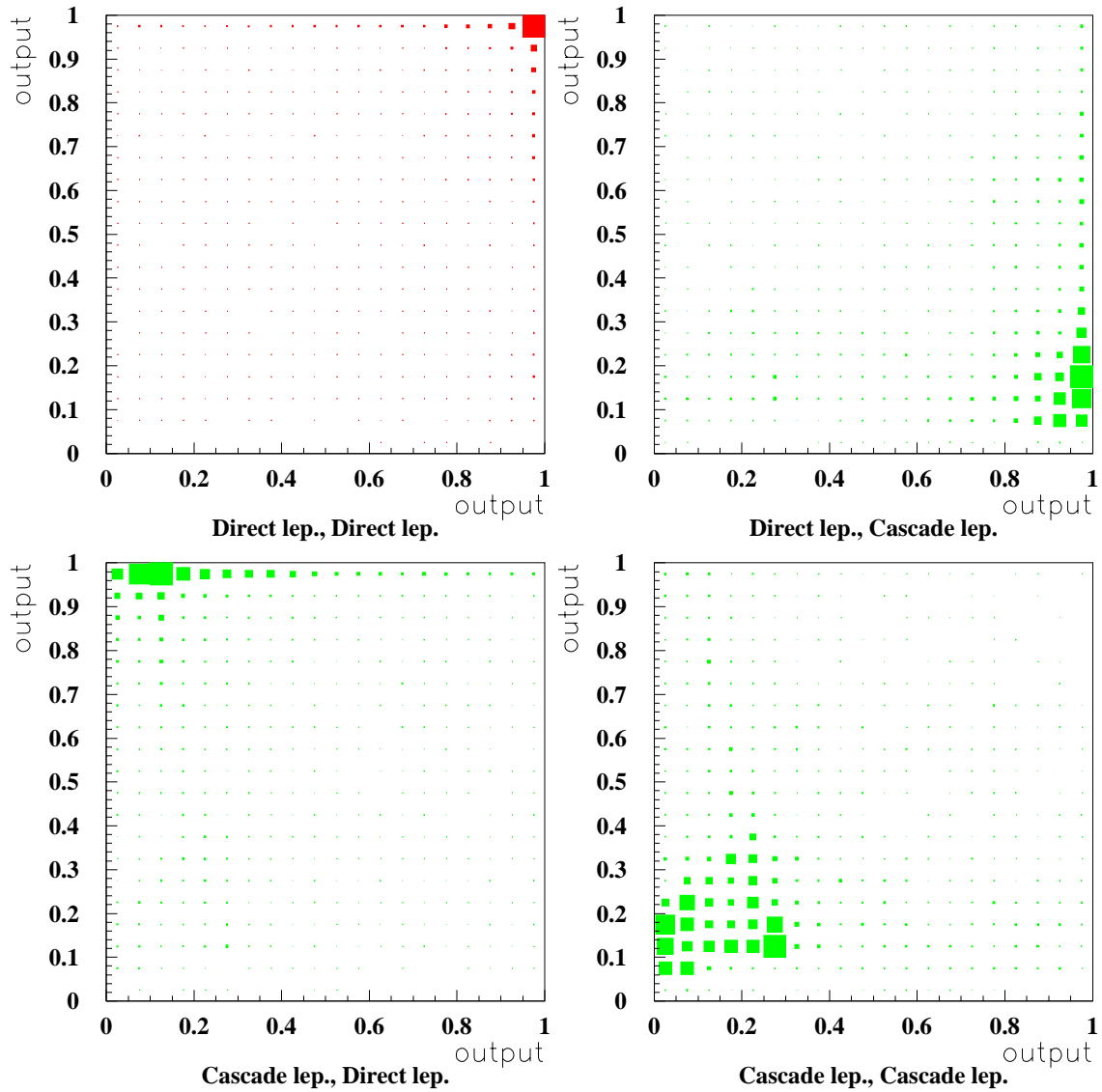


Figure 11-4. Distribution of the dilepton events as a function of the two ANN outputs (one for each lepton) for the four cases (direct \Leftrightarrow direct, direct \Leftrightarrow cascade, cascade \Leftrightarrow direct, cascade \Leftrightarrow cascade).

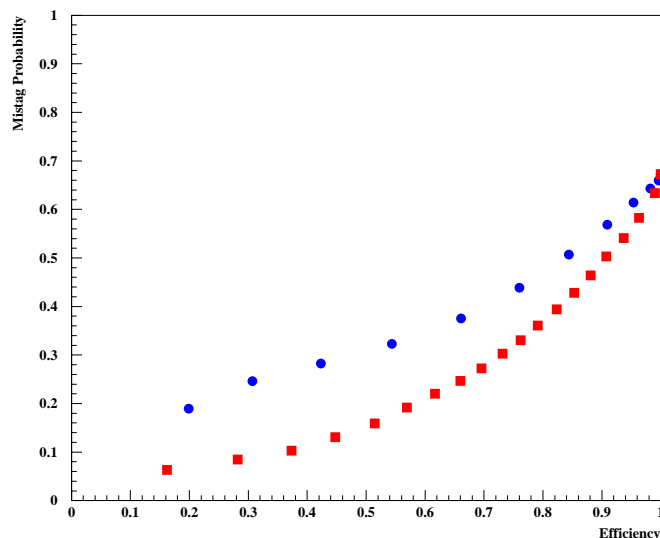


Figure 11-5. Mistag probability η as a function of the efficiency ϵ for the cut approach (circles) with the $(P_1^*, P_2^*, \theta_{lep})$ variables and for the ANN 8:8:2 (squares).

the boost. Therefore, the effect of this shift may be explored statistically by comparing the fitted value of $x_d = \Delta m_B / \Gamma$ with the true Δt and with $\Delta z / (\langle \beta \gamma \rangle c)$. In this case, for an initial value of $x_d = 0.700$, the shift is estimated to be 0.009, which is in good agreement with an independent determination of the shift (0.008) obtained with an analytical computation of the effect using the method developed in Ref. [14]. The good agreement between the two approaches shows that the effect is well controlled and this systematic bias introduced by this boost approximation can be corrected, for example by applying the shift of 0.009 calculated with the Monte Carlo data.

11.2.2.4 Measurement of Δz

This study requires a simple and robust method to determine Δz , because it must rely on the resolution function computed from Monte Carlo data.

The standard method estimates z of the vertices of the B^0 decays with the z of the point of closest approach to the origin $(0, 0)$ in the transverse plane for each lepton (**Method 1**). This estimator is a fairly good estimator of the B^0 decay vertices, since the selected leptons which are direct leptons have rather high momenta. This method does not take into account the widths of the beam in the x and y directions which are respectively $155 \mu\text{m}$ and $6.2 \mu\text{m}$. To improve the Δz resolution one must determine better the transverse coordinates (x_I, y_I) of the $\Upsilon(4S)$ decay vertex. The narrowness of

the beam in the y direction allows the choice $y_I = 0$. For the determination of x_I two different methods have been studied:

- **Method 2:** The coordinate x_I is estimated by the projection onto x axis of the intersection of the two lepton tracks in the transverse plane (see Fig. 11-6).
- **Method 3:** In the transverse plane, the intersections of each of the two lepton tracks with the x axis are computed and the vertex is estimated by the middle of the two points thus determined (see Fig. 11-6).

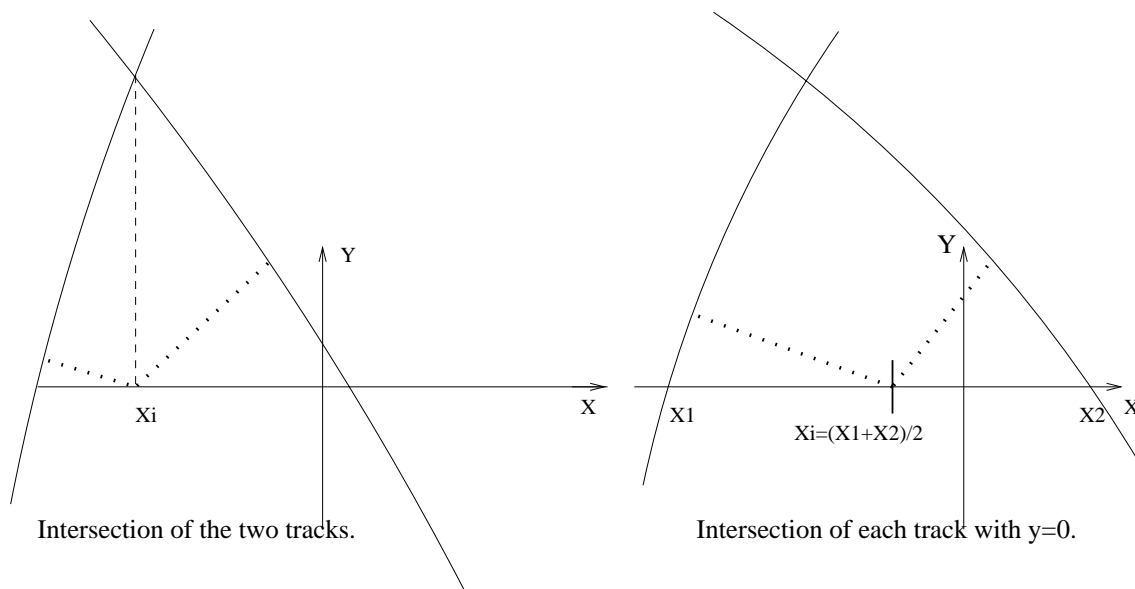


Figure 11-6. Estimation of the $\Upsilon(4S)$ decay vertex using the intersection of the tracks in the transverse plane (left), and using the middle of the intersections of the tracks with x axis (right).

Then the point of closest approach for each lepton to the decay vertex point, (x_I, y_I) , of the $\Upsilon(4S)$ is determined. The results of the various methods are compared using the rms difference and with a two-Gaussian fit to the resolution function. The results are summarized in Table 11-1 for $Aslund$ and for fully reconstructed $B\bar{B}sim$ events. Particle identification is used for all three methods.

The correction due to the beam width obtained with Methods 2 and 3 improves significantly the resolution performance and should reduce the sensitivity of the Δm_B measurement to the resolution correction. The resolution function obtained with method 2 is displayed in Fig. 11-7. This resolution function $f_{reso}(|\Delta t|)$ may be checked with the data sample, by using leptonic tracks which originate from a J/ψ decay. A preliminary study made with $B\bar{B}sim$ shows that a simple J/ψ reconstruction, based on a cut on the squared invariant mass of the leptonic pairs ($9.45 \text{ GeV} < M(l^+l^-)^2 < 9.7 \text{ GeV}$), selects 50,000 J/ψ for one year of data taking at nominal

Table 11-1. Resolution of the Δz measurement for the three methods described in text for Aslund and BBsim events.

	Aslund			BBsim		
	Method 1	Method 2	Method 3	Method 1	Method 2	Method 3
rms (μm)	217.	229.	240.	286.	277.	282.
$\sigma_{\text{narrow}}(\mu\text{m})$	$97. \pm 2$	$92. \pm 2$	$94. \pm 2$	$120. \pm 5$	$110. \pm 3$	$113. \pm 3$
$\sigma_{\text{wide}}(\mu\text{m})$	$282. \pm 5$	$304. \pm 14$	$341. \pm 10$	$360. \pm 20$	$439. \pm 31$	$459. \pm 28$
In narrow Gaussian	0.58	0.69	0.70	0.62	0.75	0.76

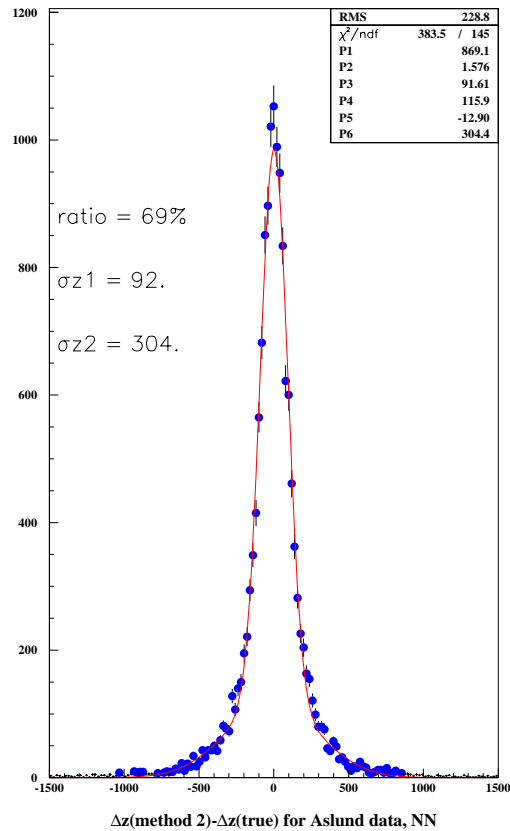


Figure 11-7. Fit with two Gaussians of the Δz resolution function.

luminosity, with a background of 12%. With this amount of data, that part of the resolution function arising from the reconstruction method may be directly determined from J/ψ decays.

11.2.2.5 The extraction of Δm_B

This study used 500,000 $B^0\bar{B}^0$, 500,000 B^+B^- and 800,000 $c\bar{c}$ generated and parametrized by `Aslund` with a perfect particle ID, and roughly the same quantity of `BBsim` events fully reconstructed with a realistic particle ID. The values and statistical errors for Δm_B , and the mistag probability η , are extracted from the fit of the leptonic asymmetry $A_{\Delta m_B}(|\Delta t|)$ to the following function:

$$A_{fit}(|\Delta t|) = \frac{f^+ \Leftrightarrow f^-}{f^+ + f^-} \cdot (1 \Leftrightarrow 2\eta) \quad (11.20)$$

with

$$f^+ = [1/2e^{-\Gamma^0|\Delta t|}(1 + \cos(\Delta m_B|\Delta t|)) + R \cdot e^{-\Gamma^+|\Delta t|}] \otimes f_{reso}(|\Delta t|) , \quad (11.21)$$

$$f^- = [1/2e^{-\Gamma^0|\Delta t|}(1 \Leftrightarrow \cos(\Delta m_B|\Delta t|))] \otimes f_{reso}(|\Delta t|) , \quad (11.22)$$

where the \otimes symbol represents the convolution of the two functions. The decay rates of the charged and neutral B mesons (Γ^+ and Γ^0) are fixed.

The results of $x_d = \Delta m_B/\Gamma = 0.71 \pm 0.03$, $R = 1.14 \pm 0.11$ obtained with `Aslund` events and perfect particle ID are consistent inside the statistical errors with the input values introduced (respectively 0.70 and 1). The value of $\eta = 9.2\%$ is in good agreement with the results obtained in Section 11.2.2.2. The comparison between `Aslund` and `BBsim` shows the same resolution, the same (cascade \Leftrightarrow direct) separation, and similar mistag probability. However there is a decrease in the efficiency, essentially due to the low efficiency of the particle ID used here (about 40% for a leptonic pair). The extrapolation of these results to (30 fb^{-1}) gives statistical errors around 1% for Δm_B .

The same fit has been performed with `BBsim` data (see Fig. 11-8), using 620,000 $B^0\bar{B}^0$ and 500,000 B^+B^- . The results, $x_d = 0.86 \pm 0.05$ and $R = 0.77 \pm 0.11$ are in good agreement with the input values ($x_d = 0.80$ and $R = 0.81$), given the statistical errors. The extrapolation of these results to (30 fb^{-1}) gives a statistical precision of 1.1% for Δm_B and about 2.5% for the ratio $R = (b_+^2 f_{+-})/(b_0^2 f_{00})$.

The main contribution to the systematic error on Δm_B and $(b_+^2 f_{+-})/(b_0^2 f_{00})$ (see Table 11-2) is the 2.5% uncertainty on the B (both charged and neutral) lifetime [11]. This term should be drastically reduced by measurements of neutral and charged B lifetimes, measured at the level of 1% with the first year of `BaBar` data. Then, the measurement of Δm_B will be limited by the uncertainty on the resolution function determined with Monte Carlo data. However, the knowledge of the resolution function may be improved by studying the resolution with real data (leptonic decays of the J/ψ).

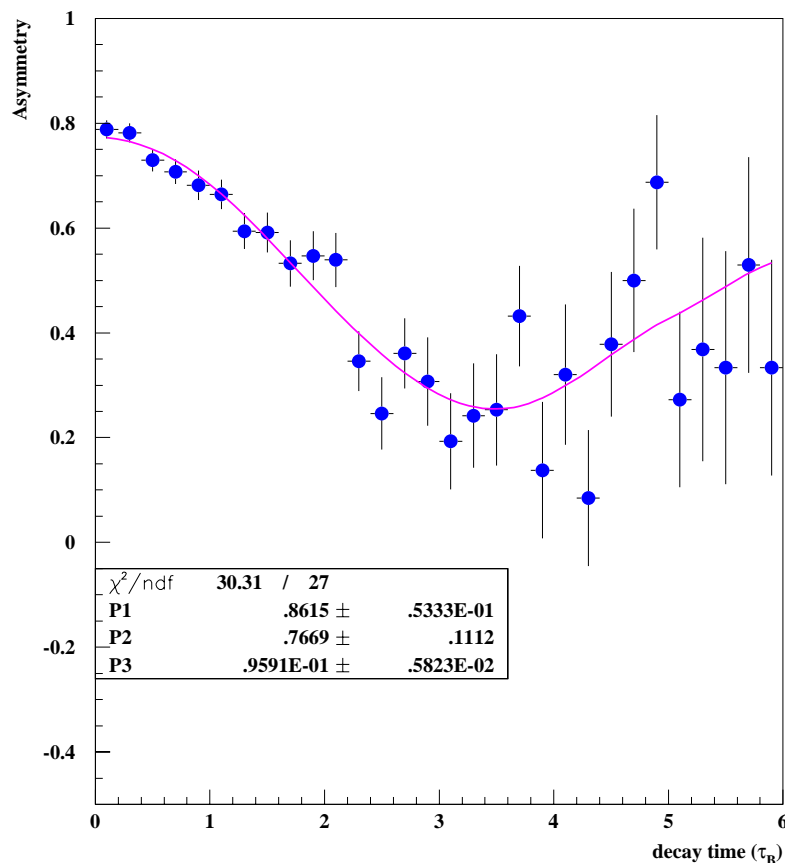


Figure 11-8. Fit of the $A_{\Delta m_B}(|\Delta t|)$ asymmetry between the “unlike” events (l^+l^-) and the “like” events (l^+l^+) + (l^-l^-) with the function $A_{fit}(|\Delta t|)$ performed with `BBSim` events.

11.2.2.6 Conclusions

This study has shown that the mixing parameter Δm_B may be extracted from the asymmetry between like- and unlike-sign dilepton events. Direct leptonic decays are selected by combining kinematical and topological discriminating variables through a neural network approach. The resolution function is determined with Monte Carlo and incorporated in the fit. In order to reduce the systematics on the Δm_B measurement, the resolution function may be checked once real data is available using J/ψ decays.

The statistical errors expected from one year of data-taking at nominal luminosity (30 fb^{-1} at the $\Upsilon(4S)$) is 1.1% for Δm_B . This will constitute the most precise determination of this parameter.

Table 11-2. Summary of the different contributions to the estimation of the systematic error on Δm_B and $(b_+^2 f_{+-})/(b_0^2 f_{00})$.

Type of systematic error	$\sigma(\Delta m_B)$ (%)	$\sigma((b_+^2 f_{+-})/(b_0^2 f_{00}))$ (%)
Correction of the resolution effect	0.6	1.4
Correction of the boost approximation	0.3	negligible
Sensitivity to Γ^0 (PDG 98 $\pm 1\sigma$)	1.2	14
Sensitivity to Γ^+ (PDG 98 $\pm 1\sigma$)	0.8	7
Correction of the $q\bar{q}$ asymmetry (20%)	0.4	negligible
Charge asymmetry $\varepsilon^+ \neq \varepsilon^-$	negligible	negligible
Mistag asymmetry $\eta^+ \neq \eta^-$	negligible	negligible
Correction of $\eta(B^0) \neq \eta(B^\pm)$	negligible	5.0

Further improvements in B -lifetime measurements are expected and therefore a reduction of the main source of systematic error cited here.

11.3 Lifetimes

11.3.1 Lifetimes and Inclusive Semileptonic Decays

This section contains a brief review of the theory of inclusive decays of heavy hadrons and a discussion of its application to the calculation of several physical quantities. The section is organized as follows. The formalism which has been developed for inclusive processes is introduced and discussed in Section 11.3.1.1. The formulae necessary for the calculation of the semileptonic and nonleptonic decay rates are summarized in Section 11.3.1.2; the reader is referred to the original references for the derivation of the expressions and for further details. In Sections 11.3.2 and 11.3.3, the formalism is applied to heavy-hadron lifetimes and semileptonic branching fractions respectively², and the theoretical predictions are compared to experimental results. Although the present experimental measurements will certainly be improved by the time BaBar is commissioned, this discussion is useful to illustrate some important applications of the theory of inclusive decays, and to discuss the limitations which may stem from the use of the so-called quark-hadron duality introduced in Section 2.2.4.2.

²The extraction of $|V_{cb}|$ from the inclusive semileptonic decay rate is not discussed here. It can be found in Chapter 8.

11.3.1.1 Theory of inclusive decays of heavy hadrons

General formalism

The basic theoretical tool used to study of heavy hadrons is the Wilson operator-product expansion (OPE) explained in Section 2.2. The expansion parameter is not necessarily the inverse heavy-quark mass m_Q , but rather the energy release, \mathcal{E} , of the process at hand. In most calculations of the inclusive rates, \mathcal{E} is of the order of the heavy-quark mass. In this case, under the hypothesis of quark-hadron duality explained in Section 2.2.4.2, the OPE is expected to give accurate predictions for the decay widths [15]–[19], [21].

Using the optical theorem, the inclusive decay rate of a hadron H_b , containing a b quark, into a final state X can be written in terms of the imaginary part of the forward matrix element of the transition operator \hat{T}

$$\Gamma(H_b \rightarrow X) = \frac{1}{2m_{H_b}} 2 \text{Im} [\langle H_b | \hat{T} | H_b \rangle] . \quad (11.23)$$

The transition operator is given by the time-ordered product (T) of the relevant effective weak Hamiltonian \mathcal{H}_{eff}

$$\hat{T} = i \int d^4x T [\mathcal{H}_{\text{eff}}(x) \mathcal{H}_{\text{eff}}(0)] . \quad (11.24)$$

The dominant space-time separation x is related to the inverse of \mathcal{E} in the process: if this is large enough, for example if $\mathcal{E} \sim m_b$, then one can perform a short-distance expansion of \hat{T} , obtaining an infinite sum of local operators of increasing dimension

$$\Gamma(H_b \rightarrow X) = \sum_i \tilde{c}_i(\mu) \frac{\langle H_b | O_i(\mu) | H_b \rangle}{2m_{H_b}} , \quad (11.25)$$

where μ is the scale at which the operators $O_i(\mu)$ have been renormalized. Since $\Gamma(H_b \rightarrow X)$ is μ -independent, the dependence of $O_i(\mu)$ on the unphysical renormalization scale (and renormalization scheme) is canceled by the corresponding dependence of the Wilson coefficients $\tilde{c}_i(\mu)$. The Wilson coefficients $\tilde{c}_i(\mu)$ include short-distance QCD effects which can be computed in perturbation theory; the nonperturbative effects are contained, instead, in the hadronic matrix elements of the local operators $O_i(\mu)$.

The coefficients $\tilde{c}_i(\mu)$ are dimensionful quantities containing powers of $1/m_b$ which increase with the dimension of the corresponding operators. For this reason, it is convenient to introduce dimensionless coefficients $c_i(\mu) = m_b^{d_i-3} \tilde{c}_i(\mu)$, where d_i denotes the dimension of the operator $O_i(\mu)$. In this way one readily sees why it is expected that the sum is dominated by the lowest-dimension operator terms, since the operator matrix elements are not expected to grow in m_b .

In the OPE, the operator with the lowest dimension which contributes to the sum in Eq. (11.25) is the dimension-three operator $\bar{b}b$. There is no dimension-four operator since the only possible one, $i\bar{b}\not{D}b$, can be reduced to $\bar{b}b$ by using the equations of motion. Thus, the first higher dimensional operator is the dimension-five chromomagnetic one, $\bar{b}\sigma_{\mu\nu}G^{\mu\nu}b$. The dimension-six operators ($O_{6,i}$),

to be defined below, will also be considered. Therefore any inclusive decay rate can be written in the form

$$\Gamma(H_b \rightarrow X) = |V_{CKM}|^2 \frac{G_F^2 m_b^5}{192\pi^3} \left[c_3(\mu) \langle H_b | O_3(\mu) | H_b \rangle + \frac{c_5(\mu)}{2m_b^2} \langle H_b | O_5(\mu) | H_b \rangle + \sum_i \frac{c_6^i(\mu)}{m_b^3} \langle H_b | O_{6,i}(\mu) | H_b \rangle + \dots \right], \quad (11.26)$$

where $O_3 = \bar{b}b$ and $O_5 = \bar{b}\sigma_{\mu\nu}G^{\mu\nu}b$. In this equation, the combination of CKM parameters, $|V_{CKM}|^2$, and the relevant kinematical factor

$$\Gamma_0 = \frac{G_F^2 m_b^5}{192\pi^3} \quad (11.27)$$

have been explicitly factored out. Γ_0 is the naive parton model result for the decay width: it is obtained by computing the inclusive rate for the decay of a free quark of mass m_b into the appropriate quark and/or lepton final states, Fig. 11-9. By the optical theorem, it can also be computed from the imaginary part of the diagram in Fig. 11-10. The absence of operators of dimension four implies that the power corrections to the parton-model result are at least of $\mathcal{O}(A_{\text{QCD}}^2/m_b^2)$. The chromomagnetic term is obtained from the imaginary part of the diagram in Fig. 11-11.

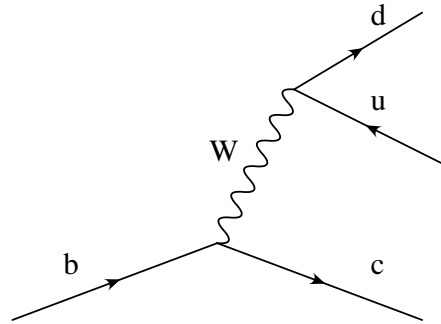


Figure 11-9. Parton-model diagram for the decay of a *b* quark.

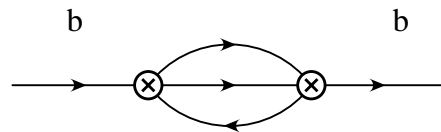


Figure 11-10. By the optical theorem, the imaginary part of this diagram gives the parton model result for the inclusive decay rate.

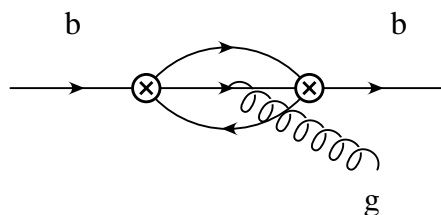


Figure 11-11. The imaginary part of this diagram gives the chromomagnetic correction to the inclusive decay rate. The spring-line represents a gluon.

The most important corrections of order $1/m_b^3$ are called *spectator effects* [16, 17]. In the parton-model approach, they arise from the diagrams shown in Figs. 11-12 and 11-13, which are referred to as Pauli-interference and W -exchange diagrams, respectively.

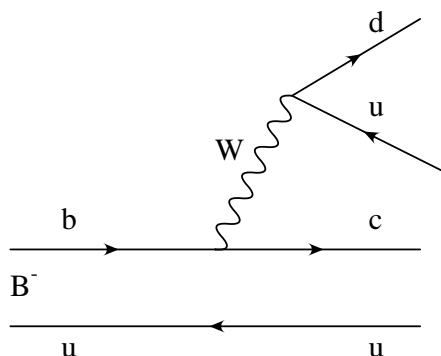


Figure 11-12. Pauli-interference (PI) diagram. Indeed, there are two identical particles, \bar{u} s, in the final state obeying the Pauli exclusion principle. The absolute square of this amplitude gives two diagrams, the conventional spectator diagram and the PI diagram of Fig. 11-14.

The first arises from the interference of two identical quarks (two \bar{u} quarks in the example of Fig. 11-12) in the final state, the second from the scattering of the two valence quarks (b and \bar{d} in the example of Fig. 11-13) inside the hadron. In the nonrelativistic language, both effects are proportional to the probability of finding two quarks at the same point (either the two \bar{u} or the b and \bar{d} quarks), *i.e.*, to the hadron wave-function at the origin. Spectator effects can also be computed from the imaginary part of the diagrams in Figs. 11-14 and 11-15. As shown in the figures, their effect, at large \mathcal{E} , is equivalent to the insertion of local operators of dimension six. By dimensionality, this implies that these diagrams contribute at $\mathcal{O}(\Lambda_{\text{QCD}}^3/\mathcal{E}^3) \sim \mathcal{O}(\Lambda_{\text{QCD}}^3/m_b^3)$ to the decay rate. Beyond the tree-level, the b -quark mass m_b appearing in the rate (11.26) must be appropriately defined in order to be consistent with the renormalization scheme used for the operators $O_i(\mu)$.

Equation (11.26) shows that, in order to predict the inclusive rates, one must evaluate both the Wilson coefficients of the different local operators and their hadronic matrix elements. The former can be computed in perturbation theory, while the latter are, in general, obtained by using some

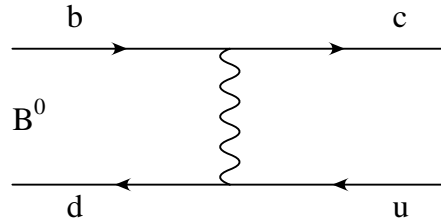


Figure 11-13. W -exchange diagram.

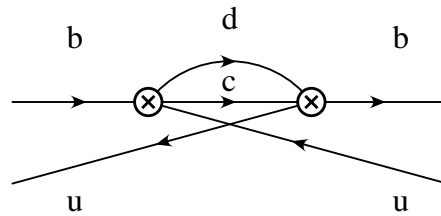


Figure 11-14. The imaginary part of this diagram corresponds to the PI diagram. In the OPE it gives rise to the four-fermion operators appearing in Eq. (11.40)

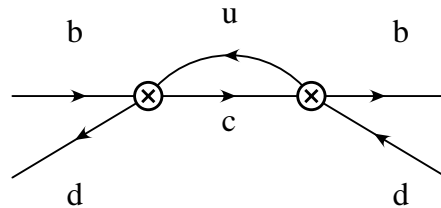


Figure 11-15. The imaginary part of this diagram corresponds to the W -exchange diagram. In the OPE it gives rise to the four-fermion operators appearing in Eq. (11.40)

nonperturbative technique, such as lattice QCD or QCD sum rules. In order to control the power corrections, the level of accuracy of the perturbative calculation of the coefficients of the leading operators must be comparable to the corrections induced by the operators of higher dimensions. Thus, for example, the inclusion of the $\mathcal{O}(1/m_b^2)$ terms makes sense only if the error on $c_3(\mu)$, which is computed up to some order α_s^n in perturbation theory, is smaller than these power-corrections.

Inclusive Decays and Heavy-Quark Expansions

The derivation of the general expression given in Eq. (11.26) relies only on the OPE at short distances. A further step can be made by expanding the forward matrix elements of the local operators in inverse powers of the heavy-quark mass (for example, by using the HQET, see Section 2.2.3). In

this way, it is possible to relate the value of the operator matrix elements to parameters that can be extracted independently from the spectrum of heavy-hadron states. For the operators of dimension three and five, one finds [18, 19, 20]

$$Z_3(\mu, m_b)\langle H_b|O_3(\mu)|H_b\rangle = 1 + \frac{\lambda_1(H_b) + 3\lambda_2(H_b)}{2m_b^2} + \mathcal{O}(1/m_b^3) \quad (11.28)$$

and

$$Z_5(\mu, m_b)\langle H_b|O_5(\mu)|H_b\rangle = 6\lambda_2(H_b) + \mathcal{O}(1/m_b), \quad (11.29)$$

where the factors Z_3 and Z_5 depend on the renormalization conditions imposed on the operators $\bar{b}b$ and $\bar{b}\sigma_{\mu\nu}G^{\mu\nu}b$. They can be computed in perturbation theory and reabsorbed in the coefficients $c_3(\mu)$ and $c_5(\mu)$. The quantities $\lambda_1(H_b)$ and $\lambda_2(H_b)$ parametrize the matrix elements of the kinetic energy and chromo-magnetic operators respectively. Contrary to the operator matrix elements themselves, the parameters $\lambda_1(H_b)$ and $\lambda_2(H_b)$ are, up to logarithmic corrections, independent of the heavy-quark mass. Estimates for the theoretical uncertainty of predictions for quantities which depend on λ_1 (and $\bar{\Lambda}$) are typically made simply by varying these parameters over the range given by various theoretical estimates. λ_2 can be directly related to physical quantities. For example, for B mesons, and up to corrections of higher order in $1/m_b$, $\lambda_2 = (M_B^2 \Leftrightarrow M_B^2)/4$. In contrast, λ_1 (like $\bar{\Lambda}$) is not a physical quantity and its value depends on the renormalization procedure used to define it. The ambiguity in the definition of λ_1 is of $\mathcal{O}(\Lambda_{QCD}^2)$. Likewise the coefficient c_3 in Eq. (11.26) is ambiguous by an additive term of $\mathcal{O}(\Lambda_{QCD}^2/m_b^2)$. The ambiguities of c_3 and λ_1 in Eq. (11.26) cancel, so that the predicted decay rate is uniquely defined (up to higher orders in $1/m_b$). When using a particular numerical value for λ_1 , one must make sure that it corresponds to consistent definitions of λ_1 and c_3 . In many theoretical models used to calculate λ_1 this is not easy, which, indeed, explains the wide spread of values for λ_1 found in the literature.

11.3.1.2 Semileptonic and nonleptonic decays

This subsection discusses semileptonic and nonleptonic decay rates in turn. For each process the effective Hamiltonian and the relevant formulae needed to obtain the theoretical predictions for the corresponding decay rate are presented. More details of the semileptonic decays can be found in Section 8.3. A general discussion of the effective Hamiltonian for nonleptonic decays, and of the calculation of the Wilson coefficients, can be found in Chapter 2 and in Appendix A.

Effective Hamiltonian and Decay Rates for Semileptonic Decays

Inclusive semileptonic decays have been used extensively for the extraction of the CKM matrix elements $|V_{cb}|$ and $|V_{ub}|$. The relevant effective Hamiltonian is given in this case by

$$\mathcal{H}_{\text{eff}}^{\text{sl}} = \frac{G_F}{\sqrt{2}} \sum_{l=e,\mu,\tau} \left\{ \bar{\ell}\gamma_\mu(1 \Leftrightarrow \gamma_5)\nu_\ell (V_{ub} \bar{u}\gamma^\mu(1 \Leftrightarrow \gamma_5)b + V_{cb} \bar{c}\gamma^\mu(1 \Leftrightarrow \gamma_5)b) + \text{h.c.} \right\}. \quad (11.30)$$

From this Hamiltonian, by using the general formula in Eq. (11.26), together with Eqs. (11.28) and (11.29), one can derive the expression for the semileptonic width [18, 19, 20, 22]:

$$\begin{aligned} \Gamma(H_b \rightarrow X_{c,u} \bar{\ell} \nu_\ell) &= |V_{(c,u)b}|^2 \frac{G_F^2 m_b^5}{192\pi^3} \left[C_0^{sl} \left(1 + \frac{\lambda_1(H_b) + 3\lambda_2(H_b)}{2m_b^2} \right) \right. \\ &\left. \Leftrightarrow \left(1 \Leftrightarrow \frac{m_{c,u}^2}{m_b^2} \right)^4 \frac{\lambda_2(H_b)}{m_b^2} + \frac{\alpha_s}{4\pi} C_1^{sl} + \dots \right]. \end{aligned} \quad (11.31)$$

The dots stand for higher-order perturbative and/or power corrections. The terms of $\mathcal{O}(1/m_b^3)$ are not written explicitly because they are expected to give negligible contributions to $\Gamma(H_b \rightarrow X_{c,u} \bar{\ell} \nu_\ell)$. This is different from what happens in nonleptonic decays. For nonleptonic decays, as explained below, the corrections of $\mathcal{O}(1/m_b^3)$ are enhanced by a large multiplicative factor and may give sizeable contributions. In Eq. (11.31), $C_0^{sl} \equiv C_0^{sl}(x_{c,u}, x_l)$ and $C_1^{sl} \equiv C_1^{sl}(x_{c,u}, x_l)$ are known phase-space factors which depend on the ratios of the final quark or lepton masses to m_b ($x_{c,u,l} \equiv m_{c,u,l}^2/m_b^2$). $C_0^{sl}(x_{c,u}, x_l)$ is given in Eq. (8.43). The expression for C_1^{sl} depends on the definition of the heavy-quark mass which is adopted beyond the lowest order in perturbation theory (pole mass, \overline{MS} -mass, etc.). A detailed discussion of the perturbative corrections to the semileptonic rate and of the dependence of C_1^{sl} on the definition of the quark mass can be found in Ref. [23].

If one uses the pole mass, except for trivial color factors, C_1^{sl} is essentially the same as the first order electro-magnetic correction occurring in $\mu \rightarrow e \nu \bar{\nu}$ decays, see Fig. 11-16. As discussed above,

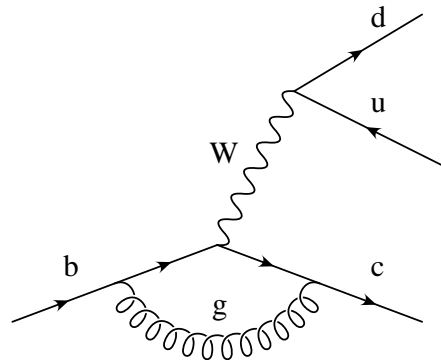


Figure 11-16. Generic first-order correction appearing in heavy-particle decays. The spring-shaped line represents a gluon.

μ -dependence enters the result because the methods for estimating λ_1 do not properly account for this scale-dependence. The effect could, in principle, be reduced if the full NLO calculation were performed. In the absence of such a calculation, BLM [23] have given a prescription for scale-setting which includes all $\alpha^n (n_f)^n$ terms correctly, using the fact that all such terms arise from fermion-loop insertions on a vector-propagator line (see Figs. 11-17 and 11-18), and hence

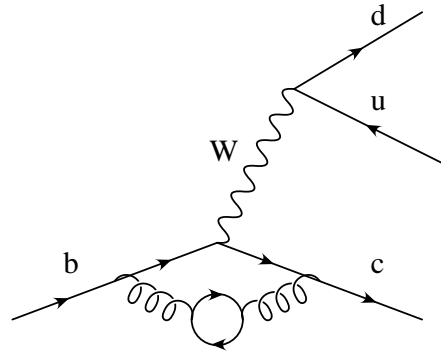


Figure 11-17. Vacuum-polarization diagram which renormalizes the coupling at the vertices of the external fermion lines.

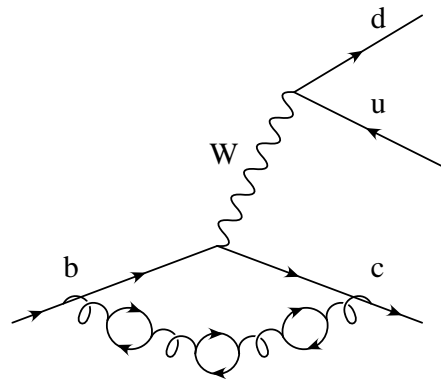


Figure 11-18. Chain of vacuum polarization diagrams.

are similar to such loop insertions in QED, which have been calculated. The BLM prescription then assumes such terms appear only in the form $\alpha^n (n_f \leftrightarrow 33/2)^n$, as this is the coefficient which controls the running of α_s . It turns out that in most of the cases where a comparison of the BLM approximation with exact second-order calculations is possible, the approximation proves to be a good one.

Effective Hamiltonian for Nonleptonic Decays

The theory of nonleptonic inclusive decays is important for predictions of the lifetimes of heavy hadrons, of their semileptonic branching fractions and of the charm yield.

For $\Delta B = 1$ nonleptonic decays, it is convenient to separate the possible cases into two different classes:

- *Decays with $\Delta C = 1$*

For $\Delta S = 0$ decays, the effective Hamiltonian is given by

$$\begin{aligned} \mathcal{H}_{\text{eff}}^{\text{nl}_1} = & \frac{G_F}{\sqrt{2}} [V_{ub}^* V_{cd} (C_1(\mu_b) O_1(\mu_b) + C_2(\mu_b) O_2(\mu_b)) \\ & + V_{cb}^* V_{ud} (C_1(\mu_b) O'_1(\mu_b) + C_2(\mu_b) O'_2(\mu_b))] , \end{aligned} \quad (11.32)$$

where the relevant operators are:

$$\begin{aligned} O_1 &= (\bar{u}_a \gamma_\mu (1 \Leftrightarrow \gamma_5) b_b) (\bar{d}_b \gamma^\mu (1 \Leftrightarrow \gamma_5) c_a) \\ O_2 &= (\bar{u}_a \gamma_\mu (1 \Leftrightarrow \gamma_5) b_a) (\bar{d}_b \gamma^\mu (1 \Leftrightarrow \gamma_5) c_b) \\ O'_1 &= (\bar{c}_a \gamma_\mu (1 \Leftrightarrow \gamma_5) b_b) (\bar{d}_b \gamma^\mu (1 \Leftrightarrow \gamma_5) u_a) \\ O'_2 &= (\bar{c}_a \gamma_\mu (1 \Leftrightarrow \gamma_5) b_a) (\bar{d}_b \gamma^\mu (1 \Leftrightarrow \gamma_5) u_b) , \end{aligned} \quad (11.33)$$

a and b are color indices and μ_b denotes the scale at which the four-fermion operators, O_i , have been renormalized. Frequently it is convenient to choose $\mu_b \sim m_b$. In general, this scale can be different from the renormalization scale of the operators appearing in the OPE in Eq. (11.25). In order to avoid confusion, the renormalization scale of the operators of the weak Hamiltonian will here be denoted by μ_b . The coefficients $C_{1,2}(\mu_b)$ are known at the NLO [24, 25]. For $\Delta C = 1$ and $\Delta S = 1$ decays, the Hamiltonian has the same form as in Eq. (11.32), with the obvious substitution $d \rightarrow s$ in Eqs. (11.32) and (11.33).

- *Decays with $\Delta C = 0$*

For $\Delta C = 0$ and $\Delta S = 0$ decays, the effective Hamiltonian has the form

$$\begin{aligned} \mathcal{H}_{\text{eff}}^{\text{nl}_2} = & \frac{G_F}{\sqrt{2}} [V_{ub}^* V_{ud} (C_1(\mu_b) O_1^u(\mu_b) + C_2(\mu_b) O_2^u(\mu_b)) \\ & + V_{cb}^* V_{cd} (C_1(\mu_b) O_1^c(\mu_b) + C_2(\mu_b) O_2^c(\mu_b)) \Leftrightarrow V_{tb}^* V_{td} \sum_{i=3,6} C_i(\mu_b) O_i(\mu_b)] , \end{aligned} \quad (11.34)$$

where

$$\begin{aligned} O_1^q &= (\bar{q}_a \gamma_\mu (1 \Leftrightarrow \gamma_5) b_b) (\bar{d}_b \gamma^\mu (1 \Leftrightarrow \gamma_5) q_a) \\ O_2^q &= (\bar{q}_a \gamma_\mu (1 \Leftrightarrow \gamma_5) b_a) (\bar{d}_b \gamma^\mu (1 \Leftrightarrow \gamma_5) q_b) \\ O_3 &= (\bar{d}_a \gamma_\mu (1 \Leftrightarrow \gamma_5) b_a) \sum_q (\bar{q}_b \gamma^\mu (1 \Leftrightarrow \gamma_5) q_b) \\ O_4 &= (\bar{d}_a \gamma_\mu (1 \Leftrightarrow \gamma_5) b_b) \sum_q (\bar{q}_b \gamma^\mu (1 \Leftrightarrow \gamma_5) q_a) \\ O_5 &= (\bar{d}_a \gamma_\mu (1 \Leftrightarrow \gamma_5) b_a) \sum_q (\bar{q}_b \gamma^\mu (1 + \gamma_5) q_b) \\ O_6 &= (\bar{d}_a \gamma_\mu (1 \Leftrightarrow \gamma_5) b_b) \sum_q (\bar{q}_b \gamma^\mu (1 + \gamma_5) q_a) . \end{aligned} \quad (11.35)$$

The sums above run over the quark flavors which are active at the scale μ_b . Thus, for $\mu_b = m_b$, the sum is over the u , d , s and c quarks. For $\Delta C = 0$ and $\Delta S = 1$ decays, the Hamiltonian has the same form as in Eq. (11.34) with the substitution $d \rightarrow s$ in Eqs. (11.34) and (11.35). The operators O_i with $i = 3-6$ are the strong-penguin operators which arise when top-quark effects (for $\mu_b \ll m_t$) are integrated out to give the effective theory. The electro-penguin operators are not included in Eq. (11.34), since they give very small contributions to the inclusive rates considered here. Note that in some exclusive decays electro-penguin operators give important contributions and cannot be ignored.

In the following, it will be convenient to introduce the Wilson coefficients $C_{\pm}(\mu_b) = C_2(\mu_b) \pm C_1(\mu_b)$ and to write their renormalization-scheme-independent parts as

$$\begin{aligned} C_{\pm}(\mu_b) &= L_{\pm}(\mu_b) \left(1 + \frac{\alpha_s(M_W) \Leftrightarrow \alpha_s(\mu_b)}{4\pi} R_{\pm} \right), \\ \eta(\mu_b) &= 2L_+(\mu_b) + L_-(\mu_b). \end{aligned} \quad (11.36)$$

The $L_{\pm}(\mu_b)$ s and $R_{\pm}(\mu_b)$ are the leading and next-to-leading order contributions to the Wilson coefficients which govern the renormalization-group evolution from M_W down to μ_b .

Nonleptonic Decay Rates

One can expand the nonleptonic rates in powers of $1/m_b$

$$\Gamma(H_b \rightarrow X_{NL}) = \Gamma_0(H_b \rightarrow X_{NL}) + \frac{\Gamma_2(H_b \rightarrow X_{NL})}{m_b^2} + \frac{\Gamma_3(H_b \rightarrow X_{NL})}{m_b^3} + \dots \quad (11.37)$$

For the leading term in $1/m_b$, one finds [26]

$$\begin{aligned} \Gamma_0(H_b \rightarrow X_{NL}) &= |V_{CKM}|^2 \Gamma_0 \Phi(x_{f_1}, x_{f_2}, x_{f_3}) \left[\eta(\mu_b) + \frac{\alpha_s(M_W) \Leftrightarrow \alpha_s(\mu_b)}{2\pi} \times \right. \\ &[2L_+^2(\mu_b)R_+(\mu_b) + L_-^2(\mu_b)R_-(\mu_b)] + \frac{\alpha_s}{2\pi} [L_+(\mu_b) \Leftrightarrow L_-(\mu_b)]^2 \mathcal{C}_{11} + \\ &\left. \frac{\alpha_s}{2\pi} [L_+^2(\mu_b) \Leftrightarrow L_-^2(\mu_b)] \mathcal{C}_{12} + \frac{\alpha_s}{2\pi} [L_+(\mu_b) + L_-(\mu_b)]^2 \mathcal{C}_{22} \right] + \Gamma_{\text{Pen}}, \end{aligned} \quad (11.38)$$

where the CKM factor, $|V_{CKM}|^2$, and the phase space, Φ , are those appropriate for the decay $b \rightarrow q_{f_1} \bar{q}_{f_2} q_{f_3}$. The coefficients $\mathcal{C}_{ij} \equiv \mathcal{C}_{ij}(\mu_b)$ depend on the final state and are known at the NLO. Their μ_b -dependence compensates, at this order, the μ_b -dependence of the coefficients $\eta(\mu_b)$, $L_{\pm}(\mu_b)$, etc. Γ_{Pen} denotes the penguin-operator contribution to the decay rate; it is only present in $b \rightarrow \bar{c}cq$ decays, with $q = d$ or s . This term is rather small and its expression is not given here. The interested reader can find the details in Ref. [26].

In the case of $\Gamma_2(H_b \rightarrow X_{NL})$, only the leading QCD corrections are known. This term can be written as [18, 19, 20, 27]

$$\Gamma_2(H_b \rightarrow X_{NL}) = \Gamma_0(H_b \rightarrow X_{NL}) \left[\frac{\lambda_1(H_b) + 3\lambda_2(H_b)}{2} \Leftrightarrow 6\mu_G^2(H_b) \frac{\Phi_1}{\Phi} \right] \Leftrightarrow 12|V_{CKM}|^2 \Gamma_0(L_+^2(\mu_b) \Leftrightarrow L_-^2(\mu_b)) \lambda_2(H_b) \Phi_2, \quad (11.39)$$

where the phase space factors, Φ_1 and Φ_2 , depend on the final-state quarks. For $b \rightarrow c\bar{u}d$ or $b \rightarrow c\bar{u}s$, neglecting the light quark masses, one has

$$\Phi_1 = (1 \Leftrightarrow x_c^2)^4, \quad \Phi_2 = (1 \Leftrightarrow x_c^2)^3.$$

For $b \rightarrow c\bar{c}d$ or $b \rightarrow c\bar{c}s$, the expressions are more complicated [28, 27] and will not be given here.

The expression for $\Gamma_3(H_b \rightarrow X_{NL})$ is given by [29, 5, 28]

$$\Gamma_3(H_b \rightarrow X_{NL}) = (16\pi^2)|V_{CKM}|^2 \Gamma_0 \left[(1 \Leftrightarrow x_c^2) \left(\frac{3}{8} \mathcal{R}_1 \Leftrightarrow \frac{1}{8} \mathcal{R}_2 \right) \Leftrightarrow \frac{\sqrt{1 \Leftrightarrow 4x_c^2}}{8} \mathcal{R}_3 \right] + \dots, \quad (11.40)$$

where the dots represent terms which are not enhanced by the factor $16\pi^2$ appearing on the right hand side of Eq. (11.40), and

$$\begin{aligned} \mathcal{R}_1 &= \left(2C_1(\mu_b)C_2(\mu_b) + \frac{C_1^2(\mu_b) + C_2^2(\mu_b)}{3} \right) \langle O_{V-A}^u \rangle \\ &\quad + 2(C_1^2(\mu_b) + C_2^2(\mu_b)) \langle T_{V-A}^u \rangle \\ \mathcal{R}_2 &= \left(2C_1(\mu_b)C_2(\mu_b) + \frac{C_1^2(\mu_b)}{3} + 3C_2^2(\mu_b) \right) \left((1 + x_c^2/2) \langle O_{V-A}^{d'} \rangle \right) \\ &\quad \Leftrightarrow (1 + 2x_c^2) \langle O_{S-P}^{d'} \rangle \\ &\quad + 2C_1^2(\mu_b) \left((1 + x_c^2/2) \langle T_{V-A}^{d'} \rangle \Leftrightarrow (1 + 2x_c^2) \langle T_{S-P}^{d'} \rangle \right) \\ \mathcal{R}_3 &= \left(2C_1(\mu_b)C_2(\mu_b) + \frac{C_1^2(\mu_b)}{3} + 3C_2^2(\mu_b) \right) \left((1 \Leftrightarrow x_c^2) \langle O_{V-A}^{s'} \rangle \right) \\ &\quad \Leftrightarrow (1 + 2x_c^2) \langle O_{S-P}^{s'} \rangle \\ &\quad + 2C_1^2(\mu_b) \left((1 \Leftrightarrow x_c^2) \langle T_{V-A}^{s'} \rangle \Leftrightarrow (1 + 2x_c^2) \langle T_{S-P}^{s'} \rangle \right). \end{aligned} \quad (11.41)$$

d' and s' denote the Cabibbo combinations coupled to the weak charged-currents and $\langle O \rangle \equiv \langle H_b | O | H_b \rangle$. Penguin contributions to \mathcal{R}_3 can be found in Ref. [30, 28]. In Eqs. (11.40) and (11.41), the operators O_{V-A}^u , T_{V-A}^u , etc., must be understood as renormalized at the scale $\mu = \mu_b$. It is certainly possible to choose $\mu \neq \mu_b$. In this case, the expressions in Eqs. (11.41) would

be more complicated. The operators appearing in Eq. (11.41) are $\Delta B = 0$, dimension-six four-fermion operators given by

$$\begin{aligned} O_{V-A}^q &= \bar{b}\gamma_\mu(1 \Leftrightarrow \gamma_5)q \bar{q}\gamma^\mu(1 \Leftrightarrow \gamma_5)b , \\ O_{S-P}^q &= \bar{b}(1 \Leftrightarrow \gamma_5)q \bar{q}(1 + \gamma_5)b \\ T_{V-A}^q &= \bar{b}t^A\gamma_\mu(1 \Leftrightarrow \gamma_5)q \bar{q}t^A\gamma^\mu(1 \Leftrightarrow \gamma_5)b , \\ T_{S-P}^q &= \bar{b}t^A(1 \Leftrightarrow \gamma_5)q \bar{q}t^A(1 + \gamma_5)b , \end{aligned} \quad (11.42)$$

where the color indices are implicit (e.g., $\bar{b}\gamma_\mu(1 \Leftrightarrow \gamma_5)q \equiv \bar{b}^b\gamma_\mu(1 \Leftrightarrow \gamma_5)q^b$), and the t^A are the generators of the $SU(3)$ color group.

In Eq. (11.40), only the $\mathcal{O}(\Lambda_{\text{QCD}}^3/m_b^3)$ contributions which are enhanced by a factor $16\pi^2$ are written explicitly. This factor comes from the difference between the phase space occurring in the imaginary part of the *two-loop* diagram in Fig. 11-10 (and Fig. 11-11), and the phase space of the *one-loop* spectator diagrams of Figs. 11-14 and 11-15. The dots stand for other terms which are not multiplied by $16\pi^2$ and, for this reason, are expected to give negligible contributions to the decay rates. They include $1/m_b^3$ corrections to the coefficients of the operators $O_3(\mu)$ and $O_5(\mu)$, terms due to the presence of two-quark operators of dimension six containing extra covariant derivatives, *etc.*

11.3.2 Lifetime Ratios

An important test of the OPE-based theory of inclusive decays, and of the heavy-quark mass expansion, is the comparison of the theoretical predictions with the experimental measurements for the heavy-hadron lifetimes and their ratios. This is the subject of this subsection. A related topic, the predictions of the semileptonic branching fractions and of the charm yield, will be discussed in Section 11.3.3.

11.3.2.1 General considerations

The differences in lifetime are studied most conveniently by considering lifetime ratios. In this way, one cancels the dependence on quantities which are poorly known, such as the b -quark mass (which, moreover, enters at the fifth power in the rate). For similar reasons, semileptonic branching fractions can be better predicted than absolute inclusive decay rates. For early work on this topic see [19, 20, 31], for recent reviews see [32] and [33]. The reader is recommended to consult these papers for more detailed discussion of the many technical points which are only briefly mentioned here.

From Equations (11.31) and (11.38) it can be seen that, neglecting higher-order corrections in $1/m_b$, the semileptonic and nonleptonic widths depend only on the CKM-factors and the quark

masses. This implies that all the heavy-hadrons have the same lifetime and semileptonic width. Lifetime differences arise either from corrections of $\mathcal{O}(1/m_b^2)$ originating from heavy-hadron “wave-function” effects, or they arise from $\mathcal{O}(1/m_b^3)$ corrections induced by Pauli-interference and W-exchange diagrams; *i.e.*, spectator corrections. There are no corrections at $\mathcal{O}(1/m_b)$. Thus it is expected that lifetime differences in the b hadrons are much smaller than for charmed hadrons.

The corrections of $\mathcal{O}(1/m_b^2)$ to lifetime-universality are due to the heavy-quark kinetic energy λ_1 and to the chromomagnetic term λ_2 which differ for different hadrons. For example $\lambda_1(B_s) \neq \lambda_1(B)$ because of $SU(3)_f$ symmetry-breaking effects, because the mass of the strange quark is much larger than the mass of the u and d quarks. (Numerically such effects are found to be small.) Likewise $\lambda_1(B) \neq \lambda_1(A_b)$ because mesons and baryons have different wave-functions, and the chromomagnetic term λ_2 vanishes for the A_b but not for the B meson.

The spectator contributions, although of $\mathcal{O}(1/m_b^3)$, are enhanced by the factor $16\pi^2$ and for this reason may give sizeable effects. Note that these corrections may have CKM factors different from those of the leading terms.

To make more specific predictions one has to evaluate the size of the expectation values for the relevant operators. While $\lambda_2(H_b)$ is known — it vanishes for A_b and Ξ_b and can be deduced for the mesons from the $B_{(s)} \Leftrightarrow B_{(s)}^*$ hyperfine splitting — $\lambda_1(H_b)$ is not known apart from a lower bound on it.

The determination of the expectation values of the four-fermion operators is also problematic. For mesonic matrix elements one has a simple yardstick against which one can calibrate the results, namely factorization. Following the notation of Ref. [29], the matrix elements of the four-fermion operators in terms of their B parameters are parametrized. For B mesons define

$$\begin{aligned} \langle B_q | O_{V-A,S-P}^q | B_q \rangle &= f_{B_q}^2 m_{B_q}^2 B_{1,2} \\ \langle B_q | T_{V-A,S-P}^q | B_q \rangle &= f_{B_q}^2 m_{B_q}^2 \epsilon_{1,2} . \end{aligned} \quad (11.43)$$

Factorization corresponds to setting $B_i = 1$ and $\epsilon_i = 0$. The value of the B parameters defined above depend on the scale at which the corresponding operators have been renormalized; further the factorization assumption can only be correct at one scale. Since factorization represents a statement about QCD dynamics, if it holds anywhere, it would be expected to be at hadronic scales $\sim 1 \Leftrightarrow 1.5$ GeV.

For the baryonic expectation values no such simple yard stick as factorization exists. Thus one has to rely on quark models to estimate the size of various matrix elements, which are expressed in terms of baryonic wavefunctions taken at zero spatial separation; the results are thus of uncertain reliability[34, 35]. For heavy baryons, specifically the A_b , the number of independent matrix elements is smaller than in the meson case. The reason is that, at lowest order in the HQET expansion, some of these matrix elements are related to each other

$$\langle A_b | O_{V-A}^q | A_b \rangle = \Leftrightarrow 2 \langle A_b | O_{S-P}^q | A_b \rangle + \mathcal{O}(1/m_b) . \quad (11.44)$$

It is also convenient to change basis by defining $T_{V-A}^q \equiv \Leftrightarrow 1/(2N_c)O_{V-A}^q + 1/2\tilde{O}_{V-A}^q$, with $\tilde{O}_{V-A}^q = \bar{b}_a\gamma^\mu(1 \Leftrightarrow \gamma_5)q_b\bar{q}_b\gamma_\mu(1 \Leftrightarrow \gamma_5)b_a$, where N_c is the number of colors. The following B parameters are then introduced:

$$\langle \Lambda_b | \tilde{O}_{V-A}^q | \Lambda_b \rangle = \Leftrightarrow \tilde{B} \langle \Lambda_b | O_{V-A}^q | \Lambda_b \rangle, \quad (11.45)$$

$$\langle \Lambda_b | O_{V-A}^q | \Lambda_b \rangle = \Leftrightarrow \frac{f_{B_q}^2 m_{B_q}^2}{6} r. \quad (11.46)$$

In the quark model, r can be related to the ratio of the squares of the wave functions determining the probability of finding the light quark in the vicinity of the b quark inside the Λ_b and the B meson

$$r = \frac{|\psi^{\Lambda_b}(0)|^2}{|\psi^B(0)|^2}. \quad (11.47)$$

11.3.2.2 Experimental measurements and theoretical predictions

At the time of this review, the average experimental results for lifetime ratios are [36]:

$$\begin{aligned} \frac{\tau(B_s)}{\tau(B)} &= 0.98 \pm 0.07; \\ \frac{\tau(B^-)}{\tau(B^0)} &= 1.06 \pm 0.04; \\ \frac{\tau(\Lambda_b)}{\tau(B^0)} &= 0.78 \pm 0.04. \end{aligned} \quad (11.48)$$

Theoretically, the difference between $\tau(B_s)$ and $\tau(B)$ is due to very small $SU(3)_f$ symmetry-breaking effects present either in $\lambda_{1,2}$ or in the matrix elements of the four-fermion operators, or due to penguin effects, which affect $\tau(B_s)$ but not $\tau(B_d)$ [30]. Precise predictions for these effects are very difficult to obtain. They have been estimated to be at most of the order of 1%. For the other ratios, the results can be written in terms of the B -parameters defined above. Thus

$$\begin{aligned} \left| \frac{\tau(B_s)}{\tau(B)} \Leftrightarrow 1 \right| &< 1\% ; \\ \frac{\tau(B^-)}{\tau(B^0)} &= 1 + 16\pi^2 \frac{f_B^2 M_B}{m_b^3} [k_1 B_1 + k_2 B_2 + k_3 \epsilon_1 + k_4 \epsilon_2] ; \\ \frac{\tau(\Lambda_b)}{\tau(B^0)} &= 1 \Leftrightarrow \frac{\lambda_1(\Lambda_b) \Leftrightarrow \lambda_1(B^0)}{2m_b^2} + c_G \frac{\lambda_2(\Lambda_b) \Leftrightarrow \lambda_2(B^0)}{m_b^2} \\ &+ 16\pi^2 \frac{f_B^2 M_B}{m_b^3} [p_1 B_1 + p_2 B_2 + p_3 \epsilon_1 + p_4 \epsilon_2 + (p_5 + p_6 \tilde{B}) r] . \end{aligned} \quad (11.49)$$

The $\tau(B_s)$ and $\tau(B)$ each represent an average of the lifetimes for the two-mass eigenstates.³ The perturbative coefficients k_i and p_i are related to the coefficients of the operators in Eqs. (11.41), the operators themselves are expressed in terms of the B -parameters B_i and ϵ_i , and the ratio r ; these depend on x_c and on the renormalization scale μ . Naively, one expects B_i and \tilde{B} to be of $\mathcal{O}(N_c^0) \sim 1$ and ϵ_i of $\mathcal{O}(1/N_c) \sim 1/3$ (however quite different results arise in more detailed calculations including renormalization and scale-dependent effects). It is dangerous to neglect the contributions of the color-suppressed parameters ϵ_i s because their coefficients are about one order of magnitude larger than those of the B_i s. The most uncertain parameter is r , for which theoretical estimates, based on quark models or QCD sum rules, give values in the range 0.1–2.0.⁴ The derivation assumes factorization at a low-scale $\mu \sim 1$ GeV to obtain the ratio $\tau(B^-)$ to $\tau(B_d)$. In this ratio the contribution coming from the differences of λ_1 and λ_2 in the B^- and B^0 mesons was neglected. c_G is the coefficient of the chromomagnetic term. The $\mathcal{O}(1/m_b^2)$ contributions to $\tau(\Lambda_b)/\tau(B^0)$ can be estimated using relations which can be derived in the HQET:

$$(m_{\Lambda_b} \Leftrightarrow m_{\Lambda_c}) \Leftrightarrow (\bar{m}_B \Leftrightarrow \bar{m}_D) = [\lambda_1(B) \Leftrightarrow \lambda_1(\Lambda_b)] \left(\frac{1}{2\bar{m}_B} \Leftrightarrow \frac{1}{2\bar{m}_D} \right) + \mathcal{O}(1/m_Q^2), \quad (11.50)$$

$$\lambda_2(B) = \frac{m_{B^*}^2 \Leftrightarrow m_B^2}{4} \quad \lambda_2(\Lambda_b) = 0, \quad (11.51)$$

where $\bar{m}_B = (m_B + 3m_{B^*})/4$ and $\bar{m}_D = (m_D + 3m_{D^*})/4$, and m_Q is either m_c or m_b . As discussed above, the individual kinetic-energy parameters λ_1 depend on the renormalization procedure. Equation (11.50) shows that in contrast, the difference $\lambda_1(B) \Leftrightarrow \lambda_1(\Lambda_b)$ is directly related to a certain combination of physical hadron masses. Using the experimental values of the hadron masses, one obtains⁵

$$\lambda_1(B) \Leftrightarrow \lambda_1(\Lambda_b) = \Leftrightarrow (0.01 \pm 0.03) \text{ GeV}^2, \\ \lambda_2(B) \simeq 0.12 \text{ GeV}^2. \quad (11.52)$$

Numerically, one obtains predictions such as [32]

$$\frac{\tau(B^-)}{\tau(B_d)} = 1 + 0.05 \cdot \left(\frac{f_B}{200 \text{ MeV}} \right)^2 \pm \sim 40\% \\ \frac{\tau(B_d)}{\bar{\tau}(B_s)} = 1 \pm \mathcal{O}(1\%) \\ \frac{\tau(\Lambda_b)}{\tau(B_d)} \simeq 0.9 \Leftrightarrow 0.95 \quad (11.53)$$

³The difference in lifetimes for the two B_s mass eigenstates is estimated to be $\simeq 0.18 \cdot (f_{B_s}/200 \text{ MeV})^2$, considerably larger than that between their average and $\tau(B)$ [4, 5, 30].

⁴However, some of these models also yield unusual values for f_B [34]. –Editors

⁵Note, however, that the higher order corrections in $(1/m_c^2)$ may introduce larger uncertainties here [37]. –Editors

There has been a recent and as yet unresolved debate in the literature about the reliability of the factorization approximation for the relevant four-fermion operators, and related differences in estimates of the theoretical uncertainty in the prediction of $\tau(B^-)/\tau(B^0)$. For two opposing viewpoints see [38] and [33]. The experimental result can, however, be easily accommodated within the uncertainties of the current data. As more precise experimental numbers become available it will be important to refine the understanding of theoretical errors. Lattice calculations are one prospect for improved accuracy here.

In contrast, the low experimental value of $\tau(\Lambda_b)/\tau(B^0)$ turns out to be a big surprise. In order to explain it, without abandoning the validity of the OPE, combined with $1/m_b$ expansion, one is forced to choose a negative value for ϵ_2 ($\epsilon_2 \sim \mp 0.3$) and a large value for r ($r \sim 1.8$). While such parameter choices are hard to justify on the basis of models; reliable, nonperturbative calculation of these parameters is needed to unambiguously test the validity of the framework .

In the absence of more precise determinations of the hadronic matrix elements, several alternative explanations of the low value of $\tau(\Lambda_b)/\tau(B^0)$ have been presented in the literature. The most popular one is that local duality, which is assumed in predicting nonleptonic widths, is violated. The mechanisms proposed to explain (and ultimately to correct) this violation are, however, rather different: a deviation from local duality due to the asymptotic nature of the OPE (this is equivalent to saying that the b quark is not sufficiently heavy for these processes); deviations due to the divergence of the OPE or to some dynamical generation of two scales; $1/m_b$ effects not present in the OPE, etc. Further theoretical investigation to test these ideas is needed.

It would be very interesting to measure separately the semileptonic branching fractions of the different heavy hadrons (also for charmed hadrons), from which the semileptonic widths could be extracted. From the knowledge of the individual semileptonic widths, it would be possible to test the validity of global duality, which is the ingredient necessary to make predictions for the semileptonic (and radiative) decay rates. It is not anticipated that there will be a difficulty with the validity of global duality.

11.3.3 The Semileptonic Branching Fraction

The semileptonic branching fraction of B mesons is defined by

$$\mathcal{B}_{SL} = \frac{\Gamma(\bar{B} \rightarrow X e \nu_e)}{\Gamma_{tot}(\bar{B})}, \quad (11.54)$$

with

$$\Gamma_{tot}(\bar{B}) = \sum_{l=e,\mu,\tau} \Gamma(\bar{B} \rightarrow X l \nu_l) + \Gamma(\bar{B} \rightarrow X_c) + \Gamma(\bar{B} \rightarrow X \bar{c}) + \Gamma_{Rare}, \quad (11.55)$$

where Γ_{Rare} includes decays to charmless final states [39], $\Gamma(B \rightarrow X_u)$, and possible contributions from new physics.

A quantity related to \mathcal{B}_{SL} is the charm yield (*i.e.*, the average number of charm particles per event) defined as

$$n_c = 1 + \lfloor (\overline{B} \rightarrow X_{\tau c}) \Leftrightarrow \mathcal{B}(\overline{B} \rightarrow \text{no charm}) \rfloor. \quad (11.56)$$

For these quantities the present experimental situation is the following:

CLEO	LEP
$\mathcal{B}_{SL} = (10.19 \pm 0.37)\%$	$(11.12 \pm 0.20)\%$
$n_c = 1.12 \pm 0.05$	1.20 ± 0.07

The LEP value for \mathcal{B}_{SL} must be corrected for the admixture from the other b hadrons which are produced together with the B -meson at the center-of-mass energy $s \sim M_z$. This gives $\mathcal{B}_{SL}^{corr} = (11.12 \pm 0.20)\% \times \tau(B)/\tau(b) = (11.4 \pm 0.2)\%$.

Theoretical uncertainties in the predictions for \mathcal{B}_{SL} come from a variety of sources: the quark masses m_b and m_c , unknown higher order radiative and power corrections, the choice of renormalization scale μ , and even the applicability of local parton-hadron duality in the various processes which contribute to (11.54). For thorough analyses, the reader is referred to [20, 40, 33]. As an illustration of the issues which arise, the sensitivity to the quark masses and the renormalization scale will be discussed here.

A convenient parametrization of the dependence of the results on $m_b \Leftrightarrow m_c$ and μ is to use the dimensionless quantities m_c/m_b and μ/m_b . Note that explicit dependence on λ_1 introduced in Section 11.3.1.1) cancels out in a branching fraction, because it is the same for all inclusive decays.

Using the HQET, the $m_b \Leftrightarrow m_c$ mass difference can be derived from the relation

$$m_b \Leftrightarrow m_c = (\overline{m}_B \Leftrightarrow \overline{m}_D) \left(1 \Leftrightarrow \frac{\lambda_1}{2\overline{m}_B \overline{m}_D} \right) + \mathcal{O}(1/m_Q^2) \quad (11.57)$$

where m_Q denotes either m_b or m_c . As explained in Section 11.3.1.1, the value of λ_1 depends on the renormalization prescription and is subject to large uncertainties. Using $\overline{m}_B = 5.31 \text{ GeV}/c^2$ and $\overline{m}_D = 1.97 \text{ GeV}/c^2$, and taking the estimate of λ_1 obtained in dimensional regularization, $\lambda_1 = \Leftrightarrow(0.4 \pm 0.2) \text{ GeV}^2$, the mass difference was originally estimated to be $m_b \Leftrightarrow m_c = (3.4 \pm 0.3 \pm 0.3) \text{ GeV}/c^2$, where the first error reflects the uncertainty in the value of λ_1 and the second takes into account higher order corrections. More recently, lower values of λ_1 have been presented in the literature, and λ_1 as small as 0–0.1 remains an open possibility. By taking $\lambda_1 = 0$ –0.1, one gets $m_b \Leftrightarrow m_c = 3.34$ –3.35. Results for \mathcal{B}_{SL} and n_c presented here are obtained by assuming the broader range

$$m_b \Leftrightarrow m_c = (3.40 \pm 0.06) \text{ GeV}/c^2. \quad (11.58)$$

Allowing the b -quark pole mass to vary in the range $m_b = 4.8 \pm 0.2 \text{ GeV}/c^2$, one obtains for the charm-to-bottom mass ratio $0.25 < m_c/m_b < 0.33$. Taking into account the uncertainty on m_c/m_b

one gets

$$\begin{aligned} \mathcal{B}_{SL} &= (12.0 \pm 1.0)\% , & n_c &= 1.20 \pm 0.06 & \mu/m_b &= 1 ; \\ \mathcal{B}_{SL} &= (10.9 \pm 1.0)\% , & n_c &= 1.21 \pm 0.06 & \mu/m_b &= \frac{1}{2} . \end{aligned} \quad (11.59)$$

This example calculation demonstrates that it is not hard to reproduce the LEP results by adjusting the input parameters m_b and μ , while the CLEO results remain outside the theoretically preferred region. This is a feature of the more complete analyses as well.

The theoretical prediction of the nonleptonic width is an essential ingredient in the calculations of these quantities. The theoretical prediction of $\mathcal{B}(B \rightarrow X_{c\bar{c}})$ is $22 \pm 6\%$ in good agreement with the experimental value obtained by the CLEO collaboration $\mathcal{B}(B \rightarrow X_{c\bar{c}}) = 23.9 \pm 3.8\%$.

This situation has led to considerable theoretical speculation, chiefly regarding mechanisms to increase the hadronic branching fraction without at the same time significantly increasing the charm fraction. These efforts fall into two classes, those that look for this possibility within the Standard Model *e.g.*, [41] and those that suggest this result is a possible indicator of beyond Standard Model physics *e.g.*, [42]. Both the experimental situation and the theoretical uncertainties of Standard Model predictions for charmless hadronic decays will have to be clarified before one can understand whether or not there are new physics effects here. The situation, however, is an interesting one and merits serious further work on both fronts.

11.3.4 B -Lifetime Ratio Measurement at BABAR

Precise measurements of exclusive B meson lifetimes are needed to fit Δm_{B_d} mixing and to extract the electroweak parameters A_{fb} and $\Gamma_{b\bar{b}}$. They are important in their own right for testing theoretical models of heavy-quark decays. For example, two calculations [19, 21] and [33] predict a lifetime difference between the B^+ and B^0 at the level of 5–10% and 1%, respectively. The current world average of all exclusive B meson lifetime measurements carries a relative error of 3% [43, 44]. The most recent averages from the LEP B lifetimes working group [44] give:

$$\tau(B_d) = 1.57 \pm 0.04 \text{ ps}, \quad \tau(B^+) = 1.67 \pm 0.04 \text{ ps}, \quad \frac{\tau(B^+)}{\tau(B_d)} = 1.07 \pm 0.04$$

These errors are too large to make a meaningful distinction between theoretical models. Measurements of these lifetimes with errors of $\sim 1\%$ are required.

The high-energy experiments capable of precision B -lifetime measurements are the LEP groups at CERN, the SLD experiment at the Stanford Linear Collider, and the CDF/D0 experiments operated at the Tevatron at Fermilab and HERA-B at DESY. LEP has finished Z^0 running and has moved on to higher energies, which are not useful for B -lifetime measurements because of

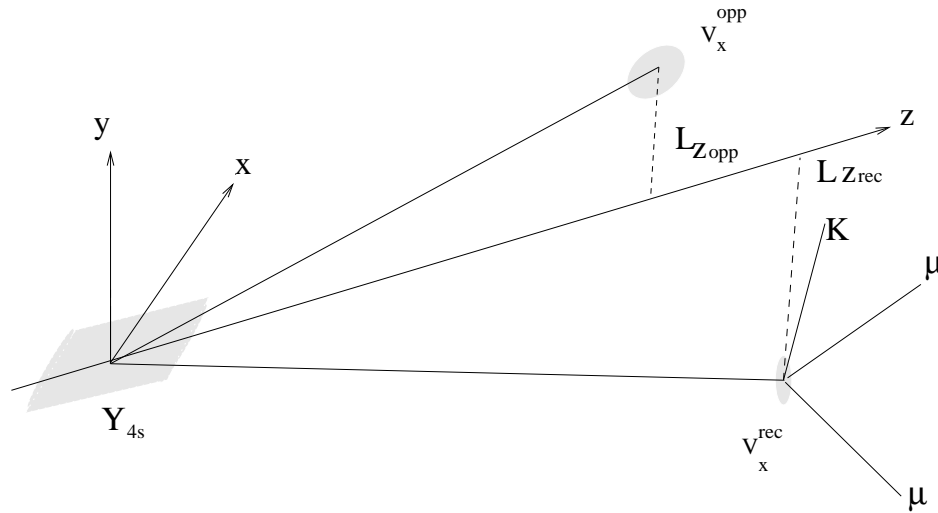


Figure 11-19. Geometry in the laboratory of the $\Upsilon(4S)$ decay to a pair of B mesons, of which one is fully reconstructed.

a much smaller event rate. It is not anticipated that SLD will operate concurrently with BaBar. Therefore LEP and SLD will eventually be statistically limited to a precision of about 2–3%. The CDF/D0 experiment will resume running in 1999 with an upgraded higher luminosity Tevatron accelerator and improved vertex detection. Their current measurements are statistically limited. They quote systematic uncertainties of order 1%. Since they anticipate collecting $\simeq 20$ times the number of B s they have in hand from Run I, they will reach an interesting level of precision. The purpose of this section is to study the error level obtainable at BaBar. It is found that, with two years at nominal luminosity (30 fb^{-1} per year), BaBar can achieve lifetime measurements at a level of precision close to the 1% required to detect departures from the spectator model. More studies are needed to substantiate this conclusion.

11.3.4.1 Strategy

The $\Upsilon(4S)$ decays exclusively to pairs of charged or neutral B mesons. For lifetime measurements, this simple configuration has the complication that no particle comes out of the $\Upsilon(4S)$ decay point, Y_{4S} , which is thus unmeasurable. Were that not the case, a lifetime measurement would consist of recording the $\Upsilon(4S)$ decay point and the decay vertices of both mesons. The decay distance and the momenta of a B meson determine its lifetime. If both B mesons are vertexed, two lifetimes measurements per event would be made. Figure 11-19 shows the geometry of the problem for the example described below. The figure has not been drawn to scale; the flight paths are of the order of $250 \mu\text{m}$ the error ellipse for a vertex point are typically $\simeq 50 \mu\text{m}$ (for a fully reconstructed B meson), or $100 \mu\text{m}$ (for a partially reconstructed one), numbers like those given in the BaBar TDR [45], and BaBar notes *e.g.*, [46]. The maximum opening angle between the trajectories of the

B mesons is 214 mrad or 12.3° . In other words, the B mesons fly almost along the electron beam (z direction). The collision region is ribbon-shaped with rms extensions of $150 \mu\text{m}$ in x , $6 \mu\text{m}$ in y and $\simeq 1 \text{ cm}$ in z . The longitudinal size of the beam is far bigger than the picture size.

In order to measure lifetimes without knowing where the production point of the B mesons is, one can infer the lifetime from Δz , the distance between the two B decay vertices projected on the beam axis. The distribution of this variable is sensitive to the (common) lifetime of the two B mesons in the event [14]. A mixing correction has to be applied in the case of neutral B mesons. Applying this method to completely reconstructed events (double-tagged sample) gives the best precision, but a price has to be paid in statistics. Conversely, partially reconstructing or only vertexing one or two B mesons gives more events, but the systematic errors are harder to control. When none of the B mesons is exclusively reconstructed, a tagging technique has to be employed. Tagged samples with no exclusive reconstruction have large intrinsic vertex errors and fits require detailed tuning. These have not yet been pursued. Table 11-3 gives rough estimates of the expected statistics for a typical BABAR year. Up to now studies have concentrated on the events with one exclusive B decay and one vertexed B and, to get a flavor of what will be achievable in the experiment, simulated data from two samples have been analyzed:

$$B^\pm \rightarrow J/\psi (\rightarrow \mu^+ \mu^-) K^\pm \quad (11.60)$$

and

$$\overline{B}_d^0/B_d^0 \rightarrow J/\psi (\rightarrow \mu^+ \mu^-) K^\pm \pi^\mp . \quad (11.61)$$

Admittedly, these modes are not typical of those that can be used to determine the lifetimes. They are all-charged, few-body final states with no open charm. They are chosen here for the initial study, for simplicity.

Table 11-3. Rough estimate of the data sample (1 sample per charge) sizes for a nominal BABAR year (30 fb^{-1} running at the $\Upsilon(4S)$).

Type of Events	Produced	ϵ	Detectable
both exclusive	9M	10^{-4}	900
1-exclusive 1-vertexed	12M	3×10^{-3}	36k

11.3.4.2 Implementation to date

Several studies were performed, which, due to lack of space, cannot all be described in detail here. They are described fully in Refs. [47, 48, 49]. The analyses were done mostly using the Aslund-parameterized fast Monte Carlo. The numbers of simulated events used are given in Table 11-4.

Table 11-4. Data samples used for the lifetime analyses. “accepted” refers to the events which satisfy the event selection criteria.

type of events		Aslund	β -Aslund	BBsim
$B^\pm \rightarrow J/\psi(\rightarrow \mu^+\mu^-)K^\pm$	generated	4000	2000	none
	accepted	2840	1064	”
	vertexed	1702	289	”
$\overline{B}_d^0/B_d^0 \rightarrow J/\psi(\rightarrow \mu^+\mu^-)K^\pm\pi^\mp$	generated	4000		4000
	accepted	2550		1000
	vertexed	1348		188

The full BBsim simulation and reconstruction chain was used for a limited statistics sample of events from the process shown in Eq. (11.61).

Event selection

Dedicated samples were generated in which one B meson decayed through the process of Eq. (11.60) or (11.61) and the other in a standard way. Monte Carlo truth lepton identification was used to obtain the J/ψ decay products. To be accepted, an event needed to have enough reconstructed tracks within the detector acceptance (in particular all the tracks from the exclusively reconstructed B meson had to be present) and suitable momentum intervals. In order to be used in the lifetime analysis, successful vertex fits to both the exclusive mode and the left-over tracks were required. The acceptance cuts retained $\simeq 30\%$ of the events. Another third were lost in the vertexing of the non reconstructed B .

Δz Results

The simplest way to extract a B meson lifetime is by fitting the $\Delta z = z^{opp} \leftrightarrow z^{rec}$ distribution. Fig. 11-19 denotes the (completely) reconstructed B by “rec,” and the other one by “opp” (for opposite). The probability density function for Δz was computed as described in Ref. [14], in the most general case of B_d events with a CP exclusive decay mode and mixing. Using a simplified formula for the cases of the charged B mesons (no mixing) and neglecting CP violation for the B_d decay, maximum likelihood fits were performed. An analytical form of the distribution is derived later, in Section 11.5.3 (see Eq. (11.93)). The results of this *Method-1* fit for Aslund were:

$$\begin{aligned}
 c\tau(B^+) &= 414 \pm 19 \mu\text{m} \\
 c\tau(B_d) &= 433 \pm 19 \mu\text{m}.
 \end{aligned}
 \tag{11.62}$$

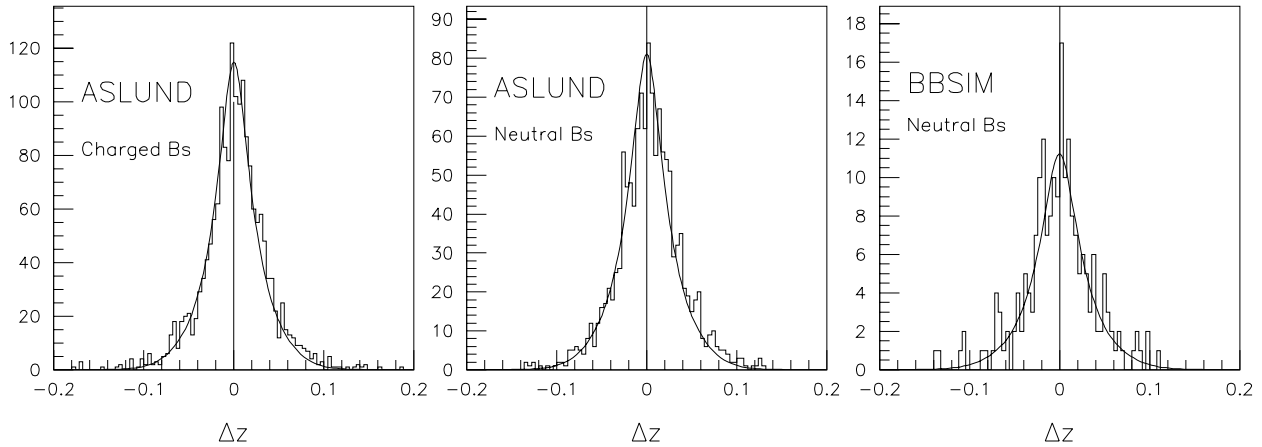


Figure 11-20. Δz fit result for events generated with `ASLUND` and `BBSim`. The curves superimposed on top of the distributions to guide the eye are the appropriate fitting functions where, for each event, the average standard deviation has been used.

For the (small) `BBSim` sample of B_d , the results are:

$$c\tau(B_d) = 453 \pm 50 \mu\text{m},$$

where the errors are purely statistical. Figure 11-20 displays the result of this fit. Only 188 events belong to the `BBSim` sample. Still the determination of the B_d lifetime is within expectations. The various distributions shown below in the description of more sophisticated lifetime determination methods compare quite well with their `ASLUND` counterparts.

The systematic errors of that method should be small for the following reasons. Minimum use of detector elements is required (the vertexing geometrical fit requires essentially only the vertex detector). Since a difference in positions is measured, the result should be quite insensitive to global detector misalignment. The main systematic error stems from the bias in the partially reconstructed B meson vertex, due to charmed particles in the final state. Other systematic effects, like the degree of approximation in the likelihood function, or the features of the real lepton identification algorithms, should be of less importance because of the quality of the J/ψ signature.

More sophisticated methods

More sophisticated methods of reconstructing the geometry and the kinematics of the events have been tried. The results look promising using the `ASLUND` fast simulation program. These results are borne out using the full `BBSim` simulation and the reconstruction software, albeit with a very

small number of events studied to date. In these methods, global kinematic and geometric fits are performed. The $\Upsilon(4S)$ decay point is fitted using one geometric constraint (the vanishing vertical beam width) and the kinematic constraints provided by the conservation of four-momentum in the $\Upsilon(4S)$ decay: the B -meson energies in the $\Upsilon(4S)$ frame. Access to the flight paths of the B mesons is thus granted and 2 determinations of the lifetime per event are possible in principle. After the fit, it is found that the only geometrical quantities which are significantly improved are the transverse coordinates, x^{opp} , y^{opp} of the non-reconstructed B meson. Since the measurement relies essentially on Δz , a great improvement in the precision of the lifetime is not expected from the fit. There is however a two-fold bonus. Firstly, since direct determinations of the reconstructed B meson flight paths are obtained, the bias from charm, which normally affects the opposite vertex, can be avoided. Secondly, with two possible measurements per event, the statistical error can be improved. These considerations led to the fits of *Method-2* and *Method-3*. The first considerations looks quite promising. Projecting Fig. 11-19 onto the x, z plane, it is straightforward to show that the lifetime is obtained from:

$$c\tau_{meth-2}^{rec} = (y^{rec} \Leftrightarrow y^{\Upsilon(4S)})M_B/P_y^{rec} \quad (11.63)$$

where P_y^{rec} is the y component of the reconstructed B meson momentum. Note that this quantity ranges from 0 to 325 MeV/c as the decay angle ($\bar{\theta}$) in the $\Upsilon(4S)$ frame varies over all values. P_y is reconstructed with a 5 MeV/c rms error. Relevant error distributions for this *Method-2* fit are shown in Fig. 11-21.

The combined fit (*Method-3*) gives two observables $c\tau_{meth-3}^{rec}$ and $c\tau^{opp}$, which can be subtracted, $\Delta c\tau$, or summed, $\Sigma c\tau$. Note that $\Delta c\tau$ looks very much like Δz . The results obtained using `Aslund` are summarized in Table 11-5. Only $\Delta c\tau$ has an average error ($\simeq 150 \mu\text{m}$) which is much less than the expectation ($\simeq 450 \mu\text{m}$). The observables which are flight paths or a sum of flight paths exhibit sensitivity to lifetimes, both through the average and the shape of the distribution. The net departure from zero of the average is due to the exponential decay distribution (convoluted with a Gaussian-like resolution function). The averages for observables including $c\tau^{opp}$ furthermore exhibit shifts towards long lifetimes because of charm. In order to correct for the charm bias, a Monte Carlo simulation has to be performed, which brings in systematic errors. Note that such a correction is needed for the simple-minded *Method-1*.

Figure 11-22 shows the error distributions of the $c\tau_{meth_2}^{rec}$, $c\tau_{meth_3}^{rec}$ and $\Delta c\tau$ observables. For the first of these, events with excessively large errors (P_y^{rec} close to zero) have to be discarded. The distributions of the same observables are shown for neutral and charged B mesons in Figs. 11-23 and 11-24. The same plots for the `BBSim` analysis are shown on the above figures. In spite of poor statistics, it can be seen that `BBSim` only brings a slight degradation of the distributions.

11.3.4.3 Extrapolation to 30 fb^{-1}

Using the `Aslund` event-selection efficiency, the estimated sizes of the exclusive B -meson data samples given in Table 11-3, and the errors given in the previous subsection, an estimate of the statistical error on the lifetime ratio of $\simeq 1.5\%$ is obtained for one year of running at the $\Upsilon(4S)$.

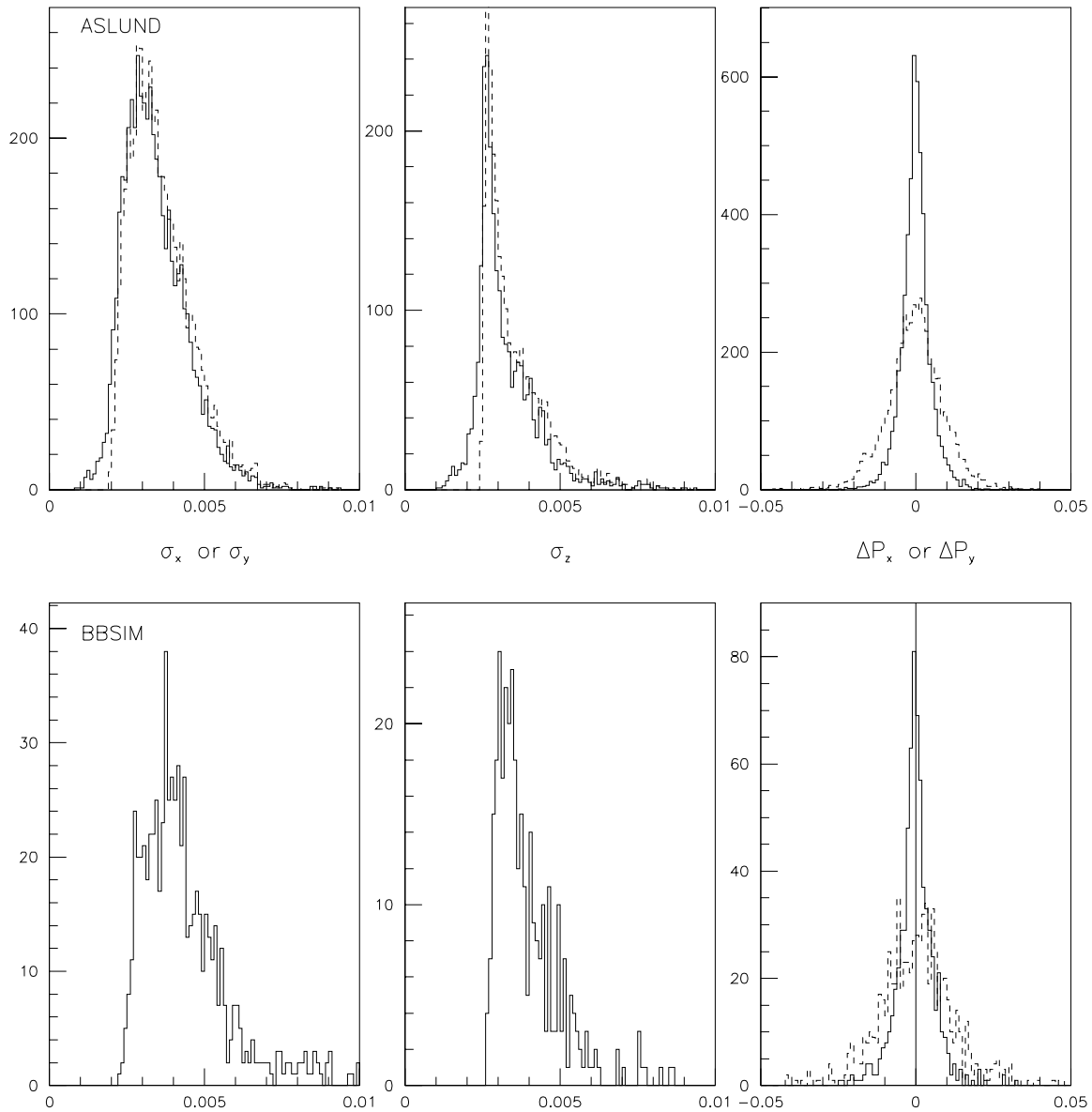


Figure 11-21. Quality of the vertex and the momentum of the reconstructed B mesons, using the geometric and kinematic constraints: left and middle: errors on x_{rec}/y_{rec} and z_{rec} coordinates expressed in cm. The full histograms show the effect of adding three kinematic constraints to a pure geometric fit (dashed lines). Right: residue in GeV/c of the P_x, P_y components. The top figures correspond to ASLUND and the bottom ones, to BBSIM.

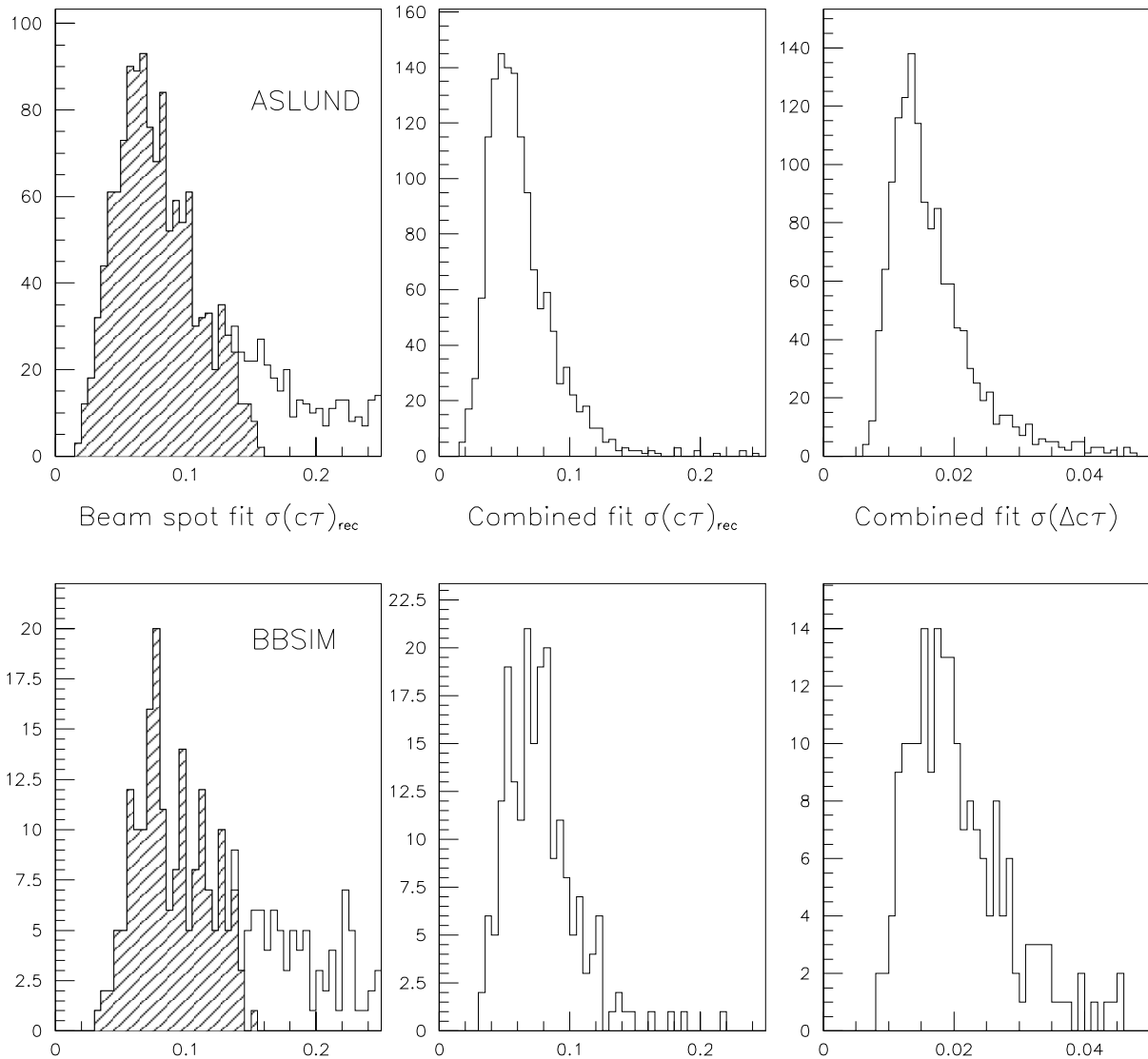


Figure 11-22. Distribution for B^0 lifetimes of the errors on: (left) $c\tau^{rec}$ in the case of the beam-spot fit with (shaded area) and without the cut $\sigma(L_z) < 800\mu m$: (center) $c\tau^{rec}$ and (right) $\Delta c\tau$ in the case of the “combined fit”. Top: ASLUND, bottom: BBSIM.

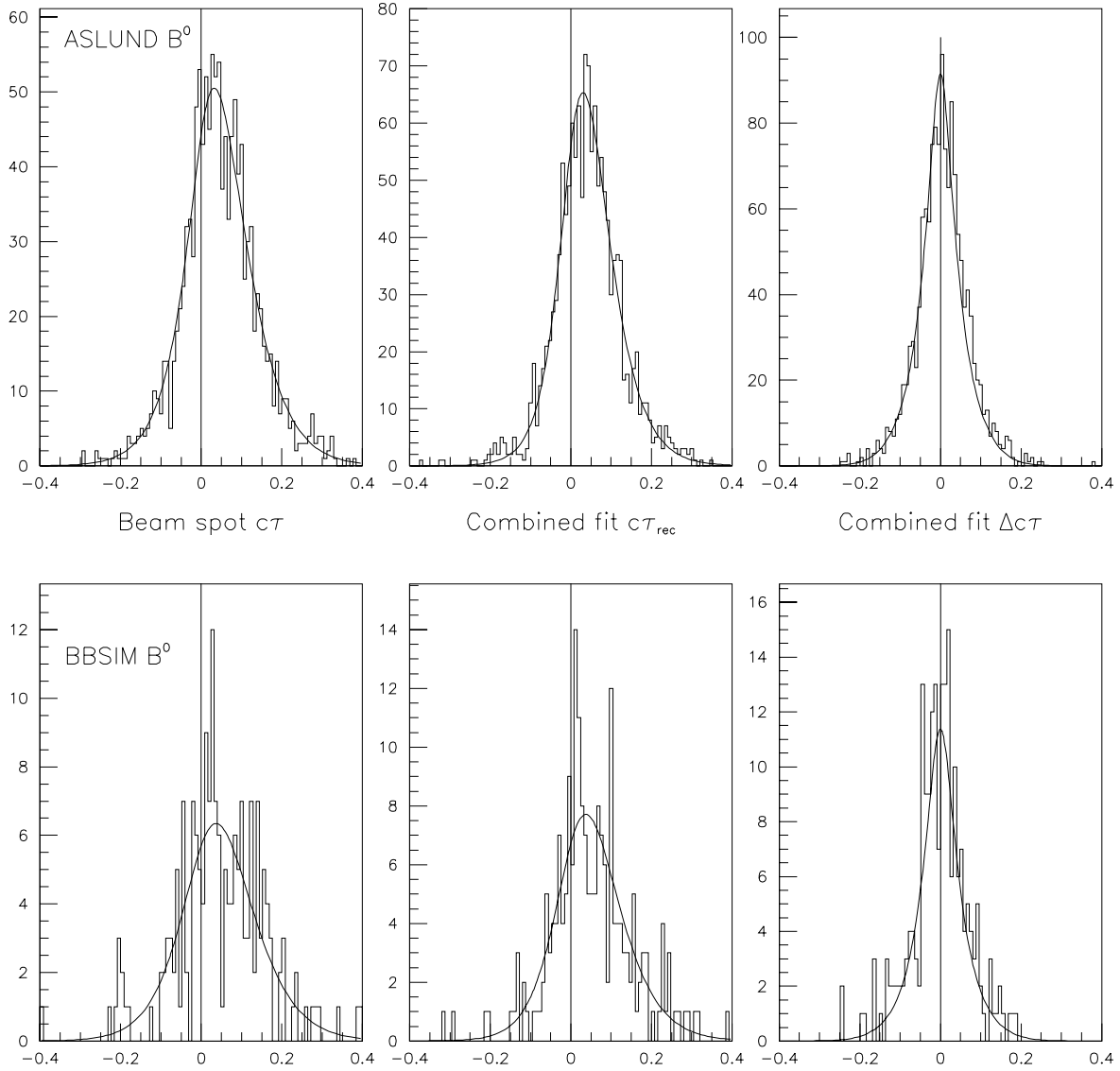


Figure 11-23. Distribution of lifetimes observables $c\tau^{rec}$ and $\Delta c\tau$ for neutral B_s . Top: Aslund, bottom: BBSim.

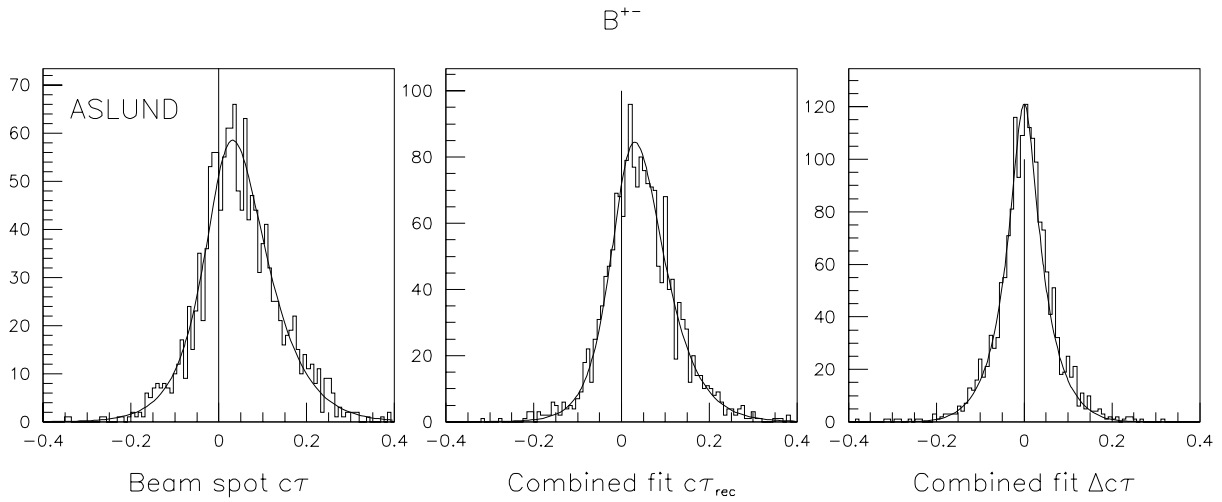


Figure 11-24. Distribution of lifetimes observables $c\tau^{rec}$ and $\Delta c\tau$ for charged B_s .

Table 11-5. Summary of straightforward and “sophisticated” methods results using Aslund. All numbers are given in μm .

		<i>Method-1</i>	<i>Method-2</i>	<i>Method-3</i>			
		$c\tau$ from Δz	$c\tau_{meth-2}^{rec}$	$c\tau_{meth-3}^{rec}$	$c\tau^{opp}$	$\Delta c\tau$	$\frac{1}{2}\Sigma c\tau$
B^+	average error		755	583		158	1170
	Max. Lik. fit	414 ± 19	455 ± 27	452 ± 20		421 ± 19	
	average		465 ± 25	461 ± 21	486 ± 20		457 ± 18
B_d	average error		780	611		162	1213
	Max. Lik. fit	433 ± 19	462 ± 30	446 ± 26		441 ± 19	
	average		471 ± 27	433 ± 23	491 ± 24		472 ± 22

In the eventual analysis, errors will be different because of many factors. The precision of the reconstructed vertex is worse for most of the reconstructible decay modes. That factor should not be too important, since the lifetime resolution is mostly determined by the vertex of the opposite B . Some increase in the statistics may come from the inclusion of semileptonic decays through missing mass techniques in the reconstructed B sample. Further degradation will unavoidably come from detector effects which have not been modeled by `Aslund` and will require stronger cuts in the event selection. The actual lepton identification will not be perfect. Finally, the background under the B -mass peak for exclusively reconstructed channels will degrade the statistics. Since these factors include both degradations and improvements, an eventual statistical error of 1.5% seems reachable for one year at nominal luminosity running at the $\Upsilon(4S)$.

Some very preliminary studies of the systematics have been performed using toy Monte Carlo simulations. The effects of detector misalignment and momentum resolution are below 0.1%. So is the uncertainty caused by the background subtraction using *e.g.*, a low-mass sideband in the B -mass plot, or other more refined techniques. The major effects are the charm bias which tends to push the opposite vertex away, and the control of the errors on the (z) position of the vertices. Further studies need to be done before claiming a 1% irreducible systematic error. A good way to master most systematic effects with data is the measurement of the charmed-meson lifetimes since their lifetimes are known to 1% (D^+) and 1.4% (D^0). $D\bar{D}$ pairs from the $c\bar{c}$ continuum have similar topologies to the $B\bar{B}$ events. Since in that case, the production vertex is known, these events could help a lot in assessing the systematics of the sophisticated *Methods-2* and *-3* which use the B -meson production point reconstruction.

11.3.4.4 Conclusions

A measurement of the ratio of the lifetimes of charged and neutral B mesons to the 1% level of precision required to test details of the decay mechanisms will be hard to achieve. More than one year at nominal luminosity will be needed to collect sufficient statistics. The level of systematic error cannot be assessed before extensive studies are made on realistic simulation data. Promising methods for using real data to control some systematic uncertainties have been identified.

11.4 Bottomonium Physics

11.4.1 $\Upsilon(4S)$ Resonance Parameters

The $\Upsilon(4S)$ state has a mass slightly above the open $B\bar{B}$ threshold. It therefore decays predominantly⁶ into $B^0\bar{B}^0$ and B^+B^- pairs, decays which are not available to the lighter resonances. This is a strong interaction process which makes the $\Upsilon(4S)$ considerably wider than the lower S states, which cannot decay strongly. The measured parameters correspond to a state $\Upsilon(10580)$, which is most probably, due to its width and overlap with excited D states, not a pure $4S$ state, but a mixture

⁶Substantial non- $B\bar{B}$ decays were once discussed, triggered by an abundance of high-momentum J/ψ mesons [50]. These can be completely explained, however, by continuum production.

of $\Upsilon(4S)$ and $\Upsilon_1(2D)$. A rich structure at higher energies is formed by more overlapping S and D states.

11.4.1.1 The $\Upsilon(10580)$ total width and Γ_{ee}

It is necessary to use a relativistic Breit–Wigner shape

$$\sigma_0(s) = 12\pi \frac{\Gamma_{ee}\Gamma(s)}{(s \leftrightarrow m^2(s))^2 + M^2\Gamma^2(s)} \quad (11.64)$$

with energy-dependent $\Gamma(s)$, in the parametrization of the resonance shape. ARGUS [51] has derived this shape from a quark pair creation model calculation [52, 53]. The matrix element for the decay $\Upsilon(10580) \rightarrow B\bar{B}$ is given by the product of a spin-dependent amplitude and an overlap integral comprising the meson and quark wave functions involved in the decay. The real part of the propagator is absorbed in a mass shift function $m(s)$, which is related to $\Gamma(s)$ by a dispersion relation.

The process $e^+e^- \rightarrow \Upsilon(10580) \rightarrow B\bar{B}$ is given to lowest order by Eq. (11.64). A remark has to be made concerning the partial width Γ_{ee} . In the derivation of the Breit Wigner cross-section, use has been made of the fact that the matrix elements are equal for

$$\mathcal{M}(e^+e^- \rightarrow \Upsilon) = \mathcal{M}(\Upsilon \rightarrow e^+e^-) \quad (11.65)$$

i.e., the production probability $e^+e^- \rightarrow \Upsilon$ equals the decay probability $\Upsilon \rightarrow e^+e^-$, if simply phase space factors are replaced by flux factors. This exchange of final and initial state is no longer possible, if a photon from bremsstrahlung of the e^+e^- is present, since the initial state energy \sqrt{s} and the resonance mass m_Υ uniquely determine the photon energy k in the production process, whereas the decay is always an integral over all k of, in principle, even infinitely many photons,

$$\Gamma_{ee}^{\text{expt}} := \sum_{n=0}^{\infty} \Gamma(\Upsilon \rightarrow e^+e^- + n\gamma). \quad (11.66)$$

The connection between Γ_{ee}^0 and $\Gamma_{ee}^{\text{expt}}$ to order α^3 , *i.e.*, of the process $\Upsilon \rightarrow e^+e^-\gamma$, is

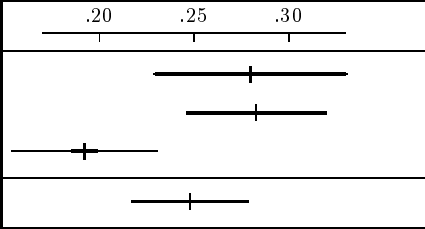
$$\Gamma_{ee}^{\text{expt}} = \Gamma_{ee}^0 \left(1 + \delta_{\text{vac}} + \delta_{\text{virt}}^{\text{final}} + \int \delta_{\text{brems}}^{\text{final}}(k) dk \right). \quad (11.67)$$

With this, one can formally rewrite the cross-section in terms of $\Gamma_{ee} = \Gamma_{ee}^{\text{expt}}$ instead of Γ_{ee}^0 . The Breit-Wigner cross-section with this substitution and first order radiative corrections is

$$\sigma(s) = \int_0^{\kappa_{\text{max}}} \sigma_0(s(1 \leftrightarrow \kappa)) \cdot \beta \kappa^\beta (1 + \delta_{\text{vert}}) d\kappa, \quad (11.68)$$

where $\beta = \frac{2\alpha}{\pi} (\ln \frac{s}{m_e^2} \leftrightarrow 1)$, and $\kappa = 2k/\sqrt{s}$ is the scaled photon energy in the e^+e^- cms.

Table 11-6. Results on the partial width Γ_{ee} of the $\Upsilon(10580)$ meson.

	Γ_{ee} [keV]	Experiment
	$0.28 \pm 0.05 \pm 0.01$	ARGUS 95 [51]
	0.283 ± 0.037	CUSB 85 [54]
	$0.192 \pm 0.007 \pm 0.038$	CLEO 85 [55]
	0.248 ± 0.031	average [56]

The energy spread of the colliding beam machine has to be taken into account. The distribution of the actual e^+e^- energy, $\sqrt{\tilde{s}}$, is assumed to have a Gaussian form with a mean energy \sqrt{s} :

$$G(\sqrt{\tilde{s}}, \sqrt{s}) = \frac{1}{\sqrt{2\pi}\Delta} \exp\left(-\frac{(\sqrt{\tilde{s}} - \sqrt{s})^2}{2\Delta^2}\right) \quad (11.69)$$

and consequently, the experimental cross-section at the mean energy \sqrt{s} is a convolution of $\sigma(\tilde{s})$ and $G(\sqrt{\tilde{s}}, \sqrt{s})$.

The fit of the resonance curve yields, at the nominal resonance mass, the following parameters:

$$\begin{aligned} \Gamma_{ee}(\Upsilon(10580)) &= (0.28 \pm 0.05 \pm 0.01) \text{ keV} \\ \Gamma_{\text{tot}}(\Upsilon(10580)) &= (10.0 \pm 2.8 \pm 2.7) \text{ MeV} \end{aligned} \quad (11.70)$$

The systematic error on the total width reflects the model uncertainty. This width is substantially smaller than the previous world average, which is obtained from fits using a parametrization valid for narrow resonances. The approximation $\Delta \gg \Gamma_{\text{tot}}$ used for its derivation is, however, not valid for the broad $\Upsilon(10580)$. Actually, a fit of this function to the ARGUS data yields a width which is about a factor two larger than the quoted result,⁷ while a convolution of a simple Breit Wigner with the Gaussian machine resolution gives $\Gamma_{\text{tot}} = (13.6 \pm 4.4) \text{ MeV}$, in agreement with the result from the more elaborate model.

The partial width Γ_{ee} is less dependent on the resonance shape, since it is given by the integral of the cross-section. Therefore, it seems reasonable to average the ARGUS result with values obtained by other collaborations, summarized in Table 11-6, although a shift to slightly higher values is expected.

11.4.1.2 The peak cross-section

The peak cross-section can be calculated from the convoluted shape, and depends on Γ_{ee} , Γ_{tot} and the machine resolution Δ . Its value as a function of Δ is shown in Fig. 11-25, using the

⁷ $\Gamma_{\text{tot}} = (21.7 \pm 3.6) \text{ MeV}$, similar to the values of CUSB, $(25 \pm 2.5) \text{ MeV}$ [54] and CLEO $(20 \pm 2 \pm 4) \text{ MeV}$ [55]. The average given by the Particle Data Group [56] is not a sensible quantity.

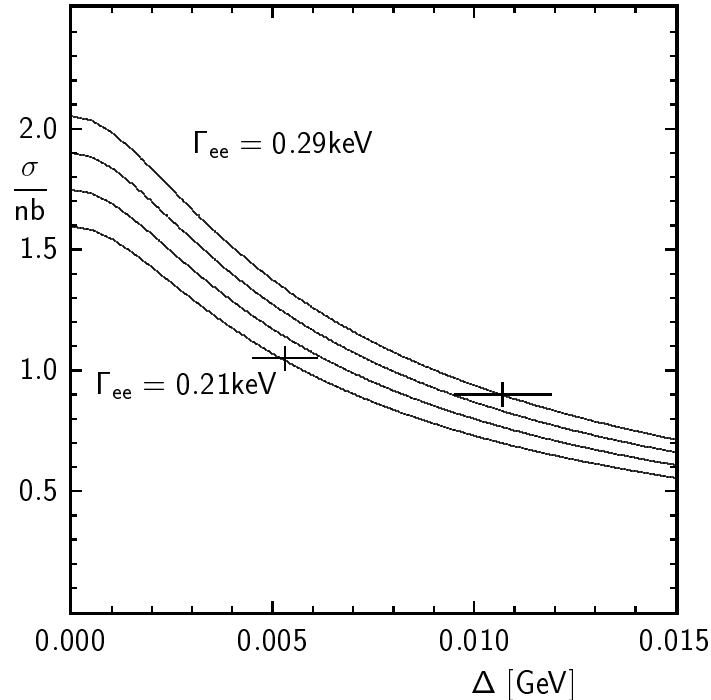


Figure 11-25. Peak cross-section of the $\Upsilon(10580)$, using $\Gamma_{\text{tot}} = 10 \text{ MeV}$ [51] and various Γ_{ee} values from 0.21 keV to 0.29 keV, versus the machine resolution $\Delta = \sigma(E_{\text{cms}})$ [57]. The crosses are the ARGUS/DORIS data (right) and CLEO/CESR (left, errors guessed).

best estimate on Γ_{tot} (from ARGUS) and four different values for Γ_{ee} within the range given by measurements at DORIS and CESR. The $(\sigma_{\text{peak}}; \Delta)$ pairs for DORIS/ARGUS and CESR/CLEO are inserted as data points. The errors on the CESR energy resolution and the systematic error due to small deviations from the peak energy at the CLEO $\Upsilon(4S)$ data taking runs (from which the cross-section is determined) are guesses. There is only a small extrapolation from CESR/CLEO to PEP-II/B $\overline{\text{A}}\text{B}\overline{\text{A}}\text{R}$ ($\Delta = 5.2 \text{ MeV}$); hence, the peak cross-section at B $\overline{\text{A}}\text{B}\overline{\text{A}}\text{R}$ is expected to be close to 1.05 nb within $\pm 0.1 \text{ nb}$.

11.4.1.3 The $\Upsilon(10580)$ mass

The $\Upsilon(10580)$ mass measurements are dominated by systematic errors in the storage ring energy [58]. The most precise value is the CLEO measurement at CESR [59], which gives

$$m_{\Upsilon(10580)} = (10580.0 \pm 3.5) \text{ MeV}/c^2 \quad (11.71)$$

A precise determination of the $\Upsilon(10580)$ mass will require sophisticated beam-energy calibration via a depolarization technique [60], which becomes possible, when the beam particles get vertically polarized by the Sokolov-Ternov effect [61]. If a beam particle is exposed to a horizontal magnetic field, its spin is tilted, and if this field is alternating in phase with the precession, the cone of

precession is opened during many revolutions and the beam is depolarized. This will also occur at energies, where the precession frequency is in phase with the orbital frequency, since constant horizontal B components are always present in storage rings. At these energies, no polarization will build up, and the technique cannot be used for beam-energy calibration.

With a time-dependent field, depolarization can be achieved at other energies, too. The depolarizing frequency f_D must match

$$f_D = f_P \Leftrightarrow n \cdot f_0 = (\gamma a \Leftrightarrow n) \cdot f_0 \quad (11.72)$$

with arbitrary integer n , where $f_P = f_0 \cdot \gamma \cdot a$ is the precession frequency, $a = (g \Leftrightarrow 2)/2 = 0.0011596521[9 \pm 1]$ the anomalous magnetic moment of the electron or positron, $\gamma = 1/\sqrt{1 \Leftrightarrow v^2/c^2}$ the Lorentz factor, and f_0 the orbital frequency. Choosing a suitable n , one can have

$$f_D = \text{frac}(\gamma a) \cdot f_0 \quad (11.73)$$

with only the fractional part of γa . Scanning f_D shows a dip in beam polarization. The correct n has to be calculated from the approximate energy. Then

$$\gamma a = \frac{f_D}{f_0} + n \quad \text{and} \quad E_{\text{beam}} = \gamma m_e. \quad (11.74)$$

In contrast to a symmetric storage ring, at BABAR/PEP-II, two beams of energy 9 GeV and 3.1 GeV respectively are used. The error on the $\Upsilon(10580)$ mass is $\Delta m = 1.70\Delta E_L \oplus 0.59\Delta E_H$. Therefore, both rings have to build up polarization and their energies have to be determined at the same time. This will probably not be possible, and the $\Upsilon(10580)$ mass will be determined only to the precision in energy difference to a nearby well-known state, *e.g.*, the $\Upsilon(2S)$, which will result in an accuracy of about ± 1 MeV.

A determination of the width is independent of the polarization capability, since only small energy differences are important, which can be reliably calculated from (dipole) magnet currents in the rings.

11.4.2 $\Upsilon(4S)$ Decays to B -Meson Pairs

The kinematics of B mesons from $\Upsilon(10580)$ decays at rest are easily calculated from the following data, where the mass scale is set by the $\Upsilon(10580)$ mass, hence no contribution from its error enters into the calculation:

$$\begin{array}{lll} m(\Upsilon(10580)) & = & 10580 \text{ MeV} \\ m(B^0) & = & 5278.8 \pm 0.2 \text{ MeV} & m(B^+) = 5278.6 \pm 0.2 \text{ MeV} \\ p(B^0) & = & 344.1 \pm 3.1 \text{ MeV} & p(B^+) = 347.1 \pm 3.1 \text{ MeV} \\ \beta & = & 0.065 \\ \gamma & = & 1.002 \end{array}$$

The decay width is

$$\Gamma(\Upsilon(10580) \rightarrow B\bar{B}) \propto p_B^3 \Phi^2(p_B). \quad (11.75)$$

The ratio of P -wave \times phase space ($\sim p^3$) alone gives

$$\frac{f_{00}}{f_{+-}} = \frac{\mathcal{B}(\Upsilon(4S) \rightarrow B^0\bar{B}^0)}{\mathcal{B}(\Upsilon(4S) \rightarrow B^+B^-)} \equiv \frac{\Gamma(\Upsilon(4S) \rightarrow B^0\bar{B}^0)}{\Gamma(\Upsilon(4S) \rightarrow B^+B^-)} = 0.97 \pm 0.04 = \frac{0.492 \pm 0.009}{0.508 \mp 0.009}. \quad (11.76)$$

However, the vertex function $\Phi(p_B)$ of an nS state has n nodes, and cannot be neglected. The vertex function is the overlap integral between the $B\bar{B}$ and $\Upsilon(10580)$ [62]. In the quark pair creation model [52], the actual momentum p_B is close to an extremum of Φ , where variation with p is very low. This leads to [63]

$$\frac{\Gamma(\Upsilon(10580) \rightarrow B^0\bar{B}^0)}{\Gamma(\Upsilon(10580) \rightarrow B^+B^-)} = 0.9999 \pm 0.0001 = \frac{0.50}{0.50}. \quad (11.77)$$

In addition, there is a QED correction to the B^+B^- decay [64] due to the electrostatic attraction, which is, for pointlike particles $\frac{f_{00}}{f_{+-}} = 1/(1 + \frac{\pi\alpha}{2\beta}) = 0.85 = \frac{(0.46 \pm 0.02)}{(0.54 \mp 0.02)}$. Form factors reduce the QED effect to $0.86 \dots 0.93$ [65, 66], and the vertex function gives another large modification, to $0.96 \dots 1.03$, depending on the model for $\Phi(p_B)$. Since $\Phi(p_B)$ varies strongly with p_B , the ratio $f_{00} : f_{+-}$ is not constant, but varies with $m_{\Upsilon(10580)}$, *i.e.*, along the resonance curve!

The ratio $\mathcal{B}(\Upsilon(4S) \rightarrow B^0\bar{B}^0) : \mathcal{B}(\Upsilon(4S) \rightarrow B^+B^-)$ is therefore taken to be 1.0 by present experiments. The remaining uncertainty is on the order of $\pm 5\%$. There are no experimental results on $f_{00} : f_{+-}$, since event ratios are always coupled to ratios of branching fractions, such as $\mathcal{B}(B^0 \rightarrow e\nu X) : \mathcal{B}(B^+ \rightarrow e\nu X)$. With improved precision on the lifetime ratio, the weak assumption.⁸ $\Gamma(B^0 \rightarrow e\nu X) : \Gamma(B^+ \rightarrow e\nu X) = 1$ and a measurement of the individual semileptonic event rates on the $\Upsilon(4S)$ could settle this point on the experimental side. A measurement at BaBar could be made by

- Comparing exclusive event rates $N(D^+l\nu) : N(D^0l\nu)$, $N(D^{*+}l\nu) : N(D^{*0}l\nu)$, or
- Using the oscillation of like-sign/opposite-sign dilepton events to determine the fraction of neutral and charged (non-oscillating) B origin.

The first method will suffer from errors on D and D^* branching fractions. The second method uses the fact that the asymmetry

$$A = \frac{N_o \Leftrightarrow N_l}{N_o + N_l} = D \cos x \frac{\Delta t}{\tau_0} \quad (11.78)$$

⁸This assumption can be checked measuring the individual branching fractions with one fully reconstructed B^0 or B^+ (or their anti-particles).

oscillates with the lifetime difference, if N_l is the number of events with two like-sign leptons from direct B decays, and N_o is the number of events with two opposite-sign leptons from direct B decays. The amplitude of this oscillation is a dilution factor

$$D = \frac{f_{00}\tau_0}{f_{00}\tau_0 + f_{+-}\tau_+} \quad (11.79)$$

from which the ratio $(f_{00}\tau_0) : (f_{+-}\tau_+)$ can be calculated.

A second method to determine f_{+-} and f_{00} separately is the reconstruction of one and two B mesons per event in various exclusive final states. This yields *e.g.*, the number of reconstructed charged B mesons

$$N_1 = N_{\Upsilon} \cdot 2 \cdot f_{+-} \cdot \mathcal{B}(B^+ \rightarrow \dots) \cdot \epsilon_{\dots}, \quad (11.80)$$

where ϵ_{\dots} is the reconstruction efficiency for the final states used. The number of events with two reconstructed charged B mesons is

$$N_2 = N_{\Upsilon} \cdot f_{+-} \cdot [\mathcal{B}(B^+ \rightarrow \dots) \cdot \epsilon_{\dots}]^2. \quad (11.81)$$

Combining these yields

$$f_{+-} = \frac{N_1^2}{4N_2N_{\Upsilon}}. \quad (11.82)$$

The same holds for events with one or two reconstructed neutral B mesons, to yield f_{00} . Instead of giving just the ratio, this method has the advantage of giving f_{00} and f_{+-} separately, thereby addressing also the question of additional substantial $\Upsilon(4S)$ decay modes.

Using a sum of charged-only “ $D\pi$ -type” states (like $D\rho$, D^*a_1) gives approximately $\mathcal{B} \cdot \epsilon = 1 \cdot 10^{-3}$ (from ARGUS/CLEO efficiencies and branching fractions). The error on f_{+-} or f_{00} will be dominated by the smallest number, N_2 , which is then for a sample of 30/fb just 15. For a 5% error, a factor 5 more in branching fraction is required, which can be achieved by including final states with one or two π^0 mesons. However, the assumption that the efficiency for the reconstruction of two B mesons in the same events is just the product of the single efficiencies may no longer be justified and requires a thorough check.

11.4.2.1 $\Upsilon(4S) \rightarrow B^0\bar{B}^0\gamma$

The neutral B pairs produced via $\Upsilon(4S)$ decays offer the possibility of a clean determination of the CP -violating parameters, since they are in a C -odd state. For this program to be implemented, it is crucial to assess the role of background processes where the $B^0\bar{B}^0$ pair is in a C -even state, such as, *e.g.*, $B\bar{B}$ pairs produced by two photon scattering (with or without undetected e^+e^- pair in the final state) or the process $e^+e^- \rightarrow B\bar{B}\gamma$. Similar analyses have been carried out for Φ -factories [67], and in particular both the S -wave resonant contribution to $\phi \rightarrow K^0\bar{K}^0\gamma$ and the nonresonant one have been studied; the predicted branching fractions are in the range $10^{-9} \Leftrightarrow 10^{-5}$ [68].

An estimate of the branching fraction of the process

$$\Upsilon(4S) \rightarrow B^0 \bar{B}^0 \gamma \quad (11.83)$$

was given in [69]. As opposed to the case of the Kaon system, it is not expected that (11.83) is dominated by resonance decay into B pairs, since the nearest known 0^+ resonance is $\chi_{b0}(10235)$, which is below the b -production threshold and is rather narrow ($\Gamma \simeq 0.5 \text{ MeV}$). The resonance $\chi_{b0}(3P)$ is also expected to be below the open b production threshold; therefore, the potentially largest contribution to (11.83) arises from processes where $\Upsilon(4S)$ decays to $B^0 \bar{B}^0 \gamma$ via an intermediate virtual B^* ; the expected enhancement of such processes is mainly produced by the small $B^* \leftrightarrow B$ mass difference. In order to compute the branching fraction of this kind of process, one needs the coupling constant $g_{B^* B \gamma}$ and the strong coupling $\Upsilon B B^*$.

The coupling $g_{B^* B \gamma}$ can be written as a sum of two terms, describing respectively the coupling of the electromagnetic current to the heavy (b) and light (d) quarks:

$$g_{B^* B \gamma} = \frac{e_b}{\Lambda_b} + \frac{e_d}{\Lambda_d} \quad (11.84)$$

In the limit $M_b \rightarrow \infty$ the mass parameter Λ_b is proportional to M_b , whereas Λ_d remains constant. The parameters $\Lambda_{b,d}$ were estimated using heavy-quark symmetry arguments, quark models and QCD sum rules (see references in [69]): the results $\Lambda_b = 5.3 \text{ GeV}$, $\Lambda_d = 0.51 \text{ GeV}$ represent intermediate values among the various determinations. The theoretical uncertainty on Λ_d (which gives rise to the dominant contribution) does not exceed 30%.

As for the strong coupling constant $\Upsilon B B^*$, no direct experimental information on this quantity can be obtained; however, it can be determined by the knowledge of the coupling $\Upsilon B B$, in the infinite M_b limit. As a matter of fact, because of the spin symmetry arising from the decoupling of the spin of the heavy quarks, the couplings $\Upsilon B B$ and $\Upsilon B B^*$ are related, and their values can be estimated from the decay width $\Upsilon(4S) \rightarrow B^0 \bar{B}^0$ [69]. This observation allows the prediction of the branching fraction (11.83):

$$\mathcal{B}(\Upsilon(4S) \rightarrow B^0 \bar{B}^0 \gamma) \simeq 3 \times 10^{-9} \quad [69] \quad ; \quad (11.85)$$

therefore, the contamination from C even $B\bar{B}$ pairs arising from a final state containing an undetected photon is negligible, and would not destroy the predictions for CP -violating effects in the process $e^+ e^- \rightarrow \Upsilon(4S) \rightarrow B^0 \bar{B}^0$.

The analogous coupling, $\Upsilon(5S) B B$, can be computed from the decays $\Upsilon(5S) \rightarrow B B$. Taking into account the mass difference between B and B^* , the production rates at the $\Upsilon(5S)$ may be predicted:

$$\Gamma(\Upsilon(5S) \rightarrow B B) : \Gamma(B B^*) : \Gamma(B^* B^*) \simeq 1 : 3 : 4, \quad (11.86)$$

to be compared to the measurement made by the CUSB Collaboration:

$$\Gamma(B B) : \Gamma(B B^*) : \Gamma(B^* B^*) \simeq 1 : 2 : 4 \quad [54, 70]. \quad (11.87)$$

It is also possible to compute the production rates of $B_s^{(*)}\bar{B}_s^{(*)}$ pairs at the $\Upsilon(5S)$; using $M_{B_s^*} = 5421$ MeV and $M_{B_d^*} = 5324.8$ MeV one gets:

$$\begin{aligned}\Gamma(\Upsilon(5S) \rightarrow B_s B_s) : \Gamma(B_d B_d) &\simeq 1 : 4 , \\ \Gamma(B_s B_s^*) : \Gamma(B_d B_d^*) &\simeq 1 : 7 , \\ \Gamma(B_s^* B_s^*) : \Gamma(B_d^* B_d^*) &\simeq 1 : 27 .\end{aligned}\tag{11.88}$$

There are however theoretical predictions for a much higher B_s^* yield at the $\Upsilon(5S)$, which are described and exploited in Sections 11.5.4 and 11.5.5, in the context of a possible upgrade of PEP-II, giving reach to B_s physics.

11.4.3 Non $B\bar{B}$ Decays of the $\Upsilon(4S)$

The radiative and hadronic transitions between bottomonia have been studied in $\Upsilon(2S)$ and $\Upsilon(3S)$ data. Data samples at BABAR will be large enough to observe these transitions for the first time with $\Upsilon(4S)$ data, and several states will be discoverable. The bottomonium family is shown in Fig.11-26 [71]. The $\chi_b(3P)$ and the $\chi_b(1D)$ and $\chi_b(2D)$ states have not yet been observed, but are predicted to have masses below open bottom threshold.

The technique of multiple photon cascades proposed in Ref. [71] can be extended to cascades originating with an $\Upsilon(4S)$. The cascades of interest are shown in Fig. 11-27.

The estimates for $\mathcal{B}(\Upsilon(4S) \rightarrow \gamma\chi_b(3^3P_J))$ were made using measurements of $\mathcal{B}(\Upsilon(3S) \rightarrow \gamma\chi_b(2^3P_J))$ and the relation:

$$\mathcal{B}(\Upsilon(4S) \rightarrow \gamma\chi_b(3^3P_J)) = \mathcal{B}(\Upsilon(3S) \rightarrow \gamma\chi_b(2^3P_J)) \times (\Gamma_{\Upsilon(3S)}/\Gamma_{\Upsilon(4S)}).\tag{11.89}$$

The most promising transition in which to observe the $\chi_b(3^3P_1)$ is $\Upsilon(4S) \rightarrow \gamma\chi_b(3^3P_1)$, $\chi_b(3^3P_1) \rightarrow \gamma\Upsilon(3S)$. The estimated branching fraction for this sequence is 2.1×10^{-5} , or 210 events per 10^7 produced $\Upsilon(4S)$ events. If both photons are reconstructed, but not the $\Upsilon(3S)$, a one-constraint kinematic fit can be used to improve the mass resolution of the $\chi_b(3^3P_1)$. The laboratory and center-of-mass energy spectra of the transition photons are shown in Fig. 11-28(a), and the unconstrained $\chi_b(3^3P_1)$ and $\Upsilon(3S)$ mass distributions are shown in Fig. 11-28(b). The 6 MeV mass resolution is much smaller than the expected $\chi_b(3P)$ mass splitting. The combined Aslund reconstruction efficiency for the two photons is 73%. Should further combinatorial background rejection be required, leptonic, di-pion, or radiative $\Upsilon(3S)$ decays can be used. These comprise about half of all $\Upsilon(3S)$ decays.

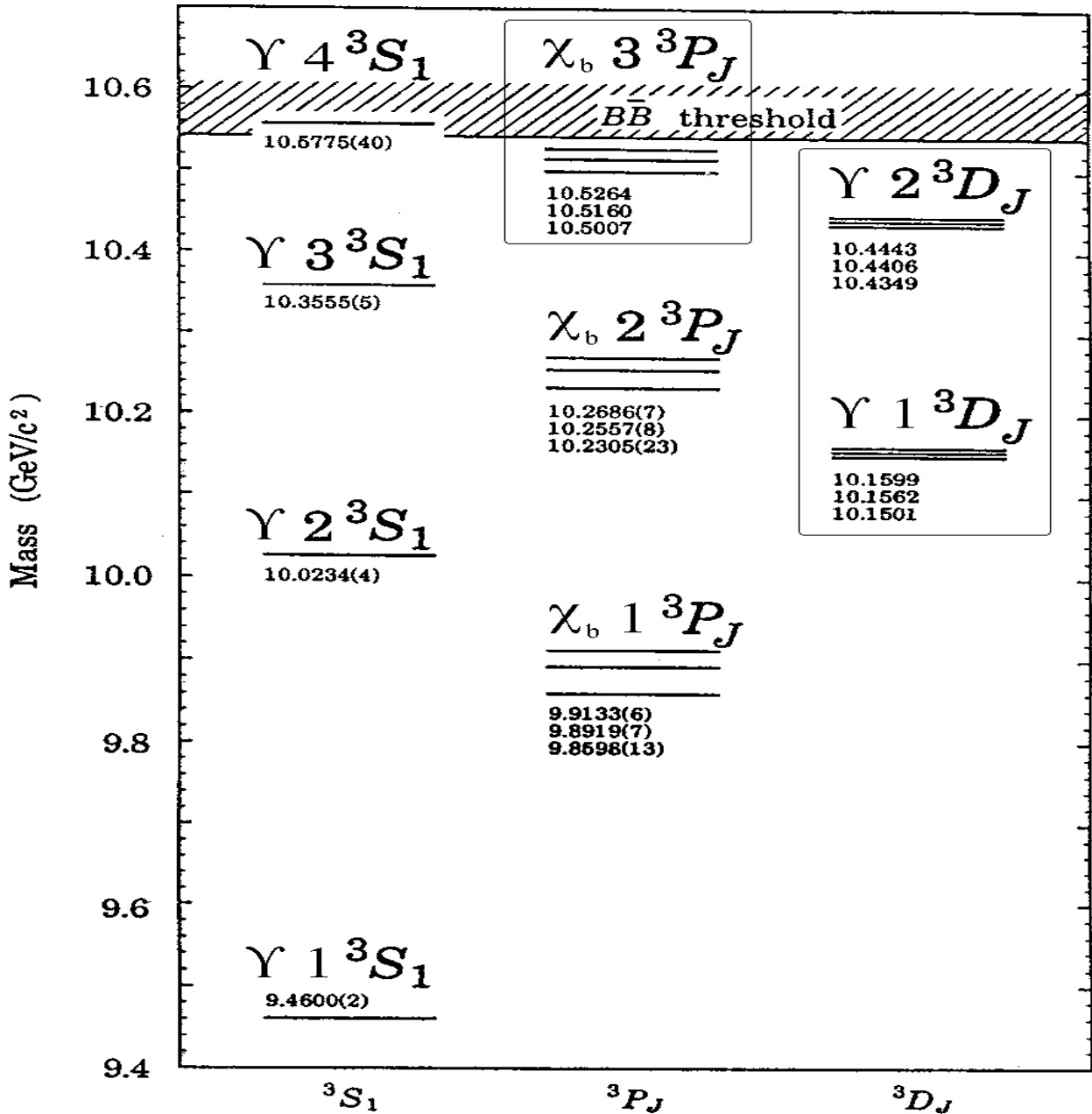


Figure 11-26. Masses of *S*, *P*, and *D* wave states in GeV/c^2 . The boxes denote states which have not yet been observed. The figure is adapted from Ref. [71].

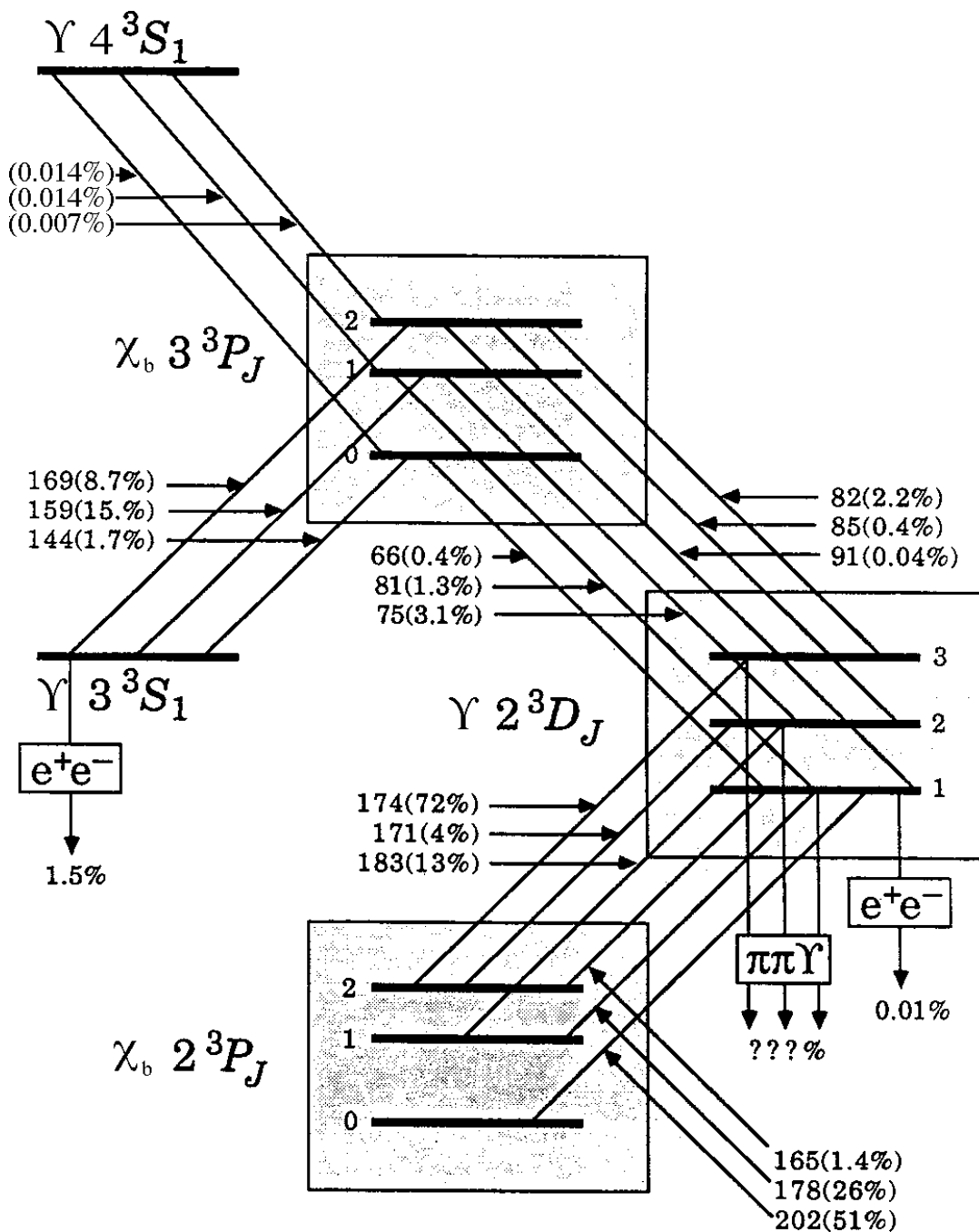


Figure 11-27. Photon cascades from the $\Upsilon(4S)$. Values within parentheses are branching fractions. The figure was adapted from Ref. [71].

97/11/05 12.23

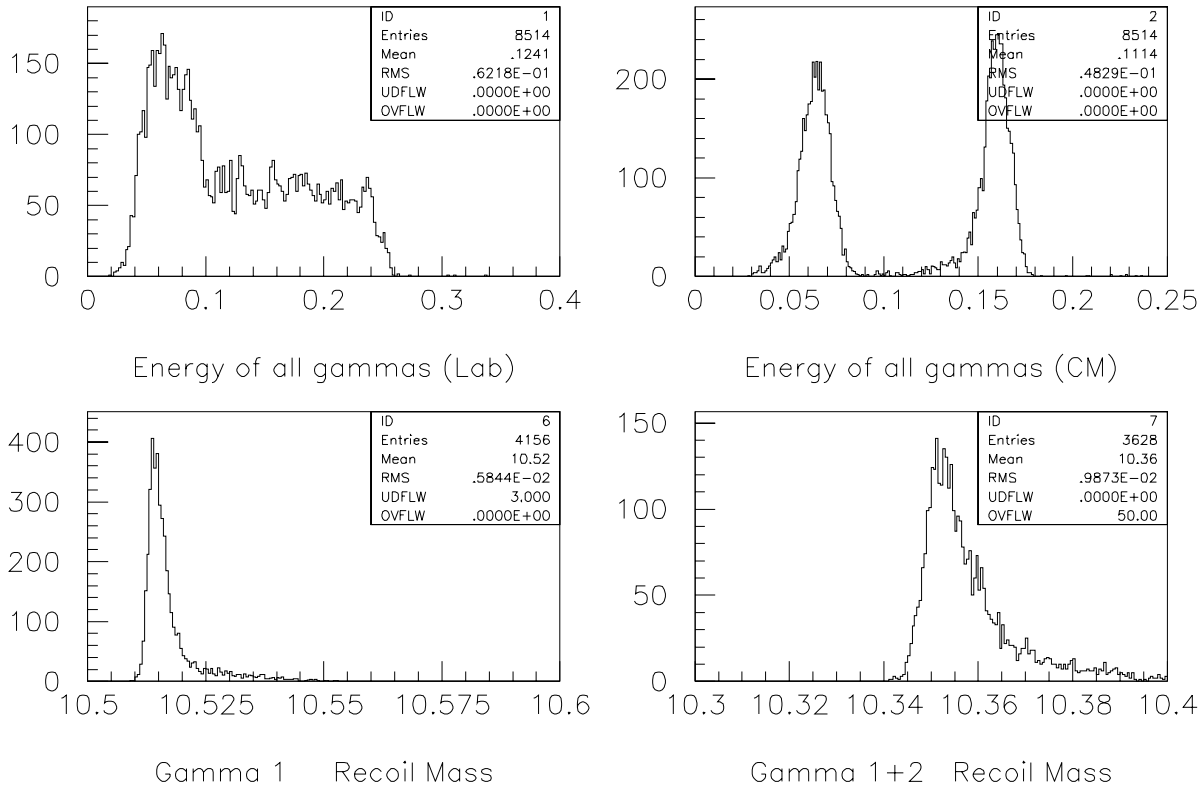


Figure 11-28. Energy of all γ rays in the (a) laboratory frame and (b) the $\Upsilon(4S)$ rest frame. The mass recoiling from the (c) primary photon and (d) the photon pair.

The D -wave (2^3P_3) state can be observed in the triple cascade $\Upsilon(4S) \rightarrow \gamma\chi_b(3^3P_2)$, $\chi_b(3^3P_2) \rightarrow \gamma\Upsilon(2^3P_3)$, $\Upsilon(2^3P_3) \rightarrow \gamma\chi_b(2^3P_2)$. The estimated branching fraction for this sequence is 2.2×10^{-6} , or 22 events per 10^7 produced $\Upsilon(4S)$ events. If only the three photons are observed, a one-constraint kinematic fit using $M(\chi_b(2^3P_2))$ can be used. If $M(\chi_b(3^3P_2))$ is estimated from $M(\chi_b(3^3P_1))$, then a second constraint is available for the kinematic fit. Since there are three transitions, cuts on any two recoil masses may be useful to establish the third transition. The laboratory energy spectra of the three photons are shown in Fig. 11-29(a), and the unconstrained $\chi_b(3^3P_1)$ and $\Upsilon(2^3D_3)$ masses are shown in Figs. 11-29(c) and (d). The combined `Aslund` reconstruction efficiency for the three photons is 60%. The 8-MeV $\Upsilon(2^3D_3)$ line width is sufficient to distinguish the $\Upsilon(2^3D_3)$ from the other $\Upsilon(2^3D_J)$ states.

97/11/05 12.06

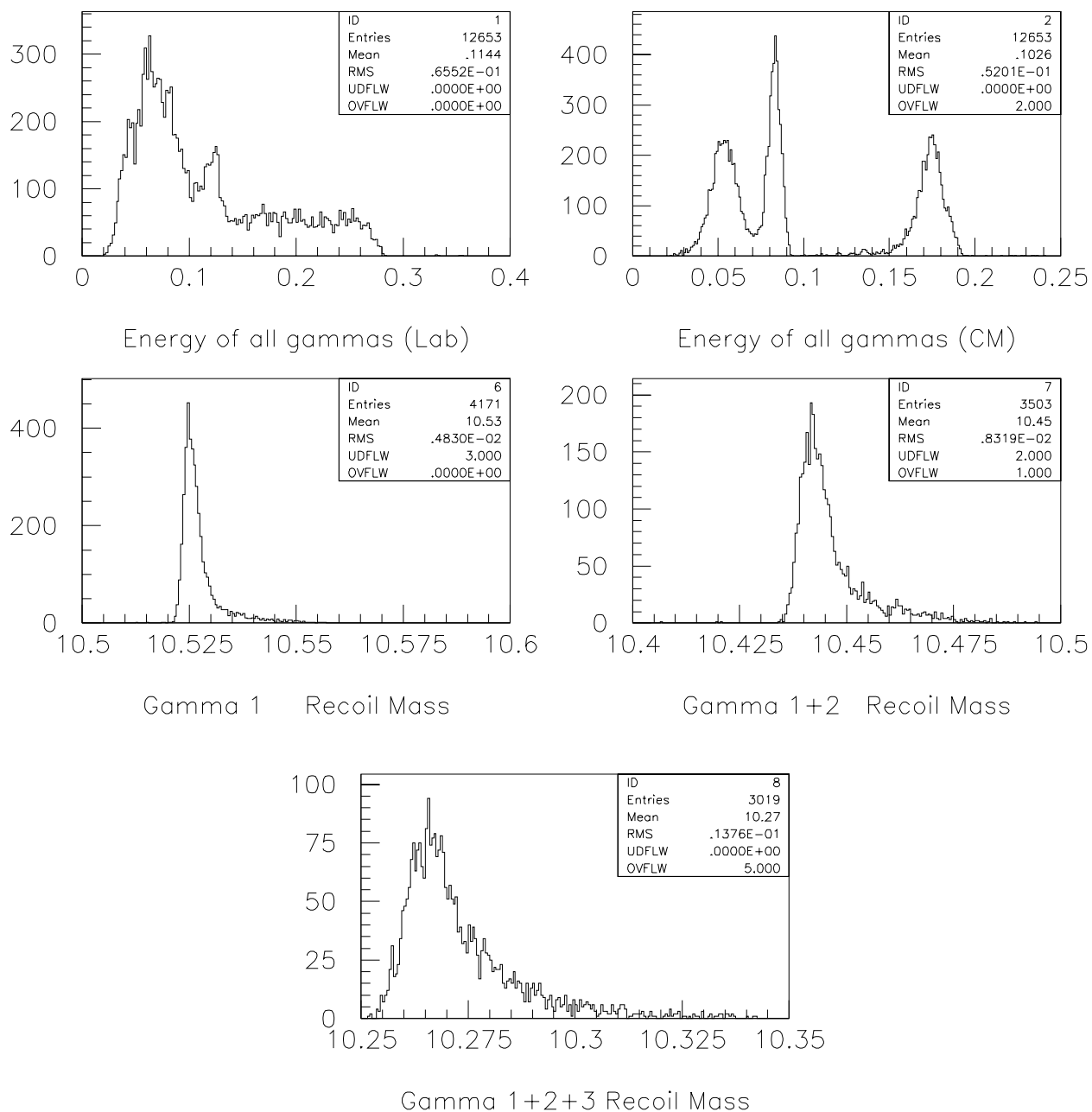


Figure 11-29. Reconstructed energy of all transition γ rays in (a) the laboratory frame and (b) the $\Upsilon(4S)$ rest frame. The mass recoiling from (c) the primary photon, (d) the primary and secondary photons, and (e) all three photons.

Table 11-7. Mass differences and widths for the two-pion transitions between Upsilon states [56].

Transition	ΔM (MeV)	$\Gamma_{\pi^+\pi^-}$ (keV)	$\Gamma_{\pi^0\pi^0}$ (keV)
$\Upsilon(2S) \rightarrow \pi\pi \Upsilon(1S)$	563	8.1	3.9
$\Upsilon(3S) \rightarrow \pi\pi \Upsilon(2S)$	332	0.7	0.5
$\Upsilon(3S) \rightarrow \pi\pi \Upsilon(1S)$	895	1.2	0.5

The two-pion transitions may be observable as well. Table 11-7 shows PDG widths and mass differences for measured two-pion transitions. The mass differences between the $\Upsilon(4S)$ and the $\Upsilon(3S)$, $\Upsilon(2S)$, and $\Upsilon(1S)$ are 225 MeV, 557 MeV, and 1120 MeV respectively. This suggests pion widths for the $\Upsilon(4S)$ of order 1 keV which corresponds to branching fractions 5×10^{-5} or ~ 500 produced decays per 10^7 $\Upsilon(4S)$ events. Should a subsequent decay of the Υ be required to suppress background, tens of events will be present in this same sample.

No calculations of $\Upsilon(2^3D_3) \rightarrow \pi\pi \Upsilon(1S)$ are available. The $\Upsilon(1^3D_3) \rightarrow \pi\pi \Upsilon(1S)$ branching fractions [72], however, have been calculated to be of order 10^{-3} . This suggests the D wave states will be detected only in radiative transitions.

11.5 The Case for $\Upsilon(5S)$ Running

The $\Upsilon(4S)$ is below the B_s production threshold. A dedicated $\Upsilon(5S)$ run will have a much lower priority than exploring CP violation at the $\Upsilon(4S)$. Only preliminary studies are presented here. Simulations were not performed for most topics discussed.

The main topics in B_s physics are mixing (determination of x_s), $\Delta\Gamma_{B_s}$ and CP violation. The state of the art anticipated for the beginning of the next decade is described in Section 11.5.1. Results are mainly expected from the CDF experiment at Fermilab. The sensitivity to x_s that can be achieved at SLD is perhaps better, but it is not certain that this experiment will run for the requisite time to perform the measurement. PEP II will not be able to compete with this accuracy, so no more will be said here on the determination of x_s . The prospects for discovering a lifetime difference $\Delta\Gamma_{B_s}$ between the mass eigenstates is more promising and is described in the feasibility study in Section 11.5.3. Such a study will benefit from the highest possible statistics. Partial B_s reconstruction techniques such as that explored in Section 11.5.2 could be important. CP violation in the B_s system is discussed in Section 7.7. For BABAR to produce B_s mesons requires running above the $\Upsilon(4S)$. Machine related issues for running above the $\Upsilon(4S)$ are treated in Sections 11.5.4 and 11.5.5.

11.5.1 CDF B_s Reach

Using Run I data (110 pb^{-1}), CDF has reported a signal of $58 \pm 12 B_s \rightarrow J/\psi \phi$, with the J/ψ decaying to muons and the ϕ decaying to K^+K^- [73]. At the peak of the CDF signal, the signal to noise ratio is $\simeq 1.3$. CDF expects 2 fb^{-1} for Run II. Scaling from Run I and factoring in trigger improvements gives $9000 B_s \rightarrow J/\psi \phi$ reconstructed for Run II [74]. The CDF x_S measurement from these data will be limited by the proper lifetime resolution of the CDF vertex detector, approximately $27 \mu\text{m}$, corresponding to an x_S reach up to about 15. CDF anticipates measuring the lifetime difference between B_{sL} and B_{sH} to 2–3%.

11.5.2 Partial B_s Reconstruction

The $\Upsilon(5S)$ energy is the most promising operating point for BABAR for physics of the B_s (see Section 11.5.4). Many physics topics use the $J/\psi \phi$ decay. In order to be competitive with CDF and others, a partial reconstruction technique may be useful. At the $\Upsilon(5S)$, the Unitary Quark Model [75] predicts the main production mechanism to be $B_s^* B_s^*$. For $B_s^* \rightarrow \gamma B_s$, $B_s \rightarrow J/\psi \phi$, the γ and the ϕ can be reconstructed with reasonable efficiency. The B_s^* has a relatively low momentum ($466 \text{ MeV}/c$) in the center of mass frame. With the approximation $p_{B_s} = 0$, and a measurement of the γ and ϕ , one can use the *missing momentum* to approximate the unmeasured J/ψ . Then, from the measured particles, the four-momenta of the B_s and the B_s^* can be reconstructed. Figures 11-30 show the missing (J/ψ) invariant mass, the B_s mass, and $\Delta M(B_s^* - B_s)$.

The ΔM resolution is 2.9 MeV , but it will not be possible to distinguish B_s^* from B_d^* based on ΔM since $\Delta M(B_s^* \leftrightarrow B_s) \simeq \Delta M(B_d^* - B_d)$. B_d are rejected because only a small fraction of B_d (or B_u) decays contain a ϕ , and these come mainly from $D^{(*)}$ and $D_s^{(*)}$. Such a ϕ is a secondary product of charm decay and is kinematically distinct from two-body $B_s \rightarrow J/\psi \phi$ decay. Figure 11-31 shows the result of applying the B_s^* partial reconstruction analysis selection criteria to $\text{Aslund } B_d^* \bar{B}_d^*$, $B_u^* \bar{B}_u^*$, and $B_s^* \bar{B}_s^*$ events (an 80k sample for each).

The plot for the latter pairs exhibits a strong peak right in the signal region despite the removal of $B_s \rightarrow J/\psi \phi$. This indicates the presence of backgrounds from other two body $B_s \rightarrow \phi X$ decays, where X is presumably other charmonia or a D^0 . While these are backgrounds to a $B_s \rightarrow J/\psi \phi$ analysis, they are potentially interesting channels for additional partial tags.

The overall efficiency for $B_s \rightarrow J/\psi \phi$ reconstruction, including geometrical acceptance, reconstruction, and K particle identification, but not branching fractions, is 49%. The partial- B_s^* tag sample can be estimated by scaling the $3.6 \times 10^7 \Upsilon(4S)$ events per 10^{33} -year by factors of

- 0.1 (for the ratio of $B_s^* B_s^*$: $\Upsilon(4S)$ cross-sections),
- 0.7 (for the PEP-II luminosity degradation factor for $\Upsilon(5S)$ running),
- $1.4 \cdot 10^{-3}$ (estimate of the $B_s \rightarrow J/\psi \phi$ branching fraction),

- 0.5 (for $\phi \rightarrow K^+ K^-$ branching fraction), and
- 2 (for the number of B_s mesons per event).

The result is that 3.6×10^3 events are expected per year. Assuming equal production of $B_d^* \bar{B}_d^*$, $B_u^* \bar{B}_u^*$, and $B_s^* \bar{B}_s^*$, the background-to-signal ratio is 27, although most of the background appears to be other potentially useful two body modes. A study of a method to suppress background from $D \rightarrow \phi X$ decays using the ϕ vertex multiplicity is included in Ref. [76].

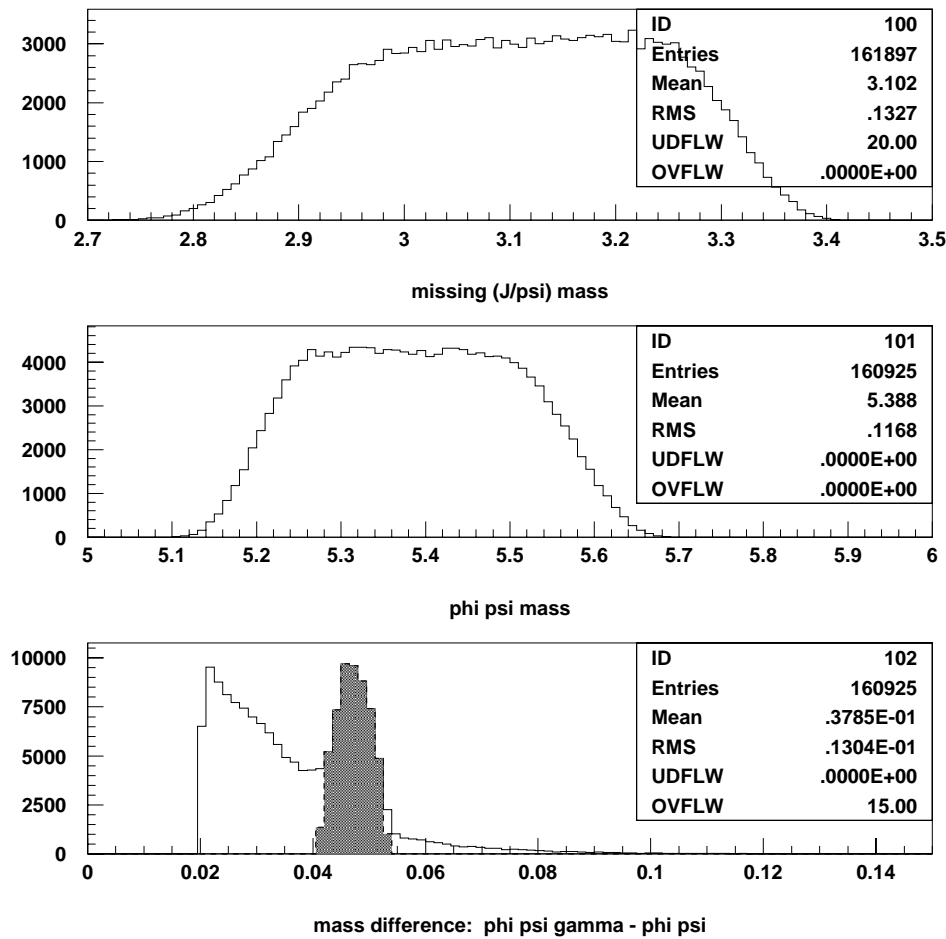


Figure 11-30. Mass plots for the partial reconstruction of the decay $B_s \rightarrow J/\psi \phi$: missing (J/ψ) mass (top); B_s pseudomass (middle); $B_s^* - B_s$ mass difference (bottom). On the bottom plot the signal has been emphasized.

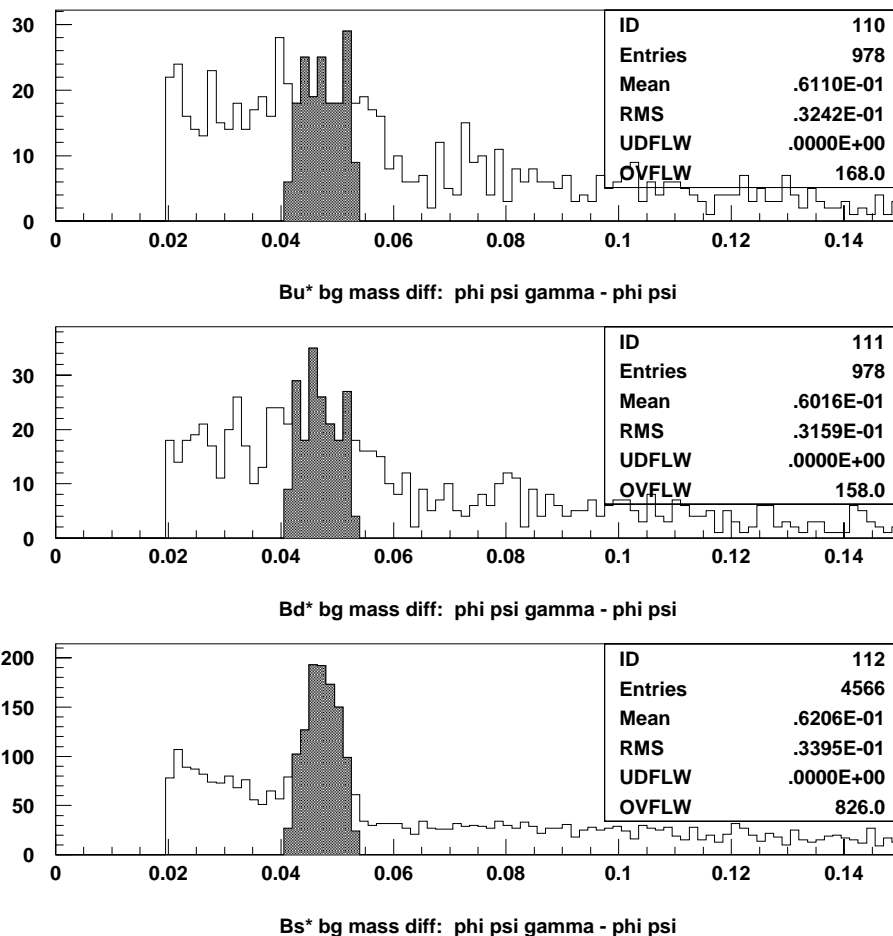


Figure 11-31. Aslund simulation of the background due to all $B^*\bar{B}^*$ pairs which are produced at the $\Upsilon(5S)$. A peak in the signal region is obvious in the bottom plot which corresponds to the $B_s^*\bar{B}_s^*$ pairs. It should presumably be interpreted as the production of other charmonium states than the J/ψ .

11.5.3 B_s -Meson Lifetime Differences

The mixing of B_s and \bar{B}_s is governed by two parameters, the mass difference Δm_{B_s} and the width difference $\Delta\Gamma_{B_s}$. An observable value of $\Delta\Gamma_{B_s}$ is expected in the Standard Model. Recent theoretical calculations [5, 30] predict

$$(\Delta\Gamma/\Gamma)_{B_s} = 0.16_{-0.09}^{+0.11}. \quad (11.90)$$

This result is comparable to the earlier calculation of [4] which gave

$$(\Delta\Gamma/\Gamma)_{B_s} = 0.18 \left(\frac{f_{B_s}}{200 \text{ MeV}} \right)^2 \quad (11.91)$$

The light B_{sL} is expected to be CP -even, with a shorter lifetime, while the heavy B_{sH} is expected to be CP -odd, with a longer lifetime.

The uncertainty in the prediction for $\frac{\Delta\Gamma_{B_s}}{\Gamma_{B_s}}$ is dominated by the decay constant f_{B_s} and the scalar ‘bag’ parameter B_{B_s} , and to a lesser extent by the b -quark mass and renormalization scale. A measurement of $\Delta\Gamma_{B_s}$ thus determines a certain linear combination of f_{B_s} and B_{B_s} . The Standard Model also predicts the ratio $\Delta m_{B_s}/\Delta\Gamma_{B_s}$. In this ratio, f_{B_s} cancels, and the uncertainty is dominated by the ratio of bag constants B_{B_s}/B_B . If this ratio is known, for instance from lattice gauge calculations, then a measurement of $\Delta\Gamma_{B_s}$ can be used to derive a value for Δm_{B_s} .

Observing a non-zero $\Delta\Gamma_{B_s}$ is not an observation of CP violation, but it does imply a natural separation of CP -even and CP -odd eigenstates by lifetime. This allows CP violation measurements to be made with lifetime-resolved and fully-reconstructed but otherwise untagged B_s events [77].

In order to obtain a sample of B_s decays, PEP-II must run at the $\Upsilon(5S)$ energy for substantial periods of time. PEP-II should be able to operate without modification at the $\Upsilon(5S)$ with 70 % of the luminosity at the $\Upsilon(4S)$. Higher luminosity is possible with expensive modifications to the machine. It is unlikely that this will be attempted until after several years of running at the $\Upsilon(4S)$.

There are two distinct approaches to measuring $\Delta\Gamma_{B_s}$. One is to neglect CP violation in the decay and measure the B_s lifetime using exclusively-reconstructed CP specific decay modes. For example, $B_s \rightarrow D_s^+ D_s^-$ is pure CP -even. The branching fraction is unknown and probably small, and the exclusive reconstruction efficiency is also small. A statistically better method (but with worse systematics) is to use $\phi\phi X$ events which may be predominantly from $B_s \rightarrow D_s^+ D_s^-$. The $B_s \rightarrow J/\psi\phi$ channel is clean experimentally but has both CP -even and CP -odd contributions. These may be separated by angular correlations, and it has been argued that CP -even modes will dominate by an order of magnitude [7]. In any case, one compares a CP -specific lifetime to the average B_s lifetime and then deduces the lifetime difference. It has been estimated that the B_d and B_s lifetimes should be identical to 1% [4, 5, 30, 31]. Note that B_s lifetime measurements which use only $B_s \rightarrow J/\psi\phi$ events, do not measure the appropriate true average B_s lifetime!

Perhaps the more obvious method of measuring $\Delta\Gamma_{B_s}$ is to fit the proper decay time distribution of inclusive B_s events to a sum of two exponential distributions, and this method is the focus of this study.

There are several complications to B -hadron-lifetime measurements, in general, at PEP-II. B or B_s mesons from $\Upsilon(4S)$ or $\Upsilon(5S)$ decays have no extra charged tracks to determine the production vertex, so the B or B_s decay lengths cannot be measured directly; only the decay length difference. Many of the decay tracks actually come from secondary D decay vertices rather than a B vertex, potentially biasing the decay length measurements.

There is also a variation in the boost parameter due to the finite momentum and angular distribution of the B or B_s in the Υ frame. For a measurement of the average B or B_s lifetime, the variation of the boost, can be averaged over, so it is of little concern. For the lifetime difference measurement, however, the variation in boost causes decay length differences which mimic lifetime differences, so the boost variation must be corrected for event by event.

The $\Upsilon(5S)$ will decay to a mixture of $B_s\bar{B}_s$, $B_s^*\bar{B}_s$, and $B_s^*\bar{B}_s^*$ events. This results in a range of B_s energies in the $\Upsilon(5S)$ frame, which further complicates the boost variations. If only events with a fully reconstructed B_s are used, the boost of the B_s is measurable, and continuum and $B\bar{B}X$ backgrounds are also eliminated. The momentum magnitude of the B_s in the $\Upsilon(5S)$ frame may then be used to classify the event as a $B_s\bar{B}_s$, $B_s^*\bar{B}_s$, or $B_s^*\bar{B}_s^*$ (without ever detecting the missing photon). From this, the boost of the other (unreconstructed, but vertexed) B_s may be calculated.

In summary, every event is now classified into one of three types, and for each event, there are two boost factors and a decay length difference.

The decay length difference distribution is required for the case of two different decay lengths. Let the two particles have decay lengths λ_x and λ_y . The probability of observing the two decays with absolute distances x and y from the production point is:

$$P(x, y, \lambda_x, \lambda_y) = \frac{1}{\lambda_x} e^{-\frac{x}{\lambda_x}} \frac{1}{\lambda_y} e^{-\frac{y}{\lambda_y}} \quad (11.92)$$

Integrating over $\Sigma = x + y$, keeping $\Delta = x \Leftrightarrow y$ constant, gives the probability of observing vertex separation Δ :

$$P(\Delta, \lambda_x, \lambda_y) = \frac{1}{\lambda_x + \lambda_y} e^{-\left[\Delta\left(\frac{\lambda_y - \lambda_x}{2\lambda_x\lambda_y}\right) + |\Delta|\left(\frac{\lambda_y + \lambda_x}{2\lambda_x\lambda_y}\right)\right]} \quad (11.93)$$

This form is still simple enough that it may be convoluted with a Gaussian distribution (or a sum of Gaussians) to include the effect of decay vertex resolution.

Since it is not known which decay vertex corresponds to which lifetime, it is necessary to use the symmetrized form:

$$P_{sym}(\Delta, \lambda_x, \lambda_y) = \frac{P(\Delta, \lambda_x, \lambda_y) + P(\Delta, \lambda_y, \lambda_x)}{2}. \quad (11.94)$$

A maximum likelihood fit may now be performed, for each of the 3 event classes. The two fit parameters are two B_s lifetimes τ_H and τ_L , and the three data are Δ , $\beta_1\gamma_1$ and $\beta_2\gamma_2$ for each event.

For the events with no B_s^* , it is known that they are 100% $B_{sH}B_{sL}$. For the other events, which have one or two B_s^* s, an equal mixture of $B_{sL}B_{sL}$, $B_{sL}B_{sH}$, $B_{sH}B_{sL}$ and $B_{sH}B_{sH}$ is expected.

For the $B_s\bar{B}_s$ case,

$$\frac{P_{sym}(\Delta, \beta_1\gamma_1 c\tau_H, \beta_2\gamma_2 c\tau_L) + P_{sym}(\Delta, \beta_1\gamma_1 c\tau_L, \beta_2\gamma_2 c\tau_H)}{2} \quad (11.95)$$

is used. For the other event classes, (in which there are one or two B_s^* s), the following form are used:

$$\begin{aligned} & \frac{1}{4} [P_{sym}(\Delta, \beta_1\gamma_1 c\tau_L, \beta_2\gamma_2 c\tau_L) + P_{sym}(\Delta, \beta_1\gamma_1 c\tau_L, \beta_2\gamma_2 c\tau_H) \\ & + P_{sym}(\Delta, \beta_1\gamma_1 c\tau_H, \beta_2\gamma_2 c\tau_L) + P_{sym}(\Delta, \beta_1\gamma_1 c\tau_H, \beta_2\gamma_2 c\tau_H)]. \end{aligned} \quad (11.96)$$

The number of events needed to distinguish two B_s widths from a single width can be estimated. The boost parameter is taken to be a constant (it actually varies by $\pm 10\%$ for $B_s^*\bar{B}_s^*$ events to $\pm 22\%$ for $B_s\bar{B}_s$ events). Vertex resolution is also neglected on the first pass of this analysis, for reasons of simplicity and cross-checking (it is, in fact, about $70 \mu\text{m}$ for each B_s meson, compared to the $400 \mu\text{m}$ decay length, if PEP-II is operated with the HER at 12 GeV. This represents a 24% resolution.). The probability of observing decay length difference Δ given individual widths Γ_x and Γ_y is

$$p(\Delta, \Gamma_x, \Gamma_y) = \frac{2\Gamma_x\Gamma_y}{\Gamma_x + \Gamma_y} e^{-\Delta\frac{\Gamma_x - \Gamma_y}{2}} e^{-|\Delta|\frac{\Gamma_x + \Gamma_y}{2}} \quad (11.97)$$

As an illustration, the case of an equal mix of HH, HL, LH, and LL events is considered (the HL+LH-only case has somewhat more statistical power). If the individual widths are $\Gamma(1 + \delta/2)$ and $\Gamma(1 \Leftrightarrow \delta/2)$, the probability becomes

$$P(\Delta, \delta) = \frac{1}{4} [p(\Delta, 1 \Leftrightarrow \delta/2, 1 \Leftrightarrow \delta/2) + p(\Delta, 1 \Leftrightarrow \delta/2, 1 + \delta/2) + p(\Delta, 1 + \delta/2, 1 \Leftrightarrow \delta/2) + p(\Delta, 1 + \delta/2, 1 + \delta/2)] \quad (11.98)$$

where units have been chosen such that the average width, Γ , is unity.

The expected χ^2 value per event can be calculated, with width difference, δ , compared to the null hypothesis of $\delta = 0$:

$$\chi^2(\delta) = \int_0^\infty d\Delta \frac{[P(\Delta, \delta) \Leftrightarrow P(\Delta, 0)]^2}{P(\Delta, \delta)} \quad (11.99)$$

This allows the calculation of how many events, N , are required to rule out a single width at a confidence level of $S\sigma$ for a given value of δ :

$$N = S^2 / \chi^2(\delta) . \quad (11.100)$$

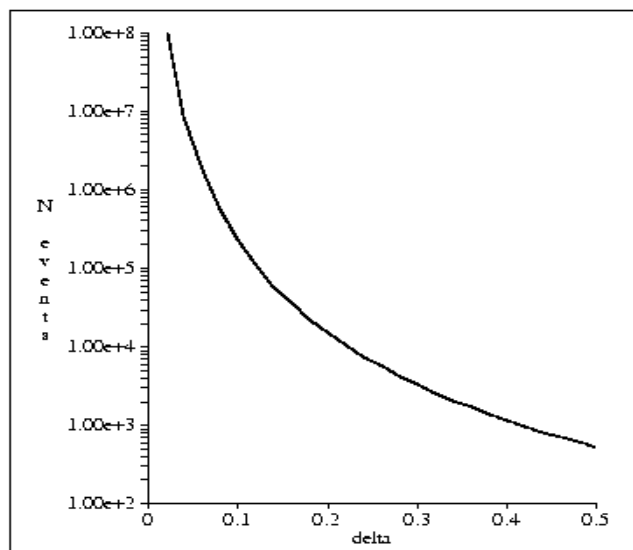


Figure 11-32. Number of events required for 3σ separation of the two B_s lifetimes as a function of δ , the width difference.

As shown in Fig. 11-32, 36000 events are required to give a 3σ signal for two widths differing by the theoretically predicted value, $\delta = 0.16$.

When the 24% resolution is included, the impact on the final numbers is surprisingly tiny, on the 3% level. This is due to the fact that most of the information on the lifetime and lifetime differences comes from the tail of the exponential distribution, where resolution does not have much effect: resolution has the strongest effect on the $t = 0$ part of the exponential.

11.5.4 B_s Production Cross-Section

The B_s production cross-section above the $\Upsilon(4S)$ has not been measured directly, although there is total cross-section data from a CESR scan [54, 55], shown in Fig. 11-33. Superimposed on the data is the cross-section prediction of the Unitarized Quark Model (UQM) [78], a coupled-channel model which is in reasonable agreement with the data. The model's predictions for B_d , and B_s production are shown in Fig. 11-33(b) and (c). In the $\Upsilon(5S)$ region, near $E_{cm}=10.87$ GeV, the model predicts the B cross-section is dominated by B^*B^* and $B_s^*B_s^*$ production. The CUSB experiment detected an excess of Doppler-broadened, monochromatic photons from B^* decay near the $\Upsilon(5S)$, and throughout the region between the $\Upsilon(4S)$ and 11.2 GeV [79, 80, 81].

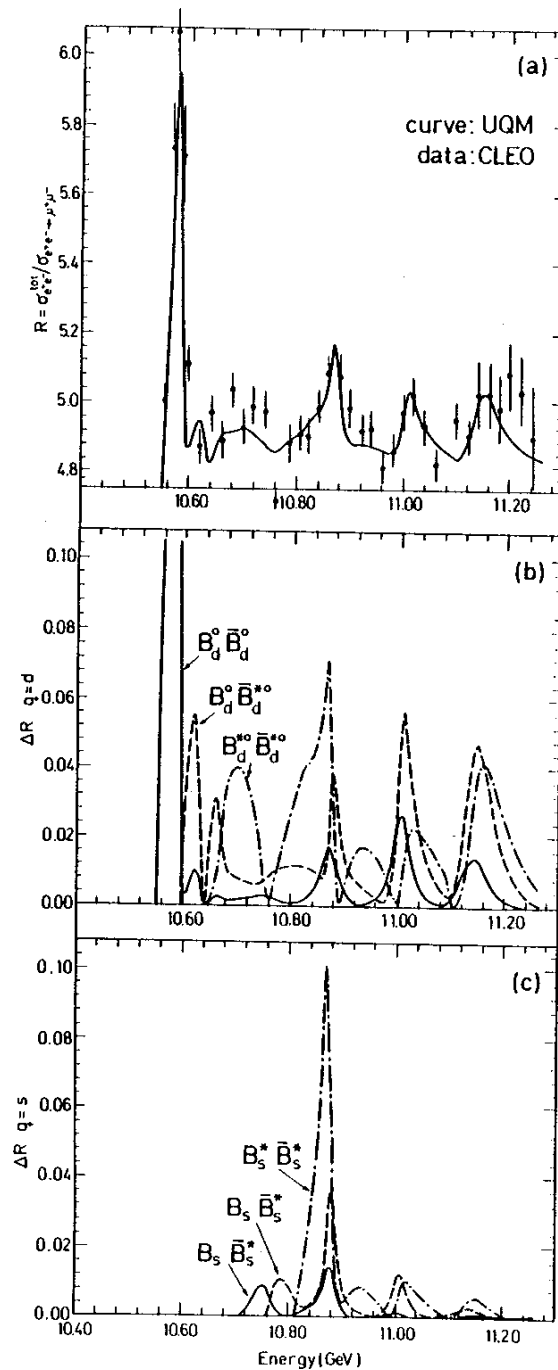


Figure 11-33. (a) Data on R from CLEO compared with the Unitarized Quark Model, (b) The contribution to R (ΔR) from non-strange neutral channels as predicted by the Unitarized Quark Model, (c) The ΔR from strange channels. The figure is taken from Ref. [75].

According to the UQM model, inclusive B_s production peaks near 10.87 GeV with a contribution to R of 0.1 unit, or approximately 1/10 of the total $\Upsilon(4S)$ rate. A final word of caution is, however, in order, since alternatives to the UQM prediction exist (see the end of Section 11.4.2).

11.5.5 PEP-II Options for Running Above the $\Upsilon(4S)$

As explained in the previous section the best place for B_s physics is to run on the $\Upsilon(5S)$ resonance. There are three options for the operation of the machine at this center-of-mass energy.

- **Basic option:** Unchanged machine and detector. The luminosity would drop by 30% because of either longer bunches or lower currents. The boost is slightly increased from 0.5585 to 0.5735. Minor modifications would have to be made to the interaction region, for instance the Q1 quadrupole setup would have to be changed. These modifications are thought to be doable in “one day.”
- **Intermediate option:** Keep a similar boost to that at the $\Upsilon(4S)$ and maximize the luminosity. This would require the installation of a new rf station for a cost of \$ 3.3 million but would have no implication on the detector. A shutdown of a few weeks would be necessary to implement this option.
- **Maximal option:** Highest boost and luminosity. The high-energy ring would run at 12 GeV. The interaction region would have to be redesigned and rebuilt. Much more rf power would have to be added. That expensive option would require a shutdown of several months.

At the time of writing, the run plan calls for running enough years on the $\Upsilon(4S)$ to do all the possible CP physics. “Enough” means of the order of three to five years, at least. Depending on the achievements of other experiments at that time a choice can be envisaged between not running on the $\Upsilon(5S)$ or one of the options outlined above.

11.6 Summary and Conclusions

In this chapter devoted to early physics accessible to BaBar, results of studies have been presented which indicate that results on B_d flavor oscillation with unprecedented precision are within reach after one good year of running. A similar conclusion for the determination of the lifetime ratio $\frac{\tau_{B^+}}{\tau_{B_d}}$ cannot be stated at this time since the studies are still in progress.

New measurements that shed light on the properties of the $\Upsilon(4S)$ and its decays to pairs of B mesons have been described. The interesting possibility of breaking new ground in Υ spectroscopy

at the $\Upsilon(4S)$ is evoked for the first time. The paper studies on B_s physics pave a rough way towards a possible physics program for future years. Partial reconstruction techniques that may find an application at the $\Upsilon(4S)$ have been pioneered.

References

- [1] A. J. Buras, M. Jamin and P. H. Weisz, *Nucl. Phys.* **B347**, 491 (1990).
- [2] S. Herrlich and U. Nierste, *Nucl. Phys.* **B419**, 292 (1994); *Phys. Rev. D* **52**, 6505 (1995); *Nucl. Phys.* **B476**, 27 (1996).
- [3] J. S. Hagelin, *Nucl. Phys.* **B193**, 123 (1981);
E. Franco, M. Lusignoli and A. Pugliese, *Nucl. Phys.* **B194**, 403 (1982);
L. L. Chau, *Phys. Rep.* **95**, 1 (1983);
A. J. Buras, W. Slominski and H. Steger, *Nucl. Phys.* **B245**, 369 (1984).
- [4] M. B. Voloshin, *et al.*, *Sov. J. Nucl. Phys.* **46**, 112 (1987).
- [5] M. Beneke, G. Buchalla and I. Dunietz, *Phys. Rev. D* **54**, 4419 (1996).
- [6] M. Beneke *et al.*, hep-ph/9808385
- [7] R. Aleksan *et al.*, *Phys. Lett. B* **316**, 567 (1993).
- [8] G. De Domenico and Ch. Yèche, “Dilepton Analysis in BABAR Experiment: Measurement of the Mixing Parameter δM_B and the Study of the T (CP) Violation Purely in Mixing,” BABAR Note # 409, (1998).
- [9] H. Albrecht *et al.*, (ARGUS Collaboration), *Phys. Lett. B* **374**, 256 (1996).
- [10] J. Bartelt *et al.*, (CLEO Collaboration), *Phys. Rev. Lett.* **71**, 1680 (1993).
- [11] Particle Data Group, *Eur. Phys. Jour. C* **3** (1998).
- [12] A. Einstein, B. Podolsky and N. Rosen, *Phys. Rev.* **47** (1935).
- [13] B. Kayser, “ CP Violation, Mixing and Quantum Mechanics,” NSF-PT-96-3 (1996), in *Proceedings of the 28th International Conference on High Energy Physics*, Warsaw, Poland, July (1996).
- [14] F. Le Diberder, “ CP Violation as Seen from the ΔZ Distribution,” BABAR Note # 42, (1990).
- [15] J. Chay, H. Georgi and B. Grinstein, *Phys. Lett. B* **247**, 399 (1990).
- [16] B. Guberina *et al.*, *Phys. Lett. B* **89**, 111 (1979);
N. Bilic, B. Guberina and J. Trampetic, *Nucl. Phys.* **B248**, 261 (1984);
B. Guberina, R. Rückl and J. Trampetic, *Z. Phys. C* **33**, 297 (1986).
- [17] M. A. Shifman and M. B. Voloshin, *Sov. J. Nucl. Phys.* **41** (1985); *JETP* **64**, 698 (1986).

- [18] I. I. Bigi, N.G. Uraltsev and A. I. Vainshtein, *Phys. Lett. B* **293**, 430 (1992); *Phys. Lett. B* **297**, 477(E) (1993).
- [19] I. I. Bigi *et al.*, *Phys. Rev. Lett.* **71**, 496 (1993); *Phys. Lett. B* **328**, 431 (1994).
- [20] *Int. J. Mod. Phys. A* **9**, 2467 (1994).
- [21] I.I. Bigi and N. Uraltsev, *Phys. Lett. B* **280**, 271 (1992).
- [22] A. V. Manohar and M. B. Wise, *Phys. Rev. D* **49**, 1310 (1994);
W. Grimus, *Fortschr. Phys.* **36**, 201 (1988).
- [23] P. Ball, M. Beneke and V. M. Braun, *Phys. Rev. D* **52**, 3929 (1995);
M. Shifman, N. Uraltsev and A. Vainshtein, *Phys. Rev. D* **51**, 2217 (1995);
I. Bigi, M. Shifman and N. Uraltsev, *Ann. Rev. Nucl. Part. Sci.* **47**, 591 (1997).
- [24] A. J. Buras and P. H. Weisz, *Nucl. Phys.* **B333**, 66 (1990);
A. J. Buras *et al.*, *Nucl. Phys.* **B370**, 69 (1992); Addendum, *Nucl. Phys.* **B375**, 501 (1992);
A. J. Buras, M. Jamin and M. E. Lautenbacher, *Nucl. Phys.* **B400**, 37 (1993); *Nucl. Phys.* **B400**, 75 (1993).
- [25] G. Altarelli *et al.*, *Nucl. Phys.* **B187**, 461 (1981);
M. Ciuchini *et al.*, *Nucl. Phys.* **B415**, 403 (1994); *Z. Phys. C* **68**, 239 (1995).
- [26] E. Bagan *et al.*, *Nucl. Phys.* **B432**, 38 (1994); *Phys. Lett. B* **342**, 362 (1995); *Phys. Lett. B* **351**, 546 (1995).
- [27] L. Koyrakh, *Phys. Rev. D* **49**, 3379 (1994).
- [28] M. Voloshin and M. Shifman *Sov. J. Nucl. Phys.* **45**, 292 1987.
- [29] M. Neubert and C. T. Sachrajda, *Nucl. Phys.* **B438**, 238 (1995).
- [30] Y.-Y. Keum and U. Nierste, *Phys. Rev. D* **57**, 4282 (1998).
- [31] I. Bigi *et al.*, in “B Decays,” S. Stone, ed., World Scientific, Singapore (1994), 2nd rev. edition.
- [32] G. Bellini, I. Bigi, and P. Dornan, *Phys. Rep.* **289**, 1 (1997) and in Ref. [29].
- [33] M. Neubert and C. Sachrajda, *Nucl. Phys.* **B483**, 339 (1997).
- [34] N. Uraltsev *Phys. Lett. B* **376**, 303 1996.
- [35] J.L. Rosner *Phys. Lett. B* **379**, 267 1996.

- [36] T. Junk, in *Proceedings of the 2nd International Conference on B Physics and CP Violation*, Honolulu, Hawaii, March (1997).
- [37] Bigi and Uraltsev ZP
- [38] I. I. Bigi, in “Continuous Advances in QCD 1996,” M. Polikarpov, ed., World Scientific, Singapore (1996).
- [39] A. Lenz, U. Nierste and G. Ostermaier, *Phys. Rev. D* **56**, 7228 (1997).
- [40] A. F. Falk, M. B. Wise, and I. Dunietz, *Phys. Rev. D* **51**, 1183, (1995).
- [41] I. Dunietz, *et al.*, *Phys. Rev. Lett.* **73**, 1075 (1994); *Eur. Phys. Jour. C* **1**, 211 (1998);
F. Close *et al.*, *Phys. Rev. D* **57**, 5653 (1998);
G. Childaze, A. F. Falk, and A. A. Petrov, *Phys. Rev. D* **58**, 034013 (1998).
- [42] A. L. Kagan *et al.*, *Phys. Rev. D* **51**, 6196 (1995);
M. Ciuchini, E. Gabrielli, and G. F. Giudice, *Phys. Lett. B* **388**, 353 (1996); *Phys. Lett. B* **293**, 489E (1997).
- [43] D. Bortoletto, “*B* Physics at Hadron Colliders,” invited talk presented at the Aspen Winter Conference on Particle Physics, January 22, (1997).
- [44] <http://wwwcn.cern.ch/~claires/lepblife.html>.
- [45] D. Boutigny *et al.*, BaBar Technical Design Report, SLAC-R-95-457, March (1995).
- [46] J. Chauveau, P. David, and Ph. Leruste, “Statistical Tools for Vertex Reconstruction. Application to the Determination of the Tagging *B* Vertex in Lepton Tagged *CP* Events,” BaBar Note # 279, (1996).
- [47] C. De la Vaissière, H. Briand, and N. Regnault, “Lifetimes with Full *B* Reconstruction,” BaBar Note # 436, (1998).
- [48] Xin Chou Lou, BaBar note in preparation.
- [49] U. Mallik *et al.*, BaBar note in preparation.
- [50] J. Alexander *et al.*, (CLEO Collaboration), *Phys. Rev. Lett.* **64**, 2226 (1990).
- [51] H. Albrecht *et al.*, (ARGUS Collaboration), *Z. Phys. C* **65**, 619 (1995);
S. Werner, Dissertation (in German), HD-IHEP 91-9, Heidelberg (1992).
- [52] A. Le Yaouancet *et al.*, *Phys. Rev. D* **8**, 2223 (1973).

- [53] A. Le Yaouanc *et al.*, *Phys. Lett. B* **71**, 397 (1977);
S. Ono, *Phys. Rev. D* **23**, 1118 (1981);
A. Le Yaouanc *et al.*, *Hadron Transitions in the Quark Model*, Gordon and Breach Science Publishing (1988).
- [54] D.M.J. Lovelock *et al.*, (CUSB Collaboration), *Phys. Rev. Lett.* **54**, 377 (1985).
- [55] D. Besson *et al.*, (CLEO Collaboration), *Phys. Rev. Lett.* **54**, 381 (1985).
- [56] R. M. Barnett *et al.*, *Phys. Rev. D* **54**, 1 (1996).
- [57] Using a Fortran program of S. Werner.
- [58] Valuable discussions with Stefan Werner and Jürgen Stiewe on the mass measurements, and useful information on PEP II from John Seeman are gratefully acknowledged.
- [59] C. Bebek *et al.*, (CLEO Collaboration), *Phys. Rev. D* **36**, 1289 (1987).
- [60] D. P. Barber *et al.*, (DORIS Machine Group, ARGUS, CRYSTAL BALL), *Phys. Lett. B* **135**, 498 (1984);
W. W. MacKay *et al.*, (CUSB, CESR), *Phys. Rev. D* **29**, 2483 (1984);
A. S. Artamov *et al.*, *Phys. Lett. B* **137**, 272 (1984);
S. E. Baru *et al.*, (MD1), *Z. Phys. C* **56**, 547 (1992).
- [61] A. A. Sokolov and I. M. Ternov, *Sov. Phys. Dokl.* **8**, 1203 (1964).
- [62] A. D. Martin and C.-K. Ng, *Z. Phys. C* **40**, 133 (1988).
- [63] S. Ono, A. I. Sanda, and N. A. Törnqvist, *Phys. Rev. D* **38**, 1619 (1988);
S. Ono, *Acta Phys. Polon.* **B15**, 201 (1984).
- [64] D. Atwood and W. J. Marciano, *Phys. Rev. D* **41**, 1736 (1990).
- [65] G. P. Lepage, *Phys. Rev. D* **42**, 3251 (1990).
- [66] N. Byers and E. Eichten, *Phys. Rev. D* **42**, 3885 (1990).
- [67] S. Nussinov and T. N. Truong, *Phys. Rev. Lett.* **63**, 2003 (1989);
N. Paver and Riazuddin, *Phys. Lett. B* **246**, 240 (1990).
- [68] F. E. Close, in “Workshop on Physics and Detectors for DAΦNE”, edited by G. Pancheri, Frascati, (1990) p. 309.
- [69] P. Colangelo, G. Corcella and G. Nardulli, *Phys. Rev. D* **54**, 1212 (1996).
- [70] J. L. Franzini *et al.*, (UCSB Collaboration), *Phys. Rev. Lett.* **65**, 2947 (1990).

-
- [71] W. Kwong and J. L. Rosner, *Phys. Rev. D* **38**, 279 (1988).
- [72] P. Moxhay, *Phys. Rev. D* **37**, 2557 (1988).
- [73] F. Abe *et al.*, *Phys. Rev. Lett.* **77**, 1945 (1996).
- [74] CDF Collaboration, Technical Design Report for Run II.
- [75] S. Ono, A. I. Sanda, and N. A. Tornqvist, *Phys. Rev. Lett.* **55**, 2938 (1985).
- [76] J. Cooke III and J. M. Izen, BABAR note in preparation.
- [77] R. Fleischer and I. Dunietz, *Phys. Rev. D* **55**, 258 (1977).
- [78] K. Heikkila , S. Ono, and N. A. Tornqvist, *Phys. Rev. D* **29**, 110 (1984); *Phys. Rev. D* **29**, 2136(E) (1984).
- [79] K. Han *et al.*, *Phys. Rev. Lett.* **55**, 36 (1985).
- [80] N.A. Tornqvist, *Acta Phys. Polon.* **B16**, 503 (1985); *Acta Phys. Polon.* **B16**, 683(E) (1985).
- [81] N.A. Tornqvist, *Phys. Rev. Lett.* **53**, 878 (1984).

This page was intentionally left blank.

Charm, τ , QCD, and Two-Photon Physics

An e^+e^- storage ring running at or near the $\Upsilon(4S)$ resonance is an excellent laboratory for studying charm, τ , QCD and two-photon physics. The $b\bar{b}$ production cross-section accounts for less than one-fifth of the total s -channel cross-section at the $\Upsilon(4S)$ (see Table 3-1). The $c\bar{c}$ cross-section is larger than that of $b\bar{b}$, and the $\tau^+\tau^-$ cross-section is almost as large. In addition, there is a large two-photon cross-section of approximately 1 nb for $e^+e^- \rightarrow e^+e^-X$ where X is a hadronic system with $W > 2$ GeV, which allows the study of processes that are difficult to access through the s -channel.

It is useful to compare the number of $c\bar{c}$ and $\tau^+\tau^-$ events which are expected at BABAR after approximately one year of running, with other data samples that will exist at that time. The design luminosity for the initial phase of PEP-II running is $3 \times 10^{33} \text{ cm}^{-2}\text{s}^{-1}$. A running period of 10^7 s at one-sixth of this luminosity would result in 5 fb^{-1} or 5 million events for each nb of cross-section. Therefore, it is expected that approximately 6 million $c\bar{c}$ and 5 million $\tau^+\tau^-$ events will be produced in the first year or so of running. The charm and tau data samples expected from other experiments at the time BABAR starts taking data are shown in Table 12-1. The integrated luminosity for CLEO assumes that 2–3 fb^{-1} will be recorded in 1998; 5.1 fb^{-1} were recorded with the CLEO II detector with no silicon detector. The largest charm samples will be from CLEO, the Fermilab fixed-target experiments E687, E791 and FOCUS, and the LEP experiments. The largest tau samples will be from CLEO and the LEP experiments.

In this chapter, the following questions regarding non- B physics are addressed:

1. How can charm decays be used at BABAR to search for physics beyond the Standard Model? In particular, $D^0\bar{D}^0$ mixing, CP violation in D decays, and rare or forbidden D decays are discussed.
2. How well can BABAR measure properties of charm decays that increase our understanding of the Standard Model or enhance our ability to make conclusive measurements in B decays? Some topics that are discussed are leptonic decay rates and decay constants, semileptonic decay rates and form factors, and hadronic decay rates and resonant substructure.
3. Can the measurements of the properties of the τ lepton be improved? What can be learned from precision measurements? The τ lifetime, decay rates, rare decays, the τ neutrino mass, CP violation, and the Lorentz structure in τ decays are all discussed.

Table 12-1. Summary of largest charm and tau samples from other experiments, expected at the time BaBar starts taking data.

e^+e^- Expts.	Data Sample Size	Charm and Tau Samples
CLEO (1999)	$\approx 12 \text{ fb}^{-1}$	16 million $c\bar{c}$ 11 million $\tau^+\tau^-$
LEP expts.	$4 \times 10^6 Z_s$ per experiment	$\approx 500,000 c\bar{c}$ $\approx 150,000 \tau^+\tau^-$ per experiment
SLD	$500 \times 10^3 Z_s$	86,000 $c\bar{c}$ 24,000 $\tau^+\tau^-$
Fixed Target Expts	Year Completed	Fully Reconstructed Charm Decays
E687 (FNAL)	1992	100,000
E791 (FNAL)	1992	200,000
FOCUS (FNAL)	1997	≈ 1 million

4. What can be learned in the area of QCD and two-photon physics? The prospects for light-meson spectroscopy in D and B decays, studies of resonance production of light-quark mesons and exotic mesons and glueballs, exclusive production of meson and baryon pairs, anomalous physics in two-photon interactions, and studies of baryon production in $e^+e^- \rightarrow q\bar{q}$ are explored.

12.1 Charm Physics

Charm decays can be used to search for new physics or to measure parameters of the Standard Model. This section describes simulation studies of BaBar's sensitivity to $D^0\bar{D}^0$ mixing and CP violation in D decays. The motivation for studying rare decays, leptonic and semileptonic decays, and nonleptonic decays is discussed, and current measurements are summarized. The section begins with an overview of the characteristics of charm decays from the $c\bar{c}$ continuum and from B decays.

Acceptance and reconstruction efficiency will depend in detail on the decay mode and the analysis. Searches for rare signals will require more stringent event selection criteria than will searches for orbitally excited charm mesons, for example. Nonetheless, the main factors that will contribute

to the expected signal rates can be summarized. Charm is produced in $e^+e^- \rightarrow c\bar{c}$ events with a cross-section of approximately 1.3 nb, producing about 2.6 million charm decays per fb^{-1} . Charm is also produced in $e^+e^- \rightarrow b\bar{b}$ events since most B mesons decay to charm. The cross-section for $e^+e^- \rightarrow \Upsilon(4S) \rightarrow B\bar{B}$ is approximately 1.05 nb, and the number of charm per B meson is approximately 1.2, so the charm production rate will be about the same as in $c\bar{c}$ events. In both continuum production and B decays, more D^0 mesons are produced than D^+ because D^{*0} final states always contain a D^0 but never a D^+ (due to kinematic constraints) and the D^{*+} decays two-thirds of the time to D^0 , and otherwise to D^+ .

Historically, e^+e^- experiments at symmetric colliders have relied on the kinematic separation of charm decays at high center-of-mass momentum (from $e^+e^- \rightarrow c\bar{c}$) to reduce backgrounds. BABAR will have excellent particle identification for hadrons over a large range of momenta and some ability to resolve charm vertices, so it might be possible to use charm decays from $b\bar{b}$ events as well as from $c\bar{c}$ events, and to use events from a wider kinematic range than those used in previous experiments.

The unshaded histograms in Fig. 12-1 show the momentum distributions for D^0 and D^+ mesons produced in $c\bar{c}$ and $b\bar{b}$ events, for the center-of-mass, (a) and (b), and laboratory, (c) and (d), frames. For both $c\bar{c}$ and $b\bar{b}$ events, the mean laboratory D momentum is about 0.5 GeV/c higher than the mean center-of-mass momentum. Separation of $c\bar{c}$ from $b\bar{b}$ events on the basis of D momentum is clearly better in the center-of-mass frame than in the laboratory frame.

The momentum distribution of kaons from charm decay depends strongly on the parent momentum and the multiplicity of the decay. The unshaded histograms in Figs. 12-2 (a)–(f) show the center-of-mass momentum distributions for kaons from $D^0 \rightarrow K^-\pi^+$, $D^+ \rightarrow K^-\pi^+\pi^+$, and $D^0 \rightarrow K^-\pi^+\pi^-\pi^+$ decays as representative two-, three- and four-body decays from $c\bar{c}$ and $b\bar{b}$ events. The unshaded histograms in Figs. 12-3 (a)–(f) show the corresponding laboratory distributions. The mean kaon momentum is about 20% higher in the laboratory frame than in the center-of-mass frame. In Fig. 12-4, a scatter plot of laboratory momenta versus center-of-mass momenta is shown for kaons from $D^+ \rightarrow K^-\pi^+\pi^+$ from $c\bar{c}$ events.

Track reconstruction is not 100% efficient due to acceptance, interactions with material, and limitations of the tracking algorithm. The cross-hatched histograms in Figs. 12-2 and 12-3 show the momentum distributions for the kaons simulated in BBSim that have corresponding reconstructed tracks. The reconstruction efficiency is about 89% for all three modes in $c\bar{c}$ events. It varies from about 86% for $D^0 \rightarrow K^-\pi^+\pi^-\pi^+$ to 91% for $D^0 \rightarrow K^-\pi^+$ in $b\bar{b}$ events. The shaded histograms in Fig. 12-1 show the momentum distributions for D decays in which all tracks were reconstructed. The efficiency for reconstructing all tracks is about 75% for D s in both $c\bar{c}$ events and $b\bar{b}$ events.

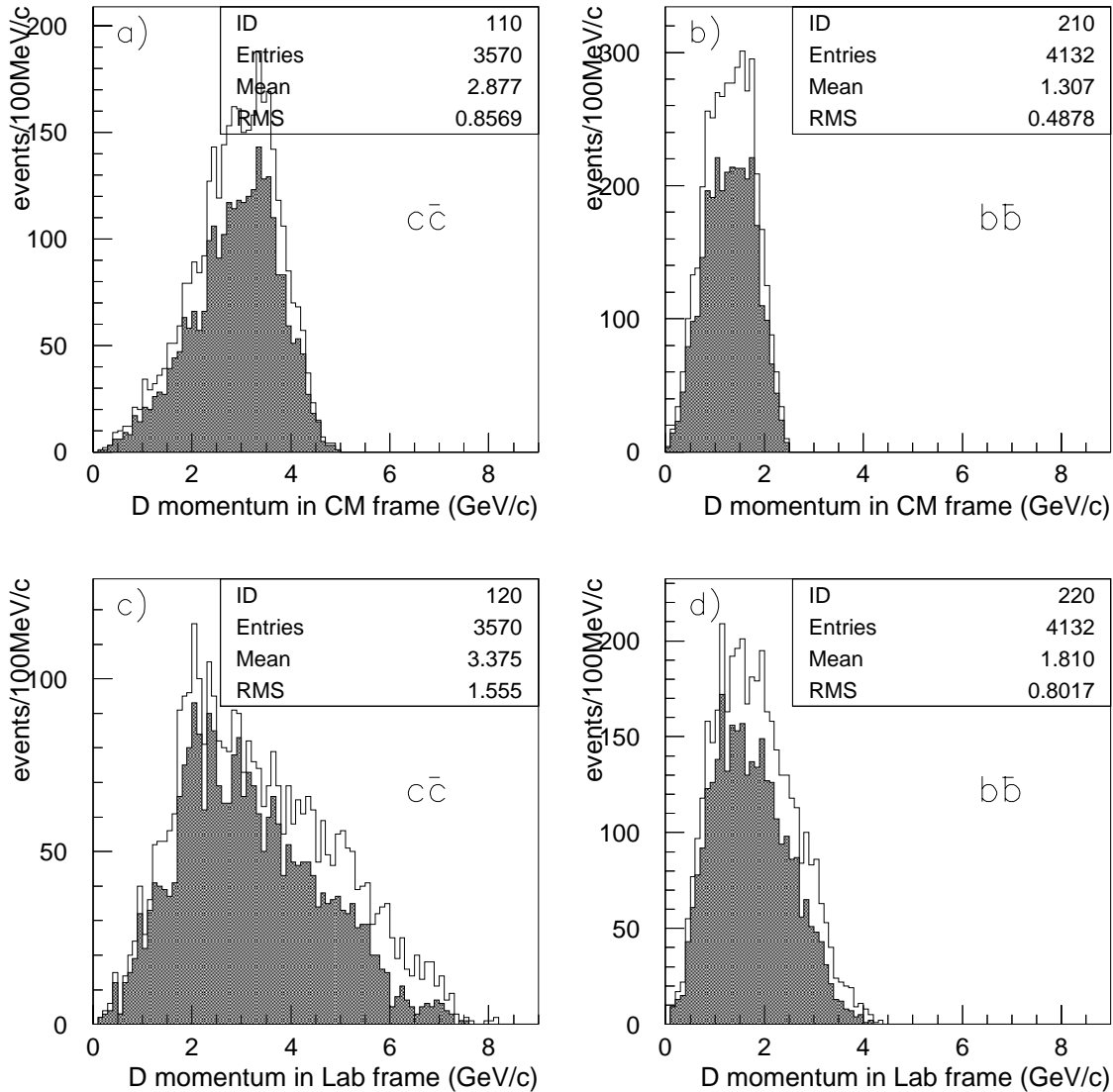


Figure 12-1. Momentum distributions for $D^0 \rightarrow K^- \pi^+$, $D^+ \rightarrow K^- \pi^+ \pi^+$ and $D^0 \rightarrow K^- \pi^+ \pi^- \pi^+$, decays. The events were produced in $c\bar{c}$ events (a, c) and $b\bar{b}$ events (b, d). Figures (a) and (b) show the center-of-mass momentum distributions. Figures (c) and (d) show the laboratory momentum distributions. The unshaded histograms correspond to the generated D mesons; the shaded histograms correspond to the D decays in which all the decay particles are reconstructed. The statistics in the upper right corner of each histogram correspond to the unshaded histograms.

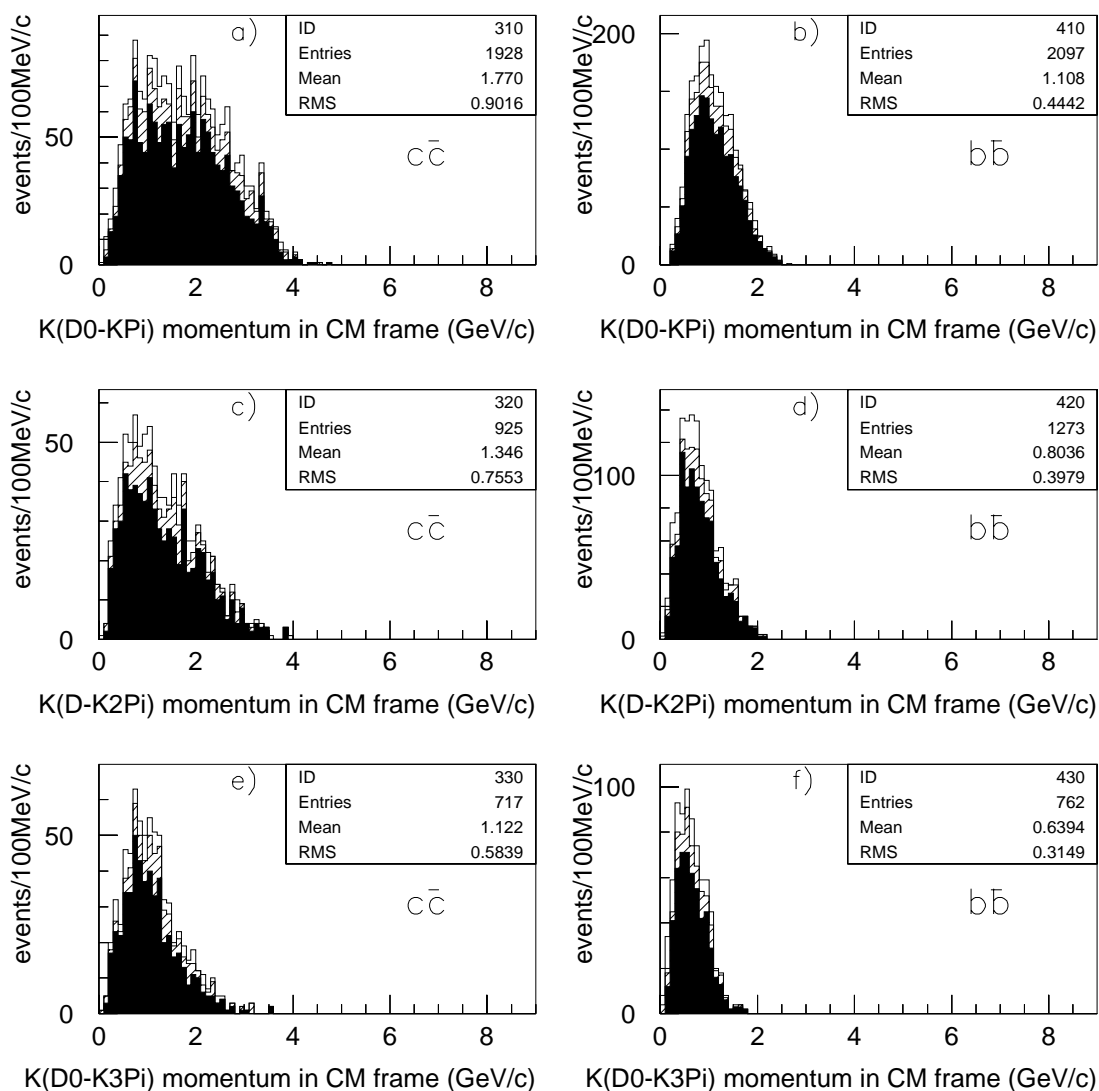


Figure 12-2. Center-of-mass momentum distributions for kaons from (a) $D^0 \rightarrow K^- \pi^+$, (c) $D^+ \rightarrow K^- \pi^+ \pi^+$, and (e) $D^0 \rightarrow K^- \pi^- \pi^+ \pi^+$ decays from $c\bar{c}$ continuum events. Distributions for kaons from D s from $b\bar{b}$ events are shown in Figures (b), (d) and (f). The unshaded histograms correspond to the generated kaons, the cross-hatched histograms to the reconstructed kaons, and the dark histograms to the kaons that are reconstructed and identified as kaons. The statistics in the upper right corner of each histogram correspond to the unshaded histograms.

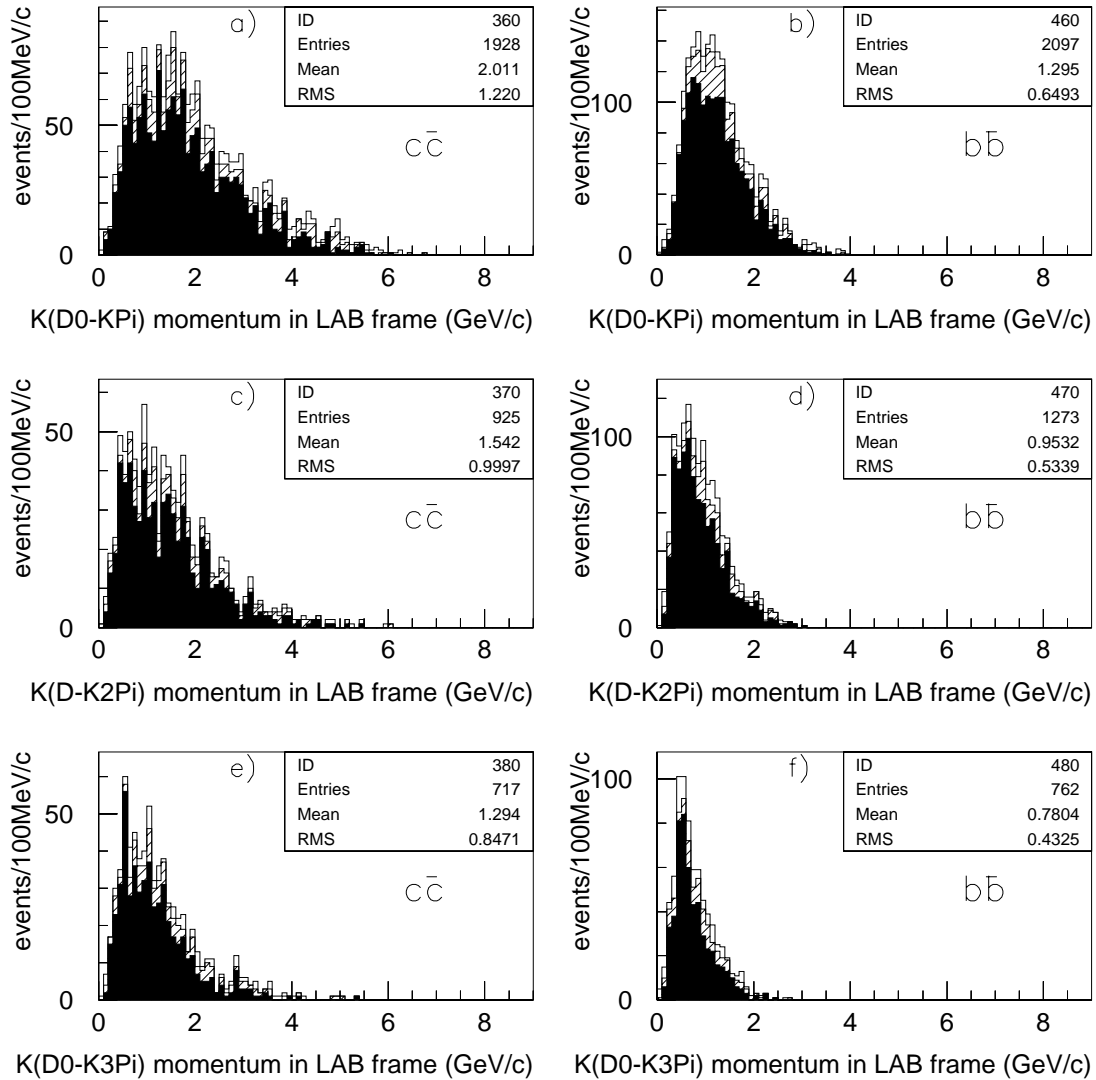


Figure 12-3. Laboratory momentum distributions for kaons from (a) $D^0 \rightarrow K^- \pi^+$, (c) $D^+ \rightarrow K^- \pi^+ \pi^+$, and (e) $D^0 \rightarrow K^- \pi^- \pi^+ \pi^+$ decays from $c\bar{c}$ continuum events. Distributions for kaons from D s from $b\bar{b}$ events are shown in Figures (b), (d) and (f). The unshaded histograms correspond to the generated kaons, the cross-hatched histograms to the reconstructed kaons, and the dark histograms to the kaons that are reconstructed and identified as kaons. The statistics in the upper right corner of each histogram correspond to the unshaded histograms.

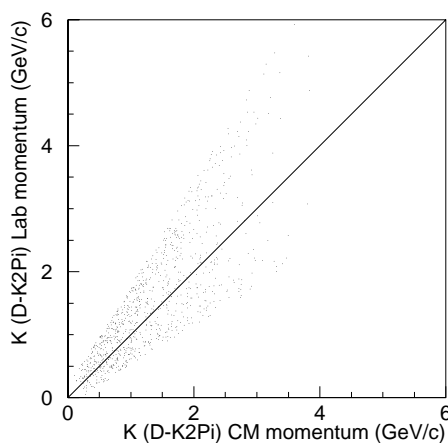


Figure 12-4. Scatter plot of laboratory versus center-of-mass momenta for kaons from $D^+ \rightarrow K^- \pi^+ \pi^+$ from $c\bar{c}$ events.

Most D decays produce at least one kaon, so the Cherenkov angle measured in the DIRC will provide good discrimination against combinatorial background. The dark histograms in Figs. 12-2 and 12-3 show the momentum distributions for the kaons simulated in `BBsim` with reconstructed tracks that are identified as kaons. Figure 12-5 shows the efficiency for kaon identification as a function of laboratory momentum in $c\bar{c}$ and $b\bar{b}$ events for the three representative D decays. The total kaon identification efficiencies vary between 81% and 85% for the three modes and the two production mechanisms.

Requiring tracks from a decay to form a common vertex also reduces combinatorial backgrounds. Fixed target experiments have required significant vertex separation in identifying charm decay candidates, and this possibility is also considered for `BABAR`. Figure 12-6 shows the component of the D decay length $\beta\gamma c\tau$ along the beam direction and perpendicular to the beam direction, for D^0 and D^+ mesons from $c\bar{c}$ events. Although the boost does increase the longitudinal flight distance of the D s moving in the forward direction in the center-of-mass frame, it decreases the longitudinal flight distance of some of the D s that are moving backwards. The fact that the D^+ lifetime is about a factor of 2.5 longer than the D^0 lifetime is evident in the distributions. Figure 12-7 shows the corresponding distributions from $b\bar{b}$ events. The decay lengths are shorter for D s from $b\bar{b}$ events since the average D momentum is lower.

In Figs. 12-8 and 12-9, the distributions of the errors on the reconstructed vertex position are shown for the three representative D decays, for D s from $c\bar{c}$ and $b\bar{b}$ events. The error is the difference between the true vertex position and the vertex position calculated for the reconstructed D decay tracks. The distributions for the x , y , and z components of the error are shown, as well as for the total error. The resolution is about $150 \mu\text{m}$, which is comparable to the transverse flight path for the D^0 and about half that for the D^+ . Vertex separation is clearly more powerful for reducing D^+ backgrounds than D^0 backgrounds due to the longer lifetime of the D^+ .

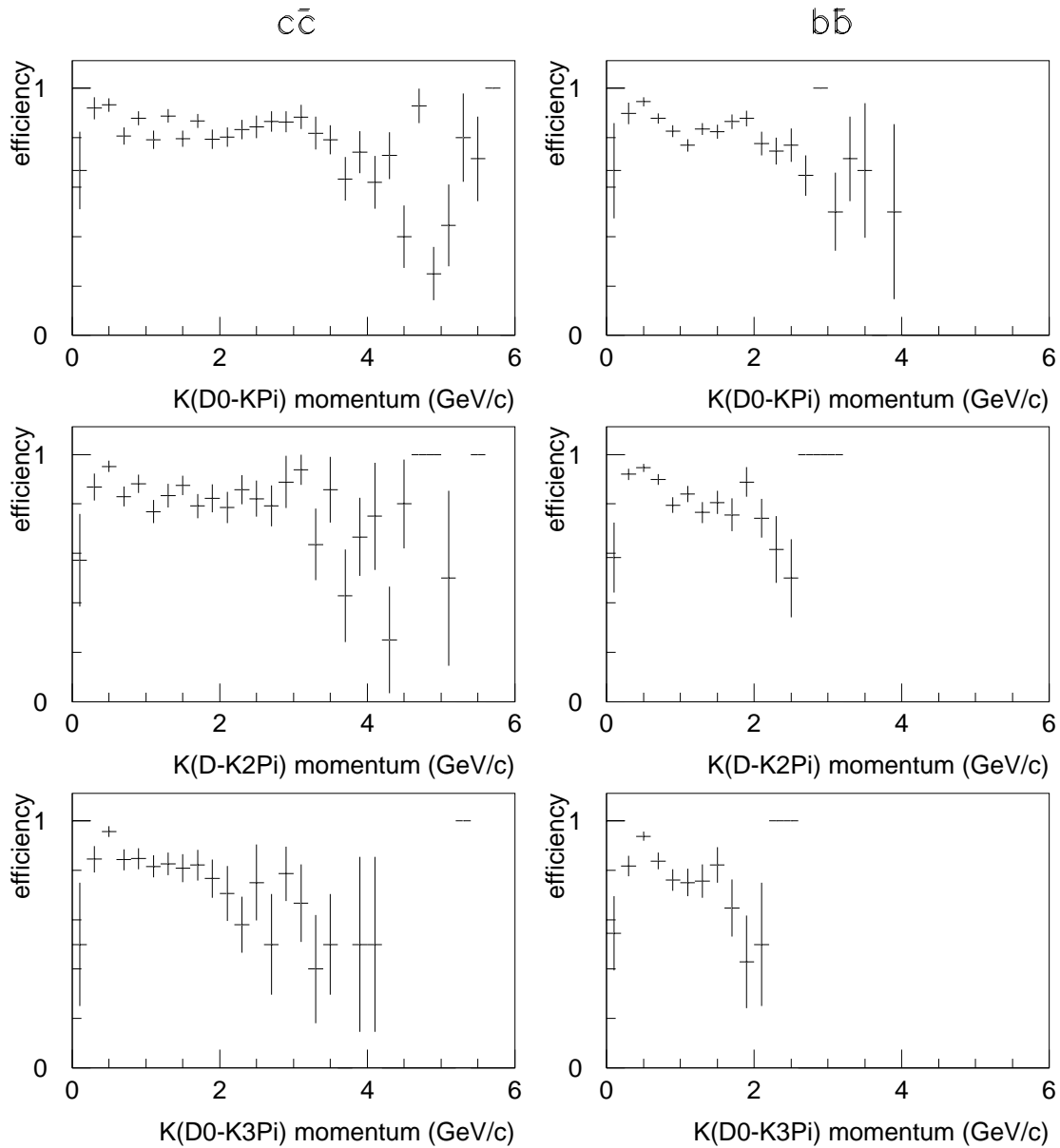


Figure 12-5. Efficiency for kaon identification as a function of laboratory momentum for three representative decay modes, for D mesons from $c\bar{c}$ and $b\bar{b}$ events.

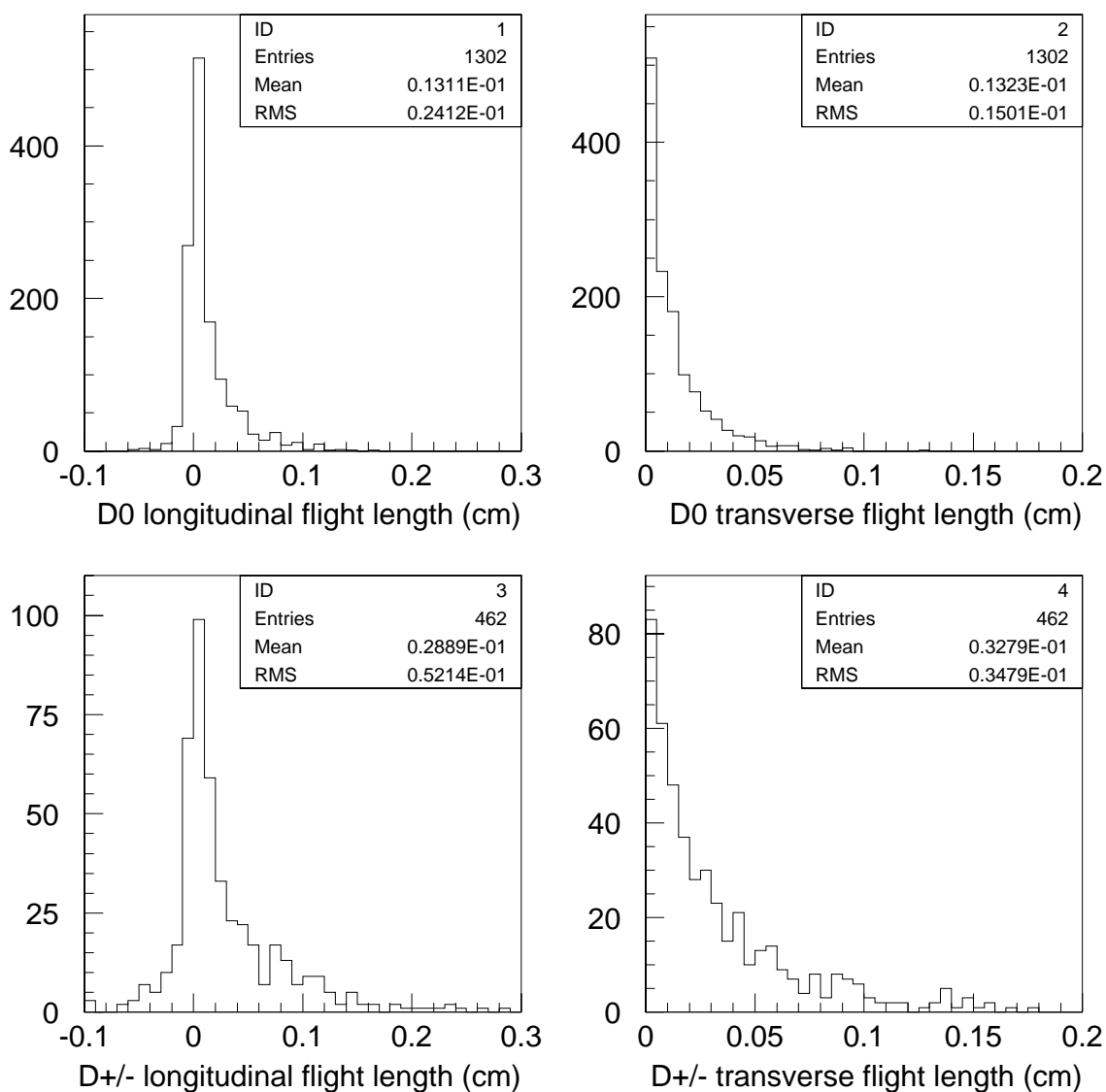


Figure 12-6. The component of the D decay length $\beta\gamma c\tau$ along the beam direction (left figures) and perpendicular to the beam direction (right figures), for D^0 (top figures) and D^{+} (bottom figures) mesons from $c\bar{c}$ events.

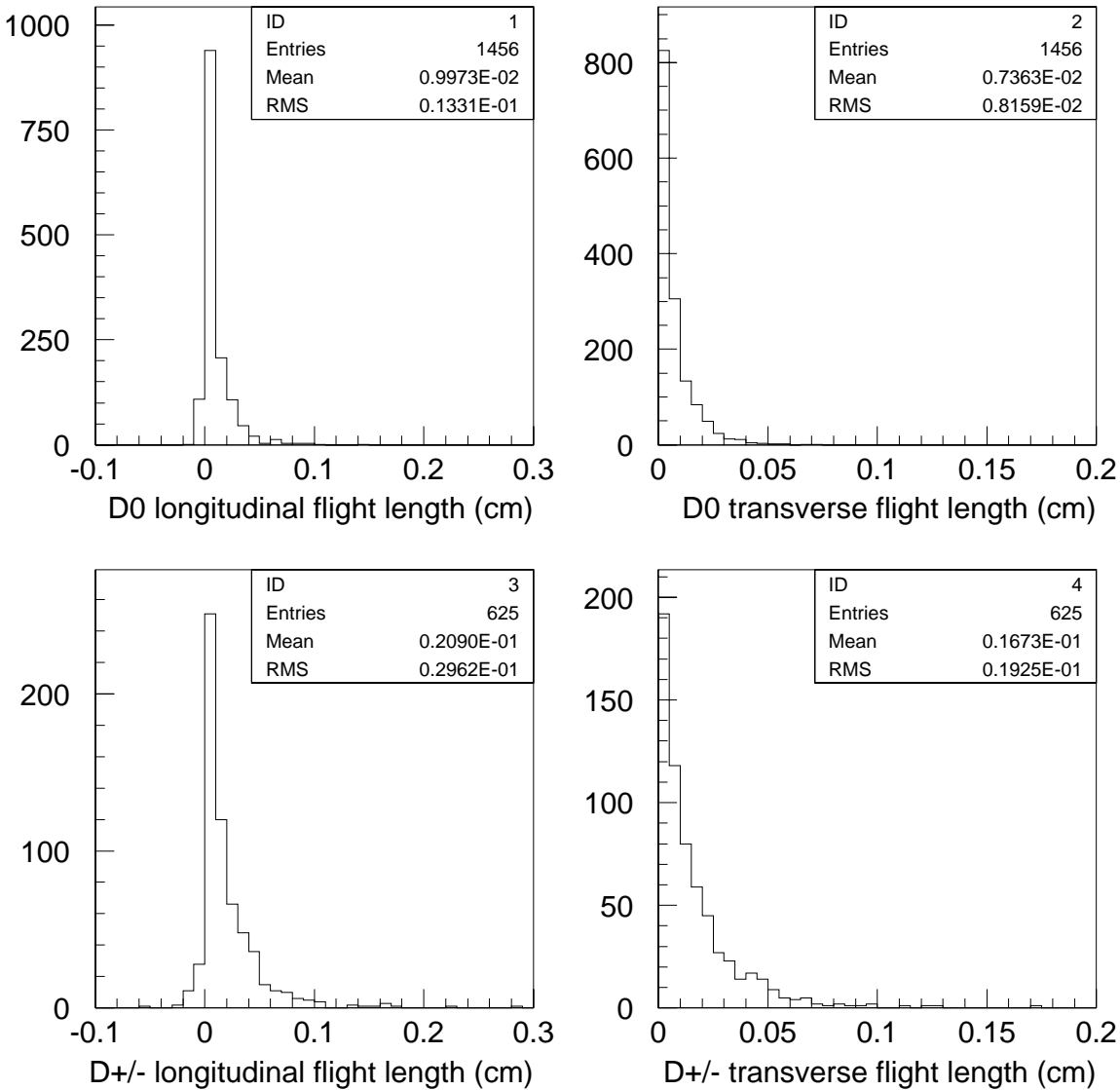


Figure 12-7. The component of the D decay length $\beta\gamma c\tau$ along the beam direction (left figures) and perpendicular to the beam direction (right figures), for D^0 (top figures) and $D^{+/-}$ (bottom figures) mesons from $b\bar{b}$ events.

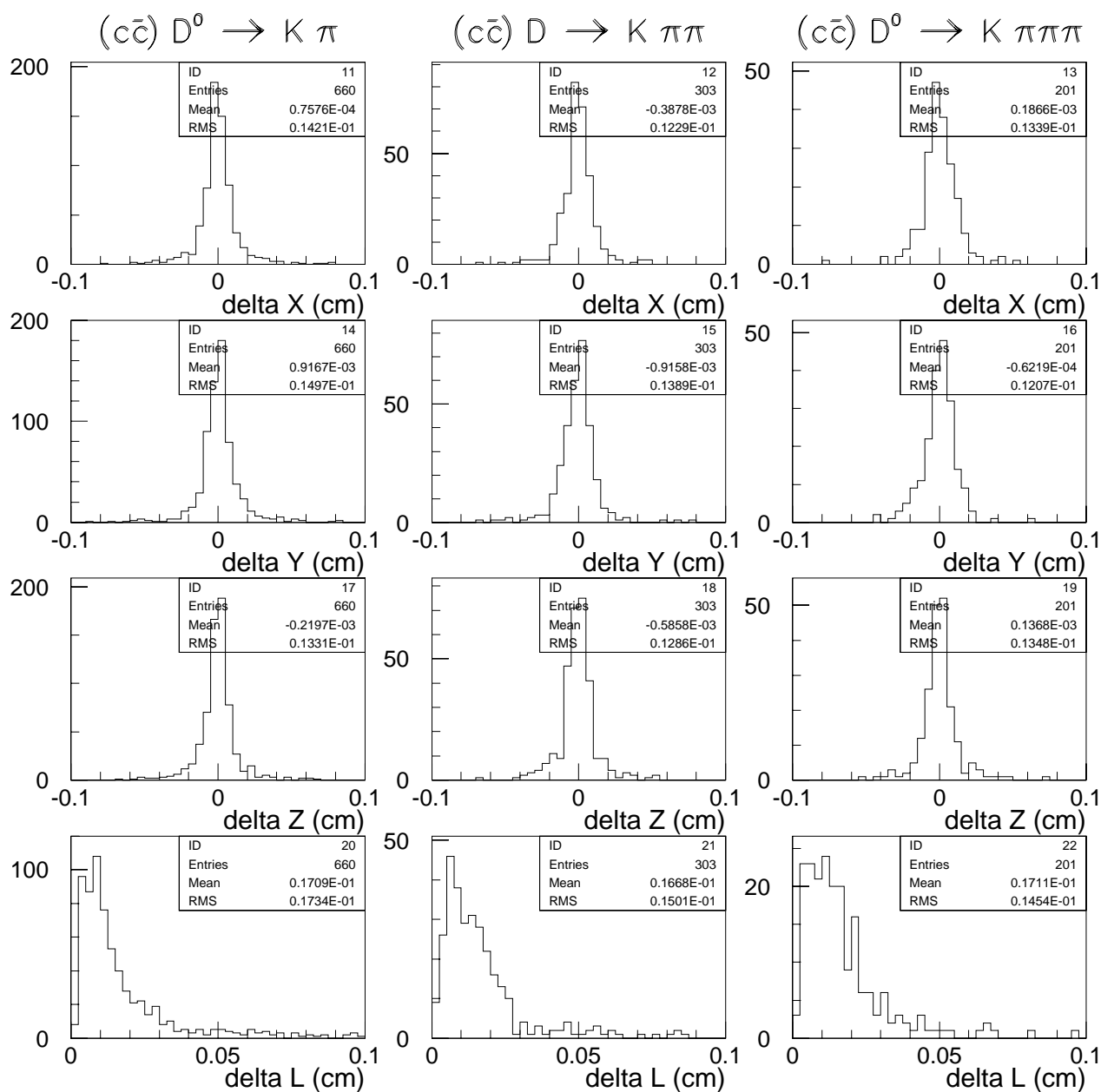


Figure 12-8. Distributions of the x , y , and z components of the error, and the total error on the reconstructed vertex position for three representative D decays, for D s from $c\bar{c}$ events. The error is calculated as the difference between the true decay point and the vertex position calculated for the reconstructed D decay tracks.

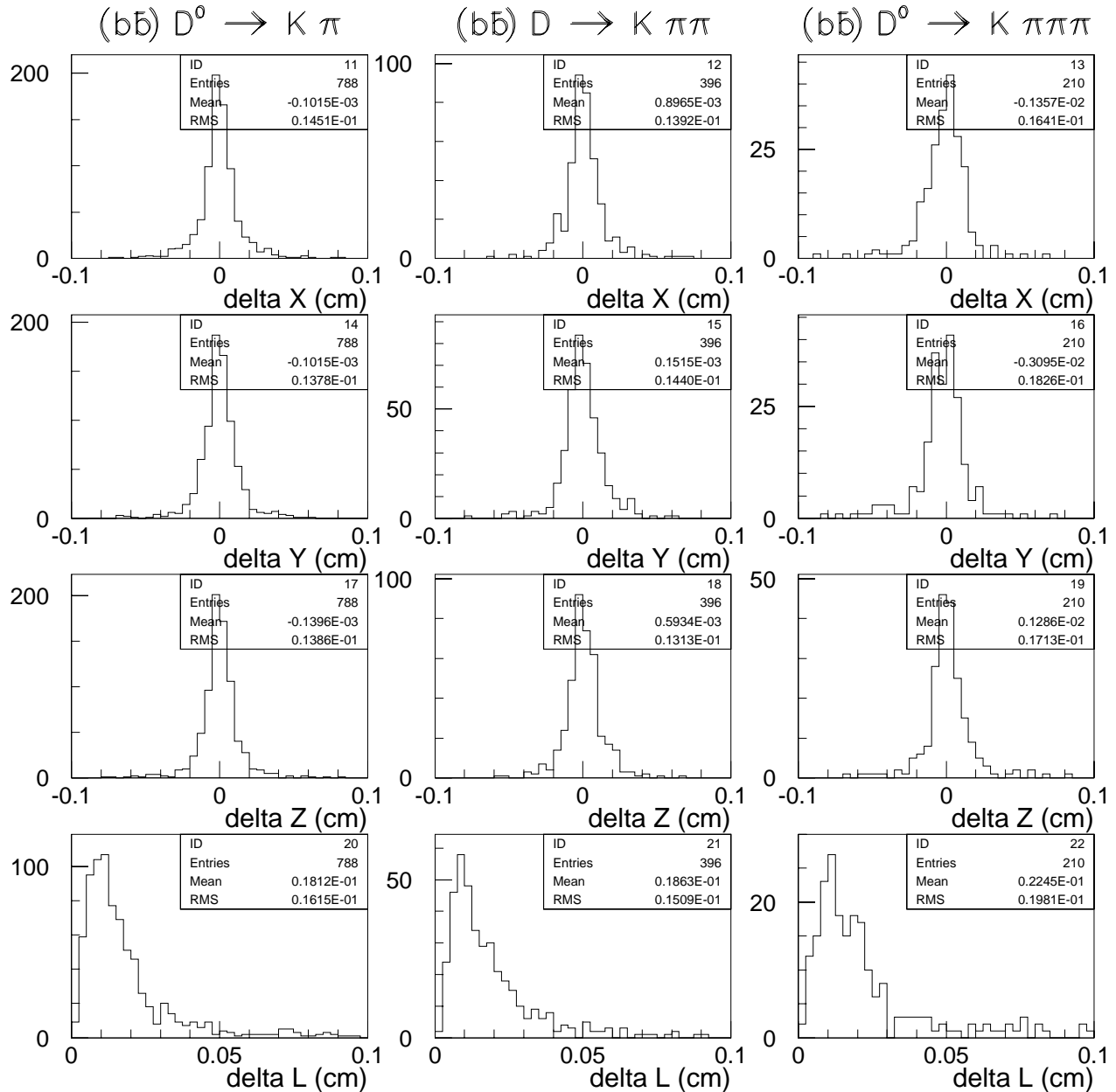


Figure 12-9. Distributions of the x , y and z components of the error, and the total error on the reconstructed vertex position for three representative D decays, for D s from $b\bar{b}$ events. The error is calculated as the difference between the true decay point and the vertex position calculated for the reconstructed D decay tracks.

12.1.1 Searches for New Physics

12.1.1.1 $D^0 \bar{D}^0$ mixing

$D^0 \bar{D}^0$ mixing is expected to be too small to measure with BABAR if the Standard Model is a complete description of physics. However, many extensions to the Standard Model can enhance the mixing via loops involving new heavy particles [1]. Theoretical estimates in these models range up to the present experimental bound. Mixing thus serves as an excellent probe for new physics, free from Standard Model effects.

Elements common to any search for $D^0 \bar{D}^0$ mixing include tagging the D flavor at production, and then observing the time evolution characteristic of mixing into the opposite flavor. This will prove that mixing has occurred, since the wrong flavor D can come from other sources such as doubly Cabibbo-suppressed (DCS) decays (for hadronic modes) or background (*e.g.*, errors in the initial flavor tag). Key limitations to the mixing measurement come from both DCS decays and errors in the tagging, as well as limited event samples of identified D mesons. The time dependence for “wrong-sign” decays can be written:

$$I(t) \propto r_D e^{-t/\tau} + \sqrt{2r_D r_{mix}} \cos \phi \frac{t}{\tau} e^{-t/\tau} + \frac{r_{mix}}{2} \left(\frac{t}{\tau}\right)^2 e^{-t/\tau} \quad (12.1)$$

Here τ is the D^0 lifetime, r_D the ratio of amplitudes squared for DCS and Cabibbo-allowed decays, r_{mix} the mixing ratio, and ϕ a phase angle for interference between the DCS and mixing amplitudes [2], where

$$r_{mix} = \frac{1}{2} \left[\left(\frac{\Delta m}{\Gamma}\right)^2 + \left(\frac{\Delta \Gamma}{2\Gamma}\right)^2 \right]. \quad (12.2)$$

Searches for $D^0 \bar{D}^0$ mixing have been conducted at e^+e^- storage rings as well as fixed target experiments. CLEO measured the ratio $\mathcal{B}(D^0 \rightarrow K^+\pi^-)/\mathcal{B}(D^0 \rightarrow K^-\pi^+)$ to be $(0.77 \pm 0.25 \pm 0.25)\%$ [3]. However, the CLEO experiment was unable to distinguish between mixing and DCS decays. The most stringent limits on mixing to date are set by Fermilab experiments E691 and E791. E691 uses the decay modes $D^0 \rightarrow K^+\pi^-$ and $D^0 \rightarrow K^+\pi^-\pi^+\pi^-$. A fit to the proper decay time distribution is performed to separate mixing from DCS amplitudes, albeit neglecting effects from interference of the decay amplitudes and potential CP violation. This results in an upper limit of $r_{mix} < 0.37\%$ at 90% CL [4]. Using the same decay modes, E791 performed a mixing analysis taking into account the possible effects of interference and CP violation [5]. With the assumption of no CP violation, they obtain a combined upper limit of $r_{mix} < 0.85\%$, assuming furthermore that no mixing-DCS interference restricts the limit to $r_{mix} < 0.33\%$. In addition, E791 has performed a mixing analysis in the semileptonic decay modes $D^0 \rightarrow K^+e^-\bar{\nu}_e$ and $D^0 \rightarrow K^+\mu^-\bar{\nu}_\mu$ that are not subject to contributions from DCS amplitudes [6]. The resulting limit of $r_{mix} < 0.50\%$ at 90% CL is the best model independent limit of $D^0 \bar{D}^0$ mixing to date. All

of the above-mentioned results were obtained by utilizing the $D^{*+} \rightarrow D^0 \pi^+$ decay chain, with its small Q value, to tag the flavor of the D at production.

At BABAR, D mesons are produced from $c\bar{c}$ initial states and as secondaries from B decays (see Section 12.1). Those produced from $c\bar{c}$ are used to optimize the lifetime measurement by choosing high momentum D mesons as well as minimizing other backgrounds. They can be uniquely selected by cutting on the momentum of the tagging D meson in the center-of-mass system. The tag efficiency is about 50% for $c\bar{c}$ using this selection criterion; background from $b\bar{b}$ becomes negligible.

To estimate the value of r_{mix} that can be positively identified, it is assumed that there are very few mixing candidates and that the DCS and mistag rates are precisely known (*e.g.*, by looking at the event distribution at short decay times relative to one lifetime). For the case of hadronic decays, the potential interference between DCS and mixing decay amplitudes is ignored. This provides a uniform way to compare possible channels for studying mixing, but a final analysis will have to be done allowing for interference in each channel. Cutting at two lifetimes to enhance the mixing fraction, the data can either be background-free, and hence just limited by statistics, or dominated by the Poisson fluctuations on the known background; the latter is assumed below. Some examples are considered using a simulation of the detector.

In general, let N_0 be the number of right-sign decays, which is determined by the tagging technique and its efficiency, as well as the D decay chosen for the mixing study. Ignoring interference with the mixing for the DCS decays, the time distribution for these decays and the initially incorrectly tagged decays is: $e^{-t/\tau}$. The mixing time distribution is proportional to $t^2 e^{-t/\tau}$.

The ratio of the number of DCS decays to the number of right-sign decays is defined as r_D , and the wrong-tag ratio as r_W . Then the number of background events expected in total is $(r_D + r_W)N_0$, with $e^{-2}(r_D + r_W)N_0$, occurring after a cut at two lifetimes. Subtracting this number of events from the observed data, the 4σ limit due to Poisson fluctuations is

$$4\sqrt{e^{-2}(r_D + r_W)N_0} \quad \text{for } t > 2 \text{ lifetimes.} \quad (12.3)$$

The total limit, extended to all times, is

$$\frac{4\sqrt{e^{-2}(r_D + r_W)}}{f} \quad (12.4)$$

where $f = 5e^{-2}$ is the fraction of mixing events with $t > 2$ lifetimes. Normalizing to N_0 , to get the fraction mixed, finally gives a limit

$$\frac{4e}{5} \sqrt{\frac{r_D + r_W}{N_0}}. \quad (12.5)$$

Note that the above analysis assumes that the final reconstructed D candidate with lifetime greater than twice the proper lifetime is always a real D . BBSim simulation studies indicate that this

assumption is sufficiently accurate for fully reconstructed hadronic D decays. For semi-leptonic decay channels, $r_D = 0$. However, in this case tight mass cuts cannot be made and background comes from misidentified D decays. The misidentification fraction r_M now replaces r_D in the above formula.

To estimate the sensitivity achievable at BABAR, as one example of a hadronic decay mode, the (right-sign) decay chain $D^{*+} \rightarrow D^0 \pi^+$, $D^0 \rightarrow K^- \pi^+$ ($\mathcal{B} = 3.83\%$) has been investigated using the BBSIM simulation of the detector response, with the exception that perfect particle identification has been assumed and is discussed below.

D^0 candidates are formed from opposite sign kaons and pions. If the invariant mass is within the accepted window, the D^0 vertex is refitted with the Kalman filter algorithm described in Section 4.5.1. The following selection criteria are applied to D^0 candidates:

- D^0 momentum in the CM frame: $p(D^0)_{CM} > 2.5 \text{ GeV}/c$ and
- D^0 invariant mass: $1.845 < m(D^0) < 1.885 \text{ GeV}/c^2$.

To reconstruct charged D^* s, a D^0 candidate is combined with a charged pion track requiring:

- Slow pion from D^* decay: $p(\pi_s)_{Lab} > 100 \text{ MeV}$ and
- Mass difference Δm : $144.5 < \Delta M < 146.5 \text{ MeV}$.

The efficiency for these selection criteria is 43%. Figure 12-10 shows the mass difference and D^0 mass distributions. The resolution of the mass difference Δm is $\sigma = 0.41 \text{ MeV}$. Remaining background in the sample is due to random combinations of pions with a real D^0 . Background with a wrong-sign D^* tag could fake a mixing signal. In this sample, the contamination of wrong-sign tags amounts to only 0.15%, considerably less than the background expected from DCS decays.

The two-body invariant mass distribution for D candidates, corresponding to real two-body D decays with a single misidentified hadron, does not peak at the D mass and hence does not contribute to the signal. Also, the combination of a real D^0 with a random pion candidate is discarded by the cut on Δm . However, D^0 decays with two misidentified hadrons could give rise to a potentially serious background when the kaon is misidentified as a pion and vice versa. It leads to a narrow peak in the mass difference and a broad enhancement around the D^0 mass. For instance, assuming a π/K misidentification probability as large as 10% gives rise to an additional background of 0.1%. Hence, with the excellent PID system of BABAR this background should be negligible. Furthermore, background could easily be reduced by a factor of 10 by requiring the mass of a D^0 candidate, calculated by interchanging the K/π assignment, to be outside a window of 10 MeV around the nominal mass. This cut introduces an inefficiency of about 6%.

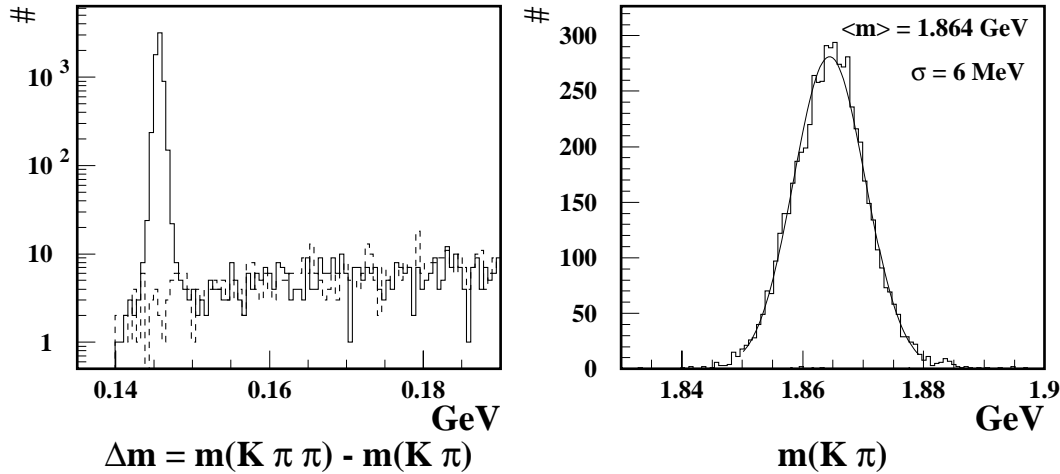


Figure 12-10. Mass difference and D^0 mass distributions for the $D^* \rightarrow D^0 \pi \rightarrow K \pi \pi$ sample. Wrong sign tags are shown as the dashed histogram. Note the logarithmic scale in the Δm plot.

To distinguish mixing from DCS amplitudes, the proper lifetime distribution must be measured. Therefore, the production and decay vertices of the D^0 have to be determined. The D^0 decay vertex is well reconstructed, with a resolution of about $50 \mu\text{m}$. However, due to the non-reconstructed other charm meson in the event, the primary vertex position cannot be determined by just fitting the remaining tracks of the event. This analysis takes advantage of the very small beam profile in the y -direction ($\sigma_y = 6 \mu\text{m}$, for comparison $\sigma_x = 160 \mu\text{m}$ and $\sigma_z \approx 1 \text{ cm}$). The D^0 direction of flight is extrapolated backwards and the primary vertex is constrained to the intersection of the D^0 momentum vector, with $y = y_{run}$ where y_{run} is the beam position in y measured for a given run (for instance, with light quark continuum events). This approach yields a resolution of the primary vertex position, *i.e.*, production vertex for the D^0 , of comparable size to the decay vertex, depending on ϕ (of course, $\sigma_y = 6 \mu\text{m}$ by construction). This results in a resolution of the proper lifetime of 0.2 ps . From this analysis, a sensitivity estimate for r_{mix} of 4.6×10^{-4} is derived for one year running at nominal luminosity. The value for $r_D = (7.57 \pm 1.2) \times 10^{-3}$ is based on the CLEO analysis [3]. Since it does not distinguish between mixing and DCS amplitudes, it serves as an upper limit on the DCS decay rate. Naively, without taking $SU(3)_F$ symmetry breaking into account, one would expect $r_D \sim \tan^4 \theta_C \approx 2.5 \times 10^{-3}$.

Other hadronic decays of interest are $D^0 \rightarrow K^+ \pi^- \pi^+ \pi^-$ (branching ratio $\mathcal{B} = 7.5\%$) and $D^0 \rightarrow K^+ \pi^- \pi^0$ ($\mathcal{B} = 13.9\%$). The reconstruction efficiencies of both decay modes have been estimated to be about 60% of the efficiency of the $K\pi$ decay mode (see Table 1 in [173]). It is assumed that the signal to wrong-sign background ratio is roughly the same as for the $K\pi$ mode (These estimates agree with the observations for $K^+ \pi^- \pi^+ \pi^-$ from E791 [5], albeit with very different

Table 12-2. Sensitivity limits for $D^0 \bar{D}^0$ mixing for different hadronic decay modes. Please refer to the text for the assumptions used.

Tag	Mode	r_D	r_W	N_0	$(r_D + r_W)N_0$	$\frac{4e}{5} \sqrt{\frac{r_D + r_W}{N_0}}$
D^*	$K \pi$	7.6×10^{-3}	1.5×10^{-3}	200000	1820	4.6×10^{-4}
D^*	$K \pi \pi \pi$	2.5×10^{-3}	1.5×10^{-3}	235000	940	2.8×10^{-4}
D^*	$K \pi \pi^0$	2.8×10^{-3}	1.5×10^{-3}	438000	1885	2.2×10^{-4}
D^\pm	$K \pi$	7.6×10^{-3}	0.8×10^{-2}	7600	120	3.1×10^{-3}

event kinematics.) For the $K^+ \pi^- \pi^0$ mode, an estimate is used for r_D , derived from hadronic decay models described in [7, 8]. For $K^+ \rho^-$, which dominates the $K^+ \pi^- \pi^0$ decay, one expects $r_D \approx 2.8 \times 10^{-3}$. In the case of $K^+ \pi^- \pi^+ \pi^-$, the results from E791 are used, derived assuming no mixing: $r_D = (0.25^{+0.36}_{-0.34} \pm 0.03)\%$ [5]. The resulting sensitivity estimates are summarized in Table 12-2. The precision of the reconstruction could be further improved by constraining and fitting the decay products to the D^0 mass.

An alternative to the D^* decay method of tagging the D flavor is to reconstruct a charged D meson in the opposite hemisphere of the center-of-mass system. Here, the decay mode $D^+ \rightarrow K^- \pi^+ \pi^+$ with a branching fraction of 9.1% is chosen. The sample is much lower in statistics compared to the D^* sample, and the combinatorial background to D^\pm is considerably higher. Although almost all of the background would not result in a wrong sign tag assuming perfect PID, with a small K/π misidentification probability, the background to the tagging procedure is estimated to be as high as $\sim 0.8\%$. Hence, this approach does not appear to be as suitable as the D^* method, even though it allows for a very good primary vertex reconstruction using both D mesons.

Table 12-2 shows the wrong-sign ratios, r_D and r_W , and the expected number of reconstructed events, N_0 , for a given tag method and decay mode assuming an integrated luminosity of 30 fb^{-1} . The last column gives the expected limit of positive identification of mixing.

Finally, semileptonic decays do not suffer from the complication of DCS amplitude; however, due to the missing neutrino, the combinatorial background is higher. For a reasonable background-to-noise ratio, it is essential to have a well-reconstructed primary vertex, not only for the lifetime measurement, but also to kinematically constrain the neutrino.

It is worth mentioning that, assuming CP conservation, it may alternatively be possible to search for mixing via the lifetime difference between different CP eigenstates [2]. This method is only sensitive to mixing if it is associated with a substantial lifetime difference, as opposed to mixing caused by mass difference.

In conclusion, with 30 pb^{-1} of data, and by combining results from different decay modes, BaBar should be able to probe $D^0 \bar{D}^0$ mixing at the level of a few $\times 10^{-4}$, with possible interference with DCS terms taken into account.

12.1.1.2 CP violation in D decays

Within the Standard Model, CP violation in the charm sector is expected to be small compared to the B sector, as it is for mixing. However, this could imply that there is room for new physics effects to be observed. Given the size of the CKM parameters involved, CP violation in $D^0 \bar{D}^0$ mixing is of order $\eta\lambda^5 \sim 10^{-4}$, while direct CP violation is of order $\eta\lambda^4 \sim 10^{-3}$, where η is the usual CKM parameter in Wolfenstein's parametrization and $\lambda = \sin\theta_c$. In the latter case, relative weak phases can only be obtained in Cabibbo suppressed decays, *e.g.*, via the interference between spectator and penguin amplitudes. In addition, D decays are known to be affected by significant strong final state interactions, which can enhance certain transition amplitudes and suppress others, thus modifying the strength of observable CP asymmetries. Specific model calculations for $D^0 \rightarrow KK, \pi\pi, K^*K$ and $D^+ \rightarrow \phi\pi, K^{*0}K^+, \rho^0\pi^-$ seem to be able to constrain quite confidently CP violation effects to be $\leq 10^{-3}$ [7, 9]. In the case of CP violation induced by mixing, the measurable CP asymmetries should definitely be a few orders of magnitude less, due to the strength of $\Delta m/\Gamma$.

New physics, such as models with an extended Higgs sector or non-minimal Supergravity or SUSY, allow for significantly larger CP asymmetries both for direct and mixing-induced CP violation [1]. In addition, through direct CP violation, Cabibbo allowed decays, such as $D \rightarrow K_s^0\pi^0, K_s^0\eta, K_s^0\phi$, could give asymmetries as large as 1% once the Standard Model constraints have been relaxed [10].

The current experimental situation is shown in Table 12-3 for charged and neutral D mesons. As shown, all the current sensitivities to the asymmetries discussed above are at least one order of magnitude higher than Standard Model predictions.

To illustrate the BaBar potentialities, the $D^0 \rightarrow K^+K^-$ decaying channel has been investigated using the Aslund simulation program. The observable considered in this analysis is the time integrated asymmetry

$$a_{CP} = \frac{N(D^0 \rightarrow K^+K^-) - N(\bar{D}^0 \rightarrow K^+K^-)}{N(D^0 \rightarrow K^+K^-) + N(\bar{D}^0 \rightarrow K^+K^-)} \quad (12.6)$$

which is related within the Standard Model to the CP violation via [14]

$$a_{CP} \simeq T_{KK} + x_D V_{KK} \quad (12.7)$$

where x_D is the mixing parameter,

$$T_{KK} = \frac{|A_{KK}|^2 - |\bar{A}_{KK}|^2}{|A_{KK}|^2 + |\bar{A}_{KK}|^2}$$

Table 12-3. Current experimental results on CP asymmetries for charged and neutral D mesons decays from E791 [11], E687 [12] and CLEO[13].

	Experiment	Mode	a_{CP}	90% CL Limits (%)
Charged	E791	$K^- K^+ \pi^-$	-0.014 ± 0.029	$-6.2 < a_{CP} < 3.4$
	E791	$\phi \pi^-$	-0.028 ± 0.036	$-8.7 < a_{CP} < 3.1$
D mesons	E791	$\bar{K}^{*0}(892)K^+$	-0.010 ± 0.050	$-9.2 < a_{CP} < 7.2$
	E791	$\pi^- \pi^- \pi^-$	-0.014 ± 0.042	$-8.6 < a_{CP} < 5.2$
Neutral	CLEO	$K^- K^+$	$+0.080 \pm 0.061$	$-2.2 < a_{CP} < 18$
	E687	$K^- K^+$	$+0.024 \pm 0.084$	$-11 < a_{CP} < 16$
D mesons	CLEO	$K_s^0 \phi$	-0.028 ± 0.094	$-18.2 < a_{CP} < 12.6$
	CLEO	$K_s^0 \pi^0$	-0.018 ± 0.030	$-6.7 < a_{CP} < 3.1$

Table 12-4. KK selection efficiencies for resonance and continuum production mechanism. Also the background over signal ratios (b/s) are reported.

selection cut	Efficiency [%]		b/s	
	$\Upsilon(4S)$	$q\bar{q}$	$\Upsilon(4S)$	$q\bar{q}$
Kaon id.	78.4	72.9	58.5	121.1
D^0 mass	77.7	71.3	0.5	1.3
D^0 vertex prob.	76.0	69.8	0.4	1.1
D^* selection	48.8	63.9	0.05	0.04

measures the direct CP violation mainly arising from the interference between different decay diagrams contributing to the same amplitude, and $V_{KK} = -2 \cdot \text{Im} \lambda$ is sensitive to the CP violation arising from the decay/mixing interference.

Experimentally the selection starts identifying $D^0(\bar{D}^0) \rightarrow K^+ K^-$, whose branching ratio is $(4.54 \pm 0.29) \times 10^{-3}$. To measure the asymmetry in Eq. (12.6) only tagged neutral D mesons can be used. For this purpose charged D^* decaying to $D^{*\pm} \rightarrow D^0 \pi^\pm$ are reconstructed, in order to use the charge of the pion produced in the D^* decay to tag the neutral D state at the production time.

Applying particle identification criteria to the two charged kaons as shown in Fig. 12-11 (using the DIRC and drift chamber dE/dx expected performances, as parametrized in Aslund) and requiring the mass difference between the reconstructed D^* and D^0 candidates to lie between

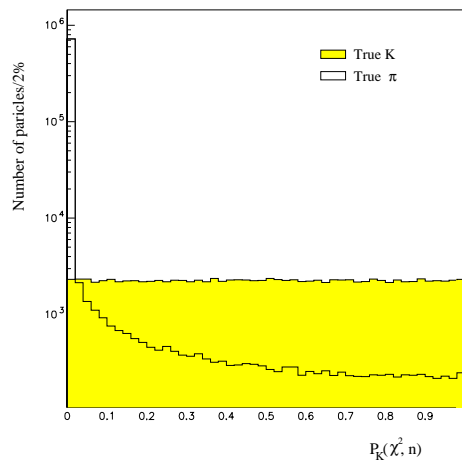


Figure 12-11. χ^2 probability built assigning kaon mass to the particles combining energy loss for ionization and Cherenkov emission angle informations. The χ^2 is defined as $\chi^2 = \frac{(r_{meas}^{DC} - r_{exp}^{DC})^2}{(\sigma_r^{DC})^2} + \frac{(r_{meas}^{DIRC} - r_{exp}^{DIRC})^2}{(\sigma_r^{DIRC})^2}$. Kaons are selected requiring $P_K(\chi^2, n) > 2\%$, which allows to retain 98% of kaons rejecting 96% of pions.

0.1430 and 0.1485 GeV/c² results in a background to signal ratio of 5%. The selection criteria efficiencies and expected background are summarized in Table 12-4.

The expected number of signal events is 1×10^5 coming either from $\Upsilon(4S)$ or from continuum events assuming an integrated luminosity of 30 fb^{-1} . This would allow a resolution on the CP asymmetry of Eq. (12.6) of 3×10^{-3} , which would still be too high to sensitively test Standard Model predictions ($\leq 10^{-3}$) but is at least one order of magnitude better than current experimental sensitivities. An improvement might come from measuring the time dependence of the asymmetry, which deserves further study.

12.1.1.3 Rare or forbidden decays

Rare charm decays are excellent hunting grounds for new physics because they involve higher order weak interaction processes that are heavily suppressed by inter-family mixing angles and by mass effects. As a result, the rates of rare charm decay processes (when estimated using short-distance Standard Model contributions) are very small, leaving plenty of room for new physics effects to be felt.

In actuality, one has to be more careful since long-distance effects can strongly alter the partonic Standard Model estimates for rare charm decay processes. For instance, the helicity-suppressed FCNC process $D^0 \rightarrow \mu^+ \mu^-$, when estimated using the effective short-distance Lagrangian for $\bar{c}u \rightarrow \mu^+ \mu^-$, gives a branching fraction of $\mathcal{O}(10^{-19})$ [15]. However, for this process, computing

Table 12-5. Experimental limits and theoretical predictions for various rare charm decays.

Mode	Exp. Limit (90% CL)	$B_{\text{Short-Distance}}$	$B_{\text{Long-Distance}}$
$D^0 \rightarrow \mu^+ \mu^-$	$< 4.2 \times 10^{-6}$ [16]	$\mathcal{O}(10^{-19})$ [15]	3×10^{-15} [15]
$D^+ \rightarrow \pi^+ \mu^+ \mu^-$	$< 1.8 \times 10^{-5}$ [18]	$\mathcal{O}(10^{-9})$ [19]	$\mathcal{O}(10^{-7})$ [19]
$D^0 \rightarrow \rho^0 \gamma$	$< \mathcal{O}(10^{-4})$ [20]	$(4 - 8) \times 10^{-13}$ [21]	$(1 - 5) \times 10^{-6}$ [21]

Table 12-6. Expected sensitivity for a 30 fb^{-1} BABAR data sample.

Mode	Expected Sensitivity
$D^0 \rightarrow \mu^+ \mu^-$	$< 4.3 \times 10^{-6}$
$D^0 \rightarrow \mu^\pm e^\mp$	$< 2.4 \times 10^{-5}$
$D^0 \rightarrow \pi^0 e^+ e^-$	$< 5.8 \times 10^{-6}$
$D^0 \rightarrow \pi^0 \mu^\pm e^\mp$	$< 1.1 \times 10^{-5}$

the effects of intermediate states, such as π^0 , η , or $\pi\pi$, yields a much larger branching ratio of $\mathcal{O}(10^{-15})$ [15]. Neither of these numbers, however, is even remotely close to the present experimental upper limit of $\mathcal{B}(D^0 \rightarrow \mu^+ \mu^-) < 4.2 \times 10^{-6}$ [16].

Table 12-5 summarizes some 90% CL for rare charm decays [17], along with theoretical estimates for these branching ratios arising from both short-distance and long-distance contributions.¹ As can be appreciated from Table 12-5, there is still a considerable gap between these experimental upper limits and the expected (long-distance) theoretical branching ratios. Indeed, for certain lepton flavor violation processes, like $D^0 \rightarrow \mu^+ e^-$, there are no theoretical expectations in the Standard Model since these processes are totally forbidden. Table 12-6 details the sensitivity expected for various rare or forbidden charm decays in a 30 fb^{-1} run at BABAR, obtained by scaling the present CLEO limits [17]. Clearly, in most cases, there is an order of magnitude discovery window to be explored.

New physics, in general, will contribute both to rare processes and to $D^0 \bar{D}^0$ mixing. For example [22], a fourth generation quark with $V_{ub'} V_{cb'}^* > 0.01$ and $m_{b'} > 100 \text{ GeV}/c^2$, gives $D^0 \rightarrow \mu^+ \mu^- > 5 \times 10^{-12}$ and $r_{\text{mix}} > 10^{-4}$. In this case, $D^0 \bar{D}^0$ mixing is a promising way to look for new physics, as values of r_{mix} of a few times 10^{-4} are accessible at BABAR. For other new physics scenarios, however, the constraints from rare decays are much more powerful. For instance, the branching ratio sensitivity for the process $D^0 \rightarrow \mu^\pm e^\mp$ shown in Table 12-6 constrains the possible couplings

¹The short-distance branching ratios for exclusive modes involving final state hadrons are taken as 10% of the inclusive partonic estimates.

and mass of a leptoquark to $[F_{eu}F_{\mu c}]^{-1/2} < 6 \times 10^{-7} [m_{lq}/100 \text{ GeV}/c^2]$ [23]. Here F_{lq} typifies the leptoquark coupling strength in units of e ($\lambda_{lq} = F_{lq}e$). For $m_{lq} \sim 100 \text{ GeV}/c^2$, the constraint on $[F_{eu}F_{\mu c}]^{-1/2}$ obtainable from mixing, in this case is only of $\mathcal{O}(10^{-2})$.

12.1.2 Purely Leptonic Decays of D and D_s

In this section, the measurement of purely leptonic decay rates of the D and D_s is motivated, and the status of experimental measurements is discussed. The mode that is experimentally most accessible is $D_s \rightarrow \mu^+ \nu_\mu$. Current measurements of $\mathcal{B}(D_s \rightarrow \mu^+ \nu_\mu)$ suffer from large statistical and/or systematic uncertainties. The quality of the measurement which will be made at BaBar will depend on several factors: recording large integrated luminosity; the performance of the BaBar muon identification system; and the hermiticity of the detector for reconstructing the momentum of the missing neutrino.

The purely leptonic decays are described theoretically by the annihilation of constituent quark and antiquark into a virtual W boson. The effect of the strong interaction can be parameterized in terms of just one factor called the decay constant. In the Standard Model the rate of the decay $M_{Q\bar{q}} \rightarrow \ell^- \bar{\nu}$, ignoring radiative correction, is predicted to be

$$\Gamma(M_{Q\bar{q}} \rightarrow \ell^- \bar{\nu}) = \frac{G_F^2}{8\pi} |V_{qQ}|^2 f_M^2 M m_\ell^2 \left(1 - \frac{m_\ell^2}{M^2}\right)^2, \quad (12.8)$$

where f_M is the decay constant, V_{qQ} is the CKM matrix element, and m_ℓ and M are the masses of the lepton and charged pseudoscalar meson $M_{Q\bar{q}}$, respectively. The decay constant f_M is a measure of the overlap of quark and antiquark at zero separation, which is necessary for them to annihilate.

The decay constants for D and B mesons have been estimated with lattice QCD, QCD sum rules, and quark potential models [24, 25, 26]. The agreement between the different approaches, however, is not very good. The decay constant also appears in numerous heavy-flavor transitions, including semileptonic and nonleptonic decays, mixing, and CP violation. Of particular interest is the B decay constant f_B , which currently limits our ability to extract $|V_{td}|$ from measurements of $B^0 \bar{B}^0$ mixing. At present it is difficult to measure purely leptonic B decays, so one must rely on theoretical calculations of f_B . It would be of great help to check these calculations against the measurements of other heavy quark decay constants such as f_{D_s} . An experimental determination of the D decay constant could be used as input to the models to reduce the theoretical uncertainty on the B decay constant. For example, HQET predicts that $f_B/f_D \approx 0.69$ when terms of order $1/m_Q$ are neglected [27]. However, the $1/m_Q$ corrections for heavy-meson decay constants are expected to be substantial and much more significant than those for weak decay form factors.

Theoretical expectations for f_D are in the range 170 to 240 MeV; f_{D_s} is expected to be about 10% larger. The theoretical predictions for f_B range from 120 to 230 MeV. Some of the predictions of

Table 12-7. Predicted D^+ , D_s , and B leptonic decay rates and branching fractions assuming $f_D = f_{D_s} = f_B = 200$ MeV, $|V_{cd}| = 0.22$, $|V_{cs}| = 0.97$, and $|V_{ub}| = 0.003$.

Decay mode	Rate (s^{-1})	Branching fraction
$D^+ \rightarrow e^+ \nu_e$	7.8×10^3	8.2×10^{-9}
$D^+ \rightarrow \mu^+ \nu_\mu$	3.3×10^8	3.5×10^{-4}
$D^+ \rightarrow \tau^+ \nu_\tau$	7.1×10^8	7.9×10^{-4}
$D_s^+ \rightarrow e^+ \nu_e$	1.6×10^5	7.5×10^{-8}
$D_s^+ \rightarrow \mu^+ \nu_\mu$	6.8×10^9	3.2×10^{-3}
$D_s^+ \rightarrow \tau^+ \nu_\tau$	6.1×10^{10}	2.9×10^{-2}
$B^- \rightarrow e^- \bar{\nu}_e$	4.1×10^0	6.6×10^{-12}
$B^- \rightarrow \mu^- \bar{\nu}_\mu$	1.8×10^5	2.8×10^{-7}
$B^- \rightarrow \tau^- \bar{\nu}_\tau$	3.9×10^7	6.3×10^{-5}

f_B from QCD sum rules were significantly lower than the predictions of lattice QCD. Several new analyses based on QCD sum rules in the heavy-quark effective theory find that radiative corrections significantly increase the value of f_B .

An asymptotic scaling law, derived in HQET [27], predicts that $f_M^2 M$ approaches a constant as M becomes large. Since the total decay rate for a heavy meson scales as M^5 , the leptonic branching fraction for the D and B mesons are expected to be very small.

The factor m_ℓ^2 in Eq. (12.8) is a consequence of helicity suppression. For small m_ℓ , the decays in which the resulting fermion and antifermion have opposite helicities are favored, but this configuration violates conservation of angular momentum when $M_{Q\bar{q}}$ is a spin-zero particle. This effect leads to a suppression of the decay rate when m_ℓ is small compared with the mass of the parent meson.

Using a value of 200 MeV for the D^+ , D_s , and B decay constants, the central values of the CKM matrix elements from the Particle Data Group (1996) [28], and the measured D^+ , D_s , and B lifetimes, the leptonic branching-fraction predictions shown in Table 12-7 are obtained. The leptonic decay rates for D_s are expected to be larger than those for D^+ because $|V_{cs}|^2$ is much larger than $|V_{cd}|^2$. In addition, the decay $D_s \rightarrow \tau^+ \nu_\tau$ has less phase-space suppression than $D^+ \rightarrow \tau^+ \nu_\tau$. Leptonic B decays are strongly suppressed by the small value of $|V_{ub}|^2$. Therefore, the leptonic heavy-quark decays that are easiest to detect experimentally are $D_s \rightarrow \mu^+ \nu_\mu$ and $D_s \rightarrow \tau^+ \nu_\tau$. The CKM matrix elements relevant for the leptonic decays of the D^+ and D_s are determined quite well from unitarity constraints, so a measurement of the leptonic decay rate for these particles provides a measurement of f_D and f_{D_s} .

Table 12-8. Summary of measurements of the decay constants for the D^+ and D_s mesons. The WA75 value is corrected by using the 1996 PDG [28] values of $\mathcal{B}(D_s^+ \rightarrow K^+ K^- \pi^+) = (4.6 \pm 1.2)\%$, and $\tau_{D_s} = (4.67 \pm 0.17) \times 10^{-13} \text{s}$, and the 1997 PDG [34] value of $\mathcal{B}(D^0 \rightarrow \ell^+ X) = (6.75 \pm 0.26)\%$ (the average of $\mathcal{B}(D^0 \rightarrow e^+ X)$ and $\mathcal{B}(D^0 \rightarrow \mu^+ X)$).

Decay constant	Decay mode	Experiment	Value (MeV)
f_D	$\mu\nu$	MARK III [35]	< 290 (90% C.L.)
f_{D_s}	$\mu\nu$	WA75 [29]	$214 \pm 43 \pm 19 \pm 42$
f_{D_s}	$\mu\nu$	CLEO II [30]	$344 \pm 37 \pm 52 \pm 42$
f_{D_s}	$\mu\nu, \tau\nu$	BES [33]	$430_{-130}^{+150} \pm 40$
f_{D_s}	$\mu\nu$	E653 [31]	$194 \pm 35 \pm 20 \pm 14$
f_{D_s}	$\tau\nu$	L3 [32]	$309 \pm 58 \pm 33 \pm 38$

Several experiments have now observed the muonic decay $D_s^+ \rightarrow \mu^+ \nu_\mu$ (Table 12-8). The first indication of $D_s^+ \rightarrow \mu^+ \nu_\mu$ was presented in 1992 by the CERN WA75 Collaboration [29]. In this fixed-target experiment, a π^- beam is incident on an emulsion target and a muon is required in the online trigger. WA75 determines a branching fraction for $D_s^+ \rightarrow \mu^+ \nu_\mu$ of $(3.6_{-1.3}^{+1.6+0.7} \pm 1.4) \times 10^{-3}$ and a D_s decay constant of $f_{D_s} = (214 \pm 43 \pm 19 \pm 42) \text{MeV}$. In both results, the last error is the systematic error on the normalization, which depends on measurements of the D^0 and D_s cross-sections from NA32, the branching fraction for $D_s \rightarrow K^+ K^- \pi^+$, and the inclusive D^0 branching fraction.

The CLEO Collaboration [30] measures the $D_s \rightarrow \mu^+ \nu_\mu$ decay rate relative to that for $D_s \rightarrow \phi\pi^+$, so the normalization is more straightforward than in the WA75 analysis. CLEO searches for $\mu\gamma$ combinations from the decay chain $D_s^* \rightarrow D_s \gamma$, $D_s \rightarrow \mu^+ \nu_\mu$. Muons are selected with a minimum momentum of 2.4 GeV/c. This removes most of the muons from B meson decays and is 33% efficient for $D_s \rightarrow \mu^+ \nu_\mu$. From a data sample corresponding to 2.1fb^{-1} , the branching ratio relative to the $\phi\pi^+$ decay mode is measured to be $\mathcal{B}(D_s \rightarrow \mu^+ \nu_\mu)/\mathcal{B}(D_s \rightarrow \phi\pi^+) = 0.245 \pm 0.052 \pm 0.074$, and the decay constant $f_{D_s} = (344 \pm 37 \pm 52 \pm 42) \sqrt{\mathcal{B}(D_s \rightarrow \phi\pi^+)/0.037} \text{MeV}$ is obtained.

The E653 Collaboration [31] has observed $23 \pm 6.0_{-0.9}^{+1.0}$ leptonic decays of $D_s^+ \rightarrow \mu^+ \nu_\mu$ from a sample of muonic one prong decays detected in the emulsion target experiment. Using the $D_s^+ \rightarrow \phi\mu^+ \nu_\mu$ yield measured previously in the same experiment, E653 obtains the branching ratio $\mathcal{B}(D_s \rightarrow \mu^+ \nu_\mu)/\mathcal{B}(D_s^+ \rightarrow \phi\mu^+ \nu_\mu) = 0.16 \pm 0.06 \pm 0.03$, and extracts the decay constant $f_{D_s} = (194 \pm 35 \pm 20 \pm 14) \text{MeV}$.

The L3 Collaboration [32] studies the leptonic decays $D^- \rightarrow \tau^- \bar{\nu}_\tau$ and $B^- \rightarrow \tau^- \bar{\nu}_\tau$ using a data sample of 1,475,000 $Z \rightarrow q\bar{q}(\gamma)$ events collected during 1994 with the L3 detector at LEP. A signal

is observed in the invariant mass distribution $M(\gamma D_s^-)$ corresponding to the decay sequence $D_s^* \rightarrow \gamma D_s^-, D_s^- \rightarrow \tau^- \bar{\nu}_\tau, \tau^- \rightarrow \ell^- \bar{\nu}_\ell \nu_\tau$. The branching fraction is determined to be $\mathcal{B}(D_s^- \rightarrow \tau^- \bar{\nu}_\tau) = 0.074 \pm 0.028 \pm 0.016 \pm 0.018$. The corresponding decay constant is $f_{D_s} = (309 \pm 58 \pm 33 \pm 38)$ MeV. In addition, L3 sets an upper limit on the branching fraction $\mathcal{B}(B^- \rightarrow \tau^- \bar{\nu}_\tau) < 5.7 \times 10^{-4}$ at 90% C.L. because no signal of $B^- \rightarrow \tau^- \bar{\nu}_\tau$ decays is observed.

The BES Collaboration [33] has fully reconstructed three events in which one of the D_s mesons decays leptonically. By normalizing to the total number of events in which at least one D_s is fully reconstructed, they extract the branching fraction $\mathcal{B}(D_s \rightarrow \mu \nu) = (1.5_{-0.6}^{+1.3+0.3})\%$ with the assumption of μ - τ universality, and the decay constant $f_{D_s} = (430_{-130}^{+150} \pm 40)$ MeV. Unlike the measurement of f_{D_s} described above, the BES measurement is not normalized to other D_s decay modes, but suffers from a very large statistical error.

12.1.3 Semileptonic Decays

In this section, the theoretical motivation for studying semileptonic decays of the D and D_s mesons is discussed, along with the status of experimental measurements of decay rates and form factors. Both CLEO and the Fermilab fixed-target experiments have contributed to measurements of decay rates for both Cabibbo-favored and Cabibbo-suppressed modes, and to studies of semileptonic D_s decays. CLEO has the highest-statistics study of the dynamics of the decay $D^0 \rightarrow K^- \ell^+ \nu$. However, the measurements of form-factor ratios in the decay $D^+ \rightarrow \bar{K}^{*0} \ell^+ \nu$ are exclusively from fixed-target experiments. This is because the study of correlations between the final state particles, necessary for extracting form-factor ratios, requires a relatively clean sample of signal events and reconstruction of the neutrino momentum. The high boost of the charm meson and the presence of silicon detectors at fixed-target experiments allows the background-to-charm signals to be suppressed and the direction of the D momentum to be determined so that the neutrino momentum can be calculated up to a quadratic ambiguity.

The quality of the measurements that will be made with BABAR will depend on many factors:

1. Recording large integrated luminosity — this is particularly important for the Cabibbo-suppressed modes;
2. The performance of the hadron identification systems — again, this is particularly important for the Cabibbo-suppressed modes where K/π separation is important;
3. The performance of the muon and electron identification systems over the full range of lepton momenta;
4. The performance of the silicon vertex detector, for suppressing non-charm background; and
5. The hermiticity of the detector, for reconstructing the momentum of the missing neutrino.

12.1.3.1 Theoretical motivation

Both B and D semileptonic decays contain a heavy quark in the initial state, so their decays to a given charmless final state are very similar. The D system thus provides a unique arena in which to test or complement ideas about hadronic physics that are essential for analyses of B decays. Such ideas include heavy quark symmetry, lattice QCD, heavy baryon chiral perturbation theory, sum rules, and quark models.

Of special interest, is that in the B rest frame a measurement of the ratio

$$\left. \frac{d\Gamma(B \rightarrow \pi e \bar{\nu}_e)/dE_\pi}{d\Gamma(D \rightarrow \pi e \bar{\nu}_e)/dE_\pi} \right|_{\text{same } E_\pi} = \left| \frac{V_{ub}}{V_{cd}} \right|^2 \left(\frac{M_B}{M_D} \right) \left| \frac{f_+^{B \rightarrow \pi}}{f_+^{D \rightarrow \pi}} \right|^2 \quad (12.9)$$

yields a value for V_{ub} if the ratio of form factors f_+ that govern $B \rightarrow \pi e \bar{\nu}_e$ and $D \rightarrow \pi e \bar{\nu}_e$ decays is known. Analogous equations apply to $B, D \rightarrow K$, $B, D \rightarrow K^*$, and $B, D \rightarrow \rho$ semileptonic decays, except that decays to vector mesons involve more form factors. The extraction of fundamental weak interaction parameters like V_{ub} thus requires theoretical predictions of hadronic form factors.

A promising and model-independent approach is to rely on symmetries to relate form factors involved in different decays. Heavy quark symmetry predicts the ratio of form factors in the semileptonic decays $B \rightarrow H$ and $D \rightarrow H$, as long as H is the same state in both cases. For example, the ratio $f_+^{B \rightarrow \pi}/f_+^{D \rightarrow \pi}$ at equal pion energies is determined by heavy quark symmetry, so a measurement of $D \rightarrow \pi e \bar{\nu}_e$ can be used towards the extraction of V_{ub} . Corrections to such relations go like $\Lambda_{QCD}(1/m_c - 1/m_b) \sim 20\%$, and preliminary indications from $B \rightarrow D^* e \bar{\nu}_e$ [36], $B \rightarrow D e \bar{\nu}_e$ [37], and $\Lambda_c \rightarrow \Lambda e \bar{\nu}_e$ [38] indicate that this may be a realistic estimate. However, very little is known about heavy-to-light decays of mesons. Comparing the q^2 dependence of B and D semileptonic form factors is therefore critical to assessing the size of $1/m$ corrections.

The Cabibbo-suppressed decays $D \rightarrow \pi e \bar{\nu}_e$ and $D \rightarrow \rho e \bar{\nu}_e$ are related by $SU(3)$ flavor symmetry to $D \rightarrow K e \bar{\nu}_e$ and $D \rightarrow K^* e \bar{\nu}_e$, which are more accessible experimentally. The disadvantage in using these decays to extract V_{ub} is that the uncertainty from combined $SU(3)$ and heavy quark symmetry violation can be rather large, perhaps 30 – 40%. Even so, there is an advantage relative to hadronic models whose uncertainties cannot be systematically quantified. Some attempts to reduce the $SU(3)$ and heavy quark uncertainties by measuring double ratios of form factors, as well as a way to constrain the shapes of form factors using dispersion relations, are described in Chapter 8.

A final symmetry that can be applied is Chiral symmetry. Combined with heavy quark symmetry, this leads to the prediction [39, 40]

$$f_+^{B \rightarrow \pi} = \frac{-1}{2f_\pi} \left[\frac{g_{B^* B \pi} f_{B^*}}{E_\pi + M_{B^*} - M_B} - \frac{g_{B^* B \pi} f_{B^*}}{M_B} + f_B \right], \quad (12.10)$$

where f_π , f_B , and f_{B^*} are the π , B and B^* decay constants, respectively, $g_{B^*B\pi}$ is an unknown coupling, and E_π is the pion energy in the B rest frame. Precisely the same formula applies to $f_+^{D \rightarrow \pi}$ after the replacements $M_B, M_{B^*} \rightarrow M_D, M_{D^*}$, $g_{B^*B\pi} \rightarrow g_{D^*D\pi}$, and $f_B, f_{B^*} \rightarrow f_D, f_{D^*}$. The prediction is valid for soft pions, with corrections of order E_π over the chiral symmetry breaking scale $\Lambda_\chi \sim 1 \text{ GeV}$. There are no $1/m$ corrections, so measurements of $B \rightarrow \pi e \bar{\nu}_e$ and $D \rightarrow \pi e \bar{\nu}_e$ close to maximum q^2 (soft pions) can provide both a test of the prediction for the shape and a clean extraction of V_{ub} if the unknown constants can be determined. The static quantities $f_B, f_{B^*}, f_D, f_{D^*}$ and f_{D_s} are ideally suited for lattice studies, and their ratios even more so, so if the overall normalization can be set by an accurate measurement of f_{D_s} , there is reason to expect reliable determinations of all the relevant decay constants. The coupling $g_{D^*D\pi}$ can be directly determined from the absolute $D^* \rightarrow D\pi$ width, or indirectly from the $D^* \rightarrow D\gamma$ branching fraction. The coupling $g_{B^*B\pi}$ is equal to $g_{D^*D\pi}$ in the infinite mass limit, and $1/m$ corrections can be eliminated if $g_{B^*B\pi}$ is amenable to lattice calculation or experimental extraction.

For example, the decay $B \rightarrow \pi \tau \bar{\nu}$ involves a second form factor that in the chiral limit is given by [39]

$$f_0 = \frac{f_B}{f_\pi}, \quad (12.11)$$

up to $1/m^2$ and E_π/Λ_χ corrections. Given the various decay constants, a helicity or angular analysis of $B \rightarrow \pi \tau \bar{\nu}$ can give $g_{B^*B\pi}$. This is a challenging but rewarding measurement that deserves consideration in the years after turn-on. It is worth noting that even data with relatively hard pions will be useful in this program, because dispersive constraints on the shape of the form factor help in extrapolating back towards zero recoil. One might reasonably hope to use this method to extract V_{ub} with 10% theoretical errors.

Symmetries are not the only theoretical tools available. Quark models and Sum Rules have enjoyed good success in describing D decays to pseudo-scalars, but have been less successful in describing form factors in decays to vectors. A comparison [24] of some of the theoretical predictions against experiment is shown in Table 12-10. For one of the form factors, A_2 , the discrepancy between theory and experiment is as large as 50 – 300%. Lattice simulations fare somewhat better, partly because they have large uncertainties for this amplitude. However, they do not predict the shapes of form factors, but rather the normalizations at a few nearby kinematic points.

Both to assess their reliability and to aid in their improvement, it is important to test the predictions of all these methods in as many D decays as possible. This includes not only B and D semileptonic decays into π , K , ρ , and K^* , but also decays of strange particles like $B_s \rightarrow \Phi \ell \bar{\nu}_\ell$ and $D_s \rightarrow \Phi \ell \bar{\nu}$. In this way more can gradually be learned about the size of heavy quark, SU(3) flavor, and chiral symmetry corrections, as well as the reliability of lattice simulations and other nonperturbative methods.

12.1.3.2 Status of experimental measurements

$D \rightarrow \bar{K}\ell^+\nu$

The most precise experimental studies of $D \rightarrow \bar{K}\ell^+\nu$ have been made for the mode $D^0 \rightarrow K^-\ell^+\nu$ because the final state contains two easily reconstructed charged particles, both of which are produced at the D decay point. In e^+e^- experiments, such as CLEO, the efficiency for reconstructing K^0 is lower than that for reconstructing a K^- because of the branching fraction for neutral kaons to decay to charged particles in the detector, and because two charged tracks must be reconstructed.

The relatively large number of reconstructed $D^0 \rightarrow K^-\ell^+\nu$ decays, and the fact that the decay rate can be expressed in terms of just one form factor $f_+(q^2)$ mean that $D^0 \rightarrow K^-\ell^+\nu$ is the only charm decay for which the q^2 dependence of the form factor has been studied. Since the value of V_{cs} is known independently, measurements of the partial decay rate determine the overall normalization of the form factor.

The sample of $D^0 \rightarrow K^-\ell^+\nu$ decay candidates from CLEO [41] is significantly larger than any previous sample, leading to the most sensitive study to date of the q^2 dependence of the form factor f_+ . The analysis will therefore be described in more detail here. The decay $D^{*+} \rightarrow D^0\pi^+$ is used to obtain a clean sample of $D^0 \rightarrow K^-\ell^+\nu$ decays, just as it is often used for $D^0 \rightarrow K^-\pi^+$. The only difference is that the D^0 is not fully reconstructed, due to the neutrino in the final state, which broadens the peak in the distribution of mass difference $\Delta M = m(K\ell\pi) - m(K\ell)$. The signal-to-background ratio for the selected events is about 3.6. The form factor itself increases roughly linearly by about a factor of two over the kinematically allowed range of q^2 . The world average result of a fit to the functional $f_+(q^2) = f_+(0)/(1 - q^2/M_P^2)$ by CLEO II [41] along with the measurements of M_P from other experiments [42, 43, 44, 45] is $M_P = 2.00 \pm 0.15$ GeV, which is somewhat lower than $M_P = M_{D_s^*} = 2.1$ GeV/ c^2 . As an alternative to the pole form, CLEO also assumed the form $f_+(q^2) = f_+(0)e^{\alpha q^2}$ and fit for the parameter α . The measured value of $\alpha = (0.29 \pm 0.04 \pm 0.06)$ GeV $^{-2}$ is about one standard deviation higher than the value used in the ISGW model [46].

The form-factor intercept $f_+(0)$ can be extracted by integrating the differential decay rate for a particular assumption for the q^2 dependence of the form factor. Using the average decay rate $\Gamma(D \rightarrow \bar{K}\ell^+\nu)$, a pole form for the q^2 dependence with $M_P = 2.1$ GeV/ c^2 , and $|V_{cs}| = 0.97$, $f_+(0) = 0.76 \pm 0.02 \pm 0.02$ is determined to be $0.76 \pm 0.02 \pm 0.02$. The first error is from the uncertainty on the decay rate and the second error is from the uncertainty in the q^2 dependence [47]. This result is consistent with theoretical predictions of quark-model, lattice gauge, and QCD sum-rule calculations, which range from 0.6 to 0.9. Theoretical predictions for the $D \rightarrow \bar{K}\ell^+\nu$ form factor are summarized and compared with the experimental measurement in Table 12-10, along with the form factors for $D \rightarrow \bar{K}^*\ell^+\nu$, which are discussed in the next subsection. In Table 12-11, the form factors are given at q_{\max}^2 and compared with the theoretical predictions of ISGW [46] and ISGW2 [48].

Table 12-9. Parameters extracted from the decay distributions for $D^+ \rightarrow \bar{K}^{*0} \ell^+ \nu$: the ratios of form factors $r_V = V(0)/A_1(0)$ and $r_2 = A_2(0)/A_1(0)$.

Experiment	$r_V = V(0)/A_1(0)$	$r_2 = A_2(0)/A_1(0)$	# of events
E691 [49]	$2.0 \pm 0.6 \pm 0.3$	$0.0 \pm 0.5 \pm 0.2$	$\sim 200, e$
E653 [50]	$2.00^{+0.34}_{-0.32} \pm 0.16$	$0.82^{+0.22}_{-0.23} \pm 0.11$	$\sim 300, \mu$
E687 [51]	$1.74 \pm 0.27 \pm 0.28$	$0.78 \pm 0.18 \pm 0.10$	$\sim 900, \mu$
E791 [52]	$1.84 \pm 0.11 \pm 0.08$	$0.71 \pm 0.08 \pm 0.09$	$\sim 3000, e$
Average	1.85 ± 0.12	0.71 ± 0.09	

$D \rightarrow \bar{K}^* \ell^+ \nu$

The largest and cleanest signals for the decay $D \rightarrow \bar{K}^* \ell^+ \nu$ are extracted from fixed-target experiments in the mode $D^+ \rightarrow \bar{K}^{*0} \ell^+ \nu$, where $\bar{K}^{*0} \rightarrow K^- \pi^+$. This mode has several advantages over the mode $D^0 \rightarrow \bar{K}^{*-} \ell^+ \nu$, with $K^{*-} \rightarrow K^- \pi^0$ or $\bar{K}^0 \pi^-$. For the $K^- \pi^+ \ell^+ \nu$ final state, all the particles in the final state (except the neutrino) are long-lived charged particles that can be reconstructed more efficiently than π^0 s or neutral kaons. The non-charm background can be studied with so-called “wrong-sign” candidates, in which the kaon charge is not consistent with the lepton charge (e.g., $K^+ \pi^- \ell^+$).² This definition of a wrong-sign background is not possible with a neutral kaon in the final state. Ratios of form factors³ $r_V = V(0)/A_1(0)$ and $r_2 = A_2(0)/A_1(0)$ have been extracted from the observed multidimensional distributions of kinematic variables for the decay $D^+ \rightarrow \bar{K}^{*0} \ell^+ \nu$ by four Fermilab fixed-target experiments [49, 50, 51, 52]. The measured form-factor ratios for all four experiments, along with the number of signal events, are shown in Table 12-9.

The world average partial decay rate for $D \rightarrow \bar{K}^* \ell^+ \nu$ can be combined with the form factor ratios to extract the form factors themselves. The resulting values of $A_1(0)$, $A_2(0)$, and $V(0)$ are given in Table 12-10, where the average measured values of the form factors are also compared with some of the theoretical predictions from QCD-inspired phenomenological models, lattice calculations, and QCD sum rules. Generally, the measured values of the axial form factors, $A_1(0)$ (which dominates the decay rate) and $A_2(0)$, are low compared with theoretical predictions. The vector form factors, on the other hand, are in reasonable agreement for both $D \rightarrow \bar{K} \ell^+ \nu$ and $D \rightarrow \bar{K}^* \ell^+ \nu$.

²This technique requires that the kaon be independently identified with a particle identification system such as Čerenkov detectors. If the kaon is not identified, the wrong-sign combination $K^+ \pi^+ \ell^-$ can be used, but then the combination of hadrons $K^+ \pi^+$ is no longer neutral.

³In these analyses, each of the three form factors is assumed to have a pole form for the q^2 dependence, with $M_P = 2.1 \text{ GeV}/c^2$ for the vector form factor and $M_P = 2.5 \text{ GeV}/c^2$ for the axial form factors.

Table 12-10. Theoretical predictions for form factors at $q^2 = 0$ for $D \rightarrow \bar{K}\ell^+\nu$ (f_+) and for $D \rightarrow \bar{K}^*\ell^+\nu$ (A_1, A_2, V) compared with experimental measurements.

	$f_+(0)$	$A_1(0)$	$A_2(0)$	$V(0)$
Experimental Average	0.76 ± 0.03	0.58 ± 0.01	0.41 ± 0.05	1.06 ± 0.08
<i>Quark Models</i>				
ISGW [46]	0.8	0.8	0.8	1.1
KS [53]	0.7	0.82	0.8	0.8
AW/GS [54, 55]	0.7	0.8	0.6	1.5
<i>Lattice Gauge</i>				
ELC [56]	$0.60 \pm 0.15 \pm 0.07$	0.64 ± 0.16	$0.41 \pm 0.28 \pm 0.04$	0.86 ± 0.24
APE [57]	0.78 ± 0.08	0.67 ± 0.11	0.49 ± 0.34	1.08 ± 0.22
UKQCD [58]	0.67 ± 0.08	$0.70^{+0.07}_{-0.10}$	$0.66^{+0.10}_{-0.15}$	$1.01^{+0.30}_{-0.13}$
<i>Sum Rules</i>				
BBD [59]	0.60	0.5	0.6	1.1

In Table 12-11, the form factors measured at $q^2 = 0$ are extrapolated to q_{max}^2 , assuming a pole form for the q^2 dependence with $M_P = 2.1 \text{ GeV}/c^2$ for the vector form factors and $M_P = 2.5 \text{ GeV}/c^2$ for the axial form factors. Future measurements of the form factors should be quoted at q_{max}^2 , as well as at $q^2 = 0$, since the value at q_{max}^2 is related to a single universal form factor in HQET, up to (large) $1/m_Q$ corrections. Form factors at $q^2 = 0$, on the other hand, are the product of the value at q_{max}^2 and a function that depends on the dynamics of the final state meson recoiling with maximum momentum in the rest frame of the initial meson. In Table 12-11, the form factor predictions are also given at q_{max}^2 of the ISGW [46] quark model and the updated predictions of ISGW2 [48]. The ISGW2 model incorporates the constraints imposed by HQET, relativistic correction factors, hyperfine distortions of wavefunctions, and form factors with more realistic high-recoil behavior. The updated predictions are in better agreement with the data. The prediction for $f_+(q_{max}^2)$ has shifted upward by about 6% due to four different effects. The prediction for $A_1(q_{max}^2)$ has decreased by about 30%, largely due to a relativistic correction. The prediction for $A_2(q_{max}^2)$ has moved closer to the measured value, but the agreement is still not very good. The net effect is that the theoretical predictions are now in better agreement with both measurements of the form factors themselves, as shown in Table 12-11.

$D_s \rightarrow \phi\ell^+\nu$

Two studies of the decay $D_s \rightarrow \phi\ell^+\nu$ are of interest. They are measurement of the branching fraction relative to $D_s \rightarrow \phi\pi^+$, which can be used to extract an absolute branching fraction for

Table 12-11. Theoretical predictions of ISGW and ISGW2 for form factors at $q^2 = q_{max}^2$ for $D \rightarrow \bar{K}\ell^+\nu$ (f_+) and for $D \rightarrow \bar{K}^*\ell^+\nu$ (A_1, A_2, V) compared with experimental measurements. Form factors measured at $q^2 = 0$ are extrapolated to q_{max}^2 assuming a pole form for the q^2 dependence with $M_P = 2.1 \text{ GeV}/c^2$ for the vector form factors and $M_P = 2.5 \text{ GeV}/c^2$ for the axial form factors.

Reference	$f_+(q_{max}^2)$	$A_1(q_{max}^2)$	$A_2(q_{max}^2)$	$V(q_{max}^2)$
Experimental Average	1.31 ± 0.04	0.68 ± 0.01	0.48 ± 0.06	1.35 ± 0.10
ISGW [46]	1.16	1.0	1.0	1.3
ISGW2 [48]	1.23	0.70	0.94	1.52

Table 12-12. Measurements of the form factors for the decay $D_s \rightarrow \phi\ell^+\nu$.

Experiment	# of events (lepton type)	Kinematic variables used in analysis	$r_V = V(0)/A_1(0)$	$r_2 = A_2(0)/A_1(0)$
E653 [60]	19 (μ)	$\cos \theta_\ell, \cos \theta_V, q^2$	$2.3_{-0.9}^{+1.1} \pm 0.4$	$2.1_{-0.5}^{+0.6} \pm 0.2$
E687 [61]	90 (μ)	$\cos \theta_\ell, \cos \theta_V, q^2, \chi$	$1.8 \pm 0.9 \pm 0.2$	$1.1 \pm 0.8 \pm 0.1$
CLEO II [62]	308 (e)	$\cos \theta_\ell, \cos \theta_V , q^2$	$0.9 \pm 0.6 \pm 0.3$	$1.4 \pm 0.5 \pm 0.3$
Average			1.4 ± 0.5	1.6 ± 0.4

$D_s \rightarrow \phi\pi^+$, and measurement of the form factors, which can be compared with those from $D^+ \rightarrow \bar{K}^{*0}\ell^+\nu$ and with theoretical predictions.

Two fixed-target experiments (E687 and E653) and CLEO have now measured the form factors in the decay $D_s \rightarrow \phi\ell^+\nu$, albeit with large uncertainties. The statistical errors are large because of limited D_s production in both fixed-target and e^+e^- machines. Also, the background level is considerably higher than that for $D^+ \rightarrow \bar{K}^{*0}\ell^+\nu$. E653 monitors their background with $K^+K^+\ell^-$ candidates. E687 and CLEO use sidebands to the ϕ peak; since the ϕ resonance is much narrower than the K^* resonance, sidebands to the K^+K^- mass peak can be used to monitor the background level and to incorporate the background in the fit.

Measurements of form factor ratios in $D_s \rightarrow \phi\ell^+\nu$ by E653, E687, and CLEO are shown in Table 12-12. The experimental average of each ratio is consistent with the value measured for the decay mode $D^+ \rightarrow \bar{K}^{*0}\ell^+\nu$ (see Table 12-9, page 811), although the value of r_2 for $D_s \rightarrow \phi\ell^+\nu$ is about two standard deviations high.

Table 12-13. Measurements of the ratio of form factors $\frac{f_+^\pi(0)}{f_+^K(0)}$ in the Cabibbo-suppressed decay $D \rightarrow \pi \ell \nu$ and Cabibbo-favored decay $D \rightarrow \bar{K} \ell \nu$. The decay mode used and the number of Cabibbo-suppressed signal events is listed in the second column.

Experiment	Mode (num. of events)	$\left \frac{V_{cd}}{V_{cs}} \right ^2 \left(\frac{f_+^\pi(0)}{f_+^K(0)} \right)^2$
CLEO [63]	$\frac{\mathcal{B}(D^+ \rightarrow \pi^0 \ell^+ \nu)}{\mathcal{B}(D^+ \rightarrow \bar{K}^0 \ell^+ \nu)}$ (58)	$0.085 \pm 0.027 \pm 0.014$
CLEO [64]	$\frac{\mathcal{B}(D^0 \rightarrow \pi^- \ell^+ \nu)}{\mathcal{B}(D^0 \rightarrow K^- \ell^+ \nu)}$ (87 ± 33)	$0.052 \pm 0.020 \pm 0.007$
Mark III [65]	$\frac{\mathcal{B}(D^0 \rightarrow \pi^- \ell^+ \nu)}{\mathcal{B}(D^0 \rightarrow K^- \ell^+ \nu)}$ (7)	$0.057_{-0.017}^{+0.038} \pm 0.005$

Cabibbo-Suppressed Semileptonic Decays of Charm Mesons

The ratio of Cabibbo-suppressed to Cabibbo-favored semileptonic decays of the D meson to a pseudoscalar meson in the final state can be used to determine the product of the ratio of CKM matrix elements $|V_{cd}/V_{cs}|$ and the ratio of form factors $f_+^\pi(0)/f_+^K(0)$. In particular,

$$\frac{\mathcal{B}(D^0 \rightarrow \pi^- e^+ \nu_e)}{\mathcal{B}(D^0 \rightarrow K^- e^+ \nu_e)} = 2 \frac{\mathcal{B}(D^+ \rightarrow \pi^0 e^+ \nu_e)}{\mathcal{B}(D^+ \rightarrow \bar{K}^0 e^+ \nu)} = 1.97 \left| \frac{V_{cd}}{V_{cs}} \right|^2 \left(\frac{f_+^\pi(0)}{f_+^K(0)} \right)^2, \quad (12.12)$$

where the factor of two difference between the two ratios arises from the $1/\sqrt{2}$ coupling of $d\bar{d}$ to the π^0 .

Table 12-13 lists three experimental results from CLEO [63, 64] and Mark III [65] for this ratio of form factors. Using $|V_{cd}/V_{cs}|^2 = 0.051 \pm 0.002$ from unitarity of the CKM matrix, the average of the Mark III and CLEO measurements can be used to extract the ratio of form factors $f_+^\pi(0)/f_+^K(0) = 1.2 \pm 0.3$. This result is consistent with theoretical predictions which range from 0.7 to 1.4 [46, 66, 67, 68, 69, 70, 71, 72].

Three Fermilab experiments [73, 74, 75] have each observed signal in the mode $D^+ \rightarrow \rho^0 \ell^+ \nu$. The results of the measurements of the decay rate relative to the corresponding Cabibbo-favored mode $\frac{\mathcal{B}(D^+ \rightarrow \rho^0 \ell^+ \nu)}{\mathcal{B}(D^+ \rightarrow \bar{K}^{*0} \ell^+ \nu)}$ are given in Table 12-14.

A model by Scora and Isgur [48] predicts that the measured ratio should equal $0.42 |V_{cd}/V_{cs}|^2 = 0.022$, not quite consistent with the experimental average given in Table 12-14.

Table 12-14. Results of the measurements of $\frac{\mathcal{B}(D^+ \rightarrow \rho^0 \ell^+ \nu)}{\mathcal{B}(D^+ \rightarrow \bar{K}^{*0} \ell^+ \nu)}$.

Experiment	Signal size (lepton)	$\frac{\mathcal{B}(D^+ \rightarrow \rho^0 \ell^+ \nu)}{\mathcal{B}(D^+ \rightarrow \bar{K}^{*0} \ell^+ \nu)}$
E653 [73]	$4.0_{-2.3}^{+2.8}(\mu)$	$0.044_{-0.025}^{+0.031} \pm 0.014$
E687 [74]	$39.2 \pm 9.0(\mu)$	$0.079 \pm 0.019 \pm 0.013$
E791 [75]	$49 \pm 17(e)$	$0.045 \pm 0.014 \pm 0.009$
	$54 \pm 18(\mu)$	$0.051 \pm 0.015 \pm 0.009$
Average		0.054 ± 0.010

12.1.4 Hadronic Charm Decays

Nonleptonic decays of charmed mesons and beauty mesons are more complicated than the corresponding semileptonic decays or the purely leptonic decays. They are also more plentiful. Cabibbo-favored charmed meson branching ratios are often as large as 1% – 10%. This makes their experimental determinations much easier than those for corresponding beauty decays where the branching ratios are typically in the range 0.1% – 1%. Studying the patterns of nonleptonic charm decays will probe the interplay of perturbative and nonperturbative physics. Nonleptonic decays also will be used in studies of $D^0 \bar{D}^0$ mixing, in studies of the masses and widths of orbitally-excited charmed mesons which test Heavy Quark Effective Theory, and in searches for direct CP violation in the charm sector. The samples of nonleptonic decays will be very large, enabling them to be used as laboratories for studying light meson spectroscopy. Some doubly Cabibbo-suppressed decay (DCSD) rates to be measured will be important for extracting physics parameters from B -meson CP violation measurements which are sensitive to the unitarity angle γ .

Earlier, in Section 12.1, the characteristics of hadronic charm decays from $c\bar{c}$ continuum production and from $B\bar{B}$ decays were discussed. In Section 12.4, hadronic D decays are discussed as a source of light mesons.

12.1.4.1 Theoretical predictions

A theoretical description of exclusive nonleptonic decays of charmed hadrons based on general principles is not yet possible. Even if the short-distance effects due to hard gluon exchange can be resummed and an effective Hamiltonian constructed at next-to-leading order [76], the evaluation of its matrix elements requires nonperturbative techniques and, at present, one has to rely on approximate methods and/or models.

The lifetime differences for charmed hadrons make it clear that the infinitely heavy quark limit is quite far from the actual situation. Therefore, the expansion in inverse powers of the heavy

quark mass characteristic of heavy quark effective theory is presumably not a useful tool in this case. In addition, the simple factorization ansatz for the matrix elements is known not to describe Cabibbo-allowed D^0 decays properly — the color-suppression factor of some contributions appears to be smaller than the value of $1/3$ expected from QCD and the data exhibit large phase differences between amplitudes with definite isospin. In some recent papers [77], the importance of nonfactorizable contributions has been stressed and their dependence on the particular process checked. In fact, there exist several decay channels that have vanishing branching ratios in the naive factorization assumption (*i.e.*, without annihilation and without rescattering effects), but are seen experimentally. For example, $D^0 \rightarrow \phi \bar{K}^0$, which only receives contributions from annihilation and/or rescattering, has a branching ratio similar to $D^0 \rightarrow \rho^0 \bar{K}^0$, which in turn, in factorization approximation, should be equal to that for $D^0 \rightarrow \omega \bar{K}^0$ and is instead roughly half of it. A recently measured channel, $D_s^+ \rightarrow \omega \pi^+$ [78], has only rescattering contributions. Moreover, only rescattering in exotic channels can be effective in this case, since resonant rescattering and (chiral-suppressed) annihilation would only feed $D_s^+ \rightarrow \rho^0 \pi^+$, which has not yet been observed. The W -exchange contribution to $D^0 \rightarrow K^0 \bar{K}^0$ vanishes, so that this amplitude also receives rescattering contributions only. However, its branching ratio is even larger than that for $D^0 \rightarrow \pi^0 \pi^0$, which receives a factorized, albeit color-suppressed, contribution. This last decay is the most evident signature of the strong breaking of flavor SU(3) symmetry in charm decays, which requires the U-spin singlet D^0 to decay only into states having U-spin equal to one. Other symmetry predictions, like the equality of D^0 decay rates into $K^+ K^-$ and $\pi^+ \pi^-$ or the $\tan^2 \theta_C$ value for the ratio of the D^+ rates into $\pi^+ \pi^0$ and $K_s \pi^+$, are also badly violated. An analysis of charm meson decay rates in terms of SU(3) reduced matrix elements has been performed [79]; however, the very importance of symmetry breaking terms requires the introduction of a large number of free parameters and a consequent lack of predictivity.

The results presented here were obtained in a phenomenological model [7, 8], which was developed to address these observations. The factorization approximation is modified by assuming one universal but arbitrary “color-suppression” parameter ξ (not necessarily $1/3$) and important corrections due to W -exchange (or annihilation) and to rescattering effects in the final states are also included. The presence of nearby resonances may well have the effect of increasing the annihilation terms relative to their naive PCAC estimates. Strong phase shifts are determined by the masses and widths of such resonances, when known. The model thus incorporates most of the ingredients needed for a realistic description of known hadronic charm decays. Its predictions allow an estimate of the channels which might prove to be the best choices for use in mixing or CP violation searches.

The model is used to describe two-body decays of charmed mesons with final states PP, PV, and PS (S being one of the lightest scalar mesons, a_0 or f_0). The factorized decay amplitudes are well known (the fitted value for ξ is 0.01). The annihilation (W -exchange) contributions depend on matrix elements of the divergence of (axial) vector currents, which are related through the

equations of motion, to scalar (pseudoscalar) densities in the following way:

$$\begin{aligned} \langle K^- \pi^+ | \partial^\mu (\bar{s} \gamma_\mu d) | 0 \rangle &= i(m_s - m_d) \langle K^- \pi^+ | \bar{s} d | 0 \rangle \equiv i(m_s - m_d) \frac{M_D^2}{f_D} W_{PP}, \\ \langle K^- \rho^+ | \partial^\mu (\bar{s} \gamma_\mu \gamma_5 d) | 0 \rangle &= i(m_s + m_d) \langle K^- \rho^+ | \bar{s} \gamma_5 d | 0 \rangle \\ &\equiv -(m_s + m_d) \frac{2M_\rho}{f_D} \epsilon^* \cdot p_K W_{PV}. \end{aligned}$$

SU(3) symmetry is assumed for the matrix elements of the densities. W_{PP} and W_{PV} are two fitted parameters ($-0.28, 0.36$).

For the lightest scalar resonances this model follows the suggestion of [80], considering them as cryptoexotic $s\bar{s}q\bar{q}$ states belonging to (incomplete) $\underline{8}$ and $\underline{1}$ SU(3) representations. The value of the form factor at $q^2=0$ for the D meson transition to a scalar mediated by the axial current is introduced as a new parameter and its fitted value (0.26) is much less than the similar quantity for other form factors.

Some details on the treatment of final state interactions, a characteristic feature of this approach, follow. The PP final states have $J^{PC} = 0^{++}$ and belong to $\underline{1}$, $\underline{8}$ and $\underline{27}$ SU(3) representations. Neglecting the $\underline{27}$ phase shift, the scalar resonances determine the phase shifts in nonexotic ($\underline{1}$ and $\underline{8}$) channels. The only experimental indication is for a resonance $K_0^*(1950)$, the other members of an octet are reconstructed using $M_{a_0}^2 = M_{K_0^*}^2 - M_K^2 + M_\pi^2$ and the Gell-Mann–Okubo formula — the f_0 - f'_0 mixing angle and the mass of the singlet are fitted parameters. The couplings are chosen in order to inhibit the decay into $\pi\pi$ of the heaviest resonance, f'_0 , as happens in the tensor nonet.

The PV final states have $J^P = 0^-$ and may belong to $\underline{1}$, $\underline{8}_D$ and $\underline{27}$ with $C = -1$, to $\underline{8}_F$ with $C = +1$ or to $\underline{10}$ and $\underline{10}^*$. The resonances $K(1830)$ and $\pi(1800)$ determine the phase shift in the nonexotic $\underline{8}_F$ channel. These same resonances are also coupled to PS in the $\underline{8}_D$ representation. The PV final states are therefore coupled by rescattering to PS channels ($|8\rangle = |8_F\rangle_{PV} + x_{PS} |8_D\rangle_{PS}$). Given the large number of exotic final states, the model also introduced a rescattering phase in one of them, $\underline{27}$, that again mixes PV and PS states ($|27_{Y=\mp 1}\rangle = |27_{Y=\mp 1}\rangle_{PV} \pm y_{PS} |27_{Y=\mp 1}\rangle_{PS}$, the sign change deriving from the opposite C properties of PV and PS states, so that $y_{PS} \neq 0$ is another sign of SU(3) violation). Unitarity requires the states $|8\rangle$ and $|27\rangle$ to be orthogonal. This is not automatic because of SU(3) breaking. The product $x_{PS} y_{PS}$ is fixed by this requirement and only x_{PS} remains as a free parameter. In the fit, $y_{PS} = -0.15$ is considerably less ($\sim 19\%$) than x_{PS} in agreement with expectations, since a nonzero x_{PS} is allowed by SU(3).

The phase shift in the nonexotic isoscalar PV and PS channels is a fitted parameter (208°), as well as those in the exotic $\underline{27}$ channels, both for D and D_s decays. Their values are quite near to each other ($\sim 44^\circ$). The results of the updated fit (56 experimental data or upper bounds [28, 78] with 15 parameters and a $\chi^2 \simeq 70$)⁴ are presented in Table 12-15, together with the predicted CP -violating

⁴This update includes some newer data [28, 78] and hence the numbers differ from the earlier fits discussed in [7, 8].

Table 12-15. Branching ratios for Cabibbo-allowed and some doubly-forbidden decays. Experimental values are from Ref. [28, 78] and theoretical predictions from Ref. [7, 8].

Decay Channel	\mathcal{B}_{exp}	\mathcal{B}_{th}	Decay Channel	\mathcal{B}_{exp}	\mathcal{B}_{th}
$D^0 \rightarrow K^- \pi^+$	3.83 ± 0.12	3.85	$D^+ \rightarrow K_S \pi^+$	1.37 ± 0.15	1.35
$D^0 \rightarrow K_S \pi^0$	1.05 ± 0.10	0.76	$D_s^+ \rightarrow K^+ K_S$	1.80 ± 0.55	2.47
$D^0 \rightarrow K_S \eta$	0.35 ± 0.05	0.45	$D_s^+ \rightarrow \pi^+ \eta$	2.0 ± 0.6	1.13
$D^0 \rightarrow K_S \eta'$	0.85 ± 0.13	0.80	$D_s^+ \rightarrow \pi^+ \eta'$	4.9 ± 1.8	5.44
$D^+ \rightarrow \bar{K}^{*0} \pi^+$	1.92 ± 0.19	2.00	$D^+ \rightarrow \rho^+ K_S$	3.30 ± 1.25	5.82
$D^0 \rightarrow \bar{K}^{*0} \pi^0$	3.10 ± 0.40	3.21	$D_s^+ \rightarrow \rho^+ \eta$	10.3 ± 3.2	8.12
$D^0 \rightarrow \rho^0 K_S$	0.60 ± 0.085	0.45	$D_s^+ \rightarrow \rho^+ \eta'$	12.0 ± 4.0	2.46
$D^0 \rightarrow K^{*-} \pi^+$	5.0 ± 0.4	4.66	$D_s^+ \rightarrow \phi \pi^+$	3.6 ± 0.9	4.55
$D^0 \rightarrow \rho^+ K^-$	10.8 ± 1.0	11.2	$D_s^+ \rightarrow \bar{K}^{*0} K^+$	3.4 ± 0.9	4.81
$D^0 \rightarrow \bar{K}^{*0} \eta$	1.90 ± 0.50	0.47	$D_s^+ \rightarrow K^{*+} K_S$	2.15 ± 0.7	1.10
$D^0 \rightarrow \bar{K}^{*0} \eta'$	< 0.11	0.004	$D_s^+ \rightarrow \rho^0 \pi^+$	< 0.29	0.01
$D^0 \rightarrow \omega K_S$	1.05 ± 0.20	0.97	$D_s^+ \rightarrow \rho^+ \pi^0$	—	0.01
$D^0 \rightarrow \phi K_S$	0.425 ± 0.05	0.414	$D_s^+ \rightarrow \omega \pi^+$	0.27 ± 0.12	0.20
$D^0 \rightarrow f_0 K_S$	0.285 ± 0.080	0.30	$D_s^+ \rightarrow f_0 \pi^+$	1.20 ± 0.50	0.69
$D^0 \rightarrow a_0^0 K_S$	—	0.10	$D^+ \rightarrow a_0^+ K_S$	—	0.13
$D^0 \rightarrow a_0^+ K^-$	—	0.49	$D_s^+ \rightarrow a_0^+ \eta$	—	0.001
$D^0 \rightarrow K^+ \pi^-$	0.029 ± 0.014	0.033	$D^+ \rightarrow \phi K^+$	< 0.013	0.003
$D^+ \rightarrow K^{*0} \pi^+$	< 0.019	0.027	$D^+ \rightarrow \rho^0 K^+$	< 0.06	0.029
$D^0 \rightarrow K^{*+} \pi^-$	—	0.038	$D^+ \rightarrow K^+ \pi^0$	—	0.055
$D^0 \rightarrow K^{*0} \pi^0$	—	0.004	$D^+ \rightarrow K^{*+} \pi^0$	—	0.057

asymmetries for the Cabibbo-forbidden decays, in Tables 12-16 and 12-17. Typically the predicted asymmetries may vary up to a factor of two due to the present uncertainty on CKM parameters. In the most favorable cases, asymmetries slightly larger than 1/1000 are predicted.

Concerning the results/predictions for branching ratios, note that the data for $D^0 \rightarrow \bar{K}^{*0} \eta$ and $D_s^+ \rightarrow \rho^+ \eta'$ are considerably larger than the fitted value, maybe pointing to a glue component [81]. For the Cabibbo doubly-forbidden decays, the model predicts the largest branching ratios ($\sim 6 \cdot 10^{-4}$) for $D^+ \rightarrow K^{+(*)} \pi^0$, (yet to be observed). In fact, the prediction is larger than the present experimental bound for $D^+ \rightarrow K^{*0} \pi^+$. The model predicts a very small branching ratio for $D^0 \rightarrow K^{*0} \pi^0$, which would in principle be a good channel for $D^0 \bar{D}^0$ mixing searches.

Table 12-16. Branching ratios and CP asymmetry predictions for Cabibbo-forbidden decays of D^+ and D_s^+ mesons. Experimental values are from Ref. [28, 78] and theoretical predictions from Ref. [7, 8].

$D^+ \rightarrow$	\mathcal{B}_{exp}	\mathcal{B}_{th}	CP asymm.	$D_s^+ \rightarrow$	\mathcal{B}_{exp}	\mathcal{B}_{th}	CP asymm.
$\pi^+\pi^0$	0.25 ± 0.07	0.185	—	$K^+\pi^0$	—	0.146	$+1.07 \cdot 10^{-3}$
$\pi^+\eta$	0.75 ± 0.25	0.38	$-0.77 \cdot 10^{-3}$	$K^+\eta$	—	0.299	$-0.05 \cdot 10^{-3}$
$\pi^+\eta'$	< 0.9	0.768	$+0.90 \cdot 10^{-3}$	$K^+\eta'$	—	0.495	$-0.64 \cdot 10^{-3}$
$K^+\bar{K}^0$	0.72 ± 0.12	0.763	$-0.52 \cdot 10^{-3}$	π^+K^0	< 0.8	0.373	$+0.48 \cdot 10^{-3}$
$\pi^+\rho^0$	< 0.14	0.104	$-1.96 \cdot 10^{-3}$	$K^+\rho^0$	< 0.29	0.198	$+0.25 \cdot 10^{-3}$
$\rho^+\pi^0$	—	0.451	$+0.89 \cdot 10^{-3}$	$K^{*+}\pi^0$	—	0.076	$-0.92 \cdot 10^{-3}$
$\rho^+\eta$	< 1.2	0.064	$-1.60 \cdot 10^{-3}$	$K^{*+}\eta$	—	0.146	$-0.41 \cdot 10^{-3}$
$\rho^+\eta'$	< 1.5	0.122	~ 0	$K^{*+}\eta'$	—	0.029	$-0.09 \cdot 10^{-3}$
$\pi^+\omega$	< 0.7	0.038	$-0.60 \cdot 10^{-3}$	$K^+\omega$	—	0.178	$-0.34 \cdot 10^{-3}$
$\pi^+\phi$	0.61 ± 0.06	0.619	$-0.09 \cdot 10^{-3}$	$K^+\phi$	< 0.05	0.008	$+1.79 \cdot 10^{-3}$
$K^+\bar{K}^{*0}$	0.42 ± 0.05	0.436	$+0.68 \cdot 10^{-3}$	$K^{*0}\pi^+$	0.65 ± 0.28	0.444	$-0.75 \cdot 10^{-3}$
$K^{*+}\bar{K}^0$	3.0 ± 1.4	1.52	$-0.19 \cdot 10^{-3}$	$K^0\rho^+$	—	1.29	$+0.36 \cdot 10^{-3}$

Table 12-17. Branching ratios and CP asymmetry predictions for Cabibbo-forbidden decays of D^0 mesons. Experimental values are from Ref. [28, 78] and theoretical predictions from Ref. [7, 8].

$D^0 \rightarrow$	\mathcal{B}_{exp}	\mathcal{B}_{th}	CP asymm.	$D^0 \rightarrow$	\mathcal{B}_{exp}	\mathcal{B}_{th}	CP asymm.
$\pi^+\pi^-$	0.152 ± 0.011	0.152	$-0.10 \cdot 10^{-3}$	$\pi^0\eta$	—	0.054	$-1.44 \cdot 10^{-3}$
$\pi^0\pi^0$	0.084 ± 0.022	0.115	$+0.51 \cdot 10^{-3}$	$\pi^0\eta'$	—	0.175	$+0.89 \cdot 10^{-3}$
K^+K^-	0.433 ± 0.027	0.427	$-0.10 \cdot 10^{-3}$	$\eta\eta$	—	0.093	$-0.51 \cdot 10^{-3}$
$K^0\bar{K}^0$	0.13 ± 0.04	0.108	$+0.26 \cdot 10^{-3}$	$\eta\eta'$	—	0.186	$-0.31 \cdot 10^{-3}$
$\pi^0\omega$	—	0.013	$-0.01 \cdot 10^{-3}$	$\eta\rho^0$	—	0.020	$-0.53 \cdot 10^{-3}$
$\pi^0\phi$	< 0.14	0.105	$-0.04 \cdot 10^{-3}$	$\eta'\rho^0$	—	0.008	$+0.01 \cdot 10^{-3}$
$\eta\phi$	< 0.28	0.080	$-0.15 \cdot 10^{-3}$	$\eta\omega$	—	0.209	$-0.02 \cdot 10^{-3}$
$K^0\bar{K}^{*0}$	< 0.16	0.052	$-0.56 \cdot 10^{-3}$	$\eta'\omega$	—	0.0002	$-3.66 \cdot 10^{-3}$
\bar{K}^0K^{*0}	< 0.08	0.062	$-0.65 \cdot 10^{-3}$	$\pi^0\rho^0$	—	0.216	$-0.01 \cdot 10^{-3}$
K^-K^{*+}	0.35 ± 0.08	0.431	$-0.04 \cdot 10^{-3}$	$\pi^+\rho^-$	—	0.485	$-0.43 \cdot 10^{-3}$
K^+K^{*-}	0.18 ± 0.10	0.290	$+0.27 \cdot 10^{-3}$	$\pi^-\rho^+$	—	0.706	$+0.34 \cdot 10^{-3}$

Among the once forbidden decays, two branching ratio predictions are particularly large, *i.e.*, larger than 1%. For $D^+ \rightarrow K^{*+} \bar{K}^0$, the recent experimental result is even larger than the model prediction [8], and a check of the model could be provided by the detection of the other, $D_s^+ \rightarrow K^0 \rho^+$. The good quality of the fit for the $D^0 \rightarrow \text{PP}$ decays is remarkable. Further checks will be given by the observation of the other channels, the largest predictions being for the $\pi^0 \eta'$ and $\eta \eta'$ final states. In the PV sector, few branching ratios have been measured, a considerable improvement would be provided by a Dalitz Plot analysis of the $\pi^+ \pi^- \pi^0$ channel, allowing the determination of the $\rho \pi$ branching ratios (and also of $f_0 \pi^0$ — predicted $\mathcal{B} = 0.025$). Predicted values are rather large and are different for each of the three charge modes. They are also different for different models, see for example the model predictions used in Chapter 6 for such modes, or [79].

An important issue concerns the predictions of the Standard Model for the D^0 dzb mixing. In this model, one can evaluate the long-distance contribution to the width difference, Γ_{12} . This quantity should be zero in the SU(3) symmetric limit, and, given the large SU(3) violations in the branching ratios, one could expect rather large values for it, *a priori* [82]. It turns out, instead, that the SU(3) cancellation is still quite effective, the contribution of Cabibbo first-forbidden states being 0.035, the contribution of allowed plus doubly-forbidden -0.033 , and the final result

$$\Gamma_{12} / \Gamma = 1.8 \times 10^{-3}.$$

This may be understood easily. Unitarity makes Γ_{12} independent of rescattering effects, which, on the other hand induce large SU(3) breaking in the branching ratios through the phase shifts related to different masses and widths of the relevant resonances. A similar calculation, using the results of [79] has been performed in [83].

12.2 τ Physics

12.2.1 Present Status

Like the bottom quark, the τ lepton is a member of the third generation which decays into particles belonging to the first and second ones. Therefore, one can expect that τ and b physics could provide some clues to the puzzle of the recurring families of leptons and quarks. In fact, one naively expects the heavier fermions to be more sensitive to whatever dynamics is responsible for the fermion mass generation. While b decays are an ideal place to look for quark mixing and CP -violating phenomena, the pure leptonic or semileptonic character of τ decays provides a much cleaner laboratory to test the structure of the weak currents and the universality of their couplings to the gauge bosons. Moreover, the τ is the only known lepton massive enough to decay into hadrons; its semileptonic decays are then an ideal tool for studying strong interaction effects in very clean conditions.

Table 12-18. Average values [85] of some basic τ parameters.

m_τ	$(1777.00^{+0.30}_{-0.27})$ MeV
τ_τ	(290.21 ± 1.15) fs
$\text{Br}(\tau^- \rightarrow \nu_\tau e^- \bar{\nu}_e)$	$(17.786 \pm 0.072)\%$
$\text{Br}(\tau^- \rightarrow \nu_\tau \mu^- \bar{\nu}_\mu)$	$(17.317 \pm 0.078)\%$
$\text{Br}(\tau^- \rightarrow \nu_\tau \pi^-)$	$(11.01 \pm 0.11)\%$
$\text{Br}(\tau^- \rightarrow \nu_\tau K^-)$	$(0.692 \pm 0.028)\%$

The last few years have witnessed a substantial change in our knowledge of τ properties. The large (and clean) data samples collected by the most recent experiments have improved considerably the statistical accuracy and, moreover, have brought a new level of systematic understanding. All experimental results obtained so far confirm the Standard Model scenario, in which the τ is a sequential lepton with its own quantum number and associated neutrino. With the increased sensitivities achieved recently, interesting limits on possible new physics contributions to the τ decay amplitudes start to emerge.

12.2.1.1 Charged-current universality

The leptonic decays $\tau^- \rightarrow l^- \bar{\nu}_l \nu_\tau$ ($l = e, \mu$) are theoretically understood at the level of the electroweak radiative corrections [84]. Within the Standard Model (neutrinos are assumed to be massless),

$$\Gamma_{\tau \rightarrow l} \equiv \Gamma(\tau^- \rightarrow \nu_\tau l^- \bar{\nu}_l) = \frac{G_F^2 m_\tau^5}{192\pi^3} f\left(\frac{m_l^2}{m_\tau^2}\right) r_{EW}, \quad (12.13)$$

where $f(x) = 1 - 8x + 8x^3 - x^4 - 12x^2 \log x$. The factor $r_{EW} = 0.9960$ takes into account radiative corrections not included in the Fermi coupling constant G_F , and the nonlocal structure of the W propagator.

Using the value of G_F measured in μ decay, Eq. (12.13) provides a relation between the τ lifetime and the leptonic branching ratios $B_l \equiv \text{Br}(\tau^- \rightarrow \nu_\tau l^- \bar{\nu}_l)$ [85]:

$$B_e = \frac{B_\mu}{0.972564 \pm 0.000010} = \frac{\tau_\tau}{(1632.1 \pm 1.4) \times 10^{-15} \text{ s}}. \quad (12.14)$$

The relevant experimental measurements are given in Table 12-18. The predicted value of B_μ/B_e is in perfect agreement with the measured ratio $B_\mu/B_e = 0.974 \pm 0.006$. As shown in Figure 12-12, the relation between B_e and τ_τ is also well satisfied by the present data.

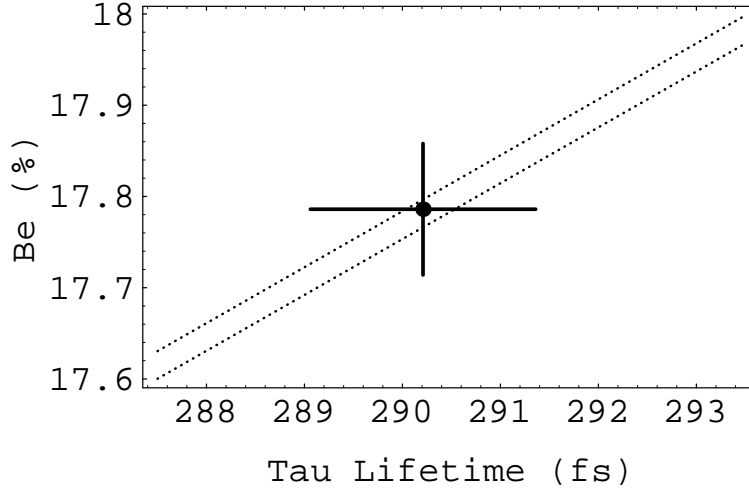


Figure 12-12. Relation between B_e and τ_τ [85]. The dotted band corresponds to Eq. (12.14).

These measurements can be used to test the universality of the W couplings to the leptonic charged currents. The B_μ/B_e ratio constrains $|g_\mu/g_e|$, while the B_e/τ_τ relation provides information on $|g_\tau/g_\mu|$. The present results are shown in Tables 12-19 and 12-20 [85], together with the values obtained from the π -decay ratio $R_{\pi \rightarrow e/\mu} \equiv \Gamma(\pi^- \rightarrow e^- \bar{\nu}_e)/\Gamma(\pi^- \rightarrow \mu^- \bar{\nu}_\mu)$, and from the comparison of the $\sigma \cdot B$ partial production cross-sections for the various $W^- \rightarrow l^- \bar{\nu}_l$ decay modes at the $p\text{-}\bar{p}$ colliders.

The decay modes $\tau^- \rightarrow \nu_\tau P^-$ ($P = \pi, K$) can also be used to test universality through the ratios

$$R_{\tau/P} \equiv \frac{\Gamma(\tau^- \rightarrow \nu_\tau P^-)}{\Gamma(P^- \rightarrow \mu^- \bar{\nu}_\mu)} = \left| \frac{g_\tau}{g_\mu} \right|^2 \frac{m_\tau^3}{2m_P m_\mu^2} \frac{(1 - m_P^2/m_\tau^2)^2}{(1 - m_\mu^2/m_P^2)^2} (1 + \delta R_{\tau/P}), \quad (12.15)$$

where the dependence on the hadronic matrix elements (the so-called decay constants $f_{\pi,K}$) factors out. Owing to the different energy scales involved, the radiative corrections to the $\tau^- \rightarrow \nu_\tau \pi^-/K^-$ amplitudes are, however, not the same as the corresponding effects in $\pi^-/K^- \rightarrow \mu^- \bar{\nu}_\mu$. The size

Table 12-19. Present constraints [85] on $|g_\mu/g_e|$.

	B_μ/B_e	$R_{\pi \rightarrow e/\mu}$	$\sigma \cdot B_{W \rightarrow \mu/e}$
$ g_\mu/g_e $	1.0005 ± 0.0030	1.0017 ± 0.0015	1.01 ± 0.04

Table 12-20. Present constraints [85] on $|g_\tau/g_\mu|$.

	$B_e \tau_\mu / \tau_\tau$	$R_{\tau/\pi}$	$R_{\tau/K}$	$\sigma \cdot B_{W \rightarrow \tau/\mu}$
$ g_\tau/g_\mu $	1.0001 ± 0.0029	1.005 ± 0.005	0.984 ± 0.020	0.99 ± 0.05

of the relative correction has been estimated [86] to be $\delta R_{\tau/\pi} = (0.16 \pm 0.14)\%$ and $\delta R_{\tau/K} = (0.90 \pm 0.22)\%$. Using these numbers, the measured $\tau^- \rightarrow \pi^- \nu_\tau, K^- \nu_\tau$ decay rates imply the $|g_\tau/g_\mu|$ ratios given in Table 12-20.

The present data verify the universality of the leptonic charged-current couplings to the 0.15% (e/μ) and 0.30% (τ/μ) level. The precision of the most recent τ -decay measurements is becoming competitive with the more accurate π -decay determination. It is important to realize the complementarity of the different universality tests. The pure leptonic decay modes probe the charged-current couplings of a transverse W . In contrast, the decays $\pi/K \rightarrow l\bar{\nu}$ and $\tau \rightarrow \nu_\tau \pi/K$ are only sensitive to the spin-0 piece of the charged current; thus, they could unveil the presence of possible scalar-exchange contributions with Yukawa-like couplings proportional to some power of the charged-lepton mass.

In the future, the tests of lepton universality will be limited by the accuracy of the measured τ lifetime. The ratio $|g_\mu/g_e|$ is directly obtained from the ratio of the two leptonic τ -decay branching ratios, which can probably be improved at a future τ -charm factory. To prove the $|g_\tau/g_\mu|$ ratio requires, however, the measurement of m_τ and τ_τ . While the τ mass can certainly be accurately measured at a threshold machine, the measurement of the τ lifetime is not accessible in a τ -charm factory. Thus, it is of great interest to know how well τ_τ can be determined at BABAR.

12.2.1.2 Hadronic decays

The τ is the only presently known lepton massive enough to decay into hadrons. Its semileptonic decays are then an ideal laboratory for studying the hadronic weak currents in very clean conditions. The decay modes $\tau^- \rightarrow \nu_\tau H^-$ probe the matrix element of the left-handed charged current between the vacuum and the final hadronic state H^- ,

$$\langle H^- | \bar{d}_\theta \gamma^\mu (1 - \gamma_5) u | 0 \rangle, \quad (d_\theta \equiv \cos \theta_C d + \sin \theta_C s). \quad (12.16)$$

Contrary to the well-known process $e^+e^- \rightarrow \gamma \rightarrow$ hadrons, which tests the electromagnetic vector current and leads to spin one states only, the semileptonic τ decay modes offer the possibility to study the properties of both vector and axial-vector currents and, furthermore, transitions to spin one as well as spin zero final states.

For the decay modes with lowest multiplicity, $\tau^- \rightarrow \nu_\tau \pi^-$ and $\tau^- \rightarrow \nu_\tau K^-$, the relevant matrix elements are already known from the measured decays $\pi^- \rightarrow \mu^- \bar{\nu}_\mu$ and $K^- \rightarrow \mu^- \bar{\nu}_\mu$. For the Cabibbo-allowed modes with $J^P = 1^-$, the matrix element of the vector charged current can also be obtained, through an isospin rotation, from the isovector part of the e^+e^- annihilation cross-section into hadrons, which measures the hadronic matrix element of the $I = 1$ component of the electromagnetic current. The $\tau \rightarrow \nu_\tau V^-$ decay width is then expressed as an integral over the

corresponding e^+e^- cross-section:

$$R_{\tau \rightarrow V} \equiv \frac{\Gamma(\tau^- \rightarrow \nu_\tau V^-)}{\Gamma_{\tau \rightarrow e}} = \frac{3 \cos^2 \theta_C}{2\pi\alpha^2 m_\tau^8} S_{EW} \int_0^{m_\tau^2} ds (m_\tau^2 - s)^2 (m_\tau^2 + 2s) s \sigma_{e^+e^- \rightarrow V^0}^{I=1}(s), \quad (12.17)$$

where the factor $S_{EW} = 1.0194$ contains the renormalization group improved electroweak correction at the leading logarithm approximation [84]. Currently, the experimental precision of the τ decay data is better than the e^+e^- one [87], which has been used for a more precise evaluation of the hadronic contribution to the photon vacuum polarization and thus for $\alpha_{QED}(M_Z)$ [88].

The exclusive τ decays into final hadronic states with $J^P = 1^+$, or Cabibbo-suppressed modes with $J^P = 1^-$, cannot be predicted with the same degree of confidence, which indicates that the decay of the τ lepton is providing new experimental hadronic information. Owing to their semileptonic character, the hadronic τ decay data are a unique and extremely useful tool to learn about the couplings of the low-lying mesons to the weak currents.

Since the hadronic matrix elements are governed by the nonperturbative regime of QCD, it is not possible at present to make first-principle calculations for exclusive decays. Nevertheless, our present knowledge of strong interactions at low energies may be used to estimate the gross features of the Lorentz-invariant form factors describing the decay amplitudes. For instance, Chiral Perturbation Theory techniques [89] can be applied to rigorously predict the low hadronic-invariant-mass behavior [90], and one can extrapolate to higher values of q^2 by using different models of resonance dynamics [91].

The determination of form factors in exclusive decays is not only required for a precise test of theoretical predictions. The separation of vector and axial-vector amplitudes and their respective spin zero and one contributions is mandatory for a number of improved phenomenological studies, like the determination of α_s and nonperturbative vacuum condensates based on moments of vector and axial spectral functions separately, or the unambiguous separation of vector contributions (in particular in the $KK\pi$ channels) for $\alpha_{QED}(M_Z)$. Just like the search for CP violation (discussed below) or the measurement of g_V^τ/g_A^τ through parity violation in hadronic decays, this can be performed with the help of a combined analysis of angular and energy distributions of the hadrons, even without reconstruction of the τ restframe. With a good K/π separation, BABAR will allow the study of, in particular, a rich variety of final states involving one or several kaons in great detail.

In the three (two) meson case, the most general ansatz for the hadronic matrix element of the quark current, $J^\mu(q_1, q_2, q_3) \equiv \langle h_1(q_1)h_2(q_2)(h_3(q_3))|V^\mu(0) - A^\mu(0)|0\rangle$, is characterized by four (two) complex form factors F_i , which are in general functions of $s_{ij} \equiv (q_i + q_j)^2$ and Q^2 ($Q^\mu \equiv \sum_i q_i^\mu$):

$$\begin{aligned} J^\mu(q_1, q_2) &= T^{\mu\nu} (q_1 - q_2)_\nu F + Q^\mu F_S, \\ J^\mu(q_1, q_2, q_3) &= T^{\mu\nu} [(q_1 - q_3)_\nu F_1 + (q_2 - q_3)_\nu F_2] + i \epsilon^{\mu\alpha\beta\gamma} q_{1\alpha} q_{2\beta} q_{3\gamma} F_3 + Q^\mu F_4. \end{aligned} \quad (12.18)$$

$T^{\mu\nu} = g^{\mu\nu} - (Q^\mu Q^\nu)/Q^2$ denotes a transverse projector. The form factors F_1 and F_2 originate from the $J^P = 1^+$ axial-vector hadronic current, and F_3 (F) from the $J^P = 1^-$ vector current;

Table 12-21. Structure functions for exclusive τ decays.

$H^{\nu*} \downarrow$	$H^\mu \longrightarrow$		
	$J^P = 1^+$	$J^P = 1^-$	$J = 0$
$J^P = 1^+$	\mathbf{W}_A $W_C W_D W_E$		
$J^P = 1^-$	$W_F W_G$ $W_H W_I$	\mathbf{W}_B	
$J = 0$	$W_{SB} W_{SC}$ $W_{SD} W_{SG}$	$W_{SF} W_{SG}$	\mathbf{W}_{SA}
		$\underbrace{\hspace{10em}}$ $h_1 h_2$	
	$\underbrace{\hspace{15em}}$ $h_1 h_2 h_3$		

they correspond to a hadronic system in a spin one state, whereas F_4 (F_S) are due to the $J = 0$ part of the axial-vector (vector) current matrix element. These form factors contain the full dynamics of the hadronic decay. For a two-pion final state, $h_1 h_2 = \pi^- \pi^0$, $F_S \equiv 0$ in the isospin symmetry limit ($m_u = m_d$). In the three pion case, $h_1 h_2 h_3 = \pi^- \pi^- \pi^+$ or $\pi^0 \pi^0 \pi^-$, Bose symmetry implies $F_2(Q^2, s_{23}, s_{13}) = F_1(Q^2, s_{13}, s_{23})$; G -parity conservation requires $F_3 \equiv 0$ for $m_u = m_d$, and F_4 vanishes when $m_u = m_d = 0$.

In the differential decay distribution, the four (two) complex form factors real “structure functions” W_X , which are defined from the hadronic tensor $H^{\mu\nu} = J^\mu J^{\nu*}$ in the hadronic rest frame [92]. For the precise definitions of W_X , see Ref. [92]. The contributions of the different F_i to W_X are summarized in Table 12-21. Almost all structure functions can be determined by studying angular distributions of the hadronic system, which allows separate analysis of the contributions from $J^P = 0^+, 0^-, 1^+$ and 1^- in a model-independent way.

While exclusive modes require some modeling of form factors, the present QCD techniques are much more powerful at the inclusive level. The total inclusive hadronic width of the τ can be systematically calculated [93, 94] by using analyticity constraints and the Operator Product Expansion. Both perturbative (to order α_s^3) and nonperturbative (which have been shown to be very suppressed) contributions have been taken into account [93, 94], together with the known electroweak corrections [84, 95]. The result turns out to be quite sensitive to the value of α_s , and

has been used to obtain one of the most precise determinations of the strong coupling constant [85]:

$$\alpha_s(m_\tau) = 0.35 \pm 0.02. \quad (12.19)$$

After evolution up to the scale M_Z , this running coupling decreases to $\alpha_s(M_Z) = 0.1217 \pm 0.0025$, in excellent agreement with the direct measurements at the Z peak. The comparison of these two determinations of $\alpha_s(\mu)$ in two extreme energy regimes, m_τ and M_Z , provides a beautiful test of the predicted running of the QCD coupling constant.

The non-strange and strange components of the τ hadronic width can also be predicted separately. Even a modest percent-level measurement of the strange component would yield a determination of the strange quark mass, with an accuracy good enough to settle the present controversies about this important parameter.

The non-strange component can be further decomposed into vector and axial-vector contributions. For final states with pions only, G parity allows the resolution of the two contributions experimentally. For a complete analysis, including *e.g.*, $KK\pi\nu_\tau$ the separation can be performed with the model-independent structure function analysis as described above. The difference between the vector and axial-vector components is a pure nonperturbative observable, which provides important information for testing our present understanding of low-energy QCD.

The invariant-mass distributions of the different components of the τ hadronic width also contains very useful information. A combined fit of certain weighted integrals of the hadronic spectrum allows [96] to simultaneously measure $\alpha_s(m_\tau)$ and the parameters characterizing the nonperturbative QCD dynamics.

A pioneering QCD analysis of the τ data has been already performed by ALEPH [97] and CLEO [98]. Their results are in good agreement with the theoretical expectations [85]. The improved precision of the future experimental studies will allow a much deeper investigation of the nonperturbative aspects of QCD.

12.2.2 Limits on the ν_τ Mass

All observed τ decays are supposed to be accompanied by neutrino emission, in order to fulfill energy-momentum conservation requirements. The present data are consistent with the ν_τ being a conventional sequential neutrino. The fact that taus are not produced by ν_e or ν_μ beams, confirms that ν_τ is different from the electronic and muonic neutrinos. LEP and SLC have confirmed the existence of three (and only three) different light neutrinos, with standard couplings to the Z . However, no direct observation of ν_τ , that is, interactions resulting from neutrinos produced in τ decay, has been made so far.

The possibility of a non-zero neutrino mass is obviously a very important question in particle physics. There is no fundamental principle requiring a null mass for the neutrino. On the contrary,

many extensions of the Standard Model predict non-vanishing neutrino masses, which could have, in addition, important implications in cosmology and astrophysics.

The first attempts to place a limit on m_{ν_τ} were done by studying the endpoint of the momentum spectrum of charged leptons from the decays $\tau^- \rightarrow \nu_\tau l^- \bar{\nu}_l$ ($l = e, \mu$). The precision that can be achieved is limited by the experimental momentum resolution of fastest particles, which deteriorates with increasing center-of-mass energy. Better limits have been set by studying the endpoint of the hadronic mass spectrum of high multiplicity τ decays. The limiting factor is then the resolution of the effective hadronic mass determination. The sensitivity to m_{ν_τ} is higher in decays where the hadronic final state peaks near the τ mass. The strongest bound up to date is the ALEPH limit [99],

$$m_{\nu_\tau} < 18.2 \text{ MeV} \quad (95\% \text{ CL}), \quad (12.20)$$

obtained from a two-dimensional likelihood fit of the visible energy and the invariant-mass distribution of $\tau^- \rightarrow (3\pi)^- \nu_\tau, (5\pi)^- \nu_\tau$ events.

For comparison, the present limits on the muon and electron neutrinos are $m_{\nu_\mu} < 170 \text{ keV}$ (90% C.L.) and $m_{\nu_e} < 15 \text{ eV}$. mass hierarchy among different generations is expected, with the neutrino mass being proportional to some power of the mass of its charged lepton partner. Assuming, for instance, the ansatz $m_{\nu_\tau}/m_{\nu_e} \sim (m_\tau/m_e)^2$, the bound (12.20) would be equivalent to a limit of 1.5 eV for m_{ν_e} . A relatively crude measurement of m_{ν_τ} may then imply strong constraints on neutrino-mass model building.

At BABAR it should be possible to push the limit on m_{ν_τ} down to the few MeV region. In addition to the usual multi-pion final states, the good kaon identification will allow to add the information from modes such as $\tau^- \rightarrow K^+ K^- \pi^- \nu_\tau$, which are kinematically constrained to rather high hadronic invariant masses but still have a sizeable ($\sim 0.2\%$) branching ratio.

12.2.3 Determination of the Strange-Quark Mass

The Cabibbo-suppressed component of the τ hadronic width,

$$R_{\tau,S} \equiv \frac{\Gamma[\tau \rightarrow \nu_\tau + \text{hadrons}; S = 1]}{\Gamma[\tau \rightarrow \nu_\tau e \bar{\nu}_e]}, \quad (12.21)$$

can be accurately predicted in QCD [93], in terms of $\alpha_s(m_\tau)$ and the running strange quark mass $m_s(m_\tau)$:

$$R_{\tau,S} = |V_{us}|^2 N_C S_{EW} \left\{ 1 + \delta'_{EW} + \delta^{(0)} + \sum_{D=2,4,\dots} \delta_{us}^{(D)} \right\}, \quad (12.22)$$

where $N_C = 3$ is the number of QCD colors, $S_{EW} = 1.0194$ and $\delta'_{EW} = 0.0010$ contain the known electroweak corrections, and $\delta^{(0)}$ is the perturbative QCD contribution (for massless quarks) to R_τ , which is known [93, 94] to $\mathcal{O}(\alpha_s^3)$. The remaining terms $\delta_{us}^{(D)}$ correspond to quark mass corrections and nonperturbative effects of dimension D ; they are suppressed by a factor $1/m_\tau^D$.

The leading $D = 2$ correction [100],

$$\delta_{us}^{(2)} = -8 \frac{m_s(m_\tau)^2}{m_\tau^2} \left\{ 1 + \frac{16}{3} \frac{\alpha_s(m_\tau)}{\pi} + 46.00 \left(\frac{\alpha_s(m_\tau)}{\pi} \right)^2 + \dots \right\}, \quad (12.23)$$

represents a $\sim -20\%$ effect, which cancels to a large extent with the perturbative $\delta^{(0)}$ contribution. The final prediction for $R_{\tau,S}$ is then very sensitive to the precise value of the strange quark mass.

A preliminary determination of m_s from $R_{\tau,S}$, $m_s(m_\tau) = (172_{-31}^{+26})$ MeV has been presented recently by ALEPH [101]. The precision of this measurement is already comparable to the best previous determinations of the strange quark mass, and clarifies the existing controversy about its size. The good capabilities of the BaBar detector for kaon identification should allow a more accurate measurement of this important parameter.

12.2.4 CP Violation in Hadronic τ Decays

CP violation has been experimentally observed only in the K meson system. The effect can be explained by a nontrivial complex phase in the CKM flavor mixing matrix. However, the fundamental origin of CP violation is still unknown. In particular the CP properties of the third fermion family are largely unexplored. Production and decay of τ leptons might offer a particularly clean laboratory to study these effects. CP violation [102] that could arise in a framework outside the conventional mechanism could be observed in semileptonic τ decays. The structure function formalism [92] allows for a systematic analysis of possible CP violation effects in the two and three meson channels.

Particularly interesting is the $\Delta S = 1$ transition $\tau \rightarrow K\pi\nu_\tau$, where possible CP -violating signals from multi Higgs boson models [103] could show up through a nonvanishing difference between the τ^+ and τ^- decay amplitudes. Transitions from the vacuum to two pseudoscalar mesons are induced through vector and scalar currents only. An exotic scalar-exchange contribution would modify the scalar form factor [see Eq. (12.18)]:

$$\tilde{F}_S = F_S + \frac{\eta_S}{m_\tau} F_H, \quad F_H(Q^2) \equiv \langle h_1(q_1)h_2(q_2)|\bar{u}d|0 \rangle. \quad (12.24)$$

The complex parameter η_S parameterizes a possible CP violation effect. Up to the small isospin-breaking terms, induced for example by the small quark mass difference, CVC implies the vanishing of F_S for the two pion ($h_1 \equiv \pi^-, h_2 \equiv \pi^0$) case. For the transition $\tau \rightarrow K\pi\nu$, the $J = 1$ form factor F is dominated by the $K^*(892)$ vector resonance contribution, while the scalar form factor F_S is expected to receive a sizable resonance contribution ($\sim 5\%$ of the decay rate) from the $K_0^*(1430)$ [104].

As indicated in Table 12-21 (page 825), interference of the vector and scalar form factors is contained in the structure functions W_{SF} and W_{SG} . Under CP , $\eta_S \rightarrow \eta_S^*$. Thus, one could

investigate the presence of a CP -violating phase through the comparison of the structure functions measured in τ^- and τ^+ decays [102]:

$$\Delta W_{SF} \equiv \frac{1}{2} \left(W_{SF}[\tau^-] - W_{SF}[\tau^+] \right) = 4\sqrt{Q^2} |\mathbf{q}_1| \frac{1}{m_\tau} \text{Im}(FF_H^*) \text{Im}(\eta_S) , \quad (12.25)$$

$$\Delta W_{SG} \equiv \frac{1}{2} \left(W_{SG}[\tau^-] - W_{SG}[\tau^+] \right) = 4\sqrt{Q^2} |\mathbf{q}_1| \frac{1}{m_\tau} \text{Re}(FF_H^*) \text{Im}(\eta_S) . \quad (12.26)$$

Any observed nonzero value of ΔW_{SF} or ΔW_{SG} would signal a true CP violation. Eqs. (12.25) and (12.26) show that the sensitivity to CP -violating effects in ΔW_{SF} and ΔW_{SG} can be fairly different. Whereas ΔW_{SF} requires nontrivial hadronic phases, ΔW_{SG} is maximal (for fixed η_S) in the absence of hadronic phases.

In essence the measurement of ΔW_{SF} analyses the difference in the correlated energy distribution of the mesons h_1 and h_2 from τ^+ and τ^- decay in the laboratory. Thus, it can be measured in e^+e^- annihilation experiments through the study of single unpolarized τ decays, even if the τ rest frame cannot be reconstructed [102, 104]. This differs from earlier studies where either polarized beams and reconstruction of the full kinematics [105] or correlated fully reconstructed τ^- and τ^+ decays were required [106].

The determination of W_{SG} , however, requires the knowledge of the full τ kinematics and τ polarization [102] (eventually to be substituted through correlation studies), which is possible with the help of vertex detectors. The corresponding distributions in this case are similar to the correlations proposed in [105, 106].

The structure function formalism [92] allows also for a systematic analysis of possible CP violation effects in the three meson case [107]. The $K\pi\pi$ and $KK\pi$ decay modes with nonvanishing vector *and* axial-vector current are of particular importance for detecting possible CP violation originating from exotic intermediate vector bosons. This would be signaled by a nonvanishing difference between the structure functions $W_X(\tau^-)$ and $W_X(\tau^+)$ with X in $\{F, G, H, I\}$. A difference in the structure functions with X in $\{SB, SC, SD, SE, SF, SG\}$ can again be induced through a CP -violating scalar exchange. CP violation in the three pion channel has been also discussed in [108] and in the $K\pi\pi$ and $KK\pi$ channels in [109], where the latter analysis is based on the “ T -odd” correlations in [92] and the vector-meson-dominance parameterizations in the last paper of [91].

12.2.5 Lorentz Structure of τ Decays

In this section, the leptonic decays $l^- \rightarrow \nu_l l'^- \bar{\nu}_{l'}$, are considered, where the lepton pair (l, l') may be (μ, e) , (τ, e) , or (τ, μ) . The most general, local, derivative-free, lepton-number conserving, four-lepton interaction Hamiltonian, consistent with locality and Lorentz invariance [85, 110],

$$\mathcal{H} = 4 \frac{G_{ll'}}{\sqrt{2}} \sum_{n, \epsilon, \omega} g_{\epsilon\omega}^n \left[\bar{l}'_\epsilon \Gamma^n (\nu_{l'})_\sigma \right] \left[(\bar{\nu}_l)_\lambda \Gamma_n l_\omega \right] , \quad (12.27)$$

contains ten complex coupling constants or, since a common phase is arbitrary, nineteen independent real parameters which could be different for each leptonic decay. The subindices ϵ, ω, σ , and λ label the chiralities (left-handed, right-handed) of the corresponding fermions, and n the type of interaction: scalar (I), vector (γ^μ), or tensor ($\sigma^{\mu\nu}/\sqrt{2}$). For given n, ϵ, ω , the neutrino chiralities σ and λ are uniquely determined. Taking out a common factor $G_{l'l}$, which is determined by the total decay rate, the coupling constants $g_{\epsilon\omega}^n$ are normalized [110] to

$$1 = \sum_{n,\epsilon,\omega} |g_{\epsilon\omega}^n/N^n|^2, \quad (12.28)$$

where $N^n = 2, 1, 1/\sqrt{3}$ for $n = S, V, T$. In the Standard Model, $g_{LL}^V = 1$ and all other $g_{\epsilon\omega}^n = 0$.

For an initial lepton polarization \mathcal{P}_l , the final charged lepton distribution in the decaying lepton rest frame is usually parametrized in the form

$$\frac{d^2\Gamma_{l\rightarrow l'}}{dx d\cos\theta} = \frac{m_l \omega^4}{2\pi^3} G_{l'l}^2 \sqrt{x^2 - x_0^2} \left\{ F(x) - \frac{\xi}{3} \mathcal{P}_l \sqrt{x^2 - x_0^2} \cos\theta A(x) \right\}, \quad (12.29)$$

where θ is the angle between the l^- spin and the final charged-lepton momentum, $\omega \equiv (m_l^2 + m_{l'}^2)/2m_l$, is the maximum l'^- energy for massless neutrinos, $x \equiv E_{l'}/\omega$ is the reduced energy, $x_0 \equiv m_{l'}/\omega$ and [85]

$$\begin{aligned} F(x) &= x(1-x) + \frac{2}{9}\rho(4x^2 - 3x - x_0^2) + \eta x_0(1-x), \\ A(x) &= 1 - x + \frac{2}{3}\delta(4x - 4 + \sqrt{1-x_0^2}). \end{aligned} \quad (12.30)$$

For unpolarized l_s , the distribution is characterized by the so-called Michel parameter ρ and the low-energy parameter η . Two more parameters, ξ and δ , can be determined when the initial lepton polarization is known. If the polarization of the final charged lepton is also measured, five additional independent parameters [28, 34] ($\xi', \xi'', \eta'', \alpha', \beta'$) appear.

For massless neutrinos, the total decay rate is given by [85]

$$\Gamma_{l\rightarrow l'} = \frac{\hat{G}_{l'l}^2 m_l^5}{192\pi^3} f\left(\frac{m_{l'}^2}{m_l^2}\right) r_{EW}, \quad \hat{G}_{l'l} \equiv G_{l'l} \sqrt{1 + 4\eta \frac{m_{l'}}{m_l} \frac{g(m_{l'}^2/m_l^2)}{f(m_{l'}^2/m_l^2)}}, \quad (12.31)$$

where $g(z) = 1 + 9z - 9z^2 - z^3 + 6z(1+z)\ln z$, and the Standard Model radiative correction r_{EW} has been included. Thus, the normalization $G_{e\mu}$ corresponds to the Fermi coupling G_F , measured in μ decay. The B_μ/B_e and $B_e\tau_\mu/\tau_\tau$ universality tests, discussed previously, actually prove the ratios $|\hat{G}_{\mu\tau}/\hat{G}_{e\tau}|$ and $|\hat{G}_{e\tau}/\hat{G}_{e\mu}|$, respectively.

In terms of the $g_{\epsilon\omega}^n$ couplings, the shape parameters in Eqs. (12.29) and (12.30) are [85]:

$$\begin{aligned}\rho &= \frac{3}{4}(\beta^+ + \beta^-) + (\gamma^+ + \gamma^-), & \xi\delta &= \frac{3}{4}(\beta^- - \beta^+) + (\gamma^+ - \gamma^-), \\ \xi &= 3(\alpha^- - \alpha^+) + (\beta^- - \beta^+) + \frac{7}{3}(\gamma^+ - \gamma^-), & & \\ \eta &= \frac{1}{2}\text{Re} \left[g_{LL}^V g_{RR}^{S*} + g_{RR}^V g_{LL}^{S*} + g_{LR}^V (g_{RL}^{S*} + 6g_{RL}^{T*}) + g_{RL}^V (g_{LR}^{S*} + 6g_{LR}^{T*}) \right],\end{aligned}\quad (12.32)$$

where

$$\begin{aligned}\alpha^+ &\equiv |g_{RL}^V|^2 + \frac{1}{16}|g_{RL}^S + 6g_{RL}^T|^2, & \alpha^- &\equiv |g_{LR}^V|^2 + \frac{1}{16}|g_{LR}^S + 6g_{LR}^T|^2, \\ \beta^- &\equiv |g_{LL}^V|^2 + \frac{1}{4}|g_{LL}^S|^2, & \beta^+ &\equiv |g_{RR}^V|^2 + \frac{1}{4}|g_{RR}^S|^2, \\ \gamma^- &\equiv \frac{3}{16}|g_{LR}^S - 2g_{LR}^T|^2, & \gamma^+ &\equiv \frac{3}{16}|g_{RL}^S - 2g_{RL}^T|^2,\end{aligned}\quad (12.33)$$

are positive-definite combinations of decay constants, corresponding to a final right-handed ($\alpha^+, \beta^+, \gamma^+$) or left-handed ($\alpha^-, \beta^-, \gamma^-$) lepton. In the Standard Model, $\rho = \delta = 3/4$, $\eta = \eta'' = \alpha' = \beta' = 0$ and $\xi = \xi' = \xi'' = 1$.

The normalization constraint (12.28) is equivalent to $\alpha^+ + \alpha^- + \beta^+ + \beta^- + \gamma^+ + \gamma^- = 1$. It is convenient to introduce [110] the probabilities $Q_{\epsilon\omega}$ for the decay of an ω -handed l^- into an ϵ -handed daughter lepton:

$$Q_{LL} = \beta^-; \quad Q_{RR} = \beta^+; \quad Q_{LR} = \alpha^- + \gamma^-; \quad Q_{RL} = \alpha^+ + \gamma^+. \quad (12.34)$$

Upper bounds on any of these (positive-semidefinite) probabilities translate into corresponding limits for all couplings with the given chiralities.

For μ decay, where precise measurements of the polarizations of both μ and e have been performed, there exist [110] upper bounds on Q_{RR} , Q_{LR} and Q_{RL} , and a lower bound on Q_{LL} . They imply corresponding upper bounds on the eight couplings $|g_{RR}^n|$, $|g_{LR}^n|$ and $|g_{RL}^n|$. The measurements of the μm and the e^- do not allow the separate determination of $|g_{LL}^S|$ and $|g_{LL}^V|$. Nevertheless, since the helicity of the ν_μ in pion decay is experimentally known to be -1 , a lower limit on $|g_{LL}^V|$ is obtained [110] from the inverse muon decay $\nu_\mu e^- \rightarrow \mu m \nu_e$. The present bounds [28, 34] on the μ -decay couplings are shown in Figure 12-13. These limits show nicely that the bulk of the μ -decay transition amplitude is indeed of the predicted V–A type.

The experimental analysis of the τ decay parameters is necessarily different from the one applied to the muon because of the much shorter τ lifetime. The measurement of the τ polarization and the parameters ξ and δ is still possible due to the fact that the spins of the $\tau^+ \tau^-$ pair produced in $e^+ e^-$ annihilation are strongly correlated. However, the polarization of the charged lepton emitted in the τ decay has never been measured. In principle, this could be done for the decay $\tau^- \rightarrow \mu^- \bar{\nu}_\mu \nu_\tau$ by stopping the muons and detecting their decay products [112]. An alternative method would be [113] to use the radiative decays $\tau \rightarrow l^- \bar{\nu}_l \nu_\tau \gamma$ ($l = e, \mu$), since the distribution of the photons

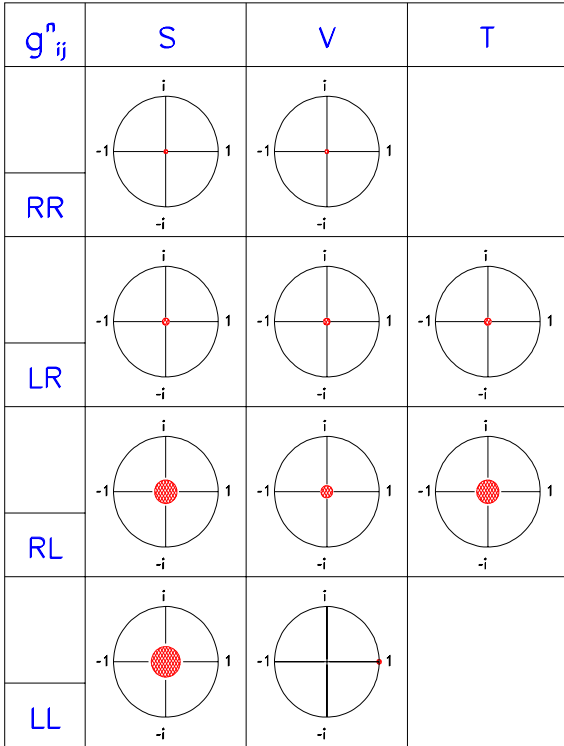


Figure 12-13. 90% CL experimental limits [28, 34] for the normalized μ -decay couplings $g_{e\omega}^n \equiv g_{e\omega}^n/N^n$.

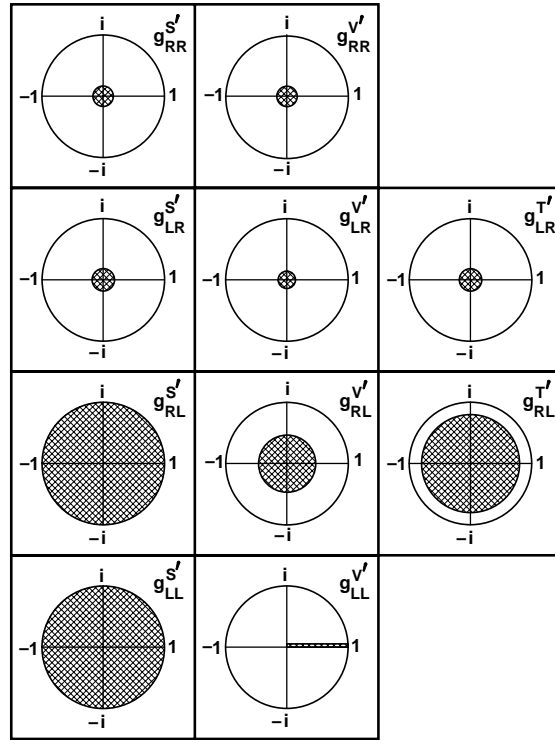


Figure 12-14. 90% CL experimental limits [111] for the normalized τ -decay couplings $g_{e\omega}^n \equiv g_{e\omega}^n/N^n$, assuming e/μ universality.

emitted by the daughter lepton is sensitive to the lepton polarization. The measurement of the inverse decay $\nu_\tau l^- \rightarrow \tau^- \nu_l$ looks far out of reach.

The most precise determination of the τ -decay parameters comes from a recent CLEO analysis [111]. The resulting constraints on the $g_{e\omega}^n$ couplings are shown in Figure 12-14.

12.2.6 Rare τ Decays

In the minimal Standard Model with massless neutrinos, there is a separately conserved additive lepton number for each generation. All present data are consistent with this conservation law. However, there are no strong theoretical reasons forbidding a mixing among the different leptons, in the same way as happens in the quark sector. Many models in fact predict lepton-flavor or even lepton-number violation at some level. Experimental searches for these processes can provide information on the scale at which the new physics begins to play a significant role.

K , π and μ decays, together with μ - e conversion, neutrinoless double beta decays and neutrino oscillation studies, have already put stringent limits [28, 34] on lepton-flavor and lepton-number violating interactions. However, given the present lack of understanding of the origin of fermion generations, one can imagine different patterns of violation of this conservation law for different mass scales. Moreover, the larger mass of the τ opens the possibility of new types of decay that are kinematically forbidden for the μ .

The CLEO Collaboration [114] has recently reported improved experimental bounds on the branching ratios of several rare τ decays to the level of 10^{-5} to 10^{-6} . With an integrated luminosity sample of 30 fb^{-1} (3×10^7 τ pairs), BABAR will be able to push these limits down by another order of magnitude.

Particularly interesting are lepton-flavor-violating (LFV) decays with no neutrinos in the final state. There are several motivations and ways to extend the standard electroweak theory leading to such rare τ decays. Restricting ourselves to models with the standard gauge structure, lepton flavor violation can arise either from (a) the mixing of heavy leptons in the leptonic charged and neutral current or (b) due to the existence of LFV Yukawa couplings to new scalar particles.

In models of type (a) the expected LFV rates will generally tend to be very suppressed by small neutrino masses. However flavor violation can occur even when neutrinos are “protected” from acquiring a mass by some symmetry such as the conservation of the *total* lepton number [115], like in models with neutral heavy leptons (NHL) [115, 116].

Neutral heavy leptons which are singlet under $SU(2)$ arise in many extensions of the electroweak theory. Being singlet, they couple to the standard gauge bosons only through their mixing with ordinary doublet neutrinos. The resulting charged- (CC) and neutral-current (NC) leptonic weak interactions have the form

$$\mathcal{L}_{CC} = \frac{g}{\sqrt{2}} W_\mu \sum_{ij} \bar{l}_{Li}^- \gamma^\mu (K_{Lij} \nu_{Lj} + K_{Hij} N_{Lj}) + h.c. , \quad (12.35)$$

$$\mathcal{L}_{NC} = \frac{g}{\cos \theta_W} Z_\mu \sum_{ij} [\bar{\nu}_{Li} \gamma^\mu P_{LLij} \nu_{Lj} + \bar{\nu}_{Li} \gamma^\mu P_{LHij} N_{Lj} + \bar{N}_{Li} \gamma^\mu P_{HLij} \nu_{Lj} + \bar{N}_{Li} \gamma^\mu P_{HHij} N_{Lj}] ,$$

where $P_{AB} = K_A^\dagger K_B$. The admixture in the CC and NC leads in general to violations of universality which limit the attainable values of the K_H matrix elements.

The presence of these NHLs can give rise to several LFV τ decays, such as $\tau \rightarrow ll'^+l'^-$, $\tau \rightarrow l\gamma$, $\tau \rightarrow l\pi^0$, $\tau \rightarrow l\eta$, $\tau \rightarrow l\eta'$, $\tau \rightarrow lK$, $\tau \rightarrow l\rho$, and $\tau \rightarrow l\phi$, where $l^{(\prime)} = e, \mu$. These processes occur at the one-loop level with at least one virtual NHL in the loop. Detailed expressions for the different decay widths can be found in [116]. The attainable branching ratio depends on the NHL mass and of course on the allowed values for the couplings K_H . In some models K_H is severely constrained by the limits on neutrino masses. However, when flavor violation occurs with massless neutrinos the only constraints on K_H follow from weak universality. For two generations of degenerated NHLs, there are three free parameters: M_N , $\sum_i |K_{H\tau i}|^2$ and $\sum_i |K_{Hl i}|^2$ leading to

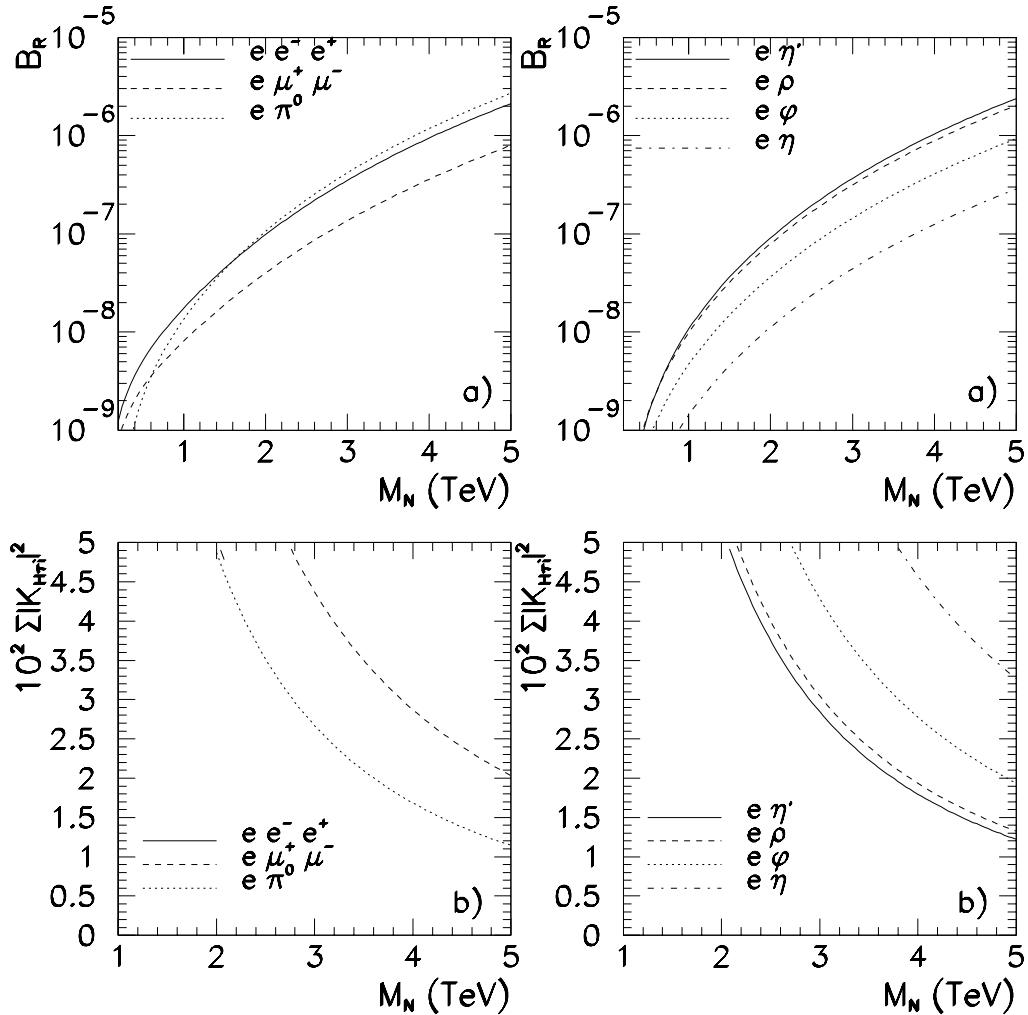


Figure 12-15. (a) Attainable τ decay branching ratios in the NHL model for maximum allowed values of the mixings $\sum_i |K_{H\tau i}|^2 \leq 0.05$ and $\sum_i |K_{Hei}|^2 \leq 0.01$. (b) Parameter region for branching ratios larger than 10^{-7} (to the right and above the curves) with maximum mixing with the first generation $\sum_i |K_{Hei}|^2 \leq 0.01$.

branching ratios as large as $\mathcal{O}(10^{-6})$ as seen in Fig. 12-15 (a). Figure 12-15 (b) displays the regions in the parameter space where the branching ratios can be larger than 10^{-7} .

Supersymmetry, both in its conventional realization, and in the alternative scenarios without R parity conservation [117, 118] provides examples of models of type (b). Supersymmetry can produce rare τ decays such as the emission of very light sneutrinos. Although this decay is kinematically ruled out in the minimal supersymmetric standard model, the emergence of a massless sneutrino is a generic feature of a class of $SU(2) \otimes U(1)$ supersymmetric models where the R_p symmetry is broken spontaneously [119]. In these models one combination of the sneutrinos remains massless because there must be a physical Nambu-Goldstone boson associated with the

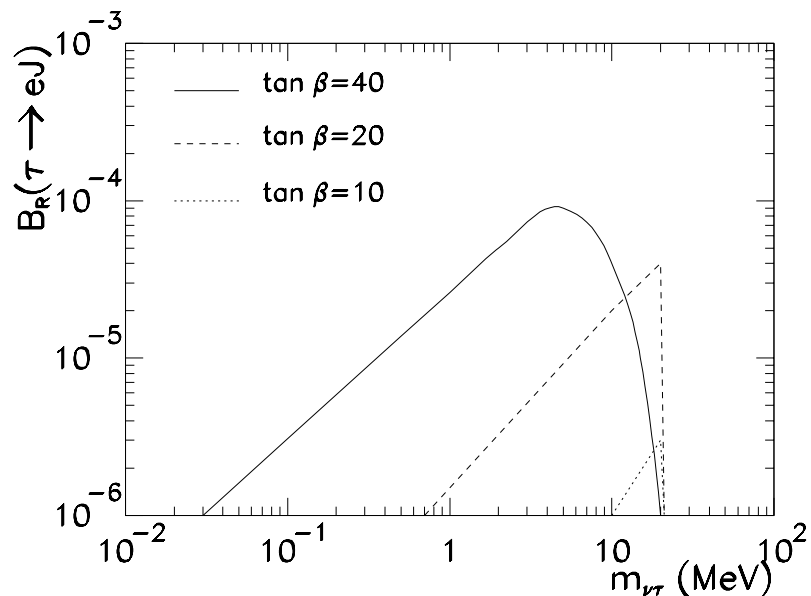


Figure 12-16. Attainable branching ratios for LFV τ decays with majoron emission, as a function of m_{ν_τ} .

spontaneous violation of lepton number symmetry. This is called the majoron and is denoted by J . The minimal SUSY model with broken R parity [119] is now ruled out by the LEP precision measurement of the invisible Z width [120]. It is, however, possible to formulate the R parity breaking model with the majoron being mainly an $SU(2) \otimes U(1)$ *singlet* so that it does not couple to the Z [118]. The scale characterizing R parity breaking is now large, *i.e.*, $v_R = \mathcal{O}(1)$ TeV.

In these models the spectrum of the τ decay is modified by single majoron emission. Figure 12-16, taken from Ref. [121], shows the attainable values of the single majoron emission τ decay branching ratios as a function of the ν_τ mass. This indicates that the flavor-violating τ decay processes with single majoron emission could lead to observable effects for a wide range of the allowed parameters.

12.2.7 τ Electric Dipole Moment

The lepton electric dipole moments d_l , which vanish in the Standard Model, are sensitive quantities to a possible lepton substructure. Moreover, they violate T and P invariance; thus, they constitute a good probe of CP violation. Owing to their chiral-changing structure, the dipole moments may provide important insights on the mechanism responsible for mass generation. In general, one expects that a fermion of mass m_f (generated by physics at some scale $M \gg m_f$) will have

induced dipole moments proportional to some power of m_f/M . Therefore, heavy fermions such as the τ should be a good testing ground for this kind of effect.

At BABAR one could search for CP violation in τ pair production, by studying CP -odd correlations between the final τ decay products. For instance, one could look for $e\mu$ final states from correlated leptonic $\tau^+\tau^-$ decays,

$$e^+e^- \rightarrow \gamma^* \rightarrow \tau^+\tau^- \rightarrow \mu^\pm e^\mp X.$$

The CP -odd $\tau^+\tau^-$ production amplitude, generated by a non-zero τ electric dipole moment, would interfere with the CP -even Standard Model one. This effect can be analyzed through the CP -odd, symmetric and traceless tensor

$$T_{ij} = (\mathbf{q}_- - \mathbf{q}_+)_i (\mathbf{q}_- \times \mathbf{q}_+)_j + (i \leftrightarrow j), \quad (12.36)$$

where i, j are Cartesian vector indices with z coordinate along the incoming electron direction and \mathbf{q}_+ and \mathbf{q}_- represent momentum vectors of the positive and negative final charged leptons.

A preliminary Monte Carlo study has been carried out [122] using the Aslund fast simulation program in the Beta analysis framework. The τ pair production has been generated with EvtGen and KORALB. In order to minimize huge backgrounds, the study has been performed with oppositely charged $e\mu$ final states. No particle identification algorithm has been used; thus, the currently accepted e and μ PID efficiency of 90% with 0.2% and 2% contamination, respectively, has been adopted. The dominant background comes from $\tau \rightarrow e\nu\bar{\nu}$ decay and a pion mis-identified as a muon from $\tau \rightarrow \pi\nu$. The event selection cuts are:

- There are only oppositely charged electron and muon candidates in the event and no photon with energy above 100 MeV. Good leptons satisfy $p_T > 0.1$ GeV/ c and $p > 0.5$ GeV/ c . This requirement completely suppresses all the generic $B\bar{B}$ and $q\bar{q}$ backgrounds.
- In order to remove lepton pair production, $p_l < 6$ GeV/ c and $p_e + p_\mu < 10$ GeV/ c has been required. Their residual contaminations are further suppressed by PID.
- Leptons are accepted within the barrel region of the BABAR detector, *i.e.*, $30^\circ < \theta_l < 130^\circ$.

The final accumulative selection efficiency of the $e\mu$ sample is 2.1%, which corresponds to $N_{e\mu} = 2 \times 10^5$ events at 10 fb^{-1} luminosity.

The most sensitive tensor element is T_{33} . The T_{33} distribution of the final $e\mu$ sample, for $d_\tau = 0$, is shown in Fig. 12-17. The mean value of the distribution is $\langle T_{33} \rangle = -0.01 \pm 0.01 \text{ GeV}^3$. This corresponds to

$$|d_\tau| \leq 1.8 \times 10^{-16} e \text{ cm} \quad (95\% \text{ CL}). \quad (12.37)$$

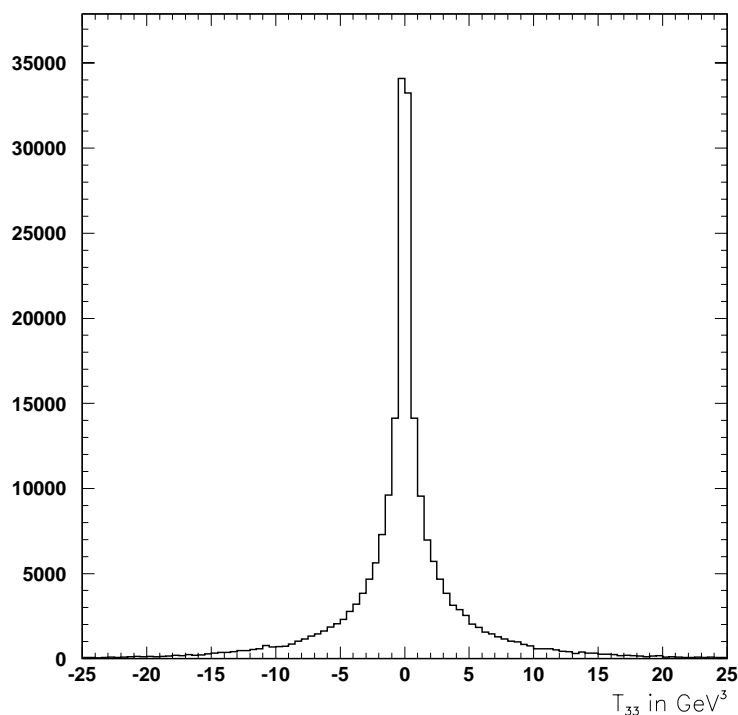


Figure 12-17. T_{33} distribution of the final $e\mu$ sample for $d_\tau = 0$.

12.3 Two-Photon Physics

The reaction $e^+e^- \rightarrow e^+e^-\gamma\gamma \rightarrow e^+e^-X$, where two virtual photons combine to give the final state X , allows a complementary probe of hadronic structure to that obtained in e^+e^- annihilation or hadron collisions. In particular, two photons couple directly to charge conjugation $C = +1$ resonances, and preferentially to those with charge $+2/3$ quarks, due to the e_q^4 dependence of the cross-section. Couplings to “exotic” mesons, such as four-quark states or glueballs, also differ from those seen in e^+e^- annihilation, and measurements of the two-photon widths $\Gamma_{\gamma\gamma}$ can help to identify such mesons. Perturbative QCD makes testable predictions for the two-photon production rates and kinematic distributions of meson and baryon pairs. Measurements of photon structure functions and jet production in two-photon reactions can also contribute significantly to our understanding of QCD.

While the total two-photon cross-section to hadrons is not small (~ 1 nb at PEP II energies), the rapid fall of the virtual photon flux with increasing W (the two-photon center-of-mass energy) has made it very difficult to use the two-photon reaction to study high-mass final states. In addition, the final states produced in two-photon processes typically have low multiplicity, making triggering and background separation difficult. The only way to compensate for this is with large integrated luminosity, coupled with a good detector. CLEO-II at Cornell has made a few steps into the

higher-mass region with several fb^{-1} of data, but the detector and trigger are not optimal for two-photon physics. Since the two-photon cross-section grows logarithmically with energy, LEP-II may also contribute, but will not achieve sufficient integrated luminosity to allow systematic studies of resonances and hadron pair production. With an excellent detector like BABAR, the PEP-II B Factory will be an ideal place to extend two-photon physics to higher masses since it will produce at least an order of magnitude higher luminosity than in present e^+e^- colliders.

The two-photon reaction is usually categorized by whether the scattered e^\pm are detected or not. In the “untagged” case, both e^+ and e^- scatter at small angles, leaving only the final state X in a typical detector. One of the best discriminants for the two-photon reaction from background processes is that the final state particles have balanced momenta perpendicular to the beam direction. Since the virtual photon fluxes each fall off as $1/q^2$, where q is the four momentum of the virtual photon, the rate is typically an order of magnitude smaller for each detected scattered lepton “tag”. The boost of an asymmetric B Factory causes the lower energy e^+ to be “pulled” out into the detector more often than in a symmetric machine, increasing the rates for detecting the singly-tagged reaction. However, this advantage cannot be fully realized with the present BABAR detector, which is without a backward endcap calorimeter.

12.3.1 Monte Carlo Simulations and BABAR Rate Estimates

A Monte Carlo simulation [123] has been used to estimate event rates and kinematics for many of the two-photon reactions of interest at PEP II. The simulation is based on one developed for the TPC/Two-Gamma experiment at PEP [124], but has been altered to allow for beam asymmetry. It generates the full $e^+e^- \rightarrow e^+e^-X$ cross-section for many different final states and allows the application of cuts on polar angles and energies. Comparing the generated events passing such cuts with measured results obtained for several reactions in the TPC/Two-Gamma experiment provides detector efficiency factors. Assuming the same efficiency factors for BABAR allows the estimation of expected rates [123]. Of course, since BABAR is, in most ways, a better detector than TPC/Two-Gamma, these efficiency factors (and the corresponding rate estimates) are probably conservatively low. Recently, the two-photon generator from CLEO [125] has been adapted to BABAR and has also been used for estimating rates. Since this generator runs under Unix, while the TPC/Two-Gamma generator does not, the CLEO generator will be added to the BABAR simulation package.

The output of the Monte Carlo generators has been converted into a form readable by the BABAR simulation package Beget/BBSim. This has allowed some of the two-photon reactions to be studied with the full detector and trigger simulations and has led to the establishment of several two-photon benchmark reactions for which minimum trigger efficiencies are specified for BABAR [126]. These simulations show that triggering on two-photon final states is straightforward and has high efficiency for $W > 2 \text{ GeV}$. However, triggering will be increasingly difficult for final state masses below about $1.5 \text{ GeV}/c^2$, especially when backgrounds are high and the desired final state has only two charged particles. Although these simulations should account for geometric and trigger efficiencies, they do not yet provide estimates of reconstruction and background cut

efficiencies. Thus, it is still prudent when trying to calculate absolute rates to apply estimated final state efficiencies (33% for all charged final states, 11% for states with one π^0 , and 8% for states with multiple π^0 s) based on experience from previous two-photon experiments. This is done for all of the rates quoted in this section. An integrated luminosity of 100 fb^{-1} is assumed, equivalent to three years of running with the expected peak luminosity of BaBar.

12.3.2 Resonance Production

12.3.2.1 Determination of $\Gamma_{\gamma\gamma}$ for $q\bar{q}$ mesons

The primary motivation for studying meson resonances with two-photon reactions is to measure their two-photon width $\Gamma_{\gamma\gamma}$, a quantity which is predictable from QCD models. As mentioned before, two photons couple to $C = +1$ mesons, and the coupling strength is stronger for those with u and c quark content, as compared with d and s quarks or gluons. In addition, production of states with $J^P = (2n + 1)^-$ by two real photons is forbidden, as are states with $J = 1$ for any parity value (Yang-Landau theorem). $\Gamma_{\gamma\gamma}$ has been measured for the pseudo-scalar mesons π^0 , η and η' , the tensor mesons $a_2(1320)$, $f_2(1270)$ and $f_2'(1525)$, the scalar $a_0(980)$ and the $\pi_2(1670)$.

The expected integrated luminosity at BaBar will extend the measurements of $\gamma\gamma$ resonance production up to masses of at least $4 \text{ GeV}/c^2$ [123]. Heavy quark states are of special interest since nonrelativistic potential model calculations are expected to be reliable. For instance, a nonrelativistic model [127] with next-to-leading-order QCD corrections predicts $\Gamma_{\gamma\gamma}(\eta_c)/\Gamma_{\mu^+\mu^-}(J/\psi) = (4/3)(1 + 1.96\alpha_s/\pi)$. This calculation, which assumes that the wave-functions for η_c and J/ψ are identical at the origin, gives $\Gamma_{\gamma\gamma}(\eta_c) = 8.2 \text{ keV}$. The measured $\Gamma_{\gamma\gamma}$ of the charmonium states η_c , χ_{c0} , and χ_{c2} disagree substantially amongst the experiments [28, 128, 129], but they are still based on only a handful of reconstructed events. Monte Carlo simulations done for BaBar, assuming the PDG average values for $\Gamma_{\gamma\gamma}$, predict that 5000–10000 events will be reconstructed in each of several decay modes for η_c , with roughly 1/2 that rate for χ_{c0} and 1/10 that rate for χ_{c2} . These large samples will give very precise measurements of the two-photon widths, with greatly reduced systematic errors as well.

The nonrelativistic quark model also leads to the following relation:

$$\frac{\Gamma_{\eta_c}}{\Gamma_{\gamma\gamma}(\eta_c)} = \frac{9\alpha_s^2(M_c)}{8\alpha^2} \left[1 + \frac{8.2}{\pi} \alpha_s(M_c) \right] \quad (12.38)$$

where the wave function at the origin cancels in the ratio of widths, so that relativistic corrections and nonperturbative QCD effects are expected to cancel. This relation should yield a precise value for $\alpha_s(M_c)$, provided that a precise measurement of $\Gamma_{\gamma\gamma}(\eta_c)$ is performed and that phase space effects due to a nonvanishing effective mass for the primary gluons emitted in the hadronic η_c decay [130] do not dominate.

There will be a characteristic flavor dependence for the two-photon production of the various states comprising a $q\bar{q}$ nonet with ideal mixing:

$$\Gamma_{\gamma\gamma}\left(\frac{(u\bar{u} + d\bar{d})}{\sqrt{2}} : \frac{(u\bar{u} - d\bar{d})}{\sqrt{2}} : s\bar{s}\right) = 25 : 9 : 2. \quad (12.39)$$

The question of which J^{PC} nonets are ideally flavor-mixed (like ρ , ω , and ϕ , or a_2 , f_2 , f_2' for the 2^{++} nonet), and which are not (like the 0^{-+} nonet), is critical to the understanding of the dynamics of flavor mixing.

The J^{PC} dependence of the production ratios is also an important characteristic. Within a 3L_J multiplet, one has in a nonrelativistic approximation

$$\Gamma_{\gamma\gamma}({}^3P_2 : {}^3P_1 : {}^3P_0) = 1 : 0 : 15/4 \quad (12.40)$$

whereas, as $m_q \rightarrow 0$, $\Gamma({}^3P_0) \rightarrow 0$. Determining the $\Gamma_{\gamma\gamma}({}^3L_J)$ for many different multiplets will provide new insight on the enigma of how to relate the small, partonic current-quark masses to the constituent-quark masses of spectroscopy. Similar relations exist for the higher multiplets [131], and enable, for example, separation of the 2^{++} radial excitation of the 3P_2 (1270), expected at ~ 1800 MeV, from the 3F_2 state which is expected to lie in the same mass region. The 3P_2 is predicted to be entirely produced in $\gamma\gamma$ collisions in the $J_z = 2$ substate. In contrast, a 3F_2 is predicted to have a $\gamma\gamma$ width from $J_z = 0$ roughly 1/3 to 1/2 of that from $J_z = 2$. So observation of a significant $J_z = 0$ contribution for a 2^{++} around 1800 MeV can help to distinguish the 3F_2 from the 3P_2 radial excitation of $f_2(1270)$.

Barnes [132] computed $\gamma\gamma$ widths of $q\bar{q}$ states based on an assumed Coulomb plus linear potential. These are in good agreement with data for the 3P_J states and so are hopefully a reasonable orientation for the sought-after radial excitations. For radially excited states with masses near 1700 MeV this gives, for $u\bar{u}$ and $d\bar{d}$ [$s\bar{s}$],

$$\begin{aligned} \Gamma_{\gamma\gamma}({}^3P_0(1700)) &= (2.1 - 2.3) \text{ keV} \quad [(0.15 - 0.2) \text{ keV}]; \\ \Gamma_{\gamma\gamma}^{\lambda=2}({}^3P_2(1700)) &= (1.5 - 2.4) \text{ keV} \quad [(0.1 - 0.2) \text{ keV}]; \\ \Gamma_{\gamma\gamma}^{\lambda=0}({}^3P_2(1700)) &= (0.05 - 0.15) \text{ keV} \quad [< 0.01 \text{ keV}]. \end{aligned} \quad (12.41)$$

These predicted values are only slightly smaller than for the 3P_J states and should be observable experimentally.

Thus, there should be a very rich spectrum of states in the 1.3–2.3 GeV/ c^2 region that could be disentangled with the help of high-statistics two-photon data. Aside from deepening our understanding of the quark model, it is important to establish the nature of all states in this region so that one may recognize the presence of non $q\bar{q}$ mesons. Even with trigger efficiencies that are lower at low mass, simulations show that BaBar should reconstruct the known $q\bar{q}$ mesons at a high

rate. For example, $\approx 10^5$ $a_2(1320)$ mesons and $\approx 10^6$ $\pi_2(1670)$ mesons should be reconstructed. Measurements of $\Gamma_{\gamma\gamma}$ for these states may be the first two-photon results obtained by BABAR and will certainly allow a thorough understanding of systematic effects needed for the study of rarer two-photon processes.

An additional test of QCD and of quark models, can be made if precision measurements of the π^0 , η , $\eta' \rightarrow \gamma\gamma$ and $\eta' \rightarrow \pi^+\pi^-\gamma$ decays are possible. Such decays are related to QCD and more generally to quark models via triangle and box anomaly diagrams [133, 134], which are expected to exist within the framework of QCD, even if they cannot be explicitly computed therein. Almost all data connected with the box anomaly diagram suffer from a lack of statistics and sometimes also from large systematic effects. Although it is very difficult to trigger on such low-mass, low-multiplicity final states in the face of large backgrounds, simulations show that BABAR might expect to accumulate at least $\sim 10^5$ fully reconstructed η and η' events. The crucial task will be to obtain a detailed understanding of the trigger and reconstruction efficiencies, so as to minimize systematic errors in the determination of the two-photon widths.

12.3.2.2 Identification of exotic mesons and glueballs

Particularly interesting is the search for exotic objects which are predicted by QCD: glueballs, hybrid $q\bar{q}g$ mesons, and 4-quark states ($qq\bar{q}\bar{q}$) or meson “molecules” ($K\bar{K}$). As photons are weakly coupled to gluons, $\gamma\gamma \rightarrow q\bar{q}g$ and $\gamma\gamma \rightarrow gg$ production are suppressed by factors of order 100–1000 compared with $\gamma\gamma \rightarrow q\bar{q}$. However, the large integrated luminosity obtainable with BABAR should allow measurements of many of these exotic states, and the ratio of their two-photon widths to normal mesons will aid in their identification.

There are lattice QCD predictions of glueballs between 1.5 GeV/ c^2 and 4 GeV/ c^2 [135], with some consensus that the lightest state is 0^{++} , while 0^{-+} and 2^{++} are the next heaviest states. A serious candidate has been observed at LEAR, the $f_0(1500)$ [136]; a possible candidate is the $f_J(2220)$ or $\xi(2230)$ [28, 137]. It will be vital to measure the two-photon widths for the 3P_0 $q\bar{q}$ states, because the lightest glueball is predicted to be $\cong 1.6$ GeV/ c^2 , which is in the vicinity of the 3P_0 nonet. The couplings to the $\gamma\gamma$ system can disentangle the pattern of these 0^{++} states and clarify the role of $f_0(1500)$ and $f_J(1710)$ in the glueball- $q\bar{q}$ mixing. As an example of the ability of BABAR to study glueball states, a Monte Carlo simulation was done for a state with the parameters of the $\pi_2(1670)$ except that a theoretically-motivated two-photon width of 1 eV was chosen instead of the $\Gamma_{\gamma\gamma} \sim 1$ keV characteristic of $q\bar{q}$ mesons. Even with such a small coupling, BABAR should reconstruct ~ 1000 such events in the final state $\pi^+\pi^-\pi^0$.

Hybrid states, where gluonic degrees of freedom are excited in the presence of the $q\bar{q}$ “seed,” are predicted to lie around 2 GeV/ c^2 . A $J^{PC} = 1^{-+}$ structure at 1.6–2.2 GeV/ c^2 , observed at Brookhaven in a π^-p reaction [138], is a candidate for such a hybrid state. The 2^{-+} sector is also interesting, as 1D_2 $q\bar{q}$ states are now becoming established in the 1.7–1.8 GeV/ c^2 mass region while lattice QCD predicts hybrid 2^{-+} states should exist in the ~ 2 GeV/ c^2 region. $\gamma\gamma \rightarrow \rho\omega$ can access the $3S$ state as it has a significant $\rho\omega$ coupling and hence, by VDM, should also couple

to $\gamma\gamma$. The hybrid state, by contrast, is expected to have a smaller $\gamma\gamma$ coupling and not couple strongly in $\rho\omega$. Any 0^{-+} in $\gamma\gamma \rightarrow \rho\omega$ may be compared with the $\pi(1800)$ hybrid candidate [139]

One of the most interesting regions for studies of exotic mesons is around $1.4 \text{ GeV}/c^2$. Here there exists the still-enigmatic $\eta(1440)$, long noted as a possible 0^{-+} glueball, which has not yet been seen in $\gamma\gamma$ reactions [140]. However, in single-tagged two-photon reactions, the X(1420) has been detected [141, 142] and identified as a spin-1 meson. The experiments could not identify the parity of this state, which determines whether it is an unwanted extra member of the 1^{++} nonet or a hybrid 1^{-+} state. Simulations suggest that at least 20000 X(1420)s will be seen in the $K^{\pm}K_s^0\pi^{\mp}$ final state with BaBar. As BaBar is without a backward endcap calorimeter, it will be difficult to identify the scattered positron that would allow separation between spin-0 and spin-1 resonances. However, with such high statistics it may be possible to use only the final state hadrons and do a Dalitz plot analysis to achieve this separation. A thorough study of $\gamma\gamma \rightarrow \eta\pi\pi$ and $K\bar{K}\pi$ might identify more such 0^{-+} states and $1^{\pm+}$ states in the $1.5\text{--}2.0 \text{ GeV}/c^2$ range.

12.3.2.3 Q^2 dependence and QCD

The $\gamma\gamma^*$ reaction, where one photon is tagged, allows a measurement of the transition form factor for mesons. For large Q^2 , where $Q^2 = \max(-q_1^2, -q_2^2)$ and q_i is the four momentum of the i 'th virtual photon, the perturbative QCD approach of Brodsky and Lepage [70, 143] results in the factorization of the amplitude into a parton distribution amplitude in the meson (or wave function) and a hard scattering amplitude computed, in leading order, from Born diagrams. The transition form factors for π^0 , η and η' have been determined by two recent experiments [144, 145], but more precise measurements of the η and η' transition form factors are needed to determine their wave functions [146]. These measurements will be difficult, but hopefully not impossible with the current BaBar detector. Addition of a backward endcap calorimeter would, of course, help to identify the “tagging” e^+ .

12.3.3 Exclusive Hadron Production and QCD

A real test of perturbative QCD predictions for exclusive hadron production from two-photon interactions can be made by analyzing data in the $W > 3 \text{ GeV}$ mass range. The exclusive productions of meson pairs or baryon-antibaryon pairs are of special interest. These processes are crossed channels of the Compton scattering of a photon from the considered meson or baryon. One advantage over Compton scattering is that a large variety of hadron pairs can be produced in two-photon interactions, whereas in Compton scattering experiments the possible targets are very limited. For large center-of-mass angles, high momenta are transferred and perturbative QCD calculations in the Born approximation are expected to account for absolute cross-sections, angular dependence, and polarizations [70, 143].

The predictions of Brodsky and Lepage [143] illustrate the sensitivity of the angular distributions to the meson wave function. For charged pions, the cross-section is essentially independent of the wave function, so that QCD predictions are almost model independent. For neutral pions, on the contrary, predictions are very sensitive to the meson wave function ϕ_M . A measurement of $\gamma\gamma \rightarrow \pi^+\pi^-$ therefore provides a test for the QCD predictions, whereas a measurement of $\gamma\gamma \rightarrow \pi^0\pi^0$ allows a determination of ϕ_M . Dimensional counting rules lead to the scaling law $d\sigma/dt \sim s^{-4}$ when s is large.

The cross-section for $\gamma\gamma \rightarrow \pi^+\pi^-$, as measured in the TPC/Two-Gamma experiment at PEP [147], is several times larger than the predictions of Brodsky and Lepage, whereas for $\gamma\gamma \rightarrow K^+K^-$ the predicted cross-section is slightly larger than the measured cross-section. It should be noted, however, that the data does not reach large values of W , where one might expect perturbative QCD to be valid. The inclusion of SU(3) flavor symmetry breaking effects [148] results in better agreement with the experimental data. In more recent results from CLEO [149] based on an integrated luminosity of 1.2 fb^{-1} , where pions and kaons could not be separated, the angular distributions are nevertheless in better agreement with theory for large values of W . Simulations using the predicted QCD cross-sections show that $> 5000 \pi^+\pi^-$ and $> 1500 \pi^0\pi^0$ events should be detected for $W > 2 \text{ GeV}$ in BABAR. (The actual detected rates in the 2–3 GeV region will be higher by a factor of a few, due to resonant contributions.) These sample sizes are at least an order of magnitude larger than those used in CLEO publications. Furthermore, the muon chambers within the BABAR IFR should distinguish pion pairs from muon pairs, reducing systematic errors in deriving the measured cross-sections. Similar event rates will be seen for K^+K^- , where the DIRC will provide excellent event-by-event separation between π and K .

The measured cross-section for $\gamma\gamma \rightarrow \rho^0\rho^0$ shows a large enhancement near threshold not seen in $\gamma\gamma \rightarrow \rho^+\rho^-$ [150], an effect which is not yet fully understood. There are also data for $\gamma\gamma \rightarrow \omega\omega$ [151, 152], and for $\gamma\gamma \rightarrow \rho\phi$ and $\omega\phi$ [153]. These data have very poor precision; BABAR should provide a major improvement that will shed light on the structure of vector mesons.

The analysis of $\gamma\gamma \rightarrow$ (baryon antibaryon) processes is similar to that for $\gamma\gamma \rightarrow$ (two mesons); yet the diagrams that contribute are much more numerous. Perturbative QCD at leading order leads to the scaling law $d\sigma/dt \sim s^{-6}$ for baryon pair production, which has to be experimentally verified in order to check that the perturbative regime has been reached. Helicity conservation implies that the baryons have opposite helicities.

The cross-section for $\gamma\gamma \rightarrow p\bar{p}$ has been measured at CLEO [154] up to $W = 3.1 \text{ GeV}$ with an integrated luminosity of 1.3 fb^{-1} . QCD based calculations by Farrar [155], using the Chernyak and Zhitnitsky wave function [156], give a cross-section one order of magnitude lower than the measured cross-section. However, radiation from isolated colored partons (“Sudakov suppression”) can have a substantial effect on the cross-section [157] and should be taken into account. On the other hand, a diquark model by Kroll [158] is in agreement with the data, but introduces further parameters because of the diquark form factor.

BaBar will detect a large number of $p\bar{p}$ events ($\approx 10^5$). Thus, in spite of the steep W dependence of the cross-section, measurements should be possible in the region $W = 3\text{--}4$ GeV where perturbative calculations are more valid. Additionally, the high statistics will allow significantly better measurements of the angular distributions. The $\gamma\gamma \rightarrow p\bar{p}$ process can be compared to the closely related Compton scattering $\gamma p \rightarrow \gamma p$ at large s and t . The $W = 3.1$ GeV results at CLEO correspond to Compton scattering of a photon beam of energy $E_\gamma = 4.5$ GeV, which is in the domain of CEBAF, while $W = 4$ GeV corresponds to Compton scattering at $E_\gamma = 8$ GeV.

The $\gamma\gamma \rightarrow \Lambda \bar{\Lambda}$ reaction has been observed at CLEO with an integrated luminosity of 3.4 fb^{-1} [159]. The cross-section is close to that for $\gamma\gamma \rightarrow p\bar{p}$, but the diquark model predicts a cross-section a factor of 3 lower than the data. One expects the ratio of the number of $\Lambda\bar{\Lambda}$ to $p\bar{p}$ to be about one half, for W greater than about 3.5 GeV. Large event samples are badly needed for this final state and should be supplied by BaBar. If sufficient data is obtained, it might be possible to test helicity conservation in this reaction.

Other baryon-antibaryon pairs can be searched for: $\Sigma^0 \bar{\Sigma}^0$ or $\Lambda \bar{\Sigma}$ are relatively difficult to identify, but $\Sigma^+ \bar{\Sigma}^+$, where $\Sigma^+ \rightarrow p\pi^0$, could be easier. Farrar *et al.* [155] predict production rates for $\Delta^+ \bar{\Delta}^+$ and $\Delta^{++} \bar{\Delta}^{++}$ much higher than for $p\bar{p}$; therefore, it is possible that these processes will be observed in spite of the broadness of the Δ .

12.4 Light-Meson Spectroscopy in B , D_s , and D Decays

Light Meson Spectroscopy is still a very active field of physics research, mostly due to the lack of final experimental evidence for a gluonic degree of freedom in the structure of light mesons. Over the last years, many experiments attempted to unravel different puzzles related to the study of the light mesons using a large variety of reactions. Studies were made using peripheral [160] and central [161] hadronic interactions, $p\bar{p}$ annihilations [162], $\gamma\gamma$ collisions [163], photo-production [164] and heavy flavor decays [165]. Dedicated experiments are actually still running or analyzing their data at CERN, BNL, FNAL, Serpukhov, and Beijing.

The basic interest in this field is the possibility of the existence of exotic states: meson resonances composed only of gluons (glueballs) or of mixtures of quarks and gluons (hybrids). These states are expected from QCD to exist and to populate the low mass region of the hadronic spectrum together with ordinary mesons with which they can mix [166]. The latest lattice calculations locate the low lying glueballs with $J^{PC} = 0^{++}$ around $1.5 \text{ GeV}/c^2$ while the $J^{PC} = 2^{++}$ is expected in the $2.2 \text{ GeV}/c^2$ region [135].

Several exotic candidates have been suggested over the last years by several experiments [167]. These include the I=0 scalars, $f_0(980)$ and $f_0(1500)$, the I=1 scalar, $a_0(980)$, the pseudoscalar, $\iota/\eta(1440)$, and the axial, $f_1(1420)$. Glueball candidates are $\theta/f_J(1710)$ and $\xi(2200)$ with as yet undefined spin. New evidence has recently been reported on the existence of an exotic $J^{PC} = 1^{-+}$

meson, $\hat{\rho}(1370)$ [168]. In addition, a series of bumps with unknown quantum numbers exist that are difficult to accommodate in the quark model. Even now, basic $q\bar{q}$ nonets have some undefined members.

One of the problems encountered in the study of light meson spectroscopy is that several resonances are superimposed in the same mass range so that only sophisticated partial wave analyses are able to separate the different contributions. However, quite often some ambiguity remains [169]. It is clear that no single experiment can answer the question of the existence of exotics — this can only be achieved by a comparison of the properties of light mesons from different production mechanisms.

New sources of light mesons that could be worthwhile exploring are the decays of B and D mesons. The number of B and D final states involving light mesons is not as rich as in charmonium decay. Nevertheless there are a few important areas in which these reactions can make important contributions. Some studies have already been performed and are giving interesting results. In particular, evidence has been presented for D_s decays to $f_0(980)$ [170, 171], $f_0(1500)$ [171], and $\theta/f_J(1700)$ [172], mesons which do not have an easy classification in the $SU(3)$ $q\bar{q}$ multiplets.

B_{ABAR}, with its high luminosity and its vertexing possibilities, due to the asymmetric e^+e^- beam energies, offers unique possibilities for performing these studies. The idea is to select one fully reconstructed B decay in channels having enough constraints to allow background-free decay chains.

In the following, the outline of a physics program that could be performed with B_{ABAR} is given. In some cases, estimates of background contributions are provided. A complete description of the simulation studies can be found in Ref. [173]. The study of these decays consists of fitting the Dalitz plots using the sum of different interfering amplitudes, each described by a Breit-Wigner lineshape and a decay angular distribution [174]. The total amplitude used to describe the Dalitz plot population is, therefore

$$|M|^2 = \left| \sum BW(m) \times J(\Omega) \times e^{i\phi} \right|^2, \quad (12.42)$$

where $BW(m)$ describes the Breit-Wigner term, $J(\Omega)$ describes the angular distributions and ϕ is the phase of the given amplitude.

Similar studies have been performed in $p\bar{p}$ annihilations at rest to pseudoscalars, where the experimental situation is much more complex due to the presence of several partial waves in the initial state. In D and B decays there is a large simplification due to the fact that the initial state is unique: a spin-0 particle.

The following simulations have been made using the Aslund program, further details can be found in Ref. [173].

12.4.1 B decays

12.4.1.1 B decays to $a_1(1260)$

The decay $B \rightarrow a_1\pi$ is an important channel for the determination of $\sin 2\alpha$. Since the $a_1(1260)$ decays dominantly via $\rho\pi$ to the 3π final state, $B \rightarrow 4\pi$ has to be investigated where a lot of background is expected ($a_2\pi$, $\rho\rho$, $\pi(1300)\pi$, ...). The expected rate of the $a_1\pi$ final state is rather small and will not allow for the determination of its lineshape. Therefore, it has to be imposed in order to extract the couplings out of the partial wave analysis of the 4π -channel. Unfortunately, static properties like mass and width of the a_1 are not well determined so far. In addition, a radial excited a_1 , a so-called $a_{1R}(1700)$ may be present in the B -Decay, which represents part of the axial current. This particle has been reported to be seen in charge exchange reactions [139] and at LEP [175], always in its 3π -mode. Therefore, it is important to study the a_1 and its radial excitations in a hadronic environment with very high statistics. This can be done very efficiently in $B \rightarrow Da_1$ decays where, in contrast to τ -decays, no phase space limit applies.

The $a_1(1260)$ meson has been observed already in B decays [28] with the branching fractions shown in Table 12-22. In these decays charge conjugation is implied. The B decay diagrams that lead to the production of the $a_1(1260)$ meson are shown in Fig. 12-18. The results from the simulations are summarized in Table 12-22. Backgrounds are rather small, for a signal of 1.9×10^3 events from the decay $\overline{B}^0 \rightarrow D^{*+}a_1^-$, $D^{*+} \rightarrow D^0\pi^+$, $D^0 \rightarrow K^-\pi^+$, the estimated background yields are the following: (B^+B^-): 31; ($c\bar{c}$): 74; total ($q\bar{q}$): 79.

One interesting channel, never studied, which could enhance the a_1 decay to $f_0\pi$ is given by the $\pi^0\pi^0\pi^\pm$ final state. This decay has also been simulated through Aslund allowing this time the a_1 to decay to $\pi^0\pi^0\pi^\pm$. The resulting estimate for this channel is also shown in the last row of Table 12-22. The resulting acceptance on the 3π Dalitz plots for the two decay modes show a rather uniform behavior.

12.4.1.2 Color-suppressed B decays

A B^0 -decay diagram that could lead to the production of neutral light mesons is shown in Fig. 12-19. Here, the decay of the X^0 system to $\pi^+\pi^-$, $K\bar{K}$, $K\bar{K}\pi$, $\eta\pi\pi$, *etc.* could be studied. Simulations have been performed imagining the X^0 system to decay to $\pi^+\pi^-$. The branching fractions for such decays are not known, so the numbers given below have been computed in units of 1×10^{-3} . The resulting figures on this channel are summarized in Table 12-23. The background estimates to the decay $\overline{B}^0 \rightarrow (\pi^+\pi^-)D^{*0}(\rightarrow \pi^0D^0(\rightarrow K^-\pi^+))$ are these: for a signal of 170 events, 52 events from B^+B^- and 16 events from $c\bar{c}$ are expected. The latter contribution may be reduced further using the jet-like structure of the continuum. These channels, therefore, depending on their branching fractions, require some careful study of backgrounds from $B\overline{B}$.

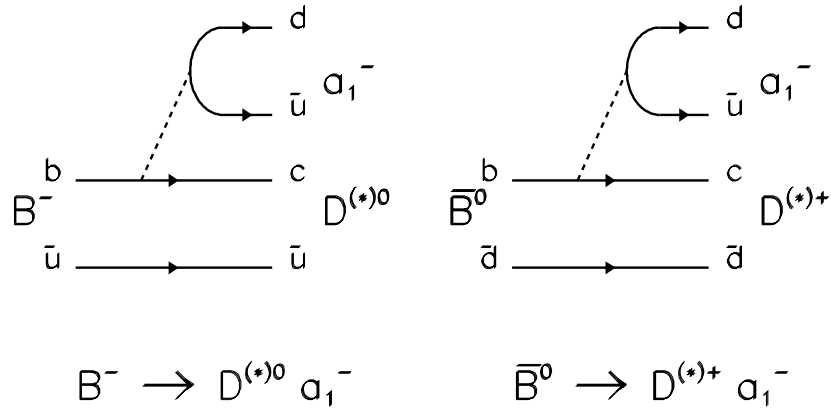

Figure 12-18. Diagrams involving B decays to a_1 .

Table 12-22. Branching fractions and estimated events for 30fb^{-1} luminosity for B decays involving the $a_1(1260)$ meson.

Channel ($a_1^\pm \rightarrow \pi^+ \pi^- \pi^\pm$)	Branching fraction (%)	Acceptance	Events
$B^- \rightarrow D^0 a_1^-$ $D^0 \rightarrow K^- \pi^+$	0.5 ± 0.4	0.38	9×10^3
$B^- \rightarrow D^{*0}(2007) a_1^-$ $D^{*0} \rightarrow \pi^0 D^0 (\rightarrow K^- \pi^+)$	1.9 ± 0.5	0.21	21×10^3
$B^0 \rightarrow D^- a_1^+$ $D^- \rightarrow K^+ \pi^- \pi^-$	0.6 ± 0.33	0.31	5×10^3
$B^0 \rightarrow D^{*-}(2010) a_1^+$ $D^{*-} \rightarrow \pi^- D^0$ $D^{*-} \rightarrow \pi^- D^0 (\rightarrow K^- \pi^+)$	1.3 ± 0.27	0.35	16×10^3
$D^{*-} \rightarrow \pi^0 D^-$ $D^{*-} \rightarrow \pi^0 D^- (\rightarrow K^+ \pi^- \pi^-)$		0.19	
Total			
$B \rightarrow D^{(*)} a_1^\pm (\rightarrow \pi^+ \pi^- \pi^\pm)$			51×10^3
$B \rightarrow D^{(*)} a_1^\pm (\rightarrow \pi^0 \pi^0 \pi^\pm)$			29×10^3

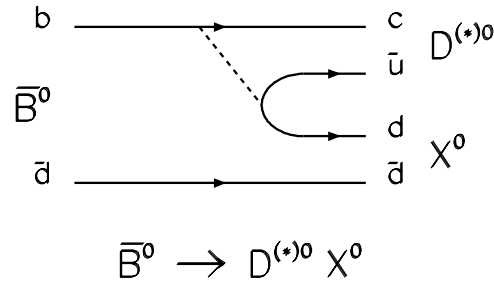


Figure 12-19. Diagram involving B^0 decays to neutral light mesons.

Table 12-23. Acceptance and event yield for a $30fb^{-1}$ luminosity in units of 1×10^{-3} branching fraction for $\bar{B}^0 \rightarrow D^0 \pi^+ \pi^-$ and $\bar{B}^0 \rightarrow D^{*0} \pi^+ \pi^-$.

Decay	Acceptance	Events
$\bar{B}^0 \rightarrow (\pi^+ \pi^-) D^{*0} (\rightarrow \pi^0 D^0 (\rightarrow K^- \pi^+))$	0.23	174
$\bar{B}^0 \rightarrow (\pi^+ \pi^-) D^{*0}$		2450
$\bar{B}^0 \rightarrow \pi^+ \pi^- D^0 (\rightarrow K^- \pi^+)$	0.41	500
$\bar{B}^0 \rightarrow \pi^+ \pi^- D^0$		3700

12.4.2 D and D_s Decays

D and D_s decay diagrams that can give information on the production of neutral light mesons are shown in Fig. 12-20. D mesons are coupled to $u\bar{u}$ states while D_s mesons are coupled to $s\bar{s}$ states.

The Dalitz plots from these decays have been studied by Mark II, Mark III, E691, E687, and ARGUS experiments, with a few hundred events and in channels which involve charged tracks only. The full reconstruction of B decays in BABAR will allow the possibility of detecting decays to channels involving γ s. D_s decays, as seen in Fig. 12-20, are coupled to mesons having $s\bar{s}$ contributions in their wavefunction. Therefore, from D_s decays, precise measurements of the branching fractions of strangeonium states could be obtained. Among the puzzles still present in light meson spectroscopy, BABAR could obtain information on the internal structure of the $f_0(980)$ meson, the $\theta/f_J(1700)$, and the E/ι puzzle. D_s decays can be obtained with high rates and relatively background free conditions using the decay channels shown in Table 12-24.

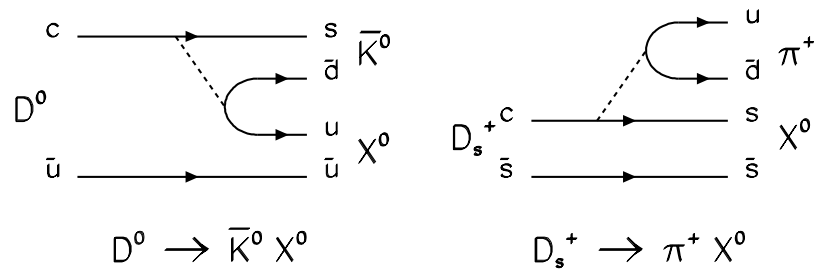


Figure 12-20. Diagrams involving D and D_s decays to light mesons.

Table 12-24. Branching fractions and events yield for a 30 fb^{-1} luminosity for B decays involving D_s meson.

Channel	Branching Fraction %	$D_s^+ \rightarrow \pi^+ \pi^- \pi^+$	$D_s^+ \rightarrow \pi^+ K^+ K^-$
$B^+ \rightarrow \bar{D}^0 D_s^+$	1.7 ± 0.6	750	1973
$B^+ \rightarrow \bar{D}^0 D_s^{*+}$	1.2 ± 1.0	303	797
$B^+ \rightarrow \bar{D}^{*0} (2007) D_s^+$	1.0 ± 0.7	282	742
$B^+ \rightarrow \bar{D}^{*0} (2007) D_s^{*+}$	2.3 ± 1.4	371	976
$B^0 \rightarrow D^- D_s^+$	0.7 ± 0.4	152	400
$B^0 \rightarrow D^{*-} (2010) D_s^+$	1.2 ± 0.6	272	715
$B^0 \rightarrow D^- D_s^{*+}$	2.0 ± 1.5	373	981
$B^0 \rightarrow D^{*-} (2010) D_s^{*+}$	1.9 ± 1.2	343	902
Total		2846	7486

Table 12-25. Acceptances for the reaction $B^0 \rightarrow D^{*-} D_s^+$, $D^{*-} \rightarrow D^0 \pi^-$, $D^0 \rightarrow K^- \pi^+$ for different D_s decay modes.

D_s Decay mode	Acceptance
$\pi^+ \pi^+ \pi^-$	0.30
$\pi^+ \pi^0 \pi^0$	0.17
$\pi^+ \eta \eta$	0.24
$\pi^+ K^+ K^-$	0.24
$\pi^+ K_s^0 K_s^0$	0.18

12.4.2.1 Study of $B^0 \rightarrow D^{*-} D_s^+$

The following decays have been simulated:

$$\begin{aligned}
 B^0 &\rightarrow D^{*-} D_s^+ \\
 &\rightarrow \pi^+ \pi^+ \pi^- \\
 &\rightarrow \pi^+ \pi^0 \pi^0 \\
 &\rightarrow \pi^+ \eta \eta \\
 &\rightarrow \pi^+ K^+ K^- \\
 &\rightarrow \pi^+ K_S^0 K_S^0
 \end{aligned}$$

with the acceptances shown in Table 12-25. The selection procedure is outlined in Fig. 12-21 where the signal is compared with backgrounds. In this case, for 42 events signal from $B^0 \rightarrow D^{*-} D_s^+$, $D^{*-} \rightarrow D^0 \pi^-$, $D^0 \rightarrow K^- \pi^+$, $D_s^+ \rightarrow \pi^+ \pi^- \pi^+ \sim 1.5$ background events may be expected from $B^+ B^-$ and 0.9 from $c\bar{c}$.

The simulation shows also a rather uniform acceptance on the Dalitz plot for $\pi^+ \pi^-$, $K^+ K^-$ and $\eta \eta$ final states, while some depletion in the high mass region can be seen in the $\pi^0 \pi^0$ and $K_S^0 K_S^0$ final states. The estimated number of events are summarized in Table 12-24.

12.4.2.2 K matrix formalism

The structure of the mysterious sector of light quark scalar mesons is still under discussion and needs information in terms of existence, lineshapes, and proper decay branching fractions of the scalar isoscalar states. The main problem in the analysis of scalar mesons is the fact that all known isoscalar scalars are overlapping and are affected by any decay threshold. However, the low mass

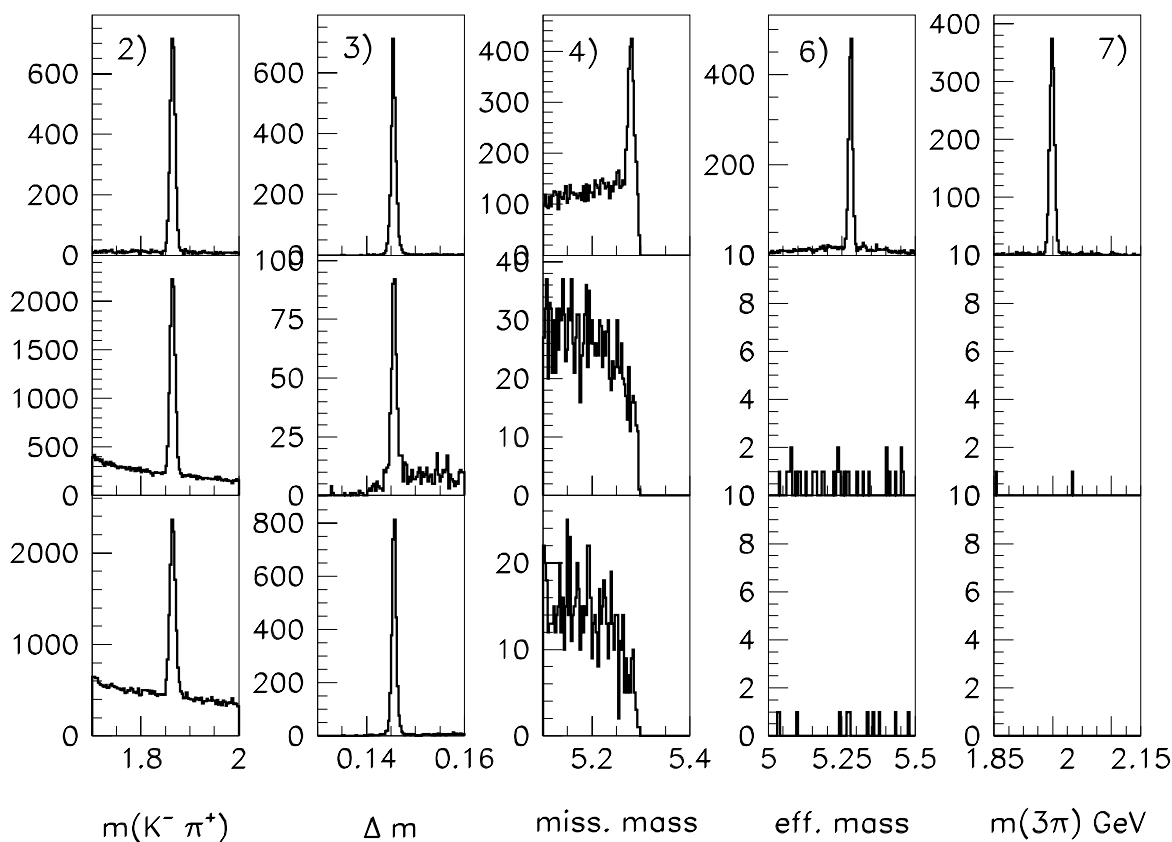


Figure 12-21. Comparison between signal (5×10^3 events, first row), $B^+ B^-$ background (0.5×10^6 events, second row) and $c\bar{c}$ continuum (1.0×10^6 events, third row) for the reaction: $B^0 \rightarrow D^{*-} D_s^+$, $D^{*-} \rightarrow D^0 \pi^-$, $D^0 \rightarrow K^- \pi^+$, $D_s^+ \rightarrow \pi^+ \pi^- \pi^+$. At stage 3) the D^0 has been required, at stage 4) the D^{*-} has been selected using the mass difference. At stage 6) a B in the missing mass to $D^* 3\pi$ has been required, at stage 7) a B in the effective mass ($D^* 3\pi$) has been required. The last figure shows the D_s signal in the 3π effective mass.

scalars are constrained by the unitarity limit condition. Therefore, a coupled channel analysis has to be applied which guarantees unitarity. Apropos of this, a powerful method for that has been developed by Chung *et al.* [176] based on a K matrix method used by the Crystal Barrel Collaboration [177] to describe the production of three pseudoscalars in $p\bar{p}$ annihilation in terms of isobar propagation. The same technique is applicable for the decay of D mesons. The work of Chung *et al.* shows how one can factorize the production and propagation of isobars in a hadronic production process. The two particle dynamics can be written in terms of the unitary S matrix with $S = I + 2i\rho T$, where I is the identity operator and $2i$ is a convention. ρ is a diagonal phase space matrix with $\rho_i = q_i/m$ with q_i being the two body breakup momentum and m being the isobar's mass. All dynamics is described by the unitary T matrix that has poles in the complex energy plane, which can be identified with resonances. To parametrize this matrix, it is useful to introduce the real hermitian K matrix with the definition $K^{-1} = T^{-1} + i\rho$, to get $T = K(I - iK\rho)^{-1}$. The K matrix describes the propagation of an isobar through its final states up to a infinite number of loops. The elements of the K matrix are sums of poles for all the individual resonances α which may occur

$$K_{ij} = \sum_{\alpha} \frac{g_{\alpha,i}(m)g_{\alpha,i}(m)}{(m_{\alpha}^2 - m^2)\sqrt{\rho_i\rho_j}} + c_{ij}, \quad (12.43)$$

where $g_{\alpha,i}(m) = m_{\alpha}\Gamma_{\alpha i}(m)$ is the mass dependent width, which includes the relative coupling strength and phase space factors as well as the angular momentum barrier of final state i to resonance α and c_{ij} and arbitrary constant. The total width of the resonance α is then $\Gamma_{\alpha} = \sum_{\alpha} \Gamma_{\alpha i}(m)$. Since the original K -matrix approach describes only two-body scattering, a production amplitude has to be introduced that can be written in terms of a P vector has exactly the same poles as the K matrix

$$P_i = \sum_{\alpha} \frac{\beta_{\alpha}g_{\alpha,i}(m)}{(m_{\alpha}^2 - m^2)\sqrt{\rho_i}} + p_i \text{ and } T = (1 - iK\rho)^{-1}P \quad (12.44)$$

where β_{α} is the production strength of the resonance α and p_i are arbitrary constants. The advantage of this method is the generality of the K -matrix, which is identical for all final states. The differences are covered by the production strength. Therefore K has to be the same as, *e.g.*, in $p\bar{p}$ interactions.

The proposed strategy for an analysis is to start with the scalar K -matrix parametrization as of the Crystal Barrel Experiment including the channels $K\bar{K}$ (K^+K^- and $K_S K_S$), $\pi\pi$ ($\pi^+\pi^-$ and $\pi^0\pi^0$) and $\eta\eta$. Other K -matrices and/or Breit-Wigner forms may be added for other partial waves depending on whether or not resonances of a given J^{PC} do or do not overlap. This should be done for each set of D -decays separately (D_s , D^{\pm} and D^0). This provides the opportunity to do cross-checks and to settle the number of poles (resonances) needed for a perfect fit. After all, it should be possible to combine all datasets to get a solution without biases from other experiments yielding masses and widths (from the complex energy plane of T) and the decay branching fractions for all individual resonances.

12.4.2.3 Study of the E/ι puzzle

The true composition of the axial mesons nonet is still uncertain, with two states $f_1(1420)$ and $f_1(1515)$ competing with being the $s\bar{s}$ member of the nonet. In addition, some pseudoscalar states have been observed in the 1.4 GeV/ c^2 region decaying to $K\bar{K}\pi$ and $\eta\pi\pi$ having a not easy classification. It is, therefore, interesting to have other inputs to the problem and D_s decays could test the internal quark structure of some of these mesons. D_s decays that could be used for this purpose are

$$D_s^+ \rightarrow (K^+K^-\pi^0)\pi^+ \quad \text{or} \quad D_s^+ \rightarrow (K_S^0K^\pm\pi^\mp)\pi^+, \quad (12.45)$$

where one looks for resonances in the $K\bar{K}\pi$ system. The results from a simulation of these channels gives a total of 11×10^3 events for the decay of $B \rightarrow D^{(*)}D_s, D_s^+ \rightarrow (K^+K^-\pi^0)\pi^+$.

12.5 Baryon Formation

The formation of hadrons is not a subject that is amenable to first principles calculation from QCD. Instead, the comparison between experiment and theory relies on the development of models. Hadron structure functions are an aspect of such modeling that is quite well developed. Models for hadron formation based on string-breaking or other phenomenological pictures are less well understood. Models have frequently been “tuned” to fit a large amount of data, at the price of introducing additional parameters with no QCD-based prediction for the values of such parameters. Further development of such models offers some prospect for clarifying this area and improving the ability to test the underlying QCD physics in a less model-dependent fashion.

One approach, developed by a UCLA collaboration [178, 179], has had some success in describing *meson* formation in $e^+e^- \rightarrow q\bar{q}$. On the other hand, *baryon* formation, though reasonably predicted by models such as those of UCLA or Lund, is considerably more complicated and far less well understood. BABAR offers an excellent environment in which to bring baryon formation models to a level of understanding comparable to that of mesons. This will require data samples of $\sim 10^8$ events with good flavor identification, in order to analyze the three-body rapidity correlation structure of baryon-meson-antibaryon events. BABAR will collect significant data running below the $B^0\bar{B}^0$ threshold for background subtraction purposes. This data sample can also be used for other studies, such as the study of hadron production mechanisms discussed here. If continuum events can be separated cleanly from $B\bar{B}$ events, then on-resonance data may also be useful for such studies.

The results to date of the UCLA model are described in [178, 179]. The flavored multiplicities and distributions in the light-quark meson sector are well predicted, employing only two inherent parameters that arise naturally in the treatment with no additional *ad hoc* parameters. However, though baryon flavor rates and distributions are approximately predicted, it is clear (a) that they

are not as well predicted as mesons, (b) the treatment of baryons involves two or three ad hoc parameters and (c) baryon formation is indeed much more complicated. This is not surprising, since each baryon requires that three quarks or antiquarks come together within a hadronic size. Typically there are also a number of mesons produced. In particular, there is the possibility of one or more mesons created in the intermediate region between baryon and antibaryon (called “popcorn” production).

Monte Carlo modeling of continuum data at ~ 10 GeV has been performed using both the Lund and UCLA approaches. The aim of such studies is not to compare Lund and UCLA models; rather it is to find ways, using Lund and UCLA as initial phenomenological models, to define a good approximate method to isolate the individual contributions of various processes. The rapidity correlations discussed here provide an example. Developing the ability to test and refine features of the models is hoped for. The aim of this initial study is thus to learn how to describe, and thereby experimentally identify, or isolate, flavored intermediate meson production. These studies were done for samples at the Monte Carlo generator level (no detector effects) of 10^7 events (compatible, with reasonable efficiency and identification rates), with $\sim 10^8$ total continuum events recorded — that is, a few years of running.⁵ The aim here is simply to indicate the type of investigation that could be done.

The method used was to look at a data sample for $pK^-\bar{\Lambda}$ production and to study the proton- K^- rapidity correlations, when the rapidity of the $\bar{\Lambda}$ is defined to be greater than that of the proton. Such “three-body” rapidity correlations are a new physics area in which a great deal remains to be learned.

The rapidity of the K^- can be greater than that of the $\bar{\Lambda}$, intermediate between the proton and the $\bar{\Lambda}$ (the case of interest here) or less than that of the proton. Loosely speaking, one expects these regions to correlate with the location in the string-breaking (quark-pair production) that produces the strange quark in the K^- . In this study, it was found that the number of events where the K^- is actually an intermediate “popcorn” meson (or daughter of such a meson) was only $\sim 6 - 11\%$ of the total observed $pK^-\bar{\Lambda}$ samples. Thus, it will be a substantial challenge to identify such production mechanisms, since there are a considerable number of cases where the K^- originates from outside the p or $\bar{\Lambda}$, some of which then “smear” into the same kinematic regions as given by the “popcorn” production mechanism. Thus, one needs to define methods for subtracting experimentally the effects of the outer production, to isolate the contribution of the intermediate or “popcorn” production process. The purpose of this study was to develop such a method, using subtractions based on a $p\bar{p}k^-$ sample, where strange meson “popcorn” production is found to be very highly suppressed. Figure 12-22 shows the result of these calculations for both the Lund and the UCLA models. The full development of this method and the details of the subtraction method are given in [180].

⁵Perhaps only one to two years of data will be needed if continuum events produced on resonance can be separated from $B\bar{B}$ events for use in such studies. The biases introduced in making such a separation will require further investigation.

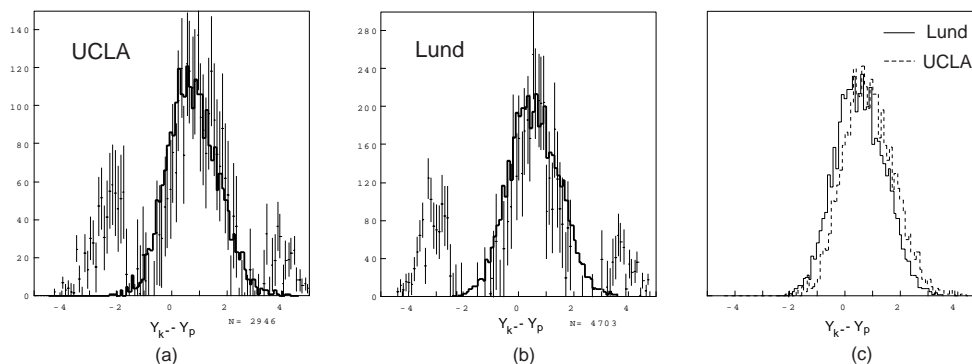


Figure 12-22. Comparison of rapidity distributions generated from “popcorn” production with that obtained from a subtraction procedure defined using $pK^- \bar{p}$ data, for (a) the UCLA model, (b) the Lund model.

The data shown are those generated from the intermediate “popcorn” production mechanism only. The curve is generated by including all production mechanisms and then applying an appropriate subtraction that can be experimentally determined from $pK^- \bar{p}$ data, but here was based on the Monte-Carlo generation of such events by the same model. The so-identified K^- popcorn signal is within 10% of the actual generated number for each Monte Carlo, centered at very close to the proper rapidity correlation value, and with approximately the proper rapidity correlation shape. It is interesting to note in Fig.12-22 that the two different models display somewhat different $Y_{K^-} - Y_p$ distributions. The purpose here, however, is not to compare the two different Monte Carlo generation models but to show how such data can be used to test the validity of particular features of the model, the focus being the inclusion of intermediate or “popcorn” meson production.

The future studies with BABAR to bring this analysis to maturity include:

- The study of whether one can use on-resonance running for this type of study, *i.e.*, whether continuum events of interest here can be separated reliably from $B\bar{B}$ events on the $\Upsilon(4S)$ resonance.
- Studies including detector and identification efficiencies, and mis-identification (such as unidentified $\bar{\Lambda}$ decays in the \bar{p} data sample).
- More studies of how to define subtractions to extract popcorn rates and distributions most reliably.

This preliminary study indicates that such investigations, which can only be carried out with continuum events at a high luminosity B Factory with good particle identification such as BABAR, can lead to a much deeper understanding of how baryons are formed.

12.6 General Conclusions on Non- B Physics

At the $\Upsilon(4S)$ resonance, the cross-sections for $c\bar{c}$, $\tau^+\tau^-$ and for two-photon processes with significant hadronic energy are each comparable to the $b\bar{b}$ cross-section. In the early stages of data analysis, studies of charm and τ physics will be available, as essential ingredients in cross-checks of the detector's performance, and as aids in developing well-understood and reliable analysis tools. Within a couple of years of the start of data-taking, the accumulated BABAR data sample should be competitive with existing data samples for charm, τ , QCD and two-photon physics, and will provide topics for early physics studies.

The particle identification offered at BABAR should provide more sensitivity than that available in current experiments, for searches for new physics (*e.g.*, $D^0\bar{D}^0$ mixing, CP violation in D or τ decays, and rare or forbidden charm and τ decays), and for measurements that increase our understanding of the Standard Model (*e.g.*, leptonic and semileptonic charm decays, and meson spectroscopy).

References

- [1] See for instance references in G. Blaylock, A. Seiden and Y. Nir, *Phys. Lett. B* **355**, 555 (1995).
- [2] Our notation follows T. Liu, *Proceedings of the Workshop on the Future of High Sensitivity Charm Experiments CHARM2000*, Batavia, IL (1994), hep-ph/9408330.
- [3] D. Cinabro *et al.*, (CLEO Collaboration), *Phys. Rev. Lett.* **72**, 1406 (1994).
- [4] J. C. Anjos *et al.*, (E691 Collaboration) , *Phys. Rev. Lett.* **60**, 1239 (1988).
- [5] E. M. Aitala *et al.*, (E791 Collaboration), *Phys. Rev. D* **57**, 13 (1998).
- [6] E. M. Aitala *et al.*, (E791 Collaboration), *Phys. Rev. Lett.* **77**, 2384 (1996).
- [7] F. Buccella *et al.*, *Phys. Rev. D* **51**, 3478 (1995).
- [8] F. Buccella, M. Lusignoli and A. Pugliese, *Phys. Lett. B* **379**, 249 (1996).
- [9] G. Burdman, “Potential for Discoveries in Charm Meson Physics,” presented at Workshop on the Tau/Charm Factory, Argonne (1995), hep-ph/9508349.
- [10] M. Gronau and S. Wakaizumi, *Phys. Rev. Lett.* **68**, 1814 (1992);
A. Le Yaouanc, L. Oliver and J. C. Raynal, *Phys. Lett. B* **292**, 353 (1992).
- [11] E. M. Aitala *et al.*, *Phys. Lett. B* **404**, 187 (1997).
- [12] P. L. Frabetti *et al.*, *Phys. Rev. D* **50**, 2953 (1994).
- [13] J. Bartlet *et al.*, *Phys. Rev. D* **52**, 4860 (1995).
- [14] Z. Z. Xing, *Phys. Rev. D* **55**, 196 (1997).
- [15] S. Pakvasa, (1997) hep-ph/9705397.
- [16] M. Alexopoulos *et al.*, *Phys. Rev. Lett.* **77**, 2380 (1996).
- [17] For a more extensive list of FCNC and lepton number violating limits, see for example, A. Freyberger *et al.*, *Phys. Rev. Lett.* **76**, 3065 (1996).
- [18] E. M. Aitala *et al.*, *Phys. Rev. Lett.* **76**, 364 (1996).
- [19] P. Singer and D.-X. Zhang, *Phys. Rev. D* **55**, 1127 (1997).
- [20] M. Selen, *Bull. Am. Phys. Soc.* **39**, 1147 (1994).

- [21] G. Burdman *et al.*, *Phys. Rev. D* **52**, 6383 (1995).
- [22] K. S. Babu *et al.*, *Phys. Lett. B* **205**, 540 (1988).
- [23] S. Davidson, D. Bailey and B. A. Campbell, *Z. Phys. C* **61**, 613 (1994).
- [24] J. Richman and P. Burchat, *Rev. Mod. Phys.* **67**, 893 (1995).
- [25] C. R. Allton, *Nucl. Phys.* **B437**, 641 (1995).
- [26] C. R. Allton *et al.*, ROME preprint 97/1164 (1997).
- [27] M. Neubert, *Phys. Rep.* **245**, 259 (1994).
- [28] R. M. Barnett *et al.*, *Phys. Rev. D* **54**, 1 (1996).
- [29] S. Aoki *et al.*, *Prog. Th. Phys.* **89**, 131 (1993).
- [30] D. Acosta *et al.*, *Phys. Rev. D* **49**, 5690 (1994).
- [31] K. Kodama *et al.*, *Phys. Lett. B* **382**, 299 (1996).
- [32] M. Acciarri *et al.*, *Phys. Lett. B* **396**, 327 (1997).
- [33] J. Z. Bai *et al.*, *Phys. Rev. Lett.* **74**, 4599 (1995).
- [34] Particle Data Group, 1997 Web Edition of Review of Particle Properties, <http://www-pdg.lbl.gov/>.
- [35] J. Adler *et al.*, *Phys. Rev. Lett.* **60**, 1375 (1988).
- [36] A. Anastassov *et al.*, (CLEO Collaboration), CLEO CONF 96-8, ICHEP96 PA05-079, in *Proceedings of the 28th International Conference on High Energy Physics*, Warsaw, Poland, 25-31 July (1996), World Scientific, Singapore (1997).
- [37] M. Athanas *et al.*, (CLEO Collaboration), *Phys. Rev. Lett.* **79**, 2208 (1997).
- [38] G. Crawford *et al.*, (CLEO Collaboration), *Phys. Rev. Lett.* **75**, 624 (1995).
- [39] G. Burdman *et al.*, *Phys. Rev. D* **49**, 2331 (1994).
- [40] G. Boyd and B. Grinstein, *Nucl. Phys.* **B442**, 205 (1995).
- [41] A. Bean *et al.*, *Phys. Lett. B* **317**, 647 (1993).
- [42] J. C. Anjos *et al.*, *Phys. Rev. Lett.* **62**, 1587 (1989).
- [43] G. Crawford *et al.*, *Phys. Rev. D* **44**, 3394 (1991).

- [44] Z. Bai *et al.*, *Phys. Rev. Lett.* **66**, 1011 (1991).
- [45] P. L. Frabetti *et al.*, *Phys. Lett. B* **315**, 203 (1993).
- [46] N. Isgur *et al.*, *Phys. Rev. D* **39**, 799 (1989).
- [47] R. L. Morrison and J. D. Richman, in *Review of Particle Properties*, Part I, p. 1565 and Part IV, p. 1602, *Phys. Rev. D* **50**, 1173 (1994).
- [48] D. Scora and N. Isgur, CEBAF Preprint CEBAF-TH-94-14 (1994).
- [49] J. C. Anjos *et al.*, *Phys. Rev. Lett.* **65**, 2630 (1990).
- [50] K. Kodama *et al.*, *Phys. Lett. B* **274**, 246 (1992).
- [51] P. L. Frabetti *et al.*, *Phys. Lett. B* **307**, 262 (1993).
- [52] E. M. Aitala *et al.*, FERMILAB-Pub97/267 (1997).
- [53] J. G. Körner and G. A. Schuler, *Z. Phys. C* **38**, 511 (1988); [*Z. Phys. C* **41**, 690(E) (1989)].
- [54] T. Altomari and L. Wolfenstein, *Phys. Rev. D* **37**, 681 (1988).
- [55] J. F. Gilman and R. L. Singleton, Jr., *Phys. Rev. D* **41**, 93 (1990).
- [56] A. Abada *et al.*, *Nucl. Phys.* **B416**, 675 (1994).
- [57] C. R. Allton *et al.*, *Phys. Lett. B* **345**, 513 (1995).
- [58] M. Nieves *et al.*, preprint SHEP-94-95-09, presented at LATTICE 94, 12th International Symposium on Lattice Field Theory, Bielefeld, Germany, Sept. 27 – Oct. 1 (1994).
- [59] P. Ball, V. M. Braun, and H. G. Dosch, *Phys. Rev. D* **44**, 3567 (1991).
- [60] K. Kodama *et al.*, *Phys. Lett. B* **309**, 483 (1993).
- [61] P. L. Frabetti *et al.*, *Phys. Lett. B* **328**, 187 (1994).
- [62] P. Avery *et al.*, (CLEO Collaboration), *Phys. Lett. B* **337**, 405 (1994).
- [63] M. S. Alam *et al.*, *Phys. Rev. Lett.* **71**, 1311 (1993).
- [64] F. Butler *et al.*, (CLEO Collaboration), *Phys. Rev. D* **52**, 2656 (1995).
- [65] J. Adler *et al.*, *Phys. Rev. Lett.* **62**, 1821 (1989).
- [66] M. Bauer, B. Stech, and M. Wirbel, *Z. Phys. C* **34**, 103 (1987).

- [67] C. A. Dominguez, *Phys. Lett. B* **207**, 499 (1988).
- [68] T. M. Aliev, A. A. Ovchinnikov, and V. A. Slobodenyuk, Trieste preprint IC/89/382 (1989).
- [69] M. Crisafulli *et al.*, *Phys. Lett. B* **223**, 90 (1989).
- [70] G. P. Lepage and S. J. Brodsky, *Phys. Rev. D* **22**, 2157 (1980).
- [71] V. Lubicz *et al.*, *Phys. Lett. B* **274**, 415 (1992).
- [72] S. Narison, *Phys. Lett. B* **337**, 163 (1994).
- [73] K. Kodama *et al.*, *Phys. Lett. B* **316**, 455 (1993).
- [74] P. L. Frabetti *et al.*, *Phys. Lett. B* **391**, 235 (1997).
- [75] E. M. Aitala *et al.*, *Phys. Lett. B* **397**, 325 (1997).
- [76] G. Altarelli *et al.*, *Nucl. Phys.* **B187**, 461 (1981);
A. J. Buras *et al.*, *Nucl. Phys.* **B370**, 69 (1992); *Nucl. Phys.* **B375**, 501 (1992) (addendum);
M. Ciuchini *et al.*, *Nucl. Phys.* **B415**, 403 (1994).
- [77] H.-Y. Cheng, *Z. Phys. C* **69**, 647 (1996);
A.N. Kamal *et al.*, *Phys. Rev. D* **53**, 2506 (1996);
A.N. Kamal, A.B. Santra and F. Ghoddoussi, *Nuo. Cim.* **111A**, 165 (1998).
- [78] R. Balest *et al.*, (CLEO Collaboration), *Phys. Rev. Lett.* **79**, 1436 (1997).
- [79] I. Hinchliffe and T. A. Kaeding, *Phys. Rev. D* **54**, 914 (1996).
- [80] J. Weinstein and N. Isgur, *Phys. Rev. D* **27**, 588 (1983).
- [81] P. Ball, J. M. Frere, and M. Tytgat, *Phys. Lett. B* **365**, 367 (1996).
- [82] L. Wolfenstein, *Phys. Lett. B* **164**, 170 (1985);
J. F. Donoghue *et al.*, *Phys. Rev. D* **33**, 179 (1986);
H. Georgi, *Phys. Lett. B* **297**, 353 (1992);
T. Ohl *et al.*, *Nucl. Phys.* **B403**, 605 (1993);
E. Golowich and A. A. Petrov, *Phys. Lett. B* **427**, 172 (1998).
- [83] T. A. Kaeding, *Phys. Lett. B* **357**, 151 (1995).
- [84] W. J. Marciano and A. Sirlin, *Phys. Rev. Lett.* **61**, 1815 (1988).
- [85] A. Pich, *Nucl. Phys. B Proc. Suppl.* **55C**, 3 (1997).

- [86] W. J. Marciano and A. Sirlin, *Phys. Rev. Lett.* **71**, 3629 (1993);
R. Decker and M. Finkemeier, *Nucl. Phys.* **B438**, 17 (1995); *Nucl. Phys. B Proc. Suppl.* **40**, 453 (1995).
- [87] S. I. Eidelman and V. N. Ivanchenko, *Nucl. Phys. B Proc. Suppl.* **55C**, 181 (1997).
- [88] M. Davier and A. Höcker, LAL-97-85, (1997) [hep-ph/9801361], and references therein.
- [89] A. Pich, *Rep. Prog. Phys.* **58**, 563 (1995).
- [90] R. Fischer, J. Wess and F. Wagner, *Z. Phys. C* **3**, 313 (1980);
G. Aubrecht, N. Chahroui and K. Slanec, *Phys. Rev. D* **24**, 1318 (1981);
A. Pich, *Phys. Lett. B* **196**, 561 (1987).
- [91] A. Pich, “QCD Tests from Tau Decay Data,” in *Proceedings of the Tau–Charm Factory Workshop*, SLAC, (1989), ed. L.V. Beers, SLAC-R-343 (1989) p. 416;
J. H. Kühn and A. Santamaria, *Z. Phys. C* **48**, 445 (1990);
M. Finkemeier and E. Mirkes, *Z. Phys. C* **69**, 243 (1996);
R. Decker *et al.*, *Z. Phys. C* **58**, 445 (1993).
- [92] J.H. Kühn and E. Mirkes, *Z. Phys. C* **56**, 661 (1992); *Z. Phys. C* **67**, 364 (1995); *Phys. Lett. B* **286**, 281 (1992);
G. Colangelo *et al.*, *Nucl. Phys. B Proc. Suppl.* **55C**, 325 (1997).
- [93] E. Braaten, S. Narison and A. Pich, *Nucl. Phys.* **B373**, 581 (1992).
- [94] F. Le Diberder and A. Pich, *Phys. Lett. B* **286**, 147 (1992).
- [95] E. Braaten and C.S. Li, *Phys. Rev. D* **42**, 3888 (1990).
- [96] F. Le Diberder and A. Pich, *Phys. Lett. B* **289**, 165 (1992).
- [97] D. Buskulic *et al.*, (ALEPH Collaboration), *Phys. Lett. B* **307**, 209 (1993); CERN-PPE/96-186 (1996);
A. Höcker, *Nucl. Phys. B Proc. Suppl.* **55C**, 379 (1997).
- [98] T. Coan *et al.*, (CLEO Collaboration), *Phys. Lett. B* **356**, 580 (1995).
- [99] R. Barate *et al.*, (ALEPH Collaboration), CERN-PPE-97-138 (1997).
- [100] A. Pich, *Nucl. Phys. Proc. Suppl.* **39BC**, 326 (1995);
A. Pich and J. Prades, *J. High Energy Phys.*, **6**, 13 (1998);
K. Maltman, hep-ph/9804298;
K. G. Chetyrkin and A. Kwiatkowski, hep-ph/9805232;
K. G. Chetyrkin, J. H. Kühn and A. A. Pivovarov, hep-ph/9805335.

- [101] S. Chen, *Nucl. Phys. Proc. Suppl.* **64**, 265 (1998).
- [102] J.H. Kühn and E. Mirkes, *Phys. Lett. B* **398**, 407 (1997).
- [103] Y. Grossman, *Nucl. Phys.* **B426**, 355 (1994) and references therein.
- [104] M. Finkemeier and E. Mirkes, *Z. Phys. C* **72**, 619 (1996).
- [105] Y. S. Tsai, *Phys. Rev. D* **51**, 3172 (1995).
- [106] C.A. Nelson *et al.*, *Phys. Rev. D* **50**, 4544 (1994) and references therein.
- [107] M. Finkemeier and E. Mirkes, in *Proceedings of Workshop on the Tau/Charm Factory*, Argonne (1995), ed. J. Repond, AIP Conf. Proc. 349, New York (1996) p. 119 [hep-ph/9508312].
- [108] S. Choi, K. Hagiwara and M. Tanabashi, *Phys. Rev. D* **52**, 1614 (1995).
- [109] U. Kilian *et al.*, *Z. Phys. C* **62**, 413 (1994).
- [110] W. Fetscher, H.-J. Gerber and K. F. Johnson, *Phys. Lett. B* **173**, 102 (1986).
- [111] J. P. Alexander *et al.*, (CLEO Collaboration), *Phys. Rev. D* **56**, 5320 (1997).
- [112] W. Fetscher, *Phys. Rev. D* **42**, 1544 (1990).
- [113] A. Stahl and H. Voss, *Z. Phys. C* **74**, 73 (1997).
- [114] G. Bonvicini *et al.*, (CLEO Collaboration), *Phys. Rev. Lett.* **79**, 1221 (1997);
D. W. Bliss *et al.*, (CLEO Collaboration), *Phys. Rev. D* **57**, 5903 (1998).
- [115] J. Bernabeu *et al.*, *Phys. Lett. B* **187**, 303 (1987);
P. Langacker and D. London, *Phys. Rev. D* **38**, 907 (1988).
- [116] M. C. Gonzalez-Garcia and J.W.F. Valle, *Mod. Phys. Lett. A* **7**, 477 (1992); *Mod. Phys. Lett. A* **9**, 2569 (1994);
S. Ilakovac and A. Pilaftsis, *Nucl. Phys.* **B437**, 491 (1995);
S. Ilakovac, B. A. Kniehl and A. Pilaftsis, *Phys. Rev. D* **52**, 3993 (1995).
- [117] G. G. Ross and J.W.F. Valle, *Phys. Lett. B* **151**, 375 (1985);
J. Ellis *et al.*, *Phys. Lett. B* **150**, 142 (1985);
R. Barbieri *et al.*, *Phys. Lett. B* **238**, 86 (1990).
- [118] A. Masiero and J.W.F. Valle, *Phys. Lett. B* **251**, 273 (1990);
P. Nogueira, J. C. Romao and J.W.F. Valle, *Phys. Lett. B* **251**, 143 (1990).

- [119] C. Aulakh and R. Mohapatra, *Phys. Lett. B* **119**, 136 (1983);
A. Santamaria and J.W.F. Valle, *Phys. Lett. B* **195**, 423 (1987); *Phys. Rev. Lett.* **60**, 397 (1988); *Phys. Rev. D* **39**, 1780 (1989).
- [120] M. C. Gonzalez-Garcia and Y. Nir, *Phys. Lett. B* **232**, 383 (1990);
P. Nogueira and J. C. Romao, *Phys. Lett. B* **234**, 371 (1990).
- [121] J. C. Romao, N. Rius and J.W.F. Valle, *Nucl. Phys.* **B363**, 369 (1991).
- [122] S. Yang, “Test of CP Invariance in $e^+e^- \rightarrow \tau^+\tau^-$ Reaction,” *BaBar Note # 399*, (1998).
- [123] D. Bauer, SLAC-400, p. 608; SLAC-373, p. 173; “Two Photon Physics at a B Factory,” *BaBar Note # 21*, (1990); “The Impact of Two Photon Physics on a B Factory Detector,” *BaBar Note # 77*, (1992).
- [124] A. R. Barker, UCSB Thesis (1988), unpublished.
- [125] Software from H.P. Paar and M. Sivertz; adapted by B. Mayer.
- [126] S. Gehrig *et al.*, “Level 1 Trigger Efficiency, Rate and Event Time Jitter Simulation Results,” *BaBar Note # 338*, (1997).
- [127] W. Kwong *et al.*, *Phys. Rev. D* **37**, 3210 (1988).
- [128] J. Dominick *et al.*, *Phys. Rev. D* **50**, 4265 (1994).
- [129] G. Crawford *et al.*, CLEO CONF95-26 (1995).
- [130] M. Consoli and J. H. Field, *Phys. Rev. D* **49**, 1293 (1994).
- [131] E. Ackleh, T. Barnes, and F. Close, *Phys. Rev. D* **46**, 2257 (1992).
- [132] T. Barnes, in *Proceedings of IX International Workshop on Gamma Gamma Physics*, La Jolla (1992), eds. D. Caldwell and H. Paar (World Scientific).
- [133] M. Chanowitz, *Phys. Rev. Lett.* **35**, 977 (1975).
- [134] M. Chanowitz, *Phys. Rev. Lett.* **44**, 59 (1980).
- [135] G. S. Bali *et al.*, *Phys. Lett. B* **309**, 378 (1993).
- [136] C. Amsler and F. E. Close, *Phys. Rev. D* **53**, 295 (1996).
- [137] J. Z. Bai *et al.*, *Phys. Rev. Lett.* **76**, 3502 (1996).
- [138] J. H. Lee *et al.*, *Phys. Lett. B* **323**, 227 (1994).
- [139] VES Collaboration, *Phys. Lett. B* **356**, 595 (1995).

- [140] H. Aihara *et al.*, *Phys. Rev. Lett.* **57**, 51 (1986).
- [141] H. Aihara *et al.*, *Phys. Rev. D* **38**, 1 (1988).
- [142] G. Gidal *et al.*, *Phys. Rev. Lett.* **59**, 2016 (1987).
- [143] S. J. Brodsky and G. P. Lepage, *Phys. Rev. D* **24**, 445 (1981).
- [144] H. Aihara *et al.*, *Phys. Rev. Lett.* **64**, 172 (1990).
- [145] J. Gronberg *et al.*, (CLEO Collaboration), *Phys. Rev. D* **57**, 33 (1998).
- [146] R. Jakob, P. Kroll and M. Raulfs, *J. Phys.* **G22**, 45 (1996).
- [147] H. Aihara *et al.*, *Phys. Rev. Lett.* **57**, 404 (1986).
- [148] M. Benayoun and V. L. Chernyak, *Nucl. Phys.* **B329**, 285 (1990).
- [149] J. Dominick *et al.*, *Phys. Rev. D* **50**, 3027 (1994).
- [150] H. Aihara *et al.*, *Phys. Rev. D* **37**, 28 (1988).
- [151] B. Barish *et al.*, CLEO CONF95-23 (1995).
- [152] H. Albrecht *et al.*, *Phys. Lett. B* **374**, 265 (1996).
- [153] H. Albrecht *et al.*, *Phys. Lett. B* **332**, 451 (1994).
- [154] M. Artuso *et al.*, *Phys. Rev. D* **50**, 5484 (1994).
- [155] G. Farrar, E. Maina and F. Neri, *Nucl. Phys.* **B259**, 702 (1985).
- [156] V. L. Chernyak and I. R. Zhitnitsky, *Nucl. Phys.* **B246**, 52 (1984).
- [157] T. Hyer, *Phys. Rev. D* **47**, 3875 (1993).
- [158] P. Kroll *et al.*, *Phys. Lett. B* **316**, 546 (1994).
- [159] S. Anderson *et al.*, *Phys. Rev. D* **56**, 2485 (1997).
- [160] A. Ostrovidov, in *Proceedings of Hadron '97*, BNL (1997);
D. I. Ryabchikov, in *Proceedings of Hadron 95*, Manchester, UK, World Scientific;
J. Dowd, in *Proceedings of Hadron 91*, University of Maryland, College Park, World Scientific.
- [161] A. Palano, in *Proceedings of the IX Workshop on Photon-Photon Collisions*, San Diego, 22–26 March (1992), World Scientific, p. 308.

- [162] C. Amsler, “Proton-Antiproton Annihilation and Meson Spectroscopy with the Crystal Barrel,” submitted to *Rev. Mod. Phys.*, hep-ex/9708025.
- [163] H. Kolanoski, in *Proceedings of the IX Workshop on Photon-Photon Collisions*, San Diego, 22–26 March (1992), World Scientific, Singapore, p. 3.
- [164] B. Diekmann, CERN-EP/86-112, (1986).
- [165] L. Kopke and N. Wermes, *Phys. Rep.***174**, 67 (1989).
- [166] T. Burnett and S. Sharpe, *Ann. Rev. Nucl. Part. Sci.* **40**, 327 (1990);
T. Barnes and F. E. Close, *Phys. Lett.* **116B**, 365 (1982);
M. Chanowitz and S. Sharpe, *Nucl. Phys.* **B222**, 211 (1983);
T. Barnes, F. E. Close and F. de Viron, *Nucl. Phys.* **B224**, 241 (1983);
N. Isgur and J. Paton, *Phys. Rev. D* **31**, 2910 (1985).
- [167] T. H. Burnett, “Physics of 0^{++} and 2^{++} Mesons” in *Proceedings of a NATO ASI on Hadron Spectroscopy and the Confinement Problem*, June 27–July 8, (1995), in London/Swansea, Plenum Press, ed. D.V. Bugg;
A. Palano, “Physics of 0^- , 1^+ and 2^- Mesons” in *Proceedings of a NATO ASI on Hadron Spectroscopy and the Confinement Problem*, June 27–July 8, (1995), in London/Swansea, Plenum Press, ed. D.V. Bugg.
- [168] D.R. Thompson *et al.*, *Phys. Rev. Lett.* **79**, 1630 (1997).
- [169] A. Palano, *Nucl. Phys. B Proc. Suppl.* **39B,C**, 287 (1995).
- [170] J. C. Anjos *et al.*, *Phys. Rev. Lett.* **62**, 125(1989).
- [171] P. L. Frabetti *et al.*, *Phys. Lett. B* **407**, 79 (1997).
- [172] P. L. Frabetti *et al.*, *Phys. Lett. B* **351**, 591 (1995).
- [173] A. Palano, “Light Meson Spectroscopy in B , D_s and D Decays,” BaBar Note # 402, (1997).
- [174] H. Albrecht *et al.*, *Phys. Lett. B* **308**, 435 (1993);
P. L. Frabetti *et al.*, *Phys. Lett. B* **331**, 217 (1994).
- [175] G. Lafferty, in *Proceedings of Hadron’97*, BNL (1997).
- [176] S. U. Chung *et al.*, *Annalen Phys.* **4**, 404 (1995).
- [177] C. Amsler *et al.*, *Phys. Lett. B* **342**, 433 (1995).
- [178] S. B. Chun and C.D. Buchanan, *Phys. Rep.***292**, 239 (1998).

- [179] S. B. Chun and C.D. Buchanan, “New Accurate Ideas on Flavor Formation in Hadronization and Connections to QCD,” in *Proceedings of the 1996 SLAC Summer Institute* (1996).
- [180] S. B. Chun and C. D. Buchanan, BaBar note in preparation.

Physics Beyond the Standard Model

The B -meson system promises to yield a fertile testing ground of the Standard Model (SM). The large data samples which will be acquired over the next decade will furnish the means to probe the Standard Model at an unprecedented level of precision. Precision measurements of low-energy processes can provide an insight to very high energy scales via the indirect effects of new interactions. Thus the B sector offers a complementary probe to the high-energy frontier in the search for new physics, and in some cases may yield constraints which surpass those from direct collider searches or exclude entire classes of models.

New physics may manifest itself in the B system in several ways:

- Two different measurements which relate to the same quantity in the Standard Model yield incompatible results for that quantity.
- $\alpha + \beta + \gamma = \pi$, but the values of the angles are inconsistent with the measured sides of the triangle.
- Asymmetries which are expected to vanish or be very small in the Standard Model are found to be significantly larger than predicted.
- Decays which are expected to be rare are found to have significantly enhanced rates
- Mixing in either B or D decays is found to differ significantly from Standard Model predictions.

These potential deviations may originate from new interactions in tree-level B decays, or by the virtual effects of new physics in loop-mediated processes (e.g., $B_d^0-\bar{B}_d^0$ mixing or penguin decays of the B), with or without the presence of new phases. Since the scale of the new physics is expected to be large compared to M_W , it is anticipated that additional tree-level contributions to B decays are suppressed (however, this need not be the case in specific scenarios, as discussed below).

This chapter concentrates on the loop effects of new interactions in flavor-changing neutral current (FCNC) B decays and in CP violation. Most classes of models which induce large effects in the FCNC decays also affect $B_d^0-\bar{B}_d^0$ mixing. However, measurements of several different rare decays may elucidate the origin of new interactions. $b \rightarrow s$ transitions provide an excellent probe of new

indirect effects as they only occur at loop level in the Standard Model, yet have relatively large rates (for loop processes) due to the massive internal top quark and the Cabibbo-Kobayashi-Maskawa (CKM) structure of the contributing penguin and box diagrams. Also, long-distance effects are expected to play a limited role due to the heavy B mass.

The following section briefly describes the situation with respect to CP violation and baryogenesis. Section 13.2 describes some general model-independent considerations for new effects in B mixing, and Section 13.3 reviews decays. The remaining sections discuss expected patterns of deviation for a number of specific types of extensions of the Standard Model: Supersymmetry, Section 13.4; Models with Extra Scalars, Section 13.5; Models with Additional Quarks, Section 13.6; Left-Right Symmetric Model, Section 13.7; and Models with Additional Strong Dynamics, Section 13.8. The summary, Section 13.9, presents a table that summarizes the different patterns of the new physics effects in these various classes of models.

13.1 Baryogenesis

The observable world is manifestly baryon asymmetric. All the stable matter is made up of baryons, with anti-baryons being created only in high-energy collisions (either in the laboratories or out in the cosmos). There is evidence that this asymmetry persists even at much larger scales. Matter and anti-matter galaxies within the same galactic cluster would result in strong γ ray emission due to annihilations. The absence of these confirms a baryon asymmetric region on the 20 Mpc scale [1]. More recently, a bound on the scale of the observable universe has been obtained by ruling out a contribution to the diffuse γ ray spectrum from particle-antiparticle annihilation [2]. The observed nuclear abundances in the stars allows us to estimate that the current baryon to photon ratio, $n_B/n_\gamma = (4 - 7) \times 10^{-10}$. This corresponds to a baryon-antibaryon asymmetry of 1 part in 10^8 in the early universe [3].

One possible explanation for the asymmetry is that it is an *ad hoc* initial condition. The other, more appealing, possibility is that the universe initially had no net baryon number, but that microphysical processes led it to develop one during its evolution from the big bang to the present epoch. The hope is that these processes may eventually be understood. There are three requirements in order for such a baryon asymmetry to develop [4]:

- (i) There must be a departure from thermal equilibrium. CPT invariance guarantees the equality of particle and anti-particle masses. Hence in thermal equilibrium both will have the same number density as dictated by Boltzmann statistics.
- (ii) There must be baryon number violation. This requirement is self explanatory.
- (iii) There must be CP violation. This is required in order for the above baryon-number-violating interactions to preferentially produce baryons. (If CP symmetry were exact, then the CP -

conjugate process that produces antibaryons would proceed at the same rate.) It is this feature of cosmological baryon asymmetry that one can potentially probe at BABAR.

There are two distinct possibilities for generating a non-zero baryon number during the thermal history of the universe. The first is using the baryon and/or lepton number, and CP -violating decays of some super-heavy particle. The departure from thermal equilibrium typically occurs because the decay rate of the particle is slower than the expansion rate of the universe (for a review, see Ref. [5]). It is possible to construct models of this kind where the phase of the CKM matrix is related to the CP -violating phase responsible for baryogenesis [6]. However, since these are processes happening at extremely high energies, it is unlikely that they have any consequences for terrestrial experiments. The one possible experimental handle on models of this kind is when the lepton-number-violating heavy particle is a Majorana neutrino [6, 7, 8, 9]. In this case the light neutrino masses can shed light on the masses of the heavy neutrinos via the see-saw mechanism for neutrino mass.

The second, and more exciting, possibility is that baryogenesis occurred at the time the electroweak group was broken ($SU(2)_L \times U(1)_Y \rightarrow U(1)_Q$) at a temperature $T \sim 100$ GeV [10] (for a review see Ref. [11]). Departure from thermal equilibrium would occur if the phase transition from the symmetric phase to the broken phase of the electroweak group were strong at first order. The anomalous coupling of the baryon number current to two $SU(2)$ gauge bosons violates baryon number. The creation or destruction of baryon number by this process is rapid at high temperatures, and turns off in the broken phase. Most importantly, the CP violation is provided by the interactions of particles that can be produced and measured in the laboratories. Thus, this scenario has experimentally testable consequences. For example, it has been found that although the three required ingredients for baryogenesis all exist within the Standard Model, the baryon asymmetry produced is too small by many orders of magnitude [12]. Not only is the phase transition not strong enough (given the current constraints on the Higgs boson mass), but the CKM mechanism of CP violation is by far not efficient enough to produce the observed baryon asymmetry. One definitely needs physics beyond the Standard Model, and more specifically new CP -violating phases, to understand the baryon asymmetry of the universe in terms of physical processes.

There are many models that generate the baryon asymmetry at the electroweak phase transition. Two well-motivated examples are models with two Higgs doublets [13, 14], and the minimal supersymmetric standard model (MSSM) [14, 15, 16]. The situation regarding the MSSM is particularly interesting. If the MSSM dynamics is responsible for baryogenesis, it predicts (amongst other things) deviations from the Standard Model expectations for $B_d^0 - \bar{B}_d^0$ mixing and the $b \rightarrow s\gamma$ decay rate that should be observable at BABAR [15].

A discovery of beyond the Standard Model CP violation at BABAR would provide the first hints of the new sources of CP violation required to explain the baryon asymmetry of the universe. It could restrict the classes of models consistent with the observed CP violation, and focus attention among

the surviving models that also have the other ingredients required for baryogenesis. Moreover, it would motivate further theoretical effort to turn what is at present a sophisticated, but still fairly rough, correspondence between the micro-physics of CP violation and the related baryon asymmetry into a more precise relationship.

13.2 Model-Independent Analysis of Mixing

In a large class of models, the only significant new physics effect on the CP asymmetries in $B^0 \rightarrow J/\psi K_S^0$ and $B \rightarrow \pi\pi$ decays is a new contribution to the $B\bar{B}$ mixing amplitude. This allows a model-independent construction of the effects on the CKM Unitarity Triangle (up to hadronic uncertainties). Furthermore, the contributions to the mixing from the Standard Model and from the new physics can be disentangled.

The analysis presented below will require accurate values for various input quantities. In particular, a good enough value for $\sin 2\alpha$ will require an isospin-based analysis and thus will be obtained only after some years of BaBar running. Likewise, accurate values of the sides of the scaled unitarity triangle $R_u = V_{ub}^* V_{ud} / V_{cb}^* V_{cd}$ and $R_t = V_{tb}^* V_{td} / V_{cb}^* V_{cd}$ will require a theoretical improvement in the modeling of charmless B decays and in the lattice calculation of f_B .

13.2.1 The Basic Assumptions and Results

Chapter 5 and Chapter 6 discuss methods to measure β and α respectively. In addition, BaBar will improve knowledge of the $B\text{--}\bar{B}$ mixing parameter, $x_d \equiv \frac{\Delta m_B}{\Gamma_B}$ (see Section 11.2.1), and of the charmless semileptonic branching ratio of the B mesons (see Chapter 8).

Within the Standard Model, these four measurements are useful in constraining the unitarity triangle. The asymmetries which measure angles of the unitarity triangle are for example (up to uncertainties arising from penguin contribution in the case of α):

$$a_{\psi K_S^0} = \sin 2\beta, \quad a_{\pi\pi} = \sin 2\alpha. \quad (13.1)$$

The measurement of x_d determines (up to uncertainties in the value of the hadronic matrix element) one side of the scaled unitarity triangle (R_t):

$$x_d = C_t R_t^2, \quad (13.2)$$

where $C_t = \tau_b \frac{G_F^2}{6\pi^2} \eta_B m_B (B_B f_B^2) m_t^2 f_2(m_t^2/m_W^2) |V_{cb}^* V_{cd}|^2$. Measurements of various inclusive and exclusive $b \rightarrow u\ell\nu$ processes will determine (up to uncertainties arising from various hadronic

models) the length of the other side of the scaled unitarity triangle (R_u):

$$\frac{\Gamma(b \rightarrow ul\nu)}{\Gamma(b \rightarrow cl\nu)} = \frac{1}{F_{\text{ps}}} \left| \frac{V_{cd}}{V_{ud}} \right|^2 R_u^2, \quad (13.3)$$

where $F_{\text{ps}} \approx 0.5$ is a phase space factor.

In the presence of new physics it is quite possible that the Standard Model predictions (13.1) and (13.2) are violated. The most likely reason is a new, significant contribution to $B-\bar{B}$ mixing that carries a CP -violating phase different from the Standard Model one. Other factors that could affect the construction of the unitarity triangle from these four measurements are unlikely to be significant [17, 18]:

- The $\bar{b} \rightarrow \bar{c}c\bar{s}$ and $\bar{b} \rightarrow \bar{u}u\bar{d}$ decays for $a_{\psi K_S^0}$ and $a_{\pi\pi}$ respectively, as well as the semileptonic B decays for R_u , are mediated by Standard Model tree-level diagrams. In most extensions of the Standard Model there is no decay mechanism that could significantly compete with these contributions. (For exceptions, which could affect the $\bar{b} \rightarrow \bar{u}u\bar{d}$ decay, see [19].)
- New physics could contribute significantly to $K-\bar{K}$ mixing. However, the small value of ε_K forbids large deviations from the Standard Model phase of the mixing amplitude.
- Unitarity of the three generation CKM matrix is maintained if there are no quarks beyond the three generations of the Standard Model. Even in models with an extended quark sector the effect on $B-\bar{B}$ mixing is always larger than the violation of CKM unitarity (for more detailed discussion of such models see Section 13.6).

The analysis presented below applies to any model which has significant new physics effects in B mixing, but not in the decay channels used to determine α and β or the K mixing phase. In all such models the relevant new physics effects in B mixing can be described by two new parameters, r_d and θ_d [20, 21, 22, 23], defined by

$$\left(r_d e^{i\theta_d} \right)^2 \equiv \frac{\langle B^0 | \mathcal{H}_{\text{eff}}^{\text{full}} | \bar{B}^0 \rangle}{\langle B^0 | \mathcal{H}_{\text{eff}}^{\text{SM}} | \bar{B}^0 \rangle}, \quad (13.4)$$

where $\mathcal{H}_{\text{eff}}^{\text{full}}$ is the effective Hamiltonian including both Standard Model and new physics contributions, and $\mathcal{H}_{\text{eff}}^{\text{SM}}$ only includes the Standard Model box diagrams. In particular, with this definition, the modification of the two CP asymmetries in (13.1) depends on a *single* new parameter, the phase θ_d :

$$a_{\psi K_S^0} = \sin(2\beta + 2\theta_d), \quad a_{\pi\pi} = \sin(2\alpha - 2\theta_d), \quad (13.5)$$

while the modification of the $B-\bar{B}$ mixing parameter x_d in (13.2) is given by the magnitude rescaling parameter, r_d :

$$x_d = C_t R_t^2 r_d^2. \quad (13.6)$$

Furthermore, since the determination of R_u from the semileptonic B decays is not affected by the New Physics, and since the unitarity triangle remains valid, the following relations between the length of its sides and its angles can be deduced:

$$R_u = \frac{\sin \beta}{\sin \alpha}, \quad (13.7)$$

$$R_t = \frac{\sin \gamma}{\sin \alpha}. \quad (13.8)$$

When α , β and γ are defined to lie in the $(0, 2\pi)$ range, they satisfy

$$\alpha + \beta + \gamma = \pi \text{ or } 5\pi. \quad (13.9)$$

The four measured quantities $a_{\psi K_S^0}$, $a_{\pi\pi}$, x_d and R_u allow one to [20]:

- Fully reconstruct the unitarity triangle and, in particular, find α , β and R_t ; and
- Find the magnitude and phase of the new physics contribution to $B-\bar{B}$ mixing, namely determine r_d and θ_d .

It is straightforward to show that the above tasks are possible in principle. Equations (13.5) and (13.7) give three equations for three unknowns, α , β , and θ_d . Once α and β are known, γ can be extracted from (13.9), R_t can then be deduced from (13.8), and finally r_d is found from (13.6).

In practice, however, the combination of experimental and theoretical uncertainties and discrete ambiguities will limit the usefulness of the above method. The methods that can be used to reduce the theoretical uncertainties in x_d and R_u , and those that can be used to constrain or remove the leading penguin effects in the α channels were discussed in previous chapters. The following section discusses the discrete ambiguities that arise in this calculation.

13.2.2 Discrete Ambiguities

A serious obstacle in carrying out the above program is an eightfold discrete ambiguity in solving for the angles of the triangle. This section describes these ambiguities. Section 13.2.3 describes how to determine the parameters in the (ρ, η) plane, and Section 13.2.4 presents the $(\sin 2\alpha, \sin 2\beta)$ plane description.

The range of each angle is defined here to be $(0, 2\pi)$. Measurement of any single asymmetry, $\sin 2\phi$, determines the corresponding angle only up to a four-fold ambiguity: $\phi, \pi/2 - \phi, \pi + \phi, 3\pi/2 - \phi$. (Once the $\rho\pi$ channel measurements provide sufficient data to carry out the full three-body analysis, Section 6.5, the four-fold ambiguity of α will likely be reduced to a two-fold choice $\phi, \pi + \phi$, but this will not occur for some time to come.)

Specifically, denote by $\bar{\alpha}$ and $\bar{\beta}$ some solution of the equations

$$a_{\psi K_S^0} = \sin 2\bar{\beta}, \quad a_{\pi\pi} = \sin 2\bar{\alpha}. \quad (13.10)$$

Thus, measurements of the two asymmetries leads to a sixteen-fold ambiguity in the values of the $\{\bar{\alpha}, \bar{\beta}\}$ pair. However, since $\bar{\alpha} = \alpha - \theta_d$ and $\bar{\beta} = \beta + \theta_d$, and unitarity is not violated, γ still satisfies the condition

$$\bar{\alpha} + \bar{\beta} + \gamma = \pi \pmod{2\pi}. \quad (13.11)$$

Then, the sixteen possibilities for γ are divided into two groups of eight that are related by the combined operation $\bar{\alpha} \rightarrow \bar{\alpha} + \pi$ and $\bar{\beta} \rightarrow \bar{\beta} + \pi$. This, in turn shifts the value of γ by 2π . However, since γ is only defined modulo 2π , the ambiguity in γ is reduced to eightfold. This reduction of the ambiguity depends only on the definition of γ . Defining

$$\phi_{\pm} = \bar{\alpha} \pm \bar{\beta}, \quad (13.12)$$

the eight possible solutions for γ are

$$\gamma = \pm\phi_+, \pi \pm \phi_+, \pi/2 \pm \phi_-, 3\pi/2 \pm \phi_- \pmod{2\pi}. \quad (13.13)$$

Note that the eight solutions come in pairs of $\pm\gamma$. This in turn implies that the ambiguity on R_t is only four-fold.

In any model where the three angles $\bar{\alpha}$, $\bar{\beta}$, and γ form a triangle, the ambiguity is further reduced [24]: the requirement that the angles are either all in the range $(0, \pi)$ or all in the range $(\pi, 2\pi)$ reduces the ambiguity in γ to four-fold. It is enough to know the signs of $a_{\psi K_S^0}$ and $a_{\pi\pi}$ to carry out this step. Finally, within the Standard Model, the bound $0 < \beta < \pi/4$ (obtained from the sign of ε_K and from $R_u < 1/\sqrt{2}$) reduces the ambiguity in γ to twofold.

When one allows for the possibility of new physics effects in the mixing, knowing the signs of $a_{\psi K_S^0}$ and $a_{\pi\pi}$ does not lead to further reduction in the ambiguity, which remains eightfold. The three angles $\bar{\alpha}$, $\bar{\beta}$ and γ are not angles that define a triangle and therefore further constraints cannot be imposed. It is possible, for example, that both γ and $\bar{\beta}$ lie in the range $(\pi/2, \pi)$. Further the sign of ε_K may not be related to the sign of η .

The following example will make the situation clear. Take

$$a_{\pi\pi} = 1/2, \quad a_{\psi K_S^0} = \sqrt{3}/2. \quad (13.14)$$

Then, the ambiguities are

$$\bar{\alpha} = \frac{\pi}{12}, \frac{5\pi}{12}, \frac{13\pi}{12}, \frac{17\pi}{12}, \quad \bar{\beta} = \frac{\pi}{6}, \frac{\pi}{3}, \frac{7\pi}{6}, \frac{4\pi}{3}. \quad (13.15)$$

The eight solutions for γ are

$$\gamma = \frac{\pi}{4}, \frac{5\pi}{12}, \frac{7\pi}{12}, \frac{3\pi}{4}, \frac{5\pi}{4}, \frac{17\pi}{12}, \frac{19\pi}{12}, \frac{7\pi}{4}. \quad (13.16)$$

If $\bar{\alpha}, \bar{\beta}, \gamma$ define a triangle, then only four solutions are allowed:

$$\{\bar{\alpha}, \bar{\beta}, \gamma\} = \left\{ \frac{\pi}{12}, \frac{\pi}{6}, \frac{3\pi}{4} \right\}, \left\{ \frac{\pi}{12}, \frac{\pi}{3}, \frac{7\pi}{12} \right\}, \left\{ \frac{5\pi}{12}, \frac{\pi}{6}, \frac{5\pi}{12} \right\}, \left\{ \frac{5\pi}{12}, \frac{\pi}{3}, \frac{\pi}{4} \right\}. \quad (13.17)$$

If $0 < \bar{\beta} < \pi/4$ as in the Standard Model, only the first two choices remain. In various special cases, the discrete ambiguity is smaller (see [25]).

In addition, for each value of γ there are two possibilities for θ_d related by $\theta_d \rightarrow \theta_d + \pi$. As long as the new physics is such that the $\Delta b = 2$ operator that contributes to $B-\bar{B}$ mixing can be separated into two $\Delta b = 1$ operators the $\theta_d \rightarrow \theta_d + \pi$ ambiguity is physical. Otherwise, it is not physical.

13.2.3 The (ρ, η) Plane

The key point in the extraction of the CKM parameters is that the angle θ_d cancels in the following sum:

$$2(\alpha + \beta) = \arcsin(a_{\psi K_S^0}) + \arcsin(a_{\pi\pi}). \quad (13.18)$$

In other words, the angle γ can be determined (up to the discrete ambiguities discussed above). In the (ρ, η) plane, a value for γ gives a ray from the origin, while a value for R_u gives a circle that is centered in the origin. The intersection point of the line and the circle gives (ρ, η) of the unitarity triangle and determines it completely.

A graphical way to carry out these calculations in the (ρ, η) plane is the following (see Fig. 13-1) [23]. One draws the four curves that correspond to Eqs. (13.1), (13.2) and (13.3) (even though only the latter is valid!). The next step is to draw the ray from the origin that passes through the intersection point of the β ray and the α circle: this is the *correct* γ ray (see the dashed line in Fig. 13-1). The intersection point of the γ ray and the R_u circle gives the *correct* vertex of the unitarity triangle, (ρ, η) , namely

$$\tan \beta = \frac{\eta}{1 - \rho}, \quad (13.19)$$

$$R_t^2 = \eta^2 + (1 - \rho)^2. \quad (13.20)$$

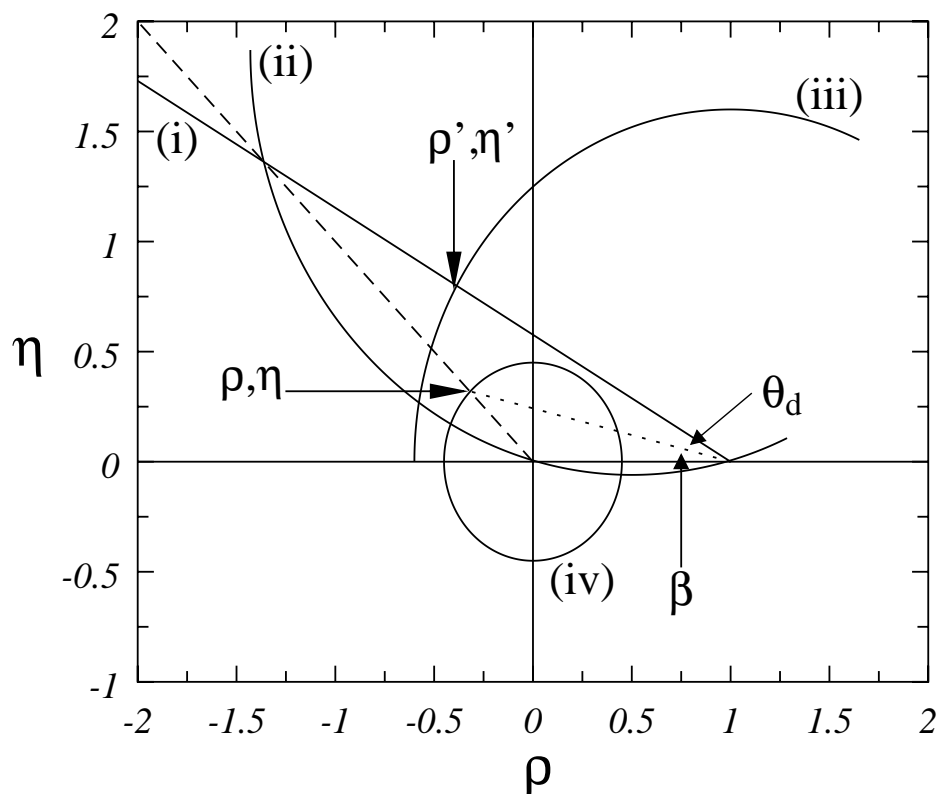


Figure 13-1. The model-independent analysis in the (ρ, η) plane: (i) The $a_{\psi K_S^0}$ ray; (ii) The $a_{\pi\pi}$ circle; (iii) The x_d circle; (iv) The R_u circle. The γ ray is given by the dashed line. The true β ray is given by the dotted line. Also shown are the true vertex of the unitarity triangle (ρ, η) and the (ρ', η') point that serves to find θ_d and r_d .

The information about the new physics contribution to $B-\bar{B}$ mixing is found from the intersection point of the β ray and the x_d circle, (ρ', η') , namely

$$\theta_d = \arctan \frac{\eta'}{1 - \rho'} - \arctan \frac{\eta}{1 - \rho}, \quad (13.21)$$

$$r_d^2 = \frac{\eta'^2 + (1 - \rho')^2}{\eta^2 + (1 - \rho)^2}. \quad (13.22)$$

13.2.4 The $(\sin 2\alpha, \sin 2\beta)$ Plane

A presentation of the various constraints in the $(\sin 2\alpha, \sin 2\beta)$ plane [20, 26, 27] is useful because the two angles are usually correlated [28]. The model independent analysis is demonstrated in Fig. 13-2. The R_u constraint gives an eight-shaped curve on which the physical values have to lie. The various solutions for Eq. (13.18) fall on two ellipses, the intersections of which with the R_u curve determine the allowed values of $\sin 2\alpha$ and $\sin 2\beta$. Note that these ellipses cross the eight-shaped curve in sixteen points but, as argued above, only eight of these points are true solutions. The inconsistent intersection points can be found by noting that the slopes of the ellipse at the consistent points should be $(\cos 2\alpha, -\cos 2\beta)$. The eight correct solutions are denoted by the filled circles in Fig. 13-2.

13.2.5 Final Comments

In the above, it was shown how to use measured values of the CP asymmetries $a_{\psi K_S^0}$ and $a_{\pi\pi}$ to find the allowed values for α and β . The presentation in the $\sin 2\alpha - \sin 2\beta$ plane is also useful for the opposite situation. Some models predict specific values for α and β . On the other hand, the models often allow new contributions to $B-\bar{B}$ mixing of unknown magnitude and phase. In this case, the predicted value of $(\sin 2\alpha, \sin 2\beta)$ is just a point in the plane, and the ellipse in Eq. (13.18) actually gives the allowed (and correlated) values of $(a_{\pi\pi}, a_{\psi K_S^0})$. Such an analysis was carried out in Ref. [29]. More generally, in any class of models where $\sin^2 \gamma$ cannot assume any value between zero and one, some regions in the $a_{\pi\pi} - a_{\psi K_S^0}$ plane are excluded [30].

As explained above, the combination of hadronic uncertainties and discrete ambiguities puts serious obstacles in the model-independent construction of the unitarity triangle. In particular, there is an eightfold ambiguity in the construction of the triangle. In order to get useful results, it will be necessary to reduce this ambiguity. One way to eliminate some of the allowed solutions can be provided by a rough knowledge of $\cos(2\alpha - 2\theta_d)$, $\cos(2\beta + 2\theta_d)$ or $\cos 2\gamma$. This can be achieved in various ways [31]. A different approach is to make further assumptions about the new physics that is responsible for the effects discussed above [25].

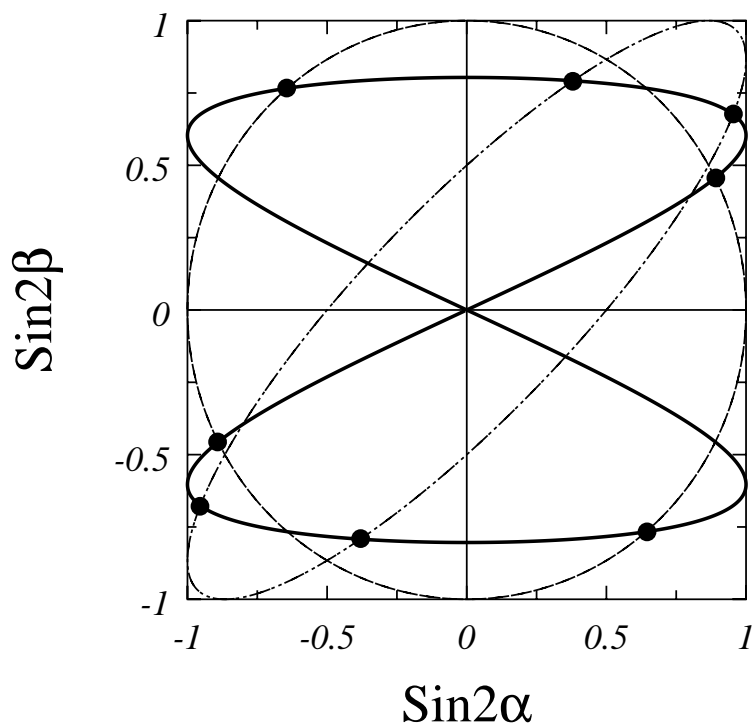


Figure 13-2. The $\alpha + \beta$ constraint (13.18) and the R_u constraint (13.7) in the $(\sin 2\alpha, \sin 2\beta)$ plane. The eight possible solutions for the unitarity triangle are given by the filled circles.

Of course, one can combine several of these measurements and assumptions to get a better handle on the true form of the unitarity triangle. It is clear, however, that the model-independent construction of the triangle at the level of accuracy required to distinguish new physics effects, while possible in principle, will pose serious theoretical and experimental challenges.

13.3 New Physics Effects in CP -Violating B Decays

This section presents a systematic analysis of the effects of new physics in the B decay amplitudes on the CP asymmetries in neutral B decays [19]. Although these are expected to be smaller than new physics effects on the mixing amplitude, they are easier to probe in some cases. Given the current uncertainties in the values of the CKM phases, and ignoring for the time being possible effects due to Standard Model penguins, the only precise predictions concerning the CP asymmetries made by the Standard Model are the following:

- (i) The CP asymmetries in all B_d decays that do not involve direct $b \rightarrow u$ (or $b \rightarrow d$) transitions have to be the same.

This prediction holds for the B_s system in an even stronger form:

- (ii) The CP asymmetries in all B_s decays that do not involve direct $b \rightarrow u$ (or $b \rightarrow d$) transitions not only have to be the same, but also approximately vanish.

Thus, the cleanest place to look for evidence of new CP -violating physics is obviously the B_s system [17, 32]. BaBar, however, will initially take data at the $\Upsilon(4S)$ where only the B_d can be studied. Once the uncertainties in these predictions due to Standard Model penguins are quantified, as is done below in Section 13.3.4, any larger deviations from it can be construed as a signal of new physics.

13.3.1 Effects in Decays

In contrast to the universal effects of the new contributions to the $B_d^0-\bar{B}_d^0$ mixing, the effects of new physics in decay amplitudes are manifestly non-universal, *i.e.*, they depend on the specific process and decay channel under consideration. Experiments on different decay modes that would measure the same CP -violating quantity in the absence of new contributions to decay amplitudes, now actually measure different CP -violating quantities. Thus, the Standard Model prediction (i), concerning B_d decays, can be violated. Even though the possibility of new physics in decay amplitudes is more constrained than that in mixing amplitudes, one could detect these smaller

effects by exploiting the fact that two experiments that should measure the same quantity, in fact, do not. This section studies this possibility. The general effects that new physics in decay amplitudes can have are presented. Then a detailed discussion of each possible decay channel, and the uncertainties in the universality predictions introduced within the Standard Model itself by sub-leading effects is undertaken. Finally, the possibility of new contributions to the B decay amplitudes is illustrated by listing the largest allowable effects in three models of new physics.

13.3.2 Formalism

This section displays the well known formulae for the decays of neutral B mesons into CP eigenstates, and highlights the relevant features that are important when more than one decay amplitude contributes to a particular process.

The time dependent CP asymmetry for the decays of states that were tagged as pure B^0 or \bar{B}^0 at production into CP eigenstates is defined as

$$a_{f_{CP}}(t) \equiv \frac{\Gamma[B^0(t) \rightarrow f_{CP}] - \Gamma[\bar{B}^0(t) \rightarrow f_{CP}]}{\Gamma[B^0(t) \rightarrow f_{CP}] + \Gamma[\bar{B}^0(t) \rightarrow f_{CP}]}, \quad (13.23)$$

and given by

$$a_{f_{CP}}(t) = a_{f_{CP}}^{\cos} \cos(\Delta Mt) + a_{f_{CP}}^{\sin} \sin(\Delta Mt) \quad (13.24)$$

where

$$a_{f_{CP}}^{\cos} = \frac{(1 - |\lambda|^2)}{1 + |\lambda|^2}; \quad a_{f_{CP}}^{\sin} = -\frac{2 \mathcal{I}m \lambda}{1 + |\lambda|^2}. \quad (13.25)$$

Here ΔM is the mass difference between the two physical states, and

$$\lambda = \left(\sqrt{\frac{M_{12}^* - \frac{i}{2}\Gamma_{12}^*}{M_{12} - \frac{i}{2}\Gamma_{12}}} \right) \frac{\langle f_{CP} | \mathcal{H} | \bar{B}^0 \rangle}{\langle f_{CP} | \mathcal{H} | B^0 \rangle} = e^{-2i\phi_M} \frac{\bar{A}}{A}, \quad (13.26)$$

where $M_{12} \gg \Gamma_{12}$ is used and thus the first fraction in Eq. (13.26) is replaced by $e^{-2i\phi_M}$, the phase of B - \bar{B} mixing.

Consider now the case where the decay amplitude A contains contributions from two terms with magnitudes A_i , CP -violating phases ϕ_i and CP -conserving phases δ_i (in what follows it will be convenient to think of A_1 giving the dominant Standard Model contribution, and A_2 giving the sub-leading Standard Model contribution or the new physics contribution):

$$A = A_1 e^{i\phi_1} e^{i\delta_1} + A_2 e^{i\phi_2} e^{i\delta_2}, \quad \bar{A} = A_1 e^{-i\phi_1} e^{i\delta_1} + A_2 e^{-i\phi_2} e^{i\delta_2}. \quad (13.27)$$

To first order in $r \equiv A_2/A_1$ Eq. (13.25) reduces to [33]

$$a_{f_{CP}}^{\cos} = -[2r \sin \phi_{12} \sin \delta_{12}] \quad (13.28)$$

and

$$a_{f_{CP}}^{\sin} = -[\sin 2(\phi_M + \phi_1) + 2r \cos 2(\phi_M + \phi_1) \sin \phi_{12} \cos \delta_{12}] \quad (13.29)$$

where $\phi_{12} = \phi_1 - \phi_2$ and $\delta_{12} = \delta_1 - \delta_2$.

In the case $r = 0$ or $\phi_{12} = 0$, one recovers the frequently studied case studied, where $a_{f_{CP}}^{\sin}$ cleanly measures the CP -violating quantity $\sin 2(\phi_M + \phi_1)$. If $r \neq 0$ and $\phi_{12} \neq 0$ one can consider two distinct scenarios:

- (a) Direct CP violation ($a_{f_{CP}}^{\cos} \neq 0$). This occurs when $\delta_{12} \neq 0$ and can be measured by a careful study of the time dependence since it gives rise to a $\cos \Delta Mt$ term in addition to the $\sin \Delta Mt$ term. Such a scenario would also give rise to CP asymmetries in charged B decays.
- (b) Different quark level decay channels that measure the same phase when only one amplitude contributes, can measure different phases if more than one amplitude contributes, *i.e.*, two different processes with the same ϕ_1 , but with different r or ϕ_2 .

The remainder of this section concentrates on the information one can obtain from $a_{f_{CP}}^{\sin}$. One can write

$$a_{f_{CP}}^{\sin} \equiv a_{f_{CP}} = -\sin 2(\phi_0 + \delta\phi), \quad (13.30)$$

where $\phi_0 = \phi_M + \phi_1$, and $\delta\phi$ is the correction to it. For small r , $\delta\phi \leq r$. However for $r > 1$, $\delta\phi$ can take any value. Thus, when cataloging values of $\delta\phi$ for various models, $\delta\phi \simeq 1$ is used to indicate such cases.

13.3.3 The Different Decay Channels

There are 12 different hadronic decay channels for the b quark: eight of them are charged-current mediated

$$\begin{aligned} (c1) \ b \rightarrow c\bar{c}s, \quad (c2) \ b \rightarrow c\bar{c}d, \quad (c3) \ b \rightarrow c\bar{u}d, \quad (c4) \ b \rightarrow c\bar{u}s, \\ (c5) \ b \rightarrow u\bar{c}d, \quad (c6) \ b \rightarrow u\bar{c}s, \quad (c7) \ b \rightarrow u\bar{u}d, \quad (c8) \ b \rightarrow u\bar{u}s, \end{aligned} \quad (13.31)$$

and four are neutral current

$$(n1) \ b \rightarrow s\bar{s}s, \quad (n2) \ b \rightarrow s\bar{s}d, \quad (n3) \ b \rightarrow d\bar{d}s, \quad (n4) \ b \rightarrow d\bar{d}d. \quad (13.32)$$

If only one Standard Model decay amplitude dominates all of these decay channels, *i.e.*, $r = 0$ in Eq. (13.29), then up to $\mathcal{O}(\lambda^2)$ (where $\lambda \approx 0.22$ is the expansion parameter in the Wolfenstein approximation), the CP asymmetries in B meson decays all measure one of the four phases,

$$\begin{aligned} \alpha &\equiv \arg\left(-\frac{V_{td}V_{tb}^*}{V_{ud}V_{ub}^*}\right), & \beta &\equiv \arg\left(-\frac{V_{cd}V_{cb}^*}{V_{td}V_{tb}^*}\right), \\ \gamma &\equiv \arg\left(-\frac{V_{ud}V_{ub}^*}{V_{cd}V_{cb}^*}\right), & \beta' &\equiv \arg\left(-\frac{V_{cs}V_{cb}^*}{V_{ts}V_{tb}^*}\right) \simeq 0. \end{aligned} \quad (13.33)$$

This situation is summarized, along with relevant decay modes in the Table 1-1 (see also [34]). Note that $\beta' < 2.5 \times 10^{-2}$ is very small in the Standard Model [35], but in principle measurable. This small value is a sub-leading correction to the clean Standard Model prediction (*ii*). Corrections to this idealized limit, as well as to the $r = 0$ limit, are studied in the next sub-section. Here the effects that new physics in b -quark decay amplitudes could have on the predictions of Eq. (13.33) are discussed.

In the Standard Model the CP asymmetries in the decay modes (*c1*) $b \rightarrow c\bar{c}s$ (e.g., $B_d \rightarrow J/\psi K_s^0$, $B_s \rightarrow D_s^+ D_s^-$), (*c2*) $b \rightarrow c\bar{c}d$ (e.g., $B_d \rightarrow D^+ D^-$, $B_s \rightarrow J/\psi K_s^0$), and (*c3*) $b \rightarrow c\bar{u}d$ (e.g., $B_d \rightarrow D_{CP}^0 \rho$, $B_s \rightarrow D_{CP}^0 K_s^0$) all measure the angle β in B_d decay and β' in B_s decays. [(*c5*) $b \rightarrow u\bar{c}d$ acts as a correction to (*c3*) and will be addressed later.] In the presence of new contributions to the $B-\bar{B}$ mixing matrix, the CP asymmetries in these modes would no longer be measuring the CKM angles β and β' . However, they would all still measure the angles $(\beta + \delta_{m_d}, \beta' + \delta_{m_s})$, where $(\delta_{m_d}, \delta_{m_s})$ are the new contributions to the $B_{(d,s)}-\bar{B}_{(d,s)}$ mixing phase. In contrast, new contributions to the b -quark decay amplitudes could affect each of these modes differently, and thus they would each be measuring different CP -violating quantities.

Several methods [36] have been proposed based on the fact that the two amplitudes (*c4*) $b \rightarrow c\bar{u}s$ and (*c6*) $b \rightarrow u\bar{c}s$ (e.g., $B_d \rightarrow D_{CP} K_s^0$, $B_s \rightarrow D_{CP} \phi$) are comparable in size, and contribute dominantly to the D^0 or \bar{D}^0 parts of D_{CP} , respectively, to extract the quantity

$$\arg(b \rightarrow c\bar{u}s) + \arg(c \rightarrow d\bar{d}u) - \arg(b \rightarrow u\bar{c}s) - \arg(\bar{c} \rightarrow \bar{d}d\bar{u}) \equiv \gamma. \quad (13.34)$$

This measurement of γ is manifestly independent of the $B-\bar{B}$ mixing phase¹.

The mode (*c7*) $b \rightarrow u\bar{u}d$ (e.g., $B_d \rightarrow \pi\pi$, $B_s \rightarrow \rho K_s^0$) measures the angles $(\beta + \gamma, \beta' + \gamma)$ in the Standard Model. This measurement can be combined with the phase (β, β') measured in the (*c1*) $b \rightarrow c\bar{c}s$ modes to yield another determination of γ that is independent of the phase in the $B-\bar{B}$ mixing matrix, e.g., comparing $a_{CP}(t)[B_d \rightarrow J/\psi K_s^0]$ to $a_{CP}(t)[B_d \rightarrow \pi\pi]$ allows the extraction of

$$\arg(b \rightarrow c\bar{c}s) - \arg(b \rightarrow u\bar{u}d) \equiv \gamma. \quad (13.35)$$

Since both of the above evaluations of γ , Eqs. (13.34) and (13.35) are manifestly independent of any phases in the neutral meson mixing matrices, the only way they can differ is if there are new contributions to the B or D meson decay amplitudes.

The remaining charged current decay mode (*c8*) $b \rightarrow u\bar{u}s$ suffers from large theoretical uncertainty since the tree and penguin contributions are similar in magnitude and is not studied here.

¹Note that CP asymmetries into final states that contain D_{CP} cannot be affected by possible new contributions to $D-\bar{D}$ mixing. One identifies D_{CP} by looking for CP eigenstate decay products like $K^+ K^-$, $\pi\pi$ or πK_s^0 . As $(\Delta\Gamma/\Gamma)_D$ is known to be tiny, the mass eigenstates cannot be identified. The relevant quantity that enters in the calculation of the CP asymmetry is the D meson decay amplitude and not the $D-\bar{D}$ mixing amplitude. Thus, the only new physics in the D sector that could affect the standard analysis are new contributions to the D decay amplitudes.

For the neutral current modes the dominant Standard Model contribution is first assumed to be from a penguin diagram with a top quark in the loop; corrections to this approximation are discussed later. Since these are loop-mediated processes even in the Standard Model, CP asymmetries into final states that can only be produced by flavor changing neutral current vertices are likely to be fairly sensitive to the possibility of new physics in the B meson decay amplitudes. The modes $(n3) b \rightarrow s\bar{d}d$ and $(n4) b \rightarrow d\bar{d}d$ however, result in CP eigenstate final states that are the same as for the charged current modes $(c8) b \rightarrow u\bar{u}s$ and $(c7) b \rightarrow u\bar{u}d$ respectively. Hence they cannot be used to study CP violation, but rather act as corrections to the charged current modes.

In the Standard Model the mode $(n1) b \rightarrow s\bar{s}s$, (e.g., $B_d \rightarrow \phi K_s^0$, $B_s \rightarrow \phi\eta'$) measures the angle β or 0 in B_d and B_s decays. One can once again try and isolate new physics in the decay amplitudes by comparing these measurements with the charged current measurements of β . Finally, $(n2) b \rightarrow s\bar{s}d$, e.g., $(B_d \rightarrow K_s^0 K_s^0, B_s \rightarrow \phi K_s^0)$ measures the angle 0 and β for Standard Model B_d and B_s decays.

13.3.4 Standard Model Corrections

All of the preceding discussion treated the idealized case where only one Standard Model amplitude contributes to a particular decay process and worked to first order in the Wolfenstein approximation. The size of the sub-leading Standard Model corrections to the above processes must be estimated in order to quantify how large the new physics effects need to be to dominate these corrections and thus to find the most promising modes to study.

There is a Standard Model penguin contribution to $(c1) b \rightarrow c\bar{c}s$. However, as is well known, this contribution has the same phase as the tree-level contribution (up to corrections of order β' , that is Cabibbo-suppressed terms) and hence $\delta\phi = 0$ in Eq. (13.30). Thus in the absence of new contributions to decay amplitudes, the decay $B^0 \rightarrow J/\psi K_s^0$ cleanly measures the phase $\beta + \delta_{m_d}$ (where δ_{m_d} denotes any new contribution to the mixing phase).

The mode $(c2) b \rightarrow c\bar{c}d$ also has a penguin correction in the Standard Model. In this case $\phi_{12} = \mathcal{O}(1)$ and the correction can be estimated as [37]

$$\delta\phi_{SM}(b \rightarrow c\bar{c}d) \simeq \frac{V_{tb}V_{td}^*}{V_{cb}V_{cd}^*} \frac{\alpha_s(m_b)}{12\pi} \log(m_b^2/m_t^2) \lesssim 0.1, \quad (13.36)$$

where the upper bound is obtained for $|V_{td}| < 0.02$, $m_t = 180 \text{ GeV}/c^2$ and $\alpha_s(m_b) = 0.2$.

The mode $(c3) b \rightarrow c\bar{u}d$ does not get penguin corrections, however there is a doubly Cabibbo-suppressed tree-level correction coming from $(c5) b \rightarrow u\bar{c}d$. Thus $B_d \rightarrow D_{CP}\rho$ gets a second contribution with different CKM elements. While in general $\delta\phi$ can be a function of hadronic matrix elements, this dependence is expected to be very weak here [38]. In the factorization approximation, the matrix elements of the leading and sub-leading amplitude are identical, as

are the final state rescattering effects. Moreover, both these cases get contributions from only one electroweak diagram, thus reducing the possibility of complicated interference patterns. Thus

$$\delta\phi_{SM}(b \rightarrow c\bar{u}d) = \frac{V_{ub}V_{cd}^*}{V_{cb}V_{ud}^*} r_{FA} \leq 0.05 \quad (13.37)$$

gives a reasonable estimate, where r_{FA} is the ratio of matrix elements with $r_{FA} = 1$ in the factorization approximation. Here $|V_{ub}/V_{cb}| < 0.11$ and a reasonable limit for the matrix elements ratio, $r_{FA} < 2$, were used to obtain the upper bound.

The technique proposed to extract γ using the modes (c4) $b \rightarrow c\bar{u}s$ and (c6) $b \rightarrow u\bar{c}s$ is manifestly independent of any ‘‘Standard Model pollution.’’

Mode (c7) $b \rightarrow u\bar{u}d$ suffers from significant Standard Model penguin pollution, which can be estimated by [37]

$$\delta\phi_{SM}(b \rightarrow u\bar{u}d) \simeq \frac{V_{tb}V_{td}^*}{V_{ub}V_{ud}^*} \frac{\alpha_s(m_b)}{12\pi} \log(m_b^2/m_t^2) \lesssim 0.4, \quad (13.38)$$

where the upper bound is for $|V_{td}| < 0.02$, $|V_{ub}| > 0.002$, $m_t = 180 \text{ GeV}/c^2$ and $\alpha_s(m_b) = 0.2$. For some B_d decays (notably $\pi\pi$ and $\rho\pi$) the effects of the Standard Model penguin can be removed by isospin-based analyses as is described in Chapter 6. However, this technique would also remove any new physics contributions to the gluonic penguin operator.

For the neutral current modes (n1) $b \rightarrow s\bar{s}s$ the dominant penguin contribution is in phase with the dominant contribution, and the sub-dominant part is Cabibbo suppressed. Thus it would appear that, in the absence of new decay amplitudes, the CP asymmetry in modes mediated by the $b \rightarrow s\bar{s}s$ transition such as $B_d \rightarrow \phi K_s^0$ and $B_d \rightarrow \eta' K_s^0$ will measure the angle $\beta - \beta' + \delta_{m_d}$ and, $\delta\phi_{SM} = \beta' \leq 0.025$. However, another source of uncertainty comes from the fact that $B_d \rightarrow \phi K_s^0$ and $B_d \rightarrow \eta' K_s^0$ can also be mediated via the tree-level $b \rightarrow u\bar{u}s$ decay and this has a different weak phase than the leading penguin diagram. For the ϕK_s^0 this contribution appears only from the $u\bar{u}$ pair rescattering into an $s\bar{s}$ pair, whereas for the $\eta' K_s^0$ it could come either from this mechanism or directly, since the η' has a significant $u\bar{u}$ component. One can use experimental data on $SU(3)$ related modes to constrain this pollution ([39] for $B_d \rightarrow \phi K_s^0$ and [40] for $B_d \rightarrow \eta' K_s^0$), and it is expected to be small. Combining these two sources of uncertainty yields

$$\delta\phi_{SM}(b \rightarrow s\bar{s}s) \leq 0.05. \quad (13.39)$$

This uncertainty can be reduced once β' is measured, using *e.g.*, $B_s \rightarrow D_s^+ D_s^-$.

Finally, (n2) $b \rightarrow d\bar{s}s$ suffers from an $\mathcal{O}(30\%)$ correction due to Standard Model penguins with up and charm quarks [41].

In summary, the cleanest modes are $b \rightarrow c\bar{c}s$ and $b \rightarrow c\bar{u}s$ since they are essentially free of any sub-leading effects. The modes $b \rightarrow c\bar{u}d$ and $b \rightarrow s\bar{s}s$ suffer only small theoretical uncertainty,

less than 0.05. For $b \rightarrow c\bar{c}d$ the uncertainty is larger, $\mathcal{O}(0.1)$, and moreover cannot be estimated reliably since it depends on the ratio of tree and penguin matrix elements. Finally, the $b \rightarrow u\bar{u}d$ and $b \rightarrow d\bar{s}s$ modes suffer from large uncertainties.

The rare decay modes $B_d \rightarrow \phi K_s^0$ and $B_d \rightarrow \eta' K_s^0$ are important in probing new physics. Since these are penguin-mediated decays in the Standard Model, they are the most sensitive of all the modes discussed above to possible contributions from new physics. Moreover, the expected branching ratios and detection efficiencies imply that the CP asymmetry in these modes is measurable in the first few years of BABAR operation (see Chapter 5).

In the analysis above examples are given for the case of B_d decays, but the discussion can be readily generalized to the B_s case, since clearly the type of the spectator quark does not affect the relative size or relative weak phase of tree and penguin contributions. This analysis makes it clear that an important part of the program for BABAR will be to study the relative sizes of penguin and tree contributions by comparing many modes. It is to be hoped that one can thereby develop better limits on the sizes of the non-leading Standard-Model contributions and hence greater sensitivity to possible new physics effects.

13.3.5 Overview of New Physics Possibilities

The remainder of this chapter presents in some detail the new physics effects expected in each of several types of extensions of the Standard Model. Here we briefly summarize some of these effects to illustrate the relevance of the preceding discussion. Table 13-1 shows the largest allowable effects on B meson decay amplitudes in three models: (a) Effective Supersymmetry², (b) Models with Enhanced Chromomagnetic Dipole Operators, and (c) Supersymmetry without R Parity. Such effects in general supersymmetric models have also been studied [42].

The observed pattern of CP asymmetries can distinguish between different classes of new contributions to the B decay amplitudes. Consider two examples:

- (1) In both models (a) and (b), the neutral current decay $b \rightarrow s\bar{s}s$ can have significant ($\mathcal{O}(1)$) corrections. In model (c) however, this mode is essentially unmodified.
- (2) The $b \rightarrow c\bar{u}d$ channel can be significantly affected in model (c), in contrast with the other two models. In those models the new decay amplitudes are penguin induced, and require the up-type quarks in the final state to be a flavor singlet ($c\bar{c}$ or $u\bar{u}$), thus giving no correction to the $b \rightarrow c\bar{u}d$ decay.

²Effective Supersymmetry denotes a class of supersymmetric extensions of the Standard Model where the third family is light ($\lesssim 1 \text{ TeV}/c^2$), in order to maintain the naturalness properties of supersymmetric theories, while the first two families are heavy ($\gg 1 \text{ TeV}/c^2$) in order to alleviate the problem with flavor-changing neutral currents.

Table 13-1. Summary of useful modes. The “Standard Model angle” entry corresponds to the angle obtained from B_d decays assuming one decay amplitude and to first order in the Wolfenstein approximation. The angle γ in the mode $b \rightarrow u\bar{c}s$ is measured after combining with the mode $b \rightarrow c\bar{u}s$. New contributions to the mixing amplitude would shift all the entries by δ_{m_d} . $\delta\phi$ (defined in Eq. (13.30)) corresponds to the (absolute value of the) correction to the universality prediction within each model: $\delta\phi_{SM}$ — Standard Model non-leading effects, $\delta\phi_a$ — Effective Supersymmetry, $\delta\phi_b$ — Models with Enhanced Chromomagnetic Dipole Operators, and $\delta\phi_c$ — Supersymmetry without R parity. 1 means that the phase can have any value. The branching ratio is taken from [43] and is an order of magnitude estimate for one of the exclusive channels that can be used in each quark decay mode. For the $b \rightarrow c\bar{u}d$ mode \mathcal{B} stands for the product $\mathcal{B}(B_d \rightarrow \bar{D}\rho) \times \mathcal{B}(\bar{D} \rightarrow f_{CP})$ where f_{CP} is a CP eigenstate.

Mode	SM angle (ϕ_0)	$\delta\phi_{SM}$	$\delta\phi_a$	$\delta\phi_b$	$\delta\phi_c$	\mathcal{B}
$b \rightarrow c\bar{c}s$	β	0	0.1	0.1	0.1	7×10^{-4}
$b \rightarrow c\bar{c}d$	β	0.1	0.2	0.6	0.6	4×10^{-4}
$b \rightarrow c\bar{u}d$	β	0.05	0	0	0.5	10^{-5}
$b \rightarrow s\bar{s}s$	β	0.04	1	1	0	10^{-5}
$b \rightarrow u\bar{u}d$	$\beta + \gamma$	0.4	0.4	1	0	10^{-5}
$b \rightarrow u\bar{c}s$	γ	0	0	0	0	10^{-6}
$b \rightarrow d\bar{s}s$	0	0.3	1	1	1	10^{-6}

Thus new physics can be probed by comparing two experiments that measure the same phase ϕ_0 in the Standard Model [see Eq. (13.30)]. If these two measurements differ by an amount greater than the Standard Model uncertainty (and the experimental sensitivity), this provides a signature for new physics *i.e.*,

$$|\phi(B \rightarrow f_1) - \phi(B \rightarrow f_2)| > \delta\phi_{SM}(B \rightarrow f_1) + \delta\phi_{SM}(B \rightarrow f_2), \quad (13.40)$$

where $\phi(B \rightarrow f)$ is the angle obtained from the asymmetry measurement in the $B \rightarrow f$ decay.

The most promising way to look for new physics effects in decay amplitudes is to compare all the B_d decay modes that measure β in the Standard Model (and the B_s decay modes that measure β' in the Standard Model). The theoretical uncertainties among all the decays considered are at most $\mathcal{O}(10\%)$, and they have relatively large rates. The best mode is $B^0 \rightarrow J/\psi K_S^0$ which has a sizeable rate and negligible theoretical uncertainty. This mode should be the reference mode to which all other measurements are compared. The $b \rightarrow c\bar{u}d$ and $b \rightarrow s\bar{s}s$ modes are also theoretically very clean. In addition, the $b \rightarrow s\bar{s}s$ being a loop-mediated process in the Standard Model, is particularly sensitive to new physics effects. In both cases the conservative upper bound on the theoretical uncertainty is less than 0.05, and this can possibly be reduced with more experimental

data. Moreover, the rates for the relevant hadronic states are $\mathcal{O}(10^{-5})$ which is not extremely small. Thus, three important relations are

$$|\phi(B_d \rightarrow J/\psi K_s^0) - \phi(B_d \rightarrow \phi K_s^0)| < 0.05, \quad (13.41)$$

$$|\phi(B_d \rightarrow J/\psi K_s^0) - \phi(B_d \rightarrow \eta' K_s^0)| < 0.05, \quad (13.42)$$

and

$$|\phi(B_d \rightarrow J/\psi K_s^0) - \phi(B_d \rightarrow D_{CP}\rho)| < 0.05. \quad (13.43)$$

Any deviation from these three relations will be a clear indication for new physics in decay amplitudes.

Although not as precise as the previous predictions, another important way to search for new physics in the B decay amplitudes is to look for violations of the relation

$$|\phi(B_d \rightarrow J/\psi K_s^0) - \phi(B_d \rightarrow D^+ D^-)| < 0.1. \quad (13.44)$$

The advantage is that the relevant rates are rather large, $\mathcal{B}(B_d \rightarrow D^+ D^-) \approx 4 \times 10^{-4}$. However, the theoretical uncertainty is large too. As long as one does not know how to calculate hadronic matrix elements it will be hard to place a conservative upper bound on the Standard Model corrections.

New physics can possibly be discovered by comparing the two ways to measure γ in the Standard Model. For example one can compare the direct determination of γ from $b \rightarrow c\bar{u}s$ and $b \rightarrow u\bar{c}s$ with the quantity $\gamma = \pi - \alpha - \beta$, where α and β are determined from $b \rightarrow u\bar{u}d$ and $b \rightarrow c\bar{c}s$, respectively. However, this approach is less promising since some of the rates are relatively small, and the theoretical uncertainties due to non-leading contributions to the α channels are significant. Thus, one would require large new physics effects in order to distinguish them from non-leading Standard Model contributions. Moreover, although an isospin-based analysis could substantially reduce the Standard Model uncertainty in $b \rightarrow u\bar{u}d$, it would simultaneously remove any isospin invariant new physics effects from this mode, thus requiring the new physics effects to be in the $b \rightarrow c\bar{u}s$ mode. (Such effects were not found in the three models studied here.)

New physics can also contribute an observable CP asymmetry in semileptonic B decays. This is measured by

$$a_{SL} \equiv \frac{N(l^+l^+) - N(l^-l^-)}{N(l^+l^+) + N(l^-l^-)}, \quad (13.45)$$

where $N(l^+l^+)$ [$N(l^-l^-)$] defines the number of times a $B^0\bar{B}^0$ pair decays into a pair of positively [negatively] charged leptons. a_{SL} is a measure of CP violation in the $B^0-\bar{B}^0$ mixing matrix and is given by

$$a_{SL} = \text{Im} \left(\frac{\Gamma_{12}}{M_{12}} \right) = \left| \frac{\Gamma_{12}}{M_{12}} \right| \sin \phi_{12}, \quad (13.46)$$

where ϕ_{12} is the phase between Γ_{12} and M_{12} . In the Standard Model, a_{SL} is unobservably small, $\sim 10^{-3}$ due to a combination of the fact that $|\frac{\Gamma_{12}}{M_{12}}| \sim 10^{-2}$ and $\sin \phi_{12} \sim m_c^2/m_b^2 \sim 10^{-1}$ due

to the GIM mechanism. Thus, new physics can enhance a_{SL} either by increasing $|\frac{\Gamma_{12}}{M_{12}}|$ or $\sin \phi_{12}$. New physics that gives large contributions to decay modes that are common to both B^0 and \bar{B}^0 can enhance both of these factors and could lead to $a_{SL} \sim 10\%$ which could be observed with about $10^6 B^0 \bar{B}^0$ pairs at BABAR [44]. Moreover, most models of new physics where new, heavy particles contribute to M_{12} but not to Γ_{12} would result in enhancements of the relative phase ϕ_{12} leading to the possibility that $a_{SL} \sim 1\%$. This has recently been explored in the context of supersymmetric models [45].

13.4 Supersymmetry

13.4.1 The Supersymmetric CP Problems

A generic supersymmetric extension of the Standard Model contains a host of new flavor and CP -violating parameters; see Grossman *et al.* [46] for a recent review. Experimental data provides strong constraints on many of these parameters. For this reason, the physics of flavor and CP violation has had a profound impact on supersymmetric model building. A discussion of CP violation in this context can hardly avoid addressing the flavor problem itself. Indeed, many of the supersymmetric models that we analyze below were originally aimed at solving flavor problems.

As concerns CP violation, one can distinguish two classes of experimental constraints. First, bounds on nuclear and atomic electric dipole moments determine what is usually called the *supersymmetric CP problem*. It involves effects that are flavor preserving and consequently appears already in the minimal supersymmetric standard model (MSSM) with universal sfermion masses and with the trilinear SUSY-breaking scalar couplings proportional to the corresponding Yukawa couplings. In such a constrained framework, the two phases of the Standard Model (δ_{KM} and θ_{QCD}) [47, 48], are augmented by two additional phases, usually denoted by ϕ_A and ϕ_B . In the more general case of non-universal soft terms there is one independent phase ϕ_{A_i} for each quark and lepton flavor. Moreover, complex off-diagonal entries in the sfermion mass matrices may provide additional sources of CP violation.

The most significant effect of ϕ_A and ϕ_B is their contribution to electric dipole moments (EDMs). In particular, the present experimental bound, $d_N < 1.1 \times 10^{-25} e \text{ cm}$ [49, 50] implies [51]

$$\left(\frac{100 \text{ GeV}}{\widetilde{m}}\right)^2 \sin \phi_{A,B} \lesssim 10^{-2} \frac{d_N}{10^{-25} e \text{ cm}}, \quad (13.47)$$

where \widetilde{m} represents the overall SUSY scale. Whether the phases are small or squarks are heavy, a fine-tuning of order 10^{-2} seems to be required, in general, to avoid too large a d_N . This is the Supersymmetric CP Problem.

A second class of experimental constraints, involving the physics of neutral mesons and, most importantly, the small experimental value of ε_K , pose the *supersymmetric ε_K problem*. The contribution to the CP -violating ε_K parameter in the neutral K system is dominated by diagrams involving Q and \bar{d} squarks in the same loop. A typical bound on the supersymmetric parameters reads [52]:

$$\left(\frac{300 \text{ GeV}/c^2}{\tilde{m}}\right)^2 \left| \frac{(\delta m_Q^2)_{12}}{m_Q^2} \frac{(\delta m_D^2)_{12}}{m_D^2} \right| \sin \phi \lesssim 0.5 \times 10^{-7}, \quad (13.48)$$

where $\phi = \arg((\delta m_Q^2)_{12}(\delta m_D^2)_{12})$, and $(\delta m_{Q,D}^2)_{12}$ are the off-diagonal entries in the squark-mass matrices in a basis where the down-quark mass matrix and the gluino couplings are diagonal. For dimensionless parameters assuming their natural values of $\mathcal{O}(1)$, the constraint (13.48) is generically violated by about seven orders of magnitude. This is the supersymmetric ε_K problem.

13.4.2 Classes of Supersymmetric Models

The supersymmetric flavor and CP problems have provided a very significant input to supersymmetry model builders. Two scales play an important role in supersymmetry: Λ_S , where the soft supersymmetry-breaking terms are generated, and Λ_F , where flavor dynamics takes place.

Both supersymmetric CP problems are solved if, at the scale Λ_S , the soft supersymmetry-breaking terms are universal and the genuine SUSY CP phases $\phi_{A,B}$ vanish. Then the Yukawa matrices represent the only source of flavor and CP violation which is relevant in low energy physics. This situation can naturally arise when $\Lambda_S \ll \Lambda_F$, for example in models where supersymmetry breaking is mediated by the Standard Model gauge interactions [53]. In the simplest scenarios, the A terms and the gaugino masses are generated by the same SUSY and $U(1)_R$ breaking source, leading to $\phi_A = 0$. In specific models also $\phi_B = 0$ in a similar way [54, 55].

The most important implication of such boundary conditions for soft terms, here called *exact universality* [56, 57], is the existence of the SUSY analogue of the GIM mechanism of the Standard Model. The CP -violating phase of the CKM matrix can feed into the soft terms via Renormalization Group (RG) evolution only with a strong suppression from light-quark masses [47, 58]. The resulting phenomenology of CP violation is hardly distinguishable from the Standard Model. For the B_d and B_s systems, the largest SUSY contribution to the mixing comes from box diagrams with intermediate charged Higgs and up quarks. It can be up to $\mathcal{O}(0.2)$ of the Standard Model amplitude for $\Lambda_S = M_{\text{Pl}}$ and $\tan \beta = \mathcal{O}(1)$ [59], and much smaller for large $\tan \beta$. The contribution is smaller in models of gauge-mediated SUSY breaking where the mass of the charged Higgs is typically $\gtrsim 300 \text{ GeV}/c^2$ [53] and $\log(\Lambda_S/M_W) \sim 5$. The SUSY contributions to $B_d - \bar{B}_d$ and $B_s - \bar{B}_s$ mixing are, to a good approximation, proportional to $(V_{tb}V_{td}^*)^2$ and $(V_{tb}V_{ts}^*)^2$, respectively, as in the Standard Model. Then, regardless of the size of these contributions, the relation

$\Delta m_{B_d}/\Delta m_{B_s} \sim |V_{td}/V_{ts}|^2$ and the CP asymmetries in neutral B decays into final CP eigenstates are the same as in the Standard Model.

When $\Lambda_F \lesssim \Lambda_S$, flavor and CP violation are not necessarily limited to the Yukawa matrices and, *a priori*, could be large. One way to suppress CP violation would be to assume that CP is an approximate symmetry of the full theory. In such a case, one expects also that the Standard Model phase δ_{KM} is $\ll 1$. Then the standard box diagrams cannot account for ε_K which must therefore arise from another source. In supersymmetry with non-universal soft terms, the source could be diagrams involving virtual superpartners, mainly squark-gluino box diagrams. Denoting the supersymmetric contribution to the $K-\bar{K}$ mixing amplitude by $(M_{12}^K)^{\text{SUSY}}$, the requirements $\text{Re}(M_{12}^K)^{\text{SUSY}} \lesssim \Delta m_K$ and $\text{Im}(M_{12}^K)^{\text{SUSY}} \sim \varepsilon_K \Delta m_K$ imply that the generic CP phases are $\geq \mathcal{O}(\varepsilon_K) \sim 10^{-3}$. Then, somewhat like the superweak scenario, all CP -violating observables (when defined appropriately) are characterized by a similar small parameter. This implies many dramatic consequences, *e.g.*, d_N just below or barely compatible with the present experimental bound and, most strikingly, that CP asymmetries in B meson decays are small, perhaps $\mathcal{O}(\varepsilon_K)$, rather than $\mathcal{O}(1)$ as expected in the Standard Model.

Another option is to assume that, as in the Standard Model, CP -violating phases are large but their effects are screened, possibly by the same physics that explains the various flavor puzzles. This usually requires Abelian or non-Abelian horizontal symmetries. Two ingredients play a major role here: selection rules that come from the symmetry and holomorphy of Yukawa and A terms that come from the supersymmetry. With Abelian symmetries, the screening mechanism is provided by *alignment* [60, 61], whereby the mixing matrices for gaugino couplings have very small mixing angles, particularly for the first two down-squark generations. With non-Abelian symmetries, the screening mechanism is *approximate universality*, where quarks of the two light families fit into an irreducible doublet of the horizontal symmetry and are, therefore, approximately degenerate [62, 63]. An extension of these ideas, aimed at screening the CP phases in the A terms, is to assume that CP is a symmetry of the Lagrangian [64], spontaneously broken by the same fields that break the horizontal symmetry. In general, it can be shown that non-universality of A terms and the requirement of an $\mathcal{O}(1)$ CKM phase imply $\phi_A \gtrsim \sin^6 \theta_C \sim J$, leading to $d_N \gtrsim 10^{-28} e$ cm. The minimal result can be reached only with almost triangular Yukawa matrices, which can be achieved with Abelian flavor symmetries. In models of non-Abelian symmetries, where the two light families are in irreducible doublets, one does not expect such a structure and typically the effective CP phases for light quarks are expected to be $\gtrsim \sin^4 \theta_C$.

As far as the third generation is concerned, the signatures of Abelian and non-Abelian models are similar. The relevant supersymmetric mixing angles are suppressed by $\mathcal{O}(V_{ub})$. The supersymmetric contribution to $B-\bar{B}$ mixing is comparable to the Standard Model contribution for squark masses around 300 GeV/ c^2 [61]. The crucial difference from exact universality does not lie, however, in the magnitude of the contributions: these may be too small to be clearly signaled in Δm_B because of the hadronic uncertainties (most noticeably in f_B). It lies instead in the fact that the phase of the supersymmetric contribution is now generically different from

that of the standard W -boson box diagrams. Therefore, in models where flavor symmetries tame the supersymmetric FCNC, observable deviations from the Standard Model predictions for CP asymmetries in B decays are possible. In some cases, non-Abelian models give relations between CKM parameters and consequently predict strong constraints on these CP asymmetries [29, 63]. Also, supersymmetric contributions to FCNC decay amplitudes could be significant and carry new phases [42]. This will induce a difference between CP asymmetries that are predicted to be equal in the Standard Model [19], for example between $B^0 \rightarrow J/\psi K_s^0$ and $B \rightarrow \phi K_s^0$.

Finally, it is possible that CP -violating effects are suppressed because squarks are heavy. If the masses of the first- and second-generation squarks m_i are larger than the other soft masses, $m_i^2 \sim 100 \tilde{m}^2$ then the Supersymmetric CP problem is solved and the ε_K problem is relaxed (but not eliminated) [62, 65, 66]. Such squark masses do not necessarily lead to naturalness problems, since these two generations are almost decoupled from the Higgs sector.

Models with the first two squark generations heavy have their own signatures of CP violation in neutral meson mixing [23]. In the neutral B system, it is possible to have $\mathcal{O}(1)$ shifts from the Standard Model predictions of CP asymmetries in the decays to final CP eigenstates. This can occur even when the squark masses of the third family are $\sim 1 \text{ TeV}/c^2$, since mixing angles can naturally be larger than in the case of horizontal symmetries (alignment or approximate universality). Again, interesting effects of CP violation appear also in the decay amplitudes [19].

To summarize, measurements of CP violation and, in particular, CP asymmetries in B decays, will provide an excellent probe of the flavor and CP structure of supersymmetry. Models of exact universality predict CP asymmetries that are very similar to the Standard Model predictions. However, all models with new, genuinely supersymmetric CP -violating phases, allow for deviations from the Standard Model. Approximate CP predicts asymmetries that are $\leq \mathcal{O}(10^{-3})$ in all modes. Horizontal symmetries allow deviations of order 0.3 from the Standard Model values. In some cases, non-Abelian flavor symmetries predict very strong correlations between various asymmetries. Models with heavy squarks allow even larger deviations (unless they are combined with approximate CP to solve the ε_K problem).

Rare B decays also provide a sensitive probe of supersymmetry [96]. As an example, the reach of rare B decays in probing the supersymmetric parameter space is compared here with that of high-energy colliders. A set of five points in the minimal supergravity (SUGRA) parameter space were chosen at Snowmass 1996 [67] for the study of supersymmetry at the NLC; point #3 is the so-called “common” point used for a comparison of SUSY studies at the NLC, LHC, and upgraded Tevatron. Once these points are chosen the sparticle mass spectra is obtained, as usual, via the SUGRA relations. Their contributions to $B \rightarrow X_s \gamma$ can then be computed. The results are displayed in the $R_7 - R_8$ plane in Fig. 13-3 (labeled 1 – 5 for each SUGRA point), where R_i is defined in Chapter 9 in terms of the Wilson coefficients C_i as $R_i \equiv C_i^{SUSY}(M_W)/C_i^{SM}(M_W) - 1$. C_7 and C_8 are the Wilson coefficients of the magnetic dipole and chromomagnetic dipole operators, respectively, which mediate the decay $B \rightarrow X_s \gamma$ (including the QCD corrections). Also shown in the figure are the constraints in this plane obtained in Chapter 9 from fits to the present data

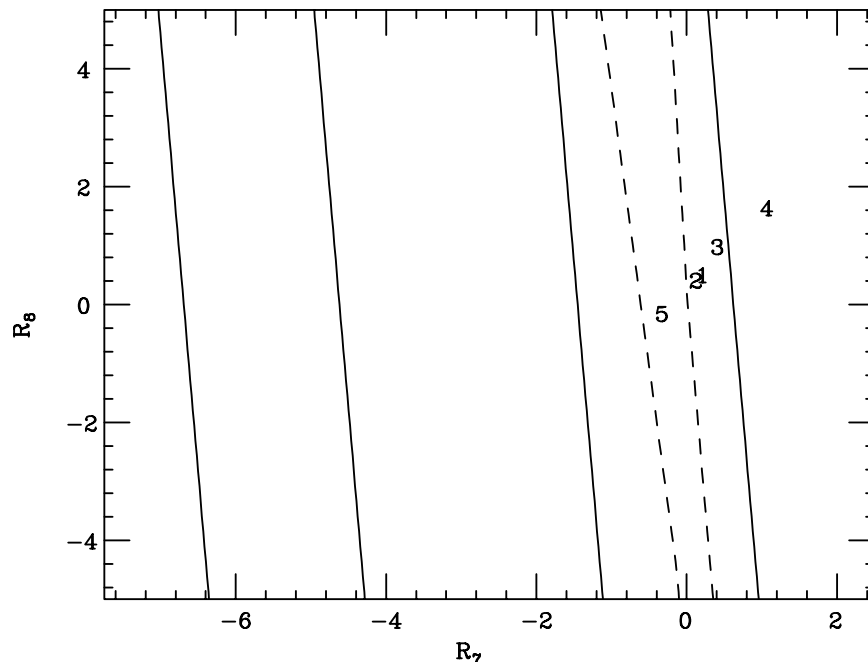


Figure 13-3. Values in the $R_7 - R_8$ plane for the five Snowmass NLC SUGRA points. The dashed bands represent the constraints placed by a future measurement of $\mathcal{B}(B \rightarrow X_s \gamma)$, assuming the SM value with 10% measurement errors, while the solid bands correspond to the presently allowed region by CLEO. The allowed regions lie inside the bands.

at CLEO (solid bands) and the anticipated bounds (dashed bands) that would be placed by a future measurement with 10% errors assuming the SM value for the branching ratio. One sees that four of the SUGRA points lie outside of the dashed bands and should be discernable from the Standard Model in the future, and in fact one of the points is already excluded by CLEO data. Thus rare B decays are indeed complementary to high-energy colliders in searching for supersymmetry.

13.4.3 Supersymmetry without R -parity

This section presents a short introduction to SUSY models where R -parity is not imposed, and lepton number (L) or baryon number (B) are not conserved by renormalizable interactions [68]. These models are characterized by several new L - and B -violating couplings involving leptons and quarks of the three generations. Some combinations of these couplings can induce large tree-level contributions to rare B decays. Since the values of the couplings is left undetermined, without further theoretical input no numerical predictions of the effects on B decays are possible. To estimate the expected size of the new physics effects, one considers models where the magnitude of the fermion masses and CKM mixing angles is explained by assuming some horizontal $U(1)$

symmetry, as discussed above [60, 61, 69]. This framework provides additional theoretical constraints resulting in a set of numerical predictions for all the interesting parameters, and allowing order of magnitude estimates of the decay rates.

13.4.3.1 *R*-parity-violating couplings

The field content of the Standard Model together with the requirement of $SU(2)_L \times U(1)_Y$ gauge invariance, implies that at the renormalizable level the most general Lagrangian possesses additional accidental $U(1)$ symmetries corresponding to conserved baryon and lepton-flavor (L_i) quantum numbers. The conservation of B , L_i and hence of total lepton number ($L = \sum_i L_i$) naturally explains nucleon stability as well as the non-observation of L and L_i -violating transitions. In SUSY extensions of the Standard Model, additional gauge and Lorentz invariant terms are allowed, which violate B , L_i , and L . Denoting collectively by \widehat{H}_α ($\alpha = 0, 1, 2, 3$) the supermultiplets containing the down-type Higgs and the left-handed lepton doublets, which transform in the same way under the gauge group, the following L_i - and L -violating superpotential terms arise

$$W_{\mathcal{L}} = \mu_\alpha \widehat{H}_\alpha \widehat{H}_u + \lambda_{\alpha\beta k} \widehat{H}_\alpha \widehat{H}_\beta \widehat{l}_k^c + \lambda'_{\alpha j k} \widehat{H}_\alpha \widehat{Q}_j \widehat{d}_k^c. \quad (13.49)$$

Here \widehat{Q}_i and \widehat{d}_i^c denote the quark-doublet and down-quark-singlet superfields, \widehat{l}_i^c are the lepton singlets and \widehat{H}_u contains the up-type Higgs field. There are also renormalizable terms which violate B , $W_{\mathcal{B}} = \lambda''_{ijk} \widehat{u}_i^c \widehat{d}_j^c \widehat{d}_k^c$, and physics at some large scale M_Λ can induce additional dimension 5 B - and L -violating (but R -parity conserving) terms like $(\Gamma'_{\alpha ijk}/M_\Lambda) \widehat{H}_\alpha \widehat{Q}_i \widehat{Q}_j \widehat{Q}_k + \dots$

To forbid the dangerous dimension 4 terms, a parity quantum number $R = (-1)^{3B+L+2S}$ (S being the spin) is assigned to each component field, and invariance under R transformations is imposed. However, even if suppressed by the Planck mass, the dimension 5 R -parity conserving terms can still induce too rapid proton decay, unless $\Gamma' \lesssim 10^{-8}$ etc. From a phenomenological point of view, the first priority is to ensure the absence of operators leading to fast nucleon decay, and in this respect other discrete symmetries can be more effective than R [70]. These interesting alternatives forbid dimension 4 and 5 B -violating terms but do not imply the same for the L -violating terms. Since a mild violation of L can be phenomenologically tolerated, SUSY extensions of the Standard Model with highly-suppressed B violation but without R parity and without L number, represent interesting alternatives to the MSSM. Henceforth, it is assumed here that B is effectively conserved, and only the L -violating terms contained in (13.49) are considered.

The first term in (13.49) can mix the fermions with the Higgsinos, resulting in too-large neutrino masses [71, 72, 73, 74]. One can ensure that neutrinos remain light by assuming universal soft SUSY-breaking terms. Universality conditions are unstable under renormalization group running [74] and non-vanishing neutrino masses will still be generated due to the evolution of the soft breaking parameters from the high scale down to low energy. This results in additional constraints

on these models. In the following, it is assumed that the induced neutrino-neutralino mixing is small enough that the experimental limits on neutrino masses are satisfied, and the effects of the bilinear term in (13.49) can be neglected.

Once the fields are rotated to the physical basis, the L -violating trilinear terms contained in (13.49) read

$$\lambda_{ijk} \widehat{L}_i \widehat{L}_j \widehat{l}_k^c + \lambda'_{ijk} \widehat{L}_i \widehat{Q}_j \widehat{d}_k^c, \quad (13.50)$$

where $\lambda_{ijk} = -\lambda_{jik}$ due to the antisymmetry in the $SU(2)$ indices. Several of the λ and λ' couplings are strongly constrained by the existing phenomenology [68]. The best limits are for couplings involving fermions of the first two generations ($i, j, k = 1, 2$) while for couplings involving more than a single third generation field the existing limits are much weaker, and in some cases no bound exists to date. This situation is interesting since in general models that can explain the observed fermion mass hierarchy also predict that the largest R -parity-violating couplings are those involving more than a single third generation field. This is the case in the models introduced in the next subsection.

13.4.3.2 R -parity violation in the framework of horizontal symmetries

Supersymmetric models with $U(1)$ horizontal symmetries have been thoroughly investigated in [60, 61, 69, 75, 76], this discussion follows that work. Besides predicting the order of magnitude of the fermion masses and CKM angles, these models can also explain the suppression of L [75] and B violation [76] in SUSY models without R -parity. In these models no additional fields are introduced in the low-energy spectrum with respect to minimal SUSY. However, each supermultiplet $\widehat{\psi}$ is assigned a charge $H(\widehat{\psi})$ of an Abelian horizontal symmetry $\mathcal{H} = U(1)_H$. \mathcal{H} is explicitly broken by a small parameter ε with charge $H(\varepsilon) = -1$, giving rise to a set of selection rules for the effective couplings of the low-energy Lagrangian [60, 61, 69]. If each of the lepton, quark, and Higgs superfields is assumed to carry positive or zero charge, the selection rule relevant for the present discussion is that the effective coupling g_{abc} for a general trilinear superpotential term $\widehat{\psi}_a \widehat{\psi}_b \widehat{\psi}_c$ is of order $g_{abc} \sim \varepsilon^{H(\widehat{\psi}_a)+H(\widehat{\psi}_b)+H(\widehat{\psi}_c)}$. Therefore, the Yukawa couplings of the leptons and down-type quarks are of order $Y_{ij}^l \sim \varepsilon^{H(\widehat{\Phi}_d)+H(\widehat{L}_i)+H(\widehat{l}_j^c)}$ and $Y_{ij}^d \sim \varepsilon^{H(\widehat{\Phi}_d)+H(\widehat{Q}_i)+H(\widehat{d}_j^c)}$, respectively (rotation to the exact quark-mass eigenstate basis does not affect the order of magnitude estimates [60, 61, 69]). Most of the L -violating trilinear couplings in (13.49) are further suppressed with respect to the corresponding Yukawa couplings. They can be estimated as

$$\lambda_{kij} \sim Y_{ij}^l \varepsilon^{H(\widehat{L}_k)-H(\widehat{\Phi}_d)} \sim \left(\frac{2\sqrt{2}G_F}{\cos^2 \beta} \right)^{1/2} m_{l_i} \varepsilon^{H(\widehat{l}_j^c)-H(\widehat{l}_i^c)+H(\widehat{L}_k)-H(\widehat{\Phi}_d)}, \quad (13.51)$$

and

$$\lambda'_{kij} \sim Y_{ij}^d \varepsilon^{H(\widehat{L}_k)-H(\widehat{\Phi}_d)} \sim \left(\frac{2\sqrt{2}G_F}{\cos^2 \beta} \right)^{1/2} m_{d_i} \varepsilon^{H(\widehat{d}_j^c)-H(\widehat{d}_i^c)+H(\widehat{L}_k)-H(\widehat{\Phi}_d)}. \quad (13.52)$$

These equations show that (i) the couplings λ and λ' involving fermions of the third generation are respectively enhanced by m_τ and m_b , and (ii) like the lepton and down-quark Yukawa couplings, the λ, λ' couplings increase with $\tan\beta$.

Next, a set of H charges and a value for the \mathcal{H} -symmetry breaking parameter ε must be defined. In general, $\varepsilon \sim 0.22$ is fixed by the magnitude of the Cabibbo angle, while the quark, lepton, and Higgs charges are chosen to reproduce the values of the fermion masses and CKM mixing angles. Besides reproducing the measured values, this framework has some predictivity in the quark sector [60, 61, 69]. It also yields estimates for ratios of neutrino masses [75, 77], and most importantly in the present context, it ensures that the L -violating couplings in (13.50), (13.51) and (13.52) are safely suppressed below the present experimental limits [72]. The following \mathcal{H} -charge assignments fit the order of magnitude of all the quark masses and CKM-mixing angles [60, 61, 69]:

$$\begin{array}{cccccc} \widehat{Q}_1 & \widehat{Q}_2 & \widehat{Q}_3 & \widehat{d}_1^c & \widehat{d}_2^c & \widehat{d}_3^c & \widehat{u}_1^c & \widehat{u}_2^c & \widehat{u}_3^c & \widehat{\Phi}_d & \widehat{\Phi}_u \\ (3) & (2) & (0) & (3) & (2) & (2) & (3) & (1) & (0) & (0) & (0) \end{array} \quad (13.53)$$

For the leptons, two different sets of charges will be used here; both fit the order of magnitude of the charged lepton masses. A different value for the squark masses $m_{\widehat{q}}$ is used in each set:

$$\begin{array}{cccccc} \widehat{L}_1 & \widehat{L}_2 & \widehat{L}_3 & \widehat{l}_1^c & \widehat{l}_2^c & \widehat{l}_3^c & m_{\widehat{l}} \text{ (GeV}/c^2) & m_{\widehat{q}} \text{ (GeV}/c^2) \\ \text{Model I :} & (4) & (2) & (0) & (4) & (3) & (3) & 100 & 170 \\ \text{Model II :} & (3) & (0) & (0) & (5) & (5) & (3) & 100 & 350 \end{array} \quad (13.54)$$

The charges of Model I coincide with the charges of the ‘‘master model’’ of [75]. While in this model new physics effects are induced dominantly by squark exchange, in Model II the leading effects are due to slepton exchange.

13.4.3.3 Coefficients and rates for the various decays

Once an estimate for the trilinear couplings in (13.49) is worked out, and a choice is made for the squarks and slepton masses, it is straightforward to evaluate the coefficients of the effective operators appearing in the general amplitudes for rare B decays such as $B^- \rightarrow l\bar{\nu}_l$ (Eq. 9.3), $B_d \rightarrow l^+l^-$ (Eq. 9.8), $b \rightarrow X_q\nu\bar{\nu}$ (Eq. 9.70) or $b \rightarrow X_q l^+l^-$ (see Ref. [78]).

For example, the coefficients appearing in (9.3) and (9.4) for the decay $B^- \rightarrow l\bar{\nu}_l$ read

$$\begin{aligned} C_A^{l_i\bar{\nu}_j} - C_A^{l_i\bar{\nu}_{j'}} &= -\frac{\lambda_{i1k}^* \lambda_{j3k}'}{4 G_F m_{\widehat{d}_k}^2} - \sqrt{2} V_{ub} \delta_{ij} \\ C_P^{l_i\bar{\nu}_j} - C_P^{l_i\bar{\nu}_{j'}} &= -\frac{\lambda_{k13}^* \lambda_{kj i}'}{2 G_F m_{\widehat{l}_k}^2} \quad (k \neq i), \end{aligned} \quad (13.55)$$

where a sum over the repeated index k is understood. The corresponding expressions for the coefficients entering the decays $B_d \rightarrow l^+ l^-$ (9.9) and $b \rightarrow X_q \nu \bar{\nu}$ (9.71) can be found in [78]. In (13.55) it was shown that these models allow decay channels where the final state neutrino ν_j has a different flavor from the charged lepton. More interestingly, lepton-flavor-violating decays such as $B_d \rightarrow l_i^+ l_j^-$ and $b \rightarrow X_q l_i^+ l_j^-$ with $i \neq j$ are also allowed, and can provide a signature for SUSY models without R -parity.

To study new physics effects in the decay $B \rightarrow X_q l^+ l^-$ the Standard Model effective Hamiltonian (9.18) has to be generalized to include several new operators that are induced by squark and slepton exchange. A detailed discussion is given in [78].

Finally, note that in SUSY models without R -parity the decay $b \rightarrow s \gamma$ is affected by the new physics only at the loop level, and hence, unlike the leptonic and semileptonic decays, it is not very sensitive to the effects discussed here.

To identify the measurements most sensitive to new physics, several observables measurable in $b \rightarrow \tau$, $b \rightarrow \nu_\tau$ and $b \rightarrow \mu$ transitions were studied, within the two different models defined in (13.53) and (13.54). For decays involving electrons in final state, the new contributions are strongly suppressed. In both models, new physics contributions to the branching ratios scale as $\tan^4 \beta$. In Model I the dominant effects come from squark exchange, and scale roughly as $(200 \text{ GeV}/m_{\tilde{q}})^4$. For light squarks ($m_{\tilde{q}} \simeq 100 \text{ GeV}/c^2$) and moderate values of $\tan \beta$ ($\gtrsim 2$) this model can predict values of the branching ratio for $B \rightarrow X_s \tau^+ \tau^-$ up to few $\times 10^{-5}$. Model II is defined in terms of a different set of lepton horizontal charges (13.54). The dominant effects come from slepton exchange and scale roughly as $(100 \text{ GeV}/m_{\tilde{l}})^4$.

Our results are collected in Tables 13-2 and 13-3. Table 13-2 lists the predictions for decays involving the transitions $b \rightarrow \tau$ and $b \rightarrow \nu_\tau$. The first five lines give the results for the decays $B^- \rightarrow \tau \bar{\nu}_\tau$, $B_q \rightarrow \tau^+ \tau^-$ and $b \rightarrow X_q \nu \bar{\nu}$. The results for the branching ratio, forward-backward asymmetry, and τ polarization asymmetries in the decay $B \rightarrow X_s \tau^+ \tau^-$ are given in the remaining entries. Table 13-3 collects the results for the corresponding processes involving final state muons. In both tables, the first column lists the Standard Model predictions for the various observables (computed in the leading order approximation). The second and third columns list the predictions of Model I and Model II, respectively.

Since $B \rightarrow X_s \mu^+ \mu^-$ and $B \rightarrow X_s \tau^+ \tau^-$ are affected by large long-distance effects, to single out the short-distance contributions, cuts were applied on the normalized dilepton invariant mass $\hat{s} = q^2/m_b^2$ with $q^2 = m_{l^+ l^-}^2$. The decay $B \rightarrow X_s \tau^+ \tau^-$ is studied in the region above the ψ' ($\hat{s} > 0.6$) while $B \rightarrow X_s \mu^+ \mu^-$ is analyzed below the resonance region ($\hat{s} < 0.4$). A comparison between the total inclusive branching ratios $\mathcal{B}(B \rightarrow X_s l^+ l^-)_{\text{no cut}}$, the branching ratio in the region within the cuts and the kinematic limits $\mathcal{B}(B \rightarrow X_s l^+ l^-)_{\hat{s} < 0.4 (\hat{s} > 0.6)}$, and only the short-distance contribution in the same region $\mathcal{B}^{\text{sd}}(B \rightarrow X_s l^+ l^-)$ shows the effects of the cuts on the total rates and their effectiveness in isolating the interesting contributions.

Table 13-2. Predictions for the various decay rates and asymmetries for $b \rightarrow \tau$ transitions in the standard model and in the R -parity-violating models discussed in the text. Model I is sensitive to operators generated by squark exchange. The lepton horizontal charges are $H(\hat{L}) = (4, 2, 0)$, $H(\hat{l}^c) = (4, 3, 3)$ while the SUSY masses are $m_{\tilde{l}} = 100 \text{ GeV}/c^2$ and $m_{\tilde{q}} = 170 \text{ GeV}/c^2$. Model II is sensitive to operators generated by slepton exchange, with horizontal charges $H(\hat{L}) = (3, 0, 0)$, $H(\hat{l}^c) = (5, 5, 3)$ and SUSY masses $m_{\tilde{l}} = 100 \text{ GeV}/c^2$ and $m_{\tilde{q}} = 350 \text{ GeV}/c^2$. In both models the value of the horizontal symmetry-breaking parameter is $\varepsilon = 0.22$.

Process	Standard Model	Model I	Model II
$\mathcal{B}(B^- \rightarrow \tau^- \bar{\nu})$	7.1×10^{-5}	7.2×10^{-5}	7.4×10^{-5}
$\mathcal{B}(B_s \rightarrow \tau^+ \tau^-)$	9.1×10^{-7}	5.7×10^{-6}	1.8×10^{-4}
$\mathcal{B}(B_d \rightarrow \tau^+ \tau^-)$	4.3×10^{-8}	1.9×10^{-7}	6.3×10^{-6}
$\mathcal{B}(b \rightarrow X_s \nu \bar{\nu})$	4.4×10^{-5}	6.7×10^{-5}	5.0×10^{-5}
$\mathcal{B}(b \rightarrow X_d \nu \bar{\nu})$	2.7×10^{-6}	3.9×10^{-6}	3.0×10^{-6}
$\mathcal{B}(b \rightarrow X_s \tau^+ \tau^-)_{\text{no cut}}$	4.9×10^{-6}	9.6×10^{-6}	1.0×10^{-5}
$\mathcal{B}(b \rightarrow X_s \tau^+ \tau^-)_{s > 0.6}$	1.5×10^{-7}	4.1×10^{-6}	4.6×10^{-6}
$\mathcal{B}^{\text{sd}}(b \rightarrow X_s \tau^+ \tau^-)_{s > 0.6}$	1.6×10^{-7}	4.1×10^{-6}	4.6×10^{-6}
$\langle A_{\text{FB}}^{\tau} \rangle_{s > 0.6}$	-0.13	0.18	-0.03
$\langle \mathcal{P}_{\text{L}}^{\tau} \rangle_{s > 0.6}$	-0.34	-0.40	-0.68
$\langle \mathcal{P}_{\text{T}}^{\tau} \rangle_{s > 0.6}$	-0.40	-0.13	-0.14
$\langle \mathcal{P}_{\text{N}}^{\tau} \rangle_{s > 0.6}$	0.05	0.00	0.01

From Table 13-2, it is apparent that in both models the decays $B^- \rightarrow \tau \bar{\nu}_{\tau}$ and $B \rightarrow X_q \nu \bar{\nu}$ do not show significant enhancements with respect to the Standard Model rates. New physics affects to some extent the rates for $B_s \rightarrow \tau^+ \tau^-$ and $B_d \rightarrow \tau^+ \tau^-$. However, in most cases the rates still remain very small. In Model II the branching ratio for $B_s \rightarrow \tau^+ \tau^-$ increases by two orders of magnitude, up to $\sim 10^{-4}$, however, this process is not relevant at B -factories running at the $\Upsilon(4S)$. A similar large enhancement for $B_d \rightarrow \tau^+ \tau^-$ could be more promising for new physics searches at BaBar.

In the muon channel, the corresponding decays $B_q \rightarrow \mu^+ \mu^-$ are sensitive to new physics effects from both models. However, even if the decay rates are enhanced by two orders of magnitude, the branching ratios are still only at the level of $\sim 2 \times 10^{-8}$ for B_d and $\sim 6 \times 10^{-7}$ for B_s .

As regards the decay $B \rightarrow X_s \mu^+ \mu^-$, the branching ratio can be enhanced at most by a factor of two (Model II). In contrast, in both models the branching ratio for the decay $B \rightarrow X_s \tau^+ \tau^-$ is enhanced by more than one order of magnitude. Notice that Model I and Model II both predict

Table 13-3. Predictions for the various decay rates and asymmetries for $b \rightarrow \mu$ transitions in the standard model and in the R -parity-violating models discussed in the text. Model I is sensitive to operators generated by squark exchange. The lepton horizontal charges are $H(\hat{L}) = (4, 2, 0)$, $H(\hat{l}^c) = (4, 3, 3)$ while the SUSY masses are $m_{\tilde{l}} = 100 \text{ GeV}/c^2$ and $m_{\tilde{q}} = 170 \text{ GeV}/c^2$. Model II is sensitive to operators generated by slepton exchange, with horizontal charges $H(\hat{L}) = (3, 0, 0)$, $H(\hat{l}^c) = (5, 5, 3)$ and SUSY masses $m_{\tilde{l}} = 100 \text{ GeV}/c^2$ and $m_{\tilde{q}} = 350 \text{ GeV}/c^2$. In both models the value of the horizontal symmetry-breaking parameter is $\varepsilon = 0.22$.

Process	Standard Model	Model I	Model II
$\mathcal{B}(B^- \rightarrow \mu^- \bar{\nu})$	3.2×10^{-7}	3.2×10^{-7}	3.3×10^{-7}
$\mathcal{B}(B_s \rightarrow \mu^+ \mu^-)$	4.3×10^{-9}	7.9×10^{-7}	7.2×10^{-7}
$\mathcal{B}(B_d \rightarrow \mu^+ \mu^-)$	2.1×10^{-10}	2.9×10^{-8}	2.7×10^{-8}
$\mathcal{B}(b \rightarrow X_s \mu^+ \mu^-)_{\text{no cut}}$	3.1×10^{-4}	3.1×10^{-4}	3.4×10^{-4}
$\mathcal{B}(b \rightarrow X_s \mu^+ \mu^-)_{\hat{s} < 0.4}$	4.3×10^{-6}	4.5×10^{-6}	8.3×10^{-6}
$\mathcal{B}^{\text{sd}}(b \rightarrow X_s \mu^+ \mu^-)_{\hat{s} < 0.4}$	3.9×10^{-6}	4.1×10^{-6}	7.7×10^{-6}
$\langle A_{\text{FB}}^\mu \rangle_{\hat{s} < 0.4}$	-0.01	0.00	0.08
$\langle \mathcal{P}_{\text{L}}^\mu \rangle_{\hat{s} < 0.4}$	-0.57	-0.56	-0.73

very similar rates even though the respective enhancements are induced by effective operators of quite a different nature. The τ polarization asymmetries \mathcal{P}_{L} and \mathcal{P}_{T} could in principle disentangle the effects of squark exchange (Model I) from the effects of slepton exchange (Model II).

In summary, order of magnitude predictions for various B decays have been made, within two representative models of SUSY without R -parity. The decays $B_q \rightarrow \tau^+ \tau^-$ and $B \rightarrow X_s \tau^+ \tau^-$ appear to be quite sensitive to the new effects since the rates can be enhanced up to one or two orders of magnitude. In the muon channel, sizeable effects were found only for the $B_q \rightarrow \mu^+ \mu^-$ decay modes. However, even with the new physics contributions, the overall rates for these decays appear to be rather small.

13.4.4 Model-Independent Analysis

Given a specific SUSY model it is in principle possible to make a full computation of all the FCNC phenomena in that context. However, given the variety of options for low-energy SUSY previously mentioned (even confining the discussion here to models with R matter parity), it is useful to extract from the whole host of FCNC processes upper limits on a set of quantities which can be readily computed in any chosen SUSY model.

The best such model-independent parameterization of FCNC effects is the mass-insertion approximation [79]. It is applied here to the most peculiar source of FCNC SUSY contributions, those that do not arise from the mere supersymmetrization of the FCNC in the Standard Model. These originate from the FC couplings of gluinos and neutralinos to fermions and sfermions [80]. One chooses a basis for the fermion and sfermion states where all the couplings of these particles to neutral gauginos are flavor diagonal; in this basis the FC is exhibited by the non-diagonality of the sfermion propagators. Denoting by Δ the off-diagonal terms in the sfermion mass matrices (*i.e.*, the mass terms relating sfermions of the same electric charge, but different flavor), the sfermion propagators can be expanded as a series in terms of $\delta = \Delta/\tilde{m}^2$ where \tilde{m} is the average sfermion mass. As long as Δ is significantly smaller than \tilde{m}^2 , one can truncate this expansion to a single term. The experimental information concerning FCNC and CP -violating phenomena then translates into an upper bound on these δ [52, 81].

The above mass-insertion method presents the major advantage that one does not need the full diagonalization of the sfermion mass matrices to perform a test of the SUSY model under consideration in the FCNC sector. It is enough to compute ratios of the off-diagonal and diagonal entries of the sfermion mass matrices and compare the results with the general bounds on the δ s that are provided here from all available experimental information.

There exist four different Δ mass insertions connecting flavors i and j along a sfermion propagator: $(\Delta_{ij})_{LL}$, $(\Delta_{ij})_{RR}$, $(\Delta_{ij})_{LR}$, and $(\Delta_{ij})_{RL}$. The indices L and R refer to the helicity of the fermion partners. The size of these Δ s can be quite different. For example, in the MSSM case there is a strong hierarchy between those connecting squarks of different helicity partners $(\Delta_{ij})_{LL} \gg (\Delta_{ij})_{LR} \gg (\Delta_{ij})_{RR}$.

The FCNC processes in B physics, which provide the best bounds on the δ_{23} and δ_{13} FC insertions, are $b \rightarrow s\gamma$ and $B_d-\bar{B}_d$ mixing, respectively. The process $b \rightarrow s\gamma$ requires a helicity flip. In the presence of a $(\delta_{23}^d)_{LR}$ mass insertion this flip can be realized by the gluino running in the loop. On the contrary, the $(\delta_{23}^d)_{LL}$ insertion requires the helicity flip to occur in the external b -quark line. Hence, a stronger bound on the $(\delta_{23}^d)_{LR}$ quantity is expected. Indeed, this is what happens: $(\delta_{23}^d)_{LL}$ is essentially not bounded, while $(\delta_{23}^d)_{LR}$ is limited to be $< 1.3 - 3 \times 10^{-2}$ for an average squark mass of 500 GeV/ c^2 and $0.3 < m_{\tilde{g}}^2/m_{\tilde{q}}^2 < 4.0$ (these bounds scale as $m_{\tilde{q}}^2$). Given the upper bound on $(\delta_{23}^d)_{LR}$ from $b \rightarrow s\gamma$, the quantity x_s of the $B_s-\bar{B}_s$ mixing is found to receive only tiny contributions from this kind of mass insertion. The only chance to obtain large values of x_s is if $(\delta_{23}^d)_{LL}$ is large, say of $\mathcal{O}(1)$. In that case x_s can easily jump up to values of $\mathcal{O}(10^2)$ or even larger.

As for the mixing $B_d-\bar{B}_d$, one obtains

$$\begin{aligned} \sqrt{\left| \text{Re} \left(\delta_{13}^d \right)_{LL}^2 \right|} &< 4.6 \cdot 10^{-2} \\ \sqrt{\left| \text{Re} \left(\delta_{13}^d \right)_{LR}^2 \right|} &< 5.6 \cdot 10^{-2} \\ \sqrt{\left| \text{Re} \left(\delta_{13}^d \right)_{LL} \left(\delta_{13}^d \right)_{RR} \right|} &< 1.6 \cdot 10^{-2} \end{aligned} \quad (13.56)$$

for $x \equiv m_{\tilde{g}}^2/m_{\tilde{q}}^2 = 0.3$ with $m_{\tilde{q}} = 500 \text{ GeV}/c^2$. The above bounds scale with $m_{\tilde{q}} (\text{GeV}/c^2)/500$ for different values of $m_{\tilde{q}}$ (at fixed x). Then, imposing the bounds (13.56), one finds that the largest possible value for $\mathcal{B}(b \rightarrow d\gamma)$ arises through gluino exchange. As expected, the $\left(\delta_{13}^d \right)_{LL}$ insertion leads to very small values of this branching ratio ($\mathcal{O}(10^{-7})$), whereas the $\left(\delta_{13}^d \right)_{LR}$ insertion allows for $\mathcal{B}(b \rightarrow d\gamma)$ ranging from few times 10^{-4} up to few times 10^{-3} for decreasing values of $x = m_{\tilde{g}}^2/m_{\tilde{q}}^2$. In the Standard Model one expects [82] $\mathcal{B}(b \rightarrow d\gamma)$ to be typically 10 to 20 times smaller than $\mathcal{B}(b \rightarrow s\gamma)$, *i.e.*, $\mathcal{B}(b \rightarrow d\gamma) = (1.7 \pm 0.85) \times 10^{-5}$. Hence a large enhancement in the SUSY case is conceivable if $\left(\delta_{13}^d \right)_{LR}$ is in the 10^{-2} range. Notice that in the MSSM one expects $\left(\delta_{13}^d \right)_{LR} < m_b^2/m_{\tilde{q}}^2 \times V_{td} < 10^{-6}$, and hence no hope at all of a sizeable contribution to $b \rightarrow d\gamma$.

The question of distinguishing SUSY effects from the Standard Model in CP -violating B decays in the present model-independent analysis is discussed next. The problem comes down to finding the range of results that is compatible with the Standard Model with a reasonable range for assumptions on model-dependent inputs. The framework of the analysis of Ref. [42] is followed. The effective Hamiltonian (\mathcal{H}_{eff}) formalism is used, including LO QCD corrections; in the numerical analysis, LO Standard Model Wilson coefficients are evaluated at $\mu = 5 \text{ GeV}/c^2$, as given in Ref. [83]. In most cases, by choosing different scales (within a reasonable range) or by using NLO Wilson coefficients, the results vary by about 20–30%. In some particular channels uncertainties are larger; such channels are not as useful for looking for beyond-Standard Model effects.

The matrix elements of the operators of \mathcal{H}_{eff} are given in terms of the following Wick contractions between hadronic states: Disconnected Emission (DE), Connected Emission (CE), Disconnected Annihilation (DA), Connected Annihilation (CA), Disconnected Penguin (DP) and Connected Penguin (CP) (either for left-left (LL) or for left-right (LR) current-current operators). Following Ref. [84, 85], where a detailed discussion can be found, instead of adopting a specific model for estimating the different diagrams, the model-dependent inputs are allowed to vary within reasonable ranges to estimate the Standard Model uncertainty (see Ref. [42]). First, only $DE = DE_{LL} = DE_{LR}$ are assumed to be different from zero (for simplicity, unless stated otherwise, the same numerical values are used for diagrams corresponding to the insertion of LL or LR operators, *i.e.*, $DE = DE_{LL} = DE_{LR}$, $CE = CE_{LL} = CE_{LR}$, *etc.*). The CE contribution is then added, by taking $CE = DE/3$. Annihilation diagrams are then included, using $DA = 0$ and $CA = \frac{1}{2}DE$ [84, 85]. Inspired by kaon decays, some enhancement of the matrix elements

of left-right (LR) operators is allowed, thus $DE_{LR} = 2DE_{LL}$ and $CE_{LR} = 2CE_{LL}$ are chosen. Penguin contractions, CP and DP , can be interpreted as long-distance penguin contributions to the matrix elements and play an important role. If, for example, $CP_{LL} = CE$ and $DP_{LL} = DE$, in some decays these terms dominate the amplitude. Finally, long-distance effects which might differentiate penguin contractions with up and charm quarks in the loop are considered, these can give rise to incomplete GIM cancellations (here $\overline{DP} = DP(c) - DP(u) = DE/3$ and $\overline{CP} = CP(c) - CP(u) = CE/3$ are assumed). For any given decay channel, whenever two terms with different CP phases contribute in the Standard Model, letting the various matrix elements vary within the above ranges, the ratio r_{SM} of the two amplitudes is estimated, the result is reported in the fifth column of Table 13-4.

As noted previously, new physics can change Standard Model predictions on CP asymmetries in B decays in two ways: by shifting the phase of the $B_d-\overline{B}_d$ mixing amplitude and by modifying both phases and absolute values of the decay amplitudes. The generic SUSY extension of the Standard Model considered here can cause all such effects.

In the SUSY case, by using the results in Eq. (12) of Ref. [52] for the Wilson coefficients and by parameterizing the matrix elements as was done for the Standard Model case discussed above, the ratios of SUSY to Standard Model amplitudes given in Table 13-4 were obtained. For each decay channel results for squark and gluino masses of $250 \text{ GeV}/c^2$ are given (r_{250} in the seventh column). The inclusion of the various terms in the amplitudes, DE , DA , *etc.*, can modify the ratio r of SUSY to Standard Model contributions up to one order of magnitude.

The simplest case occurs when one decay amplitude only appears in (or dominates) a decay process: the CP -violating asymmetry is then determined by the total phase $\phi_T = \phi_M + \phi_D$, where ϕ_D is the weak phase of the decay, while ϕ_M denotes the total mixing phase. This ideal situation is spoiled by the presence of several interfering amplitudes. If the ratios r in Table 13-4 are small, then the uncertainty on the sine of the CP phase is less than r , while if r is $\mathcal{O}(1)$, ϕ_T receives, in general, large corrections.

The results of this analysis are summarized in Table 13-4. In the third column, the values for the branching ratios of the various channels [84, 85] are given; these were obtained using QCD sum-rule form factors to evaluate DE , and $|CE| = 0.46$, based on a fit to the measured two-body B decays. The range of values given corresponds to the variation of the CKM angles and to the inclusion of the charming penguin contributions (see Ref. [84, 85] for further details). In the fourth column, the possible Standard Model decay phases when one or two decay amplitudes contribute are given for each channel, as well as the range of variation of their ratio, r_{SM} , as explained above. A few comments are necessary at this point: (a) for $B \rightarrow K_s^0 \pi^0$ the penguin contributions (with a vanishing phase) dominate over the tree-level amplitude because the latter is Cabibbo suppressed; (b) for the channel $b \rightarrow s \overline{s} d$ only penguin operators or penguin contractions of current-current operators contribute; (c) the phase γ is present in the penguin contractions of the $(\overline{b}u)(\overline{u}d)$ operator, denoted as u -penguin γ in Table 13-4; (d) $\overline{b}d \rightarrow \overline{q}q$ indicates processes occurring via annihilation diagrams which can be measured from the last two channels of Table 13-4; (e) in

the case $B \rightarrow K^+K^-$ both current-current and penguin operators contribute; (f) in $B \rightarrow D^0\bar{D}^0$ the contributions from the $(\bar{b}u)(\bar{u}d)$ and the $(\bar{b}c)(\bar{c}d)$ current-current operators (proportional to the phase γ) tend to cancel.

SUSY contributes to the decay amplitudes with phases induced by δ_{13} and δ_{23} which are denoted as ϕ_{13} and ϕ_{23} . The ratio A_{SUSY}/A_{SM} for SUSY masses of 250 GeV/ c^2 is reported in the r_{250} column of Table 13-4.

Some conclusions can be drawn from the results of Table 13-4. In the Standard Model, the first six decays measure directly the mixing phase β , up to corrections which, in most of the cases, are expected to be small. These corrections, due to the presence of two amplitudes contributing with different phases, produce uncertainties of $\sim 10\%$ in $B^0 \rightarrow K_s^0\pi^0$, and of $\sim 30\%$ in $B^0 \rightarrow D^+D^-$ and $B^0 \rightarrow J/\psi\pi^0$. In spite of the uncertainties, however, there are cases where the SUSY contribution gives rise to significant changes. For example, for SUSY masses of order 250 GeV/ c^2 , SUSY corrections can shift the measured value of the sine of the phase in $B^0 \rightarrow \phi K_s^0$ and in $B^0 \rightarrow K_s^0\pi^0$ decays by about 70%. For these decays SUSY effects are sizeable even for masses of 500 GeV/ c^2 . In $B^0 \rightarrow J/\psi K_s^0$ and $B^0 \rightarrow \phi\pi^0$ decays, SUSY effects are only about 10%, but Standard Model uncertainties are negligible. In $B^0 \rightarrow K^0\bar{K}^0$ the larger effect, $\sim 20\%$, is partially covered by the uncertainty of about 10% already existing in the Standard Model. Moreover, the rate for this channel is expected to be rather small. In $B^0 \rightarrow D^+D^-$ and $B^0 \rightarrow K^+K^-$, SUSY effects are completely obscured by the uncertainties in the estimates of the Standard Model amplitudes. In $B^0 \rightarrow D_{CP}^0\pi^0$ the asymmetry is sensitive to the mixing angle ϕ_M only, since the decay amplitude is unaffected by SUSY. This result can be used in connection with $B^0 \rightarrow K_s^0\pi^0$, since a difference in the measure of the phase is a manifestation of SUSY effects.

Turning to $B \rightarrow \pi\pi$ decays, both the uncertainties in the Standard Model and the SUSY contributions are very large. Here three independent amplitudes with different phases and of comparable size contribute. The observation of SUSY effects in the $\pi^0\pi^0$ case is hopeless. The possibility of separating SM and SUSY contributions by using the isospin analysis remains an open possibility which deserves further investigation. For a thorough discussion of the Standard Model uncertainties in $B \rightarrow \pi\pi$, see Ref. [84, 85].

In conclusion, the measurements of CP asymmetries in several channels may allow the extraction of the CP mixing phase and to disentangle Standard Model and SUSY contributions to the CP decay phase. The gold-plated decays in this respect are the $B \rightarrow \phi K_s^0$ and $B \rightarrow K_s^0\pi^0$ channels. The size of the SUSY effects is clearly controlled by the nondiagonal SUSY mass insertions δ_{ij}^d , which for illustration are assumed to have the maximal value compatible with the present experimental limits on $B_d^0-\bar{B}_d^0$ mixing.

Table 13-4. Branching ratios and CP phases for B decays. ϕ_{SM}^D denotes the decay phase in the Standard Model; T and P denote Tree and Penguin, respectively; for each channel, when two amplitudes with different weak phases are present, one is given in the first row, the other in the last one and the ratio of the two in the r_{SM} column. ϕ_{SUSY}^D denotes the phase of the SUSY amplitude, and the ratio of the SUSY to Standard Model contributions is given in the r_{250} column.

Incl.	Excl.	$\mathcal{B} \times 10^5$	ϕ_{SM}^D	r_{SM}	ϕ_{SUSY}^D	r_{250}
$b \rightarrow c\bar{c}s$	$B^0 \rightarrow J/\psi K_S^0$	40	0	–	ϕ_{23}	0.03 – 0.1
$b \rightarrow s\bar{s}s$	$B \rightarrow \phi K_S^0$	0.6 – 2	0	–	ϕ_{23}	0.4 – 0.7
$b \rightarrow u\bar{u}s$	$B \rightarrow \pi^0 K_S^0$	0.02 – 0.4	P 0	0.01 – 0.08	ϕ_{23}	0.4 – 0.7
$b \rightarrow d\bar{d}s$			T γ			
$b \rightarrow c\bar{u}d$	$B \rightarrow D_{CP}^0 \pi^0$	16	0	0.02	–	–
$b \rightarrow u\bar{c}d$			γ			
$b \rightarrow c\bar{c}d$	$B \rightarrow D^+ D^-$	30 – 50	T 0	0.03 – 0.3	ϕ_{13}	0.007 – 0.02
	$B \rightarrow J/\psi \pi^0$	2	P β	0.04 – 0.3		0.007 – 0.03
$b \rightarrow s\bar{s}d$	$B \rightarrow \phi \pi^0$	$1 - 4 \times 10^{-4}$	P β	–	ϕ_{13}	0.06 – 0.1
	$B \rightarrow K^0 \bar{K}^0$	0.007 – 0.3	u-P γ	0 – 0.07		0.08 – 0.2
$b \rightarrow u\bar{u}d$	$B \rightarrow \pi^+ \pi^-$	0.2 – 2	T γ	0.09 – 0.9	ϕ_{13}	0.02 – 0.8
$b \rightarrow d\bar{d}d$	$B \rightarrow \pi^0 \pi^0$	0.003 – 0.09	P β	0.6 – 6	ϕ_{13}	0.06 – 0.4
$b\bar{d} \rightarrow q\bar{q}$	$B \rightarrow K^+ K^-$	< 0.5	T γ	0.2 – 0.4	ϕ_{13}	0.04 – 0.1
	$B \rightarrow D^0 \bar{D}^0$	< 20	P β	only β		0.01 – 0.03

13.5 Models with Extra Scalars

The Higgs sector of the Standard Model, which has a single Higgs doublet, has not yet been experimentally tested. The possibility of an extended Higgs sector is certainly consistent with experimental data. The simplest extensions are models with several Higgs doublets; these all contain charged scalars. Below the general Multi-Higgs-Doublet Model (MHDM), and its simplest version, the Two-Higgs-Doublet Model (2HDM), will be discussed. More details can be found in *e.g.*, [86, 87].

Many models beyond the Standard Model have an extended Higgs sector. Often such models deviate from the Standard Model in other sectors too. Nevertheless, most studies of charged scalar effects are confined to the simplest cases, where no other new physics beside the extended Higgs sector is introduced. One has to keep in mind, however, that bounds on the Higgs-sector parameters, which are obtained from processes where the charged scalars are virtual, may be evaded due to cancellation from other new phenomena related to other sectors of a particular model.

13.5.1 The General MHDM

There are two major constraints on any extension of the Higgs sector of the Standard Model. First, it is an experimental fact that $\rho = m_W^2/(m_Z^2 \cos^2 \theta_W)$ is very close to 1 [88]. It is known [86] that in a model with only Higgs doublets, the tree-level value of $\rho = 1$ is automatic without adjustment of any parameters in the model, whereas models with Higgs particles in larger, higher multiplets do not maintain this relationship. Second, there are strong experimental limits on flavor-changing neutral currents (FCNC). In the Standard Model, tree-level FCNC are absent because fermion mass matrices and Higgs-fermion couplings are simultaneously diagonalized. In general, this ceases to be true in a model with a nonminimal Higgs sector. An elegant way to avoid this problem is based on a theorem by Glashow and Weinberg [89] called Natural Flavor Conservation (NFC): tree-level FCNC mediated by Higgs bosons will be absent if all fermions of a given electric charge couple to no more than one Higgs doublet. This can be achieved by imposing extra symmetries. With such symmetries, the Higgs couplings to fermions are constrained but not unique. There are five possibilities to couple the Higgs doublets to the known three types of massive fermions (up-type quarks, down-type quarks, and charged leptons). Summary of these possibilities is given in Table 13-5. For *Model III* at least three Higgs doublets are needed, for *Model I* one is enough, while for the other models two are sufficient. It does, of course, make a difference if the number of Higgs doublets is larger than the minimal one.

For a general MHDM the Yukawa interactions are given by

$$\mathcal{L}_Y = \overline{Q}_{L_i} F_{ij}^D \Phi_d D_{R_j} + \overline{Q}_{L_i} F_{ij}^U \tilde{\Phi}_u U_{R_j} + \overline{L}_{L_i} F_{ij}^E \Phi_e E_{R_j} + \text{h.c.} \quad (13.57)$$

Table 13-5. Summary of all the possibilities of MHDM. The numbers in the table show which Higgs doublet couples to which fermion type.

	Model				
	<i>I</i>	<i>I'</i>	<i>II</i>	<i>II'</i>	<i>III</i>
d (down-type quarks)	1	1	1	1	1
u (up-type quarks)	1	1	2	2	2
e (charged leptons)	1	2	1	2	3

Where left-handed quark doublets are denoted by Q_{L_i} , and left-handed lepton doublets by L_{L_i} . Right-handed quark singlets are denoted by D_{R_i} and U_{R_i} , and right handed charged lepton singlets by E_{R_i} . The sub-index i is a generation index ($i = 1, 2, 3$). Higgs doublets are denoted by Φ_j (where j runs from 1 to n , the number of Higgs doublets), and $\tilde{\Phi}_j = i\sigma_2\Phi_j^*$. Sub-indices d , u and e denote the Higgs doublet that couples to the down-type quarks, up-type quarks, and charged leptons, respectively. F^U and F^D are general 3×3 Yukawa matrices and one can choose a basis where one of them is real and diagonal. For massless neutrinos, F^E can be chosen real and diagonal.

In a general MHDM, with n Higgs doublets, there are $2n$ charged and $2n$ neutral scalar fields. After spontaneous symmetry breaking two charged fields and one neutral field become the would-be Goldstone boson “eaten” by the W^\pm and the Z in order to acquire their masses, and $2(n - 1)$ charged and $2n - 1$ neutral scalars are left as physical particles. The Yukawa interaction of the physical charged scalars with fermion mass eigenstates is given by [90]

$$\mathcal{L}_Y^\pm = (2\sqrt{2}G_F)^{1/2} \sum_{i=2}^n (X_i \bar{U}_L V M_D D_R + Y_i \bar{U}_R M_U V D_L + Z_i \bar{N}_L M_E E_R) H_i^+ + \text{h.c.} \quad (13.58)$$

M_D , M_U , and M_E are the diagonal mass matrices of down-type quarks, up-type quarks, and charged leptons, respectively. H_i^+ denotes the positively charged physical scalars. Left-handed neutrino fields are denoted by N_L , and the CKM matrix by V . X_i , Y_i and Z_i are complex coupling constants that arise from the mixing matrix for charged scalars. An important feature of the charged scalar-fermion interactions is that they are proportional to the fermion masses. Hence, effects are stronger in processes involving heavy fermions, real or virtual.

There are relations between X_i , Y_i , and Z_i [87]. However, as long as the charged scalars are not degenerate, and as far as the coupling to fermions are concerned, already for 4HDM, these relations are not relevant. Consequently, in order to exploit the most general MHDM, one usually assumes that one of the charged scalars is much lighter than the others and that all the heavy charged scalars effectively decouple from the fermions. Then, there is effectively only the single light charged scalar, and the sub-indices of H_i , X_i , Y_i , and Z_i can be dropped. Thus, in this model there are

several new parameters: the mass of the lightest charged scalar, m_H , and the coupling constants, X , Y , and Z . These couplings are arbitrary complex numbers. There are, of course, bounds on the values of these parameters obtained (mainly) from low-energy data: neutral meson mixing, rare K and B decays, Z boson interactions, and CP -violating effects. These bounds are summarized in [87].

When imposing NFC, within the framework of MHDM, CP violation could arise in charged scalar exchange if there are at least three Higgs doublets [91]. In principle, CP violation may be explicit or spontaneous. The requirement of spontaneous CP violation forces $\delta_{KM} = 0$ [92]. In this case, CP non-invariance arises solely from charged scalar exchange. However, experimental data on the neutron electric dipole moment and $b \rightarrow s\gamma$ exclude this possibility [93, 27]. On the other hand, explicit CP violation is allowed where CP violation can arise from both charged scalar exchange and W^\pm exchange. In both cases, CP violation in the Higgs sector is manifest in phases that appear in the combinations XY^* , XZ^* , and YZ^* . Note that some of the charged scalars must be nondegenerate for CP violation to arise from the Higgs sector [94].

13.5.2 B Physics Implications

The presence of a charged Higgs boson can affect several B physics observables. Many rare decays can be significantly enhanced, sometimes by more than an order of magnitude. A detailed discussion can be found in [87]. The possible implication for CP asymmetries is discussed below.

In the multi-scalar framework, because the charged-Higgs couplings are proportional to the Yukawa couplings, the charged Higgs effect on tree-level decays is very small and can be neglected. The B – \bar{B} mixing amplitude receives extra contributions from box diagrams, where one or two of the W 's are replaced by the charged Higgs. Thus, the mixing phase is affected by the new charged-scalar exchange phase through the mixing dependence on $\text{Im}(XY^*)$. Thus, in principle, large deviations from the Standard Model prediction are possible. However, the upper bound on $\mathcal{B}(b \rightarrow s\gamma)$ constrains the shift in the mixing phase to be small (< 0.02) [27].

The effect on penguin amplitudes can be much larger. Due to the large top-quark mass, the charged Higgs-top loop can generate a large contribution. The bound on $\text{Im}(XY^*)$ from $\mathcal{B}(b \rightarrow s\gamma)$ implies that this new contribution is below the 10% level for the amplitude in $B^0 \rightarrow J/\psi K_s^0$ [95]. (Since the relevant hadronic matrix elements are not known, this effect can only be estimated.) However, the effect on decays, which are dominated by penguins in the Standard Model, can be much larger, up to $\mathcal{O}(1)$. Therefore, MHDMs can have detectable signals, for example, that the CP asymmetry in $B^0 \rightarrow J/\psi K_s^0$ is not equal to the one in $B^0 \rightarrow \phi K_s^0$.

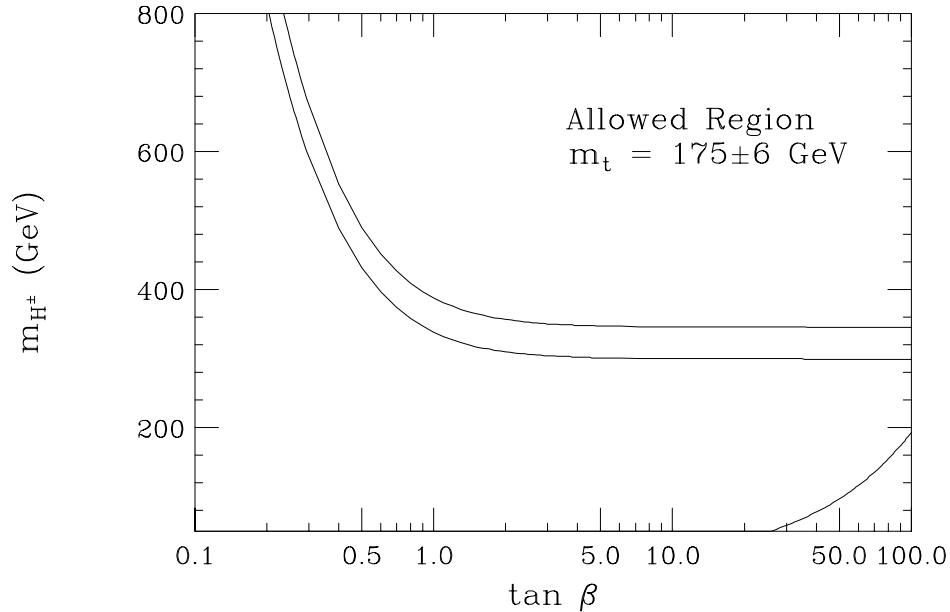


Figure 13-4. Constraints in the charged Higgs mass- $\tan \beta$ plane from the CLEO bound on $\mathcal{B}(B \rightarrow X_s \gamma)$. The excluded region is that to the left and below the curves. The top (bottom) line corresponds to $m_t^{\text{phys}} = 181(169)$ GeV/ c^2 . Also displayed is the restriction $\tan \beta/m_{H^\pm} > 0.52$ GeV $^{-1}$, which arises from measurements of $B \rightarrow X \tau \nu$ as discussed in [97].

13.5.3 2HDM

Model II of 2HDM has been widely discussed in the literature because it is the simplest version of MHDM and because this version is realized in the Higgs sector of the MSSM. In 2HDM, there are only two parameters in the charged Higgs sector, m_H and $\tan \beta$ where

$$Z = X = \tan \beta, \quad Y = \cot \beta, \quad \tan \beta = \frac{v_u}{v_d}. \quad (13.59)$$

where v_u (v_d) is the vacuum expectation value of the doublet that couples to the up- (down-) type quarks.

The main differences between the general MHDM and the 2HDM are (i) In 2HDM there is no CP violation in the Higgs sector, and (ii) The bound on the charged scalar mass from $b \rightarrow s \gamma$ is larger, $m_H \gtrsim 260$ GeV/ c^2 [96] as shown in Fig. 13-4. The second difference is due to the fact that $XY = 1$ in 2HDM. Thus, due to its large mass and real couplings, the potential effects of the charged scalar in 2HDM are limited.

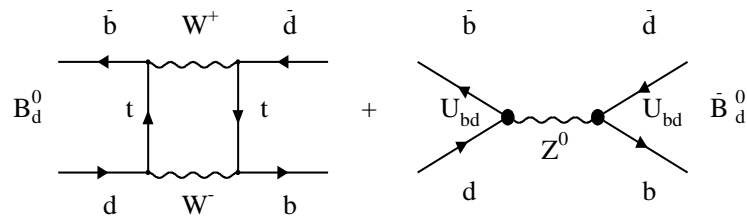


Figure 13-5. Standard Model and Z -mediated FCNC diagrams for $B_d^0 - \bar{B}_d^0$ mixing.

13.6 Models with Additional Quarks

13.6.1 Isosinglet Quarks

There are many extensions of the Standard Model, where additional fermions with nonstandard $SU(2) \otimes U(1)$ assignments naturally occur. This is the case, for example, of the grand-unified theory (GUT) based on E_6 , where each fermion family forms a $\underline{27}$ representation of E_6 , which contains, apart from the 15 standard chiral fermions, a vector-like isosinglet quark of charge $-1/3$, a vector-like doublet of leptons, and two extra neutrinos. We designate as vector-like, fermions whose left-handed and right-handed components transform in the same way under the Standard Model gauge group. The 27 representation of E_6 is a subgroup of the E_8 of the heterotic string. In other models, extra fermion representations beyond the usual Standard Model representations are needed and also contain isosinglet down quarks [98, 99]. Models with isosinglet up quarks are rarer, but the phenomenology of such quarks in D mesons is striking. For definiteness, we will concentrate here on a model where a $Q = -1/3$ vector-like isosinglet quark is added to the Standard Model.

Apart from the fact that isosinglet quarks naturally arise within an E_6 GUT, their addition to the Standard Model provides a simple solution [100] to the strong CP problem [101], through the Barr-Nelson mechanism [102]. At a more phenomenological level, models with isosinglet quarks provide the simplest self-consistent framework to study deviations of unitarity of the CKM matrix as well as flavor-changing neutral currents. We will show that the presence of FCNC can have an important impact on the value of CP asymmetries in neutral B -meson decays. In the isosinglet down-quark models, the zero weak isospin leads to flavor changing neutral currents when quarks of the same charge mix. For extra down quarks the FCNC of $b \rightarrow d$ and $b \rightarrow s$ lead to $B_d^0 - \bar{B}_d^0$ and $B_s^0 - \bar{B}_s^0$ mixing, respectively, at tree level. These processes are shown in Fig. 13-5 along with a Standard Model mixing diagram. Similar diagrams for $d \rightarrow s$ also contribute to $K^0 - \bar{K}^0$ mixing.

One can analyze the predominant effects of such additional quarks by truncating the mixing to include just the single new quark that mixes the most, giving a 3×4 charged-current quark-mixing

matrix V [98, 99, 103, 104]. Since V is not unitary, there is also a nontrivial neutral current mixing matrix, denoted as U .

For the four-down-quark model, the 3×4 mixing matrix depends on six mixing angles and three phases, as does the mixing matrix [105] for four full generations (although such matrices are different for more than four quarks [99, 103]). In this type of model, FCNC and deviations from 3×3 unitarity are closely related and both are naturally suppressed because of the large mass of the additional quark. Indeed taking into account the order of magnitude of the mass terms, one can readily show that

$$V_{4i} = \mathcal{O}(m/M) \quad (13.60)$$

where M is the mass of the fourth mass eigenstate and m represents the relevant lighter down-quark mass, which implies, for the flavor-changing Z couplings,

$$U_{ij} = \mathcal{O}(m^2/M^2). \quad (13.61)$$

The Z flavor-changing couplings that are relevant to the neutral B , B_s , and K systems are, $-U_{db} = V_{4d}^* V_{4b}$, $-U_{bs} = V_{4b}^* V_{4s}$, and $-U_{sd} = V_{4s}^* V_{4d}$, respectively. When the mixing matrix is parameterized by extending the standard parameterization of the CKM matrix to a fourth quark, the leading order terms in the new angles and phases for U_{db} are

$$U_{db} = -s_{34}(s_{34}V_{td}^* + s_{14}e^{-i\delta_{14}} - s_{24}e^{i\delta_{24}}s_{12}), \quad (13.62)$$

where $V_{td} = (s_{12}s_{23} - s_{13}e^{i\delta_{13}})$, $V_{ub} = s_{13}e^{-\delta_{13}}$, $V_{cD} = s_{24}e^{-i\delta_{24}}$, and $V_{uD} = s_{14}e^{-i\delta_{14}}$, where D is the isosinglet down quark. In Section 13.2 a model-independent analysis to search for such non-Standard-Model contributions to the mixing was presented.

Analyses have been performed with constraints on the V elements and on the FCNC U s from all relevant charged current, neutral current, FCNC, and mixing experiments [106]. These analyses allow small but sufficient values for the elements of U so that the Z -mediated FCNC diagram can contribute significantly to the phases in $B_d^0-\bar{B}_d^0$ and $B_s^0-\bar{B}_s^0$ mixing, as well as to the $\sin\gamma$ experiments [98, 99, 103, 104, 107, 108]. The allowed range in the $(a_{J/\psi K_S^0}, a_{\pi\pi})$ plane is the entire plane for the four-down-quark model, as contrasted with the Standard Model, where the allowed range is $0.3 < \sin 2\beta < 0.9$ (see Chapter 14 for the Standard Model constraints). Experiments aiming to measure $\sin\gamma$ may find any value between -1 and $+1$ as opposed to the allowed range of $0.3 < \sin\gamma < 1$ of the Standard Model. In the $\rho - \eta$ plane, defined now as the location of $V_{ub}^*/|V_{cb}V_{cd}|$, negative η is allowed so that the allowed region in the four-down-quark model is an annulus about the origin. The zero values of η occur when the new phases δ_{14} or δ_{24} are providing the CP violation found in K decays.

While these models lead to unitarity quadrangles (or higher polygons), the restrictions from prior data require that the fourth side is less than a tenth of the base, making study of the sides of the triangle a difficult way to isolate this model. The phases or angles measured in CP violation experiments give much more dramatic changes from Standard Model effects.

13.6.2 Fourth Generation

While it is known that there are only three species of light neutrinos, this does not rule out the possibility of a fourth sequential generation with a very massive neutrino flavor. If a fourth generation (FG) exists it may be of significant importance in B physics as well as other low-energy processes. Its precise impact is difficult to evaluate in all generality, since there is a significant increase in the number of free parameters in comparison to the three-generation case. In addition to the masses of the b' and t' quarks, the 4×4 CKM mixing matrix has six angles and three phases. One indication for the existence of the fourth generation in B physics would be the lack of closure of the unitarity triangle [109]; with a fourth generation the unitarity triangle becomes a unitarity quadrangle. However, if the magnitudes of the additional CKM elements are small it may be difficult to distinguish a quadrangle with one small side from the conventional triangle.

In order to gauge the impact of a fourth generation it is necessary to have some constraints on the new parameters. In almost all cases, the fourth generation leptons play essentially no role in low-energy physics provided they are associated with their own conserved lepton number. The fourth generation possibility remains in agreement with precision electroweak measurements [110] and direct searches as long as: the neutrino mass is greater than one-half the Z mass; the mass splitting between the t' and b' is $\leq 100\text{--}130 \text{ GeV}/c^2$; and the masses of the charged fourth generation fermions are above the LEP-II production threshold, *i.e.*, $m_{FG} \geq 85 \text{ GeV}/c^2$ [111]. Assuming no other new physics sources, measurements of the ratio $R_b = \Gamma(Z \rightarrow b\bar{b})/\Gamma(Z \rightarrow \text{hadrons})$ at LEP and SLD also provide correlated information about the t' mass and two of the CKM elements. The reasonable agreement of the most recent data with the expectations of the three-generation Standard Model implies that

$$1 \approx |V_{tb}|^2 + |V_{t'b}|^2 (m_{t'}/m_t)^2. \quad (13.63)$$

Searches at hadron colliders (assuming $m_{t'} > m_{b'}$) have excluded a light b' with a mass below $\simeq 105 \text{ GeV}/c^2$ via its flavor-changing decay mode [112] and, except for conspiratorial possibilities [113], strongly indicate that $m_{t'} > m_t \simeq 175 \text{ GeV}/c^2$. The masses of the fourth-generation quarks are also constrained from above by requiring that scattering amplitudes (such as those associated with elastic $t't'$ scattering through Z and Higgs exchange) satisfy perturbative unitarity [114], which leads to the constraint $m_{t',b'} \leq 500 \text{ GeV}/c^2$. Analyses of the strength of the fourth-generation-fermion Higgs-Yukawa coupling would lead to similar, perhaps somewhat stronger yet more model dependent, constraints [115]. Summarizing, it would thus appear that $m_{b',t'}$ must lie in the ranges $105 < m_{b'} < 500 \text{ GeV}/c^2$ and $175 < m_{t'} < 500 \text{ GeV}/c^2$ subject to the additional constraint that $|m_{t'} - m_{b'}| \leq 100 - 130 \text{ GeV}/c^2$. One must also be careful of the fourth-generation-fermion contributions to the oblique parameters in electroweak precision measurements.

If there is a fourth generation, present knowledge of the CKM matrix, even its conventional 3×3 submatrix, becomes compromised. As is emphasized by the PDG [88], many of the constraints on the CKM elements arise from the assumed unitarity of the 3×3 matrix. Recall that only the

magnitudes of the elements $V_{ij}, i < j = 3$ have been *directly* measured and that almost all our remaining knowledge of the CKM elements is inferred from loop-induced processes such as ϵ_K as well as $B-\bar{B}$ and $K-\bar{K}$ mixing. Fortunately, some clarification of the value of $|V_{tb}|$ will occur when the cross-section for single top production is measured during the next Tevatron run.

In the B system, in addition to the failure of the triangle to close, the fourth generation opens up a number of intriguing possibilities which arise from new weak-scale contributions to the Wilson coefficients, $C_i(M_W)$, of the operators that control the B decay Hamiltonian which originate from penguin and box graphs. In the three-generation Standard Model, t -quark loops are by far the largest contributors to these coefficients, but significant t' contributions are also possible. For example, for the rare processes $b \rightarrow s/d \gamma$, $b \rightarrow s/d g$, $b \rightarrow s/d \ell^+ \ell^-$ and $b \rightarrow s/d \nu \bar{\nu}$, the augmentation of the values of the operator coefficients at the weak scale due to fourth generation contributions takes the form

$$C_i(M_W) \simeq V_{tb} V_{ts,d}^* F_i(x_t) + V_{t'b} V_{t's,d}^* F_i(x_{t'}), \quad (13.64)$$

where the F_i are standard Inami-Lim functions and as usual $x_{t,t'} = m_{t,t'}^2/M_W^2$. In addition to obvious rate and distribution modifications that can arise from these new terms, they are also seen to provide new sources for CP violation since there are now two large contributions to the C_i with different CKM phases. For example, in the three-generation Standard Model, the expected size of CP violation in $b \rightarrow s \gamma$ is of the order of 1% since the charm penguin contribution is mass suppressed. If a fourth generation exists, this CP violation can be significantly larger than 10%.

In the three-generation Standard Model, and in many new physics scenarios (*e.g.*, charged Higgs bosons), the ratio of the amount of $B_s-\bar{B}_s$ and $B_d-\bar{B}_d$ mixing directly yields the ratio of CKM elements $|V_{ts}/V_{td}|$ up to an overall ‘ $SU(3)$ ’-violating factor ξ , which can be estimated, *e.g.*, from lattice calculations. If a fourth generation is present, this direct connection is lost and one obtains

$$\frac{\Delta M_s}{\Delta M_d} = \xi \frac{\sum_{ij} \eta_{ij} V_{ib}^* V_{is} V_{jb} V_{js}^* G(x_i, x_j)}{\sum_{ij} \eta_{ij} V_{ib}^* V_{id} V_{jb} V_{jd}^* G(x_i, x_j)}, \quad (13.65)$$

where η_{ij} are QCD correction factors and $G(x_i, x_j)$ are known box functions, and the sum extends over both t and t' . Neglecting the t' the conventional result is recovered. An immediate implication of this expression is that the range of values expected for the parameter x_s in the three-generation Standard Model, $10 \leq x_s \leq 30$ [116], would be significantly extended. Other measures of the ratio $|V_{ts}/V_{td}|$ are also affected; *e.g.*, even if one neglects long-distance corrections, the ratio of the $b \rightarrow d \gamma$ to $b \rightarrow s \gamma$ branching fractions would no longer provide direct information on the CKM matrix elements. This follows immediately from the expression above for the Wilson coefficients, C_i . The rates for both $K^+ \rightarrow \pi^+ \nu \bar{\nu}$ and the CP -violating process $K_L^0 \rightarrow \pi^0 \nu \bar{\nu}$ [117] can be significantly modified (in either direction) by fourth generation contributions. Again, this prevents one from directly extracting information on V_{td} .

Fourth-generation effects may also be observable in the D system due to the rather large mass of the b' quark. Processes that are conventionally long-distance dominated in the three-generation

Standard Model would become short-distance dominated and enhanced. Some examples [118] include $D-\bar{D}$ mixing, $D \rightarrow \mu^+\mu^-$, and radiative D decays, which would be dominated by b' boxes and penguins, and might occur with rates close to the current experimental bounds. Given the complexity of B physics in the presence of a fourth generation, data from the D and K systems would be necessary to unravel its detailed nature.

13.7 Left-Right Symmetric Model

The Left-Right Symmetric Model (LRM) [119], which is based on the extended gauge group $SU(2)_L \times SU(2)_R \times U(1)$, can lead to interesting new effects in the B system [120]. Due to the extended gauge structure there are both new neutral and charged gauge bosons, Z' , W_R^\pm , in addition to those present in the Standard Model. In this scenario the left- (right-) handed fermions of the Standard Model are assigned to doublets under the $SU(2)_{L(R)}$ group. The Higgs fields which can directly generate Standard Model fermion masses are thus in *bi-doublet* representations, *i.e.*, they transform as doublets under both $SU(2)$ groups. The LRM is quite robust and possesses a large number of free parameters which play an interdependent role in the calculation of observables and in the existing constraints on the model resulting from various experiments.

As far as B physics and the subsequent discussion are concerned there are several parameters of direct interest; the structure and spontaneous symmetry breaking of the extended gauge sector accounts for a reasonable number of these. The most obvious free parameter is the ratio of the $SU(2)_R$ and $SU(2)_L$ gauge couplings $0.55 < \kappa = g_R/g_L \leq 2$. Whereas g_L is directly related to e as usual through $\sin^2 \theta_W$, g_R is unconstrained except through the definition of electric charge and naturalness arguments; GUT embedding scenarios generally suggest that $\kappa \leq 1$. The extended gauge symmetry is broken in two stages. First the $SU(2)_L \times SU(2)_R \times U(1)$ symmetry is broken down to the Standard Model via the action of Higgs fields that transform either as doublets or triplets under $SU(2)_R$. This choice of Higgs representation determines both the mass relationship between the Z' and W_R (analogous to the condition that $\rho = 1$ in the Standard Model) as well as the nature of neutrino masses; in particular, the Higgs triplet choice allows for the implementation of the see-saw mechanism and yields a heavy right-handed neutrino. After complete symmetry breaking the resulting W_L-W_R mixing is described by two parameters, a real mixing angle, ϕ , and a phase, α . Note that it is usually $t_\phi = \tan \phi$ which appears in expressions directly related to observables. The additional phase, as always, can be a new source of CP violation. (However, in discussing processes in which the right-handed neutrinos do not participate, as is the case in B decays, this angle can be thought of as an overall phase of the right-handed CKM matrix, V_R , to be discussed below.) The mixing between W_L and W_R results in the mass eigenstates $W_{1,2}$, with a ratio of masses, $r = M_1^2/M_2^2$, (with $M_2 \simeq M_R$). In most models t_ϕ is naturally of order r or less in the large M_2 limit. Of course, W_1 is the state directly produced at both the Tevatron and LEP-II and is identical to the Standard Model W in the $\phi \rightarrow 0$ limit. Note that when ϕ is non-zero, W_1

no longer couples to a purely left-handed current. Of course, if a heavy right-handed neutrino is indeed realized, then the effective *leptonic* current coupling to W_1 remains purely left-handed as far as low-energy experiments are concerned. As is well-known, one of the strongest constraints on this model arises from polarized μ decay [121], which is trivial to satisfy in this case.

Additional parameters arise in the quark sector; in principle the effective mass matrices for the Standard Model fermions may be non-Hermitian implying that the two matrices involved in the bi-unitary transformation needed to diagonalize them will be unrelated. This means that the elements of the mixing matrix, V_R , appearing in the right-handed charged current for quarks will be *unrelated* to the corresponding elements of $V_L = V_{CKM}$. V_R will then involve three new angles as well as six additional phases all of which are *a priori* unknown parameters. Needless to say the additional phases can be a further source of CP violation. The possibility that V_L and V_R may be unrelated is often overlooked when considering the potential impact of the LRM on low-energy physics and there has been very little detailed exploration of this more general situation. Clearly as the elements of V_R are allowed to vary, the impact of the extended gauge sector on B physics will be greatly effected. There are many well-known constraints on the LRM: universality, the apparent observed unitarity of the CKM matrix, $B^0 - \bar{B}^0$ mixing, the $K_L^0 - K_S$ mass difference [122], and direct W' searches at the Tevatron [123]. They are quite sensitive to variations in V_R [124], but W_2 masses as low as $450 \text{ GeV}/c^2$ can be accommodated by the present data. To be safe, however, one generally assumes that $M_2 > 600 - 800 \text{ GeV}/c^2$, implying that the magnitude of t_ϕ is less than a few times 10^{-2} . A completely updated, detailed study of the possible structure of V_R has yet to be performed and is badly needed.

As a last point, it is important be reminded that the extended Higgs sector associated with both the breaking of the LRM group down to $U(1)_{em}$ and the complete generation of fermion masses may also have an important role to play in low-energy physics through both the existence of complex Yukawa and/or flavor-changing neutral current type couplings. However, this sector of the LRM is highly model dependent and is of course quite sensitive to the detailed nature of the fermion-mass-generation problem. For purposes of brevity and simplicity it will be ignored in the following discussion which will focus only on the effects associated with $W_{1,2}$ exchange.

The influence of the LRM may be felt in both tree- and loop-level processes in the B system. In particular, at the loop level the decays $b \rightarrow s\gamma$ and $b \rightarrow s\ell^+\ell^-$ [96, 125, 126] may arguably provide the cleanest environment for new physics searches since they are both reasonably well understood within the Standard Model given the potential complexity of strong-interaction dynamics. In the LRM, the decay $b \rightarrow s\gamma$ has been examined in some detail and many interesting features have been uncovered [127]. In particular it has been shown that left-right mixing terms associated with $t_\phi \neq 0$ can be enhanced by a helicity flip factor of $\sim m_t/m_b$ and can lead to significantly different predictions than the Standard Model, even when $V_L = V_R$ and W_2 is very heavy as can be seen from Fig. 13-6. Of course, given the large parameter space of the LRM, it is generally quite simple to satisfy the experimental constraints from both CLEO [128] and ALEPH [129], obtaining essentially the Standard Model result *without* being in the Standard Model limit of the

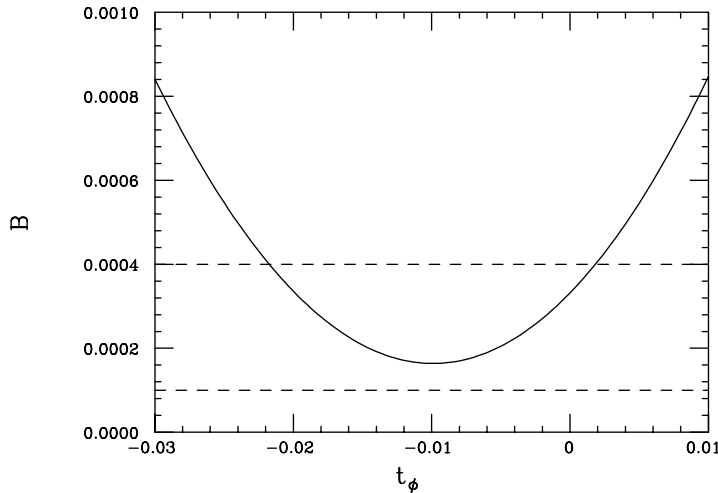


Figure 13-6. Prediction for the $b \rightarrow s\gamma$ branching fraction for $m_t(m_t) = 170 \text{ GeV}/c^2$ and $\kappa = 1$ as a function of $\tan \phi$ in the LRM at essentially NLO assuming $V_L = V_R$ and $M_2 = 1.6 \text{ TeV}/c^2$. The 95% CL allowed region from CLEO lies between the dashed lines.

theory. In this case observables associated with the decay $b \rightarrow s\ell^+\ell^-$ must be used to distinguish the LRM from the Standard Model. (Another possibility would be to measure the polarization of the photon.) One of the most important aspects associated with the $b \rightarrow s\ell^+\ell^-$ calculations is the extension of the complete operator basis in the Standard Model (10 operators) to a basis with 24 operators which form two independent subsets of 12 each which do not mix under renormalization. This generalization allows for both the obvious L \rightarrow R doubling as well as new operators with mixed helicity structures. In the LRM the decay $b \rightarrow s\gamma$ probes a combination of the operator coefficients $C_{7L,R}(\mu \sim m_b)$, while $b \rightarrow s\ell^+\ell^-$ probes $C_{7L,R}$, $C_{9L,R}$, and $C_{10L,R}$ at the same scale. Note that this extension of the operator basis implies that the conventional model-independent analysis of $b \rightarrow s\gamma$ and $b \rightarrow s\ell^+\ell^-$ by Hewett [96, 126] would *not* apply in this case and that the Standard Model expressions for the lepton spectrum and asymmetries would have to be augmented. The determination of the matching conditions for these 24 operators at the EW scale is far from trivial due to the very large number of free parameters and, in addition to new tree graphs, 116 one-loop graphs must also be calculated [130].

To show the power of the $b \rightarrow s\ell^+\ell^-$ decay mode in probing the LRM, Fig. 13-7 displays the predictions for both the lepton pair mass distribution and the leptonic forward-backward asymmetry of the Standard Model with five sample points of the LRM parameter space. These five points yield the *same* rate for the decay $b \rightarrow s\gamma$ as does the Standard Model and satisfy *all* other constraints, such as $K_L^0-K_S^0$ and $B^0-\bar{B}^0$ mixing, and the Tevatron searches. As can be seen from this figure, the give LRM predictions for $b \rightarrow s\ell^+\ell^-$ differ not only from the Standard Model but also from each other. Of course there is nothing unique about these five points since the volume of LRM parameter space satisfying the above constraints is quite large.

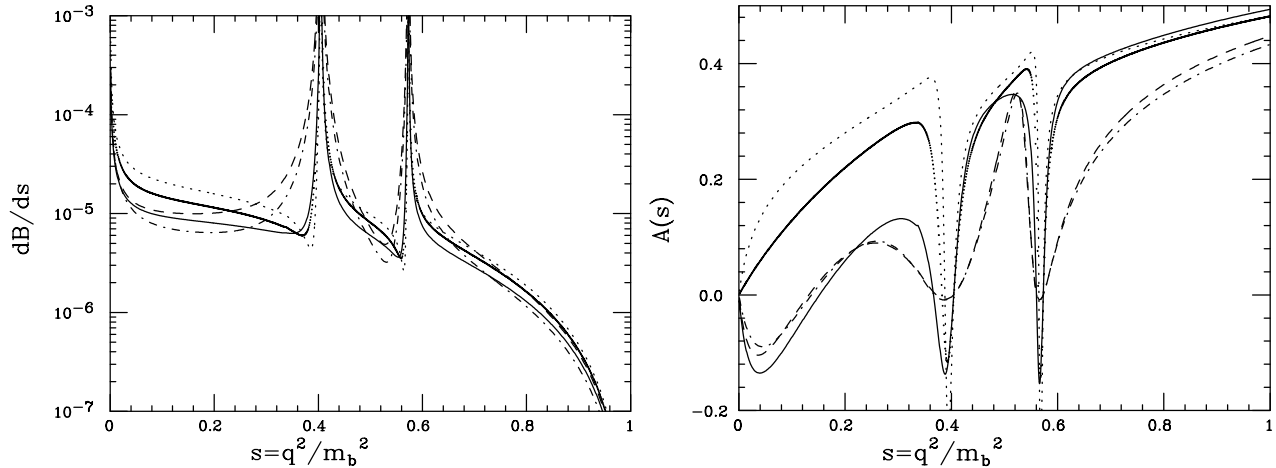


Figure 13-7. Differential decay distribution and lepton forward-backward asymmetry for the decay $b \rightarrow sl^+\ell^-$ in the Standard Model (solid) and four points in the LRM parameter space, which yield the Standard Model value for the $b \rightarrow s\gamma$ branching fraction and satisfy all other existing experimental constraints.

The possibility that the hadronic current describing the $b \rightarrow c$ transition has a large right-handed component has been a subject of discussion for some time [120, 131]. This right-handed piece need not originate from the LRM [132] though this is the most logical possibility. It is now known that this right-handed interaction cannot be dominant [133] or even of the same magnitude as the left-handed one. The L3 Collaboration [133], for example, measured both the lepton and missing energy spectra in semileptonic b decay and compared it with various theoretical predictions. Assuming a left-handed leptonic current, as in the LRM at low energies, both the $(V + A) \times (V - A)$ and $V \times (V - A)$ hypotheses were excluded indicating that the strength of the right-handed coupling was less than that for the left-handed coupling. However, no fit to the possible right-handed fraction was performed. Presently, the greatest sensitivity to the relative strength, $\xi = |\xi|e^{i\Delta}$, of the right-handed to the left-handed $b \rightarrow c$ coupling comes from the CLEO form factor analysis of the $B \rightarrow D^*l\nu$ decay [134] as well as the determination of the Λ_b polarization performed by ALEPH [135] and DELPHI [136].

A two-fold analysis of the CLEO data allowing for right-handed couplings has been performed [137]. In the first analysis the published CLEO measurements of the leptonic forward-backward asymmetry and the D^* polarization were combined with determinations of V_{cb} [138]. A simultaneous fit for the allowed values of $|\xi|$ and $\cos \Delta$ was then obtained with sample results shown in Fig.13-8 for the two HQET parameterizations [139]. Inclusion of the more recent unpublished data results in a somewhat smaller allowed region and leaves room for possible right-handed couplings, depending on which HQET functions are employed in the fit. In order to obtain increased sensitivity to right-handed currents, a second independent fit to the decay χ distribution was performed, where χ is the angle between the W^* and D^* event planes. This result strengthens the case for possible right-handed interactions and favors the same parameter space regime. It is

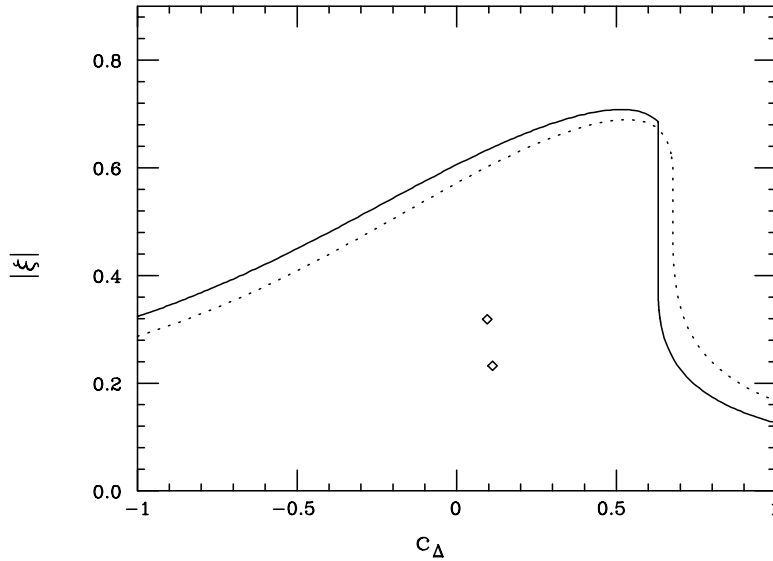


Figure 13-8. 95% CL allowed parameter space for the right-handed coupling strength as a function of $\cos \Delta$ obtained from a simultaneous fit to the published CLEO data using HQET. The solid (dotted) curve uses the Neubert (Close and Wambach) parameterization. The upper (lower) data point corresponds to the location of the χ^2 minimum for the Neubert (Close and Wambach) cases.

clear that all of these measurements need to be repeated with a simultaneous fit to the form factors for $B \rightarrow D^* l \nu$, allowing for right-handed currents.

It is interesting to note that the regions of $|\xi|$ and $\cos \Delta$ parameter space favored by the ALEPH [135] and DELPHI [136] measurements of the Λ_b polarization are in agreement [137] with those obtained in the above fits to CLEO data with central values near $|\xi| \simeq 0.3 - 0.4$ and $\cos \Delta \simeq 0.7 - 0.8$. It is also possible that these apparently anomalous Λ_b results simply reflect the rather poor understanding at present of the strong interaction [140, 141]. Future measurements may allow these two possibilities to be distinguished as has been discussed in Ref. [137]. If right-handed currents with these typical parameter values are indeed present, then CP -violating asymmetries of the order of 5% should be anticipated in the $B \rightarrow D^* l \nu$ channel.

If right-handed couplings do exist, they may play an important role in addressing the B semileptonic decay and charm counting problems [142] as suggested by Voloshin [120]. Given the parameter space allowed by the CLEO fit and using the LRM to complete the theoretical framework, an examination was made to determine if right-handed currents could significantly reduce the theoretical expectations [85, 143] for these quantities in comparison to the Standard Model. For values of the LRM parameters r and t of order 0.01 with $\kappa = 1$, a significant reduction in both the quantities B_ℓ and n_c were obtained in certain limited (or fine-tuned) parameter space regions. These results suggest that $(V_R)_{cb}$ is near unity. Interestingly, projecting the selected LRM

parameters back onto the $|\xi| - \cos \Delta$ space used in the CLEO/ALEPH/DELPHI analysis above results in a region consistent with the indications of right-handed couplings from those data sets near $|\xi| \simeq 0.35$ and $\cos \Delta \simeq 0.7$.

13.8 Models with Additional Strong Dynamics

The possibility that the mechanisms for Electroweak Symmetry Breaking (EWSB) and/or the generation of fermion masses involve new strong dynamics has a wide variety of consequences in flavor physics. In these scenarios, a mechanism for dynamical EWSB involves strong dynamics leading to the breaking of a global chiral symmetry and, as a consequence, the presence of at least three massless Goldstone bosons. In this minimal picture, these states are absorbed by the electroweak gauge bosons, giving rise to their longitudinal polarizations and to their masses m_W and m_Z . This is the basic idea in technicolor (TC) models [144] where, in analogy with QCD, a new gauge interaction among technifermions breaks the chiral symmetry giving rise to large technifermion masses as well as triggering EWSB. At this point, there appears to be little connection with flavor physics since the standard fermions remain massless. Although it is possible that the scale underlying fermion mass generation is much higher than the EWSB scale, it is necessary to communicate these two scales in such a way that EWSB turns on the actual fermion mass terms. For instance, this is the case in Extended Technicolor (ETC) models [145], where both technifermions and ordinary fermions transform under the ETC group, which breaks at some high-energy scale Λ_{ETC} down to technicolor and the Standard Model groups. The exchange of ETC gauge bosons between technifermions and ordinary fermions generates four-fermion interactions that turn into fermion mass terms when technifermion condensation takes place. On the other hand, ETC gauge boson exchange tends to give large FCNC effects. The experimental bounds from processes such as $K^0 - \bar{K}^0$ mixing imply that only very small quark masses of $\mathcal{O}(1)$ MeV/ c^2 could be generated if simple QCD-like dynamics applies to the ETC gauge interactions. Several solutions to this problem have been proposed, with the common feature being the appearance of a large anomalous dimension which enhances the value of fermion masses without the need for lower ETC scales. Such is the case in walking technicolor [146] and sub-critical amplification [147]. These models are relatively successful in generating the masses of the lighter two generations without conflict with FCNC. However, the generation of a large mass for the top quark remains problematic even in this modified ETC picture, requiring a rather low ETC mass scale and resulting in large effects, for instance in FCNC processes involving top-quark loops [148]. However, if most of the top mass is generated via top condensation [149], with the ETC-generated masses not larger than $\mathcal{O}(1)$ GeV/ c^2 , the problem is circumvented. This is the scenario in Topcolor-assisted Technicolor (TaTC) [150]: EWSB and small fermion masses are generated by TC/ETC, whereas the top-quark mass is dynamically generated via top condensation.

13.8.1 FCNC Effects in Topcolor-Assisted Technicolor

The basic Topcolor mechanism requires the spontaneous breaking of $SU(3)_1 \times SU(3)_2$ down to $SU(3)_c$ at an energy scale Λ . The $SU(3)_1$ interacts strongly with the third-generation quarks. After Topcolor breaking there is, in addition to the massless gluons, a remnant octet of massive, colored, vector particles, the top gluons. Their strong interaction with the third-generation quarks is above critical in the top direction, implying a non-zero $\langle \bar{t}_L t_R \rangle$, and thus generating a large top-quark mass dynamically. The top condensate breaks the top-quark chiral symmetry, which leads to the existence of a triplet of massless Goldstone modes, the top pions. Since EWSB is mostly due to techni-pion condensation, there will be a set of physical states π_t leftover after mixing with the techni-Goldstone-bosons. The physical top pions are then orthogonal to the states that are absorbed by the W and the Z . In addition, there is a scalar h_t (top Higgs), which together with top gluons and top pions constitute the minimal particle content of Topcolor models. The top-gluon masses are of order Λ , the top-Higgs mass is approximately $m_{h_t} \simeq 2m_t$, and the top pions acquire masses in the range of a few hundred GeV/c^2 from explicit ETC-quark masses [150].

In addition to this model-independent content, there will be other particles associated with important although model-dependent details. For example, in order to avoid b -quark condensation while having top condensation it may be necessary to introduce either additional gauge bosons or fermions. In the standard TaTC the isospin breaking is induced by introducing a $U(1)_1 \times U(1)_2$ interaction. As before, the third generation is strongly coupled to the $U(1)_1$. This group breaks down to $U(1)_Y$ at the scale Λ [150, 151], which implies the existence of a Z' with a mass at this high-energy scale. Although they are not strong enough to generate a large b -quark mass, the Topcolor interactions of the b are likely to lead to the presence of scalars and pseudoscalars, also with masses in the few hundred GeV/c^2 range. These “ b pions,” together with the top pions and the tree-level interactions of the Z' , lead to interesting phenomenological consequences in B physics.

The tree-level couplings of the Z' are non-universal and stronger with the third generation. When the quark fields are rotated to the mass eigenstate basis, flavor-changing neutral couplings of the Z' appear. Thus, Z' exchange induces tree-level transitions such as $B_q \rightarrow \ell^+ \ell^-$, $b \rightarrow q \ell^+ \ell^-$, $b \rightarrow q \bar{\nu} \nu$, with $q = (s, d)$. These and other effects of the Z' were studied in Refs. [151, 152]. Large deviations from the Standard Model are possible in $B_s \rightarrow \tau^+ \tau^-$, $b \rightarrow s \tau^+ \tau^-$ and $b \rightarrow s \bar{\nu} \nu$, due to the strong coupling of the Z' to the third generation leptons. Direct searches [153] as well as constraints from electroweak precision measurements [154] imply a lower bound of approximately $m_{Z'} > 1.50 \text{ TeV}/c^2$. However, even for these masses, the enhancements are generally of order one for the decays listed above, and in some cases even larger, depending on details of the model parameters. Thus, measurements of these branching ratios are of interest for such models.

The effects of scalars and pseudoscalars are mostly confined to one-loop contributions to the various FCNC vertices. However, in the case of the b pions, there is an important tree-level effect in $B^0 - \bar{B}^0$ mixing [155]. These scalar states, present if the Topcolor interaction couples strongly to b_R , lead to the flavor changing neutral vertex

$$\frac{m_t}{\sqrt{2}f_{\pi_t}} \phi_b \left\{ D_L^{bs*} \bar{s}_L b_R + D_R^{bs} \bar{b}_L s_R \right\}, \quad (13.66)$$

where ϕ_b stands for a scalar or pseudoscalar b pion, and $D_{L,R}^{bs}$ are the (b, s) elements of the rotations that diagonalize the left and right-handed down sectors. In TaTC, the top-pion decay constant is estimated to be $f_{\pi_t} \simeq (50 - 70)$ GeV [150], so the interaction in (13.66) is strong. More interestingly, it mediates tree-level $B^0 - \bar{B}^0$ mixing and translates into a stringent constraint on models generating the light masses and therefore the quark-rotation matrices [151, 156], which must produce a largely suppressed value of *either* D_L^{bs} or D_R^{bs} . The reason for this is that these two parameters always enter multiplicatively in mixing.

One-loop contributions of Topcolor scalars are generally more difficult to avoid since they tend to be additive. In addition to the b pions, the top pions couple strongly to b and t quarks, also with strength $m_t/\sqrt{2}f_{\pi_t}$. Thus, there are one-loop contributions to $b \rightarrow s$ transitions with a top quark and a top pion or a b pion in the loop. These are generally proportional to some linear combination of D_L^{bs} and D_R^{bs} . For instance, the potential effects in $b \rightarrow s\gamma$ were studied in [151], where it was found that agreement with the experimental measurement could be achieved for a large portion of the available parameter space. This is possible, in part due to cancellations between the top pion and b pion contributions. Although the situation is similar in $b \rightarrow s\ell^+\ell^-$ decays, the cancellations do not always occur for the same set of values of the parameters, implying that the combination of experimental observations of these two types of decay modes will be complementary in constraining Topcolor models.

It is possible to construct Topcolor models without the $U(1)$ groups, and therefore without a Z' . This is the case, for example, if the strong $SU(3)_1$ simply does not couple to b_R , thus making it unnecessary to use $U(1)$ couplings to have a sub-critical coupling to the b quark, while having a critical strength to generate m_t . In addition, in these scenarios there are no b pions. Several models along these lines have been considered [151, 157, 158]. In all cases, in order to cancel anomalies, a new set of fermions must be included. Also, it is necessary to couple more Standard Model quark doublets to $SU(3)_1$, which leads to the presence of additional scalar and pseudoscalar states. As a consequence, these realizations of Topcolor are already highly constrained by indirect observables. For instance, $D^0 - \bar{D}^0$ mixing [151] and the Z hadronic width and its width to charm R_c [158], tightly constrain most such models. It is, however, interesting to notice that none of these constraints decidedly rules out these scenarios. On the other hand, the absence of the b pions in these models, implies that there will be no cancellation of the top-pion contributions to $b \rightarrow s\gamma$ and $b \rightarrow s\ell^+\ell^-$. Thus, rare B processes are very sensitive to these scenarios. In general, the use of several processes in FCNC B decays will help to disentangle the more model-dependent details, and will begin to test more fundamental aspects of the Topcolor idea, such as the top-pion decay constant f_{π_t} , and its mass.

13.8.2 Model-Independent Analysis

The absence of a unified theoretical picture in strong dynamics scenarios, together with the difficulty in computation inherent to them, suggests the need for a more general analysis. One that may capture some of the essential aspects that might be present in the various, otherwise dissimilar, theories. For instance, it is possible that although the basic mechanism of technicolor theories may be correct, the dynamics might be very different from that usually assumed on the basis of QCD. The same can be said of mechanisms for generating fermion masses. Another possibility is that top condensation is the underlying mechanism for the generation of a large top-quark mass (and perhaps even EWSB) but the correct theory [159] has not yet been fully developed. In any case a model-independent analysis, when possible, provides a complementary alternative to model building.

The study of deviations from the Standard Model in a model-independent analysis requires the most general parametrization of the relevant interactions compatible with the Standard Model symmetries. The resulting effective interactions can be divided into interactions among the degrees of freedom of the EWSB sector, and those of fermions with the Standard Model gauge bosons. The effective Lagrangian involving the Goldstone bosons associated with the breaking of $SU(2)_L \times U(1)_Y$, as well as the transverse gauge bosons, resembles the chiral Lagrangian for the interactions of pions and photons in low-energy QCD [160]. The coefficient of the leading-order term, \mathcal{L}_0 , is associated with the masses of the W and the Z gauge bosons. The next-to-leading-order Lagrangian \mathcal{L}_1 receives contributions from extensions of the Standard Model. For instance, \mathcal{L}_1 gives contributions to the two-point functions entering in the electroweak parameters S , T , and U ; as well as to the three- and four-point functions, implying nonstandard self-interactions of the gauge bosons. Bounds on deviations from the Standard Model predictions for the triple-gauge boson vertices (TGV) [161] can be obtained from one-loop contributions to oblique electroweak parameters or directly via di-boson production at LEP-II and the Tevatron. Bounds from these sources [162] already constrain the $WW\gamma$ couplings κ_γ and λ_γ to values smaller than 1. Nonstandard TGV contribute to FCNC transitions [163] such as $b \rightarrow s\gamma$, $b \rightarrow d\gamma$, $b \rightarrow sl^+l^-$, $b \rightarrow dl^+\ell^-$, *etc.* For instance, the CLEO observation of $b \rightarrow s\gamma$ constrains κ_γ [164] and is competitive with the collider bounds. Future collider measurements might improve the bounds below the 10% level. However, current bounds allow for important effects in rare B decays, such as the dilepton modes, where also the W^+W^-Z couplings are tested.

On the other hand, it was recently shown that effects of \mathcal{L}_1 involving fermions were potentially observable if these belong to the third generation, despite the fact that \mathcal{L}_1 itself does not contain fermions. Among these, are one-loop vertex corrections that include internal gauge boson lines as well as an internal top-quark. These terms in the effective Lagrangian are not bound by electroweak precision observables, since these involve external fermions that are light compared to the weak scale. These new contributions can be regarded as nonstandard corrections to the longitudinal gauge-boson propagators, *i.e.*, the propagators of the electroweak Goldstone bosons. Their effects

were first considered in R_b and $B^0-\bar{B}^0$ mixing in Ref. [165]. However, FCNC processes such as $b \rightarrow sl^+\ell^-$, $b \rightarrow s\bar{\nu}\nu$ and $K \rightarrow \pi\bar{\nu}\nu$ were shown to be more sensitive to these terms in the effective Lagrangian [166]. For instance, enhancements of up to factors of two in the branching fractions of $b \rightarrow sl^+\ell^-$ processes, are allowed by the parameter space to which these terms are constrained by the experimental values of R_b , and B and K mixing.

Yet another distinct possibility is that the interactions of the electroweak gauge bosons with the Standard Model fermions are affected by new strong dynamics [167]. These effects have been considered in various forms and contexts in the literature. Considering only the third-generation quarks, the dimension-four operators parametrizing the nonstandard interactions with the gauge bosons are

$$\frac{g}{4c\theta_W}Z^\mu \left\{ \kappa_L^{NC}\bar{t}_L\gamma_\mu t_L + \kappa_R^{NC}\bar{t}_R\gamma_\mu t_R \right\} + \frac{g}{\sqrt{2}}W^\mu \left\{ \kappa_L^{CC}\bar{t}_L\gamma_\mu b_L + \kappa_R^{CC}\bar{t}_R\gamma_\mu b_R + \text{h.c.} \right\}, \quad (13.67)$$

where κ_L^{NC} , κ_R^{NC} , κ_L^{CC} , and κ_R^{CC} are couplings induced by new physics at the high-energy scale.³ They enter in one-loop-induced FCNC in rare B decays, such as $b \rightarrow s\gamma$ and $b \rightarrow sl^+\ell^-$. These couplings are constrained already by flavor-conserving electroweak measurements [168, 169]. In some cases the flavor-changing processes are the most constraining. For instance, the bound from Z decays is $\kappa_R^{CC} < 0.30$ [168], whereas the $b \rightarrow s\gamma$ constraint gives a bound that is better than 0.1 [170]. It is also possible to incorporate bounds on dimension-five operators, such as the electric and magnetic dipole moments of the top quark. A thorough analysis of the effects at the Z is carried out in Ref. [171]. Although these couplings are in principle of higher dimension, and therefore naively expected to be suppressed compared to dimension four operators, their effects may be the leading ones in some extensions of the Standard Model. The bounds from $b \rightarrow s$ transitions on the top magnetic dipole moment, for instance, are considered in Ref. [172].

Future measurements of FCNC processes in B and K decays will help to disentangle all the possible contributions to these transitions, and perhaps will give a first look at the nature of the new dynamics residing at much higher energies.

13.9 Summary

This chapter has reviewed only a small subset of the many theories that introduce particles and interactions beyond those of the Standard Model. In many cases significant differences between these models and Standard Model predictions are found. The patterns of these differences change from model to model. A summary of some of the effects is given in Table 13-6. As with all new measurements, data from BaBar can be used to constrain these models. Even when such data are also consistent with the Standard Model, this will not eliminate many of these theories,

³Additionally, one could consider similar neutral-current couplings for the b quark. However, these are highly constrained by direct measurements at the Z pole.

Table 13-6. *Model-dependent effects of new physics in various processes.*

Model	CP Violation		Rare Decays	$D^0-\bar{D}^0$ Mixing
	$B_d^0-\bar{B}_d^0$ Mixing	Decay Ampl.		
MSSM	$\mathcal{O}(20\%)$ SM Same Phase	No Effect	$B \rightarrow X_s \gamma$ – yes $B \rightarrow X_s l^+ l^-$ – no	No Effect
SUSY – Alignment	$\mathcal{O}(20\%)$ SM New Phases	$\mathcal{O}(1)$	Small Effect	Big Effect
SUSY – Approx. Universality	$\mathcal{O}(20\%)$ SM New Phases	$\mathcal{O}(1)$	No Effect	No Effect
R-Parity Violation	Can Do	Everything	Except Make	Coffee
MHDM	\sim SM/New Phases	Suppressed	$B \rightarrow X_s \gamma, B \rightarrow X_s \tau \tau$	Big Effect
2HDM	\sim SM/Same Phase	Suppressed	$B \rightarrow X_s \gamma$	No Effect
Quark Singlets	Yes/New Phases	Yes	Saturates Limits	$Q = 2/3$
Fourth Generation	\sim SM/New Phases	Yes	Saturates Limits	Big Effect
LRM – $V_L = V_R$	No Effect	No Effect	$B \rightarrow X_s \gamma, B \rightarrow X_s l^+ l^-$	No Effect
– $V_L \neq V_R$	Big/New Phases	Yes	$B \rightarrow X_s \gamma, B \rightarrow X_s l^+ l^-$	No Effect
DEWSB	Big/Same Phase	No Effect	$B \rightarrow X_s \ell \ell, B \rightarrow X - s \nu \bar{\nu}$	Big Effect

though in many cases further data may limit the available parameter space. In the more exciting eventuality that the results are not consistent with Standard Model predictions, the full pattern of the discrepancies both in rare decays and in CP -violating effects will help point to the preferred extension, and possibly rule out others. In either case there is much to be learned.

References

- [1] G. Steigman, *Ann. Rev. Astr. Ap.* **14**, 339 (1976).
- [2] A. Cohen, A. DeRujula and S. Glashow, *Astro. Phys. J.* **495**, 539 (1998).
- [3] E. Kolb and M. Turner, "The Early Universe," Addison-Wesley (1990).
- [4] A. Sakharov, *JETP Lett.* **5**, 24 (1967).
- [5] K. Olive, (1994) hep-ph/9404352.
- [6] M. Worah, *Phys. Rev. D* **53**, 3902 (1996).
- [7] M. Fukugita and T. Yanagida, *Phys. Lett. B* **174**, 45 (1986).
- [8] M. Luty, *Phys. Rev. D* **45**, 455 (1992).
- [9] W. Buchmuller and M. Plumacher, *Phys. Lett. B* **389**, 73 (1996).
- [10] V. Kuzmin, V. Rubakov and M. Shaposhnikov, *Phys. Lett. B* **155**, 36 (1985).
- [11] A. Cohen, D. Kaplan and A. Nelson, *Ann. Rev. Nucl. Part. Sci.* **43**, 27 (1993).
- [12] P. Huet and E. Sather, *Phys. Rev. D* **51**, 379 (1995).
- [13] A. Cohen, D. Kaplan and A. Nelson, *Phys. Lett. B* **263**, 86 (1991).
- [14] P. Huet and A. Nelson, *Phys. Rev. D* **53**, 4578 (1996).
- [15] M. Worah, *Phys. Rev. Lett.* **79**, 3810 (1997).
- [16] M. Carena *et al.*, *Nucl. Phys.* **B503**, 387 (1997).
- [17] Y. Nir and D. Silverman, *Nucl. Phys.* **B345**, 301 (1990).
- [18] C. O. Dib, D. London and Y. Nir, *Int. J. Mod. Phys. A* **6**, 1253 (1991);
T. Goto *et al.*, *Phys. Rev. D* **53**, 6662 (1996).
- [19] Y. Grossman and M. Worah, *Phys. Lett. B* **395**, 241 (1997).
- [20] J. M. Soares and L. Wolfenstein, *Phys. Rev. D* **47**, 1021 (1993).
- [21] N. G. Deshpande, B. Dutta and S. Oh, *Phys. Rev. Lett.* **77**, 4499 (1996).
- [22] J. P. Silva and L. Wolfenstein, *Phys. Rev. D* **55**, 5331 (1997).

- [23] A. G. Cohen *et al.*, *Phys. Rev. Lett.* **78**, 2300 (1997).
- [24] Y. Nir and H. R. Quinn, *Phys. Rev. D* **42**, 1473 (1990).
- [25] Y. Grossman, Y. Nir, and M. P. Worah, *Phys. Lett. B* **407**, 307 (1997).
- [26] Y. Nir and U. Sarid, *Phys. Rev. D* **47**, 2818 (1993).
- [27] Y. Grossman and Y. Nir, *Phys. Lett. B* **313**, 126 (1993).
- [28] C. O. Dib *et al.*, *Phys. Rev. D* **41**, 1522 (1990).
- [29] R. Barbieri, L. J. Hall and A. Romanino, *Phys. Lett. B* **401**, 47 (1997).
- [30] Y. Grossman *et al.*, *Nucl. Phys.* **B511**, 69 (1998).
- [31] Y. Grossman and H. R. Quinn, *Phys. Rev. D* **56**, 7259 (1997).
- [32] Y. Grossman, *Phys. Lett. B* **380**, 99 (1996).
- [33] M. Gronau, *Phys. Lett. B* **300**, 163 (1993).
- [34] H. Quinn, in Particle Data Book, *Phys. Rev. D* **54**, 507 (1996).
- [35] A. J. Buras, in *Proceedings of the 28th International Conference on High-energy Physics*, Warsaw, Poland (1996), hep-ph/9610461.
- [36] M. Gronau and D. London, *Phys. Lett. B* **253**, 483 (1991);
M. Gronau and D. Wyler, *Phys. Lett. B* **265**, 172 (1991);
I. Dunietz, *Phys. Lett. B* **270**, 75 (1991); *Phys. Rev. D* **52**, 3048 (1995).
- [37] M. Gronau and D. London, *Phys. Rev. D* **55**, 2845 (1997).
- [38] Y. Koide, *Phys. Rev. D* **40**, 1685 (1989).
- [39] Y. Grossman, G. Isidori and M. Worah, *Phys. Rev. D* **58**, 057504 (1998).
- [40] D. London and A. Soni, *Phys. Lett. B* **407**, 61 (1997).
- [41] R. Fleischer, *Phys. Lett. B* **341**, 205 (1994).
- [42] M. Ciuchini *et al.*, *Phys. Rev. Lett.* **79**, 978 (1997);
R. Barbieri and A. Strumia, *Nucl. Phys.* **B508**, 3 (1997).
- [43] T. E. Browder and K. Honscheid, *Prog. Part. Nucl. Phys.* **35**, 81 (1995).
- [44] Y. Grossman, J. Pelaéz and M. Worah, *Phys. Rev. D* **58**, 096009 (1998).

- [45] L. Randall and S. Su, MIT-CTP-2755, hep-ph/9807377.
- [46] Y. Grossman, Y. Nir and R. Rattazzi, (1997) hep-ph/9701231.
- [47] M. Dugan, B. Grinstein and L. J. Hall, *Nucl. Phys.* **B255**, 413 (1985).
- [48] S. Dimopoulos and S. Thomas, *Nucl. Phys.* **B465**, 23 (1996).
- [49] K. F. Smith *et al.*, *Phys. Lett. B* **234**, 191 (1990).
- [50] I. S. Altarev *et al.*, *Phys. Lett. B* **276**, 242 (1992).
- [51] W. Fischler, S. Paban and S. Thomas, *Phys. Lett. B* **289**, 373 (1992).
- [52] F. Gabbiani *et al.*, *Nucl. Phys.* **B477**, 321 (1996).
- [53] M. Dine *et al.*, *Phys. Rev. D* **53**, 2658 (1996).
- [54] M. Dine, A. Nelson and Y. Shirman, *Phys. Rev. D* **51**, 1362 (1995).
- [55] M. Dine, Y. Nir and Y. Shirman, *Phys. Rev. D* **55**, 1501 (1997).
- [56] S. Dimopoulos and H. Georgi, *Nucl. Phys.* **B193**, 150 (1981).
- [57] N. Sakai, *Z. Phys. C* **11**, 153 (1981).
- [58] A. Romanino and A. Strumia, *Nucl. Phys.* **B490**, 3 (1997).
- [59] S. Bertolini *et al.*, *Nucl. Phys.* **B353**, 591 (1991).
- [60] Y. Nir and N. Seiberg, *Phys. Lett. B* **309**, 337 (1993).
- [61] M. Leurer, Y. Nir and N. Seiberg, *Nucl. Phys.* **B420**, 468 (1994).
- [62] M. Dine, A. Kagan and R.G. Leigh, *Phys. Rev. D* **48**, 4269 (1993).
- [63] R. Barbieri *et al.*, *Nucl. Phys.* **B493**, 3 (1997).
- [64] Y. Nir and R. Rattazzi, *Phys. Lett. B* **382**, 363 (1996).
- [65] A. Pomarol and D. Tommasini, *Nucl. Phys.* **B466**, 3 (1996).
- [66] A. G. Cohen, D. B. Kaplan and A. E. Nelson, *Phys. Lett. B* **388**, 588 (1996).
- [67] M. N. Danielson *et al.*, in *Proceedings of New Directions for High-Energy Physics*, Snowmass, CO (1996), ed. D.G. Cassel *et al.*

- [68] C. S. Aulakh and R.N. Mohapatra, *Phys. Lett. B* **119**, 136 (1982);
I.-H. Lee, *Phys. Lett. B* **138**, 121 (1984); *Nucl. Phys.* **B246**, 120 (1984);
S. Dawson, *Nucl. Phys.* **B261**, 297 (1985);
G. Ross and J. Valle, *Phys. Lett. B* **151**, 375 (1985);
J. Ellis *et al.*, *Phys. Lett. B* **150**, 142 (1985);
R. N. Mohapatra, *Phys. Rev. D* **34**, 679 (1986);
S. Dimopoulos and L. J. Hall, *Phys. Lett. B* **207**, 210 (1987);
V. Barger, G. F. Giudice, and T. Han, *Phys. Rev. D* **40**, 2987 (1989);
D. E. Brahm, L. J. Hall, and S. Hsu, *Phys. Rev. D* **42**, 1860 (1990);
K. S. Babu and R. N. Mohapatra, *Phys. Rev. Lett.* **64**, 1705 (1990);
R. M. Godbole, P. Roy, and X. Tata, *Nucl. Phys.* **B401**, 67 (1993);
I. Hinchliffe and T. Kaeding, *Phys. Rev. D* **47**, 279 (1993);
K. S. Babu and R. N. Mohapatra, *Phys. Rev. Lett.* **75**, 2276 (1995);
A. S. Joshipura and M. Nowakowski, *Phys. Rev. D* **51**, 2421 (1995);
F. de Campos *et al.*, *Nucl. Phys.* **B451**, 3 (1995);
M. Hirsch, H. Klapdor-Kleingrothaus and S. Kovalenko, *Phys. Rev. Lett.* **75**, 17 (1995);
G. Bhattacharyya, J. Ellis and K. Sridhar, *Mod. Phys. Lett.* **A10**, 1583 (1995).
- [69] M. Leurer, Y. Nir and N. Seiberg, *Nucl. Phys.* **B398**, 319 (1993).
- [70] L. E. Ibañez and G. G. Ross, *Nucl. Phys.* **B368**, 3 (1992).
- [71] L. J. Hall and M. Suzuki, *Nucl. Phys.* **B231**, 419 (1984).
- [72] T. Banks *et al.*, *Phys. Rev. D* **52**, 5319 (1995).
- [73] A.Y. Smirnov and F. Vissani, *Nucl. Phys.* **B460**, 37 (1996);
R. Hempfling, *Nucl. Phys.* **B478**, 3 (1996);
B. de Carlos and P. L. White *Phys. Rev. D* **54**, 3427 (1996);
H. P. Nilles and N. Polonsky, *Nucl. Phys.* **B484**, 33 (1997).
- [74] E. Nardi, *Phys. Rev. D* **55**, 5772 (1997).
- [75] Y. Grossman and Y. Nir, *Nucl. Phys.* **B448**, 30 (1995).
- [76] V. Ben-Hamo and Y.Nir, *Phys. Lett. B* **339**, 77 (1994).
- [77] F. M. Borzumati *et al.*, *Phys. Lett. B* **384**, 123 (1996).
- [78] D. Guetta and E. Nardi, *Phys. Rev. D* **58**, 012001 (1998).
- [79] L. J. Hall, V.A. Kostelecky and S. Raby, *Nucl. Phys.* **B267**, 415 (1986).
- [80] M. J. Duncan, *Nucl. Phys.* **B221**, 285 (1983);
J. F. Donoghue, H. P. Nilles and D. Wyler, *Phys. Lett. B* **128**, 55 (1983);
A. Bouquet, J. Kaplan and C. A. Savoy, *Phys. Lett. B* **148**, 69 (1984).

- [81] F. Gabbiani and A. Masiero, *Nucl. Phys.* **B322**, 235 (1989);
J. S. Hagelin, S. Kelley and T. Tanaka, *Nucl. Phys.* **B415**, 293 (1994);
E. Gabrielli, A. Masiero and L. Silvestrini, *Phys. Lett. B* **374**, 80 (1996).
- [82] A. Ali, *Nucl. Instr. Methods* **A384**, 8 (1996).
- [83] M. Ciuchini *et al.*, *Z. Phys. C* **68**, 239 (1995).
- [84] M. Ciuchini *et al.*, *Nucl. Phys.* **B501**, 271 (1997); *Nucl. Phys.* **B512**, 3 (1998).
- [85] A. Lenz, U. Nierste and G. Ostermeyer, *Phys. Rev. D* **56**, 7228 (1997).
- [86] J. F. Gunion *et al.*, “The Higgs Hunter’s Guide,” Addison-Wesley Publishing Company, Reading, MA, (1990) and references therein.
- [87] Y. Grossman, *Nucl. Phys.* **B426**, 355 (1994).
- [88] C. Caso *et al.*, *Eur. Phys. Jour. C* **3**, 1 (1998).
- [89] S. L. Glashow and S. Weinberg, *Phys. Rev. D* **15**, 1958 (1977).
- [90] C. Albright, J. Smith and S.-H. H. Tye, *Phys. Rev. D* **21**, 711 (1980).
- [91] S. Weinberg, *Phys. Rev. Lett.* **37**, 657 (1976).
- [92] G. C. Branco, *Phys. Rev. Lett.* **44**, 504 (1980).
- [93] P. Krawczyk and S. Pokorski, *Nucl. Phys.* **B364**, 10 (1991).
- [94] S. Weinberg, *Phys. Rev. D* **42**, 860 (1990).
- [95] X-G. He, *Phys. Rev. D* **53**, 6326 (1996).
- [96] J. L. Hewett and J. D. Wells, *Phys. Rev. D* **55**, 5549 (1997).
- [97] P. Krawczyk and S. Pokorski, *Phys. Rev. Lett.* **60**, 182 (1988);
Y. Grossman, H. Haber, and Y. Nir, *Phys. Lett. B* **357**, 630 (1995).
- [98] F. del Aguila and J. Cortés, *Phys. Lett. B* **156**, 243 (1985);
M. Shin, M. Bander, and D. Silverman, *Phys. Lett. B* **219**, 381 (1989);
Y. Nir and D. Silverman, *Phys. Rev. D* **42**, 1477 (1990);
D. Silverman, *Phys. Rev. D* **45**, 1800 (1992).
- [99] G. C. Branco and L. Lavoura, *Nucl. Phys.* **B278**, 738 (1986).
- [100] L. Lavoura, (1996) hep-ph/9611268.
- [101] R. D. Peccei in “CP Violation,” ed. C. Jarlskog, World Scientific, Singapore (1989).

- [102] A. Nelson, *Phys. Lett. B* **136**, 387 (1984);
S. M. Barr, *Phys. Rev. Lett.* **53**, 329 (1984).
- [103] G. C. Branco *et al.*, *Phys. Rev. D* **48**, 1167 (1993);
G. Barenboim *et al.*, *Phys. Lett. B* **422**, 277 (1998).
- [104] W.-S. Choong and D. Silverman, *Phys. Rev. D* **49**, 1649 (1994);
D. Silverman, *Int. Jour. Mod. Phys. A***11**, 2253 (1996); *Phys. Rev. D* **58**, 095006 (1998).
- [105] F. J. Botella and L. L. Chau, *Phys. Lett. B* **168**, 97 (1986);
H. Harari and M. Leuler, *Phys. Lett. B* **181**, 123 (1986).
- [106] C. Albajar *et al.*, (UA1 Collaboration), *Phys. Lett. B* **262**, 163 (1991);
A. J. Buras and R. Fleischer, “Quark mixing, CP violation and rare decays after the top quark discovery,” to appear in *Heavy Flavours II*, eds. A. J. Buras and M. Lindner, Advanced Series on Directions in High Energy Physics, World Scientific (1997);
G. Barenboim and F. J. Botella, *Phys. Lett. B* **433**, 385 (1998);
Y. Grossman, Z. Ligeti and E. Nardi, *Nucl. Phys.* **B465**, 369 (1996); *Nucl. Phys.* **B480**, 753(E) (1996);
S. Abachi *et al.*, (D0 Collaboration), FERMILAB-CONF-96/253-E, presented at the 28th International Conference on High Energy Physics, Warsaw, Poland (1996);
Y. Grossman, Y. Nir and R. Rattazzi, “CP violation beyond the Standard Model,” in *Heavy Flavours II*, eds. A. J. Buras and M. Lindner, Advanced Series on Directions in High Energy Physics, World Scientific (1997), 755.
- [107] L. Lavoura and J. P. Silva, *Phys. Rev. D* **47**, 1117 (1993).
- [108] V. Barger, M. S. Berger and R. J. Phillips, *Phys. Rev. D* **52**, 1663 (1995).
- [109] Y. Nir and H. Quinn, in *B Decays*, edited by S. Stone, World Scientific, Singapore (1992).
- [110] G. Altarelli, R. Barbieri and F. Caravaglios, *Int. J. Mod. Phys. A***13**, 1031 (1988);
G. Altarelli, hep-ph/9710434.
- [111] Some general search review ????????
- [112] S. Abachi *et al.*, (D0 Collaboration), *Phys. Rev. Lett.* **78**, 3818 (1997).
- [113] M. Carena, H. E. Haber and C.E.M. Wagner, *Nucl. Phys.* **B472**, 55 (1996);
J. F. Gunion, D. W. McKay and H. Pois, *Phys. Lett. B* **344**, 339 (1994).
- [114] M. S. Chanowitz, M. A. Furman and I. Hinchliffe, *Nucl. Phys.* **B153**, 402 (1979).
- [115] S. K. Kang and G. T. Park, *Int. J. Mod. Phys. A***12**, 553 (1997);
S. K. Kang, *Phys. Rev. D* **54**, 7077 (1996).

- [116] F. Parodi, P. Roudeau and A. Siocchi, hep-ph/9802289.
- [117] T. Hattori, T. Hasuike and S. Wakaizumi, hep-ph/9804412.
- [118] J. L. Hewett in *Proceedings of the LAFEX International School on High Energy Physics (LISHEP95)*, Rio De Janiero, Brazil, February (1995);
G. Burdman *et al.*, *Phys. Rev. D* **52**, 6383 (1995).
- [119] R. N. Mohapatra, *Unification and Supersymmetry*, Springer, New York, (1986);
P. Langacker and S. U. Sankar, *Phys. Rev. D* **40**, 1569 (1989);
T. Hayashi, *Prog. Th. Phys.* **98**, 143 (1997).
- [120] The possibility of right-handed currents playing an important role in tree level B decays has been recently revived by M. B. Voloshin, *Mod. Phys. Lett. A* **12**, 1823 (1997) .
- [121] A. Jodiddo *et al.*, *Phys. Rev. D* **34**, 1967 (1986); *Phys. Rev. D* **37**, 237 (1988);
J. Imazoto, *et al.*, *Phys. Rev. Lett.* **69**, 877 (1992).
- [122] G. Beall, M. Bander, and A. Soni, *Phys. Rev. Lett.* **48**, 848 (1982).
- [123] F. Abe, *et al.*, (CDF Collaboration), *Phys. Rev. Lett.* **74**, 2900 (1995); *Phys. Rev. D* **55**, 5263 (1997) ;
S. Abachi, *et al.*, (D0 Collaboration), *Phys. Rev. Lett.* **76**, 3271 (1996);
B. Abbott, *et al.*, (D0 Collaboration), paper submitted to the XVIII International Symposium on Lepton Photon Interactions, Hamburg, Germany, July 28–August 1 (1997).
- [124] T. G. Rizzo, *Phys. Rev. D* **50**, 325 (1994).
- [125] For a survey of models and the restrictions imposed by the CLEO results on $b \rightarrow s\gamma$, see J. L. Hewett, “Top-Ten Models Constrained by $b \rightarrow s\gamma$,” (1994) hep-ph/9406302.
- [126] J. L. Hewett, *Phys. Rev. D* **53**, 4964 (1996);
A. J. Buras and M. Münz, *Phys. Rev. D* **52**, 186 (1995);
A. F. Falk, M. Luke and M. Savage, *Phys. Rev. D* **49**, 3367 (1994);
A. Ali and C. Greub, *Phys. Lett. B* **361**, 146 (1995);
C. Greub, T. Hurth and D. Wyler, *Phys. Lett. B* **380**, 385 (1996); *Phys. Rev. D* **54**, 3350 (1996); K. Chetyrkin, M. Misiak and M. Münz, *Phys. Lett. B* **400**, 206 (1997);
G. Buchalla, G. Isidori and S. J. Rey, *Nucl. Phys.* **B511**, 594 (1998);
C. Greub and T. Hurth, (1997) hep-ph/9704350 and hep-ph/9708214, and references therein.
- [127] D. Cocolicchio *et al.*, *Phys. Rev. D* **40**, 1477 (1989);
G. M. Asatryan and A. N. Ioannisyian, *Yad. Fiz.* **51**, 1350 (1990);
K. S. Babu, K. Fujikawa and A. Yamada, *Phys. Lett. B* **333**, 196 (1994);
P. Cho and M. Misiak, *Phys. Rev. D* **49**, 5894 (1994);

- T. G. Rizzo, *Phys. Rev. D* **50**, 3303 (1994) and (1997) hep-ph/9705209;
G. Bhattacharyya and A. Raychaudhuri, *Phys. Lett. B* **357**, 119 (1995).
- [128] M.S. Alam, *et al.*, (CLEO Collaboration), *Phys. Rev. Lett.* **74**, 2885 (1995).
- [129] R. Barate, (ALEPH Collaboration), *Phys. Lett. B* **429**, 169 (1998).
- [130] T.G. Rizzo, hep-ph/9705209 and hep-ph/9802401.
- [131] M. Gronau and S. Wakaizumi, *Phys. Rev. Lett.* **68**, 1814 (1992).
- [132] G.-H. Wu, K. Kiers and J. N. Ng, *Phys. Rev. D* **56**, 5413 (1997);
B. Grzadkowski and J. Wudka, *Phys. Lett. B* **364**, 46 (1995) and references therein.
- [133] M. Acciarri *et al.*, (L3 Collaboration), *Phys. Lett. B* **351**, 375 (1995).
- [134] J. E. Duboscq *et al.*, (CLEO Collaboration), *Phys. Rev. Lett.* **76**, 3898 (1996);
S. Sanghera *et al.*, (CLEO Collaboration), *Phys. Rev. D* **47**, 791 (1993);
M. Athanas *et al.*, (CLEO Collaboration), *Phys. Rev. Lett.* **79**, 2208 (1997);
H. Albrecht *et al.*, (ARGUS Collaboration) *Z. Phys. C* **57**, 533 (1993);
A. Anastassov *et al.*, (CLEO Collaboration), CLEO CONF 96-8, paper contributed to the
28th International Conference on High Energy Physics, Warsaw, Poland, 25–31 July (1996).
- [135] D. Buskulic *et al.*, (ALEPH Collaboration), *Phys. Lett. B* **365**, 367 (1996); *Phys. Lett. B* **365**,
437 (1996).
- [136] Newer, still unpublished results from both the ALEPH and DELPHI Collaborations confirm
and strengthen the earlier published low Λ_b polarization results. See P. Brückman in the
Proceedings of the 28th International Conference on High Energy Physics, eds. Z. Ajduk
and A.K. Wroblewski, World Scientific (1997), p. 910.
- [137] T.G. Rizzo, *Phys. Rev. D* **58**, 055009 (1998).
- [138] A. J. Buras, (1997) hep-ph/9711217.
- [139] M. Neubert, *Phys. Rev. D* **245**, 259 (1994);
F. E. Close and Wambach, *Phys. Lett. B* **348**, 207 (1995).
- [140] A. Falk and M. Peskin, *Phys. Rev. D* **49**, 3320 (1994);
F. Close *et al.*, *J. Phys.* **G18**, 1716 (1992).
- [141] V.A. Saleev, *Phys. Lett. B* **426**, 384 (1998).
- [142] I. Bigi *et al.*, *Phys. Lett. B* **323**, 408 (1994).

- [143] E. Bagan *et al.*, *Nucl. Phys.* **B432**, 3 (1994); *Phys. Lett. B* **342**, 362 (1995); *Phys. Lett. B* **351**, 546 (1995); *Phys. Lett. B* **374**, 363(E) (1996);
M. Neubert and C. T. Sachrajda, *Nucl. Phys.* **B483**, 339 (1997).
- [144] S. Weinberg, *Phys. Rev. D* **19**, 1277 (1979);
L. Susskind, *Phys. Rev. D* **20**, 2619 (1979).
- [145] S. Dimopoulos and L. Susskind, *Nucl. Phys.* **B155**, 237 (1980);
E. Eichten and K. Lane, *Phys. Lett. B* **90**, 125 (1980).
- [146] B. Holdom, *Phys. Rev. D* **24**, 1441 (1981); *Phys. Lett. B* **150**, 301 (1985);
K. Yamawaki, M. Bando and K. Matumoto, *Phys. Rev. Lett.* **56**, 1335 (1986);
T. Appellequist, D. Karabali and L.C.R. Wijewardhana, *Phys. Rev. Lett.* **57**, 957 (1986).
- [147] T. Appellequist *et al.*, *Phys. Lett. B* **220**, 223 (1989);
V.A. Miransky and K. Yamawaki, *Mod. Phys. Lett.* **A4**, 129 (1989).
- [148] L. Randall and R. Sundrum, *Phys. Lett. B* **312**, 148 (1993);
B. Grinstein, Y. Nir and J. Soares, *Phys. Rev. D* **48**, 3960 (1993).
- [149] W. Bardeen, C. T. Hill and M. Lindner, *Phys. Rev. D* **241**, 1647 (1990).
- [150] C. T. Hill, *Phys. Lett. B* **345**, 483 (1995).
- [151] G. Buchalla *et al.*, *Phys. Rev. D* **53**, 5185 (1996).
- [152] G. Burdman, *Phys. Rev. D* **52**, 6400 (1995).
- [153] K. Cheung and R. Harris, in *Proceedings of the 1996 DPF/DPB Summer Study, New Directions for High Energy Physics*, Snowmass, Colorado, June (1996), hep-ph/9610382.
- [154] R. S. Chivukula and J. Terning, *Phys. Lett. B* **385**, 209 (1996).
- [155] D. Komiris, *Phys. Lett. B* **358**, 312 (1995).
- [156] K. Lane, *Phys. Rev. D* **54**, 2204 (1996).
- [157] G. Burdman, in *Proceedings of the 1996 DPF/DPB Summer Study, New Directions for High Energy Physics*, Snowmass, Colorado, June (1996), hep-ph/9611265 .
- [158] G. Burdman and D. Komiris, *Phys. Lett. B* **403**, 101 (1997).
- [159] B. Dobrescu and C. T. Hill, FERMILAB-PUB-97-409/T, (1997), hep-ph/9712319.
- [160] A. Longhitano, *Phys. Rev. D* **22**, 1166 (1980); *Nucl. Phys.* **B188**, 118 (1981);
T. Appellequist and G. Wu, *Phys. Rev. D* **48**, 3235 (1993).

- [161] K. Hagiwara *et al.*, *Nucl. Phys.* **B282**, 253 (1987); *Phys. Lett. B* **283**, 353 (1992); *Phys. Rev. D* **48**, 2182 (1993).
- [162] B. Abbott *et al.*, (D0 Collaboration), contributed paper to the XVIII Symposium on Lepton-Photon Interactions. July 28–August 1, Hamburg, Germany. See also D. Ward, to appear in *Proceedings of the 1997 Meeting of European Physical Society*, Jerusalem, Israel (1997).
- [163] S. P. Chia, *Phys. Lett. B* **240**, 465 (1990);
K. A. Peterson, *Phys. Lett. B* **282**, 207 (1992);
K. Numata, *Z. Phys. C* **52**, 691 (1991);
T. G. Rizzo, *Phys. Lett. B* **315**, 471 (1993);
G. Baillie, *Z. Phys. C* **61**, 667 (1994).
- [164] S. Stone and S. Playfer, *Int. J. Mod. Phys. A* **10**, 4107 (1995).
- [165] J. Bernabéu *et al.*, *Phys. Rev. Lett.* **78**, 2902 (1997).
- [166] G. Burdman, *Phys. Lett. B* **409**, 443 (1997).
- [167] R. Peccei and X. Zhang, *Nucl. Phys.* **B337**, 269 (1990);
R. Peccei, S. Peris and X. Zhang, *Nucl. Phys.* **B349**, 305 (1991).
- [168] S. Dawson and G. Valencia, *Phys. Rev. D* **53**, 1721 (1996).
- [169] B. Dobrescu and J. Terning, *Phys. Lett. B* **416**, 129 (1998).
- [170] K. Fukikawa and A. Yamada, *Phys. Rev. D* **49**, 5890 (1994)
- [171] O.J.P. Éboli, M.C. Gonzalez-Garcia and S. F. Novaes, *Phys. Lett. B* **415**, 75 (1997).
- [172] J. L. Hewett and T. G. Rizzo, *Phys. Rev. D* **49**, 319 (1994).

This page was intentionally left blank.

Overall Determinations of the CKM Matrix

The goal of this chapter is to combine all the relevant measurements to constrain the CKM matrix. Fitting the four independent CKM parameters to all available measurements provides the most precise determination of these parameters. Moreover, the compatibility between the various measurements tests the CKM picture of quark mixing.

Of the four CKM parameters, one, $\lambda = |V_{us}|$, is known to an accuracy of 1%. The other three, which are less accurately known, are conventionally parameterized by either the Wolfenstein parameters $(A, \bar{\rho}, \bar{\eta})$ [see Eq. (1.88)], or by the set $(A, \sin 2\alpha, \sin 2\beta)$. The first set is simply related to moduli of various CKM combinations and is therefore convenient for presenting the existing constraints. The second set is simply related to CKM phases and will therefore be convenient for presenting future constraints from CP asymmetries in B decays.

The determination of the CKM parameters is complicated by theoretical uncertainties that enter the interpretation of the measurements. Section 14.1 describes the way that these uncertainties may be handled. Since the A parameter is better determined than the remaining two parameters, it is convenient to present the results of the fitting procedure in either the $(\bar{\rho}, \bar{\eta})$ plane or the $(\sin 2\alpha, \sin 2\beta)$ plane. Section 14.2 presents the individual constraints corresponding to relevant observables in the $(\bar{\rho}, \bar{\eta})$ plane and in the $(\sin 2\alpha, \sin 2\beta)$ plane.

The individual constraints define allowed regions in the two-parameter planes. However, combining them does not simply correspond to determining the overlap of the individual regions. One reason is that correlations between $\bar{\rho}$ and $\bar{\eta}$ appear when combining several measurements. A second, more subtle, reason is that the correlations with the third unknown parameter (A) are not taken into account. The situation is further complicated by the fact that theoretical parameters estimated by various means enter the calculation, and it is not clear how to handle the various estimates and their error. In statistical terms, no probability density can be assumed for these parameters. In Section 14.3 a method which avoids these problems and combines all the observables in a statistically meaningful way is proposed. The present knowledge of $(\bar{\rho}, \bar{\eta})$ and $(\sin 2\alpha, \sin 2\beta)$ is studied and then the impact of BABAR measurements under different scenarios is presented.

It may be found in the future, that no single choice of CKM parameters is consistent with all measurements. This would indicate that there is a contribution from physics beyond the Standard Model. In a wide variety of models, new physics affects only $B^0 \bar{B}^0$ mixing but not B decays. For these, a model-independent determination of the unitarity triangle can still be performed. This is discussed in the previous Chapter in Section 13.2, where it is explicitly shown that the contributions

to mixing from the Standard Model and those from the new physics can be disentangled. A serious obstacle in this analysis is an eight-fold ambiguity in determining the angles of the unitarity triangle from the CP asymmetries. Section 13.2 also explains how the eight-fold ambiguity may be reduced by performing additional measurements or by making additional assumptions on the nature of the new physics.

14.1 The Problem of Theoretical Uncertainties

Generally, theoretical uncertainties arise from limitations in the computations that relate the CKM parameters to the experimental observables. Sometimes calculations of limited accuracy are available. If these calculations are made in the framework of a systematic expansion, it is possible to estimate the magnitude of the error incurred in truncating the expansion. This error can be treated much as any systematic error.

Often, however, there is no reliable method of performing the necessary calculations. One then resorts to models, heuristic arguments and, on occasion, simply educated guesses. Not surprisingly such “theoretical predictions” span a range of values. How does one ascertain the error in the determination of CKM parameters when this type of theoretical guesswork is used? There is no easy answer. It is incorrect to quote the range of theoretical “predictions” as the theoretical error; however, this remains the most popular method (see, *e.g.*, the PDG value[1] for $|V_{ub}|$). In the absence of trustworthy calculations, it is most sensible to quote separately the extracted CKM value for each distinct “prediction” as presented in Section 14.3.

Eventually many, if not all, calculations of hadronic matrix elements will be carried out by simulations of QCD on the lattice. These will not be calculations of absolute precision, but will be controlled, in the same sense as any systematic expansion. Errors associated with statistical fluctuations, finite lattice size, and the extrapolation to the continuum can all be reliably estimated, much like truncation errors in a perturbative calculation. The one exception to the rule is in the errors associated with modeling QCD as some simplified theory, such as “quenched QCD.” Much like in the model calculations of the above paragraph, the errors associated with extrapolations between theories are uncontrolled.

14.2 Individual Constraints on the Unitarity Triangle

The unitarity of the CKM matrix gives the following relation:

$$V_{ud}V_{ub}^* + V_{cd}V_{cb}^* + V_{td}V_{tb}^* = 0. \quad (14.1)$$

The term “Unitarity Triangle” refers to a geometrical presentation of this relation in the complex plane, where the side corresponding to $V_{cd}V_{cb}^*$ is chosen real and rescaled to unit length. More details can be found in Chapter 1, but for our purposes it is convenient to collect some formulae here. In the extended Wolfenstein parametrization [2] [3]

$$\begin{aligned} V_{ud}V_{ub}^* &= A\lambda^3(\bar{\rho} + i\bar{\eta}), \\ V_{cd}V_{cb}^* &= -A\lambda^3, \\ V_{td}V_{tb}^* &= A\lambda^3(1 - \bar{\rho} - i\bar{\eta}). \end{aligned} \quad (14.2)$$

The apex of the unitarity triangle is located at $(\bar{\rho}, \bar{\eta})$. The sides are given by

$$R_u = \left| \frac{V_{ub}^*V_{ud}}{V_{cb}^*V_{cd}} \right| = \sqrt{\bar{\rho}^2 + \bar{\eta}^2}, \quad (14.3)$$

$$R_t = \left| \frac{V_{td}V_{tb}^*}{V_{cb}^*V_{cd}} \right| = \sqrt{(1 - \bar{\rho})^2 + \bar{\eta}^2}. \quad (14.4)$$

The relation between the $(\bar{\rho}, \bar{\eta})$ and $(\sin 2\alpha, \sin 2\beta)$ parameters is given by

$$\sin 2\alpha = \frac{2\bar{\eta}[\bar{\eta}^2 + \bar{\rho}(\bar{\rho} - 1)]}{[\bar{\eta}^2 + (1 - \bar{\rho})^2][\bar{\eta}^2 + \bar{\rho}^2]}, \quad \sin 2\beta = \frac{2\bar{\eta}(1 - \bar{\rho})}{\bar{\eta}^2 + (1 - \bar{\rho})^2}. \quad (14.5)$$

Note that a mapping of $\bar{\eta} \rightarrow -\bar{\eta}$ yields a mapping of $(\sin 2\alpha, \sin 2\beta) \rightarrow (-\sin 2\alpha, -\sin 2\beta)$. Thus, any observable that represents a region in the $(\bar{\rho}, \bar{\eta})$ plane that is symmetric with respect to the $\bar{\rho}$ axis, yields a region in the $(\sin 2\alpha, \sin 2\beta)$ plane that is symmetric with respect to the origin (see *e.g.*, $|V_{ub}/V_{cb}|$ and Δm_{B_d}).

In this section the constraints from individual measurements in the $(\bar{\rho}, \bar{\eta})$ plane and in the $(\sin 2\alpha, \sin 2\beta)$ plane are discussed. The method used for displaying the constraints is the following. Statistical errors, systematic uncertainties, and controlled theoretical uncertainties are added in quadrature and a 95% CL contour is determined. The remaining, uncontrolled theoretical uncertainties are treated by scanning the quantity over a reasonable range. The bounds presented in the following plots result from linearly adding these two uncertainties.

The measurements used in this section are summarized in Table 14-1. In this table, the experimental measurements have been separated from the model-dependent estimates of theoretical parameters. As stressed in the introduction, λ is already known to a high precision and will be considered as fixed. Extraction of the CKM parameters from the observables depends on a number of theoretical parameters which are somewhat uncertain and model-dependent. It also relies on a set of more “hidden” values believed to be known accurately and are considered as fixed. The values of other parameters used in this section are given in Table 14-2.

Table 14-1. Measured values of the CKM parameters and other observables that provide constraints on the apex of the unitarity triangle in the $(\bar{\rho}, \bar{\eta})$ plane, as well as on the A parameter. Theoretical uncertainties are marked with a *.

Observable	Process	Measurement
$ V_{ub}/V_{cb} $	$B \rightarrow X_u \ell \nu$	$0.08 \pm 0.005 \pm 0.02^*$ [1, 4]
$ V_{cb} $	$B \rightarrow D^* \ell \nu$	0.040 ± 0.002 [1]
λ	$K^+ \rightarrow \pi^0 e^+ \nu$	0.2205 ± 0.0018 [1]
Δm_{B_d}	$B_d - \bar{B}_d$ oscillations	$0.471 \pm 0.016 \text{ ps}^{-1}$ [5]
ϵ_K	CP violation in $K^0 - \bar{K}^0$ mixing	$(2.258 \pm 0.018) \times 10^{-3}$ [1]
Δm_{B_s}	$B_s - \bar{B}_s$ oscillations	$> 12.4 \text{ ps}^{-1}$ @ 95% CL [5]

Table 14-2. *Theoretical input parameters and other measured parameters.*

Variable	Value	Reference
QCD parameters		
η_B	0.55 ± 0.01	[10]
η_1	1.38 ± 0.2	[9]
η_2	0.57 ± 0.01	[10]
η_3	0.47 ± 0.04	[11]
Running Quark masses		
\overline{m}_t	$167 \pm 6 \text{ GeV}/c^2$	[7]
\overline{m}_b	$4.7 \pm 0.13 \text{ GeV}/c^2$	[7]
\overline{m}_c	$1.3 \pm 0.3 \text{ GeV}/c^2$	[8]
m_{B_d}	$5279.2 \text{ MeV}/c^2$	[8]
m_{B_s}	$5369.3 \text{ MeV}/c^2$	[8]
m_{K^0}	$497.7 \text{ MeV}/c^2$	[8]
Electroweak parameters		
$\alpha_s(m_Z)$	0.117 ± 0.005	[7]
$\alpha(m_Z)$	1/128	[1]
m_W	$80.41 \pm 0.1 \text{ GeV}/c^2$	[8]
$\sin^2 \theta_W$	0.23	[1]
B factors and decay constants		
B_K	0.6 – 1.0	[12]
$f_{B_d} \sqrt{B_{B_d}}$	160 – 240 MeV	[12]
$f_{B_s} \sqrt{B_{B_s}}$	200 – 280 MeV	[12]
ξ_s^2	1.12 – 1.48	[12]
Inami & Lim functions [13]		
$S_0(x_t)$	2.36	[13]
$S_0(x_t, x_c)$	2.31×10^{-3}	[13]
$S_0(x_c)$	2.62×10^{-4}	[13]

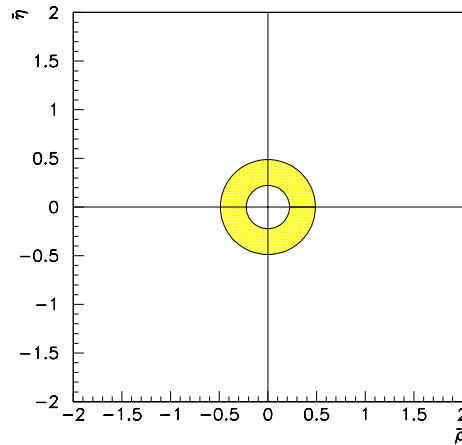


Figure 14-1. The $|V_{ub}/V_{cb}|$ constraint in the $(\bar{\rho}, \bar{\eta})$ plane. Experimental errors are treated statistically and the range of theoretical uncertainties is scanned (see text).

14.2.1 The $|V_{ub}/V_{cb}|$ Constraint

The measurement of $|V_{ub}/V_{cb}|$ constrains the length R_u of the unitarity triangle through Equation (14.3). The CKM matrix elements $|V_{ub}|$ and $|V_{cb}|$ are measured in semileptonic B decays using two independent methods (see Chapter 8). An endpoint analysis in inclusive semileptonic B decays yields a direct determination of $|V_{ub}/V_{cb}|$ [4], while measurements of branching fractions of exclusive final states such as $B \rightarrow (\pi, \rho)\ell\nu$ measure $|V_{ub}|$ [14]. For normalization, the world average of $|V_{cb}|$ measurements is used [1]. The model-dependence in either method is quite substantial but the final ranges are, however, in good agreement. The results of the inclusive analysis are used because the uncertainties are slightly smaller.

The $|V_{ub}/V_{cb}|$ measurement defines an annulus in the $(\bar{\rho}, \bar{\eta})$ plane centered at (0,0). Figure 14-1 shows the annulus obtained for the present experimental and theoretical uncertainties. The upper and lower contours are specified by $R_u^{max} + 1.96\sigma_{R_u}$ and $R_u^{min} - 1.96\sigma_{R_u}$, respectively. Here $R_u^{min} = 0.266$ and $R_u^{max} = 0.444$ represent the maximal and minimal bounds obtained from scanning the theoretical uncertainties and $\sigma_{R_u} = 0.022$ is the combined statistical and systematic error. The corresponding constraint in the $(\sin 2\alpha, \sin 2\beta)$ plane is shown in Figure 14-2. The shaded area represents the allowed region. The four “wings” at small $|\sin 2\beta|$ values result from mappings of small $\bar{\eta}$ values. Note that for $\bar{\rho} = 0$ one obtains $\sin 2\alpha = \sin 2\beta$.

It is expected that the theoretical uncertainties in $|V_{cb}|$ and $|V_{ub}|$ can be reduced to about 5% and 10%, respectively (see Chapter 8).

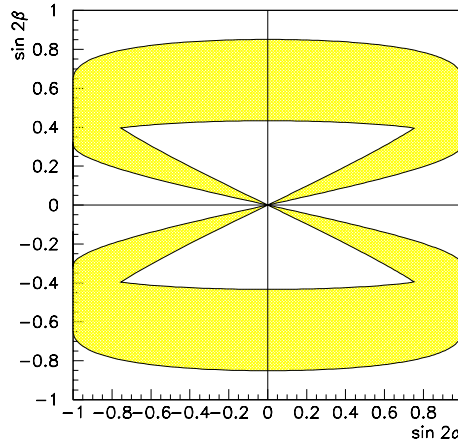


Figure 14-2. The $|V_{ub}/V_{cb}|$ constraint in the $(\sin 2\alpha, \sin 2\beta)$ plane.

14.2.2 The Δm_{B_d} Constraint

The measurement of $B_d - \bar{B}_d$ oscillations yields a determination of $|V_{td}V_{tb}^*|$ because of the dominance of the t quark in the electroweak loop. This in turn fixes the length R_t in the unitarity triangle through Equation (14.6). The oscillation frequency, which is given by the mass difference between the heavy and light B_d states, has been measured to be $\Delta m_{B_d} = 0.471 \pm 0.016 \text{ ps}^{-1}$. The prediction for Δm_{B_d} is obtained from the $\Delta B = 2$ effective Hamiltonian, yielding (see Chapter 11)

$$\Delta m_{B_d} = \frac{G_F^2}{6\pi^2} \eta_B m_{B_d} m_W^2 f_{B_d}^2 B_{B_d} S_0(x_t) |V_{td}V_{tb}^*|^2, \quad (14.6)$$

where G_F is the Fermi constant, η_B is a QCD correction factor calculated in NLO [10], m_{B_d} is the B_d^0 mass, m_W is the W mass, f_{B_d} is the B -decay constant, B_{B_d} parameterizes the value of the hadronic matrix element, the Inami-Lim function $S_0(x_t)$ [13] gives the electroweak loop contribution of the top quark without QCD corrections and $x_t = \bar{m}_t^2/m_W^2$. The numerical values of the theoretical input parameters are summarized in Table 14-2.

Note that $f_{B_d} \sqrt{B_{B_d}}$ has a theoretical uncertainty of 20% from systematic errors in the lattice calculations. Combined with the theoretical uncertainty in $|V_{cb}|$, this yields a rather large range for R_t despite the 3% combined experimental error. The central value for R_t is given by

$$R_t = 1.0 \times \left| \frac{0.04}{V_{cb}} \right| \left| \frac{V_{td}V_{tb}^*}{8.6 \times 10^{-3}} \right| \quad (14.7)$$

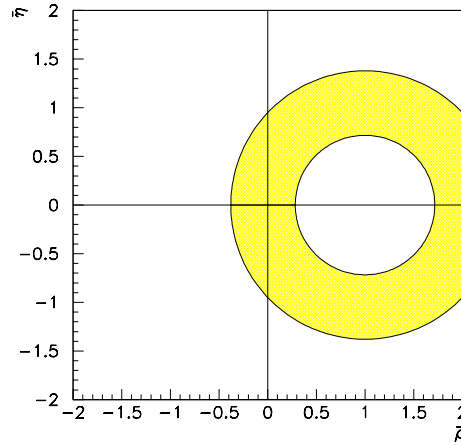


Figure 14-3. The Δm_{B_d} constraint in the $(\bar{\rho}, \bar{\eta})$ plane. Experimental errors are treated statistically and the range of theoretical uncertainties is scanned (see text).

where

$$|V_{td}V_{tb}^*| = 8.6 \times 10^{-3} \left[\frac{\Delta m_{B_d}}{0.471 \text{ ps}^{-1}} \right]^{\frac{1}{2}} \left[\frac{0.2 \text{ GeV}}{f_{B_d} \sqrt{B_{B_d}}} \right] \left[\frac{2.36}{S_0(x_t)} \right]^{\frac{1}{2}} \left[\frac{0.55}{\eta_B} \right]^{\frac{1}{2}}. \quad (14.8)$$

The Δm_{B_d} measurement defines an annulus centered at (1,0) in the $(\bar{\rho}, \bar{\eta})$ plane. The annulus obtained with the present uncertainties is plotted in Figure 14-3. The two bounds are specified by $R_t^{max} + 1.96\sigma_{R_t}$ and $R_t^{min} - 1.96\sigma_{R_t}$, where $R_t^{max} = 1.32$ and $R_t^{min} = 0.88$ are obtained from scanning the theoretical parameters within their uncertainties and $\sigma_{R_t} = 0.063$ represents the total experimental error. The corresponding region constrained in the $(\sin 2\alpha, \sin 2\beta)$ plane is shown in Figure 14-4, and is indicated by the shaded area. The bulk area results from mappings of $\bar{\rho} < 1$ points, while the arcs near (1,-1) and (-1,1) come from mappings of $\bar{\rho} > 1$ points.

The dominant theoretical uncertainty could be significantly reduced if f_{B_d} were determined directly through a measurement of $\mathcal{B}(B^+ \rightarrow \mu^+ \nu_\mu)$ with adequate precision. Since this is a $\bar{b} \rightarrow \bar{u}$ transition, which is also helicity-suppressed, the branching fraction is predicted to be $\sim 2 \times 10^{-7}$. Thus, the entire data set ever collected in BaBar will be needed to obtain an f_{B_d} measurement with better than 10% precision. The $B^+ \rightarrow \tau^+ \nu_\tau$ decay is enhanced by $(m_\tau/m_\mu)^2 \sim 250$ compared to the muonic channel, but this mode is experimentally much more difficult due to backgrounds and the presence of two or three ν s in the final state (see Chapter 11).

The CKM combination $|V_{td}V_{tb}^*|$ may be also obtained from Cabbibo suppressed electromagnetic penguin processes such as $B \rightarrow X_d \gamma$, $B \rightarrow X_d l^+ l^-$, or $B \rightarrow X_d \nu \bar{\nu}$. None of these modes is presently observed. See Chapter 9 for discussion of these modes.

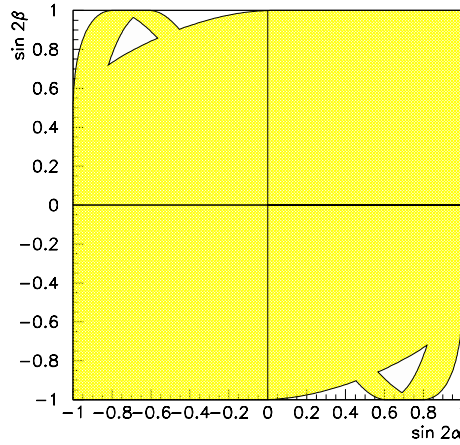


Figure 14-4. The Δm_{B_d} constraint in the $(\sin 2\alpha, \sin 2\beta)$ plane.

Another way of improving the determination of R_t is through a measurement of $B_s - \bar{B}_s$ oscillations,

$$R_t^2 = \xi_s^2 \frac{m_{B_s}}{m_{B_d}} \frac{\Delta m_{B_d}}{\Delta m_{B_s}} \frac{1 - \lambda^2(1 - 2\bar{\rho})}{\lambda^2}, \quad (14.9)$$

with

$$\xi_s = \frac{f_{B_s} \sqrt{B_{B_s}}}{f_{B_d} \sqrt{B_{B_d}}}. \quad (14.10)$$

The advantage of this determination over the one from Δm_{B_d} alone is, first, that the dependence on m_t and $|V_{cb}|$ has been eliminated and, second, that the ratio f_{B_s}/f_{B_d} can be more precisely determined than each decay constant itself. Lattice calculations give $\xi_s^2 = 1.30 \pm 0.18$ [12]. Presently only a lower limit on the oscillation frequency of $\Delta m_{B_s} > 12.4 \text{ps}^{-1}$ @ 95% CL has been obtained. This provides an upper bound of $|V_{td}/V_{ts}| < 0.25$ @ 95% CL, which can be translated into an upper bound for R_t , yielding

$$R_t < 0.92\xi_s. \quad (14.11)$$

This bound represents a circle centered at $(1,0)$ in the $(\bar{\rho}, \bar{\eta})$ plane, excluding all values outside. Once Δm_{B_s} has been measured, Equation (14.9) will specify an annulus. Finally, note that the LEP search for B_s oscillations yields more information than just the 95% CL limit used here. In Section 14.3.2.2 a more complete technique that uses this information is presented.

14.2.3 The ϵ_K Constraint

CP violation in $K^0\bar{K}^0$ mixing is described by the parameter ϵ_K ,

$$\epsilon_K = \frac{\exp(i\pi/4) \Im M_{12}}{\sqrt{2} \Delta m_K}, \quad (14.12)$$

where Δm_K is the $K_L^0 - K_S^0$ mass difference. The off-diagonal mass matrix element M_{12} is obtained from the $\Delta S = 2$ effective Hamiltonian with contributions from both the c quark and t quark in the electroweak loop, yielding

$$M_{12} = \frac{G_F^2}{12\pi^2} f_K^2 B_K m_K m_W^2 [\lambda_c^{*2} \eta_1 S_0(x_c) + \lambda_t^{*2} \eta_2 S_0(x_t) + 2\lambda_c^* \lambda_t^* \eta_3 S_0(x_c, x_t)] \quad (14.13)$$

where f_K is the kaon decay constant, m_K is the K^0 mass, η_1 [11], η_2 [10] and η_3 [11] are QCD correction factors calculated in NLO, $\lambda_q = V_{qd}V_{qs}^*$ for $q = c, t$ and $S_0(x_q)$ represent the electroweak loop contributions without QCD corrections. The main source of theoretical uncertainty comes from the B_K parameter, which parameterizes the value of the hadronic matrix element [15] [16] [17] [18] [19]. In order to represent the spread of the different calculations of B_K , values are taken to be in the range $B_K = 0.6 - 1.0$ (see Appendices C, D).

Using the unitarity relations $\Im \lambda_c = \Im \lambda_t$, and neglecting the factor $\Re \lambda_t / \Re \lambda_c \sim \mathcal{O}(\lambda^4)$ in the evaluation of $\Im(\lambda_c \lambda_t)$ one obtains

$$\epsilon_K = C_\epsilon B_K \Im \lambda_t \{ \Re \lambda_c [\eta_1 S_0(x_c) - \eta_3 S_0(x_c, x_t)] - \Re \lambda_t \eta_2 S_0(x_t) \} \exp(i\pi/4), \quad (14.14)$$

where all well-measured quantities have been combined in the numerical constant

$$C_\epsilon = \frac{G_F^2}{6\sqrt{2}\pi^2} \frac{f_K^2 m_K m_W^2}{\Delta m_K} = 3.78 \times 10^4. \quad (14.15)$$

Using $\Im \lambda_t = \bar{\eta} A^2 \lambda^5$, $\Re \lambda_c = -\lambda(1 - \frac{1}{2}\lambda^2)$, $\Re \lambda_t = (1 - \frac{1}{2}\lambda^2)A^2 \lambda^5(1 - \bar{\rho})$ and $V_{cb} = A\lambda^2$, one finds

$$\bar{\eta} \{ (1 - \bar{\rho}) \eta_2 S_0(x_t) |V_{cb}|^2 + \eta_3 S_0(x_c, x_t) - \eta_1 S_0(x_c) \} |V_{cb}|^2 B_K = 1.23 \times 10^{-6}. \quad (14.16)$$

This specifies a hyperbola in the $(\bar{\rho}, \bar{\eta})$ plane. Note that the error contribution from $|V_{cb}|$ is about as large as that from B_K because of the $|V_{cb}|^4$ dependence. Taking all uncertainties into account, two hyperbolic bands in the $(\bar{\rho}, \bar{\eta})$ plane are obtained as depicted in Figure 14-5. Depending on the choice of $|V_{cb}|$ and B_K , the hyperbolae have a singularity in the range $\bar{\rho} = 1.35 - 1.41$.

The corresponding region in the $(\sin 2\alpha, \sin 2\beta)$ plane is shown in Figure 14-6. The light-shaded area (a) is the allowed region obtained from the positive $\bar{\eta}$ values, while the dark-shaded area (b) results from the negative $\bar{\eta}$ values. The large negative $\bar{\rho}$ values from the hyperbola are mapped into

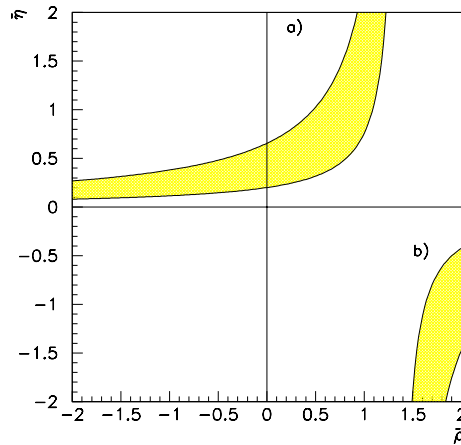


Figure 14-5. The $|\epsilon_K|$ constraint in the $(\bar{\rho}, \bar{\eta})$ plane. Experimental errors are treated statistically and the range of theoretical uncertainties is scanned (see text).

the “wing” at $(0,0)$, while $\bar{\rho}$ values between one and the singularity are mapped into the “wing” of large $\sin 2\alpha$ and negative $\sin 2\beta$ values. The tip of this “wing” would have extended to the origin if for practical reasons $\bar{\rho}$ had not been constrained to values below 1.25. Note that within the Standard Model, the measured sign of $\mathcal{R}e \epsilon_K$ implies that $\sin 2\beta$ is positive if $\bar{\rho}$ values are constrained to ≤ 1 .

14.2.4 The Status of ϵ'/ϵ

Direct CP violation in neutral kaon decays is described by the parameter ϵ' . The prediction yields [20]

$$\epsilon'/\epsilon = \mathcal{I}m \lambda_t F(x_t) = |V_{cb}|^2 \lambda \bar{\eta} F(x_t), \quad (14.17)$$

where $F(x_t)$ represents a sum of top-mass-dependent functions that also depend on $A_{\overline{MS}}$ and hadronic matrix elements, which in turn depend on the charm-quark mass and the strange-quark mass. Thus, the determination of $F(x_t)$ suffers from large theoretical uncertainties specifying a range of $0.85 \leq F(x_t) \leq 2.75$ [6, 21]. In addition, the present two measurements have large experimental errors and are barely consistent with each other:

$$\mathcal{R}e(\epsilon'/\epsilon) = (7.4 \pm 5.9) \times 10^{-4} \text{ (E731)[22]}, \quad (14.18)$$

$$\mathcal{R}e(\epsilon'/\epsilon) = (23 \pm 6.5) \times 10^{-4} \text{ (NA31)[23]}. \quad (14.19)$$

As is clear from Eq. (14.17), the ϵ'/ϵ measurement specifies a horizontal band in the $(\bar{\rho}, \bar{\eta})$ plane. However, given the very large theoretical uncertainties entering the calculations, no firm conclusion

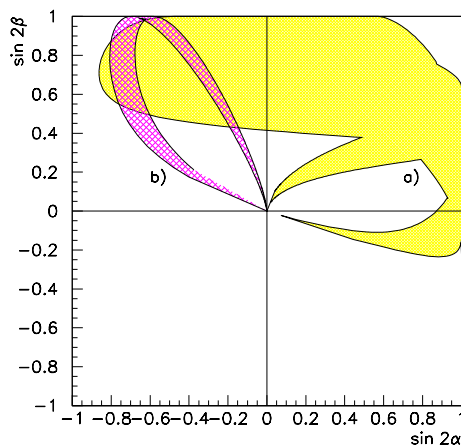


Figure 14-6. The $|\epsilon_K|$ constraint in the $(\sin 2\alpha, \sin 2\beta)$ plane. Regions (a) and (b) correspond to the two hyperbolic bands in Figure 14-5.

can presently be drawn on the unitarity triangle. Two new improved rounds of experiments have started to take data, so that improved results may be expected by the time BABAR starts taking data.

14.2.5 Impact of $K \rightarrow \pi\nu\bar{\nu}$ Decays

The rare kaon decays $K^+ \rightarrow \pi^+\nu\bar{\nu}$ [29] and $K_L \rightarrow \pi^0\nu\bar{\nu}$ [30] are theoretically very clean. Both modes are dominated by short-distance Z -penguins and box diagrams. While the neutral mode only has contributions from the top quark in the electroweak loop, the charged mode acquires additional sizable contributions from the charm quark. $K_L^0 \rightarrow \pi^0\bar{\nu}\nu$ proceeds almost exclusively via direct CP violation, allowing the cleanest determination of $\mathcal{I}m V_{ts}^*V_{td}$ and in turn, η . $K^+ \rightarrow \pi^+\nu\bar{\nu}$ is CP conserving and allows a clean determination of $|V_{td}V_{ts}^*|$. The present experimental bound $\mathcal{B}(K_L^0 \rightarrow \pi^0\nu\bar{\nu}) \leq 1.8 \times 10^{-6}$ [24] lies about five orders of magnitude above the Standard Model prediction [25] and about two orders of magnitude above the bound that can be deduced using model-independent isospin relations [26] from the experimental upper bound on the charged mode [27]. Significant constraints from the neutral mode can be expected only if a dedicated experiment is performed.

The branching fraction for $K^+ \rightarrow \pi^+\nu\bar{\nu}$ can be expressed in terms of $\bar{\rho}$ and $\bar{\eta}$ [7],

$$\mathcal{B}(K^+ \rightarrow \pi^+\nu\bar{\nu}) = 8.33 \times 10^{-6} |V_{cb}|^4 X(x_t)^2 \frac{(\sigma\bar{\eta})^2 + (\rho_0 - \bar{\rho})^2}{\sigma}, \quad (14.20)$$

where

$$\sigma = \left(1 - \frac{1}{2}\lambda^2\right)^{-2}, \quad \rho_0 = 1 + \frac{P_0(X)}{X(x_t)} \frac{\lambda^4}{|V_{cb}|^2}, \quad (14.21)$$

and $X(x_t)$ and $P_0(X)$ represent the electroweak loop contributions in NLO for the top quark and for the charm-quark contribution, respectively. The uncertainties in $X(x_t)$ due to scale-dependence and $\Lambda_{\overline{MS}}$ are about 1%, while $P_0(X)$ shows a strong dependence on both the renormalization scale μ_c and $\Lambda_{\overline{MS}}$. The range for $P_0(X)$, *i.e.*, $P_0(X) = 0.40 \pm 0.06$, leads to an overall theoretical uncertainty in the branching fraction of about 7%.

Equation (14.20) specifies an ellipse centered at $(\rho_0, 0)$ in the $(\bar{\rho}, \bar{\eta})$ plane with major axis $\bar{\rho}_1 = r_0$ and minor axis $\bar{\eta}_1 = r_0/\sigma$, where

$$r_0 = \frac{1}{|V_{cb}|^2 X(x_t)} \left[\sqrt{\frac{\sigma \mathcal{B}(K^+ \rightarrow \pi^+ \nu \bar{\nu})}{8.33 \times 10^{-6}}} \right]. \quad (14.22)$$

With present accuracy, $\sigma = 1$ is appropriate and Eq. (14.20) specifies a circle in the $(\bar{\rho}, \bar{\eta})$ plane.¹ First evidence for $K^+ \rightarrow \pi^+ \nu \bar{\nu}$ was presented recently [28]. From the one observed event, a branching fraction of $\mathcal{B}(K^+ \rightarrow \pi^+ \nu \bar{\nu}) = (4.2_{-3.5}^{+9.7}) \times 10^{-10}$ is measured, which is consistent with the SM range of $\mathcal{B}(K^+ \rightarrow \pi^+ \nu \bar{\nu}) = (9.1 \pm 3.2) \times 10^{-11}$ [29]. Due to the large experimental errors, this mode does not yet give new information for determining the apex of the unitarity triangle in the $(\bar{\rho}, \bar{\eta})$ plane. In the next round of experiments, however, new constraints from this mode are expected.

The branching fraction for $K_L^0 \rightarrow \pi^0 \nu \bar{\nu}$ in terms of η is given by [7]

$$\mathcal{B}(K_L^0 \rightarrow \pi^0 \nu \bar{\nu}) = 3.29 \times 10^{-5} \eta^2 |V_{cb}|^4 X^2(x_t). \quad (14.23)$$

Equation (14.23) specifies a horizontal line in the $(\bar{\rho}, \bar{\eta})$ plane.

14.2.6 Determination of $\sin 2\beta$

A measurement of $\sin 2\beta$ from *e.g.*, the CP asymmetry in the $B \rightarrow \psi K_S$ decays will simply specify a band $\langle \sin 2\beta \pm \sigma(\sin 2\beta) \rangle$ in the $(\sin 2\alpha, \sin 2\beta)$ plane. For representation in the $(\bar{\rho}, \bar{\eta})$ plane, it is first necessary to determine the angle β . Due to a four-fold ambiguity, four different angles are obtained: β , $\frac{\pi}{2} - \beta$, $\beta + \pi$, and $\frac{3\pi}{2} - \beta$. In the Standard Model, those two solutions which extend into the negative $\bar{\eta}$ plane are excluded. In a search for new physics, all four solutions need to be considered. Each solution is bounded by a pair of rays in the $(\bar{\rho}, \bar{\eta})$ plane, each originating at $(1, 0)$ and given by $\beta \pm \sigma_\beta$, where

$$\sigma_\beta = \frac{1}{2} \frac{1}{\cos 2\beta} \sigma(\sin 2\beta). \quad (14.24)$$

¹Note that in this approximation $\bar{\rho} = \rho$ and $\bar{\eta} = \eta$.

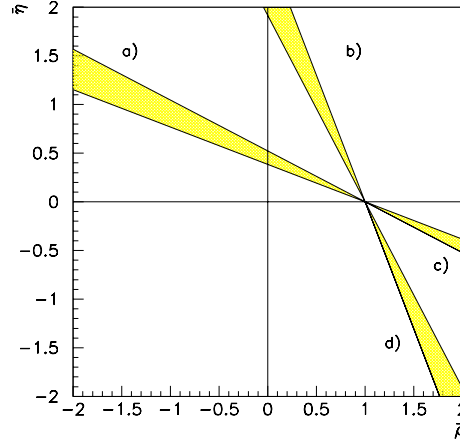


Figure 14-7. Impact of $\sin 2\beta$ measurements in the $(\bar{\rho}, \bar{\eta})$ plane. The four regions result from the four-fold ambiguity: (a) β , (b) $\pi/2 - \beta$, (c) $\pi + \beta$, and (d) $3\pi/2 - \beta$.

The resulting picture is shown in Figure 14-7 for $\sin 2\beta = 0.750 \pm 0.076$.

14.2.7 Determination of $\sin 2\alpha$

A measurement of $\sin 2\alpha$ from *e.g.*, the CP asymmetry in the $B \rightarrow \pi\pi$ decay (in the case that penguins were negligible) would specify a band $\langle \sin 2\alpha \pm \sigma(\sin 2\alpha) \rangle$ in the $(\sin 2\alpha, \sin 2\beta)$ plane. As concerns the $(\bar{\rho}, \bar{\eta})$ plane, the locus of all points $(\bar{\rho}, \bar{\eta})$ forming a unitarity triangle with fixed angle α is a circle centered at

$$(x_\alpha, y_\alpha) = \left(\frac{1}{2}, \frac{\cot \alpha}{2} \right), \quad (14.25)$$

with a radius

$$r_\alpha = \frac{1}{2} \frac{1}{\sin \alpha}. \quad (14.26)$$

The resulting error on the determination of r_α is given by

$$\sigma_{r_\alpha} = \frac{1}{2\sqrt{2}} \frac{\sin 2\alpha}{\cos 2\alpha} \frac{1}{(1 - \cos 2\alpha)^{\frac{3}{2}}} \sigma(\sin 2\alpha) = \frac{r_\alpha y_\alpha}{\cos 2\alpha} \sigma(\sin 2\alpha). \quad (14.27)$$

The error σ_{r_α} shows singularities at $\alpha = n\pi$ and $\alpha = \frac{m}{4}\pi$, with integer n and odd integer m . The first singularity reflects the fact that for $\alpha = 0$ or $\alpha = \pi$ no triangle is obtained. The second singularity accounts for the fact that for angles $\alpha \sim \frac{m}{4}\pi$, $\sin 2\alpha$ is near one. Since it cannot exceed one, the positive error has to become appropriately small, so that the product of $\frac{\sigma(\sin 2\alpha)}{\cos 2\alpha}$ remains finite. The latter argument applies also for the extraction of the error for β and γ .

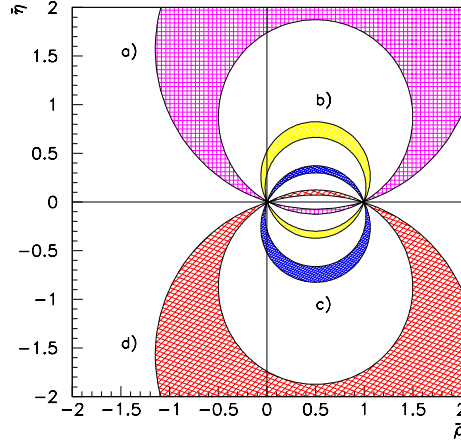


Figure 14-8. Impact of $\sin 2\alpha$ measurements in the $(\bar{\rho}, \bar{\eta})$ plane. The four regions result from the four-fold ambiguity: (a) $\pi/2 - \alpha$, (b) α , (c) $\alpha + \pi$, and (d) $3\pi/2 - \alpha$.

Since α is extracted from $\sin 2\alpha$, we are faced with a four-fold ambiguity: α , $\frac{1}{2}\pi - \alpha$, $\alpha + \pi$, and $\frac{3}{2}\pi - \alpha$. The ambiguity yields four distinct circles:

$$\begin{aligned}
 y_\alpha &= \pm \frac{1}{2} \cot \alpha && \text{for } \alpha, \alpha + \pi, \\
 y_\alpha &= \pm \frac{1}{2} \tan \alpha && \text{for } \frac{\pi}{2} - \alpha, \frac{3\pi}{2} - \alpha, \\
 r_\alpha &= \frac{1}{2} \frac{1}{\sin \alpha} && \text{for } \alpha, \alpha + \pi, \\
 r_\alpha &= \frac{1}{2} \frac{1}{\cos \alpha} && \text{for } \frac{\pi}{2} - \alpha, \frac{3\pi}{2} - \alpha.
 \end{aligned} \tag{14.28}$$

Each solution specifies a sickle-shaped region in the $(\bar{\rho}, \bar{\eta})$ plane centered at $(\frac{1}{2}, \sqrt{(r_\alpha \pm \sigma_{r_\alpha})^2 - \frac{1}{4}})$ with upper and lower bounds $r_\alpha \pm \sigma_{r_\alpha}$, respectively. All four solutions are sketched in Figure 14-8 for $\sin 2\alpha = 0.70 \pm 0.2$. The intersection with the rays specifying β will yield the allowed range for the apex $(\bar{\rho}, \bar{\eta})$. In general, there are four solutions each in the positive and negative $\sin 2\beta$ hemispheres.

In the case that penguin diagrams are not negligible in the α modes, α must be derived, either from an isospin analysis or from a full Dalitz plot analysis of $B \rightarrow \rho\pi$, but both of these will require several years' data taking (see Chapter 6 for a detailed discussion). In the first few years of BABAR running, neither of these analyses seems likely to be possible. In that case, a theoretical systematic error of order 0.2 on $\sin 2\alpha$ is unavoidable. This error might be reduced by improving the understanding of penguin effects through interplay between additional measurements and refined theoretical models.

14.3 The Determination of the CKM Parameters

14.3.1 Method for Extracting CKM Parameters

14.3.1.1 Measurements

Several measurements (Section 14.2) contain information about the unknown CKM parameters, $(A, \bar{\rho}, \bar{\eta})$ or $(A, \sin 2\alpha, \sin 2\beta)$. Given the measurement of an observable $Y^{meas} = \langle Y \rangle \pm \sigma_Y$ (the meaning of the uncertainty σ_Y is discussed later), a statistical handling of the unknown parameters is performed by constructing

$$\chi^2(A, \bar{\rho}, \bar{\eta}) = \sum_Y \left[\frac{\langle Y \rangle - Y(A, \bar{\rho}, \bar{\eta})}{\sigma_Y} \right]^2, \quad (14.29)$$

where $Y(A, \bar{\rho}, \bar{\eta})$ represents the theoretical description of the Y observable. By minimizing the χ^2 with respect to the three parameters one gets the best estimates $(\hat{A}, \hat{\rho}, \hat{\eta})$ that satisfy $\chi^2(\hat{A}, \hat{\rho}, \hat{\eta}) = \chi^2_{min}$. There are two aspects in minimizing the χ^2 :

- Assuming the model is right, one obtains the best estimates of the three fitted parameters at the minimum of the χ^2 function. In addition 95% CL contours can be obtained.
- This procedure may be used as a test of the compatibility between the data and its theoretical description. This assumes that the χ^2 variable fluctuates around the χ^2_{min} value according to a true χ^2 distribution. Using a χ^2 -distributed variable assumes, however, that each observable that contributes is Gaussian distributed. This is certainly not the case for most of the observables under consideration because of the uncontrolled theoretical uncertainties.

14.3.1.2 Handling of errors

While it is reasonable to assume that measurements have Gaussian errors ($Y^{meas} = \langle Y \rangle \pm \sigma_Y$), as explained in Section 14.1 it is certainly not the case for uncontrolled theoretical parameters. These are, for instance, $f_{B_d} \sqrt{B_{B_d}}$ for Δm_{B_d} , B_K for $|\epsilon_K|$ or the model-dependent part in the extraction of $|\frac{V_{ub}}{V_{cb}}|$. In the procedure adopted here, each of the theoretical parameters is scanned inside its bounds, and for each given set of values, M , of these uncontrolled theoretical parameters, the χ^2 function can be built and minimized,

$$\chi^2_M(A, \bar{\rho}, \bar{\eta}) = \sum_Y \left[\frac{\langle Y \rangle - Y_M(A, \bar{\rho}, \bar{\eta})}{\sigma_Y} \right]^2. \quad (14.30)$$

14.3.1.3 Statistical interpretation

For a given M , the consistency between theory and data can be tested by using a cutoff on the $(\chi_M^2)_{min}$ probability after the minimization. If the probability is lower than the cutoff, this theoretical model M is no longer considered. In the following, a cutoff value of 5% is used for the probability P , $P((\chi_M^2)_{min}) > 5\%$. Measurements are therefore considered as ways to reject theoretically inconsistent sets of parameters. If all sets of theoretical parameters M are rejected, there is a consistency problem between data and theory.

For a given model M satisfying $P((\chi_M^2)_{min}) > 5\%$, a 95% CL contour can be obtained in the $(\bar{\rho}, \bar{\eta})$ or $(\sin 2\alpha, \sin 2\beta)$ plane. Scanning over different realistic sets of values M yields new parameter estimates $(\hat{A}, \hat{\rho}, \hat{\eta})$ or $(\hat{A}, \sin \hat{2}\alpha, \sin \hat{2}\beta)$, depicted by points in various figures and contours that are continuously distributed. By considering the set of all the contours, the 95% CL contour for $(\bar{\rho}, \bar{\eta})$ is obtained from the external envelope of all the contours. This procedure should not be construed as assuming a flat probability distribution for theoretical parameters. Instead, we are determining whether theory and experiment remain consistent within a reasonable range of theoretical parameters.

14.3.1.4 Summary of the method

The method can be summarized in the following terms:

- Choose a set of CKM parameters to be determined.
- Choose a set of measurements $Y^{meas} = \langle Y \rangle \pm \sigma_Y$ where the uncertainty σ_Y is of experimental type (Gaussian).
- Scan a set M of theoretical parameters within a reasonable range;
- Build and minimize a χ_M^2 for each model M .
- Keep all models satisfying a χ_M^2 probability greater than a given cutoff. If no model survives, invoke a consistency problem between data and theory (suggesting possible new physics).
- In a two-parameter space, draw the 95% CL contours for each model satisfying the probability cut. The external envelope of all these contours represents the overall 95% CL contour.

14.3.2 Present Constraints on the Unitarity Triangle

The individual experimental constraints on the CKM parameters were discussed in Section 14.2. In this section, the results of the methodology outlined above for extracting the CKM parameters

Table 14-3. Present (1998) knowledge of the parameters entering the χ^2 calculation. For measurements, a real error is quoted, while for model-dependent quantities, a range is quoted.

Measurements		
$ V_{cb} $	0.040 ± 0.002	[1]
Δm_{B_d}	$0.471 \pm 0.016 \text{ ps}^{-1}$	[5]
$ \epsilon_K $	$(2.258 \pm 0.018)10^{-3}$	[1]
$ \frac{V_{ub}}{V_{cb}} $	$\langle \frac{V_{ub}}{V_{cb}} \rangle \pm .003$	Chapter 8
\overline{m}_t	$167 \pm 6 \text{ GeV}/c^2$	[7]
Δm_{B_s}	Amplitude method	[5]
Model-Dependence		
$\langle \frac{V_{ub}}{V_{cb}} \rangle$	[.06, .1]	[1] and Chapter 8
B_K	[0.6, 1.]	Appendix C, D
$f_{B_d}\sqrt{B_{B_d}}$	[160, 240] MeV	Appendix C

using all the experimental constraints together are presented. The currently measured values of the various observables, and the most significant theoretical uncertainties associated with their interpretation in terms of CKM elements as used in this section, are summarized in Table 14-3.

14.3.2.1 Constraints in the $(\overline{\rho}, \overline{\eta})$ plane

As described in Section 14.2, the present constraints on the unitarity triangle come mainly from the observables $Y = |V_{cb}|, |\frac{V_{ub}}{V_{cb}}|, |\epsilon_K|, \Delta m_{B_d}$. Explicitly the χ^2 reads²

$$\chi_M^2(A, \overline{\rho}, \overline{\eta}) = \left(\frac{\langle |V_{cb}| \rangle - |V_{cb}|(A)}{\sigma_{cb}} \right)^2 + \left(\frac{\langle |V_{ub}/V_{cb}| \rangle - |V_{ub}/V_{cb}|(\overline{\rho}, \overline{\eta})}{\sigma_{ub}} \right)^2 + \left(\frac{\langle \Delta m_{B_d} \rangle - \Delta m_{B_d}(A, \overline{\rho}, \overline{\eta})}{\sigma_{\Delta m}} \right)^2 + \left(\frac{\langle |\epsilon_K| \rangle - |\epsilon_K|(A, \overline{\rho}, \overline{\eta})}{\sigma_\epsilon} \right)^2, \quad (14.31)$$

where the errors appearing are of experimental type only, as explained in Section 14.1. In particular, for $|\frac{V_{ub}}{V_{cb}}|$ the error σ_{ub} is purely experimental, while the mean value of $\langle |\frac{V_{ub}}{V_{cb}}| \rangle$ will be varied

²Additional information from the top-quark mass is also taken into account, by introducing \overline{m}_t as a new parameter to be fitted with the constraint $\overline{m}_t = 167 \pm 6 \text{ GeV}$. Since this gives no further constraint it will be omitted in the text, however it is considered implicitly in each fit.

within theoretical bounds due to models. The model-dependent terms here are:³

$$M = \left(\left\langle \left| \frac{V_{ub}}{V_{cb}} \right| \right\rangle, f_{B_d} \sqrt{B_{B_d}}, B_K \right).$$

First, in order to illustrate the individual effect of varying each of the theoretical parameters,

$$M = \left(\left\langle \left| \frac{V_{ub}}{V_{cb}} \right| \right\rangle, f_{B_d} \sqrt{B_{B_d}}, B_K \right)$$

the minimization is performed several times, varying only one of the parameters at a time, within the (conservative) bounds of Table 14-3, while keeping the others at their central values. The effect on the fitted values in the $(\bar{\rho}, \bar{\eta})$ plane of scanning each of the theoretical parameters in turn is illustrated in Fig. 14-9.

For the present knowledge of the unitarity triangle (without including limits on Δm_{B_s} ; see the next section for a discussion including these), all the experimental information contained in Table 14-3 is used to build the χ^2 (Eq. (14.31)). All the model-dependent terms $M = \left(\left\langle \left| \frac{V_{ub}}{V_{cb}} \right| \right\rangle, f_{B_d} \sqrt{B_{B_d}}, B_K \right)$ within the conservative bounds of Table 14-3 are scanned. For each M , the χ^2 is minimized using the MINUIT package [31] and the resulting 95% CL is drawn if the contour survives the cut $\mathcal{P}(\chi_{min}^2) > 0.05$. The overall envelope of all the contours describes the optimized constraints on the $\bar{\rho}$ and $\bar{\eta}$ parameters at 95% CL.

Using this method, the contributions from experiment and from theory may be resolved; a single contour represents what the constraints would be, given a certain value for every theoretical input.

It is also worth noting that the overall 95% CL contour obtained by this method is smaller than that obtained by simply taking the intersection of the individual constraints, as can be seen from Figure 14-10. As explained earlier, this is due to the fact that correlations arise between the estimates when combining several measurements and that all three parameters $(A, \bar{\rho}, \bar{\eta})$ are explicitly taken into account in the fit.

14.3.2.2 Including Δm_{B_s} properly

As discussed in Section 14.2, a measurement of the B_s oscillation frequency is useful in constraining the CKM parameters. This frequency can be written as:

$$\Delta m_{B_s} = \frac{G_F^2}{6\pi^2} \eta_B m_{B_s} m_W^2 S_0(x_t) f_{B_s} \sqrt{B_{B_s}} |V_{tb}^* V_{ts}|^2, \quad (14.32)$$

³To be precise, a part of the error on the extraction of $|V_{cb}|$ is also of theoretical nature. However, it was checked that the results do not change while ignoring the model-dependent error and incorporating it in the experimental error.

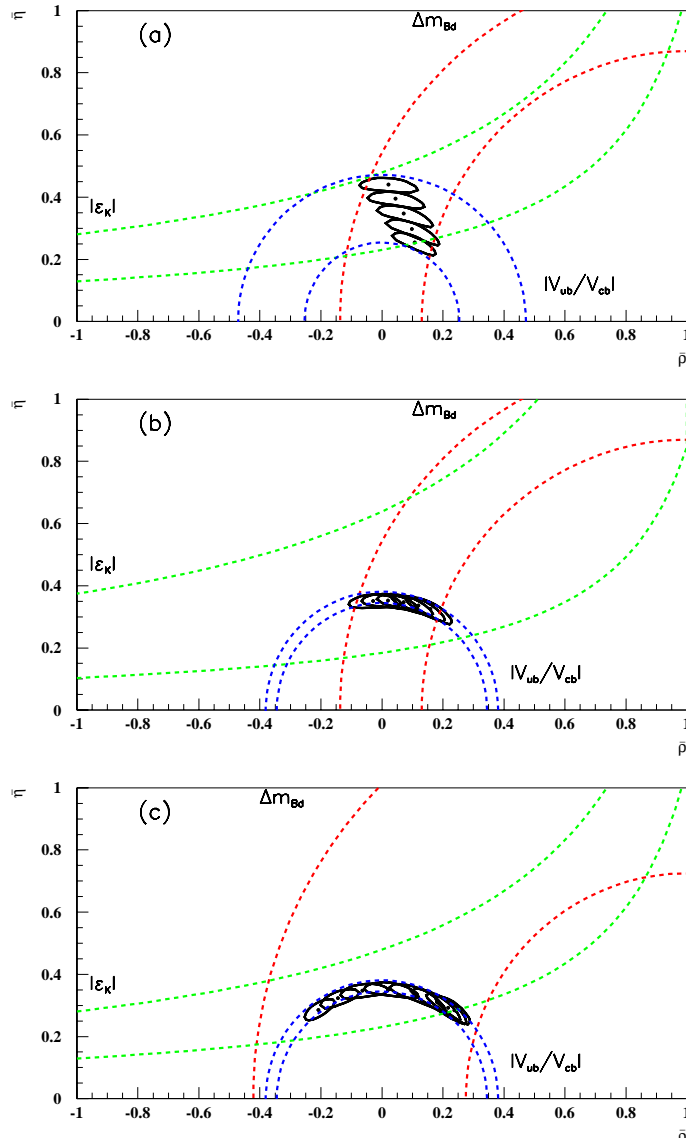


Figure 14-9. The three figures indicate the effects on the determination of the CKM parameters $(\bar{\rho}, \bar{\eta})$ of the various theoretical uncertainties. In each of the three figures, the χ^2 minimization is performed for several different values of one theoretical parameter, the other two each being held constant at their central values. The figures should be contrasted with Fig. 14-10 where all three are allowed to vary simultaneously. For each of the minimizations, the 95% CL contour is drawn and the point near the center locates the fitted estimate of the point $(\bar{\rho}, \bar{\eta})$. In each case, the dashed lines correspond to the “minimum and maximum limit” contours obtained when allowing all the degrees of freedom (experimental ones and the free theoretical one in each case) to vary within their allowed range. Plot (a) corresponds to a variation of $|V_{ub}/V_{cb}|$, plot (b) to a variation of B_K and plot (c) to a variation of $f_{B_d}\sqrt{B_{B_d}}$.

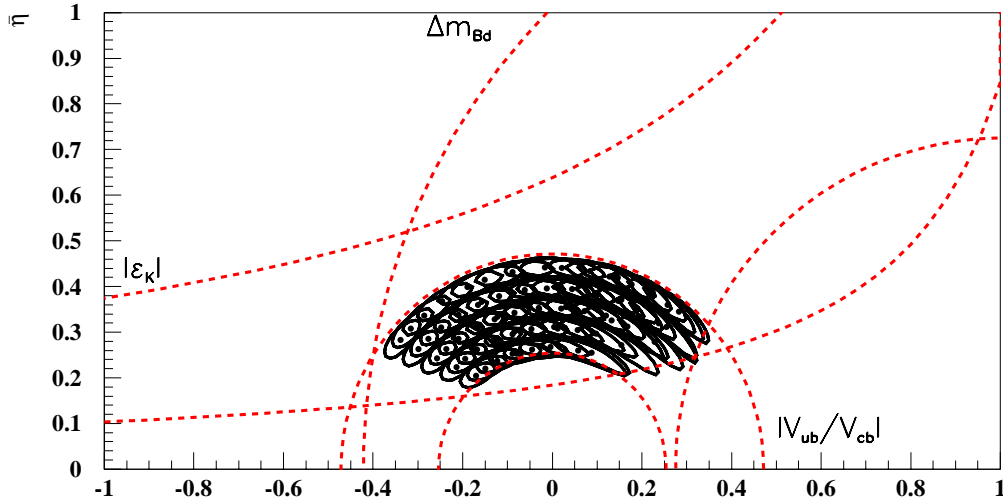


Figure 14-10. The overall 95% CL for $(\bar{\rho}, \bar{\eta})$ in 1998 without including limits on Δm_{B_s} . Each contour (with its minimum represented as a point) is a 95% CL obtained with one fixed set of theoretical parameters. These parameters are scanned within the boundaries of Table 14-3 and the set of all these contours represents the best constraints on $\bar{\rho}$ and $\bar{\eta}$ at 95% CL. Also shown as dotted lines are the individual constraints brought by the different measurements: they are obtained by varying coherently all the uncertainties (experimental and theoretical) in order to produce the maximum and minimum variation in this plane, and they are represented for illustrative purposes only.

where, in comparison with the formula for Δm_{B_d} (see 14.6):

- The CKM factor appearing is $|V_{tb}^* V_{ts}|^2$, which depends apparently weakly on $(\bar{\rho}, \bar{\eta})$ (to first order this term is simply $A^2 \lambda^4$). However, as the fit is performed on the full set of parameters $A, \bar{\rho}, \bar{\eta}$, the correlations induce a reduction of the allowed $(\bar{\rho}, \bar{\eta})$ region. In other words one does not need to incorporate explicitly the ratio $\frac{\Delta m_{B_s}}{\Delta m_{B_d}}$ to observe an improvement on the unitarity triangle. This is taken into account naturally in the full fit.
- The pseudoscalar decay constant (times the Bag factor) for the B_s , $f_{B_s} \sqrt{B_{B_s}}$, is different from that for the B_d . Models predict an uncertainty as large as for the B_d (see Table 14-3). However, the ratio (ξ_s) is better known (see Table 14-3). To account for this constraint in the scan, only the couple of values $(f_{B_d} \sqrt{B_{B_d}}, f_{B_s} \sqrt{B_{B_s}})$ which satisfies:

$$1.12 < \xi_s^2 = \left[\frac{f_{B_s} \sqrt{B_{B_s}}}{f_{B_d} \sqrt{B_{B_d}}} \right]^2 < 1.48 \quad (14.33)$$

have been used in the scan.

Presently, the B_s oscillation frequency has not been measured; therefore only 95% CL lower limits have been determined. The most stringent lower limit on the B_s oscillation frequency is obtained by combining all results from ALEPH, CDF, DELPHI, OPAL, and SLD. By using the “amplitude method” [32] the LEP B Oscillation Working Group yields a lower limit of $\Delta m_{B_s} > 12.4 \text{ ps}^{-1}$ at 95% CL [5]. It also turns out that the “amplitude method” is the best procedure for including Δm_{B_s} in the χ^2 minimization, as it contains much more information than a 95% CL lower limit and it can be implemented easily into the χ^2 minimization, whereas a 95% CL limit cannot.

The basic principle of the method is the following: neglecting detector effects and mistagging, the probability density for observing the decay of a \bar{B}_s meson at time t if a B_s was produced at time $t = 0$ is

$$\mathcal{P} = \frac{1}{\tau} e^{-t/\tau} \frac{1 - \cos(\Delta m_{B_s} t)}{2}, \quad (14.34)$$

while that for observing the decay of a B_s meson is

$$\mathcal{P} = \frac{1}{\tau} e^{-t/\tau} \frac{1 + \cos(\Delta m_{B_s} t)}{2}, \quad (14.35)$$

where τ is the B_s lifetime. The “amplitude method” modifies the oscillation term ($1 \pm \cos \Delta m_{B_s} t$) by ($1 \pm \mathcal{A} \cos \Delta m_{B_s} t$), where an amplitude \mathcal{A} has been introduced. This method consists of measuring the values of \mathcal{A} for various Δm_{B_s} frequencies. This provides a real measurement and it has been checked that the behavior of the likelihood function with respect to \mathcal{A} is parabolic in the region $|\mathcal{A}| \leq 1$ (*i.e.*, the errors are Gaussian). For each value of the frequency Δm_{B_s} , \mathcal{A} and its uncertainty $\sigma_{\mathcal{A}}$ are obtained (Figure 14-11). For each Δm_{B_s} value, if \mathcal{A} is compatible with zero, one deduces that there is no visible oscillation at this frequency. If \mathcal{A} is compatible with unity, one concludes that at this frequency an oscillation is observed. The Δm_{B_s} 95% CL limit was set at the frequency for which $\mathcal{A} + 1.645 \sigma_{\mathcal{A}} = 1$.

In the analysis presented here, for each set of the free parameters $(A, \bar{\rho}, \bar{\eta})$ the value of Δm_{B_s} is computed from Eq. (14.32), and the corresponding measured value and uncertainty for the amplitude ($\mathcal{A}^{mes}, \sigma_{\mathcal{A}}^{mes}$) are obtained. This amplitude is then compared to the one expected if the tested value of Δm_{B_s} was the correct one ($\mathcal{A} = 1$) and a χ^2 term is built and added to the global χ^2 ,

$$\chi_M^2(A, \bar{\rho}, \bar{\eta})_{new} = \chi_M^2(A, \bar{\rho}, \bar{\eta})_{old} + \left(\frac{\mathcal{A}^{mes} - 1}{\sigma_{\mathcal{A}}^{mes}} \right)^2. \quad (14.36)$$

In addition, it is required for each set, that the values of Δm_{B_d} and Δm_{B_s} correspond to a choice of parameters that is consistent with the allowed range of $f_{B_d} \sqrt{B_{B_d}} / f_{B_s}$, or the case is automatically excluded.

Once the experimental information on Δm_{B_s} has been included, the constraints on the CKM parameters come from the set of measured values of Table 14-3, adding the amplitude information of Fig. 14-11. As usual, all model-dependent parameters are scanned within the ranges indicated in Table 14-3 and the 1998 best knowledge of the $(\bar{\rho}, \bar{\eta})$ parameters is the overall 95% CL contour

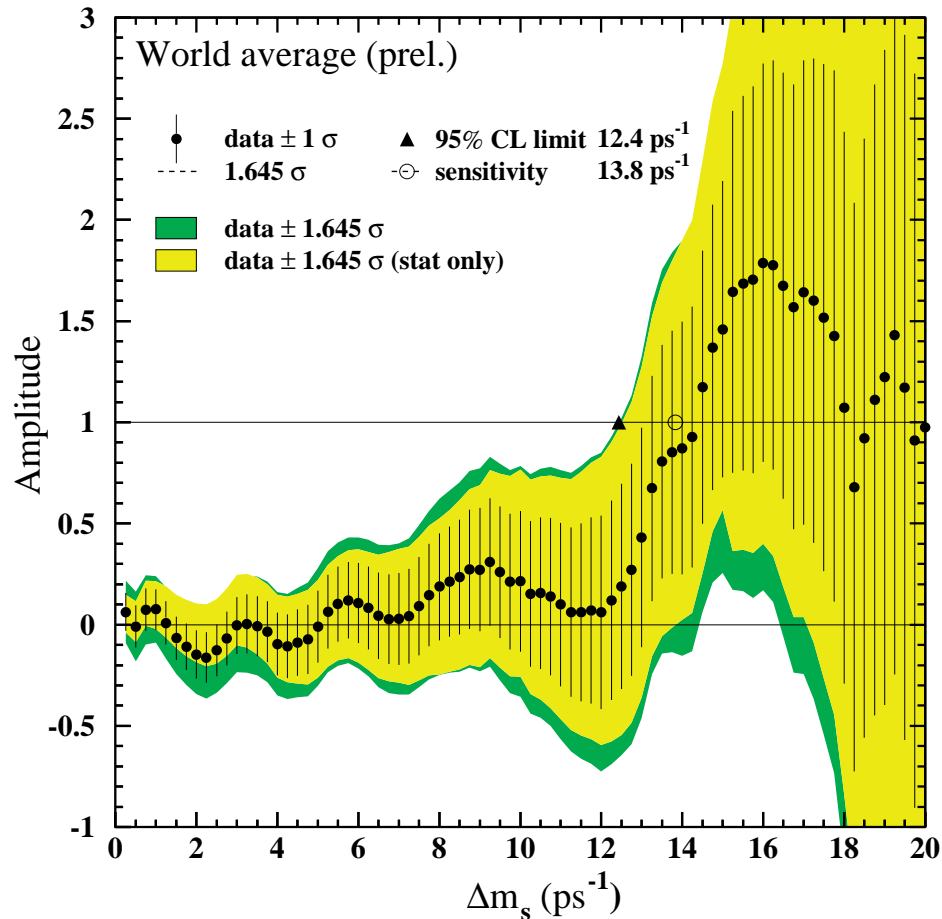


Figure 14-11. Combined amplitude measurements of the ALEPH, CDF, DELPHI, OPAL, and SLD collaborations. The dots indicate the measured \mathcal{A} and the error bar the uncertainty on the amplitude $\sigma_{\mathcal{A}}$. The line indicates the value $\mathcal{A} + 1.645 \sigma_{\mathcal{A}}$. The crossing point of this line with the value $\mathcal{A} = 1$ gives the 95% CL limit (12.4 ps^{-1}).

obtained using the envelope of all the contours (see Fig. 14-12). Note that this treatment makes more detailed use of the information in Fig. 14-11 than the extraction of a simple bound. The fact that this method leads to a slightly less restricted region surviving at the 95% confidence level than is implied by the line labeled Δm_{B_s} alone, is due to the fact that more degrees of freedom are used in this full fit. The total area allowed by the full fit is, of course, much reduced compared with that allowed by the Δm_{B_s} constraint alone.

It is clear from the comparison of Figs. 14-10 and 14-12 that the inclusion of Δm_{B_s} information reduces the allowed region for the $(\bar{\rho}, \bar{\eta})$ parameters. The zone corresponding to $\bar{\rho}$ values around -0.3 does not satisfy anymore the cutoff on the χ^2 probability and has thus disappeared from Fig. 14-12.

Therefore using a crude approximation, the following ranges of allowed values summarize the constraints obtained (at 95% CL):

- $-0.15 < \bar{\rho} < 0.35$
- $0.20 < \bar{\eta} < 0.45$

although the full $(\bar{\rho}, \bar{\eta})$ plane result is more complex than this.

14.3.2.3 Constraints in the $(\sin 2\alpha, \sin 2\beta)$ plane

Ambiguities

When the χ_M^2 function is computed in the basis $(A, \sin 2\alpha, \sin 2\beta)$, ambiguities in α and β arise. Indeed the pair $(\bar{\rho}, \bar{\eta})$ can be related uniquely to the pair (α, β) by simple trigonometry,

$$\begin{aligned}\bar{\rho}(\alpha, \beta) &= \frac{\tan \beta}{\tan \beta - \tan(\alpha + \beta)}, \\ \bar{\eta}(\alpha, \beta) &= -\frac{\tan \beta \tan(\alpha + \beta)}{\tan \beta - \tan(\alpha + \beta)}.\end{aligned}\tag{14.37}$$

However there are four solutions for relating (α, β) to $(\sin 2\alpha, \sin 2\beta)$:

$$\begin{aligned}\alpha_1 &= \frac{1}{2} \arcsin(\sin 2\alpha), & \beta_1 &= \frac{1}{2} \arcsin(\sin 2\beta) \\ \alpha_2 &= \frac{\pi}{2} - \frac{1}{2} \arcsin(\sin 2\alpha), & \beta_2 &= \frac{1}{2} \arcsin(\sin 2\beta) \\ \alpha_3 &= \frac{1}{2} \arcsin(\sin 2\alpha), & \beta_3 &= \frac{\pi}{2} - \frac{1}{2} \arcsin(\sin 2\beta) \\ \alpha_4 &= \frac{\pi}{2} - \frac{1}{2} \arcsin(\sin 2\alpha), & \beta_4 &= \frac{\pi}{2} - \frac{1}{2} \arcsin(\sin 2\beta)\end{aligned}\tag{14.38}$$

The angles α_1 and β_1 are defined to be in the range $(0, \pi/2)$.

Building the χ^2 requires the description of all observables in terms of $A, \sin 2\alpha, \sin 2\beta$. Since theoretical calculations of an observable Y are given in terms of the independent set of parameters $Y(A, \bar{\rho}, \bar{\eta})$, the transformation to $Y(A, \sin 2\alpha, \sin 2\beta)$ requires a choice of i in Eq. (14.38) to express $Y(A, \bar{\rho}(\alpha_i, \beta_i), \bar{\eta}(\alpha_i, \beta_i))$. In other words, the fact that for each set of values $(\sin 2\alpha, \sin 2\beta)$

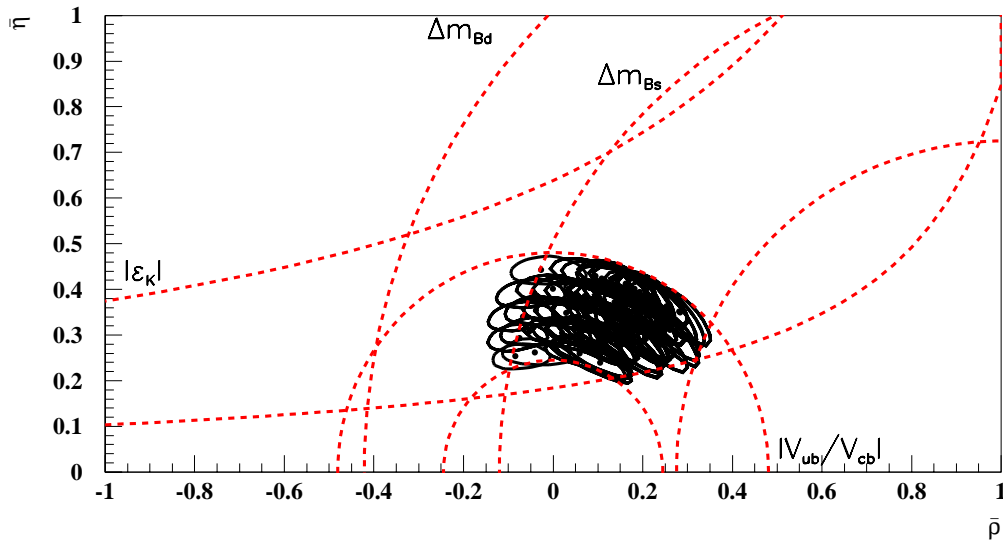


Figure 14-12. The overall 95% CL for $(\bar{\rho}, \bar{\eta})$ in 1998, including the limits on Δm_{B_s} via the amplitude measurements (described in the text). Each contour is a 95% CL obtained with one fixed set of theoretical parameters. These parameters are scanned within the boundaries of Table 14-3 and the set of all these contours represents the best constraints on $\bar{\rho}$ and $\bar{\eta}$ at 95% CL. Also shown (for illustrative purposes only) as dotted lines, are the individual constraints brought by the different measurements: they are obtained by varying coherently all the uncertainties (experimental and theoretical) to produce the maximum and minimum variation in this plane. For Δm_{B_s} , the dotted line represents the constraint obtained by taking the ratio $\frac{\Delta m_{B_s}}{\Delta m_{B_d}}$ using simply the limit $\Delta m_{B_s} > 12.4 ps^{-1}$ and the upper value of $\xi_s^2 = 1.48$.

there are four possible sets of values $(\bar{\rho}, \bar{\eta})$ means that at each point in the $(\sin 2\alpha, \sin 2\beta)$ plane, the fit has to be performed four times and then the minimum value among the four resulting χ^2 must be chosen.

Present knowledge of $(\sin 2\alpha, \sin 2\beta)$

Using the same ingredients as in Section 14.3.2, the present knowledge of the parameters $A, \sin 2\alpha, \sin 2\beta$ is obtained by minimizing a χ^2 of the form

$$\chi_M^2(A, \sin 2\alpha, \sin 2\beta) = \min_{i \in [1,4]} \sum_Y \left[\frac{\langle Y \rangle - Y_M(A, \bar{\rho}(\alpha_i, \beta_i), \bar{\eta}(\alpha_i, \beta_i))}{\sigma_Y} \right]^2 \quad (14.39)$$

for a given theoretical model M and an ambiguity $i = 1, \dots, 4$ (from Eq. (14.38)). Using the observables from Table 14-3 and Δm_{B_s} , Figure 14-13 displays the best knowledge about $(\sin 2\alpha, \sin 2\beta)$ in 1998. Here again the external envelope of the contours indicates the overall 95% CL region for the $(\sin 2\alpha, \sin 2\beta)$ parameters, while one single contour describes the errors obtained neglecting any model-dependence.

Two important remarks can be made for B factories:

- From indirect measurements (and model-dependence), $\sin 2\beta$ is already constrained to lie in the range $[0.4, 0.8]$ (95% CL). Therefore, the first task of BABAR is to use the clean $J/\psi K_S^0$ mode to check the direct measurement of this asymmetry. Any sizeable disagreement with this range would be most interesting. It would indicate either that the errors on model-dependent parameters are here underestimated, or that new physics is playing a role. If the result is compatible, BABAR will allow the reduction of this range.
- $\sin 2\alpha$ can presently have any value (except near -1). The goal of a B factory should therefore be to *measure* this value.

14.3.3 Including BABAR CP Asymmetry Measurements

14.3.3.1 Method for including CP asymmetry measurements

If real measurements (*i.e.*, with Gaussian errors) are achievable for $\sin 2\alpha$ and $\sin 2\beta$ (with errors $\sigma_\alpha, \sigma_\beta$ and a correlation $c_{\alpha\beta}$), the way to include them in the global fit of the CKM parameters is to add to the χ^2 a term of the form

$$\chi_{\text{BABAR}}^2(\sin 2\alpha, \sin 2\beta) = B^T W B \quad (14.40)$$

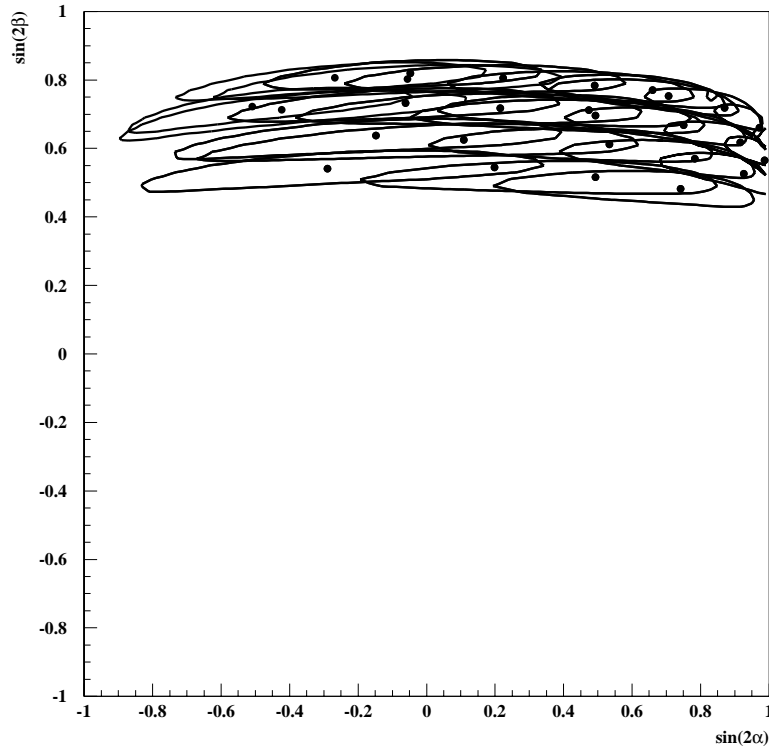


Figure 14-13. Present (1998) knowledge of the $(\sin 2\alpha, \sin 2\beta)$ parameters (at 95% CL), including Δm_{B_s} limits. The fit is performed in the $(A, \sin 2\alpha, \sin 2\beta)$ basis. Each contour (with its minimum represented as a point) is a 95% CL obtained with one fixed set of theoretical parameters. These parameters are scanned within the boundaries of Table 14-3 and the set of all these contours represents the best knowledge on $(\sin 2\alpha, \sin 2\beta)$ at 95% CL.

where B is a column vector, $B = \begin{pmatrix} \langle \sin 2\alpha \rangle - \sin 2\alpha \\ \langle \sin 2\beta \rangle - \sin 2\beta \end{pmatrix}$, and W is the weight matrix defined as the inverse of the correlation matrix, $W^{-1} = \begin{pmatrix} \sigma_\alpha^2 & c_{\alpha\beta} \\ c_{\alpha\beta} & \sigma_\beta^2 \end{pmatrix}$. In the $A, \bar{\rho}, \bar{\eta}$ representation, the χ^2 is expressed in terms of those parameters by using equations (14.5).

One cannot, however, avoid a level of model-dependence when extracting α , and, as is clear from Chapter 6, the final result for α (after extraction of the penguin contribution) has non-Gaussian errors. In order to get an idea of the impact of BaBar measurements on the determination of the unitarity triangle at some hypothetical future time, the strategy is as follows:

- $\sin 2\beta = 0.750 \pm 0.076$ will be used as an example of a real measurement, obtained for 30 fb^{-1} . The error is an example of the typical value that might be expected for this integrated luminosity, and comes from combining several of the modes described in Chapter 5. The central value is arbitrary, and was chosen to be compatible with the present allowed range. The error will be scaled by a factor of $\sqrt{N_1}/\sqrt{N_2}$ for higher statistics.
- For α , the results of the 2-pion and 3-pion studies of Chapter 6 will be combined, once enough statistics are available. The full likelihood distributions of those two analyses will be transformed into a χ^2 , mapping the whole $(\bar{\rho}, \bar{\eta})$ plane. This χ^2 incorporates the model-dependence introduced with penguins in the 2-pion study. In the interests of a conservative estimate of performance for this study, this dependence has been allowed to vary over a rather generous range. The 3-pion analysis extracts the penguin contribution directly from the data. Note that the α determination is used directly here, since this is the quantity delivered by the full 3-pion analysis with penguins, which disentangles (to some extent) the ambiguities otherwise brought by a simpler analysis.
- As more and more data are accumulated by B factories, better estimates of the quantities $|V_{cb}|$ and $|\frac{V_{ub}}{V_{cb}}|$ will be obtained. Some improvements are therefore input, which are “educated guesses” (taken from the conclusions of Chapter 8). The improvements expected in $f_{B_d}\sqrt{B_{B_d}}$, B_K , $|\epsilon_K|$ and Δm_{B_d} being less clear, the present estimates and uncertainties have been kept.

This combination is performed for illustrative reasons only. Indeed, much will depend, in the “real” future, on what the measured central values actually are. The transformation from α, β to $(\bar{\rho}, \bar{\eta})$ is highly nonlinear, and the Jacobian involved can lead to very different χ^2 areas depending on the measured central values. Furthermore, much depends, in the 2-pion and 3-pion analyses, on the branching fractions of the neutral modes, which are presently very uncertain.

14.3.3.2 Results for 30 fb^{-1}

With 30 fb^{-1} of data accumulated at the $\Upsilon(4S)$, it is expected (although it is not certain) from Chapter 6, that with the presently available knowledge of the penguin pollution, it will not be possible to extract the true value of $\sin 2\alpha$. This measurement is therefore not used for this limited luminosity. For β , the estimate $\sin 2\beta = 0.750 \pm 0.076$ is used, as explained above, and is treated as if it were a real measurement (*i.e.*, with Gaussian errors). The other numbers come from Table 14-4. The results derived from the overall combination of the information from all the measurements (*i.e.*, $|V_{cb}|$, $|\frac{V_{ub}}{V_{cb}}|$, $|\epsilon_K|$, Δm_{B_d} and Δm_{B_s} amplitudes and $\sin 2\beta$) are displayed in Fig.14-14.

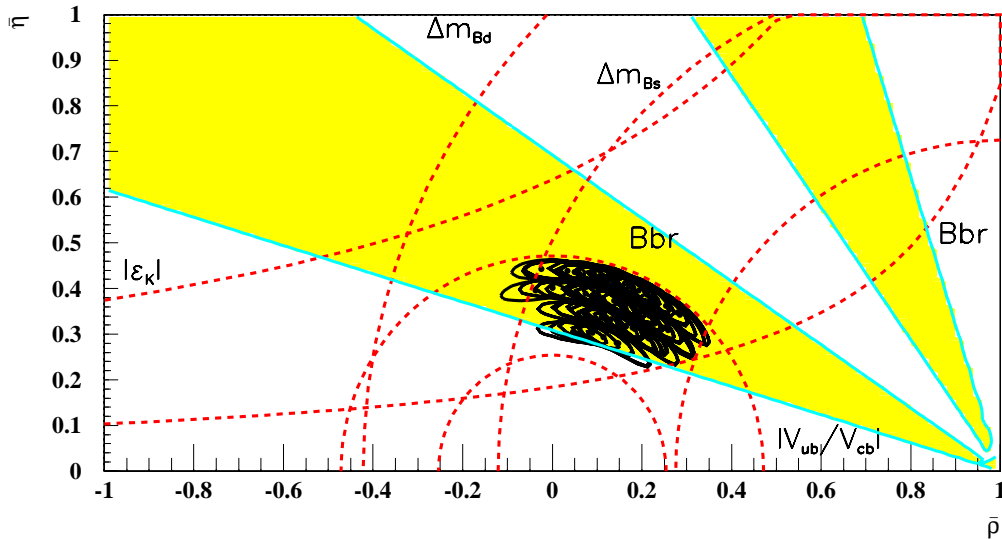


Figure 14-14. Combination of all observables for BABAR with 30 fb^{-1} of integrated luminosity at the $\Upsilon(4S)$, using data from Table 14-4. For each set of the scanned values of $(|V_{ub}/V_{cb}|, f_{B_d} \sqrt{B_{B_d}}, f_{B_s} \sqrt{B_{B_s}} (\xi_s^2), B_K)$ the 95% CL contour is drawn and the point locates the fitted estimate of the point $(\bar{\rho}, \bar{\eta})$, if its χ_M^2 probability is greater than 5%. The dotted lines correspond to the 95% CL for each constraint alone. The full (lightly shaded) contours correspond to the 95% CL obtained from the BABAR $\sin 2\beta$ measurements alone without any information on α .

14.3.3.3 Results for 90 fb^{-1}

Here it is assumed that a measurement of α has been performed. In the 3-pion case, the penguin pollution is *extracted* from the data, while for the 2-pion analysis, the model-dependence is incorporated in the (very) conservative range $0.15 < \frac{|P|}{|T|} < 0.62$ (see Chapter 6). There is no inclusion of a 4-pion analysis, although in fact some constraint may be possible from that mode.

The measurement of $\sin 2\beta$ has improved and also an improvement on the understanding of $|V_{ub}/V_{cb}|$ is foreseen. The measurements which have been used are detailed in Table 14-5. The constraints coming from the combination of the information from all the observables are shown in Figure 14-15.

14.3.3.4 Results for 180 fb^{-1}

Here the resolution of the penguin and tree contributions in the 3-pion mode is expected to be better. The measurement of $\sin 2\beta$ is improved, according to the increased integrated luminosity. The measurements used are detailed in Table 14-6 and the constraints coming from the combination of all the observables are displayed in Fig. 14-16.

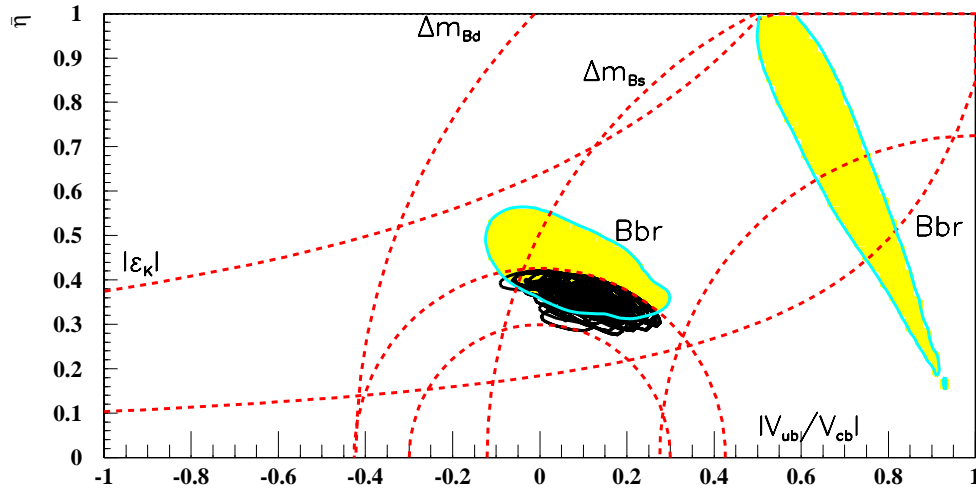


Figure 14-15. Combination of all observables for BABAR with 90 fb^{-1} integrated luminosity at the $\Upsilon(4S)$, using data from Table 14-5. For each set of the scanned values of $(\langle |V_{ub}| \rangle, f_{B_d} \sqrt{B_{B_d}}, f_{B_s} \sqrt{B_{B_s}} (\xi_s^2), B_K)$ the 95% CL contour is drawn and the point locates the fitted estimate of the point $(\bar{\rho}, \bar{\eta})$ if its $\chi^2_{M \text{ min}}$ probability is greater than 5%. The dotted lines correspond to the 95 % CL for each constraint alone. The full (lightly shaded) contours correspond to the 95% CL obtained from the BABAR $\sin 2\beta$ and α measurements alone; they include the model-dependence in the extraction of penguin pollution for the $\pi\pi$ mode.

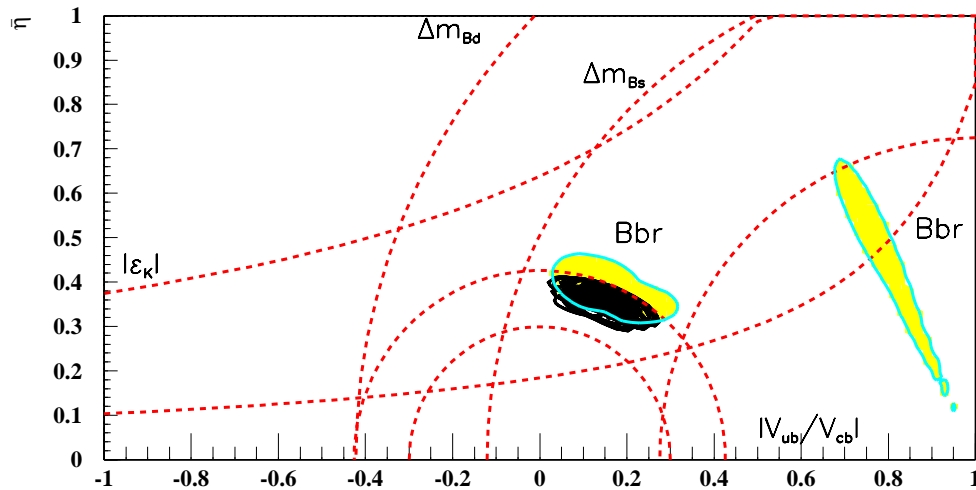


Figure 14-16. Combination of all observables for BABAR 180 fb^{-1} integrated luminosity at the $\Upsilon(4S)$, using data from Table 14-6. For each set of the scanned values of $(\langle |V_{ub}| \rangle, f_{B_d} \sqrt{B_{B_d}}, f_{B_s} \sqrt{B_{B_s}} (\xi_s^2), B_K)$ the 95% CL contour is drawn and the point locates the fitted estimate of the point $(\bar{\rho}, \bar{\eta})$ if its $\chi^2_{M \text{ min}}$ probability is greater than 5%. The dotted lines correspond to the 95 % CL for each constraint alone. The full (lightly shaded) contours correspond to the BABAR CP-measurement-alone 95% CL including the model-dependence in the extraction of penguin pollution for the $\pi\pi$ mode.

Table 14-4. Set of measurements and model-dependent parameters used in the CKM determination for a BABAR-integrated luminosity of 30 fb^{-1} at the $\Upsilon(4S)$.

Measurements		
$ V_{cb} $	0.040 ± 0.002	[1]
Δm_{B_d}	$0.471 \pm 0.016 \text{ ps}^{-1}$	[5]
$ \epsilon_K $	$(2.258 \pm 0.018)10^{-3}$	[1]
$ \frac{V_{ub}}{V_{cb}} $	$\langle \frac{V_{ub}}{V_{cb}} \rangle \pm .002$	Chapter 8
\bar{m}_t	$167 \pm 6 \text{ GeV}/c^2$	[7]
Δm_{B_s}	Amplitude method	[5]
$\sin 2\beta$	0.75 ± 0.076	Chapter 5
Model-Dependence		
$\langle \frac{V_{ub}}{V_{cb}} \rangle$	[.06, .1]	Chapter 8
B_K	[0.6, 1.]	Appendix C, D
$f_{B_d} \sqrt{B_{B_d}}$	[160., 240.] MeV	Appendix C
$f_{B_s} \sqrt{B_{B_s}}$	[200., 280.] MeV	Appendix C
ξ_s^2	[1.12, 1.48]	[12]

14.3.3.5 Conclusions from this analysis

The inclusion of BABAR measurements clearly improves our knowledge of $(\bar{\rho}, \bar{\eta})$, *i.e.*, the CKM matrix elements and the description of CP violation. The above projections may well vary, depending on many yet unknown factors. For example:

- Central values measured for $\sin 2\beta$ and α . In particular, incompatibility with present $\sin 2\beta$ estimates.
- Uncertain branching fractions ($\mathcal{B}(B^0 \rightarrow \pi^0 \pi^0)$, $\mathcal{B}(B^0 \rightarrow \rho^0 \pi^0)$).
- Experimental improvements on $|V_{cb}|$, $|\frac{V_{ub}}{V_{cb}}|$, Δm_{B_d} , Δm_{B_s} .
- Theoretical improvements on $f_{B_d} \sqrt{B_{B_d}}$, B_K and understanding of the penguin pollution (by testing the models).

Table 14-5. Set of measurements and model-dependent parameters used in the CKM determination for a BaBar-integrated luminosity of 90 fb^{-1} running at the $\Upsilon(4S)$.

Measurements		
$ V_{cb} $	0.040 ± 0.002	[1]
Δm_{B_d}	$0.471 \pm 0.016 \text{ ps}^{-1}$	[5]
$ \epsilon_K $	$(2.258 \pm 0.018)10^{-3}$	[1]
$ \frac{V_{ub}}{V_{cb}} $	$\langle \frac{V_{ub}}{V_{cb}} \rangle \pm .002$	Chapter 8
\overline{m}_t	$167 \pm 6 \text{ GeV}/c^2$	[7]
Δm_{B_s}	Amplitude method	[5]
$\sin 2\beta$	0.75 ± 0.050	Chapter 5
α	$1.347 + \chi^2(\alpha)$	Chapter 6
Model-Dependence		
$\langle \frac{V_{ub}}{V_{cb}} \rangle$	[.07, .09]	Chapter 8
B_K	[0.6, 1.]	Appendix C, D
$f_{B_d}\sqrt{B_{B_d}}$	[160., 240.] MeV	Appendix C
$f_{B_s}\sqrt{B_{B_s}}$	[200., 280.] MeV	Appendix C
ξ_s^2	[1.12, 1.48]	[12]

14.3.4 Determination of $f_{B_d}\sqrt{B_{B_d}}$ and B_K using CP Asymmetries

Since the measurement of just two sides of the unitarity triangle is sufficient to predict its angles, one can use the BaBar measurements of the angles to constrain the sides, and therefore to determine the theoretical parameters describing these observables. The main theoretical parameters are: $(\langle |\frac{V_{ub}}{V_{cb}}| \rangle, f_{B_d}\sqrt{B_{B_d}}, B_K)$. It is interesting to study $f_{B_d}\sqrt{B_{B_d}}$ and B_K together, since they can both be obtained from QCD lattices. To illustrate the gain that BaBar could bring to the knowledge of these two parameters, the values of the models that survived the χ^2 probability cut at 5% in the full fit are represented in Fig. 14-17. In the two-dimensional plot, $f_{B_d}\sqrt{B_{B_d}}$ is plotted vs. B_K for the present values (Table 14-3) and for the BaBar projection for 90 fb^{-1} (Table 14-5). $|\frac{V_{ub}}{V_{cb}}|$ and $f_{B_s}\sqrt{B_{B_s}}$ are still varied within the boundaries indicated in the tables.

While almost the whole $(f_{B_d}\sqrt{B_{B_d}}, B_K)$ plane is presently allowed (apart from large values of $f_{B_d}\sqrt{B_{B_d}}$ with low values of B_K , which is presently confirmed by lattice results) the inclusion of constraints from BaBar restricts the allowed values to a smaller region. Here again, results may

Table 14-6. Set of measurements and model-dependent parameters used in the CKM determination for a BABAR-integrated luminosity of 180 fb^{-1} running at the $\Upsilon(4S)$.

Measurements		
$ V_{cb} $	0.040 ± 0.002	[1]
Δm_{B_d}	$0.471 \pm 0.016 \text{ ps}^{-1}$	[5]
$ \epsilon_K $	$(2.258 \pm 0.018)10^{-3}$	[1]
$ \frac{V_{ub}}{V_{cb}} $	$\langle \frac{V_{ub}}{V_{cb}} \rangle \pm .002$	Chapter 8
\overline{m}_t	$167 \pm 6 \text{ GeV}/c^2$	[7]
Δm_{B_s}	Amplitude method	[5]
$\sin 2\beta$	0.75 ± 0.035	Chapter 5
α	$1.347 + \chi^2(\alpha)$	Chapter 6
Model-Dependence		
$\langle \frac{V_{ub}}{V_{cb}} \rangle$	[.07, .09]	Chapter 8
B_K	[0.6, 1.]	Appendix C, D
$f_{B_d}\sqrt{B_{B_d}}$	[160., 240.] MeV	Appendix C
$f_{B_s}\sqrt{B_{B_s}}$	[200., 280.] MeV	Appendix C
ξ_s^2	[1.12, 1.48]	[12]

vary depending on the measured central values for $\sin 2\beta$ and α . Also, to achieve the most accurate measurement, a precise knowledge of $|\frac{V_{ub}}{V_{cb}}|$ is important.

Such constraints would probably represent the first real measurements (in the model-independent sense) of $f_{B_d}\sqrt{B_{B_d}}$ and B_K , the direct measurements of these quantities being difficult. These values could then be used as a means to check the precision of the QCD lattice predictions.

14.3.5 In Case of Incompatibility

All previous combinations assume the Standard Model description for every observable. Since a χ^2 is used, the method allows a test of this assumption. Indeed, the $\mathcal{P}_M(\chi_{min}^2)$ cut is seen as a way to reject theoretical parameters incompatible with data, therefore determining the allowed range of such parameters within the Standard Model. However, if all theoretically-allowed values of the parameters were to be rejected, as for example in Fig. 14-18, this would be a possible indication of new physics. One should then ask the following questions:

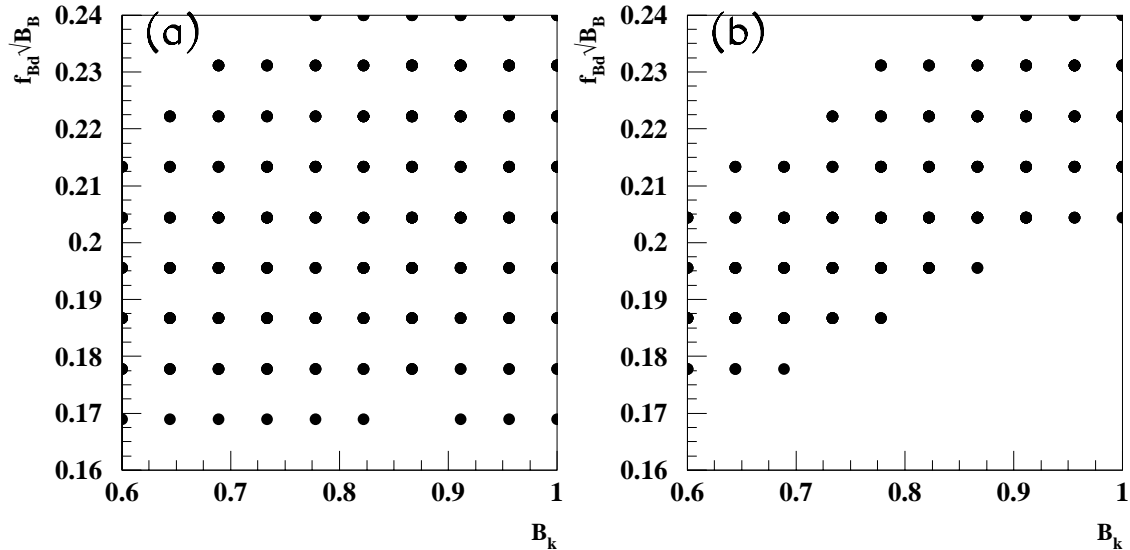


Figure 14-17. Display of the theoretical values of $f_{B_d} \sqrt{B_{B_d}}$ and B_K which survive the probability cut $\mathcal{P}(\chi_{min}^2) > 0.05$, (a) for the present situation and (b) for the projection to 90 fb^{-1} . Experimental values were taken from Table 14-3 and Table 14-5 and other theoretical parameters (i.e., $\langle |V_{ub}/V_{cb}| \rangle$ and $f_{B_s} \sqrt{B_{B_s}}$) were scanned according to the ranges indicated in the tables.

- Are the data reliable? In particular, are the quoted errors reasonable?
- Is the range scanned for theoretical parameters reasonable? In particular many “hidden” quantities enter the theoretical calculations (see Table 14-2). To what level are they certain? Inverting the problem, $B_{\text{A}B\text{A}R}$ can provide the set of parameters that can describe the data, and theorists can then study if they can accommodate these values within the Standard Model.
- Is it new physics? This would be particularly plausible if the measured CP asymmetry in the clean $J/\psi K_S^0$ mode is very different from 0.7 (in particular, no asymmetry), since here the theoretical prediction is very clean.

In searching for incompatibility with the Standard Model, it is also important to examine those channels where the Standard Model predicts small or vanishing asymmetries, since these may have significant asymmetries in many models — see, in particular, the discussion in Section 13.2.

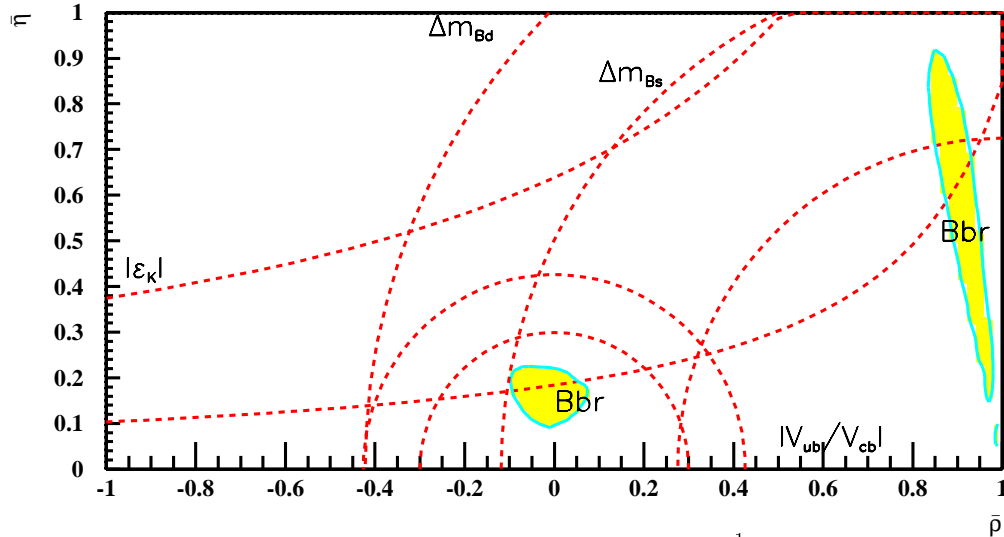


Figure 14-18. Combination of all observables for BABAR with 90 fb^{-1} integrated luminosity at the $\Upsilon(4S)$, using data from Table 14-5 except for $\sin 2\beta = 0.30 \pm 0.050$. In this case the allowed values for the point $(\bar{\rho}, \bar{\eta})$ obtained from $(\alpha, \sin 2\beta)$ is incompatible with the $|\frac{V_{ub}}{V_{cb}}|$ measurement. As a consequence the $\chi^2_{M \text{ min}}$ probability cut of 5% is never satisfied and no 95% CL contours are drawn.

14.3.6 Other Possible Future Constraints

The Fleischer-Mannel idea to constrain the range of gamma from combined $B_{u,d} \rightarrow \pi K$ branching ratios, discussed in Section 7.5.3, could prove useful. However, the most recent data [5] (which appeared since that section was written) suggests that it will not provide a strong restriction, so it will not be considered further here.

14.3.6.1 $K \rightarrow \pi \nu \bar{\nu}$ decays

The rare decay mode $K^+ \rightarrow \pi^+ \nu \bar{\nu}$ is theoretically clean (see Section 14.2.5). The only sizeable uncertainty comes from the parameter $P_0(X) = 0.40 \pm 0.06$. To investigate the effect of adding-in a constraint from here, $P_0(X)$ will be scanned in the range 0.34 to 0.46 (where the effect of this uncertainty is quite small), along with the other parameters that have uncontrolled theoretical uncertainties. This new constraint is taken into account by adding a term to the global χ^2 ,

$$\chi^2_M(A, \bar{\rho}, \bar{\eta}) = \chi^2_M(A, \bar{\rho}, \bar{\eta}) + \left(\frac{\langle \mathcal{B}(K^+ \rightarrow \pi^+ \nu \bar{\nu}) \rangle - \mathcal{B}(K^+ \rightarrow \pi^+ \nu \bar{\nu})(A, \bar{\rho}, \bar{\eta})}{\sigma_{K^+}} \right)^2. \quad (14.41)$$

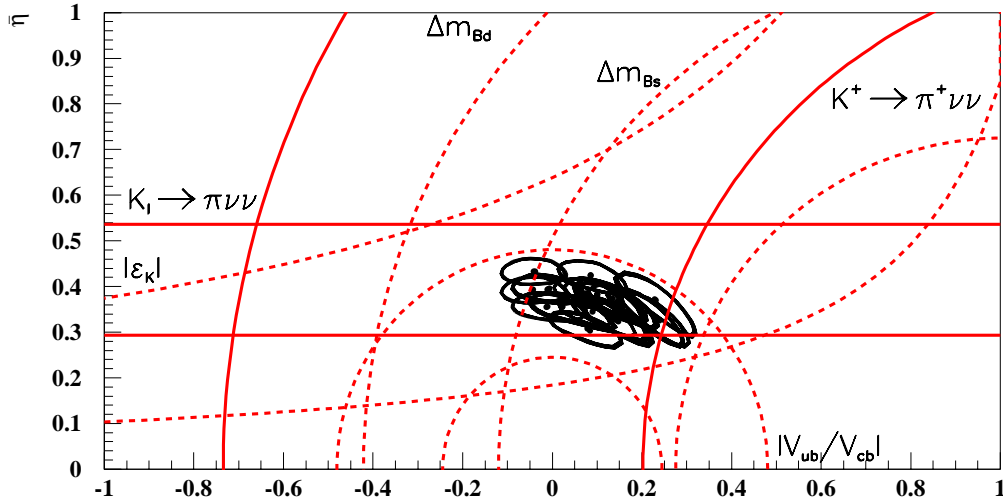


Figure 14-19. For each set of the scanned values of $(\langle |V_{ub}/V_{cb}| \rangle, f_{B_d} \sqrt{B_{B_d}}, f_{B_s} \sqrt{B_{B_s}}, (\xi_s^2), B_K)$ the 95% CL contour is drawn and the point locates the fitted estimate of the point $(\bar{\rho}, \bar{\eta})$ if the χ_M^2 min probability is greater than 5%. The lines correspond to the “minimum and maximum limit” contours obtained when varying coherently all the uncertainties (experimental and theoretical) to produce some maximum and minimum variation of the constraints. The measurements are $|V_{cb}|, |V_{ub}/V_{cb}|, |\varepsilon_K|, \Delta m_{B_d}, \Delta m_{B_s}$ and the two rare K decays $K^+ \rightarrow \pi^+ \nu \bar{\nu}$ and $K_L^0 \rightarrow \pi^0 \nu \bar{\nu}$.

The $K_L^0 \rightarrow \pi^0 \nu \bar{\nu}$ decay is even cleaner, theoretically. The resulting constraint is taken into account by adding a simple term to the global χ_M^2 ,

$$\chi_M^2(A, \bar{\rho}, \bar{\eta}) = \chi_M^2(A, \bar{\rho}, \bar{\eta}) + \left(\frac{\langle \mathcal{B}(K_L^0 \rightarrow \pi^0 \nu \bar{\nu}) \rangle - \mathcal{B}(K_L^0 \rightarrow \pi^0 \nu \bar{\nu})(A, \eta)}{\sigma_{K_L^0}} \right)^2. \quad (14.42)$$

No uncontrolled theoretical parameters beyond $M = \langle |V_{ub}/V_{cb}| \rangle, f_{B_d} \sqrt{B_{B_d}}, f_{B_s} \sqrt{B_{B_s}}, (\xi_s^2), B_K$ are needed in this case.

The impact of these two rare K decays results in the $(\bar{\rho}, \bar{\eta})$ plane is demonstrated in Fig. 14-19, assuming that future measurements would give:

$$\mathcal{B}(K^+ \rightarrow \pi^+ \nu \bar{\nu}) = (1.0 \pm 0.1) \times 10^{-10},$$

$$\mathcal{B}(K_L^0 \rightarrow \pi^0 \nu \bar{\nu}) = (3.0 \pm 0.3) \times 10^{-11},$$

while for $|V_{cb}|, |V_{ub}/V_{cb}|, |\varepsilon_K|, \Delta m_{B_d}$, and Δm_{B_s} , the present data are used (see Table 14-3).

Comparing Fig.14-19 with Fig. 14-12, it can be seen (as already pointed out in Ref. [29]) that measurements of these two rare kaon decays bring stringent constraints on the CKM parameters.

14.4 Conclusions

In this chapter, the different observables that constrain the CKM matrix elements have been surveyed: $(A, \bar{\rho}, \bar{\eta})$, or equivalently $(A, \sin 2\alpha, \sin 2\beta)$.

A statistically meaningful way of combining them has been described, by differentiating measurements from theoretical parameters that rely on model assumptions. In particular, it has been shown that this combination gives better results than a naive intersection of the individual constraints.

An optimal way of integrating the Δm_{B_s} limits using the method of amplitudes has been described. The present knowledge (in 1998) of the unitarity triangle has been given. Working in the $(A, \sin 2\alpha, \sin 2\beta)$ representation, the conclusions are that $\sin 2\beta$ is presently constrained by indirect measurement $0.45 < \sin 2\beta < 0.85$ (95% CL) while $\sin 2\alpha$ can essentially take any value. The implications for BaBar are that CP asymmetries for the β modes provide an immediate test of the Standard Model. For α , the goal is to measure this parameter.

Just as measuring the sides of the unitarity triangle allows the angles to be constrained, measuring the two angles α and β allows the sides of the triangle to be constrained without any model-assumption. This translates into a measurement of the theoretical parameters, $f_{B_d} \sqrt{B_{B_d}}$ and B_K , which can then be compared with lattice results.

It should be emphasized that the illustrative exercise of combining all observables with the potential BaBar CP asymmetry measurements relies presently on a choice of yet uncertain parameters (such as the branching fractions of B^0 into 3-pion final states, and on the actual central values of the CKM parameters). Improvements are foreseen on the experimental side ($|V_{cb}|$, $|\frac{V_{ub}}{V_{cb}}|$, rare K decays, . . .) and on the theoretical side ($f_{B_d} \sqrt{B_{B_d}}$, ξ_s , B_K). Also, with the large statistics in many channels accumulated by the BaBar detector, theorists will test the models of hadronic B decays, and get a better understanding of the yet unfamiliar world of penguins. This in turn will allow the reduction of some of the theoretical uncertainties present in the analyses described in this book, and so tighten the tests of the Standard Model discussed here.

The studies in this book show something of both the challenges and the opportunities that PEP-II and BaBar will present. Much remains to be done in completing the detector, improving the simulations and reconstruction software, and refining the studies presented. However, it is already clear that there is exciting discovery potential, as well as an important long term program to exploit fully the capabilities of this facility. The beginning of data taking in 1999 is eagerly anticipated.

References

- [1] C. Caso *et al.*, *Eur. Phys. Jour. C* **3**, 1 (1998).
- [2] L. Wolfenstein, *Phys. Rev. Lett.* **51**, 1945 (1983).
- [3] A.J. Buras, M. E. Lautenbacher and G. Ostermeier, *Phys. Rev. D* **50**, 3433 (1994).
- [4] M. Athanas *et al.*, *Phys. Rev. Lett.* **73**, 3503 (1994).
- [5] J. Alexander, talk given at 29th International Conference on High Energy Physics in Vancouver, July 22-29, (1998).
- [6] G. Buchalla, A. J. Buras and M. E. Lautenbacher, *Rev. Mod. Phys.* **68**, 1125 (1996).
- [7] A.J. Buras and R. Fleischer, hep-ph/9704376, to appear in *Heavy Flavours II*, World Scientific (1997), eds. A.J. Buras and M. Lindner.
- [8] R. M. Barnett *et al.*, *Phys. Rev. D* **54**, 1 (1996).
- [9] S. Herrlich and U. Nierste, *Nucl. Phys.* **B419**, 292 (1994).
- [10] A. J. Buras, M. Jamin and P. H. Weisz, *Nucl. Phys.* **B347**, 491 (1990).
- [11] S. Herrlich and U. Nierste, *Phys. Rev. D* **52**, 6505 (1995); *Nucl. Phys.* **B476**, 27 (1996).
- [12] C. Sachradja, "Heavy Flavour Physics," XVIII International Symposium on Lepton and Photon Interactions, July- 28 - August 1 (1997), Hamburg, Germany; hep-th/9711386.
- [13] T. Inami and C. S. Lim, *Prog. Th. Phys.* **65**, 297 (1981).
- [14] J. Alexander *et al.*, *Phys. Rev. Lett.* **77**, 5000 (1994).
- [15] W. A. Bardeen, A. J. Buras and J. M. Gerard, *Phys. Lett. B* **211**, 343 (1988).
- [16] J. Flynn, in *Proceedings of 28th International Conference on High Energy Physics*, Warsaw , Poland (1996), hep-lat/9611016.
- [17] A. Pich and E. de Rafael, *Phys. Lett. B* **158**, 477 (1985);
J. Prades *et al.*, *Z. Phys. C* **51**, 287 (1991).
- [18] J. F. Donoghue, F. Golowich and B. R. Holstein, *Phys. Lett. B* **119**, 412 (1982).
- [19] R. Decker, *Nucl. Phys. B Proc. Suppl.* **7A**, 180 (1990);
S. Narrison, *Phys. Lett. B* **351**, 369 (1995).

-
- [20] A. J. Buras, M. Jamin and M. E. Lautenbacher, *Phys. Lett. B* **389**, 749 (1996).
- [21] A. J. Buras, M. Jamin and M. E. Lautenbacher, *Nucl. Phys.* **B408**, 209 (1993).
- [22] L. K. Gibbons *et al.*, *Phys. Rev. Lett.* **70**, 70 (1993).
- [23] G. D. Barr *et al.*, *Phys. Lett. B* **317**, 233 (1993).
- [24] A.J.S. Smith, talk given in the 18th International Symposium on Lepton Photon Interactions, Hamburg, Germany (1997).
- [25] A. J. Buras, in *Proceedings of 28th International Conference on High Energy Physics*, Warsaw, Poland (1996), hep-ph/9610461.
- [26] Y. Grossman and Y. Nir, *Phys. Lett. B* **398**, 163 (1997).
- [27] S. Adler *et al.*, (E787 Collaboration), *Phys. Rev. Lett.* **77**, 1421 (1996).
- [28] S. Adler *et al.*, (E787 Collaboration), *Phys. Rev. Lett.* **79**, 2204 (1997).
- [29] G. Buchalla and A. J. Buras, *Nucl. Phys.* **B412**, 106 (1996).
- [30] G. Buchalla and A. J. Buras, *Nucl. Phys.* **B398**, 285 (1993); *Nucl. Phys.* **B400** 225 (1993).
- [31] F. James, "MINUIT," CERN Program Library D506.
- [32] H.-G Moser and A. Roussarie, *Nucl. Instr. Methods* **A394**, 491 (1997).

This page was intentionally left blank.

A

The Effective $|\Delta|B| = 1$ Hamiltonian

A key quantity entering all chapters of this book is the effective $|\Delta|B| = 1$ -Hamiltonian $\mathcal{H}^{|\Delta B|=1}$ triggering the decay of the B -meson. This appendix summarizes the points necessary for the correct use of $\mathcal{H}^{|\Delta B|=1}$ in physical applications, sketches its origin and explains some of the physics terminology associated with $\mathcal{H}^{|\Delta B|=1}$.

To obtain the decay rate of the B meson into some final state f , one must first calculate the transition amplitude \mathcal{M} for $B \rightarrow f$. In general there are many contributions to \mathcal{M} , each of which is pictorially represented by a Feynman diagram such as the one in Fig. 2-1. Yet one cannot simply take the Standard Model diagrams to obtain \mathcal{M} : At short distances much smaller than $\hbar c/\Lambda_{QCD}$ the strong interaction can be described perturbatively by the exchange of gluons. When traveling over a distance of order $\hbar c/\Lambda_{QCD}$, however, quarks and gluons hadronize and QCD becomes non-perturbative. Therefore the physics from different length scales, or, equivalently, from different energy scales must be treated separately. The theoretical tool for this is the *operator product expansion* (OPE) which was explained in Section 2.1. The decay amplitude \mathcal{M} is expressed as

$$\mathcal{M} = -\frac{G_F}{\sqrt{2}} V_{CKM} \sum_j C_j \langle f|O_j|B \rangle \left[1 + \mathcal{O}\left(\frac{m_b^2}{M_W^2}\right) \right]. \quad (\text{A.1})$$

Here the C_j are the Wilson coefficients, which contain the information on the short-distance physics defined at some scale μ . All dependence on heavy masses $M \gg \mu$ such as m_t , M_W or the masses of new undiscovered heavy particles is contained in the C_j . By convention one factors out $G_F/\sqrt{2}$ and the CKM factors, which are denoted by V_{CKM} in (A.1). The quantity $\langle f|O_j|B \rangle$ is the matrix element of the local operator O_j for the $B \rightarrow f$ transition in question. Thus, formally, (A.1) separates the physics from different distances. Due to the property of asymptotic freedom hard QCD effects can be included perturbatively in the Wilson coefficients, *i.e.*, by the calculation of Feynman diagrams with quarks and gluons. The $\langle f|O_j|B \rangle$ includes long-distance effects and cannot be evaluated from perturbation theory. In principle such quantities can be evaluated using sophisticated non-perturbative methods such as lattice calculation or QCD sum rules. However often these calculations are not available and one is forced to rely instead on model-based estimates for these quantities. The terms of order $\frac{m_b^2}{M_W^2}$ in A.1 represent the fact that the sum over operators is implicitly truncated to include only the leading dimension six (four-quark) operators.

An important feature of the OPE in (A.1) is the universality of the coefficients C_j ; they are independent of the external states, *e.g.*, their numerical value is the same for all final states f

in (A.1). Therefore one can view the C_j 's as effective coupling constants and the O_j 's as the corresponding interaction vertices. Thus one can set up the *effective Hamiltonian* or decays with a given quantum number transition

$$\mathcal{H}^{|\Delta B|=1} = \frac{G_F}{\sqrt{2}} V_{CKM} \sum_j C_j O_j + \text{h.c.} \quad (\text{A.2})$$

An amplitude calculated from $\mathcal{H}^{|\Delta B|=1}$, defined at a scale of order m_b , in principle reproduces the corresponding Standard Model result up to corrections of order m_b^2/M_W^2 as indicated in (A.1). The set of operators O_j needed in (A.2) depends on the flavor structure of the physical process under consideration. For example the $\Delta B = \Delta C = 1$ decay of Fig. 2-2 requires the two operators of (2.4) and (2.5) in the effective Hamiltonian. These operators are generated by the tree-level W exchange diagram and QCD corrections to it, see Fig. 2-2.

The Hamiltonian for $\Delta B = 1$, $\Delta C = \Delta S = 0$ transitions, however, comprises more operators because it must also accommodate for the penguin diagram with an internal top quark of Fig. 2-3. The corresponding operator basis reads:

$$\begin{aligned} O_1^c &= \bar{d}_\alpha \gamma_\mu (1 - \gamma_5) c_\beta \bar{c}_\beta \gamma^\mu (1 - \gamma_5) b_\alpha, & O_1^u &= \bar{d}_\alpha \gamma_\mu (1 - \gamma_5) u_\beta \bar{u}_\beta \gamma^\mu (1 - \gamma_5) b_\alpha, \\ O_2^c &= \bar{d}_\alpha \gamma_\mu (1 - \gamma_5) c_\alpha \bar{c}_\beta \gamma^\mu (1 - \gamma_5) b_\beta, & O_2^u &= \bar{d}_\alpha \gamma_\mu (1 - \gamma_5) u_\alpha \bar{u}_\beta \gamma^\mu (1 - \gamma_5) b_\beta, \\ O_3 &= \sum_{q=u,d,s,c,b} \bar{d}_\alpha \gamma_\mu (1 - \gamma_5) b_\alpha \bar{q}_\beta \gamma^\mu (1 - \gamma_5) q_\beta, \\ O_4 &= \sum_{q=u,d,s,c,b} \bar{d}_\alpha \gamma_\mu (1 - \gamma_5) b_\beta \bar{q}_\beta \gamma^\mu (1 - \gamma_5) q_\alpha, \\ O_5 &= \sum_{q=u,d,s,c,b} \bar{d}_\alpha \gamma_\mu (1 - \gamma_5) b_\alpha \bar{q}_\beta \gamma^\mu (1 + \gamma_5) q_\beta, \\ O_6 &= \sum_{q=u,d,s,c,b} \bar{d}_\alpha \gamma_\mu (1 - \gamma_5) b_\beta \bar{q}_\beta \gamma^\mu (1 + \gamma_5) q_\alpha, \\ O_8 &= -\frac{g}{8\pi^2} \bar{d} \sigma^{\mu\nu} [m_d L + m_b R] T^a b \cdot G_{\mu\nu}^a. \end{aligned} \quad (\text{A.3})$$

These operators are depicted in Figure A-1. O_1 and O_2 are called *current-current* operators, O_{3-6} are *four-fermion penguin operators* and O_8 is the *chromomagnetic (penguin) operator*.¹ They come with different CKM factors, the corresponding Hamiltonian reads:

$$\mathcal{H}^{|\Delta B|=1} = \frac{G_F}{\sqrt{2}} \left\{ \sum_{j=1}^2 C_j (\xi_c^* O_j^c + \xi_u^* O_j^u) - \xi_t^* \sum_{j=3}^6 C_j O_j - \xi_t^* C_8 O_8 \right\} + \text{h.c.}, \quad \xi_q = V_{qb}^* V_{qd} \quad (\text{A.4})$$

¹In the literature one often finds O_8 with the opposite sign. In QCD the sign of the quark-gluon coupling is not fixed, the sign in (A.3) complies with the result for C_8 in Table A-1, if the Feynman rule for the quark-gluon coupling is chosen as $+ig$.

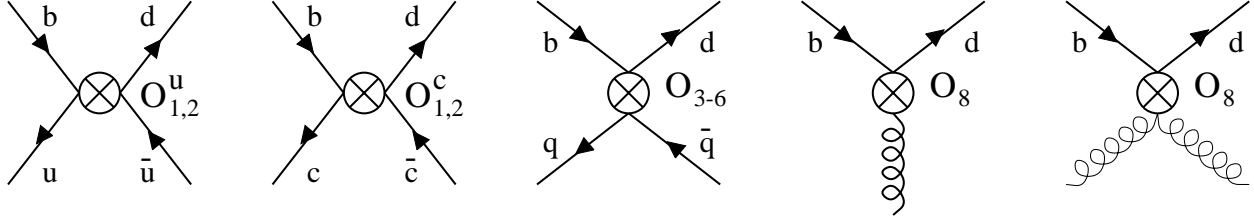


Figure A-1. Effective operators of (A.3). There are two types of fermion-gluon couplings associated with the chromomagnetic operator O_8 .

The Wilson coefficients and the operator matrix elements obtained from taking a matrix element of (A.4) each depend on the arbitrary choice of renormalization scale μ . The C_j 's contain $\alpha_s(\mu) \ln(\mu/M_W)$. Conversely the matrix elements $\langle f|O_j|B \rangle$ must contain logarithms of the form $\ln(\mu/m_b)$ multiplied with $\alpha_s(\mu)$. In the sum in (A.4) these logarithms combine to $\ln(m_b/M_W)$ since any physical quantity, such as a matrix element of $\mathcal{H}^{|\Delta B|=1}$, must be μ -independent. The choice of the scale μ determines the division between the hard QCD interactions included in the C_j 's and the soft-QCD effects included in the matrix elements $\langle f|O_j|B \rangle$. C_j contains the QCD effects from all scales between μ and M_W and $\langle f|O_j|B \rangle$ comprises the strong interaction effects from all energies below μ . (Sometimes μ is therefore called *factorization* scale, meaning the scale that factorizes hard from soft physics; in the context of B Physics this language is a little confusing, since there is another quantity with a similar name, namely the scale at which the factorization approximation to the matrix elements can be expected to work well.) *A priori* one may choose μ arbitrarily, but in practice one wants to shift all the perturbative QCD corrections into C_j and to choose μ as small as possible. Many non-perturbative methods to calculate $\langle f|O_j|B \rangle$ only work for relatively small μ .

Conversely, for perturbation theory to work radiative corrections must be small. If μ is too small, the quantity $\alpha_s(\mu) \ln(\mu/M_W)$ is of the order of 1, *i.e.*, the large logarithm spoils the perturbative series. A partial remedy for this problem is the application of the renormalization group to sum the large logarithms, $\alpha_s(\mu)^n \ln^n(\mu/M_W)$, $n = 1, 2, \dots$, to all orders of perturbation theory as explained in Section 2.1.3. The minimal way to do this is the *leading logarithmic approximation*; the corresponding expression is usually called LO (for *leading order*) result. The LO expression for C_1 and C_2 can be found in (2.8). The summed logarithms can be reproduced by using the LO expansion for the running QCD coupling constant:

$$\alpha_s(\mu) = \frac{\alpha_s(\mu_0)}{1 + 2\beta_0 \alpha_s(\mu_0)/(4\pi) \cdot \ln(\mu/\mu_0)}, \quad \beta_0 = \frac{23}{3}. \quad (\text{A.5})$$

Here β_0 is the first term of the QCD β -function that controls the running of α_s . Setting $\mu_0 = M_W$ one can insert (A.5) into (2.8) and expand $C_{1,2}(\mu)$ in terms of $\alpha_s(M_W)$ to rediscover the summed logarithm. One must choose μ not to differ too much from m_b in order to keep $\ln(\mu/m_b)$ small. A typical choice is $m_b/2 \lesssim \mu \lesssim 2m_b$. Ideally, the μ -dependence cancels between the Wilson coefficients and the operator matrix elements. If it in fact did so then the choice of μ would not be an issue. However most methods to estimate the matrix elements do not give any scale dependence,

and thus, when the sum in (A.1) is performed, calculations encounter a residual μ -dependence. With a leading order perturbative calculation significant residual scale dependence of the result is likely. The numerical range obtained for the predicted observable, when μ is varied in some “reasonable” interval around m_b , is often used to estimate a “theoretical error” of the calculation (other such errors may arise from uncertainties in the matrix element calculation itself). However there is no good way to determine what range of μ represents a “reasonable” variation.

The residual μ -dependence of the LO result can be very large. Thus the leading log approximation is not sufficient for the predictions of high precision experiments like BaBar. Scale dependence is generally reduced once a *next-to-leading order* calculation of the coefficients is made. There are also conceptual reasons for calculating *next-to-leading order* (NLO) corrections, for example the important question of the correct definition of quark masses is a NLO issue (see *e.g.*, the review article [1]). In the NLO the coefficients and therefore (in principle) the matrix elements receive corrections of the form $1 + \mathcal{O}(\alpha_s)$ and also the coupling constant expansion (A.5) changes.

An new feature arises in NLO results, which is often treated incorrectly (or simply ignored). If we calculate a Wilson coefficient $C_j(\mu)$ beyond the leading-log approximation, the result depends on the *renormalization scheme*, which is related to the way one treats divergent loops in Feynman diagrams. Just as in the case of the scale dependence, this *scheme dependence* must cancel when Wilson coefficients and correctly defined matrix elements are combined. This phenomenon can be easily illustrated for the case of a single operator Q and its coefficient C : Let C, C' be the coefficients in two different renormalization schemes. The matrix elements must also differ; in general these two results are related as

$$\begin{aligned} C' &= C (1 + \alpha_s r) \\ \langle f|Q|B \rangle' &= \langle f|Q|B \rangle (1 - \alpha_s r). \end{aligned} \quad (\text{A.6})$$

Hence

$$C' \langle f|Q|B \rangle' = C \langle f|Q|B \rangle (1 + \mathcal{O}(\alpha_s^2)), \quad (\text{A.7})$$

so that physical observables agree within the calculated order. The OPE defines the short-distance physics involving heavy masses like M_W and m_t to belong to the C_j 's, while the long-distance physics is contained in the matrix elements. But a constant number like r in (A.6) can be attributed to either of them! Hence scheme dependences are inevitable. There is no unique definition of anything like a “scheme-independent” Wilson-coefficient. In inclusive decay rates such as $\Gamma(B \rightarrow \text{no charm})$ the sum of matrix elements entering this calculation can be calculated perturbatively using the property of quark hadron-duality, see Section 2.2.4.2. In that case the scheme dependence is under perfect control and cancels as in (A.7). However, for exclusive final states we must use non-perturbative methods to calculate $\langle f|Q|B \rangle$. In lattice calculations and QCD sum rules one can control the scheme and scale dependence, although the scale and scheme matching problems can be formidable. However with many popular methods used to obtain $\langle f|Q|B \rangle$ this is not possible. For example, in the vacuum insertion approximation neither a scale dependence nor any scheme

dependence of the matrix elements is predicted. The same is true for calculations that rely on meson form factor models. Such models can thus at best be correct for a single scale and scheme choice, but typically they contain little or no information to help specify what choice is appropriate.

The numerical values for the renormalization group improved Wilson coefficients can be found in Table A-1. The NLO coefficients are listed for two popular schemes, the *naive dimensional regularization* (NDR) scheme and the *Hooft-Veltman* (HV) scheme. These results have been independently obtained by the Rome and Munich groups [2]. The situation with C_8 is special: To obtain C_{1-6} in Table A-1 one must calculate one-loop diagrams. The calculation of C_8 , however, already involves two-loop diagrams in the leading order. This implies that even the LO expression for C_8 is scheme-dependent. The tabulated value corresponds to the commonly used “effective” coefficient C_8 introduced in [3], which is defined in a scheme-independent way. To know the NLO value for C_8 one must calculate three-loop diagrams. The operator basis in (A.3) is badly suited for this calculation, and hence a different one has been used [4]. For the basis in (A.3) the NLO value for C_8 is not known; we therefore leave the corresponding rows open.

The operators in (A.3) are sufficient for the calculation of $\Delta B = 1$ transitions in the lowest order of the weak interaction with short-distance QCD corrections to any desired order in α_s . These transitions correspond to Standard Model diagrams with a single W -boson and the appropriate number of gluons. If one wants to include electromagnetic effects or higher orders in G_f , one must invoke extra operators. The important radiative decay mode $B \rightarrow X_s \gamma$ involves the *electromagnetic (penguin) operator* O_7 :

$$O_7 = -\frac{e}{8\pi^2} \bar{d} [m_d L + m_b R] \sigma_{\mu\nu} b \cdot F^{\mu\nu}.$$

The corresponding quark-photon coupling looks like the fourth diagram of Fig. A-1 with the gluon replaced by a photon line. Likewise Standard Model diagrams of order G_F^2 involve an extra W - or Z -boson and generate new operators such as electroweak penguin operators. Interesting semileptonic decays such as $B \rightarrow X_s e^+ e^-$ require operators with external quarks and lepton lines. These operators are only relevant for Chapter 9 and are discussed there. The inclusion of electromagnetic corrections not only induces new operators, but also modifies the values of the coefficients in Table A-1 by small terms of order $\mathcal{O}(\alpha)$.

New physics can modify the effective Hamiltonian (A.4). Whatever the physics beyond the Standard Model may be, it is associated with new particles much heavier than the b quark. Hence new physics will modify the Wilson coefficients of Table A-1. New physics effects will be more visible in C_{3-8} , which are loop suppressed in the Standard Model, than in the large coefficients $C_{1,2}$ stemming from the tree-level W exchange. Also new physics may generate new operators in addition to those in (A.3). Stated differently, a coefficient which is exactly zero in the Standard Model can obtain a non-zero value in non-standard scenarios.

Table A-1. Wilson coefficients in the leading and next-to-leading order. The NLO running of α_s has been used in both the LO and NLO coefficients. $\alpha_s(M_Z) = 0.112, 0.118, 0.124$ implies $\alpha_s(4.8 \text{ GeV}) = 0.196, 0.216, 0.238$. The corresponding values of the five-flavor QCD scale parameter $\Lambda_{\overline{\text{MS}}}$ are 159, 226, and 312 MeV. The dependence on $m_t(m_t)$, here taken as 168 GeV, is negligible. The NLO coefficients are listed for the NDR and HV scheme. There are two different conventions for the HV scheme, here we use the one adopted in [2]. The HV coefficients tabulated in [1] are related to our C_j^{HV} 's by $C_j^{HV}([1]) = [1 + 16/3 \cdot \alpha_s(\mu)/(4\pi)] C_j^{HV}$.

$\alpha_s(M_Z)$	scheme	μ GeV	C_1	C_2	C_3	C_4	C_5	C_6	C_8
0.112	LO	4.8	-0.229	1.097	0.010	-0.024	0.007	-0.029	-0.146
		2.4	-0.325	1.149	0.015	-0.033	0.009	-0.043	-0.161
		9.6	-0.155	1.062	0.007	-0.016	0.005	-0.019	-0.133
	NDR	4.8	-0.160	1.066	0.011	-0.031	0.008	-0.035	
		2.4	-0.245	1.110	0.017	-0.043	0.009	-0.052	
		9.6	-0.093	1.036	0.008	-0.021	0.006	-0.023	
	HV	4.8	-0.177	0.993	0.009	-0.024	0.007	-0.026	
		2.4	-0.260	1.020	0.014	-0.033	0.010	-0.038	
		9.6	-0.111	0.975	0.006	-0.015	0.005	-0.017	
0.118	LO	4.8	-0.249	1.108	0.011	-0.026	0.008	-0.031	-0.149
		2.4	-0.361	1.169	0.017	-0.036	0.010	-0.048	-0.166
		9.6	-0.167	1.067	0.007	-0.018	0.005	-0.020	-0.135
	NDR	4.8	-0.174	1.073	0.013	-0.034	0.009	-0.038	
		2.4	-0.272	1.124	0.020	-0.047	0.010	-0.060	
		9.6	-0.100	1.039	0.008	-0.024	0.006	-0.025	
	HV	4.8	-0.192	0.993	0.010	-0.026	0.008	-0.028	
		2.4	-0.286	1.022	0.016	-0.036	0.011	-0.042	
		9.6	-0.120	0.972	0.006	-0.017	0.005	-0.018	
0.124	LO	4.8	-0.272	1.120	0.012	-0.028	0.008	-0.035	-0.153
		2.4	-0.403	1.194	0.019	-0.040	0.011	-0.055	-0.172
		9.6	-0.180	1.073	0.008	-0.019	0.006	-0.022	-0.138
	NDR	4.8	-0.190	1.082	0.014	-0.037	0.009	-0.043	
		2.4	-0.303	1.142	0.022	-0.054	0.011	-0.069	
		9.6	-0.108	1.042	0.009	-0.025	0.007	-0.028	
	HV	4.8	-0.208	0.993	0.011	-0.028	0.008	-0.031	
		2.4	-0.316	1.025	0.018	-0.040	0.012	-0.048	
		9.6	-0.129	0.970	0.007	-0.018	0.006	-0.019	

References

- [1] G. Buchalla, A. J. Buras and Markus E. Lautenbacher, *Rev. Mod. Phys.* **68**, 1125 (1996).
- [2] G. Altarelli *et al.*, *Nucl. Phys.* **B187**, 461 (1981);
A. J. Buras and P. H. Weisz, *Nucl. Phys.* **B333**, 66 (1990);
A. J. Buras *et al.*, *Nucl. Phys.* **B370**, 69 (1992); Addendum *ibid.*, **B375**, 501 (1992); *Nucl. Phys.* **B400**, 37 (1993);
M. Ciuchini *et al.*, *Nucl. Phys.* **B415**, 403 (1994).
- [3] M. Ciuchini *et al.*, *Phys. Lett. B* **316**, 127 (1993); *Phys. Lett. B* **334**, 137 (1994); *Nucl. Phys.* **B421**, 41 (1994).
- [4] M. Misiak and M. Münz, *Phys. Lett. B* **400**, 206 (1997).

This page was intentionally left blank.

B

Some Remarks on Form-Factor Models

B.1 Introduction

B.1.1 Why Use Quark Models?

It is not known how to compute a form factor from full QCD from first principles. In the last few years various methods have been developed to avoid using a model in extracting information from exclusive semileptonic B decays. Lattice calculations (see Appendix C) and QCD sum rules approaches (see Appendix D) give some results and some constraints. However, no method leads to complete predictions for the full range of q^2 and for all final states. In the early stage of the experimental analysis, models are still an indispensable tool which enters *e.g.*, the Monte Carlo simulations. However it is important to be aware of the theoretical limitations of such models.

This appendix contains some critical remarks on form-factor models that are frequently used in semileptonic B decays. This is not meant to deny the intuitive understanding they provide, or their practical utility, but rather to make the user aware of certain problems that are inherent in such models. A comprehensive list of all models on the market is beyond the scope of this appendix. The focus here is to give a general “classification” of models referring to their physical input and to review briefly the limitations of each class of models.

It is not possible to find any model prescription which is satisfactory in all situations. Although various ideas which have been proposed are each subjected to critical review below, each has some particular advantages. The best choice of a model depends on the specific application.

There are some theoretical constraints which must be fulfilled by a reasonable model. These come from the underlying field theory, namely QCD. The most stringent of these constraints are the following:

- Compatibility with symmetries (chiral as well as heavy-quark symmetry)
- Compatibility with analyticity and unitarity bounds
- Compatibility with the behavior of QCD in the deep euclidean region.

One can impose in addition agreement with QCD-based calculations where they exist, such as

- Compatibility with lattice data, and
- Compatibility with the various sum rule calculations.

In estimating the model-dependence of a result, only models that satisfy these constraints reasonably well and that have a certain degree of success in fitting data for measured B decays should be included.

However, many of the models predict not only the form factor for a single exclusive decay, but also the form factors for a whole class of decays. A model that yields a reasonable form factor by these criteria for example for the $0^- \rightarrow 0^-$ transition between ground state mesons is not automatically a “good” model for transitions into excited states.

This problem reflects a deeper drawback in using models. Once a model is employed to predict a process or to extract a fundamental parameter, one has no control over the systematic uncertainties induced by the model. In this there is a sharp distinction between a *model* and an *approximation*. For this reason controlled approximations are always preferable over the application of models, wherever they are possible.

The focus here is on models for semileptonic-decay form factors. These model form factors are frequently also used for a computation of exclusive two-body nonleptonic decays. This relies on the additional, theoretically not well justified, assumption of factorization. However, this *ad hoc* prescription describes the present data on exclusive nonleptonic two-body B decays in a reasonable way, so that it is frequently viewed as giving at least a reasonable estimate for the as-yet-unmeasured decay rates. We shall not consider this point any further here, since it is discussed in Chapter 10.

B.1.2 General Features of Quark Models for Form Factors

Before the different versions of quark models are discussed in some detail, a few general remarks and an outline of a classification scheme are in order.

The spirit of practically all quark models is quantum mechanical, as opposed to field theoretical; the concept is based on potentials giving rise to bound states, and the number of particles involved is fixed (*i.e.*, the valence quarks only). Most models include some relativistic effects. However, *relativistic effects* or a *relativistic model* mean in most cases (at least in the present context) that either the nonrelativistic approach is supplemented by relativistic corrections (*i.e.*, the next-to-leading terms in the v/c expansion) or that a two-body equation with a form for the three-dimensional wave function motivated, for example, by the Dirac equation is used to determine the wave function for the bound state of quarks.

However, most such models yield wave functions that are not fully Lorentz-covariant, and hence a specific reference frame has to be picked in which to apply the approximations. This is usually taken to be the rest frame of the initial hadron. Some aspects of the hadronic physics, such as the wave functions at the origin or the mass-spectrum of states, can be reproduced by these models, once the potential is adjusted appropriately. A model that satisfies such constraints is sometimes called a *spectroscopic model*.

In order to model a form factor one has to perform a further step to access the q^2 dependence. In general there are two ways this is done:

- The form factor is calculated for a fixed value of q_0^2 , *e.g.*, within a spectroscopic model, and then an ansatz for the q^2 dependence, motivated by some phenomenological picture, is used. This is often called a *hybrid model*.
- The overlap of the initial and final state wave functions is computed directly, where the final state wave function is boosted according to the value of q^2 . Such calculations are here called *full quark model calculations*.

The full quark model calculations may again be divided into purely nonrelativistic approaches and (semi-)relativistic ones. The former are based on ordinary quantum mechanics, where it is known and well defined how to boost (*i.e.*, how to Galilei transform) a two-particle wave function. While such an approach has the advantage that it naturally incorporates the normalization at q_{\max}^2 implied by the heavy-mass limit, it does not reproduce the observed q^2 dependence [1]. This results in two shortcomings:

- much too small ρ^2 (or charge radii for light-quark systems)¹ and
- much too small values of the form factors at large recoil, at least if one uses the standard Gaussian wave functions.

Even in a $B \rightarrow D$ transition v/c for the D meson in the rest frame of the B can be as large as 0.7, not to speak about the large internal velocities of the light quark inside the mesons. Thus a purely nonrelativistic approach over the full range of q^2 is clearly not justified. Of course the situation is even worse for the $B \rightarrow \pi$ transitions.

Various ways have been suggested to include relativistic effects. Starting from full quantum field theory one obtains a formulation in terms of the Bethe-Salpeter amplitude [3], which fulfills a complicated integral equation involving an interaction kernel. At this stage everything is still fully

¹The ISGW [2] potential model appears to be nonrelativistic, but contrary to many statements, except for some features are zero recoil, the ISGW model for form factors is not really a nonrelativistic full quark model, because *e.g.*, the slopes of the form factors are not taken at the values predicted by the nonrelativistic calculation. The claim is that the change parametrizes some of the relativistic effects.

Lorentz covariant. The kernel, as well as the Bethe-Salpeter amplitude, depend on the space time coordinates of the two fields involved in the bound state; this dependence may be rewritten in terms of relative and cms-motion, and hence a *relative time* coordinate appears. It is the dependence on this variable which makes this approach practically intractable, unless some approximations are made.

One common approximation is to neglect the dependence on the relative time variable, in which case the interaction kernel is simply an instantaneous potential, and the Bethe-Salpeter amplitude becomes a two-particle wave function, depending on the (cms)-time variable and the cms- and relative space coordinates. This approximation makes the Bethe-Salpeter approach tractable, at the cost of having the boosted wave-function only crudely approximated. In order to compute a form factor in this approach, an additional approximation has to be made. This is the so-called “triangle approximation” [4] which allows one to express the current matrix elements in terms of an integral over the Bethe-Salpeter amplitudes of the two hadrons only. Through these assumptions one ends up with something close to the three-dimensional quantum-mechanical approach, except for an additional quark pair contribution which is the only remnant of field theory. This will be discussed in some detail in Section B.3.

All other methods are not based on quantum field theory, but rather on semi-relativistic two-particle equations, motivated by the success of the three-dimensional Dirac or Salpeter equations. These approaches, applied as spectroscopic models, can reproduce the mass spectrum in a satisfactory way (by a clever choice of the potential). However the computation of form factors requires knowledge of the relativistic boosts. These are not known, and so require some ansatz, in general not covariant. Yet, this is up to now the most practicable approach, and presently the most active trend. This will be considered in some more detail in Section B.3.

Table B-1 summarizes the classification of models used in this appendix. Most of the models suggested in the literature fall into one of these classes. The last column gives a “prototype” of the corresponding model, simply to provide an example. The intent here is not to evaluate all the models in the literature nor to make any specific suggestion which models are preferable over others; this will anyway depend on the physical circumstances which have to be described by the model.

A more detailed discussion of the various models and their classification follows. In the next section we shall consider the *hybrid models* (that is *quark models combined with a phenomenological ansatz*) together with a few remarks on *purely phenomenological models*. Section B.3 discusses the full quark model calculations, in which the q^2 dependence is obtained from the wave function overlap.

Table B-1. Schematic classification of the various models. The last column contains the reference to the corresponding “prototype” model.

Quark Model combined with phenomenological ansatz	Vector-Meson-Dominance models with	normalization at $q^2 = 0$		[5]
		normalization at q_{max}^2		[6]
	phenomenological ansatz for relativistic effects		[2], [7]	
	constraints from QCD	deep euclidean q^2		[8]
		Heavy-Quark Symmetry		[7], [9]
Form factors from overlap of nonrelativistic wave functions				[10], [11]
relativistic approaches	three-dimensional approach	approximation of Bethe-Salpeter amplitudes	Lorentz contraction	[12], [13], [14], [15]
			pseudo-potential	[16]
	Bakamjian-Thomas relativistic quantum mechanics	instant form		[17], [18]
		point form		[19]
		light-front	longitudinal frame	[20], [21]
	transverse frame		[22], [23]	
	Bethe-Salpeter approach in Mandelstam triangle approximation			

B.2 Hybrid Models and Purely Phenomenological Models

The *hybrid quark models* circumvent the problem of the boost by using the quark model only for a convenient value q_0^2 of the momentum transfer and applying a more or less ad hoc ansatz for the q^2 dependence. In other words, a quark model is only used to obtain the normalization of the chosen q^2 dependence. The hybrid models can be divided into those which use a true quantitative normalization by quark models, and others, which borrow only qualitative features from quark models (purely phenomenological models). However, all the comments on the relevance of particle pole dominance which are discussed for the former below, are also valid for the latter.

B.2.1 Hybrid Models

In Hybrid Models there are two natural choices $q_0^2 = q_{\max}^2$ or $q_0^2 = 0$. The first choice $q_0^2 = q_{\max}^2$ is an obvious one from both the heavy-quark symmetry point of view as well as from the point of view of spectroscopic models. At this kinematic point the initial as well as the final state particle have the same rest frame and the form factor at this point which is simply the overlap of two rest frame wave functions, which can be taken from a spectroscopic model. Prototypes of these models are *e.g.*, the model by Altomari and Wolfenstein [6], the two types of the Isgur, Scora, Grinstein, Wise model, ISGW I [2] and ISGW II [7]. Here the normalization is given simply by the wave function overlap of the initial and the final state meson.

The second choice $q_0^2 = 0$ is the kinematic point at which the final state particle has its maximal momentum in the rest frame of the decaying one. Here, one may compute the form factors as simple wave function overlaps in the infinite momentum frame. Prototypes here are the model by Wirbel, Bauer and Stech [5], the models by Körner and Schuler [8], and the NRSX model [9].

There are infinitely many possible choices for the q^2 dependence. In most cases, (multi-)pole ansatz for the q^2 dependence are used, except for ISGW I, where Gaussians were adopted. These have been abandoned in the later ISGW2 version in favor of a multipole ansatz because the ISGW I models yield much too small values for the form factors at large recoil due to the steeply falling wave functions.

The general motivation of these ansätze is simply that one expects a smooth q^2 behavior of the form factors. The reason for the (multi-)pole ansatz is twofold. Close to q_{\max}^2 one expects a single state to dominate the q^2 behavior in the heavy-to-light case, implying a vector meson dominance (VMD) form of the q^2 dependence. This is discussed in more detail below. Secondly, in the Euclidean region $q^2 \rightarrow -\infty$, perturbative QCD based on the ideas of Brodsky and Lepage [26] predicts that the q^2 behavior in the deep Euclidean is multipole-like.

B.2.2 Discussion of the Idea of Nearby-Pole Dominance

More explicitly, motivation for such an ansatz for the q^2 dependence comes from quantum field theory. Consider the vector current between two pseudoscalar mesons M_i and M_f . It can be shown that this transition matrix element may be written as

$$\langle M_i(p) | \bar{Q} \gamma_\mu q | M_f(p') \rangle = f_V(q^2) \left(p_\mu + p'_\mu - \frac{m^2 - m'^2}{q^2} q_\mu \right) + f_0(q^2) q_\mu \quad (\text{B.1})$$

where $q = p - p'$ is the momentum transfer of the process. The form factors f_V and f_0 satisfy dispersion relations, which have the form

$$f_V(q^2) = \int_0^\infty \frac{ds}{2\pi} \frac{\rho_V(s)}{q^2 - s + i\epsilon} \quad (\text{B.2})$$

$$f_0(q^2) = \int_0^\infty \frac{ds}{2\pi} \frac{\rho_0(s)}{q^2 - s + i\epsilon}$$

where we do not discuss the possibility of subtractions. The two spectral functions ρ_V and ρ_0 may be related to intermediate states $|X(p_X)\rangle$ such that the matrix element (B.1) may be understood as a subsequent process in which the current creates the intermediate state which then decays into a final state $|M_i(p)M_f(p')\rangle$. This yields the matrix element $\langle 0 | \bar{Q} \gamma_\mu q | M_i(p)M_f(p') \rangle$ which is related through crossing symmetry (*i.e.*, analytic continuation of the variable q^2) to (B.1).

It is tempting to assume that, because of the denominators under the integrals, the main contribution in the region $0 \leq q^2 \leq q_{\text{max}}^2 = (m - m')^2$ to the integrals in (B.2) comes from states with masses closest to this region, which are the states with masses right above q_{max}^2 . Due to the structure of the form factors the intermediate states relevant for ρ_V are 1^- states, and hence one may think of approximating ρ_V by $\rho_V(s) = R_V(m_*^2)(2\pi)\delta(s - m_*^2)$ where m_*^2 is the mass of the lowest vector particle with the correct flavor quantum numbers. Correspondingly, the states for ρ_0 have to be 0^- states, and thus we get

$$f_V(q^2) \approx \frac{R_V(m_*^2)}{q^2 - m_*^2} \quad (\text{B.3})$$

$$f_0(q^2) \approx \frac{R_0(m_{**}^2)}{q^2 - m_{**}^2}$$

where m_{**} is the mass of the lowest scalar resonance with the correct flavor quantum numbers. As examples, for the $b \rightarrow u$ transitions the lowest vector particle is the B^* , while in the scalar channel the lowest state is one of the B^{**} s.

Thus this approximation gives a function for the q^2 dependence of the form factors, where the normalization is given by $R_V(m_*^2)$ and $R_0(m_{**}^2)$. One does not know how to compute these

quantities from the underlying field theory. Hence the normalization is taken from a different source, namely from a quark model.

There are many *ad-hoc* modifications of this simple ansatz such a dipole-form which is using the second power of the denominators in (B.3).

One would expect that the nearest pole indeed can dominate the behavior of a form factor close to q_{\max}^2 , if this pole is isolated, meaning that the density of states in this region is small. Intuitively one expects that this may be reasonable for the $b \rightarrow u$ decays close to q_{\max}^2 involving the vector channel, since there is only a single isolated state below the $B\pi$ threshold. On the other hand, for the $b \rightarrow c$ transitions there will be a larger number of B_c -states below the BD threshold, which will cause deviations from the simple pole even close to q_{\max}^2 .

On the other hand, these decays are probably well described by *full quark model calculations*. The relation between the dispersion relation and the wave function picture has been discussed by Jaffe and Mende [27] where they point out that the large “charge” radius of a “loosely bound” confined system can only be reproduced by a complicated behavior of the spectral functions, since the simple pole always yields a much smaller charge radius of the order of the Compton wavelength of the intermediate state.

The idea of nearby-pole dominance or VMD is central to the ansatz for the q^2 dependence in hybrid models. Some problems related to it are discussed below. More details can be found in [28], [29]).

- For heavy-to-light transitions in the region close to $q^2 = 0$ one is far away from the region $q^2 \sim q_{\max}^2 \sim m_B^2$ where one would assume that the dominance of the nearest pole is a good approximation. The extrapolation using a simple pole will certainly not be safe.
- For heavy-to-heavy transitions there will be many closely spaced nearby states (*e.g.*, the family of B_c states in the $b \rightarrow c$ transitions) which may fake anomalous thresholds, yielding a more complicated q^2 behavior of the form factor (*cf.* Jaffe and Mende [27]).
- The usual ansatz uses only the functional dependence on q^2 with a normalization (*i.e.*, a residue) fixed by a quark model. The residue obtained in this way is in general unrelated to the “true” residue one would obtain from a dispersion relation.
- Pure pole dominance, *e.g.*, in Altomari, Wolfenstein and Wirbel, Stech, Bauer, is in contradiction with certain expectations from QCD, such as the asymptotic behavior at large negative q^2 and heavy-quark symmetry in the case of heavy-to-heavy transitions.

Hence the conclusion is that simple pole dominance can at best be expected to be a good approximation close to q_{\max}^2 in the case of a heavy-to-light transition such as a semileptonic $B \rightarrow \pi$ decay. In this region the pole form has deeper root in QCD given by the idea of uniting heavy-quark symmetry with chiral symmetry [30].

Given these problems efforts have been made to modify the ansatz. In particular, one may impose heavy-quark symmetry on a model for heavy-to-heavy transitions using the wave function at $q^2 = 0$. Given the dependence on the masses one may reconstruct a form of the Isgur Wise function (see Neubert and Rickert [31]). This does, however, not result in a pole-like dependence.

One may also try to make a pole ansatz consistent with heavy-quark symmetry as it is done in the NRSX model [9]. Here the powers are fixed according to heavy-quark symmetry relations. Yet, the NRSX model remains not fully consistent with heavy-quark symmetry because of the properties of the quark model used at $q^2 = 0$ [13].

The constraints from asymptotic QCD have been imposed by Körner and Schuler (KS) [8]; they require that some of the form factors must be chosen to be dipoles. Clearly this ansatz departs from the simple single resonance pole-dominance picture. The usual argument is that it corresponds to several particle poles, as in the nucleon isoscalar form factor, or it may not correspond to particle poles at all, rather it reflects a more complicated structure.

On the other hand, certain relativistic models support the idea of a pole ansatz, although the physical content of the models is based on wave functions and is thus unrelated to the VMD idea. In particular, according to Jaffe and Mende [27] this wave function picture should be matched to a situation with many closely spaced nearby poles. As an example, in the model of [32], the dipole like behavior is connected with the Coulomb-like behavior of the wave functions.

In conclusion, one must consider the (multi-)pole ansatz as having little to do with the dominance of a nearby singularity, rather they have a “flexible” meaning: “pole” or “dipole” may be considered, with poles fixed at physical masses or not, at large q^2 or in the physically limited range $0 < q^2 < q_{\text{max}}^2$, for one or another set of invariant form factors.

B.2.3 Purely Phenomenological Models

There is a class of models which uses qualitatively some of the ideas described above, but they do not make quantitative use of a quark model. In this sense they are purely phenomenological and use only general theoretical constraints. Models of this kind are [33] [13] [34] [35], the main motivation of which is to have more flexibility in order to get a better fit to data on *e.g.*, D decays.

As far as the physical input is concerned, these models use either the concepts of pole dominance or QCD constraints (mainly heavy-quark symmetries) considered above or features of the “full quark models” discussed below. We shall not discuss this class here any further.

B.3 Full Quark Model Approaches

Full quark-model calculations here refers to any approach which calculates the form factors completely within the framework of a quark model. In general such models fall into two classes. The first class are the models based on the formally covariant Bethe-Salpeter approach and the second class are the three-dimensional wave function approaches.

Following the trend of current research the **full quark-model calculations** discussed below are those where the form factors are calculated through the current operator matrix-elements of ordinary three-dimensional wave functions. It should be stressed that, although intrinsically quantum-mechanical, such models always aim at some sort of **relativistic** treatment.

B.3.1 Bethe-Salpeter Approach

The **Bethe-Salpeter approach** has been investigated in the past by Gudehus, Böhm, Joos and Krammer [24], with a full combined study of spectroscopy and decays; a later study was performed by Körner. An even more recent Bethe-Salpeter approach, somewhat outside the scope of the usual quark models, includes the idea of spontaneous breaking of chiral symmetry [36]. One known difficulty of this approach is that it is not possible to reproduce the orbital excitation spectrum with the vector exchange confining kernel which is often used to respect chiral symmetry. If the full nonperturbative gluon propagator is used for the kernel, there is the additional danger of getting large spin-spin confining forces. A very recent example of the application of this approach to heavy-flavor decay form factors is found in [25].

In the Bethe-Salpeter approach one retains the triangle approximation [4] in the Mandelstam expansion of current matrix elements. The main advantage of this formulation is that, if one uses a covariant interaction kernel in the bound state equation, each term in the expansion is covariant by itself; therefore, even in the triangle approximation, one obtains automatically frame-invariant form factors. Nevertheless, this sort of invariance is rather formal because these approaches are not really based on local field theory, but rather on phenomenological assumptions for the interaction kernel, or even on a direct phenomenological ansatz for the Bethe-Salpeter amplitudes. An ansatz for the interaction kernel in general is not compatible with a field theory based on a local Lagrangian. In other words, a local field theory would yield a certain kernel, but the reverse, namely that some guess for the kernel can be cast into the form of a local field theory, is not in general true.

Furthermore, in solving the Bethe-Salpeter bound state equation one sometimes resorts to approximations built from a picture which only applies (if at all) in the hadron rest frame. Nevertheless, this is a weaker assumption than those necessary in three-dimensional models, where one has also to choose particular frames to calculate the form factors themselves.

The difficulties of the approach are mainly related to the relative energy dependence. This complicates the analysis, since this dependence is neither easily deduced from theory nor easily obtained from data; one has then to formulate additional assumptions. Hence in general, the connection with the underlying theory is lost. From the technical side, the analysis is complicated by the number of independent components of the Bethe-Salpeter amplitude due to spin.

B.3.2 Three-Dimensional Approaches

The general idea of the **three-dimensional approach** is to deduce three-dimensional wave functions for the states in motion from the corresponding wave functions at rest, where the latter are calculated in standard spectroscopic quark models. The direct connection to the spectroscopic quark models is an advantage, since such models have been checked in various other applications. In addition, the three-dimensional wave function has a probabilistic interpretation, which is not the case for the full multi-time Bethe-Salpeter amplitude.

The main disadvantage is the lack of covariance in general; the values assigned to the invariant form factors depend on a choice of frame for the calculation. Since models are in any case approximate, the lack of explicit covariance in the form factors is perhaps not a problem, provided one understands in what frame the model's approximation is reasonable. With the exception of the pseudopotential approach, these models retain only the simplest configurations with conserved particle number. They neglect pair creation or annihilation effects. Despite their drawbacks, the three-dimensional approaches have been studied extensively in the recent period.

A partial solution to the covariance problem is given by the **Bakamjian-Thomas formalism**. This approach is not related to field theory. It allows a rather general instantaneous interaction between quarks, and one can obtain a covariant result in the sense that one has the correct commutation relations for the boost operators. The spectrum and the states are fully covariant and one can deduce consistently the relation between wave functions in different frames. It has to be stressed again that this type of covariance is formal and is not related to the covariance of the underlying local field theory. In particular, the results from this approach are not superior to any other model approach only because of this formal covariance.

Within this approach using this formal covariance, the form factors in the heavy-mass limit do not depend on the particular frame in which the calculation has been performed. This will be discussed in more detail below. Unfortunately this method applies only for heavy-to-heavy transitions and not heavy-to-light transitions.

There are relations between the three-dimensional approach and the Bethe-Salpeter ansatz. In many cases the triangle approximation of the Bethe-Salpeter approach serves as a theoretical reference, from which one derives a three-dimensional approach. Within this point of view in general the translation of the Bethe-Salpeter triangle approximation into a three-dimensional formalism

yields a pair contribution, which corresponds to creation or annihilation of quark-antiquark pairs by the current. Such terms are a natural consequence of field theory; however, they are not included in most three-dimensional quark models (a notable exception is the recent works of Faustov *et al.* [37]). Neglecting these contributions is in agreement with the simplifying postulate of the impulse approximation (*i.e.*, a quantum mechanical treatment), which is inherent in the usual quark models. We note that in the infinite momentum approach these terms vanish under certain kinematical conditions, which are unfortunately unphysical (see below).

An approach which lies in between the Bethe-Salpeter method and certain three-dimensional formulations has been proposed by Melikhov *et al.* [23]. It has been shown to be equivalent to both methods under certain conditions and with some assumptions (see below).

B.3.3 Classification of Three-Dimensional Approaches

Among the three-dimensional approaches there are again various different assumptions made. The most common ones are the following:

- Direct identification of the form factors in the $m_Q \rightarrow \infty$ limit with nonrelativistic overlaps; prototypes of this kind are discussed by Ali *et al.*, [10], and Suzuki *et al.*, [11].
- Models of the Wirbel, Stech, Bauer type, which deduce the three-dimensional wave function in the infinite momentum frame from an explicit four-dimensional wave function (*e.g.*, from an harmonic oscillator model). Prototypes of these models are the Wirbel, Stech, Bauer model using the infinite momentum frame at $q^2 = 0$, with nonrelativistic structure for the spin wave function [5], and the modified Wirbel, Stech, Bauer quark model with a semi-relativistic treatment of the spin, which is quoted in [31].
- Approaches with a definite general prescription to deduce wave function in motion from the wave function at rest.

The last type of approach represents the present main trend, and it can again be divided into two groups. One consists of the models based on an intuitive approximation of the Lorentz transformation for wave functions, and the second are the so-called Bakamjian-Thomas formulations, which incorporate in particular many of the numerous infinite momentum frame approaches.

B.3.3.1 Intuitive approximations of the Lorentz transformation for wave functions

In the four-dimensional Bethe-Salpeter formulation, the transformation of wave functions between two frames is trivial: it amounts simply to the Lorentz transformation of space-time coordinates

or momenta and to the standard Lorentz boost for the spins. However, this requires the knowledge of the full relative time dependence, which is not available. For the three-dimensional wave function models the difficulty is simply moved elsewhere, since it corresponds to the Bethe-Salpeter amplitude at equal times. Hence there is no longer any dependence on the relative time, but the price paid is loss of Lorentz covariance. The Lorentz transformations of the wave function is not a priori defined in this treatment; one needs some additional assumptions or modeling to obtain the boost. In fact, the instantaneous wave function in some frame is related to the Bethe-Salpeter amplitude in another frame, *e.g.*, in the hadron rest frame, with constituents taken at different times. No simple exact relation exists to the instantaneous, equal time wave function of the rest frame, which is the input provided by the spectroscopic models. Approximate linear relations are taken from some intuition and are generally based on the idea of weak binding. All approximate prescriptions contain the usual Lorentz transformation of spin, or its Pauli spinor version with Wigner rotations. But they differ in the way they relate space coordinates or momenta in the wave functions in the rest frame to those in motion. The typical prescriptions are the following:

- The naive Lorentz contraction prescription, which can be derived from the assumption of weak relative time dependence of the Bethe-Salpeter amplitude in the rest frame. This dates back to Brodsky and Primack [12], Licht and Pagnamenta [38], and has been developed further in the old Orsay quark model [1] [13]. Some more recent discussion can be found in Ahmady *et al.* [14] and by Veseli and Olsson [15].
- The “pseudopotential” approach as discussed in [16], [39], and [37].

The latter is basically a reformulation of the Bethe-Salpeter formalism in a three-dimensional form, with the wave function being the equal-time Bethe-Salpeter amplitude. Hence it would be equivalent to the Bethe-Salpeter approach, if all terms in the pseudopotential expansion were included and if the three-dimensional wave functions were calculated dynamically in each frame. However only the simplest, lowest-order terms in the expansion can be included in practice. Moreover, the wave function is not actually calculated in each frame from the Bethe-Salpeter bound state equation; usually (see especially Faustov [16]) one tries to deduce the wave function in motion from the one in the rest frame, once the rest frame wave function is calculated.

This requires an assumption for the relation between the quark momenta in the laboratory frame and those in the rest frame, where the wave function is known. In [16], it is assumed that quarks are quasi-free, and approximately on their mass shell in the laboratory frame. Based on this the corresponding momenta in the rest frame are computed from a Lorentz boost of the hadron. Another approximation, first exposed in [39] and used in more recent papers [37], is to neglect the Lorentz transformation of the momenta and to retain only the Wigner rotations of spin.

Another approach has been suggested by Colangelo *et al.* [40]. They identify certain kinematic conditions chosen to minimize the effect of the wave function transformation. In this way approximate covariance is obtained.

B.3.3.2 Relativistic quantum mechanics à la Bakamjian-Thomas

The basic ideas of the approach can be found in the papers by Bakamjian and Thomas [41], by Osborn [42], and by Keister-Polyzou [43]. The approach constructs a boost-covariant theory with a fixed number of constituents and an arbitrary direct interaction between the quarks. This is achieved by the construction of an exact unitary representation of the Poincaré group, that is the Hamiltonian H and the boost operators \mathbf{K} . This approach is still purely quantum mechanical and has no a-priori connection to field theory, although Close and Osborn [44] have discussed an approximate connection to QED, using a v^2/c^2 expansion.

One important advantage of the approach is that, since the boost operators are constructed explicitly, one can implement covariance at least formally. The Hamiltonian and therefore its eigenstates are covariant. One obtains a well-defined relation between the momenta in the rest frame wave function and those for the wave function in motion, thereby avoiding the need for uncontrolled approximations to give this behavior.

The difficulty is that the simple one-quark current operators such as $\gamma^\mu, \gamma^\mu\gamma^5$ are not covariant under the Bakamjian-Thomas boosts. Obtaining a covariant current operator is a much more difficult task which is possible only using multi-body operators. Hence form factors calculated by keeping only the standard current operators are not covariant in general. Therefore there are once again, in practice, a variety of inequivalent models according to various choices of reference frames, as it is seen below.

Various forms of the Bakamjian-Thomas approach correspond to the different choices of how to describe the dynamics [45]. There is the instant form formulation of Le Yaouanc *et al.* [17]; the intuitive formulation of Close and Wambach [18], which has been found to be a special case of in the instant form formulation [17]; the light-front form given in [46] and [47]; and the point form of [43] and [19]. In the instant form of the Bakamjian-Thomas approach, concrete calculations have been performed up to now only in the $m_Q = \infty$ limit and thus apply presently only to heavy-to-heavy processes.

The current trend is to use the Bakamjian-Thomas approach in the infinite momentum frame. Most of the quark models formulated in the light front approach can be obtained from the Bakamjian-Thomas method by going to this frame. This has been shown in [48]. Exceptions to this rule are the Wirbel-Bauer-Stech model [5] and the one developed by Dziembovski [49].

In the following the discussion is restricted to models relevant for heavy-quark decays. One must first note a few problems of the infinite momentum frame versions of quark models. Since the current operators such as γ_μ are not covariant under the boost operators, results depend on the choice of the direction of various vectors with respect to the infinite momentum frame axis. One agrees to choose the positive light-cone component of the current J_+ , which involves only those components of quark fields, which are projected out in the light cone formalism. However, there is still further freedom to choose the reference frame: either a “transverse” frame as proposed by

Jaus [22] or a longitudinal frame as in Dubin and Kaidalov [21], Narodetskii *et al.*, and Simula, [20] [50]. Here transverse and longitudinal are defined by the direction of the three-dimensional momentum transfer with respect to the direction of the infinite momentum.

In the infinite momentum transverse frame the region $q^2 > 0$ is inaccessible. This is a serious drawback for semileptonic decays, where $q^2 > 0$. There have been two suggestions to overcome this problem:

- One starts from the $q^2 < 0$ transverse frame expression and extrapolates the light-front integral directly (see Jaus [22]).
- One uses for the analytic continuation a new “double dispersion relation” expression as suggested by Melikhov [23].

For similar reasons, for high spin hadrons, in the infinite-momentum-frame, the physical results depend on the choice of the helicity states used to identify the form factors in the quark model calculation.

In conclusion, the infinite momentum frame approach has many ambiguities, some of which compel rather unphysical choices. In contrast, in the instant form, it is sufficient to choose a frame, for instance the rest frame of one hadron; no further choice of current and spin components is necessary since the models are rotationally invariant.

The main advantage of the infinite momentum frame is the possibility of suppressing the pair contribution, which is difficult to evaluate and not included. However, this suppression occurs only in the transverse frame, which is unphysical for semileptonic decays. In the longitudinal frame, there is no suppression of the pair contribution, and one finds a strange behavior of the form factors near q_{\max}^2 , as *e.g.*, a decrease of $f_+^{B \rightarrow \pi}$ as $q^2 \rightarrow q_{\max}^2$.

The $m_Q = \infty$ limit of models à la Bakamjian-Thomas has been investigated in detail in [51]. In the instant form one can obtain covariance and heavy-quark symmetry for the form factors. In addition, the Bjorken sum rule can be derived by using the completeness of states in motion. Furthermore, the covariance found in this limit implies the identity of instant and light-front forms in the heavy-quark limit. This allows for an interesting check for the infinite momentum frame calculations, which suffer from complicated features at $q^2 > 0$; *e.g.*, one should obtain the same ρ^2 as in the instant form in passing to the limit of heavy quarks, independent of frame choice. This has indeed been verified. The point form seems to lead to the same conclusions: the $m_Q = \infty$ limit yields covariant expression with correct heavy-quark symmetry properties [19]. Hence in the $m_Q = \infty$ limit the heavy-quark symmetry all forms of dynamics yield covariant and heavy-quark symmetric results.

Off the limit $m_Q = \infty$ the Bakamjian-Thomas approach still suffers from serious defects at order $(1/m_Q)$, in particular for heavy-to-light transitions. These problems are

- Lack of covariance of form factors,
- Lack of gauge invariance [52], and
- Violations of Heavy-Quark Symmetry in the infinite momentum frame version [23].

B.3.4 Connection between Bethe-Salpeter Formalism and Three-Dimensional Models

There is a relation between the “triangle” diagram approximation to the current matrix-element in the four-dimensional Mandelstam formalism for the Bethe-Salpeter equations and the three-dimensional approach. The connection is established by performing the integration over the relative energy variable, which is possible when the only dependence on this variable originates from the poles of the propagators [12]. Hence this relation is not valid in general; it applies only for special cases in which, *e.g.*, the vertex functions are constant or at least independent of the relative energy variable.

In addition, this relation neglects the pair contribution, which automatically is given through the reduction of the triangle diagram to a three-dimensional expression, but which is not usually taken into account in the direct three-dimensional approaches. Therefore, for the relation to be exact, the pair contribution must vanish. This happens if two conditions are met [53]:

1. The infinite momentum frame or light front coordinates are used.
2. Transverse frames are used.

As mentioned above, the transverse frames cannot be used to calculate directly in the $q^2 > 0$ region. Thus one needs some extrapolation or analytic continuation if one wants to exploit the attractive property of pair-contribution suppression in the transverse frames.

In this respect the dispersion approach of Melikhov [23] has certain advantages:

- Melikhov derives an equivalence for $q^2 < 0$ between the triangle approximation within a certain category of vertex functions and the light-front formulation in the transverse frame, without pairs. These vertex functions are those which are independent of relative energy in the rest frame of the hadron. However, this equivalence is not fully general because of the possibility of “subtractions” needed in the dispersion relation for high-spin hadrons. For example, for axial-current matrix elements of $0^- \rightarrow 1^-$ transitions, the equivalence is lost because Melikhov adopts a modified spectral function to enforce NLO heavy-quark symmetry.

- He proposes a general expression for the analytic continuation to $q^2 > 0$.
- He cures the problems of the violation of heavy-quark symmetry in non-leading order by introducing subtractions.

However, there is a price to pay for these improvements. First, one has to depart from the intuitive picture of three-dimensional wave functions; in particular, the expressions for the analytic continuation into the physically relevant region $0 < q^2 < q_{\max}^2$ are very complex. Furthermore, the subtractions are not supported by the infinite momentum wave function framework, which means that this approach is somewhat outside the wave function picture.

B.3.5 Quantitative Predictions of Three-Dimensional Models

To perform an actual computation in three-dimensional approaches, one first has to choose a specific mass operator or spectroscopic model from which the wave functions at rest are calculated. In discussing results of models for form factors, one has to note that these results arise always from a particular approach to the treatment of hadrons in motion and a particular model for the wave functions at rest. For instance, the notion “ISGW model” can be either understood as meaning their specific spectroscopic model (a nonrelativistic potential model) or their phenomenological ansatz for form factors. Therefore, in any discussion referring to models for form factors, one must pay attention to the question of whether one is discussing the model which obtains the rest frame wave functions or the one for deducing from them the form factors themselves. Of course, the two should be discussed separately from a theoretical point of view, and one could be reasonable while the other is not.

Some issues concerning spectroscopic models and wave functions used in practical calculations, which seem to have been often underestimated up to are the following:

- Many predictions are still formulated with wave functions taken from nonrelativistic spectroscopic models. It appears that relativistic spectroscopic models with relativistic kinetic energy (such as [54], [55] and [56]) yield notably different wave functions, which exhibit an exponential behavior over a large range of r , and thus have a larger average momentum [32]. It is obvious on general physical grounds that they should be preferred to nonrelativistic ones. In addition such relativistic wave functions are very close to wave functions measured in lattice NRQCD [57]. For both these reasons model predictions formulated with relativistic wave functions, are preferable.
- The standard harmonic oscillator wave-function is used in a good number of models. It appears very unsatisfactory in crucial cases, in spite of the fact that the overlap with the exact wave function may be very close to unity. A better criterion for evaluating the quality

of the approximation for the wave function is the integral of squared difference between the two wave functions. Using this criterion, an exponential approximation to the ground state wave function appears far better, in particular for relativistic wave equations.

To illustrate the strong sensitivity to wave functions, let us give a typical example in the Bakamjian-Thomas framework. With a relativistic wave function, one obtains a dipole behavior of the Isgur-Wise function $\xi(w)$:

$$\xi(w) \approx \left(\frac{2}{w+1} \right)^2. \quad (\text{B.4})$$

From this one gets $\rho^2 \approx 1.0$ compared to $\rho^2 \sim 1.2$ for the harmonic oscillator approximation to the same wave function. For a nonrelativistic wave function one finds $\rho^2 = 1.3$ for the ISGW nonrelativistic wave function, and $\rho^2 = 1.4$ for the harmonic oscillator approximation to the same wave functions.

The same sensitivity to the choice of the wave function is true for the heavy-to-light transitions at large recoil. At present, the model of Melikhov uses harmonic oscillator wave functions; a similar treatment applied to exact relativistic wave functions might change the predictions for large recoil significantly.

B.4 Conclusions

In conclusion, the large multiplicity of models is due in part to the existence of competing general physical ideas: pole dominance versus wave function pictures. Within these classes there are again many subdivisions according to further assumptions or the ways chosen to solve the remaining problems. For the pole dominance models there is the way to pick the normalization point as well as the difficulty to implement asymptotic QCD constraints. For the full quark model calculations there is the difficulty of implementing the aspects of relativity, in particular the boost of the wave functions.

Finally we want to comment on the implementation of radiative corrections. Since models are obviously not based on local field theory, they miss an important consequence of quantum field theory, namely radiative corrections. In particular, in QCD one may compute the short distance contributions perturbatively. In the cases in which the matrix elements under consideration are renormalized under a change of scale, one may use perturbation theory to calculate the dependence on this renormalization scale. On the other hand, physical results should not depend on the renormalization scale, and hence the nonperturbative matrix elements which are evaluated using models, have to exhibit an appropriate scale dependence which has to match the one of the short distance contribution.

None of the models incorporate such an effect. However, as long as we discuss only semileptonic decays, which are induced by the left-handed current, this is not a severe problem, since in full QCD the operator of the left-handed current does not depend on the renormalization scale. Thus in this case the radiative corrections can be taken into account consistently by multiplying the result for the long-distance matrix element (obtained by a model) with the appropriate short-distance coefficient, which in this particular case does not depend on the scale.

Typically these long-distance matrix elements are evaluated at the scale of the mass of the heavy quark. This is, however, still a perturbative scale and hence one may still perform a perturbative calculation, which will exhibit terms enhanced by large logarithms of the heavy-quark mass. These terms may be resummed by using Heavy-Quark Effective Theory, which again will introduce a dependence of the short-distance part on the renormalization scale, this time even for the left-handed current. As in full QCD, this dependence of the short-distance contribution has to cancel against a corresponding dependence of the matrix element, which is evaluated by a model. Also here, none of the models incorporates any scale dependence, showing that again the models are not consistent with QCD as a field theory.

Again, despite all the critical comments made above, there is no choice but to use models to estimate rates for as yet unmeasured decays. Analyses to extract physical parameters such as V_{ub} also depend on models, see Section 8.2. A range of models should be considered in any such study. However models which have been shown not to satisfy the kind of constraints discussed at the beginning of this appendix should no longer be used.

References

- [1] A. Le Yaouanc *et al.*, *Phys. Rev. D* **15**, 844 (1977) and references therein.
- [2] N. Isgur *et al.*, *Phys. Rev. D* **39**, 799 (1989).
- [3] E. E. Salpeter and H. A. Bethe, *Phys. Rev.* **84**, 1232 (1951).
- [4] S. Mandelstam, *Proc. Roy. Soc. Lond.* **A233**, 248 (1955).
- [5] M. Wirbel, B. Stech and M. Bauer, *Z. Phys. C* **29**, 637 (1985).
- [6] T. Altomari and L. Wolfenstein, *Phys. Rev. D* **37**, 681 (1988).
- [7] D. Scora and N. Isgur, *Phys. Rev. D* **52**, 2783 (1995)
- [8] J. G. Körner and G. A. Schuler, *Z. Phys. C* **38**, 511 (1988); *Z. Phys. C* **41**, 690(E) (1989).
- [9] M. Neubert *et al.*, “Exclusive Weak Decays of *B*-Mesons,” in **Heavy Flavours**, eds. A.J. Buras and M. Lindner, World Scientific, Singapore (1992).
- [10] A. Ali, T. Ohl and T. Mannel, *Phys. Lett. B* **298**, 195 (1993).
- [11] T. B. Suzuki *et al.*, *Prog. Th. Phys.* **91**, 757 (1994).
- [12] S. Brodsky and J. Primack, *Ann. Phys.* **52**, 315 (1969).
- [13] R. Aleksan *et al.*, *Phys. Rev. D* **51**, 6235 (1995).
- [14] M. R. Ahmady, R. R. Mendel and J. D. Talman, *Phys. Rev. D* **52**, 254 (1995).
- [15] S. Veseli and M. G. Olsson, *Phys. Lett. B* **367**, 302 (1996); *Z. Phys. C* **71**, 287 (1996); *Phys. Rev. D* **54**, 886 (1996).
- [16] R. N. Faustov, *Nuo. Cim.* **69**, 37 (1970).
- [17] A. Le Yaouanc *et al.*, *Phys. Lett. B* **365**, 319 (1996).
- [18] F. E. Close and A. Wambach, *Nucl. Phys.* **B412**, 169 (1994); *Phys. Lett. B* **348**, 207 (1995); A. Wambach, *Nucl. Phys.* **B434**, 647 (1995).
- [19] B. Keister, *Phys. Rev. D* **46**, 3188 (1992).
- [20] F. Cardarelli *et al.*, *Phys. Lett. B* **332**, 1 (1994);
N. B. Demchuk *et al.*, *Phys. Atom. Nuclei* **59**, 2152 (1996); and references [50].

- [21] A. Dubin and A. Kaidalov, *Sov. J. Nucl. Phys.* **56**, 237 (1993) . They find the Isgur-Wise scaling relations in an approach based on Feynman diagrams.
- [22] W. Jaus, *Phys. Rev. D* **53**, 1349 (1996); *Phys. Rev. D* **54**, 5904(E) (1996); *Z. Phys. C* **54**, 611 (1992); *Phys. Rev. D* **41**, 3394 (1990).
- [23] D. Melikhov, *Phys. Rev. D* **53**, 2460 (1996); *Phys. Lett. B* **380**, 363 (1996); *Phys. Lett. B* **394**, 385 (1997); *Phys. Rev. D* **56**, 7089 (1997);
D. Melikhov and N. Nikitin, (1996) 9609503.
- [24] M. Böhm, H. Joos and M. Krammer, *Acta Phys. Austr. Suppl.* **XI**, 3 (1973).
- [25] M. A. Ivanov *et al.*, *Phys. Lett. B* **416**, 29 (1998).
- [26] S. J. Brodsky and G. P. Lepage. See for instance the references given by S. J. Brodsky, (1997) hep-ph/9710288, Ref. [10], especially *Phys. Rev. D* **22**, 2157 (1980), Section IV.
- [27] R. L. Jaffe and P. M. Mende, *Nucl. Phys.* **B369**, 189 (1992).
- [28] A. Le Yaouanc and O. Pène, *Third Workshop on the Tau-Charm Factory*, 1–6 June (1993), Marbella, Spain, hep-ph/9309230.
- [29] A. Le Yaouanc *et al.*, “Leptonic and semileptonic decays of D mesons at a τ - c factory” (1995) in *Proposal for a Tau-Charm Factory*, ed. J. Kirkby, P. Roudeau, etc. (to be published).
- [30] R. Casalbuoni *et al.*, *Phys. Rep.* **281**, 145 (1997) and references therein.
- [31] M. Neubert and V. Rieckert, *Nucl. Phys.* **B382**, 97 (1992).
- [32] V. Morenas *et al.*, *Phys. Lett. B* **408**, 357 (1997).
- [33] M. Gourdin, A. N. Kamal and X. Y. Pham, *Phys. Rev. Lett.* **73**, 3355 (1994); *Phys. Lett. B* **354**, 447 (1995).
- [34] B. Stech, (1996) hep-ph/9608297.
- [35] M. Neubert and B. Stech, “Nonleptonic Weak Decays of B Mesons,” to be published in the 2nd edition of **Heavy Flavours**, eds. A. J. Buras and M. Lindner, World Scientific, Singapore (1997), hep-ph/9705292 .
- [36] A. Le Yaouanc *et al.*, *Phys. Rev. D* **31**, 137 (1985).
- [37] R. N. Faustov, V. O. Galkin and A. Yu. Mishurov, *Phys. Lett. B* **356**, 516 (1995); *Phys. Lett. B* **367**, 391(E) (1996).
- [38] A. L. Licht and A. Pagnamenta, *Phys. Rev. D* **2**, 1150 (1970).

- [39] R. N. Faustov, *Ann. Phys.* **78**, 176 (1973).
- [40] P. Colangelo, G. Nardulli, and L. Tedesco, *Phys. Lett. B* **272**, 344 (1991).
- [41] B. Bakamjian and L. H. Thomas, *Phys. Rev.* **92**, 1300 (1953).
- [42] H. Osborn, *Phys. Rev.* **176**, 1514 (1968).
- [43] B. D. Keister and W. N. Polyzou, *Adv. Nucl. Phys.* **20**, 225 (1991).
- [44] F. E. Close and H. Osborn, *Phys. Rev. D* **2**, 2127 (1970).
- [45] P.A.M. Dirac, *Rev. Mod. Phys.* **21**, 392 (1949).
- [46] M. Terent'ev, *Sov. J. Nucl. Phys.* **24**, 106 (1976).
- [47] I. G. Aznauryan, A. S. Bagdasaryan and N. L. Ter-Isaakyan, *Phys. Lett. B* **112**, 393 (1982).
- [48] A. Le Yaouanc, L. Oliver, O. Pène and J.-C. Raynal, to be published.
- [49] Z. Dziembowski, C. J. Martoff and P. Żyła, *Phys. Rev. D* **50**, 5613 (1994).
- [50] S. Simula, *Phys. Lett. B* **373**, 193 (1996);
I. L. Grach, I. M. Narodetskii and S. Simula, *Phys. Lett. B* **385**, 317 (1996).
- [51] Reference ([17]);
Y. A. Le Yaouanc *et al.*, *Phys. Lett. B* **386**, 304 (1996); *Phys. Lett. B* **387**, 582 (1996);
Ref. [32];
V. Morenas *et al.*, *Phys. Lett. B* **386**, 315 (1996); *Phys. Rev. D* **56**, 5668 (1997); LPTHE
96/99, PCCF RI 9706 (1997), hep-ph/9710298.
- [52] A. Le Yaouanc, L. Oliver, O. Pène and J.-C. Raynal, to be published.
- [53] L. L. Frankfurt and M. I. Strikman, *Nucl. Phys.* **B148**, 107 (1979).
- [54] S. Godfrey and N. Isgur, *Phys. Rev. D* **32**, 189 (1985).
- [55] P. Cea *et al.*, *Phys. Lett.* **206B**, 691 (1988);
P. Colangelo, G. Nardulli and M. Pietroni, *Phys. Rev. D* **43**, 3002 (1991).
- [56] S. Veseli and I. Dunietz, MADPH-96-947, FERMILAB-PUB-96/144-T (1996).
- [57] A. Duncan, E. Eichten and H. Thacker, *Phys. Lett. B* **303**, 109 (1993).

C

Standard Model Parameters from Lattice QCD

This appendix contains a compilation of the main lattice results for hadronic parameters which are relevant for b physics. The principal sources of uncertainty and prospects for future improvements are also briefly discussed. More details can be found, for example, in the two recent reviews [1] and [2], and in references therein.

In the lattice formulation of quantum field theory space-time is approximated by a discrete mesh, a “lattice,” of points and the physical quantities of interest are evaluated numerically by computing the corresponding functional integrals. For these computations to make sense it is necessary for the lattice to be sufficiently large to accommodate the particles being studied ($L \gg 1$ fm say, where L is the spatial length of the lattice), and for the spacing between neighboring points, a , to be sufficiently small to control the systematic errors induced by the space-time discretization ($a\Lambda_{\text{QCD}} \ll 1$). The number of lattice points in any given simulation is limited by the available computing resources; current simulations are performed with about 16–20 points in each spatial direction (up to about 64 points if the effects of quark loops are neglected, *i.e.*, in the so-called “quenched” approximation). Thus it is possible to work on lattices which have a spatial extent of about 2 fm and a lattice spacing of 0.1 fm, probably satisfying the above requirements.

In studying heavy-flavor physics discretization errors may be important even when the condition $a\Lambda_{\text{QCD}} \ll 1$ is satisfied. The reason is that for heavy quarks Q , with $m_Q \gg \Lambda_{\text{QCD}}$, the discretization errors which are of $\mathcal{O}(am_Q)$, become large. Moreover, at values of the lattice spacing used in current simulations ($a^{-1} \sim 2\text{--}4$ GeV), $am_b \sim 1.3\text{--}2.5$ so that one cannot directly put the bottom quark on the lattice. Nevertheless, predictions for physical quantities which are of interest in b physics can be obtained by using the scaling laws of the HQET. This is done by combining calculations performed in a range of masses around the charm mass, which allow the study of dependence of the physical quantities on the heavy-quark mass, with the direct calculation of the same quantities using the lattice HQET at lowest order in $1/m_Q$. This strategy has been widely used to predict the B -meson leptonic decay constant, the $B^0\text{--}\bar{B}^0$ mixing amplitude *etc.* For charm quarks, for which $am_c \sim 0.3\text{--}0.6$, several methods to reduce the discretization errors have been proposed and are listed in Section C.2.

The lattice method is illustrated in Section C.1. A summary of the principal sources of uncertainty on the theoretical predictions with this approach is given in Section C.2. The remainder of the appendix contains a brief review of lattice results for the following quantities:

- (i) quark masses, Section C.3;
- (ii) leptonic decay constants, Section C.4;
- (iii) $\Delta B = 2$ and $\Delta S = 2$ transition amplitudes, Section C.5;
- (iv) form factors for exclusive semileptonic D - and B -decays and radiative B -decays, Section C.6;
- (v) parameters of the HQET, Section C.7.

Finally, a brief description of the methods proposed for the calculation of the nonleptonic two-body decay amplitudes, which are so important in B physics, can be found in Section C.8.

C.1 Evaluation of Physical Quantities in Lattice Simulations

Physical quantities, such as hadronic masses and operator matrix elements, are obtained in lattice simulations by the direct computation of correlation functions of multi-local operators composed of quark and gluon fields (in Euclidean space):

$$\langle 0 | O(x_1, x_2, \dots, x_n) | 0 \rangle = \frac{1}{Z} \int [DA_\mu][D\psi][D\bar{\psi}] e^{-S} O(x_1, x_2, \dots, x_n), \quad (\text{C.1})$$

where Z is the partition function

$$Z = \int [DA_\mu][D\psi][D\bar{\psi}] e^{-S}, \quad (\text{C.2})$$

S is the action and the integrals are over quark and gluon fields at each space-time point. In Eq. (C.1), $O(x_1, x_2, \dots, x_n)$ is a multi-local operator; the choice of O governs the physics which can be studied. The two most frequently encountered cases are those for which $n=2$ or 3, that is two- and three-point functions.

Lattice computations evaluate two point correlation functions of the form

$$C_2(t_x) \equiv \sum_{\mathbf{x}} \langle 0 | T \{ J_h(\mathbf{x}) J_h^\dagger(0) \} | 0 \rangle, \quad (\text{C.3})$$

where $x \equiv (\mathbf{x}, t_x)$. J_h is an interpolating operator with the appropriate quantum numbers to be coupled to the hadron h whose properties are to be examined. For sufficiently large positive t_x one obtains:

$$C_2(t_x) \simeq \frac{e^{-m_h t_x}}{2m_h} |\langle 0 | J_h | h \rangle|^2 + \frac{e^{-m_{h'} t_x}}{2m_{h'}} |\langle 0 | J_h | h' \rangle|^2 + \dots \quad (\text{C.4})$$

where m_h is the mass of the hadron h , which is assumed to be the lightest one which can be created by the operator J_h^\dagger . The contribution from each heavier hadron, h' with mass $m_{h'}$ say, is suppressed by the exponential factor $\exp(-(m_{h'} - m_h)t_x)$ with respect to the first term on the right-hand side of Eq. (C.4) and can be neglected at large time differences. In lattice simulations the correlation function C_2 is computed numerically, and by fitting the results to the expression in Eq. (C.4) both the mass m_h and the matrix element $|\langle 0 | J_h | h \rangle|$ can be determined. In principle, from the study of the time dependence of C_2 , also the masses and matrix elements of the higher-mass states can be extracted.

The summation in Eq. (C.3) implies that the hadron h is at rest, but of course it is also possible to give it a non-zero momentum, \mathbf{p} say, by taking the Fourier transform with the appropriate weighting factor $\exp(i\mathbf{p}\cdot\mathbf{x})$.

As an example of the above procedure consider the case in which h is the B meson and J_h is the axial current A_μ (with the flavor quantum numbers of the B meson). In this case one obtains the value of the leptonic decay constant f_B ,

$$\langle 0 | A_\mu | B(p) \rangle = f_B p_\mu . \quad (\text{C.5})$$

It will also be useful to consider three-point correlation functions:

$$C_3(t_x, t_y) = \sum_{\mathbf{x}, \mathbf{y}} e^{i\mathbf{p}\cdot\mathbf{x}} e^{i\mathbf{q}\cdot\mathbf{y}} \langle 0 | J_2(\mathbf{x}, t_x) \hat{O}(\mathbf{y}, t_y) J_1^\dagger(\mathbf{0}, 0) | 0 \rangle , \quad (\text{C.6})$$

where, J_1 and J_2 are the interpolating operators for hadrons h_1 and h_2 respectively, \hat{O} is a local operator, and it is assumed that $t_x > t_y > 0$. Inserting complete sets of states between the operators in Eq. (C.6) yields

$$C_3(t_x, t_y) = \frac{e^{-E_1 t_y}}{2E_1} \frac{e^{-E_2(t_x - t_y)}}{2E_2} \langle 0 | J_2 | h_2(\mathbf{p}, E_2) \rangle \times \\ \langle h_2(\mathbf{p}, E_2) | \hat{O} | h_1(\mathbf{p} + \mathbf{q}, E_1) \rangle \langle h_1(\mathbf{p} + \mathbf{q}, E_1) | J_1^\dagger | 0 \rangle + \dots , \quad (\text{C.7})$$

where $E_1 = \sqrt{m_1^2 + (\mathbf{p} + \mathbf{q})^2}$, $E_2 = \sqrt{m_2^2 + \mathbf{p}^2}$ and the points of ellipsis represent the contributions from heavier states. The exponential factors, $\exp(-E_1 t_y)$ and $\exp(-E_2(t_x - t_y))$, ensure that for large time separations t_y and $t_x - t_y$ the contributions from the lightest states dominate. With the exception of the matrix element $\langle h_2 | \hat{O} | h_1 \rangle$, all the elements on the right-hand side of Eq. (C.7) can be determined from two-point correlation functions. Thus by computing two- and three-point

correlation functions the matrix element $\langle h_2 | \hat{O} | h_1 \rangle$ can be determined. The computation of three-point correlation functions is useful in studying $B^0 - \bar{B}^0$ mixing amplitudes, semileptonic decays, and radiative weak decays of heavy hadrons.

The study of the hadron spectrum on the lattice also allows the determination of another class of fundamental parameters, the quark masses (see also Section C.3). Hadron masses depend on the (short-distance) bare quark masses, m_{bare} , related to the mass parameters, the Wilson hopping parameters, which appear in the lattice action. By requiring that the hadron spectrum agrees with the experimental data, it is possible to determine m . An alternative method is based on the use of the Ward Identities (WI) which relate the divergence of the lattice (non-singlet) axial-vector (vector) current, $A_\mu^{\text{latt}} = \bar{\psi}_1 \gamma_\mu \gamma_5 \psi_2$ ($V_\mu^{\text{latt}} = \bar{\psi}_1 \gamma_\mu \psi_2$), to the pseudoscalar (scalar) density, $P^{\text{latt}} = \bar{\psi}_1 \gamma_5 \psi_2$ ($S^{\text{latt}} = \bar{\psi}_1 \psi_2$), e.g.,

$$m_{\text{bare}}^1 + m_{\text{bare}}^2 = Z_{AP} \frac{\langle \partial_\mu A_\mu^{\text{latt}}(x) O(x_1, \dots, x_n) \rangle}{\langle P^{\text{latt}}(x) O(x_1, \dots, x_n) \rangle}, \quad (\text{C.8})$$

where Z_{AP} is a suitable renormalization factor. At tree-level $Z_{AP} = 1$. In order to extract $m_{\text{bare}}^{1,2}$, the WI are computed for values of the mass parameters corresponding to the physical values of the hadron masses containing the flavors 1 and 2.

The renormalized quark masses in a continuum renormalization scheme, for example in the \overline{MS} scheme, can be computed from m_{bare} by using the relation

$$m^{\overline{MS}}(\mu) = Z_m(\mu a, \alpha_s(\mu)) m_{\text{bare}}, \quad (\text{C.9})$$

where $Z_m(\mu a, \alpha_s(\mu))$ is a short-distance matching factor, relating the bare mass in the lattice regularization and the renormalized one in the continuum \overline{MS} scheme.

Both Z_{AP} and Z_m can be obtained in perturbation theory since they involve only short-distance physics. Experience has taught, however, that the coefficients in lattice perturbation theory can be large, leading to significant uncertainties (frequently of $\mathcal{O}(10\%)$ or more). This is also true in the calculation of the renormalization constants of many composite lattice operators which enter in the evaluation of the hadronic weak matrix elements. For this reason, nonperturbative techniques to evaluate the renormalization constants which relate the bare lattice operators to the renormalized ones have been developed using chiral Ward identities where possible [3] or by imposing an explicit renormalization condition [4] (see also Refs. [5, 6]), thus effectively removing this source of uncertainty in many important cases.

This brief summary of lattice computations of hadronic matrix elements concludes with a word about the determination of the lattice spacing a . It is conventional to introduce the parameter $\beta = 6/g_0^2(a)$, where $g_0(a)$ is the bare coupling constant in the theory with the lattice regularization. It is β (or equivalently $g_0(a)$) which is the input parameter in the simulation, and the corresponding lattice spacing is then determined by requiring that some physical quantity (which is computed in lattice units) is equal to the experimental value. For example, one may compute the pion leptonic

decay constant in lattice units, af_π , and determine the lattice spacing a by dividing the result by 131 MeV.

C.2 Main Sources of Uncertainty

Although lattice computations provide the opportunity, in principle, to evaluate the nonperturbative QCD effects in weak decays of heavy quarks from first principles and with no model assumptions or free parameters, in practice the precision of the results is limited by the sources of uncertainty in these computations are the following:

- *Statistical errors:* The functional integrals in Eq. (C.1) are evaluated by Monte Carlo techniques. This leads to sampling errors, which decrease as the number of field configurations included in the estimate of the integrals is increased.
- *Discretization errors:* These are artifacts due to the finiteness of the lattice spacing. Much effort is being devoted to reducing these errors either by performing simulations at several values of the lattice spacing and extrapolating the results to the continuum limit ($a = 0$), or by “improving” the lattice formulation of QCD so that the error in a simulation at a fixed value of a is formally smaller [7]–[8].
- *Extrapolations to physical quark masses:* It is generally not possible to use physical quark masses in simulations. For the light (u and d) quarks the masses must be chosen such that the corresponding π mesons are sufficiently heavy to be insensitive to the finite volume of the lattice. For the heavy quarks Q (*i.e.*, for c , and particularly for b) the masses must be sufficiently small so that the discretization errors, which are of $\mathcal{O}(m_Q a)$ or $\mathcal{O}(m_Q^2 a^2)$, are small. The results obtained in the simulations must then be extrapolated to those corresponding to physical quark masses.
- *Finite volume effects:* Results are required to be independent of the lattice volume treated. In most cases of interest, the errors due to finite volume effects are much smaller than the other systematic errors (*e.g.*, those due to the finiteness of the lattice spacing), provided that the light-quark masses are not too small (see the previous item).
- *Quenching:* In most current simulations the matrix elements are evaluated in the “quenched” approximation, in which the effects of virtual quark loops are neglected. It is rather difficult to estimate the error coming from the use of the quenched approximation. Moreover, quenching effects are expected to depend on the quantity being studied and can be relatively small in some cases and larger in others. Unquenched calculations are beginning to be performed, although at present the statistical precision reached in the determination of physical quantities is generally much poorer in the unquenched computations than in quenched.

For almost all the quantities discussed in this appendix, the results have been obtained in the quenched approximation. In these cases, the quoted errors include the statistical uncertainties and a (conservative) estimate of effects coming from discretization and extrapolation. *They do not include, however, the systematic error due to the quenched approximation.* In a few cases, namely the leptonic decay constants and the $K^0-\bar{K}^0$ mixing amplitude, the existing calculations in the full theory allow at least an estimate of the quenching error. This has been included only in the value of \hat{B}_K given below.

C.3 Quark Masses

The systematic study of quark masses is a relatively new subject of investigation for lattice QCD. For this reason, most of the present activity in this field is devoted to understanding and quantifying the systematic errors. So far, three main sources of uncertainty in the lattice estimates of quark masses have been identified: i) discretization errors, which are certainly important in the case of the standard unimproved Wilson action; ii) the matching constants between the lattice and the continuum schemes (*e.g.*, Z_{AP} and Z_m in Eqs. (C.8) and (C.9)); iii) the error induced by the use of the quenched approximation.

Consider for example the mass of the strange quark m_s , which is an important parameter for the theoretical predictions of the CP violation parameter ϵ'/ϵ , see Chapter 14. If the lattice spacing and the mass of the light quarks are determined by using the ρ and π masses, the mass of the strange quark can be fixed either by using the mass of the pseudoscalar meson m_K or that of one of the vector mesons containing strange quarks (m_{K^*} or m_ϕ). In the absence of systematic errors, the different determinations of the strange-quark mass should coincide. At fixed lattice spacing and in the quenched approximation this is not always the case. For example the hyperfine splitting is affected by systematic errors and the determinations of the strange-quark mass using pseudoscalar or vector mesons may be different. This is precisely what has been found by the CP-PACS collaboration, which has studied the light-quark masses for a variety of values of the lattice spacing and has also attempted an extrapolation to the continuum limit. They find

$$\begin{aligned}\overline{m}_s(2 \text{ GeV}) &= (110 \pm 2) \text{ MeV} && \text{from } m_K \\ \overline{m}_s(2 \text{ GeV}) &= (133 \pm 6) \text{ MeV} && \text{from } m_\phi ,\end{aligned}\tag{C.10}$$

where $\overline{m}_s(\mu)$ is the mass of the strange quark renormalized in the \overline{MS} -scheme at the scale μ . The difference between the two values given above represents an irreducible uncertainty of the present calculations.

Up to logarithmic corrections, the masses of the light hadrons can be expanded in powers of the quark masses. For example, using chiral perturbation theory, one expects

$$\begin{aligned} m_P^2 &= B_P (m^1 + m^2) + C_P (m^1 + m^2)^2 + C'_P (m^1 - m^2)^2 + \dots \\ m_V &= A_V + B_V (m^1 + m^2) + C_V (m^1 + m^2)^2 + C'_V (m^1 - m^2)^2 + \dots, \end{aligned} \quad (\text{C.11})$$

where m_P and m_V denote the masses of the pseudoscalar and vector mesons composed of two light quarks of mass m^1 and m^2 . Lattice data show that the nonlinear terms in the expansions of Eq. (C.11) become important only if large values of the quark masses are considered. For masses of $\mathcal{O}(m_s)$, or smaller (but not for masses of $\mathcal{O}(m_c)$), these non-linearities are very small and very difficult to detect within the accuracy of the present calculations. In the linear approximation, the determinations of m_s and of $\overline{m} = (\overline{m}_u + \overline{m}_d)/2$ are not independent because their ratio can be expressed in terms of ratios of the kaon and pion masses. For this reason, lattice predictions for \overline{m}_s and for the mass of the lightest quarks $\overline{m} = (\overline{m}_u + \overline{m}_d)/2$ are strongly correlated and should not be considered as independent predictions. Nevertheless, since differences may arise in the different treatment of the data, and for comparison with QCD sum rules, in Table C-1 also presents the results for \overline{m} . The same table also gives the lattice results for $\overline{m}_c(\overline{m}_c)$, for which one expects that there are still sizeable discretization errors. The lattice results for $\overline{m}_b(\overline{m}_b)$ have been obtained using either the lattice HQET or NRQCD. Discussion of the results is postponed until Section C.7.

The extraction of the quark masses involves several steps for which the different groups have used different approaches (*e.g.*, the perturbative or nonperturbative determination of the matching coefficients and the extrapolation of the mass to the continuum limit). This makes a comparison of the results from different groups difficult. For this reason, and because the situation is rapidly evolving, the results from the different collaborations are presented separately; the spread of the results is indicative of the systematic errors still present in the determination of the quark masses. For a complete set of references see [9]. The quoted errors from each group include statistical errors plus estimates of discretization and continuum extrapolation errors. Further work is needed to understand systematic uncertainties and eventually to obtain unquenched results which have smaller uncertainties.

In the lattice community it has become customary to give the quark masses at the renormalization scale $\mu = 2$ GeV, which is the typical scale in numerical simulations ($a \sim 2\text{--}4$ GeV). With QCD sum rules, the standard renormalization scale is instead $\mu = 1$ GeV. To make the comparison easier, here $\overline{m}_q(1 \text{ GeV})/\overline{m}_q(2 \text{ GeV}) = 1.39$ is used and results are given both at $\mu = 2$ GeV and at $\mu = 1$ GeV. A particularly appropriate choice as the reference value for future comparisons would be the renormalization-group invariant quark mass \widehat{m}_q defined as

$$\widehat{m}_q = R(\mu)\overline{m}_q(\mu), \quad (\text{C.12})$$

where

$$R(\mu) = \left(\frac{\beta_0 \alpha_s(\mu)}{2 \pi} \right)^{-2\gamma_0/\beta_0} \left\{ 1 + \frac{\alpha_s(\mu)}{\pi} \left(\frac{\beta_1 \gamma_0}{\beta_0^2} - 2 \frac{\gamma_1}{\beta_0} \right) + \dots \right\}. \quad (\text{C.13})$$

Table C-1. Results for the light-quark mass $\overline{m} = (\overline{m}_u + \overline{m}_d)/2$, \overline{m}_s and \overline{m}_c from the lattice. All the results have been obtained in the quenched approximation. Only results where the NLO corrections have been included are given. Infinite values of β symbolize results obtained after extrapolation to the continuum limit.

	Yr	β	$\overline{m}(2 \text{ GeV})/\text{MeV}$	$\overline{m}(1 \text{ GeV})/\text{MeV}$
SESAM	97	6.0	5.5 ± 0.5	7.6 ± 0.7
QCDSF	97	6.0–6.2	5.1 ± 0.2	7.1 ± 0.3
APE	97	6.0–6.2	5.7 ± 0.8	7.9 ± 0.1
CP-PACS	97	∞	4.2 ± 0.1	5.7 ± 0.2
LNAL	97	∞	3.8 ± 0.6	5.2 ± 0.8
	Yr	β	$\overline{m}_s(2 \text{ GeV})/\text{MeV}$	$\overline{m}_s(1 \text{ GeV})/\text{MeV}$
APE	94	6.0–6.4	128 ± 18	178 ± 25
SESAM	97	6.0	166 ± 15	231 ± 21
QCDSF	97	6.0–6.2	112 ± 5	156 ± 7
APE	97	6.0–6.2	130 ± 19	181 ± 25
CP-PACS m_K	97	∞	110 ± 2	152 ± 3
CP-PACS m_ϕ	97	∞	133 ± 6	185 ± 8
LNAL	97	∞	110 ± 23	153 ± 32
	Yr	β	$\overline{m}_c(\overline{m}_c)/\text{GeV}$	
APE	94	6.0–6.4	1.60 ± 0.27	
APE	97	6.0–6.2	1.66 ± 0.23	

The explicit expressions for the mass anomalous-dimension constants $\gamma_{0,1}$ can be found in Appendix D, Equation (D-17).

C.4 Leptonic Constants of Pseudoscalar Heavy Mesons

This section reviews the current status of calculations of the leptonic decay constants f_D and f_B . The definition of the leptonic decay constant for pseudoscalar mesons has already been given in Eq. (C.5). This definition corresponds to the normalization in which $f_{\pi^+} \simeq 131 \text{ MeV}$. The two principle sources of uncertainty in the calculations of the decay constants are those due to discretization errors and to quenching.

For a heavy quark with mass m_Q , the product $m_Q a$ is large and can be an important source of mass-dependent discretization errors. This has been addressed in two ways. Some studies have used the Sheikholeslami-Wohlert (SW or clover) improved action [10] together with improved operators [8], which removes tree-level $\mathcal{O}(a)$ errors, leaving ones of $\mathcal{O}(\alpha_s m_Q a)$. In the near future recently developed techniques are expected to reduce the discretization errors still further, to $\mathcal{O}(m_Q^2 a^2)$ [5, 11]. The second approach introduces a revised normalization of the quark fields in simulations using the standard Wilson fermion action. This is designed to remove higher-order effects in $m_Q a$ from the heavy-quark propagator, but only at tree level in the strong interactions. The theoretical significance of this normalization factor is not completely clear; in particular, it does not eliminate all the $\mathcal{O}(m_Q a)$ effects. The nonrelativistic normalization is often denoted “KLM” in the literature, after some of its originators [12, 13]. In some of the more recent series of simulations, computations are performed at a sequence of lattice spacings and the results are extrapolated to the continuum limit.

The second principal source of uncertainty in the calculations of the decay constants is quenching. Its effects are only now beginning to be studied, and early indications suggest that the values of the decay constants may increase when the effects of quark loops are fully included. It is still too early to draw a firm conclusion on this point.

In the quenched case, the results for f_D and f_B obtained using different approaches for correcting discretization errors are mutually consistent and give for the central values: $180 \text{ MeV} \leq f_D \leq 220 \text{ MeV}$ and $150 \text{ MeV} \leq f_B \leq 200 \text{ MeV}$. The errors quoted by the authors are typically about 20–30 MeV for f_D and 30–40 MeV for f_B . From a compilation of the most recent results, using rather conservative estimates of the errors, our averages for the decay constants are given by

$$\begin{aligned} f_D &= 200 \pm 30 \text{ MeV} , & f_{D_s} &= 220 \pm 30 \text{ MeV} , \\ f_B &= 170 \pm 35 \text{ MeV} , & f_{B_s} &= 195 \pm 35 \text{ MeV} , \end{aligned} \quad (\text{C.14})$$

$$f_{D_s}/f_D = 1.10 \pm 0.06 , \quad f_{B_s}/f_B = 1.14 \pm 0.08 . \quad (\text{C.15})$$

This section concludes with a comment on the validity of the asymptotic scaling law for the decay constants. For sufficiently large masses of the heavy quark, the decay constant of a heavy-light pseudoscalar meson P scales with its mass m_P as follows:

$$f_P = \frac{A}{\sqrt{m_P}} \left[\alpha_s(m_P)^{-2/\beta_0} \{1 + \mathcal{O}(\alpha_s(m_P))\} + \mathcal{O}\left(\frac{1}{m_P}\right) \right] , \quad (\text{C.16})$$

where A is independent of m_P . Using the leading term of this scaling law, a value of 200 MeV for f_D would correspond to $f_B \simeq 120 \text{ MeV}$. Results from the lattice computations, however, indicate that f_B is significantly larger than this and thus that the $\mathcal{O}(1/m_P)$ corrections on the right-hand side of Eq. (C.16) are considerable. The coefficient of the $\mathcal{O}(1/m_P)$ corrections is typically found to be between 0.5 and 1 GeV, on the large side of theoretical expectations.

C.5 B^0 - \bar{B}^0 and K^0 - \bar{K}^0 Mixing

B^0 - \bar{B}^0 mixing provides important constraints for the determination of the angles of the unitarity triangle (for a review and references to the original literature see Chapter 11). Strong interaction effects are contained in the matrix element of the $\Delta B=2$ operator:

$$\langle \bar{B}^0 | \bar{b}\gamma_\mu(1-\gamma_5)q \bar{b}\gamma^\mu(1-\gamma_5)q | B^0 \rangle = \frac{8}{3} f_B^2 m_B^2 B_B(\mu). \quad (\text{C.17})$$

The dimensionless quantity $B_B(\mu)$ is better determined than f_B in lattice calculations, so that the theoretical uncertainties in the value of the matrix element of the four fermion operator are dominated by ignorance of f_B .

$B_B(\mu)$ is a scale-dependent quantity for which lattice results are most often quoted after translation to the \overline{MS} scheme. The next-to-leading order (NLO) renormalization group invariant B -parameter, \hat{B}_B^{nlo} , is defined by

$$\hat{B}_B^{\text{nlo}} = b_B^{\text{nlo}}(\mu) B_B(\mu) = \alpha_s(\mu)^{-2/\beta_0} \left(1 + \frac{\alpha_s(\mu)}{4\pi} J_{n_f} \right) B_B(\mu), \quad (\text{C.18})$$

where $\beta_0 = 11 - 2n_f/3$ and J_{n_f} is obtained from the one- and two-loop anomalous dimensions of the $\Delta B=2$ operator by [14],

$$J_{n_f} = \frac{1}{2\beta_0} \left(\gamma_0 \frac{\beta_1}{\beta_0} - \gamma_1 \right), \quad (\text{C.19})$$

with $\beta_1 = 102 - 38n_f/3$, $\gamma_0 = 4$, and $\gamma_1 = -7 + 4n_f/9$. In the discussion below $\mu = m_b$ is used.

\hat{B}_B can be obtained by computing the matrix element either by using the lattice HQET at lowest order in $1/m_b$ [15, 16], or with propagating b quarks.

The main difficulty in trying to determine the value of B_B using static heavy quarks is that large perturbative corrections are encountered when calculating the four-fermion operator matrix element in some standard renormalization scheme (*e.g.*, the \overline{MS} scheme) in full QCD from those measured on the lattice in the HQET. To this source of uncertainty, one has to add that coming from higher-order corrections in the heavy-quark expansion which have not been included in the calculations. For these reasons, at present, the estimates of B_B in the static theory add little to the information obtained with propagating quarks, and hence here only the results for the latter case are given.

Calculations with propagating heavy quarks are reported in Table C-2. All results are given at a common scale $m_b = 5 \text{ GeV}$ and then converted to \hat{B}_B at NLO. The results show no observable dependence on the lattice spacing, although the authors of Ref. [17] perform a linear extrapolation to the continuum limit, which is the reason for the relatively large error in the corresponding

Table C-2. Results for the mixing parameter B_B obtained in the quenched approximation using propagating b quarks. The authors' results for $B_B(\mu)$ at scale μ or for $B_B(m_b)$ with $m_b = 5$ GeV are quoted. They are then scaled to m_b and converted to \hat{B}_B^{nl0} , the renormalization group invariant B parameter. The results may differ slightly from those in the original articles owing to rescaling to the particular choice of parameters used here: authors' numbers are shown in upright type, rescaled numbers in oblique type. Infinite values of β symbolize results obtained after extrapolation to the continuum limit.

	Yr	β	μ/GeV	$B_B(\mu)$	$B_B(m_b)$	\hat{B}_B^{nl0}
BBS [17]	97	∞	2	1.02(13)	0.96(12)	1.53(19)
JLQCD [19]	96	6.3			0.840(60)	1.34(10)
JLQCD [19]	96	6.1			0.895(47)	1.42(7)
BS [18]	96	∞	2	0.96(6)(4)	0.90(6)(4)	1.44(9)(6)
ELC [20]	92	6.4	3.7	0.86(5)	0.84(5)	1.34(8)
BDHS [21]	88	6.1	2	1.01(15)	0.95(14)	1.51(22)

result. Although the quoted errors are largely statistical, the different groups treat the perturbative matching in different ways, so that it is not appropriate simply to perform a weighted average. An estimate based on the results in Table C-2 is

$$\hat{B}_B^{\text{nl0}} = 1.4(1) . \quad (\text{C.20})$$

In estimating the error here, it has been assumed that the results are almost independent of the lattice spacing and no attempt has been made to quantify the effects of quenching. The second error in the result from Ref. [18] is the authors' estimate of the quenching errors.

The relevant phenomenological quantity for $B^0-\bar{B}^0$ mixing is $f_B^2 \hat{B}_B$. Taking the result in Eq. (C.20) above for \hat{B}_B^{nl0} , with $f_B = 170(35)$ MeV from Eq. (C.14), gives

$$f_B \sqrt{\hat{B}_B^{\text{nl0}}} = 201(42) \text{ MeV} \quad (\text{C.21})$$

as the lattice estimate. An interesting dimensionless quantity is the ratio

$$\xi \equiv \frac{f_{B_s} \sqrt{\hat{B}_{B_s}}}{f_{B_d} \sqrt{\hat{B}_{B_d}}} . \quad (\text{C.22})$$

For propagating quarks, combining the result $f_{B_s}/f_B = 1.14(8)$ from Eq. (C.14) with $B_{B_s}/B_B = 1.00(3)$ [22] gives

$$\xi = 1.14(8) . \quad (\text{C.23})$$

A direct extraction of the matrix element gives the ratio $r_{sd} \equiv \xi^2 m_{B_s}^2 / m_{B_d}^2 = 1.54(13)(32)$ [17]. In the static case, Giménez and Martinelli [16] find $r_{sd} = 1.43(7)$ by combining $f_{B_s}/f_B = 1.17(3)$ and $B_{B_s}/B_B = 1.01(1)$, and $r_{sd} = 1.35(5)$ from a direct evaluation of the four-quark matrix element measured on the same gauge configurations. The results of the two methods are quite consistent and future calculations should improve on the precision of r_{sd} .

The above results are largely from quenched calculations. For B_{B_s}/B_B , numerical evidence suggests a small increase on two-flavor dynamical configurations [18], but the chiral loop estimate [23, 24] is for a decrease of -0.04 in the ratio. Reliable simulations with dynamical quarks are needed before the size of quenching effects can be determined with confidence.

This section ends with a brief presentation of the results for the kaon B -parameter B_K (see Chapter 11). This quantity has been computed for a variety of lattice fermion actions and using several (perturbative and nonperturbative) methods to renormalize the relevant four-fermion operator

$$O^{\Delta S=2} = \bar{s}\gamma_\mu(1-\gamma_5)d\bar{s}\gamma^\mu(1-\gamma_5)d. \quad (\text{C.24})$$

With staggered fermions some preliminary results exist also in the unquenched case and the extrapolation of the quenched results to the continuum limit has been attempted by several groups. For a recent review see, for example, Ref. [24] and references therein. In the quenched approximation, taking into account the most recent results of the JLQCD collaboration [25], for the operator renormalized in the \overline{MS} scheme

$$B_K(\mu = 2 \text{ GeV}) = 0.61 \pm 0.06. \quad (\text{C.25})$$

From the above result, one can derive the following value for the renormalization group invariant B -parameter

$$\hat{B}_K = 0.84 \pm 0.07 \pm 0.12, \quad (\text{C.26})$$

In the above equation the second error (which is absent in Eq. (C.25)) is an estimate of the error induced by the use of the quenched approximation following Ref. [24].

C.6 Semileptonic Decays of D and B Mesons

This section discusses semileptonic decays of D and B mesons, considering in turn the cases in which the c quark decays into an s or d quark and the b quark decays into a c or u quark. The relevant form factors are defined in the helicity basis given below.

When the final state is a pseudoscalar meson P , parity implies that only the vector component of the $V-A$ weak current contributes to the decay, and there are two independent form factors, f^+ and f^0 , defined by

$$\langle P(k)|V^\mu|B(p)\rangle = f^+(q^2) \left[(p+k)^\mu - \frac{m_B^2 - m_P^2}{q^2} q^\mu \right]$$

$$+ f^0(q^2) \frac{m_B^2 - m_P^2}{q^2} q^\mu, \quad (\text{C.27})$$

where q is the momentum transfer, $q = p - k$, and $B(p)$ denotes either a B or D meson.

When the final-state hadron is a vector meson V , there are four independent form factors:

$$\langle V(k, \varepsilon) | V^\mu | B(p) \rangle = \frac{2V(q^2)}{m_B + m_V} \epsilon^{\mu\gamma\delta\beta} \varepsilon_\beta^* p_\gamma k_\delta \quad (\text{C.28})$$

$$\begin{aligned} \langle V(k, \varepsilon) | A^\mu | B(p) \rangle &= i(m_B + m_V) A_1(q^2) \varepsilon^{*\mu} - i \frac{A_2(q^2)}{m_B + m_V} \varepsilon^* \cdot p (p+k)^\mu \\ &+ i \frac{A(q^2)}{q^2} 2m_V \varepsilon^* \cdot p q^\mu, \end{aligned} \quad (\text{C.29})$$

where ε is the polarization vector of the final-state meson, and $q = p - k$. The form factor A_0 is given in terms of those defined above by $A_0 = A + A_3$, with

$$A_3 = \frac{m_B + m_V}{2m_V} A_1 - \frac{m_B - m_V}{2m_V} A_2. \quad (\text{C.30})$$

C.6.1 Semileptonic D Decays

The decays $D \rightarrow K \ell^+ \nu_\ell$ and $D \rightarrow K^* \ell^+ \nu_\ell$ provide a good test for lattice calculations since the relevant CKM matrix element V_{cs} is well constrained in the standard model. The form factors for the decays $D \rightarrow \pi \ell^+ \nu_\ell$ and $D \rightarrow \rho \ell^+ \nu_\ell$ can also be computed in lattice simulations. Charm quarks are light enough to be simulated directly (though one still needs to be wary of mass-dependent discretization errors). Furthermore, strange quarks can also be simulated directly, so for $D \rightarrow K$ or K^* decays there is only one quark for which a chiral extrapolation (to the actual light-quark mass) needs to be performed. For semileptonic D meson decays the whole physical phase space can be sampled,¹ while keeping the spatial momenta of the initial and final state mesons small in order to minimize the momentum-dependent discretization errors.

Although the lattice calculations actually measure the q^2 dependence of the form factors, the standard practice, followed here, is to quote values at $q^2 = 0$. In contrast to the case for B decays to be discussed below, this involves only an interpolation and so is relatively well controlled. Reference [2] and references therein give detailed discussions of the q^2 -dependence of the form factors.

Lattice results for the $D \rightarrow K^{(*)}, \pi, \rho$ form factors are summarized in Table C-3. The lattice results were all obtained from quenched simulations and no group has performed a continuum extrapolation. Table C-3 contains a summary based on the more recent results from UKQCD [26],

¹In addition, one obtains the form factors for unphysical, negative values of q^2 .

Table C-3. Summary of lattice and experimental results for $D \rightarrow K, K^*$ and $D \rightarrow \pi, \rho$ semileptonic decay form factors at $q^2 = 0$. The experimental numbers are taken from the survey in Ref. [30].

	$D \rightarrow K, K^*$		$D \rightarrow \pi, \rho$
	lattice	expt	lattice
$f^+(0)$	0.73(7)	0.76(3)	0.65(10)
$V(0)$	1.2(2)	1.07(9)	1.1(2)
$A_1(0)$	0.70(7)	0.58(3)	0.65(7)
$A_2(0)$	0.6(1)	0.41(5)	0.55(10)

WUP [27], LANL [28] and APE [29] which all use either the improved SW action or the Wilson action with a KLM normalization. The summary values presented in Table C-3 include the recent experimental world averages [30] for $D \rightarrow K, K^*$ decays. Again the quoted uncertainties include statistical and discretization errors, but do not attempt to estimate the uncertainty introduced by the quenched approximation.

C.6.2 Semileptonic $B \rightarrow D$ and $B \rightarrow D^*$ Decays

Semileptonic $B \rightarrow D^*$ and, more recently, $B \rightarrow D$ decays are used to determine the V_{cb} element of the CKM matrix. Heavy-quark symmetry is rather powerful in controlling the theoretical description of these heavy-to-heavy quark transitions, as described in Chapter 2.

In the heavy-quark limit all six form factors in Eqs. (C.27)–(C.29) are related and there is just one universal form factor $\xi(\omega)$, known as the Isgur–Wise (IW) function which contains all the nonperturbative QCD effects. Specifically:

$$\begin{aligned}
 f^+(q^2) &= V(q^2) = A_0(q^2) = A_2(q^2) \\
 &= \left[1 - \frac{q^2}{(m_B + m_D)^2} \right]^{-1} A_1(q^2) = \frac{m_B + m_D}{2\sqrt{m_B m_D}} \xi(\omega), \quad (\text{C.31})
 \end{aligned}$$

where $\omega = v_B \cdot v_D$ is the velocity transfer variable. Here the label D represents the D or D^* meson as appropriate (pseudoscalar and vector mesons are degenerate in this leading approximation). Vector current conservation implies that the IW-function is normalized at zero recoil, *i.e.*, that $\xi(1) = 1$.

The relations in Eq. (C.31) are valid up to perturbative and power corrections. Allowing for corrections to the heavy-quark limit, the relevant quantities are the $\mathcal{F}_i(\omega)$, the “physical form factors” given by the IW-function combined with perturbative and power corrections.

Table C-4. Values of the Slope of the IW-function of a heavy meson, obtained using lattice QCD. BSS note that $\rho_{u,d}^2$ is 12% smaller than ρ_s^2 , but do not quote a separate result. The first error quoted is statistical while the second is an estimate of systematic effects such as light-quark mass extrapolation and lattice effects, but not quenching.

	Yr	$\rho_{u,d}^2$	ρ_s^2	using
LANL [28]	96	0.97(6)		f_+
UKQCD [31]	95	$0.9(\frac{2}{3})(\frac{4}{2})$	$1.2(\frac{2}{2})(\frac{2}{1})$	f_+
UKQCD [32]	94	$0.9(\frac{4}{5})(\frac{9}{1})$	$1.2(\frac{3}{3})(\frac{7}{1})$	A_1
BSS [33]	93		1.24(26)(33)	f_+
BSS [33]	93		1.41(19)(38)	f_+

In order to understand the shape of the physical form factor, it is convenient to expand the \mathcal{F}_i as a power series in $\omega - 1$. For $B \rightarrow D^*$ decays, one writes the expansion as

$$\mathcal{F}(\omega) = \mathcal{F}(1) \left[1 - \hat{\rho}^2 (\omega - 1) + \hat{c} (\omega - 1)^2 + \dots \right]. \quad (\text{C.32})$$

The slope parameter $\hat{\rho}^2$ differs from the slope parameter ρ^2 of the IW function itself by heavy-quark symmetry violating corrections,

$$\hat{\rho}^2 = \rho^2 + (0.16 \pm 0.02) + \text{power corrections}. \quad (\text{C.33})$$

The principal difficulty for lattice calculations is to separate the physical heavy-quark mass dependence due to power corrections from the unphysical one due to mass-dependent discretization errors. One must also address the question of lattice-to-continuum matching. The lattice determinations of the slope of the IW function are summarized in Table C-4. Since ‘the’ IW function is different for different light degrees of freedom, the results in the table are labeled with subscripts u, d or s as appropriate.

A first lattice study of the semileptonic decays $\Lambda_b \rightarrow \Lambda_c \ell \nu_\ell$ and $\Xi_b \rightarrow \Xi_c \ell \nu_\ell$ has recently been performed [34], giving predictions for the decay distributions and the baryonic Isgur-Wise function. The interested reader can consult Ref. [34] for details.

C.6.3 Semileptonic $B \rightarrow \rho$ and $B \rightarrow \pi$ Decays and the Rare Decay $\bar{B} \rightarrow K^* \gamma$

This subsection considers the heavy-to-light semileptonic decays $B \rightarrow \rho$ and $B \rightarrow \pi$ which are now being used experimentally to determine the V_{ub} matrix element. Several groups have evaluated form factors for these decays using lattice simulations [27, 29, 35, 36]. The rare radiative decay

$\bar{B} \rightarrow K^* \gamma$ which is related by heavy-quark and light-flavor symmetries to the $B \rightarrow \rho$ semileptonic decay will also be discussed.

Form factors for semileptonic $B \rightarrow \pi$ decays were defined above in Eq. (C.27) and for $B \rightarrow \rho$ decays in Eq. (C.29). For completeness, form factors for the matrix element of the magnetic moment operator responsible for the short-distance contribution to the $\bar{B} \rightarrow K^* \gamma$ decay are given:

$$\langle K^*(k, \varepsilon) | \bar{s} \sigma_{\mu\nu} q^\nu b_R | B(p) \rangle = \sum_{i=1}^3 C_\mu^i T_i(q^2), \quad (\text{C.34})$$

where $q = p - k$, ε is the polarization vector of the K^* and

$$C_\mu^1 = 2\varepsilon_{\mu\nu\lambda\rho} \varepsilon^{*\nu} p^\lambda k^\rho, \quad (\text{C.35})$$

$$C_\mu^2 = \varepsilon_\mu^* (m_B^2 - m_{K^*}^2) - \varepsilon \cdot q (p + k)_\mu, \quad (\text{C.36})$$

$$C_\mu^3 = \varepsilon_\mu^* \cdot q \left(q_\mu - \frac{q^2}{m_B^2 - m_{K^*}^2} (p + k)_\mu \right). \quad (\text{C.37})$$

T_3 does not contribute to the physical $\bar{B} \rightarrow K^* \gamma$ amplitude for which $q^2 = 0$, and $T_1(0)$ and $T_2(0)$ are related by,

$$T_1(q^2=0) = iT_2(q^2=0). \quad (\text{C.38})$$

Hence, for the process $\bar{B} \rightarrow K^* \gamma$, one needs to determine T_1 and/or T_2 at the on-shell point $q^2=0$.

Heavy-quark symmetry is less predictive for heavy-to-light decays than for heavy-to-heavy ones. In particular, there is no normalization condition at zero recoil corresponding to the condition $\xi(1) = 1$, which is so useful in the extraction of V_{cb} . Heavy-quark symmetry does, however, give useful scaling laws for the behavior of the form factors with the mass of the heavy quark at fixed ω . Moreover, the heavy-quark spin symmetry relates the $B \rightarrow V$ matrix elements [37, 38] (where V is a light vector particle) of the weak current and magnetic moment operators, thereby relating the amplitudes for the two processes $\bar{B}^0 \rightarrow \rho^+ l^- \bar{\nu}_l$ and $\bar{B} \rightarrow K^* \gamma$, up to $SU(3)$ flavor symmetry breaking effects.

For fixed ω the scaling laws for the form factors given by heavy-quark symmetry are as follows

$$f(q^2(\omega))|_{\omega \text{ fixed}} = M^{\nu_f} \gamma_f \left(1 + \frac{\delta_f}{M} + \frac{\epsilon_f}{M^2} + \dots \right), \quad (\text{C.39})$$

where f labels the form factor, M is the mass of the heavy-light meson and γ_f, δ_f , etc. include calculable logarithmic corrections. The leading M dependences, M^{ν_f} , are listed in Table C-5. Lattice calculations with propagating quarks use a range of quark masses around the charm mass and generally employ these scaling relations to extrapolate to the B mass: this is the case for results from ELC, APE and UKQCD. In the limit $M \rightarrow \infty$ the relations

$$A_1(q^2(\omega)) = 2iT_2(q^2(\omega)), \quad V(q^2(\omega)) = 2T_1(q^2(\omega)) \quad (\text{C.40})$$

Table C-5. Leading M dependence of form factors for heavy-to-light decays in the helicity basis. The dependence follows from heavy-quark symmetry applied at fixed velocity transfer ω . Note that only three of the four A_i form factors for $B \rightarrow \rho \ell \nu_\ell$ are independent.

form factor	t -channel exchange	leading M dependence	form factor	t -channel exchange	leading M dependence
$B \rightarrow \rho \ell \nu_\ell$			$B \rightarrow \pi \ell \nu_\ell$		
V	1^-	$M^{1/2}$	f^+	1^-	$M^{1/2}$
A_1	1^+	$M^{-1/2}$	f^0	0^+	$M^{-1/2}$
A_2	1^+	$M^{1/2}$	$B \rightarrow K^* \gamma$		
A_3	1^+	$M^{3/2}$	T_1	1^-	$M^{1/2}$
A_0	0^-	$M^{1/2}$	T_2	1^+	$M^{-1/2}$

are also found for any fixed ω . The UKQCD collaboration have checked the validity of the relations in Eq. (C.40) [39], finding that they are well satisfied in the infinite mass limit. However, at the B mass the ratio $V/2T_1$ already shows significant deviations from its limiting value of 1. There are also kinematic constraints on the form factors at $q^2 = 0$:

$$f^+(0) = f^0(0), \quad T_1(0) = iT_2(0), \quad A_0(0) = A_3(0), \quad (\text{C.41})$$

which are very useful to constrain the lattice results.

From lattice simulations one can obtain the form factors only for part of the physical phase space. In order to control discretization errors one requires that the three-momenta of the B , π and ρ mesons be small in lattice units. This implies that the form factors are determined at large values of momentum transfer $q^2 = (p_B - p_{\pi,\rho})^2$. In the near future, one can expect to be able to compare the lattice form factor calculations directly with experimental data at large q^2 . A proposal in this direction was made by UKQCD [39] for $\overline{B}^0 \rightarrow \rho^+ l^- \overline{\nu}_l$ decays.

It is clear that one would also like to know the full q^2 dependence of the form factors, which involves a large extrapolation in q^2 from the high values where lattice calculations produce results, down to $q^2 = 0$. In particular the radiative decay $\overline{B} \rightarrow K^* \gamma$ occurs at $q^2 = 0$, so that existing lattice simulations cannot make a direct calculation of the necessary form factors. Attempts to constrain the q^2 dependence of the form factors using dispersion relations can be found in Refs. [32, 40].

For now one can only rely on model input to guide q^2 extrapolations. In addition one can ensure that any assumed q^2 -dependence of the form factors is consistent with the requirements imposed by heavy-quark symmetry, as shown in Eq. (C.39), together with the kinematical relations of Eq. (C.41). Even with these constraints, however, current lattice data do not by themselves distinguish a preferred q^2 -dependence. Fortunately, more guidance is available from light-cone sum rule analyses [41, 42] which lead to scaling laws for the form factors at fixed (low) q^2 rather than

Table C-6. Lattice results for $\overline{B}^0 \rightarrow \pi^+ l^- \overline{\nu}_l$ using various ansätze for the form factor f^+ . The decay rates are values for $\Gamma(\overline{B}^0 \rightarrow \pi^+ l^- \overline{\nu}_l)/V_{ub}^2 \text{ps}^{-1}$. ELC [35] and APE [29] results are from their method ‘b’, which uses the heavy-quark scaling laws of Eq. (C.39) to extrapolate from D to B mesons at fixed ω .

	Yr	β	c_{sw}	Rate	$f^+(0)$
UKQCD [36]	97	6.2	1	$8.5^{(33)}_{(14)}$	0.27(11)
WUP [27]	97	6.3	0		0.43(19)
APE [29]	95	6.0	1	8 ± 4	0.35(8)
ELC [35]	94	6.4	0	9 ± 6	0.30(14)(5)

Table C-7. $\overline{B}^0 \rightarrow \rho^+ l^- \overline{\nu}_l$ results from lattice simulations. The decay rates are values for $\Gamma(\overline{B}^0 \rightarrow \rho^+ l^- \overline{\nu}_l)/|V_{ub}|^2 \text{ps}^{-1}$. ELC [35] and APE [29] results are from their method ‘b’, which uses the heavy-quark scaling laws of Eq. (C.39) to extrapolate from D to B mesons at fixed ω .

	Yr	β	c_{sw}	Rate	$V(0)$	$A_1(0)$	$A_2(0)$
UKQCD [36]	97	6.2	1	$16.5^{(35)}_{(23)}$	$0.35^{(6)}_{(5)}$	$0.27^{(5)}_{(4)}$	$0.26^{(5)}_{(3)}$
WUP [27]	97	6.3	0		0.65(15)	0.28(3)	0.46(23)
APE [29]	95	6.0	1	12 ± 6	0.53(31)	0.24(12)	0.27(80)
ELC [35]	94	6.4	0	14 ± 12	0.37(11)	0.22(5)	0.49(21)(5)

at fixed ω as in Eq. (C.39). In particular all form factors scale like $M^{-3/2}$ at $q^2 = 0$:

$$f(0) = M^{-3/2} \gamma'_f \left(1 + \frac{\delta'_f}{M} + \frac{\epsilon'_f}{M^2} + \dots \right). \quad (\text{C.42})$$

It is important to use ansätze for the form factors compatible with as many of the known constraints as possible.

Lattice results for $\overline{B}^0 \rightarrow \pi^+ l^- \overline{\nu}_l$, $\overline{B}^0 \rightarrow \rho^+ l^- \overline{\nu}_l$ and $\overline{B} \rightarrow K^* \gamma$ are reported in Tables C-6, C-7, and C-8 respectively.

The UKQCD results for $\overline{B}^0 \rightarrow \pi^+ l^- \overline{\nu}_l$ and $\overline{B}^0 \rightarrow \rho^+ l^- \overline{\nu}_l$ come from constrained fits [36]. Their values for the form factors extrapolated to $q^2 = 0$ agree well with light-cone sum rule calculations, which work best at low q^2 . The fitted form factors also agree with experimental results for the rates and ratio-of-rates of these semileptonic decays. However, note that the extrapolated form factors are model-dependent and that this dependence is not explicit in the quoted errors in these tables, but is demonstrated by the spread of results obtained by different groups.

Table C-8. Lattice results for $\overline{B} \rightarrow K^* \gamma$. Values for $T(0) \equiv T_1(0) = iT_2(0)$ are quoted only from models which satisfy the light-cone sum rule scaling relation, Eq. (C.42), at $q^2 = 0$.

	Yr	β	c_{sw}	$T(0)$	$T_2(q_{\text{max}}^2)$
UKQCD [36]	97	6.2	1	0.16($\frac{2}{1}$)	0.25(2)
LANL [43]	96	6.0	0	0.09(1)	
APE [44]	96	6.0	1	0.09(1)(1)	
BHS [45]	94	6.3	0	0.101(10)(28)	0.325(33)(65)

Table C-8 lists the values of $T(0) \equiv T_1(0) = iT_2(0)$ for $\overline{B} \rightarrow K^* \gamma$, together with the directly measured $T_2(q_{\text{max}}^2)$. All groups find that T_2 has much less q^2 dependence than T_1 , although the lattice data again do not themselves distinguish a preferred q^2 dependence. In order to make a distinction, one can apply the light-cone sum rule scaling relation at $q^2 = 0$, see Eq. (C.42), which states that $T(0)$ has a leading $M^{-3/2}$ behavior. The table lists results from form factor fits which satisfy this scaling law. By using the UKQCD result (with statistical error only) obtained from a combined fit to $B \rightarrow V$ decays [36]

$$T(0) = 0.16(\frac{2}{1}), \quad (\text{C.43})$$

one can estimate the ratio (given at leading order in QCD and up to $\mathcal{O}(1/m_b^2)$ corrections)

$$R_{K^*} = \frac{\Gamma(\overline{B} \rightarrow K^* \gamma)}{\Gamma(b \rightarrow s \gamma)} = 4 \left(\frac{m_B}{m_b} \right)^3 \left(1 - \frac{m_{K^*}^2}{m_B^2} \right)^3 |T(0)|^2 = 16(\frac{4}{3})\%, \quad (\text{C.44})$$

which is consistent with the experimental result 18(7)% from CLEO. Discrepancies between R_{K^*} calculated using $T(0)$ and the experimental ratio $\Gamma(\overline{B} \rightarrow K^* \gamma)/\Gamma(b \rightarrow s \gamma)$ could reveal the existence of long-distance effects in the exclusive decay. At present, within the precision of the experimental and lattice results, there is no evidence for them.

C.7 The Parameters of the HQET

The Heavy-Quark Effective Theory discussed in Chapter 2 is proving to be a particularly useful tool for lattice studies in charm and beauty physics. The nonperturbative strong interaction effects can be parametrized in terms of matrix elements of local operators, which appear as factors in the expansion coefficients. Lattice simulations of the HQET provide the opportunity of computing these matrix elements numerically and this section briefly describes some of the calculations of some of the following quantities:

- $\bar{\Lambda}$, the mass difference between the heavy hadron and the heavy quark that it contains;
- λ_1 , the kinetic energy of the heavy quark;
- λ_2 , the matrix element of the chromomagnetic operator.

In practice, the heavy-quark mass must be defined at short distances (otherwise experimentally measurable quantities cannot be expressed in terms of the mass using perturbation theory), and below the \overline{MS} mass is used. The discussion is presented simply in terms of the mass itself. Clearly once a definition of the mass is chosen, the definition of $\bar{\Lambda}$ is then given. (The quantity $\bar{\Lambda}$, sometimes called the binding energy of the heavy quark, includes the energy of the light quark(s), as well as the binding energy of the meson.) In all the three examples to be discussed below, results are presented from lattice calculations using static heavy quarks.

C.7.1 The Evaluation of the Mass of a Heavy Quark

The first example given here is the lattice determination of the mass of a heavy quark (*e.g.*, the b quark), up to and including the terms of $\mathcal{O}(\Lambda_{\text{QCD}})$, but neglecting terms of $\mathcal{O}(\Lambda_{\text{QCD}}^2/m_b)$.

In Section C.4, the computation of the decay constant of a meson containing a heavy quark was discussed. In the HQET this parameter is obtained by evaluating correlation functions of the form:

$$C(t) = \sum_{\mathbf{x}} \langle 0 | A_4(\mathbf{x}, t) A_4(\mathbf{0}, 0) | 0 \rangle \quad (\text{C.45})$$

with Lagrangian density

$$\mathcal{L} = \bar{h} D_4 h, \quad (\text{C.46})$$

where h represents the field of the static quark. For sufficiently large values of the time t ,

$$C(t) \simeq Z^2 e^{-\mathcal{E}t} + \dots, \quad (\text{C.47})$$

where the points of ellipsis represent contributions from excited states. The value of f_B in the static limit is obtained from the prefactor Z . In addition, however, from the exponent \mathcal{E} it is possible to obtain the $\mathcal{O}(\Lambda_{\text{QCD}})$ contribution to m_b . Performing the matching of the heavy-quark propagator in full QCD and in the HQET gives [46]

$$\mathcal{E} = m_B - (m_b^{\text{pole}} - \delta m), \quad (\text{C.48})$$

where m_B is the mass of the B meson and m_b^{pole} is the pole mass of the b quark. Although the bare Lagrangian (C.46) was chosen to have no mass term, higher order perturbative corrections generate such a term and

$$\delta m = \sum_{n=1}^{\infty} \left(\frac{\alpha_s}{4\pi} \right)^n \frac{X_n}{a} \quad (\text{C.49})$$

represents the perturbation series generating the mass. Both \mathcal{E} and δm diverge linearly with the lattice spacing, so that they are not physical quantities. m_b^{pole} is also unphysical and in perturbation theory contains renormalon ambiguities [47, 48]. These ambiguities cancel those also present in δm in the difference on the right-hand side of Eq. (C.48). Thus it is possible to determine the value of a physical (short-distance) definition of the quark mass, such as $\overline{m}_b \equiv m_b^{\overline{MS}}(m_b^{\overline{MS}})$ from the computed value of \mathcal{E} . In practice, however, the subtraction of the linear divergence, which is performed in perturbation theory, leads to large numerical cancellations and hence to significant uncertainties. In Ref. [49] it was found that

$$\overline{m}_b = 4.15 \pm 0.05 \pm 0.20 \text{ GeV} . \quad (\text{C.50})$$

The first error on the right-hand side of Eq. (C.50) is due to uncertainties in the lattice evaluation of \mathcal{E} and in the value of the lattice spacing. However, the larger error of 200 MeV or so is the estimate of the uncertainty due to the truncation of the perturbation series for δm at one-loop order. Evaluation of higher-order terms in this series is urgently needed to reduce the uncertainty in the computed value of \overline{m}_b .

A similar approach, using NRQCD [50], gives

$$\overline{m}_b = 4.16 \pm 0.15 \text{ GeV} , \quad (\text{C.51})$$

in good agreement with the static result of Eq. (C.50). In Eq. (C.51) the uncertainty due to the truncation of the perturbative series has not been included in the error.

C.7.2 Kinetic Energy of a Heavy Quark

The next example considered here is the evaluation of the kinetic energy of the heavy quark λ_1 , which appears in many applications of the HQET. On the lattice one starts with the evaluation of the matrix element of the bare operator

$$\lambda_1^{\text{bare}} = - \frac{\langle B | \overline{h} (i\mathbf{D})^2 h | B \rangle}{2M_B} \quad (\text{C.52})$$

$$= -(0.69 \pm 0.03 \pm 0.03) a^{-2}, \quad (\text{C.53})$$

where the numerical result is taken from a simulation on a $24^3 \times 60$ lattice at $\beta = 6.0$ with the SW-action [51]. Taking the lattice spacing to be $2.0 \pm 0.2 \text{ GeV}$, one sees that the magnitude of the result is about 2.8 GeV^2 , to be compared to the expected physical corrections of $\mathcal{O}(A_{\text{QCD}}^2) \sim 0.1 \text{ GeV}^2$. Of course, the large result is due to the presence of power divergences, in this case they are quadratic, *i.e.*, they are of $\mathcal{O}(a^{-2})$. In one-loop perturbation theory, the power divergence is equal to $-5.19 \alpha_s a^{-2}$, which, depending on the value taken for the coupling constant α_s , is in the range $(0.67 - 0.93)a^{-2}$ (the choice of a suitable definition of the coupling constant is

a representation of ignorance of the higher-order perturbative corrections, the range given here comes from frequently used definitions). The uncertainty is greater than the terms to be evaluated, which are of $\mathcal{O}(\Lambda_{\text{QCD}}^2)$. Clearly, in order for the lattice result to be useful for phenomenological applications, the perturbative calculations must be performed to higher orders. This is the main conclusion of this subsection.

It is also possible to subtract the power divergences nonperturbatively. In Refs. [46, 51] a subtracted kinetic energy operator,

$$\bar{h}\mathbf{D}_S^2 h \equiv \bar{h}\mathbf{D}^2 h - \frac{c}{a^2}\bar{h}h, \quad (\text{C.54})$$

was defined, with the subtraction constant c fixed by imposing that the matrix element of this operator vanishes between quark states at rest (in the Landau Gauge). The corresponding value of λ_1 , which is now free of quadratic divergences, was found to be²

$$\lambda_1 = a^{-2}Z_{\mathbf{D}_S^2}(a^2\lambda_1^{\text{bare}} - a^2c) \quad (\text{C.55})$$

$$= 0.09 \pm 0.14 \text{ GeV}^2. \quad (\text{C.56})$$

Of course the large relative error in Eq. (C.56) is due to the large cancellation between the two terms in the parentheses in Eq. (C.55). In Eq. (C.55), $Z_{\mathbf{D}_S^2}$ is the normalization constant required to obtain the continuum, \overline{MS} , value of λ_1 from the subtracted lattice one.

The difficulties described here arise because of the mixing of the kinetic energy operator $\bar{h}(i\mathbf{D})^2 h$ with $\bar{h}h/a^2$. Since $\bar{h}h$ is a conserved current in the HQET, its matrix elements are the same between all hadronic states. This means that the difference of the matrix elements of the kinetic energy operator between any two different beauty hadrons is a physical quantity. In Ref. [51] it was found that

$$\lambda_1(B_s) - \lambda_1(B_d) = -0.09 \pm 0.04 \text{ GeV}^2. \quad (\text{C.57})$$

This difference is the leading contribution to the following combination of masses

$$\lambda_1(B_s) - \lambda_1(B_d) = \frac{\overline{m}_{B_s} - \overline{m}_{B_d} - (\overline{m}_{D_s} - \overline{m}_{D_d})}{\frac{1}{2}(1/m_D - 1/m_B)} + \mathcal{O}\left(\frac{\Lambda_{\text{QCD}}^3}{m_Q}\right), \quad (\text{C.58})$$

where, for example, \overline{m}_B is the spin-averaged mass of the B meson (with the corresponding light valence quark)

$$\overline{m}_B = \frac{1}{4}(3m_{B^*} + m_B), \quad (\text{C.59})$$

and m_Q is the mass of the heavy quark Q ($Q = b$ or c). Where appropriate, the subscript d or s denotes the presence of the corresponding light valence quark. The experimental value of the first term on the right-hand side of Eq. (C.58) is $-0.06 \pm 0.02 \text{ GeV}^2$, in very good agreement with the result in Eq. (C.57). It must, however, be remembered that the $\mathcal{O}(\Lambda_{\text{QCD}}^3/m_c)$ corrections to this result may be significant.

²Note that the central value in Eq. (C.56) has the opposite sign to that of many other estimates using various definitions of λ_1 .

C.7.3 The Matrix Element of the Chromomagnetic Operator

The chromomagnetic operator, $\bar{h}\frac{1}{2}\sigma_{ij}G^{ij}h$, does not mix with the operator $\bar{h}h$, and hence its matrix elements are free of power divergences. The parameter λ_2 , defined as

$$\lambda_2 \equiv \frac{1}{2m_B} \frac{1}{3} \langle B | \bar{h} \frac{1}{2} \sigma_{ij} G^{ij} h | B \rangle, \quad (\text{C.60})$$

gives the first term in the hyperfine splitting in the B meson system:

$$m_{B^*}^2 - m_B^2 = 4\lambda_2. \quad (\text{C.61})$$

The lattice results for λ_2 are all significantly smaller (by about a factor of two) than the values deduced from the physical masses of the B^* and B mesons. In two recent lattice computations the authors found:

$$m_{B^*}^2 - m_B^2 = \begin{cases} 0.28 \pm 0.02 \pm 0.04 \text{ GeV}^2 & \text{Ref. [15]} \\ 0.28 \pm 0.06 \text{ GeV}^2 & \text{Ref. [51]} \end{cases} \quad (\text{C.62})$$

to be compared to the experimental value of $0.485 \pm 0.005 \text{ GeV}^2$.

One possible source for the discrepancy between the lattice results and the experimental value is the unusually large one-loop contribution to the renormalization constant relating the lattice and continuum chromomagnetic operator [52]. This renormalization constant is about 1.85 at one-loop order, and so one may wonder whether the higher order terms might give a significant contribution. Other possible contributions to the discrepancy might be the use of the quenched approximation, or that the relation between λ_2 and the hyperfine splitting may be significantly modified by higher order corrections in $1/m_b$. It is important to clarify the source of this discrepancy.

Lattice calculations of the hyperfine splitting using propagating heavy quarks also give a result which is smaller than the experimental one. This is a different problem, however, which is related to the presence of a spurious chromomagnetic term of $\mathcal{O}(a)$ present in the lattice action. This interpretation is confirmed by the fact that the computed value of the splitting increases as the action is “improved” to remove this term, in agreement with expectations.

C.8 Exclusive Nonleptonic Decays of Heavy Mesons

Exclusive nonleptonic decays are, in principle, an important source of fundamental information on the properties of weak decays of heavy quarks. Unfortunately current theoretical understanding of the nonperturbative QCD effects in these processes is rather primitive, and one is forced to make assumptions based on factorization and/or quark models. Lattice computations of the corresponding matrix elements are also difficult [53]. They need to be performed in Euclidean space, where

there is no distinction between *in*- and *out*-states. The quantities which one obtains directly in lattice computations are the (real) averages such as

$$\langle M_1 M_2 | \mathcal{H}_W | B \rangle = \frac{1}{2} (\text{in} \langle M_1 M_2 | \mathcal{H}_W | B \rangle + \text{out} \langle M_1 M_2 | \mathcal{H}_W | B \rangle), \quad (\text{C.63})$$

where M_1 and M_2 are mesons. It is therefore not possible to obtain directly any information about the phase due to final state interactions, and hence to determine the matrix elements reliably. Maiani and Testa [53] also showed that the quantities which are obtained from the large time behavior of the corresponding correlation functions are the unphysical form factors in which the final state mesons are at rest, *e.g.*,

$$\langle M_1(\mathbf{p}_{M_1} = \mathbf{0}) M_2(\mathbf{p}_{M_2} = \mathbf{0}) | \mathcal{H}_W | B \rangle. \quad (\text{C.64})$$

For $K \rightarrow \pi\pi$ decays chiral perturbation theory can then be used to obtain the physical form factors with reasonable accuracy. For D - and B -meson decays this is not possible. The publication of the Maiani-Testa [53] theorem stopped the exploratory work on the numerical evaluation of two-body nonleptonic decays. These early, and not very accurate papers, studied the non-penguin contributions to D -meson decay amplitudes [54].

The Maiani-Testa theorem implies that it is not possible to obtain the phase of the final state interactions without some assumptions about the amplitudes. The importance of developing reliable quantitative techniques for the evaluation of nonperturbative QCD effects in nonleptonic decays cannot be overstated, and so attempts to introduce “reasonable” assumptions to enable calculations to be performed (and compared with experimental data) are needed urgently. Ciuchini *et al.*, [55, 56] have recently shown that by making a “smoothness” hypothesis about the decay amplitudes it is possible to extract information about the phase of two-body nonleptonic amplitudes. Studies to see whether their proposals are practicable and consistent are currently beginning.

References

- [1] H. Wittig, *Int. J. Mod. Phys.* **A12**, 4477 (1997).
- [2] J. M. Flynn and C. T. Sachrajda, SHEP 97/20, to appear in *Heavy Flavours II*, eds. A. J. Buras and M Lindner, World Scientific (1997), hep-lat/9710057.
- [3] L. H. Karsten and J. Smit, *Nucl. Phys.* **B183**, 103 (1981);
M. Bochicchio *et al.*, *Nucl. Phys.* **B262**, 331 (1985);
L. Maiani and G. Martinelli, *Phys. Lett. B* **178**, 265 (1986);
G. Martinelli *et al.*, *Phys. Lett. B* **311**, 241 (1993); *Phys. Lett. B* **317**, 660(E) (1993).
- [4] G. Martinelli *et al.*, *Nucl. Phys.* **B445**, 81 (1995).
- [5] M. Lüscher *et al.*, *Nucl. Phys.* **B478**, 365 (1996);
M. Lüscher and P. Weisz, *Nucl. Phys.* **B479**, 429 (1996);
M. Lüscher *et al.*, *Nucl. Phys.* **B491**, 323 (1997).
- [6] M. Lüscher *et al.*, *Nucl. Phys.* **B491**, 344 (1997).
- [7] K. Symanzik, “Mathematical Problems in Theoretical Physics,” *Lecture Notes in Physics* **153** (1982) 429 P, eds. R. Schrader *et al.*, Springer, New York; *Nucl. Phys.* **B226**, 187 (1983);
Nucl. Phys. **B226**, 205 (1983).
- [8] G. Heatlie *et al.*, *Nucl. Phys.* **B352**, 266 (1991);
H. Hoerber *et al.*, *Nucl. Phys. Proc. Suppl.* **63**, 218 (1998).
- [9] T. Bhattacharya and R. Gupta, *Nucl. Phys. Proc. Suppl.* **63**, 95 (1998).
- [10] B. Sheikholeslami and R. Wohlert, *Nucl. Phys.* **B259**, 572 (1985).
- [11] G. Martinelli *et al.*, *Phys. Lett. B* **411**, 141 (1997).
- [12] G. P. Lepage and P. B. Mackenzie, *Phys. Rev. D* **48**, 2250 (1993).
- [13] A. X. El-Khadra, A. S. Kronfeld and P. B. Mackenzie, *Phys. Rev. D* **55**, 3933 (1997).
- [14] A. J. Buras, M. Jamin and P. H. Weisz, *Nucl. Phys.* **B347**, 491 (1990).
- [15] A. K. Ewing *et al.*, (UKQCD Collaboration), *Phys. Rev. D* **54**, 3526 (1996).
- [16] V. Giménez and G. Martinelli, *Phys. Lett. B* **398**, 135 (1997).
- [17] C. Bernard, T. Blum and A. Soni, *Nucl. Phys. B Proc. Suppl.* **53**, 382 (1997).
- [18] A. Soni, *Nucl. Phys. B Proc. Suppl.* **47**, 43 (1996).

- [19] S. Aoki *et al.*, (JLQCD Collaboration), *Nucl. Phys. B Proc. Suppl.* **47**, 433 (1996).
- [20] A. Abada *et al.*, (ELC Collaboration), *Nucl. Phys.* **B376**, 172 (1992).
- [21] C. Bernard *et al.*, *Phys. Rev. D* **38**, 3540 (1988).
- [22] C. Bernard, to be published in *Proceedings of the 7th International Symposium on Heavy Flavor Physics*, Santa Barbara, CA, July (1997), hep-ph/9709460.
- [23] S. R. Sharpe and Y. Zhang, *Phys. Rev. D* **53**, 5125 (1996).
- [24] S. R. Sharpe, *Nucl. Phys. B Proc. Suppl.* **53**, 181 (1997).
- [25] S. Aoki *et al.*, *Nucl. Phys. B Proc. Suppl.* **53**, 349 (1997); hep-lat/9705035 and hep-lat/9710073.
- [26] K.C. Bowler *et al.*, (UKQCD Collaboration), *Phys. Rev. D* **51**, 4905 (1995).
- [27] S. Güsken, private communication, paper in preparation.
- [28] T. Bhattacharya and R. Gupta, *Nucl. Phys. B Proc. Suppl.* **42**, 935 (1995); *Nucl. Phys. B Proc. Suppl.* **47**, 481 (1996).
- [29] C. R. Allton *et al.*, (APE Collaboration), *Phys. Lett. B* **345**, 513 (1995).
- [30] A. Ryd, talk presented at Seventh International Symposium on Heavy Flavors, Santa Barbara, CA, July (1997).
- [31] K.C. Bowler *et al.*, (UKQCD Collaboration), *Phys. Rev. D* **52**, 5067 (1995).
- [32] L. Lellouch, *Acta Phys. Polon.* **B25**, 1679 (1994); *Nucl. Phys.* **B479**, 353 (1996).
- [33] C.W. Bernard, Y. Shen and A. Soni, *Nucl. Phys. B Proc. Suppl.* **34**, 483 (1994); *Phys. Lett. B* **317**, 164 (1993).
- [34] K. C. Bowler *et al.*, (UKQCD Collaboration), *Phys. Rev. D* **57**, 6948 (1998).
- [35] A. Abada *et al.*, *Nucl. Phys.* **B416**, 675 (1994).
- [36] L. Del Debbio *et al.*, (UKQCD Collaboration), *Phys. Lett. B* **416**, 392 (1998).
- [37] N. Isgur and M. B. Wise, *Phys. Rev. D* **42**, 2388 (1990).
- [38] P. A. Griffin, M. Masip and M. McGuigan, *Phys. Rev. D* **42**, 5751 (1994).
- [39] J. M. Flynn *et al.*, (UKQCD Collaboration), *Nucl. Phys.* **B461**, 327 (1996).
- [40] D. Becirevic, LPTHE–Orsay preprint 97/16, hep-ph/9707271.

- [41] A. Ali, V. Braun and H. Simma, *Z. Phys. C* **63**, 437 (1994).
- [42] P. Ball and V. M. Braun, *Phys. Rev. D* **55**, 5561 (1997).
- [43] R. Gupta and T. Bhattacharya, *Nucl. Phys. B Proc. Suppl.* **47**, 473 (1996).
- [44] A. Abada *et al.*, (APE Collaboration), *Phys. Lett. B* **365**, 275 (1996).
- [45] C. Bernard, P. Hsieh and A. Soni, *Phys. Rev. Lett.* **72**, 1402 (1994).
- [46] M. Crisafulli *et al.*, *Nucl. Phys.* **B457**, 594 (1995).
- [47] M. Beneke and V. M. Braun, *Nucl. Phys.* **B426**, 301 (1994).
- [48] I. I. Bigi *et al.*, *Phys. Rev. D* **50**, 2234 (1994).
- [49] V. Giménez, G. Martinelli and C. T. Sachrajda, *Phys. Lett. B* **393**, 124 (1997).
- [50] C. Davies *et al.*, *Phys. Rev. Lett.* **73**, 2654 (1994).
- [51] V. Giménez, G. Martinelli and C. T. Sachrajda, *Nucl. Phys.* **B486**, 227 (1997).
- [52] J. M. Flynn and B. R. Hill, *Phys. Lett. B* **264**, 173 (1991).
- [53] L. Maiani and M. Testa, *Phys. Lett. B* **245**, 585 (1990).
- [54] C. Bernard, J. Simone and A. Soni, *Nucl. Phys. B Proc. Suppl.* **17**, 504 (1990);
A. Abada *et al.*, *Nucl. Phys. B Proc. Suppl.* **17**, 518 (1990).
- [55] M. Ciuchini *et al.*, *Phys. Lett. B* **380**, 353 (1996).
- [56] L. Silvestrini, *Nucl. Phys. A (Proc. Suppl.)* **54**, 276 (1997).

This page was intentionally left blank.

D

Standard Model Parameters from QCD Sum Rules

The method of QCD sum rules has been extensively applied to the calculation of the hadronic parameters which are relevant for the physics at the B factories. This appendix outlines the main aspects of the approach, referring to [1] for more comprehensive reviews.

The basic quantities investigated in the QCD sum rule approach [2] are the correlation functions defined at the Euclidean momentum $Q^2 = -q^2$:

$$\Pi(Q^2) = i \int d^4x e^{iq \cdot x} \langle \text{vac} | T (J(x) J(0)^\dagger) | \text{vac} \rangle \quad (\text{D.1})$$

(omitting possible Lorentz indices), where $|\text{vac}\rangle$ represents the QCD nonperturbative vacuum. The local currents J are made of quark (or gluon) fields and have the same quantum numbers of the hadrons one is interested in, *e.g.*, $\bar{b}(x)\Gamma d(x)$ with $\Gamma = i\gamma_5, \gamma_\mu$ for the B, B^* mesons, $\bar{q}_i(x)\gamma_\mu q_j(x)$ for light vector mesons, analogous three-quark operators with baryons quantum numbers, *etc.* Thus, Eq. (D.1) represents the Fourier transform of the nonperturbative propagation amplitude of mesons or baryons from $0 \rightarrow x$.

The connection of $\Pi(Q^2)$ to the relevant hadrons is realized by a dispersive representation, allowed by the analyticity in Q^2 of the right-hand side of Eq. (D.1):

$$\Pi(Q^2) = \frac{1}{\pi} \int_{th}^{\infty} ds \frac{\rho(s)}{s + Q^2} + (\text{subtractions}), \quad (\text{D.2})$$

where the spectral function $\rho(s) = \text{Im}\Pi(s)$ contains information on the physical hadronic states with the quantum numbers of J , their masses, coupling constants, *etc.*

The left-hand side of (D.1) can be evaluated in QCD at large $Q^2 \gg \Lambda_{QCD}^2$ by means of the Operator Product Expansion (OPE) which organizes the result in terms of a sum of products of the short-distance perturbative coefficients times coefficients that are a set of nonperturbative quark and gluon operator vacuum matrix elements divided by inverse powers of Q^2 corresponding to the dimension of the matrix element. Terms are ordered in increasing dimensionality of the matrix elements. This expansion (D.1) in powers of $1/Q^2$ can be written:

$$\Pi(Q^2)_{QCD} = \sum_k C_{2k}(Q^2, \alpha_s, \mu) \frac{\langle \text{vac} | \mathcal{O}_{2k}(\mu) | \text{vac} \rangle}{(Q^2)^k}, \quad (\text{D.3})$$

where C_{2k} are Wilson coefficients, calculable in perturbative QCD to a given order in α_s . The vacuum matrix elements (called vacuum condensates) $\langle \text{vac} | \mathcal{O}_{2k}(\mu) | \text{vac} \rangle$ systematically account for the effects of the nonperturbative QCD vacuum. Indeed, the lowest dimension, $k = 0$, term in (D.3) is the, purely perturbative, asymptotic freedom contribution to $\Pi(Q^2)$, since the relevant operator is the trivial unit operator. This is the only term which survives for asymptotically large Q^2 . Knowledge of the vacuum condensates up to some dimension allows the extrapolation in Q^2 from the asymptotic freedom region down to relatively “moderate” Q^2 , closer to the hadronic mass scales. Both the operators \mathcal{O}_{2k} and the corresponding coefficients C_{2k} depend on a renormalization mass scale μ , separating short- from long-distance physics.

QCD sum rules are obtained by imposing, according to a generalized version of “quark-hadron duality” [3], the requirement that the two descriptions (D.2) and (D.3) match in a suitable range of Q^2 . In this way, hadronic properties (such as masses, coupling constants, *etc.*) in (D.2) can be related to QCD parameters (quark masses, α_s , vacuum condensates).

The vacuum expectation values cannot be computed in perturbative QCD, but must be either estimated in some nonperturbative framework or inferred phenomenologically from applications of QCD sum rules to cases where the hadronic spectral density $\rho(s)$ is particularly well known. Being universal, the values of the condensates so determined can then be used to make predictions in other channels of interest (provided care is taken to ensure that renormalization-scale matching is properly accounted for).

The lowest dimension vacuum expectation values, and their currently used values, are given by (q denotes light quarks):

- D=3: $\langle \text{vac} | \bar{q}q | \text{vac} \rangle (1 \text{ GeV}) = -(225 \pm 25 \text{ MeV})^3$, obtained using PCAC, in the SU(3) limit (SU(3) breaking corrections are discussed, *e.g.*, in [4]);
- D=4: $\langle \text{vac} | \alpha_s G_{\mu\nu}^2 | \text{vac} \rangle = 0.04 \pm 0.02 \text{ GeV}^4$ [5];
- D=5: $\langle \text{vac} | g_s \bar{q} \sigma_{\mu\nu} G^{\mu\nu} | \text{vac} \rangle = m_0^2 \langle \text{vac} | \bar{q}q | \text{vac} \rangle$ with $m_0^2 = 0.8 \pm 0.2 \text{ GeV}^2$ [6];
- D=6: $\langle \text{vac} | (\bar{q}q)^2 | \text{vac} \rangle$ is usually obtained by the assumption of factorization (otherwise called vacuum saturation), namely that it is given by the product of two dimension 3 vacuum matrix elements.

Even dimension vacuum condensates in (D.3) are obtained by multiplying the above listed condensates by quark masses, defined at the same scale.

Clearly, since only a limited number of condensates are quantitatively known, the procedure is sensible if the OPE expansion (D.3) is rapidly converging in the “duality” range of Q^2 , so that the sum can be truncated to the first few terms. This would make the method both economical, *i.e.*, depending on few parameters incorporating the general features of nonperturbative QCD, and

predictive at the same time. Uncertainties in results also arise because the order in α_s at which the perturbative Wilson coefficients have been calculated is limited and yet the scale at which the condensates can be evaluated by matching to the dispersive expression is quite low. Thus results in some cases can have unphysical apparent scale-dependence.

In practical applications, a phenomenological ansatz to parameterize the hadronic spectral function $\rho(s)$ is needed. It generally consists of the contributions of the lowest lying hadronic states $\rho(s)_H$ — in many cases a δ -function or a Breit-Wigner centered at the ground state — plus a “continuum” of hadronic higher excitations and multi-particle states starting at some threshold s_0 . According to parton model ideas, above the threshold s_0 duality between hadrons and asymptotically free quarks and gluons is assumed. This leads to the identification of the continuum with the perturbatively calculable $\rho(s)_{AF}$. Accordingly, in this parametrization s_0 represents the threshold for the onset of asymptotic freedom, and:

$$\rho(s) = \rho(s)_H + \theta(s - s_0)\rho(s)_{AF}. \quad (\text{D.4})$$

Technically, the dispersive integrals Eq. (D.2) are modified by convoluting $\rho(s)$ with suitable weight functions, in order to improve convergence, eliminate dependence on subtraction constants, emphasize the contribution of the ground state one is interested in, and minimize the role of the model for the continuum of hadronic states (in particular, the sensitivity of the results to the threshold s_0 , which cannot be fixed a priori). Different choices for the hadronic weight functions identify several types of QCD sum rules:

- Hilbert, or power moments, sum rules follow from n -times differentiation of $\Pi(Q^2)$:

$$\mathcal{M}_n(Q^2) = \frac{(-1)^n}{n!} \left(\frac{d}{dQ^2} \right)^n \Pi(Q^2) = \frac{1}{\pi} \int_{th}^{\infty} ds \frac{\rho(s)}{(s + Q^2)^{n+1}} \quad (\text{D.5})$$

and of the corresponding OPE expansion in $1/Q^2$ in (D.3). For heavy quarks b and c , which already bring a large mass scale into the game by their masses, moments at $Q^2 = 0$ have been considered also with the corresponding OPE expansion in inverse powers of the heavy mass $m_{b,c}$. Clearly, the $1/s^{n+1}$ integration for large n in (D.5) strongly emphasizes contribution to the dispersive expression from the hadronic ground state. On the other hand, larger n is found to increase the size of both the perturbative QCD corrections and the contribution of higher dimension contributions in the OPE. Since a truncation of the OPE is unavoidable because only a limited number of condensates are well determined, in practice a compromise must be made in choosing the actual values of n at which QCD sum rules can best be numerically exploited.

- Laplace, or exponential, sum rules are obtained by Borel transform of (D.2), which results into an exponential weight [2] formally derivable from the limit $n \rightarrow \infty$, $Q^2 \rightarrow \infty$, $Q^2/n = 1/\sigma$ in (D.5):

$$\mathcal{M}(\sigma) = \frac{1}{\pi} \int_{th}^{\infty} ds \exp(-\sigma s) \rho(s). \quad (\text{D.6})$$

In this case the relevant OPE expansion is in powers of the (a priori arbitrary) variable σ . A benefit of borelization is that the higher dimensional contributions are suppressed, in addition to higher powers in σ , by factorial factors, so that an improved convergence of the OPE is expected in this case. Similar to the previous case, large σ in (D.6) would emphasize the lowest lying hadronic states and minimize the continuum, at the cost of increasing the power corrections. Therefore, for this kind of sum rules, a suitable range of σ must be chosen as a compromise, such that the lowest hadronic state dominates and at the same time the OPE truncation can be justified.

- Gaussian sum rules, where the spectral function is weighted by a Gaussian centered at a reference point \hat{s} , can be generated from the previous ones [7]:

$$G(\sigma, \hat{s}) = \frac{1}{\sqrt{4\pi\sigma}} \frac{1}{\pi} \int_{th}^{\infty} ds \exp[-(s - \hat{s})^2/4\sigma] \rho(s); \quad (\text{D.7})$$

- Finite energy sum rules (FESR) [8], that can be derived using the Cauchy theorem:

$$\frac{1}{\pi} \int_0^{s_0} ds s^{n-1} \rho(s)_H = -\frac{1}{2\pi i} \oint_{C(|s_0|)} ds s^{n-1} \Pi(s)_{OPE} \quad (\text{D.8})$$

($n = 1, 2, \dots$), which results into the relation

$$\frac{1}{\pi} \int_0^{s_0} ds s^{n-1} \rho(s)_H = \frac{s_0^n}{n} \mathcal{F}_n(s_0) - (-1)^N C_{2n} \langle \text{vac} | \mathcal{O}_{2n} | \text{vac} \rangle, \quad (\text{D.9})$$

where the $\mathcal{F}_n(s_0)$ originate from the contour integration of the perturbative term. Eq. (D.9) also naturally follows either from (D.6) and from (D.7) [5]. The advantage of FESR is that of projecting out operators of a given dimension. On the other hand, the positive power of s in (D.9) enhances the contribution of less known higher-lying hadronic states in the dispersive expression, hence to introduce a strong dependence on the continuum threshold s_0 , so that only the first few values of n can be considered in practical applications.

Since they refer to observable quantities, in principle the predictions of the above QCD sum rules should be independent of n and s_0 , or σ and s_0 , *etc.* Therefore, sum rules are exploited by numerically looking for a (hopefully wide) “stability window”, *i.e.*, a range in n and s_0 , or in σ and s_0 , where the OPE expansion and the hadronic dispersive contribution match each other [9] such that the quantity to be predicted is reasonably stable against changes of such variables. An additional criterion to identify the window is that both the $O(\alpha_s)$ corrections and the higher power corrections must represent small corrections (up to an assigned size) to the leading perturbative terms in (D.3), in order to ensure a hierarchy of contributions to the OPE and thus justify the truncation of the series to the lowest orders in α_s and in the dimensional operators. Consequently, although they are based on field theory and hence on “first principles,” QCD sum rules must be considered as an approximate nonperturbative framework, where results are derived

from the numerical “optimization” procedure outlined above, rather than a direct computational scheme. Such optimization procedures, together with the uncertainties in the actual input values of condensates and of Λ_{QCD} , produce uncertainties in the final result which, combined with the systematic uncertainty intrinsic to the method, cannot be made arbitrarily small. Nonetheless, the method has the advantage that it offers the possibility of deriving predictions for the hadronic quantities using (relatively) simple calculations.

Similar considerations can be applied in order to extend the method of QCD sum rules to the calculation of hadronic form factors. In this case, the basic objects to study are three-point correlators of the kind [10, 11]:

$$\Pi_\mu(p, p', q) = i^2 \int d^4x d^4y e^{i(p' \cdot x - p \cdot y)} \langle \text{vac} | T \left(J_2(x) J_\mu^{V,A}(0) J_1(y) \right) | \text{vac} \rangle , \quad (\text{D.10})$$

where $q = p - p'$, the currents J_1 and J_2 interpolate the hadrons, and $J_\mu^{V,A}$ are weak currents. In analogy to (D.2), the connection of (D.10) to hadronic data is obtained through spectral representations involving double spectral functions $\rho(s, s', q^2)$. Similarly to (D.4), the spectral representation is saturated by the lowest-lying hadronic states $\rho(s, s', q^2)_H$, containing the required form factor $F(q^2)$, plus a QCD continuum starting at thresholds s_0, s'_0 , and modeled by the quark-gluon calculation $\rho(s, s', q^2)_{AF}$. Moreover, for Euclidean (and large) p^2, p'^2 , and q^2 the left-hand side of (D.10) can be expressed as an OPE in the framework of QCD, accounting for the asymptotic freedom contribution plus nonperturbative vacuum condensates. QCD sum rules are finally obtained by matching these alternative representations, and the convergence of both the dispersive representation and the OPE can be improved by convolution with appropriate weight functions. For example, the analogue of the Laplace moments (D.6) reads as follows ($t = q^2$):

$$\mathcal{M}(\sigma, \sigma', t) = \frac{1}{(2\pi)^2} \int ds ds' \rho(s, s', t) e^{-s\sigma} e^{-s'\sigma'} , \quad (\text{D.11})$$

and the optimization in the variables σ, σ' and s_0, s'_0 must be performed on (D.11) to obtain predictions for the form factors.

Another possibility to study form factors is represented by the light-cone QCD sum rule approach, where, instead of (D.10), one analyzes current correlators with one of the hadrons as an external state [12, 13, 14, 15]:

$$\Omega_\mu(p, p', q) = i \int d^4x e^{ip' \cdot x} \langle \text{vac} | T \left(J_2(x) J_\mu^{V,A}(0) \right) | H_1(p) \rangle . \quad (\text{D.12})$$

With $p^2 = M_{H_1}^2$ now fixed, a dispersion relation in the variable p'^2 at fixed t is assumed to hold for (D.12), as usual parameterized in terms of the required form factor plus a higher lying continuum. The OPE is now applied to the T-product on the right-hand side of (D.12), the difference with the previous formulation being that “non-forward” operator matrix elements, *i.e.*, between $\langle \text{vac} |$ and $| H_1(p) \rangle$, must be taken into account. The OPE expansion now involves contributions to the light-cone wave function of the H_1 hadron, *e.g.*, hadronic matrix elements of operators ordered

for increasing twist, rather than dimension. The wave functions can be modeled (and their value at particular points, together with several moments, can be determined by QCD sum rules) in the case of some light hadrons (for example, the π and the ρ). This kind of QCD sum rule has some advantages for light-to-light and heavy-to-light form factors. This approach is discussed in further detail in Section D.4.

To study hadrons containing one heavy quark in the limit $m_Q \rightarrow \infty$, or using the heavy-quark expansion in $1/m_Q$, the QCD sum rule approach can be directly, and very naturally, formulated in the framework of HQET [16]. In this case, the relevant correlators involve the hadron interpolating currents made of the appropriate heavy-quark fields. For example: $\tilde{J} = \bar{q}\gamma_5 h_Q(v)$ with $Q = b, c$ for the B and D mesons respectively, where v is the heavy quark four-velocity, $\bar{q}(\gamma_\mu - v_\mu)h_Q(v)$ for B^* and D^* , and analogous trilinear constructions for beauty baryons. Moreover, the heavy-to-heavy $b \rightarrow c$ weak vector and axial-vector currents are expressed as $\tilde{J}_\mu^V = \bar{h}_c(v')\gamma_\mu h_b(v)$ and $\tilde{J}_\mu^A = \bar{h}_c(v')\gamma_\mu\gamma_5 h_b(v)$, respectively. Accordingly, instead of (D.1) and (D.10), the basic two- and three-point functions will have the form:

$$\tilde{\Pi}(\omega) = i \int d^4x e^{ik \cdot x} \langle \text{vac} | T \left(\tilde{J}(x) \tilde{J}(0)^\dagger \right) | \text{vac} \rangle \quad (\text{D.13})$$

($k = \omega v$) and

$$\tilde{\Pi}_\mu(\omega, \omega', q^2) = i^2 \int d^4x d^4y e^{i(k' \cdot x - k \cdot y)} \langle \text{vac} | T \left(\tilde{J}_2(x) \tilde{J}_\mu^{V,A}(0) \tilde{J}_1(y) \right) | \text{vac} \rangle \quad . \quad (\text{D.14})$$

Dispersion relations in ω and ω' , analogues to (D.2), connect such Green functions to the hadronic states. On the other hand, for large negative ω , (D.13) and (D.14) can be expanded by means of the OPE, which can be directly obtained by the application of the Feynman rules of HQET. Then, the procedure for obtaining QCD sum rules exactly follows the steps previously outlined for the low mass case. Clearly, the hadronic states and the relevant observables involved here are those pertinent to the HQET, and the connection to the full QCD can be obtained through appropriate (calculable) QCD coefficients. The $1/m_Q$ corrections to the infinite mass limit have been assessed in some cases by studying the relevant higher-dimensional operator matrix elements in the framework of QCD sum rules and HQET.

In what follows we collect the most recent QCD sum rule determinations of Standard Model parameters which are relevant to the physics at the B Factory. Since a large number of predictions can be found in the literature for each quantity of interest, with different numerical inputs, it is difficult to compile an exhaustive review. Therefore, as a rule, in addition to considering only updated estimates, we selected results that make use of consistent values of the input parameters. Unweighted numerical averages of these results are quoted as “best” values, with an uncertainty “conservatively” determined as the largest deviation from the mean value, without attempting to combine the individual errors. Hence these errors are in no way statistical. Earlier determinations are quoted in the list of references.

D.1 Quark Masses

In this section we collect the results of the most recent QCD sum rule determinations of the current quark masses, which represent input parameters in the theoretical estimates of some B and D meson matrix elements. The running masses depend on the renormalization scale μ through the renormalization group equation:

$$\mu \frac{d}{d\mu} m_q(\mu) = -\gamma(\alpha_s) m_q(\mu), \quad (\text{D.15})$$

where γ has the expansion:

$$\gamma(\alpha_s) = \gamma_0 \frac{\alpha_s}{\pi} + \gamma_1 \left(\frac{\alpha_s}{\pi}\right)^2 + \gamma_2 \left(\frac{\alpha_s}{\pi}\right)^3 + \gamma_3 \left(\frac{\alpha_s}{\pi}\right)^4 + \mathcal{O}(\alpha_s^5). \quad (\text{D.16})$$

The lowest order coefficients, for $N_c = 3$ and N_f flavors, read as follows:

$$\gamma_0 = 2, \quad \gamma_1 = \frac{101}{12} - \frac{5}{18} N_f, \quad \gamma_2 = \frac{1}{32} \left[1249 - \left(\frac{2216}{27} + \frac{160}{3} \zeta(3) \right) N_f - \frac{140}{81} N_f^2 \right], \quad (\text{D.17})$$

$\zeta(x)$ being the Riemann ζ function. The coefficient γ_3 , in the \overline{MS} scheme, has recently been computed [17]: $\gamma_3 = 88.5256$, for $N_c = 3$ and $N_f = 3$.

Using the scale dependence of α_s ($L = \ln(\mu^2/\Lambda^2)$):

$$\alpha_s(\mu) = \frac{4\pi}{\beta_0} \frac{1}{L} \left\{ 1 - \frac{2\beta_1}{\beta_0^2} \frac{\ln L}{L} + \frac{4\beta_1^2}{\beta_0^4 L^2} \left[\left(\ln L - \frac{1}{2} \right)^2 + \frac{\beta_2 \beta_0}{8\beta_1^2} - \frac{5}{4} \right] \right\} + \mathcal{O}\left(\frac{\ln^2 L}{L^3}\right), \quad (\text{D.18})$$

with

$$\beta(\alpha_s) = -\frac{\beta_0}{2\pi} \alpha_s^2 - \frac{\beta_1}{4\pi^2} \alpha_s^3 - \frac{\beta_2}{64\pi^3} \alpha_s^4 + \mathcal{O}(\alpha_s^5), \quad (\text{D.19})$$

and

$$\beta_0 = 11 - \frac{2}{3} N_f, \quad \beta_1 = 51 - \frac{19}{3} N_f, \quad \beta_2 = 2857 - \frac{5033}{9} N_f + \frac{325}{27} N_f^2, \quad (\text{D.20})$$

(the α_s^5 contribution, in the \overline{MS} scheme, has been recently computed in [18]), the scale dependence of the light-quark masses can be expressed as:

$$m_q(\mu) = \widehat{m}_q R(\alpha_s). \quad (\text{D.21})$$

Here, the μ -independent parameter \widehat{m}_q is the so called renormalization invariant mass, and

$$R(\alpha_s) = \left(\frac{\beta_0}{2} \frac{\alpha_s}{\pi} \right)^{2\gamma_0/\beta_0} \left\{ 1 + \left(2\frac{\gamma_1}{\beta_0} - \frac{\beta_1 \gamma_0}{\beta_0^2} \right) \frac{\alpha_s}{\pi} + \frac{1}{2} \left[\left(2\frac{\gamma_1}{\beta_0} - \frac{\beta_1 \gamma_0}{\beta_0^2} \right)^2 + 2\frac{\gamma_2}{\beta_0} - \frac{\beta_1 \gamma_1}{\beta_0^2} - \frac{\beta_2 \gamma_0}{16\beta_0^2} + \frac{\beta_1^2 \gamma_0}{2\beta_0^3} \right] \left(\frac{\alpha_s}{\pi} \right)^2 + \mathcal{O}(\alpha_s^3) \right\}. \quad (\text{D.22})$$

Table D-1. Recent QCD sum rule determinations of the combination $\overline{m}_u + \overline{m}_d$, in the \overline{MS} scheme at the scale $\mu = 1$ GeV.

$\overline{m}_u + \overline{m}_d$ (MeV)	Ref.	method
15.2 ± 2.0	[21]	FESR
12.0 ± 2.5	[22]	Laplace and FESR

Predictions for the scale-independent ratios between the light u -, d -, and s -quark masses are obtained at the next-to-leading order in chiral perturbation theory, from the measured masses of pseudoscalar mesons [19, 20]. The results are [20]:

$$\frac{m_s}{m_d} = 18.9 \pm 0.8 \quad , \quad \frac{m_u}{m_d} = 0.553 \pm 0.043 \quad , \quad \frac{m_s}{\frac{1}{2}(m_u + m_d)} = 24.4 \pm 1.5 \quad . \quad (\text{D.23})$$

D.1.1 Non-Strange-Quark Masses: $m_u + m_d$

Recent QCD sum rule determinations of the combination $\overline{m}_u + \overline{m}_d$, in the \overline{MS} scheme at the scale $\mu = 1$ GeV, are reported in Table D-1, where the method adopted in each determination is also mentioned. Individual values of \overline{m}_u and \overline{m}_d can be obtained using Table D-1 and the ratios (D.23).

In [21], finite energy sum rules are applied to the pseudoscalar meson channel, *i.e.*, to the correlator of the non-strange axial current divergence $\partial_\mu(\overline{u}\gamma^\mu\gamma_5 d)$, proportional to $\overline{m}_u + \overline{m}_d$. The QCD contribution includes two-loop corrections in the perturbative expression and up to $D = 6$ nonperturbative condensates. The hadronic spectral function is expressed in terms of the pion pole and of higher resonances and is constrained to satisfy the behavior predicted by chiral perturbation theory at the (3π) threshold. In [22], the 3-loop order is included in the perturbative part, and an improved parameterization of the hadronic spectral function is used.

The results collected in Table D-1 can be conservatively summarized in the value

$$(\overline{m}_u + \overline{m}_d)(1 \text{ GeV}) = 13.4 \pm 3.8 \text{ MeV} \quad . \quad (\text{D.24})$$

Other QCD sum rule calculations of m_u and m_d can be found in [23] and references therein.

Table D-2. The most recent QCD sum rule determinations of the strange-quark mass \overline{m}_s , in the \overline{MS} scheme at the scale $\mu = 1 \text{ GeV}$.

\overline{m}_s (MeV)	Ref.	method
189 ± 32	[25]	Laplace
203.5 ± 20	[26]	Laplace
140 ± 20	[27]	Laplace
189 ± 28	[21]	FESR
146 ± 32	[22]	Laplace, FESR

D.1.2 Strange-Quark Mass: m_s

The most recent QCD sum rule determinations of the strange-quark mass \overline{m}_s , in the \overline{MS} scheme at the scale $\mu = 1 \text{ GeV}$, are collected in Table D-2 (reference to the previous literature can be found in [24]).

The determinations in [25, 26, 27] are the results from Laplace QCD sum rules applied to the scalar channel, *i.e.*, to the correlator of the strangeness changing vector current divergence, which is proportional to $m_s - m_u$. In [25], the correlator of the strangeness changing axial current divergences (proportional to $m_s + m_u$) was also considered, but in this case the data needed to reconstruct the hadronic spectral function, in particular the information on higher ($K\pi\pi$) resonances, are more uncertain than in the scalar channel.

In [25], the calculation of the perturbative contribution to the sum rule is performed including $\mathcal{O}(\alpha_s^2)$ corrections, whereas in [26, 27] the complete $\mathcal{O}(\alpha_s^3)$ expression is considered, including the α_s^4 corrections to the β function and to the anomalous dimension of the quark mass [17, 18]. The QCD nonperturbative part of the OPE includes condensates up to dimension 6. Moreover, in [25, 26] the hadronic spectral function is reconstructed by assuming the dominance of the scalar $|S| = 1$, $K_0^*(1430)$, and $K_0^*(1950)$ ($K\pi$) resonances and is normalized at the ($K\pi$) threshold as dictated by chiral perturbation theory. In [27], the hadronic spectral function is reconstructed by using an Omnés representation and the complete available information on the ($K\pi$) scalar system, including the measured $I = 1/2$ ($K\pi$) phase shift. The resulting spectral function is also found to satisfy numerically the chiral perturbation theory condition at threshold.

In each determination, the quoted uncertainty accounts for the dependence on $\Lambda_{\overline{MS}}^{(3)} = 280 - 480 \text{ MeV}$, and the variation of the parameters of the QCD sum rule (Borel variable σ and continuum threshold s_0) in the “duality” range. Therefore, the significant difference between [27] and [25, 26] mainly reflects the systematic uncertainty related to the different procedures to input the available

Table D-3. Two recent determinations of the pole mass M_c .

M_c (GeV)	Ref.	method
1.46 ± 0.05	[30]	Laplace
1.41 ± 0.03	[31]	Laplace, Hilbert moments

experimental information on the scalar $K\pi$ channel in the parameterization of the hadronic spectral function.

The determinations [21, 22] quoted in Table D-2 are obtained from the QCD sum rule calculations of the up- and down-quark masses reported in Table D-1, using the chiral perturbation theory ratios (D.23). The results collected in Table D-2 can be conservatively summarized by the value

$$\bar{m}_s(1 \text{ GeV}) = 172 \pm 52 \text{ MeV} . \quad (\text{D.25})$$

D.1.3 Charm-Quark Mass: M_c

The starting object is the two-point correlator of the charm vector current: $V_\mu = \bar{c}\gamma_\mu c$. The hadronic spectral function makes use of experimental data on the e^+e^- cross-section into $\bar{c}c$, in particular of the precise information on the charmonium vector states. The perturbative QCD part of the sum rule is determined at the two-loop accuracy, whereas the nonperturbative contribution mainly depends on the gluon condensate $\langle\alpha_s G^2\rangle$, which is independently determined. Two recent determinations of the pole mass M_c are reported in Table D-3 (for previous determinations see [28]). The two-loop relation between the (perturbatively renormalized) pole mass and the \overline{MS} running mass is given by:

$$M_Q = \bar{m}_Q(M_Q^2) \left\{ 1 + \frac{4}{3} \left(\frac{\alpha_s(M_Q^2)}{\pi} \right) + K_Q \left(\frac{\alpha_s(M_Q^2)}{\pi} \right)^2 \right\} \quad (\text{D.26})$$

with $K_c = 13.3$, $K_b = 12.4$ [29].

Reference [30] carries out the sum rule analysis directly in terms of the pole mass, while Ref. [31] determines the running quark mass, which is then related to the pole mass through Eq. (D.26).

In both Refs. [30] and [31] the infinite heavy-quark mass limit (nonrelativistic limit) of the sum rules is also studied (without resummation of the Coulomb pole); the results indicate reasonably small $\frac{1}{M_c}$ corrections, of the order of 15 – 20%, so that higher order terms are not expected to change the pole mass significantly.

Table D-4. A compilation of the four most recent QCD sum rule results for the beauty-quark pole mass M_b .

M_b (GeV)	Ref.	method
4.72 ± 0.05	[33]	Laplace
4.62 ± 0.02	[31]	Laplace, Hilbert moments
4.827 ± 0.007	[34]	Hilbert moments
4.60 ± 0.02	[35]	Hilbert moments

As a result, we quote the value

$$M_c = 1.45 \pm 0.10 \text{ GeV} . \quad (\text{D.27})$$

D.1.4 Beauty-Quark Mass: M_b

In Table D-4 we present a compilation of the four most recent QCD sum rule results for the beauty-quark pole mass M_b . Previous determinations can be found in [32].

In this case, the relevant two-point correlator involves the beauty vector current: $V_\mu = \bar{b}\gamma_\mu b$. The hadronic contribution to the spectral function is obtained by summing over the first six known $\Upsilon(nS)$ resonances. As for the “theoretical” side of the sum rules and the OPE, the perturbative contribution is largely dominant over the condensate terms. Therefore the α_s corrections can play a substantial role in the determination of M_b . In the determination [35] the three-loop, $\mathcal{O}(\alpha_s^2)$, contributions are included in the sum rule, which is an improvement on the other calculations quoted in Table D-4, and the Coulomb pole resummation is performed. In Ref. [34] a nonrelativistic heavy-quark expansion is made, and the Coulomb pole resummation is also performed.¹

The determinations in Table D-4 can be conservatively averaged in the result

$$M_b = 4.71 \pm 0.13 \text{ GeV} \quad (\text{D.28})$$

where the error essentially accounts for the difference between the determination in [34] and the results in [33, 31, 35].

¹There is an infrared ambiguity, called the renormalon ambiguity, which potentially affects heavy-quark pole masses (both charm and beauty) [36, 37]; the order of magnitude of the uncertainty from this effect value can be estimated to be $\mathcal{O}(100 \text{ MeV})$.

D.2 Leptonic Constants of Pseudoscalar Heavy Mesons

The pseudoscalar meson leptonic decay constant f_P is defined as:

$$\langle 0 | J_\mu^A | P(p) \rangle = i f_P p_\mu \quad (\text{D.29})$$

where J_μ^A is the relevant axial-vector current and the normalization is such that $f_\pi = 132$ MeV.

For mesons composed of a heavy quark Q and a light antiquark \bar{q} , HQET predicts an expansion in the inverse powers (*modulo* logs) of the heavy-quark mass $m_Q \gg \Lambda_{QCD}$ of the following form ([16] and references therein):

$$f_P \sqrt{m_P} = \hat{C}(M_Q) F_{ren} \left[1 + \frac{A}{M_Q} + \dots \right], \quad (\text{D.30})$$

where F_{ren} is a renormalized, universal nonperturbative constant, independent of the heavy-quark mass, and $\hat{C}(M_Q)$ is a perturbative QCD coefficient. The power terms represent the corrections to the $M_Q \rightarrow \infty$ result, due to heavy flavor- and spin-symmetry breaking, and are related to matrix elements of higher dimension HQET operators.

In Table D-5 we list the most recent QCD sum rule determinations of f_{D_d} and f_{B_d} , for values of the heavy-quark masses compatible with the figures reported in the previous section. In these calculations, the light-quark masses m_u and m_d are usually neglected, as their effect would be irrelevant in comparison to the expected overall accuracy of the method. Previous results can be found in Ref. [38].

The relevant two-point correlators involve the heavy-light pseudoscalar density $J = \bar{q} i \gamma_5 Q$. The determinations [39] result from QCD sum rules with finite-quark masses M_c and M_b , with values determined from charmonium and bottomonium as previously discussed and where both Hilbert moments and Laplace sum rule techniques have been employed. On the QCD side, the perturbative contributions are evaluated up to two-loop accuracy, and nonperturbative condensates up to $D = 6$ have been included in the OPE. The hadronic spectral functions are parameterized in terms of the pseudoscalar meson pole, proportional to f_P^2 , plus a continuum modeled by perturbative QCD. Reproducing the experimental values of the B - and D -meson masses is used as a condition to determine the “duality windows” in which the QCD sum rules for the leptonic constants should work reliably. The reported uncertainties are those characteristic of the optimal analysis of the sum rules, as well as the range of input quark masses. Indeed, the determination of f_B turns out to be rather sensitive to the value of the beauty-quark mass, and in particular the largest values of f_B are obtained in correspondence to the smaller values of M_b . Such heavy-quark mass effect is less significant in the determination of f_D . An additional potential uncertainty is represented by the choice of the argument of α_s because scale-dependence is still significant at the presently available order of perturbative calculation.

Table D-5.

f_D (MeV)	f_B (MeV)	Ref.	method
188 ± 48	160 ± 25	[39]	Hilbert moments
172 ± 20	168 ± 18	[39]	Laplace
	169 ± 30	[40]	Laplace (HQET)
170 ± 30 [41]	180 ± 40	[16]	Laplace (HQET)

Table D-6.

f_{D_s}/f_D	f_{B_s}/f_B	Ref.	method
1.21 ± 0.06	1.22 ± 0.02	[39]	Laplace and moments
	1.09 ± 0.03	[42]	Laplace
1.15 ± 0.04	1.16 ± 0.04	[43]	Laplace
$1.17 \pm 0.03 \pm 0.03$	$1.20 \pm 0.04 \pm 0.03$	[44]	Laplace

The determinations of f_B in Refs. [40, 16] follow from Laplace QCD sum rules, directly formulated in HQET. In this framework, both F_{ren} and the coefficient of the first power correction A in (D.30) have been determined by QCD sum rules for the relevant operator matrix elements, with two-loop perturbative parts and operators up to $D = 5$ in the OPE. The uncertainty reported in Table D-5 follows from QCD sum rule uncertainties on the HQET parameters quoted in [40, 16] and the chosen ranges of heavy-quark masses. The contribution of the power corrections turns out to be non-negligible for f_B and quite large for f_D . In addition, the leading order α_s contributions to the f_P sum rule are significant.

Our conservative averages for the results in Table D-5 are

$$f_D = 188 \pm 48 \text{ MeV} \quad ; \quad f_B = 178 \pm 42 \text{ MeV} . \quad (\text{D.31})$$

The same method allows a determination of the light SU(3)-flavor breaking ratios f_{D_s}/f_D and f_{B_s}/f_B by including corrections of the order m_s in the QCD side of the sum rule. A compilation of the most recent determinations of these quantities is presented in Table D-6.

Our conservative averages for the results in Table D-6 are

$$f_{D_s}/f_D = 1.19 \pm 0.08 \quad ; \quad f_{B_s}/f_B = 1.16 \pm 0.09 . \quad (\text{D.32})$$

The experimental determination of f_{D_s} is $f_{D_s} = 241 \pm 21 \pm 30$ MeV [45], whereas only an upper limit exists for f_D : $f_D < 290$ MeV at 90% CL [46].

D.3 B_{B_d} and B_K

The parameters B_{B_d} and B_K are defined by the matrix elements

$$\langle \bar{B}_d^0 | (\bar{b}\gamma^\mu(1 - \gamma_5)d)(\bar{b}\gamma_\mu(1 - \gamma_5)d) | B_d^0 \rangle = 2(1 + \frac{1}{N_c})(f_B m_B)^2 B_{B_d}(\mu) \quad (\text{D.33})$$

(and similarly for the Kaon system), and represent the deviation from the vacuum saturation expression of the $B - \bar{B}$ and $K^0 - \bar{K}^0$ mixing matrix elements. By definition, such parameters are scale-dependent. Their leading order dependence on the renormalization scale is given by:

$$B_{B_d}(\mu) = \hat{B}_{B_d}(\alpha_s(\mu))^{6/23}; \quad B_K(\mu) = \hat{B}_K(\alpha_s(\mu))^{2/9}, \quad (\text{D.34})$$

where \hat{B} is a renormalization invariant quantity, and the different powers of $\alpha_s(\mu)$ are due to the different number of active quark flavors to be considered for the B and K system.

In [9, 47, 48] the parameter \hat{B}_K is derived from the analysis of the two-point correlator of the $\Delta S = 2$ four-quark operator: $O_{\Delta S=2} = (\bar{s}\gamma^\mu(1 - \gamma_5)d)(\bar{s}\gamma_\mu(1 - \gamma_5)d)$. In this approach, the B_K parameter is determined at the crossing-related unphysical point $t = 4m_K^2$, where the hadronic spectral function takes contribution from the strangeness two KK intermediate state. Then, the result must be extrapolated to the point $t = 0$, pertinent to the matrix element analogous to (D.33).

The approach followed in [49] is the calculation of the three-point function of $O_{\Delta S=2}$ and the currents interpolating K^0 and \bar{K}^0 . In this case, there is an ambiguity related to the identification of the convenient kinematical variables to be used in the double dispersion relation, and to the identification of the nonfactorizable term [49].

Therefore, a systematic uncertainty is connected to the choice of the type of QCD sum rule. Both approaches also suffer from systematic uncertainties due to the lack of a complete calculation of the perturbative α_s correction, so that there is residual un-physical dependence on the choice of μ .

The most recent determination of \hat{B}_K from the two-point function is: $\hat{B}_K = 0.55 \pm 0.09$ [48], while three-point function sum rules give: $\hat{B}_K = 0.4 - 0.9$ [49]. This situation can be summarized by the conservative value

$$\hat{B}_K = 0.65 \pm 0.25. \quad (\text{D.35})$$

In [50] the parameter \hat{B}_{B_d} has been determined using a sum rule analysis of the two-point correlator of the $O_{\Delta B=2}$ operator in (D.34), with the result:

$$\hat{B}_{B_d} = 1.00 \pm 0.15. \quad (\text{D.36})$$

This result suggests that the violation of vacuum saturation approximation in the B channel does not exceed 15%. Results compatible with (D.36) were found in earlier applications of three-point sum rules [51].

D.4 Heavy-to-Light Decay Form Factors from Light-Cone Sum Rules

In exclusive decays of B mesons involving only light quarks in the final state there is a large region of the allowed phase space for which the decay products have large energy: up to $E \sim m_b/2 \sim 2.5$ GeV at maximum recoil in the B rest frame. This potentially upsets the Wilson operator product expansion since contributions of operators of high dimension to the sum rules are accompanied by powers of Em_b/M^2 , where the Borel parameter $M^2 \sim m_b\Lambda$ and $\Lambda \sim 1$ GeV. This problem is exactly analogous to the breakdown of the QCD sum rule calculations of the pion form factor at large momentum transfers [10, 11]. A detailed discussion can be found in [52]. A radical remedy is provided by the light-cone sum rule approach [13, 14, 15] in which the operator product expansion is organized according to the twist of the operators rather than their dimension. This allows the resummation, in a certain approximation, of an infinite series of contributions $\sim (Em_b/M^2)^k$, $k = 1, 2, \dots$. The resummation uses results on the asymptotic behavior of exclusive processes at large momentum transfer [53]. In cases where the maximum energy is, however, not very large, it is not clear a priori whether this deficiency of the standard approach is numerically relevant. For D decays, both methods are equally applicable and yield comparable results [54, 55]. For B decays, one has to examine case by case.

The t -dependence of all the numerous form factors in question cannot be given here. In a few cases, however, we provide a simple parametrization of the t -dependence using the function

$$F(t) = \frac{F(0)}{1 + a_F t/m_B^2 + b_F t^2/m_B^4} \quad (\text{D.37})$$

which has been found to reproduce the sum rule results to an accuracy better than 0.5% over the entire range of t . The reader is invited to consult the original papers for details and precise definitions.

D.4.1 Semileptonic Decays

Semileptonic decays have historically attracted most of the attention, especially the simplest of them, $B \rightarrow \pi l \bar{\nu}_l$ [56, 57, 58, 59, 60, 61, 62, 63, 64]. The hadronic matrix element is parametrized by two form factors

$$\langle \pi | \bar{u} \gamma_\mu b | B \rangle = f_+(t)(p_B + p_\pi)_\mu + f_-(t)(p_B - p_\pi)_\mu, \quad (\text{D.38})$$

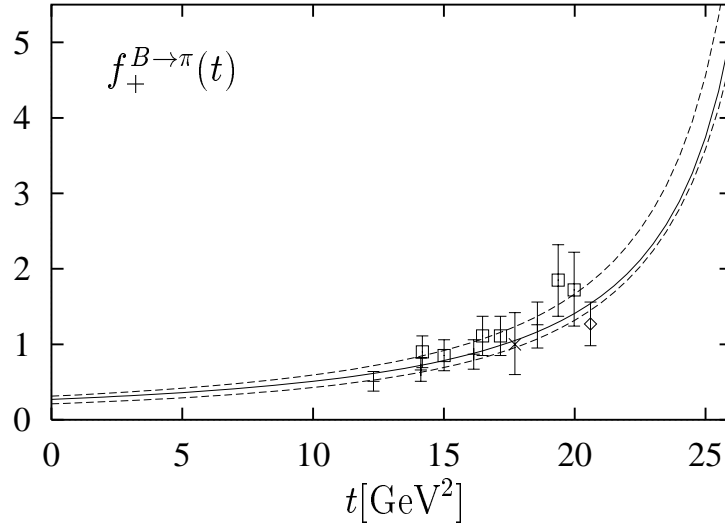


Figure D-1. The prediction [65] for the $B \rightarrow \pi$ form factor $f_+^{B \rightarrow \pi}$ from light-cone sum rules (solid) and the theoretical uncertainties (dashed), in comparison to lattice results [90].

where only $f_+(t)$ is important for $l = e, \mu$. Table D-7 gives the more recent and reliable predictions. The recently calculated $O(\alpha_s)$ correction [65, 66] to f_+ is taken into account. Results of the traditional (here called “three-point”) and light-cone sum rules appear to be in good agreement. Both methods predict a t -dependence of the form factor f_+ which is comparable to vector-dominance. The prediction of the light-cone sum rule [65] is shown in Fig. D-1. The second form factor f_- is usually combined with f_+ in the scalar form factor $f_0(t) = f_+(t) + t/(m_B^2 - m_\pi^2)f_-(t)$. The latter form factor was also calculated using three-point [67] and light-cone [64] sum rules. It can be measured in $B \rightarrow \pi \tau \bar{\nu}_\tau$.

Semileptonic $B \rightarrow \rho e \bar{\nu}$ decays have been controversial for some time, with a considerable dispersion of results ([61] and references therein). There are four independent form factors

$$\begin{aligned} \langle \rho, \lambda | \bar{u} \gamma_\mu (1 - \gamma_5) b | B \rangle = & -i(m_B + m_\rho) A_1(t) e_\mu^{*(\lambda)} + \frac{i A_2(t)}{m_B + m_\rho} (e^{*(\lambda)} p_B) (p_B + p_\rho)_\mu \\ & + \frac{i A_3(t)}{m_B + m_\rho} (e^{*(\lambda)} p_B) (p_B - p_\rho)_\mu + \frac{2V(t)}{m_B + m_\rho} \epsilon_\mu^{\alpha\beta\gamma} e_\alpha^{*(\lambda)} p_{B\beta} p_{\rho\gamma} \end{aligned} \quad (\text{D.39})$$

of which only $V(t)$, $A_1(t)$ and $A_2(t)$ contribute to the decay rate. These form factors were recently reexamined in [52] (see Fig. D-2) with the conclusion that the existing three-point sum rules are not reliable and the light-cone approach is more appropriate in this case. It is found that all three form factors rise with t , contrary to some of the earlier predictions. The results are summarized in Tables D-7 and D-8.

Table D-7. Form factors from light-cone sum rules with functional t dependence fitted to Eq. (D.37). The first (second) value of $f_+^{B \rightarrow \pi}$ is obtained with the twist 2 wave function from [14] (asymptotic twist 2 wave function) of the pion.

FF	$F(0)$	a_F	b_F
$f_+^{B \rightarrow \pi}$ [65]	0.27 ± 0.05	-1.50	0.52
	0.25 ± 0.05	-1.65	0.67
$f_+^{B \rightarrow \pi}$ [66]	0.30 ± 0.03	-1.32	0.21
	0.25 ± 0.03	-1.72	0.72
$f_0^{B \rightarrow \pi}$ [64]	0.30 ± 0.05	-0.84	0.03
$f_+^{B \rightarrow K}$ [60]	0.33 ± 0.05	-1.14	0.05
$F_1^{B \rightarrow K^*}$ [74]	0.32 ± 0.05	-	-
$A_1^{B \rightarrow \rho}$ [52]	0.27 ± 0.05	-0.42	-0.29
$A_2^{B \rightarrow \rho}$ [52]	0.28 ± 0.05	-1.34	0.38
$V^{B \rightarrow \rho}$ [52]	0.35 ± 0.07	-1.51	0.47

Table D-8. Decay rates in units ps^{-1} . $\Gamma_L(\Gamma_T)$ denotes the decay rates into a longitudinally (transversely) polarized ρ . The widths for $B \rightarrow (K, K^*)\mu^+\mu^-$ do not include long-distance corrections.

channel	Γ	Γ_L/Γ	Γ_T/Γ
$B \rightarrow \pi e \bar{\nu}$ [65]	$ V_{ub} ^2 (7.5 \pm 2.5)$	-	-
$B \rightarrow \pi \tau \bar{\nu}$ [64]	$ V_{ub} ^2 (6.1 \pm 2.3)$	-	-
$B \rightarrow \rho e \bar{\nu}$ [52]	$ V_{ub} ^2 (13.5 \pm 4)$	0.34 ± 0.04	0.66 ± 0.04
$B \rightarrow K^* \gamma$ [74]	$3.0 \cdot 10^{-5}$	-	-
$B \rightarrow K \mu^+ \mu^-$ [77]	$1.7 \cdot 10^{-7}$	-	-
$B \rightarrow K^* \mu^+ \mu^-$ [76]	$7.8 \cdot 10^{-7}$	-	-

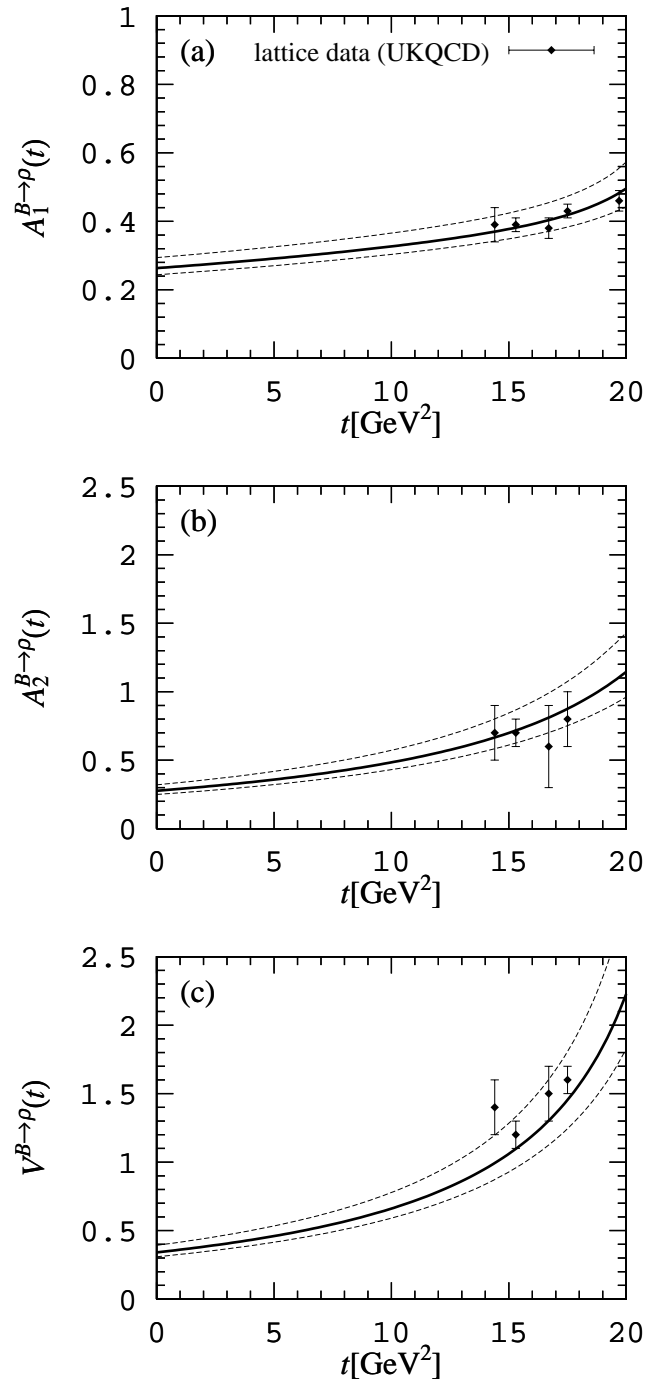


Figure D-2. The predictions [52] for the $B \rightarrow \rho$ form factors from light-cone sum rules (solid) and the theoretical uncertainties (dashed), in comparison to lattice results [90].

D.4.2 Rare Decays

There exists a rich variety of rare radiative decays induced by flavor-changing neutral currents, of which $B \rightarrow K^* \gamma$ has received the most attention [68, 69, 70, 71, 72, 73, 74]. It is determined by a single form factor, defined by

$$\langle K^*, \lambda | \bar{s} \sigma_{\mu\nu} q^\nu b | B \rangle = 2i \epsilon_{\mu\nu\rho\sigma} e^{*(\lambda)\nu} p_B^\rho p_{K^*}^\sigma F_1(t). \quad (\text{D.40})$$

Calculations exist both within the three-point and light-cone sum rule framework, although one may argue [52, 74] that the light-cone approach is advantageous. It has to be noted that the discrepancy between the approaches is somewhat masked by different groups using different parameters. Other decays studied are $B_s \rightarrow K^* \gamma$, $B_u \rightarrow \rho(\omega) \gamma$ and $B_s \rightarrow \phi \gamma$ [74]. In addition, the $B \rightarrow K^* \ell^+ \ell^-$, $B \rightarrow K \ell^+ \ell^-$ decay form factors have been calculated using the three-point sum rules in [75] and very recently using the light-cone approach in [76, 77]. The relevant form factors are too numerous to be presented here. The results are summarized in Table D-8. We note that the results of [74, 76] need to be updated using the revised light-cone distribution amplitudes of the vector meson [78] and surface terms for the continuum subtraction [52]. To improve [76], one should also take into account the SU(3)-violating asymmetry in the K -meson light-cone distributions. However these corrections are not expected to cause significant numerical changes.

The light-cone sum rule method can also be used to estimate the long-distance contributions of four-fermion operators to the decay $B^+ \rightarrow \rho^+ \gamma$ [79, 80] which appear to be of order 20% of the short-distance contribution to the decay rate. The same approach was applied to the decay $B \rightarrow \mu \bar{\nu}_\mu \gamma$ [79, 81]. The ratio of the decay widths with and without a photon is estimated to be $R_B^\mu \sim 20$ [79]. Recently, an estimate of the long-distance effect in the decay $B \rightarrow K^* \gamma$ was obtained [82] using the three-point sum rules. The overall correction to the form factor (D.40) is found to be small, not more than about 5%.

D.4.3 Strong Coupling Constants

The strong couplings of B mesons to pions have been studied in much detail, most of all, the $B^* B \pi$ coupling:

$$\langle B^{*+} \pi^- | B^0 \rangle = -g_{B^* B \pi} p_\mu^\pi \epsilon(B^*)^\mu. \quad (\text{D.41})$$

In order to estimate this matrix element from the sum rules based on the Wilson operator expansion, one needs to apply the soft-pion approximation [83, 84, 85, 86] which introduces additional uncertainties. A more advanced method is to use the light-cone expansion [63] which allows calculation of the strong coupling to the pion within the same framework and with the same accuracy as the corresponding $B \rightarrow \pi$ form factors. The light-cone sum rule [63] yields $g_{B^* B \pi} = 29 \pm 6$ where

the theoretical uncertainty is a rough estimate. This value of the $B^* B\pi$ coupling is then used to extrapolate the $B \rightarrow \pi$ form factor f_+ by the B^* -pole approximation in the region of large t , near the kinematical threshold. In the same framework, the strong coupling constants of the scalar and axial B mesons with the pion have been estimated yielding the following predictions for the observable strong decay widths [87]: $\Gamma(B(0^{++}) \rightarrow B\pi) \simeq \Gamma(B(1^{++}) \rightarrow B^*\pi) \simeq 360$ MeV. An analogous method was used in [88] to obtain the $BB^*\rho$ coupling.

D.4.4 The Heavy-Quark Limit

The behavior of the heavy-to-light decay form factors in the heavy-quark limit has been the subject of numerous discussions. One should distinguish between different regions of the momentum transfer. At small recoil $m_b^2 - t \sim O(m_b)$ the quark-mass dependence of form factors is given by the heavy-quark effective theory (HQET) and one can check that both three-point and light-cone sum rules obey these scaling laws explicitly. At large recoil, $m_b^2 - t \sim O(m_b^2)$, HQET is not applicable and the b -quark mass dependence has to be studied using different methods [53]. This analysis indicates that heavy-to-light form factors generically scale as $\sim 1/m_b^{3/2}$ at maximum recoil. The form factors calculated by the light-cone sum rules have the expected behavior [52, 15, 64, 74], while for usual three-point sum rules the heavy-quark limit at maximum recoil does not exist. For realistic values of the b -quark mass these scaling laws have to be applied with great caution and large corrections are expected, see [74] for $B \rightarrow K^*\gamma$, [63] for the $B^*B\pi$ coupling and [52] for $B \rightarrow \rho e\bar{\nu}$ decays.

D.4.5 Theoretical Accuracy and Possible Developments

The analysis of theoretical uncertainties in the sum rule methods is a difficult issue in general. On the average, present calculations of form factors have roughly 15–30% accuracy, which translates to an uncertainty of order 30–60% in the decay rates. As far as the sum rule parameters are concerned, the main sources of errors are the high sensitivity to the b -quark mass and the uncertainty in f_B . A typical strategy is to consider ratios of sum rules, in which the dependence on m_b and f_B is reduced (see, *e.g.*, [60, 74]). From the theoretical side, significant uncertainties are due to unknown radiative corrections. Taking them into account is relatively straightforward, but laborious. First results on the radiative corrections for $B \rightarrow \pi$ have already been obtained [65, 66], the corresponding results for $B \rightarrow \rho$ form factors are expected to appear soon [89].

Higher twist contributions, another source of uncertainty, so far were only studied for $B \rightarrow \pi e\bar{\nu}$ [63]. Their estimate for other decays requires, as a first step, a systematic study of light-cone distributions of vector mesons (and photons) beyond leading twist.

We expect that by working out radiative and higher-twist corrections to the sum rules, one can increase the accuracy and reliability of predictions considerably. With some better knowledge of m_b and f_B , the errors in form factors can potentially be reduced to $\sim 10\%$ (20% in the decay rates). Higher accuracy than this does not appear feasible for the sum rule method.

References

- [1] L. J. Reinders, H. Rubinstein and S. Yazaki, *Phys. Rep.* **127**, 1 (1985);
S. Narison, *QCD Spectral Sum Rules*, World Scientific (1989);
M. A. Shifman (*ed.*), *Vacuum Structure and QCD Sum Rules*, North Holland (1992).
- [2] M. A. Shifman, A. I. Vainshtein and V. I. Zakharov, *Nucl. Phys.* **B147**, 385 (1979).
- [3] J. J. Sakurai, *Phys. Lett. B* **46**, 207 (1973);
K. Ishikawa and J. J. Sakurai, *Z. Phys. C* **1**, 117 (1979);
J. S. Bell and R. A. Bertlmann, *Z. Phys. C* **4**, 11 (1980).
- [4] Y. Chung *et al.*, *Z. Phys. C* **25**, 151 (1984);
H. G. Dosch, M. Jamin and S. Narison, *Phys. Lett. B* **220**, 251 (1989).
- [5] R. A. Bertlmann *et al.*, *Z. Phys. C* **39**, 231 (1988). Here, also the determinations of the D=6 four-fermion condensates, $\langle \text{vac} | \alpha_s \bar{q} \Gamma q \bar{q} \Gamma q | \text{vac} \rangle$ with Γ any Dirac matrix, are critically reviewed.
- [6] V. M. Belyaev and B.L. Joffe, *JETP* **57**, 716 (1983);
A. A. Ovchinnikov and A. A. Pivovarov, *Sov. J. Nucl. Phys.* **48**, 721 (1988).
The analysis of the $SU(3)$ corrections to this quantity can be found in M. Beneke and H. G. Dosch, *Phys. Lett. B* **284**, 116 (1992).
- [7] R. A. Bertlmann, G. Launer and E. de Rafael, *Nucl. Phys.* **B250**, 61 (1985).
- [8] A. A. Logunov, L. D. Soloviev and A. N. Tavkhelidze, *Phys. Lett. B* **24**, 181 (1967);
K. G. Chetyrkin and N. V. Krasnikov, *Nucl. Phys.* **B119**, 174 (1977);
K. G. Chetyrkin, N. V. Krasnikov and A. N. Tavkhelidze, *Phys. Lett. B* **76**, 83 (1978).
- [9] A. Pich and E. de Rafael, *Phys. Lett. B* **158**, 477 (1985).
- [10] B. L. Ioffe and A.V. Smilga, *Phys. Lett. B* **114**, 353 (1982);
Nucl. Phys. **B216**, 373 (1983).
- [11] V. A. Nesterenko and A. V. Radyushkin, *Phys. Lett. B* **115**, 410 (1982).
- [12] N.S. Craigie and J. Stern, *Nucl. Phys.* **B305**, 109 (1983).
- [13] I. Balitsky, V. M. Braun and A. V. Kolesnichenko, *Nucl. Phys.* **B312**, 509 (1989).
- [14] V. M. Braun and I. E. Filyanov, *Z. Phys. C* **44**, 157 (1989).
- [15] V. L. Chernyak and I. R. Zhitnitsky, *Nucl. Phys.* **B345**, 137 (1990).

- [16] M. Neubert, *Phys. Rep.* **245**, 259 (1994).
- [17] K. G. Chetyrkin, *Phys. Lett. B* **404**, 161 (1997);
J.A.M. Vermaseren, S. A. Larin and T. van Ritbergen, *Phys. Lett.* **B405**, 327 (1997).
- [18] T. van Ritbergen, J.A.M. Vermaseren, S. A. Larin, *Phys. Lett. B* **400**, 379 (1997).
- [19] J. Gasser and H. Leutwyler, *Nucl. Phys.* **B250**, 465 (1985)
H. Leutwyler, *Nucl. Phys.* **B337**, 108 (1990);
J. Donoghue, B. Holstein and D. Wyler, *Phys. Rev. Lett.* **69**, 3444 (1992).
- [20] H. Leutwyler, *Phys. Lett. B* **378**, 313 (1996).
- [21] C. A. Dominguez and E. de Rafael, *Ann. Phys.* **174**, 372 (1987).
- [22] J. Bijnens, J. Prades and E. de Rafael, *Phys. Lett. B* **348**, 226 (1995).
- [23] V. L. Eletsky and B.L. Ioffe, *Phys. Rev. D* **48**, 1441 (1993);
C. Adami, E.G. Drukarev and B.L. Ioffe, *Phys. Rev. D* **48**, 2304 (1993);
X. Jin, M. Nielsen and J. Pasupathy, *Phys. Rev. D* **51**, 3688 (1993).
- [24] S. Narison *et al.*, *Nucl. Phys.* **B212**, 365 (1983);
S. C. Generalis, *J. Phys.* **G16** L 117 (1990);
C. A. Dominguez, C. van Gend and N. Paver, *Phys. Lett. B* **241**, 241 (1991);
K. G. Chetyrkin *et al.*, *Phys. Rev. D* **51**, 5090 (1995);
S. Narison, *Phys. Lett. B* **358**, 113 (1995).
- [25] M. Jamin and M. Münz, *Z. Phys.* **C66**, 633 (1995).
- [26] K. G. Chetyrkin, D. Pirjol and K. Schilcher, *Phys. Lett.* **B404**, 337 (1997).
- [27] P. Colangelo *et al.*, *Phys. Lett.* **B408**, 340 (1997).
- [28] V. A. Novikov *et al.*, *Phys. Rep.* **41**, 1 (1978);
J. S. Bell and R. A. Bertlmann, *Nucl. Phys.* **B187**, 285 (1981);
K. J. Miller and M. G. Olsson, *Phys. Rev. D* **25**, 1247 (1982);
S. Narison, *Phys. Lett. B* **197**, 405 (1987); *Phys. Lett.* **B216** 191 (1989).
- [29] N. Gray *et al.*, *Z. Phys. C* **48**, 673 (1990).
- [30] C. A. Dominguez, G.R. Gluckman and N. Paver, *Phys. Lett. B* **333**, 184 (1994).
- [31] S. Narison, *Phys. Lett. B* **341**, 73 (1994).
- [32] See Refs. [1]; M. B. Voloshin, *Sov. J. Nucl. Phys.* **29**, 703 (1979);
R. A. Bertlmann, *Nucl. Phys.* **B204**, 387 (1982);
M. B. Voloshin and Yu. M. Zaitsev, *Sov. Phys. Usp.* **30**, 553 (1987).

- [33] C. A. Dominguez and N. Paver, *Phys. Lett. B* **293**, 197 (1992).
- [34] M. A. Voloshin, *Int. J. Mod. Phys. A* **10**, 2865 (1995).
- [35] M. Jamin and A. Pich, *Nucl. Phys.* **B507**, 334 (1997).
- [36] I. I. Bigi *et al.*, *Phys. Rev. D* **50**, 2234 (1994).
- [37] M. Beneke and V. M. Braun, *Nucl. Phys.* **B426**, 301 (1994).
- [38] T. M. Aliev and V.L. Eletsky, *Sov. J. Nucl. Phys.* **38**, 936 (1983);
C. A. Dominguez and N. Paver, *Phys. Lett. B* **197**, 423 (1987); *Phys. Lett. B* **199**, 596(E) (1987);
S. Narison, *Phys. Lett. B* **198**, 104 (1987);
L. J. Reinders, *Phys. Rev. D* **38**, 947 (1988).
- [39] C. A. Dominguez, in *Proceedings of the Third Workshop on the Tau-Charm Factory*, Marbella, Spain, 1-6 June (1993), Ed. J. Kirkby and R. Kirkby, Editions Frontières, p. 357.
- [40] E. Bagan *et al.*, *Phys. Lett. B* **278**, 457 (1992);
P. Ball, *Nucl. Phys.* **B421**, 593 (1994).
- [41] M. Neubert, *Phys. Rev. D* **45**, 2451 (1992).
- [42] P. Blasi *et al.*, *Phys. Rev. D* **49**, 238 (1994).
- [43] S. Narison, *Phys. Lett. B* **322**, 247 (1994).
- [44] T. Huang and C. W. Luo, *Phys. Rev. D* **53**, 5042 (1996).
- [45] J. D. Richman, in *Proceedings of the 28th International Conference on High Energy Physics*, Warsaw, Poland, 25-31 July 1996, Eds. Z. Ajduk and A. K. Wroblewski, World Scientific, Singapore (1996), p. 193.
- [46] R. M. Barnett *et al.*, *Phys. Rev. D* **54**, 1 (1996).
- [47] J. Prades *et al.*, *Z. Phys. C* **51**, 287 (1991).
- [48] S. Narison, *Phys. Lett. B* **351**, 369 (1995).
- [49] K. G. Chetyrkin *et al.*, *Phys. Lett. B* **174**, 104 (1986);
R. Decker, *Nucl. Phys.* **B277**, 661 (1986);
L. J. Reinders and S. Yazaki, *Nucl. Phys.* **B288**, 789 (1987);
N. Bilic, C.A. Dominguez and B. Guberina, *Z. Phys. C* **39**, 351 (1988).
- [50] S. Narison and A. A. Pivovarov, *Phys. Lett. B* **327**, 341 (1994).

- [51] L. J. Reinders and S. Yazaki, *Phys. Lett. B* **212**, 245 (1988);
A. A. Ovchinnikov and A. A. Pivovarov, *Phys. Lett. B* **207**, 333 (1988).
- [52] P. Ball and V. M. Braun, *Phys. Rev. D* **55**, 5561 (1997).
- [53] V. L. Chernyak and A. R. Zhitnitsky, *JETP Lett.* **25**, 510 (1977); *Yad. Fiz.* **31**, 1053 (1980);
A. V. Efremov and A. V. Radyushkin, *Phys. Lett. B* **94**, 245 (1980); *Teor. Mat. Fiz.* **42**, 147 (1980);
G. P. Lepage and S. J. Brodsky, *Phys. Lett. B* **87**, 359 (1979); *Phys. Rev.* **D22**, 2157 (1980);
V. L. Chernyak, V.G. Serbo and A. R. Zhitnitsky, *JETP Lett.* **26**, 594 (1977); *Sov. J. Nucl. Phys.* **31**, 552 (1980).
- [54] T. M. Aliev, V. L. Eletskii and Ya. I. Kogan, *Sov. J. Nucl. Phys.* **40**, 527 (1984).
- [55] P. Ball, V. M. Braun and H. G. Dosch, *Phys. Rev. D* **44**, 3567 (1991).
- [56] C. A. Dominguez and N. Paver, *Z. Phys.* **C41**, 217 (1988).
- [57] A. A. Ovchinnikov, *Phys. Lett. B* **229**, 127 (1989).
- [58] P. Ball, V. M. Braun and H. G. Dosch, *Phys. Lett. B* **273**, 316 (1991).
- [59] S. Narison, *Phys. Lett. B* **283**, 384 (1992).
- [60] V. M. Belyaev, A. Khodjamirian and R. Rückl, *Z. Phys.* **C60**, 349 (1993).
- [61] P. Ball, *Phys. Rev. D* **48**, 3190 (1993).
- [62] N. Paver and Riazuddin, *Phys. Lett. B* **320**, 364 (1994).
- [63] V. M. Belyaev *et al.*, *Phys. Rev. D* **51**, 6177 (1995).
- [64] A. Khodjamirian and R. Rückl, in *Heavy Flavours II*, edited by A. J. Buras and M. Linder, World Scientific, Singapore (1998), p. 345;
A. Khodjamirian, R. Rückl and C. W. Winhart, *Phys. Rev. D* **58**, 054013 (1998) .
- [65] A. Khodjamirian *et al.*, *Phys. Lett. B* **410**, 275 (1997);
A. Khodjamirian, R. Rückl, S. Weinzierl, C. W. Winhart and O. Yakovlev, *paper in preparation*.
- [66] E. Bagan, P. Ball and V. M. Braun, *Phys. Lett.* **B417**, 154 (1998).
- [67] P. Colangelo and P. Santorelli, *Phys. Lett. B* **327**, 123 (1994).
- [68] C. A. Dominguez, N. Paver and Riazuddin, *Phys. Lett. B* **214**, 459 (1988).
- [69] T. M. Aliev, A. A. Ovchinnikov and V. A. Slobodenyuk, *Phys. Lett. B* **237**, 569 (1990).

- [70] N. Paver and Riazuddin, *Phys. Rev. D* **45**, 978 (1992).
- [71] P. Ball, Preprint TUM-T31-43/93 (1993), hep-ph/9308244 (unpublished).
- [72] P. Colangelo *et al.*, *Phys. Lett. B* **317**, 183 (1993).
- [73] S. Narison, *Phys. Lett. B* **329**, 354 (1994).
- [74] A. Ali, V.M. Braun and H. Simma, *Z. Phys.* **C63**, 437 (1994).
- [75] P. Colangelo *et al.*, *Phys. Rev. D* **53**, 3672 (1996).
- [76] T. M. Aliev, *et al.*, *Phys. Rev. D* **56**, 4260 (1997).
- [77] T. M. Aliev *et al.*, *Phys. Lett. B* **400**, 194 (1997).
- [78] P. Ball and V. M. Braun, *Phys. Rev. D* **54**, 2182 (1996).
- [79] A. Khodjamirian, G. Stoll and D. Wyler, *Phys. Lett. B* **358**, 129 (1995).
- [80] A. Ali and V. M. Braun, *Phys. Lett. B* **359**, 223 (1995).
- [81] G. Eilam, I. Halperin and R. R. Mendel, *Phys. Lett. B* **361**, 137 (1995).
- [82] A. Khodjamirian *et al.*, *Phys. Lett. B* **402**, 167 (1997).
- [83] V. L. Eletsky and Ya. I. Kogan, *Z. Phys.* **C28**, 155 (1985).
- [84] A. A. Ovchinnikov, *Sov. J. Nucl. Phys.* **50**, 519 (1989).
- [85] P. Colangelo *et al.*, *Phys. Lett. B* **339**, 151 (1994).
- [86] A.G. Grozin and O.I. Yakovlev, *Eur. Phys. Jour. C* **2**, 721 (1998).
- [87] P. Colangelo *et al.*, *Phys. Rev.* **D52**, 6422 (1995).
- [88] T. M. Aliev *et al.*, *Phys. Rev. D* **53**, 355 (1996).
- [89] P. Ball and V.M. Braun, hep-ph/9805422, to appear in *Phys. Rev. D*.
- [90] J. M. Flynn, in *Proceedings of the 28th International Conference on High-Energy Physics (ICHEP 96)*, Warsaw, Poland, ed. Z. Ajduk and A. K. Wroblewski, World Scientific, Singapore (1996), p. 335.